MINERALOGY AND GEOCHEMISTRY OF IRON-OXIDES IN THE OLYMPIC DAM IOCG-DEPOSIT AND ADJACENT PROSPECTS, SOUTH AUSTRALIA

Max Robert Verdugo Ihl

This thesis is submitted for the degree of Doctor of Philosophy

in the

School of Chemical Engineering and Advanced Materials,

Faculty of Engineering, Computer and Mathematical Sciences

at

The University of Adelaide

THE UNIVERSITY of ADELAIDE

April 2020

TABLE OF CONTENTS

ABSTRACT ..... **xi**

DECLARATION ..... **xv**

ACKNOWLEDGEMENTS ..... **xvii**

PREFACE ..... **xix**

CHAPTER 1: INTRODUCTION **1**

1.1 Research objectives and thesis structure 10

1.2 References 15

CHAPTER 2: TEXTURES AND U-W-SN-MO SIGNATURES IN HEMATITE FROM THE OLYMPIC DAM CU-U-AU-AG DEPOSIT, SOUTH AUSTRALIA: DEFINING THE ARCHETYPE FOR IOCG DEPOSITS **21**

Abstract 25

2.1 Introduction 25

2.2 Geological background 26

2.3 Sampling approach 27

2.4 Methodology 27

2.5 Petrography and trace element distribution in granitophile-rich hematite 28

2.5.1 Categories of granitophile-rich hematite 30

2.5.2 Zoned hematite – primary zonation patterns and their overprint 31

2.5.3 Grain-scale trace element distribution – LA-ICP-MS maps 33

2.5.3.1 Element maps for zoned hematite 34

2.5.3.2 Element maps for other categories of granitophile-rich hematite 35

2.6 Compositional data 35

2.6.1 Electron probe microanalysis 35

2.6.2 LA-ICP-MS trace element data 35

2.6.2.1 Granitophile elements: U(-Pb), W, Sn, Mo and Th 36

2.6.2.2 Rare earth elements and yttrium 37

2.6.2.3 Arsenic and antimony 38

2.6.2.4 Transition metals: Cr, Mn, Co, Ni, Cu and Zn 39
2.6.2.5 High field strength elements: Sc, Ti, V, Zr(-Hf) and Nb(-Ta) 40
2.7 Discussion 40
2.7.1 Incorporation of granitophile elements in hematite 40
2.7.2 REY and other trace element signatures in hematite – evolving fluids 42
2.7.3 Chemical oscillators and recycling trace elements during their overprint 43
2.7.4 Hematite from the Olympic Dam orebody – defining the archetype for IOCG deposits 45
2.8 Outlook and implications 46
2.9 Acknowledgements 46
2.10 References 46

CHAPTER 3: DEFINING EARLY STAGES OF IOCG SYSTEMS: EVIDENCE FROM IRON-OXIDES IN THE OUTER SHELL OF THE OLYMPIC DAM DEPOSIT, SOUTH AUSTRALIA 49

Abstract 53
3.1 Introduction 53
3.2 Geological background 54
3.3 Sampling and methodology 56
3.4 Results 57
3.4.1 Iron oxide distributions 57
3.4.2 Petrography 60
3.4.3 Mineralogy and trace elements distribution in iron oxides 61
3.4.3.1 Silician magnetite 61
3.4.3.2 Transition to (pseudo)mushketovite 63
3.4.3.3 Hematite 65
3.4.4 Trace element concentrations in iron oxides 66
3.4.4.1 HFSE and associated elements 68
3.4.4.2 Granitophile elements U-W-Sn-Mo 68
3.4.4.3 Other trace elements 68
3.4.4.4 Rare earth elements 68
3.5 Discussion 70
3.5.1 Mineralogy and signatures of early Fe-oxides: constraints on a granite-derive fluid 70
3.5.2 Geochemical modelling – conditions for early Fe-oxide formation 71

3.5.3 Proposed geological model for the IOCG system at Olympic Dam 71
3.6 Conclusions and implications 73
3.7 Acknowledgements 74
3.8 References 74

CHAPTER 4: COPPER-ARSENIC NANOPARTICLES IN HEMATITE: FINGERPRINTING FLUID-MINERAL INTERACTION 79

Abstract 83
4.1 Introduction 84
4.2 Samples and Methodology 85
4.3 Results 87
4.3.1 Nanoscale Characterisation of Cu-As Zoned and Weave-Twinned Hematite ... 87
4.3.2 High-Resolution HAADF STEM Imaging of Hematite 95
4.4 Discussion and Summary 97
4.4.1 Can Fluid Inclusions be Fingerprinted at the Nanoscale? 97
4.4.2 Trace Element Mobilisation during Fluid-Mineral Interaction: Trapping Metal Nanoparticles 98
4.5 Implications 100
4.6 Acknowledgements 101
4.7 References 101

CHAPTER 5: TRACE ELEMENT REMOBILISATION FROM W-SN-U-PB ZONED HEMATITE: NANOSCALE INSIGHTS INTO OPEN SYSTEM BEHAVIOUR OF A MINERAL GEOCHRONOMETER 105

Abstract 109
5.1 Introduction 109
5.2 Methodology 111
5.3 Results 112
5.3.1 Grain-scale characterisation: textures, FIB-sampling and trace element data for hematite 112
5.3.2 HAADF STEM imaging and trace element distributions at the nanoscale 112
5.3.3 Two-fold hematite superstructure with oxygen vacancies 115
5.4 Discussion 118
5.4.1 Tracing pseudomorphic replacement reactions from micro to nano scale 118
5.4.2 Trace element incorporation into and release from hematite 119

5.4.3 Trace-element mobility in a mineral geochronometer: implications for U-Pb geochronology 121
5.5 Implications 121
5.6 Conclusions 122
5.7 Acknowledgements 122
5.8 References 122

CHAPTER 6: NANOMINERALOGY OF HYDROTHERMAL MAGNETITE FROM ACROPOLIS, SOUTH AUSTRALIA: GENETIC IMPLICATIONS FOR IRON–OXIDE COPPER GOLD MINERALIZATION 125

Abstract 129
6.1 Introduction 130
6.2 Geological background 132
6.3 Methodology 134
6.4 Results 135
6.4.1 Sampling 135
6.4.2 Petrography and mineral chemistry 136
6.4.3 Minor and trace element signatures 140
6.4.4 Nanoscale magnetite characterization 142
6.4.5 High-resolution imaging 149
6.5 Discussion 157
6.5.1 Exsolution and order-disorder phenomena in spinels 157
6.5.2 Behavior of minor/trace elements in magnetite 158
6.5.3 Magnetite formation at Acropolis 159
6.6 Implications 161
6.7 Acknowledgements 164
6.8 References 165

CHAPTER 7: FERRO-TSCHERMAKITE WITH SHORT RANGE DISORDER IDENTIFIED IN SILICIAN MAGNETITE 171

Abstract 175
7.1 Introduction and Background 176
7.2 Methodology 179
7.3 Results and Discussion 180
7.4 Implications 185

7.5 Acknowledgements 186
7.6 References cited 186

CHAPTER 8: VAPOUR TRANSPORT OF MAGNETITE IN VOLCANOES: EVIDENCE FROM IGNEOUS PYROXENE PAIR INCLUSIONS AND S-BEARING SUBLIMATE COATINGS 191

Abstract 197
8.1 Introduction 198
8.2 Samples and methodology 201
8.3 Results 202
8.3.1 Mineralogy and mineral chemistry 202
8.3.2 Nanoscale characterisation 207
8.4 Discussion 211
8.5 Implications and conclusions 216
8.6 Acknowledgements 216
8.7 References 217

CHAPTER 9: SUMMARY, RECOMMENDATIONS AND CONCLUDING REMARKS 221

9.1 Summary 223
9.1.1 Geochemistry and mineralogy of hematite and magnetite from the Olympic Dam deposit 225
9.1.2 Trace element remobilisation in hematite by fluid-mineral interaction 227
9.1.3 Magnetite nanomineralogy from IOCG and -kin systems 229
9.2 Recommendations 232
9.2.1 Hematite geochemistry and additional microanalysis 233
9.2.2 Nanomineralogy of Acropolis titanohematite 236
9.2.3 Granitophile element bearing hematite in IOCG system along the Chilean Iron Belt: Geochronological implications 237
9.3 Concluding remarks 240
9.4 References 241

CHAPTER 10: SUPPLEMENTARY AND ADDITIONAL MATERIAL 247

SUPPLEMENTARY MATERIAL A: for Chapter 2 249
Electronic Appendix A for Chapter 2 250

Electronic Appendix B for Chapter 2 259
Electronic Appendix C for Chapter 2 262
Electronic Appendix D for Chapter 2 292
SUPPLEMENTARY MATERIAL B: for Chapter 3 293
Electronic Appendix A for Chapter 3 294
Electronic Appendix B for Chapter 3 297
Electronic Appendix C for Chapter 3 319
SUPPLEMENTARY MATERIAL C: for Chapter 4 334
Electronic Appendix A for Chapter 4 335
SUPPLEMENTARY MATERIAL D: for Chapter 5 342
Electronic Appendix A for Chapter 5 343
Electronic Appendix B for Chapter 5 345
Electronic Appendix C for Chapter 5 347
SUPPLEMENTARY MATERIAL E: for Chapter 6 349
Electronic Appendix A for Chapter 6 350
SUPPLEMENTARY MATERIAL F: for Chapter 7 365
Electronic Appendix A for Chapter 7 366
SUPPLEMENTARY MATERIAL G: for Chapter 8 375
Electronic Appendix A for Chapter 8 376
ADDITIONAL MATERIAL H: Silician Magnetite: Si–Fe-Nanoprecipitates and Other Mineral Inclusions in Magnetite from the Olympic Dam Deposit, South Australia 384
ADDITIONAL MATERIAL I: Advances and opportunities in ore mineralogy 386
ADDITIONAL MATERIAL J: ~1760 Ma magnetite-bearing protoliths in the Olympic Dam deposit: Implications for ore genesis and regional metallogeny 388
ADDITIONAL MATERIAL K: A multi-technique evaluation of hydrothermal hematite U-Pb isotope systematics: Implications for ore deposit geochronology 390
ADDITIONAL MATERIAL L: Hematite geochemistry and geochronology resolve genetic and temporal links among iron-oxide copper gold systems, Olympic Dam district, South Australia 392
ADDITIONAL MATERIAL M: Zircon at the nanoscale records metasomatic processes leading to large magmatic-hydrothermal ore systems 394
ADDITIONAL MATERIAL N: Synthesis of U-Pb doped hematite using a hydrated ferric oxide approach 396

ADDITIONAL MATERIAL O: Defining IOCG signatures through compositional data analysis: A case study of lithogeochemical zoning from the Olympic Dam deposit, South Australia 398
ADDITIONAL MATERIAL P: Mineralization-alteration footprints in the Olympic Dam IOCG district, South Australia: The Acropolis prospect 400
ADDITIONAL MATERIAL Q: Numerical modelling of rare earth element fractionation trends in garnet: a tool to monitor skarn evolution 402
ADDITIONAL MATERIAL R: Trace element signatures in U-W-Sn-Mo zoned hematite from the IOCG deposit at Olympic Dam, South Australia 404
ADDITIONAL MATERIAL S: Copper nanoparticles along fluid inclusion trails in hematite 410
ADDITIONAL MATERIAL T: Metal-bearing nanoparticles in hematite 414
ADDITIONAL MATERIAL U: Tungsten-bearing nanoparticles in hematite: insights into open system behaviour of mineral geochronometers 418
ADDITIONAL MATERIAL V: Crystal structural modifications in U-rich, oscillatory-zoned hematite 422
ADDITIONAL MATERIAL W: Nanoscale study of silician magnetite from IOCG systems: examples from the Olympic Dam district, South Australia 424
ADDITIONAL MATERIAL X: Why detailed mineralogy is important: understanding evolution of the Olympic Dam iron-oxide-copper-gold system, South Australia 428
ADDITIONAL MATERIAL Y: Oscillatory-zoned hematite: a reliable U-Pb mineral geochronometer 432
ADDITIONAL MATERIAL Z: U-Pb doped synthetic reference material for in-situ hematite geochronology 434
ADDITIONAL MATERIAL AA: The U-Pb systematics of hydrothermal hematite: insights from the IOCG system at Olympic Dam, South Australia 436
ADDITIONAL MATERIAL BB: Chloro-hydroxy-zircon nanoprecipitates fingerprint fertility and mineralization potential of granitic magmas 440
ADDITIONAL MATERIAL CC: Multivariate statistical analyses of LA-ICP-MS trace element data for iron-oxides: examples from genetically distinct ore deposits from South Australia 444
ADDITIONAL MATERIAL DD: Copula Functions as A Tool for Statistical Modelling of Trace Element Signatures in Iron-Oxides: Examples from South Australian Ore Deposits 446

ADDITIONAL MATERIAL EE: Defining IOCG signatures through compositional data analysis: a case study of lithogeochemical zoning at Olympic Dam, South Australia..... 448
ADDITIONAL MATERIAL FF: Mineralization signatures of the magnetite-dominant Acropolis prospect, Olympic Dam IOCG district, South Australia 452
ADDITIONAL MATERIAL GG: 'Invisible' Au in pyrite from Olympic Dam deposit, South Australia: bridging textures with statistical analyses 458
ADDITIONAL MATERIAL HH: Oscillatory growth patterns in hematite defined by Si-Fe- nanoprecipitates: ore enrichment processes in BIFs 462
ADDITIONAL MATERIAL II: A Multiplatform approach to unravelling geological problems: a case study from Olympic Dam, South Australia 466

CHAPTER 11: REFERENCES.....471

ABSTRACT

Iron-oxide copper gold (IOCG) mineralisation is defined by an abundance of hematite and/or magnetite. The predominance of one Fe-oxide over the other and their textural relationships can, however, differ significantly within a single deposit or within the same metallogenic province, as a response to variations in the genetic conditions. Analysis of Fe-oxides, bridging scales of observation from deposit down to the nanoscale, highlights different formation conditions within deposits and prospects from the ~1.6 Ga Olympic Dam district, South Australia. In addition, Fe-oxides from the ~5.3-1.6 Ma El Laco Volcanic Complex (Chile), which are debated in terms of magmatic and/or hydrothermal origins, were analysed for comparison with those formed in IOCG systems.

At Olympic Dam, a characteristic oscillatory-zoned hematite, containing up to wt% concentrations of U-W-Sn-Mo ('granitophile' elements), is the predominant Fe-oxide over the ~6 km-strike and ~2 km-depth of the breccia-hosted mineralisation. Complex textural and compositional zoning patterns within the hematite indicate overprinting and replacement of pre-existing minerals, including earlier hematite, during subsequent episodes of fluid-assisted brecciation and mineralisation. A diverse range of features at the micron- to nanoscale indicates that pseudomorphic replacement of hematite occurred via coupled dissolution and reprecipitation reactions leading to grain-scale (re)mobilisation of minor/trace elements. Primary geochemical signatures are nevertheless partially or selectively preserved. This allows the use of hematite as a reliable U-Pb geochronometer.

Mineralogical-geochemical study of Fe-oxides from the *outer shell*, a weakly-mineralised domain between the host granite and the Olympic Dam orebody, allows for re-interpretation of deposit formation. Iron-oxide assemblages comprise oscillatory-zoned, silician magnetite, high field strength element-bearing hematite, and various interconversion products between the two

oxides. Formation of such assemblages is associated with early alkali-calcic alteration (calc-silicate inclusions in silician magnetite), breakdown of magmatic Fe-Ti-oxides, and replacement of igneous magnetite by silician magnetite. Geochemical modelling at 400 °C suggests magnetite-replacement at pH/fO_2 conditions that coincide with stability shifts of K-feldspar → sericite, and ilmenite → rutile. *Outer shell* formation was initiated at the depth of granite emplacement (~6-8 km), following volatile release from fluids ponding at intrusion margins. Mineralisation continued during uplift to shallower depth, with cupola collapse following extensive fluid release that facilitated brecciation and orebody formation.

Nanoscale analysis of Fe-oxides by scanning transmission electron microscopy using Z-contrast imaging and mapping provides further insights into ore-forming processes. Fingerprinting of fluid-mineral interactions during subsequent overprint of U-W-Sn-Mo-bearing hematite show that twins provide pathways for fluid percolation and trap elements exchanged during cycles of coupled dissolution-reprecipitation. Metal nanoparticles (NP) are also trapped within pores developed during transient porosity, which can be hosted by fluid inclusions. Unusual Cu-As-zoning at the micron-scale correlates with Cu-(As)-NPs along fluid inclusion trails and Si-Al-K-bearing twin planes linking such metal enrichment to hydrolytic alteration. W-Pb-enrichment occurs along 2-3 nm-wide twin crests and as W-(Pb)-bearing NPs in hematite displaying ‘granitophile element’-signature with preferential removal of W and preservation of Sn, as shown by grain-scale element patterns. A two-fold superstructure model with oxygen vacancies is constructed to explain W-release from hematite. Nanoscale features observed in relation to twins also allow prediction of disturbances to the U/Pb-systematics of hematite with implications for geochronology.

Nanomineral inclusions in magnetite are valuable petrogenetic indicators that can clarify ore-forming processes. At Acropolis, vein titanomagnetite, within ~1.6 Ga volcanic rocks, features nanoscale inclusions with ulvöspinel-hercynite pairs and ilmenite-trellis exsolutions followed by subsequent overprinting (rutile replacement of Ti-phases). Spinel-group

associations and ilmenite/magnetite oxythermobarometry supports hydrothermal-magnetite formation at ≥500 °C. Silician magnetite from Wirrda Well hosts nanoinclusions of the rare Al-amphibole, tschermakite. Considering the metamorphism of the host ~1.85 Ma granite, the presence of tschermakite could represents a metamorphic phase that crystallised prior to IOCG-style mineralisation. In contrast, magnetite from Fe-ores at El Laco contains nm-scale inclusions of paired clinopyroxenes (augite-pigeonite/clinoenstatite) with intergrowths indicative of rapid growth and exsolution at low pressures/high temperatures, typical of crystallisation from melts. Sulfur-bearing coatings on comparable but finer-grained pyroxene-bearing magnetite are indicative of 'magnetite flotation' via attachment to bubbles of vapour+fluid, allowing transport from a deep magma reservoir to surface.

Iron-oxides show remarkable variation in compositional signatures and nanoscale heterogeneity. Detailed petrographic, geochemical and mineralogical analysis of Fe-oxides represents a rich and often untapped source of information that can assist in constraining ore formation conditions and contribute to improved genetic models.

DECLARATION

I certify that this work contains no material which has been accepted for the award of any other degree or diploma in my name in any university or other tertiary institution and, to the best of my knowledge and belief, contains no material previously published or written by another person, except where due reference has been made in the text. In addition, I certify that no part of this work will, in the future, be used in a submission in my name for any other degree or diploma in any university or other tertiary institution without the prior approval of the University of Adelaide and where applicable, any partner institution responsible for the joint award of this degree.

I acknowledge that copyright of published works contained within this thesis resides with the copyright holder(s) of those works.

I give permission for the digital version of my thesis to be made available on the web, via the University's digital research repository, the Library Search and also through web search engines, unless permission has been granted by the University to restrict access for a period of time.

I acknowledge the support I have received for my research through the provision of an Australian Government Research Training Program Scholarship.

Signed: Date: 15/04/2020

ACKNOWLEDGEMENTS

I would like to first, and foremost acknowledge the major efforts and contributions of my supervisors and particularly my principal supervisor, Dr. Cristiana L. Ciobanu; without her this work would not have been possible. Being your student was a challenging yet also rewarding experience. Thank you for your guidance and for pushing me to think more critically, and for caring and dedicating yourself so much to the successes of your students. I extend my thanks to Prof. Dr. Nigel J. Cook, who supported both Cristi and her students during these last few years in achieving many of the ambitious goals within the FOX project. Thank you for your willingness and dedication invested in the editing of countless drafts, and for being a pillar for both Cristi and the FOXes. I extend my gratitude to my external supervisor, Dr. Kathy Ehrig, who opened Olympic Dam to us and gave us the opportunity to conduct research on this fascinating deposit. Thank you for sharing with us your insights and experience with this deposit that you have amassed over the years and providing so much help.

I recognise the exceptional work of the Adelaide Microscopy staff, and especially thank Drs. Sarah E. Gilbert, Benjamin P. Wade, Ashley Slattery and Animesh Basak, who have continuously assisted our analytical work and contributed in various ways. Your support is greatly acknowledged, and you have my honest gratitude for your dedication and your readiness to help.

Thank you to fellow students and colleagues Drs. Danielle Schmandt, Nick Owen, Mark Rollog, Alkis Kontonikas-Charos and Jing Xu for being part of my experience here in Adelaide. I am glad that I had the opportunity to meet and share with you during the last few years, and hope to see you again in a not so distant future!

Heartfelt thanks and appreciation to my fellow FOXes: Marija Dmitrijeva, William Keyser and Liam Courtney-Davies: esteemed colleagues, partners in crime and, most importantly, dear

friends. I am grateful that you all were part of this team, thank you for your support along this arduous journey. Thank you Will for being my office buddy, Marija for sharing your code and Liam for rarely and *reluctantly* joining me for *a* drink to discuss geological topics and share our perspectives on several matters; thank you all!

Thank you, Frances, for all your love. Getting to know you over the last four years has been one of my greatest joys ever since I came to Adelaide. Your support during the last months of my candidature was extremely important to me.

Lastly, I want to thank my family and, specifically, my dear mother Wera for all her love, continuous and unconditional support and for encouraging me throughout my life; many of my accomplishments would have not been possible without or because of you.

PREFACE

This thesis comprises a portfolio of articles and manuscripts, which are either published or under review in international, peer-reviewed journals. The journals in which these papers are published or have been submitted to are *'Ore Geology Reviews'* (**Chapter 2**, published), *'Mineralium Deposita'* (**Chapter 3**, published), *'Minerals'* (**Chapter 4**, published), *'Mineralogical Magazine'* (**Chapter 5**, published), *'American Mineralogist'* (**Chapter 6**, in press), *'American Mineralogist'* (**Chapter 7**, submitted) and *'Earth and Planetary Science Letters'* (**Chapter 8**, in revision). All 7 chapters are closely related and summarise key findings and interpretations, to be read as standalone contributions. Recommendations have been made in **Chapter 9**, as a direct result of the key findings of this research.

The four published articles, one article in press and two submitted manuscripts, which form the basis of this thesis are:

1. Verdugo-Ihl, M.R., Ciobanu, C.L., Cook, N.J., Ehrig, K.J., Courtney-Davies, L., Gilbert, S., 2017. Textures and U-W-Sn-Mo signatures in hematite from the Olympic Dam Cu-U-Au-Ag deposit, South Australia: Defining the archetype for IOCG deposits. *Ore Geology Reviews* 91, 173–195. https://doi.org/10.1016/j.oregeorev.2017.10.007

2. Verdugo-Ihl, M.R., Ciobanu, C.L., Cook, N.J., Ehrig, K., Courtney-Davies, L., 2020. Defining early stages of IOCG systems: evidence from iron-oxides in the outer shell of the Olympic Dam deposit, South Australia. *Mineralium Deposita* 55, 429–452. https://doi-org/10.1007/s00126-019-00896-2

3. Verdugo-Ihl, M.R., Ciobanu, C.L., Slattery, A., Cook, N.J., Ehrig, K.J., Courtney-Davies, L., 2019. Copper-arsenic nanoparticles in hematite: fingerprinting fluid-mineral interaction. *Minerals* 9(7), 388. https://doi.org/10.3390/min9070388

4. Verdugo-Ihl, M.R., Ciobanu, C.L., Cook, N.J., Ehrig, K., Slattery, A., Courtney-Davies, L., 2020. Trace-element remobilisation from W–Sn–U–Pb zoned hematite: Nanoscale insights into a mineral geochronometer behaviour during interaction with fluids. *Mineralogical Magazine* 84, 502–516. https://doi.org/10.1180/mgm.2020.49

5. Verdugo-Ihl, M.R., Ciobanu, C.L., Cook, N.J., Ehrig, K., Slattery, A., Courtney-Davies, L., Dmitrijeva, M. Nanomineralogy of hydrothermal magnetite from Acropolis, South Australia: Genetic implications for IOCG mineralization. *American Mineralogist*, in press. https://doi.org/10.2138/am-2020-7557

6. Verdugo-Ihl, M.R., Ciobanu, C.L., Cook, N.J., Ehrig, K., Slattery, A., Courtney-Davies, submitted. Ferro-tschermakite with short range disorder identified in silician magnetite, *American Mineralogist.*

7. Verdugo-Ihl, M.R., Ciobanu, C.L., Cook, N.J., Tornos, F., Ehrig, K., Slattery, A., Xu, J., Courtney-Davies, L., Hanchar, J.M., in revision. Vapour transport of magnetite in volcanoes: evidence from igneous pyroxene pair inclusions and S-bearing sublimate coatings. *Earth and Planetary Science Letters*.

Chapter 9 contains supplementary material for all chapters outlined above, as well as additional material comprising co-authored publication abstracts, conference abstracts and posters and co-authored conference abstracts that have been generated during the Ph.D. candidature.

The supplementary material is as follows:

A. Supplementary material for Chapter 2 (*Ore Geology Reviews*).

B. Supplementary material for Chapter 3 (*Mineralium Deposita*).

C. Supplementary material for Chapter 4 (*Minerals*).

D. Supplementary material for Chapter 5 (*Mineralogical Magazine*).

E. Supplementary material for Chapter 6 (*American mineralogist*, in press).

F. Supplementary material for Chapter 7 (*American Mineralogist*, in review).

G. Supplementary material for Chapter 8 (*Earth and Planetary Science Letters*, in revision).

Abstracts of co-authored articles

H. Ciobanu, C.L., **Verdugo-Ihl, M.R.**, Slattery, A., Cook, N.J., Ehrig, K., Courtney-Davies, L., Wade, B.P., 2019. Silician Magnetite: Si–Fe-Nanoprecipitates and Other Mineral Inclusions in Magnetite from the Olympic Dam Deposit, South Australia. *Minerals* 9(5), 311. https://doi.org/10.3390/min9050311

I. Cook, N.J., Ciobanu, C.L., Ehrig, K.J., Slattery, A., **Verdugo-Ihl, M.R.**, Courtney-Davies, L., Gao, W., 2017. Advances and opportunities in ore mineralogy. *Minerals* 7(12), 233. https://doi.org/10.3390/min7120233

J. Courtney-Davies, L., Ciobanu, C.L., **Verdugo-Ihl, M.R.**, Cook, N.J., Ehrig, K., Wade, B.P., Zhu, Z-Y., Kamenetsky, V.S., 2020 ~1760 Ma magnetite-bearing protoliths in the Olympic Dam deposit: Implications for ore genesis and regional metallogeny. *Ore Geology Reviews* 118, 103337. https://doi.org/10.1016/j.oregeorev.2020.103337

K. Courtney-Davies, L., Tapster, S.R., Ciobanu, C.L., Cook, N.J., **Verdugo-Ihl, M.R.**, Ehrig, K.J., Kennedy, A.K., Gilbert, S.E., Condon, D.J., Wade, B.P., 2019. A multi-technique evaluation of hydrothermal hematite U-Pb isotope systematics: Implications for ore deposit geochronology. *Chemical Geology* 513, 54–72. https://doi.org/10.1016/j.chemgeo.2019.03.005

L. Courtney-Davies, L., Ciobanu, C.L., **Verdugo-Ihl, M.R.**, Dmitrijeva, M., Cook, N.J., Ehrig, K., Wade, B.P., 2019. Hematite geochemistry and geochronology resolve genetic and temporal links among iron-oxide copper gold systems, Olympic Dam district, South Australia. *Precambrian Research* 335, 105480. https://doi.org/10.1016/j.precamres.2019.105480

M. Courtney-Davies, L., Ciobanu, C.L., **Verdugo-Ihl, M.R.**, Slattery, A., Cook, N.J., Dmitrijeva, M., Keyser, W., Wade, B.P., Dominick, U.I., Ehrig, K., Xu, J., Kontonikas-Charos, A., 2019. Zircon at the nanoscale records metasomatic processes leading to large magmatic-hydrothermal ore deposits. *Minerals* 9(6), 364. https://doi.org/10.3390/min9060364

N. Courtney-Davies, L., Ciobanu, C.L., Richardson, M.W., Prosser, N., **Verdugo-Ihl, M.R.**, Wade, B.P., Gilbert, S.E., Ehrig, K., Cook, N.J., 2019. Synthesis of U-Pb doped hematite using a hydrated ferric oxide approach. *Journal of Crystal Growth* 513, 48–57. https://doi.org/10.1016/j.jcrysgro.2019.02.053

O. Dmitrijeva, M., Ehrig, K.J., Ciobanu, C.L., Cook, N.J., **Verdugo-Ihl, M.R.**, Metcalfe, A.V., 2019. Defining IOCG signatures through compositional data analysis: A case study of lithogeochemical zoning from the Olympic Dam deposit, South Australia. *Ore Geology Reviews* 105, 86–101. https://doi.org/10.1016/j.oregeorev.2018.12.013

P. Dmitrijeva, M., Ciobanu, C.L., Ehrig, K.J., Cook, N.J., Metcalfe, A. V., **Verdugo-Ihl, M.R.**, McPhie, J., 2019. Mineralization-alteration footprints in the Olympic Dam IOCG district, South Australia: The Acropolis prospect. *Journal Geochemical Exploration* 205, 106333. https://doi.org/10.1016/j.gexplo.2019.106333

Q. Xu, J., Ciobanu, C.L., Cook, N.J., Zheng, Y., Li, X., Wade, B.P., **Verdugo-Ihl, M.R.**, Gao, W., Zhu, Q., 2020. Numerical modelling of rare earth element fractionation trends in garnet: a tool to monitor skarn evolution. *Contributions to Mineral and Petrology* 175, 30. https://doi.org/10.1007/s00410-020-1670-7

First author conference abstracts (poster presentations)

R. Verdugo-Ihl, M.R., Ciobanu, C.L., Cook, N.J., Ehrig, K., Courtney-Davies, L., Gilbert, S.E. 2017. Trace element signatures in U-W-Sn-Mo zoned hematite from the IOCG deposit at Olympic Dam, South Australia. Mineral Resources to Discover. Proceedings of the 14th SGA Biennial Meeting, Québec, Canada, August 20th-23rd, 2017. ISBN: 978-2-9816898-0-1, Vol. 3, pp. 967–970.

S. Verdugo-Ihl, M.R., Ciobanu, C.L., Cook, N.J., Slattery, A., Ehrig, K. 2018. Copper Nanoparticles along fluid inclusion trails in hematite. Goldschmidt Conference 2018, Boston, U.S.A., August 12th-17th.

T. Verdugo-Ihl, M.R., Ciobanu, C.L. Cook, N.J., Courtney-Davies, L., Ehrig, K., Slattery, A. 2019. Tungsten-bearing nanoparticles in hematite: insights into open system behaviour of mineral geochronometers. TIGeR Conference 2019, Curtin University, Perth, W.A., Australia, September 11th-13th, pp. 66–67.

First author conference abstracts (oral presentation)

U. Verdugo-Ihl, M.R., Ciobanu, C.L., Cook, N.J., Slattery, A., Ehrig, K., Courtney-Davies, L., 2018. Metal-bearing nanoparticles in hematite. Proceedings of the 15th Quadrennial IAGOD Symposium, August 28th-31st, Salta, Argentina, pp. 189–190.

Co-authored conference abstracts

V. Ciobanu, C.L., Slattery, A., **Verdugo-Ihl, M.R.**, Courtney-Davies, L., Cook, N.J., Ehrig, K., 2017. Crystal structural modifications in U-rich, oscillatory-zoned hematite. Goldschmidt Conference 2018, Boston, U.S.A., August 12th-17th.

W. Ciobanu, C.L., **Verdugo-Ihl, M.R.**, Slattery, A., Cook, N.J., Ehrig, K., Courtney-Davies, L., 2018. Nanoscale study of silician magnetite from IOCG systems: examples from the Olympic Dam district, South Australia. Proceedings of the 15th Quadrennial IAGOD Symposium, August 28th-31st, Salta, Argentina, pp. 185–186.

X. Cook, N.J., Ehrig, K., Ciobanu, C.L., Courtney-Davies, L., **Verdugo-Ihl, M.R.**, Rollog, M., Schmandt, D.S., Owen, N.D., Macmillan, E., Kontonikas-Charos, A., Krneta, S., Dmitrijeva, M., 2018. Why detailed mineralogy is important: understanding evolution of the Olympic Dam iron-oxide-copper-gold system, South Australia. Proceedings of the 15th Quadrennial IAGOD Symposium, August 28th-31st, Salta, Argentina, pp. 371–372.

Y. Courtney-Davies, L., Ciobanu, C.L., Cook, N.J., **Verdugo-Ihl, M.**, Tapster, S.R., Condon, D.J., Kennedy, A.K., Ehrig, K., Wade, W.P., Gilbert, S.E., 2017. Oscillatory-zoned hematite: a reliable U-Pb mineral geochronometer. Goldschmidt Conference 2017, Paris, France, August 13th-18th.

Z. Courtney-Davies, L., Richardson, M.W., Gilbert, S.E., Ciobanu, C.L., **Verdugo-Ihl, M.**, Cook, N.J., Ehrig, K., Wade, B.P., 2018. U-Pb doped synthetic reference material for in-situ hematite geochronology. Geoanalysis 2018 Conference, Sydney, Australia, July 10th-14th.

AA. Courtney-Davies, L., Ciobanu, C.L., Tapster, S.R., Cook, N.J., Ehrig, K., Kennedy, A.K., Condon, D.J., **Verdugo-Ihl, M.**, Wade, B.P., Gilbert, S.E., 2018. The U-Pb systematics of hydrothermal hematite: insights from the IOCG system at Olympic Dam, South Australia. Proceedings of the 15th Quadrennial IAGOD Symposium, August 28th-31st, Salta, Argentina, pp. 171–172.

BB. Courtney-Davies, L., Ciobanu, C.L., **Verdugo-Ihl, M.**, Slattery, A., Cook, N.J., Ehrig, K., 2019. Chloro-hydroxy-zircon nanoprecipitates fingerprint fertility and mineralization potential of granitic magmas. TIGeR Conference 2019, Curtin University, Perth, W.A., Australia, September 11th-13th, pp. 51–52.

CC. Dmitrijeva, M., Ciobanu, C.L., Metcalfe, A.V., Cook, N.J., **Verdugo-Ihl, M.R.**, Keyser, W., Ehrig, K., 2017. Multivariate statistical analyses of LA-ICP-MS trace element data for iron-oxides: examples from genetically distinct ore deposits from South Australia. 18th International Association for Mathematical Geosciences Conference 2017, Perth, Australia, September 2nd-9th, p. 110.

DD. Dmitrijeva, M., Metcalfe, A.V., Ciobanu, C.L., Cook, N.J., **Verdugo-Ihl, M.R.**, Keyser, W.M., Ehrig, K. Copula Functions as a Tool for Statistical Modelling of Trace Element Signatures in Iron-Oxides: Examples from South Australian Ore Deposits. International Association of Mathematical Geosciences 2017, Perth, Australia, September 2nd-9th, p. 207.

EE. Dmitrijeva, M., Ehrig, K.J., Ciobanu, C.L., Cook, N.J., **Verdugo-Ihl, M.R.**, Metcalfe, A.V., 2018. Defining IOCG signatures through compositional data analysis: a case study of lithogeochemical zoning at Olympic Dam, South Australia. Proceedings of the 15th Quadrennial IAGOD Symposium, August 28th-31st, Salta, Argentina, pp. 246–247.

FF. Dmitrijeva, M., Ciobanu, C.L., Ehrig, K.J., Metcalfe, A. V., **Verdugo-Ihl, M.R.**, McPhie, J., Cook, N.J., 2019. Mineralization signatures of the magnetite-dominant Acropolis prospect, Olympic Dam IOCG district, South Australia. ASEG Extended Abstracts 2019, 1–5. https://doi.org/10.1080/22020586.2019.12073050

GG. Dmitrijeva, M., **Verdugo-Ihl, M.R.**, Ehrig, K.J., Ciobanu, C.L., Cook, N.J., 2019. 'Invisible' Au in pyrite from Olympic Dam deposit, South Australia: bridging textures with statistical analyses. TIGeR Conference 2019, Curtin University, Perth, W.A., Australia, September 11th-13th, pp. 52–53.

HH. Keyser, W., Ciobanu, C.L., **Verdugo-Ihl, M.**, Cook, N.J., Slattery, A., Ehrig, K., 2019. Oscillatory growth patterns in hematite defined by Si-Fe- nanoprecipitates: ore enrichment processes in BIFs. TIGeR Conference 2019, Curtin University, Perth, W.A., Australia, September 11th-13th, pp. 54–55.

II. Netting, A.K.O, Wade, B.P., **Verdugo-Ihl, M.R.**, Courtney-Davies, L., Ciobanu, C.L., Cook, N.J., Ehrig, K., Slattery, A., Gilbert, S., Neubauer, K., 2019. A Multiplatform approach to unravelling geological problems: a case study from Olympic Dam, South Australia, 2019. 16th European Workshop on Modern Developments and Applications in Microbeam Analysis (EMAS 2019), Norwegian University of Technology and Science,

Trondheim, Norway, 19th-23rd May. Microscopy and Microanalysis 25 (Suppl. 2), 2432–2433. https://doi.org/10.1017/S1431927619012893

The final chapter of this thesis (**Chapter 10**) consists of a complete reference list of all publications cited within any of the manuscripts, chapters and supplementary materials submitted as a component of this thesis.

CHAPTER 1

INTRODUCTION

CHAPTER 1: INTRODUCTION

Formation of iron-oxide copper gold (IOCG) systems is broadly attributed to magmatic-hydrothermal processes that precipitate abundant hematite (α-Fe_2O_3), magnetite (Fe_3O_4), or a combination of both, in addition to economic quantities of commodities including Cu, Au and Ag, with subordinate U and REE, among many other elements (Hitzman et al., 1992; Barton, 2014). In South Australia, IOCG-style deposits are by far the most economically significant contributors to the mineral resource sector in the state. Banded iron formations (BIF; Keyser et al., 2018, 2019a) are also substantial contributors. Importantly, these two types of deposit, which both occur in the eastern Gawler Craton, are Fe-oxide dominant. This has prompted the question of whether Fe-oxides can be used as petrogenetic indicators to infer a range of conditions during mineralisation and/or subsequent overprinting. Despite being formed by very different processes, some provinces feature superposition of IOCG- and BIF-type deposits. This was recently demonstrated by new geochronological data supporting the incorporation of Fe-rich protoliths from pre-existing BIF lithologies within IOCG mineralisation at the Olympic Dam Cu-U-Au-Ag deposit (Courtney-Davies et al., 2020a), possibly contributing to the total metal endowment. Since both magnetite and hematite react to and record physiochemical changes in their formation environments, they can be used to constrain the evolution of a deposit, if sufficiently linked to textural and compositional variations at the deposit scale within a well-defined temporal framework (Dmitrijeva et al., 2018; Keyser et al., 2018, 2019a; Courtney-Davies et al., 2019a, 2020b).

Within South Australia, several dozen IOCG systems of Mesoproterozoic age occur within the Olympic Cu-Au Province, a ~700 km-long N-S trending metallogenic belt on the eastern margin of the Gawler Craton (Skirrow et al., 2007; Reid, 2019, and references therein; Fig. 1.1).

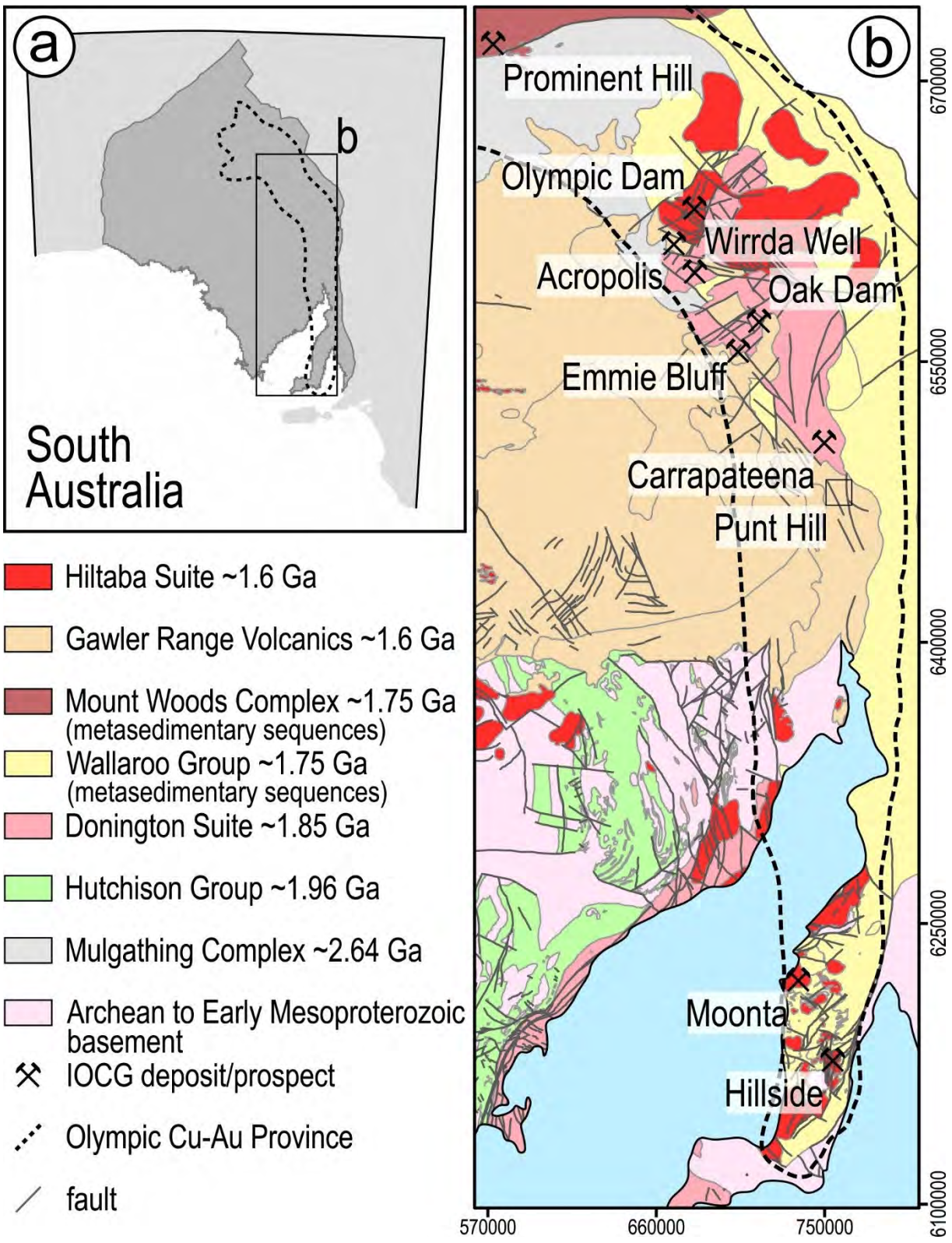

Fig. 1.1. (a) Location of the Gawler Craton in South Australia and (b) geological map of the eastern margin of the Gawler Craton highlighting important IOCG deposits and/or prospects within the Olympic Cu-Au province. Map data sourced from https://map.sarig.sa.gov.au.

This metallogenic province shows a close spatial and temporal association with development of the ~1.6 Ga Gawler Silicic Large Igneous Province (SLIP; Allen et al., 2008), which

comprises the Gawler Range Volcanics (GRV; Blissett et al., 1993) and the comagmatic Hiltaba Suite (HS) intrusive rocks. Although several deposits and prospects are hosted directly within Gawler SLIP lithologies (e.g., Olympic Dam, Acropolis), others are confined to older lithologies, such as the Wirrda Well prospect, which is located in the southern part of the Olympic Dam district and hosted within ~1.85 Ga Donington Suite granitoids.

Despite being hosted by different lithologies, each of these systems features regional- to deposit-scale alteration footprints comparable to those at Olympic Dam (Mauger et al., 2016; Kontonikas-Charos et al., 2017). Although many of these deposits/prospects are attributed to similar ore-forming processes and formed under broadly similar genetic conditions, the predominance of one Fe-oxide over the other, the composition of the Fe-oxides, and their textural relationships can, however, differ significantly within a single deposit, or across a district. These differences are also reflected in various styles of mineralisation (e.g., breccia-hosted at Olympic Dam deposit; Ehrig et al., 2012, 2017; vein-hosted at Acropolis; Dmitrijeva et al., 2019a; McPhie et al., 2020), and suggest a response to varying genetic conditions, e.g., proximity to source (?), variations in source, mineralisation environment – and not least, the degree of subsequent reworking/overprint of mineralisation. Two of the satellite prospects within the Olympic Dam district, Acropolis and Wirrda Well, show apparent differences relative to each another and to Olympic Dam. Comparative studies are thus valuable, since they could represent different temperature/depth expressions of a similarly-rooted hydrothermal system.

Whether the deposits are magnetite- or hematite-dominant, Fe-oxides are major phases throughout all stages of the evolution of IOCG systems *sensu lato*, and therefore have the potential to track their evolution unlike any other mineral. A holistic, multi-technique approach to Fe-oxide characterisation, bridging scales of observation from deposit-scale, within single drillholes, in hand specimens, polished sections and down to the nanoscale, can provide the means to highlight similarities or differences relating individual deposit/prospect formation

conditions. Integration of these results allow not only new deposit models but valuable constraints on metallogenetic evolution across the ~1.6 Ga Olympic Dam district. Beyond this, comparison with magnetite from Fe-oxide rich mineralisation from the Plio-Pleistocene El Laco Volcanic Complex (Chile), which is strongly debated in terms of a magmatic and/or hydrothermal origin (e.g., Tornos et al., 2016; Ovalle et al., 2018), and contrasts starkly with the South Australian IOCG systems, serves as a good opportunity for comparison. This comparison enables the application of insights gained from the study of South Australian IOCGs to decipher formation conditions at El Laco, and determine the similarities and differences between magmatic-hydrothermal Fe-oxide systems in the broader sense.

Interest in the characterisation of Fe-oxides has expanded quickly over the past decade due to the growing realisation that these common minerals can contain an extraordinary amount of information. The ease of minor/trace element compositional characterisation has advanced thanks to the increasing availability of laser ablation inductively coupled plasma mass spectrometry (LA-ICP-MS), which permits rapid acquisition of trace element concentration data coupled with far lower minimum limits of detection when compared with other conventional microbeam techniques (e.g., electron probe microanalysis; EPMA). The trace element compositions of magnetite from multiple geological settings has been extensively characterised by LA-ICP-MS (Cook et al., 2016, references therein, and many subsequent publications).

In contrast to magnetite, geochemical characterisation of hematite has been largely overlooked until recently, such that there is a significant gap with respect to its potential use as a petrogenetic indicator. In addition, very few studies have attempted to resolve the compositional variation of magnetite at the nanoscale (e.g., Huberty et al., 2012; Xu et al., 2014; Deditius et al., 2018), and even less so for hematite, to understand how these phases adapt to trace element incorporation and, thus, define petrologically useful minor/trace element signatures.

Although hematite from Olympic Dam had been known to contain U for some time (Oreskes, 1990), the study by Ciobanu et al. (2013) was the first to recognise the compositional complexity of this hematite, which is characterised by up to several wt.% of lattice-bound U, Mo, W, and radiogenic Pb, among other elements. Ciobanu et al. (2013) presented the first LA-ICP-MS maps of zoned hematite and assessed its potential suitability as a mineral geochronometer for dating hematite-bearing ores. This contribution served as a foundation for subsequent research aimed at developing a matrix-matched reference material for routine hematite geochronology by LA-ICP-MS (Courtney-Davies et al., 2016, 2019b), for validating the capabilities and limitations of the hematite geochronometer (Courtney-Davies et al., 2019c), and also for consolidating its use in dating IOCG mineralisation at Olympic Dam (Courtney-Davies et al., 2020b), and elsewhere in the region (e.g., $^{207}Pb/^{206}Pb$: Acropolis at 1590.6 ± 6.5 and Wirrda Well at 1598.9 ± 6.3 Ma; Courtney-Davies et al., 2019a), BIF-style mineralisation in South Australia (Keyser et al., 2019a), and most recently, much younger Fe-oxides containing only a few ppm U (Verdugo-Ihl et al., submitted, a).

Importantly, these studies predict that datable, U-bearing hematite exists not only at Olympic Dam and nearby prospects, but worldwide, which has tremendous potential for constraining the lifespan of hematite-rich IOCG mineralisation, and improves or contributes to refining existing genetic models and exploration criteria at the scale of a metallogenic province. Deposit-scale studies using large whole-rock datasets and *state-of-the-art* statistical analyses have also been able to reconcile the U-W-Sn-Mo ('granitophile' elements) signature in hematite at the deposit-scale, both in the hematite-dominant breccia complex at Olympic Dam (Dmitrijeva et al., 2019b), and even partially in prospects where magnetite vein predominate (e.g., Acropolis; Dmitrijeva et al., 2019b). Importantly, this mineral signature is also recognised in younger systems of possible IOCG affiliation elsewhere (e.g., Rosen, Bulgaria; Sillitoe et al., 2020).

The advantages of dedicated nanoscale analysis of Fe-oxides by transmission electron microscopy (TEM), including high angle annular dark field (HAADF) scanning (S/)TEM have been increasingly recognised in recent years, and used to solve petrogenetic questions in ore geology. For instance, nanoscale analysis of granoblastic hematite from high-grade ores in the Peculiar Knob deposit, Mt. Woods Inlier, South Australia (Keyser et al., 2019b), have shown the presence of nm-wide baddeleyite lamellae within Zr-rich hematite (up to ~650 ppm). These results have contributed to a re-assessment of the source for this mineralisation, previously considered as of BIF origin, which is now though to be potentially derived from Fe-rich sediments containing detrital Zr-bearing titanomagnetite that originated from mafic lithologies that where metamorphosed during the Kimban Orogeny. At Olympic Dam, a similar but more comprehensive nanoscale study focused on silician magnetite from the *outer shell* has shown an eclectic range of nanomineral inclusions, including Si-Fe-nanoprecipitates, (ferro)actinolite, diopside and epidote, which characterise early, alkali-calcic alteration within the deposit that is otherwise poorly preserved (Ciobanu et al., 2019).

With the exception of early work (Oreskes, 1990), and the reconnaissance work of Ciobanu et al. (2013), no previous published study had addressed the Fe-oxide mineralogy of IOCG systems within the Olympic Dam district or elsewhere within the Olympic Cu-Au Province in any detail. A substantial gap in knowledge thus existed at the start of the present project with respect to the role of Fe-oxides in these systems, thus providing the basis for a major research collaboration between BHP Olympic Dam, The University of Adelaide and the South Australian Government. During the duration of this candidature, other contributions have been published as a result of collaborative work, notably Fe-oxide geochemistry and dating at Acropolis and Wirrda Well (Courtney-Davies et al., 2019a), and a comprehensive nanoscale study focused on silician magnetite from the *outer shell* at Olympic Dam (Ciobanu et al., 2019). Iron-oxides readily record evidence of overprinting by brecciation and fluid-mineral interaction, causing element (re)mobilisation in some cases, which appears to be an important

characteristic of IOCG systems. The remarkable variation in compositional signatures and, particularly the nanoscale heterogeneity of Fe-oxides represents a rich source of information that can be exploited. This does however necessitate detailed petrographic, geochemical and mineralogical analysis underpinned by an in-depth understanding of what has been analysed. Attempts to define ore deposit types based on geochemical signature (Dupuis and Beaudoin, 2011) can fail or be compromised by inadequate or insufficiently detailed characterisation.

The objectives of this project were to use Fe-oxides geochemical signatures, characterised by distinct minor and trace element associations, to define and underpin the evolution of IOCG systems during the lifespan of the mineralisation, using the archetype Olympic Dam and adjacent prospects as an example (Fig. 1.1). One important aspect of this work was to understand the distribution, and fundamental reasons behind incorporation and release of minor/trace elements. The research also aimed to understand minor/trace element behaviour within Fe-oxides during overprinting by fluid-mineral interaction or subsolidus reactions, i.e., the presence of elements of interest in solid solution (structurally bound) *versus* sub-micron-scale inclusions of discrete phases. Together, this knowledge could be used to develop or improve genetic models for IOCG deposits. Despite their simple stoichiometries, Fe-oxides show remarkable variation in terms of compositional signatures, owing to their crystal structures, which can accommodate various types of substitution mechanisms, and nanoscale heterogeneity. Detailed petrographic, geochemical and mineralogical analysis of Fe-oxides therefore represents a rich, and largely untapped source of complementary information that can assist in constraining ore formation conditions and contribute to improved genetic models, particularly in those deposits or mineral systems in which they are volumetrically dominant phases.

1.1 Research objectives and thesis structure

This thesis is a contribution to the overarching research project 'Trace elements in iron-oxides: deportment, distribution and application in ore genesis, geochronology, exploration and mineral processing'. The aim of the research reported in this thesis was to address key questions regarding the formation of the world-class Olympic Dam deposit, the archetype of IOCG systems, by the analysis of Fe-oxides, the most abundant and defining component within these systems.

The broad objective of this project was to characterise both magnetite and hematite and their interconversion products, minerals which per definition constitute the bulk of IOCG systems, as either the dominant gangue mineral, or – in some cases – ore minerals. The analytical approach involved advanced microanalytical techniques capable of characterisation at the micron- to nanoscales. These included conventional petrography by reflected light optical and back scatter electron (BSE) microscopy, complemented by compositional analysis using EPMA and LA-ICP-MS techniques, and dedicated nanoscale analysis by HAADF S/TEM. Collectively, these methods can define variations in the geochemical signatures of major, minor and trace elements related to their formation conditions at the deposit-scale at Olympic Dam, its satellite prospects and in other kin-deposits or genetically related analogues worldwide. The studied deposits feature different types of magnetite and hematite, which also occur in different proportions, that were analysed to identify the cause of different compositional signatures and their variations at different scales. Linking such geochemical signatures to Fe-oxide nanomineralogy, can in turn be used to further assess and constrain Fe-oxide formation, since Fe-oxides can form over a wide range of physiochemical conditions and are sufficiently refractory to preserve them. In this context, nanomineral inclusions in Fe-oxides are valuable petrogenetic indicators that can provide additional criteria to discriminate between a wide range of formation scenarios.

The main body of this thesis comprises seven chapters (**Chapters 2** to **8**), which are stand-alone manuscripts that can be read independently. All are, however, interlinked by the common theme of how the mineralogy, mineral chemistry and nanoscale features of Fe-oxides can assist with constraining the genesis of ore deposits. The first three chapters (**Chapters 2**, **3** and **4**) were published during the course of the Ph.D. candidature, whereas **Chapters 5** to **8** were under review at the time of thesis submission. This thesis can be divided into three parts, comprising: (i) deposit-scale characterisation of Fe-oxides at Olympic Dam (**Chapters 2** and **3**), which facilitated (ii) detailed, follow-up nanoscale studies on hematite from the same deposit (**Chapters 4** and **5**), and (iii) nanoscale case-studies on magnetite from satellite prospects within the Olympic Dam district (**Chapters 6** and **7**) and the El Laco deposit in northern Chile (**Chapter 8**).

Chapter 2 (Verdugo-Ihl et al., 2017) focuses on the geochemistry and mineralogy of hematite, the most abundant Fe-oxide phase within the Olympic Dam orebody and the major gangue mineral in the ore (making up 30-80 % of the orebody) of the deposit. Emphasis is placed on a conspicuously oscillatory and sectorially zoned hematite characterised by up to several wt.% of U, W, Sn and Mo (collectively defined as 'granitophile' elements). This hematite is recognised as the predominant variety over the ~6 km-strike and ~2 km-depth of the breccia-hosted mineralisation. Such hematite displays complex textural patterns linked to compositional changes, which are attributable to overprinting and replacement of pre-existing minerals, including earlier generations of hematite, during subsequent cycles of mineral-fluid interaction and brecciation. A diverse range of features at the micron-scale supports the overprint of hematite via coupled dissolution and reprecipitation reactions leading to grain-scale (re)mobilisation of minor/trace elements. Despite this, primary geochemical signatures can be partially preserved.

Chapter 3 (Verdugo-Ihl et al., 2020a) addresses the mineralogy and geochemistry of Fe-oxides from the *outer shell* of the Olympic Dam orebody, a weakly-mineralised domain

adjacent to the host granite. The study allows for a re-interpretation of deposit formation. Iron-oxide-bearing assemblages in the *outer shell* comprise oscillatory-zoned, silician magnetite, a sub-type of hematite containing high field strength elements, and various products of the interconversion between the two oxides (i.e., pseudomorphic replacements). Formation of such assemblages is associated with early alkali-calcic alteration, as supported by the presence of calc-silicate inclusions in silician magnetite, breakdown of magmatic Fe-Ti-oxides, and the replacement of igneous magnetite by silician magnetite. Geochemical modelling at 400 °C suggests that magnetite-replacement took place at pH and fO_2 conditions that coincide with stability shifts of K-feldspar to sericite, and ilmenite to rutile. Formation of the o*uter shell* could have been initiated at the depth of granite emplacement (~6-8 km), following volatile release from fluids ponding at the intrusion margins. Mineralisation continued during uplift to shallower depth, with cupola collapse following extensive fluid release that facilitated brecciation and orebody formation.

Topical analysis of hematite by nanoscale characterisation using Z-contrast imaging by HAADF STEM, accompanied by STEM-EDX mapping, provides further insights into ore-forming processes at Olympic Dam with valuable implications for hematite U-Pb geochronology. **Chapter 4** (Verdugo-Ihl et al., 2019) fingerprints the products of fluid-mineral interactions at the nanoscale that are generated during overprinting of U-W-Sn-Mo-bearing hematite. Results demonstrate the role of twins in providing fluid-pathways and facilitating fluid percolation. The same twins can also act as traps for elements exchanged during coupled dissolution-reprecipitation reactions. During these reactions, metal nanoparticles can nucleate and be trapped within fluid inclusions that developed as pores during generation of transient porosity. Unusual Cu-As-zoning at the micron-scale as shown by LA-ICP-MS mapping correlates with the presence of Cu(-As)-nanoparticles along fluid inclusion trails and Si-Al-K-bearing twin planes at the nanoscale visible on HAADF STEM images, thus linking such metal enrichment to hydrolytic alteration.

Discrete enrichment of W and Pb is shown along 2-3 nm-wide twin crests and as W(-Pb)-bearing nanoparticles in hematite displaying 'granitophile'-signature, with preferential removal of W and preservation of Sn, as depicted by grain-scale compositional patterns (**Chapter 5**; Verdugo-Ihl et al., 2020b). A two-fold superstructure model with oxygen vacancies is constructed to explain W-release from hematite, relating to observed superstructures and lattice-scale motifs. Nanoscale features observed in relation to twins also allow for the prediction of disturbances to the U-Pb-systematics of hematite with implications for geochronology.

Chapter 6 (Verdugo-Ihl et al., in press) addresses the nanomineralogy of Ti-rich and -poor magnetite varieties from magnetite veins hosted within ~1.6 Ga GRV lithologies and HS granite in the Acropolis prospect. Primary titanomagnetite, comparable with magmatic magnetite in granites across the district, features ilmenite-trellis and two-phase ulvöspinel-hercynite nanoparticles as exsolution products from magnetite solid solutions ($magnetite_{ss}$) due to increasing fO_2 and cooling. Titanium-poor magnetite, however, is characterised by finest, monophase nanoparticles of spinel *sensu stricto* only. Following exsolution of ilmenite and ulvöspinel-hercynite, subsequent overprint of magnetite via mineral-buffered reactions, interpreted in the context of vein-reopening, recycles and redistributes elements that form densely-mottled and orbicular clusters of sub-µm inclusions comprising hercynite±gahnite+TiO_2 polymorphs and rare Sc-Ti-phases. Order-disorder phenomena observed in two TiO_2 polymorphs, anatase and rutile, are evidence for subtly fO_2-buffered reactions from anatase (reducing) to rutile (more oxidising) conditions. Nano-thermooxybarometry using ilmenite-magnetite pairs provide re-equilibration temperatures in the range of ~570-510±50 °C from primary to orbicular magnetite, whereas Ti-poor magnetite may have formed at even higher temperatures (670±50 °C using X_{Mg}-in-magnetite thermometry). The lack of calc-silicate nanoparticles, like those known from silician magnetite in IOCG systems with prevailing rock-buffered alteration of host lithologies (Olympic Dam),

can be explained by open-fracture circulation of hydrothermal fluids at Acropolis, which inhibits the additional supply of Si, Ca, K, etc. during magnetite precipitation.

Unlike Acropolis, silician magnetite is the predominant magnetite variety at the Wirrda Well prospect. **Chapter 7** (Verdugo-Ihl et al., in review, b) describes, drawing on HAADF S/TEM data, how such magnetite hosts nanoinclusions of the rare Al-amphibole, tschermakite. Considering that the host ~1.85 Ma granite has undergone metamorphism, tschermakite is interpreted to represent a metamorphic phase that formed prior to the main magmatic-hydrothermal event, at ~1.6 Ga, that deposited IOCG-style mineralisation across the district.

In contrast to the chapters detailing studies of Fe-oxides from IOCG deposits in South Australia, **Chapter 8** (Verdugo-Ihl et al., in revision, c) is a case-study from the well-preserved ~5.3-1.6 Ma El Laco deposit, northern Chile, which hosts magnetite mineralisation kin to that of Kiruna-type iron oxide-apatite deposits. Currently, there are two contrasting models proposed to explain formation of the massive magnetite-orebodies, prompting considerable debate in the literature. One of these invokes direct crystallisation from immiscible, Fe-rich melts whereas the other considers transport to surface by so-called “magnetite flotation” during magma degassing. The latter mechanism has been considered sufficiently robust to also explain formation of giant, Kiruna-type deposits. Micron- to nanoscale observations on magnetite from stratabound mineralisation and on magnetite occurring as micron-sized inclusions hosted by hydrothermal hematite, shows that they are genetically linked. Both magnetites host the same nm-scale paired inclusions of clinopyroxenes (augite-pigeonite and/or clinoenstatite) with intergrowths indicative of rapid growth and exsolution at low pressure and relatively high temperatures typical for melts (e.g., basalts). However, pyroxene-bearing magnetite inclusions in the hematite are markedly finer-grained, by roughly one order of magnitude, than magnetite from stratabound mineralisation. The fine magnetite inclusions trapped in hematite display S-bearing coatings and are interpreted to represent the products of magnetite transport from a magma reservoir to surface by a S-bearing vapour-fluid mixture that precipitated the host

hematite. Evidence presented in this chapter represents new nanoscale support for magnetite flotation and also allows for a discrimination between massive and floated magnetite at El Laco. Most importantly for the overall debate, the new evidence allows floatation to be ruled out as a mechanism for large-scale accumulation of Fe in volcanic settings, instead favouring initial magnetite formation out of a melt.

Chapter 9 provides a summary of the key findings and implications of this research. This chapter also highlights several open research questions and potential future avenues of investigation.

Additional material, including supplementary material associated with **Chapters 2** to **8**, co-authored publications, and conference contributions presented during this candidature are compiled in **Chapter 10**. A complete reference list for all chapters is provided in **Chapter 11**.

1.2 References

Allen, S.R., McPhie, J., Ferris, G., Simpson, C., 2008. Evolution and architecture of a large felsic Igneous Province in western Laurentia: The 1.6 Ga Gawler Range Volcanics, South Australia. Journal of Volcanology and Geothermal Research 172, 132–147. https://doi.org/10.1016/j.jvolgeores.2005.09.027

Barton, M.D., 2014. Iron Oxide(–Cu–Au–REE–P–Ag–U–Co) Systems, in: Treatise on Geochemistry. Elsevier, pp. 515–541. https://doi.org/10.1016/B978-0-08-095975-7.01123-2

Blissett, A.H., Creaser, R.A., Daly, S.J., Flint, R.B., Parker, A.J., 1993. Gawler Range Volcanics, in: Drexel, J.F., Preiss, W. V., Parker, A.J. (Eds.), The Geology of South Australia. Vol. 1, The Precambrian, Bulletin 54. Geological Survey of South Australia, pp. 107–124.

Ciobanu, C.L., Verdugo-Ihl, M.R., Slattery, A., Cook, N.J., Ehrig, K., Courtney-Davies, L., Wade, B.P., 2019. Silician Magnetite: Si–Fe-Nanoprecipitates and Other Mineral Inclusions in Magnetite from the Olympic Dam Deposit, South Australia. Minerals 9, 311. https://doi.org/10.3390/min9050311

Ciobanu, C.L., Wade, B.P., Cook, N.J., Schmidt Mumm, A., Giles, D., 2013. Uranium-bearing hematite from the Olympic Dam Cu–U–Au deposit, South Australia: A geochemical tracer and reconnaissance Pb–Pb geochronometer. Precambrian Research 238, 129–147. https://doi.org/10.1016/j.precamres.2013.10.007

Cook, N., Ciobanu, C., George, L., Zhu, Z.-Y., Wade, B., Ehrig, K., 2016. Trace Element Analysis of Minerals in Magmatic-Hydrothermal Ores by Laser Ablation Inductively-Coupled Plasma Mass Spectrometry: Approaches and Opportunities. Minerals 6, 111. https://doi.org/10.3390/min6040111

Courtney-Davies, L., Zhu, Z., Ciobanu, C.L., Wade, B.P., Cook, N.J., Ehrig, K., Cabral, A.R., Kennedy, A., 2016. Matrix-matched iron-oxide laser ablation ICP-MS U-Pb geochronology using mixed solution standards. Minerals 6(3), 85. https://doi.org/10.3390/min6030085

Courtney-Davies, L., Ciobanu, C.L., Verdugo-Ihl, M.R., Dmitrijeva, M., Cook, N.J., Ehrig, K., Wade, B.P., 2019a. Hematite geochemistry and geochronology resolve genetic and temporal links among iron-oxide copper gold systems, Olympic Dam district, South Australia. Precambrian Research 335, 105480. https://doi.org/10.1016/j.precamres.2019.105480

Courtney-Davies, L., Ciobanu, C.L., Richardson, M.W., Prosser, N., Verdugo-Ihl, M., Wade, B.P., Gilbert, S.E., Ehrig, K.J., Cook, N.J., 2019b. Synthesis of U-Pb doped hematite using a hydrated ferric oxide approach. Journal of Crystal Growth 513, 48–57. https://doi.org/10.1016/j.jcrysgro.2019.02.053

Courtney-Davies, L., Tapster, S.R., Ciobanu, C.L., Cook, N.J., Verdugo-Ihl, M.R., Ehrig, K.J., Kennedy, A.K., Gilbert, S.E., Condon, D.J., Wade, B.P., 2019c. A multi-technique evaluation of hydrothermal hematite U Pb isotope systematics: Implications for ore deposit geochronology. Chemical Geology 513, 54–72. https://doi.org/10.1016/j.chemgeo.2019.03.005

Courtney-Davies, L., Ciobanu, C.L., Verdugo-Ihl, M.R., Cook, N.J., Ehrig, K.J., Wade, B.P., Zhu, Z., Kamenetsky, V.S., 2020a. ~1760 Ma magnetite-bearing protoliths in the Olympic Dam deposit, South Australia: Implications for ore genesis and regional metallogeny. Ore Geology Reviews 118, 103337. https://doi.org/10.1016/j.oregeorev.2020.103337

Courtney-Davies, L., Ciobanu, C.L., Tapster, S.R., Cook, N.J., Ehrig, K., Crowley, J.L., Verdugo-Ihl, M.R., Wade, B.P., Condon, D.J., 2020b. Opening the Magmatic-Hydrothermal Window: High-Precision U-Pb Geochronology of the Mesoproterozoic Olympic Dam Cu-U-Au-Ag Deposit, South Australia. Economic Geology, in press. https://doi.org/10.5382/econgeo.4772

Deditius, A.P., Reich, M., Simon, A.C., Suvorova, A., Knipping, J., Roberts, M.P., Rubanov, S., Dodd, A., Saunders, M., 2018. Nanogeochemistry of hydrothermal magnetite. Contributions to Mineralogy and Petrology 173, 46. https://doi.org/10.1007/s00410-018-1474-1

Dmitrijeva, M., Metcalfe, A. V., Ciobanu, C.L., Cook, N.J., Frenzel, M., Keyser, W.M., Johnson, G., Ehrig, K., 2018. Discrimination and Variance Structure of Trace Element Signatures in Fe-Oxides: A Case Study of BIF-Mineralisation from the Middleback Ranges, South Australia. Mathematical Geosciences 50, 381–415. https://doi.org/10.1007/s11004-018-9734-1

Dmitrijeva, M., Ciobanu, C.L., Ehrig, K.J., Cook, N.J., Metcalfe, A. V., Verdugo-Ihl, M.R., McPhie, J., 2019a. Mineralization-alteration footprints in the Olympic Dam IOCG district, South Australia: The Acropolis prospect. Journal of Geochemical Exploration 205, 106333. https://doi.org/10.1016/j.gexplo.2019.106333

Dmitrijeva, M., Ehrig, K.J., Ciobanu, C.L., Cook, N.J., Verdugo-Ihl, M.R., Metcalfe, A. V., 2019b. Defining IOCG signatures through compositional data analysis: A case study of lithogeochemical zoning from the Olympic Dam deposit, South Australia. Ore Geology Reviews 105, 86–101. https://doi.org/10.1016/j.oregeorev.2018.12.013

Dupuis, C., Beaudoin, G., 2011. Discriminant diagrams for iron oxide trace element fingerprinting of mineral deposit types. Mineralium Deposita 46, 319–335. https://doi.org/10.1007/s00126-011-0334-y

Ehrig, K., Kamenetsky, V.S., McPhie, J., Cook, N.J., Ciobanu, C.L., 2017. Olympic Dam iron oxide Cu-U-Au-Ag deposit, in: Phillips, G.N. (Ed.), Australian Ore Deposits. The Australasian Institute of Mining and Metallurgy, Melbourne, pp. 601–610.

Ehrig, K., McPhie, J., Kamenetsky, V., 2012. Geology and Mineralogical Zonation of the Olympic Dam Iron Oxide Cu-U-Au-Ag Deposit, South Australia, in: Hedenquist, J.W., Harris, M., Camus, F. (Eds.), Geology and Genesis of Major Copper Deposits and Districts of the World: A Tribute to Richard H. Sillitoe, Special Publication 16. Society of Economic Geologists, pp. 237–267. https://doi.org/10.5382/SP.16.11

Hitzman, M.W., Oreskes, N., Einaudi, M.T., 1992. Geological characteristics and tectonic setting of Proterozoic iron oxide (Cu-U-Au-REE) deposits. Precambrian Research 58, 241–287. https://doi.org/10.1016/0301-9268(92)90121-4

Huberty, J.M., Konishi, H., Heck, P.R., Fournelle, J.H., Valley, J.W., Xu, H., 2012. Silician magnetite from the Dales Gorge Member of the Brockman Iron Formation, Hamersley Group, Western Australia. American Mineralogist 97, 26–37. https://doi.org/10.2138/am.2012.3864

Keyser, W., Ciobanu, C.L., Cook, N.J., Dmitrijeva, M., Courtney-Davies, L., Feltus, H., Gilbert, S., Johnson, G., Ehrig, K., 2019a. Iron-oxides constrain BIF evolution in terranes with protracted geological histories: The Iron Count prospect, Middleback Ranges, South Australia. Lithos 324–325, 20–38. https://doi.org/10.1016/j.lithos.2018.10.035

Keyser, W., Ciobanu, C.L., Cook, N.J., Feltus, H., Johnson, G., Slattery, A., Wade, B.P., Ehrig, K., 2019b. Mineralogy of Zirconium in Iron-Oxides: A Micron- to Nanoscale Study of Hematite Ore from Peculiar Knob, South Australia. Minerals 9, 244. https://doi.org/10.3390/min9040244

Keyser, W., Ciobanu, C.L., Cook, N.J., Johnson, G., Feltus, H., Johnson, S., Dmitrijeva, M., Ehrig, K., Nguyen, P.T., 2018. Petrography and trace element signatures of iron-oxides in deposits from the Middleback Ranges, South Australia: From banded iron formation to ore. Ore Geology Reviews 93, 337–360. https://doi.org/10.1016/j.oregeorev.2018.01.006

Kontonikas-Charos, A., Ciobanu, C.L., Cook, N.J., Ehrig, K., Krneta, S., Kamenetsky, V.S., 2017. Feldspar evolution in the Roxby Downs Granite, host to Fe-oxide Cu-Au-(U) mineralisation at Olympic Dam, South Australia. Ore Geology Reviews 80, 838–859. https://doi.org/10.1016/j.oregeorev.2016.08.019

Krneta, S., Cook, N.J., Ciobanu, C.L., Ehrig, K., Kontonikas-Charos, A., 2017. The Wirrda Well and Acropolis prospects, Gawler Craton, South Australia: Insights into evolving fluid conditions through apatite chemistry. Journal of Geochemical Exploration 181, 276–291. https://doi.org/10.1016/j.gexplo.2017.08.004

Mauger, A.J., Ehrig, K., Kontonikas-Charos, A., Ciobanu, C.L., Cook, N.J., Kamenetsky, V.S., 2016. Alteration at the Olympic Dam IOCG–U deposit: insights into distal to proximal feldspar and phyllosilicate chemistry from infrared reflectance spectroscopy. Australian Journal of Earth Sciences 63, 959–972. https://doi.org/10.1080/08120099.2016.1264474

McPhie, J., Ehrig, K.J., Kamenetsky, M.B., Crowley, J.L., Kamenetsky, V.S., 2020. Geology of the Acropolis prospect, South Australia, constrained by high-precision CA-TIMS ages. Australian Journal of Earth Sciences 67(5), 699-716. https://doi.org/10.1080/08120099.2020.1717617

Oreskes, N., 1990. Uranium content of Olympic Dam hematite: Implications for fluid chemistry and ore depositional mechanisms. Program with Abstracts, 8th Quadrennial IAGOD Conference, Ottawa, Canada, p. A137.

Ovalle, J.T., La Cruz, N.L., Reich, M., Barra, F., Simon, A.C., Konecke, B.A., Rodriguez-Mustafa, M.A., Deditius, A.P., Childress, T.M., Morata, D., 2018. Formation of massive iron deposits linked to explosive volcanic eruptions. Scientific Reports 8, 14855. https://doi.org/10.1038/s41598-018-33206-3

Reid, A., 2019. The Olympic Cu-Au Province, Gawler Craton: A Review of the Lithospheric Architecture, Geodynamic Setting, Alteration Systems, Cover Successions and Prospectivity. Minerals 9, 371. https://doi.org/10.3390/min9060371

Sillitoe, R.H., Magaranov, G., Mladenov, V., Creaser, R.A., 2020. Rosen, Bulgaria: A newly recognized iron oxide-copper-gold district. Economic Geology 104, 897–904. https://doi.org/10.5382/econgeo.4731

Skirrow, R.G., Bastrakov, E.N., Barovich, K., Fraser, G.L., Creaser, R.A., Fanning, C.M., Raymond, O.L., Davidson, G.J., 2007. Timing of Iron Oxide Cu-Au-(U) Hydrothermal Activity and Nd Isotope Constraints on Metal Sources in the Gawler Craton, South Australia. Economic Geology 102, 1441–1470. https://doi.org/10.2113/gsecongeo.102.8.1441

Tornos, F., Velasco, F., Hanchar, J.M., 2016. Iron-rich melts, magmatic magnetite, and superheated hydrothermal systems: The El Laco deposit, Chile. Geology 44, 427–430. https://doi.org/10.1130/G37705.1

Verdugo-Ihl, M.R., Ciobanu, C.L., Cook, N.J., Ehrig, K.J., Courtney-Davies, L., Gilbert, S., 2017. Textures and U-W-Sn-Mo signatures in hematite from the Olympic Dam Cu-U-Au-Ag deposit, South Australia: Defining the archetype for IOCG deposits. Ore Geology Reviews 91, 173–195. https://doi.org/10.1016/j.oregeorev.2017.10.007

Verdugo-Ihl, M.R., Ciobanu, C.L., Slattery, A., Cook, N.J., Ehrig, K., Courtney-Davies, L., 2019. Copper-Arsenic Nanoparticles in Hematite: Fingerprinting Fluid-Mineral Interaction. Minerals 9, 388. https://doi.org/10.3390/min9070388

Verdugo-Ihl, M.R., Ciobanu, C.L., Cook, N.J., Ehrig, K.J., Courtney-Davies, L., 2020a. Defining early stages of IOCG systems: evidence from iron oxides in the outer shell of the Olympic Dam deposit, South Australia. Mineralium Deposita 55, 429–452. https://doi.org/10.1007/s00126-019-00896-2

Verdugo-Ihl, M.R., Ciobanu, C.L., Cook, N.J., Ehrig, K., Slattery, A., Courtney-Davies, L., 2020b. Trace element remobilisation from W-Sn-U-Pb zoned hematite: Nanoscale insights into open system behaviour of a mineral geochronometer. Mineralogical Magazine 84(4), 502–516. https://doi.org/10.1180/mgm.2020.49

Verdugo-Ihl, M.R., Courtney-Davies, L., Ciobanu, C.L., Cook, N.J., Ehrig, K., Tornos, F., Hanchar, J.M., submitted, a. Hematite U-Pb age constraints on the timing of IOCG mineralization along the Atacama Fault Zone, Chile. Abstract, SEG 2020 Vision, Celebrating a Century of Discovery, September 15-18. Whistler, B.C., Canada.

Verdugo-Ihl, M.R., Ciobanu, C.L., Cook, N.J., Ehrig, K., Slattery, A., Courtney-Davies, L., Dmitrijeva, M. Nanomineralogy of hydrothermal magnetite from Acropolis, South Australia: Genetic implications for iron-oxide copper gold mineralization. American Mineralogist, in press. https://doi.org/10.2138/am-2020-7557.

Verdugo-Ihl, M.R., Ciobanu, C.L., Cook, N.J., Ehrig, K., Slattery, A., Courtney-Davies, L., in review b. Ferro-tschermakite with short range disorder identified in silician magnetite. American Mineralogist.

Verdugo-Ihl, M.R., Ciobanu, C.L., Cook, N.J., Tornos, F., Ehrig, K., Slattery, A., Xu, J., Courtney-Davies, L., Hanchar, J.M., in revision c. Vapour transport of magnetite in volcanoes: evidence from igneous pyroxene pair inclusions and S-bearing sublimate coatings. Earth and Planetary Science Letters.

Xu, H., Shen, Z., Konishi, H., 2014. Si-magnetite nano-precipitates in silician magnetite from banded iron formation: Z-contrast imaging and ab initio study. American Mineralogist 99, 2196–2202. https://doi.org/10.2138/am-2014-4964

CHAPTER 2

TEXTURES AND U-W-SN-MO SIGNATURES IN HEMATITE FROM THE OLYMPIC DAM CU-U-AU-AG DEPOSIT, SOUTH AUSTRALIA: DEFINING THE ARCHETYPE FOR IOCG DEPOSITS

Max R. Verdugo-Ihl [1], Cristiana L. Ciobanu [1], Nigel J. Cook [1],

Kathy J. Ehrig [2], Liam Courtney-Davies [1], and Sarah Gilbert [3]

[1]*School of Chemical Engineering, The University of Adelaide, Adelaide, SA 5005, Australia;*

[2]*BHP Olympic Dam, Adelaide, SA 5000, Australia;*

[3]*Adelaide Microscopy, The University of Adelaide, Adelaide, SA 5005, Australia*

Article published in *Ore Geology Reviews* (2017) 91:173−195.

Statement of Authorship

Title of Paper	Textures and U-W-Sn-Mo signatures in hematite from the Olympic Dam Cu-U-Au-Ag deposit, South Australia: Defining the archetype for IOCG deposits
Publication Status	☑ Published ☐ Accepted for Publication ☐ Submitted for Publication ☐ Unpublished and Unsubmitted w ork w ritten in manuscript style
Publication Details	Verdugo-Ihl, M.R., Ciobanu, C.L., Cook, N.J., Ehrig, K.J., Courtney-Davies, L., Gilbert, S., 2017. Textures and U-W-Sn-Mo signatures in hematite from the Olympic Dam Cu-U-Au-Ag deposit, South Australia: Defining the archetype for IOCG deposits. Ore Geology Reviews 91, 173–195, https://doi.org/10.1016/j.oregeorev.2017.10.007.

Principal Author

Name of Principal Author (Candidate)	Max R. Verdugo-Ihl		
Contribution to the Paper	Performed analytical work, evaluation and interpretation of results and prepared the manuscript.		
Overall percentage (%)	60		
Certification:	This paper reports on original research I conducted during the period of my Higher Degree by Research candidature and is not subject to any obligations or contractual agreements with a third party that would constrain its inclusion in this thesis. I am the primary author of this paper.		
Signature		Date	15.04.2020

Co-Author Contributions

By signing the Statement of Authorship, each author certifies that:

i. the candidate's stated contribution to the publication is accurate (as detailed above);

ii. permission is granted for the candidate in include the publication in the thesis; and

iii. the sum of all co-author contributions is equal to 100% less the candidate's stated contribution.

Name of Co-Author	Cristiana L. Ciobanu		
Contribution to the Paper	Helped to define the direction of the manuscript, guided manuscript preparation and assisted with the interpretation of the results and evaluation of the manuscript.		
Overall percentage (%)	20		
Signature		Date	15.04.2020

Name of Co-Author	Nigel J. Cook		
Contribution to the Paper	Assisted with the preparation and evaluation of the manuscript.		
Overall percentage (%)	10		
Signature		Date	15.04.2020

Name of Co-Author	Kathy J. Ehrig		
Contribution to the Paper	Assisted with the evaluation of the manuscript.		
Overall percentage (%)	5		
Signature		Date	15.04.2020

Name of Co-Author	Liam Courtney-Davies		
Contribution to the Paper	Assisted with data collection.		
Overall percentage (%)	2.5		
Signature		Date	15.04.2020

Name of Co-Author	Sarah Gilbert		
Contribution to the Paper	Assisted with acquisition and processing of LA-ICP-MS data.		
Overall percentage (%)	2.5		
Signature		Date	15.04.2020

Ore Geology Reviews 91 (2017) 173–195

Contents lists available at ScienceDirect

Ore Geology Reviews

journal homepage: www.elsevier.com/locate/oregeorev

Textures and U-W-Sn-Mo signatures in hematite from the Olympic Dam Cu-U-Au-Ag deposit, South Australia: Defining the archetype for IOCG deposits

Max R. Verdugo-Ihl[a,*], Cristiana L. Ciobanu[a], Nigel J. Cook[a], Kathy J. Ehrig[b], Liam Courtney-Davies[a], Sarah Gilbert[c]

[a] School of Chemical Engineering, The University of Adelaide, Adelaide, SA 5000, Australia
[b] BHP Olympic Dam, Adelaide, SA 5000, Australia
[c] Adelaide Microscopy, The University of Adelaide, Adelaide, SA 5000, Australia

ARTICLE INFO

Keywords:
Hematite
Trace elements
U-W-Sn-Mo compositional zoning
Olympic Dam
Iron-oxide copper gold deposits
Laser ablation inductivcly coupled plasma mass spectrometry

ABSTRACT

The textural characteristics and trace element geochemistry of hematite with U-W-Sn-Mo signatures from the Cu-U-Au-Ag orebody at Olympic Dam, South Australia, are documented. Olympic Dam is the archetype for iron-oxide copper–gold (IOCG) deposits where hematite is by far the most abundant mineral in the orebody. The deposit is located within hematite-bearing breccias (> 5% Fe) hosted by the ~1.6 Ga Roxby Downs Granite (RDG). Although such breccias are mostly derived from RDG, they also include volcanic clasts and sedimentary rocks. Samples cover the ~6 km strike length and ~2 km vertical extent of mineralisation, including hematite from the aforementioned lithologies. Hematite with U-W-Sn-Mo ('granitophile' elements) signatures is recognised throughout all lithologies and parts of the deposit. Hematite enriched in granitophile elements is represented by a variety of textures, of which zoned hematite, defined by oscillatory zonation patterns, is the most prominent and can be tied to the age of the RDG, and thus initiation of the IOCG system as confirmed by published U-Pb geochronology. Other categories of hematite with granitophile signatures include hematite resulting from replacement of pre-existing minerals (e.g., carbonates and feldspars), as well as replacement of previous oscillatory-zoned hematites. Matrix and vacuole filling hematite from volcanoclastic-dominated intervals also carry 'granitophile' signatures. In addition, some colloform types which likely post-date primary IOCG mineralisation are also rich in 'granitophile' elements. Trace element mapping and spot analysis by laser ablation inductively coupled plasma mass spectrometry (LA-ICP-MS) defines complex trace element signatures of hematite, which, in addition to the 'granitophile' elements, also comprise rare earth elements, high field strength elements, chalcogens and transition metals.

The distinct geochemical signature, characterised by enrichment in the 'granitophile' elements (up to wt% levels of U and W within individual zones, and up to thousands of ppm Mo and Sn) prevails throughout the hematite in the deposit irrespective of textures. Iron-oxides have been repeatedly formed, reworked and overprinted by subsequent cycles of brecciation, fluid-mineral reaction, remobilization, element redistribution and recrystallisation. Coupled dissolution-replacement reactions are discussed as having played a major role in the modification of textural and geochemical patterns in hematite, but also allow for widespread preservation of primary geochemical signatures. Despite its simple chemistry, the crystal-structural modularity of hematite can adapt and retain evolving fluid signatures. The reported trace element signatures are fully concordant with conceptual frameworks for the genesis of IOCG systems, and may be an inherent, albeit hitherto under-reported characteristic of other IOCG systems. Hematite is probably by far the most important W-, Sn- and Mo-bearing phase in the deposit by mass.

1. Introduction

An inherent feature of all iron-oxide copper gold (IOCG) deposits is the abundance of Fe-oxides, as either hematite (α-Fe_2O_3) and/or magnetite (Fe_3O_4), generally making the Fe-oxides by far the most dominant minerals (Hitzman et al., 1992). Iron-oxides are valuable sources of petrogenetic information, as they commonly contain trace elements at measurable concentrations, with patterns and variations among these trace elements that reflect evolving physiochemical conditions.

* Corresponding author.
E-mail address: max.verdugoihl@adelaide.edu.au (M.R. Verdugo-Ihl).

http://dx.doi.org/10.1016/j.oregeorev.2017.10.007
Received 11 August 2017; Received in revised form 8 October 2017; Accepted 10 October 2017
Available online 12 October 2017
0169-1368/ © 2017 Elsevier B.V. All rights reserved.

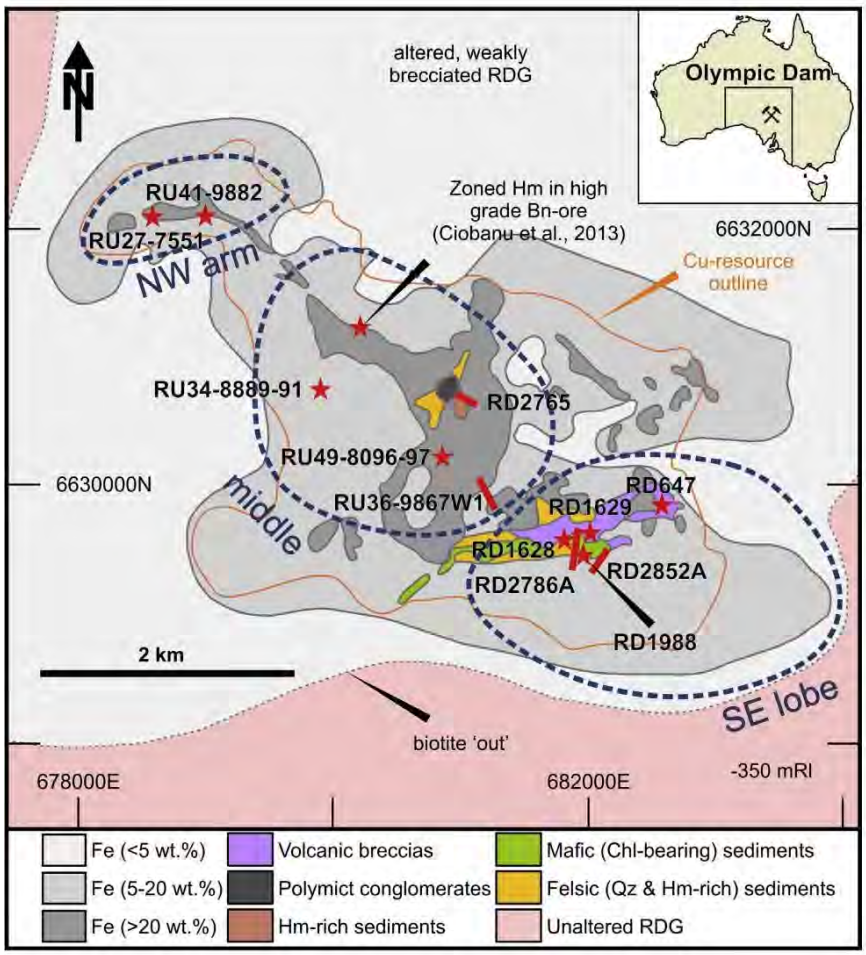

Fig. 1. Simplified geological sketch outlining the Olympic Dam Breccia Complex after Ehrig et al. (2012), indicating locations of sampled drillholes (stars: vertical drillhole; rectangles: oriented drillholes) and the distribution of main lithological units. The simplified map is projected at the −350 m RL mine grid below surface.

Recent literature is largely focused on trace element studies of mineral signatures by laser-ablation inductively-coupled plasma mass spectrometry (LA-ICP-MS; Cook et al., 2016 and references therein). Trace element signatures of magnetite from end-member IOCG deposits *sensu lato*, such as Kiruna (Sweden) and El Laco (Chile), have been obtained to constrain the debate on their magmatic versus hydrothermal origins (e.g., Dare et al., 2015; Knipping et al., 2015a,b; Broughm et al., 2017). Except for preliminary studies of hematite from Olympic Dam (OD) and satellite deposits such as Island Dam (e.g., Ciobanu et al., 2013, 2015; Cook et al., 2016; Keyser et al., 2017; Verdugo-Ihl et al., 2017), trace element geochemistry of Fe-oxides from IOCG-systems *sensu stricto*, and specifically hematite have not been studied in any great detail, despite being the main products of hydrothermal alteration, and therefore closely associated with the mineralising processes itself. The aforementioned studies have shown that hematite can incorporate a wide range of trace elements, including high field strength elements (HFSE), rare earth elements (REE) and Y (hereafter REY) and that these compositions vary with textures, location in the deposit and interconversion with magnetite. But more notable, oscillatory-zoned hematite from OD stands out by its enrichment in U (and radiogenic Pb), W, Sn, and Mo (hereafter 'granitophile' elements) (Ciobanu et al., 2013, 2015; Cook et al., 2016; Verdugo-Ihl et al., 2017). The incorporation of U and its decay products within the lattice of zoned hematite facilitates its use as a mineral geochronometer for directly dating hydrothermal ore-forming processes in IOCG deposits (Ciobanu et al., 2013; Courtney-Davies et al., 2016, 2017).

In this contribution, we document textural characteristics and trace element geochemistry of hematite from the Cu-U-Au-Ag orebody at OD (Ehrig et al., 2012), South Australia, the largest known IOCG system on Earth and considered the archetype of the IOCG deposit class (Hitzman et al., 1992). We address the petrography and trace element geochemistry of OD hematite, with emphasis on distinctive types enriched in U, W, Mo and Sn, which often display spectacular grain-scale compositional zonation. Other sub-types of hematite with granitophile-rich signatures are also documented as they can help track the sequence of incorporation and remobilisation of such elements during deposit evolution. The combination of textural and trace element data offers insights into the processes responsible for the genesis and overprinting of IOCG-deposits, as well as providing a temporal context for regional metallogenic events.

2. Geological background

Olympic Dam is a Cu-U-Au-Ag deposit (10,400 Mt @ 0.77% Cu, 250 ppm U_3O_8, 1 ppm Ag and 0.32 ppm Au; BHP Billiton, 2016) located in the central-northern part of the Olympic Cu-Au Province, South Australia. The Olympic Cu-Au Province is a N-S-trending metallogenic belt that extends ca. 700 km along the eastern margin of the Archean to Mesoproterozoic Gawler Craton. IOCG-style mineralisation in the province is spatially- and temporally-associated with a magmatic event at

~1.6–1.58 Ga that derived in the formation of a silicic large igneous province, encompassing the Hiltaba Suite (HS) and co-magmatic, bimodal Gawler Range Volcanics (GRV) (Fanning et al., 1988). These magmatic rocks intruded and unconformably overlie basement units, which in the OD district correspond to metasedimentary rocks of the Hutchison Group, deformed granitoids of the Donington Suite (ca. 1.85–1.81 Ga), and Wallaroo Group equivalents (ca. 1.76–1.74 Ga).

The deposit is hosted within the Olympic Dam Breccia Complex (ODBC; Reeve et al., 1990), which is confined to the Roxby Downs Granite (RDG; Fig. 1), an altered HS granitoid considered to form at a depth of 6–8 km (Creaser, 1989; Kontonikas-Charos et al., 2017a). Proximal to the deposit, the RDG displays a gradational continuum from altered, through fractured to brecciated lithologies, associated with an increase in the degree of Fe-metasomatism and multiple episodes of brecciation and replacement. The deposit formed beneath, and partly within, an active sedimentary basin, as indicated by locally well-preserved fragments of subaqueous sedimented facies incorporated within the breccias (McPhie et al., 2011, 2016). At least two generations of predominantly mafic-ultramafic dykes occur in the deposit: an early generation of GRV-associated dykes, roughly synchronous with IOCG mineralisation (Huang et al., 2016); and superimposed dolerites affiliated to ~820 Ma Gairdner Dyke swarms (Huang et al., 2015). At the deposit scale, OD is mineralogically zoned, featuring a roughly concentric vertical and lateral zonation with respect to Cu(-Fe)-sulphides from an outer/deeper pyrite-chalcopyrite (Py-Cp) zone through chalcopyrite-bornite (Cp-Bn) to a bornite-chalcocite (Bn-Cc) zone enclosing the largely sulphide-barren inner core (Ehrig et al., 2012). Such a pattern is considered to represent a primary feature of hypogene ore precipitation (Ciobanu et al., 2017). Additionally, a polymetallic signature is recognised at deposit margins (galena, sphalerite, and fahlores in the SE lobe). Unlike the sulphides, the distribution of U-minerals (uraninite, coffinite and brannerite) does not appear to follow a systematic deposit-scale zonation, although the proportion of uraninite tends to increase with Fe content (Ehrig et al., 2012).

Within the orebody, hematite is the main Fe-oxide, irrespective of sulphide zone, although magnetite can be locally dominant at depth and at deposit margins (Ehrig et al., 2012; Ciobanu et al., 2015). Copper grade broadly correlates with the intensity of Fe-metasomatism, meaning that the resource outline coincides with Fe-rich domains (Fig. 1).

High-precision U-Pb dating of magmatic and hydrothermal zircon in the RDG and ODBC shows that the earliest stages of brecciation and hydrothermal alteration are coeval with RDG crystallisation at ~1594 Ma (e.g., Jagodzinski, 2005). This temporal constraint is supported by U-Pb geochronological data for oscillatory-zoned hematite from two locations in the deposit, which overlap with the zircon ages (Ciobanu et al., 2013; Courtney-Davies et al., 2016).

3. Sampling approach

The present study was carried-out on a sample suite (58 hand specimens derived from 17 drillholes) representative of hematite in the ODBC throughout the ~6 km strike length through the SE lobe, the middle, and the NW arm and ~2 km depth of the deposit in the SE lobe (Table 1; Figs. 1 and 2; Electronic Appendix Fig. A1). The sampled lithologies include: (i) granite-rich breccias, generally clast-supported, containing fine-grained hematite as a matrix component and variably-altered granitic clasts; (ii) matrix-supported hematite-rich breccias, containing abundant hematite as clasts/replacements, but also as matrix/infill, and more intensely reworked clasts of granitic composition, in addition to rock-flour that may show fluidization textures; (iii) heterolithic breccias, containing hematite, altered granite and pervasively altered volcanic clasts occasionally displaying irregular, amoeboid-like margins, some of which are GRV-derived. The sample suite also contains all representative ore types (Electronic Appendix Fig. A1a–e), including high-grade bornite- and chalcocite-ores from the NW arm and middle parts of the deposit, respectively. In addition, sedimentary rocks comprising bedded clastic facies with hematite-rich, silty-sandstones with gradational or faulted contacts to hematite-rich breccia (Electronic Appendix Fig. A1f, g) were sampled from the upper part of the deposit in the SE lobe and from the sulphide-poor middle part of the deposit. Drillhole RD647 in the SE lobe is representative for thicker sequences of breccias with volcanic clasts. Those samples richest in hematite occur towards the centre of deposit and are characterized by the presence of different textural types of hematite cemented in a highly porous matrix consisting predominantly of finer hematite, minor amounts of other gangue components, and generally lack Cu(-Fe)-sulphides.

Although not continuously sampled across the 2 km vertical extent of the mineralisation, the deepest Cp-Py zone is sampled from the last 150 m in drillhole RD1988 whereas the uppermost Cp-Bn and Bn-Cc zones are sampled from ~300 m in drillhole RD2852A (Fig. 2a, b). In the latter, a sulphide-poor, Au-rich interval occurs underneath the Bn-Cc zone. A third, low-angle drillhole, RD2786A, intersecting deeper mineralisation from RD1988 was sampled as it contains one of the most diverse lithologies, including sedimentary rocks, granites, altered mafic dikes, etc. Both RD2786A and RD2852A drillholes intersect mineralisation with a pronounced polymetallic mineral signature (tennantite-dominant fahlores are present). A selection of representative elements are plotted from whole rock assays (data from BHP Olympic Dam; see also Ehrig et al., 2012) to show correlation with lithologies and sampled intervals (Fig. 2). Both Sn and W concentrations show a strong correlation with increasing Fe content in the SE lobe (Fig. 2d, e).

4. Methodology

One-inch diameter polished blocks were prepared and subsequently examined in reflected light microscopy and using a FEI Quanta 450 scanning electron microscope (SEM) equipped with a back-scattered electron (BSE) detector and an energy dispersive X-ray spectrometer (EDS). All instrumentation is housed at Adelaide Microscopy, The University of Adelaide. A small volume of electron probe data was collected to verify compositional zonation patterns using a Cameca SX-Five Electron Probe Microanalyzer operated at 15 kV and 20 nA. Details of standards, wavelengths and minimum limits of detection are given in Electronic Appendix B.

The main body of trace element data reported here was obtained by laser-ablation inductively-coupled plasma mass spectrometry (LA-ICP-MS) operating in spot analysis mode, using a RESOlution-LR 193 nm excimer laser microprobe coupled to an Agilent 7700cx Quadrupole ICP-MS. The analysed grains were pre-selected for LA-ICP-MS analysis based on textures, compositional zonation and relationships with co-existing minerals. Methodology followed established practices in the same laboratory (e.g., Ciobanu et al., 2013; Ismail et al., 2014; Xu et al., 2016). Details of operating conditions, reference standards and isotopes measured are given in Electronic Appendix B. Beam size varied from 29 to 51 μm, with 43 μm most commonly used for zoned hematite, depending upon the size and homogeneity of the analysed domains or grains. The reference materials BHVO-2G, GSD-1G and NIST-610 were used as external standards. Analysis time for each spot analysis was a uniform 60 s, comprising a 30-s measurement of background (laser-off), and 30-s analysis of the unknown (laser-on). All data reduction was performed using Glitter software (van Achterbergh et al., 2001). Internal calibration was achieved using ideal stoichiometric concentration of Fe in hematite as FeO in wt% (89.9810). For comparative purposes, concentrations below minimum limit of detection (< mdl) were treated as equal to that mdl value.

Element mapping by LA-ICP-MS was conducted using the same instrument by ablating sets of parallel line rasters in a grid across an area in the sample using laser repetition rates of 10 Hz and a fluence of 3.5 J/cm^{-2}. Beam sizes of 7 and, more commonly, 11 μm, and scan speeds of 7 and 11 μm/s respectively were chosen, resulting in the desired sensitivity of the elements of interest and adequate spatial

Table 1
Sample list and key characteristics.

Deposit area	Drillhole	Sample	Depth (m)	Sulphide-zone	Key characteristics
SE lobe	RD1988	RX7293B	1618.5	Cp-Bn	
		RX7294GM/BW	1768.7	Py-Cp	
		RX7295GM/BW	1808.8	Py-Cp	
	RD2786A	LCD02	1772	Py-Cp	
		MV023	1772.3	Py-Cp	
		MV024	1783	Py-Cp	
		LCD03	1785	Py-Cp	
		LCD04/MV025	1808.2	Cp-Bn	
		LCD05	1821.5	Cp-Bn	
		MV026	1826.2	Py-Cp	
		LCD06	1898.7	Cp-Bn	Sedimentary facies
		MV027	1908.1	Cp-Bn	Sedimentary facies
		LCD07	1930	Cp-Bn	
		MV031	1950.10	Py-Cp	
		MV032	1989.1	Cp-Bn	
		MV034	2062.3	Cp-Bn	
		MV028	2109.4	Py-Cp	
		LCD09	2133.4	Py-Cp	Sedimentary facies
	RD2852A	RX6581	419.5	Bn-Cc	
		RX6583	488	Bn-Cc	
		RX6584	489.3	Bn-Cc	
		RX6585	490.4	Bn-Cc	
		RX6587	548.4	Bn-Cc	
		RX6601	617.2	Bn-Cc	
		RX6607	658.3	Bn-Cc	
		RX6609	679.5	Bn-Cc	
		RX6610	680.3	Cp-Bn	
		RX6612	682.3	Cp-Bn	
		RX6626	789.3	Cp-Bn	
	RD647	MV092	379.4	Sulphide-poor	
		LCD32	651.4	Cp-Bn	
		MV093A/B	757.4	Sulphide-poor	Granoblastic hematite filling vacuole(?)
		MV094	819.7	Sulphide-poor	
		LCD35	821.8	Sulphide-poor	
	RD1628	LCD36	507.9	Sulphide-poor	Fine-grained sedimentary fragments
		LCD39	665	Sulphide-poor	Fine-grained sedimentary fragments
	RD1629	CLC109	705	Sulphide-poor	Fine-grained sedimentary fragments
Middle	RU36-9867W1	MV095	119.2	Sulphide-poor	
		MV096	145.8	Sulphide-poor	
		MV097	177.2	Sulphide-poor	
		MV099	349	Cp-Bn	
		MV100	384.8	Py-Cp	
	RU49-8096	CLC046	220.15	Cp-Bn	
		CLC047	226.15	Cp-Bn	
	RU49-8097	CLC050B	93.5	Bn-Cc	
	RD2765	MV103	509.8	Sulphide-poor	
		MV104	583.5	Sulphide-poor	
		MV101	650.60	Sulphide-poor	Sedimentary facies
		MV105	665.30	Sulphide-poor	
	RU34-8889	CLC052	28.25	Bn-Cc	
	RU34-8890	CLC053A/B	26.3	Bn-Cc	
		CLC054A/B	26.75	Bn-Cc	
	RU34-8891	CLC055	34.5	Bn-Cc	
		CLC056	41.5	Bn-Cc	
	Hand specimen	CLC057	Underground (unlocated)	Cp-Bn	
NW arm	RU41-9882	CLC201A/B/C	62.85	Cp-Bn	
	RU27-7551	MV043	187.60	Bn-Cc	
		MV048	336.7	Cp-Bn	

resolution. Re-deposition during mapping was minimized by pre-ablating each line prior to data collection. A 10-s background acquisition was acquired at the start of each line and, to allow for cell wash-out, gas stabilization and computer processing, a delay of 20 s was used after each line. Spot analyses, with acquisition of 60 s signal (laser-on), were conducted on the standards at the start and end of each mapping run.

Individual line-profiles were processed together and compiled into 2-D images displaying the combined background-subtracted intensities for each element using the program Iolite (e.g., Woodhead et al., 2007).

5. Petrography and trace element distribution in granitophile-rich hematite

Petrographic aspects and LA-ICP-MS maps showing grain-scale trace element distributions for the U-(Pb)-W-Sn-Mo-rich hematite in the Olympic Dam orebody are shown in Figs. 3–12, and Electronic Appendix Figs. A1, 3–9. This type of hematite is identified in several textural categories with variable concentrations of U + Pb + W + Sn + Mo and with different concentrations of the individual elements relative to one another (Electronic Appendix C; see also below).

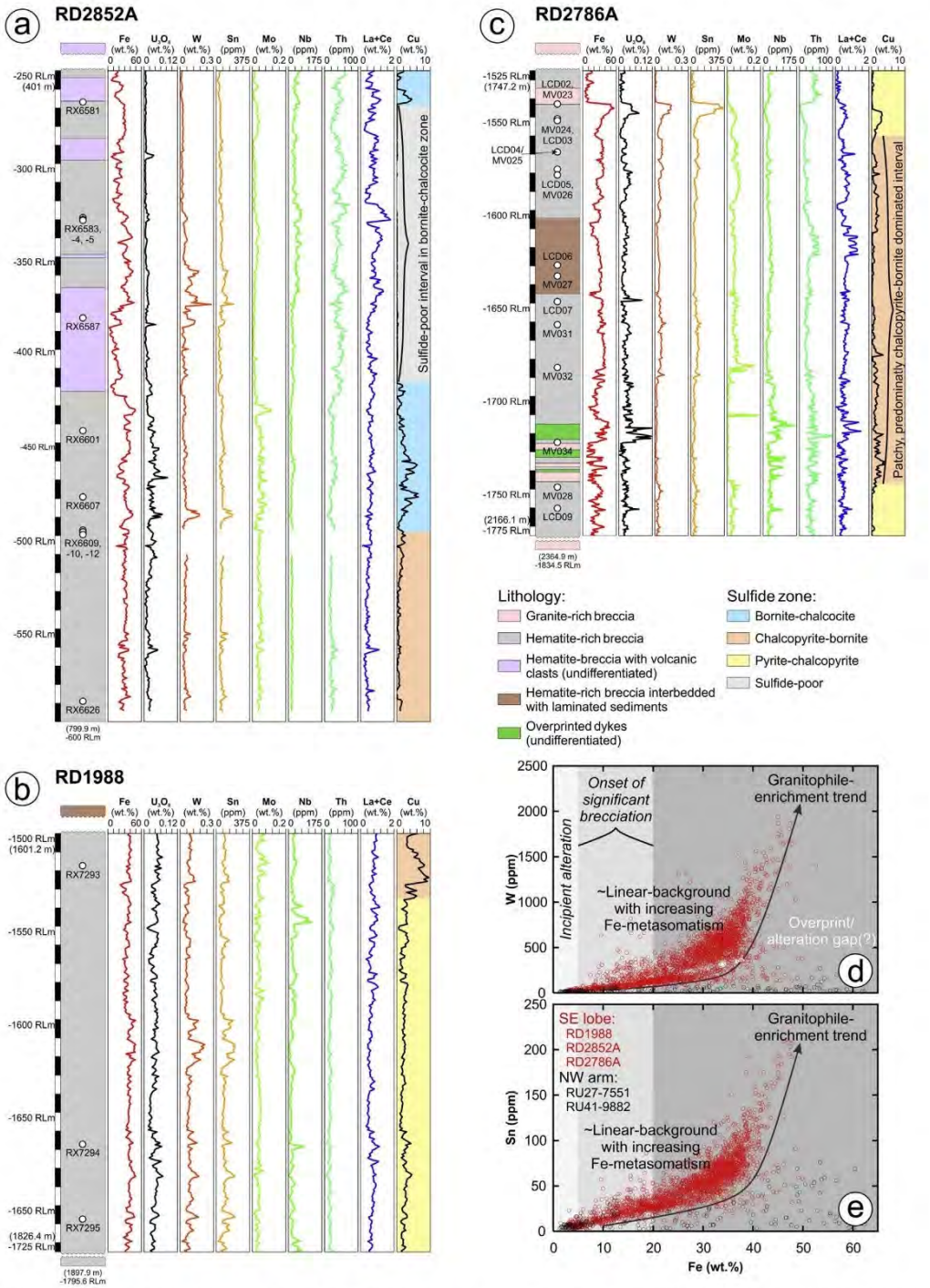

Fig. 2. Simplified drillhole logs showing schematic representations of profiles for selected elements and lithologies: (a) RD2852A; (b) RD1988; and (c) RD2786A. Whole-rock assay data was generally collected at ~1 m intervals. Note the locally good correlation between Fe and W, which is also mimicked by Sn enrichment. For comparative purposes, drillhole logs were projected on the absolute mine-grid depth (RLm) as both RD2852A and RD2786A are drilled sub-vertically. Whole-rock assay data for (d) W *vs.* Fe, and (e) Sn *vs.* Fe.

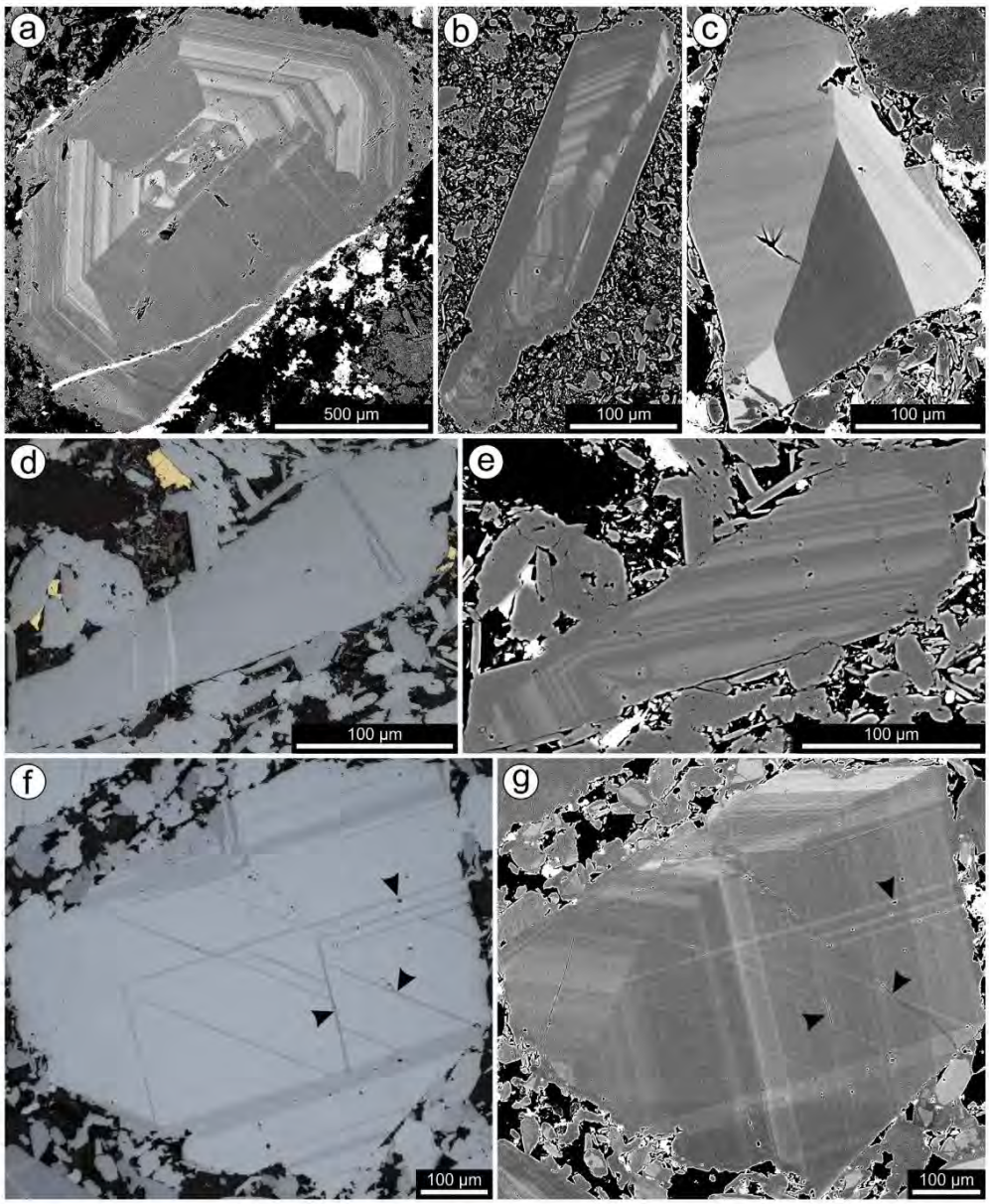

Fig. 3. Back-scattered electron (BSE) (a–c, e, g) and reflected light (d, f) microphotographs of oscillatory-zoned hematite showing types of zonation patterns and twinning. (a) Basal section of a euhedral, coarse-grained oscillatory-zoned hematite cross-cut by a barite veinlet (bright). Note the presence of darker domains (LA-ICP-MS maps in Fig. 9; sample was repolished). (b) Section approximately parallel to the *c*-axis showing a zonation pattern attributable to changes in the growth habit. (c) Reworked zoned hematite fragment (note slightly rounded edges), showing strong BSE-intensity contrast between different domains; note faint chemical-oscillations are still recognizable. (d–g) Relationships between sets of twins and zonation patterns. Note 3-sets of twins in (f), of which one has the direction of the chemical pattern, the other two are clearly visible on the BSE image. (e) Same grain as previous. Hematite overgrowths can be distinguished from the zoned domain. Set of twins, not recognizable in BSE image, cross-cut the zonation pattern and the overgrowth.

5.1. Categories of granitophile-rich hematite

The distinct categories of granitophile-rich hematite are separated by prevailing textures as follows: (1) grain-scale oscillatory and/or sectorial zonation patterns – **zoned hematite** (Fig. 3); (2) hematite that replaces either siderite and/or ankerite **(carbonate replacement hematite**, 2a**),** or feldspars (**feldspar replacement hematite**, 2b) (Fig. 4a, b); (3) **granoblastic hematite** aggregates, which fill vugs in volcanic clasts (Fig. 5a; Electronic Appendix Fig. A1d); (4) **matrix fine-grained hematite** in volcanoclastic breccias (Fig. 4b); (5) **colloform/crustiform hematite** (Fig. 5c–e); and (6) secondary hematite replacing zoned hematite (**overprinted zoned hematite**).

All the above categories of hematite occur within hydrothermal breccias that also comprise other minerals, including Cu-(Fe)-sulphides and gangue phases, such as quartz, sericite, barite, carbonates, fluorite and accessory minerals, which vary in abundance. The accessory minerals are commonly represented by U- and REE-minerals, as well as others (e.g., zircon, rutile, and rare tourmaline). In addition, there are

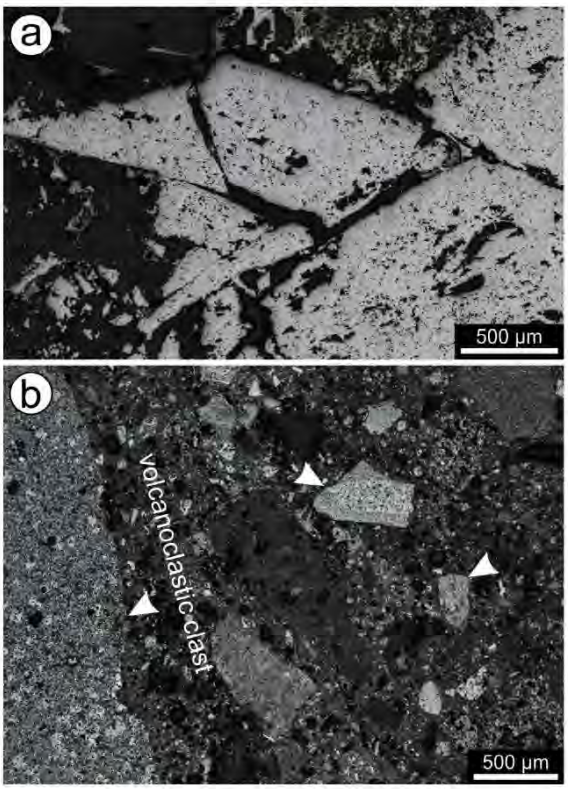

Fig. 4. Reflected-light microphotographs showing replacement hematite categories. (a) Carbonate replacement hematite showing fine-grained hematite filling coarse grains with rhombic, euhedral habit (inferred as carbonates). (b) Feldspar replacement hematite (arrowed), displaying core-to-rim zonation within volcanoclastic breccia; note also the fine-grained matrix hematite.

variable amounts of hematite poor in trace elements present in any sample containing the granitophile-rich hematite categories we focus on here. Such hematite is generally porous when replacing clasts or pre-existing minerals, occurs as single or lamellar aggregates within the breccia matrix, and often forms μm-sized, stubby grains as rims or inclusions within sulphides. Except for the stubby type, none of the other categories are readily distinguishable from some of the granitophile-rich categories studied here.

Several categories of granitophile-rich hematite are fine-grained aggregates that fill 'shapes', with morphology and/or characteristics attributable to pseudomorphic replacement of pre-existing minerals, either precursors to zoned hematite (carbonates, feldspars; categories 2a and b, respectively), or postdating an earlier generation of zoned hematite (overprinted zoned hematite; category 6). In the latter, relicts of non-replaced hematite can be occasionally recognised by their conspicuous zoning. Some categories of granitophile-rich hematite are not widespread across the deposit. For example, the carbonate-replacement type is presented only in samples from high-grade chalcocite ores in the middle part of the deposit (drillholes RU34-8889-91). This type stands out by its occurrence as fine aggregates that fill coarser (mm- to cm-sized) grains (Fig. 4a; Electronic Appendix Fig. A1e). In contrast, one of the widest ranges of texture is displayed by hematite from volcanoclastic breccias from the SE lobe (drillhole RD647; Figs. 4b and 5; Electronic Appendix Fig. A1d). These include fine-grained hematite filling subhedral grains with core-to-rim zonation suggestive of pseudomorphically replaced feldspar phenocrysts (category 2b; Fig. 4b), and aggregates of polygonal hematite occurring throughout mm-size clasts, hinting at vacuole filling (category 3; Fig. 5a). The latter hematite displays a 'basket-weave' texture (Fig. 5b). The nature of such a texture is the subject of nanoscale investigation.

Colloform hematite is fine-grained and occurs as crusts or radial aggregates around vugs, cementing earlier generations of lamellar hematite in the sericite (± Fe-rich chlorite) matrix (NW arm; drillhole RU27-7551; Fig. 5c–d), or within reworked breccia fragments elsewhere in the deposit. The colloform bands can develop concentric growth-zoning by subsequent cycles of precipitation, marked by differences in their width but otherwise homogeneous, and seemingly devoid of inclusions (Fig. 5f–e).

Zoned hematite (category 1), the main focus of the present study, is by far the richest in granitophile elements and has been studied throughout the entire deposit. Other categories, although they may have wider occurrence, are only included for purposes of comparison and assessment of the zoned category. Zoned hematite is most abundant within the SE-lobe, irrespective of the lithological complexity (sedimentary rocks, volcanoclastic breccias), and tends to decrease in abundance from deeper to shallower parts of the deposit. The sedimentary rock sequences in the SE-lobe display graded bedding and consist of silty, fine-grained sandstones with interstitial, fine-grained, unzoned hematite and sericite (Electronic Appendix Fig. A1f). In this case, the zoned grains occur along the stratification and are particularly abundant and coarser at boundaries between different grain size fractions. Zoned hematite is also common throughout the sulphide-poor interval in drillhole RD2852A in the SE lobe, which also contains Au-Cu alloys (Fig. 2a). Towards the deposit centre, zoned hematite is generally subordinate to its overprinted analogue (6). Notably, zoned hematite is present within samples from the contact between the ODBC and stratified sedimentary rock packages at shallow levels, where, in addition to zoned hematite, other textural types of (unzoned) hematite are recognised in the sedimentary stratification (Electronic Appendix Fig. A1g). Although the present study includes fewer samples from the NW-arm of the deposit, these samples nonetheless show the existence of zoned hematite as elsewhere in the deposit. Importantly, these samples include U-rich, high-grade bornite ore (Electronic Appendix Fig. A1b, h). In drillhole RU27-7551 from the NW arm, zoned hematite is rare but it can be also traced by the presence of overprinted varieties (6).

5.2. *Zoned hematite – primary zonation patterns and their overprint*

Zoned hematite varies in size, from a few μm to exceptional, mm-sized grains, and comprises isolated, single grains, as well as aggregates (Figs. 3 and 6). The most common variety of zoned hematite is represented by euhedral to subhedral, single grains with average sizes in the range of a few tens to hundreds of μm, with sections perpendicular, or along the *c*-axis (Fig. 3a, b). Fragments of crystals are also common, particularly in the sedimentary rocks (Figs. 3c and 6f). Polysynthetic twinning (Fig. 3d) is another common feature in zoned hematite, most often observed in coarser grains as one to rarely three sets of lamellae, where the latter is typical of equant grains (Fig. 3f). Occasionally, BSE images can reveal a correlation between chemical banding and twinning (Fig. 3e, g).

Zoning observable on the BSE images is represented by variations on the theme of oscillatory patterns at scales extending from a few tens of μm down to sub-μm size (Fig. 6). One common pattern features zonation correlated to grain morphology, expanding from the core to the margin whether in aggregates, in grains with prismatic-elongate habit (Figs. 3b and 6a), or within basal sections, as defined by their hexagonal or octagonal outlines (Figs. 3a and 6b). In many cases, the oscillatory pattern displays complexities such as difference in growth rhythms, suggesting either various growth cycles, or changes in the growth rate (Fig. 6a–c). Although less common, zoned hematite can show morphologies with a clast-like appearance and internal oscillatory patterns, which do not correlate with the grain outline (Figs. 3c and 6f). Within some grains, there are domains with darker or brighter

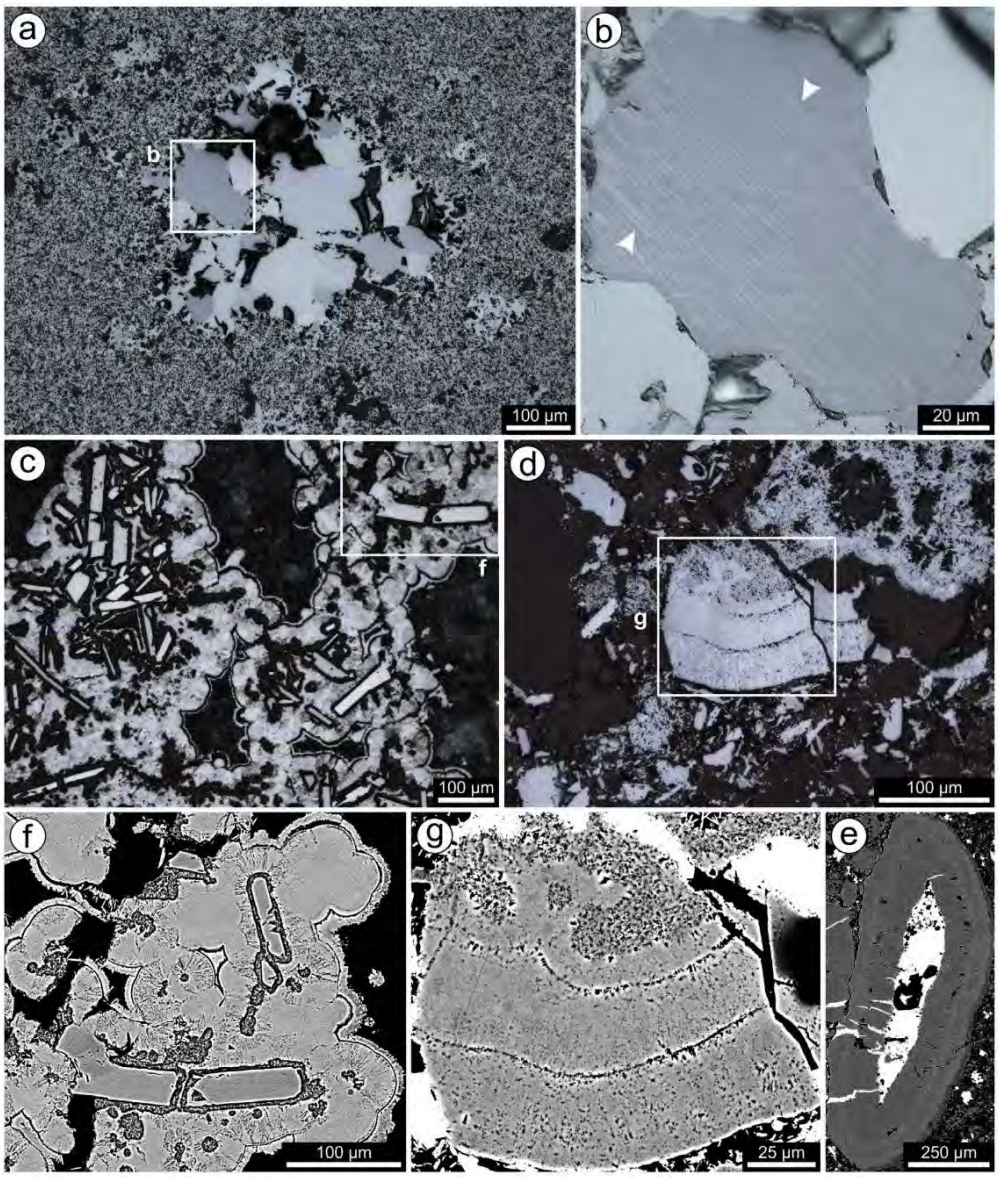

Fig. 5. Reflected light microphotographs (a–d) and BSE images (f–e) of other granitophile-rich hematite categories. (a, b) Granoblastic hematite filling vugs (vacuoles). In (b) note the basket-weave texture. (c–g) Colloform hematite from the NW arm and volcanics in SE lobe in (e). In (c) concentric bands surround lamellar hematite. (d) The bands are formed by fibrous hematite with radial arrangement relative to cores. (f, g) BSE images showing the presence of pores and no mineral inclusions present. (e) Concentric bands around a barite core.

intensities on BSE images that can be weakly zoned to unzoned, and either share coherent mutual boundaries with the oscillatory-zoned domains, or not (Fig. 3a–c). Such patterns may represent sectorial zoning, or, alternatively, reflect a new growth regime overprinting an initial grain (see below). Further complexity in the zonation patterns relates to grains that are affected by fracturing and development of porosity, with parts of the grain undergoing re-orientation of fragments displaying zonation followed by replacement (Fig. 6b, c; see below), or, in other examples, a second cycle of rhythmic growth (Fig. 6a, d).

Throughout the deposit, most primary zonation patterns in zoned hematite are variably overprinted, sometimes resulting in partial to complete obliteration of the primary textures (Fig. 7a). Many samples contain examples of both partially unaltered and overprinted zoned hematites coexisting in the immediate vicinity of one another. Overprinting processes are reflected in the generation of a wide variety of 'new' textures (Fig. 7). New core-to-rim patterns can be inferred from reworked domains where a darker shade on BSE images correlates with the presence of pores (Fig. 7b). Exceptionally, tiny blades of REE-fluorocarbonates occur throughout such grains. Overgrowths, consisting of acicular aggregates of hematite depleted in granitophile elements, are observed around zoned hematite (Fig. 7c). Boundaries that display intense darkening on BSE images (depletion in granitophile elements) are considerably common. These are often associated with pores, some of which may retain µm to sub-µm inclusions in them (Fig. 7d, e). The most commonly observed inclusions are U(± Pb)-minerals (uraninite, rarely coffinite), W-minerals (scheelite or

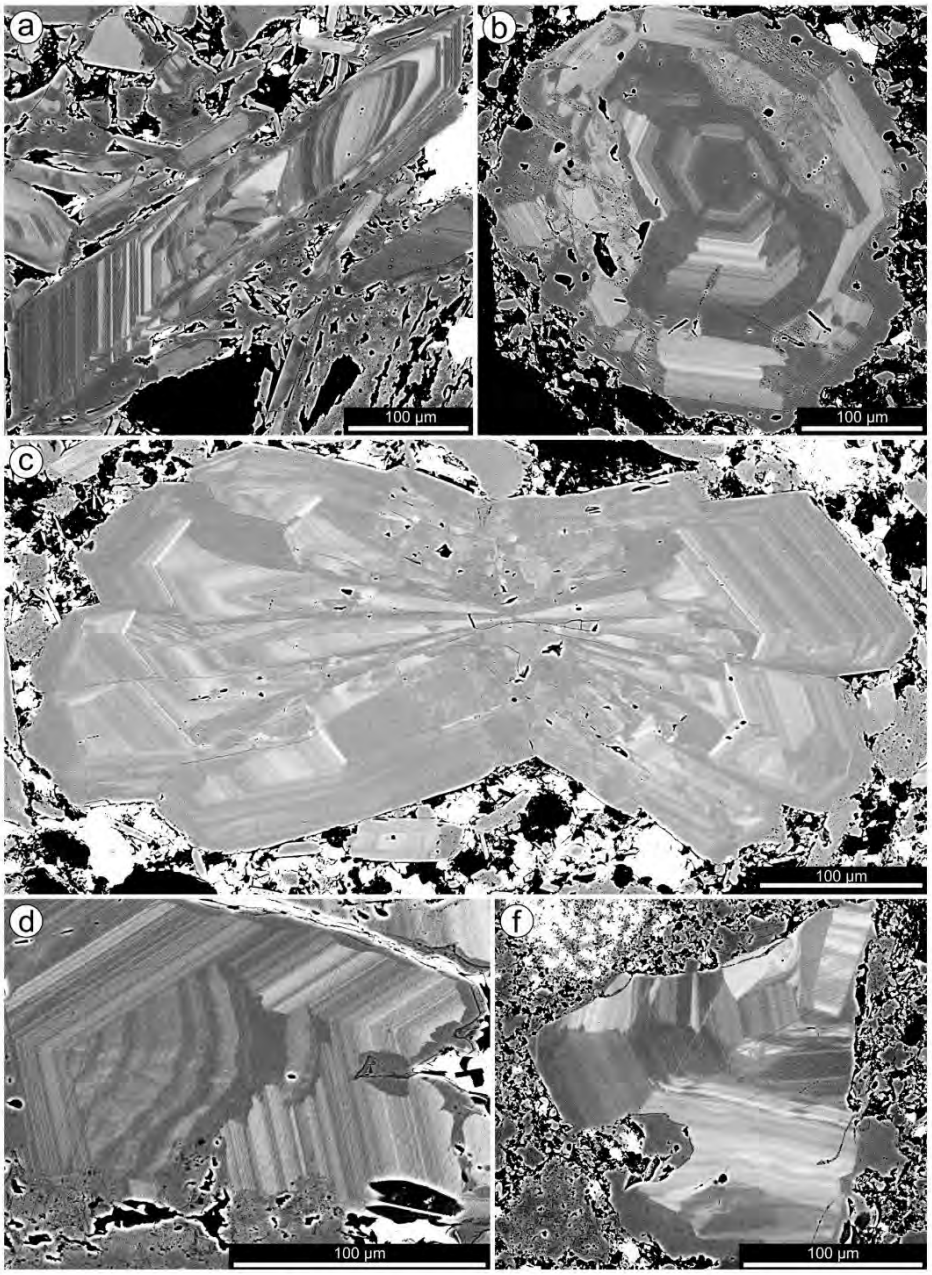

Fig. 6. BSE images showing complex oscillatory zoning patterns and incipient overprint. (a) Core to rim zonation in single grain cut parallel to the *c*-axis. (b) Core-to-rim zonation in octahedral basal section. Note parts of the grain showing reworking of zonation in areas marked by porosity. (c) Typical aggregate of oscillatory zoned hematite. Note zonation outlines growth in two directions (twins?) outwards from the middle part. (d) Detail of aggregate shown in Fig. 9b displaying two oscillatory zoning cycles marked by reversal growth direction. Although the inward cycle is an overprint, U and W are preserved. (f) Oscillatory zoned-grain with a 'clast'-like appearance.

ferberite), cassiterite, as well as REE-minerals (commonly monazite) or rare Nb(± Ti)-oxides.

5.3. Grain-scale trace element distribution – LA-ICP-MS maps

The correlation between the textures described above and trace element associations are illustrated by grain-scale element maps (Figs. 8–12; Electronic Appendix Fig. A3–9). The complexity of zonation patterns, in terms of inter-element correlations, within zoned hematite is highlighted on Figs. 8–10. In all cases, there is an intrinsic correlation between the zonation visible on BSE images and the presence of granitophile elements, in which the brightest areas are enriched in U(+Pb), and/or W, or to a combination of granitophile elements in different proportions.

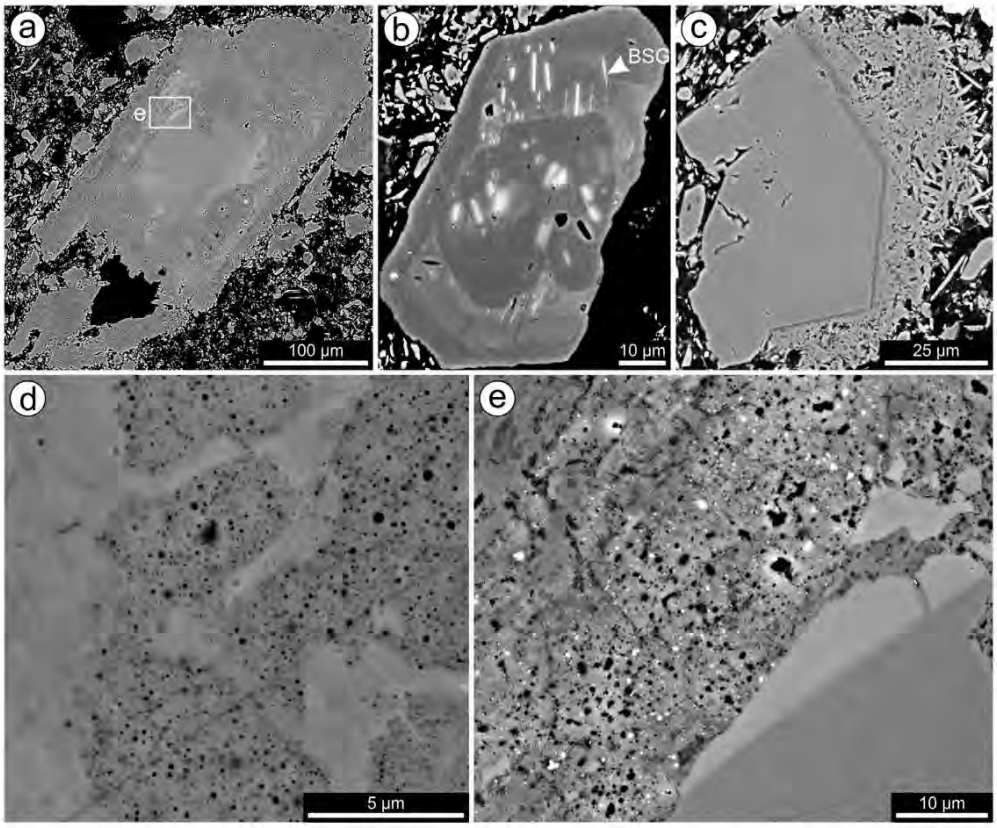

Fig. 7. BSE images showing aspects of zoned hematite overprint. (a) Advanced replacement marked by pores, darkening and irregular grain margins. Zoned relict recognizable in the core. (b) Reworking of zoned hematite with recrystallised core and REE-fluorocarbonates from bastnäsite-synchysite group (BSG) as lamellar inclusions. (c) Replaced zoned hematite with outwards lamellar overgrowth. (d-e) Details of patterns resulting during overprint in (a) showing high porosity (d) and inclusions attached to pores (e).

5.3.1. Element maps for zoned hematite

Zoned hematite grains from the middle part of the deposit are represented by the element maps shown in Fig. 8 (sample CLC046). This grain displays distinct inter-correlations between granitophile elements throughout different domains of sectorial and oscillatory zonation. In the sectorial domain, moderate concentrations of W correlate with highest concentrations of Mo, but the brightest areas on the BSE images correlate with highest U + Pb + W + Sn. The margins of the oscillatory-zoned grain show an inverse correlation between W + Sn (rich) and U + Pb (poor). In all maps of zoned hematite, there is a strong correlation between U and radiogenic Pb (^{206}Pb and ^{207}Pb). The brightest areas on the zonation patterns are therefore those with high U (+Pb), followed by W, whereas areas enriched in Sn or Mo can appear comparatively dark on the BSE images.

Partial overprinting of oscillatory-zoned hematite from the chalcocite-bornite zone of the mineralisation in the SE lobe is shown by element maps in Fig. 9 (sample RX6607). One of the most remarkable aspects revealed by mapping is the decoupling between granitophile elements in domains that show overprinting (recognizable by a darkening on BSE images; Fig. 9). In this case, the area is strongly depleted in W + Mo yet shows unchanged zonation with respect to Sn. Uranium, although not so enriched in this grain, and also ^{206}Pb (not shown), partially correlates with Sn. Oscillatory zonation with respect to Nb towards the margin is retained but the element is locally depleted within the core. Other elements (not shown) that mimic the distribution of Sn (unchanged zoning), or W (changed zoning) are Al + V and Mn + Co (very low), respectively. Reincorporation of granitophile elements such as W and U(+Pb) into secondary oscillatory zonation patterns (Fig. 6d) within the same grain is also observed in aggregates with intensive overprinting within the same sample (Fig. 9b).

Zoned hematite in samples from the chalcopyrite-pyrite zone in the deepest part of the SE lobe (RX7294) displays oscillatory zonation patterns with good spatial correlation between all the granitophile elements (Fig. 10). In addition, the zonation includes REE (e.g., Ce, Y), also overlapping with areas of the grains in which Th is present. Such elements are, however, only present at low concentrations in zoned hematite within the orebody. Other elements (not shown on the maps) present within the zonation pattern are Mn, V and Al (enriched in the grain margins), Ga, As, and Nb (low concentrations but nonetheless zoned).

Element maps of hematite grains from sulphide-poor intervals in the SE lobe, intersected by drillhole RD2852A (Fig. 11; sample RX6584) show some of the most complex trace element distributions. The mapped grain fragment displays a weak zonation on the BSE image, in which a darker band separates distinct inner and outer domains with only weak contrast between one another. The inner domain shows enrichment in Sn, W, Al and Ga (generally not distinctly zoned in other mapped grains), with scattered U, ^{206}Pb, Mo and Sb (noisy). Manganese is enriched in parts of the inner domain in which other elements are relatively depleted. Uranium, ^{206}Pb, Mo and Al are at their maximum concentrations in the outer domain. The darker band is characterized by a strong enrichment in As and Sb, also correlating with Cu, suggesting the presence of these metals within the hematite grain.

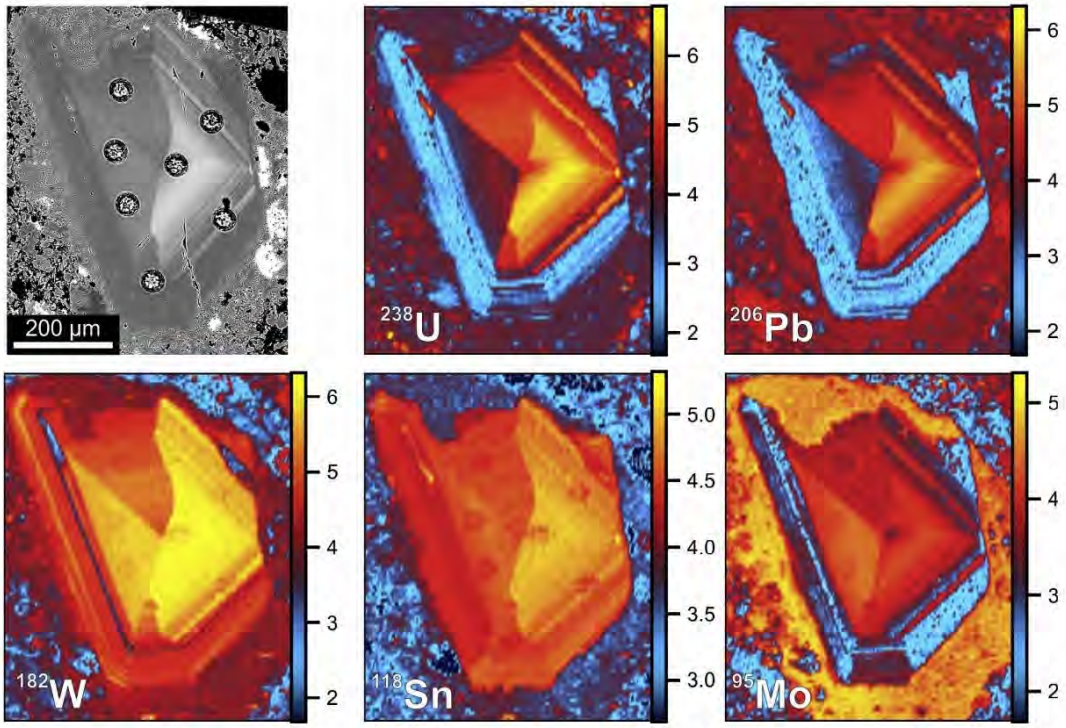

Fig. 8. LA-ICP-MS maps of zoned hematite (sample CLC046, RU49-8096). Scales in counts-per-second (logarithmic scale, 10^n). Spots on the BSE image (upper left) are previously acquired laser-ablation spot analysis.

5.3.2. Element maps for other categories of granitophile-rich hematite

Element maps (Fig. 12a) of granoblastic hematite from a volcanic clast shown in Fig. 5a (sample MV93A, SE lobe) show Sn as the granitophile element with highest concentration whereas U, W and Mo (not shown) are much lower and have a slight inverse correlation to Sn. Highest concentrations are observed for V towards the margin of the vug, inversely correlating with Nb (inner part). Titanium shows a positive correlation with Sn, albeit with two areas that are very high. LREE (Ce) (not shown) are also present throughout the middle part of the aggregate. Interestingly, Zn is present outside the margin of the vug, and correlates with Mn (not shown).

Colloform hematite from the NW lobe (sample MV048) shows complex distribution patterns (Fig. 12b) that reproduce the concentric zoning observed on BSE images. The darkest areas on the BSE image comprise fine-grained mixtures of Fe-hydroxides and silicates (depleted in Fe, enriched in Si and Al, not shown). The brightest bands correlate with highest concentrations of ^{206}Pb, U, Th, HREE (Yb), as well as Mo and to a lower extent Sn and W (not shown). This is the only case we have mapped which shows Pb at higher concentrations than U (see below). In contrast, the darkest areas on BSE and their margins are richer in LREE (Ce). An interesting feature is the presence of As at relatively high concentrations throughout the concentric banding. Other elements not shown on the figure (Sb, Cu, Zn and Ga) partially mimic the As distribution.

6. Compositional data

6.1. Electron probe microanalysis

Although the present work has used LA-ICP-MS methods to provide quantitative trace element data for hematite, a limited EPMA study was carried out to confirm the presence of lattice-bond granitophile-elements in zoned hematite and to assess, at the smaller scale of the microprobe beam, the variation within a single, particularly U-rich, zoned grain. Representative EPMA analyses of bright and dark domains on the BSE image of this grain from the SE lobe (RD2852A) are presented in Fig. 13. EPMA data are provided in Electronic Appendix D. Observed zonation patterns reflect bi-modal alternation between granitophile-rich hematite and end-member hematite (Fig. 13b). Concentrations of MgO, Al_2O_3, SiO_2, P_2O_5, CaO, TiO_2, V_2O_3, Cr_2O_3, MnO, NiO, ZnO, ZrO_2 and Nb_2O_5 are negligible in both bright and dark domains, mostly below their respective limits of detection and rarely exceeding 0.1 wt%. Uranium concentrations can be high, reaching a maximum concentration of 2.33 wt% UO_3, equivalent to 0.013 atoms per formula unit (apfu). Spot analyses with higher U are accompanied by variable, but sometimes higher, concentrations of W (in this case up to 1.61 wt% WO_3 or 0.011 apfu, Fig. 13b). Even though concentrations of both U and W are typically higher within brighter domains on the BSE image, Fig. 13b indicates that a degree of decoupling of the two elements has occurred within some zones. Generally in the present sample suite, most of the measured elements in zoned hematite are subordinate to W. Irrespective of spot location within the zoned grain, Sn concentrations consistently exceed the minimum limit of detection, albeit at low concentrations, reaching a maximum of up to 0.14 wt% SnO_2. Molybdenum is also present, reaching a maximum of 0.18 wt% MoO_3, although normally subordinate to other granitophile-elements, and decreasing towards grain margins.

6.2. LA-ICP-MS trace element data

This study comprises 1037 spot analyses of zoned hematite, 194 of *carbonate-replacement hematite*, 96 analyses of replaced zoned hematites, 50 of colloform hematite, 22 of granoblastic hematite, including the finer hematite matrix, and 12 analyses of *feldspar-replacement*

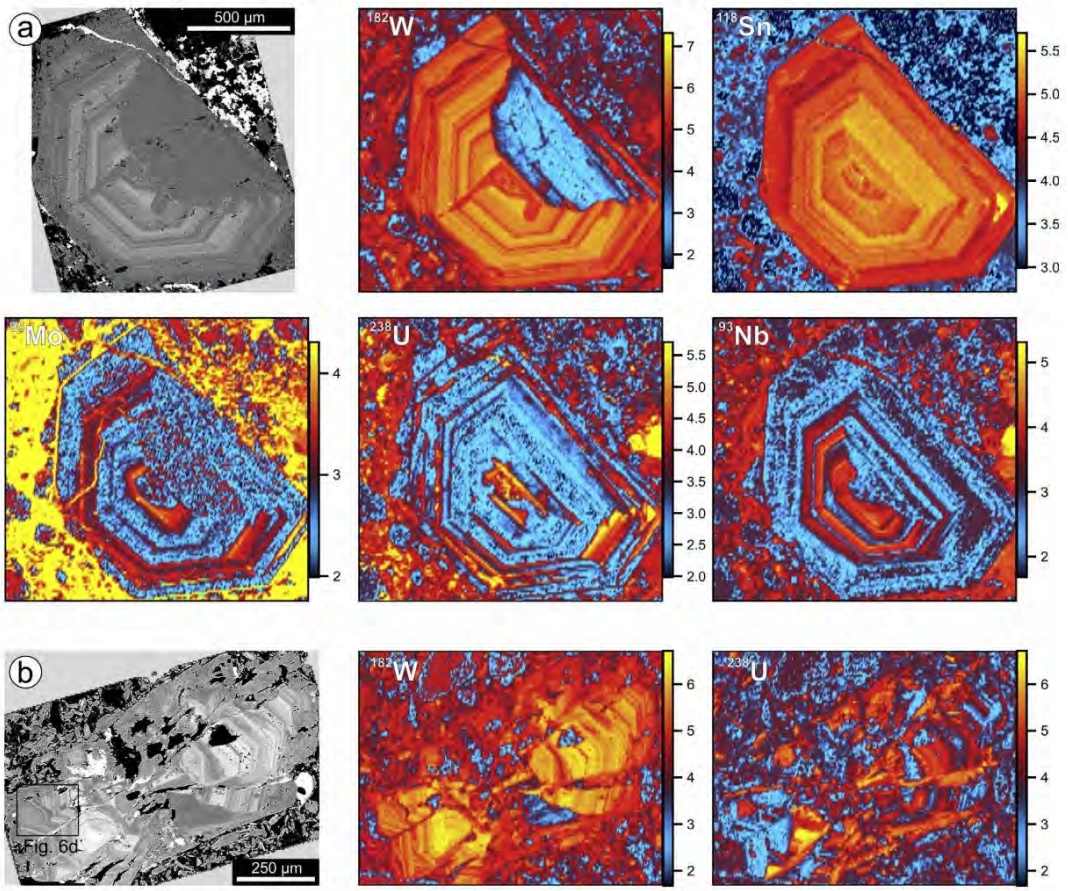

Fig. 9. LA-ICP-MS maps of two zoned hematite grains (a, b) in sample RX6607 (RD2852A). Scales in counts-per-second (logarithmic scale, 10^n). BSE images of mapped areas are shown for comparison.

hematite. The study is intentionally biased towards coarser, granitophile-rich grains that could be readily analysed by LA-ICP-MS using larger spot sizes. For all textural types, time-resolved LA-ICP-MS profiles show smooth, flat signals for the granitophile elements and others, indicating homogeneous distributions of these elements in the ablated volumes (Electronic Appendix Fig. A2). There are, however, examples of noisier signals that attest to the presence of discrete inclusions of phases containing Cu, REE, Th, Nb, W, Sn, U and Pb. These spot analyses were either excluded from the data presented, or the integrated time-intervals were reduced to avoid undue influence from these inclusions. Summary statistics for the dataset are presented in Electronic Appendix C; ternary and bivariate scatterplots for the data are shown in Figs. 15 and 16, respectively.

6.2.1. Granitophile elements: U(-Pb), W, Sn, Mo and Th

Across the deposit, hematite from the categories considered here, regardless of textural type and lithological association, is characterized by measurable concentrations of U, W, Sn and Mo. Lead is also measured within such hematites, in most cases as radiogenic Pb (see below). Normally, the concentrations of granitophile elements in zoned hematite vary in the range of some hundreds to a few thousands of ppm, following the order of abundance $W \gtrsim Sn \gtrsim U \gtrsim Mo$, not uncommonly with values across several orders of magnitude, particularly for U. Typical concentrations of these elements vary in the ranges of 20–370 ppm U, 1800–8900 ppm W, 300–1100 ppm Sn and 50–330 ppm Mo. Molybdenum concentrations are, in general, more consistent than those of U and display more limited variation, albeit at lower absolute concentrations. Despite U, Sn and Mo being typically subordinate to W, they can reach significant concentrations in individual spot analyses (10000–20000 ppm), and in rare cases, may even be present at higher concentrations than W (e.g., up to ca. 27000 ppm Sn and ca. 12000 ppm Mo).

A series of cumulative plots (Fig. 14) depict the variation in the concentrations of granitophile elements in hematite, commonly over several orders of magnitude within individual samples, or across sampled drillcore intervals. Neither the range of absolute values nor their variation show any significant differences with respect to vertical position in the deposit or sulphide zone (i.e., concentrations are broadly comparable in zoned hematite from different sulphide zones).

The zoned hematite clearly displays the highest maximum and mean concentrations of granitophile elements, followed closely by the carbonate-replacement category (600–1100 ppm U, 330–680 ppm W, 610–1200 ppm Sn, and 30–50 ppm Mo), and then by overprinted zoned hematite (490–960 ppm U, 120–440 ppm W, 120–300 ppm Sn, and 20–50 ppm Mo). The carbonate replacement category, restricted to the middle part of the deposit, displays a relatively consistent composition across the dataset, without the marked variance shown by zoned hematite (compare Fig. 14a, c). Particularly, U concentrations in carbonate replacement hematite show markedly less scatter than U concentrations in zoned hematite (Fig. 14c).

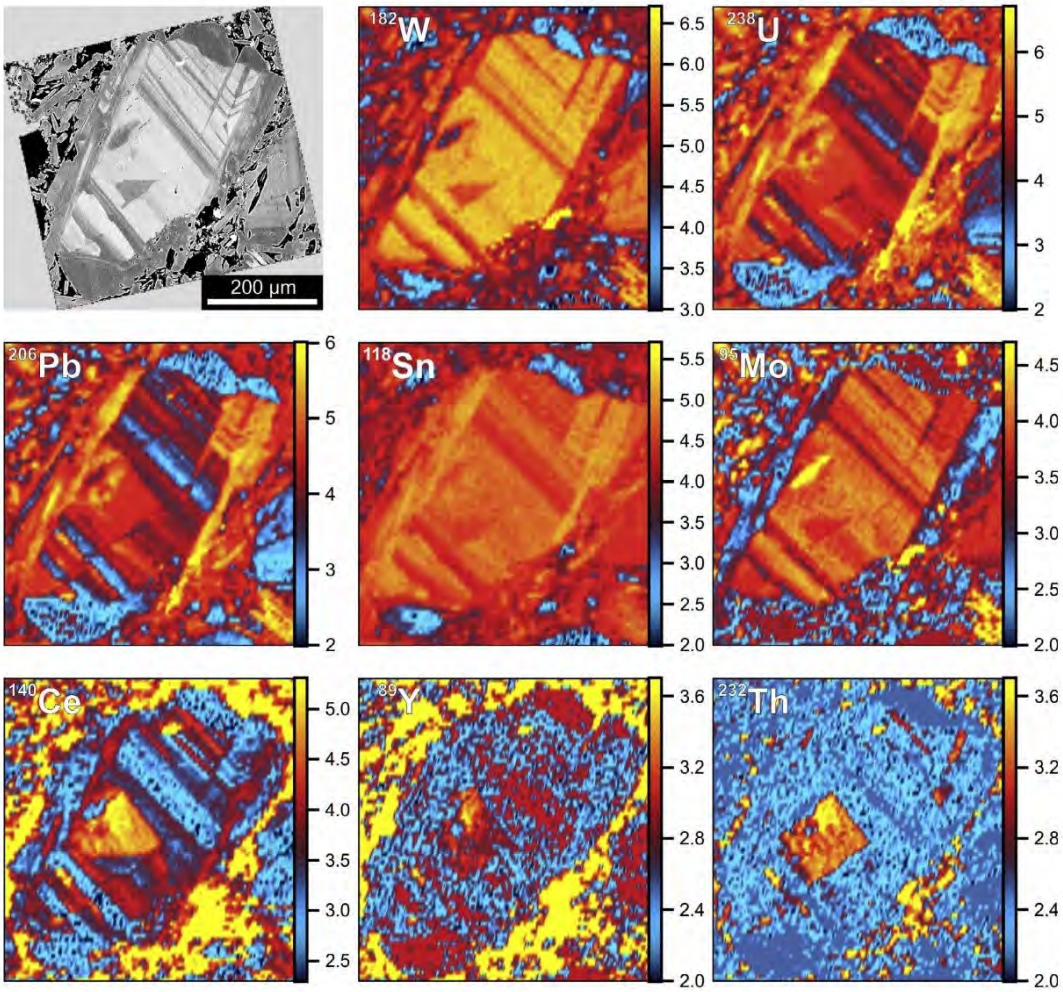

Fig. 10. LA-ICP-MS maps of zoned hematite (sample RX7294, RD1988). Scales in counts-per-second (logarithmic scale, 10^n). BSE images of mapped areas are shown for comparison.

Despite the lack of marked differences in concentrations between sulphide zones, the dataset shows that zoned hematite from the SE lobe has a particularly pronounced granitophile signature. Whereas U, Sn and Mo concentrations in zoned hematite are comparable across the deposit, W is distinctly more enriched in the SE-lobe relative to the central area or the NW-arm. This feature is seen on ternary diagrams for granitophile elements (Fig. 15). A discrimination between other textural types in terms of the relative abundance of these elements can also be seen.

Other textural types, although generally exhibiting lower concentrations of granitophile elements, can nevertheless be characteristically enriched in one of these elements. Tin concentrations, for example, can reach up to 200 ppm in granoblastic hematite whereas U, W, and Mo are < 10 ppm (Fig. 14c).

Variation in the concentrations of granitophile elements in hematite is exemplified by a plot of U *vs.* Mo + Sn + W (Fig. 16a). The considerable spread in zoned hematite and lesser variance in other textural types can be seen clearly. Concentrations of Th are much lower than U or the other granitophile elements. The element is, however, distinctly enriched (sample averages of up to ~150 ppm) in carbonate replacement hematite and overprinted hematite (typical ranges of 60–120 and 90–140 ppm Th, respectively). Fig. 16b shows a positive but rather weak correlation between Th and U in zoned hematite, and a stronger correlation among the other categories. Concentrations of Th discriminate colloform hematite (6–15 ppm) from zoned and granoblastic hematite (< 1 ppm). Radiogenic Pb, the product of U and Th decay, is also present in hematite, at concentrations that can exceed 1000 ppm. A strong correlation is seen between U and Pb (Fig. 16c), where Pb corresponds to an estimate the total lead amount calculated from the individual ^{206}Pb, ^{207}Pb and ^{208}Pb abundances. Notably astray from the main correlation, however, is the colloform hematite with comparatively high Pb concentrations and lower U/Pb ratios, suggesting a different, or later formation, in which ^{206}Pb, ^{207}Pb and ^{208}Pb from *in situ* decay of U and Th is supplemented by additional radiogenic lead, possibly migrated from the decay of U- and Th-bearing minerals unable to retain Pb within their structures.

6.2.2. Rare earth elements and yttrium

Despite the abundance of other REE- and Y-bearing minerals at OD, hematite is a significant host for REY. ΣREY (the sum of all REE, La to Lu, and Y) varies over 5 orders of magnitude, from fractions of a ppm, to as much as 1000 ppm (Fig. 16d, e). ΣREY values for zoned hematite span the entire range but are, on average, among the lowest of all categories, together with granoblastic hematite, which contains 1–12 ppm

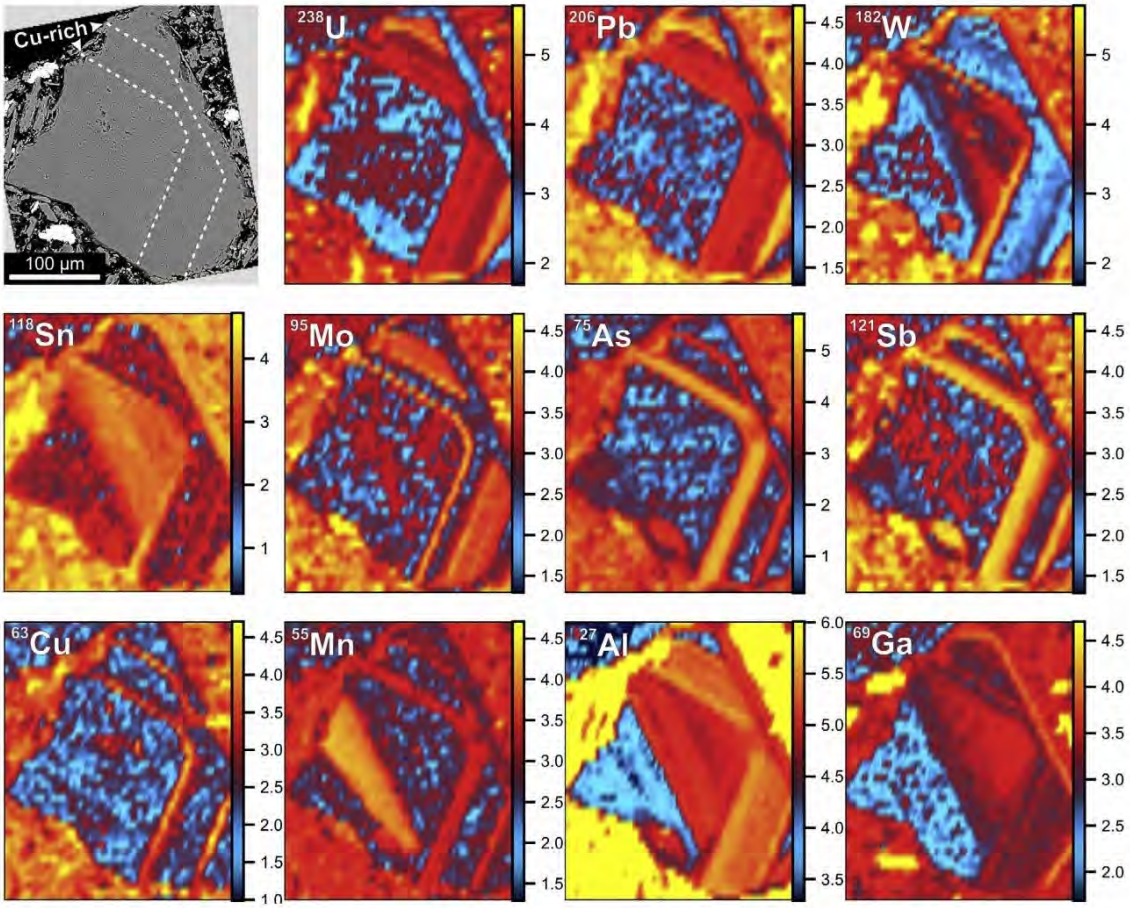

Fig. 11. LA-ICP-MS maps of zoned hematite (sample RX6584, RD2852A). Scales in counts-per-second (logarithmic scale, 10^n). BSE images of mapped areas are shown for comparison.

ΣREY, and rarely surpasses 150 ppm. Other textural types commonly have higher and more consistent ΣREY than zoned hematite (e.g., colloform hematite, which can reach up to ca. 300 ppm). A comparison of chondrite-normalized REY-fractionation trends for different categories is shown in Fig. 17. Different textural types of hematite can be distinguished based on their REY-patterns, however some types display marked variability within and between samples (particularly true for granitophile-zoned hematite).

The zoned hematite grains which are relatively enriched in ΣREY generally show REY-fractionation patterns defined by LREE-enrichment, concave trends and smooth slopes, which flatten or become slightly, but steadily enriched in HREE (Fig. 17a). Such a trend is, however, more common in zoned hematite from the SE-lobe at depth, although, individual samples from other localities may contain grains showing similar trends. More commonly, however, zoned hematite contains very low amounts of ΣREY, with several REE at or below their respective minimum limits of detection, producing erratic fractionation trends that are accentuated on logarithmic plots. One common trend (Fig. 17b) shows a sinuous fractionation with slight LREE-enrichment and a pronounced negative Y-anomaly. One specific example is highlighted on Fig. 17b (sample MV031) which depicts a smooth, LREE-enriched trend with a marked positive Eu-anomaly, atypical for zoned hematite across the deposit. Less commonly, zoned hematite may also feature distinct HREE-enrichment (Fig. 17c), a pattern that may be accompanied by more to less pronounced, negative Eu-anomalies.

Other textural types show chondrite-normalized REY-fractionation trends that can be distinguished from those of zoned hematite. Carbonate-replacement hematite (ΣREY: 25–45 ppm) features fractionation trends characterized by slight LREE-enrichment, negative Eu-anomalies and an overall continuous HREE enrichment (Fig. 17d), similar to patterns observed in some overprinted hematites, which also have comparable ΣREY (30–55 ppm). Hematite replacing feldspar shows fractionation-patterns characterized by slight LREE-enrichment and otherwise smooth patterns with small positive Eu- and negative Y-anomalies (Fig. 17e), resembling and in the same range as fine-grained hematite matrix, whereas granoblastic hematite shows less-enriched trends. Colloform hematite displays fractionation patterns characterized by smooth, flat slopes with slight positive Eu- and negative Y-anomalies (Fig. 17f), albeit with subtle differences between individual samples.

6.2.3. *Arsenic and antimony*

Arsenic and Sb are both measured in all textural types of hematite, varying in concentrations (Fig. 16f), typically with As > Sb, but within similar concentration ranges. Typical ranges for zoned hematite are 2–26 ppm As, and 2–13 ppm Sb, although higher concentrations are measured in some spots. Zoned hematite from the NW arm and deposit centre appear to have only moderate concentrations of As and Sb compared to most analyses of zoned hematite from the SE lobe. Typically, colloform hematite shows characteristically high As and Sb, as does the matrix hematite. In general, As and Sb concentrations correlate positively for most textural types, although colloform hematites do not

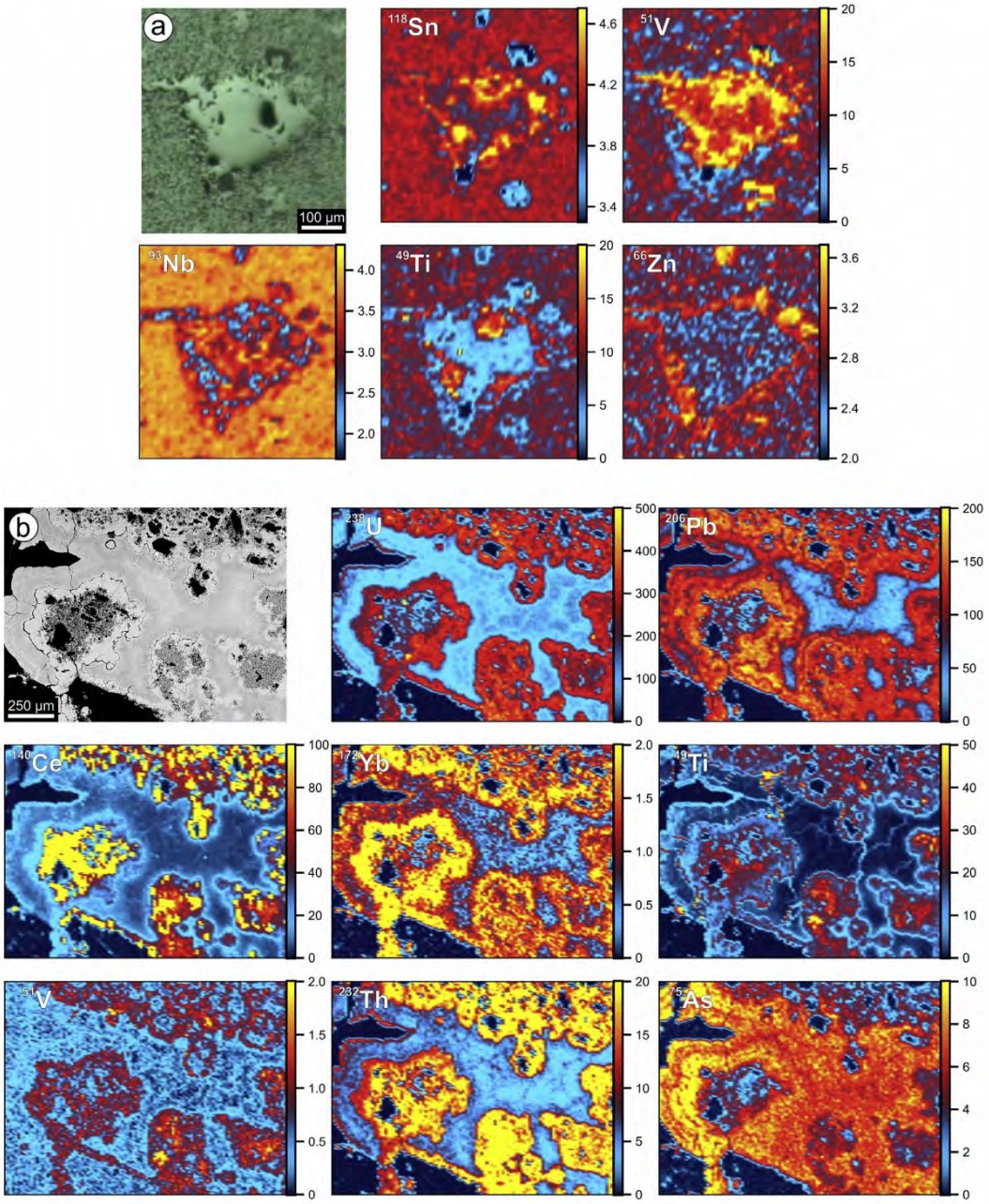

Fig. 12. LA-ICP-MS element maps of (a) granoblastic hematite (sample MV093, RD647) and (b) colloform hematite (MV048, RU27-7551). Scales in counts-per-second (logarithmic scale, 10^n). ^{49}Ti and ^{51}V on (a), and ^{238}U, ^{206}Pb, ^{140}Ce, ^{49}Ti, ^{232}Th and ^{75}As on (b) are linearly scaled (n·1000). Upper left images of the ablated area are an optical micrograph (a) and BSE image (b).

follow this trend and appear to be uncorrelated (relatively constant As concentrations but Sb varying over ca. 1–2 orders of magnitude).

6.2.4. Transition metals: Cr, Mn, Co Ni, Cu and Zn

Increased Ni, Cu and Zn concentrations show a strong positive correlation with higher As + Sb (Fig. 16f), raising the possibility of sulphide inclusions, which are common in replacement and overprinted textural types. Some zoned hematites from the SE-lobe show comparatively low concentrations of Ni + Cu + Zn despite higher As + Sb. Zoned hematite from the NW arm and deposit centre appear to have only moderate concentrations of Ni, Cu and Zn compared to most analyses of zoned hematite from the SE lobe.

Chromium, Mn and Co do not appear to be particularly enriched in OD hematite. All three elements are generally found at concentrations < 100 ppm, with Mn > Co. Among the different textural types, zoned hematite contains the lowest Cr, Mn and Co contents (together

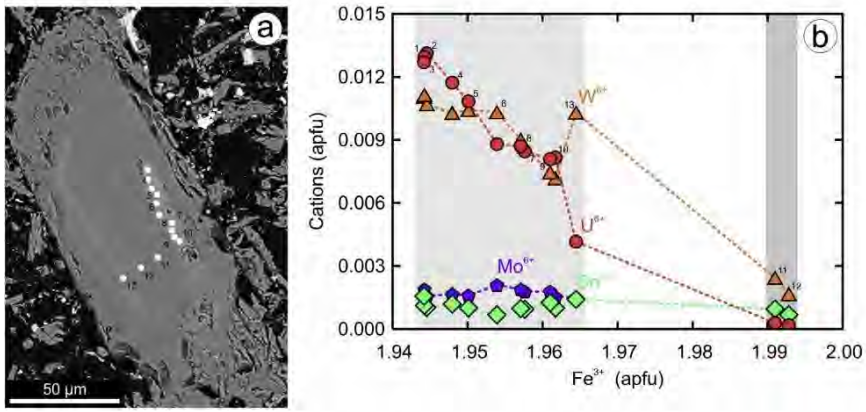

Fig. 13. (a) BSE micrograph of U-rich zoned hematite (sample RX6583, RD2852A) and location of spots analysed by EPMA (numbered white dots). (b) Compositional variation between different domains within the zonation pattern depicted by Fe^{3+} *vs.* U^{6-}, W^{6-}, Sn^{4+} and Mo^{6-} in atoms-per-formula-unit (apfu). Hematite formulae calculated based on 3 apfu O.

commonly < 20 ppm), whereas other types contain higher concentrations. Chromium does not correlate with other transition metals, while Mn and Co appear to be slightly correlated, with both showing concentrations in comparable ranges and increased concentrations in carbonate replacement hematites (28–62 ppm Mn, 15–27 ppm Co) and overprinted hematites (40–92 ppm Mn, 12–21 ppm Co).

6.2.5. High field strength elements: Sc, Ti, V, Zr(-Hf) and Nb(-Ta)

Compared to the granitophile elements, concentrations of HFSE are not particularly high in zoned hematite. They can, however, reach significant concentrations in other textural categories, such as in replacement-types, granoblastic and colloform hematite. Typically, V is present in zoned hematite at concentrations < 10 ppm and Nb is present at somewhat higher concentrations. There is however a marked increase in the Nb concentration in zoned hematite from volcanics in the SE lobe (up to ~2800 ppm), although individual samples from the middle part of the deposit (up to ~2000 ppm) and from the NW arm (up to ~1800 ppm) can also reach considerable amounts. Both elements are, however, clearly enriched in other categories relative to zoned hematite, reaching up to a few hundreds of ppm V, and a few thousands of ppm Nb: 440–1400 ppm Nb and 280–390 ppm V in carbonate replacement hematite, and 700–2700 ppm Nb and 100–200 ppm V in replaced zoned hematite. Niobium correlates positively with Ti + V (Fig. 16g) and a good correlation between V + Nb and Sc + Ti + Y + Zr is also seen (Fig. 16h). While the majority of zoned hematite shows significant scatter irrespective of location, carbonate-replacement and overprinted zoned hematite can be effectively discriminated by their particular HFSE signatures, plotting generally together as a group, or at least close to one another. Irrespective of textural type, concentrations of Nb are mimicked by Ta, even if at low concentrations, giving good correlations albeit with considerable scatter.

Typically, zoned hematite is poor in Ti, contrasting with other textural types, which have higher concentrations: hematite replacing feldspar (consistent concentrations in the range 1400–2400 ppm), granoblastic hematite (400–1000 ppm), and colloform hematite (160–1200 ppm). Granoblastic hematite also displays the relatively highest concentrations of Sc and Zr among the different textural types, albeit at very low concentrations (< 5 ppm Sc, < 10 ppm Zr). Hafnium is also present at measurable concentrations.

7. Discussion

Hematite from OD displays a variety of textures accompanied by distinctive trace element signatures and REY-fractionation trends. As shown here, and previously (Ciobanu et al., 2013, 2015; Cook et al., 2016; Verdugo-Ihl et al., 2017), a granitophile-signature prevails throughout the hematite in the deposit irrespective of textures.

7.1. Incorporation of granitophile elements in hematite

Hematite incorporates elements in VI-coordinated positions, permitting accommodation of a wide range of foreign cations at concentrations that can attain wt% levels. Substituting cations include those with higher oxidation states as shown by X-ray absorption near-edge spectroscopy (XANES) studies for U^{6+} (Duff et al., 2002) and W^{6+} (Kreissl et al., 2016) in synthetic and natural hematite (α-Fe_2O_3). Raman spectral evidence was also given for W^{6+} in hematite from an oxidation zone in the Western Rhodopes, Bulgaria (Tarassov et al., 2002).

The presence of U(-Pb), W, Sn and Mo in the lattice of zoned hematite from OD, for which LA-ICP-MS and transmission electron microscopy (TEM) data were reported by Ciobanu et al. (2013), is here attested to by EPMA data for the first time. The necessity to consider Me^{6+} (Me: U, W, Mo) in U-rich hematite from OD (up to 0.013 apfu, assuming U^{6+}) is based on vacancy-induced crystal-structure modifications (long-range superstructures) following the proposed substitution: $2Fe^{3+} \leftrightarrow Me^{6+} + \square$ (Ciobanu et al., 2013). A preliminary TEM study of W-rich hematite (up to 0.018 apfu) from OD shows instead a simpler, $2a$ superstructure (Liu and Ciobanu, 2016). Atomic-scale high-angular annular dark field scanning-TEM imaging of W-rich (up to 0.022 apfu) hematite which also contains a 10–20 nm-sized inclusion of ferberite ($FeWO_4$) shows defect-free, compositionally homogenous hematite, except for the presence of darker areas, a few nm in width, where the $2a$ superlattice is present suggesting O vacancies (Ciobanu et al., 2016). In this case, coherent lattice fringes imaged across the boundary between hematite and ferberite imply structural isomorphism (solid solution) between the two minerals. Considering the decrease in the oxidation state of Fe in hematite with O vacancies (Chen et al., 2008), such as the darker areas, the oxygen-deficient sites could act as catalyst for $W^{6+} \rightarrow 3Fe^{2+}$ substitution. This mechanism is different to the one suggested by EXAFS spectra showing similarities between the W^{6+} and Fe^{3+} position in substituted hematite (Kreissl et al., 2016).

Comparable suggestions for substitutional mechanisms involving Fe^{2+} have been put forward to explain incorporation of Sn in hematite with up to 2.26 wt% SnO_2 (~0.024 apfu Sn) in oscillatory-zoned hematite from placer deposits in Canadian Creek, Yukon, Canada (Barkov et al., 2008). These authors discussed several substitutional mechanisms but concluded that the most likely is $Sn^{4+} + Fe^{2+} \leftrightarrow 2Fe^{3+}$, whereby co-present Al^{3+} would minimise lattice strain.

In contrast to the granitophile elements discussed in the above paragraphs, very little is known about the presence of Mo in natural hematite. This can however be considered, like U or W, to have a

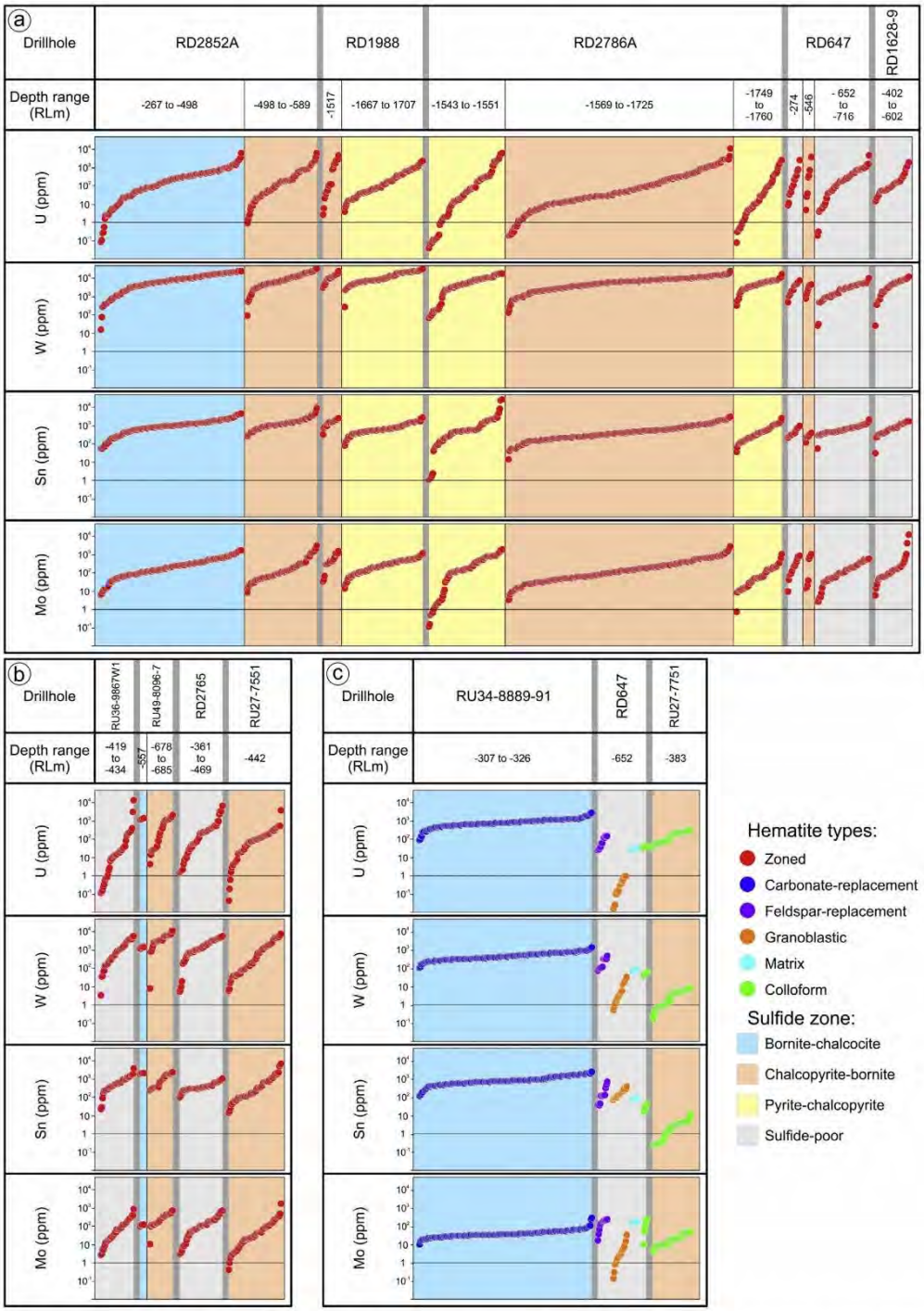

Fig. 14. Diagrams showing granitophile element concentrations in individual analyses arranged in ascending order by sulphide zones and textural type. (a) Zoned hematite, SE lobe. (b) Zoned hematite, deposit middle and NW arm. (c) Other textural categories in SE lobe, middle and NW arm.

hexavalent oxidation state. The assumption of a higher oxidation state for U, W and Mo in early hydrothermal fluids at OD is, however, somewhat contradictory to that made for 'primary' uraninite (Macmillan et al., 2016a). In uraninite, a change in the oxidation state from U^{4+} to U^{6+} was invoked to track the evolution from the earliest (primary) to latest, partially replaced, recrystallised, or newly-precipitated generations of uraninite. XANES studies are necessary on each of the two minerals to assess the oxidation states of the substituting

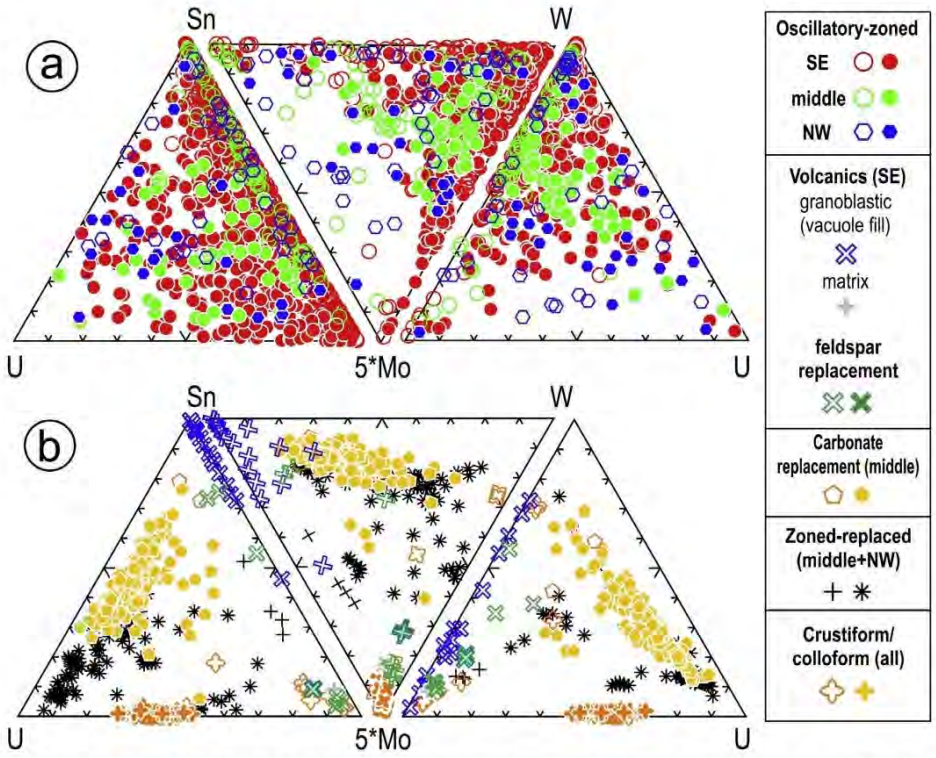

Fig. 15. Ternary plots of U-Sn-Mo(*5), W-Sn-Mo(*5) and U-W-Mo(*5) showing relative enrichment of granitophile elements in different textural types of hematite. (a) Granitophile-zoned hematite from the SE lobe, the deposit middle, and the NW arm. (b) Other categories from various locations. Filled symbols correspond to U-rich hematite (> 122 ppm).

elements.

7.2. REY and other trace element signatures in hematite – evolving fluids

Concentrations of REY within OD hematite are subordinate to those in other minerals that are better REY-carriers, e.g., uraninite (Macmillan et al., 2016a), or apatite (Krneta et al., 2017). Nonetheless, some categories of hematite contain up to tens or hundreds ppm ΣREY, e.g., zoned hematite from depth in the SE lobe, and carbonate replacement plus zoned overprinted categories. Although the measured REY concentrations likely relate not only to lattice-bound elements substituting for Fe (e.g., map in Fig. 10) but also to the presence of discrete, sub-μm-sized REE-mineral inclusions, the consistency of chondrite-normalized REY-fractionation trends (Fig. 17) suggests that REY signatures can be used as geochemical tracers for fluid evolution at OD. In hydrothermal systems, the transport and deposition of REE is controlled by the stability and availability of suitable ligands to complex REE, and the relative solubilities of REE-bearing phases. Experimental and thermodynamic calculations of REE stability, transport and deposition conclude that chloride and sulfate species dominate solution transport whereas fluoride, carbonate and phosphate are important as depositional ligands (Migdisov et al., 2016 and references therein).

The subtle variations in zoned hematite, otherwise characterized by comparable, slightly concave, relatively LREE-enriched fractionation trends, relate mostly to Eu- and Y-anomalies. The transition from a negative to a positive Eu-anomaly can be correlated with the strong effect of pH in constraining the dominant REE-(chloride) aqueous transport complexes, impacting on the relative stabilities of Eu^{2+} versus Eu^{3+}. Fluids of variable pH from mildly acidic (sericite-stable) to alkaline (carbonate-buffered) are interpreted to explain comparable changes in Eu-anomalies recorded by apatite from early to late hydrothermal stages at OD (Krneta et al., 2017). The presence of a strong negative Y-anomaly, recorded in one-third of the analysed hematites, is suggestive of co-precipitation of relatively Y-rich phases such as xenotime or monazite.

The slightly HREE-enriched fractionation trends recorded in carbonate replacement and overprinted zoned hematite can be related either to down-T fractionation, or to depositional controls offered by HREE-fluoride stability relative to that of LREE-chloride complexes (Migdisov et al., 2016). On the other hand, highly acidic HF-rich fluids can transport $NbF_2(OH)_3$ complexes, and such acidic fluids, if they interact with carbonates, will be neutralised (Timofeev et al., 2015). This depositional mechanism can also explain the high concentrations of Nb (thousands of ppm) and other HFSE (V, Th) in carbonate replacement and overprinted zoned hematite categories.

All other categories of hematite: volcanic-hosted (except zoned hematite from the same samples, which resemble zoned hematite elsewhere) and colloform, display similar REY fractionation patterns. These feature relatively flat trends, slightly LREE-rich for volcanic-hosted categories, and slight variation in the size and sign of Eu- and/or Y-anomalies, but are distinct from those shown by zoned hematite (Fig. 17). Such trends are comparable with chondrite-normalized REY patterns for some Fe-oxides and/or hydroxides observed from BIF-supergene environments (e.g., Keyser et al., in review). The latter are interpreted to represent the signatures of low-T (< 250 °C) submarine thermal springs associated with young volcanoes (Michard et al., 1993). Comparable seafloor paleo-vents could have been associated with formation of volcanic-hosted (granoblastic, matrix and feldspar replacement) hematite considering that these rocks may well have formed in a submarine environment.

Volcanic-hosted and colloform hematites are, however, clearly distinguishable from one another in terms of the concentrations of other

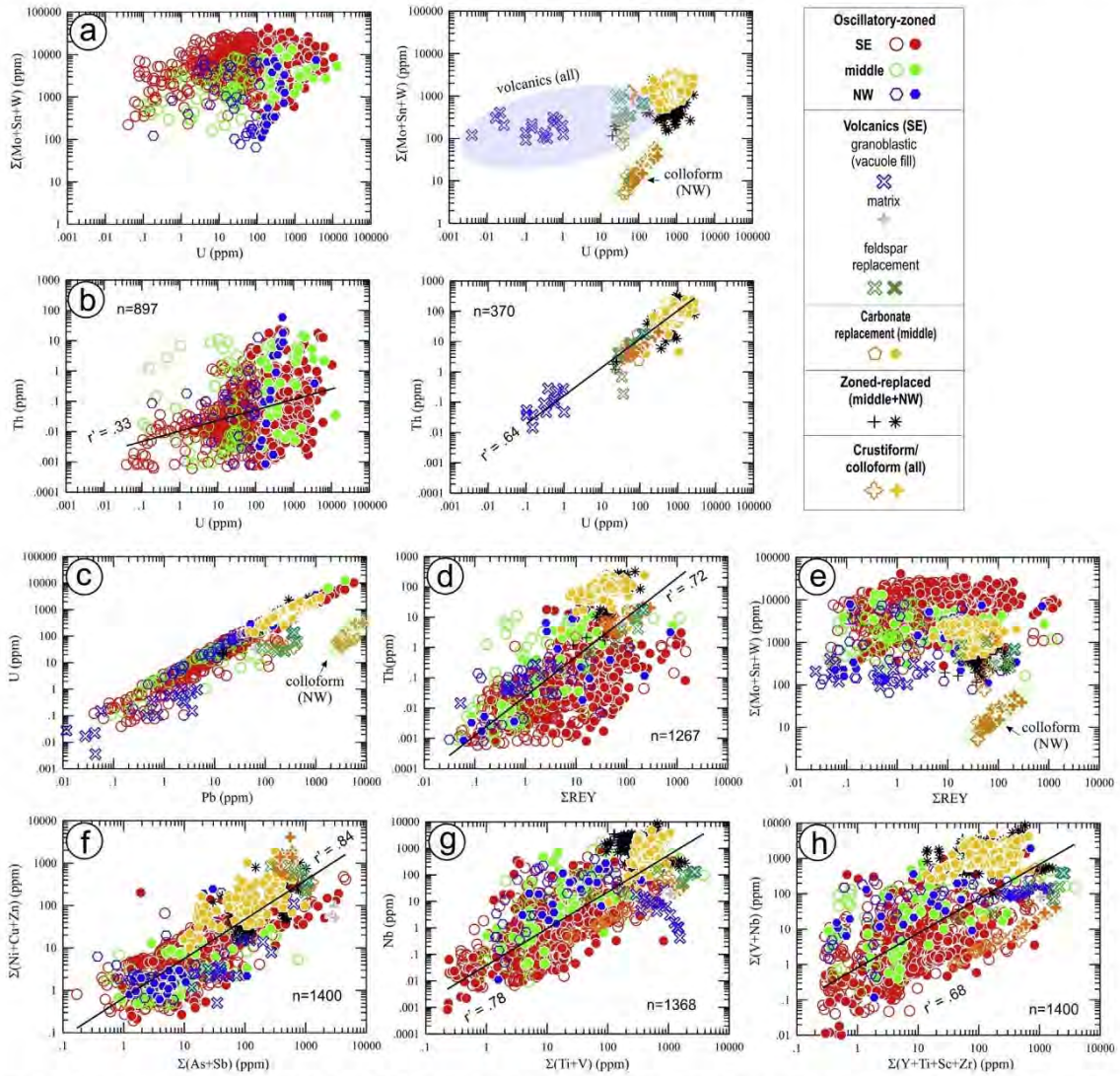

Fig. 16. Scatterplots for selected trace elements. (a) U *vs.* Mo + Sn + W, (b) U *vs.* Th, (c) Pb *vs.* U, (d) ΣREY *vs.* Th, (e) ΣREY *vs.* Mo + Sn + W, (f) As + Sb *vs.* Ni + Cu + Zn, (g) Ti + V *vs.* Nb, and (h) Sc + Ti + Y + Zr *vs.* V + Nb. Filled symbols correspond to U-rich hematite (> 122 ppm).

trace elements, notably their Sn-Ti-Zr-Sc and Cu-Zn-As signatures (Figs. 12 and 16). Colloform hematite from the NW arm is an outlier on most of the plots (Figs. 15b and 16), but particularly on those involving Th, U and radiogenic Pb. They may plausibly represent a much younger (post-IOCG) hematite, not least because they also strongly resemble colloform magnetite within veinlets from ~820 Ma Gairdner dikes documented from OD (Apukhtina et al., 2016).

The relatively strong correlations between different groups of elements including REY, chalcophile, transition metals and HFSE (Fig. 16f–h) in all granitophile-rich hematite categories show the complex evolution of trace element signatures across the OD deposit. Multivariate statistical analysis will be employed to better define such signatures and their potential for spatial ore vectoring.

7.3. Chemical oscillators and recycling trace elements during their overprint

Oscillatory zoning, in which chemical composition varies from core to rim, is a common feature of crystal growth from fluids of complex chemistry if ionic diffusion in the solid is much slower than that in the fluid. Such processes have been reproduced experimentally using major-element variation in solid-solution series (e.g., $(Ba,Sr)SO_4$; Putnis et al., 1992). Chemical-oscillatory growth can be controlled by either extrinsic (external) or intrinsic (internal) factors. Macroscopic and cellular automata models have simulated experimentally-produced patterns in $(Ba,Sr)SO_4$ without an external template, proving that spontaneous spatiotemporal patterns can be generated by non-linear systems driven away from thermodynamic equilibrium (L'Heureux and Katsev, 2006). Of direct relevance here is that, in such models, small fluctuations in element concentrations within aqueous solution may contribute to the development of oscillatory zoning by causing noise-induced transitions in the crystal growth, thus explaining both the textural variety and differences in the relative concentrations of the granitophile elements measured or mapped in zoned hematite (Figs. 3, 6, 8–11 and 15a). Such incredible variation, sometimes observed between grains in the same sample, as well as the lack of obvious, reproducible trends throughout the deposit, may be indicative of

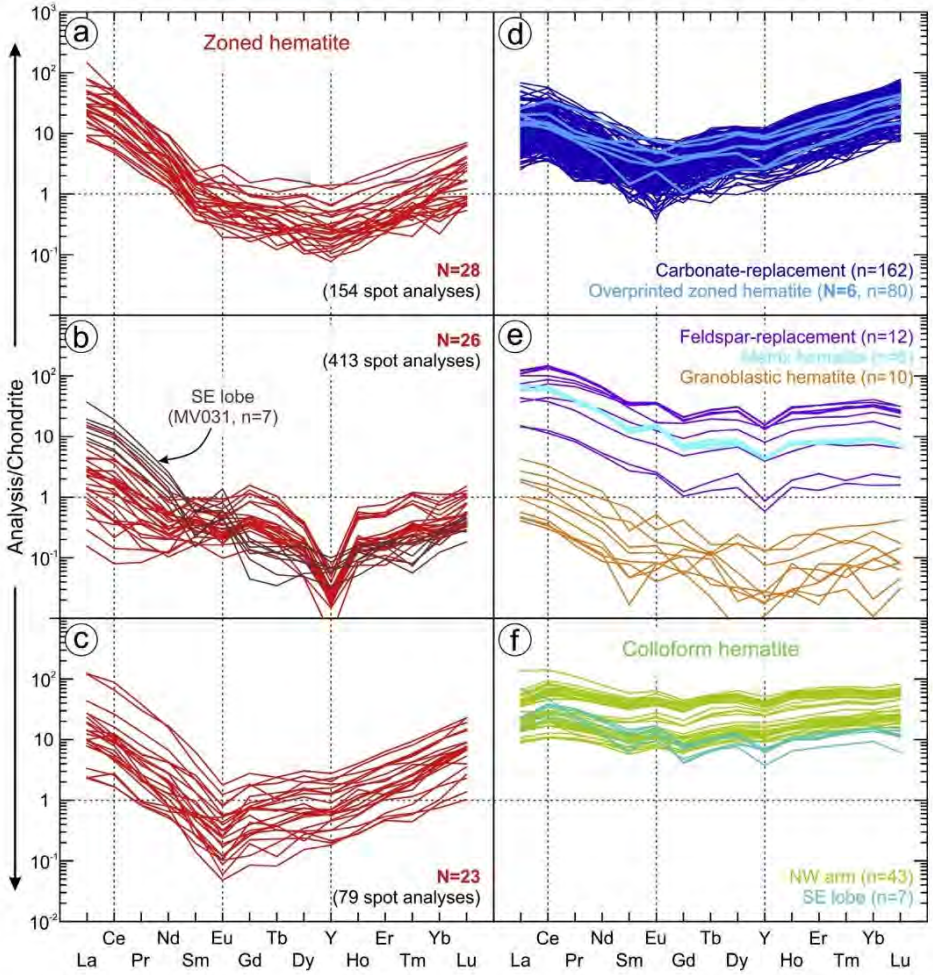

Fig. 17. Chondrite-normalized REY-fractionation trends for granitophile-rich hematite categories as marked. The trends depicted for zoned hematite (a-c) are not specific to any location or lithology in the deposit. N = sample averages (geometric mean); n = number of spot analyses. See text for additional explanation.

self-organising phenomena whereby small rather than systematic compositional variation within the same fluids induces chemical oscillations during hematite growth. The REY-fractionation trends for zoned hematite, which typically lack systematic trends within an individual sample, from one sample to another, or throughout the deposit, also support this idea.

Textural characterization and element mapping of zoned hematite shows several key aspects instructive for understanding overprinting in terms of cation exchange, nucleation of inclusions, partial replacement and recrystallisation (Fig. 18). Whereas, the zoned hematite generally displays variations on the theme of pseudomorphic replacement that are generically attributable to reactions that couple dissolution with reprecipitation reactions (CDRR; Putnis, 2002), there are two major lines of fluid-hematite interaction shown schematically in Fig. 18.

The first type (1), also discussed in previous studies (Ciobanu et al., 2013; Cook et al., 2016), is characterized by corrosive replacement boundaries presumably produced by acidic, HF-rich (?) fluids leading to intense porosity, obliteration of zoning, and strong depletion of trace elements, particularly the granitophile elements (case 1a). A range of minute mineral inclusions formed from the removed trace elements can be trapped within the pores. These inclusions display a continuous range of textures, and vary in density, from scattered to dense swarms, even within grains from the same sample. CDRR reactions are promoted by transient porosity and depending upon the rates of reaction, some pores remain open whereas others are rapidly closed and obliterated (Putnis, 2015). Such inclusions may provide the ingredients for a second generation of granitophile-rich hematite, the overprinted zoned type, should the grain undergo re-crystallisation (case 1b). The most compelling case is represented by the observation of REE-fluorocarbonates within the recrystallised patterns (Fig. 7b). This is also further support for the presumption of F-rich fluids (case 1c).

The second type (2) is, however, new and shows fluids at disequilibrium only with respect to certain elements, leading to selective removal of, for example, W but not Sn (case 2a). The textures can be considered to evolve via sharp interface boundaries since zonation patterns are well preserved. The same can be invoked to explain recycling of granitophile elements, e.g., Mo, into subsequent cycles of zoning with chalcophile elements, e.g., Cu, As, Sb (case 2b), typifying hematite from sulphide-poor intervals.

Such selective removal of trace elements can be suggested by redox changes in the fluid, affecting elements with differences in the stability of cationic oxidation states (Sn^{4+} versus W^{6+}). Reducing fluids can be associated with sulphide-depleted intervals featuring barite veining, in which native copper and Cu-Au alloys are also stable (Ciobanu, 2015).

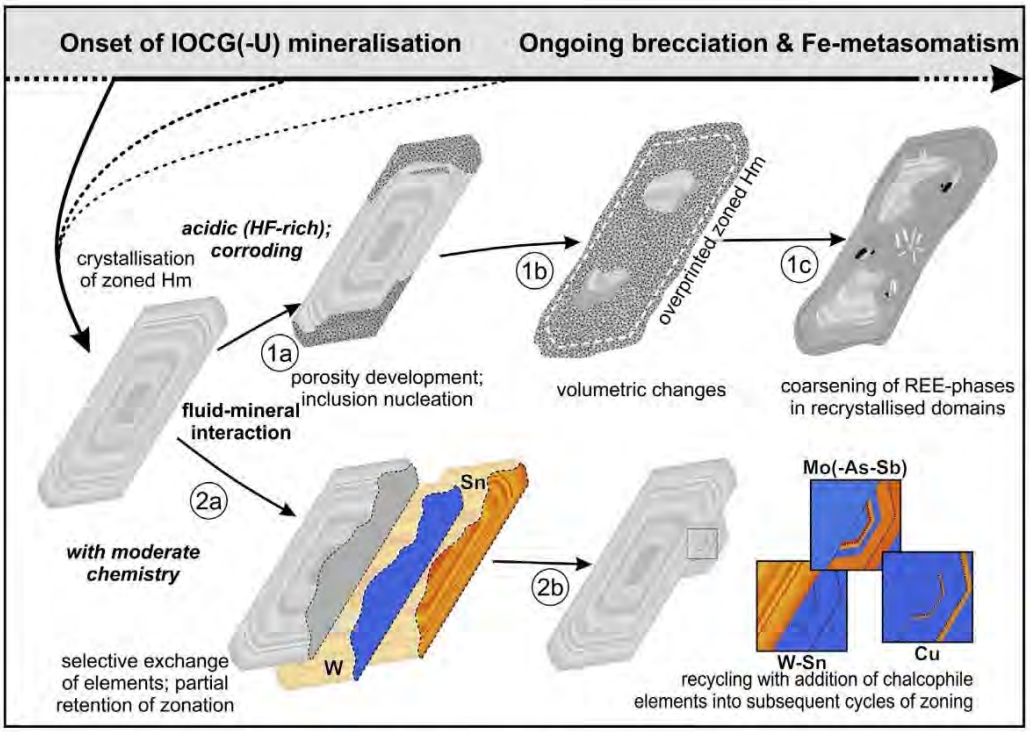

Fig. 18. Schematic showing the main types of zoned hematite overprint preserving granitophile-rich signatures. Textures and trace element signatures are interpreted to result from coupled dissolution reprecipitation reactions but with various scenarios for the fluids as marked. See text for additional explanation.

Case 2a is just ~200 m away from 2b.

Both types of interaction preserve, albeit in different ways, the initial granitophile signatures of zoned hematite either in new, recrystallised grains, or as discrete mineral inclusions. At OD, comparable selective trace element removal has been shown for uraninite during strain-induced radiogenic decay of U (Macmillan et al., 2016b), as well as CDRR-driven replacement of uraninite by Cu-Fe-sulphides (Macmillan et al., 2016c). The hypotheses discussed above will be constrained in the future by nanoscale studies of hematite addressing the relative orientation of the hematite across replacement boundaries.

7.4. Hematite from the Olympic Dam orebody – defining the archetype for IOCG deposits

Taken together, the complexity of trace element signatures as defined here, particularly the links between the U-W-Sn-Mo signatures with REY, HFSE and chalcophile elements (Cu, Zn, As, Sb) in hematite, the major component of the deposit, represents a proof-of-concept for the conceptual framework of IOCG system genesis, which predicts enrichment in such elements (Groves et al., 2010 and references therein). In such models, metal sources are tied to magmas originating from metasomatised subcontinental lithospheric mantle with transfer of volatiles and metals between (volatile-rich) alkaline basic and ultrabasic magmas, and felsic melts formed in the lower crust. Such melts are the source for bimodal magmatism in the upper crust as proven at OD (Huang et al., 2015) and elsewhere in the Olympic Cu-Au Province (e.g., at Hillside; Conor et al., 2010).

The maar setting assigned to OD in such schematics is, however, incompatible with recent studies that have addressed and reconstructed sedimentary successions observed at upper levels of the deposit (McPhie et al., 2016), or the proposed depth of granite emplacement (Kontonikas-Charos et al., 2017a). In addition, the obliteration of transient porosity developed during CDR reactions confines metals and allows for preservation of geochemical signatures as discussed here for hematite and elsewhere for feldspars and uraninite (Kontonikas-Charos et al., 2017a,b; Macmillan et al., 2016a,b,c). Such evidence, as well as the preservation of high-T, primary Cu-(Fe)-sulphides throughout the vertical zonation (Ciobanu et al., 2017), suggest that Cu-U mineralisation formed at depth, prior to RDG uplift.

Recent LA-ICP-MS U-Pb dating of zoned hematite using the same sample suite across OD (Courtney-Davies et al., 2017) has shown two distinct hematite age groups. The oldest group, including some of the published ages for the high-grade ore (Ciobanu et al., 2013; Courtney-Davies et al., 2016) and spanning the vertical sulphide-zonation in the SE lobe (confirmed by high-precision ID-TIMS U-Pb dating; Courtney-Davies et al., 2017) closely resembles U-Pb zircon ages for the RDG (1593.9 ± 0.5 Ma; Jagodzinski, 2014), thus clearly relating mineralisation to emplacement of the host granite. Based on the consistency of the oldest hematite ages and the prominent enrichment of U, W Sn and Mo in hematite, a granitic source for the hydrothermal fluids is inferred. Ongoing high-precision dating of zoned hematite from volcanoclastic rocks and sedimentary rocks will provide a time-space framework for the deposit evolution.

Olympic Dam was one deposit considered to define IOCG mineralisation as a distinct style (Hitzman et al., 1992) but ongoing work highlights the ingredients necessary to refine broader IOCG models. The U-W-Sn-Mo signature, retained throughout the different textural types of hematite described here, can be considered one of the defining characteristics of such an archetype. Despite its simple chemistry, the crystal-structural modularity of hematite can adapt and retain evolving fluid signatures so long as the main type of fluid-rock interaction is via coupling dissolution with re-precipitation rates.

8. Outlook and implications

The widespread presence of hematite enriched in granitophile elements is hitherto unreported from other locations, although enrichment in individual elements is well-documented in the literature. For example, maximum concentrations of up to 4.96 wt% WO_3 (~0.034 apfu W), accompanied by 0.13 wt% SnO_2 (~0.001 apfu Sn), are documented from epithermal veins with exotic Cu-Bi-sulphosalts (Banska Stiavnica, Slovak Republic; Sejkora et al., 2015). Simultaneous enrichment of both W and Sn in hematite, whether as discrete mineral inclusions or lattice-bound substitution, thus appears to be relatively common, even if a simultaneous enrichment in U and Mo is less commonly reported. Nonetheless, hematite from other IOCG systems in the Olympic Cu-Au Province, South Australia, and also from the Carajás Province, Brazil, possess trace-element signatures that resemble those observed at OD (Courtney-Davies et al., 2016). Comparable W ± Sn-enriched signatures were recently recognised in the skarn-like overprint of BIF-mineralisation from the Island Dam prospect (located ~17 km SE from the OD deposit; Keyser et al., 2017), further emphasizing that enrichment in granitophile elements is a common feature of Fe-oxides across the Olympic Cu-Au Province. In IOCG systems with skarn alteration, however, garnets from the granite series preferentially partition comparable concentrations of granitophile elements instead of Fe-oxides (e.g., Hillside deposit, Yorke Peninsula; Ismail et al., 2014). An association of U with Fe-oxides appears widespread (e.g., Karkhanavala, 1958; Wernicke and Lippolt, 1993), yet wt% levels, such as those reported by Ciobanu et al. (2013), or in this study have not been published for hematite from hydrothermal deposits elsewhere.

CDR-reactions are recognised as driving element exchange during hydrothermal alteration in IOCG-systems and, as shown here, are important for partially preserving the granitophile signatures throughout various hematite categories. CDRR are invoked as a fundamental requisite for formation of IOCG-systems, whereby sodic alteration (albitization) contributes towards the total available REE budget (Kontonikas-Charos et al., 2014, 2018). Indeed, such reactions are shown to be widespread at OD across disparate mineral groups (e.g., Macmillan et al., 2016a,b, Kontonikas-Charos et al., 2017b). As noted by Ciobanu et al. (2017), CDRR may be characteristic for, and inherent to, formation of giant, high-grade deposits of this type.

As seen from OD, Fe-oxides are among the minerals that have been repeatedly formed, reworked and overprinted by subsequent cycles of brecciation, fluid-mineral reaction, remobilization and recrystallisation within the same sample (Ciobanu et al., 2013; Cook et al., 2016), and throughout the orebody as shown here. Despite this, aspects of the primary geochemical signatures survive these processes and can therefore be traced.

Lastly, the presence of granitophile elements in hematite carries relevance for definition of a hypothetical future resource. Locally, concentrations of W and Sn in hematite correlate with total Fe content from whole-rock assay data, indicating increase with the degree of Fe-metasomatism (Fig. 2d, e). Hematite is already recognised as the 4th most important U-bearing phase at OD after uraninite, coffinite and brannerite (Ehrig et al., 2012), and is probably by far the most important W-, Sn- and Mo-bearing phase in the deposit by mass.

Acknowledgements

This work is a contribution to the 'FOX' project (Trace elements in iron oxides: deportment, distribution and application in ore genesis, geochronology, exploration and mineral processing), supported by BHP Olympic Dam and the South Australian Government Mining and Petroleum Services Centre of Excellence. We extend thanks to staff at Adelaide Microscopy, particularly Benjamin Wade, for assistance with microanalysis. Last but not least, we acknowledge valuable comments from reviewers Ian Graham and Alexandre Cabral and *Ore Geology Reviews* Chief Editor Franco Pirajno, which helped us improve expression of our results and interpretations.

Appendix A. Supplementary data

Supplementary data associated with this article can be found, in the online version, at http://dx.doi.org/10.1016/j.oregeorev.2017.10.007.

References

Apukhtina, O.B., Kamenetsky, V.S., Ehrig, K., Kamenetsky, M.B., McPhie, J., Maas, R., Meffre, S., Goemann, K., Rodemann, T., Cook, N.J., Ciobanu, C.L., 2016. Postmagmatic magnetite–apatite assemblage in mafic intrusions: a case study of dolerite at Olympic Dam, South Australia. Contrib. Mineral. Petrol. 171. https://http://dx.doi.org/10.1007/s00410-015-1215-7.

Barkov, A.Y., Martin, R.F., Shi, L., LeBarge, W., Fedortchouk, Y., 2008. Oscillatory zoning in stanniferous hematite and associated W- and Bi-rich minerals from Canadian Creek, Yukon, Canada. Can. Mineral. 46, 59–72. http://dx.doi.org/10.3749/canmin.46.1.59.

BHP Billiton, 2016. Annual Report 2016. http://www.bhpbilliton.com/~/media/bhp/documents/investors/annual-reports/2016/bhpbillitonannualreport2016.pdf?la=en.

Broughm, S.G., Hanchar, J.M., Tornos, F., Westhues, A., Attersley, S., 2017. Mineral chemistry of magnetite from magnetite-apatite mineralization and their host rocks: examples from Kiruna, Sweden, and El Laco, Chile. Miner. Deposita (in press). https://doi.org/10.1007/s00126-017-0718-8.

Chen, Z., Cvelbar, U., Mozetič, M., He, J., Sunkara, M.K., 2008. Long-range ordering of oxygen-vacancy planes in α-Fe_2O_3 nanowires and nanobelts. Chem. Mater. 20 (9), 3224–3228. http://dx.doi.org/10.1021/cm800288y.

Ciobanu, C.L., 2015. Trace element signatures in sulphides at Olympic Dam and satellite prospects. Unpublished report for BHP Billiton Olympic Dam, 260 pp.

Ciobanu, C.L., Wade, B.P., Cook, N.J., Schmidt Mumm, A., Giles, D., 2013. Uranium-bearing hematite from the Olympic Dam Cu–U–Au deposit, South Australia: a geochemical tracer and reconnaissance Pb–Pb geochronometer. Precambr. Res. 238, 129–147. http://dx.doi.org/10.1016/j.precamres.2013. 10.007.

Ciobanu, C.L., Cook, N.J., Ehrig, K., Wade, B.P., Kamenetsky, V.S., 2015. Trace element signatures in iron oxides from the Olympic Dam IOCG deposit, South Australia. 13th SGA Biennial Meeting 2015. Miner. Resour. Sustainable World 3, 1071–1074.

Ciobanu, C.L., Cook, N.J., Ehrig, K., Courtney-Davies, L., Keyser, W., Wade, B.P., Maunders, C., Kamenetsky, V.S., 2016. Towards a suitable natural standard for routine U-Pb dating of iron oxides. Abstract, Australian Earth Sciences Convention, Adelaide.

Ciobanu, C.L., Cook, N.J., Ehrig, K., 2017. Ore minerals down to the nanoscale: Cu-(Fe)-sulphides from the iron oxide copper gold deposit at Olympic Dam, South Australia. Ore Geol. Rev. 81, 1218–1235. http://dx.doi.org/10.1016/j.oregeorev.2016.08.015.

Conor, C., Raymond, O., Baker, T., Teale, G., Say, P., Lowe, G., 2010. Alteration and mineralisation in the Moonta-Wallaroo Cu–Au mining field region, Olympic Domain, South Australia. In: In: Porter, T.M. (Ed.), Hydrothermal Iron Oxide Copper-Gold and Related Deposits, vol. 3. PGC Publishing, Adelaide, pp. 1–24.

Cook, N.J., Ciobanu, C.L., George, L., Zhu, Z.-Y., Wade, B., Ehrig, K., 2016. Trace element analysis of minerals in magmatic-hydrothermal ores by laser ablation inductively-coupled plasma mass spectrometry: approaches and opportunities. Minerals 6 (4), 111. http://dx.doi.org/10.3390/min6040111.

Courtney-Davies, L., Zhu, Z., Ciobanu, C.L., Wade, B.P., Cook, N.J., Ehrig, K., Cabral, A.R., Kennedy, A., 2016. Matrix-matched iron-oxide laser Ablation ICP-MS U-Pb geochronology using mixed solution standards. Minerals 6 (3), 85. http://dx.doi.org/10.3390/min6030085.

Courtney-Davies, L., Ciobanu, C.L., Cook, N.J., Verdugo-Ihl, M., Tapster, S.R., Condon, D. J., Kennedy, A.K., Ehrig, K., Wade, B/P., Gilbert, S.E. 2017. Oscillatory-zoned hematite: a reliable U-Pb mineral geochronometer. Abstract, Goldschmidt 2017, Paris, France, August 13–18.

Creaser, R.A., 1989. The Geology and Petrology of Middle Proterozoic felsic Magmatism of the Stuart Shelf, South Australia. Unpublished PhD thesis, La Trobe University.

Dare, S.A.S., Barnes, S.-J., Beaudoin, G., 2015. Did the massive magnetite "lava flows" of El Laco (Chile) form by magmatic or hydrothermal processes? New constraints from magnetite composition by LA-ICP-MS. Miner. Deposita 50, 607–617. http://dx.doi.org/10.1007/s00126-014-0560-1.

Duff, M.C., Coughlin, J.U., Hunter, D.B., 2002. Uranium co-precipitation with iron oxide minerals. Geochim. Cosmochim. Acta 66, 3533–3547. http://dx.doi.org/10.1016/S0016-7037(02)00953-5.

Ehrig, K., McPhie, J., Kamenetsky, V., 2012. Geology and Mineralogical Zonation of the Olympic Dam Iron Oxide Cu-U-Au-Ag Deposit, South Australia. In J.W. Hedenquist, M. Harris, F. Camus (Eds.), Geology and Genesis of Major Copper Deposits and Districts of the World: A Tribute to Richard H. Sillitoe, Society of Economic Geologists, Special Publication 16, pp. 237–267.

Fanning, C.M., Flint, R.B., Parker, A.J., Ludwig, K.R., Blissett, A.H., 1988. Refined Proterozoic evolution of the Gawler Craton, South Australia, through U-Pb zircon geochronology. Precambr. Res. 40–41, 363–386. http://dx.doi.org/10.1016/0301-9268(88)90076-9.

Groves, D.I., Bierlein, F.P., Meinert, L.D., Hitzman, M.W., 2010. Iron Oxide Copper-Gold (IOCG) deposits through earth history: implications for origin, lithospheric setting, and distinction from other epigenetic iron oxide deposits. Econ. Geol. 105, 641–654. http://dx.doi.org/10.2113/gsecongeo.105.3.641.

Hitzman, M.W., Oreskes, N., Einaudi, M.T., 1992. Geological characteristics and tectonic

setting of Proterozoic iron oxide (Cu-U-Au-REE) deposits. Precambr. Res. 58, 241–287. http://dx.doi.org/10.1016/0301-9268(92)90121-4.

Huang, Q., Kamenetsky, V.S., McPhie, J., Ehrig, K., Meffre, S., Maas, R., Thompson, J., Kamenetsky, M., Chambefort, I., Apukhtina, O., Hu, Y., 2015. Neoproterozoic (ca. 820–830 Ma) mafic dykes at Olympic Dam, South Australia: links with the Gairdner Large Igneous Province. Precambr. Res. 271, 160–172. http://dx.doi.org/10.1016/j.precamres.2015.10.001.

Huang, Q., Kamenetsky, V.S., Ehrig, K., McPhie, J., Kamenetsky, M., Cross, K., Meffre, S., Agangi, A., Chambefort, I., Direen, N.G., Maas, R., Apukhtina, O., 2016. Olivine-phyric basalt in the Mesoproterozoic Gawler silicic large igneous province, South Australia: examples at the Olympic Dam Iron Oxide Cu–U–Au–Ag deposit and other localities. Precambr. Res. 281, 185–199. http://dx.doi.org/10.1016/j.precamres.2016.05.019.

Ismail, R., Ciobanu, C.L., Cook, N.J., Teale, G.S., Giles, D., Schmidt Mumm, A.S., Wade, B., 2014. Rare earths and other trace elements in minerals from skarn assemblages, Hillside iron oxide–copper–gold deposit, Yorke Peninsula, South Australia. Lithos 184–187, 456–477. http://dx.doi.org/10.1016/j.lithos. 2013.07.023.

Jagodzinski, E.A., 2005. Compilation of SHRIMP U-Pb geochronological data Olympic Domain, Gawler Craton, South Australia. Geoscience Australia Record 2005/20.

Jagodzinski, E.A., 2014. The Age of Magmatic and Hydrothermal Zircon at Olympic Dam. In: Proceedings of 2014 Australian Earth Sciences Convention (AESC), Sustainable Australia, Newcastle, NSW, Australia, 7–10 July 2014; vol. 110, p. 260.

Karkhanavala, M.D., 1958. On radioactive uraniferous iron oxides. Geochim. Cosmochim. Acta 15, 229–236. http://dx.doi.org/10.1016/0016-7037(58)90060-7.

Keyser, W.M., Ciobanu C.L., Cook, N.J., Courtney-Davies L., Ehrig K., Gilbert S., McPhie, J., 2017. Links between sedimentary protoliths and IOCG-skarn alteration, Island Dam, South Australia, Extended abstract, 14th Biennial SGA Conference, Québec, Canada, vol. 3, pp. 935-938.

Keyser, W., Ciobanu, C.L., Cook, N.J., Johnson, G., Feltus, H., Johnson, S., Dmitrijeva, M., Ehrig, K., Nguyen, P.T. (in review) Petrography and trace element signatures of iron-oxides in deposits from the Middleback Ranges, South Australia: from banded iron formation to ore. Ore Geol. Rev.

Knipping, J.L., Bilenker, L.D., Simon, A.C., Reich, M., Barra, F., Deditius, A.P., Lundstrom, C., Bindeman, I., Munizaga, R., 2015a. Giant Kiruna-type deposits form by efficient flotation of magmatic magnetite suspensions. Geology 43, 591–594. http://dx.doi.org/10.1130/G36650.1.

Knipping, J.L., Bilenker, L.D., Simon, A.C., Reich, M., Barra, F., Deditius, A.P., Wälle, M., Heinrich, C.A., Holtz, F., Munizaga, R., 2015b. Trace elements in magnetite from massive iron oxide-apatite deposits indicate a combined formation by igneous and magmatic-hydrothermal processes. Geochim. Cosmochim. Acta 171, 15–38. http://dx.doi.org/10.1016/j.gca. 2015.08.010.

Kontonikas-Charos, A., Ciobanu, C.L., Cook, N.J., 2014. Albitization and redistribution of REE and Y in IOCG systems: Insights from Moonta-Wallaroo, Yorke Peninsula, South Australia. Lithos 208–209, 178–201. http://dx.doi.org/10.1016/j.lithos.2014.09.001.

Kontonikas-Charos, A., Ciobanu, C.L., Cook, N.J., Ehrig, K., Krneta, S., Kamenetsky, V.S., 2017a. Feldspar evolution in the Roxby Downs Granite, host to Fe-oxide Cu-Au-(U) mineralisation at Olympic Dam, South Australia. Ore Geol. Rev. 80, 838–859. http://dx.doi.org/10.1016/j.oregeorev.2016.08.019.

Kontonikas-Charos, A., Ciobanu, C.L., Cook, N.J., Ehrig, K., Ismail, R., Krneta, S., Basak, A., 2017b. Feldspar mineralogy and rare earth element (re)mobilization in iron-oxide copper gold systems from South Australia: a nanoscale study. Mineral. Mag. http://dx.doi.org/10.1180/minmag.2017. 081.040.

Kontonikas-Charos, A., Ciobanu, C.L., Cook, N.J., Ehrig, K., Krneta, S., Kamenetsky, V.S., 2018. Rare earth element geochemistry of feldspars: examples from Fe-oxide Cu-Au systems in the olympic Cu-Au Province, South Australia. Mineral. Petrol. http://dx.doi.org/10.1007/s00710-017-0533-z. in press.

Kreissl, S., Bolanz, R., Göttlicher, J., Steininger, R., Tarassov, M., Markl, G., 2016. Structural incorporation of W^{6-} into hematite and goethite: a combined study of natural and synthetic iron oxides developed from precursor ferrihydrite and the preservation of ancient fluid compositions in hematite. Am. Mineral. 101, 2701–2715. http://dx.doi.org/10.2138/am-2016-5690.

Krneta, S., Ciobanu, C.L., Cook, N.J., Ehrig, K., Kontonikas-Charos, A., 2017. Rare earth element behaviour in apatite from the Olympic Dam Cu–U–Au–Ag deposit, South Australia. Minerals 7 (8), 135. https://http://dx.doi.org/10.3390/min7080135.

L'Heureux, I., Katsev, S., 2006. Oscillatory zoning in a (Ba, Sr)SO4 solid solution: macroscopic and cellular automata models. Chem. Geol. 225 (3), 230–243. http://dx.doi.org/10.1016/j.chemgeo.2005.08.017.

Liu, Y., Ciobanu, C.L., 2016. Crystal-Structural and Nanoscale Characterization of Iron Oxides From the Olympic Dam Cu-U-Au-Ag Deposit. Unpublished Research Report, The University of Adelaide, South Australia.

Macmillan, E., Ciobanu, C.L., Ehrig, K., Cook, N.J., Pring, A., 2016a. Chemical zoning and lattice distortion in uraninite from Olympic Dam, South Australia. Am. Mineral. 101, 2351–2354. http://dx.doi.org/10.2138/am-2016-5753.

Macmillan, E., Cook, N.J., Ehrig, K., Ciobanu, C.L., Pring, A., 2016b. Uraninite from the Olympic Dam IOCG-U-Ag deposit: linking textural and compositional variation to temporal evolution. Am. Mineral. 101, 1295–1320. http://dx.doi.org/10.2138/am-2016-5411.

Macmillan, E., Ciobanu, C.L., Ehrig, K., Cook, N.J., Pring, A., 2016c. Replacement of uraninite by bornite via coupled dissolution-reprecipitation: evidence from texture and microstructure. Can. Mineral. 54, 1369–1383. http://dx.doi.org/10.3749/canmin.1600031.

McPhie, J., Kamenetsky, V.S., Chambefort, I., Ehrig, K., Green, N., 2011. Origin of the supergiant Olympic Dam Cu-U-Au-Ag deposit, South Australia: Was a sedimentary basin involved? Geology 39, 795–798. http://dx.doi.org/10.1130/G31952.1.

McPhie, J., Orth, K., Kamenetsky, V., Kamenetsky, M., Ehrig, K., 2016. Characteristics, origin and significance of Mesoproterozoic bedded clastic facies at the Olympic Dam Cu–U–Au–Ag deposit, South Australia. Precambr. Res. 276, 85–100. http://dx.doi.org/10.1016/j.precamres.2016.01.029.

Michard, A., Michard, G., Stüben, D., Stoffers, P., Cheminée, J., Binard, N., 1993. Submarine thermal springs associated with young volcanos: the Teahitia vents, Society Islands, Pacific Ocean. Geochim. Cosmochim. Acta 57, 4977–4986. http://dx.doi.org/10.1016/S0016-7037(05)80003-1.

Migdisov, A., Williams-Jones, A.E., Brugger, J., Caporuscio, F.A., 2016. Hydrothermal transport, deposition, and fractionation of the REE: Experimental data and thermodynamic calculations. Chem. Geol. 439, 13–42. http://dx.doi.org/10.1016/j.chemgeo.2016.06.005.

Putnis, A., 2002. Mineral replacement reactions: from macroscopic observations to microscopic mechanisms. Mineral. Mag. 66, 689–708. http://dx.doi.org/10.1180/0026461026650056.

Putnis, A., 2015. Transient porosity resulting from fluid-mineral interaction and its consequences. Rev. Mineral. Geochem. 80, 1–23. http://dx.doi.org/10.2138/rmg.2015.80.01.

Putnis, A., Fernandez-Diaz, L., Prieto, M., 1992. Experimentally produced oscillatory zoning in the (Ba, Sr)SO4 solid solution. Nature 358, 743–745. https://doi.org/http://dx.doi.org/10.1038/358743a0.

Reeve, J.S., Cross, K.C., Smith, R.N., Oreskes, N., 1990. Olympic Dam Copper-Uranium-gold-silver Deposit. In: F.E. Hughes (Ed.), Geology of the Mineral Deposits of Australia and Papua New Guinea, Australasian Institute of Mining and Metallurgy, pp. 1009–1035.

Sejkora, J., Števko, M., Ozdín, D., Pršek, J., Jeleň, S., 2015. Unusual morphological forms of hodrušite from the Rozália vein, Hodruša-Hámre near Banská Štiavnica (Slovak Republic). J. Geosci. 60, 11–22. http://dx.doi.org/10.3190/jgeosci.188.

Tarassov, M., Mihailova, B., Tarasova, E., Konstantinov, I., 2002. Chemical composition and vibrational spectra of tungsten-bearing goethite and hematite from Western Rhodopes, Bulgaria. Eur. J. Mineral. 14, 977–986. http://dx.doi.org/10.1127/0935-1221/2002/0014-097.

Timofeev, A., Migdisov, A.A., Williams-Jones, A.E., 2015. An experimental study of the solubility and speciation of niobium in fluoride-bearing aqueous solutions at elevated temperature. Geochim. Cosmochim. Acta 158, 103–111. http://dx.doi.org/10.1016/j.gca.2015.02.015.

van Achterbergh, E., Ryan, C.G., Jackson, S.E., Griffin, W.L., 2001. Data reduction software for LA-ICP-MS. In: P.J. Sylvester (Ed.), Laser-ablation-ICPMS in the Earth Sciences: Principles and Applications. Mineralogical Association of Canada, Short Course Series Ottawa, Ontario, Canada, vol. 29, pp. 239–243.

Verdugo-Ihl, M.R., Ciobanu, C.L., Cook., N.J., Courtney-Davies, L., Ehrig, K.J., Gilbert, S., 2017. Trace element signatures in U-W-Sn-Mo zoned hematite from the IOCG deposit at Olympic Dam, South Australia, Extended abstract, 14th Biennial SGA Conference, Québec, Canada, vol. 3, pp. 967-970.

Wernicke, R.S., Lippolt, H.J., 1993. Botryoidal hematite from the Schwarzwald (Germany): heterogeneous uranium distributions and their bearing on the helium dating method. Earth Planet. Sci. Lett. 114, 287–300. http://dx.doi.org/10.1016/0012-821X(93)90031-4.

Woodhead, J.D., Hellstrom, J., Hergt, J.M., Greig, A., Maas, R., 2007. Isotopic and elemental imaging of geological materials by laser ablation inductively coupled plasma-mass spectrometry. Geostand. Geoanal. Res. 31, 331–343. http://dx.doi.org/10.1111/j.1751-908X.2007.00104.x.

Xu, J., Ciobanu, C.L., Cook, N.J., Zheng, Y., Sun, X., Wade, B.P., 2016. Skarn formation and trace elements in garnet and associated minerals from Zhibula copper deposit, Gangdese Belt, southern Tibet. Lithos 262, 213–231. http://dx.doi.org/10.1016/j.lithos.2016.07.010.

CHAPTER 3

DEFINING EARLY STAGES OF IOCG SYSTEMS: EVIDENCE FROM IRON-OXIDES IN THE OUTER SHELL OF THE OLYMPIC DAM DEPOSIT, SOUTH AUSTRALIA

Max R. Verdugo-Ihl [1], Cristiana L. Ciobanu [1], Nigel J. Cook [1],

Kathy Ehrig [2] and Liam Courtney-Davies [1]

[1]*School of Chemical Engineering, The University of Adelaide, Adelaide, SA 5005, Australia;*

[2]*BHP Olympic Dam, Adelaide, SA 5000, Australia*

Article published in *Mineralium Deposita* (2020) 55:429−452.

Statement of Authorship

Title of Paper	Defining early stages of IOCG systems: evidence from iron-oxides in the outer shell of the Olympic Dam deposit, South Australia.
Publication Status	☑ Published ☐ Accepted for Publication ☐ Submitted for Publication ☐ Unpublished and Unsubmitted w ork w ritten in manuscript style
Publication Details	Verdugo-Ihl, M.R., Ciobanu, C.L., Cook, N.J., Ehrig, K., Courtney-Davies, L. Defining early stages of IOCG systems: evidence from iron-oxides in the outer shell of the Olympic Dam deposit, South Australia. Mineralium Deposita 55, 429-452, https://doi-org/10.1007/s00126-019-00896-2.

Principal Author

Name of Principal Author (Candidate)	Max R. Verdugo-Ihl		
Contribution to the Paper	Performed analytical work, evaluation and interpretation of results and prepared the manuscript.		
Overall percentage (%)	60		
Certification:	This paper reports on original research I conducted during the period of my Higher Degree by Research candidature and is not subject to any obligations or contractual agreements with a third party that would constrain its inclusion in this thesis. I am the primary author of this paper.		
Signature		Date	15.04.202020

Co-Author Contributions

By signing the Statement of Authorship, each author certifies that:

i. the candidate's stated contribution to the publication is accurate (as detailed above);

ii. permission is granted for the candidate in include the publication in the thesis; and

iii. the sum of all co-author contributions is equal to 100% less the candidate's stated contribution.

Name of Co-Author	Cristiana L. Ciobanu		
Contribution to the Paper	Helped to define the direction of the manuscript, guided manuscript preparation and assisted with the interpretation of the results and evaluation of the manuscript.		
Overall percentage (%)	25		
Signature		Date	15.04.2020

Name of Co-Author	Nigel J. Cook		
Contribution to the Paper	Assisted with the preparation and evaluation of the manuscript.		
Overall percentage (%)	10		
Signature		Date	15.04.2020

Name of Co-Author	Kathy Ehrig		
Contribution to the Paper	Assisted with the evaluation of the manuscript.		
Overall percentage (%)	3		
Signature		Date	15.04.2020

Name of Co-Author	Liam Courtney-Davies		
Contribution to the Paper	Assisted with data collection and the evaluation of the manuscript.		
Overall percentage (%)	2		
Signature		Date	15.04.2020

Mineralium Deposita (2020) 55:429–452
https://doi.org/10.1007/s00126-019-00896-2

ARTICLE

Defining early stages of IOCG systems: evidence from iron oxides in the outer shell of the Olympic Dam deposit, South Australia

Max R. Verdugo-Ihl[1] · Cristiana L. Ciobanu[1] · Nigel J. Cook[1] · Kathy J. Ehrig[2] · Liam Courtney-Davies[1]

Received: 13 November 2018 / Accepted: 6 May 2019 / Published online: 12 June 2019
© Springer-Verlag GmbH Germany, part of Springer Nature 2019

Abstract

The IOCG deposit at Olympic Dam (South Australia) is hosted within the Roxby Downs Granite, which displays a weakly mineralised contact to the orebody (hereafter 'outer shell'). In a mineralogical-geochemical characterisation of Fe-oxides from the outer shell, we show silician magnetite (Si-magnetite) and HFSE-bearing hematite define the early stages of alkali-calcic alteration. This association forms in the presence of hydrothermal K-feldspar and calc-silicates via overprinting of magmatic magnetite and ilmenite breakdown. Geochemical modelling, at ≥ 400 °C, shows such reactions occur at pH-fO_2 conditions coinciding with shifts from K-feldspar to sericite, and ilmenite to rutile stability. The subsequent Si-magnetite+siderite association forms down-T in the absence of K-feldspar. Transition from granular to bladed morphologies in Si-magnetite is part of a series of Fe-oxide interconversions, followed by formation of zoned, U-W-Sn-Mo-bearing hematite. Enrichment in REE, Y and U in Si-magnetite and the prevalence of U-W-Sn-Mo-bearing hematite support a granite-derived fluid. Combined, petrographic and geochemical evidence show a transition among Fe-oxides from the outer shell to the orebody attributable to the evolution of the same fluid. Unusual massive magnetite intervals and Fe-oxide nodules in granite are considered due to either the presence of inherited lithologies, metasomatic products, or the result of magnetite-rich, crystal mush forming in the melt. We propose a model, corroborated by recently published data including high-precision U-Pb dating of magmatic zircon and hydrothermal hematite, in which an 'outer shell' is initiated at the 6–8 km depth of granite emplacement during volatile release from fluids ponding at intrusion margins. Granite cupola collapse at shallower levels (2–3 km?) follows via uplift along faults, facilitating intense brecciation and ore formation.

Keywords IOCG · Olympic Dam · Fe-metasomatism · Silician magnetite · HFSE-bearing hematite

Introduction

Iron oxide copper gold (IOCG) deposits encompass magnetite- to hematite-rich end-members (Barton 2014 and references therein). In recent years, Cu-Au-poor, magnetite-rich system such as Kiruna (Sweden) and El Laco (Chile) have been termed 'iron oxide apatite' (IOA) deposits. We refer to them as deposits that are kin to but distinct from those of the IOCG class sensu stricto. Evolution schemes for IOCG systems consider regional-scale alteration haloes centred on fluid sources of various origins, in which Fe-oxide associations generally change from higher-temperature magnetite- to lower-temperature hematite-dominant assemblages (Barton 2014 and references therein), even if both spatially co-exist in many cases. The genetic scheme underpinning such a model stipulates that fluids change from mildly alkaline/neutral pH to more acidic, resulting in three main stages: (i) barren Na(-Ca)-alteration, (ii) K-alteration (K-feldspar and/or biotite), and (iii) hydrolytic (sericite)-alteration. However, IOCG deposits rarely preserve well-defined zonation, either due to telescoping of alteration patterns during evolution of the system, or to superimposed geological events. Olympic Dam (OD) is, however, a well-preserved, mineralogically and geochemically zoned, intrusion-hosted IOCG deposit (Ehrig et al. 2012),

Editorial handling: D. Huston

Electronic supplementary material The online version of this article (https://doi.org/10.1007/s00126-019-00896-2) contains supplementary material, which is available to authorized users.

✉ Max R. Verdugo-Ihl
max.verdugoihl@adelaide.edu.au

[1] School of Chemical Engineering, The University of Adelaide, Adelaide, SA 5005, Australia

[2] BHP Olympic Dam, Adelaide, SA 5000, Australia

ideal for studying relationships between co-existing Fe-oxides. The orebody is hosted within hematite+sericite alteration, whereas magnetite is present predominantly at depth and at the outer margins of the deposit (Ehrig et al. 2012 and references therein).

Relationships between textures and trace element signatures preserved in hematite and magnetite, supported by statistical analyses, can be used to correlate the formation and subsequent overprinting of Fe-oxides, as shown for banded iron formations (BIF) (e.g. Dmitrijeva et al. 2018; Keyser et al. 2018). Within the context of IOCG system, detailed studies of Fe-oxides and the products of their interconversions can facilitate new insights into their genesis, since Fe-oxides react sensitively to changes in their physio-chemical environments of formation. Following advances in laser ablation inductively coupled-plasma mass spectrometry (LA-ICP-MS) and other microbeam techniques (see Cook et al. 2016, 2017), a large volume of geochemical, isotopic, and nanoscale data has become available to assist with interpretation of deposit genesis. Recent geochemical and mineralogical studies on Fe-oxides ascribed to the broader IOCG clan have, however, focused almost exclusively on magnetite rather than hematite, examples of the latter being relatively few (e.g. Dare et al. 2015; Knipping et al. 2015; Verdugo-Ihl et al. 2017a).

In this contribution, we address the mineralogy and geochemistry of magnetite and hematite from the outer shell of the OD deposit, defined here as low-grade Cu mineralisation hosted in brecciated granite immediately outside the resource outline. We aim to define the associations of the two Fe-oxides with emphasis on recognising the early stages of IOCG systems and their trace element signatures relative to an outer alteration envelope, inherited lithologies and the host intrusion. Iron oxide formation is interpreted through geochemical modelling. The overall aim is to incorporate the results into a geological model that builds upon recent published data on the Olympic Dam deposit.

Geological background

The Olympic Cu-Au Province lies on the eastern margin of the Archean to Mesoproterozoic Gawler Craton, comprising the world-class Olympic Dam Cu-U-Au-Ag deposit and several other IOCG deposits/prospects (Fig. 1a). Mineralisation is broadly spatially and temporally associated with a craton-scale tectonothermal event at ~ 1.6 Ga that formed the Gawler Silicic Large Igneous Province (Allen et al. 2008). The latter consists of extrusive (Gawler Range Volcanics; GRV) and intrusive (Hiltaba Intrusive Suite; HIS) magmatism of bimodal character (Blissett et al. 1993). HIS granitoids and GRV intrude and unconformably overlie older basement units including metasedimentary rocks of the ~ 2.0–1.85 Ga Hutchison Group and syntectonic granitoids associated with the short-lived Cornian Orogeny (~ 1.86–1.85 Ga Donington Suite; Jagodzinski 2005). Meta(volcano)sedimentary rocks from the ~ 1.76–1.74 Ga Wallaroo Group, which host Fe-rich horizons (BIFs?) (Cowley et al. 2003; Fig. 1a) occur in the OD district. Ultramafic and mafic magmatism is recorded as dikes of (i) intensely altered picrites considered of HIS affiliation (e.g. Huang et al. 2016) and (ii) relatively fresh dolerites attributed to the ~ 820 Ma Gairdner Dyke Swarm (Huang et al. 2015).

The orebody is located within the Olympic Dam Breccia Complex (ODBC; Reeve et al. 1990), hosted within the Roxby Downs Granite (RDG; Fig. 1b), part of the HIS-affiliated Burgoyne Batholith composed of quartz monzodiorite, quartz monzonite and granite (Creaser 1996). Depth of emplacement (~ 6–8 km) was estimated for quartz monzodiorite from locations distal to OD (Creaser 1996). Studies prior to 2000 recognised the unusual character of the deposit, which was initially considered 'a new type of stratabound sediment-hosted Cu-U-Au deposit' with no obvious lateral sulfide zoning (Roberts and Hudson 1983). Models subsequently evolved to 'hydrothermal and phreatomagmatic breccias' formed in an active hydrothermal system with localised diatremes and concentric, lateral and vertical sulfide zoning relative to a barren core (Reeve et al. 1990) becoming an integral component of the then new class of IOCG deposits (Hitzman 2000 and references therein). REE-enriched hematite breccias were recognised as the products of progressive hydrothermal brecciation and Fe-metasomatism of the host granite, allowing hypothetical structural collapse in the upper part of the complex to be proposed (Oreskes and Einaudi 1990). The 'shallow', maar-diatreme setting became a paradigm for studies that followed. For example, despite comparable or overlapping fluid inclusion temperature and stable isotope signatures (~ 400 °C, 10 ‰ $\delta^{18}O$, and ~ 200–400 °C, 9 ‰ $\delta^{18}O$), for magnetite and hematite associations, respectively), two fluids were postulated: (i) a deep-seated hydrothermal fluid of magmatic(?) origin; and (ii) shallow, surficial-derived waters (Oreskes and Einaudi 1992). Based on this, a 'fluid-mixing model' was introduced (Haynes et al. 1995), in which a deep-seated intrusion within the RDG injects hot fluids into a maar, above which overlying basalt provides basalt-derived groundwater and forming vertical columns of zoned Cu-(Fe)-sulfide ores.

Intense drilling in the last decades has allowed for comprehensive sampling throughout the entire mineralised area at OD. Comprehensive resource block modelling, combined with petrological, mineralogical, lithogeochemical studies, U-Pb dating and REE-in-apatite modelling, provides new data and interpretations of the local setting and ore-forming processes at OD. Based on amphibole-plagioclase geobarometry in granite proximal to OD, the RDG emplacement depth is also estimated at 6–8 km

Miner Deposita (2020) 55:429–452

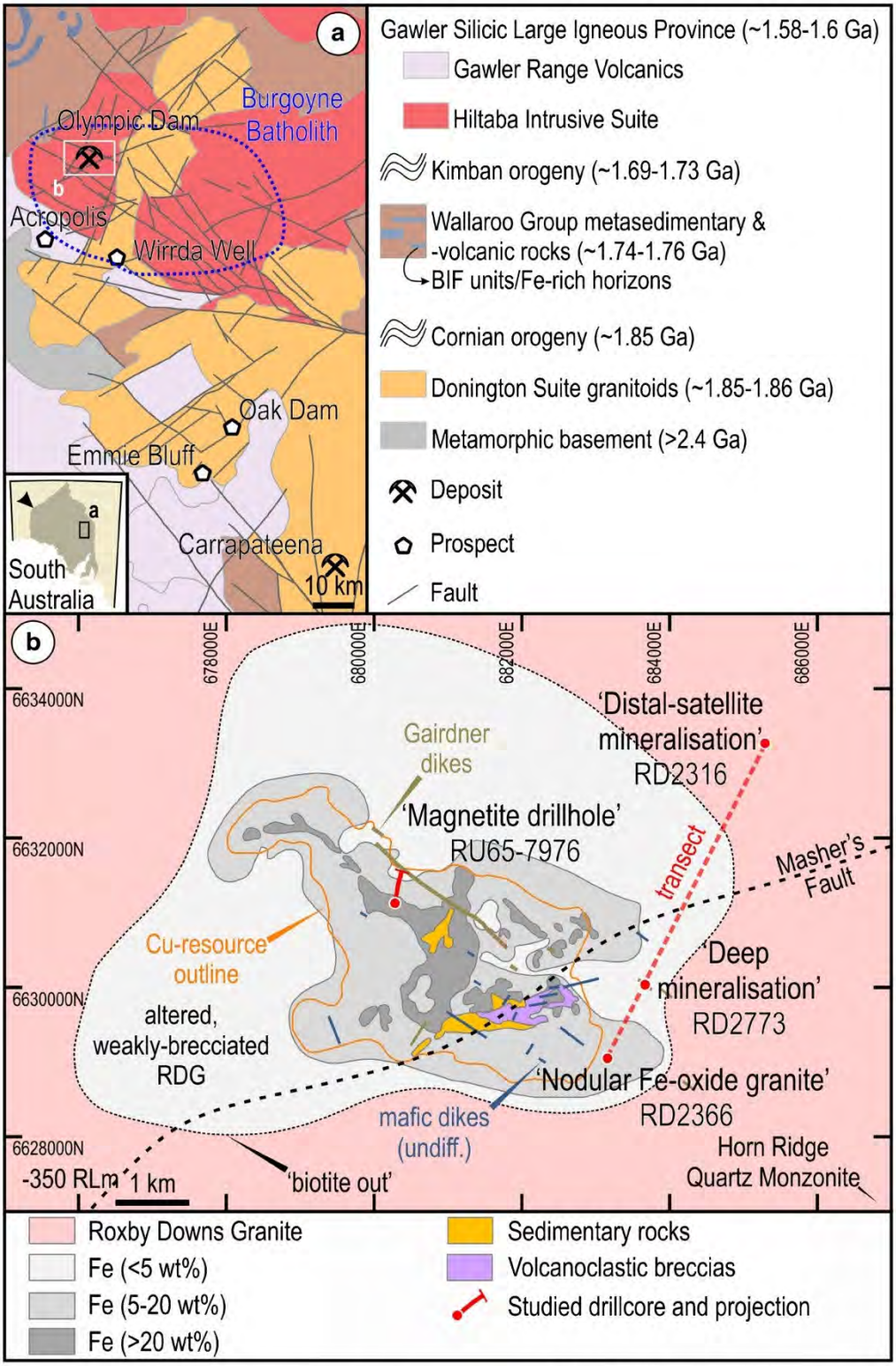

Fig. 1 (**a**) Geological map of the Olympic Dam area outlining the main basement units and extent of the Gawler Craton (arrowed in inset). Data sourced from Geological Survey of South Australia (https://map.sarig.sa.gov.au/). (**b**) Sketch of the Olympic Dam deposit showing main lithologies and projection of sampled drillholes

(Kontonikas-Charos et al. 2017). High-precision (CA-ID-TIMS) U-Pb dating of magmatic zircon in RDG outside the deposit yielded a weighted age of 1593.87 ± 0.21 Ma (2σ error; Cherry et al. 2018), suggesting no distinct magmatic pulses, although this is yet to be tested at depth and on the SE part of the deposit. Lithological complexity relates to the presence of other, presumably roughly coeval, magmatic rocks, such as the Horn Ridge Quartz Monzonite, as well as abundant mafic enclaves in the RDG (Kontonikas-Charos et al. 2017; Krneta et al. 2017). Such enclaves, combined with feldspar rapakivi textures support magma mingling at depth (Kontonikas-Charos et al. 2017).

Mineralisation, considered broadly coeval with RDG crystallisation, as indicated by U-Pb LA-ICP-MS dating of hydrothermal, U-W-Sn-Mo-bearing hematite (Ciobanu et al. 2013; Courtney-Davies et al. 2016; Apukhtina et al. 2017), is now shown to be ~ 1–3 Ma younger than the host granite based on high-precision U-Pb ID-TIMS dating of hematite (average weighted age of 1592.1 ± 0.88 Ma, 2σ error; Courtney-Davies et al. 2018). The association between Cu mineralisation and degree of Fe-metasomatism is shown by the close correspondence between the Cu-resource outline (≥ 0.3 wt% Cu) and the outer boundary of the 5–20 wt% Fe contour from the ODBC (Fig. 1b; Ehrig et al. 2012). The deposit features an inwards and upwards zonation comprising pyrite+chalcopyrite, chalcopyrite+bornite and bornite+chalcocite orezones throughout the 7-km-strike- and 2-km-depth-extent of the deposit (Ehrig et al. 2012). Hypogene vertical zoning is supported by nanoscale study of Cu-Fe-sulfides showing associations interpretable as exsolutions along cooling paths from ≤ 400 °C solid solutions within the system Cu-Fe-S (Ciobanu et al. 2017). Hematite is the main Fe-oxide within the deposit, irrespective of sulfide-zone, whereas magnetite, where present, is mostly associated with pyrite+chalcopyrite. The earliest hematite present throughout the entire deposit is oscillatory-zoned with respect to U-W-Sn-Mo, considered as a 'granitophile element' signature, typical of IOCG systems in the Gawler Craton and likely elsewhere (Ciobanu et al. 2013, 2015; Courtney-Davies et al. 2016; Verdugo-Ihl et al. 2017a, b). Multivariate statistical analysis of a large whole-rock dataset supports this signature throughout the deposit (Dmitrijeva et al. 2019). The contours of the 'IOCG signature', defined from 39 elements by principal component analysis (PCA), overlap with the isolines of ≥ 20 wt% Fe and the sericite-K-feldspar stability boundary.

Copper mineralisation (pyrite+chalcopyrite±Fe-oxides) also occurs in less-altered and -brecciated granite immediately outside the orebody, here defined as the outer shell. The granite preserves assemblages indicative of alkali-calcic metasomatism (newly formed, Ba-rich K-feldspar, calc-silicates) based on data shown here and previously (Cook et al. 2017; Kontonikas-Charos et al. 2017, 2018; Ciobanu et al. 2018). Large-scale, alkali-alteration (hydrothermal albite and K-feldspar) surrounding and underneath OD is indicated by infrared reflectance spectroscopy mapping of drillcores along a 14 km-long transect (Mauger et al. 2016).

Although magnetite is the main Fe-oxide, hematite and interconversion products among the two Fe-oxides are also reported in various associations/relationships with siderite, fluorapatite and chlorite. Such associations were used to: (i) define a generic, outer and deeper 'reduced Fe-oxide assemblage' (Ehrig et al. 2012); (ii) support evidence for an 'inherited BIF origin of magnetite' in a carbonate-hosted magnetite interval (Ciobanu et al. 2014); and (iii) propose the existence of an 'early, deep magnetite-fluorapatite mineralisation' type on the SE side of the deposit (drillhole RD2773; Fig. 1b) (Apukhtina et al. 2017).

The 'earliest' IOCG-stage magnetite was reported from mineralisation throughout a felsic, porphyritic unit ('Felsic unit', also referred to as the 'quartz-phyric felsic dyke'; Ehrig et al. 2012), which is intersected from ~ 2 km down in drillhole RD2773 (Fig. 2) (Apukhtina et al. 2017). The same authors considered the Felsic unit to be coeval with RDG based on LA-ICP-MS U-Pb zircon dating (1591 ± 11 Ma). However, the uncertainty on this age cannot resolve potential timing differences between the two magmatic phases and the question of which Fe-oxides in the outer shell at OD are the earliest thus remains open.

The presence of older, pre-Hiltaba Fe-rich lithologies is inferred from preliminary U-Pb LA-ICP-MS magnetite dating that yielded a 1769 ± 58 Ma age for a massive magnetite interval from drillhole RU65–7976 (OD11; Fig. 1b; Ciobanu et al. 2014). Such Fe-rich lithologies may potentially represent entrapped BIF blocks preserved in the granite. In contrast, spherulitic magnetite as young as ~ 820 Ma is inferred from dating of accessory minerals in Gairdner dikes (Apukhtina et al. 2016).

The manifestation of the IOCG event within the outer shell at OD is confirmed from U-Pb LA-ICP-MS dating of hematite and accessory minerals from the DM (Apukhtina et al. 2017) and is reinforced by U-Pb ID-TIMS dating of hematite from the outer shell (1587.6 ± 3.2 Ma; sample MV005A; RD2366; Courtney-Davies et al. 2019). The age of magnetite in the outer shell is, however, as yet unconstrained.

Samples and methodology

The present study aims to understand the role of Fe-oxides in defining the early stage of IOCG mineralisation and whether these trends can be discriminated from signatures inherited from precursor rocks. The sample suite comprises three nearly vertical drillholes located along a ~ 4.7 km-long transect on

Miner Deposita (2020) 55:429–452

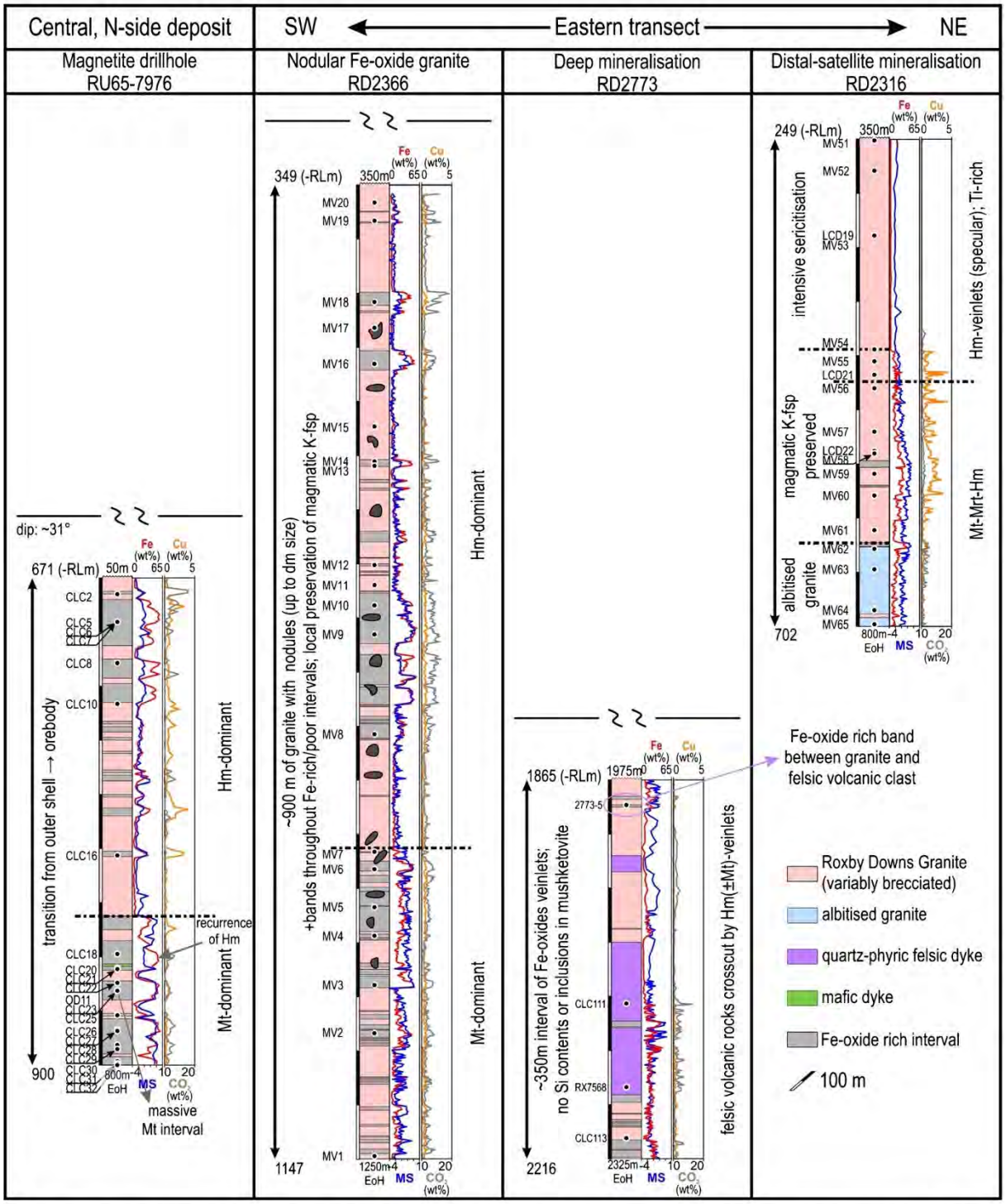

Fig. 2 Simplified lithologies of the studied drillholes showing sample locations. Logs of Cu, Fe, CO_2 show correlation between Cu mineralisation and Fe-metasomatism. Note variability in CO_2 among the different locations. Coincidence between MS and increased Fe is indicative of magnetite-rich intervals; magnetic susceptibility (MS) is logarithmically scaled (10^n). Except for drillhole RD2366, these drillholes have been previously studied, and we use the same nomenclature for consistency

the eastern side of the deposit, and a fourth, sub-horizontal hole drilled from underground on the central-north margin of the orebody, together covering a vertical extent of ~ 2 km (Fig. 2). The intersected granite in these locations displays different degrees of alteration, presence of other lithologies and the mode of occurrence of Fe-oxides (Figs. 1b and 2; ESM 3).

Sample characterisation involved examination by reflected light optical microscopy and scanning electron microscopy using a FEI Quanta 450 instrument operated at 20 or 25 kV in back-scattered electron (BSE) mode. A CAMECA SX-Five electron probe microanalyzer (EPMA) operated at 15 kV, beam currents of 20 and 100 nA, and focused ~ 1 μm beam, was used to verify Fe-oxide stoichiometry. Data reduction was performed using 'Probe for EPMA' (e.g. Donovan et al. 2016).

Trace element LA-ICP-MS analysis of Fe-oxides was conducted on a RESOlution-LR 193 nm ArF excimer laser microprobe (Australian Scientific Instruments) coupled to an Agilent 7900cx quadrupole ICP-MS. Spot analysis was biased towards coarse-grained Fe-oxides that could be readily analysed using larger spot sizes (up to 51 μm). Spot analysis comprised measurement of background (30 s) followed by acquisition of signal during ablation (30 or 40 s). Iron, measured as ^{57}Fe, was used as the internal standard element, assuming ideal stoichiometries for hematite and magnetite. GSD-1G or BHVO-2G and NIST-610 were employed as external reference materials and used for instrument drift correction and trace element quantification. Maximum sensitivity and low oxide interference production was achieved by daily optimization of the ICP-MS system. Off-line data reduction was performed in 'Glitter' (van Achterbergh et al. 2001). Evident contributions from inclusions were minimised by avoiding their interference from the integrated intervals, otherwise such analyses were rejected. Analysis of Fe-oxides featuring a consistent presence of homogeneously distributed inclusions at the scale of the ablation spot includes their contribution in the integrated signal. Reported Pb contents correspond to total Pb concentrations calculated from the individual abundances of ^{206}Pb, ^{207}Pb and ^{208}Pb. LA-ICP-MS intensity maps, scaled in counts-per-second (cps), were obtained by ablating sets of parallel, adjacent lines over rectangular grids. The individual lines were compiled and processed into 2-D images displaying the combined background-subtracted intensities using 'Iolite' (Paton et al. 2011). Obtained intensities were scaled individually to enhance features of interest; if not stated otherwise, logarithmic scales are used (10^n).

All instrumentation employed for microanalytical work is housed at Adelaide Microscopy, The University of Adelaide. Further details on the aforementioned methods, operating conditions and reference materials are given in ESM 1.

Results

Iron oxide distributions

The sample suite encompasses distinct Fe-oxide textures, including rhythmically banded (Fig. 3a), veinlets (Fig. 3b, c), scalloped and orbicular/nodular morphologies (Fig. 3d–h), brecciated veins (Fig. 3i) and cm-sized pockets of Fe-oxides associated with sulfides (Fig. 3j). Centimetre-scale hematite veinlets are present throughout the RDG, particularly on the eastern side.

The Magnetite Drillhole displays a downwards transition from hematite- to magnetite-dominant intervals in its lower third (Fig. 2), but also with local m- to cm-scale recurrences among Fe-oxides. Iron oxides are present as accumulations of dark-grey, fine-grained intervals (metres to tens of metres in thickness) within the granite. Sporadically, unusual rhythmic banding of coarse hematite and gangue is observed (Fig. 3a). Massive, ~ 10 m-wide magnetite intervals with a siderite matrix (Fig. 2) are also present. The altered granite displays pink (hematite-), to greenish (chlorite-altered) colours (Fig. 3b, d) and lacks magmatic feldspar and mafic minerals. Iron oxides cement matrix- to clast-supported granite breccias in which coarse- and fine-grained granite varieties can co-exist (Fig. 3b). Advanced replacement of granite by Fe-oxide+carbonate assemblages can result in scalloped boundaries (Fig. 3d).

The Nodular Fe-oxide Granite (RD2366) intersects metres to tens of metres thick intervals of Fe-oxides within variably brecciated and altered granite (Fig. 2). The brecciated granite can be still recognisable as pink-coloured clasts. The nodules, which are scattered throughout the drillhole, have different colours (Fig. 3e–h), can be enveloped by sulfides, may occur adjacent to 'exotic' clasts (Fig. 3f), or display irregular, sub-rounded morphologies (Fig. 3h). Despite advanced alteration, the granite still retains relicts of magmatic K-feldspar, although newly formed, Ba-bearing, K-felspar is also present.

The Deep Mineralisation (DM) represents the deepest sampled interval (drillhole RD2773, from a depth of ~ 1975–2325 m EoH) and intersects the Felsic unit (Fig. 2). Magnetite and hematite are generally observed together from

Fig. 3 Photographs of hand-specimens representative of the different mode of occurrence of Fe-oxides. (**a**) Rhythmically banded hematite and gangue representing the category termed 'hematite replacement of carbonates' (RU65-7976). (**b**) Clast-supported granite breccia with interstitial Fe-oxides. Note grain-size variation between adjacent granite clasts. (**c**) Iron oxide veinlets in the sericite-altered Felsic unit (DM). (**d**) Scalloped boundary between magnetite+siderite and chlorite-altered (green) granite. (**e–h**) Morphology and colour variation of 'nodules' within granite (RD2366). Note presence of 'exotic' clast (sedimentary rock or microgranite?) in (**f**). (**i**) Breccia vein containing Ti-hematite. (**j**) Fe-oxides associated with sulfide mineralisation in altered granite (DSM). Ap-apatite; Chl-chlorite; Cp-chalcopyrite; Fl-fluorite; Hm-hematite; Mt-magnetite; Py-pyrite; Qtz-quartz; Sd-siderite; Ser-sericite; the same abbreviations are used henceforth

Miner Deposita (2020) 55:429–452

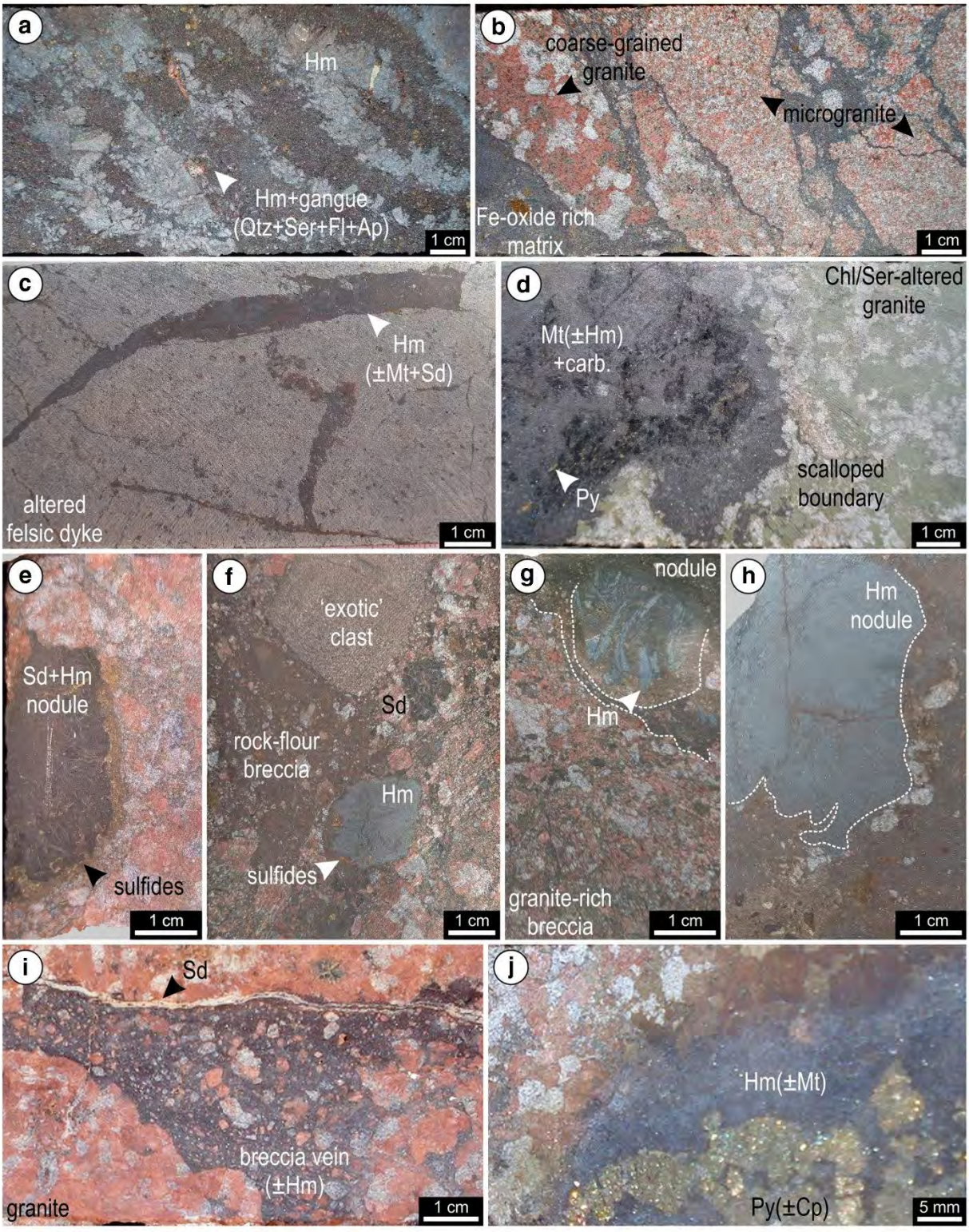

the contact downwards with associated increase in Cu grade. Both the RDG and the Felsic unit are strongly altered to assemblages of sericite/chlorite+hematite. Felsic volcanic rocks also occur as clasts or metre-thick intervals throughout the brecciated granite. Iron oxides occur scattered as disseminations and/or pockets in the granite and within crosscutting veinlets in the Felsic unit (Fig. 3c).

In the Distal Satellite Mineralisation (DSM; RD2316) (Fig. 1b), the intersected granite displays sodic alteration beneath an interval in which magmatic K-feldspar is broadly preserved (Fig. 2). Copper mineralisation coincides with the latter, lower interval between depths of 450 m and ~ 700 m in rocks which also display the most intense Fe-metasomatism. In contrast, the albitised interval is weakly to unmineralised. Unusually abundant molybdenite occurs throughout the mineralisation, forming aggregates up to cm-size. Assemblages of REE-fluorocarbonates and molybdenite replace feldspars, or fill veinlets of intense brecciation in the upper section of the drillhole. Such veinlets can locally develop into domains of rock-flour milling and brecciation of the granite (Fig. 3i). As in the Magnetite Drillhole, hematite is dominant in the ~ 330 m-thick upper section as veinlets and co-exists with magnetite downwards; the latter becoming increasingly more abundant with depth (Fig. 2).

As shown here, the depth of transition from hematite to magnetite in the outer shell varies among the different locations (Fig. 2); shallowest for DSM (~ 470 m), similar for the Magnetite and Nodular Fe-oxide Granite drillholes (830 and 860 m, respectively), and below a depth of ~ 2.2 km in the DM.

Petrography

Texturally, magnetite and hematite are intimately associated on the scale of a polished block, with a few exceptions in which one Fe-oxide markedly predominates over the other. Co-existing textural varieties indicating pseudomorphic replacement of magnetite by hematite (martite), or vice versa (mushketovite) are observed. However, there are also varieties of bladed, acicular or feathery magnetite that can result from overprinting of granular magnetite (see below) rather than conversion from pre-existing hematite. This textural type is hereafter termed (pseudo)mushketovite.

In the DSM, magnetite is progressively replaced by hematite unambiguously illustrating martitisation, commonly associated with sulfide deposition (Fig. 4a, b). Otherwise, martitisation as such is not widely preserved at OD. Coarse-grained, twinned hematite, either bladed or granular, can host subordinate magnetite in veinlets from the Felsic unit (DM). Samples from the contact between granite and a block of felsic volcanic rock differ, in that both magnetite and hematite appear to replace pre-existing grains of a feldspar(?)-rich band (~ 2 cm-wide; Fig. 4c; ESM 3, Fig. 3). Mushketovite sensu stricto can be recognised, since replacement of hematite by magnetite is clearly observed along twins (Fig. 4d). Examples of (pseudo)mushketovite are seen in the Magnetite Drillhole and Nodular Fe-oxide Granite from ~ 850 m downwards. In contrast, martite cannot be unequivocally constrained from the prevailing Fe-oxide textures in either location.

In the Magnetite Drillhole, hematite textures are comparable to those from the orebody (680–830 -RLm, RU65–7976). Least-altered magnetite is preserved in a 10 m-thick interval of massive magnetite (> 70 vol%), with siderite±quartz-apatite gangue (sample OD11; ESM 3, Fig. 1). All other samples feature combinations of granular, inclusion-bearing magnetite, (pseudo)mushketovite and hematite (Fig. 4e–g). Fibrous (pseudo)mushketovite may fill oval shapes with variable internal textures including radial and weave-like textures (Fig. 4h, i). Replacement of both magnetite varieties by siderite is common (Fig. 4g, h).

The Nodular Fe-oxide Granite displays the greatest lithological variation among the sampled drillcores (ESM 3, Fig. 3). In Fe-rich intervals, a fine-grained groundmass shows a transition from spotted to patchy, lace-like domains attributable to metasomatism without brecciation (Fig. 5a–c). Such textures are defined by intergrowths between siderite-quartz gangue, Fe-oxides, mostly hematite, and pyrite+chalcopyrite. Lace-like domains show coarsening towards 'proto-nodules' with larger, bladed hematite (Fig. 5c), adjacent to veinlets filled with similar assemblages. Comparable assemblages are seen throughout the nodules and within banded intervals. At upper levels, the nodules/bands consist of specular hematite, with either (i) a compact, 'feather-like' growth (Fig. 5d), or (ii) long laths of hematite within siderite-quartz gangue (Fig. 5e). Nodules or bands with less-abundant Fe-oxides display margins featuring the same siderite-quartz-sulfide assemblages. Feathery magnetite intergrown with siderite(±sulfides) can form nodules at depth (Fig. 5f). Some strongly metasomatised domains also display 'proto-nodules' with skeletal magnetite present within siderite (Fig. 5g). Lamellar aggregates of hematite and magnetite with marginal Si-magnetite (Fig. 5h) can be replaced by magnetite+siderite+sulfide assemblages (Fig. 5h). Replacement of pre-existing phenocrysts (feldspar?) can also be inferred from Fe-oxide+sulfide textures in the metasomatised granite (Fig. 5i).

Magmatic magnetite, ilmenite and titanite are present throughout granite from all locations and the Felsic unit, albeit with breakdown of ilmenite to rutile-hematite symplectites and fields of rutile inclusions (Fig. 6a, b). These textures are attributable to overprinting of typical magmatic Fe-Ti-oxide precursor phases. Coarse, hydrothermal, Nb-W-bearing rutile may form adjacent to such areas. Zoned, Ti- and U-W-Sn-Mo-bearing hematite (Fig. 6b–d) forms on behalf of ilmenite breakdown and magnetite replacement.

Miner Deposita (2020) 55:429–452

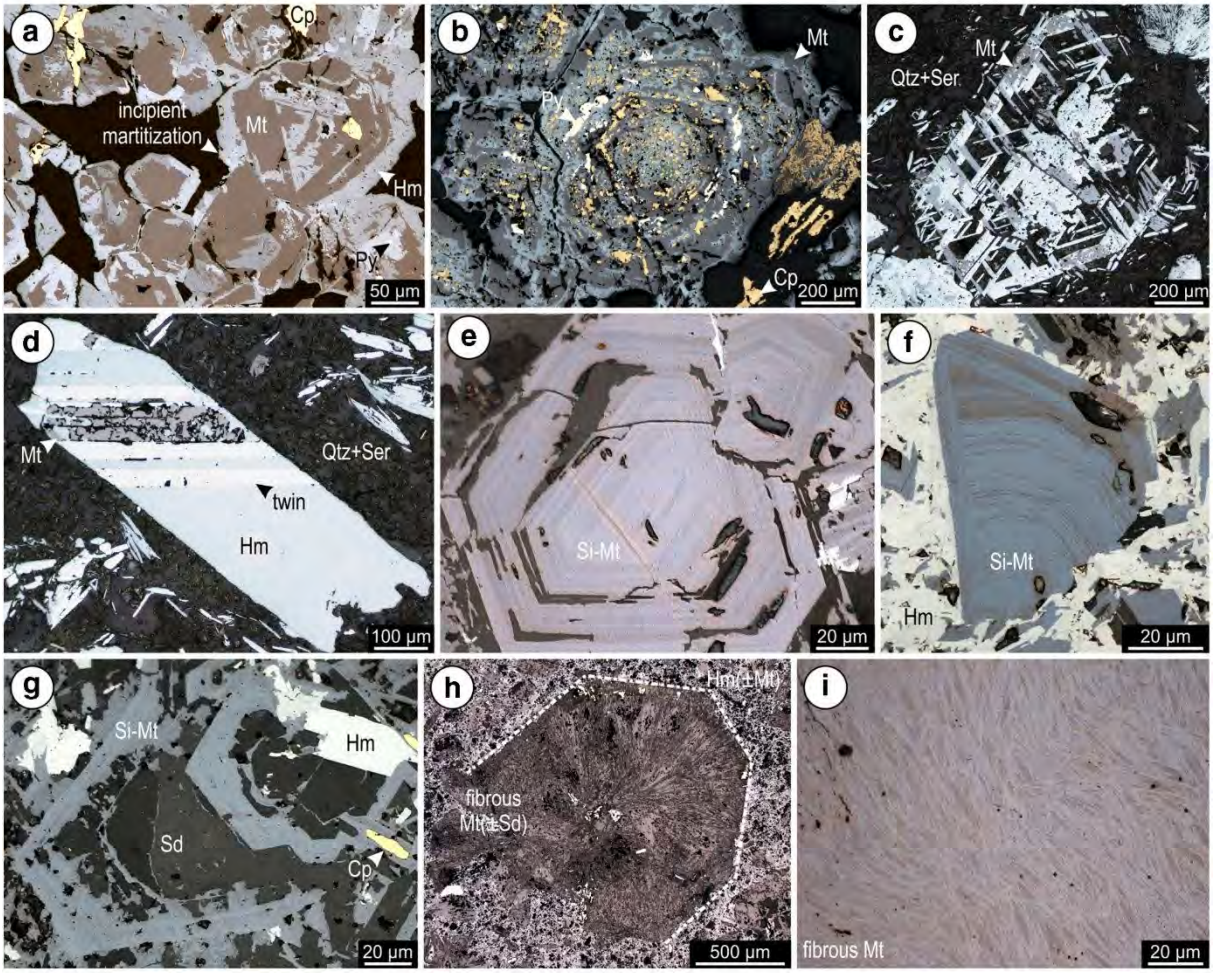

Fig. 4 Reflected light micrographs of Fe-oxides from the DSM (**a**, **b**), DM (**c**, **d**), and RU65–7976 (e-i). (**a**) Aspects of gradational martitisation and (**b**) mottled texture of sulfides formed during martitisation. (**c**) Lamellar hematite texture suggestive of feldspar replacement(?); note incipient mushketovitization. (**d**) Twinned hematite with selective magnetite replacement along twin planes. (**e**–**g**) Silician magnetite with granular morphology; note association with hematite in (**e**) and advanced replacement by siderite in (**g**). (**h**, **i**) Aspects of fibrous (pseudo)mushketovite aggregates

Mineralogy and trace elements distribution in iron oxides

Each main type of Fe-oxide was studied in terms of textures down to the sub-micron scale prior to EPMA analysis (ESM 2). Magnetite stoichiometry was calculated by normalising to 32 O atoms per formula unit (apfu), as per Huberty et al. (2012). Hematite formulae were calculated based on 3 O apfu. Grains or aggregates representative of the main types of Fe-oxides were mapped by LA-ICP-MS to establish grain-scale patterns of trace element distributions.

Silician magnetite An important characteristic of magnetite throughout the outer shell, except for the veins from the Felsic unit, is the presence of inclusions. These vary in size, from micron- to nanoscale, abundance and mineralogy from one location to another and within individual grain populations (Fig. 7a–f). Magnetite in all cases is Si-bearing at the µm-scale and can thus be defined as silician magnetite (Si-magnetite). The smallest (nm-scale) inclusions account for the apparent oscillatory zoning observable at the micron scale (Fig. 7a). Rarely, mottled, ring-shaped cores develop into octahedral to dodecahedral crystal faces (Fig. 7b). Representative of the broadest range of textures and size of Si-magnetite is the massive interval (sample OD11), in which several grain-size populations co-exist (Fig. 7c): (i) smallest, few-µm in size; (ii) medium, tens of µm in size; and (iii) a rarer, coarser-grained group, > 100 µm in size.

Trails of sub-µm size inclusions are a conspicuous feature of finer grains and radially crosscut the zoning (Fig. 7e, f). Various styles of oscillatory zonation are recognised, with respect to periodicity, band widths and inclusion abundance

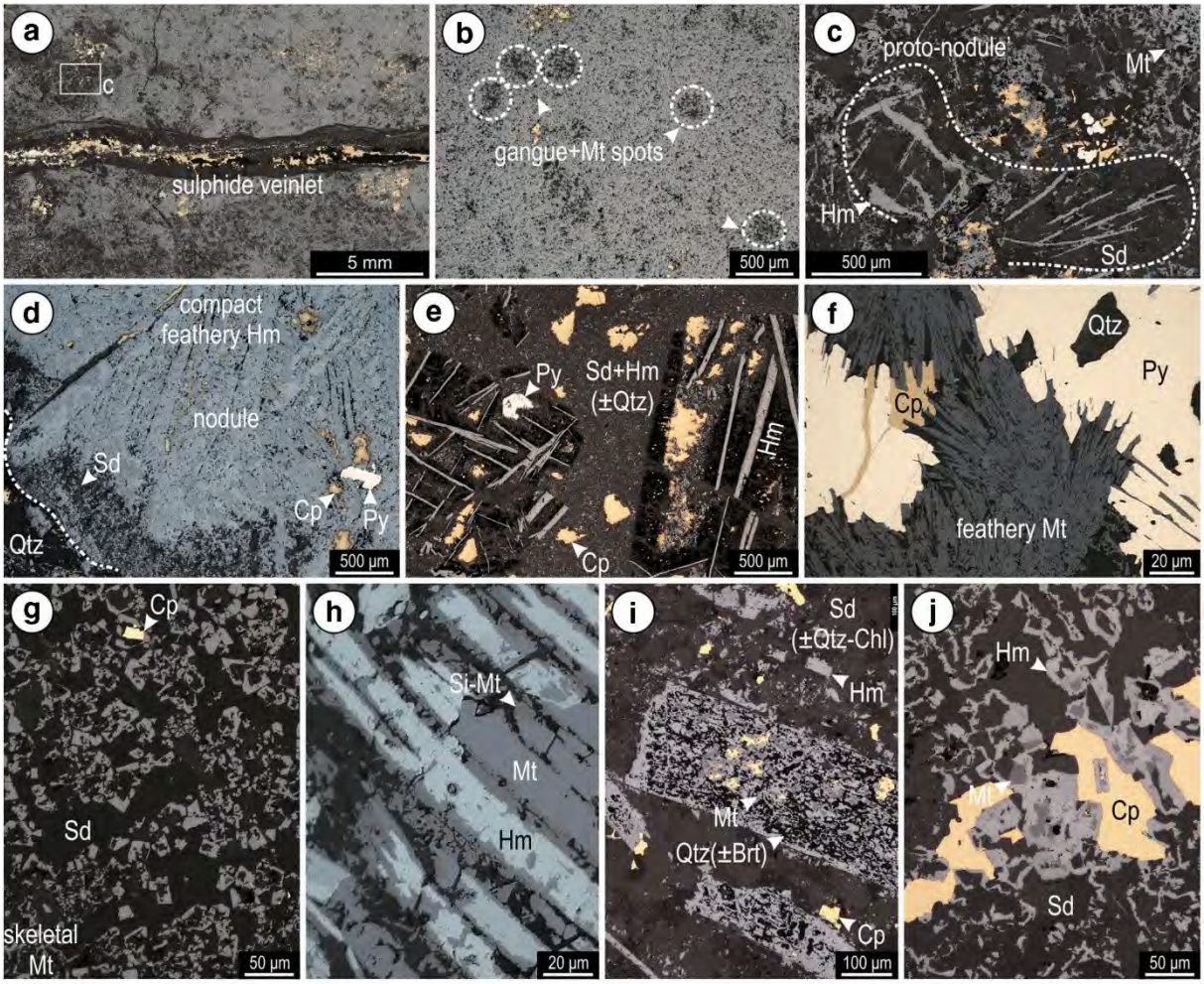

Fig. 5 Reflected light micrographs of Fe-oxides from the Nodular Fe-oxide Granite. (**a**–**i**) Fe-metasomatism in granite; see text. (**d**, **e**) Hematite- and gangue-rich nodules and bands; note siderite margins or matrix and association with sulfides. (**f**) Magnetite-rich nodule with feathery magnetite growth in siderite- and sulfide-rich matrix. (**g**) Skeletal magnetite in siderite within metasomatised granite. (**h**) Replacement of hematite by magnetite with Si-magnetite overgrowth. (**i**, **j**) Magnetite+hematite and siderite replacing feldspar(?); note crosscutting relationships with chalcopyrite in (**j**)

(Fig. 7d–f). Importantly, replacement of magmatic magnetite (trellis ilmenite, hercynite+ilmenite blebs) by Si-magnetite is also observed (Fig. 7g–i).

Oxide components routinely detected by EPMA at high concentrations in Si-magnetite are SiO_2, CaO and MgO (up to 4.46, 1.23 and 0.91 wt%, respectively) (ESM 2). Concentrations of these elements generally correlate with one another as seen from transects across oscillatory-zoned grains (ESM 3, Fig. 5a, b). Silician magnetite from the DSM displays comparable trends to those shown by magnetite from the outer shell at OD, although it features higher Ti and V contents (up to 0.41 wt% TiO_2, and 0.08 wt% V_2O_3). In contrast, magmatic magnetite from the RDG within the Nodular Fe-oxide Granite contains negligible SiO_2 and neither CaO nor MgO, but consistent, albeit low, concentrations of TiO_2 (0.21–0.33 wt%) and V_2O_3 (0.03–0.06 wt%).

LA-ICP-MS element maps for Si-magnetite from the Magnetite Drillhole (Fig. 8a, b) and the DSM (Fig. 8c) show contrasting trace element distributions (ESM 3, Figs. 6, 7, 8). Trace element concentrations in magnetite from the same sample can vary within individual grains, and at the scale of a few hundreds of µm between adjacent grains, despite them displaying similar textures. REE enrichment within high-Si domains, as shown by the close match between Ce and/or Y and Si maps is common to all studied samples. In contrast, U-W-Sn-Mo are enriched in grains from the massive magnetite interval (sample OD11; U in Fig. 8a) but not in other samples from the same drillhole (e.g. CLC29). Moreover, U and ^{206}Pb are

Miner Deposita (2020) 55:429–452

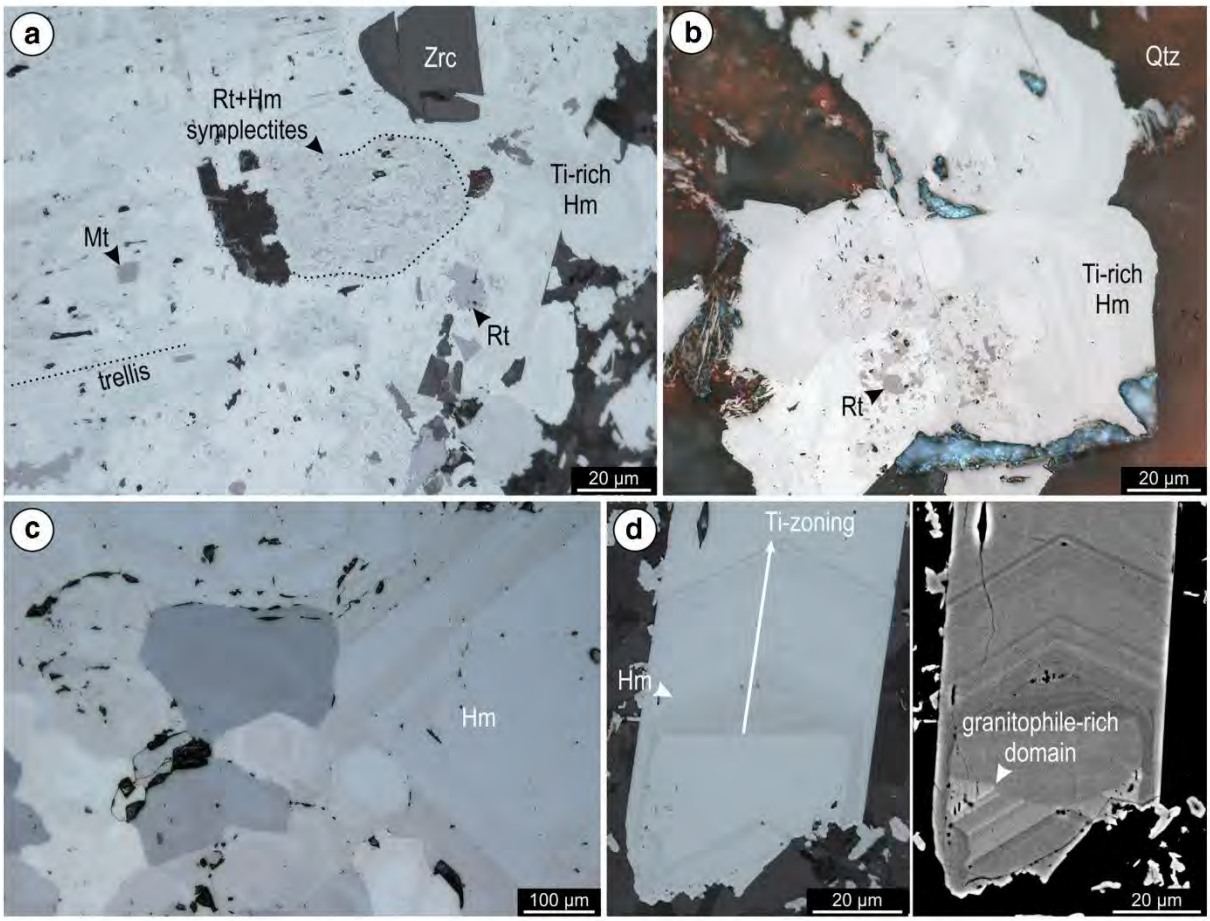

Fig. 6 Reflected light micrographs of Fe-(Ti)-oxides (**a**, **b**) and zoned hematite (**c**, **d**). Breakdown products of magmatic magnetite and ilmenite (**a**) with overgrowth of Ti-rich, zoned hematite (**b**). Note tiny rutile inclusions, in both cases. Typical HFSE zonation in early hematite (**c**, **d**), and also zonation with respect to U-W-Sn-Mo in the corresponding BSE-image in (**d**). Abbreviations: Rt-rutile; Zrc-zircon

depleted in grains strongly enriched in Sn, W and Mo within the same mapped area (sample OD11). Specific to this interval is also the strong enrichment in As, Sb and partly Co, which correlates with Sn, W and Mo, whereas REE correlate positively with U. Except for a comparable enrichment in REE, the Si-magnetite from other samples from this drillhole is relatively depleted in such trace elements, possibly associated with extensive overprinting. In contrast, Si-magnetite from DSM shows elevated concentrations of HFSE, as seen by the enrichment of V and Sc; the latter element positively correlates with REE. Concentrations of U-W-Sn-Mo are otherwise low.

Transition to (pseudo)mushketovite In contrast to martitisation, the transition from overprinted, Si-magnetite to (pseudo)mushketovite is defined by a continuum of textural aspects from granular to bladed, acicular, feathery or fibrous magnetite (Fig. 9). Variable degrees of overprinting are observed as re-shaping of Si-magnetite grains by superimposed fracturing/brecciation or local dissolution/reprecipitation (Fig. 9a). The strongest illustration of (pseudo)mushketovite is the formation of bladed textures within newly formed (reprecipitated) domains (Fig. 9b). Recrystallization of rim or core domains is expressed by a spectrum of textures indicative of superimposed (newly formed) zonation patterns, inclusion digestion and/or coarsening (Fig. 9c, d).

Hematite aggregates formed by blades with fan-, radial- or mesh-like arrangements could be considered mushketovite sensu stricto (Fig. 9e, f). However, the presence of Si-magnetite rims and overall magnetite-like shape of some of these aggregates could hint at dissolution-reprecipitation of a pre-existing Si-magnetite. Comparably, dense Si-bearing inclusions (Fig. 9g, h) are also characteristic of short, acicular magnetite aggregates filling such granular shapes (Fig. 4h, i). Such inclusions may display different orientations and vary in size and

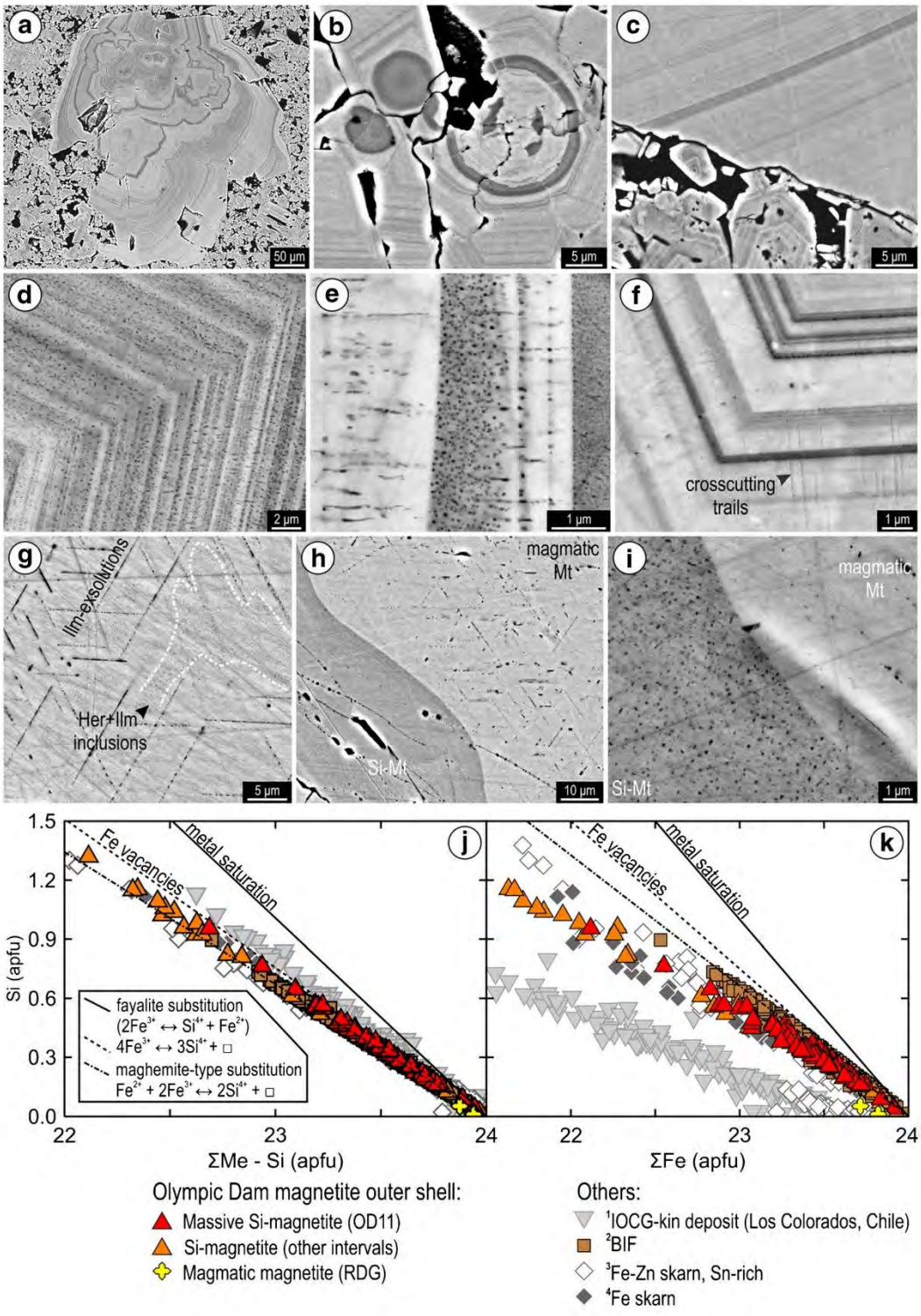

abundance throughout the same blade (Fig. 9h). Overall, these textures are similar to those observed in overprinted, granular Si-magnetite.

LA-ICP-MS element maps of mushketovite show marked compositional differences between the various components (Fig. 10a; ESM 3, Fig. 9). Decoupling of HFSE is observed,

Miner Deposita (2020) 55:429–452

◀ **Fig. 7** BSE-images of Si-magnetite (**a**–**f**). (**a**–**c**) Variation in size and style of zonation in Si-magnetite from polygonal aggregates (**a**) to ring-shaped patterns (**b**); note that smallest grains are clustered with inclusions (**c**). (**d**–**f**) Oscillatory zonation marked by micro- to nanoscale inclusions of Si-rich phases; note inclusions trails crosscutting the growth zones in (**e**, **f**). (**g**–**i**) BSE images of magmatic magnetite overprinted by Si-magnetite; note trellis exsolutions with ilmenite and hercynite+ilmenite inclusions typical RDG magnetite in (**g**). (**j**–**k**) Compositional variation of magnetite in terms of: (**j**) Si vs. ∑Me-Si, or (**k**) ∑Fe in apfu, compared to magnetite stoichiometries from other deposits. References: (1) Deditius et al. (2018); (2) Huberty et al. (2012); (3) Wang et al. (2017); (4) Ohkawa et al. (2007). ∑Me corresponds to the sum of all measured cations, whereas ∑Fe represents Fe^{2+}+Fe^{3+}. Abbreviations: Her-hercynite; Ilm-ilmenite

in which Ti is relatively enriched in the overgrowth, whereas V, Nb, Sn and W are concentrated in the middle of the lamellae. A preferential enrichment of REE is observed in the overgrowth. Unlike the Si-magnetite discussed above, there is an antithetic relationship between U and ^{206}Pb in the central part of the lamellae relative to its margin.

Hematite Hematite shows a continuum of textures from the orebody to the outer shell. Some of the most striking features of hematite grains or aggregates relate to zoning patterns combining HFSE and U-W-Sn-Mo, exemplified by the LA-ICP-MS element maps of hematite from the Fe-rich matrix (sample MV05; Fig. 10b) and the hematite-rich nodules (sample MV19; Fig. 10c) from the Nodular Fe-oxide Granite. Stunning oscillatory zonation patterns are displayed by Th, V and Nb in hematite within the Fe-oxide-rich matrix. In contrast, hematite from the nodules shows the highest Th and Nb concentrations (up to ~290 and ~6,900 ppm, respectively), albeit with only subtle zonation.

Hematite from the rhythmic banded intervals in the Magnetite Drillhole shows comparable trace element enrichment trends (ESM 3, Fig. 12). Lath-shaped hematite displays

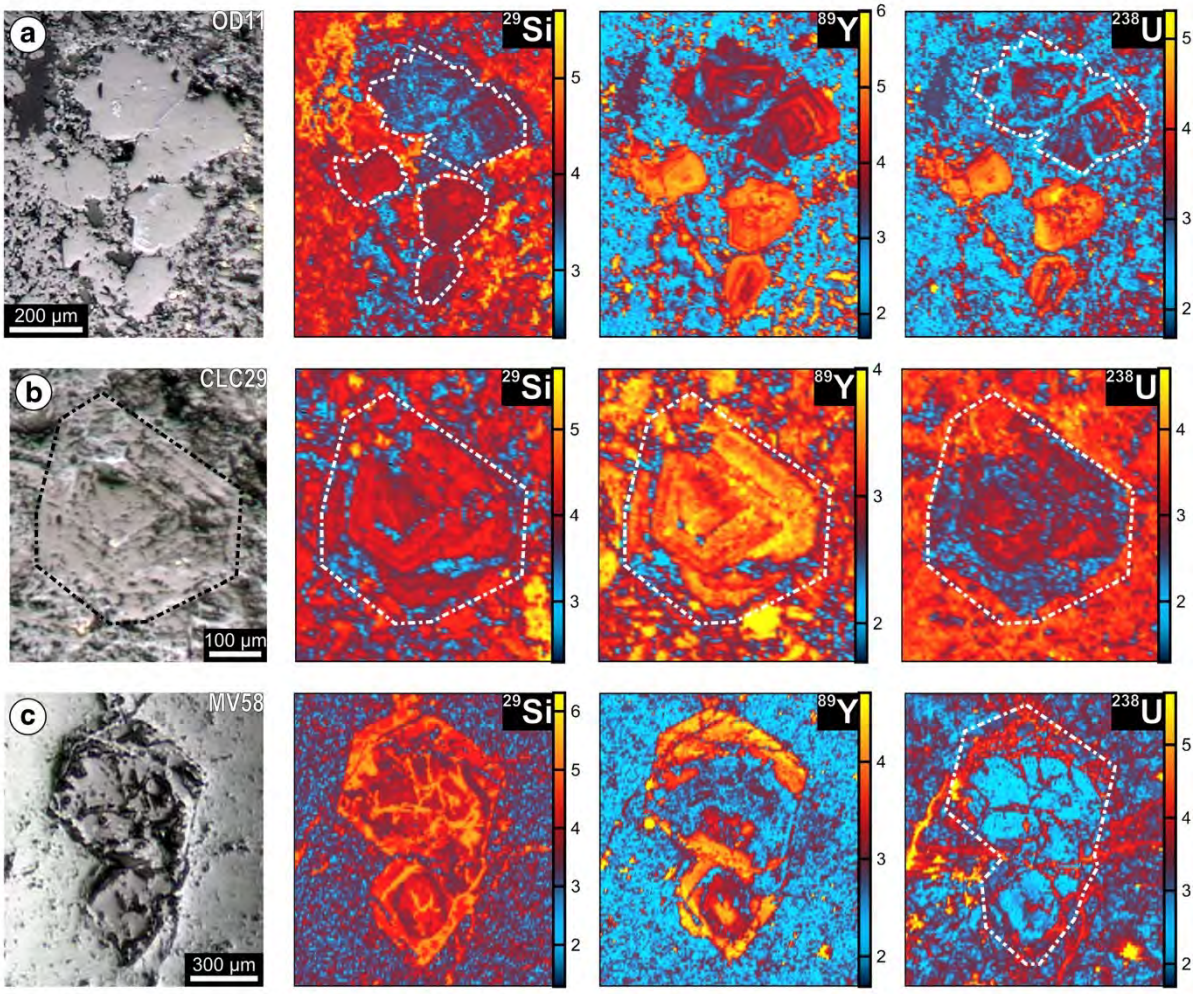

Fig. 8 LA-ICP-MS element maps of Si-magnetite (reflected light images to the left). Note variation in size and replacement by gangue from (**a**) to (**c**)

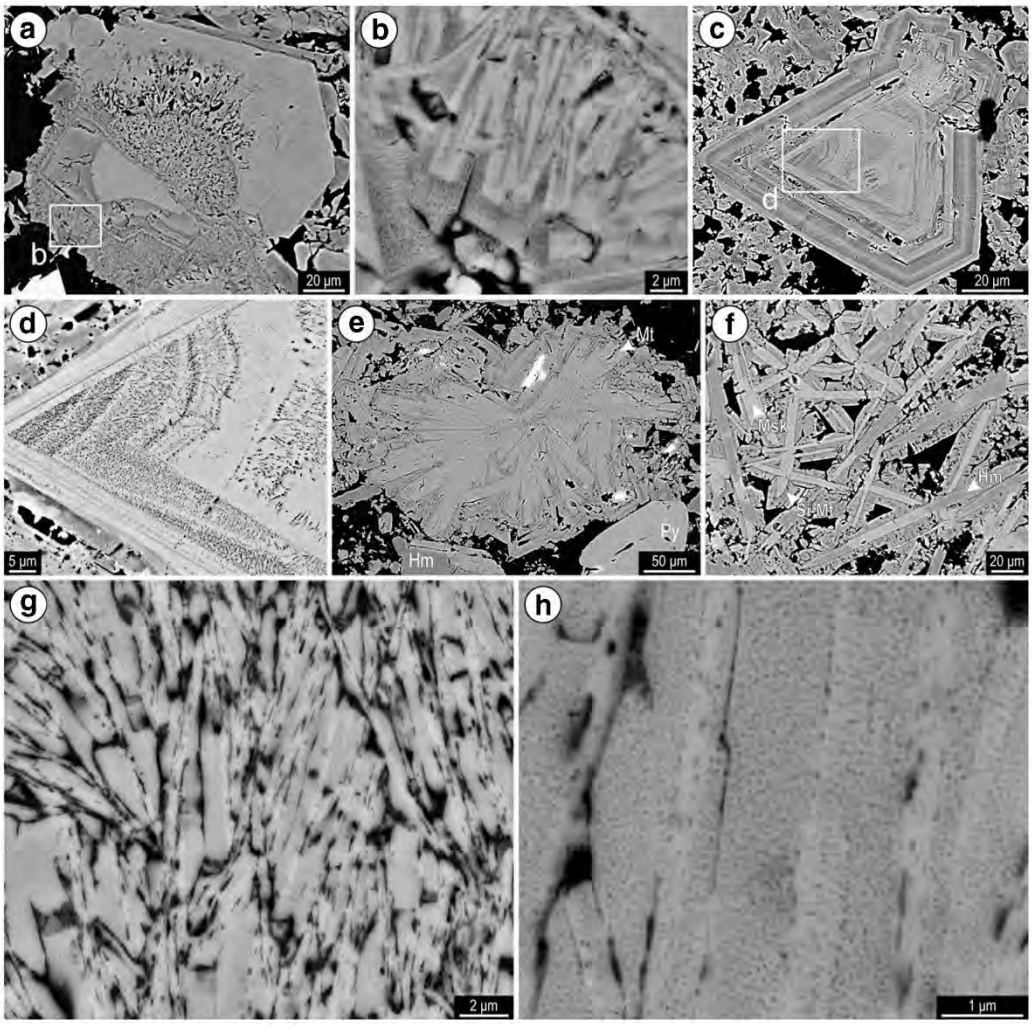

Fig. 9 BSE-images showing aspects of (**a**–**d**) Si-magnetite overprint and (**e**–**h**) (pseudo)mushketovite displaying variation in the morphology, arrangement and distribution of inclusions. (**a**, **c**) Core-to-margin patterns of dissolution-reprecipitation products of Si-magnetite. (**b**) Inclusion redistribution and magnetite recrystallisation in a reworked margin showing development of lamellar-like habit (incipient (pseudo)mushketovite). (**d**) Superimposed, inwards-oriented, oscillatory-growth cycle. (**e**, **f**) Radial and mesh-like arrangement of mushketovite with marginal Si-magnetite; in each case, dusty inclusions of U-, W, and Sn-bearing minerals can occur within the magnetite and/or hematite. (**g**) Splinter aggregate forming weaving textures in Fig. 4 h and i. (**h**) Aspect of inclusions within blades typical of the aggregate in (**g**)

both oscillatory (e.g. Th, Ti, Nb) and sector zoning (inverse patterns between Lu and W), which is notable given that these laths are polygranular.

The anomalous HFSE concentrations in hematite from the Nodular Fe-oxide Granite are measurable by EPMA (ESM 2). Concentrations of Nb (up to 1.72 wt% Nb_2O_5; 0.02 apfu Nb) and Ti (0.93 wt% TiO_2; 0.018 apfu Ti) are obtained for hematite-rich nodules (sample MV19). The two elements correlate strongly ($r^2 = 0.92$), concordant with the substitution scheme: $Nb^{5+} + Ti^{4+} + \leftrightarrow 3Fe^{3+}$. Concentrations of Al_2O_3 (0.11–0.19 wt%), SnO_2 (0.07–0.10 wt%) and V_2O_3 (0.06–0.09 wt%) are always subordinate to Nb_2O_5.

Trace element concentrations in iron oxides

Selected scatterplots (Fig. 11) and chondrite-normalised REY fractionation trends (ESM 3, Fig. 15), show that both location and textures exert important control over trace element signatures. Time-resolved LA-ICP-MS profiles typically show

Fig. 10 LA-ICP-MS element maps and corresponding reflected light (**a**, **c**) or BSE (**b**) micrographs Fe-oxides. (**a**) Lamellar aggregate of magnetite with hematite cores and Si-magnetite overgrowths featuring contrasting compositions relative to the three domains; note that magnetite in the middle part is Si-free. (**b**, **c**) Zoned hematite displaying variation of zonation themes relative to HFSE and U-W-Sn-Mo. ^{118}Sn in linear scale ($n \cdot 10^5$) in (**b**) ▶

Miner Deposita (2020) 55:429–452

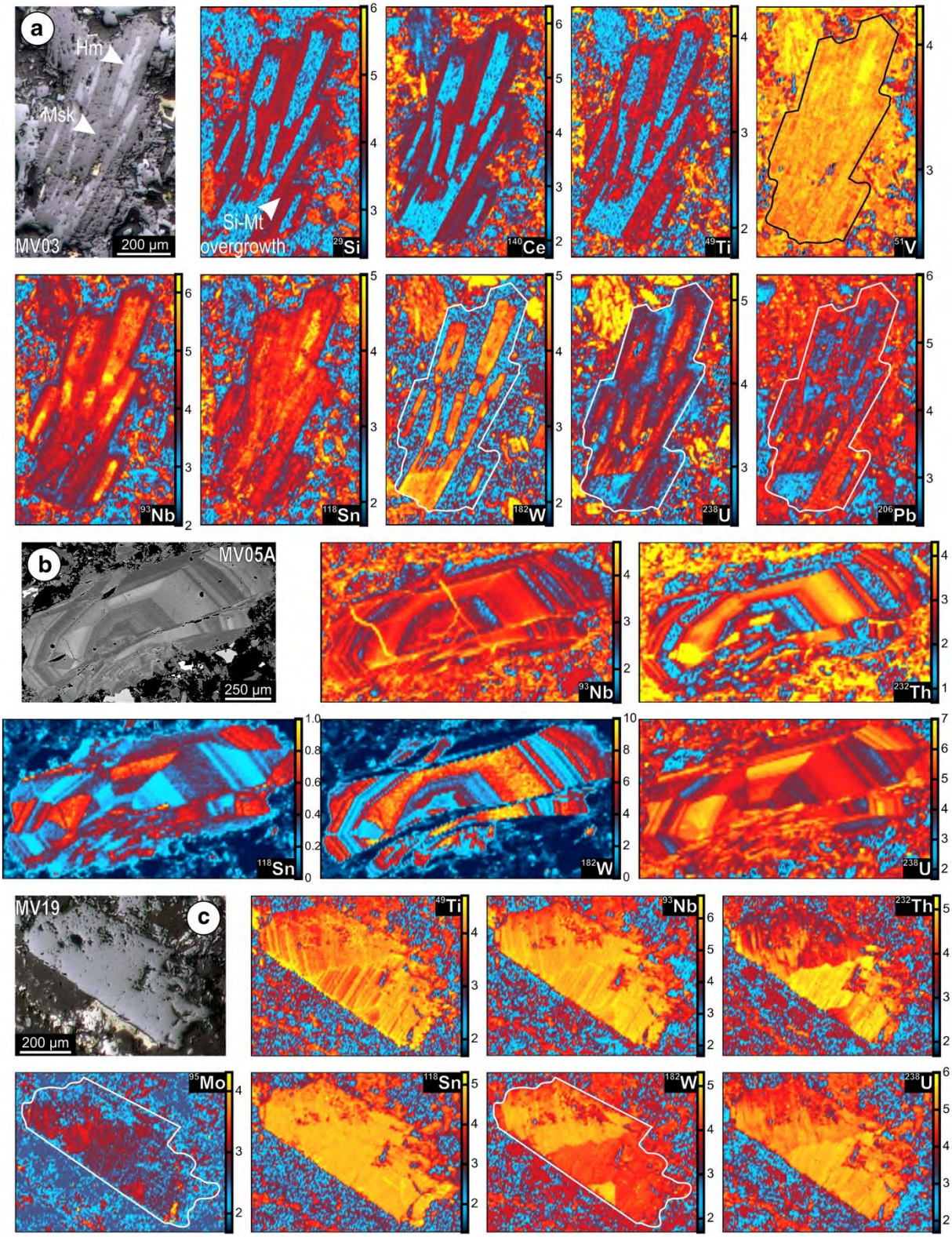

smooth signals for most measured elements at higher concentrations, indicating homogeneous distribution within the ablated volumes (ESM 3, Fig.13). Summary statistics of the dataset are presented in ESMs 2 and 3.

HFSE and associated elements Titanium and V are generally present at measurable concentrations, displaying positive correlations across the dataset (Fig. 11a), typically with V contents ~ 1–2 orders of magnitude lower than Ti. Both V and Ti can reach significant concentrations in magmatic magnetite, up to ~ 910 and 11,500 ppm, respectively. Hematite from veinlets within the upper section of the DSM features the highest Ti contents (up to ~ 34,800 ppm in individual spot analyses or ~ 13,900 ppm as sample/texture means). Scandium contents are generally low across the dataset (rarely > 10 ppm; Fig. 11b), although Sc is distinctly richer in the DSM and DM (averages of up to ~ 57 ppm). In the lower section of the DSM, hematite contains up to ~ 360 ppm Sc. HFSE correlate strongly with Ti, particularly for hematite. Niobium concentrations are generally higher in hematite than magnetite, including hematite replacing carbonates(?) in the rhythmically banded interval (up to ~ 5,000 ppm Nb), zoned hematite from hematite-rich nodules (~ 6,900 ppm), and other bladed, polygranular hematites in both the Nodular Fe-oxide and Magnetite Drillholes (sample CLC31; ~ 8,800 ppm). Niobium and Th are strongly coupled across the dataset (Fig. 11c). Zoned hematite from the nodules displays the highest Th contents (up to ~ 290 ppm; sample MV19). Such hematites also display increased Sn and V contents. Thorium and Nb concentrations are the lowest within magmatic magnetite and both Si-magnetite and mushketovite from DM and DSM. Mushketovite from the DM mimics the overall low contents of all elements within the hematite hosts. Zirconium, Hf and Ta have the lowest concentrations (< 2 ppm).

Granitophile elements U-W-Sn-Mo Hematite categories other than martite from the DSM and hematite veinlets within the Felsic unit are strongly enriched in U-W-Sn-Mo (Fig. 11d). Zoned hematite from the Magnetite Drillhole (sample CLC10) contains the highest concentrations (up ~ 18,300 ppm W, ~ 5,300 ppm U, ~ 5,000 ppm Sn and ~ 1,500 ppm Mo in individual analyses). Within other categories of hematite (e.g. replacement of carbonates?), enrichment of these elements can commonly exceed 1,000 ppm, typically with W≳Sn≳U≳Mo. In contrast, martite displays some of the lowest (< 10 ppm) concentrations of U-W-Sn-Mo, generally mimicking the low abundances of these elements in co-existing Si-magnetite. However, these elements can be significantly enriched in Si-magnetite and (pseudo)mushketovite from both the magnetite and nodular Fe-oxides drillholes. In general, Mo + Sn + W contents in (pseudo)mushketovite are within the range of hematite from the same location, whereas Si-magnetite is lower still in these elements; U concentrations are nonetheless comparable for all categories. Concentrations of U in Si-magnetite from the Magnetite Drillhole reach sample averages of up to ~ 83 ppm; individual spot analyses display up to ~ 2,800 ppm U. Total Pb typically ranges between 1.1 and ~ 100 ppm across the dataset, with sample averages as high as ~ 640 ppm in bladed, polycrystalline hematite from the nodules. Individual spot analyses may reach up to ~ 3,900 ppm Pb, although generally with a greater common-Pb component.

Other trace elements Arsenic and Sb concentrations are consistent across the dataset, varying within narrow ranges (3.1–37.9 and 0.78–17.3 ppm, respectively) and with good correlations (Fig. 11f). These elements can be enriched at up to ~ 940 ppm As in hematite and ~ 410 ppm Sb in (pseudo)mushketovite from the Nodular Fe-oxide Granite. Otherwise, Sb concentrations are ~ 1 order of magnitude lower than As.

Transition metals are not significantly enriched in any of the studied Fe-oxides and nor do they show strong correlations. Individually, however, they can be enriched within certain categories. Manganese concentrations (typically < 150 ppm) vary within ~ 1 order of magnitude across the dataset, and are relatively higher in Si-magnetite, martite after Si-magnetite (DSM) and in (pseudo)mushketovite. Zinc (typically < 100 ppm) correlates with Mn and is higher in magnetite (both silician and magmatic) relative to other Fe-oxide categories. Si-magnetite from the DM features particularly high Mn and Zn (Fig. 11g). Except in magmatic magnetite (up to ~ 420 ppm), Cr concentrations are low across the dataset (< 10 ppm).

Rare earth elements ∑REY varies over 4 orders of magnitude across the dataset and are relatively enriched in Si-magnetite and (pseudo)mushketovite (ESM 3, Fig. 15e). Higher ∑REY correlates with increased U contents, particularly in Si-magnetite from the Magnetite Drillhole. Concentrations are distinctly lower in both DSM and DM. Higher ∑REY (up to ~ 4,400 ppm) in individual analyses are recorded for Si-magnetite in sample OD11. Concentrations of Si correlate with ∑REY, displaying similar trends as U vs. ∑REY for magnetite. ∑REY concentrations in hematite can reach up to ~ 760 ppm, although always subordinate to those in Si-magnetite.

Chondrite-normalised fractionation patterns for REY in Si-magnetite (ESM 3, Fig. 15a) exhibit variation over ~ 4 orders of magnitude. Magnetite and Nodular Fe-oxide Granites are the highest, displaying weak positive Ce-anomalies, LREE-enrichment and a marked negative Eu anomaly. However, Si-magnetite displays variable HREE-enrichment, with either smooth, flat to concave slopes and generally no Y-anomaly. Magnetite from the massive interval (sample OD11) stands out by pronounced HREE-enrichment and a positive, albeit weak, Y-anomaly (ESM 3, Fig. 15a). Fractionation trends for

Miner Deposita (2020) 55:429–452

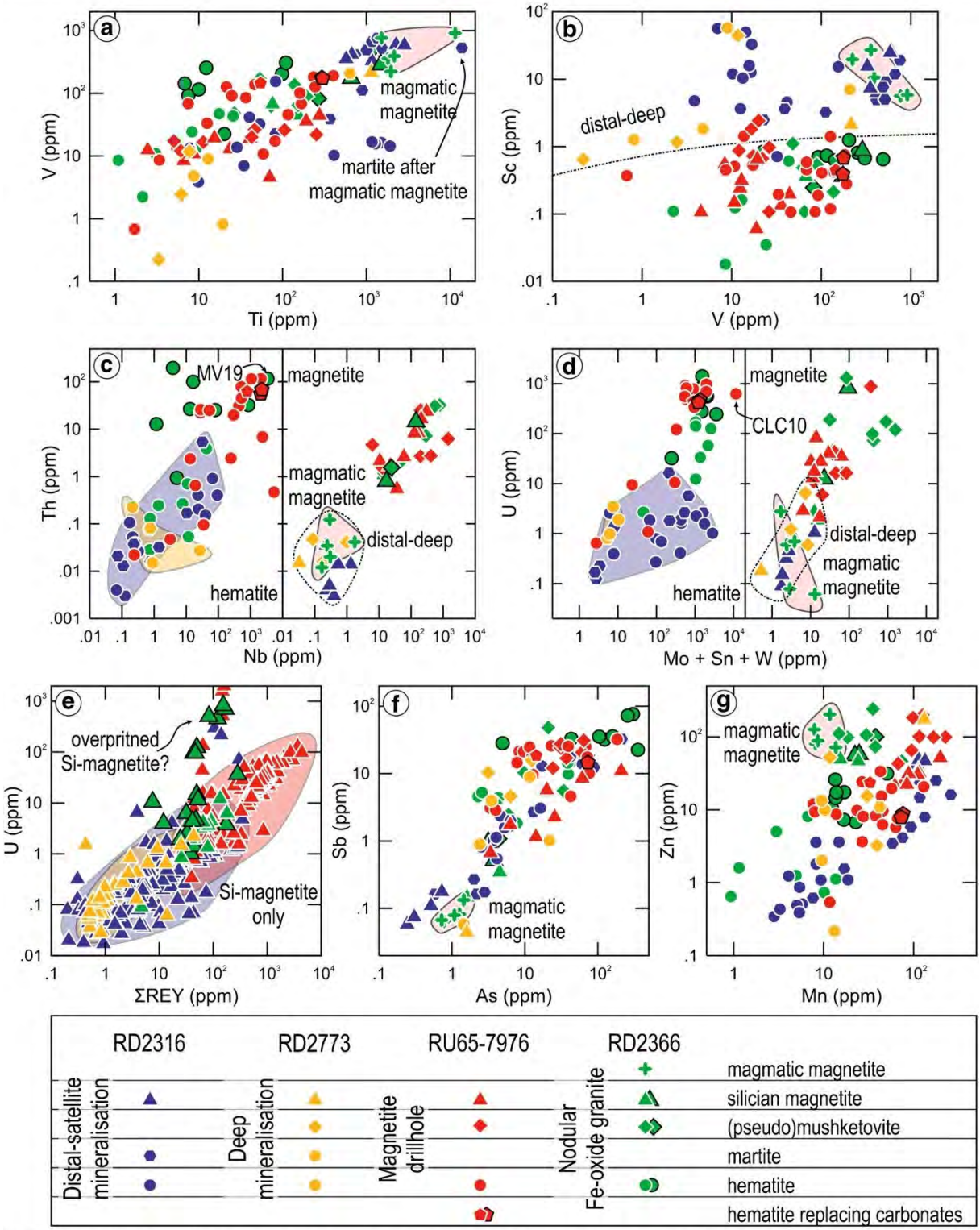

Fig. 11 Scatter plots of sample/texture-averages (geometric means) for selected element(/-groups)-pairs. (**a**) V vs. Ti; (**b**) Sc vs. V, (**c**) Th vs. Nb, (**d**) U vs. Mo+Sn+W, (**e**) U vs. ∑REY (Si-magnetite only), (**f**) Sb vs. As, (**g**) Zn vs. Mn. Black outline indicates analysed Fe-oxides from bands/nodules

Si-magnetite from other locations are similar but commonly noisier with decreasing ∑REY.

Fractionation patterns for (pseudo)mushketovite from both the Magnetite and Nodular Fe-oxide Granites resemble the trends for Si-magnetite (ESM 3, Fig. 15b), albeit with minor or no Eu anomaly for the Nodular Fe-oxide Granite. DM mushketovite is overall low in ΣREY (values close to or at typical minimum detection limits) but display distinct fractionation trends with convex MREE-enrichment and negative Y-anomalies. Martite after Si-magnetite from the DSM displays REY fractionation trends that no longer resemble precursor Si-magnetite, with slight LREE-enrichment and overall concave slopes.

Chondrite-normalised REY fractionation patterns for hematite vary considerably, although they partly overlap (ESM 3, Fig. 15c, d). Hematite from both Magnetite Drillhole and Nodular Fe-oxide Granite, irrespective of textures, show LREE-enrichment and consistent upwards HREE pattern. In contrast, the DSM and DM show distinct, flatter REY trends, with conspicuous negative Y-anomalies (ESM 3, Fig. 15d).

Discussion

Mineralogy and signatures of early Fe-oxides: constraints on a granite-derived fluid

Silician magnetite, documented throughout the outer shell at OD, was clearly one of the earliest hydrothermal Fe-oxides marking the onset of the IOCG system, since this directly overprints magmatic magnetite. However, this is not necessarily true for all the Si-magnetite associated with siderite, e.g. the 1.76 Ga BIF-inferred magnetite (Ciobanu et al. 2014). Both the massive magnetite and nodular granite locations show highest REY and U, hinting at their unusual, overprinted(?) character (Fig. 11e). Such elements are characteristic of the IOCG footprint at OD tied to in-situ alteration of the RDG, they can therefore be considered granite-derived (Kontonikas-Charos et al. 2017; Dmitrijeva et al. 2019). The best proof would be dating of magnetite throughout the outer shell, but the presence of high common-Pb renders U-Pb dating difficult, particularly for the nodular granite.

Magnetite with (calc)-silicate inclusions as present in the Si-magnetite at OD (Ciobanu et al. 2018, 2019), is reported from Los Colorados, an IOCG-kin deposit in the Chilean Iron Belt (CIB) (Deditius et al. 2018). Moreover, REY fractionation trends of magnetite from younger deposits within the central Andes, which were used to discriminate hydrothermal from magmatic origin of the El Laco deposit (Dare et al. 2015), are similar to REY trends of Si-magnetite shown here.

Differences between Si-magnetite from several deposit types become apparent when plotted in terms of Si vs. other cations/Fe (Fig. 7j, k). Silician magnetite from OD broadly overlaps with magnetite from BIFs and skarns along the γ-Fe_2O_3-$\square_{0.5}Fe_{1.5}SiO_4$ substitution trend, with ordered vacancies (Fig. 7j), but is slightly offset from Los Colorados. The presence of Si-magnetite nanoprecipitates in both the BIF example and at OD is concordant with such compositional overlap (Xu et al. 2014; Ciobanu et al. 2018). However, higher-temperature formation (> 350 °C) can be inferred from the presence of abundant calc-silicate inclusions in the Si-magnetite here and at Los Colorados (Ciobanu et al. 2018; Deditius et al. 2018). Calculated temperatures for quartz-magnetite deposition at OD lie in the range 400–500 °C, based on $\delta^{18}O$ measurements of quartz-magnetite pairs, and some of the halite-saturated (up to 42 wt% eqv. NaCl), 3-phase fluid inclusions give temperatures at ~ 389 °C (Oreskes and Einaudi 1992). The high temperature environment of less-evolved hydrothermal fluids from this stage may explain why compositional signatures of Si-magnetite closely resemble those from skarns (calc-silicate rocks), deposits in which metasomatism and high-saline fluids account for prograde stages (Meinert et al. 2005).

Differences between the four locations are mostly emphasised by the REY trends of the interconversion products, attributable to local conditions during fluid-rock interaction. The unusual character of DM relative to the other locations is highlighted by the REY trends of mushketovite (ESM 3, Fig. 15), which regionally compares with feldspars from calc-silicate metasomatites/skarns from elsewhere in the Olympic Cu-Au Province (Ismail et al. 2014; Kontonikas-Charos et al. 2014). Nonetheless, the hematite REY trends are comparable to those from the deposit (Verdugo-Ihl et al. 2017a) and thus distinct from younger, sediment-hosted hematite (from the upper, middle part of the orebody) which displays a positive Eu anomaly (Ciobanu et al. 2015).

U-Pb dating of hematite displaying enrichment in U-W-Sn-Mo from the outer shell or the orebody yields overlapping ages within ~ 1.6 Ma of one another (cf. MV05 and LCD04; Courtney-Davies et al. 2019). However, the shell hematite carries a distinct HFSE signature (Ti, and Th, in particular; Fig. 10), which is uncharacteristic for orebody hematite (Cook et al. 2016; Verdugo-Ihl et al. 2017a). This implies the zoned hematite in the outer shell preserves an earlier signature, an interpretation supported by the observation of hematite forming directly from breakdown of magmatic Fe-(Ti)-oxides (Fig. 6), which become more enriched in U-W-Sn-Mo and HFSE-depleted in the orebody with the evolution of the hydrothermal system. This close association between precursor magmatic accessories and the Ti-Th-bearing hematite is evidence for granite sourcing the HFSE signature.

Altogether, the petrography and geochemistry shows a transition among Fe-oxides from the outer shell to the orebody attributable to the same fluid, which can be the 'hotter', granite-derived fluid of Haynes et al. (1995), or the 'deep-seated hydrothermal fluid' of Oreskes and Einaudi (1992).

Miner Deposita (2020) 55:429–452

However, the observed signatures (no distinct Fe-oxide populations with Cr, Ni, Co enrichment) do not support presence of a second, mafic-affiliated fluid ('surficial, basalt-derived fluid') as introduced by Haynes et al. (1995).

Geochemical modelling—conditions for early Fe-oxide formation

Typical IOCG fluids are estimated from fluid inclusion studies at OD, and elsewhere, as being initially CO_2-rich, medium to hyper-saline and with temperatures up to ~ 450 °C (e.g. Oreskes and Einaudi 1992; Pollard 2001; Morales Ruano et al. 2002; Bastrakov et al. 2007). Apatite geochemistry in the outer shell also supports Cl-rich fluids at this stage (Krneta et al. 2016, 2018), associated with breakdown of magmatic feldspars and mafic minerals in the RDG (Kontonikas-Charos et al. 2017). Such fluid-rock reactions could have supplied Si, Ca, Al, and Mg to form Si-magnetite and calc-silicates inclusions as discussed here.

A shift towards slightly acidic conditions (via pH variation) is produced during replacement of K-feldspar by sericite. Although widely considered a redox reaction, pH-controlled (non-redox) reactions (mildly acidic fluids) can also convert magnetite into hematite via transient maghemite ($\square_{0.33}Fe^{3+}{}_{0.67}Fe^{3+}{}_2O_4$; Bosi et al. 2019), i.e. by removal of Fe^{2+} and creating vacancies in the magnetite structure (Otake et al. 2007, 2010 and references therein). Despite maghemite sensu stricto not being detected as such in this study, pervasive transformation of magnetite into a vacancy-bearing maghemite-like structure takes place via formation of γ-$\square_{0.5}Fe_{1.5}SiO_4$ representing the Si-magnetite nanoprecipitates (1–3 nm-wide, along preferential $\{111\}_{magnetite}$) reported by Ciobanu et al. (2019) from the same samples.

At the same time, formation of hydrothermal rutile indicates a fO_2 increase leading to destabilisation of ilmenite and subsequent formation of HFSE-bearing hematite. Using aqueous stability diagrams at 400 °C, these assemblages can be formed at pH-fO_2 conditions coinciding with shifts from K-feldspar to sericite, and ilmenite to rutile, stability (pH = 4.2; log fO_2 = −24; Fig. 12a). The fitted conditions, although constrained by pH variation across the sericite-K-feldspar stability boundary coincides with the magnetite-hematite boundary, explaining the intimate association between the two Fe-oxides and their interconversion products. This intimate association between hematite and magnetite suggests that small-scale fluctuations of fluid parameters were persistent throughout this stage.

The most widespread Si-magnetite nonetheless formed in association with siderite, either via co-crystallisation (skeletal Si-magnetite+siderite; Fig. 5g), or replacement (Fig. 5d–f) during granite Fe-metasomatism by CO_2-rich fluids. Assemblages from the Magnetite Drillhole, in which siderite replaces Si-magnetite and sericite obliterates K-feldspar, can be estimated to have formed as a result of temperature decrease on aqueous stability diagrams at 300 °C (Fig. 12b), i.e. more reduced conditions (log $fO_2 < -30$) relative to the higher-temperature assemblage and slightly acidic conditions at this temperature (pH ~ 4.5). The fluctuation in pH or temperature along the siderite-magnetite boundary may explain the spectrum of (pseudo)mushketovite textures observed (Fig. 9), many of which are pseudomorphic replacements and overgrowths resulting from locally controlled dissolution-reprecipitation reactions.

The lack of extensive martitisation could be attributed to the stability of maghemite-vacancy ordered structure relative to hematite in the presence of SiO_2, as seen from experiments of Si-supported magnetite catalysis up to ~ 500 °C (Lund and Dumesic 1981). Martitisation of Si-magnetite in the DSM may however result from interaction with more acidic (HF-bearing?) fluids than elsewhere.

Proposed geological model for the IOCG system at Olympic Dam

Our data shows a continuum of aspects in which host RDG undergoes Fe-metasomatism, from overprint of magmatic Fe-Ti-oxides to formation of hydrothermal Fe-oxides with recognisable textures and signatures indicating granitic affiliation. A convergence between magmatic hydrothermal processes forming large ore deposits of IOCG or porphyry Cu + Mo + Au type is discussed in the literature with recognition of calc-alkaline/mildly alkaline magmatism sourcing the metals (Richards and Mumin 2013). Previous geological models of OD have introduced a fluid-mixing scheme in which magmatically derived fluids are produced not by the host granite but by a hypothetically, deeper-seated intrusion (Haynes et al. 1995). The deep emplacement of RDG (6–8 km) cannot be reconciled with the narrow age difference between magmatic zircon and hydrothermal hematite even considering rapid uplift/exhumation rates (e.g. ~ 2.5 mm annually in high-tectonic orogenic areas; Tkachev 2011), ruling out models of ore formation in shallow environments (e.g. Haynes et al. 1995).

Despite being spatially separated, the magnetite-to-hematite transition occurs at comparable depths (~ 850 m) in the two locations closest to the orebody outline (Nodular Fe-oxide Granite and Magnetite Drillhole) inferring shell continuity. Nonetheless, deep faulting and compartmentation could explain the apparent drop-down of the DM by > 1 km, inferring that the contact between the orebody and outer shell is locally displaced. Such faulting also explains the presence of deeper hematite (~ 2 km) from the SE part of the orebody (Verdugo-Ihl et al. 2017a) below the magnetite/hematite boundary, ~ 2 km to the east of the Nodular Fe-oxide Granite location. There is, however, no significant age difference between this hematite (1584 ± 5 Ma; Courtney-Davies et al. 2019) and other

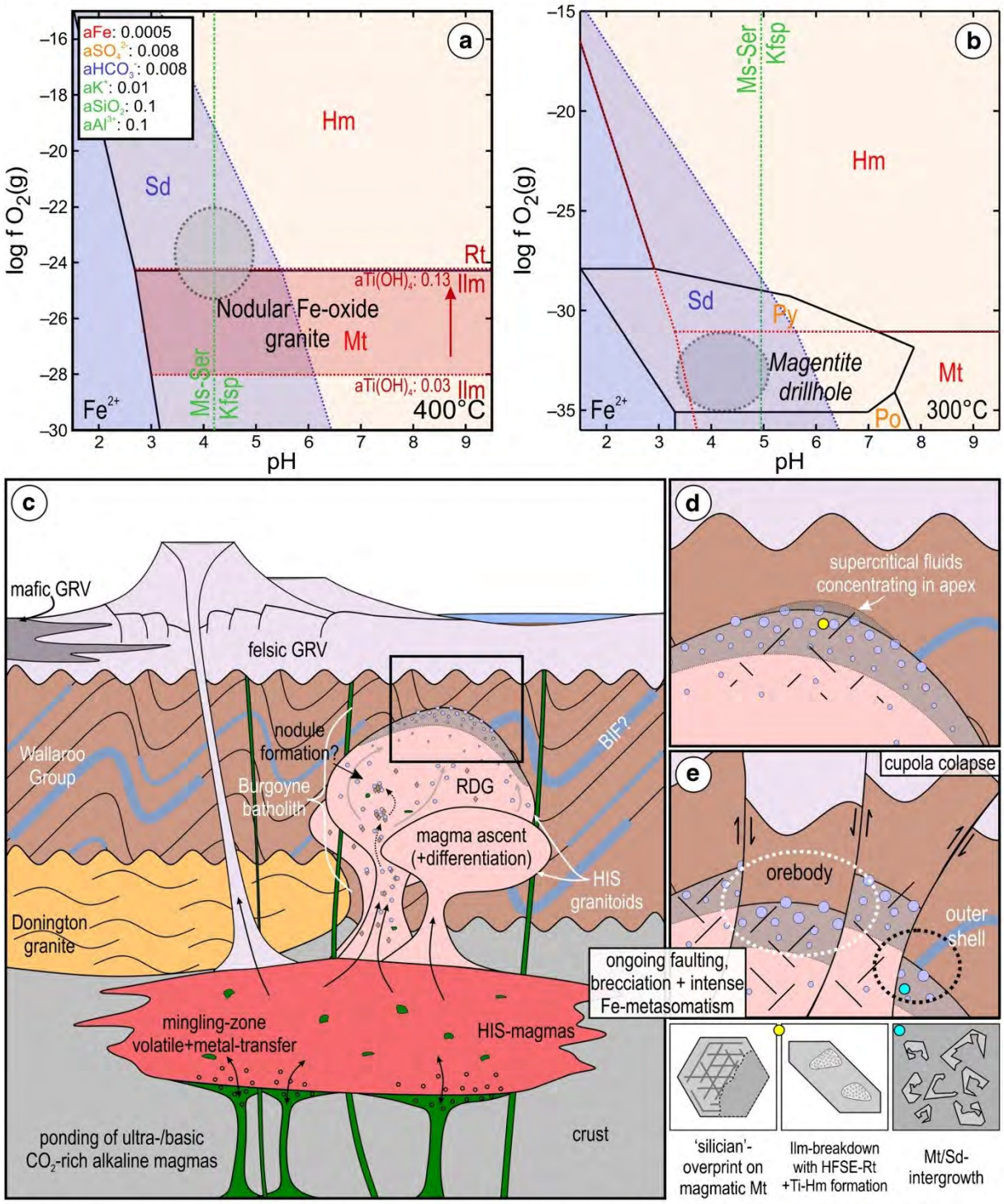

Fig. 12 Log$fO_{2(g)}$-pH diagrams showing inferred formation conditions (dashed circles) of early Si-magnetite and HFSE-bearing hematite (**a**) and Si-magnetite-siderite (**b**) at activities shown in (**a**). Fluid parameters adapted from Krneta et al. (2018) and reasoning therein. Diagrams obtained using the Geochemist's Workbench and an expanded database at 400 °C with SUPCRTBL (Zimmer et al. 2016) and $Ti(OH)_4$ data from Knauss et al. (2001). (**c**–**e**) Schematic showing the spatiotemporal model for Fe-oxides formation in the outer shell at OD as discussed in the text. Abbreviations: Ms-muscovite

ages at ~ 1589 Ma, inferring the onset of mineralisation at a depth of at least 2–3 km, during granite uplift.

Considering all the above, we propose a geological model as shown schematically in Fig. 12c–e. Magma mingling between granitic and underplating alkaline-ultramafic melts (picrite) can be inferred for parent magma of the Burgoyne Batholith at depth (Fig. 12c). This is concordant with generic IOCG models with metal fertilisation by volatile transfer taking place still deeper, at the crust-lithosphere boundary (Groves et al. 2010).

The country rocks for the Burgoyne Batholith include sheared Donington Suite granite, Wallaroo Group metasedimentary rocks and superjacent GRV extrusive activity, which was likely ongoing. Unroofing of such lithologies during RDG uplift could explain presence of volcanic and sedimentary rocks, featuring IOCG mineralisation throughout the ODBC, as thick as ~ 800 m, vertically oriented blocks in the SE part of the deposit (Ehrig et al. 2012).

A process of nodule formation can be initiated at this stage if we consider the model of magnetite flotation via volatile transport recently put forward for IOCG-kin deposits (e.g. Ovalle et al. 2018 and references therein) to create accumulations of Fe-(Ti)-oxides, originally as a crystal mush. In the OD case, CO_2-rich fluids could also explain the association between magnetite and siderite in the nodules and throughout the metasomatized granite. Although the primary textures within such magnetite nodules are obliterated, this mechanism of Fe-transfer from the underplating mafic magma would also explain the overall Fe-enrichment in RDG through magma assimilation. Alternatively, these nodules could represent enclaves (mafic rocks, older Donington granite or sedimentary rocks?) or self-patterning relating to granite metasomatism.

At the stage when granite crystallisation resulted in accumulation of hydrothermal fluids in supercritical state on the outer margins and in the apex of the RDG, tectonic activity and/or fluid overpressure initiate volatile-fluid separation triggering the onset of reactions in the OD 'outer shell' (Fig. 12d). Granite, together with the roofing country rocks, undergo brecciation during faulting, uplift and cupola collapse due to the build-up and release of volatiles (Fig. 12e). The orebody will form in the collapsed cupola at the same time as the outer shell undergoes interconversion between Fe-oxides at shallower depths (2–3 km?).

Conclusions and implications

Silician magnetite co-exists with HFSE-hematite throughout the outer shell at Olympic Dam. This association is tied to earliest overprint of magmatic Fe-Ti-oxides and inherits characteristics from the precursor phases, defining the onset of hydrothermal activity. The discovery of silician magnetite as a main species is important because it can be linked to granite metasomatism during alkali-calcic alteration, since Si and associated Ca, Mg and Ti are sourced from breakdown of magmatic silicates. Intricate, μm-scale associations of both Fe-oxides and their interconversion products are ubiquitous and characteristic of the outer shell, although a general, upwards transition from magnetite to hematite is recognisable.

Trace element signatures of Fe-oxides show common trends related to certain element groups but also differences attributable to local conditions. Of these, the relative enrichment in REY and U in silician magnetite proximal to deposit and the more prominent U-W-Sn-Mo signature in hematite towards the deposit, support a granite-derived fluid; none of the trends indicate a mafic-affiliation (Cr, Ni, Co). Altogether, petrographic and geochemical evidence show a transition among Fe-oxides from the outer shell to the orebody attributable to the evolution of the same fluid.

Activity diagrams shows formation conditions for: (i) early Fe-oxide associations being controlled by the shift from K-feldspar to sericite, and ilmenite to rutile + hematite stabilities, at 400 °C, and (ii) magnetite-siderite association forming at ~ $3.5 < pH < 5$ (sericite-stable) and fO_2 below the magnetite-hematite buffer, at 300 °C. The fitted conditions, next to mineral buffers, allow for interpretation of persistent small-scale fluctuations of fluid parameters, concordant with textural observation.

Distribution of Fe-oxides throughout the different parts of the shell and relative to the orebody indicates block/fault-compartmentation with highest offset in the SE part of the deposit. Corroborated by newly published data and high-precision U-Pb dating of magmatic zircon and hydrothermal U-W-Sn-Mo hematite, a new model is suggested for the IOCG system at Olympic Dam. At the stage when the host granite has crystallised, volatile-fluid separation due to overpressure and/or tectonic activity triggered mineral reactions accounting for formation of early Fe-oxides in the outer shell. Further uplift and cupola collapse at shallower depth (2–3 km?) released the main hydrothermal fluids sourcing the mineralisation and at the same time, leading to interconversion between Fe-oxides in the surrounding shell.

These results highlight the importance of combining detailed petrographic and geochemical studies at different scales of observation. Siderite may yet prove a key mineral in understanding the origin of the reported magnetite-bearing assemblages, if stable isotope signatures are resolved at appropriate scales (e.g. by nanoSIMS). The extent of IOCG alteration relative to individual intrusive bodies in the Burgoyne Batholith is yet to be rigorously constrained. We stipulate that silician magnetite is typical of early, alkali-calcic alteration stages of IOCG mineralisation, particularly in intrusion-hosted deposits. Identification may however require dedicated nanoscale studies. The co-existence of Si-magnetite and HFSE-bearing hematite could be an important pathfinder for early IOCG mineralisation.

Acknowledgments We extend thanks to the staff of Adelaide Microscopy, particularly Sarah Gilbert and Benjamin Wade, who assisted with LA-ICP-MS and EPMA, respectively. Constructive comments from Peter Pollard, an anonymous reviewer, Associate Editor David Huston and Editor-in-Chief Bernd Lehmann are appreciated, and helped improve the manuscript.

Funding information This work is a contribution to the 'FOX' project (Trace elements in iron oxides: deportment, distribution and application in ore genesis, geochronology, exploration and mineral processing), supported by BHP Olympic Dam and the South Australian Government Mining and Petroleum Services Centre of Excellence. N.J.C. acknowledges support from the ARC Research Hub for Australian Copper-Uranium (Grant IH130200033).

References

Allen SR, McPhie J, Ferris G, Simpson C (2008) Evolution and architecture of a large felsic Igneous Province in western Laurentia: The 1.6 Ga Gawler Range Volcanics, South Australia. J Volcanol Geotherm Res 172:132–147. https://doi.org/10.1016/j.jvolgeores.2005.09.027

Apukhtina OB, Kamenetsky VS, Ehrig K, Kamenetsky MB, McPhie J, Mass R, Meffre S, Goemann K, Rodemann T, Cook NJ, Ciobanu CL (2016) Postmagmatic magnetite–apatite assemblage in mafic intrusions: a case study of dolerite at Olympic Dam, South Australia. Contrib Mineral Petrol 171:15. https://doi.org/10.1007/s00410-015-1215-7

Apukhtina OB, Kamenetsky VS, Ehrig K, Kamenetsky MB, Mass R, Thompson J, McPhie J, Ciobanu CL, Cook NJ (2017) Early, deep magnetite-fluorapatite mineralization at the Olympic Dam Cu-U-Au-Ag deposit, South Australia. Econ Geol 112:1531–1542. https://doi.org/10.5382/econgeo.2017.4520

Barton MD (2014) Iron oxide(–Cu–Au–REE–P–Ag–U–Co) systems. In: Turekian K, Holland H, Scott SD (eds) Treatise on Geochemistry, vol 13, 2nd edn. Elsevier, New York, pp 515–541. doi: https://doi.org/10.1016/B978-0-08-095975-7.01123-2

Bastrakov EN, Skirrow RG, Davidson GJ (2007) Fluid evolution and origins of iron oxide Cu-Au prospects in the Olympic Dam District, Gawler Craton, South Australia. Econ Geol 102:1415–1440. https://doi.org/10.2113/gsecongeo.102.8.1415

Blissett AH, Creaser RA, Daly SJ, Flint RB, Parker AJ (1993) Gawler Range Volcanics. In: Drexel JF, Preiss WV, Parker AJ (eds) The Geology of South Australia. Vol. 1, The Precambrian, South Australia Geological Survey, Bulletin 54, pp 107–124

Bosi F, Biagioni C, Pasero M (2019) Nomenclature and classification of the spinel supergroup. Eur J Mineral 31:183–192. https://doi.org/10.1127/ejm/2019/0031-2788

Cherry AR, Ehrig K, Kamenetsky VS, McPhie J, Crowley JL, Kamenetsky MB (2018) Precise geochronological constraints on the origin, setting and incorporation of ca. 1.59 Ga surficial facies into the Olympic Dam Breccia Complex, South Australia. Precambrian Res 315:162–178. https://doi.org/10.1016/j.precamres.2018.07.012

Ciobanu CL, Wade BP, Cook NJ, Schmidt Mumm A, Giles D (2013) Uranium-bearing hematite from the Olympic Dam Cu–U–Au deposit, South Australia: a geochemical tracer and reconnaissance Pb–Pb geochronometer. Precambrian Res 238:129–147. https://doi.org/10.1016/j.precamres.2013.10.007

Ciobanu CL, Cook NJ, Wade BP, Ehrig K (2014) Ore minerals down to nanoscale: petrogenetic implications. Acta Geol Sin-Engl 88:1441–1443. https://doi.org/10.1111/1755-6724.12382_2

Ciobanu CL, Cook NJ, Ehrig K, Wade BP, Kamenetsky VS (2015) Trace element signatures in iron oxides from the Olympic Dam IOCG deposit, South Australia. In: Mineral Resources in a Sustainable World, Proceedings of the 13th SGA Biennial Meeting, Nancy, France, 24-27 August 2015. 3:1071–1074

Ciobanu CL, Cook NJ, Ehrig K (2017) Ore minerals down to the nanoscale: Cu-(Fe)-sulphides from the iron oxide copper gold deposit at Olympic Dam, South Australia. Ore Geol Rev 81:1218–1235. https://doi.org/10.1016/j.oregeorev.2016.08.015

Ciobanu CL, Verdugo-Ihl MR, Slattery A, Cook NJ, Ehrig KJ, Courtney-Davies L (2018) Nanoscale study of silician magnetite from IOCG systems: examples from the Olympic Dam District, South Australia. In: Proceedings of the 15th Quadrennial International Association on the Genesis of Ore Deposits symposium, Salta, Argentina, 28-31 August 2018. pp 185–186

Ciobanu CL, Verdugo-Ihl MR, Slattery A, Cook NJ, Ehrig K, Courtney-Davies L, Wade BP (2019) Silician magnetite: Si–Fe-nanoprecipitates and other mineral inclusions in magnetite from the Olympic Dam deposit, South Australia. Minerals 9:311. https://doi.org/10.3390/min9050311

Cook N, Ciobanu CL, George L, Zhu Z-Y, Wade B, Ehrig K (2016) Trace element analysis of minerals in magmatic-hydrothermal ores by laser ablation inductively-coupled plasma mass spectrometry: approaches and opportunities. Minerals 6:111. https://doi.org/10.3390/min6040111

Cook NJ, Ciobanu CL, Ehrig K, Slattery A, Verdugo-Ihl MR, Courtney-Davies L, Gao W (2017) Advances and opportunities in ore mineralogy. Minerals 7:233. https://doi.org/10.3390/min7120233

Courtney-Davies L, Zhu Z, Ciobanu CL, Wade BP, Cook NJ, Ehrig K, Cabral AR, Kennedy A (2016) Matrix-matched iron-oxide laser ablation ICP-MS U–Pb geochronology using mixed solution standards. Minerals 6:85. https://doi.org/10.3390/min6030085

Courtney-Davies L, Ciobanu CL, Tapster SR, Cook NJ, Ehrig KJ, Kennedy AK, Condon DJ, Verdugo-Ihl MR, Wade BP, Gilbert SE (2018) The U-Pb systematics of hydrothermal hematite: insights from the IOCG system at Olympic Dam, South Australia. In: Proceedings of the 15th Quadrennial International Association on the Genesis of Ore Deposits symposium, Salta, Argentina, 28-31 August 2018. pp 171–172

Courtney-Davies L, Tapster SR, Ciobanu CL, Cook NJ, Verdugo-Ihl MR, Ehrig KJ, Kennedy AK, Gilbert SE, Condon DJ, Wade BP (2019) A multi-technique evaluation of hydrothermal hematite U–Pb isotope systematics: Implications for ore deposit geochronology. Chem Geol 513:54–72. https://doi.org/10.1016/j.chemgeo.2019.03.005

Cowley W, Conor C, Zang W (2003) New and revised Proterozoic stratigraphic units on northern Yorke Peninsula. Mesa J 29:46–58

Creaser RA (1996) Petrogenesis of a Mesoproterozoic quartz latite-granitoid suite from the Roxby Downs area, South Australia. Precambrian Res 79:371–394. https://doi.org/10.1016/S0301-9268(96)00002-2

Dare SAS, Barnes S-J, Beaudoin G (2015) Did the massive magnetite "lava flows" of El Laco (Chile) form by magmatic or hydrothermal processes? New constraints from magnetite composition by LA-ICP-MS. Mineral Deposita 50:607–617. https://doi.org/10.1007/s00126-014-0560-1

Deditius AP, Reich M, Simon AC, Suvorova S, Knipping J, Roberts MP, Rubanov S, Dodd A, Saunders M (2018) Nanogeochemistry of hydrothermal magnetite. Contrib Mineral Petrol 173:46. https://doi.org/10.1007/s00410-018-1474-1

Dmitrijeva M, Metcalfe AV, Ciobanu CL, Cook NJ, Frenzel M, Keyser WM, Johnson G, Ehrig K (2018) Discrimination and variance structure of trace element signatures in Fe-oxides: a case study of BIF-

mineralisation from the Middleback Ranges, South Australia. Math Geosci 50:381–415. https://doi.org/10.1007/s11004-018-9734-1

Dmitrijeva M, Ehrig KJ, Ciobanu CL, Cook NJ, Verdugo-Ihl MR, Metcalfe AV (2019) Defining IOCG signatures through compositional data analysis: a case study of lithogeochemical zoning from the Olympic Dam deposit, South Australia. Ore Geol Rev 105:86–101. https://doi.org/10.1016/j.oregeorev.2018.12.013

Donovan JJ, Singer JW, Armstrong JT (2016) A new EPMA method for fast trace element analysis in simple matrices. Am Mineral 101: 1839–1853. https://doi.org/10.2138/am-2016-5628

Ehrig K, McPhie J, Kamenetsky V (2012) Geology and mineralogical zonation of the Olympic Dam iron oxide Cu-U-Au-Ag deposit, South Australia. In: Hedenquist JW, Harris M, Camus F (eds) Geology and genesis of major copper deposits and districts of the world: a tribute to Richard H. Sillitoe. Soc of Econ Geol Spec Pub 16:237–267. https://doi.org/10.5382/SP.16.11

Groves DI, Bierlein FP, Meinert LD, Hitzman MW (2010) Iron oxide copper-gold (IOCG) deposits through Earth history: Implications for origin, lithospheric setting, and distinction from other epigenetic iron oxide deposits. Econ Geol 105:641–654. https://doi.org/10.2113/gsecongeo.105.3.641

Haynes DW, Cross KC, Bills RT, Reed MH (1995) Olympic Dam ore genesis: a fluid-mixing model. Econ Geol 90:281–307. https://doi.org/10.2113/gsecongeo.90.2.281

Hitzman MW (2000) Iron-oxide-Cu-Au deposits: What, where, when, and why. In: Porter TM (ed) Hydrothermal Iron Oxide Copper-Gold & Related Deposits: A Global Perspective. PGC Publishing, Adelaide, vol. 1, pp 9–25

Huang Q, Kamenetsky VS, McPhie J, Ehrig K, Meffre S, Mass R, Thompson J, Kamenetsky M, Chambefort I, Apukhhtina O, Hu Y (2015) Neoproterozoic (ca. 820–830 Ma) mafic dykes at Olympic Dam, South Australia: Links with the Gairdner Large Igneous Province. Precambrian Res 271:160–172. https://doi.org/10.1016/j.precamres.2015.10.001

Huang Q, Kamenetsky VS, Ehrig K, McPhie J, Kamenetsky M, Cross K, Meffre S, Agangi A, Chambefort I, Direen NG, Mass R, Apukhtina O (2016) Olivine-phyric basalt in the Mesoproterozoic Gawler silicic large igneous province, South Australia: Examples at the Olympic Dam Iron Oxide Cu–U–Au–Ag deposit and other localities. Precambrian Res 281:185–199. https://doi.org/10.1016/j.precamres.2016.05.019

Huberty JM, Konishi H, Heck PR, Fournelle JH, Valley JW, Xu H (2012) Silician magnetite from the Dales Gorge Member of the Brockman Iron Formation, Hamersley Group, Western Australia. Am Mineral 97:26–37. https://doi.org/10.2138/am.2012.3864

Ismail R, Ciobanu CL, Cook NJ, Teale GS, Giles D, Schmidt Mumm A, Wade B (2014) Rare earths and other trace elements in minerals from skarn assemblages, Hillside iron oxide–copper–gold deposit, Yorke Peninsula, South Australia. Lithos 184–187:456–477. https://doi.org/10.1016/j.lithos.2013.07.023

Jagodzinski EA (2005) Compilation of SHRIMP U-Pb geochronological data, Olympic Domain, Gawler Craton, South Australia, 2001–2003. Geoscience Australia, Record 2005/20. 197 pp.

Keyser W, Ciobanu CL, Cook NJ, Johnson G, Feltus H, Johnson S, Dmitrijeva M, Ehrig K, Nguyen PT (2018) Petrography and trace element signatures of iron-oxides in deposits from the Middleback Ranges, South Australia: from banded iron formation to ore. Ore Geol Rev 93:337–360. https://doi.org/10.1016/j.oregeorev.2018.01.006

Knauss KG, Dibley MJ, Bourcier WL, Shaw HF (2001) Ti(IV) hydrolysis constants derived from rutile solubility measurements made from 100 to 300°C. Appl Geochem 16:1115–1128. https://doi.org/10.1016/S0883-2927(00)00081-0

Knipping JL, Bilenker LD, Simon AC, Reich M, Barra F, Deditius AP, Lundstrom C, Bindeman I, Munizaga R (2015) Giant Kiruna-type deposits form by efficient flotation of magmatic magnetite suspensions. Geology 43:591–594. https://doi.org/10.1130/G36650.1

Kontonikas-Charos A, Ciobanu CL, Cook NJ (2014) Albitization and redistribution of REE and Y in IOCG systems: insights from Moonta-Wallaroo, Yorke Peninsula, South Australia. Lithos 208–209:178–201. https://doi.org/10.1016/j.lithos.2014.09.001

Kontonikas-Charos A, Ciobanu CL, Cook NJ, Ehrig K, Krneta S, Kamenetsky VS (2017) Feldspar evolution in the Roxby Downs Granite, host to Fe-oxide Cu-Au-(U) mineralisation at Olympic Dam, South Australia. Ore Geol Rev 80:838–859. https://doi.org/10.1016/j.oregeorev.2016.08.019

Kontonikas-Charos A, Ciobanu CL, Cook NJ, Ehrig K, Ismail R, Krneta S, Basak A (2018) Feldspar mineralogy and rare-earth element (re)mobilization in iron-oxide copper gold systems from South Australia: a nanoscale study. Mineral Mag 82:S173–S197. https://doi.org/10.1180/minmag.2017.081.040

Krneta S, Ciobanu CL, Cook NJ, Ehrig K, Kontonikas-Charos A (2016) Apatite at Olympic Dam, South Australia: a petrogenetic tool. Lithos 262:470–485. https://doi.org/10.1016/j.lithos.2016.07.033

Krneta S, Ciobanu CL, Cook NJ, Ehrig K, Kontonikas-Charos A (2017) Rare earth element behaviour in apatite from the Olympic Dam Cu–U–Au–Ag deposit, South Australia. Minerals 7:135. https://doi.org/10.3390/min7080135

Krneta S, Ciobanu C, Cook N, Ehrig K (2018) Numerical modeling of REE fractionation patterns in fluorapatite from the Olympic Dam deposit (South Australia). Minerals 8:342. https://doi.org/10.3390/min8080342

Lund CRF, Dumesic JA (1981) Strong oxide-oxide interactions in silica-supported magnetite catalysts. 1. X-ray diffraction and Mössbauer spectroscopy evidence for interaction. J Phys Chem 85:3175–3180. https://doi.org/10.1021/j150621a034

Mauger AJ, Ehrig K, Kontonikas-Charos A, Ciobanu CL, Cook NJ, Kamenetsky VS (2016) Alteration at the Olympic Dam IOCG–U deposit: insights into distal to proximal feldspar and phyllosilicate chemistry from infrared reflectance spectroscopy. Aust J Earth Sci 63:959–972. https://doi.org/10.1080/08120099.2016.1264474

Meinert LD, Dipple G M, Nicolescu S (2005) World skarn deposits. In: Hedenquist JW, Thompson JFH, Goldfarb RJ, Richards JP (eds) Econ Geol 100th Anniv Vol, Society of Economic Geologists, Littleton, pp 299–336. https://doi.org/10.1130/0091-7613(1993)021

Morales Ruano S, Both RA, Golding SD (2002) A fluid inclusion and stable isotope study of the Moonta copper–gold deposits, South Australia: evidence for fluid immiscibility in a magmatic hydrothermal system. Chem Geol 192:211–226. https://doi.org/10.1016/S0009-2541(02)00197-3

Ohkawa M, MiyaharaA M, Ohta E, Hoshino K (2007) Silicon-substituted magnetite and accompanying iron oxides and hydroxides from the Kumano mine, Yamaguchi prefecture, Japan: reexamination of the so-called maghemite (γ-Fe_2O_3). J Mineral Petrol Sci 102:182–193. https://doi.org/10.2465/jmps.050706

Oreskes N, Einaudi MT (1990) Origin of rare earth element-enriched hematite breccias at the Olympic Dam Cu-U-Au-Ag deposit, Roxby Downs, South Australia. Econ Geol 85:1–28. https://doi.org/10.2113/gsecongeo.85.1.1

Oreskes N, Einaudi MT (1992) Origin of hydrothermal fluids at Olympic Dam: preliminary results from fluid inclusions and stable isotopes. Econ Geol 87:64–90. https://doi.org/10.2113/gsecongeo.87.1.64

Otake T, Wesolowski DJ, Anovitz LM, Allard LF, Ohmoto H (2007) Experimental evidence for non-redox transformations between magnetite and hematite under H_2-rich hydrothermal conditions. Earth Planet Sci Lett 257:60–70. https://doi.org/10.1016/j.epsl.2007.02.022

Otake T, Wesolowski DJ, Anovitz LM, Allard LF, Ohmoto H (2010) Mechanisms of iron oxide transformations in hydrothermal systems.

Geochim Cosmochim Acta 74:6141–6156. https://doi.org/10.1016/j.gca.2010.07.024

Ovalle JT, La Cruz NL, Reich M, Barra F, Simon AC, Konecke BA, Rodriguez-Mustafa MA, Deditius AP, Childress TM, Morata D (2018) Formation of massive iron deposits linked to explosive volcanic eruptions. Sci Rep 8:14855. https://doi.org/10.1038/s41598-018-33206-3

Paton C, Hellstrom J, Paul B, Woodhead J, Hergt J (2011) Iolite: freeware for the visualisation and processing of mass spectrometric data. J Anal At Spectrom 26:2508–2518. https://doi.org/10.1039/c1ja10172b

Pollard PJ (2001) Sodic(−calcic) alteration in Fe-oxide–Cu–Au districts: an origin via unmixing of magmatic H_2O–CO_2–NaCl + $CaCl_2$–KCl fluids. Mineral Deposita 36:93–100. https://doi.org/10.1007/s001260050289

Reeve JS, Cross KC, Smith RN, Oreskes N (1990) Olympic Dam copper-uranium-gold-silver deposit. In: Hughes FE (ed) Geology of the Mineral Deposits of Australia and Papua New Guinea. Australasian Institute of Mining and Metallurgy, Melbourne, pp 1009–1035

Richards JP, Mumin AH (2013) Magmatic-hydrothermal processes within an evolving earth: Iron oxide-copper-gold and porphyry Cu±Mo ±Au deposits. Geology 41:767–770. https://doi.org/10.1130/G34275.1

Roberts DE, Hudson GRT (1983) The Olympic Dam copper-uranium-gold deposit, Roxby Downs, South Australia. Econ Geol 78:799–822. https://doi.org/10.2113/gsecongeo.78.5.799

Tkachev AV (2011) Evolution of metallogeny of granitic pegmatites associated with orogens throughout geological time. Geol Soc Lond Spec Publ 350:7–23. https://doi.org/10.1144/SP350.2

van Achterbergh E, Ryan CG, Jackson SE, Griffin WL (2001) Data reduction software for LA-ICP-MS. in: Sylvester PJ (ed) Laser-Ablation-ICPMS in the Earth Sciences; Principles and Applications. Mineralogical Association of Canada, Short Course Series 29. pp 239–243

Verdugo-Ihl MR, Ciobanu CL, Cook NJ, Ehrig KJ, Courtney-Davies L, Gilbert S (2017a) Textures and U-W-Sn-Mo signatures in hematite from the Olympic Dam Cu-U-Au-Ag deposit, South Australia: defining the archetype for IOCG deposits. Ore Geol Rev 91:173–195. https://doi.org/10.1016/j.oregeorev.2017.10.007

Verdugo-Ihl MR, Ciobanu CL, Cook NJ, Courtney-Davies L, Ehrig KJ, Gilbert S (2017b) Trace element signatures in U-W-Sn-Mo zoned hematite from the IOCG deposit at Olympic Dam, South Australia. In: Mineral Resources to Discover, Proceedings of the 14th Biennial SGA Conference, Quebec City, QC, Canada, 20–23 August 2017. pp 967–970

Wang X, Wei W, Lv X, Fan X, Wang S (2017) Stanniferous magnetite composition from the Haobugao skarn Fe-Zn deposit, southern Great Xing'an Range: implication for mineral depositional mechanism. Geol J 53:1823–1839. doi: https://doi.org/10.1002/gj.3009

Xu H, Shen Z, Konishi H (2014) Si-magnetite nano-precipitates in silician magnetite from banded iron formation: Z-contrast imaging and ab initio study. Am Mineral 99:2196–2202. https://doi.org/10.2138/am-2014-4964

Zimmer K, Zhang Y, Lu P, Chen Y, Zhang G, Dalkilic M, Zhu C (2016) SUPCRTBL: a revised and extended thermodynamic dataset and software package of SUPCRT92. Comput Geosci 90:97–111. https://doi.org/10.1016/j.cageo.2016.02.013

Publisher's note Springer Nature remains neutral with regard to jurisdictional claims in published maps and institutional affiliations.

CHAPTER 4

COPPER-ARSENIC NANOPARTICLES IN HEMATITE: FINGERPRINTING FLUID-MINERAL INTERACTION

Max R. Verdugo-Ihl [1], Cristiana L. Ciobanu [1], Ashley Slattery [2],

Nigel J. Cook [1], Kathy Ehrig [3] and Liam Courtney-Davies [1]

[1]School of Chemical Engineering and Advanced Materials, The University of Adelaide, Adelaide, SA 5005, Australia;

[2]Adelaide Microscopy, The University of Adelaide, Adelaide, SA 5005, Australia;

[3]BHP Olympic Dam, Adelaide, SA 5000, Australia

Article published in *Minerals* (2019) 9(7):388.

Statement of Authorship

Title of Paper	Copper-arsenic nanoparticles in hematite: fingerprinting fluid-mineral interaction
Publication Status	☑ Published ☐ Accepted for Publication ☐ Submitted for Publication ☐ Unpublished and Unsubmitted work written in manuscript style
Publication Details	Verdugo-Ihl, M.R., Ciobnau, C.L., Slattery, A., Cook, N.J., Ehrig, K.J., Courtney-Davies, L., 2019. Copper-arsenic nanoparticles in hematite: fingerprinting fluid-mineral interaction. Minerals 9(7), 388, https://doi.org/10.3390/min9070388.

Principal Author

Name of Principal Author (Candidate)	Max R. Verdugo-Ihl		
Contribution to the Paper	Performed analytical work, evaluation and interpretation of results and prepared the manuscript.		
Overall percentage (%)	55		
Certification:	This paper reports on original research I conducted during the period of my Higher Degree by Research candidature and is not subject to any obligations or contractual agreements with a third party that would constrain its inclusion in this thesis. I am the primary author of this paper.		
Signature		Date	15.04.2020

Co-Author Contributions

By signing the Statement of Authorship, each author certifies that:

i. the candidate's stated contribution to the publication is accurate (as detailed above);

ii. permission is granted for the candidate in include the publication in the thesis; and

iii. the sum of all co-author contributions is equal to 100% less the candidate's stated contribution.

Name of Co-Author	Cristiana L. Ciobanu		
Contribution to the Paper	Helped to define the direction of the manuscript, guided manuscript preparation and assisted with data acquisition, the interpretation of the results and evaluation of the manuscript.		
Overall percentage (%)	25		
Signature		Date	15.04.2020

Name of Co-Author	Ashley Slattery		
Contribution to the Paper	Performed HAADF-STEM data acquisition.		
Overall percentage (%)	7.5		
Signature		Date	15.04.20

Name of Co-Author	Nigel J. Cook		
Contribution to the Paper	Assisted with the preparation and evaluation of the manuscript.		
Overall percentage (%)	7.5		
Signature		Date	15.04.2020

Name of Co-Author	Kathy Ehrig		
Contribution to the Paper	Assisted with the evaluation of the manuscript.		
Overall percentage (%)	3		
Signature		Date	15.04.2020

Name of Co-Author	Liam Courtney-Davies		
Contribution to the Paper	Assisted with the evaluation of the manuscript.		
Overall percentage (%)	2		
Signature		Date	15.04.2020

minerals

MDPI

Article

Copper-Arsenic Nanoparticles in Hematite: Fingerprinting Fluid-Mineral Interaction

Max R. Verdugo-Ihl [1,*], Cristiana L. Ciobanu [1], Ashley Slattery [2], Nigel J. Cook [1], Kathy Ehrig [3] and Liam Courtney-Davies [1]

1 School of Chemical Engineering and Advanced Materials, The University of Adelaide, Adelaide, SA 5005, Australia
2 Adelaide Microscopy, The University of Adelaide, Adelaide, SA 5005, Australia
3 BHP Olympic Dam, Adelaide, SA 5000, Australia
* Correspondence: max.verdugoihl@adelaide.edu.au; Tel.: +61-831-33093

Received: 2 June 2019; Accepted: 25 June 2019; Published: 27 June 2019

Abstract: Metal nanoparticles (NP) in minerals are an emerging field of research. Development of advanced analytical techniques such as Z-contrast imaging and mapping using high-angle annular dark field scanning transmission electron microscopy (HAADF STEM) allows unparalleled insights at the nanoscale. Moreover, the technique provides a link between micron-scale textures and chemical patterns if the sample is extracted in situ from a location of petrogenetic interest. Here we use HAADF STEM imaging and energy-dispersive X-ray spectrometry (EDX) mapping/spot analysis on focused ion beam prepared foils to characterise atypical Cu-As-zoned and weave-twinned hematite from the Olympic Dam deposit, South Australia. We aim to determine the role of solid-solution versus the presence of discrete included NPs in the observed zoning and to understand Cu-As-enrichment processes. Relative to the grain surface, the Cu-As bands extend in depth as (sub)vertical trails of opposite orientation, with Si-bearing hematite NP inclusions on one side and coarser cavities (up to hundreds of nm) on the other. The latter host Cu and Cu-As NPs, contain mappable K, Cl, and C, and display internal voids with rounded morphologies. Aside from STEM-EDX mapping, the agglomeration of native copper NPs was also assessed by high-resolution imaging. Collectively, such characteristics, corroborated with the geometrical outlines and negative crystal shapes of the cavities, infer that these are opened fluid inclusions with NPs attached to inclusion walls. Hematite along the trails features distinct nanoscale domains with lattice defects (twins, 2-fold superstructuring) relative to hematite outside the trails, indicating this is a nanoprecipitate formed during replacement processes, i.e., coupled dissolution and reprecipitation reactions (CDRR). Transient porosity intrinsically developed during CDRR can trap fluids and metals. Needle-shaped and platelet Cu-As NPs are also observed along (sub)horizontal bands along which Si, Al and K is traceable along the margins. The same signature is depicted along nm-wide planes crosscutting at 60° and offsetting (012)-twins in weave-twinned hematite. High-resolution imaging shows linear and planar defects, kink deformation along the twin planes, misorientation and lattice dilation around duplexes of Si-Al-K-planes. Such defects are evidence of strain, induced during fluid percolation along channels that become wider and host sericite platelets, as well as Cl-K-bearing inclusions, comparable with those from the Cu-As-zoned hematite, although without metal NPs. The Cu-As-bands mapped in hematite correspond to discrete NPs formed during interaction with fluids that changed in composition from alkali-silicic to Cl- and metal-bearing brines, and to fluid rates that evolved from slow infiltration to erratic inflow controlled by fault-valve mechanism pumping. This explains the presence of Cu-As NPs hosted either along Si-Al-K-planes (fluid supersaturation), or in fluid inclusions (phase separation during depressurisation) as well as the common signatures observed in hematite with variable degrees of fluid-mineral interaction. The invoked fluids are typical of hydrolytic alteration and the fluid pumping mechanism is feasible via fault (re)activation. Using a

Minerals **2019**, *9*, 388

nanoscale approach, we show that fluid-mineral interaction can be fingerprinted at the (atomic) scale at which element exchange occurs.

Keywords: HAADF-STEM; hematite; Cu-(As) nanoparticles; fluid-mineral interaction; fluid-inclusions

1. Introduction

The abundance and potential significance of nanoparticles in rocks and ores is gaining recognition, as analytical capabilities expand, allowing detailed characterisation of their physical states and quantification of their chemical compositions. Nanoparticulate phases may have geochemical behaviour that differs significantly from that of their larger mineral analogues due to far greater surface area relative to mass (e.g., [1]). Metal-bearing nanoparticles (NPs) hosted within minerals, particularly sulphides, have drawn research attention because of their potential economic significance and because they can represent evidence in support of petrogenetic models. Among the best studied examples is nanoparticulate "invisible gold" within arsenian pyrite, or arsenopyrite. Inferences for the presence of discrete Au NPs, alongside lattice-bound (solid solution) gold within arsenian pyrite were validated for the first time by direct imaging of high-As (thousands ppm) pyrite using transmission electron microscopy (TEM) [2]. This type of observation has been used in combination with trace element data to determine an empirical solubility limit for structurally-bound Au in pyrite as a function of increasing As-content [3]. Gold NPs have recently been identified in hydrothermal fluids, suggesting that gold transport may occur in both dissolved (complexed) and particulate form [4]. The identification of nanoparticulate platinum group element (PGE)-minerals has been used to discuss PGE enrichment and ore-forming processes in layered-intrusions (e.g., [5–7]).

Breaking the paradigm of invisible gold in As-bearing pyrite, an alternative mechanism was put forward [8], which could explain the formation of Au NPs. Ciobanu et al. [8] invoked devolatilization processes resulting in precipitation of Au-telluride NPs within As-free pyrite during fluid-rock interaction. Such a process was considered to occur via a coupled dissolution and reprecipitation reaction (CDRR), during which transient porosity develops, explaining the persistent presence of pores wherever NPs were observed. The pore-attached NPs were interpreted as the "frozen expression" of fluid inclusions. Comparable CDRR processes were invoked to explain the presence of composite, pore-attached nanoparticulate clausthalite (PbSe) and Bi-bearing phases within chalcopyrite [9]. In this case, the Se was already present in solid solution within the Cu-Fe-sulphide and Pb (from U-decay) was supplied by an interacting hydrothermal fluid, accounting for NP precipitation. The role of transient porosity in trapping metals has been validated by experimental work supporting the "Bi-Au collector" model [10]. Gold scavenged by a Bi-melt is precipitated from hydrothermal fluids and incorporated in pores along the reaction interface as Bi-Au NPs/fine particles. Experimental work demonstrating the development of CDRR shows that rapid closure of external porosity, due to ripening of the pores, can effectively trap fluids, including low-T melts, as fluid inclusions and/or mineral precipitates during CDRR [11].

In comparison with sulphides, relatively little is known about the presence of NPs in Fe-oxides. Nanoscale studies of NPs in magnetite (e.g., [12–14]) have been used to identify conditions of ore-formation. In contrast, the potential constraints that could be obtained from NPs in hematite remain largely unexplored. The formation of uraninite NPs associated with pores in hematite has previously been attributed to CDRR processes [15], with the U locally sourced from U-rich domains in the precursor, overprinted hematite.

Quantitative compositional data obtained by laser-ablation inductively-coupled-plasma mass-spectrometry (LA-ICP-MS) may only represent bulk, volume-averaged results whenever the mineral in question is heterogeneous down to the nanoscale, a phenomenon that may impact on accurate petrogenetic interpretations [16]. An adequate understanding of the distribution and

speciation of trace elements (i.e., within solid-solution or as discrete phases) can often only be achieved by systematic studies using a combination of microanalytical techniques with different scales of observation [15,17,18]. High-resolution imaging using Z-contrast techniques, such as high-angle annular dark-field (HAADF) scanning transmission electron microscopy (STEM) on material extracted in-situ from the surface of a polished specimen, using a focused ion beam (FIB) scanning electron microscope (SEM) platform, has proven particularly valuable for correct interpretation of micron-scale geochemical data [17,19–21]. TEM methods can also be used to resolve and image sub-micrometre-size fluid inclusions [22], making the technique valuable for understanding complex trace element signatures associated with their presence, although they are limited to what remains of the fluid inclusions after TEM-sample preparation.

The sample selected for this study originates from the iron oxide Cu-Au (IOCG) system at the Olympic Dam deposit, South Australia [23]. The deposit is hosted within a breccia complex, confined to the Mesoproterozoic Roxby Downs Granite. Discovery of hematite containing lattice-bound U and radiogenic Pb and displaying oscillatory zoning patterns allowed U-Pb dating using LA-ICP-MS, providing geologically meaningful ages [24]. Subsequent high-precision U-Pb ID-TIMS dating of hematite (1592.1 ± 0.88 Ma; [25]) indicates that mineralisation occurred shortly after granite emplacement (U-Pb zircon age 1593.87 ± 0.21 Ma; [26]).

The oscillatory zoned hematite is present throughout the entire Olympic Dam deposit, with zonation patterns defined by the element association U-(Pb)-W-Sn-Mo [27]. Moreover, such hematite displays a variety of textures, including varied twinning patterns and overprints. Among the latter, pseudomorphic replacement of oscillatory zoned hematite by another hematite with a distinct, different trace element signature can show a "new" zoning arrangement that can partially overlap pre-existing patterns or may display evidence of selective removal of some pre-existing elements [27]. The present study is carried out on a representative sample displaying such an overprint, in which compositional maps obtained by LA-ICP-MS depict spatially overlapping grain-scale zonation patterns in hematite expressed by U-W-Sn-Mo, superimposed by Cu, As and Sb [27]. Hematite from this sample is also characterised by unusual weave-twinning, such as those described as basket-weave twins in volcaniclastic breccias at the Olympic Dam deposit [27].

Although naturally-occurring end-member Cu-Fe-oxides (e.g., cuprospinel, $CuFe_2O_4$; [28]) are relatively scarce, limited Cu^{2+} substitution in octahedral coordination is considered for both magnetite and hematite. Copper incorporation into hematite, however, has only been documented from experimental studies of hematite nanostructures (e.g., [29]). Incorporation of Sb (and As) into hematite can be inferred by the existence of rhombohedral, ilmenite-type oxides (e.g., melanostibite: $Mn^{2+}(Sb_{0.5}{}^{5+}Fe_{0.5}{}^{3+})O_3$; [30]) that could build limited solid-solution with hematite, although charge-balance would require substituting divalent cations (e.g., Fe^{2+}).

In this context, the sample studied here represents an ideal opportunity to test whether Cu, As (and Sb) incorporation in natural hematite specimens could be explained by substitution, or if these elements occur as discrete phases. We therefore assess the incorporation of Cu, and As in hematite down to the nanoscale to determine the role of solid-solution versus the presence of discrete inclusions (NPs). Secondly, we aim to understand the processes involved in the Cu-As-enrichment of hematite.

2. Samples and Methodology

The studied hematite derives from a sulphide-poor interval in the south-eastern part of the Olympic Dam deposit. This interval comprises a hematite breccia containing clasts of volcanic rocks and is notable for the presence of a diverse range of trace minerals including native copper, Cu-Au-alloys, electrum, and Pb-Bi-tellurides [31]. The grains studied are derived from a single polished block in which oscillatory zoned, U-W-Sn-Mo-bearing hematite shows two conspicuous features: (i) unusual zoning with respect to Cu and As (Figure 1); and (ii) weave-twinning patterns (Figure 2).

Minerals **2019**, *9*, 388

Four TEM-foils were extracted using established dual-beam FIB-SEM methods [16] using a FEI Helios Nanolab 600 instrument (FEI, Hillsboro, OR, USA). Three foils (foils #1, #2 and #3) were cut across the Cu-As bands from both sides of the grain (domain A and B; Figure 1b), whereas a fourth (foil #4) was cut across the weave-twining pattern in another hematite grain (Figure 2). HAADF STEM imaging and energy-dispersive X-ray spectrometry (EDX) spot analysis and mapping were conducted with an ultra-high resolution, probe corrected, FEI Titan Themis STEM (FEI, Hillsboro, OR, USA) operated at 200 kV. This instrument is equipped with a X-FEG Schottky source and Super-X EDX geometry. The Super-X EDX detector provides geometrically symmetric EDX detection with an effective solid angle of 0.8 Sr. Probe correction delivered sub-Ångstrom spatial resolution and an inner collection angle greater than 50 mrad was used for HAADF imaging with a Fischione detector.

Indexing of diffraction patterns obtained from Fast-Fourier-Transformed (FFT) images was conducted with WinWulff© (version 1.5.2) and publicly available data from the American Mineralogist Crystal Structure Database (http://rruff.geo.arizona.edu/AMS/amcsd.php). Crystal structure models were generated in CrystalMaker® (version 10.2) and STEM for xHREM™ Version 4.1 software. All instruments are housed at Adelaide Microscopy, The University of Adelaide. Complete STEM EDX maps and additional figures are shown as Supplementary Materials Figures S1–S7.

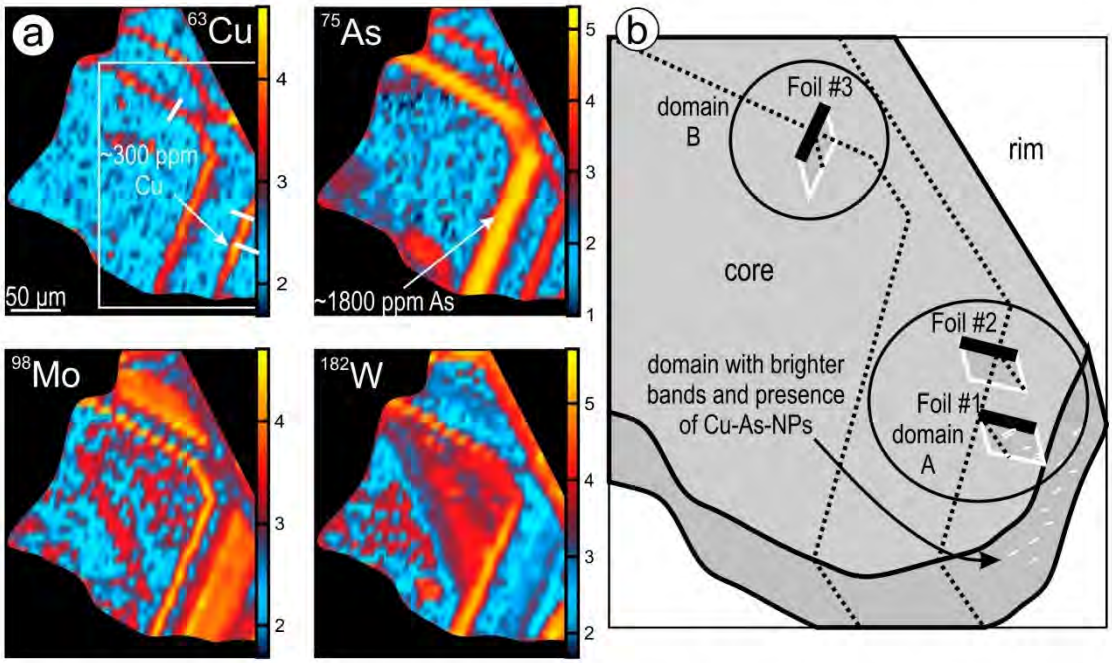

Figure 1. (**a**) LA-ICP-MS element maps of hematite (grain #1) displaying oscillatory zoning with respect to Cu and As. The distributions of both elements partially overlap with other metals such as Mo and W (modified from [27]). Other metal/metalloids showing zoning in this grain are Sb, Sn, and U. Intensities are in counts-per-second (logarithmic scale, 10^n). Concentrations of Cu and Sb in the bands can reach up to ~300 and ~200 ppm, respectively, whereas As concentrations are an order of magnitude higher (up to ~1800 ppm). Locations of FIB cuts for extraction of S/TEM foils are shown as white bars. (**b**) 3D schematic showing the location of the three foils (foils #1–3) relative to zoning and trails observed at depth (dashed black lines). Two domains (A and B) are defined relative to the sides of the grain in which domain A features bright bands (dashed white lines) hosting Cu-As NPs. Note the variable orientation of trails relative to the grain core.

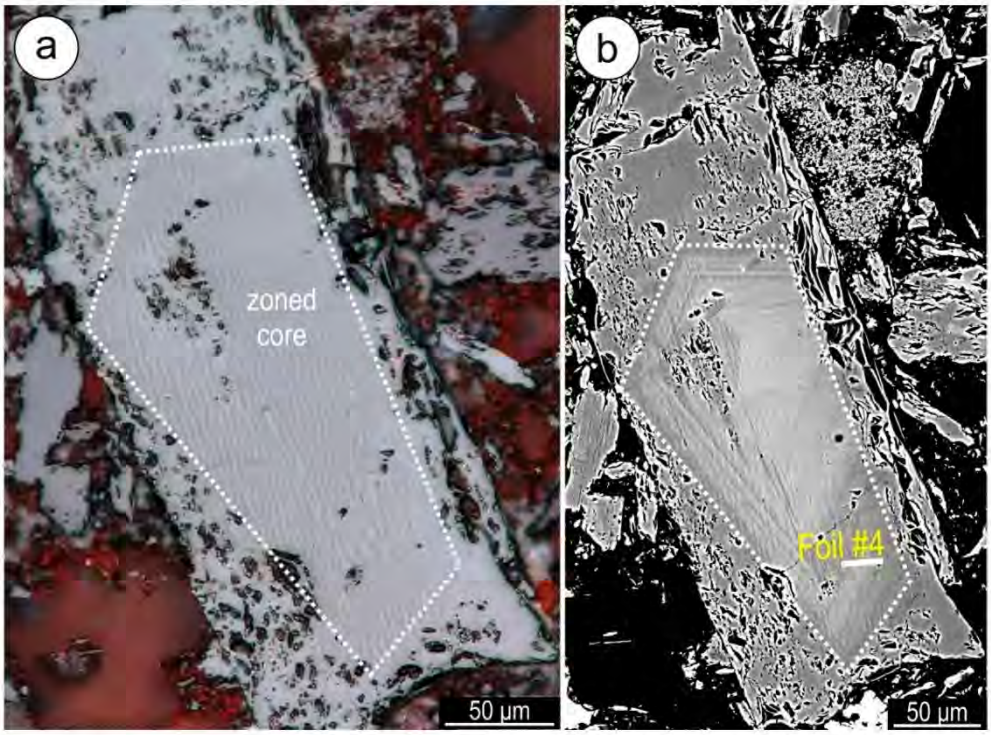

Figure 2. (**a**) Reflected light microphotograph of weave-twinned hematite (grain #2) and (**b**) back scattered electron image of the same grain showing oscillatory zonation patterns. Note the two textures overlap with one another within the grain core (dashed line). Location of extracted foil (Foil #4) is marked on (**b**). Obtained foil shown in Supplementary Material Figure S1.

3. Results

3.1. Nanoscale Characterisation of Cu-As Zoned and Weave-Twinned Hematite

HAADF STEM imaging of the three foils from the zoned Cu-As hematite shows oriented trails tens of microns in length consisting of darker inclusions and cavities (Figures 3 and 4). Domain A also displays brighter bands (up to ~300 nm in width and ~2–3 µm in length) with variable orientations relative to the trails (Figure 3a).

Orientation of trails is at ~50–60° relative to the surface in both domains, but subvertical trails are also observed in domain B (Figure 3c). This indicates that the banding with respect to Cu and As on the surface of the grain changes both inwards and outwards with depth relative to the grain core (Figure 1b). The trails are densely populated, but the distribution of inclusions and cavities is asymmetric (Figure 4). The smallest inclusions can form linear arrays along one side of the trail, whereas a diverse range of inclusions and cavities, from NPs (<50 nm) to fine particles >300 nm in size, occur on the other side, in some cases organised along linear splays (Figure 4b–d). The smallest inclusions are nanoparticles of Si-(Al-K)-Cl-bearing hematite (?), hereafter termed $NP_{Si\text{-}Hm}$ (Figure 5a–c). The coarsest cavities display relatively well-defined, geometrical, negative crystal outlines featuring walls towards rounded voids (Figure 5d,e). Such cavities are surrounded by $NP_{Si\text{-}Hm}$.

Mapping of the bright bands shows the presence of Cu-As NPs with acicular and hexagonal morphologies in the middle part of the bands (Figure 6a,b; Supplementary Material Figure S2). STEM EDX profiles across these NPs give a relatively steady Cu/As molar ratio of ~3.2–3.7 and indicate a distinct Si-K-Al geochemical signature on the margins of the NPs (Figure 6c). Such ratios are somewhat higher than stoichiometric domeykite (Cu_3As), possibly suggesting that these are composed of intergrowths between domeykite and another Cu-rich arsenide phase such as algodonite (Cu_6As; [32]).

STEM EDX maps of coarser cavities show detectable concentrations of Cu, As and occasionally, also Mo and W, as well as Cl, K, Si, Al, C, and minor Ca (Figures 7 and 8; Supplementary Material

Minerals **2019**, *9*, 388

Figures S3–S6). Both Cu and As show higher concentration (agglomerated Cu-As and native Cu NPs) particularly towards the outer margins of the voids (Figures 7 and 8b). The speciation of the NPs differs within the two domains, whereby the Cu-As NPs are found only in domain B, which lacks the bright bands.

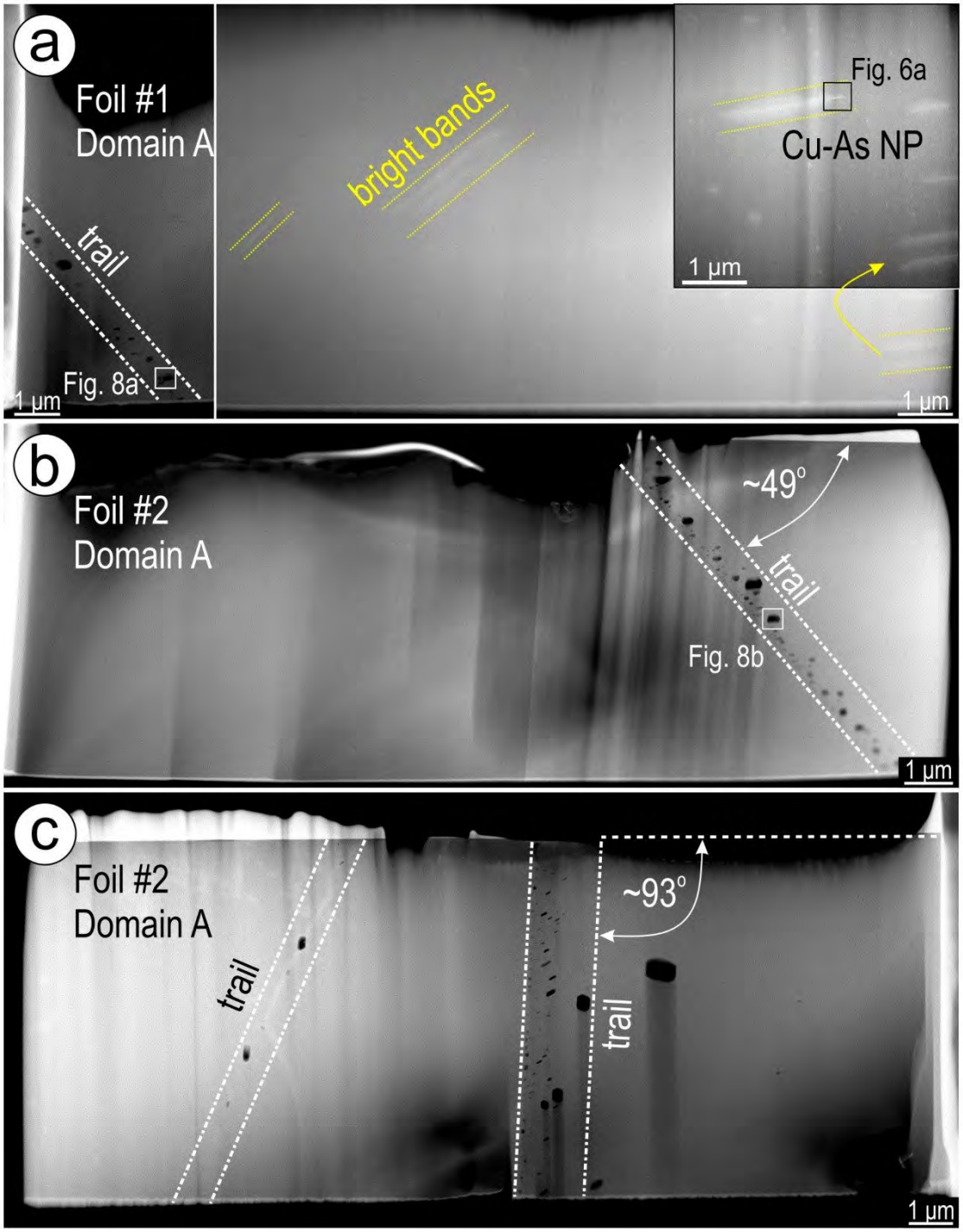

Figure 3. (**a**–**c**) HAADF STEM images of foils from grain 1 (foils #1–3) showing textures of Cu-As-zoned hematite. Trails of inclusions and cavities (white lines) with (sub)vertical orientation differ to (sub)horizontal, bright bands (yellow lines) observed in domain A. Inset in (**a**) shows one of the Cu-As NP along the "bright bands". Note that the foils are oriented from the core of the hematite grain (left) to its margin (right) in all cases for comparison with the schematic shown as Figure 1b.

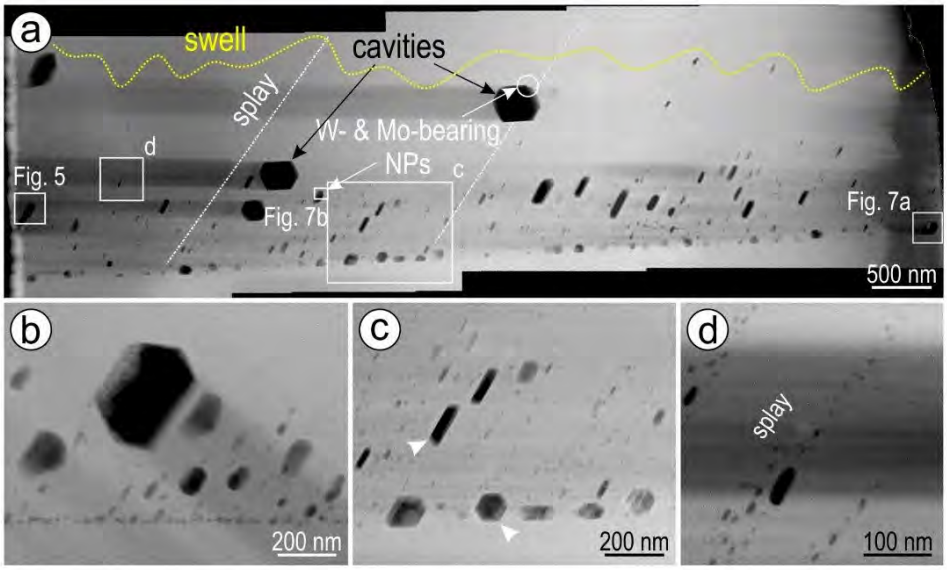

Figure 4. HAADF STEM images showing distribution of inclusions and cavities along trails in hematite. (**a**) Trail representative for the asymmetric distribution of inclusions and cavities (subvertical trail in Figure 3c rotated at 90°). Note that the coarsest inclusions are placed within swells (yellow line) on one side of the trail. (**b**) Variation across trail width (several hundred nm; foil #2) showing the finest inclusions (<20 nm) as a continuous array on one side expanding into coarsest cavities (~300–400 nm size) on the other side. Swarms of small inclusions are present throughout the area. (**c**) Detail of trail in (**a**) showing a mixture of inclusions and cavities along the array defining the trail on one side. Note hexagonal to tabular morphologies (arrowed) of cavity/inclusions but with swarms of NPs still present throughout the area. (**d**) Detail from (**a**) showing distribution of inclusions/cavities along diagonal splays propagating from one side of the trail.

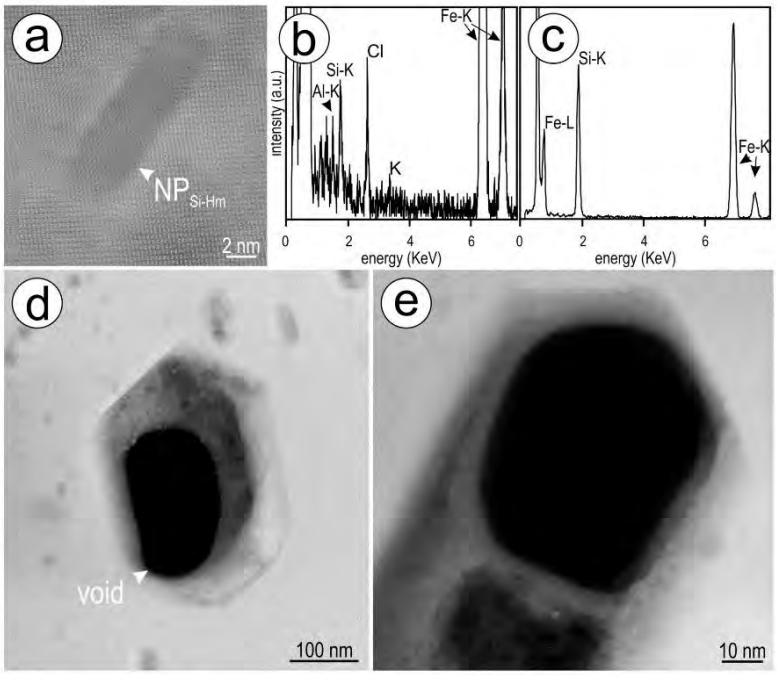

Figure 5. (**a**) HAADF STEM image of a NP interpreted as Si-bearing hematite ($NP_{Si\text{-}Hm}$). (**b**,**c**) Representative STEM EDX spectra showing composition of $NP_{Si\text{-}Hm}$. Note the presence of Si and Fe in both cases. Common to such NPs is the presence of Cl; note strong peak in (**b**). Minor Al, and trace K can occasionally be present. (**d**,**e**) HAADF STEM images showing cavities with negative crystal shapes with hexagonal outline showing rounded voids.

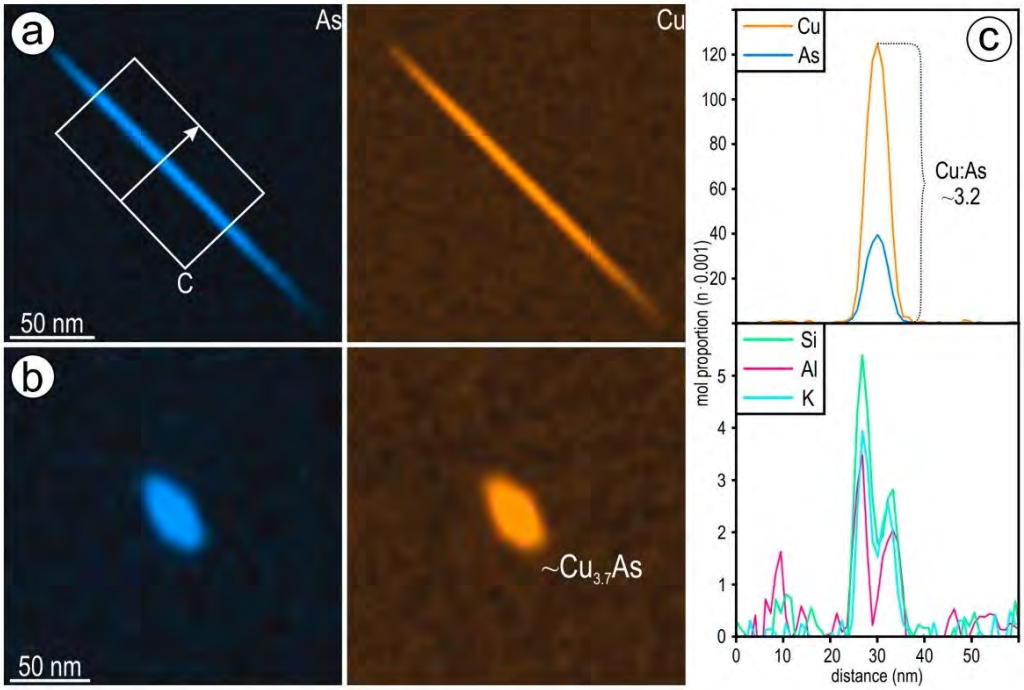

Figure 6. STEM EDX maps of Cu-As NPs hosted within bright bands (foil #1) with acicular (needle in (**a**)) and hexagonal (**b**) morphology. (**c**) Integrated, molar-profile across Cu-As-needle shown in (**a**). Note the positive correlation between Si, K and Al (sericite?) on the margins of the Cu-As NP. The profiles correspond to background-subtracted intensities to avoid interference from the copper grid.

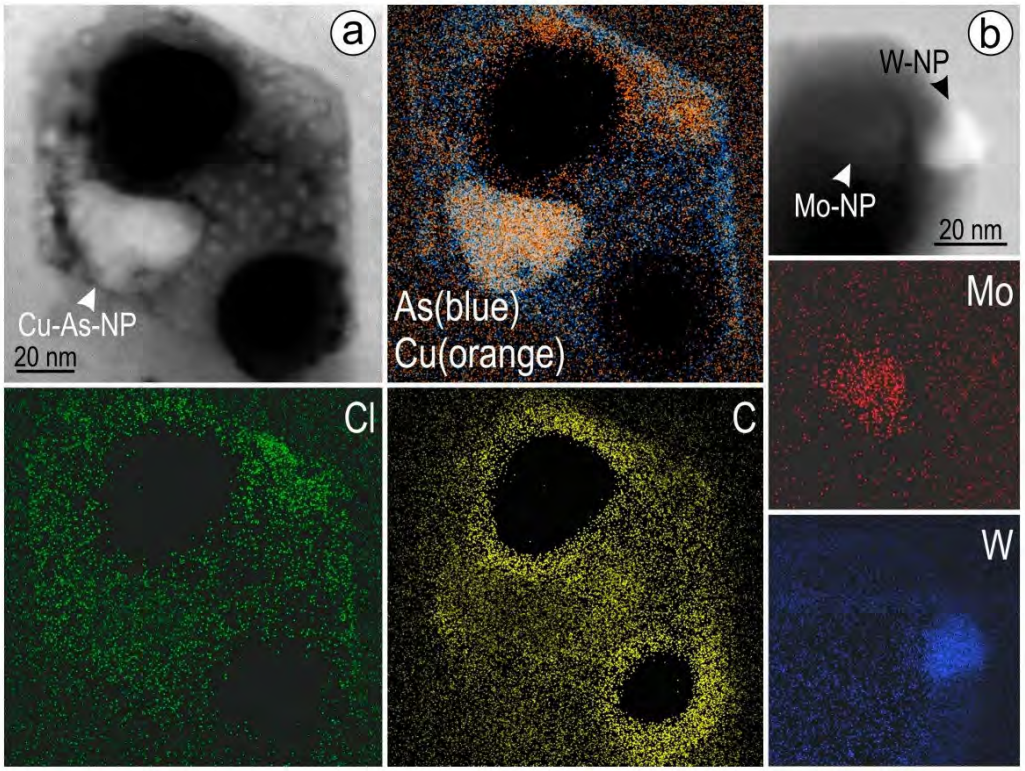

Figure 7. HAADF STEM image (upper left, right) and STEM EDX element maps (foil #3, domain B; extended maps are shown in Supplementary Material Figures S3 and S4) of (**a**) coarse negative crystal shaped cavity showing the presence of Cu, As, Cl and C, and (**b**) the presence of W and Mo NPs within the cavity. Copper and As are highest and overlap, indicating a Cu-As NP. The other elements are likely retained on the wall of the cavity. Note the rounded voids are empty.

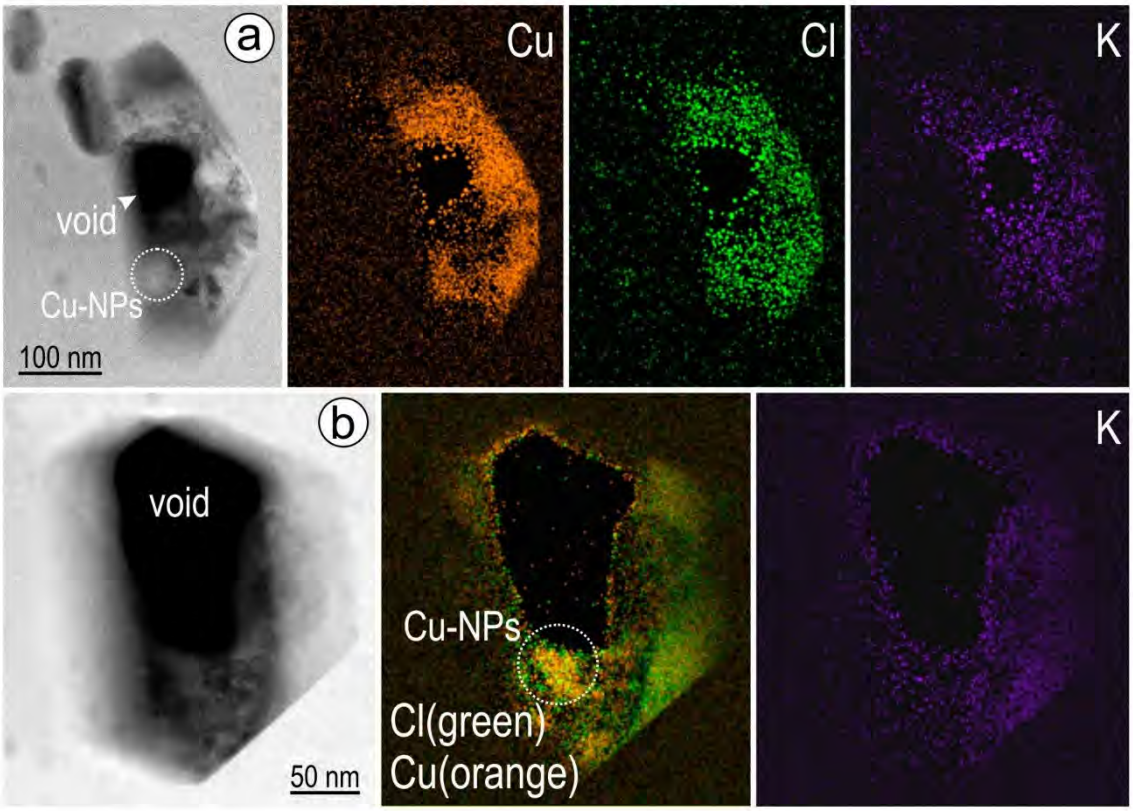

Figure 8. HAADF STEM images (left) and STEM EDX maps (extended maps in Supplementary Material Figures S4 and S5; foil #1–2 in (**a**,**b**), respectively) showing native Cu NPs within negative crystal shaped cavities from domain A. Note the presence of Cl and K within the cavities.

High-resolution imaging of one cluster of NPs from one of the cavities mapped in Figure 7a shows agglomeration of Cu NPs (Figure 9a). Nanoparticle morphology was observed to change under exposure to the beam. An atomic arrangement that can be indexed as the [100] zone axis of native copper is documented from one of the larger NP (Figure 9b). The substrate of the NPs contains measurable Si (spectrum in Figure 9c). Compositional information of the native copper NPs is also shown by the spectrum in Figure 9d, in which Fe is conspicuously absent.

The hematite foil obtained from grain 2 (foil #4) shows differences between the upper and the lower margin (Supplementary Material Figure S1). At the upper part, domains of variable widths display two crosscutting sets of 'lamellae' at an orientation of ~60° to one another (Figure 10a). In detail, the two sets also feature different morphologies, whereby the thinnest (no more than a few nm wide) are planes containing measurable concentrations of Si-Al-K and become host to platelets of sericitic mica (Figure 10b; see below), even though the contents of many of these have been lost during FIB milling. The second set of lamellae are twins crosscut and offset by the Si-Al-K-bearing planes. The planes themselves also show kink deformation between two twins (Figure 10c). In contrast to the Si-Al-K-planes, the twins can be as wide as ~150–200 nm but they narrow down towards edges with lanceolate terminations (Figure 10d). Sharp, rectangular domains of hematite close to the Si-Al-K-planes shows slight misorientation relative to enclosing hematite, indicating presence of glide planes (Figure 10e). Nucleation of sericite platelets can take place between such glide planes (Figure 10e). Imaging of hematite on the $[12\bar{1}]$ zone axis across simple twins show splits of main reflections along rows parallel to (021)* lattice vector on FFT image (inset Figure 10d). Groups of satellite reflections along the same directions mark conjugated pairs of twins, and Si-Al-K-planes (and/or sericite) on FFTs (inset, Figure 10c). Trails of inclusions and cavities resembling those in foils #1–3 are present in the lower part of the same foil (Figure 11a,b). These are seen to propagate into splays

leading to stubby, hexagonal-shaped platelets (Figure 11c,d). Although they appear empty (cf. BF and HAADF STEM images, Figure 11), they partially preserve areas with the same Si-Al-K-bearing element association as the inferred "sericite" platelets at the upper part of the foil.

STEM EDX mapping of two areas representative of upper and lower parts of the foil (Figures 12 and 13) show that they contain measurable concentrations of Si, Al, K, but the lower area differs in that it also shows Cl as a component of some of the K-bearing platelets (Figure 13). Additionally, the trails and splays feature the presence of Pb and Ti, respectively. Spotty concentrations of Cl and K also occur along the trails, whereas Si and Al appear homogeneously distributed. On the other hand, compositional heterogeneity is also observed in the upper part of the foil, between wider and thinner planes, whereby the latter contain only Al (Figure 12).

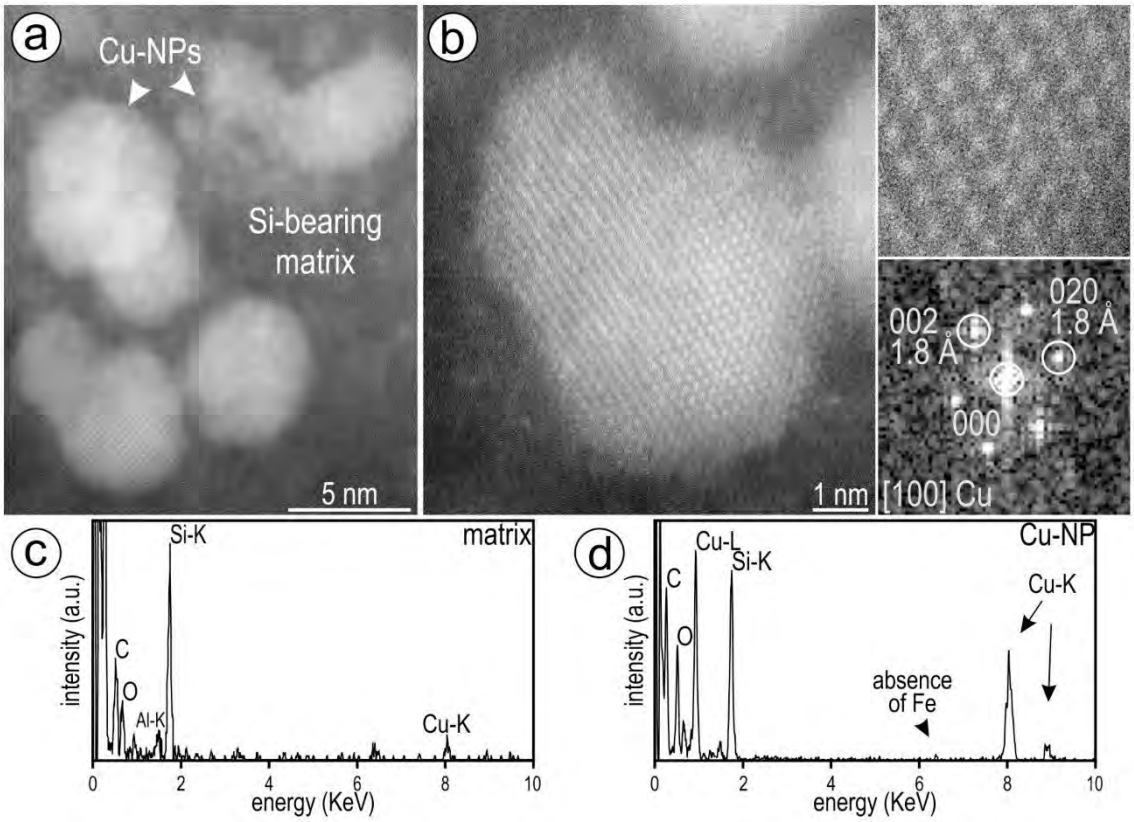

Figure 9. (**a**,**b**) Atomic-scale resolution images of native copper NPs. (**a**) Agglomeration of Cu NPs placed adjacent to the empty void in Figure 8a. (**b**) Distribution of Cu atoms in one of the NPs in (**a**) showing a square arrangement (cropped area upper right side) corresponding to zone axis [100] in native copper as indexed from FFT in the image bottom right. (**c**,**d**) STEM EDX spectra of substrate and Cu NPs. Note absence of Fe in both spectra. The carbon peaks on both spectra are partially due to the contamination in the chamber during prior high-resolution imaging.

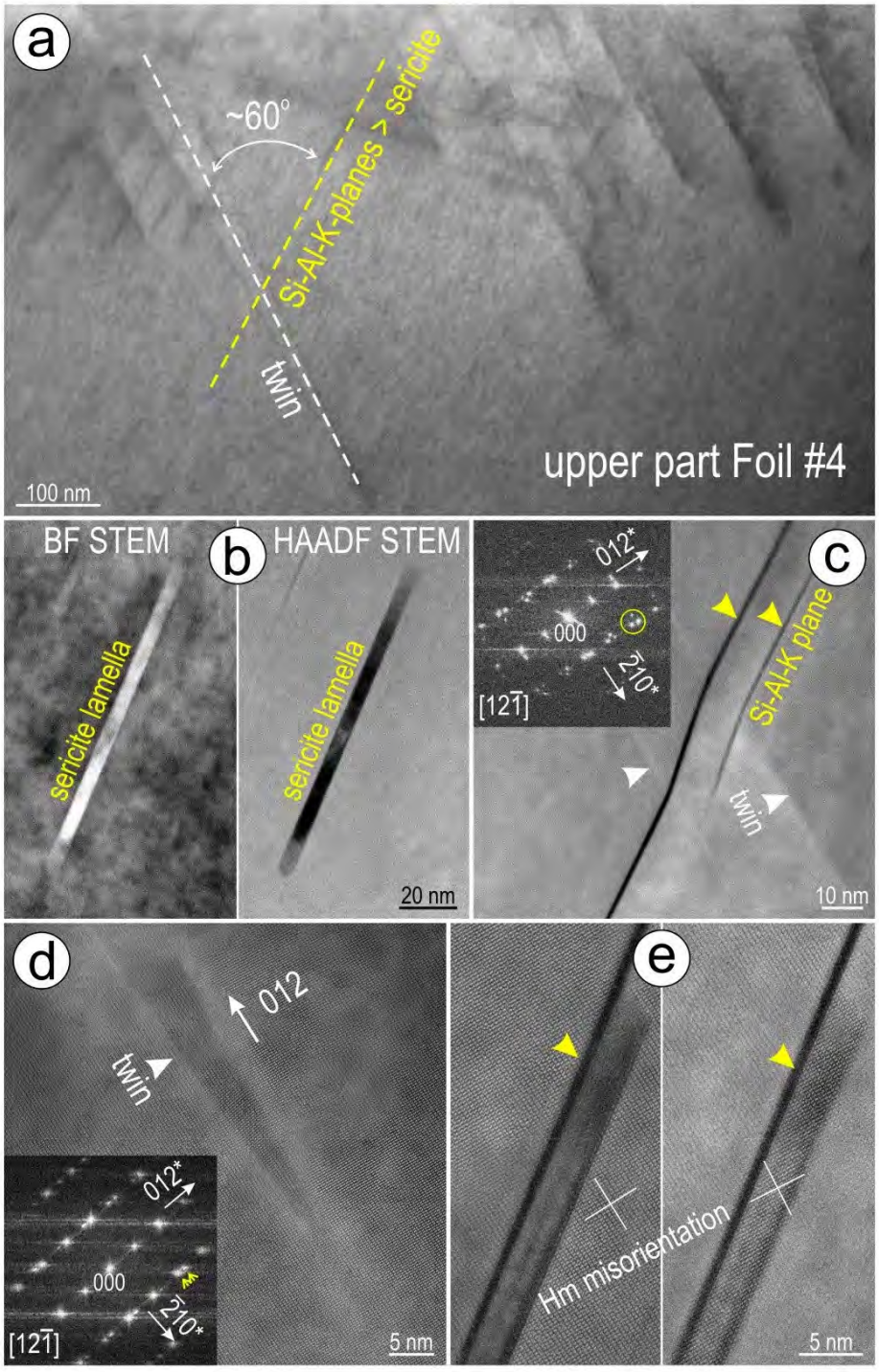

Figure 10. (**a**) HAADF (and bright field (BF) where marked) STEM images showing aspects of weaved-twin hematite at the upper part of foil #4. (**a**) Sets of twins and crosscutting Si-Al-K planes crosscutting at ~60°. (**b**) Platelets of sericite found in continuation of Si-Al-K planes. Comparison between BF and HAADF STEM images shows much of the filling is lost most likely plucked out during the FIB milling. (**c**) Conjugate sets of Si-Al-K planes (yellow arrows) crosscutting twins (white arrows) in hematite imaged on [12$\bar{1}$] zone axis. Such crosscutting relationships are marked by groups of satellite reflections (circled) along ($\bar{2}$10)* and parallel lattice vectors as shown on the FFT (inset). (**d**) Twinned hematite imaged on the [12$\bar{1}$] zone axis. The twin planes along (012) directions are marked by a split in reflections along the ($\bar{2}$10)* and parallel lattice vectors (FFT in inset). (**e**) Sliver of hematite adjacent to a Si-Al-K-plane (yellow arrow) imaged on the same [12$\bar{1}$] zone axis but with different focus to show the slight misorientation (white crosses) relative to the enclosing hematite.

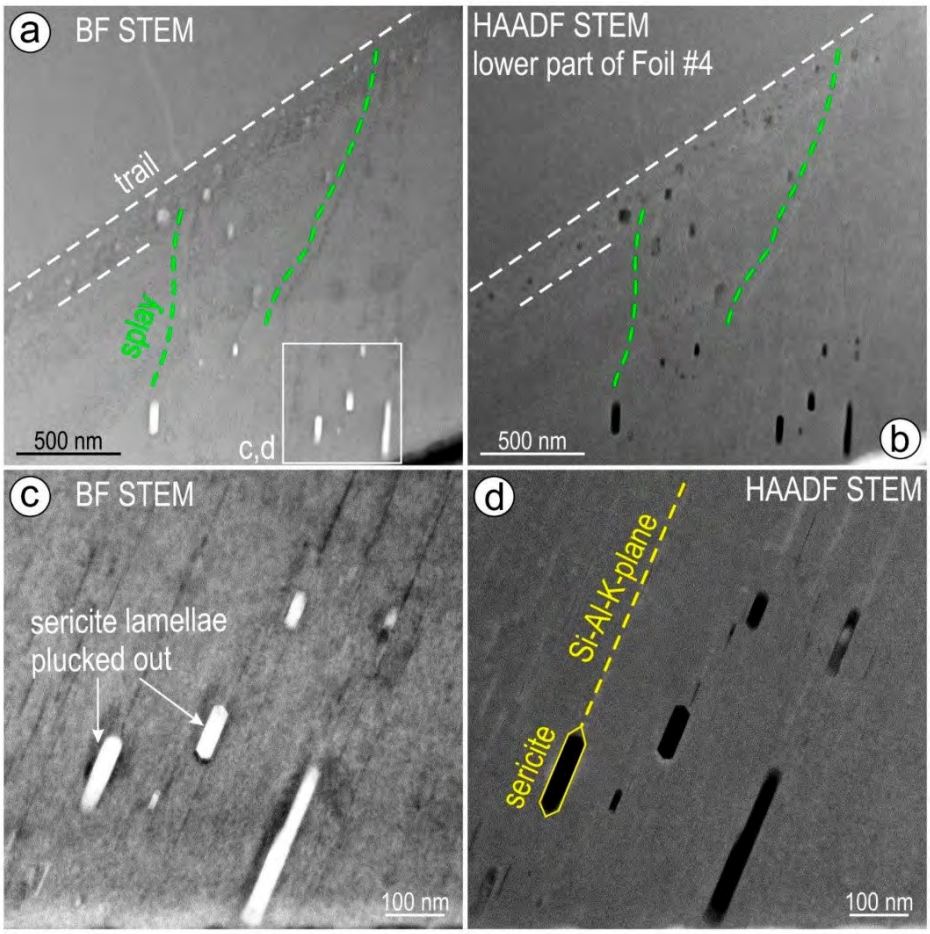

Figure 11. Images in BF and HAADF STEM modes as marked, showing aspects of hematite in the lower part of foil #4. (**a**,**b**) Trail of inclusions and cavities (white lines) with branching splays (green) towards fields of hexagonal platelets. (**c**,**d**) Detail of the platelets interpreted as sericite lamellae formed in continuation of Si-Al-K-planes.

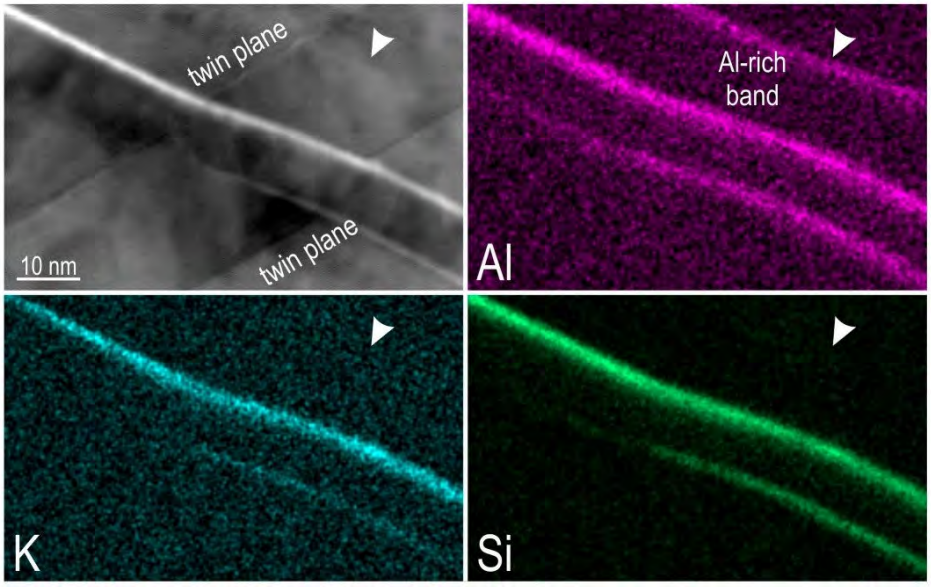

Figure 12. Bright field STEM image (top left) and STEM EDX maps of the Si-Al-K-bearing planes crosscutting twins at the upper part of foil #4. Note some of the planes are only depicted by Al (arrowed).

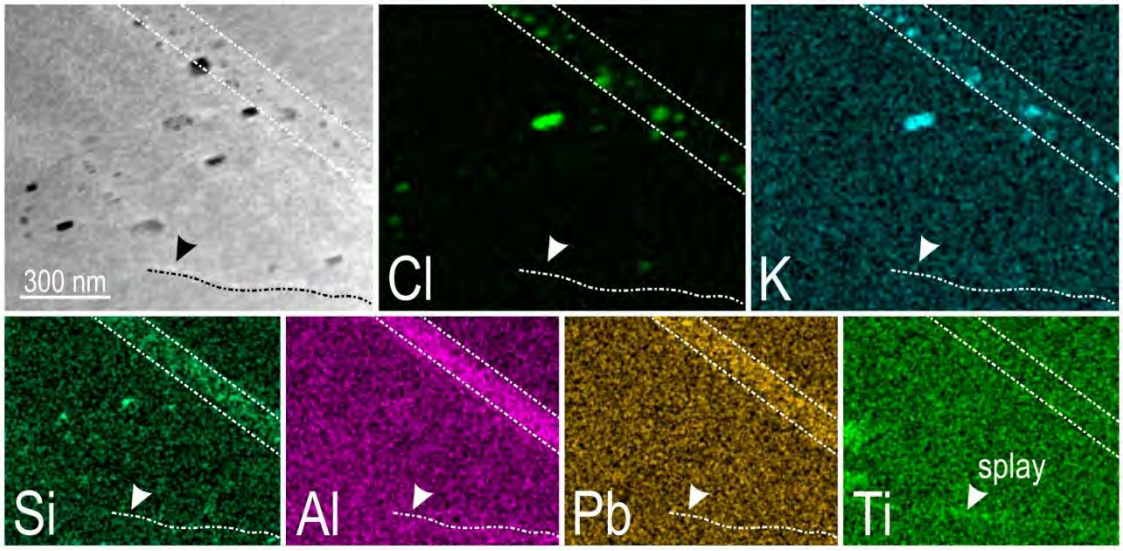

Figure 13. HAADF STEM image (left) and STEM EDX maps of the trail at the lower part of foil #4 (part of area shown in Figure 11). Note Cl and K show high concentrations either within the trail or along splays, whereas other elements, including Pb, are evenly distributed across the width of the trail. In contrast, Ti is present outside of the trail.

3.2. *High-Resolution HAADF STEM Imaging of Hematite*

Atomic scale imaging of hematite throughout all foils was undertaken on two zone axes, i.e., $[2\bar{2}1]$ for the Cu-As-zoned grain and $[12\bar{1}]$ for the weave-twinned grain. Interpretation of HAADF STEM images was based upon: (i) STEM simulation; and (ii) crystal models on the two respective axes obtained from the images (Figure 14). The bright spots on the images correspond to Fe atoms which show two distinct dumbbell patterns with good fit to the STEM simulations.

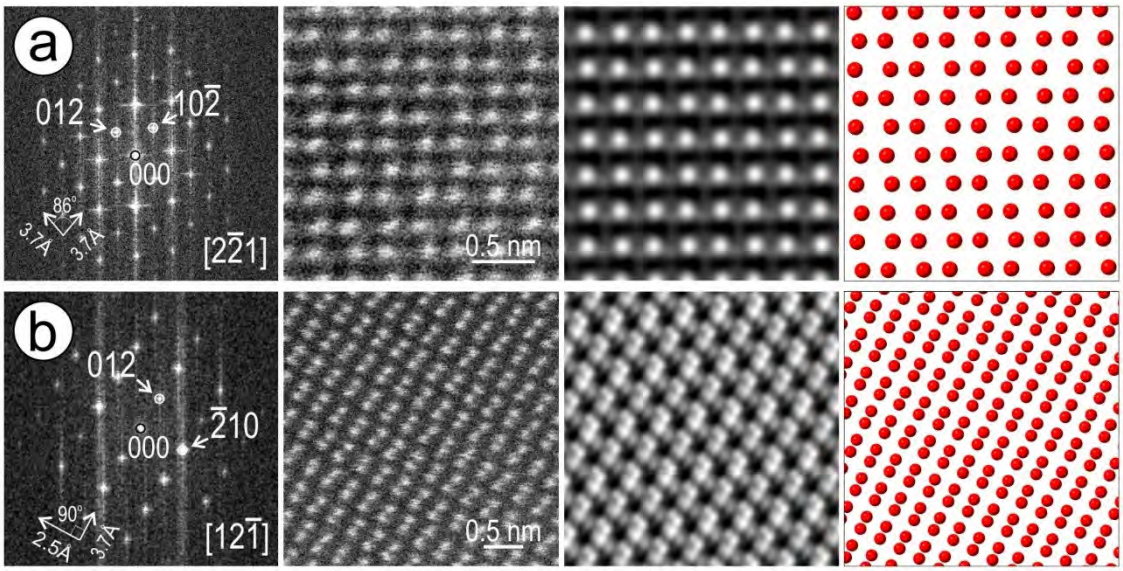

Figure 14. Assessment of atomic arrangements on HAADF STEM images obtained from hematite oriented on the two zone axes as marked. Each zone axis is represented by (**a**) and (**b**) rows, showing, from left to right: FFT, HAADF STEM image, STEM simulation and crystal structural model (space filling) of hematite. Red spheres represent Fe atoms. Indexing using crystallographic information data for hematite (a = 5.0355 Å, c = 13.7471 Å; space group $R\bar{3}c$; [33]).

In all cases, the hematite represents a single grain as it shows continuous orientation throughout the foil, except for areas surrounding the trails in foils #1–3. In the Cu-As-zoned hematite, the lattice is free of defects (Figure 15a). In contrast, hematite close to the larger cavities displays sets of twinned nanodomains with 120° rotation relative to one another on [001] zone axis (Figure 15b). Such nanodomains are evidence for local recrystallisation since these changes in orientation are observed against the surrounding hematite titled on the [2$\bar{2}$1] zone axis. Moreover, domains of lattice superstructuring are also present close to the walls of the cavities (Figure 15c). The micro-twins are shown by sets of satellite reflections on the [001] zone axis (Figure 15d). The two-fold superstructure is also shown as satellite reflections at 1/2 (012)* and 1/2 [$\bar{1}$02]* lattice vectors (Figure 15e). High-resolution imaging of weaved-twinned hematite shows lattice scale defects related to crosscutting relationships between the twins and the Si-Al-K-planes (Figure 16). The most common defects are displacements of twin boundaries at the junction with these planes. The magnitude of such displacements varies from one to several atom arrays with an increase of the Si-Al-K-plane width (Figure 16a,b).

More complex lattice scale defects are observed with respect to duplex planes crosscutting the twins (Figure 16c,d). In such cases, kink deformation is observed along the wider twin planes whereas nanodomains with misorientation surround the tips of the thinner Si-Al-K-planes. The twin planes also show linear defects at the crest of the twin propagating downwards into planar defects (Figure 16e).

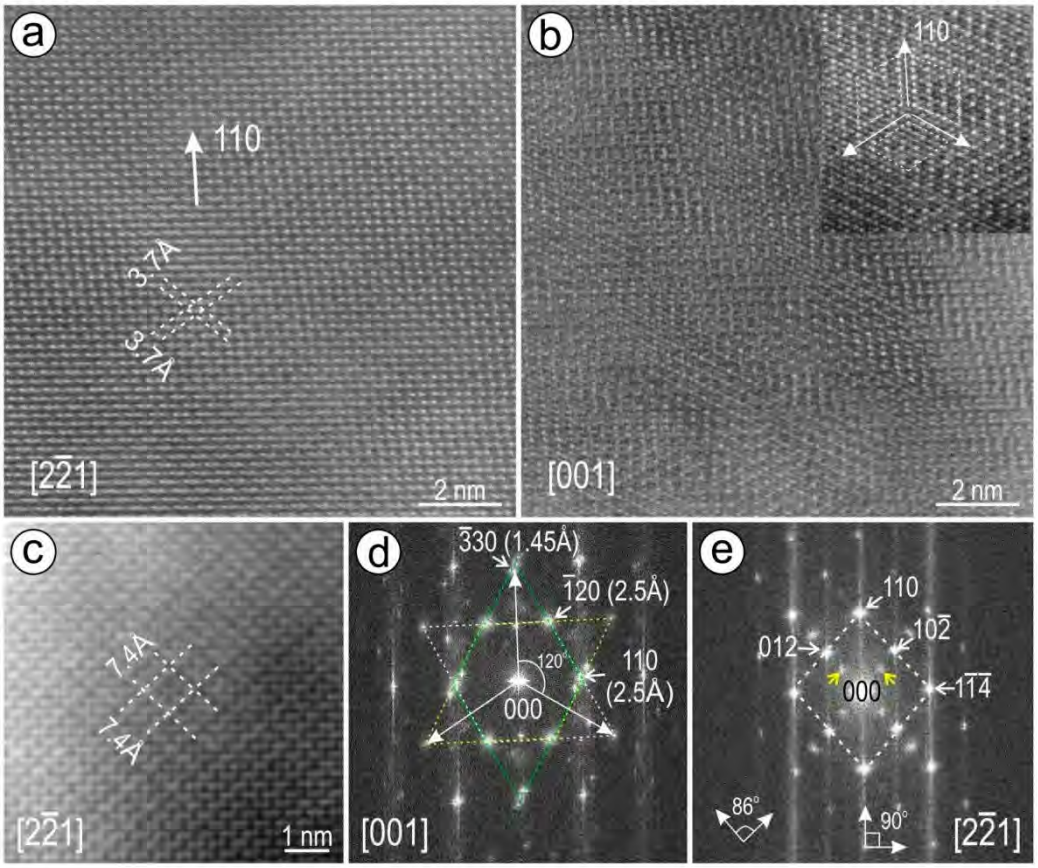

Figure 15. (**a**–**c**) High resolution HAADF STEM images of hematite on zone axes as marked. (**a**) Dumbbell atomic arrangement of Fe atoms on [2$\bar{2}$1] zone axis. (**b**,**c**) Nanoscale domains with twins and 2-fold superstructure in hematite from areas surrounding coarse inclusions/cavities adjacent to trails (foils #1–2). Note three sets of nanotwins on $[001]_{hematite}$ in (**b**) also highlighted by dashed lines in the inset. The double spacing of the superstructure relative to the simple structure of hematite on [2$\bar{2}$1] zone axis is marked by dashed lines in (**c**) and (**a**), respectively. (**d**) and (**e**) FFT patterns corresponding to images in (**b**) and (**c**). The three sets of twins are marked by different colours in (**d**), Satellite reflections at 1/2 (012) and (10$\bar{2}$) are marked by yellow arrows in (**e**).

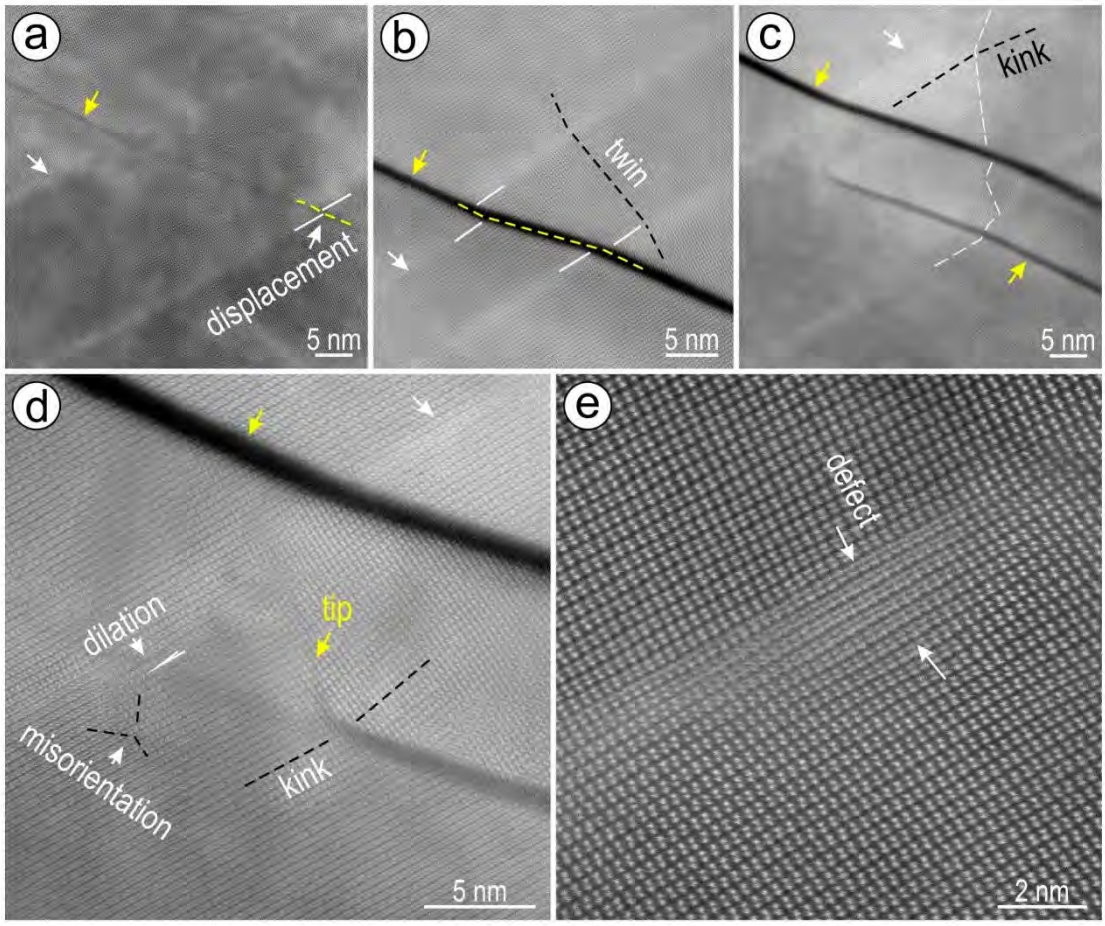

Figure 16. Atomic-scale resolution images showing lattice scale defects associated with crosscutting relationships between Si-Al-K-planes (yellow arrowheads) and twins (white arrowheads) in the weave-twinned hematite (foil #4). (**a**,**b**) Twin displacements (white bars) with increasing magnitude relative to increasing width of the planes. Note kink bends along the Si-Al-K-planes (dashed yellow lines). Single column atomic arrangement across the twin is marked by black dashed line following ($\bar{2}10$) direction. (**c**,**d**) More complex defects in areas with duplex Si-Al-K-planes crosscutting a twin. (**c**) Kink deformation (white dashed line) along the direction of the twin (dashed black line). (**d**) Detail around the tip of Si-Al-K-plane in (**c**) showing nanodomain misorientation, lattice dilation and kink bends as marked. (**e**) Linear defect at the twin plane crest propagating into a planar defect (arrowed).

4. Discussion and Summary

4.1. Can Fluid Inclusions be Fingerprinted at the Nanoscale?

The observations presented here show that cavities with negative crystal shapes (Figure 5c,d) have a topography which is chemically traceable from K, Cl, and C-bearing surfaces (Figures 7 and 8). These elements are commonly associated with fluids trapped as fluid inclusions within a host mineral [34]. If so, the rounded voids/holes within the negative crystal shaped cavities are attributable to vapour bubbles, whereas the Cu-(As) NPs imaged on the walls of the same cavities (Figures 7 and 8) correspond to solid phase components of the inclusions. The geometrical morphologies displayed by the coarser cavities can be related to the maturation of fluid inclusions during processes of re-equilibration, as has been proved experimentally ([35] and references therein).

Although fluid inclusion studies are often undertaken to track the fluid evolution of hydrothermal ore deposits, these are generally carried out on transparent rather than (semi)opaque host minerals such as hematite. Fluid inclusions in iron-oxides have nonetheless been addressed in several studies, for example from hematite from banded iron ores and crosscutting Au-Pd-Pt-quartz veins

from Quadrilátero Ferrífero, Brazil [36,37]. In both cases, two- and three-phase fluid inclusions were documented, some of which display comparable hexagonal shapes as those reported here. The Quadrilátero Ferrífero hematite in the veins also contains measurable concentrations of Na, K, CO_2 and SO_4; the solid phases, however, could not be identified [37].

The cavities imaged and mapped in the present study can therefore be interpreted as relicts of fluid inclusions forming along trails in hematite that have been opened during foil cutting and milling. The mapped concentrations of K and Cl (Figures 7 and 8) would represent a fingerprint of the fluid ± clathrate phases, such as sylvite (KCl). Similarly, the measured C may be correlated with a CO_2-bearing vapour phase partially released during foil preparation. In addition, the metals (Cu, Mo, W) and As trapped as NPs within fluid inclusions (Figures 7 and 8) represent components of a 3-phase (liquid-vapour-solid) system. Copper NPs are present in domain A which preserves Cu-As NPs along bands (Figure 6) outside of those trails containing fluid inclusions, whereas Cu-As NPs are present within the fluid inclusions occurring along trails from domain B. The presence of Cl is also detected within the smaller NPs (Figure 5a,b) as well as in the inclusions along splays from the weave-twinned hematite (Figure 13). The lack of detectable Na is possibly an intrinsic feature of the fluids preserved within the hematite but might equally be due to analytical conditions during sample preparation (lost by volatilization?).

4.2. Trace Element Mobilisation during Fluid-Mineral Interaction: Trapping Metal Nanoparticles

The formation of metal NPs of two distinct types, associated with trails of fluid inclusions and along Cu-As-bearing bands mapped with continuous appearance at the micron-scale (Figure 1) can be discussed in the context of fluid-mineral interaction during events that allow for, and facilitate changes in fluid chemistry and rates of fluid influx (Figure 17). Assuming that weave-twinned hematite represents the precursor mineral at the initial stage for the formation of metal NPs, the twin planes provide zones of weakness allowing percolation of Si-Al-K-bearing fluids (Figure 17a). If so, chemical disequilibrium between such a fluid and the host hematite facilitates reactions that result in precipitation of nm-wide Si-Al-K-phases and sericite lamellae placed discontinuously along the Si-Al-K-planes of fluid percolation (Figure 17b). We can assume that the infiltration takes place along a conjugate set of twins in hematite with 60° rotation relative to the twins observed and that these twins were obliterated in the course of reaction. Alternatively, fluid flow has a preferential direction relative to the grain orientation and infiltration is driven along parting planes in hematite rather than along pre-existing twins. Either way, the fact that a Si-Al-K-fluid interacts with pre-existing hematite is proven by the lattice defects (shown in Figure 16) and in mapping of these planes and sericite platelets in hematite (Figure 12). Formation of sericite is entirely consistent with the hydrolytic alteration observed at Olympic Dam [23] and in IOCG systems elsewhere ([38] and references therein).

A second stage in this model (Figure 17c,d) starts with metal-bearing brines percolating the same assemblage. Two different fluid rates can be inferred at this stage: (i) steady-state percolation along the Si-Al-K-planes; and (ii) erratic fluid focussing associated with strong pressure fluctuation. In case (i), a metal-bearing brine replaces pre-existing Si-Al-K-bearing bands leading to formation of Cu-As NPs (Figure 17c). The bands nevertheless preserve the initial signature along the margins (Figure 6; Supplementary Material Figure S2). In case (ii), fluid-focussing of this brine along the affected Cu-As-bearing bands initiates replacement fronts that couple dissolution with reprecipitation rates, a process leading to transient porosity along the reaction front (Figure 17d). Such pores can trap products formed during CDRR, and in this case, we suggest they could pool fluids, evolving into fluid inclusions. The misorientation of nanodomains and -twins in hematite are evidence that this is a newly formed hematite that precipitated in areas immediately surrounding the fluid inclusions (Figure 15). The latter are hosted within swells (Figure 17d) located on one side of the trail and linked to one another by splays to the smallest inclusions of $NP_{Si\text{-}Hm}$, an observation suggestive of abrupt pressure fluctuation as considered for fault-valve mechanisms in orogenic Au deposits (e.g., [39]). Formation of

metal-dominant NPs within three-phase fluid inclusions (Figure 17e) can be considered in the context of fault-valve depressurisation leading to phase separation and metal precipitation from the brines.

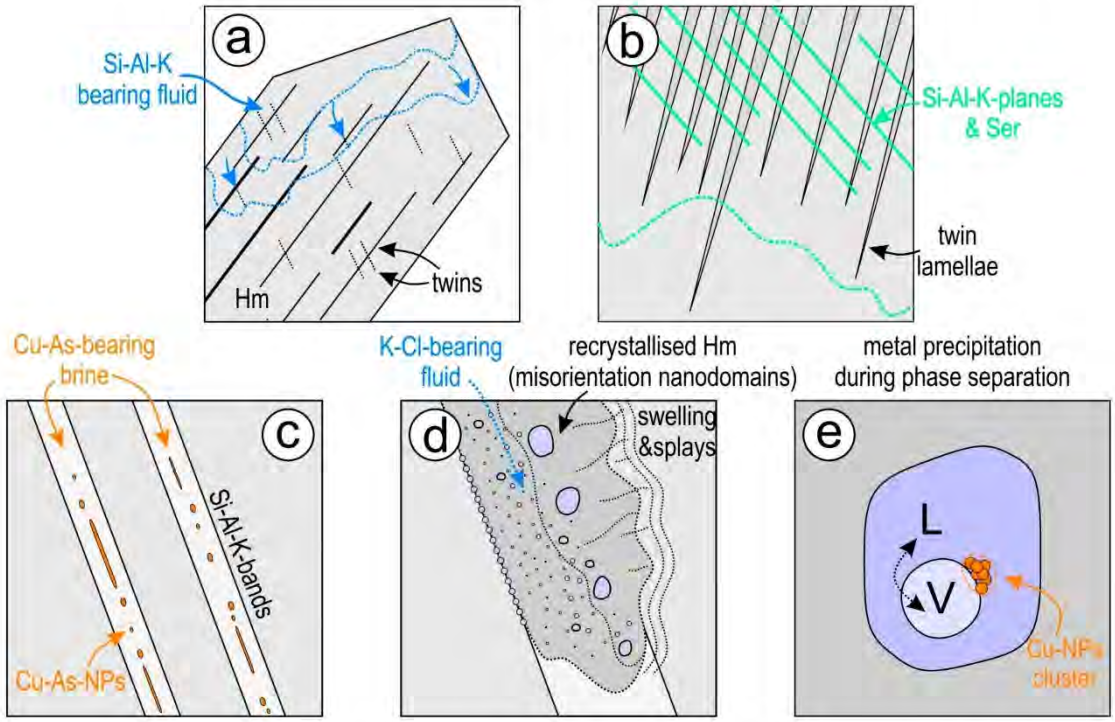

Figure 17. Schematic showing formation of metal NPs along fluid inclusion trails in hematite during fluid-mineral interaction. (**a**) Plan view of weave-twinned hematite interacting with incoming Si-Al-K-bearing fluids typical of hydrolytic alteration in IOCG systems. (**b**) Cross-section of a reacted domain within hematite in which the channels of fluid percolation led to nm-wide Si-Al-K-planes that become coarser bands and/or sericite platelets. Various defects occur in hematite at the junction between the twins and fluid channels. (**c**,**d**) The fluid compositionally evolves into a Cl- and metal-bearing brine that interacts with the pre-existing Si-Al-K planes and sericite. Initially, rates of fluid percolation are slow, and the reaction leads to formation of Cu-As NPs with variable Cu/As ratios, whereas some of the Si-Al-K-filling of the planes is removed (**c**). Rapid and/or erratic fluid flow driven by fault-valve mechanisms produce fronts of reaction via CDRR along preferential sets of Cu-As-enriched and Si-Al-K-depleted bands (**d**). This leads to formation of complex trails with smallest Si-hematite NPs on one side and coarsest fluid inclusions within swells on the other side of the trail. The reacted area along the trails is filled with nanoprecipitates of hematite (dark grey) recognised by nanodomains with 2-fold superstructures, twins and misorientation. Fluid inclusions are trapped within transient pores produced during CDRR development. (**e**) Metal-bearing NPs (Cu-, Cu-As-, Mo-, and W-bearing NPs) are precipitated within the fluid inclusions during fluid-vapour phase separation. The latter is induced by sudden depressurization during fault-valve fluid pumping.

Formation of fluid inclusion-hosted NPs, close to the interface between the vapour bubble and fluid is attributable to a decrease in metal solubility in the fluid at the stage of phase separation. The suggested mechanism involving pressure fluctuation leading to metal discharge is comparable with devolatilization during hydrofracturing as considered for pore-attached Au-telluride NPs occurring within As-free pyrite [8]. Two metal source(s) are possible for the observed NPs: (i) Cu, As, Mo, W and Pb are remobilised from the hematite itself during superimposed CDRR processes, the primary hematite being oscillatory zoned with respect to U-(Pb)-W-Sn-Mo, as well as with Cu and As in this case [27]; and (ii) Cu and As are sourced from pre-existing Cu-(Fe)-sulphides from the enclosing hematite breccia, a scenario considered feasible in the context of the sulphide-poor interval from which the sample originates.

The fault-valve mechanism invoked for phase separation can be attributed to fault (re)activation. This is possible considering the presence of steeply dipping faults, with ~1 km vertical drop, along which the breccia formed [23].

In summary, the two hematite grains, although apparently unrelated at the micron-scale, have common geochemical signatures, and also display nanoscale aspects that allows interpretation of a shared genetic history. The Cu-As-bands exposed on the surface of analysed hematite (grain #1) extend as inclusion trails with two opposite directions at depth, with the same grain featuring sub-horizontal Cu-As-rich bands (Figures 1 and 3). This indicates that such grains represent the equivalent of the weave-twinned hematite studied from grain #2 (Figure 2) but differ in having undergone more intense interaction with fluids. The textural and compositional variation between inclusions trails and Cu-As-bands throughout the same foil indicates that fluid flow was focussed along preferential directions within the volume of the same grain. The type of weave-twinned hematite studied from grain #2 is less affected by interaction with fluids and preserves characteristics intrinsic to its primary crystallisation. At this stage, it is unclear whether the twinning patterns represent characteristics inherited from the rock protolith, e.g., hematite replacing a pre-existing feldspar as is reported for hematite from Olympic Dam [40]. Alternatively, such weave-twin patterns may occur in hematite within breccias containing rock-flour milling produced during fault (re)activation. At Olympic Dam, several breccia types are polymict and contain volcanic clasts. The Si-hematite NPs found here within the reacted hematite requires further study, as this feature is likely more widespread in ores of various types and would represent a key texture for recognition of overprinting events. For example, Si-bearing hematite (up to 1.51 wt. % SiO_2) has been documented from hematite grains with oscillatory zoning at the micron scale in banded ion formation ores (Middleback Ranges, South Australia; [41]).

5. Implications

The results presented here attest to the importance of CDRR and the generation of transient porosity in the formation of NPs associated with fluid inclusions, and how these impact on observed trace element signatures measured at the micron-scale (e.g., by LA-ICP-MS). If characterized at appropriate scales of observation, such features represent evidence for open system behaviour in hematite and other minerals, with broad applicability to a range of geochemical systems.

Demonstration of open system behaviour at the nanoscale carries implications for the decoupling and mobilization of daughter radionuclides from their parent isotopes (e.g., [42,43]. In turn, such pseudo-fractionation would cause a modification of isotope systematics affecting accurate interpretations of U-Pb microbeam-dating of hematite [24,44], or other minerals. This is particularly valid whenever the replacement process is highly selective and allows primary zonation patterns to be at least partially preserved [27].

This study further highlights the advantages of HAADF STEM imaging as a valuable technique to understand and correctly interpret trace element compositional data. The presence of Cu within hematite at Olympic Dam represents additional evidence for the simultaneous introduction of Fe, Cu, and U.

Supplementary Materials: Supporting figures (Figures S1–S7) are available at http://www.mdpi.com/2075-163X/9/7/388/s1. Figure S1. Low-magnification HAADF STEM image of the foil (foil #4) from the weave-twinned hematite showing areas of interest. Ser-sericite; Hm-hematite. Figure S2. HAADF STEM and STEM EDX maps of Cu-As NP with acicular morphology hosted within bright band (foil #1). Note the presence of Si, K and Al surrounding the margins of the needle and/or proximal to it. Ser-sericite. Figure S3. HAADF STEM and STEM-EDX maps of hexagonal cavity in Foil #3 (domain B) featuring the presence of voids and a Cu-As NP. Though F-Kα partially overlaps with Fe-Lα in the lower energy spectrum, note that enrichment of F is observed within the cavity, rather than outside, in the host hematite. Figure S4. HAADF STEM and STEM-EDX maps of cavity hosting W- and Mo-bearing NPs (foil #3, domain B). Although the EDX peak position of Mo-Lα partially overlaps with that of Pb-Mα, the presence of characteristic Mo-Kα peaks is observed in the higher energy interval of the spectrum. Figure S5. HAADF STEM and STEM-EDX maps of large cavity in foil #1 displaying the presence of a void and strong enrichment in Cu correlating with Cl. Native copper NPs are observed proximal to the void. Figure S6. HAADF STEM and STEM-EDX maps of cavity in foil #2 (domain A) displaying the presence of a void and compositional heterogeneity within the inclusion (compare distributions of Ca versus Si and Al).

Figure S7. Representative STEM EDX spectra for observed NPs within cavities or directly hosted by hematite. The spectra are scaled individually to emphasise features of interest; typical hematite spectrum is shown (top left) for comparison. Note the relative differences between the Fe-K and Cu-K intensities in hematite host relative to the Cu-As-bearing NP.

Author Contributions: M.R.V.-I. and C.L.C. conceived this contribution and conducted all analytical work, assisted by A.S. (HAADF STEM imaging). K.E. provided sample material and guidance. The manuscript was written by M.R.V.-I., C.L.C. and N.J.C., with contributions from K.E., L.C.-D. and A.S.

Funding: This research is a contribution to the FOX project "Trace elements in iron-oxides: deportment, distribution and application in ore genesis, geochronology, exploration and mineral processing", supported by BHP Olympic Dam and the South Australian Government Mining and Petroleum Services Centre of Excellence. N.J.C. acknowledges support from the ARC Research Hub for Australian Copper-Uranium (Grant IH130200033).

Acknowledgments: We extend thanks to the staff of Adelaide Microscopy, particularly Sarah Gilbert and Benjamin Wade, who have assisted the FOX project in various ways. We kindly thank four anonymous reviewers for their positive feedback and constructive comments that helped us improve this manuscript.

Conflicts of Interest: The authors declare no conflicts of interest.

References

1. Reich, M.; Hough, R.M.; Deditius, A.; Utsunomiya, S.; Ciobanu, C.L.; Cook, N.J. Nanogeoscience in ore systems research: Principles, methods, and applications. *Ore Geol. Rev.* **2011**, *42*, 1–5. [CrossRef]
2. Palenik, C.S.; Utsunomiya, S.; Reich, M.; Kesler, S.E.; Wang, L.; Ewing, R.C. "Invisible" gold revealed: Direct imaging of gold nanoparticles in a Carlin-type deposit. *Am. Mineral.* **2004**, *89*, 1359–1366. [CrossRef]
3. Reich, M.; Kesler, S.E.; Utsunomiya, S.; Palenik, C.S.; Chryssoulis, S.L.; Ewing, R.C. Solubility of gold in arsenian pyrite. *Geochim. Cosmochim. Acta* **2005**, *69*, 2781–2796. [CrossRef]
4. Hannington, M.; Garbe-Schönberg, D. Detection of gold nanoparticles in hydrothermal fluids. *Econ. Geol.* **2019**, *114*, 397–400. [CrossRef]
5. Wirth, R.; Reid, D.; Schreiber, A. Nanometer-sized platinum-group minerals (PGM) in base metal sulfides: New evidence for an orthomagmatic origin of the Merensky Reef PGE ore deposit, Bushveld Complex, South Africa. *Can. Mineral.* **2013**, *51*, 143–155. [CrossRef]
6. Junge, M.; Wirth, R.; Oberthür, T.; Melcher, F.; Schreiber, A. Mineralogical siting of platinum-group elements in pentlandite from the Bushveld Complex, South Africa. *Miner. Depos.* **2015**, *50*, 41–54. [CrossRef]
7. Baurier-Aymat, S.; Jiménez-Franco, A.; Roqué-Rosell, J.; González-Jiménez, J.M.; Gervilla, F.; Proenza, J.A.; Mendoza, J.; Nieto, F. Nanoscale Structure of Zoned Laurites from the Ojén Ultramafic Massif, Southern Spain. *Minerals* **2019**, *9*, 288. [CrossRef]
8. Ciobanu, C.L.; Cook, N.J.; Utsunomiya, S.; Kogagwa, M.; Green, L.; Gilbert, S.; Wade, B. Gold-telluride nanoparticles revealed in arsenic-free pyrite. *Am. Mineral.* **2012**, *97*, 1515–1518. [CrossRef]
9. Owen, N.D.; Ciobanu, C.L.; Cook, N.J.; Slattery, A.; Basak, A. Nanoscale Study of Clausthalite-Bearing Symplectites in Cu-Au-(U) Ores: Implications for Ore Genesis. *Minerals* **2018**, *8*, 28. [CrossRef]
10. Tooth, B.; Ciobanu, C.L.; Green, L.; O'Neill, B.; Brugger, J. Bi-melt formation and gold scavenging from hydrothermal fluids: An experimental study. *Geochim. Cosmochim. Acta* **2011**, *75*, 5423–5443. [CrossRef]
11. Putnis, C.V.; Tsukamoto, K.; Nishimura, Y. Direct observations of pseudomorphism: Compositional and textural evolution at a fluid-solid interface. *Am. Mineral.* **2005**, *90*, 1909–1912. [CrossRef]
12. Xu, H.; Shen, Z.; Konishi, H. Si-magnetite nano-precipitates in silician magnetite from banded iron formation: Z-contrast imaging and ab initio study. *Am. Mineral.* **2014**, *99*, 2196–2202. [CrossRef]
13. Deditius, A.P.; Reich, M.; Simon, A.C.; Suvorova, A.; Knipping, J.; Roberts, M.P.; Rubanov, S.; Dodd, A.; Saunders, M. Nanogeochemistry of hydrothermal magnetite. *Contrib. Mineral. Petrol.* **2018**, *173*, 46. [CrossRef]
14. Ciobanu, C.L.; Verdugo-Ihl, M.R.; Slattery, A.; Cook, N.J.; Ehrig, K.; Courtney-Davies, L.; Wade, B.P. Silician Magnetite: Si–Fe-Nanoprecipitates and Other Mineral Inclusions in Magnetite from the Olympic Dam Deposit, South Australia. *Minerals* **2019**, *9*, 311. [CrossRef]
15. Cook, N.J.; Ciobanu, C.L.; Ehrig, K.; Slattery, A.; Verdugo-Ihl, M.R.; Courtney-Davies, L.; Gao, W. Advances and Opportunities in Ore Mineralogy. *Minerals* **2017**, *7*, 233. [CrossRef]

16. Ciobanu, C.L.; Cook, N.J.; Utsunomiya, S.; Pring, A.; Green, L. Focussed ion beam–transmission electron microscopy applications in ore mineralogy: Bridging micro- and nanoscale observations. *Ore Geol. Rev.* **2011**, *42*, 6–31. [CrossRef]
17. Ciobanu, C.; Cook, N.; Maunders, C.; Wade, B.; Ehrig, K. Focused Ion Beam and Advanced Electron Microscopy for Minerals: Insights and Outlook from Bismuth Sulphosalts. *Minerals* **2016**, *6*, 112. [CrossRef]
18. Cook, N.; Ciobanu, C.; George, L.; Zhu, Z.-Y.; Wade, B.; Ehrig, K. Trace Element Analysis of Minerals in Magmatic-Hydrothermal Ores by Laser Ablation Inductively-Coupled Plasma Mass Spectrometry: Approaches and Opportunities. *Minerals* **2016**, *6*, 111. [CrossRef]
19. Keyser, W.; Ciobanu, C.L.; Cook, N.J.; Feltus, H.; Johnson, G.; Slattery, A.; Wade, B.P.; Ehrig, K. Mineralogy of Zirconium in Iron-Oxides: A Micron- to Nanoscale Study of Hematite Ore from Peculiar Knob, South Australia. *Minerals* **2019**, *9*, 244. [CrossRef]
20. Xu, J.; Ciobanu, C.L.; Cook, N.J.; Slattery, A. Crystals from the scheelite-powellite solid-solution series at the nanoscale: The Zhibula Cu skarn, Gangdese Belt, Tibet. *Minerals* **2019**, *9*, 340. [CrossRef]
21. Courtney-Davies, L.; Ciobanu, C.L.; Verdugo-Ihl, M.R.; Slattery, A.; Cook, N.J.; Dmitrijeva, M.; Keyser, W.; Wade, B.P.; Dominick, U.I.; Ehrig, K.; et al. Zircon at the nanoscale records metasomatic processes leading to large magmatic-hydrothermal ore deposits. *Minerals* **2019**, *9*, 364. [CrossRef]
22. Viti, C.; Frezzotti, M.-L. Transmission electron microscopy applied to fluid inclusion investigations. *Lithos* **2001**, *55*, 125–138. [CrossRef]
23. Ehrig, K.; McPhie, J.; Kamenetsky, V. Geology and Mineralogical Zonation of the Olympic Dam Iron Oxide Cu-U-Au-Ag Deposit, South Australia. In *Geology and Genesis of Major Copper Deposits and Districts of the World: A Tribute to Richard H. Sillitoe, Special Publication 16*; Hedenquist, J.W., Harris, M., Camus, F., Eds.; Society of Economic Geologists: Littleton, CO, USA, 2012; pp. 237–267.
24. Ciobanu, C.L.; Wade, B.P.; Cook, N.J.; Schmidt Mumm, A.; Giles, D. Uranium-bearing hematite from the Olympic Dam Cu–U–Au deposit, South Australia: A geochemical tracer and reconnaissance Pb–Pb geochronometer. *Precambrian Res.* **2013**, *238*, 129–147. [CrossRef]
25. Courtney-Davies, L.; Ciobanu, C.L.; Tapster, S.R.; Cook, N.J.; Ehrig, K.J.; Kennedy, A.K.; Condon, D.J.; Verdugo-Ihl, M.R.; Wade, B.S.; Gilbert, S.E. The U-Pb systematics of hydrothermal hematite: Insights from the IOCG system at Olympic Dam, South Australia. In Proceedings of the 15th Quadrennial International Association on the Genesis of Ore Deposits Symposium, Salta, Argentina, 28–31 August 2018; pp. 171–172.
26. Cherry, A.R.; Ehrig, K.; Kamenetsky, V.S.; McPhie, J.; Crowley, J.L.; Kamenetsky, M.B. Precise geochronological constraints on the origin, setting and incorporation of ca. 1.59 Ga surficial facies into the Olympic Dam Breccia Complex, South Australia. *Precambrian Res.* **2018**, *315*, 162–178. [CrossRef]
27. Verdugo-Ihl, M.R.; Ciobanu, C.L.; Cook, N.J.; Ehrig, K.J.; Courtney-Davies, L.; Gilbert, S. Textures and U-W-Sn-Mo signatures in hematite from the Olympic Dam Cu-U-Au-Ag deposit, South Australia: Defining the archetype for IOCG deposits. *Ore Geol. Rev.* **2017**, *91*, 173–195. [CrossRef]
28. Nickel, E.H. The new mineral cuprospinel ($CuFe_2O_4$) and other spinels from an oxidized ore dump at Baie Verte, Newfoundland. *Can. Mineral.* **1973**, *11*, 1003–1007.
29. Gotić, M.; Dražić, G.; Musić, S. Hydrothermal synthesis of α-Fe_2O_3 nanorings with the help of divalent metal cations, Mn^{2+}, Cu^{2+}, Zn^{2+} and Ni^{2+}. *J. Mol. Struct.* **2011**, *993*, 167–176. [CrossRef]
30. Moore, P.B. Substitutions of the type ($Sb_{0.5}^{5+}Fe_{0.5}^{3+} \rightleftarrows Ti^{4+}$): The crystal structure of melanostibite. *Am. Mineral.* **1968**, *53*, 1104–1109.
31. Ciobanu, C.L. *Trace element signatures in sulfides at Olympic Dam and satellite prospects: A reconnaissance study for ore vectoring using Cu-(Fe)-sulfides in Iron Oxide Copper Gold Deposits*; The University of Adelaide: Adelaide, Australia, 2015; Unpublished Report.
32. Subramanian, P.R.; Laughlin, D.E. The As–Cu (arsenic-copper) system. *Bull. Alloy Phase Diagrams* **1988**, *9*, 605–618. [CrossRef]
33. Maslen, E.N.; Streltsov, V.A.; Streltsova, N.R.; Ishizawa, N. Synchrotron X-ray study of the electron density in α-Fe_2O_3. *Acta Crystallogr. Sect. B Struct. Sci.* **1994**, *50*, 435–441. [CrossRef]
34. Roedder, E. Fluid inclusions. *Rev. Mineral.* **1984**, *12*, 646.
35. Bodnar, R.J. Reequilibration of fluid inclusions. In *Fluid inclusions: Analysis and interpretation, Short Course 32*; Samson, I., Anderson, A., Marshal, D., Eds.; Mineralogical Association of Canada: Ottawa, ON, Canada, 2003; pp. 213–230.

36. Rosiere, C.A.; Rios, F.J. The origin of hematite in high-grade iron ores based on infrared microscopy and fluid inclusion studies: The example of the Conceição Mine, Quadrilátero Ferrífero, Brazil. *Econ. Geol.* **2004**, *99*, 611–624. [CrossRef]
37. Lüders, V.; Romer, R.L.; Cabral, A.R.; Schmidt, C.; Banks, D.A.; Schneider, J. Genesis of itabirite-hosted Au–Pd–Pt-bearing hematite-(quartz) veins, Quadrilátero Ferrífero, Minas Gerais, Brazil: Constraints from fluid inclusion infrared microthermometry, bulk crush-leach analysis and U–Pb systematics. *Miner. Depos.* **2005**, *40*, 289–306. [CrossRef]
38. Barton, M.D. Iron Oxide(–Cu–Au–REE–P–Ag–U–Co) Systems. In *Treatise on Geochemistry*; Elsevier: Amsterdam, The Netherlands, 2014; Volume 13, pp. 515–541, ISBN 9780080959757.
39. Sibson, R.H.; Robert, F.; Poulsen, K.H. High-angle reverse faults, fluid-pressure cycling, and mesothermal gold-quartz deposits. *Geology* **1988**, *16*, 551. [CrossRef]
40. Verdugo-Ihl, M.R.; Ciobanu, C.L.; Cook, N.J.; Ehrig, K.J.; Courtney-Davies, L. Defining early stages of IOCG systems: Evidence from iron oxides in the outer shell of the Olympic Dam deposit, South Australia. *Miner. Depos.* **2019**, 1–24. [CrossRef]
41. Keyser, W.; Ciobanu, C.L.; Cook, N.J.; Johnson, G.; Feltus, H.; Johnson, S.; Dmitrijeva, M.; Ehrig, K.; Nguyen, P.T. Petrography and trace element signatures of iron-oxides in deposits from the Middleback Ranges, South Australia: From banded iron formation to ore. *Ore Geol. Rev.* **2018**, *93*, 337–360. [CrossRef]
42. Rollog, M.; Cook, N.J.; Guagliardo, P.; Ehrig, K.; Kilburn, M. In situ spatial distribution mapping of radionuclides in minerals by nanoSIMS. *Geochemistry Explor. Environ. Anal.* **2018**. [CrossRef]
43. Rollog, M.; Cook, N.J.; Guagliardo, P.; Ehrig, K.; Ciobanu, C.L.; Kilburn, M. Detection of trace elements/isotopes in Olympic Dam copper concentrates by nanoSIMS. *Minerals* **2019**, *9*, 336. [CrossRef]
44. Courtney-Davies, L.; Tapster, S.R.; Ciobanu, C.L.; Cook, N.J.; Verdugo-Ihl, M.R.; Ehrig, K.J.; Kennedy, A.K.; Gilbert, S.E.; Condon, D.J.; Wade, B.P. A multi-technique evaluation of hydrothermal hematite U Pb isotope systematics: Implications for ore deposit geochronology. *Chem. Geol.* **2019**, *513*, 54–72. [CrossRef]

© 2019 by the authors. Licensee MDPI, Basel, Switzerland. This article is an open access article distributed under the terms and conditions of the Creative Commons Attribution (CC BY) license (http://creativecommons.org/licenses/by/4.0/).

CHAPTER 5

TRACE ELEMENT REMOBILISATION FROM W-SN-U-PB ZONED HEMATITE: NANOSCALE INSIGHTS INTO OPEN SYSTEM BEHAVIOUR OF A MINERAL GEOCHRONOMETER

Max R. Verdugo-Ihl [1], Cristiana L. Ciobanu [1], Nigel J. Cook [1],

Kathy Ehrig [3], Ashley Slattery [2], and Liam Courtney-Davies [1]

[1]*School of Chemical Engineering and Advanced Materials, The University of Adelaide, Adelaide, SA 5005, Australia;*

[2]*Adelaide Microscopy, The University of Adelaide, Adelaide, SA 5005, Australia;*

[3]*BHP Olympic Dam, 10 Franklin St, Adelaide SA, 5000, Australia*

Article published in *Mineralogical Magazine* (2020) 84(4):502−516.

Statement of Authorship

Title of Paper	Trace element remobilisation from W-Sn-U-Pb zoned hematite: Nanoscale Insights into open system behaviour of a mineral geochronometer
Publication Status	☑ Published ☐ Accepted for Publication ☐ Submitted for Publication ☐ Unpublished and Unsubmitted w ork w ritten in manuscript style
Publication Details	Verdugo Ihl, M.R., Ciobanu, C.L., Cook, N.J., Ehrig, K., Slattery, A., Courtney-Davies, L., 2020. Trace element remobilisation from W-Sn-U-Pb zoned hematite: Nanoscale insights into a mineral geochronometer behaviour during interaction with fluids. Mineralogical Magazine 84, 502–516. https://doi.org/10.1180/mgm.2020.49.

Principal Author

Name of Principal Author (Candidate)	Max R. Verdugo-Ihl		
Contribution to the Paper	Performed analytical work, evaluation and interpretation of results and prepared the manuscript.		
Overall percentage (%)	55		
Certification:	This paper reports on original research I conducted during the period of my Higher Degree by Research candidature and is not subject to any obligations or contractual agreements with a third party that would constrain its inclusion in this thesis. I am the primary author of this paper.		
Signature		Date	15.04.2020

Co-Author Contributions

By signing the Statement of Authorship, each author certifies that:

i. the candidate's stated contribution to the publication is accurate (as detailed above);

ii. permission is granted for the candidate in include the publication in the thesis; and

iii. the sum of all co-author contributions is equal to 100% less the candidate's stated contribution.

Name of Co-Author	Cristiana L. Ciobanu		
Contribution to the Paper	Helped to define the direction of the manuscript, guided manuscript preparation and assisted with data acquisition, the interpretation of the results and evaluation of the manuscript.		
Overall percentage (%)	25		
Signature		Date	15.04.2020

Name of Co-Author	Nigel J. Cook		
Contribution to the Paper	Assisted with the preparation and evaluation of the manuscript.		
Overall percentage (%)	10		
Signature		Date	15.04.2020

Name of Co-Author	Kathy Ehrig		
Contribution to the Paper	Assisted with the evaluation of the manuscript.		
Overall percentage (%)	4		
Signature		Date	15.04.2020

Name of Co-Author	Ashley Slattery		
Contribution to the Paper	Performed HAADF-STEM data acquisition.		
Overall percentage (%)	4		
Signature		Date	15.04.20

Name of Co-Author	Liam Courtney-Davies		
Contribution to the Paper	Assisted with the evaluation of the manuscript.		
Overall percentage (%)	2		
Signature		Date	15.04.2020

Mineralogical Magazine (2020), **84**, 502–516
doi:10.1180/mgm.2020.49

CAMBRIDGE UNIVERSITY PRESS

Article

Trace-element remobilisation from W–Sn–U–Pb zoned hematite: Nanoscale insights into a mineral geochronometer behaviour during interaction with fluids

Max R. Verdugo-Ihl[1]*, Cristiana L. Ciobanu[1], Nigel J. Cook[2], Kathy Ehrig[3], Ashley Slattery[4] and Liam Courtney-Davies[1]

[1]School of Chemical Engineering and Advanced Materials, The University of Adelaide, Adelaide, SA 5005, Australia; [2]School of Civil, Environmental and Mining Engineering, The University of Adelaide, Adelaide, SA 5005, Australia; [3]BHP Olympic Dam, 10 Franklin St, Adelaide SA, 5000, Australia; and [4]Adelaide Microscopy, The University of Adelaide, Adelaide, SA, 5005, Australia

Abstract

Preferential removal of W relative to other trace elements from zoned, W–Sn–U–Pb-bearing hematite coupled with disturbance of U–Pb isotope systematics is attributed to pseudomorphic replacement via coupled dissolution reprecipitation reaction (CDRR). This hematite has been studied down to the nanoscale to understand the mechanisms leading to compositional and U/Pb isotope heterogeneity at the grain scale. High-Angle Annular Dark Field Scanning Transmission Electron Microscopy (HAADF STEM) imaging of foils extracted *in situ* from three locations across the W-rich to W-depleted domains show lattice-scale defects and crystal structure modifications adjacent to twin planes. Secondary sets of twins and associated splays are common, but wider (up to ~100 nm) inclusion trails occur only at the boundary between the W-rich and W-depleted domains. STEM energy-dispersive X-ray mapping reveals W- and Pb-enrichment along 2–3 nm-wide features defining the twin planes; W-bearing nanoparticles occur along the splays. Tungsten and Pb are both present, albeit at low concentrations, within Na–K–Cl-bearing inclusions along the trails. HAADF STEM imaging of hematite reveals modifications relative to ideal crystal structure. A two-fold hematite superstructure ($a = b = c = 10.85$ Å; $\alpha = \beta = \gamma = 55.28°$) involving oxygen vacancies was constructed and assessed by STEM simulations with a good match to data. This model can account for significant W release during interaction with fluids percolating through twin planes and secondary structures as CDRR progresses from the zoned domain, otherwise apparently undisturbed at the micrometre scale. Lead remobilisation is confirmed here at the nanoscale and is responsible for a disturbance of U/Pb ratios in hematite affected by CDRR. Twin planes can provide pathways for fluid percolation and metal entrapment during post-crystallisation overprinting. The presence of complex twinning can therefore predict potential disturbances of isotope systems in hematite that will affect its performance as a robust geochronometer.

Keywords: HAADF STEM, W–Sn–U–Pb-bearing hematite, metal (re)mobilisation, nanoparticles, twinning, open system, geochronology

(Received 14 March 2020; accepted 10 June 2020; Accepted Manuscript published online: 16 June 2020; Associate Editor: Jason Harvey)

Introduction

The primary distribution of trace elements in minerals and the subsequent (re)mobilisation of those elements is relevant for understanding rock-forming processes and critical for accurate age determination of ore-forming events. Rapid advances in microbeam techniques provide ever increasing spatial resolution and greater sensitivity (lower minimum limits of detection) allowing unparalleled insights into grain-scale compositional zoning and how primary patterns are reshaped during subsequent events (e.g. for U–(Pb)–W–Sn–Mo hematite; Verdugo-Ihl *et al.*, 2017). Pseudomorphic replacement via coupled dissolution replacement reaction (CDRR; Putnis, 2009 and references therein) are readily recognisable from preserved complex compositional patterns and are a widespread phenomenon responsible for local-scale mineral transformation and trace-element remobilisation in hydrothermal ores (Cook *et al.*, 2017, and references therein).

Numerous examples of pseudomorphic mineral replacement during fluid–rock interaction demonstrate the role of the interface at the reaction front in preserving crystallographic information from parent to reprecipitated phase (e.g. Putnis, 2009). Thus, in order to determine whether the identified replacement takes place via CDDR, or by other mechanisms, a crystallographic assessment of the relationships between the parent and product phases is necessary (e.g. Xia *et al.*, 2009; Macmillan *et al.*, 2016*a*).

Comparatively few studies have addressed replacement via CDRR in which the product is the same phase as the parent but with grain-scale modification of the trace/minor element endowment, such as in zoned hematite from the Olympic Dam deposit, South Australia (Verdugo-Ihl *et al.*, 2017).

Hematite is demonstrated to be a reliable U–Pb geochronometer, in some cases generating analytical precision (0.05%) comparable to conventional mineral geochronometers such as zircon (Courtney-Davies *et al.*, 2019, 2020). The U–Pb systematics of this type of hematite, addressed by microbeam techniques

*Author for correspondence: Max R. Verdugo-Ihl, Email: max.verdugoihl@adelaide.edu.au
Cite this article: Verdugo-Ihl M.R., Ciobanu C.L., Cook N.J., Ehrig K., Slattery A. and Courtney-Davies L. (2020) Trace-element remobilisation from W–Sn–U–Pb zoned hematite: Nanoscale insights into a mineral geochronometer behaviour during interaction with fluids. *Mineralogical Magazine* **84**, 502–516. https://doi.org/10.1180/mgm.2020.49

© The Mineralogical Society of Great Britain and Ireland 2020

and high-precision isotope dilution thermal ionisation mass spectrometry (ID–TIMS) using microsampled material from U-rich domains (Courtney-Davies *et al.*, 2019), show both the closed and open system behaviour of U–Pb isotopes. These phenomena can be linked to replacement processes, as inferred from the modification of primary crystal zoning, and is relevant for U–Pb age determination of hematite by laser-ablation inductively coupled plasma mass spectrometry (LA-ICP-MS) and other techniques.

The incorporation and release of trace elements in and from minerals depends upon the ability of an individual crystal structure to adjust compositional changes via structural modifications of certain periodicity. Despite the simple composition, five crystal structural modifications of Fe_2O_3 have been defined from nanoscale studies (Lee and Xu, 2016). Moreover, the structural complexity of Fe_2O_3 has been described as a homologous series of nFeO·$m$$Fe_2O_3$ compounds based on experiments at high pressure and temperature (Bykova *et al.*, 2016). Such homology is underpinned, in particular, by the formation of non-stoichiometric Fe_2O_{3-x} phases ($x = 0.2$, 0.44) involving oxygen release. Transmission electron microscopy (TEM) studies have shown long-range modulation as ordered O vacancies in various hematite superstructures (Chen *et al.*, 2008). Metal substitution has also been invoked as an alternative explanation for TEM data that shows the presence of long-range satellite reflections in high-U hematite (up to 2.6 wt.% UO_3; Ciobanu *et al.*, 2013). Recently, another model has been proposed based on *ab initio* molecular dynamic simulations, in which substitution of U^{6+} for Fe^{3+} takes place producing a short-range, two-fold superstructure of hematite (McBriarty *et al.*, 2018).

None of these models has, however, been previously assessed by direct visualisation of atoms in the crystal structure. Such supporting evidence is obtainable using the atomic-scale resolution capabilities of contemporary scanning/TEM (STEM) instrumentation with Z-contrast technique imaging such as high-angle annular dark field (HAADF) STEM (e.g. van Tendeloo *et al.*, 2012; Ciobanu *et al.*, 2016).

In this study, we employ this technique to assess the incorporation of trace elements into, and their release from, compositionally zoned hematite, in which W (and Sn) is present at higher concentrations than either U or Pb (Verdugo-Ihl *et al.*, 2017). The study was carried out on oscillatory-zoned hematite from a bornite–chalcocite-bearing sulfide interval in the SE part of the Olympic Dam deposit (Fig. 1). This sample displays a clear decoupling between W and Sn, whereas U and Pb show relative enrichment in the core and margin but with patchy distribution between them (Fig. 2*a*; Verdugo-Ihl *et al.*, 2017). The ID–TIMS age determination of this grain measured high-common Pb components within analysed volumes, manifest as a non-linear spread of datapoints on a Tera–Wasserburg diagram, where an intercept cannot be formed (Fig. 2*b,c*; Courtney-Davies *et al.*, 2019).

The high levels of measured common Pb in the ID–TIMS dataset is due to microsampling of material from further below the studied hematite grain, as shown by anomalously high levels of Th/U compared to other zoned-hematite grains, and comparatively low measured proportions of ^{204}Pb in the LA-ICP-MS dataset from the same grain. Therefore, when using the laser ablation method, the smaller analysed volume is a far more representative measurement of true common Pb components in this case. Trace-element remobilisation processes are relevant for understanding the deportment of economically important minor

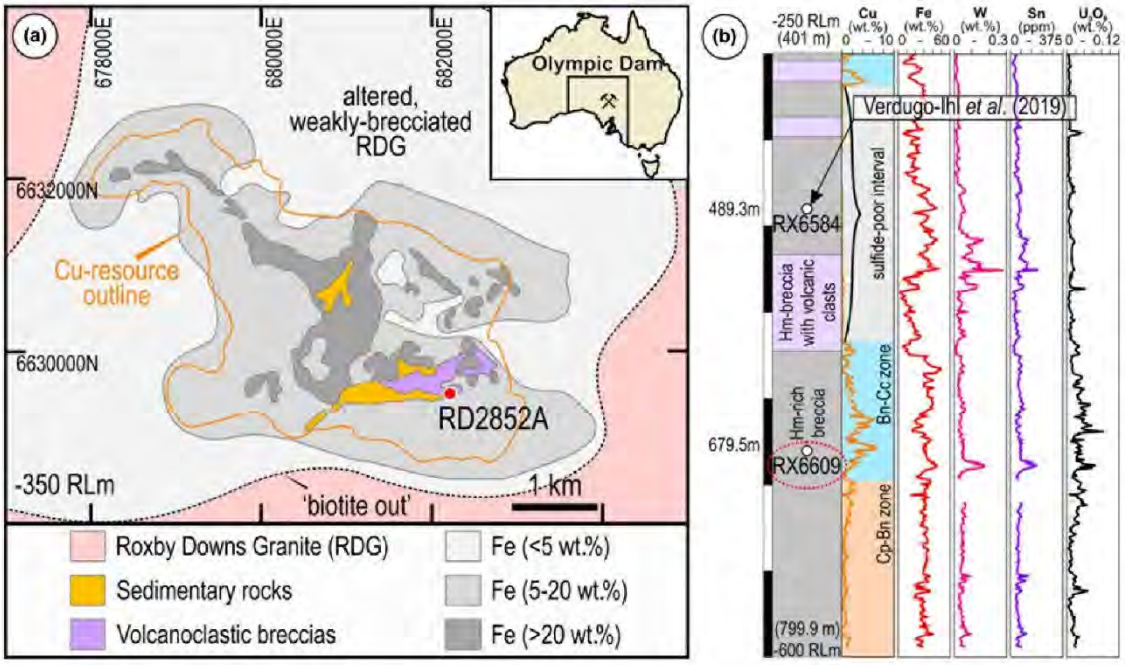

Fig. 1. (*a*) Sketch of the Olympic Dam deposit outlining the main lithologies and location of sampled drillhole (red dot; RD2852A) projected at the –350 m RL mine grid below surface. Deposit location within Australia shown in inset. (*b*) Simplified lithology in RD2852A displaying selected element assays. Location of Cu–As-zoned hematite discussed in the text is also shown (sample RX6584). Abbreviations: Bn – bornite; Cc – chalcocite; Cp – chalcopyrite; Hm – hematite.

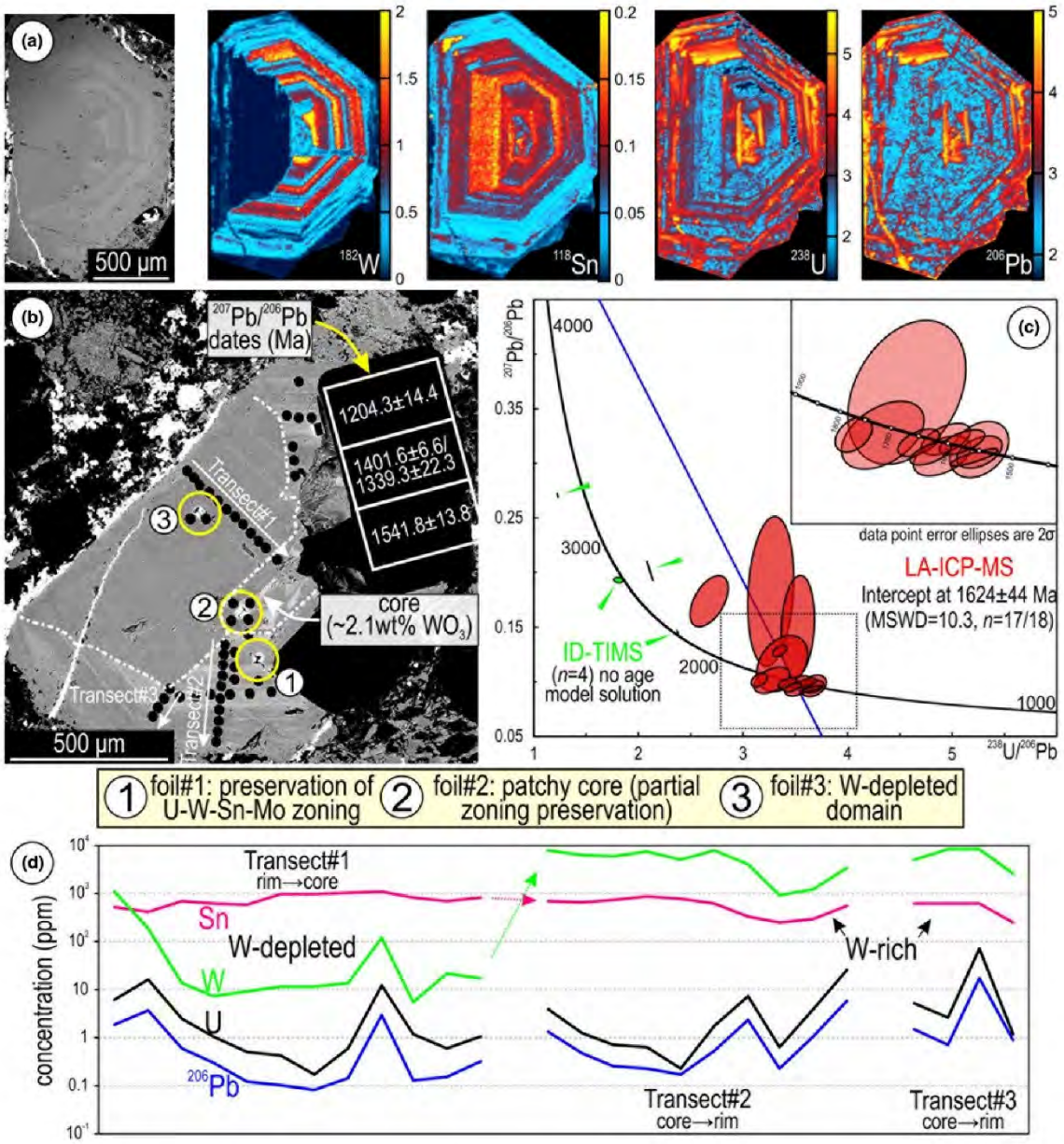

Fig. 2. (*a*) BSE image and corresponding LA-ICP-MS trace-element maps of the zoned hematite investigated. W and Sn in linear scale (n-10^6); U and Pb are logarithmically scaled (10^n). Intensities (counts-per-second, cps) scaled individually to enhance features of interest. (*b*) BSE image of the same grain re-polished after mapping showing locations of FIB-prepared S/TEM foils. (*c*) Plot of both LA-ICP-MS and ID-TIMS U–Pb data (modified from Courtney-Davies *et al.*, 2019). LA-ICP-MS age determination of hematite presented on a Tera–Wasserburg diagram (see text for further details), providing a geologically meaningful intercept age, whereas ID-TIMS data from microsampled domains could not form an intercept due to high common Pb content. (*d*) LA-ICP-MS transects across selected domains as shown in (*b*).

elements but also for modelling ore-forming processes and for interpretation of geochronological data. We have undertaken detailed nanoscale investigations to understand grain-scale heterogeneity, the mechanisms involved, the identity of the reprecipitation products, and how the processes leading to decoupling of parent–daughter isotope pairs took place. The results carry implications for understanding how grain-scale element remobilisation can affect the performance of mineral geochronometers.

Methodology

The sample investigated was re-polished for new micro- and nanoscale analysis after mapping and geochronology (Verdugo-Ihl *et al.*, 2017; Courtney-Davies *et al.*, 2019). The new work comprised reflected light optical and scanning electron microscopy using a FEI Quanta 450 instrument in back-scattered electron (BSE) mode to assess the hematite grain in terms of micro-scale textures

on the newly polished surface. Several LA-ICP-MS spot analysis transects were conducted to assess quantitatively variation in the concentration of trace elements throughout different grain domains. LA-ICP-MS methodology followed Verdugo-Ihl *et al.* (2020) using a RESOlution-LR 193 nm ArF excimer laser microprobe coupled to an Agilent 7900cx quadrupole ICP-MS. ^{57}Fe was used as the internal standard element, assuming a stoichiometric Fe content in hematite. External reference materials GSD-1 G and NIST-610 were used for instrument drift correction and trace-element quantification. A laser spot diameter of 43 µm, pulse repetition rate of 5 Hz and fluence of 3.5 J/cm^2 were used. Data reduction was performed in *Glitter* (van Achterbergh *et al.*, 2001). Analysis comprised measurement of 47 isotopes, including four Pb isotopes: ^{24}Mg, ^{27}Al, ^{28}Si, ^{31}P, ^{43}Ca, ^{45}Sc, ^{49}Ti, ^{51}V, ^{52}Cr, ^{55}Mn, ^{59}Co, ^{60}Ni, ^{63}Cu, ^{66}Zn, ^{69}Ga, ^{75}As, ^{88}Sr, ^{89}Y, ^{90}Zr, ^{93}Nb, ^{95}Mo, ^{118}Sn, ^{121}Sb, ^{137}Ba, ^{139}La, ^{140}Ce, ^{141}Pr, ^{146}Nd, ^{147}Sm, ^{153}Eu, ^{157}Gd, ^{159}Tb, ^{163}Dy, ^{165}Ho, ^{166}Er, ^{169}Tm, ^{172}Yb, ^{175}Lu, ^{178}Hf, ^{181}Ta, ^{182}W, ^{204}Pb, ^{206}Pb, ^{207}Pb, ^{208}Pb, ^{232}Th and ^{238}U.

Three thinned foils (~20 µm × ~6 µm × ~100 nm in dimension) were prepared using procedures for dual-beam FIB-SEM methods as outlined in Ciobanu *et al.* (2011) using an FEI Helios Nanolab 600 instrument. HAADF STEM imaging and energy-dispersive X-ray (EDX) spectrometry, in both spot analysis and mapping modes, were conducted with an ultra-high resolution, probe-corrected FEI Titan Themis S/TEM operated at 200 kV. This instrument is equipped with an X-FEG Schottky source and Super-X EDX geometry. The Super-X EDX detector provides geometrically symmetric EDX detection with an effective solid angle of 0.8 sr. Probe correction delivered sub-Ångstrom spatial resolution and an inner collection angle greater than >50 mrad was used for HAADF imaging with a Fischione detector.

Indexing of Fast-Fourier-Transform (FFT) patterns was conducted using *WinWulff*© (version 1.6) and publicly available data from the *American Mineralogist* Crystal Structure Database (http://rruff.geo.arizona.edu/AMS/amcsd.php). Crystal structure models and the superstructure was built using *CrystalMaker*® (version 10.2). STEM simulations were obtained using xHREM™ (version 4.1). All instruments are housed at Adelaide Microscopy, The University of Adelaide.

Results

Grain-scale characterisation: textures, FIB sampling and trace-element data for hematite

The analysed hematite occurs as a single, euhedral grain and is unusually coarse (millimetre-sized) relative to the fine-grained hematite in the surrounding breccia matrix (Fig. 3*a*). Two sets of twins are observed, both cross-cutting the boundary with the W-depleted domain, which is, nonetheless, marked by microtextures such as an abundance of pores/inclusions and fractures. Nanoscale sampling by FIB-SEM targeted the grain-scale textural variation across this boundary: (1) directly across the zoning; (2) addressing partially preserved zoning within the patchy core; and (3) within the W-depleted domain (Fig. 3*b*). Twin planes with a width of a few micrometres are intersected at depth in each foil (Fig. 3*c–e*). In the patchy core, trails of sub-micrometre inclusions occur either parallel to the twin plane or dipping towards it (see below).

Trace-element LA-ICP-MS data (Fig. 2*d*; Supplementary Material 1, Table S1) show compositional variation between the W-rich and -depleted domains. Transects collected along compositional zoning, as well as individual analyses on the patchy zoning in the core, show distinctly high W, typically >2500 ppm (maximum 8640), and one order of magnitude lower Sn concentrations (≳250 to ~860 ppm); the two elements are positively correlated. Across the W-depleted domain however, the transect shows that Sn remains relatively unaffected, displaying similar concentration ranges (420–1100 ppm) as in the high-W domains whereas W is markedly lower (<100 ppm). A comparison between concentration values obtained along the transects indicates W-depletion by roughly three orders of magnitude (Fig. 2*d*). Uranium and Pb concentrations do not differ significantly between these two domains, being typically <26 and 6 ppm, respectively, although both appear to be slightly more enriched wherever zoning is preserved.

HAADF STEM imaging and trace-element distributions at the nanoscale

The twin planes are associated with splays (appearing brighter on HAADF STEM images), branching to nm-size fractures or across inclusion trails (Fig. 4*a–c*). However, relative enrichment in W–Pb (see below) occurs along the twin plane only in the area furthest away from the targeted replacement boundary (foil #1; Fig. 4*d,e*). The direction or trace of the twin within the plane of view is defined hereafter as the twin crest. Tungsten-bearing nanoparticles (W-NPs) are present associated with splays in both locations outside the W-depleted domain (i.e. the zoned area and the patchy core; foils #1 and #2; Fig. 4*f,g*). These W-NPs are concentrated along dense, short sets of splays within bands, up to 200–300 nm wide, in the patchy grain core (foil #2; Fig. 4*h,i*). They are distinct from the coarser inclusions (up to ~100 nm in diameter) along the trails (Fig. 4*b*), which have different compositions. Unlike in the other locations, twins within the W-depleted domain display locally developed scalloped-shaped crests (Fig. 4*j*) and lack measurable enrichment in trace elements.

STEM EDX mapping indicates measurable concentrations of W and Pb along both splays and twin crests in the zoned area (foil #1), with higher concentrations of W relative to Pb (Fig. 5*a–c*). Although both elements are evenly distributed along the twin crests, both Pb and W are preferentially concentrated in the middle and sides of these crests, respectively (Fig. 5*d,e*). However, the W-NPs occurring along splays adjacent to such twins (Fig. 4*f*) show no measurable Pb (Fig. 6*a–c*). Inclusions along the trails (foil #2) display various element associations, including small Si-rich domains within a matrix containing elevated concentrations of Cl, K and Na (Fig. 6*d*). Tungsten, Pb, Sn, and As concentrations are low and erratic throughout these inclusions. The trails hosting the inclusions are depleted in W relative to the host hematite (Fig. 6*d*). The W-NPs from splays adjacent to the trails in the same patchy core (foil #2) also show some measurable Si (Fig. 6*e*), which is not seen in those W-NPs from hematite in which zonation is preserved (foil #1; Fig. 6*a–c*).

High-resolution imaging of hematite shows a range of defects, including subtle lattice misorientations and localised crystal structural modifications relative to adjacent twin planes (Figs. 7, 8). A direct correlation is observed between the W–Pb-bearing, minor twins and lattice-scale modifications in hematite (Fig. 7). These effects are observed within irregular halos adjacent to the twin crest (Fig. 7*a*). The width of twin crests varies and locally displays dilation (open space) along its direction, features which are associated with loss of HAADF signal intensity (Fig. 7*b,c*).

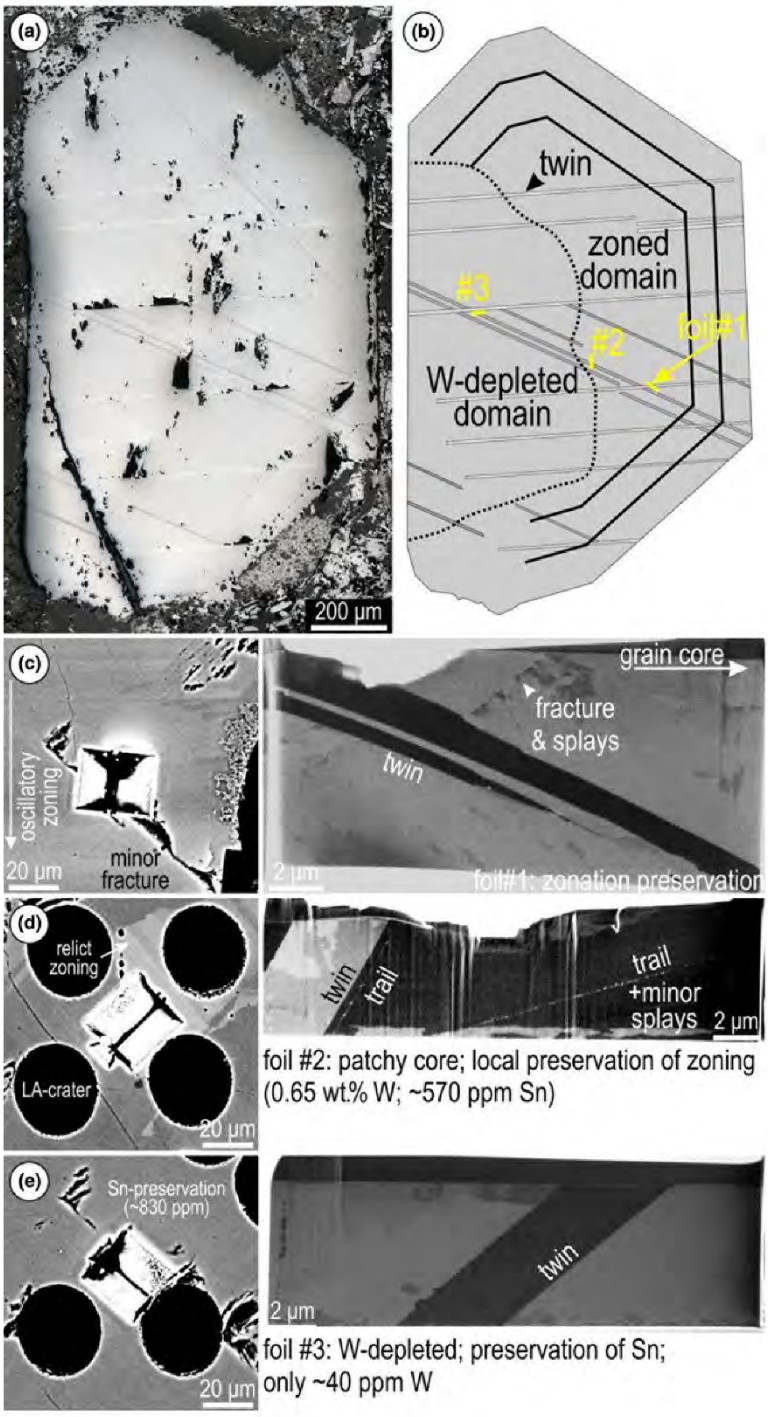

Fig. 3. (*a*) Reflected light image of hematite after re-polishing and (*b*) sketch showing distribution of main sets of twins and studied domains. (*c–e*) BSE images of extracted S/TEM-foil locations and corresponding foils imaged in secondary electron (immersion mode) showing relevant textures in hematite.

Misorientation directions in hematite can also be expressed as sets of 'shears' oblique to the twin plane (Fig. 7*d*). The shears are associated with variation in atom brightness and with satellite reflections displaying long-range modulation on Fast Fourier Transform (FFT) patterns (Fig. 7*e* and inset). There is however a wider spectrum of lattice modifications within nanodomains along the margins of the twin (Fig. 7*f* and inset).

In the W-depleted area, lattice distortions and defects are observed on either side of major twin planes (Fig. 8). Misorientation in hematite occurs as domains a few nanometres

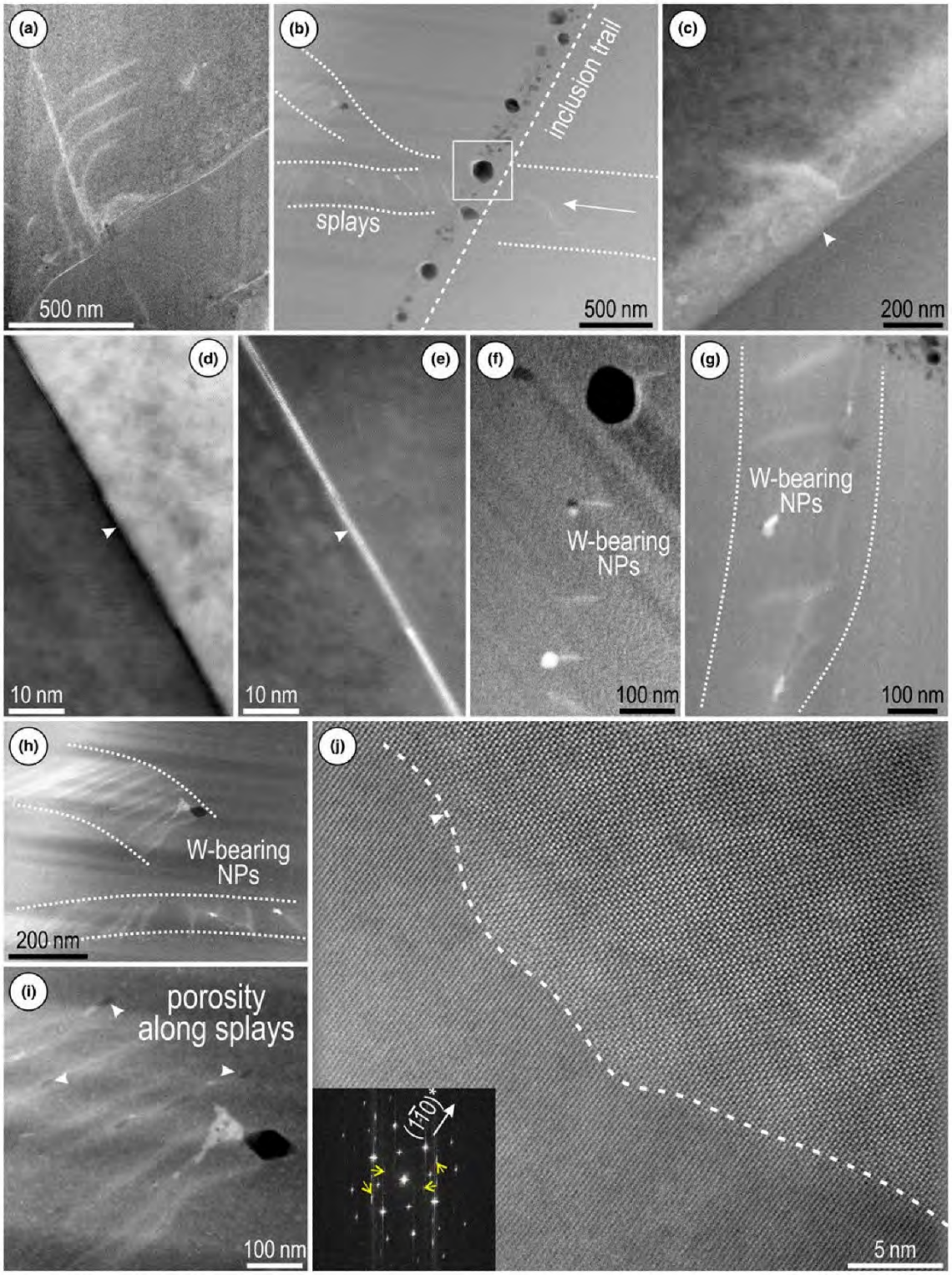

Fig. 4. HAADF STEM (*a–c*, *e–j*) and BF STEM (*d*) images of hematite from the three sampled domains. (*a*) Splays (brighter on image) oblique to minor twin. (*b*) Inclusion trail showing bimodal size distribution crosscutting splays. (*c*) Splay at twin plane interface (arrowed) in the W-depleted domain. (*d*, *e*) Twin imaged in BS and HAADF STEM modes showing W–Pb-enrichment along the crest (arrowed). (*f*) W-bearing NPs associated with splays. (*g*) W-bearing NPs associated with splays along band (dotted line) close to inclusion trail in the patchy grain core (foil #2). (*h*, *i*) W-bearing NPs and pores (arrowed) along bands delineating parallel sets of splays. (*j*) Scalloped boundary at the twin interface (dashed line) in the W-depleted domain. FFT pattern (inset) shows twinning along $\langle 1\bar{1}0 \rangle$ directions (twin reflections marked by yellow arrows) on $[2\bar{2}1]_{Hm}$ (orientation for the upper side).

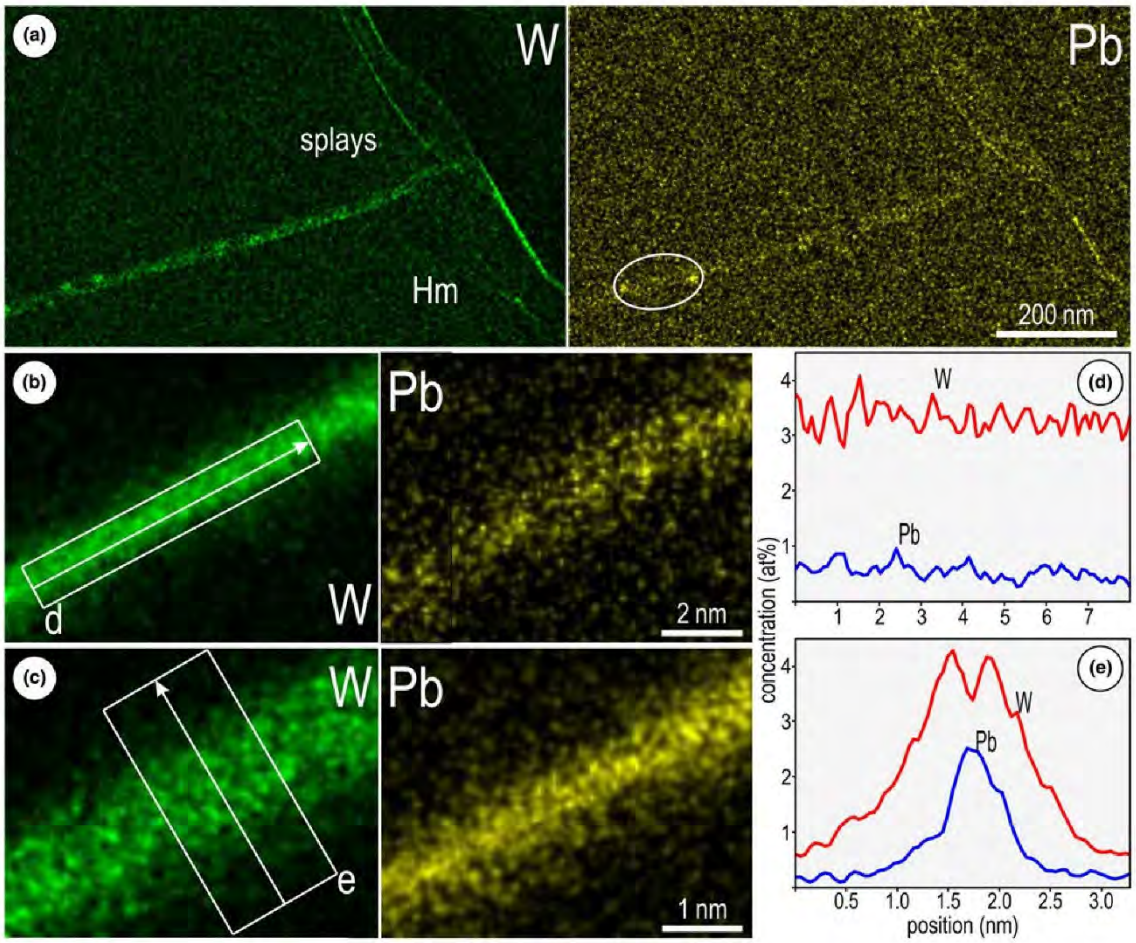

Fig. 5. (*a*) STEM-EDX maps of hematite (Hm) from the area preserving zoning (foil # 1) showing W–Pb-enrichment along splay (*a*) and twin crest (*b*, *c*). (*d*, *e*) STEM-EDX profiles obtained along and across the twin-crests in (*b*) and (*c*) as marked showing the relative concentrations and distribution of the two elements.

in size displaying subtle variation in contrast and development of stripes throughout the images (Fig. 8*a*). In detail, nm-wide defects are recognisable as atom displacements induced by screw dislocations (Fig. 8*b* and inset). Additionally, gaps of darker contrast occur between the cation arrays (bright dots), depicted as periodic defects by satellite reflections with wave-modulation on FFT patterns (Fig. 8*c* and inset). In contrast, nm-wide defects displaying atom stretching are identified from images with no effects on FFT patterns (Fig. 8*d*–*f*).

Two-fold hematite superstructure with oxygen vacancies

In order to understand whether the observations could be reconciled with crystal structural modifications of hematite, including development of superstructures, the samples were imaged by tilting each specimen on multiple main zone axes. The zone axes used for STEM simulations and crystal structure models were obtained from indexing of FFT patterns, which were in turn assessed against simulated electron diffractions (ED; Fig. 9). HAADF STEM images of least affected hematite show good fits with the simulations and crystal structure models. The latter indicate that the bright dots on all zone axes imaged here correspond to columns of equal number of Fe atoms, thus no intensity variation should be expected on the HAADF STEM images (Fig. 9).

The three zone axes shown in Fig. 9*a*–*c* can also display a variation in signal intensity that correlates with the appearance of satellite reflections on FFT patterns (Fig. 10). We observed that in each of these cases, the satellites occur at ½ distance to the main reflections, thus suggesting two-fold superstructures. Because such images were obtained from both W-bearing and -depleted hematite, we assume that vacancies in the oxygen sites could play the main role in the observed changes, rather than metal substitution for Fe. This is especially clear in areas adjacent to the W–Pb-crests shown in Fig. 7.

For simplicity, we used $[001] \equiv [0001]_H$ (space group $R\bar{3}c$ with hexagonal axes) zone axis which shows alternating Fe–O–O–Fe atoms along $\langle 100 \rangle$, $\langle 010 \rangle$ and $\langle 1\bar{1}0 \rangle$ vectors (Supplementary Material 2, Fig. S1). After building a two-fold superstructure of hematite as a trigonal primitive cell (T) with rhombohedral axes, defined as: $a = b = c = 10.85$ Å; $\alpha = \beta = \gamma = 55.28°$, the same metal–oxygen arrays are present on $\langle 1\bar{1}0 \rangle$ and conjugate directions on the corresponding $[111]_T$ zone axis (Supplementary

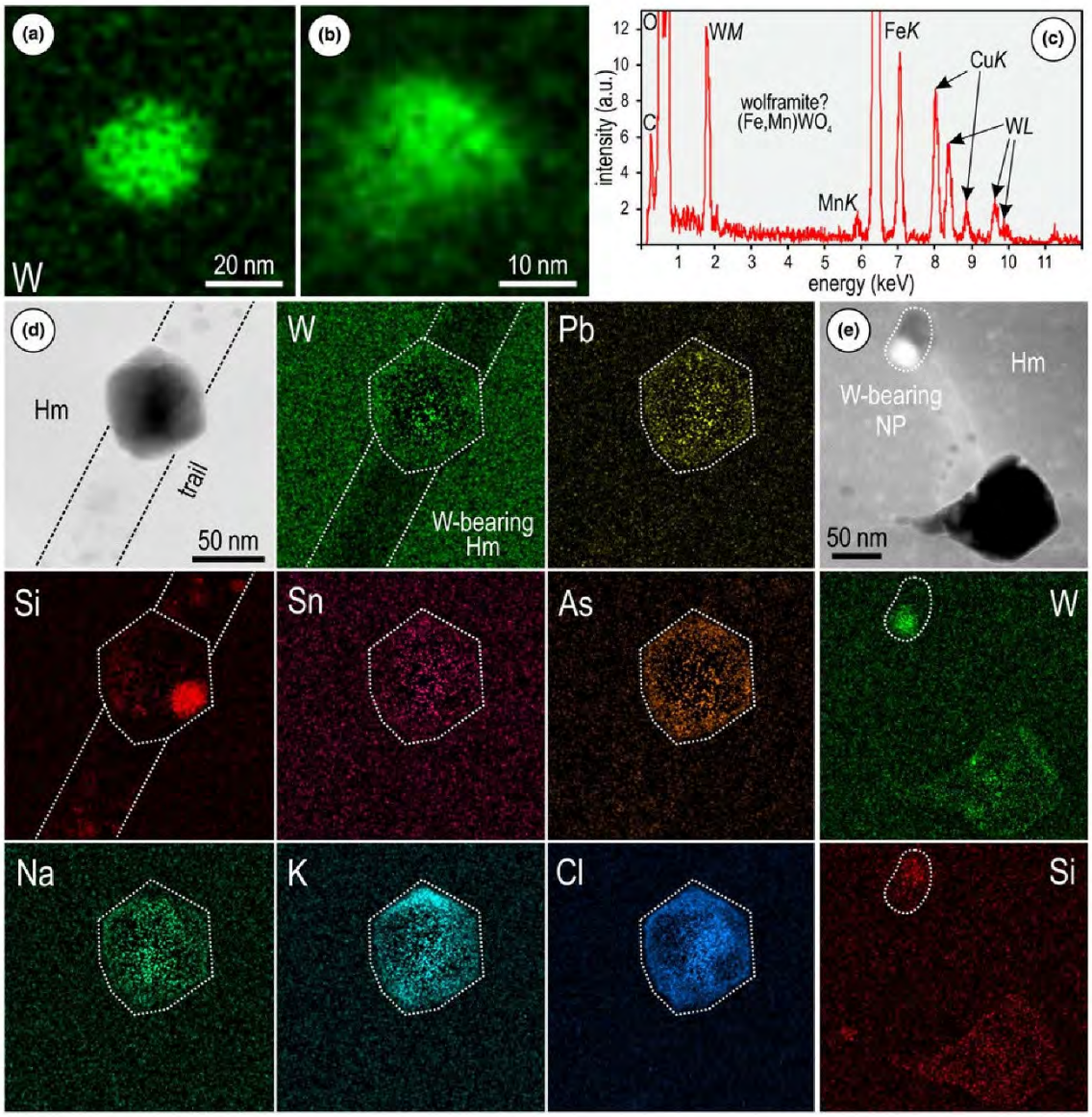

Fig. 6. STEM-EDX maps of NPs and inclusions within hematite (Hm) from foil #1 (*a*, *b*) and foil # 2 (*d*, *e*). (*a*, *b*) W-bearing NPs attached to the splays shown in Fig. 4*f*. (*c*) EDX spectrum of a W-bearing NP showing Mn as a minor element associated with Fe, suggesting wolframite as a species within the NPs. (*d*) Euhedral inclusion in hematite (Hm) along the trail shown in Fig. 4*b* (area marked by rectangle) displaying a complex element association (Na, K, Cl) indicative of fluid inclusions and attached Si-NPs. Note presence of W and Pb within the inclusion but not along the trail. (*e*) W-bearing NPs attached to a Si-bearing pore typical of splays in hematite from the patchy core. Note Si and W are also mapped within a larger cavity at the end of the splay.

Material 2, Fig. S1*a*). We create arrays of Fe–O–v–Fe–v–O–Fe by removing corresponding O column clusters from the aforementioned directions within the extended structure (Supplementary Material 2, Fig. S1*b*). For simplicity, no Fe or O positions were modified. We use the crystallographic information obtained (Supplementary Material 3) representing the two-fold superstructure simulations of ED and STEM patterns (Fig. 10). There is a good fit between the FFT patterns and ED simulations in terms of the distribution of satellite reflections in all three cases selected, thus confirming the choice of the supercell.

The STEM simulations on $[111]_T$ show the superstructure as a honeycomb motif in which the six brightest spots (Fe) placed at the vertices of a hexagon are interlocked with six fainter/smaller spots forming the vertices of a second hexagon (Fig. 10*a*; Supplementary Material 2, Fig. S2). The pattern also features a well-defined darker ring around each Fe atom at the centre of the hexagonal motif. In the corresponding crystal model, the vertices of the fainter hexagon overlap with O atoms between an Fe atom and an O vacancy (Fig. 10*a*). Such results suggest that removal of O clusters induces three effects on the STEM images:

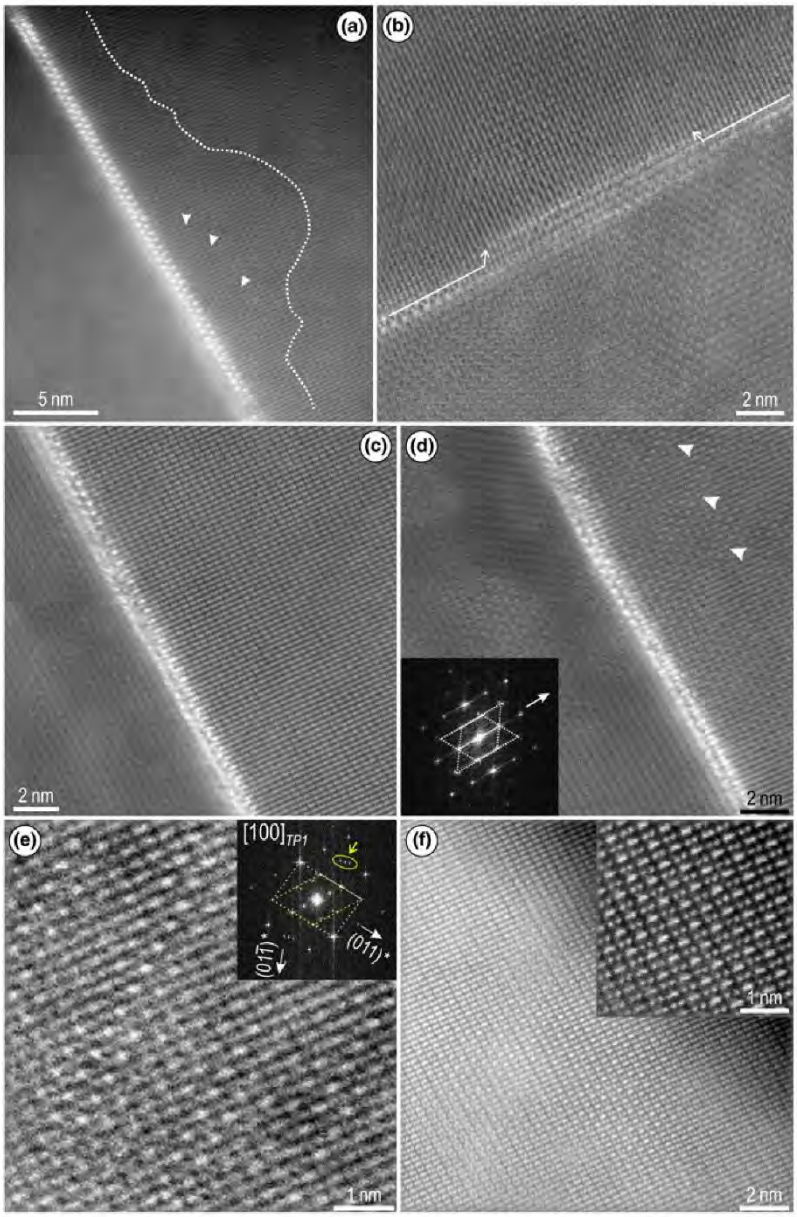

Fig. 7. HAADF STEM images showing details of W–Pb-enriched twin planes on $[12\bar{1}]_{Hm}$ undergoing superstructuring to $[1\bar{1}1]_T$ from areas with preserved zonation (foil # 1). (*a*) Halo (dotted line) imaged on one side of the twin crest displaying defects as darker strips (arrowed) with irregular distribution. Note this is the narrowest twin crest as a tight 'zip' between two-bright atoms (W, Pb). (*b*, *c*) Local dilation (arrowed) along the twin crests leading to open spaces between the two 'zipped' bright atoms. (*d*) Defects as sets of periodic shears (arrowed) within hematite. FFT pattern (inset) shows disorder along $(\bar{2}10)^* \equiv (0\bar{1}1)_T^*$ associated with such shears. Twin motifs highlighted by dotted lines. (*e*) Image and FFT pattern (inset) showing details of shear-modulation from hematite in (*d*). Dashed lines show the basic motif on $[100]_T$ in white and superimposed rhombic motif in yellow. Long-range wave-modulation along (011)* shown as groups of satellite reflections arrowed and circled. (*f*) Twin side displaying superstructuring with domains displaying enhanced intensity variation of alternating Fe atoms dumbbells (inset). See text for additional explanation.

(1) enhanced brightness of the Fe atoms that are not directly adjacent to O vacancies; (2) a 'darkening' as an inner ring around each Fe atom within the honeycomb motif; and (3) production of 'phantom' spots centred on O atoms between Fe and O vacancies adjacent to the vacancies (Fig. 10*a*).

The STEM simulation for the two dumbbell patterns show somewhat comparable effects to those of the vacancies (Fig. 10*b*, *c*; Supplementary Material 2, Fig. S2). On $[1\bar{1}1]_T$ orientation, a 2×2-squarish pattern highlighted by dark bands (effect 2) and faint, 'phantom' squares (effect 3) occurring between two adjacent vacancies, both expressed on the HAADF STEM images (Fig. 10*b*). On $[100]_T$ zone axis, rows of brighter Fe atoms occur with 2×2 periodicity along the $\langle 0\bar{1}1 \rangle$ and $\langle 011 \rangle$ directions (Fig. 10*c*). Such variation in intensity relates to a combination of alternating O and vacancy sites along the columns between the Fe-atom pairs (effect 1) with phantom squares (effect 3) between two adjacent vacancies creating a superimposed rhombic pattern (Fig. 10*c*). The latter is well-expressed by the enhanced intensity of dumbbell pairs along the *b* and *c* axes on some of the HAADF STEM images (Fig. 7*f* and inset).

Intensity variation on HAADF STEM is also expected to be produced by mixed sites and/or Fe positions substituted with heavier atoms (W, Sn, U, Pb), but this not considered in the current model. For example, atom brightening effects were obtained for U-substituted hematite (~10.9 wt.% UO_3) using the two-fold superstructure (P1, trigonal) from McBriarty *et al.* (2018) (Supplementary

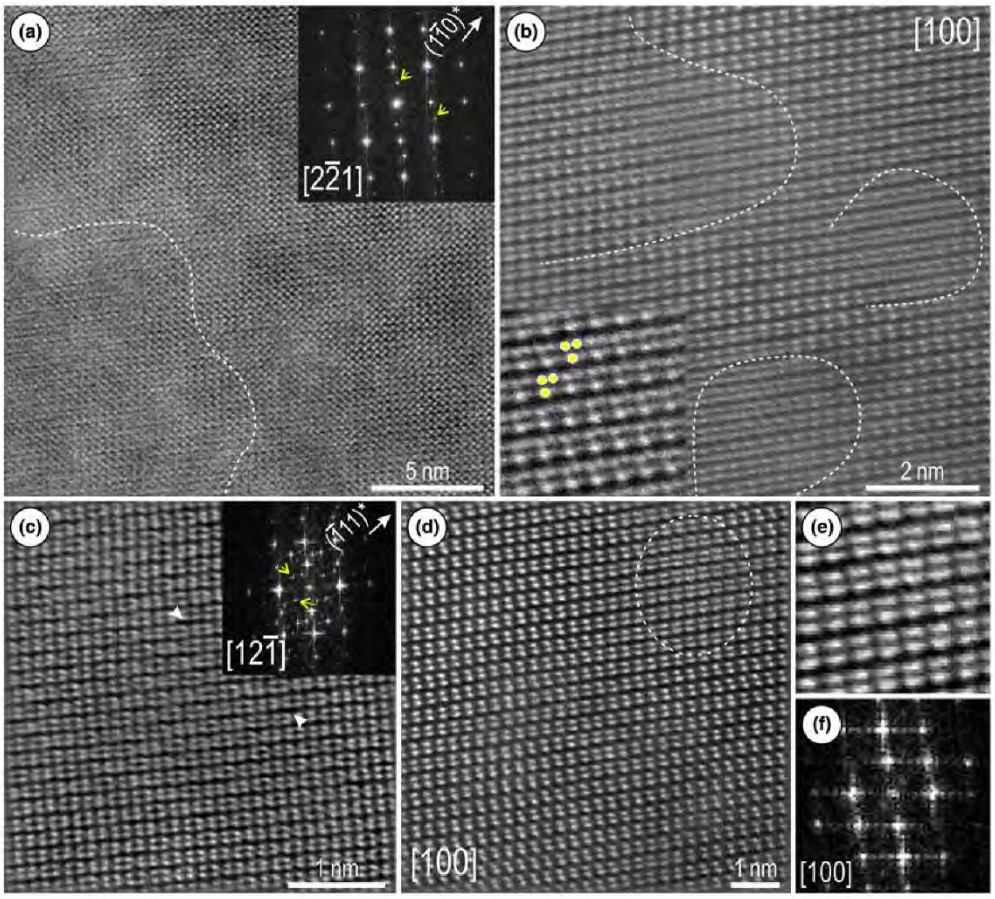

Fig. 8. HAADF STEM images of hematite (Hm) from the W-depleted domain on zone axes as marked (using hexagonal axes) and showing lattice-scale defects and partial superstructuring. (*a*) Domain with superstructuring on $[2\bar{2}1]_{Hm}$ zone axis (dashed line) showing bands (image) and satellite reflections (arrowed). (*b*) Defects on $[100]_{Hm}$ within domains marked by a dashed line showing splitting of Fe columns (inset, marked as dots) by screw dislocations. (*c*) Widening 'gaps' between adjacent rows of Fe dumbbells (arrowed) imaged on $[12\bar{1}]_{Hm}$ producing satellite reflections with modulation on $(\bar{1}11)^*$ imaged (arrowed on FFT, inset). (*d*, *e*) Atom-stretching defects (dashed line on (*d*)) on $[100]_{Hm}$. (f) FFT pattern corresponding to images in (*d*) and (*e*).

Material 2, Fig. S3). Moreover, the scheme of vacancies might vary locally as W and O release is coupled. As more data are acquired, a combination of the two models can be produced.

Discussion

Tracing pseudomorphic replacement reactions from micro to nano scale

Linking observations from micrometre to the nanometre scale, we show how trace-element remobilisation is reflected by crystal-structural order/disorder phenomena at different stages of CDRR.

The fact that a two-fold hematite superstructure is recognised within nanodomains close to the W–Pb-bearing twin crests (Fig. 7) is evidence for the reaction onset, because hematite still retains the W–Sn–U–Pb zonation at the micrometre scale (Figs. 2, 3). Fluid percolation at this stage induces compositional changes at the nanoscale, illustrated by the relative enrichment of W and Pb along the crests of minor twins and conjugated splays (Fig. 5).

As the infiltration rates increase, hematite–fluid interaction is expressed by the appearance of abundant W–Pb-bearing NPs hosted in wider trails and splays, characteristic for the patchy core with relict zoning (Fig. 6*d*–*e*). These splays can be associated with dilation and/or strain associated with fluid-percolation and are comparable with fractures or deformed bands in seismically deformed zircon (Kusiak *et al.*, 2019). Each of these displays complex composition and includes non-formula elements introduced by the fluid. The inclusions along the trails are comparable to those interpreted as fluid inclusions in Cu–As-zoned hematite (Verdugo-Ihl *et al.*, 2019), and represent a further example of how transient porosity, which is intrinsic to CDRR mechanisms, can trap metals and fluid produced during the reaction (Putnis *et al.*, 2005). As shown by Verdugo-Ihl *et al.* (2019), the reprecipitated hematite records two-fold superstructuring close to the inclusion trails.

Recognition of the same two-fold hematite superstructure in the W-depleted domain, displaying preferential removal of W but not Sn (Fig. 2*a*), implies that the reprecipitate transfers the structural identity from earlier stages of replacement. The highest lattice-scale disorder (e.g. screw dislocation defects, or misorientation domains) is nonetheless recorded at this stage when higher rates of infiltration produced lattice strain.

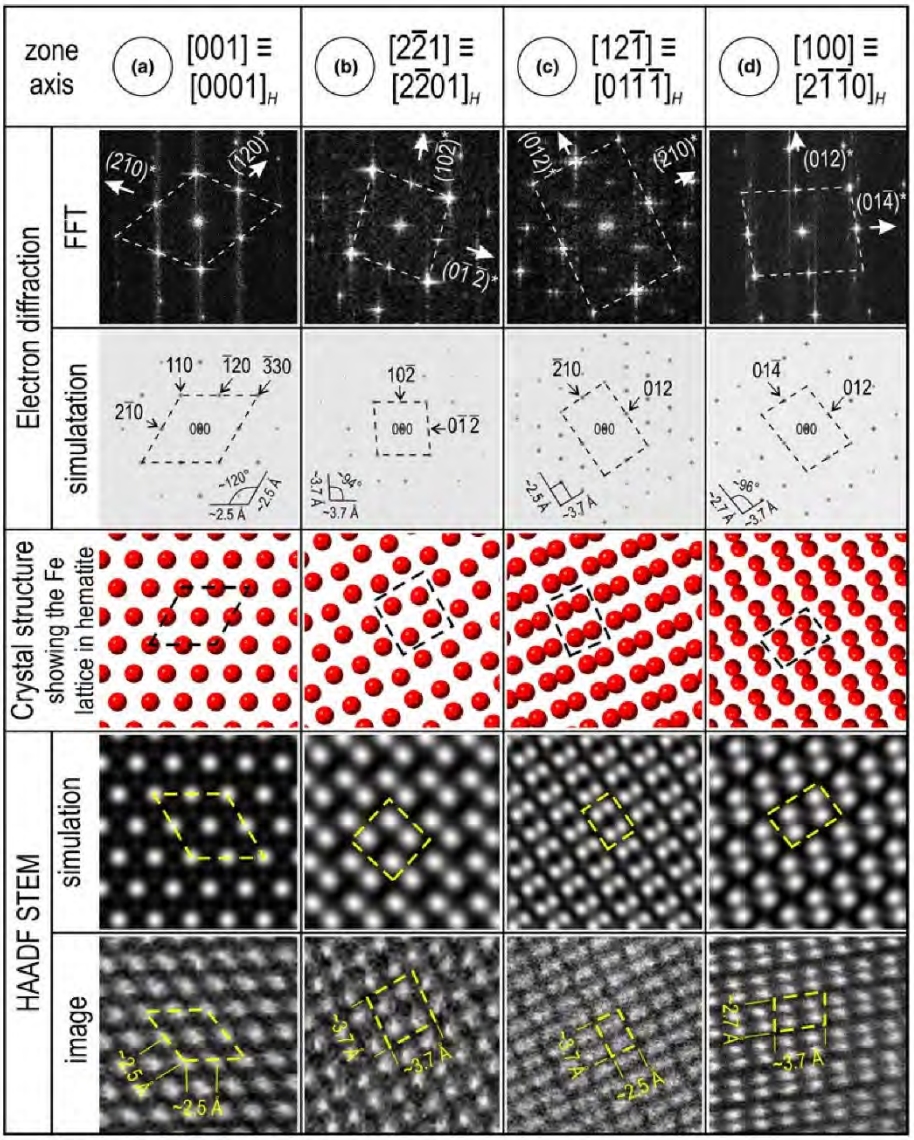

Fig. 9. (*a–d*) Assessment of atomic arrangements on HAADF STEM images obtained from hematite oriented on four main zone axes as marked. For simplicity, indexing of hematite with hexagonal axes (space group $R\bar{3}c$) is shown with three indices but the corresponding four index hexagonal (*H*) zone axis is also given. Crystal structure used for models from Maslen *et al.* (1994). The main repeating motif for each zone axis is marked by dashed lines.

The formation of twins can be constrained as post-dating primary crystal growth as they crosscut initial hematite zoning (Figs 2, 3), but pre-date the replacement reactions. Although the twin planes clearly provide fluid pathways and metal traps, they are not obliterated during progression of CDRR. This effectively means that crystallographic information (including twin orientations) is transmitted from the parent to the new-formed hematite.

Trace-element incorporation into and release from hematite

Although our model for a two-fold hematite superstructure, based on abundant oxygen vacancies (up to $x = 0.75$ to accentuate the vacancy effect on STEM simulations), may be stable only as nanodomains, it reproduces the HAADF STEM images better than the metal vacancy plus protonated oxygen model (McBriarty *et al.*, 2018), or the earlier O vacancy models that do not consider a trigonal symmetry (e.g. Chen *et al.*, 2008). This is nonetheless a simplification of the hematite studied as substitution of several metals (W, Sn, U, Pb) for Fe occurs at varying concentrations throughout both the parent and reprecipitated hematite but has not been considered in the model. HAADF STEM imaging of (Pb, Bi)$_{1-x}$Fe$_{1+x}$O$_{3-y}$ compounds show perovskite-like blocks separated by crystallographic shear planes at different periodicities (Abakumov *et al.*, 2011). Such crystallographic shear planes are also typical of wave-modulation in tungsten compounds with anion deficiency, such as W_nO_{3n-x} ($x = 1, 2$)

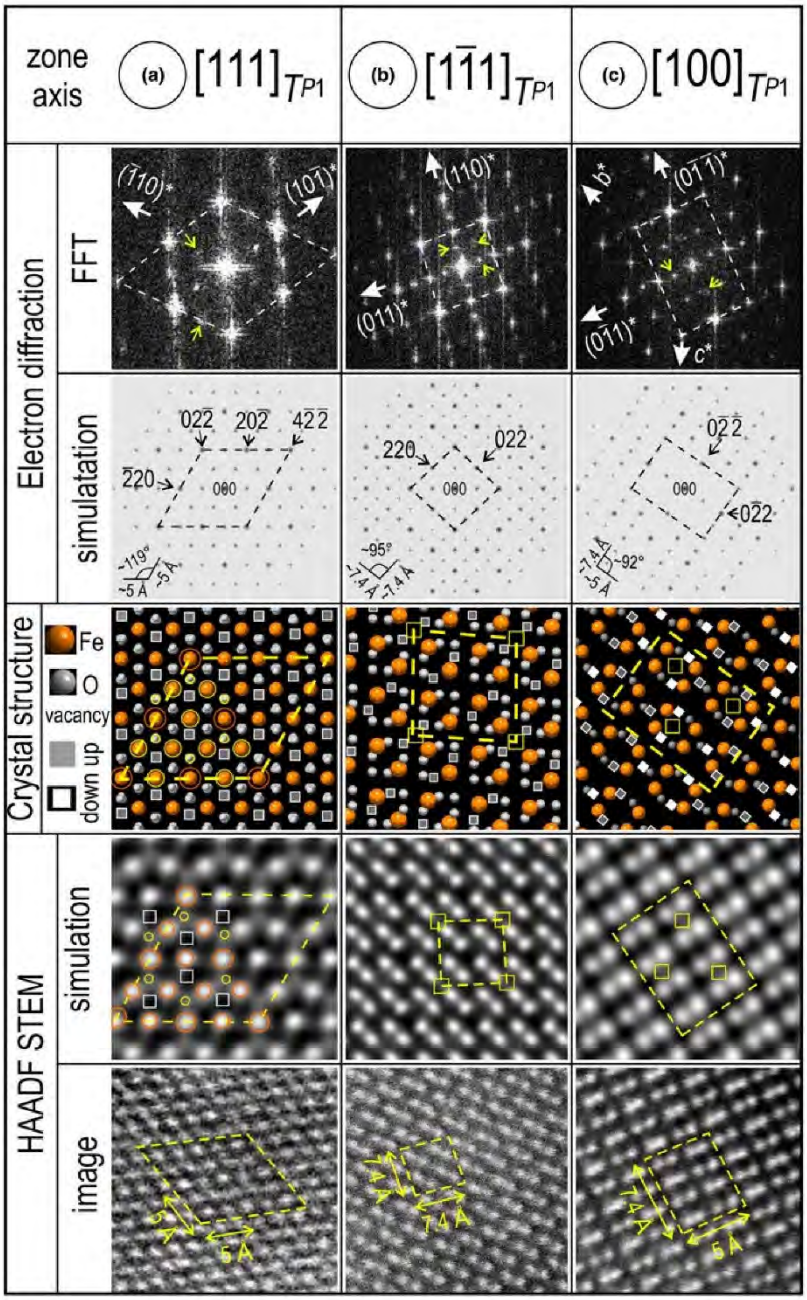

Fig. 10. (*a–c*) Two-fold superstructure with oxygen vacancies in hematite on zone axes as indicated. The three zone axes shown represent a trigonal primitive cell (T) indexed using rhombohedral axes, defined as: $a = b = c = 10.85$ Å; $\alpha = \beta = \gamma = 55.28°$. The main repeating motif for each zone axis is marked by dashed lines. Note they represent 2 × wider 2 motifs relative to corresponding zone axes in hematite from Fig. 9*a–c*. Yellow circles and squares show the 'phantom' effects induced on HAADF STEM simulations and images.

(Abakumov *et al.*, 2006, and references therein) and could explain some of the shear-dislocation defects imaged for hematite (Figs. 7*d*,*f*, 10).

Fluid–mineral interaction during coupled dissolution–reprecipitation is effective in stripping W from hematite, with concentrations reduced by three orders of magnitude whereas Sn behaves as an immobile element (concentrations remain unchanged). If the formation of O vacancies is associated with near complete W release from hematite (enrichment within the twin crest; Fig. 7), this could explain preferential removal relative to Sn if we consider the stability of the two elements during interaction with a fluid that does not show significant f_{O_2} variation (hematite remains stable). At temperatures between 350 and 250°C, W can form two aqueous complexes (H_2WO_4 and HWO_4^-) depending upon fluid pH (low or slightly higher, respectively; Wang *et al.*, 2019). At similar temperature conditions, Sn(IV) has a much lower solubility (Brugger *et al.*, 2016, and references therein) and probably remains in the hematite. It is clear from the micro-scale maps (Fig. 2) that U and Pb, are partially remobilised but are not depleted to the same extent as

W. Moreover, Pb is observed along the twin crests and splays but not in the W-bearing NPs in the same area (Figs 5, 6*a–c*), implying it might not be removed from hematite but rather introduced by the fluids. Nonetheless, both elements are observed in the same inclusions along the trails (Fig. 6*d*), indicating strongly that they partially share the same fate in terms of (re)mobilisation during CDRR.

Trace-element mobility in a mineral geochronometer: implications for U–Pb geochronology

The presence of Pb in hematite can be attributed primarily to decay of U (and Th); thus these elements are coupled on the grain-scale element maps (Fig. 2*a*). Moreover, LA-ICP-MS data for the U–Pb-rich zones are comparable across the W-rich and -depleted domains, indicating that these elements have not been remobilised substantially. Although total Pb concentrations do not exceed ~5 ppm in the affected areas (Supplementary Material 1, Table S1), they can nevertheless be mapped here at the nanoscale (Fig. 5).

Even if in such small quantities and over distances of 1 µm, grain-scale (re)mobilisation of Pb leads to modification of U–Pb isotopic systematics (Fig. 2*b,c*) and thus impacts on the accuracy and precision of hematite age determination at different scales of spatial resolution. This interpretation, invoking Pb migration, is drawn from LA-ICP-MS U–Pb age determination along the high W–U-rich zones of the grain, which produces a spread of reversely to normally discordant data clustering along concordia on a Tera–Wasserburg diagram (Fig. 2*b,c*). Although arguable in terms of potential analytical artefacts generated by the lack of a matrix-matched reference material, the $^{207}Pb/^{206}Pb$ date obtained (1597 ± 12 Ma) is in agreement with more robust ages from Olympic Dam (Courtney-Davies *et al.*, 2019; 2020).

Disturbance of isotope systematics attributed to coupled dissolution–reprecipitation was invoked for compositionally zoned monazite displaying decoupled U–Pb ages (Weinberg *et al.*, 2020). This case differs, however, from that presented here in that Weinberg *et al.* (2020) report no obvious link between U–Pb age, composition, and spot analysis position in the case of the monazite they studied. These authors speculate about a behaviour analogous to hematite as previously reported by the present authors (Verdugo-Ihl *et al.*, 2017). We endorse such an interpretation while adding that the spatial relationship between domains from which elements have been remobilised and those where the elements have been reprecipitated might only be recognisable at resolutions approaching atomic-scale, i.e. at scales below which accurate age determination can be performed. Mobilisation of radiogenic Pb in zircon is also shown at the micrometre scale for otherwise pristine, oscillatory zoned zircon (Kusiak *et al.*, 2013). In our case, the clear disturbance of U–Pb ratios is observed in parts of the grain where evidence for the onset of CDDR is preserved. Analogous to the Pb enrichment we have mapped along twin crests 2–3 nm in width, Pb-rich domains some ~50 nm wide were documented from monazite that displayed discordant U–Th–Pb ages (Seydoux-Guillaume *et al.*, 2003).

Atom probe tomography (APT) has been used to demonstrate nm-scale Pb mobility resulting in high $^{207}Pb/^{206}Pb$, recognised as isolated nanoclusters enriched in incompatible elements within Hadean zircon (Valley *et al.*, 2014). The authors interpreted this as evidence for intra-grain element mobility without implications for age accuracy at the resolution of a SIMS spot analysis, thus concluding closed rather than open system (U–Pb) behaviour in zircon at the micrometre scale. The presence of Pb as metallic Pb-nanospheres, Pb-oxide NPs, or Pb-bearing clusters, has been documented in zircon and monazite affected by ultra-high temperature (UHT) metamorphism (Kusiak *et al.*, 2013, 2015, 2019; Whitehouse *et al.*, 2017; Seydoux-Guillaume *et al.*, 2019). The formation of Pb nanospheres at the same time as healing of radiation damage in zircon during the UHT event prohibits Pb loss from zircon, as shown by nanoSIMS age determination, i.e. distinct model ages for metamorphism (nanospheres) and crystallisation of host zircon (Lyon *et al.*, 2019). Likewise, APT age determination of Pb-bearing clusters in monazite (Seydoux-Guillaume *et al.*, 2019) returned an age interval considered to represent the duration of the UHT event rather than Pb/Th open-system behaviour. However, $^{208}Pb/^{232}Th$ ages extracted from these analyses were subsequently shown as inaccurate, as previous studies had overestimated systematically the $^{208}Pb/^{232}Th$ ratio (Fougerouse *et al.*, 2020).

Previous examples are distinct from the hematite discussed here, in which Pb-bearing twin crests are opened by dilational jogs and pores (Figs. 5 and 7), indicating mineral interaction with fluids derived outside the grain. Overprinting of Pb-bearing sulfides/chalcogenides and U-bearing minerals (hematite, uraninite, etc.), is observed in Olympic Dam ores (Macmillan *et al.*, 2016a,b; Verdugo-Ihl *et al.*, 2017; 2019; Rollog *et al.*, 2019a) and can provide a source of Pb external to the grain. However, whether this hematite grain has lost radiogenic Pb, or gained unsupported Pb, during fluid–mineral interaction is difficult to unequivocally determine without nanoscale age determination or U/Pb ratio measurements of or within the individual domains (nanoSIMS or APT). To constrain conclusively Pb diffusion, or Pb gain within hematite, mapping of fine oscillatory zones by nanoSIMS might resolve differences in U/Pb and Pb/Pb at a much higher spatial resolution than LA-ICP-MS. Therefore, although we show evidence for Pb clusters being trapped along fluid-inclusion trails (Fig. 6*d*), we cannot fingerprint the pathways of such Pb relative to host hematite.

Implications

This study documents an example of 'isomineral' pseudomorphic replacement (W-bearing hematite by hematite) which is traceable by compositional and crystal-structural modifications. We show that hematite will carry crystallographic information from initial dissolution to the final stages of reprecipitation.

The results emphasise the importance of multiple sets of twin planes and their secondary structures (splays) in driving fluid percolation and providing traps for released metals. Twin boundaries were previously discussed as planes of oxidation and element redistribution, e.g. in twinned sphalerite (Šrot *et al.*, 2003; Ciobanu *et al.*, 2011). Twin-controlled fluid–mineral interaction during sericite alteration is demonstrated in Cu–As-bearing hematite from a location at Olympic Dam, ~200 m above the present sample (Verdugo-Ihl *et al.*, 2019). It is probable that the primary zoned hematite from this part of the deposit, close to a major fault system, with ~800 m vertical displacement, was affected during fault reactivation as suggested from Fe oxides study in the immediate outer shell (Verdugo-Ihl *et al.*, 2020).

Isotope disturbances in radioactive minerals from Olympic Dam have been demonstrated for compositionally zoned uraninite exhibiting lattice distortion (Macmillan *et al.*, 2016*b*). Microstructural analysis has shown crystal-plastic deformation of uraninite via formation and migration of defects and

dislocations into tilt boundaries with implication for the incorporation and release of daughter radioisotopes. Multi-technique evaluation of hematite U–Pb isotope systematics, has shown the presence of common Pb in domains of oscillatory zoned hematite overprinted by micro-fracturing, indicating open system behaviour of such grains (e.g. sample LCD4; Courtney-Davies *et al.*, 2019). Indeed, open-system behaviour of either hematite or uraninite, can be postulated from the widespread decoupling of daughter radionuclides from parent isotopes that has been documented in various minerals from Olympic Dam (Rollog *et al.*, 2019*b*,*c*). Regardless, and dependent on fluid parameters and composition of the parent hematite, replacement products of CDRR can be highly variable in terms of the trace-element endowment of the reprecipitate and associated nanomineral inclusions. For example, uraninite rather than Pb-bearing NPs are produced along the interface between a reprecipitated hematite grain core rich in REE–fluorocarbonate inclusions and the U–W–Sn–Mo-zoned margin (Cook *et al.*, 2017; Verdugo-Ihl *et al.*, 2017).

Further work to clarify open *versus* closed system behaviour at the nanoscale should include determination of the ages of distinct domains in the hematite studied here. Such studies would also solve an important problem for the Olympic Dam deposit, whether trace-element remobilisation is confined to the brecciation event within a few Ma of the onset of IOCG system formation (Courtney-Davies *et al.*, 2020), or is due to a later overprint event, hundred(s) of Ma after formation.

Conclusions

Key observations resulting from this study are:

(1) Grain-scale remobilisation of trace elements (W and Pb) during coupled dissolution–reprecipitation reactions is associated with crystal structural modifications in hematite.
(2) A two-fold hematite superstructure model with oxygen vacancies was constructed and assessed by STEM simulations and shows good agreement with HAADF STEM imaging. This model accounts for W release from the studied hematite but could be further tested for W incorporation into this mineral.
(3) Lead mobilisation, confirmed here at the nanoscale, is responsible for U–Pb isotope disturbances in hematite. This implies that perturbations of isotopic systems in mineral geochronometers are readily traceable at the nanoscale despite being invisible at the micrometre scale.
(4) Twinning in minerals provides ideal pathways for fluid percolation and metal entrapment and thus their presence, particularly as conjugate sets, can be an indicator of open system behaviour, thus directly affecting the robustness of the hematite geochronometer, although this would need to be validated by further work.

Supplementary material. To view supplementary material for this article, please visit https://doi.org/10.1180/mgm.2020.49.

Acknowledgements. This work was funded by the 'FOX' project (Trace elements in iron oxides: deportment, distribution and application in ore genesis, geochronology, exploration and mineral processing), supported by BHP Olympic Dam and the South Australian Government Mining and Petroleum Services Centre of Excellence. N.J.C. acknowledges support from the ARC Research Hub for Australian Copper–Uranium (Grant IH130200033). We appreciate the positive and constructive comments of two journal reviewers and Principal Editor Roger Mitchell.

References

Abakumov, A.M., Hadermann, J., Bals, S., Nikolaev, I.V., Antipov, E.V. and Van Tendeloo, G. (2006) Crystallographic shear structures as a route to anion-deficient perovskites. *Angewandte Chemie International Edition*, **45**, 6697–6700. https://dx.doi.or/10.1002/anie.200602480

Abakumov, A.M., Batuk, D., Hadermann, J., Rozova, M.G., Sheptyakov, D.V., Tsirlin, A.A., Niermann, D., Waschkowski, F., Hemberger, J., Van Tendeloo, G. and Antipov, E.V. (2011) Antiferroelectric $(Pb,Bi)_{1-x}Fe_{1+x}O_{3-y}$ perovskites modulated by crystallographic shear planes. *Chemistry of Materials*, **23**, 255–265. https://dx.doi.org/10.1021/cm102907h

Brugger, J., Liu, W., Etschmann, B., Mei, Y., Sherman, D.M. and Testemale, D. (2016) A review of the coordination chemistry of hydrothermal systems, or do coordination changes make ore deposits? *Chemical Geology*, **447**, 219–253. https://dx.doi.org/10.1016/j.chemgeo.2016.10.021

Bykova, E., Dubrovinsky, L., Dubrovinskaia, N., Bykov, M., McCammon, C., Ovsyannikov, S.V., Liermann, H.-P., Kupenko, I., Chumakov, A.I., Rüffer, R., Hanfland, M. and Prakapenka, V. (2016) Structural complexity of simple Fe_2O_3 at high pressures and temperatures. *Nature Communications*, **7**, 10661. https://dx.doi.org/10.1038/ncomms10661

Chen, Z., Cvelbar, U., Mozetič, M., He, J. and Sunkara, M.K. (2008) Long-range ordering of oxygen-vacancy planes in α-Fe_2O_3 nanowires and nanobelts. *Chemistry of Materials*, **20**, 3224–3228. https://dx.doi.org/10.1021/cm800288y

Ciobanu, C.L., Cook, N.J., Utsunomiya, S., Pring, A. and Green, L. (2011) Focussed ion beam-transmission electron microscopy applications in ore mineralogy: Bridging micro- and nanoscale observations. *Ore Geology Reviews*, **42**, 6–31. https://dx.doi.org/10.1016/j.oregeorev.2011.06.012

Ciobanu, C.L., Wade, B.P., Cook, N.J., Schmidt Mumm, A. and Giles, D. (2013) Uranium-bearing hematite from the Olympic Dam Cu–U–Au deposit, South Australia: A geochemical tracer and reconnaissance Pb–Pb geochronometer. *Precambrian Research*, **238**, 129–147. https://dx.doi.org/10.1016/j.precamres.2013.10.007

Ciobanu, C., Cook, N., Maunders, C., Wade, B. and Ehrig, K. (2016) Focused ion beam and advanced electron microscopy for minerals: Insights and outlook from bismuth sulphosalts. *Minerals*, **6**, 112. https://dx.doi.org/10.3390/min6040112

Cook, N., Ciobanu, C., Ehrig, K., Slattery, A., Verdugo-Ihl, M., Courtney-Davies, L. and Gao, W. (2017) Advances and opportunities in ore mineralogy. *Minerals*, **7**, 233. https://dx.doi.org/10.3390/min7120233

Courtney-Davies, L., Tapster, S.R., Ciobanu, C.L., Cook, N.J., Verdugo-Ihl, M.R., Ehrig, K.J., Kennedy, A.K., Gilbert, S.E., Condon, D.J. and Wade, B.P. (2019) A multi-technique evaluation of hydrothermal hematite U Pb isotope systematics: Implications for ore deposit geochronology. *Chemical Geology*, **513**, 54–72. https://dx.doi.org/10.1016/j.chemgeo.2019.03.005

Courtney-Davies, L., Ciobanu, C.L., Tapster, S.R., Cook, N.J., Ehrig, K., Crowley, J.L., Verdugo-Ihl, M.R., Wade, B.P. and Condon, D.J. (2020) Opening the magmatic-hydrothermal window: High-precision U-Pb geochronology of the Mesoproterozoic Olympic Dam Cu-U-Au-Ag deposit, South Australia. *Economic Geology* (in press).

Fougerouse, D., Kirkland, C., Saxey, D., Seydoux-Guillaume, A.-M., Rowles, M.R., Rickard, W.D. and Reddy, S.M. (2020) Nanoscale Isotopic Dating of Monazite. *Geostandards and Geoanalytical Research*, in press. https://dx.doi.org/10.1111/ggr.12340

Kusiak, M.A., Whitehouse, M.J., Wilde, S.A., Wilde, S.A., Nemchin, A.A. and Clark, C. (2013) Mobilization of radiogenic Pb in zircon revealed by ion imaging: Implications for early Earth geochronology. *Geology*, **41**, 291–294. https://dx.doi.org/10.1130/G33920.1

Kusiak, M.A., Dunkley, D.J., Wirth, R., Whitehouse, M.J., Wilde, S. and Marquardt, K. (2015) Metallic lead nanospheres discovered in ancient zircons. *Proceedings of the National Academy of Science*, **112**, 4958–4963. https://dx.doi.org/10.1073/pnas.1415264112

Kusiak, M.A., Kovaleva, E., Wirth, R., Klötzli, U., Dunkley, D.J., Yi, K. and Lee, S. (2019) Lead oxide nanospheres in seismically deformed zircon grains.

Geochimica et Cosmochimica Acta, **262**, 20–30. https://dx.doi.org/10.1016/j.gca.2019.07.026

Lee, S. and Xu, H. (2016) Size-dependent phase map and phase transformation kinetics for nanometric iron(III) oxides ($\gamma \rightarrow \varepsilon \rightarrow \alpha$ pathway). *The Journal of Physical Chemistry C*, **120**, 13316–13322. https://dx.doi.org/10.1021/acs.jpcc.6b05287

Lyon, I.C., Kusiak, M.A., Wirth, R., Whitehouse, M.J., Dunkley, D.J., Wilde, S.A., Schaumlöffel, D., Malherbe, J. and Moore, K.L. (2019) Pb nanospheres in ancient zircon yield model ages for zircon formation and Pb mobilization. *Scientific Reports*, **9**, 13702. https://dx.doi.org/10.1038/s41598-019-49882-8

Macmillan, E., Ciobanu, C.L., Ehrig, K., Cook, N.J. and Pring, A. (2016*a*) Replacement of uraninite by bornite via coupled dissolution-reprecipitation: Evidence from texture and microstructure. *The Canadian Mineralogist*, **54**, 1369–1383. https://dx.doi.org/10.3749/canmin.1600031

Macmillan, E., Ciobanu, C.L., Ehrig, K., Cook, N.J. and Pring, A. (2016*b*) Chemical zoning and lattice distortion in uraninite from Olympic Dam, South Australia. *American Mineralogist*, **101**, 2351–2354. https://dx.doi.org/10.2138/am-2016-5753

Maslen, E.N., Streltsov, V.A., Streltsova, N.R. and Ishizawa, N. (1994) Synchrotron X-ray study of the electron density in alpha-Fe_2O_3. *Acta Crystallographica B*, **50**, 435–441. https://dx.doi.org/10.1107/S0108768194002284

McBriarty, M.E., Kerisit, S., Bylaska, E.J., Shaw, S., Morris, K. and Ilton, E.S. (2018) Iron vacancies accommodate uranyl incorporation into hematite. *Environmental Science & Technology*, **52**, 6282–6290. https://dx.doi.org/10.1021/acs.est.8b00297

Putnis, A. (2009) Mineral replacement reactions. Pp. 87–124 in: *Thermodynamics and Kinetics of Water-Rock Interactions* (E.H. Oelkers and J. Schott, editors). Reviews in Mineralogy and Geochemistry, **70**, Mineralogical Society of America, Chantilly, Virginia, USA. https://dx.doi.org/10.2138/rmg.2009.70.3

Putnis, C.V., Tsukamoto, K. and Nishimura, Y. (2005) Direct observations of pseudomorphism: compositional and textural evolution at a fluid-solid interface. *American Mineralogist*, **90**, 1909–1912. https://dx.doi.org/10.2138/am.2005.1990

Rollog, M., Cook, N.J., Guagliardo, P., Ehrig, K., Ciobanu, C.L. and Kilburn, M. (2019*a*) Detection of trace elements/isotopes in Olympic Dam copper concentrates by nanoSIMS. *Minerals*, **9**, 336. https://dx.doi.org/10.3390/min9060336

Rollog, M., Cook, N.J., Guagliardo, P., Ehrig, K. and Kilburn, M. (2019*b*) In situ spatial distribution mapping of radionuclides in minerals by nanoSIMS. *Geochemistry: Exploration, Environment, Analysis*, **19**(3), 245–254. https://dx.doi.org/10.1144/geochem2018-038

Rollog, M., Cook, N.J., Guagliardo, P., Ehrig, K.J. and Kilburn, M. (2019*c*) Radionuclide-bearing minerals in Olympic Dam copper concentrates. *Hydrometallurgy*, **189**, 105153. https://dx.doi.org/10.1016/j.hydromet.2019.105153

Seydoux-Guillaume, A.-M., Goncalves, P., Wirth, R. and Deutsch, A. (2003) Transmission electron microscope study of polyphase and discordant monazites: Site-specific specimen preparation using the focused ion beam technique. *Geology*, **31**, 973–976. https://dx.doi.org/10.1130/G19582.1

Seydoux-Guillaume, A.-M., Fougerouse, D., Laurent, A.T., Gardés, E., Reddy, S.M. and Saxey, D.W. (2019) Nanoscale resetting of the Th/Pb system in an isotopically-closed monazite grain: A combined atom probe and transmission electron microscopy study. *Geosciences Frontiers*, **10**, 65–76. https://dx.doi.org/10.1016/j.gsf.2018.09.004

Šrot, V., Rečnik, A., Scheu, C., Šturm, S. and Mirtič, B. (2003) Stacking faults and twin boundaries in sphalerite crystals from the Trepča mines in Kosovo. *American Mineralogist*, **88**, 1809–1816. https://dx.doi.org/10.2138/am-2003-11-1222

Valley, J.W., Cavosie, A.J., Ushikubo, T., Reinhard, D.A., Lawrence, D.F., Larson, D.J., Clifton, P.H., Kelly, T.F., Wilde, S.A., Moser, D.E. and Spicuzza, M.J. (2014) Hadean age for a post-magma-ocean zircon confirmed by atom-probe tomography. *Nature Geosciences*, **7**, 219–223. https://dx.doi.org/10.1038/ngeo2075

van Achterbergh, E., Ryan, C.G., Jackson, S.E. and Griffin, W.L. (2001) Data reduction software for LA-ICP-MS. Pp. 239–243 in: *Laser-ablation-ICPMS in the Earth Sciences; Principles and applications* (Sylvester P.J., editor). Short Course Series, **29.** Mineralogical Association of Canada.

Van Tendeloo, G., Bals, S., Van Aert, S., Verbeeck, J. and Van Dyck, D. (2012) Advanced electron microscopy for advanced materials. *Advanced Materials*, **24**, 5655–5675. https://dx.doi.org/10.1002/adma.201202107

Verdugo-Ihl, M.R., Ciobanu, C.L., Cook, N.J., Ehrig, K.J., Courtney-Davies, L. and Gilbert, S. (2017) Textures and U-W-Sn-Mo signatures in hematite from the Olympic Dam Cu-U-Au-Ag deposit, South Australia: Defining the archetype for IOCG deposits. *Ore Geology Reviews*, **91**, 173–195. https://dx.doi.org/10.1016/j.oregeorev.2017.10.007

Verdugo-Ihl, M.R., Ciobanu, C.L., Slattery, A., Cook, N.J., Ehrig, K. and Courtney-Davies, L. (2019) Copper-arsenic nanoparticles in hematite: Fingerprinting fluid–mineral interaction. *Minerals*, **9**, 388. https://dx.doi.org/10.3390/min9070388

Verdugo-Ihl, M.R., Ciobanu, C.L., Cook, N.J., Ehrig, K.J. and Courtney-Davies, L. (2020) Defining early stages of IOCG systems: evidence from iron oxides in the outer shell of the Olympic Dam deposit, South Australia. *Mineralium Deposita*, **55**, 429–452. https://dx.doi.org/10.1007/s00126-019-00896-2

Wang, X.-S., Timofeev, A., Williams-Jones, A.E., Shang, L.-B. and Bi, X.-W. (2019) An experimental study of the solubility and speciation of tungsten in NaCl-bearing aqueous solutions at 250, 300, and 350°C. *Geochimica et Cosmochimica Acta*, **265**, 313–329. https://dx.doi.org/10.1016/j.gca.2019.09.013

Weinberg, R.F., Wolfram, L.C., Nebel, O., Hasalová, P., Závada, P., Kylander-Clark, A.R.C. and Becchio, R. (2020) Decoupled U-Pb date and chemical zonation of monazite in migmatites: The case for disturbance of isotopic systematics by coupled dissolution-reprecipitation. *Geochimica et Cosmochimica Acta*, **269**, 398–412. https://dx.doi.org/10.1016/j.gca.2019.10.024

Whitehouse, M.J., Kusiak, M.A., Wirth, R., and Ravindra Kumar, G.R. (2017) Metallic Pb nanospheres in ultra-high temperature metamorphosed zircon from southern India. *Mineralogy and Petrology*, **111**, 467–474. https://dx.doi.org/10.1007/s00710-017-0523-1

Xia, F., Brugger, J., Chen, G., Ngothai, Y., O'Neill, B., Putnis, A. and Pring, A. (2009) Mechanism and kinetics of pseudomorphic mineral replacement reactions: A case study of the replacement of pentlandite by violarite. *Geochimica et Cosmochimica Acta*, **73**, 1945–1969. https://dx.doi.org/10.1016/j.gca.2009.01.007

CHAPTER 6

NANOMINERALOGY OF HYDROTHERMAL MAGNETITE FROM ACROPOLIS, SOUTH AUSTRALIA: GENETIC IMPLICATIONS FOR IRON–OXIDE COPPER GOLD MINERALIZATION

Max R. Verdugo-Ihl [1], Cristiana L. Ciobanu [1], Nigel J. Cook [1], Kathy Ehrig [2],

Ashley Slattery [3], Liam Courtney-Davies [1], and Marija Dmitrijeva [1]

[1]*School of Chemical Engineering and Advanced Materials, The University of Adelaide, Adelaide, SA 5005, Australia;*

[3]*BHP Olympic Dam, 10 Franklin St, Adelaide SA, 5000, Australia;*

[2]*Adelaide Microscopy, The University of Adelaide, Adelaide, SA 5005, Australia*

Article accepted for publication in *American Mineralogist*, October 4th, 2020.

Statement of Authorship

Title of Paper	Nanomineralogy of hydrothermal magnetite from Acropolis, South Australia: Genetic implications for iron–oxide copper gold mineralization
Publication Status	☐ Published ☑ Accepted for Publication ☐ Submitted for Publication ☐ Unpublished and Unsubmitted w ork w ritten in manuscript style
Publication Details	Verdugo-Ihl, M.R., Ciobnau, C.L., Cook, N.J., Ehrig, K., Slattery, A., Courtney-Davies, L., Dmitrijeva, M. Nanomineralogy of hydrothermal magnetite from Acropolis, South Australia: Genetic implications for iron–oxide copper gold mineralization. American Mineralogist, in press. https://doi.org/10.2138/am-2020-7557.

Principal Author

Name of Principal Author (Candidate)	Max R. Verdugo-Ihl		
Contribution to the Paper	Performed analytical work, evaluation and interpretation of results and prepared the manuscript.		
Overall percentage (%)	55		
Certification:	This paper reports on original research I conducted during the period of my Higher Degree by Research candidature and is not subject to any obligations or contractual agreements with a third party that would constrain its inclusion in this thesis. I am the primary author of this paper.		
Signature		Date	15.04.2020

Co-Author Contributions

By signing the Statement of Authorship, each author certifies that:

i. the candidate's stated contribution to the publication is accurate (as detailed above);

ii. permission is granted for the candidate in include the publication in the thesis; and

iii. the sum of all co-author contributions is equal to 100% less the candidate's stated contribution.

Name of Co-Author	Cristiana L. Ciobanu		
Contribution to the Paper	Helped to define the direction of the manuscript, guided manuscript preparation and assisted with data acquisition, the interpretation of the results and evaluation of the manuscript.		
Overall percentage (%)	25		
Signature		Date	15.04.2020

Name of Co-Author	Nigel J. Cook		
Contribution to the Paper	Assisted with the preparation and evaluation of the manuscript.		
Overall percentage (%)	10		
Signature		Date	15.04.2020

Name of Co-Author	Kathy Ehrig		
Contribution to the Paper	Assisted with the evaluation of the manuscript.		
Overall percentage (%)	3		
Signature		Date	15.04.2020

Name of Co-Author	Ashley Slattery		
Contribution to the Paper	Performed HAADF-STEM data acquisition.		
Overall percentage (%)	3		
Signature		Date	15.04.20

Name of Co-Author	Liam Courtney-Davies		
Contribution to the Paper	Assisted with the evaluation of the manuscript.		
Overall percentage (%)	2		
Signature		Date	15.04.2020

Name of Co-Author	Marija Dmitrijeva		
Contribution to the Paper	Assisted with the evaluation of compositional data analysis and geological modelling.		
Overall percentage (%)	2		
Signature		Date	15.04.2020

Nanomineralogy of hydrothermal magnetite from Acropolis, South Australia: Genetic implications for iron-oxide copper gold mineralization

MAX R. VERDUGO-IHL[1,*], CRISTIANA L. CIOBANU[1], NIGEL J. COOK[1], KATHY EHRIG[2], ASHLEY SLATTERY[3], LIAM COURTNEY-DAVIES[1], MARIJA DMITRIJEVA[1]

[1] *School of Chemical Engineering and Advanced Materials, The University of Adelaide, Adelaide, SA 5005, Australia*

[2] *BHP Olympic Dam, 10 Franklin Street, Adelaide SA, 5000, Australia*

[3] *Adelaide Microscopy, The University of Adelaide, Adelaide, SA, 5005, Australia*

ABSTRACT

Magnetite is the dominant Fe-oxide at the Acropolis IOCG prospect, Olympic Dam district, South Australia. Complementary microbeam techniques, including scanning transmission electron microscopy (STEM), are used to characterize titanomagnetite from veins in volcanic rocks and Ti-poor magnetite from a granite body with uplifted position in the volcanic sequence. A temperature of 670±50 °C is estimated for Ti-poor magnetite using X_{Mg}-in-magnetite thermometry. Titanomagnetite, typified by Ti-rich trellis lamellae of ilmenite in magnetite, also displays sub-µm inclusions forming densely mottled and orbicular subtypes of titanomagnetite with increasing degree of overprinting. STEM analysis shows nanoparticles (NPs) of spinels and TiO_2 polymorphs, anatase and rutile. These vary as: dense, finest-scale, monophase-NPs of spinel *sensu stricto* in Ti-poor magnetite; two-phase, ulvöspinel-hercynite NPs in primary titanomagnetite; and coarser clusters of NPs (hercynite±gahnite+TiO_2-polymorphs), in mottled and orbicular subtypes. Nano-thermobarometry using ilmenite-magnetite pairs gives temperatures in the range ~510-570 (±50) °C, with mineral-pair re-equilibration from primary to orbicular titanomagnetite constrained by changes in fO_2 from

* Corresponding author. e-mail address: max.verdugoihl@adelaide.edu.au

ilmenite-stable to magnetite+hematite-stable conditions. Epitaxial relationships between spinel and Fe-Ti-oxides along trellis lamellae and among phases forming the NPs support exsolution from magnetite$_{ss}$, followed by replacement via mineral-buffered reactions. Lattice-scale intergrowths between ulvöspinel and ilmenite within NPs are interpreted as exsolution recording cooling under O_2-conserving conditions, whereas the presence of both TiO_2-polymorphs displaying variable order-disorder phenomena is evidence for subtly fO_2-buffered reactions from anatase (reducing) to rutile (more oxidizing) stabilities. Transient formation of O-deficient phases is retained during replacement of ilmenite by anatase displaying crystallographic-shear planes. Development of dense inclusion mottling and orbicular textures are associated with NP coarsening and clustering during vein re-opening. Fluid-assisted replacement locally recycles trace elements, forming gahnite NPs or discrete Sc-Ti-phases. Hydrothermal titanomagnetite from Acropolis is comparable with magmatic magnetite in granites across the district and typifies early, alkali-calcic alteration. Open-fracture circulation, inhibiting additional supply of Si, Ca, K, etc. during magnetite precipitation, prohibits formation of silician magnetite hosting calc-silicate NPs, as known from IOCG systems characterized by rock-buffered alteration of host lithologies. Obliteration of trellis textures during subsequent overprinting could explain the scarcity of this type of hydrothermal magnetite in other IOCG systems.

Keywords: titanomagnetite, HAADF STEM, nanoparticles, spinels, Fe-Ti-oxides, IOCG, Acropolis

INTRODUCTION

Magnetite and related spinel group minerals are common accessories in igneous rocks, forming during magmatic crystallization, often before the rock-forming silicates (Bowles et al. 2011). The ubiquitous presence of Ti in igneous magnetite and the occurrence of ilmenite lamellae along crystallographic directions (trellis titanomagnetite) has prompted development

of thermobarometric models based upon magnetite-ilmenite pairs with equilibration T-fO_2 conditions constrained from experimental studies (e.g., Buddington and Lindsley 1964). Such models have been widely applied to magnetite-ilmenite pairs at the micron-scale, and recently also at the nanoscale (Righter et al. 2014).

Titanomagnetite formed from Fe-rich melts display the greatest Ti concentrations and most varied textures. These represent the main ore component of large Fe-Ti-V-deposits hosted by layered intrusions (e.g., Zhou et al. 2005). Sizable accumulations of Ti-bearing, trellis-free magnetite are known from several deposits and are subject to an ongoing debate in recent literature in terms of magmatic versus hydrothermal origins. The Los Colorados deposit (Chile) is one example where nanoscale characterization of magnetite has been used to support a hydrothermal origin (Deditius et al. 2018).

In contrast, silician magnetite is known from deposits spanning the magmatic-hydrothermal spectrum, as well as in banded iron formation deposits (Ciobanu et al. 2019). Recent studies using scanning transmission electron microscopy (STEM), and particularly Z-contrast imaging techniques, have shown that silician magnetite contains Si-Fe-nanoprecipitates and other nanoscale silicate inclusions (Xu et al. 2014; Ciobanu et al. 2019). Likewise, comparable STEM studies have shown the ultrafine nature of spinel-ilmenite associations from titanomagnetite in layered intrusions, thus providing new petrogenetic insights into their genesis (Gao et al. 2019a, 2019b).

Hydrothermal magnetite is one of the Fe-oxides typifying alteration in iron-oxide cooper gold (IOCG) deposits, and is a predominant Fe-oxide at Acropolis, Olympic Dam district, South Australia (e.g., Ehrig et al. 2017; Fig. 1a). Acropolis magnetite is reported as Ti-rich, with trellis-type lamellae (Krneta et al. 2017; Courtney-Davies et al. 2019a).

We address the Acropolis magnetite at the micron- and nanoscales to understand how minor and trace element geochemical signatures relate to nanoscale features. We show that magnetite nanomineralogy can support genetic interpretation of spinel associations and their

transformations using atomic-scale, Z-contrast imaging. The results provide new petrogenetic insights allowing formation conditions for IOCG mineralization in the Olympic Dam district and elsewhere to be constrained.

GEOLOGICAL BACKGROUND

The Olympic Dam deposit and two prospects located ~20-25 km to the south, Acropolis and Wirrda Well, represent a spectrum of IOCG-style mineralization in the Olympic Dam district, the best metal endowed part of the Mesoproterozoic Olympic Cu-Au Province, eastern Gawler Craton (Fig. 1). Although they share brecciation and IOCG-type alteration, they differ in terms of host lithologies and predominant mineralization styles (Ehrig et al. 2017).

The Acropolis prospect, placed on the eastern side of the largest geophysical anomaly in the district (e.g., Dmitrijeva et al. 2019a; McPhie et al. 2020), ~10 times larger than Olympic Dam. Mineralization is predominantly hosted within rocks from the Gawler Range Volcanics (GRV) but also in a granite of Hiltaba Suite (HS) affiliation (Fig. 1a, b; McPhie et al. 2020). Uranium-Pb high-precision, chemical abrasion-isotope-dilution-thermal ionization mass spectrometry (CA-ID-TIMS) dating of zircon from GRV and HS granite yield 1594.03±0.68 Ma and 1594.88±0.50 Ma, respectively (McPhie et al. 2020), not clearly resolving the temporal relationships between these rocks, even though the slightly older age for the HS granite could be correlated with fault uplift of this block (Fig. 1c).

Lithologies of the GRV are predominantly interpreted as lavas and ignimbrites with relationships to the granite obscured by intense brecciation (McPhie et al. 2020; Fig. 1). The Acropolis HS granite age is ~1 My older than the Roxby Down Granite host to the mineralized breccia body at Olympic Dam (for which CA-ID-TIMS zircon dating yields 1593.03±0.21 Ma and 1593.28±0.26 Ma; Cherry et al. 2018; Courtney-Davies et al. 2020). These data suggest sequential stages of granite emplacement within a ~1 My timeframe throughout the district.

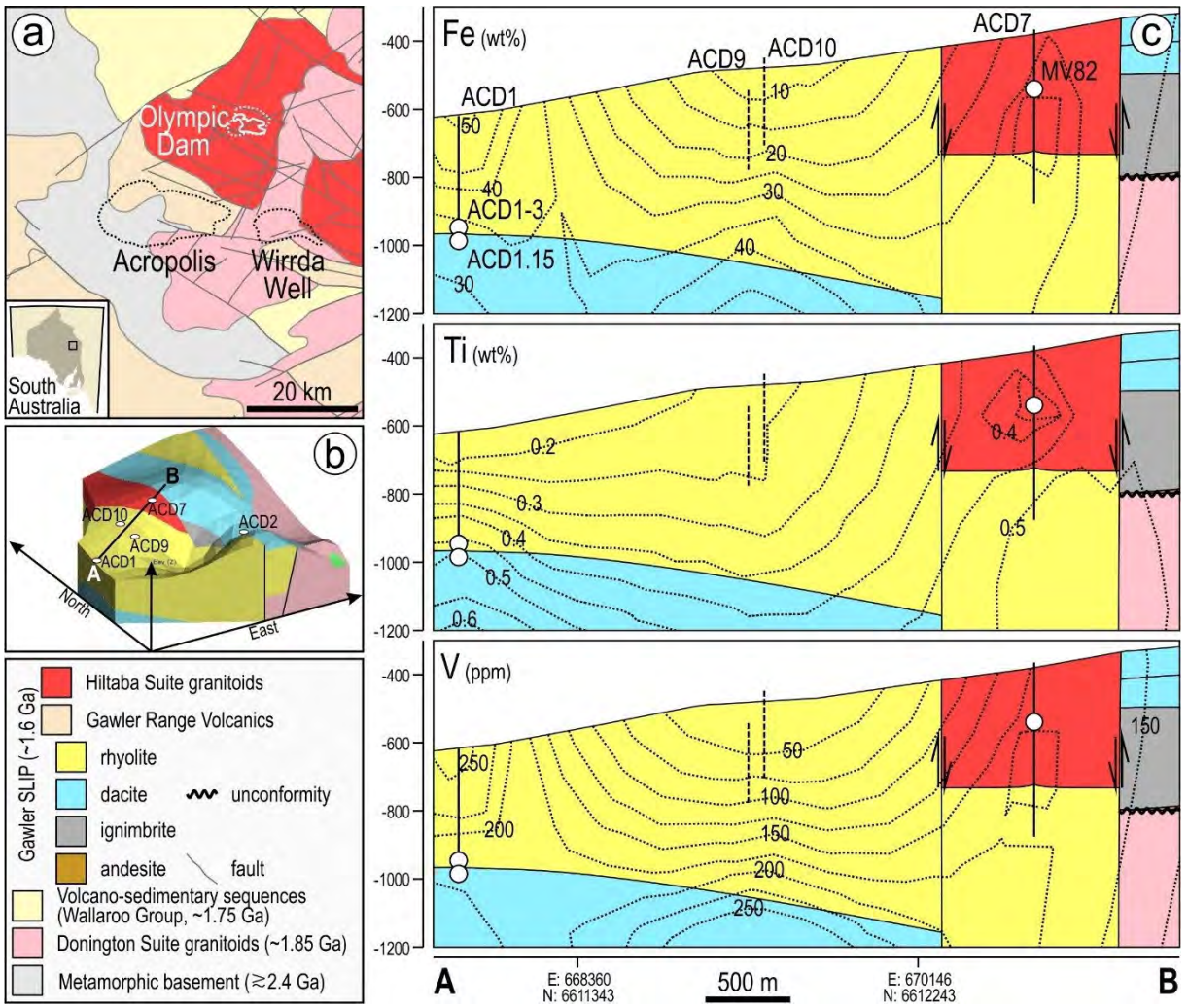

Fig. 1. (a). Geological map of the Olympic Dam district, Gawler Craton, South Australia (inset), showing the location of Acropolis (data sourced from https://map.sarig.sa.gov.au). Outline of geophysical anomalies surrounding the deposits/prospects shown as dotted lines. (b) 3D, oblique view of Acropolis and (c) cross-section showing isolines for Fe, Ti and V (Leapfrog model adapted from Dmitrijeva et al. 2019a). Note the Fe and V anomalies beneath drillholes ACD9/10 suggesting mineralization open at depth. The location of U-bearing hematite previously dated by Courtney-Davies et al. (2019a) from drillhole ACD2 is also marked on (b).

Whereas pervasive alkali-calcic+magnetite alteration followed by hydrolytic alteration is ubiquitous in IOCG prospects across the district, albeit with differences in the degree of telescoping, intensity and mineralogy depending on host lithologies (e.g., Dmitrijeva et al. 2019a, 2019b), the magnetite-vein style mineralization is distinct at Acropolis. High-temperature (440-550 °C) formation was estimated from oxygen isotope data for Acropolis magnetite (Oreskes and Einaudi 1992). Principal component (PC) analysis on whole-rock data discriminated between ‘magnetite’ (Fe-V-Ni-Co) and ‘hematite’ (Ca-P-U-Th-REE-W-Sn-Sb)

signatures as PC1 loadings (Dmitrijeva et al. 2019a). This highlights the presence of the 'U-W-Sn-Mo' element association in the mineralization footprint, a group of elements considered of 'granitophile affiliation' in hematite and throughout the orebody at Olympic Dam (Verdugo-Ihl et al. 2017; Dmitrijeva et al. 2019a).

Using hematite, a newly assessed mineral geochronometer from Olympic Dam (Courtney-Davies et al. 2019b), laser-ablation inductively-coupled-plasma mass-spectrometry (LA-ICP-MS) U-Pb dating of dating of hematite from Acropolis (ACD 2; Fig. 1b) produced a $^{207}Pb/^{206}Pb$ age of 1590.6±6.5 Ma (Courtney-Davies et al. 2019a). Moreover, comparable hematite geochemistry and geochronology were recognized to resolve genetic and temporal links among IOCG systems in the district since ages of ~1.6 Ga from Wirrda Well hematite are within statistical overlap with hematite from both Olympic Dam (1591.27±0.89 Ma; U-Pb ID-TIMS; Courtney-Davies et al. 2020) and Acropolis (Courtney-Davies et al. 2019a).

METHODOLOGY

Petrographic and geochemical characterization at the micron-scale comprised scanning electron microscopy using a FEI Quanta 450 instrument in back-scattered electron (BSE) mode and electron probe microanalysis (EPMA) using a CAMECA SX-Five electron probe microanalyzer. Trace element data was collected using LA-ICP-MS conducted on an ASI RESOlution-LR 193 nm ArF excimer laser microprobe coupled to an Agilent 7900cx quadrupole ICP-MS. See Supplemental[1] for further details.

Thin-foils were prepared by FIB-SEM methods as outlined in Ciobanu et al. (2011) using a FEI Helios Nanolab 600 instrument. The foils were extracted across exsolution lamellae. HAADF STEM imaging and energy-dispersive X-ray (EDX) spectrometry were conducted with an ultra-high-resolution, probe corrected FEI Titan Themis S/TEM operated at 200 kV. This instrument is equipped with a X-FEG Schottky source and Super-X EDX geometry. The Super-X EDX detector provides geometrically symmetric EDX detection with an effective solid

[1] Deposit item

angle of 0.8 sr. Probe correction delivered sub-Ångstrom spatial resolution and an inner collection angle greater than 50 mrad was used for HAADF imaging with a Fischione detector.

Indexing of diffraction patterns was conducted with WinWulff© (v1.6) and publicly available data from the American Mineralogist Crystal Structure Database (http://rruff.geo.arizona.edu/AMS/amcsd.php). Crystal structure models were generated in CrystalMaker® (v10.4.6) and STEM for xHREM™ (v4.1). All instruments are housed at Adelaide Microscopy, The University of Adelaide.

RESULTS

Sampling

Samples were selected from the main lithologies that host magnetite mineralization at Acropolis: HS granite; GRV rhyolite and GRV dacite; Fig. 1c). These were collected from two drillholes, ~4 km apart, that intersect intervals with the highest Fe content (Fig. 1c; Supplemental[1] Fig. A1).

The samples represent different levels of mineralization, ~400 m apart vertically, whereby the HS-hosted magnetite lies at upper levels (540 m) and GRV-hosted magnetite is positioned lower in the system (950 and 990 m; Fig. 1c; Supplemental[1] Fig. A1). Although the mineralization style is dominantly as cm- to dm-size veins/veinlets, it can also form localized stockworks (Supplemental[1] Fig. A2). The dominant Fe-oxide at Acropolis is magnetite, given the good correlation with high magnetic susceptibly, but hematite is also present, particularly as martite in the upper parts of each drillhole (Supplemental[1] Fig. A1). Although Fe-rich intervals attributable to Ti-rich magnetite (in the range 0.6-1.9 wt.% Ti), a ~100 m-long section of the HS-hosted magnetite interval is Ti-poor (~0.14 wt.% Ti; Supplemental[1] Fig. A1). The Ti/V ratio in whole rock is relatively constant (~30) throughout the Ti-rich magnetite-bearing intervals, whereas in the Ti-poor interval and upper intervals that contain more hematite, the

Ti/V ratio is lower (Supplemental[1] Fig. A1). Magnetite from ACD7 (sample MV82) contains cm-sized grains of interstitial apatite (Supplemental[1] Fig. A2d).

Petrography and mineral chemistry

The nanoscale study was carried out on three polished blocks that were prepared from vein magnetite; samples details are given in Supplemental[1] Figures A3-6 and accompanying petrographic background. The Ti-poor magnetite displays 120° triple junctions between grains (Fig. 2a), indicating equilibrium crystallization but lacks micron-scale inclusions, except for erratic Mg-silicates. In contrast, the Ti-rich magnetite displays dense sets of <111> and/or $<100>_{lamellae}$, which are generally consistent with trellis exsolutions of ilmenite formed during cooling of titaniferous magnetite (e.g., Buddington and Lindsley 1964; Fig. 2b, c). Such Ti-rich lamellae can, however, show more complex orientations within domains throughout a single grain, as observed in the rhyolite-hosted sample (ACD1-3; Fig. 2c), as well as wider sets of fractures filled by secondary minerals (Fig. 3a). A further characteristic of the Ti-rich magnetite is the presence of sub-micron inclusions, either as orbicular arrangements, with wide morphological variation, or as densely mottled fields between the Ti-rich lamellae (Fig. 3a, b). These fields are mostly separated from the lamellae by areas apparently free of inclusions, but with margins outlined by coarser inclusions (Fig. 3a, b). In contrast, dacite-hosted Ti-rich magnetite shows much finer/rarer inclusions at this scale of observation (Fig. 3c). The orbicular Ti-rich magnetite displays inclusion-rich mottled cores surrounded by concentric rhythms of inclusions (Fig. 3d). Some of the orbicular patterns crosscut lamellar sets (Fig. 3d), whereas others engulf subsets of such lamellae (Fig. 3a).

Microprobe data (Supplemental[1] Table A1) obtained from both Ti-poor and -rich varieties of magnetite (except the dense mottled type) were collected across inclusion-bearing domains avoiding the Ti-rich lamellae. Crystal-chemical formulae calculated on a basis of 32 oxygen indicate distinct compositions and can be given as:

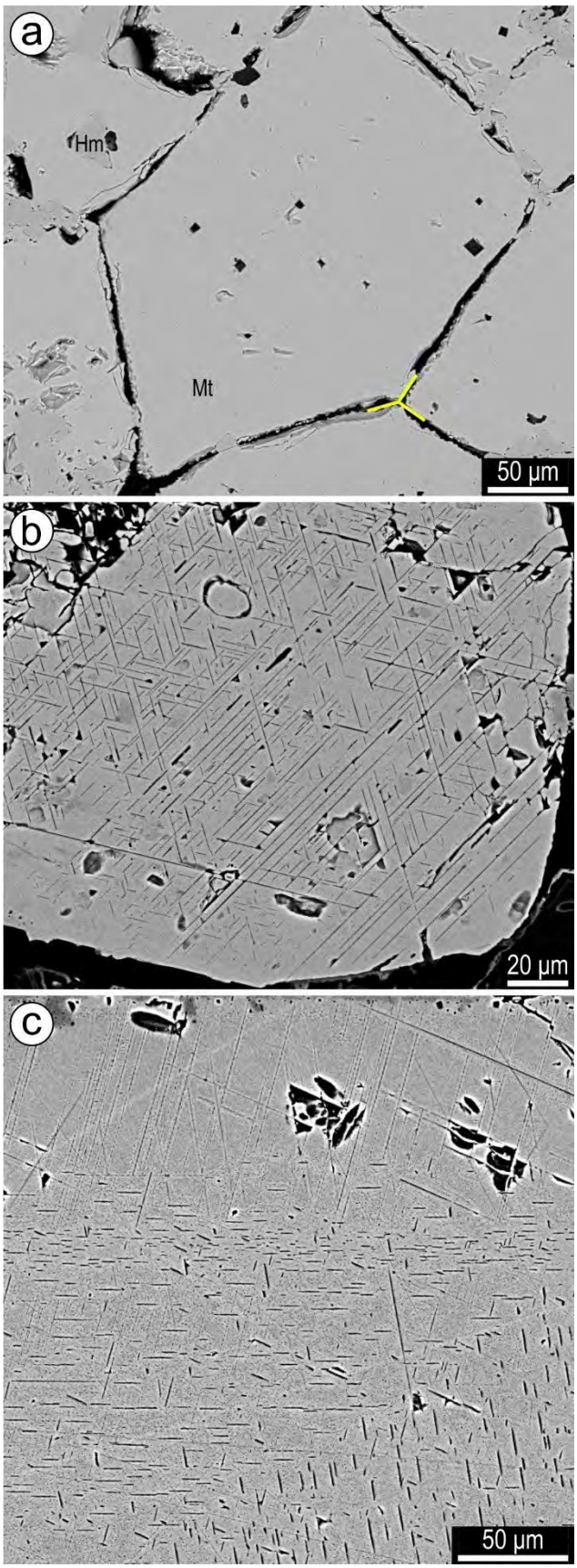

Fig. 2. BSE images showing typical aspects of (a) Ti-poor magnetite and (b, c) Ti-rich, trellis magnetite. In (a), 120° triple junctions (marked) show equilibrium crystallization; no micron-scale textures are observable, except sporadic (secondary) Mg-silicate inclusions. (b, c) Ti-rich lamellar sets of <111> and <100> orientations defining 'trellis' titanomagnetite. Note variable density and complexity of lamellae in (c).

(i) Ti-poor (MV82):

$$(Fe_{7.81}Mg_{0.2}Mn_{0.02})^{2+}_{\sum=8.03}(Fe_{15.84}Al_{0.1})^{3+}_{\sum=15.94}(Si_{0.02}Ti_{0.01})^{4+}_{\sum=0.03}O_{32}$$

(ii) Ti-rich, primary trellis type (ACD1.15):

$$(Fe_{8.4}Ca_{0.01}Zn_{0.01})^{2+}_{\sum=8.42}(Fe_{15.02}Al_{0.13}V_{0.02})^{3+}_{\sum=15.17}(Ti_{0.41}Si_{0.01})^{4+}_{\sum=0.42}O_{32}$$

(iii) Ti-rich, orbicular type (ACD1.3):

$$(Fe_{8.12}Mg_{0.06})^{2+}_{\sum=8.18}(Fe_{15.46}Al_{0.16}V_{0.02})^{3+}_{\sum=15.64}(Ti_{0.17}Si_{0.01})^{4+}_{\sum=0.18}O_{32}$$

Using calculations from Ferracutti et al. (2015), these formulae give mean mol.% spinel compositions of: (i) $Mt_{96.4}Mgf_{2.55}Spl_{0.64}Her_{0.64}Ulv_{0.07}$; (ii) $Mt_{96.1}Ulv_{2.64}Her_{0.84}Gah_{0.09}$; and (iii) $Mt_{96.38}Ulv_{1.09}Her_{0.99}Spl_{0.76}Mgf_{0.76}Gah_{0.03}$, where Gah=gahnite ($ZnAl_2O_4$); Her=hercynite ($FeAl_2O_4$); Mgf=magnesioferrite ($MgFe_2O_4$); Mt=magnetite ($Fe^{2+}Fe^{3+}{}_2O_4$); Spl=spinel *sensu stricto* ($MgAl_2O_4$); and Ulv=ulvöspinel ($TiFe_2O_4$). Compositions (ii) and (iii) do not, however, reflect the titanomagnetite as a whole, since they do not include the Ti-rich lamellae. Considering the density of these lamellae (Fig. 2b), an increase in the Ulv content (~10-15 mol.%) can be estimated at least for some grains/domains assuming an approximate Ilm/Mt ratio of ~1:5 in primary titanomagnetite (prior to any overprint).

Such compositional variation reflects the presence of inclusions and/or unavoidable subsurface Ti-rich lamellae in the Ti-rich varieties. Aside from Ti, Mg and Al, Zn and V are also commonly above minimum limits of detection. The two Ti-rich varieties, containing up to 3.1 wt.% TiO_2 (or 4.7 mol.% ulvöspinel) and displaying trellis lamellae are hereafter called titanomagnetite. Magnesium is higher in the Ti-poor magnetite, and highest in parts of the transect across the orbicular magnetite (Fig. 3e). The highest concentrations of Ti are recorded adjacent to trellis lamellae in the orbicular magnetite forming an ‘ilmenite’ trend whereas the other analyses from the clusters of points plot along a trend of different slope with respect to Ti versus Fe^{2+} (Fig. 3f). Aluminum is present throughout all samples at relatively constant values. Although all these elements are considered as lattice-hosted within magnetite, they are enriched

across the inclusion fields within the orbicular type, implying that those inclusions are Ti-, Al- and Mg-bearing oxides.

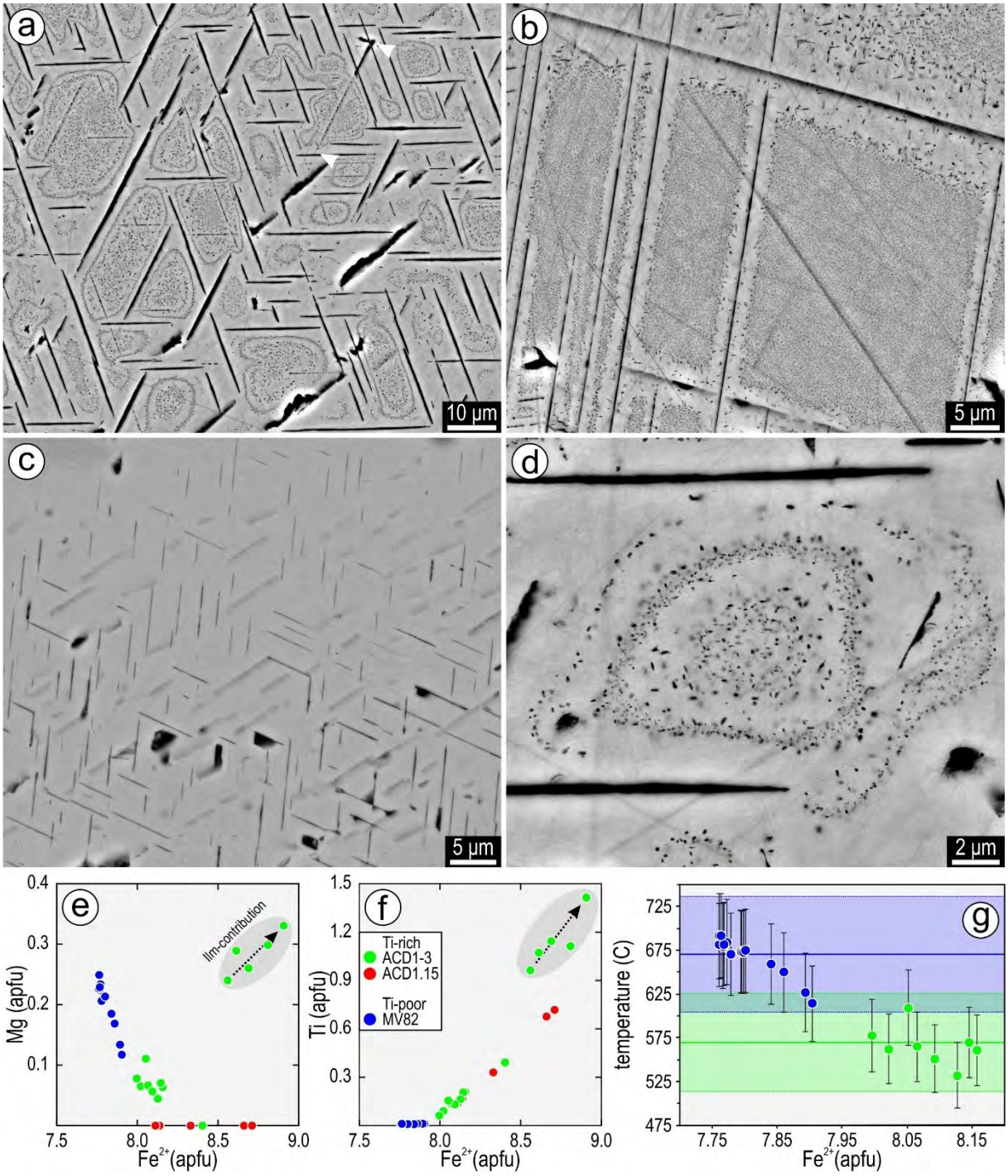

Fig. 3. (a-c) BSE images illustrating inclusion fields in trellis titanomagnetite: (a) orbicular; (b) densely mottled; and (c) faint, hardly visible at this resolution. (d) Detail of orbicular texture showing concentric bands of inclusions surrounding a mottled core. Note crosscutting relationships between bands of inclusions and trellis lamellae, also arrowed in (a). (e, f) Mg versus Fe^{2+}, and Ti versus Fe^{2+} plots for Ti-poor and -rich magnetite varieties. The upper trend in (b) defines ilmenite (Ilm; arrowed). apfu–atoms per formula unit). (g) Fe^{2+} versus temperature plot for Ti-poor (blue) and Ti-rich, orbicular (green) magnetite using the X_{Mg} geothermometer (Canil and Lacourse 2020). Averages are marked by thicker lines.

EPMA data for magnetite were used to estimate formation temperature using the empirical geothermometer of Canil and Lacourse (2020). Results indicate average formation temperatures of ~570±40 °C for orbicular magnetite and ~670±50 °C for Ti-poor magnetite (Fig. 3g).

Minor and trace element signatures

Trace element data obtained by LA-ICP-MS (Supplemental[1] Table A2) show comparable ranges of concentration for the two types of titanomagnetite. They are consequently treated together and compared with the Ti-poor magnetite (Fig. 4a). Element concentrations in titanomagnetite measured by LA-ICP-MS are comparable to those measured by EPMA. Aside from elevated Ti (between 8,200 and 15,600 ppm), this sub-type is also enriched in a limited number of elements, including Al (1,760−3,240 ppm), V (390−480 ppm), Mg (34−1,470 ppm) and Zn (68−330 ppm). Trace elements measured at relatively high concentrations include: Mn (41−330 ppm), Ga (37−55 ppm), Ni (27−47 ppm), Sc (19−41 ppm), Co (21−34 ppm) and Sn (5.6−16 ppm). Concentrations of other trace elements are ≲5 ppm.

Titanium-poor magnetite shows a broadly similar geochemical signature. Enrichment patterns are, however, subtly different. Compared to titanomagnetite, Ti-poor magnetite is distinctly enriched in Mg (1,150−3,250 ppm), Mn (155−680 ppm), Co (116−130 ppm) and Ni (60−65 ppm). Other elements at high concentrations include Al (1,440−1,560 ppm), Ti (371−420 ppm) and V (230−250 ppm). Consistent, albeit low, concentrations of Zn (64−77 ppm), Ga and Sn (~15 ppm), and Sc (~5 ppm) are measured. As with titanomagnetite, Mg and Mn display large variance.

Elements consistently above minimum detection limits and with arithmetic means ≥5 ppm were used for PCA. The resultant dendrogram (Fig. 4b) shows three groups: (1) Ti-Sc-Zn-Ga-Al-V, (2) Mg and (3) Ni-Sn-Mn-Co. Except for Al, Group 3 defines the titanomagnetite-signature at Acropolis. Groups 2 and 3, however, are representative of Ti-poor magnetite.

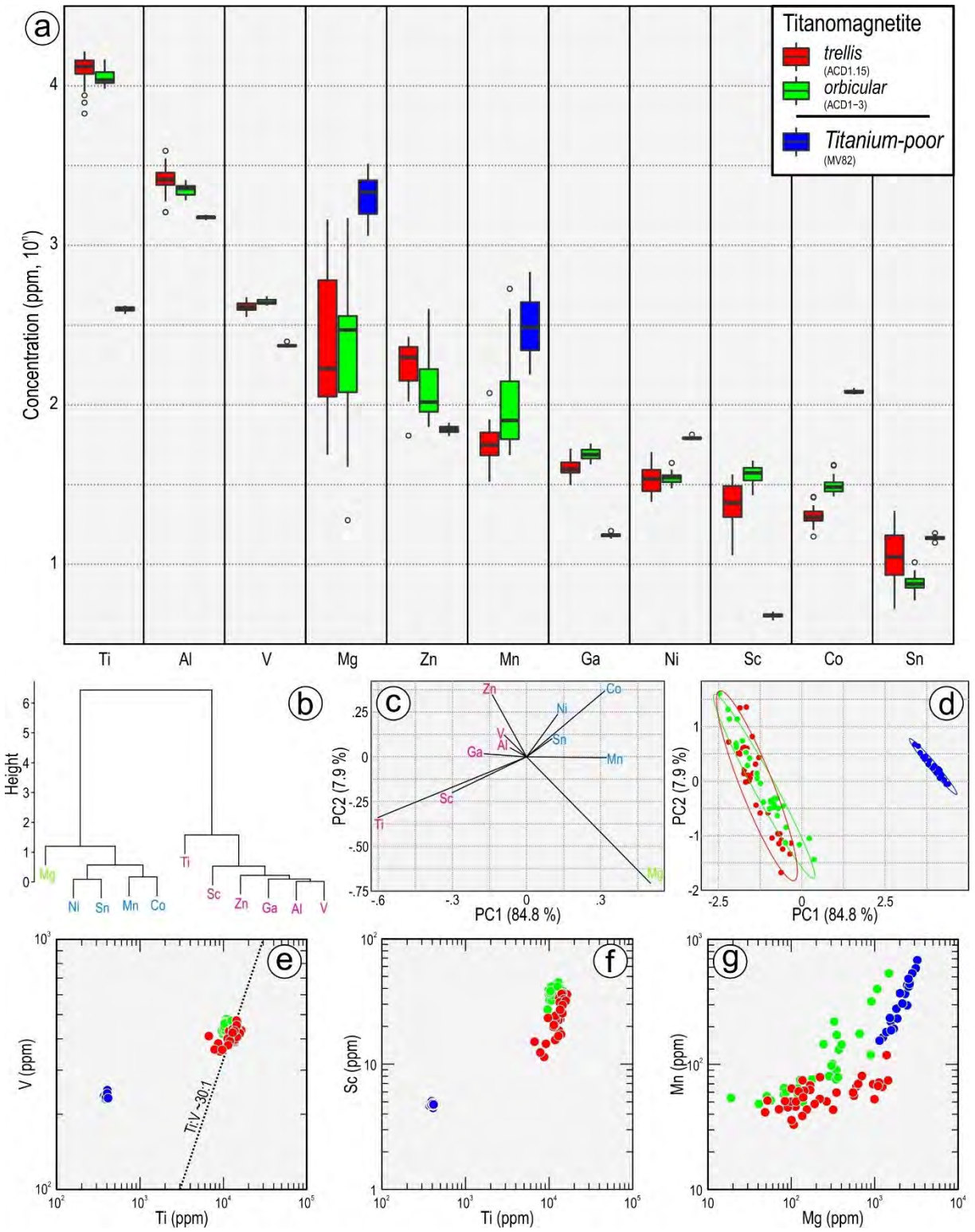

Fig. 4. LA-ICP-MS trace element data. (a) Boxplot of selected trace element concentration data ordered by descending median values. (b) Hierarchical cluster dendrogram showing trace element discriminating Ti-poor (left) and Ti-rich (right) magnetite. (c, d) Loadings of the centered log-ratio transformed elements projected on a PC1 versus PC2 plot, and corresponding principal components scores, showing element associations typical of the two magnetite varieties. Note that orbicular (green) is a subtype of the Ti-rich magnetite. Plots in (b-d) obtained using procedures described by Dmijtreva et al. (2019a). (e, f) Scatterplots of V versus Ti and Sc versus Ti, showing distinct clusters for the magnetite varieties. Note that Ti:V ratios in Ti-rich magnetite correlates with whole rock Ti:V contents (~30:1). (g) Mn versus Mg plot showing positive correlations, albeit stronger and steeper slope for Ti-poor variety.

Except for Zn in Group 1 and Sn in Group 3, oxidation states of elements within Group 1 are higher (tri- or tetravalent) than in Groups 2 and 3 (predominantly divalent), potentially suggesting differences in behavior during overprinting of magnetite. Loadings of the centered log-ratio transformed elements are shown in the PC1 versus PC2 projection (Fig. 4c). Principal component scores projected onto PC1 versus PC2 (Fig. 4d) highlight relative differences between the Ti-poor magnetite and titanomagnetite samples.

Differences in minor/trace element endowment between the two magnetite types is expressed on bivariate plots. The good correlation between Ti and V at the drillhole-scale relates to the nearly constant concentrations of these elements in trellis-textured magnetite (Fig. 4e), in which the mean Ti:V-ratio (ppm/ppm basis) is 28.4 (±4.6, 1σ), compared to 1.7±0.06 in Ti-poor magnetite. Whereas Ti-poor magnetite generally shows a narrow range of composition and well-defined clusters on the biplots, titanomagnetite shows greater spread (e.g., Sc versus Ti; Fig. 4f). Magnesium and Mn display a positive correlation in Ti-poor magnetite (R^2=0.91; Fig. 4g).

Nanoscale characterization

The nanoscale study was carried out on six S/TEM foils (Table 1; Supplemental[1] Figs. A3-A5) prepared across selected grains displaying the textures introduced above for the trellis and orbicular titanomagnetite, as well as for Ti-poor magnetite. In all cases, the selected samples show inclusion fields with variable density, morphology and distribution relative to lamellar networks (Supplemental[1] Figs. A7 and A8).

HAADF STEM imaging shows at least two distinct phases making up the Ti-rich trellis lamellae (Fig. 5a-c). Primary titanomagnetite is characterized by sets of <111> and $<100>_{lamellae}$, tens to several hundreds of nm in width, some of which are interrupted due to overprinting (Fig. 5a). In this case, fields of inclusions are ubiquitously present between any given sets of lamellae.

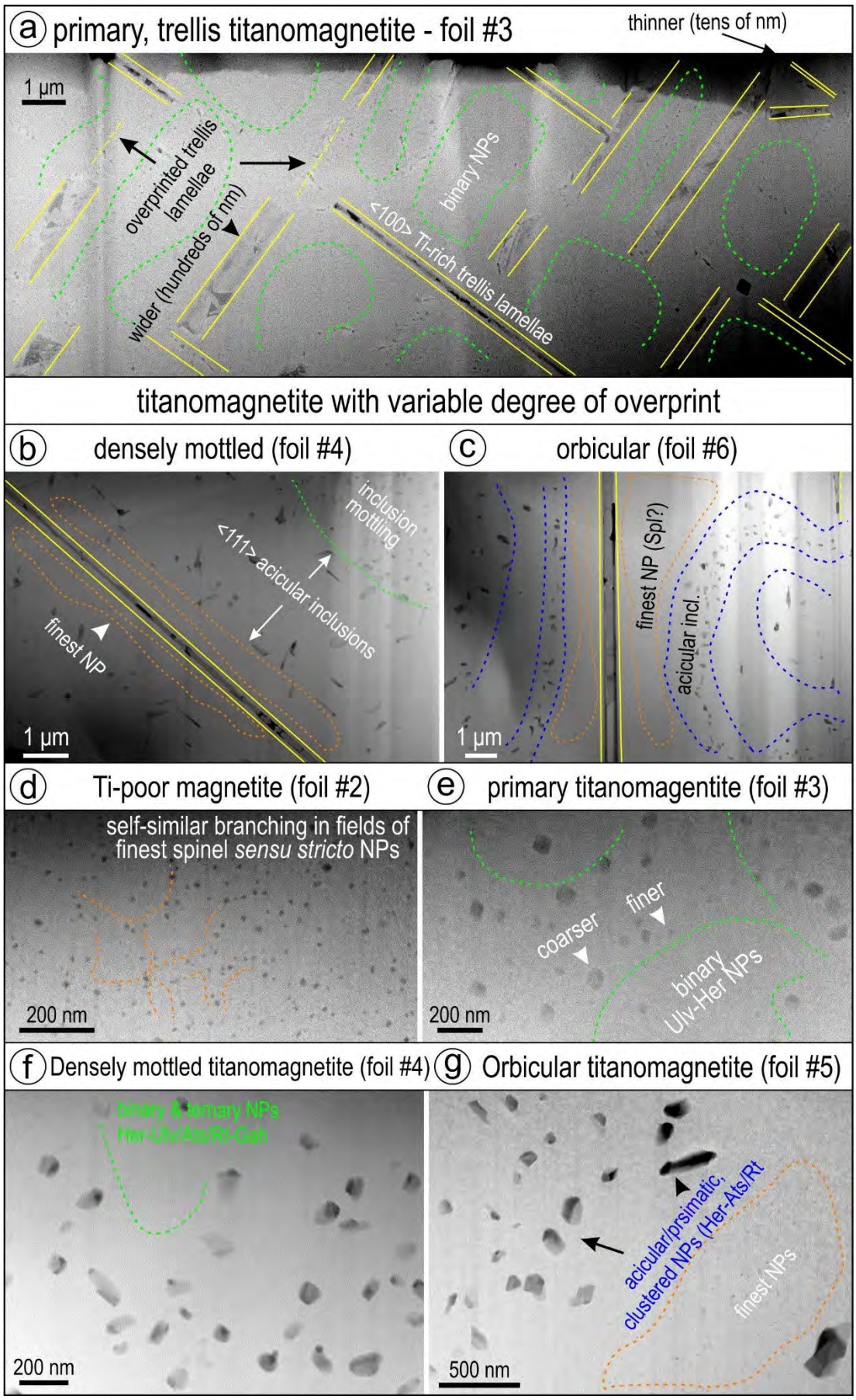

Fig. 5. HAADF-STEM images showing nanoscale aspects of magnetite as marked. (a-c) Relationships between trellis lamellae (yellow) and inclusions fields in titanomagnetite varieties. (d-g) Details of inclusion distribution, size and associations as marked. See text for further explanations.

In the other varieties of titanomagnetite (foils #4-6), the inclusions display much wider variation in size, morphology and spatial relationship with the lamellae (Fig. 5b, c; Supplemental[1] Figs. A5d-f and A6d-f). In these cases, each lamella is surrounded by a ~0.5-1 μm-wide interval mottled with single-phase, finest particles, each ≲5-10 nm in diameter, followed by a zone of acicular and composite inclusions, either forming <111> networks (foil #4), or concentric bands (foils #5, 6; Fig. 5b, c). Densely mottled inclusions form distinct fields in titanomagnetite from foil #4, whereas scarcer but coarser, clustered inclusions occur in the orbicular type (Fig. 5b, c; Supplemental[1] Figs. A7d-f, and A8d-f).

The Ti-poor magnetite is instead characterized throughout the sample by ubiquitous, finest-scale particles with self-similar branching (Fig. 5d). In contrast, two populations of binary inclusions (up ~50 nm and ~10 nm) occur in the primary titanomagnetite (Fig. 5e). Increased inclusion size (up to hundreds of nm) is observed within binary and ternary inclusions throughout the densely mottled areas in titanomagnetite with partial overprint (foil #4; Fig. 5f). Orbicular titanomagnetite shows less dense but clustered inclusions, with individual particles displaying a pronounced tendency to acicular/prismatic habits (Fig. 5g).

STEM EDX mapping of inclusion fields shows the ubiquitous presence of Al irrespective of inclusion associations. Overall, Mg and Ti are prevalent in the Ti-poor and -Ti-rich magnetite varieties, respectively (Fig. 6). Monophase, Al-Mg-bearing inclusions are typical of Ti-poor magnetite (Fig. 6a), whereas Ti-Al and Ti-Al-Zn characterize binary and ternary inclusions from titanomagnetite (Fig. 6b-d). A discrete Ti-Sc-bearing phase was identified in only one of the Al-Ti-rich, acicular inclusions (Fig. 6e, f).

HAADF STEM imaging and STEM EDX mapping of individual inclusions assisted the identification of phases within the inclusion fields (Figs. 7 and 8). Aside from magnetite, four other spinels are identified: ulvöspinel, hercynite, gahnite and spinel *sensu stricto*. Discrimination between different Ti-Fe-bearing phases, or among TiO_2 polymorphs (anatase or rutile) was only possible following high-resolution imaging.

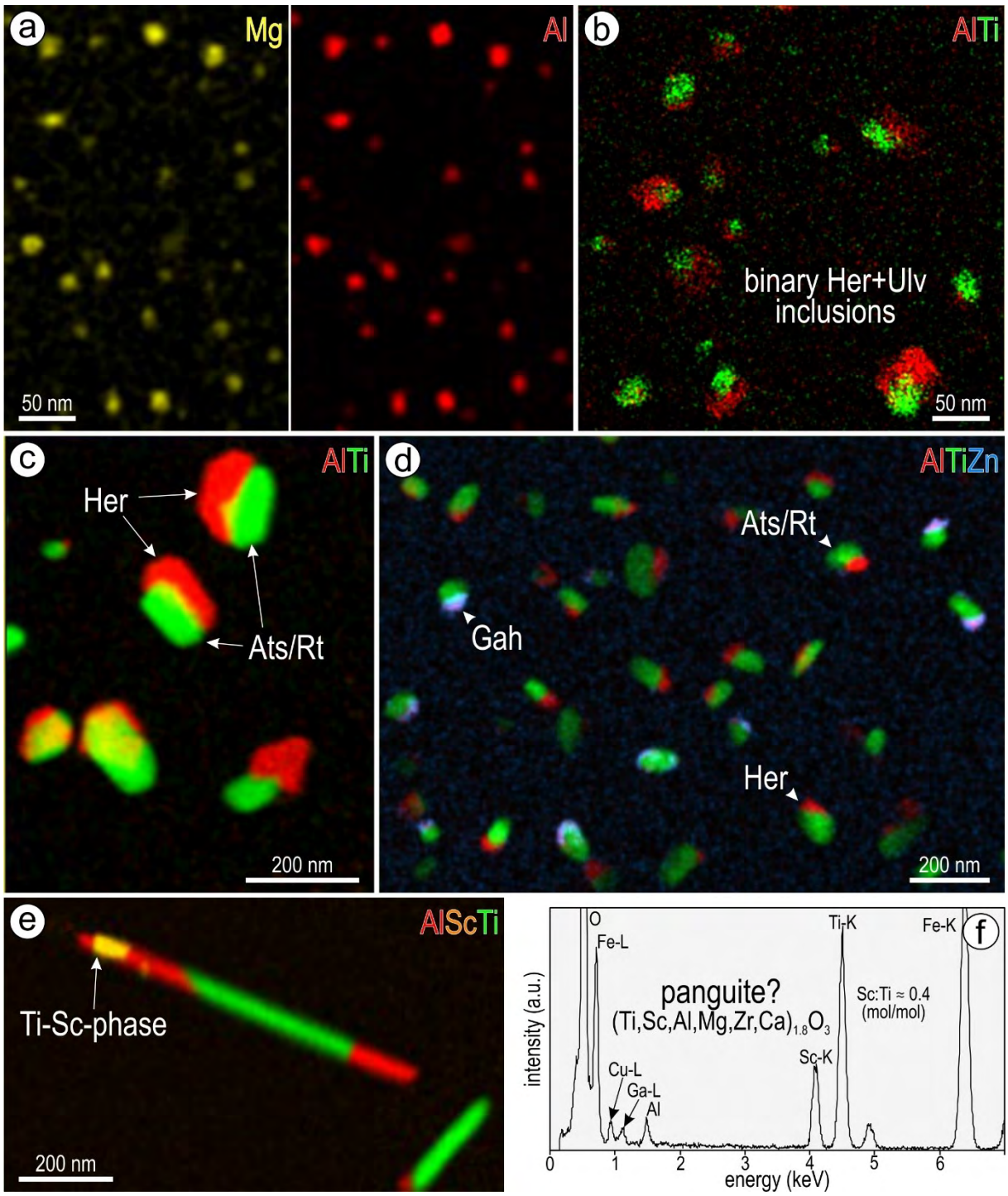

Fig. 6. STEM-EDX maps of inclusion fields from different magnetite varieties. (a) Spinel *sensu stricto* in Ti-poor magnetite. (b) Binary hercynite (Her)-ulvöspinel (Ulv) inclusions in primary, trellis magnetite. (c) Hercynite-anatase/rutile (Ats/Rt) inclusions in orbicular titanomagnetite. (d) Two/three-phase inclusions [hercynite associated either with gahnite (Gah) and/or TiO_2 polymorphs (Ats/Rt)] in densely mottled titanomagnetite. (e) Titanium-Sc-phase part of an acicular inclusion of hercynite+TiO_2 and (f) corresponding EDX spectrum. Molar Sc:Ti ratios suggest that it could be an Fe-bearing variety of panguite.

Across all samples, most individual inclusions have sizes within the nanoparticle range (<100 nm; NP), but in the orbicular titanomagnetite such NPs typically form clusters of several

hundred nm in size (Fig. 7). The smallest NPs (<10 nm) are typically single-phase, either spinel *sensu stricto* or gahnite; the latter is identified from areas surrounding the trellis lamellae (Figs. 7a, b and 8a, b). The bleb-like single or binary-phase spinel inclusions are slightly rounded to sub-euhedral, with typical cubic section (Fig. 7c-f). Binary spinel NPs (up to 30-50 nm in size), are composed of ulvöspinel associated with either hercynite or gahnite.

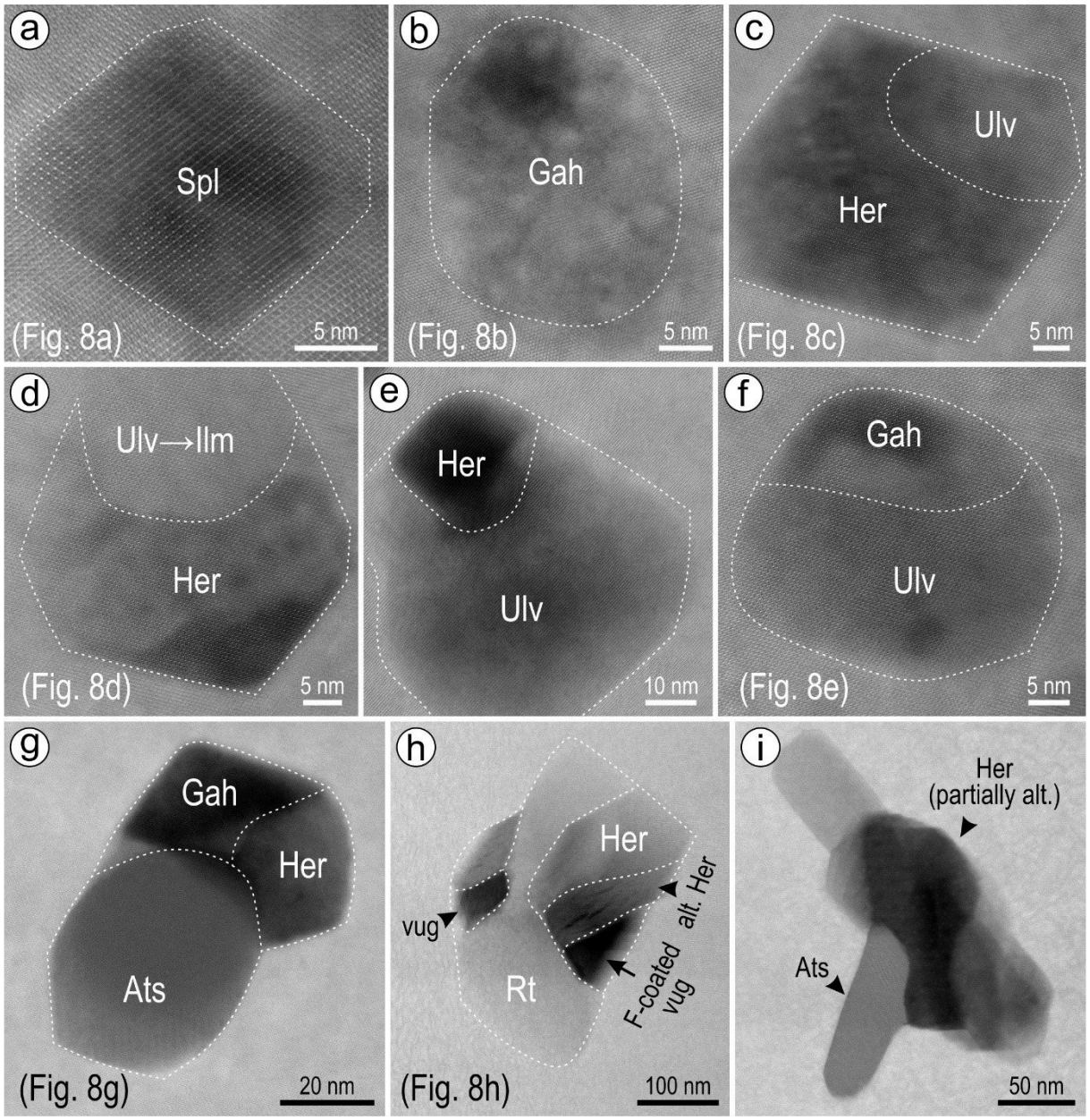

Fig. 7. HAADF-STEM images of individual nanoparticles (NP) (a-f) and composite NP clusters (g-i): (a, b) Smallest NPs with single spinel composition; (c-f) two-spinel association in the same NP; note curvilinear mutual boundaries; and (g-i) clusters of spinels and Ti-oxides. Note fluorine (F) coating vughs and alteration of hercynite in the NP cluster from (h). Ats–anatase; Gah–gahnite; Her–hercynite.

These display curvilinear mutual boundaries and are typical of primary and partially overprinted titanomagnetite (foils #3 and 4; Figs. 7c-f and 8c-e). In contrast, TiO_2 (anatase or

rutile) associated with spinels are mostly observed in the clustered NPs. Each displays a distinct morphology and can also comprise three phases (gahnite+hercynite+rutile/anatase; Figs. 7g-i and 8f-h). Vughs, with margins containing measurable F are observed marginal to the larger clusters (Figs. 7h and 8h). EDX spectra show the presence of Ti in both spinel *sensu stricto* and gahnite, whereas hercynite and ulvöspinel are relatively stoichiometric (Fig. 8i-l). Minor Mg is also confirmed in the spinel inclusions, within either gahnite or hercynite.

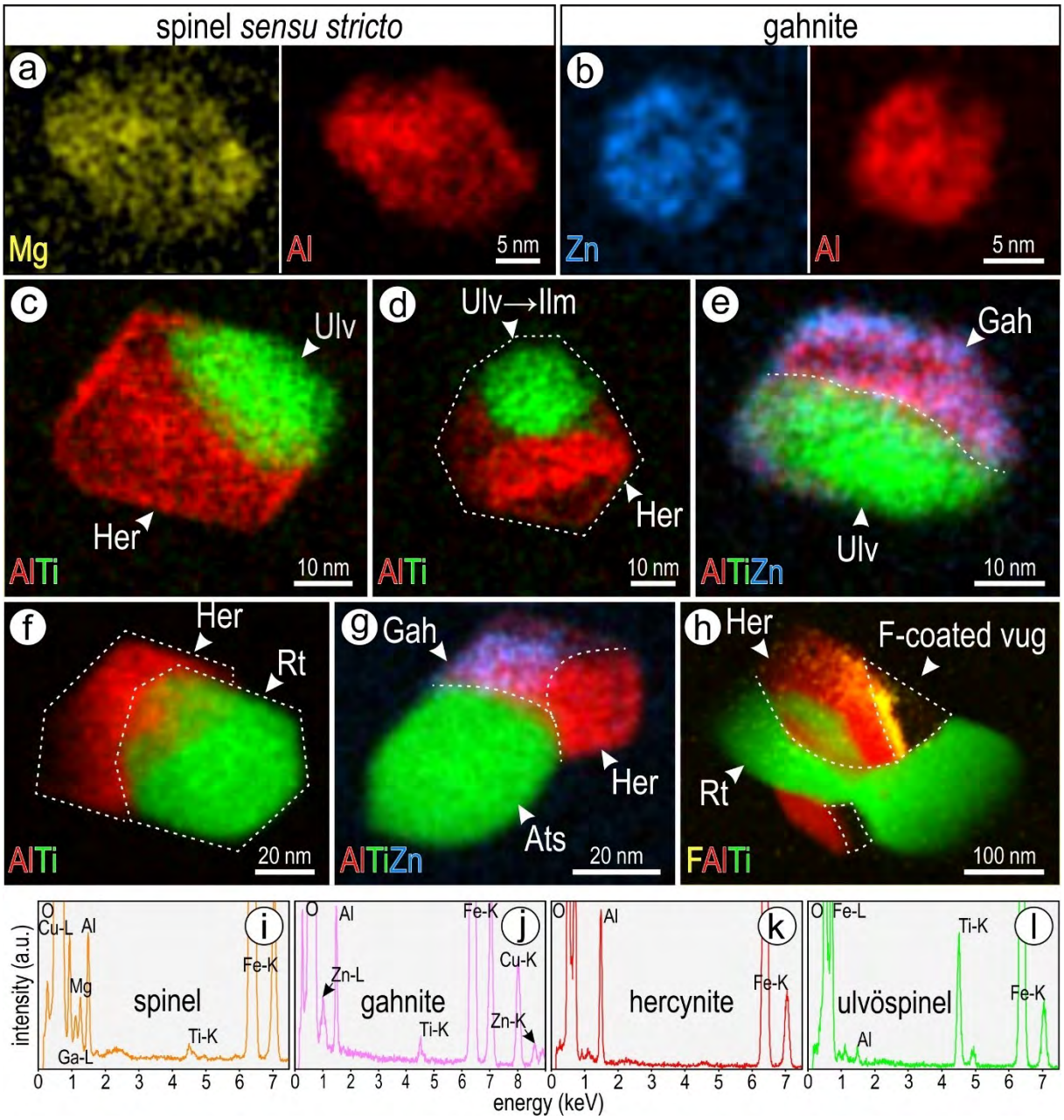

Fig. 8. STEM-EDX maps of NPs and clusters from Figure 6a-e, g, h and an additional binary NP in (f). (i-l) Spectra representative of the 4 different spinel phases as marked. Note the presence of minor Ti in spinel *sensu stricto*. Abbreviations as in Figure 7.

In titanomagnetite, ilmenite ($FeTiO_3$) and TiO_2 are present along the Ti-rich lamella, with sparse hercynite (or Al-secondary phases) or gahnite present on the margins (Fig. 9a, b). EDX spot analysis on co-existing magnetite immediately adjacent to the ilmenite is almost Ti-free; ilmenite from the same lamellae contains variable amounts of Mn, whereas the TiO_2 (rutile in this case) is stoichiometric (Fig. 9c-e). Ilmenite from the orbicular titanomagnetite contains higher concentrations of Mn and Mg.

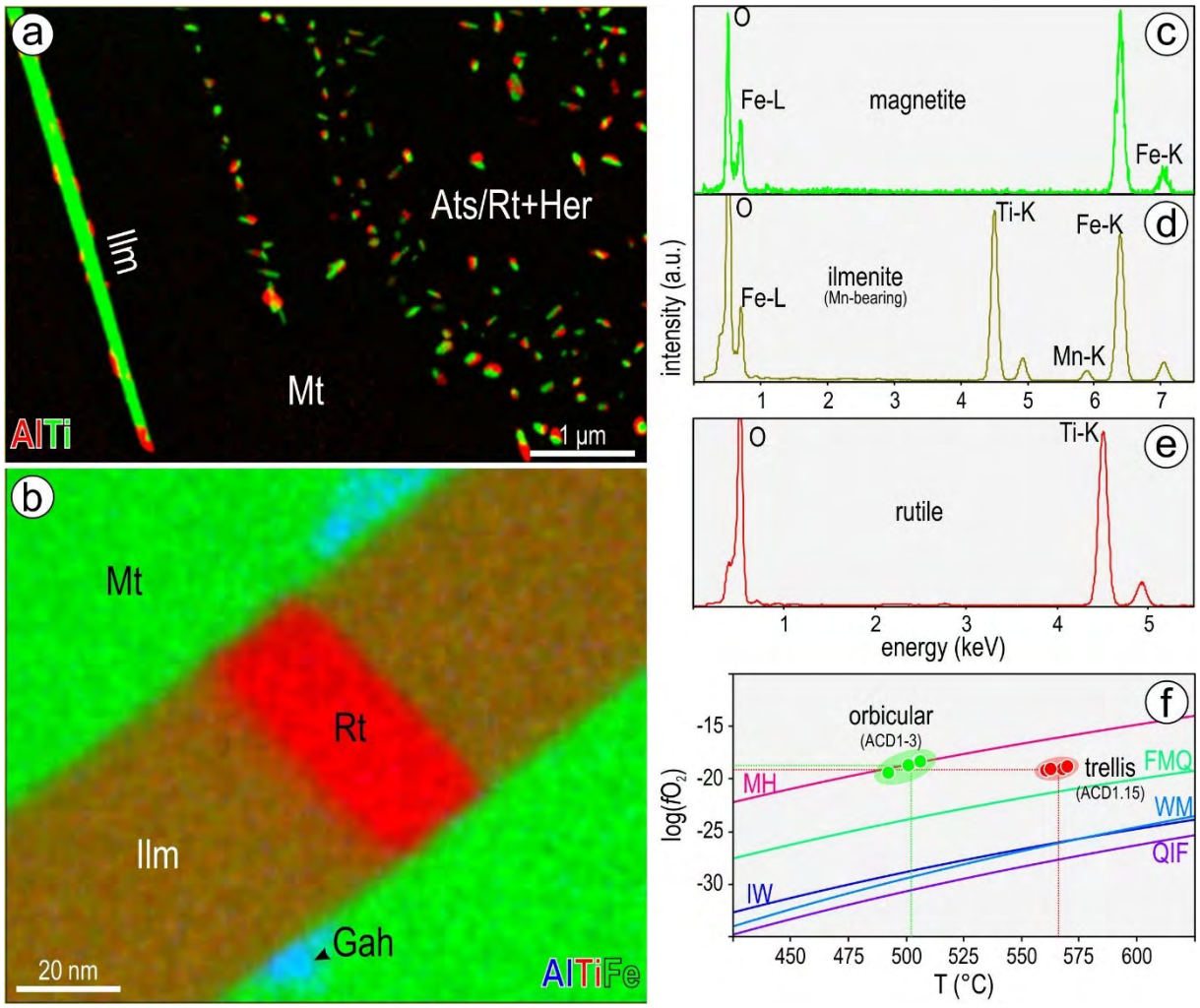

Fig. 9. STEM-EDX maps of ilmenite lamellae in orbicular (a) and primary (b) titanomagnetite. (c-e) EDX spectra of phases in (b). (f) logfO_2 *versus* temperature plot showing ilmenite-magnetite equilibration conditions in the trellis and orbicular magnetite. Nano-thermooxybarometry results (see Supplemental[1] Table A3) are obtained from STEM-EDX spectra integrated over larger domains. Stability of buffering assemblages calculated from data provided in Frost (1991). Abbreviations as in Figure 7; MH–magnetite-hematite; FMQ–fayalite-magnetite-quartz; WM–wüstite-magnetite; IW–iron-wüstite; QIF–quartz-iron-fayalite.

EDX analyses integrated over areas hundreds of nm^2 within magnetite and adjacent ilmenite were obtained for application of nano-thermooxybarometry for the two cases where magnetite

and ilmenite co-exist (Supplemental[1] Table A3). Results give temperatures of ~560 °C at logfO_2 values of -19, and ~510 °C, at slighter higher fO_2, for the trellis-only and orbicular varieties, respectively (Fig. 8f). The higher value lies between the magnetite-hematite (MH) and fayalite-magnetite-quartz (FMQ) buffers, whereas the lower one plots along the MH line (Fig. 9f). Such results indicate that equilibration between magnetite and ilmenite took place at T-fO_2 conditions within reasonable limits for a natural assemblage.

High-resolution imaging

Titanium-rich trellis lamellae, typical of primary titanomagnetite grains, comprise ilmenite and rutile with mutual epitaxial relationships to one another and to the host magnetite (Fig. 10a-d). Rutile occurs as ~40 nm-wide domains along the ilmenite, the dominant mineral filling the lamella. The three-phase association, imaged on $[1\bar{1}0]_{\mathrm{Mt}}$, $[120]_{\mathrm{Ilm}}$ and $[001]_{\mathrm{Rt}}$ (Fig. 10a inset), shows sharp mutual boundaries, albeit with local disordered domains. Magnetite and ilmenite (Ilm) are well-aligned with $(111)_{\mathrm{Mt}}$ parallel to c_{Ilm}, whereby the small difference between $d_{(111)}$ (~4.8 Å) and d_{c} (~4.7 Å) is adjusted by a boundary with small atom jogs (Fig. 10b). Likewise, the rutile (Rt) - ilmenite boundary shows good alignment between $(\bar{2}10)_{\mathrm{Ilm}}$ and a_{Rt} allowed by the close match between $d_{\bar{2}10}$ ~2.6 Å and d_a ~3 Å (Fig. 10c). Coherent, stepwise boundaries, albeit with some degree of atom disorder, are also present between the two oxides (Fig. 10d).

Comparable epitaxial relationships between spinels and anatase (Ats) with specimen tilted on $[1\bar{1}0]_{\mathrm{Mt}}$ and $[02\bar{1}]_{\mathrm{Ats}}$ are imaged from NPs within titanomagnetite (Fig. 10e, f). In clustered NPs from orbicular magnetite, an atom-scale jogged boundary is seen between the two phases along which individual cells form epitaxial intergrowths along $(111)_{\mathrm{Mt}}//(112)_{\mathrm{Ats}}$ (Fig. 10e) Likewise, the same <111> directions in the spinel structure are congruent with <112> directions in anatase, as observed at 3-phase (gahnite-anatase-magnetite) junctions (Fig. 10f).

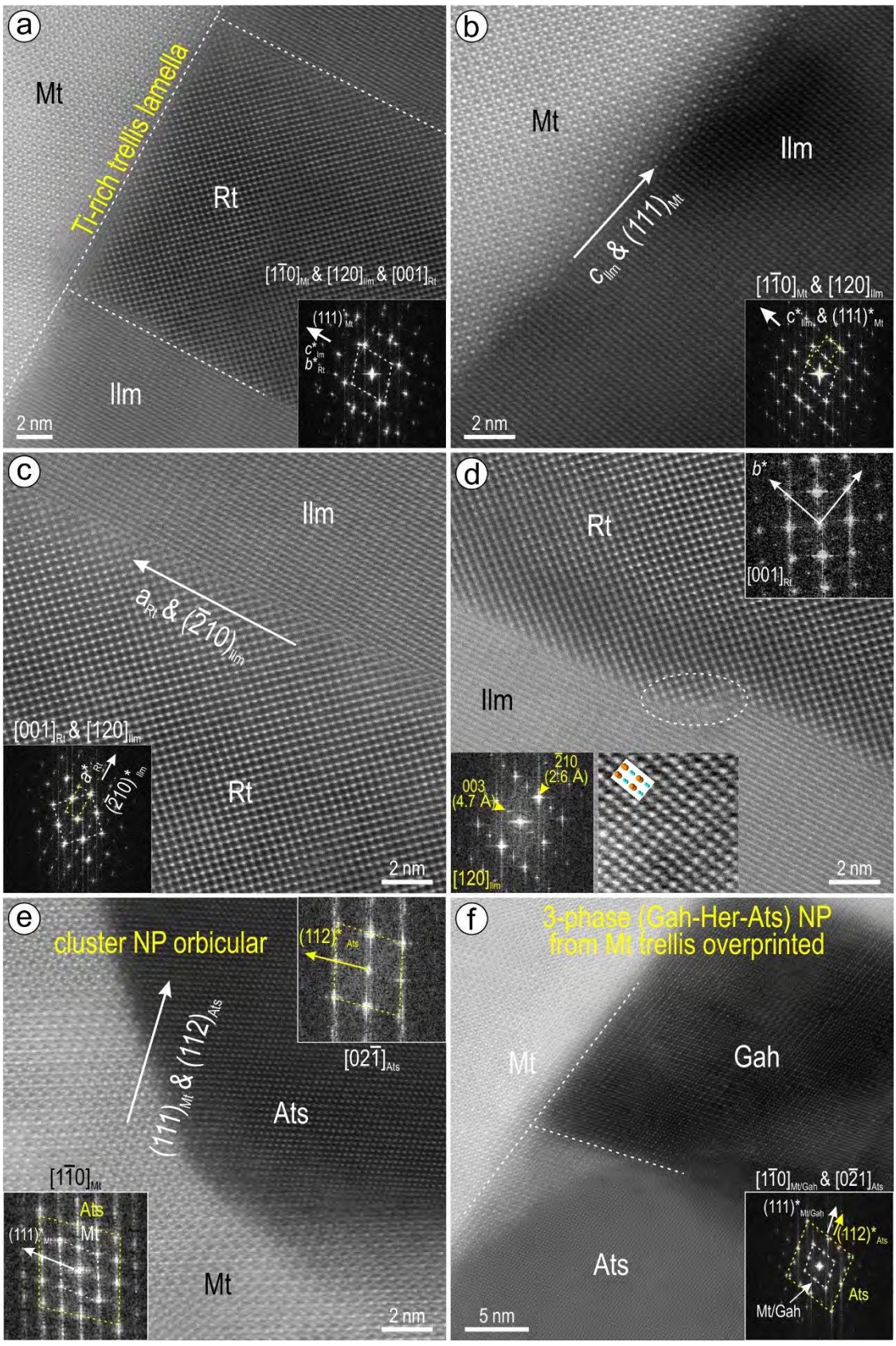

Fig. 10. HAADF STEM images showing phase relationships along Ti-rich, trellis lamellae and within spinel-TiO_2 NPs as marked. (a-d) High-resolution images of association from Figure 9b showing epitaxial relationships between magnetite (Mt)-ilmenite (Ilm) and rutile (Rt) as imaged and indexed from FFT patterns (insets). Marginal atom-scale disorder (dotted line) in (d). (e, f) 2-and 3-phase boundary in NPs showing coherent intergrowths between anatase (Ats) and spinel structures. Gah–gahnite. Images in (e) and (f) are details of NPs shown in Figure 7i and g, respectively.

Although the $d_{<112>}$ spacing in anatase (~2.3 Å) is close to $d_{<011>}$ in rutile (~2.5 Å) TiO_2 phase identification is possible based on the measured angles between the respective conjugate directions in the two phases (~104° and 114°, respectively). For some of the imaged TiO_2 inclusions, this assessment is combined with data obtained after tilting to view a second zone axis.

Lattice-scale defects are observed in spinels forming either single or multi-phase NPs (Fig. 11). Lattice misorientation is recognizable within core to margin domains of spinel in some of the smallest NPs (Fig. 11a). This type of lattice disorder is shown as streaking along <111>* directions on fast Fourier Transform (FFT) patterns (Fig. 11a inset). Gahnite displays intensity loss (darkening) along <111> directions, indicative of crystal-chemical changes along defects of d_{111} width (Fig. 11b). Primary, straight or curvilinear boundaries between spinels become irregular or lobate, clearly defining domains of ulvöspinel to anatase transformation (Fig. 11c).

Spinel group minerals share identical cubic symmetry (space group *Fd*3*m*) and thus are difficult to discriminate from one another. On HAADF STEM images, however, they display very distinctive patterns for different zone axes (Fig. 11d-f). On the $[1\bar{1}0]$zone axis, a centered rhombic motif is defined by brighter atoms corresponding to double atom columns in octahedral (M) sites, whereas all the other atoms have identical intensity, irrespective of tetragonal (T) or M locations (crystal model and STEM simulation; Fig. 11d and insets). Each brighter spot (double-atom column) is surrounded by a ring of ten smaller spots which, in magnetite, show the same size and intensity (Fig. 11d). In spinel *sensu stricto*, the T sites predominantly occupied by Mg, appear relatively darker within this ring (Fig. 11e).

Nanometer-wide defects occur along the *c* axis in the gahnite (Fig. 11f, g). These are displayed either by (i) linear arrays with atomic disorder separating domains with lattice distortion (Fig. 11f), or (ii) ordering of atoms within dumbbells along the *c* axis (Fig. 11h).

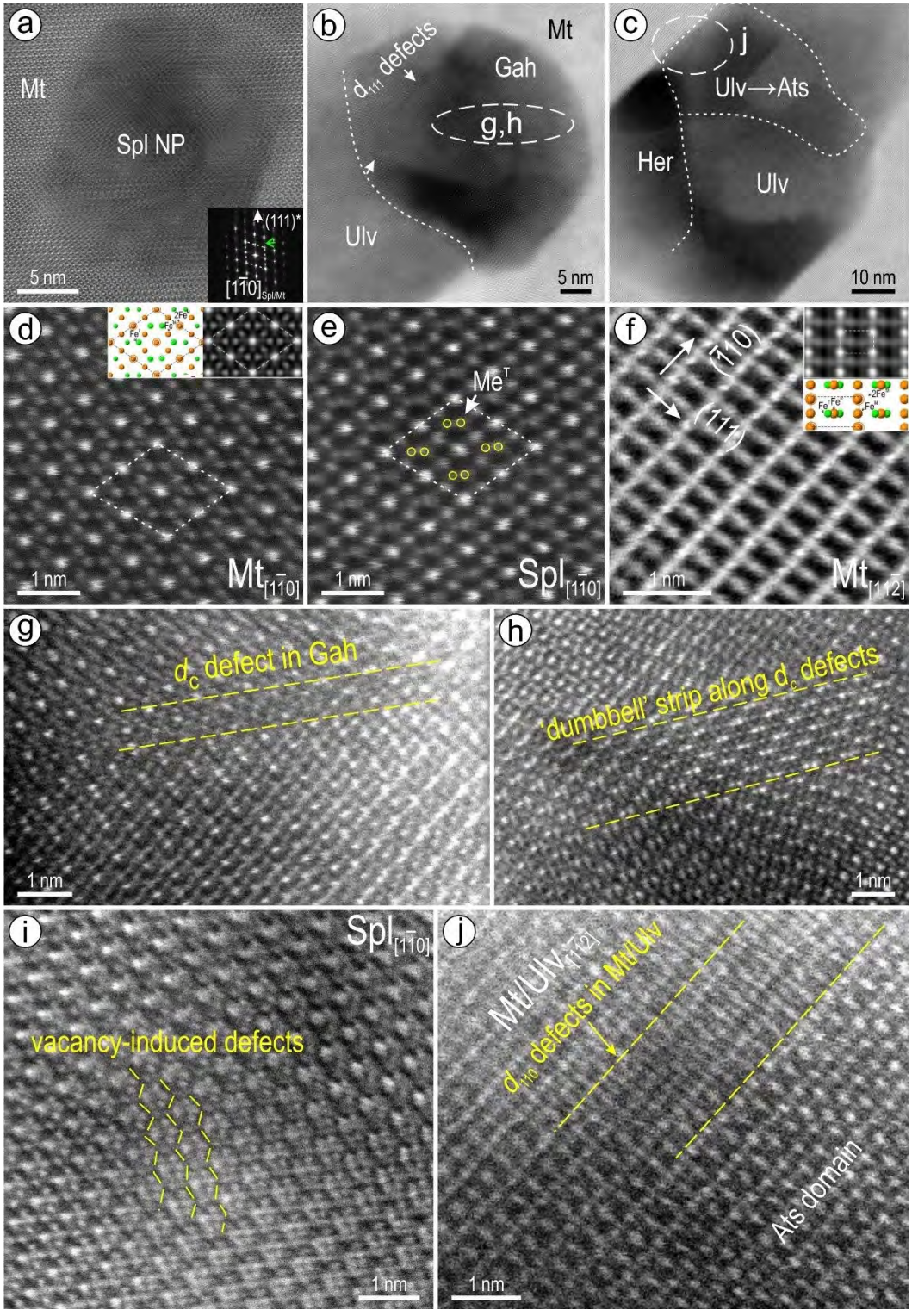

Fig. 11. HAADF STEM images showing lattice-scale defects in spinel species from NPs hosted in magnetite (Mt). (a) Lattice distortion in spinel *sensu stricto* (Spl) with (111)* disorder (inset FFT; arrowed). (b) Gahnite (Gah) displaying d_{111} defects. (c) Lobate domain in ulvöspinel (Ulv) replaced by anatase (Ats). (d-f) Atomic-scale images of spinel structure on two main zone axes as marked. Insets show STEM simulations (from Ciobanu et al. 2019) and crystal structure models. Note lower intensity for cations in tetragonal sites (T; circled) in spinel (e) relative to magnetite (d). (g, h) Linear defects showing atom disorder and dumbbell arrangement along *c* axis in gahnite. (i) Defects in spinel imaged on [1$\bar{1}$0] zone axis attributable to formation of metastable maghemite $(Fe^{3+}_{0.67}\ \square_{0.33})Fe^{3+}_{2}O_4$-vacancy; Bosi et al. 2019). (j) Defects along (110) in ulvöspinel at the boundary to anatase domains (area circled in c).

Displacement of the ten-atom ring in the spinel structure (Fig. 11i) is attributable to transition to metal-vacancy spinel structures (e.g., derivatives of maghemite, as shown in studies of silician magnetite; Xu et al. 2014; Ciobanu et al. 2019). Defects along (110) occur at domain boundaries between magnetite and anatase formed by replacement of ulvöspinel (Fig. 11j).

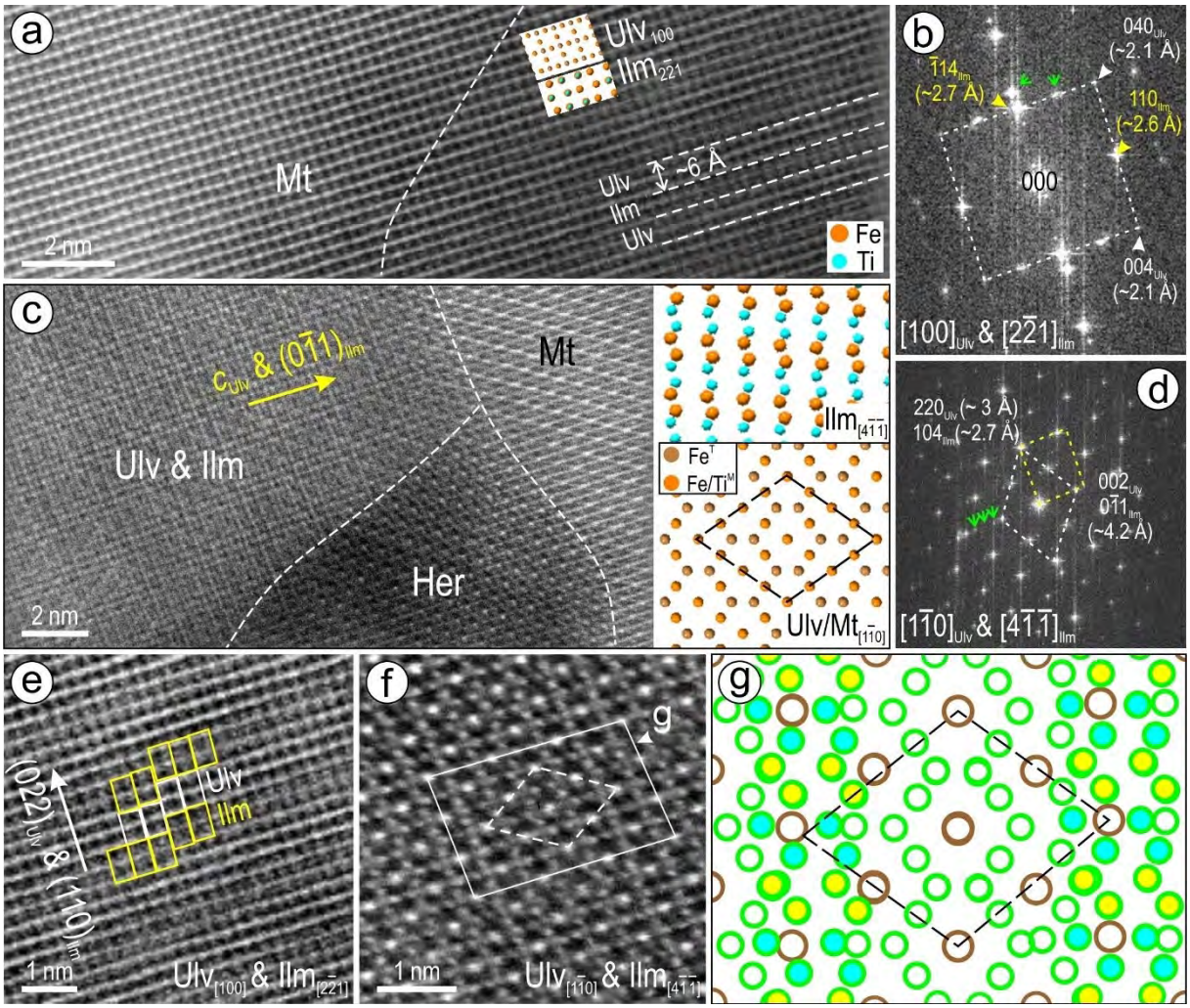

Fig. 12. HAADF STEM images (a, c, e, f), FFT patterns (b, d) and model (g) showing transformation of ulvöspinel (Ulv) to ilmenite (Ilm). Images obtained by tilting the NP from Figure 7d on two zone axes as marked. Coherent intergrowths between $[100]_{\mathrm{Ulv}}$ and $[2\bar{2}1]_{\mathrm{Ilm}}$ and $[1\bar{1}0]_{\mathrm{Ulv}}$ and $[4\bar{1}\bar{1}]_{\mathrm{Ilm}}$ (c and d, respectively). Green arrows on FFT patterns show satellite reflections indicating disorder. (e) Detail from (a) showing stepwise offset of Ulv-Ilm intergrowths. (f, g) Atomic-scale image and model of intergrowths in (c). Full circles represent ilmenite atoms overlapping the spinel structure using crystal models for the two phases shown in (c). See text for additional explanation.

Transformation of ulvöspinel to ilmenite, although rarely preserved, was imaged on two zone axes for the same NP hosted by titanomagnetite (Fig. 12). This is expressed as stacks of ~6 Å-period intergrowths between the two phases, corresponding to widths of ~$2d_{\bar{1}14}$ ilmenite and $2d_{022}$ in ulvöspinel, when the specimen is tilted on $[100]_{\mathrm{Ilm}}$ and $[2\bar{2}1]_{\mathrm{Ulv}}$ orientations (Fig.

12a, b). Coherent intergrowths are also observed along c_{Ulv} and $(0\bar{1}1)_{\mathrm{Ilm}}$ when the specimen is tilted on $[1\bar{1}0]_{\mathrm{Ulv}}//[4\bar{1}\bar{1}]_{\mathrm{Ilm}}$ zone axes (Fig. 12c, d). The 6 Å-period stacks are displaced along b_{Ulv} direction (Fig. 12e), correlating with the occurrence of satellite reflections on FFT patterns (Fig. 12b inset). Superposition of dumbbell atom pairs along $(104)_{\mathrm{Ilm}}$ with $(220)_{\mathrm{Ulv}}$ directions is seen by the presence of an additional ring of atoms in the spinel structure (Fig. 12f, g).

Both anatase and rutile are identified either within NPs, or along trellis lamellae (Figs. 13, 14). Anatase, forming from ulvöspinel in the domains shown in Figure 11c, was constrained from two zone axes: $[\bar{1}10]$ and $[\bar{1}1\bar{1}]$ (Fig. 13a, b), of which the dumbbell motif of Ti atoms on $[\bar{1}1\bar{1}]$ zone axis is discriminative compared to rutile. In both cases, FFT patterns show satellite reflections indicative of an underlining ulvöspinel structure. Anatase from clustered NPs (Fig. 10f) is often identified on $[02\bar{1}]$ zone axes with epitaxial orientation to $[1\bar{1}0]_{\mathrm{Mt}}$ (Fig. 13c).

Rutile on $[001]$ zone axis formed along trellis lamellae displays satellite reflections at ½ a^* and b^* (Fig. 13d), corresponding to an ilmenite precursor (as also shown in Fig. 10c, d). Comparable satellite reflections and disorder are associated with the presence of a second, sub-lattice in $[001]_{\mathrm{Rt}}$, identified in NPs from orbicular magnetite (Fig. 13e). Rutile and ilmenite are found as epitaxial intergrowths imaged on $[101]_{\mathrm{Rt}}//[\bar{1}1\bar{2}]_{\mathrm{Ilm}}$ zone axes (Fig. 13f) from trellis lamellae in orbicular magnetite.

In titanomagnetite with dense inclusion fields, the overprint along the trellis lamellae is shown by formation of anatase with sheared domains (Fig. 14). In this case, $[010]_{\mathrm{Ilm}}$ is identified as a relict within anatase (Fig. 14a-c). Anatase imaged on $[010]$ zone axis displays blocks sheared along the (102) direction and the FFT pattern indicates satellite reflections at ½ a^* and c^* (Fig. 14d, e). Atomic displacement is associated with crystallographic shear (CS) planes parallel to c_{Ats} and periodicity at d_{102} of ~9-10 Å (Fig. 14f, g).

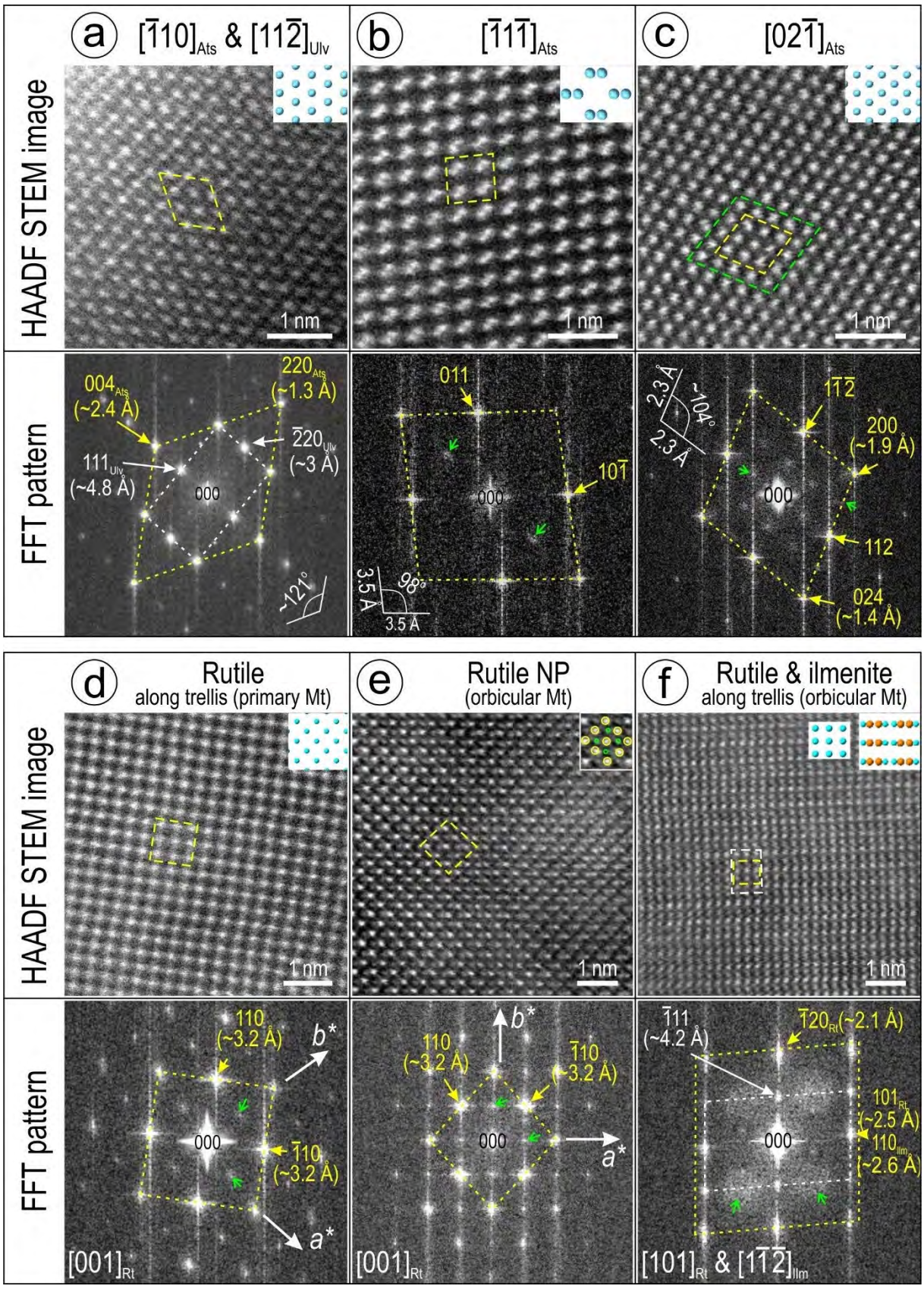

Fig. 13. High-resolution images and corresponding FFT patterns for TiO_2 polymorphs. (a-c) Anatase on three zone axes as marked. Images correspond to NPs in Figure 11c (a, b) and Figure 10c (c). (d-f) Rutile imaged on the same zone axis, [001], showing disorder (green arrows on FFTs). A second cation sublattice (green circles on inset) is imaged in (e), and is intergrown with ilmenite are shown in (f).

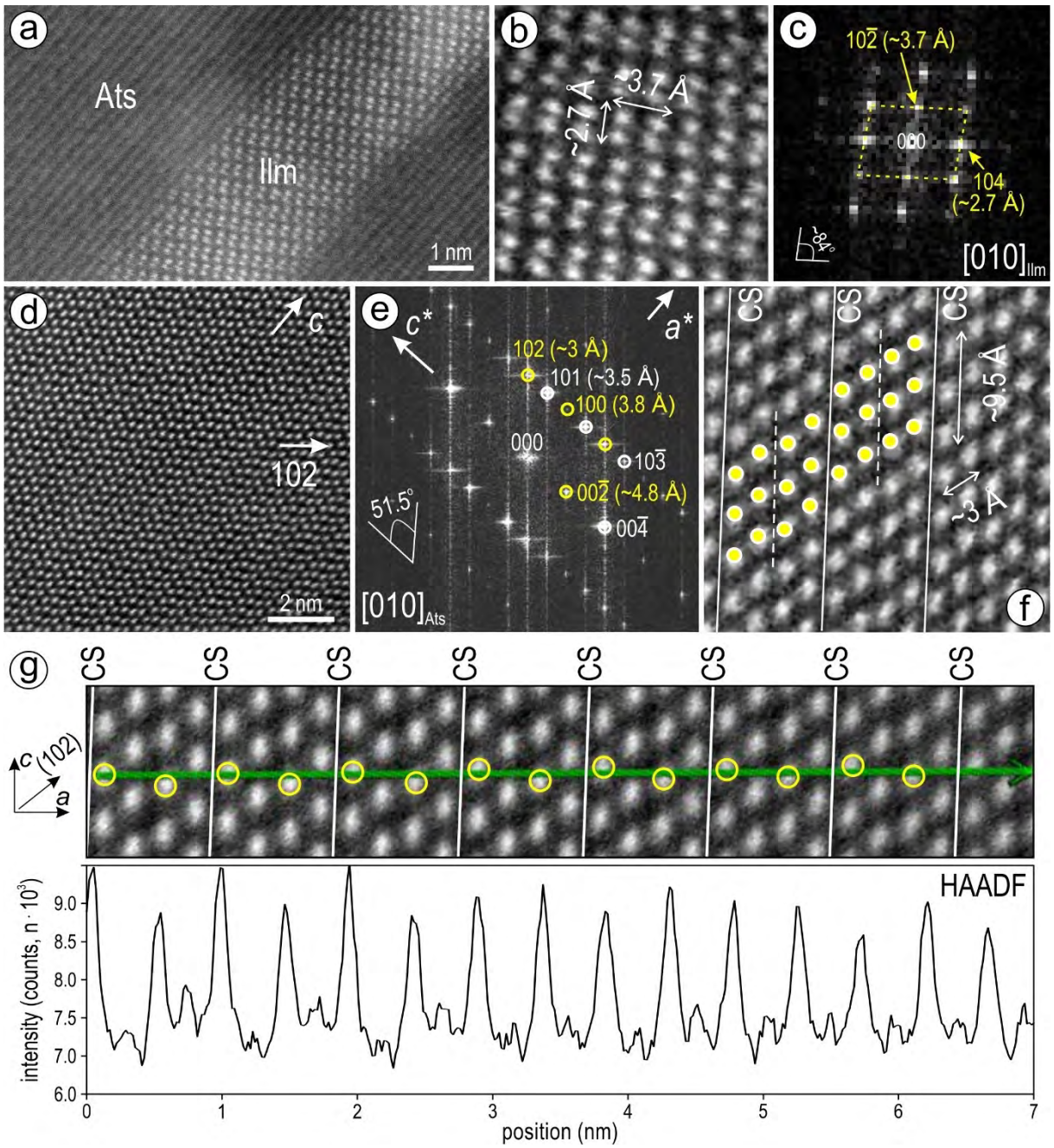

Fig. 14. HAADF STEM images and corresponding FFT patterns for ilmenite (Ilm) and anatase (Ats) with crystallographic shear (CS) planes (from trellis lamella in foil #4). (a-c) Relict $[010]_{Ilm}$ with misfit orientation to host $[010]_{CS-Ats}$. (d-f) Anatase on [010] showing CS along *c* axis and atom displacement along (102). Yellow circles on FFT pattern in (e) indicate satellite reflections attributable to CS planes. Atom shifts shown for Ti (full circles) in (f). (g) Intensity profile (highest intensity as open circles on the image) along (a) showing the regular shifts induced by CS planes.

DISCUSSION

Exsolution and order-disorder phenomena in spinels

Epitaxial relationships between spinels and Fe-Ti-oxides, either along trellis lamellae or within NPs (Fig. 10), show crystallographic control of formation processes, supporting:

exsolution, followed by replacement via mineral-buffered reactions or coupled dissolution reprecipitation reactions (CDRR).

Whereas spinel *sensu stricto* forms via exsolution of Al and Mg driven by comparable chemical gradients, bi-component spinel NPs likely originate from a two-step process: (i) Ulv-Her-Gah spinel solid solution ($Ulv_{74.0}Her_{23.4}Gah_{2.6}$) as a first exsolution product from $magnetite_{ss}$ in primary titanomagnetite ≳550 °C; and (ii) subsequent exsolution of individual components, supported by curvilinear boundaries among spinels (Fig. 7c-f).

A wide miscibility gap is reported for the $FeAl_2O_4$-Fe_2TiO_4 join in the system FeO-Al_2O_3-TiO_2 <1000 °C (e.g., Muan et al. 1972), which encompasses the $spinel_{ss}$ for binary Ulv-Her NPs. Even though the exsolution processes invoked here lie along the Ulv-Her join in the system FeO-Fe_2O_3-Al_2O_3-TiO_2 (for which data are unavailable), we can assume this is feasible given evidence for a sub-solidus state in a first stage of binary spinel NPs separation from magnetite (consistent composition, mutual boundaries; Figs. 7 and 8).

Moreover, binary hercynite-ulvöspinel NPs associations are present not only in granite-hosted magnetite from Olympic Dam with comparable density of trellis lamellae (Ciobanu et al. 2019) but also within titanomagnetite from the Fe-rich Panzhihua layered intrusion, China (Gao et al. 2017; 2019a), albeit with a somewhat lower density of trellis exsolution compared to that shown here (Fig. 2b).

The range of defects and lattice-scale order-disorder phenomena and the presence of relict or metastable phases (maghemite) (Fig. 11) are indicative of smallest-scale overprinting at disequilibrium conditions. Coherent lattice-scale intergrowths between ulvöspinel and ilmenite (Fig. 12) are illustrative of sub-solidus exsolution caused by vacancy relaxation in spinel and recording cooling under O_2-conserving conditions like those considered for lunar basalts or experimentally-obtained (micron-scale) ilmenite-ulvöspinel intergrowths (Lattard 1995). Non-redox processes have also been invoked to explain ilmenite superstructuring in titanomagnetite ores from the Panzhihua Fe-rich layered intrusion (Gao et al. 2019b).

The presence of two TiO_2 polymorphs, in most cases displaying disorder phenomena (underlining spinel structure, relicts or intergrowths with precursor ilmenite) in exsolution products from titanomagnetite (Figs. 13 and 14), represents further evidence of phase transformations by redox-controlled reactions, whereby excess rutile favors an increase in fO_2 (Padayachee et al. 2020). Rutile is well-known for its ability to form shear structures during TiO_2 oxidation (van Landuyt and Amelinckx 1970). CS defects, such as those shown here for anatase (Fig. 14), have been documented in TEM studies of non-stoichiometric, O-deficient rutile (Blanchin et al. 1981). High-resolution S/TEM studies have also shown O-vacancy superstructuring in O-deficient anatase displaying (103) and (101) CS planes with cubic-TiO-based structures in Ti_nO_{2n-1} (Ciancio et al. 2012). Although this is different to the CS planes along c_{Ats} with (102) displacements, there is great variability in the orientation of such planes, which are generally known as mechanisms for accommodation of anion deficiency in oxides, including those with TiO_2-related structures (Batuk et al. 2013).

Behavior of minor/trace elements in magnetite

Aluminum, the second most abundant element in all varieties of magnetite, is exsolved as nanoparticles of hercynite and gahnite in titanomagnetite, and spinel in Ti-poor magnetite (sample MV82). In contrast, Mg from the Ti-poor magnetite, although a major component of the spinel NPs, is retained in host magnetite since the Mg/Al ratio (≥1; mol..%/mol.%) is greater than 0.5 in stoichiometric spinel and no other Mg-bearing species is observed.

Zinc is measured at hundreds of ppm in both varieties of titanomagnetite and forms gahnite NPs, either in association with the other phases or alone. Such observations imply that the interacting fluid readily redistributed Zn, which was reprecipitated as gahnite NPs in samples that display trellis to orbicular textural transition. Such processes account for the considerable variation in Zn distribution at the micron-scale (Fig. 4a). A comparable process is also seen for trace Sc (≲45 ppm), which is observed as a discrete Ti-Sc-NP (Fig. 6e). Scandium may have been enriched in the pervading fluid since it is enriched in the orbicular magnetite relative to

trellis sub-type (Fig. 4a). In contrast, the hundreds of ppm V consistently measured could not be identified as either discrete phases or enriched in domains at the nanoscale.

Lower- temperature replacement reactions (<500 °C) display difference in HFSE mobility, e.g., Sc is more mobile than V, whereas Zn appears most easily remobilized (Figs. 7b and 8b). Element mobility during exsolutions can be attributed to solid state diffusion with variable kinetic rates, i.e., faster towards crystallographic planes in magnetite leading to trellis exsolutions, and slower for formation of NPs. Following coarsening of individual NPs, formation of three-component NP clusters, some of which show pores and additional fluid-related elements (e.g., F; Figs. 7h and 8h), can be attributed to a local increase in fluid percolation rates, while still preserving self-similar sub-systems operating within the same magnetite grain. Such a scenario can explain the greater textural variability across micron- to nanoscale patterns that appear during the transition from trellis to orbicular titanomagnetite (Fig. 5).

Magnetite formation at Acropolis

The Ti-rich and -poor magnetite types from Acropolis show nanoscale inclusions different to those described from hydrothermal magnetite, which is silician rather than Ti-bearing in other IOCG systems from the Olympic Dam district. The titanomagnetite, dominant at Acropolis, is similar in terms of textures to the magmatic magnetite from the granite hosting the Olympic Dam deposit (Ciobanu et al. 2019; Verdugo-Ihl et al. 2020). This raises the question of how Acropolis magnetite could have formed if we consider the same type of source for IOCG-forming hydrothermal fluids related to HS intrusions.

The discrepancy between inclusion populations in magnetite could be explained if we consider different regimes of fluid-rock interaction during alteration of host lithologies relative to mineralization. At Olympic Dam, the same rock-buffered reactions, also CDRR-driven, are documented from early stage alkali-calcic to late sericite-hematite alteration (Macmillan et al. 2016; Kontonikas-Charos et al. 2017; Verdugo-Ihl et al. 2017), whereas vein-filling

mineralization at Acropolis is fluid-buffered. This implies that the elements released during host rock alteration cannot provide cations (e.g., Si, Ca, Mg, etc.) for inclusion nucleation in Acropolis magnetite, as invoked for the formation of the abundant calc-silicates within silician magnetite from Olympic Dam (Ciobanu et al. 2019; Verdugo-Ihl et al. 2020).

Temperatures of ~550±50 °C for fluids (ilmenite-magnetite nano-thermooxybarometry) are within the ranges considered for alkali-calcic alteration in IOCG- or porphyry-style deposits (Richards and Mumin 2013). This temperature estimate provides a minimum limit for exsolution of the two-spinel NPs typical of Ti-rich magnetite at Acropolis.

Since the host lithologies at Acropolis show comparable IOCG-type alteration as the host granite at Olympic Dam (Dmitrijeva et al. 2019a, 2019b), hydrolytic alteration partially telescopes vein-magnetite precipitated from fluids circulating along an open fracture system, with the upper parts of the system dominated by abundant hematite and Cu-rich sulfides. Telescoping during vein-reopening is also recorded at depth by the re-shaping of trellis magnetite through the densely mottled fields with two- or three-phase spinel NPs and ultimately resulting in the orbicular Ti-rich magnetite.

The spinel-bearing magnetite can be interpreted as the result of distinct fluid pulses or, more likely, a further case of initial trellis magnetite overprinted by interaction with hot (~600±50 °C) fluids (Fig. 3g). Such Ti-depleted magnetite would recrystallize and only retain low contents of minor elements (Mg, Al), whereas re-cycling of Ti could contribute towards formation of Ti-bearing hematite (Courtney-Davies et al. 2019a) and rutile, either in the same sample or elsewhere in the prospect. Unlike layered intrusions, in which different generations of spinel and ilmenite exsolutions can coexist in the same magnetite (Tan et al. 2016; Gao et al. 2017, 2019a, 2019b), the present study shows transformation of spinel+ilmenite exsolutions in magnetite from Acropolis during interaction with fluids at increasing fO_2 conditions. Such reactions are mineral-buffered (presence of two TiO_2 polymorphs) and result in a variety of micron- to nanoscale textures.

The elevated temperature of such fluids can be associated with continuing magmatic activity within the district, if we consider the differences in age between HS granites and GRV rocks dated by high-precision methods at Acropolis and Olympic Dam (Cherry et al. 2018; McPhie et al. 2020; Courtney-Davies et al. 2020). The HS granite intersected in drillhole ACD7 is unlikely to be the source of the mineralizing fluids as the geochemical footprint of the IOCG mineralization signature is not centered on this body (Dmitrijeva et al. 2019b) and the dated U-bearing hematite, potentially indicative of source proximity, is located to the SE (Courtney-Davies et al. 2019a). The initial, relatively high Ti-content in these fluids, enhanced by high halogen contents (Tanis et al. 2016), may also suggest an intrusion with slightly more mafic composition.

Considering the steeply dipping veins at Acropolis, sub-vertical faults with multiple reactivation episodes would focus fluids sourced from an intrusion located beneath the present level of intersected lithologies. Although the wide alteration footprint is indicative of veins reaching the surficial fracture network, the temperature estimates for the mineralizing fluids (500-600 °C) indicate a formation depth of at least ~2 km.

IMPLICATIONS

The nanomineralogy of magnetite represents a rich and often untapped source of petrogenetic information that can contribute to improved genetic models for IOCG and related deposits. This approach shows the risks associated with using geochemical signatures alone to discriminate among deposit types, without detailed mineral characterization to assess dynamic variability.

Acropolis magnetite, typified by the presence of NP of spinel group minerals, has formed from hot fluids, which circulated through veins in volcanic sequences and granite. Magnetite records the history of fluid percolation during vein re-opening leading to progressive overprinting of the Ti-rich variety and resulting in self-patterning, expressed as inclusion mottling and rhythmic orbicular textures. At the nanoscale, these processes are associated with

NP clustering and coarsening, as well as replacement of ulvöspinel by anatase/rutile. Two-spinel NPs (ulvöspinel-hercynite or ulvöspinel-gahnite) and finest, monophase NPs of spinel *sensu stricto*, epitaxial relationships between spinel and Fe-Ti-oxides along trellis lamellae and within NPs support a model of exsolution from magnetite solid solutions, followed by replacement via mineral-buffered reactions.

Lattice-scale intergrowths documented between ulvöspinel and ilmenite are attributable to cooling under O_2-conserving conditions. Overprinting at disequilibrium conditions is recorded by order-disorder phenomena (defects, metastable phases, relicts), subtly fO_2-buffered reactions from anatase (reducing) to rutile (more oxidizing) stabilities, transient formation of O-deficient phases such as CS-modulated anatase. At such conditions, NP nucleation is dependent upon availability of Al, Ti, Zn and Mg and their relative concentrations. Recycling of these elements during replacement via CDRR leads to formation of gahnite NPs or discrete Sc-Ti-phases, whereas V is largely immobile.

Although published data indicate that $\delta^{56}Fe$ and $\delta^{18}O$ values largely overlap for magnetite crystallized from silicate melt and magnetite crystallized from early Cl-bearing magmatic-hydrothermal fluids (e.g., Troll et al. 2019; Childress et al. 2020), this study draws attention to the potential implications for accurate determination of Fe and O isotope signatures brought about by changing conditions during re-equilibration and subsequent recrystallization of phases within the magnetite. The effect on the Fe and O isotopic signatures is not necessarily determined by the mass/volume of the NPs, but by a change in Fe and O signatures within extensively overprinted domains of the host magnetite as a whole, i.e., leading to uneven grain-scale trace element redistribution during dissolution and subsequent reprecipitation. Whereas some of these elements (e.g., Al, Ti) are preserved within the volumes where the fluid-mineral interaction operated, there is no guarantee that the Fe and O signatures would have been preserved during re-equilibration. Therefore, if no proper sample characterization is conducted at appropriate scales, this could lead to a misinterpretation of magmatic versus hydrothermal

signatures, or inaccurate temperature estimates. Confirmation of this effect would, however, require more in-depth studies.

Since the trellis magnetite at Acropolis is within the lower range of TiO_2 content (up to 3.09 wt.%) and the temperature estimates are typical of alkali-calcic alteration in IOCG systems, why is this type of magnetite not more commonly reported? There are at least two reasons why magnetite with comparable TiO_2 contents will not display trellis exsolution. One, as shown here for the Ti-rich orbicular magnetite, is the obliteration of such primary textures during subsequent fluid-assisted overprinting. Secondly, and more generic, development of trellis textures is restricted by fO_2 conditions, as outlined by the oxy-exsolution model of Buddington and Lindsley (1964). In this model, magnetite-ulvöspinel solid solution (Mt-Ulv_{ss}) can lead to ilmenite-magnetite intergrowths (trellis textures) during sub-solidus oxidation of the Mt-Ulv_{ss}, even when the reactions driving fO_2 increase are outside the magnetite grain, e.g., controlled by alteration of country rocks. At Acropolis, disequilibrium of ulvöspinel NPs retaining transient anatase formation, or the presence of the same Ti-oxide along some of the trellis features, indicates gradual, subtle fO_2 increase between the initial trellis exsolution (ilmenite stable) to the latest orbicular stage (rutile- towards hematite-stable) in the studied Ti-rich magnetite (Fig. 9f). Trellis magnetite should be a characteristic feature of the alkali-calcic alteration in IOCG systems if fO_2 variation remains under the hematite-magnetite buffer for a sufficiently long time to allow ilmenite-magnetite re-equilibration.

An abundance of apatite in magnetite-dominant, relatively sulfide-poor, IOCG systems, has led to definition of a so-called iron oxide apatite (IOA) deposit sub-type within the broader IOCG clan (e.g., Williams et al. 2010). Acropolis has been considered an IOA-IOCG system based on locally abundant and sometimes cm-sized, pegmatitic apatite associated with magnetite (Ehrig et al. 2017; Krneta et al. 2017). Hydrothermal apatite is also abundant in the outer shell at Olympic Dam (Krneta et al. 2016; Apukhtina et al. 2017) but this does not survive hydrolytic alteration within the deposit. It is likely that 'IOA' mineralization represents an

initial, transient stage of any IOCG system, preserved as such only when that system does not evolve towards more oxidized/acidic conditions.

Trellis-textured titanomagnetite in which various spinel species form fields of exsolution are well-known from iron ores associated with layered intrusions (e.g., Arguin et al. 2018; Gao et al. 2019a) but magnetite with such textures is much rarer in hydrothermal ores. It has been recently reported from several Chinese localities including those in the Daye district (Hu et al. 2020), which share some common characteristics with Acropolis in terms of geological setting. Hu et al. (2020) identified Ti-bearing, trellis-textured magnetite as vein and fracture filling within diorite porphyry and overlaying albitized andesite and considered this magnetite typical of IOA mineralization and a useful guide for such deposits in the region. In contrast, Ti-bearing magnetite from Los Colorados, also considered of IOA type, displays oscillatory zoning with respect to Ti (0.1-0.4 wt.% TiO_2), among other elements (Deditius et al. 2018). Nanoscale study of such magnetite reveals a broad range of included silicates, ulvöspinel and 'Ti-rich magnetite'.

Hydrothermal titanomagnetite from Acropolis is clearly comparable with magmatic magnetite hosted by granites at Olympic Dam and elsewhere, and should typify an early, alkali-calcic stage of alteration. Open-fracture circulation, inhibiting additional supply of elements (Si, Ca, K, etc.) during magnetite precipitation, prohibits formation of silician magnetite as a host for calc-silicate NPs. The same type of approach, if applied to magnetite from mineralization spanning the magmatic-hydrothermal spectrum, would give insights into the early, high-T stages of deposit evolution, particularly porphyries and skarns.

ACKNOWLEDGMENTS

This is a contribution to the project "Trace elements in iron oxides: deportment, distribution and application in ore genesis, geochronology, exploration and mineral processing" supported by BHP Olympic Dam and the South Australian Mining and Petroleum Services Centre of Excellence. We extend thanks to Sarah Gilbert and Benjamin Wade (Adelaide Microscopy), who assisted with analytical

work. N.J.C. acknowledges support from the ARC Research Hub for Australian Copper-Uranium (Grant IH130200033). We appreciate the insightful comments of Adam Simon and an anonymous reviewer.

REFERENCES

Apukhtina, O.B., Kamenetsky, V.S., Ehrig, K., Kamenetsky, M.B., Maas, R., Thompson, J., McPhie, J., Ciobanu, C.L., and Cook, N.J. (2017) Early, deep magnetite-fluorapatite mineralization at the Olympic Dam Cu-U-Au-Ag deposit, South Australia. Economic Geology, 112, 1531–1542. https://doi.org/10.5382/econgeo.2017.4520

Arguin, J.-P., Pagé, P., Barnes, S.-J., Girard, R., and Duran, C. (2018) An integrated model for ilmenite, Al-spinel, and corundum exsolutions in titanomagnetite from oxide-rich layers of the Lac Doré Complex (Québec, Canada). Minerals, 8, 476. https://doi.org/10.3390/min8110476

Batuk, D., Batuk, M., Abakumov, A.M., Tsirlin, A.A., McCammon, C., Dubrovinsky, L., and Hadermann, J. (2013) Effect of lone-electron-pair cations on the orientation of crystallographic shear planes in anion-deficient perovskites. Inorganic Chemistry, 52, 10009–10020. https://doi.org/10.1021/ic4012845

Blanchin, M.G., Bursill, L.A., Hutchison, J.L., and Gai, P.L. (1981) Direct observation of disorder within crystallographic shear defects in deformed and non-stoichiometric rutiles. Journal de Physique Colloques 42 (Suppl. C3), 95-112. https://doi.org/10.1051/jphyscol:1981310

Bosi, F., Biagioni, C., and Pasero, M. (2019) Nomenclature and classification of the spinel supergroup. European Journal of Mineralogy, 31, 183–192. https://doi.org/10.1127/ejm/2019/0031-2788

Bowles, J.F.W., Howie, R.A., Vaughan, D.J., and Zussman, J. (2011) Rock-forming Minerals: Non-Silicates: Oxides, Hydroxides and Sulphides. The Geological Society of London, 920 pp.

Buddington, A.F., and Lindsley, D.H. (1964) Iron-titanium oxide minerals and synthetic equivalents. Journal of Petrology, 5, 310–357. https://doi.org/10.1093/petrology/5.2.310

Canil, D., and Lacourse, T. (2020) Geothermometry using minor and trace elements in igneous and hydrothermal magnetite. Chemical Geology, 541, 119576. https://doi.org/10.1016/j.chemgeo.2020.119576

Cherry, A.R., Ehrig, K., Kamenetsky, V.S., McPhie, J., Crowley, J.L., and Kamenetsky, M.B. (2018) Precise geochronological constraints on the origin, setting and incorporation of ca. 1.59 Ga surficial facies into the Olympic Dam Breccia Complex, South Australia. Precambrian Research, 315, 162–178. https://doi.org/10.1016/j.precamres.2018.07.012

Childress, T.M., Simon, A.C., Reich, M., Barra, F., Arce, M., Lundstrom, C.C., and Bindeman, I.N. (2020) Formation of the Mantoverde iron oxide-copper-gold (IOCG) deposit, Chile: insights from Fe and O stable isotopes and comparisons with iron oxide-apatite (IOA) deposits. Mineralium Deposita, 55, 1289–1504. https://doi.org/10.1007/s00126-019-00936-x

Ciancio, R., Vittadini, A., Selloni, A., Aruta, C., Scitti di Uccia, U., Rossi, G., and Carlino, E. (2012) Atomic structure and crystallographic shear planes in epitaxial TiO_2 anatase thin films. Microscopie, September 2012, 50–56. https://doi.org/10.4081/microscopie.2012.4985

Ciobanu, C.L., Cook, N.J., Utsunomiya, S., Pring, A., and Green, L. (2011) Focussed ion beam–transmission electron microscopy applications in ore mineralogy: Bridging micro- and nanoscale observations. Ore Geology Reviews, 42, 6–31. https://doi.org/10.1016/j.oregeorev.2011.06.012

Ciobanu, C.L., Verdugo-Ihl, M.R., Slattery, A., Cook, N.J., Ehrig, K., Courtney-Davies, L., and Wade, B.P. (2019) Silician Magnetite: Si–Fe-Nanoprecipitates and Other Mineral Inclusions in Magnetite from the Olympic Dam Deposit, South Australia. Minerals, 9, 311. https://doi.org/10.3390/min9050311

Courtney-Davies, L., Ciobanu, C.L., Verdugo-Ihl, M.R., Dmitrijeva, M., Cook, N.J., Ehrig, K., and Wade, B.P. (2019a) Hematite geochemistry and geochronology resolve genetic and temporal links

among iron-oxide copper gold systems, Olympic Dam district, South Australia. Precambrian Research, 335, 105480. https://doi.org/10.1016/j.precamres.2019.105480

Courtney-Davies, L., Tapster, S.R., Ciobanu, C.L., Cook, N.J., Verdugo-Ihl, M.R., Ehrig, K.J., Kennedy, A.K., Gilbert, S.E., Condon, D.J., and Wade, B.P. (2019b) A multi-technique evaluation of hydrothermal hematite U-Pb isotope systematics: implications for ore deposit geochronology. Chemical Geology, 513, 54–72. https://doi.org/10.1016/j.precamres.2019.105480

Courtney-Davies, L., Ciobanu, C.L., Tapster, S.R., Cook, N.J., Ehrig, K., Crowley, J.L., Verdugo-Ihl, M.R., Wade, B.P., and Condon, D.J. (2020) Opening the Magmatic-Hydrothermal Window: High-Precision U-Pb Geochronology of the Mesoproterozoic Olympic Dam Cu-U-Au-Ag Deposit, South Australia. Economic Geology, in press. https://doi.org/10.5382/econgeo.4772

Deditius, A.P., Reich, M., Simon, A.C., Suvorova, A., Knipping, J., Roberts, M.P., Rubanov, S., Dodd, A., and Saunders, M. (2018) Nanogeochemistry of hydrothermal magnetite. Contributions to Mineralogy and Petrology, 173, 46. https://doi.org/10.1007/s00410-018-1474-1

Dmitrijeva, M., Ciobanu, C.L., Ehrig, K.J., Cook, N.J., Metcalfe, A. V., Verdugo-Ihl, M.R., and McPhie, J. (2019a) Mineralization-alteration footprints in the Olympic Dam IOCG district, South Australia: The Acropolis prospect. Journal of Geochemical Exploration, 205, 106333. https://doi.org/10.1016/j.gexplo.2019.106333

Dmitrijeva, M., Ehrig, K.J., Ciobanu, C.L., Cook, N.J., Verdugo-Ihl, M.R., and Metcalfe, A.V. (2019b) Defining IOCG signatures through compositional data analysis: A case study of lithogeochemical zoning from the Olympic Dam deposit, South Australia. Ore Geology Reviews, 105, 86–101. https://doi.org/10.1016/j.oregeorev.2018.12.013

Ehrig, K., Kamenetsky, V.S., McPhie, J., Apukhtina, O., Ciobanu, C.L., Cook, N.J., Kontonikas-Charos, A., and Krneta, S. (2017) The IOCG-IOA Olympic Dam Cu-U-Au-Ag deposit and nearby prospects, South Australia. Proceedings, 14th SGA Biennial Meeting 2017, Mineral Resources to Discover, p. 823–826.

Ferracutti, G.R., Gargiulo, M.F., Ganuza, M.L., Bjerg, E.A., and Castro, S.M. (2015) Determination of the spinel group end-members based on electron microprobe analyses. Mineralogy and Petrology, 109, 153–160. https://doi.org/10.1007/s00710-014-0363-1

Frost, B.R. (1991) Introduction to oxygen fugacity and its petrologic importance, in: Lindsley, D.H. (Ed.), Oxide Minerals. De Gruyter, Berlin, Boston, pp. 1–10. https://doi.org/10.1515/9781501508684-004.

Gao, W., Ciobanu, C.L., Cook, N.J., Huang, F., Meng, L., and Gao, S. (2017) Petrography and trace element signatures in silicates and Fe–Ti oxides from the Lanjiahuoshan deposit, Panzhihua layered intrusion, Southwest China. Lithos, 294-295, 164–183. https://doi.org/10.1016/j.lithos.2017.10.003

Gao, W., Ciobanu, C.L., Cook, N.J., Slattery, A., Huang, F., and Wang, D. (2019a) Nanoscale study of lamellar exsolutions in clinopyroxene from olivine gabbro: Recording crystallization sequences in iron-rich layered intrusions. American Mineralogist, 104, 244–261. https://doi.org/10.2138/am-2019-6764

Gao, W., Ciobanu, C.L., Cook, N.J., Slattery, A., Huang, F., and Song, D. (2019b) Nanoscale study of titanomagnetite from the Panzhihua Layered Intrusion, Southwest China: Multistage exsolutions record ore formation. Minerals, 9, 513. https://doi.org/10.3390/min9090513

Hu, H., Li, J., Harlov, D.E., Lentz, D.R., McFarlane, C.R.M., and Yang, Y.-H. (2020) A genetic link between iron oxide-apatite and iron skarn mineralization in the Jinniu volcanic basin, Daye district, eastern China: Evidence from magnetite geochemistry and multi-mineral U-Pb geochronology. Geological Society of America Bulletin, 132, 899–917. https://doi.org/10.1130/B35180.1

Kontonikas-Charos, A., Ciobanu, C.L., Cook, N.J., Ehrig, K., Krneta, S., and Kamenetsky, V.S. (2017) Feldspar evolution in the Roxby Downs Granite, host to Fe-oxide Cu-Au-(U) mineralisation at Olympic Dam, South Australia. Ore Geology Reviews, 80, 838–859. https://doi.org/10.1016/j.oregeorev.2016.08.019

Krneta, S., Ciobanu, C.L., Cook, N.J., Ehrig, K., and Kontonikas-Charos, A. (2016) Apatite at Olympic Dam, South Australia: A petrogenetic tool. Lithos, 262, 470–485. https://doi.org/10.1016/j.lithos.2016.07.033

Krneta, S., Cook, N.J., Ciobanu, C.L., Ehrig, K., and Kontonikas-Charos, A. (2017) The Wirrda Well and Acropolis prospects, Gawler Craton, South Australia: Insights into evolving fluid conditions through apatite chemistry. Journal of Geochemical Exploration, 181, 276–291. https://doi.org/10.1016/j.gexplo.2017.08.004

Lattard, D. (1995) Experimental evidence for the exsolution of ilmenite from titaniferous spinel. American Mineralogist, 80, 968–981. https://doi.org/10.2138/am-1995-9-1013

Macmillan, E., Cook, N.J., Ehrig, K., Ciobanu, C.L., and Pring, A. (2016) Uraninite from the Olympic Dam IOCG-U-Ag deposit: Linking textural and compositional variation to temporal evolution. American Mineralogist, 101, 1295–1320. https://doi.org/10.2138/am-2016-5411

McPhie, J., Ehrig, K.J., Kamenetsky, M.B., Crowley, J.L., and Kamenetsky, V.S. (2020) Geology of the Acropolis prospect, South Australia, constrained by high-precision CA-TIMS ages. Australian Journal of Earth Sciences, 67, 699–716. https://doi.org/10.1080/08120099.2020.1717617

Muan, A., Hauck, J., and Löfall, T. (1972) Equilibrium studies with a bearing on lunar rocks. Proceedings, Third Lunar Science Conference, 3, 185–196.

Oreskes, N., and Einaudi, M.T. (1992) Origin of hydrothermal fluids at Olympic Dam: preliminary results from fluid inclusions and stable isotopes. Economic Geology, 87, 64–90. https://doi.org/10.2113/gsecongeo.87.1.64

Padayachee, D., Mahomed, A.S., Singh, S., and Friedrich, H.B. (2020) The effect of the TiO_2 anatase:rutile ratio and interface for the oxidative activation of n-octane. ACS Catalysis, 10, 2211–2220. https://doi.org/10.1021/acscatal.9b04004

Richards, J.P., and Mumin, A.H. (2013) Magmatic-hydrothermal processes within an evolving Earth: Iron oxide-copper-gold and porphyry Cu±Mo±Au deposits. Geology, 41, 767–770. https://doi.org/10.1130/G34275.1

Righter, K., Keller, L.P., Rahman, Z., and Christoffersen, R. (2014) Redox-driven exsolution of iron-titanium oxides in magnetite in Miller Range (MIL) 03346 nakhlite: Evidence for post crystallization oxidation in the nakhlite cumulate pile? American Mineralogist, 99, 2313–2319. https://doi.org/10.2138/am-2014-4926

Tan, W., Liu, P., He, H.P., Wang, C.Y., and Liang, X.L. (2016) Mineralogy and Origin of Exsolution in Ti-rich Magnetite from Different Magmatic Fe-Ti Oxide-bearing Intrusions. The Canadian Mineralogist, 53, 539–553. https://doi.org/10.3749/canmin.1400069

Tanis, E.A., Simon, A., Zhang, Y., Chow, P., Xiao, Y., Hanchar, J.M., Tschauner, O., and Shen, G. (2016) Rutile solubility in NaF–NaCl–KCl-bearing aqueous fluids at 0.5–2.79 GPa and 250–650 °C. Geochimica et Cosmochimica Acta, 177, 170–181. https://doi.org/10.1016/j.gca.2016.01.003

Troll, V.R., Weis, F.A., Jonsson, E., Andersson, U.B., Majidi, S.A., Högdahl, K., Harris, C., Millet, M.A., Chinnasamy, S.S., Kooijman, E., and Nilsson, K.P. (2019) Global Fe-O isotope correlation reveals magmatic origin of Kiruna-type apatite-iron-oxide ores. Nature Communications, 10, 1712. https://doi.org/10.1038/s41467-019-09244-4

Van Landuyt, J. and Amelinckx, S. (1970) Shear structures in titanium oxide. Materials Research Bulletin, 5(4), 267–274. https://doi.org/10.1016/0025-5408(70)90123-6

Verdugo-Ihl, M.R., Ciobanu, C.L., Cook, N.J., Ehrig, K.J., and Courtney-Davies, L. (2020) Defining early stages of IOCG systems: evidence from iron oxides in the outer shell of the Olympic Dam deposit, South Australia. Mineralium Deposita, 55, 429–452. https://doi.org/10.1007/s00126-019-00896-2

Verdugo-Ihl, M.R., Ciobanu, C.L., Cook, N.J., Ehrig, K.J., Courtney-Davies, L., and Gilbert, S. (2017) Textures and U-W-Sn-Mo signatures in hematite from the Olympic Dam Cu-U-Au-Ag deposit, South Australia: Defining the archetype for IOCG deposits. Ore Geology Reviews, 91, 173–195. https://doi.org/10.1016/j.oregeorev.2017.10.007

Williams, P.J. (2010) Classifying IOCG deposits, in: Corriveau, L., Mumin, H. (Eds.), Exploring for Iron Oxide Copper-Gold Deposits: Canada and Global Analogues, Short Course Notes, Geological Association of Canada, pp. 23–38.

Xu, H., Shen, Z., and Konishi, H. (2014) Si-magnetite nano-precipitates in silician magnetite from banded iron formation: Z-contrast imaging and ab initio study. American Mineralogist, 99, 2196–2202. https://doi.org/10.2138/am-2014-4964

Zhou, M.-F., Robinson, P.T., Lesher, C.M., Keays, R.R., Zhang, C.-J., and Malpas, J. (2005) Geochemistry, petrogenesis and metallogenesis of the Panzhihua gabbroic layered intrusion and associated Fe–Ti–V oxide deposits, Sichuan Province, SW China. Journal of Petrology, 46, 2253–2280. https://doi.org/10.1093/petrology/egi054

CHAPTER 7

FERRO-TSCHERMAKITE WITH SHORT RANGE DISORDER IDENTIFIED IN SILICIAN MAGNETITE

Max R. Verdugo-Ihl [1], Cristiana L. Ciobanu [1], Nigel J. Cook [1], Kathy Ehrig [2],

Ashley Slattery [3], Liam Courtney-Davies [1]

[1]*School of Chemical Engineering and Advanced Materials, The University of Adelaide, Adelaide, SA 5005, Australia;*

[3]*BHP Olympic Dam, 10 Franklin St, Adelaide SA, 5000, Australia;*

[2]*Adelaide Microscopy, The University of Adelaide, Adelaide, SA 5005, Australia*

Article submitted to *American Mineralogist*, April 17th, 2020.

Statement of Authorship

Title of Paper	Ferro-tschermakite with short range disorder identified in silician magnetite
Publication Status	☐ Published ☐ Accepted for Publication ☑ Submitted for Publication ☐ Unpublished and Unsubmitted work written in manuscript style
Publication Details	Verdugo-Ihl, M.R., Ciobnau, C.L., Cook, N.J., Ehrig, K.J., Slattery, A., Courtney-Davies, L. Ferro-tschermakite with short range disorder identified in silician magnetite. Submitted to *American Mineralogist*.

Principal Author

Name of Principal Author (Candidate)	Max R. Verdugo-Ihl		
Contribution to the Paper	Performed analytical work, evaluation and interpretation of results and prepared the manuscript.		
Overall percentage (%)	55		
Certification:	This paper reports on original research I conducted during the period of my Higher Degree by Research candidature and is not subject to any obligations or contractual agreements with a third party that would constrain its inclusion in this thesis. I am the primary author of this paper.		
Signature		Date	15.04.2020

Co-Author Contributions

By signing the Statement of Authorship, each author certifies that:

i. the candidate's stated contribution to the publication is accurate (as detailed above);

ii. permission is granted for the candidate in include the publication in the thesis; and

iii. the sum of all co-author contributions is equal to 100% less the candidate's stated contribution.

Name of Co-Author	Cristiana L. Ciobanu		
Contribution to the Paper	Helped to define the direction of the paper, assisted with data acquisition and processing, interpretation of the results and the preparation and evaluation of the manuscript.		
Overall percentage (%)	25		
Signature		Date	15.04.2020

Name of Co-Author	Nigel J. Cook		
Contribution to the Paper	Helped to define the direction of the paper, assisted with interpretation of the results and the preparation and evaluation of the manuscript.		
Overall percentage (%)	10		
Signature		Date	15.04.2020

Name of Co-Author	Ashley Slattery		
Contribution to the Paper	Performed HAADF-STEM data acquisition.		
Overall percentage (%)	4		
Signature		Date	15.04.20

Name of Co-Author	Kathy Ehrig		
Contribution to the Paper	Assisted with the evaluation of the manuscript.		
Overall percentage (%)	4		
Signature		Date	15.04.2020

Name of Co-Author	Liam Courtney-Davies		
Contribution to the Paper	Assisted with the evaluation of the manuscript.		
Overall percentage (%)	2		
Signature		Date	15.04.2020

LETTER

Ferro-tschermakite with short range disorder identified in silician magnetite

MAX R. VERDUGO-IHL[1,*], CRISTIANA L. CIOBANU[1], NIGEL J. COOK[1], KATHY EHRIG[2], ASHLEY SLATTERY[3], LIAM COURTNEY-DAVIES[1]

[1] *School of Chemical Engineering and Advanced Materials, The University of Adelaide, Adelaide, SA, 5000, Australia*

[2] *BHP Olympic Dam, 10 Franklin St., Adelaide, South Australia 5000, Australia*

[3] *Adelaide Microscopy, The University of Adelaide, Adelaide, SA, 5000, Australia*

ABSTRACT

Silician magnetite hosted by ~1.85 Ga lithologies in the Wirrda Well prospect, Olympic Dam district, South Australia, was examined at the nanoscale using high angle annular dark field scanning transmission electron microscopy (HAADF STEM) imaging, STEM energy-dispersive X-ray spectrometry mapping and spot analysis, and supported by STEM simulations. Among the inclusions imaged in magnetite is an unusually high-Al (3.24 a.p.f.u.) amphibole, identified as ferro-tschermakite, $K_{0.06}(Ca_{1.21}Na_{0.37}Fe_{0.2}Mn_{0.04})_{1.82}(Al_{1.89}Fe^{2+}_{1.86}Mg_{1.18}Ti_{0.06})_5(Si_{6.65}Al_{1.35})_8O_{22}(OH)_2$. Randomly distributed defects are observed along $b_{\text{ferro-tschermakite}}$, forming 3-chain units coherently intergrown within the 2-chain amphibole structure when viewed on [001] zone axis. This type of short-range stacking disorder is widely reported from pyriboles. Observed textures and phase assemblages are attributable to a two-stage evolution: (i) amphibole inclusion growth under oriented stress during prograde metamorphism of magnetite at ~1735–1690 Ma; and (ii) hydrothermal, post-metamorphic alteration of assemblages by local fluid-percolation along fractures and zone boundaries at ~1.59 Ga. HAADF STEM imaging shows stacking disorder in pyriboles relates directly to the presence of double A-site cavities of high complexity in terms of charge balance requirements, explaining the scarcity of regular sequences in natural samples. Magnetite records petrogenetic

processes by accommodating variable ranges of nanomineral inclusions and preserving them over geological time scales.

Keywords: ferro-tschermakite, short range disorder, pyriboles, silician magnetite, HAADF STEM

INTRODUCTION AND BACKGROUND

Scanning transmission electron microscopy (STEM) enables imaging of minerals and their intergrowths at the nanoscale, offering insight into petrological processes that cannot be constrained by other techniques. Mineral inclusions in magnetite are increasingly reported from nanoscale studies using Z-contrast STEM imaging techniques of minerals from deposits spanning the magmatic-hydrothermal spectrum (Xu et al. 2014; Deditius et al. 2018; Ciobanu et al. 2019; Gao et al. 2019a, b; Yin et al. 2019; Verdugo Ihl et al. in review). Whereas crystallographically-oriented inclusions of magnetite are common in pyroxenes from igneous and metamorphic rocks (Fleet et al. 1980), inclusions of magnetite in amphibole, or vice-versa, are largely unreported.

Amphiboles are a large group of inosilicates with general formula: $AB_2C_5T_8O_{22}W_2$, where A = vacancy (□), Na, K, Ca, Pb, Li; B = Na, Ca, Mn^{2+}, Fe^{2+}, Mg, Li; C = Mg, Fe^{2+}, Mn^{2+}, Al, Fe^{3+}, Mn^{3+}, Ti^{4+}, Li; T = Si, Al, Ti^{4+}, Be; and W = (OH), F, Cl, O^{2-} (Hawthorne et al. 2012). Tschermakite, a monoclinic calcic amphibole with *C*2/*m* structure and end-member formula: $^{A}\square^{B}Ca_2^{C}(Mg_3Al_2)^{T}(Si_6Al_2)O_{22}{}^{W}(OH)_2$ is a rare Al-rich species only documented from a handful of localities. The tschermakite crystal structure has been refined from a specimen at the contact between anorthosite and amphibolite from Fiskenaesset, Greenland (Abdu and Hawthorne 2009). The formal description of ferro-tchermakite, ideally $^{A}\square^{B}Ca_2^{C}(Fe^{2+}{}_3Al_2)^{T}(Si_6Al_2)O_{22}{}^{W}(OH)_2$, from the Ploumanac'h granitic complex, France, has been given by Oberti et al. (2018). Although high Al content in amphibole is considered an indicator of high-pressure metamorphism, identification of "one of the most aluminous

examples of hornblende" (tschermakite; up to 3.3 atoms per formula unit (apfu) Al) in low-pressure metacarbonates from Vermont, USA (Léger and Ferry 1991), prompted a preliminary thermodynamic model of P-T-X phase stability for tremolite-tschermakite solid solution in the system K_2O-CaO-MgO-Al_2O_3-SiO_2-H_2O-CO_2.

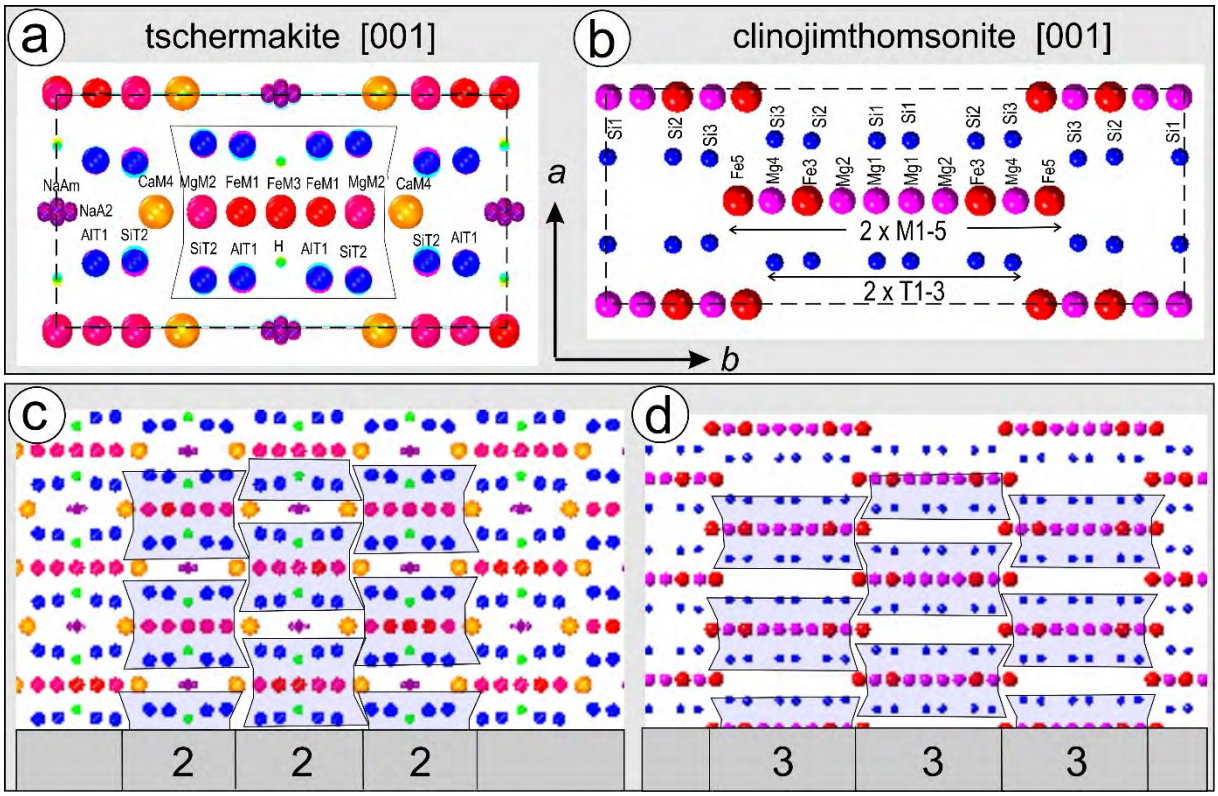

Figure 1. (a, b) Crystal structures of tshermakite and clinojimthomsonite projected onto [001] showing atom occupancy in cation sites as marked. Crystallographic information data from Abdu and Hawthorne (2009) and Veblen and Burnham (1978). M=octahedral; T=tetrahedral; A=cavity with variable site occupancy. (c, d) Extended structures with overlays showing I-beams in the same minerals. Digits refer to the number of chains in each I-beam.

When projected along the *c* axis, the basic amphibole structure can be visualized as two double-chains of SiO_4 tetrahedra (T1 and T2) sandwiching a strip of cations (M1, M2 and M3 octahedra), collectively making up what is known as an *I-beam* stack, two chains in width (Fig. 1a; Putnis 1992). Order-disorder (OD) phenomena in amphiboles, particularly short-range order (SRO), was previously considered as induced by bond-valence requirements at A sites (Na), corroborated with the arrangement of M4 cations (Ca) over adjacent O3 anions (Hawthorne et

al. 2005) and assessed in both synthetic and natural tschermakite (e.g., Najorka and Gottschalk 2003; Abdu and Hawthorne 2009).

Lattice scale intergrowths between different *I-beam* stacked structures, comprising ordered or disordered slabs of variable width (e.g., Champness 2002, and references therein) have been documented in high-resolution (HR)-TEM studies of the pyribole polysomatic series (e.g., Veblen and Buseck 1979). Aside from pyroxene and amphibole (1- and 2-chains wide), new pyriboles include those with triple chains of *I-beams* (jimthompsonite and clinojimthompsonite) and alternating double and triple chains (chesterite) identified in metamorphic rocks from Chester, Vermont (Veblen and Burnham 1978; Fig. 1b). Pyribole sequences of various combinations and OD ranges have been documented at the nanoscale but so far, with the exception of those above, no others are known as distinct mineral species, implying they may be metastable polysomes intrinsic to growth processes (see review in Champness 2002).

Silician magnetite, known from many deposit types, can accommodate vacancy-bearing Si-Fe-nanoprecipitates with widths as multiple d_{111} magnetite, as shown for banded iron formation (BIF) and iron-oxide copper gold (IOCG) deposits (Xu et al. 2014; and review of silician magnetite in Ciobanu et al. 2019). In the outer shell from the ~1.6 Ga IOCG deposit at Olympic Dam (South Australia), silician magnetite contains abundant nanoscale inclusions of (ferro)actinolite, one of several calc-silicates formed during alkali-calcic alteration of host granite (Ciobanu et al. 2019; Verdugo-Ihl et al. 2020). Based on trace element geochemistry, silician magnetite is also known from the Cu-(Au) prospect at Wirrda Well, also within the Olympic Dam district where mineralization belongs to the same ~1.6 Ga IOCG event defining the Olympic Cu-Au Province (1598.9 ± 6.3 Ma $^{207}Pb/^{206}Pb$ age obtained from U-bearing hematite; Courtney-Davies et al. 2019). The Wirrda Well prospect is, however, hosted by an older, ~1.85 Ga granite (Donington Suite; DS) that experienced burial metamorphism at conditions from granulite to greenschist facies during the 1735–1690 Ma Kimban orogeny

(Reid 2019, and references therein). Numerous mafic dikes, some of which are penecontemporaneous with the DS suite, as well as shear zones, are typical of the geological setting at Wirrda Well (e.g., Courtney-Davies et al. 2019).

The present STEM study addresses characterization of silician magnetite from Wirrda Well with the aim of understanding the petrogenetic significance of nm-scale mineral inclusions in the context of protracted magmatic-metamorphic history. Comparison with magnetite from other deposits/prospects in the district constrains mineral signatures recorded during the early stages of IOCG systems.

METHODOLOGY

Two S/TEM-foils were extracted from one magnetite grain using established dual-beam FIB-SEM methods with a FEI Helios Nanolab 600 instrument (see Ciobanu et al. 2011). High Angle Annular Dark Field (HAADF) STEM imaging and energy-dispersive X-ray spectrometry (EDX) spot analysis/mapping of the foils were conducted with an ultra-high resolution, probe-corrected FEI Titan Themis S/TEM instrument operated at 200 kV. This is equipped with a X-FEG Schottky source and Super-X EDX geometry. The Super-X EDX detector provides geometrically symmetric EDX detection with an effective solid angle of 0.8 Sr. Probe correction delivered sub-Ångstrom spatial resolution and an inner collection angle greater than 50 mrad was used for HAADF imaging with a Fischione detector. Indexing of diffraction patterns was conducted with WinWulff© (v1.6) and publicly available data from the American Mineralogist Crystal Structure Database (http://rruff.geo.arizona.edu/AMS/amcsd.php). Crystal structure models were generated in CrystalMaker® (v10.4.6) and STEM for xHREM™ (v4.1). Magnetite composition along transects close to the FIB-cut samples was obtained using electron probe microanalysis (EPMA) using a CAMECA SX-Five electron probe microanalyzer. Analytical procedures are

given in Supplemental[2] Table 1. All instruments are housed at Adelaide Microscopy, The University of Adelaide.

RESULTS AND DISCUSSION

The studied magnetite derives from a cm-wide band intersecting the contact between altered Donington granite and a mafic dyke (?) at a depth of ~1,891 m RL (drillhole WRD33, sample WW33.12B; Supplemental[1] Fig. A1a, b). Fine-grained sulfides (pyrite+chalcopyrite) form trails crosscutting the magnetite band. Alteration comprises chlorite with various Fe/Mg ratios and K-feldspar/sericite. Magnetite displays zonation patterns with respect to dusty, Si-bearing inclusions, and is marginally replaced by hematite and infilled by sulfides and secondary chlorite+quartz, as seen along the distinct zone boundaries in the analyzed grain. The STEM study was carried out on two foils, extracted from: (i) across a sharp boundary -foil #1; and densely-mottled inclusion core-foil #2 (Supplemental[1] Fig. A1c, d).

EPMA data for magnetite (Supplemental[1] Table 1) shows up to 4.39 wt.% SiO_2, 2.33 wt.% Al_2O_3, and measurable concentrations of MgO, CaO and TiO_2 (<1 wt.% each). There is no significant difference between the transects for the two domains on plots of Si *vs.* ΣMe-Si and Si *vs.* ΣMe (Supplemental[1] Fig. A1e, f). HAADF STEM imaging of the two foils shows zonation with respect to inclusions in foil #1, but pervasively distributed inclusions in foil #2 (Supplemental[1] Fig. A2). In both foils, there are also coarser inclusions/clots, which are identified from STEM EDX spectra as plagioclase, rutile, chlorite and sericite (Supplemental[1] Fig. A3). EDX mapping of areas from both foils nonetheless show that the dominant inclusions are nanorod-like, Si-Fe bearing precipitates with minor, albeit variable Al-Mg-Ca-content (Supplemental[1] Figs. A4-5).

[2] Deposit item

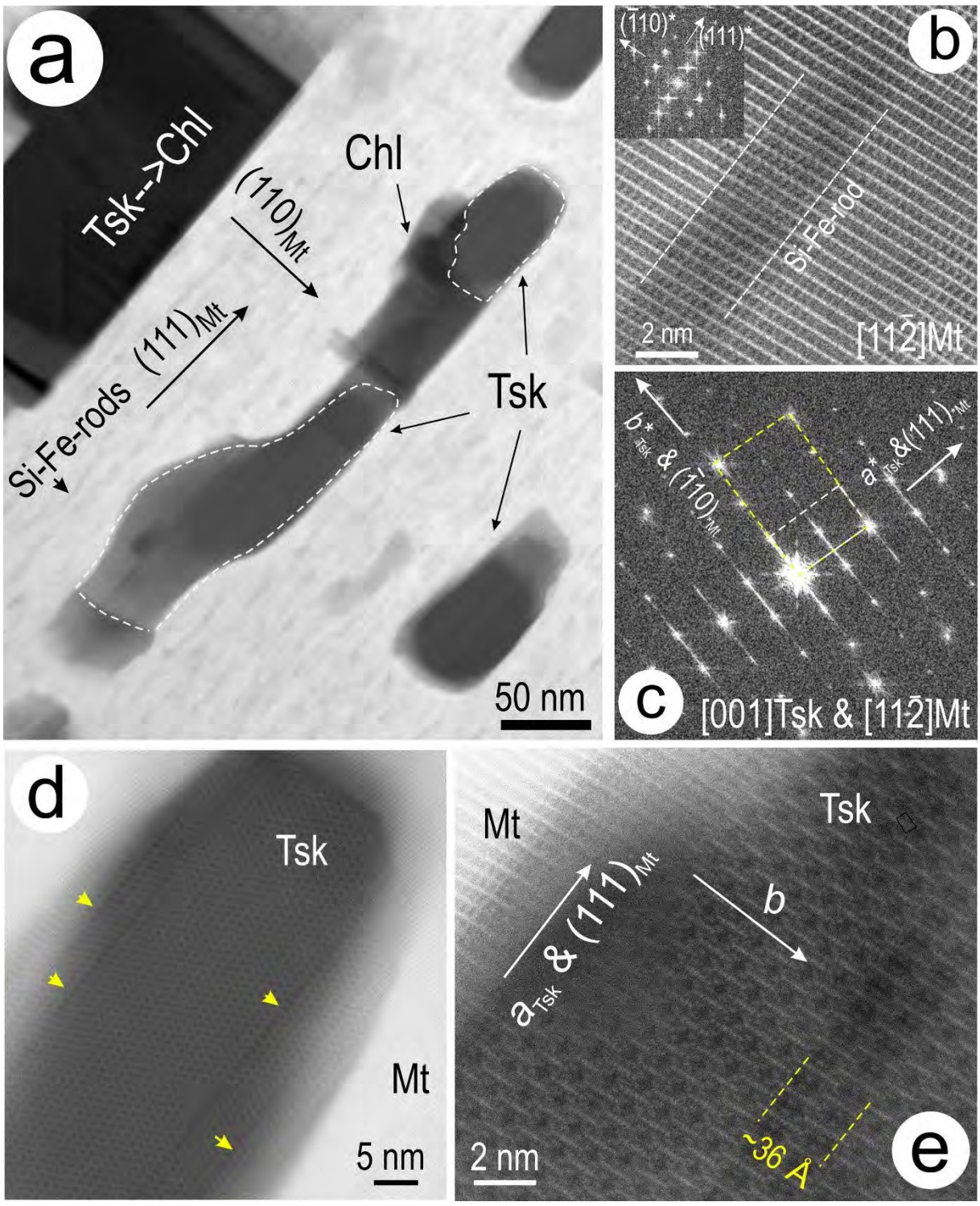

Figure 2. HAADF STEM images (a, b, d, e) and Fast Fourier Transform (FFT) pattern (c) for tschermakite (Tsk) inclusions in silician magnetite. (a) Tschermakite and Si-Fe-rods oriented along <111> in magnetite. Chlorite (Chl) replaces amphibole. (b) Si-Fe-rod in magnetite and FFT (inset). (c-e) FFT pattern corresponding to image in (e) and images showing epitaxial intergrowths between magnetite and tschermakite on directions as marked. Yellow and white dashed lines in (c) mark magnetite and tschermakite motifs. Arrowheads in (d) indicate stacking disorder in tschermakite.

Stubby grains of Al-rich amphibole, each up to several hundred nm in length and tens of nm wide (Supplemental[1] Fig. A6) are present at the contact to the inclusion-free zone in magnetite (Supplemental[1] Fig. A2). This amphibole, and also Si-Fe-nanorods (several nm wide) forming a dense mottling throughout the area, are oriented parallel to <111>$_{magnetite}$ (Fig. 2a-c). All amphibole grains display disorder on *b* axis, imaged as single- or double-$b_{amphibole}$ -wide defects occurring along the *a* axis (Fig. 2c-e; Supplemental[1] Fig. A6). EDX analysis shows the ubiquitous presence of Si-Fe-nanorods in magnetite, with incipient amphibole nucleation (Fig. 3a; Supplemental[1] Fig. A4).

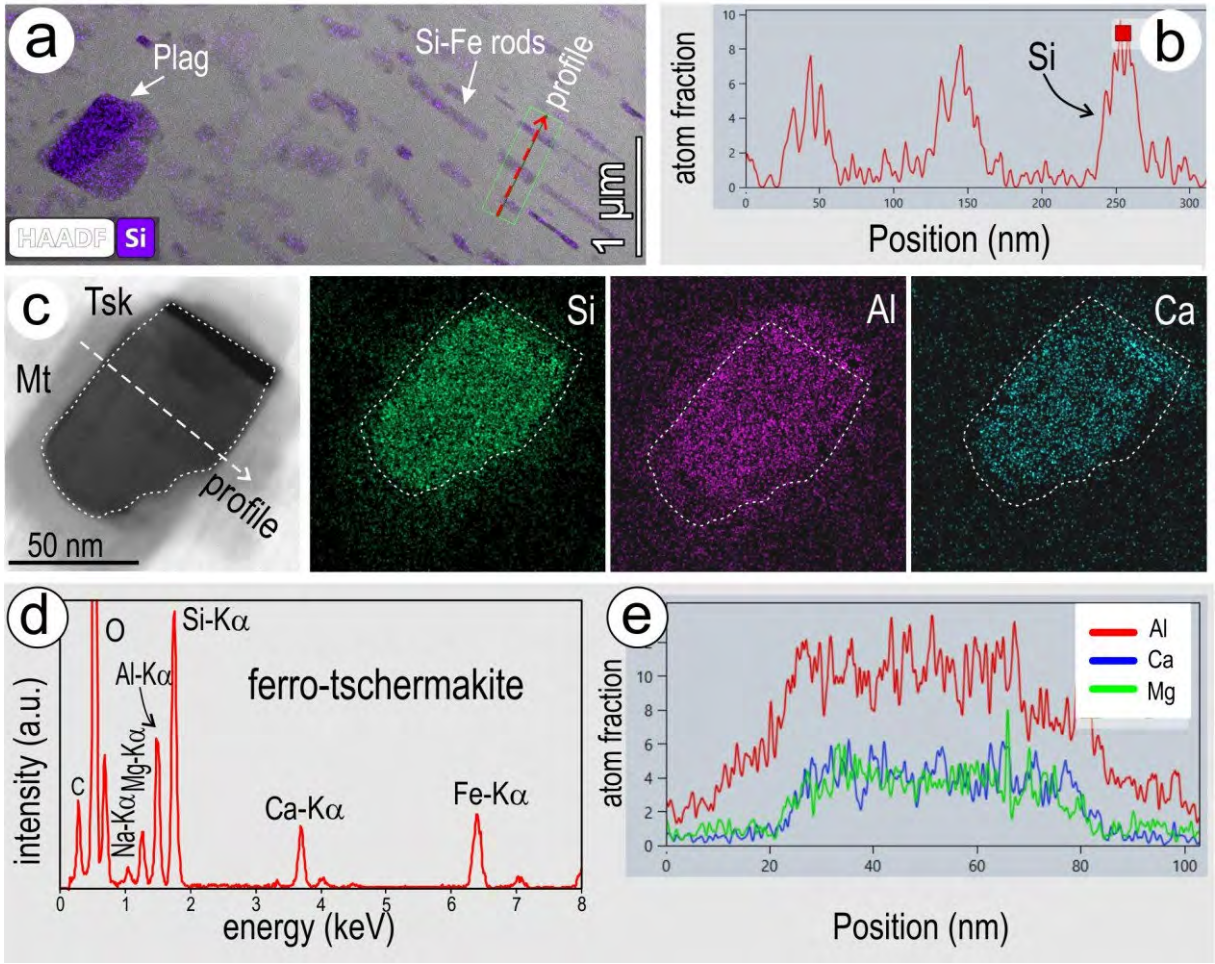

Figure 3. (a) HAADF STEM image and superimposed Si map showing Si-Fe rods and plagioclase (Plag) inclusion. (b) STEM EDX profile through magnetite and across Si-Fe rods indicated in (a). (c) HAADF STEM image and STEM EDX element maps of tschermakite inclusion for selected elements. Mt–magnetite, Tsk–tschermakite. (d) Integrated STEM EDX spectrum for ferrotschermakite inclusion in (c). (e) EDX signals for Al, Ca and Mg across the inclusion in (c).

An integrated STEM EDX spectra across the mapped amphibole gives the mean formula $^{A}K_{0.06}{}^{B}(Ca_{1.21}Na_{0.37}Fe_{0.2}Mn_{0.04})_{1.82}{}^{C}(Al_{1.89}Fe^{2+}{}_{1.86}Mg_{1.18}Ti_{0.06})_{5}{}^{T}(Si_{6.65}Al_{1.35})_{8}O_{22}{}^{W}(OH)_{2}$, corresponding to ferro-tschermakite (Fig. 3b, c; Supplemental[1] Table 2). Although elements such as Na and Ca (occupying A and C sites) are likely to be higher than measured due to volatility under beam, the data fits the crystal-chemistry of ferro-tschermakite well. Total a.p.f.u. Al is 3.24, comparable with the 3.18 total a.p.f.u. Al in ferro-tschermakite reported from Ploumanac'h (Oberti et al. 2018). The prevalence of Al over other cations in the M sites is also shown on the EDX profile (Fig. 3d).

Randomly distributed defects along $b_{\text{ferro-tschermakite}}$ form 3-chain units coherently intergrown within the 2-chain amphibole structure when viewed on [010] zone axis (Fig. 4a). This type of short-range disorder, widely reported from pyriboles (Veblen and Buseck 1979; Champness 2002, and references therein), was also encountered as triple and quadruple chains in synthetic amphibole with x_{Tsk}=0.13 (2.83 wt.% Al_2O_3) from the tremolite-tschermakite solid solution. These synthetic amphiboles were obtained at 750 ºC and 500 MPa in 40-day runs, whereas defect-free structures with X_{tsk}=0.39 (8 wt.% Al_2O_3) were obtained using shorter (5-day) runs at slightly higher T (800 ºC) and far higher P (1,500 MPa) (Najorka and Gottschalk 2003). The HAADF STEM imaging and STEM simulations match the structural units in the amphibole structure very well, particularly the cation strip along the *b* axis interrupted by a diamond-shaped, dark motif representing the A site with occupancy of light atoms (Fig. 4a-c). Configuration and occupancy of sites defining SRO in amphiboles (A2, Am and C4; see ideal structure in Fig. 1A) were discussed for tschermakite using EPMA data and Mossbauer spectroscopy (Abdu and Hawthorne 2009). Although we cannot constrain precise SRO atomic configurations from the present study, we find that the occurrence of triple chain defects in the amphibole are well-accommodated by SRO, i.e., two diamond-shaped motifs for one M-cation strip with 10 atoms surrounded on each side by triple Si-chains (Fig. 4d). This implies that SRO sites depicted in amphibole structures are present in other pyriboles, as shown here for the triple

chain type. On the other hand, SRO disorder, considered to be a key factor in the stability of tschermakite (Abdu and Hawthorne 2009), can be accommodated by lattice-scale pyribole intergrowths, but entropy and enthalpy issues may prohibit their stability over longer ranges, thus explaining their scarcity in natural samples.

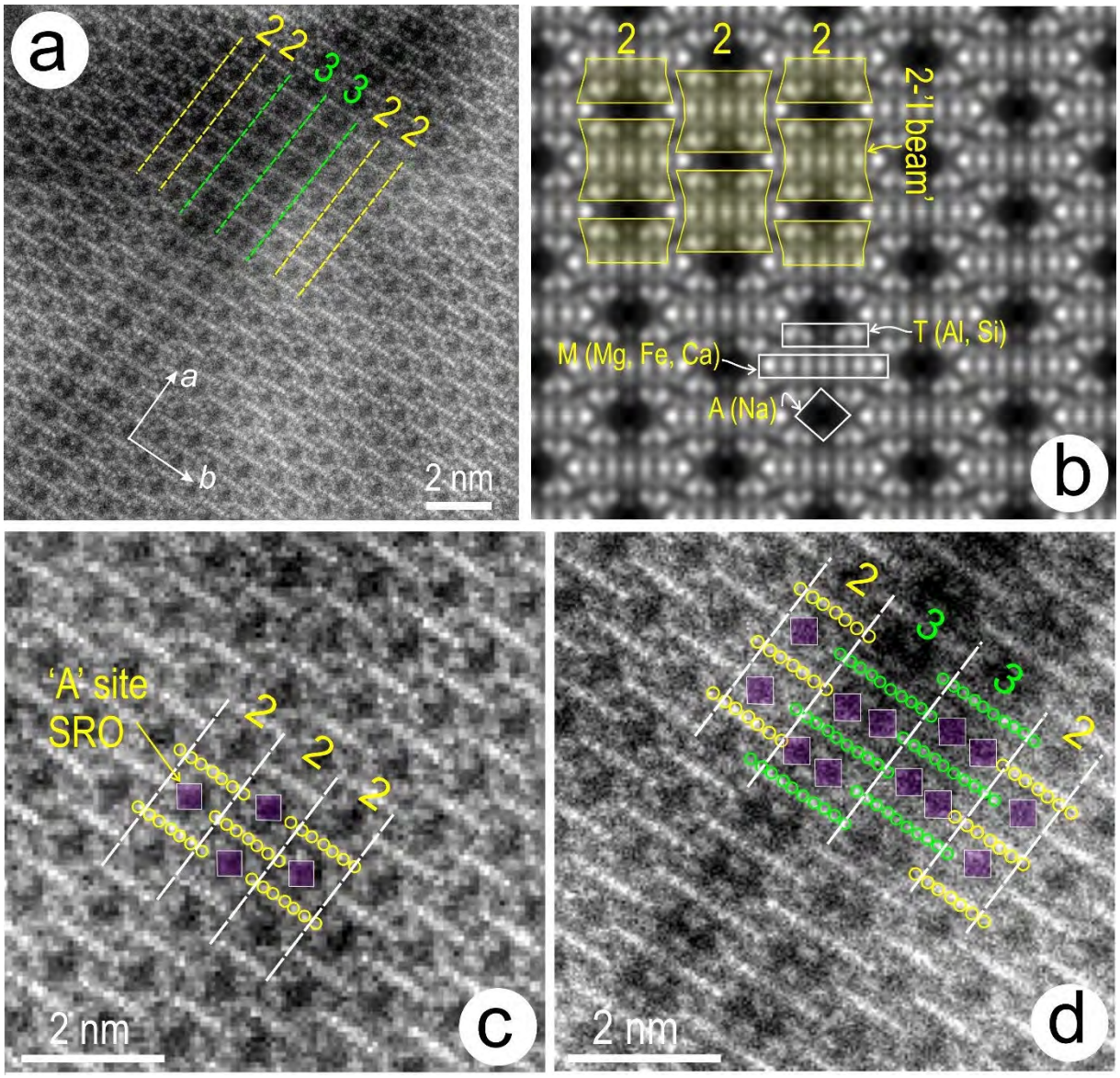

Figure 4. High-resolution HAADF STEM images and STEM simulation in (b) showing stacking disorder in tschermakite on [001] zone axis. (a) Double stack of 3-chain pyribole in the 2-chain amphibole sequence. (b) STEM simulation with overlays showing I-beams and cation sites on the image (compare with models in Figure 1). Note cations in M and T sites as bright dots whereas the A site is marked as a diamond-shaped motif. (c, d) Details from (a) showing ordered and disordered tschermakite. The M cation chains along b are marked by 7 and 10 atoms (yellow and green circles) for the double- and triple-chains structures, respectively. Note the double diamond-shaped motif between the 7- and 10-atom chains in (d).

IMPLICATIONS

Coherent nanoscale intergrowths between spinel group minerals and aluminous, Ca-amphibole are reported as lamellar exsolutions in chromite from high-pressure terranes such as podiform chromitite from the Nakhl Massif, Semail Ophiolite, Oman (Chen et al. 2019). Such a scenario is, however, unlikely for the studied magnetite, in which conditions are constrained to the lower/middle crust with maximum P-T-X conditions attained during amphibolite facies metamorphism affecting granites and dolerite dikes at. 1735–1690 Ma.

Wirrda Well magnetite preserves textures and phase assemblages attributable to a two-stage evolution: (i) amphibole inclusion growth under oriented stress during prograde metamorphism; and (ii) post-metamorphism alteration of assemblages by local fluid-percolation along fractures and zone boundaries. Intra-grain fabrics, e.g., rotation during crystal growth with mineral clots at the junctions between zones of changing direction of inclusion orientation (Supplemental[1] Fig A2) support magnetite accumulation via metamorphic segregation. Impurities such as Si, Al, Mg, Ca, etc., were likely provided by alteration of pre-exiting lithologies, particularly at granite-dolerite contacts (Supplemental[1] Fig A1). Plagioclase+amphibole assemblages in magnetite are concordant with experimental studies showing P-T conditions compatible with amphibolite facies metamorphism (~600-800 ºC, 2-5 kbar; Najorka and Gottschalk 2003). Although these experiments indicate that x_{Tsk} increases with pressure above 2 kbar, tschermakite with the highest Al content (up to 3.3. apfu Al; Léger and Ferry 1991) is found in low-pressure metacarbonates, indicating that co-existing phases can strongly buffer the assemblages, as indicated by P-T-X phase equilibria. Formation of Si-Fe-nanorods in magnetite during prograde metamorphism is supported by amphibole growth along these structures. The retrograde reactions that formed chlorite+sericite are, however, attributable to superimposed (~1.6 Ga) IOCG fluids.

The short-range disorder recorded by pyribole stacks in ferro-tschermakite indicates disequilibrium growth conditions that could provide important clues for SRO formation in

amphiboles if experiments could be designed to make use of the magnetite-hematite buffer. Identification of double A-site cavities between cation strips in 2- and 3-chain pyriboles by HAADF STEM imaging (Fig. 4) provides a direct link between conceptual models for short range disorder in minerals based on local clusters of atoms with complex charge balance configuration considered responsible for SRO in amphiboles (Hawthorne et al. 2005) on one side, and the widespread occurrence of disordered rather than ordered pyribole sequences (Veblen and Buseck 1979) on the other.

HAADF STEM imaging of minerals can also provide valuable insights into the evolution of geological terranes with protracted histories. The assemblage described here represents a ~1735–1690 Ma metamorphic window preserved in magnetite inherited from ~1.85 Ga lithologies, with an IOCG-fluid overprint at ~1.6 Ga.

ACKNOWLEDGEMENTS

This is a contribution to the 'FOX' project (Trace elements in iron oxides: deportment, distribution and application in ore genesis, geochronology, exploration and mineral processing), supported by BHP Olympic Dam and the South Australian Government Mining and Petroleum Services Centre of Excellence.

REFERENCES CITED

Abdu, Y.A., and Hawthorne, F.C. (2009) Crystal structure and Mössbauer spectroscopy of tschermakite from the Ruby locality at Fiskenaesset, Greenland. The Canadian Mineralogist, 47, 917–926. https://doi.org/10.3749/canmin.47.4.917

Champness, P.E. (2002) Applications of Transmission Electron Microscopy. In: Advances in Imaging and Electron Physics, vol. 121, p. 53–90, Academic Press. https://doi.org/10.1016/S1076-5670(02)80025-8

Chen, T., Jin, Z., Zhang, J., and Wang, L. (2019) Calcium amphibole exsolution lamellae in chromite from the Semail ophiolite: Evidence for a high-pressure origin. Lithos, 334–335, 273–280. https://doi.org/10.1016/j.lithos.2019.03.020

Ciobanu, C.L., Cook, N.J., Utsunomiya, S., Pring, A., and Green, L. (2011) Focussed ion beam–transmission electron microscopy applications in ore mineralogy: Bridging micro- and nanoscale observations. Ore Geology Reviews, 42, 6–31. https://doi.org/10.1016/j.oregeorev.2011.06.012

Ciobanu, C.L., Verdugo-Ihl, M.R., Slattery, A., Cook, N.J., Ehrig, K., Courtney-Davies, L., and Wade, B.P. (2019) Silician Magnetite: Si–Fe-Nanoprecipitates and Other Mineral Inclusions in Magnetite from the Olympic Dam Deposit, South Australia. Minerals, 9, 311. https://doi.org/10.3390/min9050311

Courtney-Davies, L., Ciobanu, C.L., Verdugo-Ihl, M.R., Dmitrijeva, M., Cook, N.J., Ehrig, K., and Wade, B.P. (2019) Hematite geochemistry and geochronology resolve genetic and temporal links among iron-oxide copper gold systems, Olympic Dam district, South Australia. Precambrian Research 335, 105480. https://doi.org/10.1016/j.precamres.2019.105480

Deditius, A.P., Reich, M., Simon, A.C., Suvorova, A., Knipping, J., Roberts, M.P., Rubanov, S., Dodd, A., and Saunders, M. (2018) Nanogeochemistry of hydrothermal magnetite. Contributions to Mineralogy and Petrology, 173, 46. https://doi.org/10.1007/s00410-018-1474-1

Fleet, M.E., Bilcox, G.A., and Barnett, R.L. (1980) Oriented magnetite inclusions in pyroxenes from the Grenville Province. Canadian Mineralogist, 18, 89–99.

Gao, W., Ciobanu, C.L., Cook, N.J., Slattery, A., Huang, F., and Wang, D. (2019a) Nanoscale study of lamellar exsolutions in clinopyroxene from olivine gabbro: Recording crystallization sequences in iron-rich layered intrusions. American Mineralogist, 104, 244–261. https://doi.org/10.2138/am-2019-6764

Gao, W., Ciobanu, C.L., Cook, N.J., Slattery, A., Huang, F., and Song, D. (2019b) Nanoscale study of titanomagnetite from the Panzhihua Layered Intrusion, Southwest China: Multistage exsolutions record ore formation. Minerals, 9, 513. https://doi.org/10.3390/min9090513

Hawthorne, F.C., Della Ventura, G., Oberti, R., Robert, J.-L., and Iezzi, G. (2005) Short-range order in minerals: Amphiboles. The Canadian Mineralogist, 43, 1895–1920. https://doi.org/10.2113/gscanmin.43.6.1895

Hawthorne, F.C., Oberti, R., Harlow, G.E., Maresch, W.V., Martin, R.F., Schumacher, J.C., and Welch, M.D. (2012) Nomenclature of the amphibole supergroup. American Mineralogist, 97, 2031–2048. https://doi.org/10.2138/am.2012.4276

Léger, A., and Ferry, J.M. (1991) Highly aluminous hornblende from low-pressure metacarbonates and a preliminary thermodynamic model for the Al content of calcic amphibole. American Mineralogist, 76, 1002–1017.

Najorka, J., and Gottschalk, M. (2003) Crystal chemistry of tremolite–tschermakite solid solutions. Physics and Chemistry of Minerals, 30, 108–124. https://doi.org/10.1007/s00269-002-0291-1

Oberti, R., Boiocchi, M., Hawthorne, F.C., and Ciriotti, M.E. (2018) Ferro-tschermakite from the Ploumanac'h granitic complex, Brittany, France: mineral description. European Journal of Mineralogy, 30, 171–176. https://doi.org/10.1127/ejm/2018/0030-2700

Putnis, A. (1992) Introduction to Mineral Sciences. Cambridge University Press, Cambridge, U.K.

Reid, A. (2019) The Olympic Cu-Au Province, Gawler Craton: A Review of the Lithospheric Architecture, Geodynamic Setting, Alteration Systems, Cover Successions and Prospectivity. Minerals, 9, 371. https://doi.org/10.3390/min9060371

Veblen, D.R., and Burnham, C.W. (1978) New biopyriboles from Chester, Vermont: II. The crystal chemistry of jimthompsonite, clinojimthompsonite, and chesterite, and the amphibole-mica reaction. American Mineralogist, 63, 1053–1073.

Veblen, D.R., and Buseck, E.R. (1979) Chain-width order and disorder in biopyriboles. American Mineralogist, 64, 687–700.

Verdugo-Ihl, M.R., Ciobanu, C.L., Cook, N.J., Ehrig, K.J., and Courtney-Davies, L. (2020) Defining early stages of IOCG systems: evidence from iron oxides in the outer shell of the Olympic Dam deposit, South Australia. Mineralium Deposita, 55, 429–452. https://doi.org/10.1007/s00126-019-00896-2

Verdugo-Ihl, M.R., Ciobanu, C.L., Cook, N.J., Ehrig, K.J., Slattery A., Courtney-Davies, L and Dmitrijeva M. Nanomineralogy of hydrothermal magnetite from Acropolis, South Australia: Genetic implications for iron-oxide copper gold mineralization. American Mineralogist, in press. https://doi.org/10.2138/am-2021-7557

Xu, H., Shen, Z., and Konishi, H. (2014) Si-magnetite nano-precipitates in silician magnetite from banded iron formation: Z-contrast imaging and ab initio study. American Mineralogist, 99, 2196–2202. https://doi.org/10.2138/am-2014-4964

Yin, S., Wirth, R., Ma, C.Q., Xu, J.N. (2019) The role of mineral nanoparticles at a fluid-magnetite interface: Implications for trace-element uptake in hydrothermal systems. American Mineralogist, 104, 1180–1188. https://doi.org/10.2138/am-2019-6996

CHAPTER 8

VAPOUR TRANSPORT OF MAGNETITE IN VOLCANOES: EVIDENCE FROM IGNEOUS PYROXENE PAIR INCLUSIONS AND S-BEARING SUBLIMATE COATINGS

Max R. Verdugo-Ihl[1]*, Cristiana L. Ciobanu[1], Nigel J. Cook[1],

Fernando Tornos[2], Kathy Ehrig[3], Ashley Slattery[4],

Jing Xu[1,5], Liam Courtney-Davies[1], John M. Hanchar[6]

[1] *School of Chemical Engineering and Advanced Materials, The University of Adelaide, Adelaide, SA 5005, Australia*

[2] *Instituto de Geociencias (CSIC-UCM), Dr. Severo Ochoa 7, 28040 Madrid, Spain*

[3] *BHP Olympic Dam, 10 Franklin Street St, Adelaide SA, 5000, Australia*

[4] *Adelaide Microscopy, The University of Adelaide, Adelaide, SA, 5005, Australia*

[5] *Key Laboratory of Mineral Resources, Institute of Geology and Geophysics, Chinese Academy of Sciences, Beijing 100029, China*

[6] *Department of Earth Sciences, Memorial University of Newfoundland, St. John's, NL A1B 3X5, Canada*

Article submitted to *Earth and Planetary Science Letters*, December 12th, 2019.

Statement of Authorship

Title of Paper	Vapour transport of magnetite in volcanoes: evidence from igneous pyroxene pair inclusions and S-bearing sublimate coatings
Publication Status	☐ Published ☐ Accepted for Publication ☑ Submitted for Publication ☐ Unpublished and Unsubmitted w ork w ritten in manuscript style
Publication Details	Verdugo-Ihl, M.R., Ciobanu, C.L., Cook, N.J., Tornos, F., Ehrig, K., Slattery, A., Xu, J., Courtney-Davies, L., Hanchar, J.M. Vapour transport of magnetite in volcanoes: evidence from igneous pyroxene pair inclusions and S-bearing sublimate coatings. Submitted to *Earth and Planetary Science Letters*.

Principal Author

Name of Principal Author (Candidate)	Max R. Verdugo-Ihl		
Contribution to the Paper	Performed analytical work, evaluation and interpretation of results and prepared the manuscript.		
Overall percentage (%)	55		
Certification:	This paper reports on original research I conducted during the period of my Higher Degree by Research candidature and is not subject to any obligations or contractual agreements with a third party that would constrain its inclusion in this thesis. I am the primary author of this paper.		
Signature		Date	15.04.2020

Co-Author Contributions

By signing the Statement of Authorship, each author certifies that:

i. the candidate's stated contribution to the publication is accurate (as detailed above);

ii. permission is granted for the candidate in include the publication in the thesis; and

iii. the sum of all co-author contributions is equal to 100% less the candidate's stated contribution.

Name of Co-Author	Cristiana L. Ciobanu		
Contribution to the Paper	Helped to define the direction of the manuscript, guided manuscript preparation and assisted with data acquisition, the interpretation of the results and evaluation of the manuscript.		
Overall percentage (%)	20		
Signature		Date	15.04.2020

Name of Co-Author	Nigel J. Cook		
Contribution to the Paper	Assisted with the preparation and evaluation of the manuscript.		
Overall percentage (%)	10		
Signature		Date	15.04.2020

Name of Co-Author	Fernando Tornos		
Contribution to the Paper	Provided sample material and assisted with the evaluation of the manuscript.		
Overall percentage (%)	4		
Signature	On behalf of the co-author,	Date	15.04.2020

Name of Co-Author	Kathy Ehrig		
Contribution to the Paper	Assisted with the evaluation of the manuscript.		
Overall percentage (%)	3		
Signature		Date	15.04.2020

Name of Co-Author	Ashley Slattery		
Contribution to the Paper	Performed and assisted with HAADF-STEM data acquisition.		
Overall percentage (%)	3		
Signature		Date	15.04.2020

Name of Co-Author	Jing Xu		
Contribution to the Paper	Assisted with data processing and the evaluation of the manuscript.		
Overall percentage (%)	2		
Signature		Date	15.04.2020

Name of Co-Author	Liam Courtney-Davies		
Contribution to the Paper	Assisted with the evaluation of the manuscript.		
Overall percentage (%)	2		
Signature		Date	15.04.2020

Name of Co-Author	John M. Hanchar		
Contribution to the Paper	Assisted with the evaluation of the manuscript.		
Overall percentage (%)	1		
Signature	on behalf of the co-author,	Date	15.04.2020

Vapour transport of magnetite in volcanoes: evidence from igneous pyroxene pair inclusions and S-bearing sublimate coatings

Max R. Verdugo-Ihl[1]*, Cristiana L. Ciobanu[1], Nigel J. Cook[1], Fernando Tornos[2], Kathy Ehrig[3], Ashley Slattery[4], Jing Xu[1,5], Liam Courtney-Davies[1], John M. Hanchar[6]

[1] *School of Chemical Engineering and Advanced Materials, The University of Adelaide, Adelaide, SA 5005, Australia*

[2] *Instituto de Geociencias (CSIC-UCM), Dr. Severo Ochoa 7, 28040 Madrid, Spain*

[3] *BHP Olympic Dam, 10 Franklin Street St, Adelaide SA, 5000, Australia*

[4] *Adelaide Microscopy, The University of Adelaide, Adelaide, SA, 5005, Australia*

[5] *Key Laboratory of Mineral Resources, Institute of Geology and Geophysics, Chinese Academy of Sciences, Beijing 100029, China*

[6] *Department of Earth Sciences, Memorial University of Newfoundland, St. John's, NL A1B 3X5, Canada*

ABSTRACT

The well-preserved, ~5.3-1.6 Ma El Laco Volcanic Complex (Chilean Andes) hosts massive magnetite mineralisation akin to that of Kiruna-type iron oxide-apatite deposits. Two contrasting and hotly contended models are proposed to explain formation of the massive magnetite-orebodies. One invokes direct crystallisation from immiscible, Fe-rich melts whereas the other considers transport to the surface by magnetite floatation during magma degassing, a mechanism considered efficient enough to form giant, Kiruna-type deposits. We provide evidence to discriminate between massive and floated magnetite at El Laco and rule out efficient floatation as a mechanism for large-scale accumulation of Fe in volcanoes. Micron- to nanoscale study of magnetite from stratabound mineralisation and occurring as micron-sized inclusions within 'nut'-shaped hematite from steam-heated alteration products show they are genetically linked to Fe-rich melts. They both host nm-scale inclusion pairs of clinopyroxenes

(augite-pigeonite and/or clinoenstatite) with intergrowths indicative of rapid growth and exsolution at low pressure and relatively high temperatures, typical of basaltic rocks. However, they differ in size by one order of magnitude, in which the finest, hematite-hosted magnetite can show sulfur-bearing coatings. These represent sublimates of vapour transporting magnetite (and debris) as a vapour-fluid mixture, followed by precipitation of 'nut'-shaped hematite within cavities and gas escape tubes due to temperature decrease. The lack of analogous alteration in the massive orebodies disproves magnetite flotation as a major ore-forming process. Nanoscale evidence from inclusions in magnetite represents a hitherto unexplored criteria to support a magmatic, effusive origin, at low pressures but high temperatures, for the stratabound magnetite orebodies at El Laco and elsewhere.

Keywords: El Laco, magnetite, HAADF STEM, clinopyroxene exsolution, vapour transport, sulfur-bearing sublimates

Introduction

Flotation of magmatic magnetite is proposed as an effective ore-forming mechanism in relatively young volcanic systems, such as at El Laco and Los Colorados (Chilean Andes; Fig. 1), to explain the occurrence of tabular, massive magnetite deposits (Knipping et al., 2015; Ovalle et al., 2018). At El Laco, where the volcanic edifice is best preserved, mineralisation is attributed to venting of a magnetite-fluid suspension along conduits that tap into a deeper magma reservoir (Ovalle et al., 2018). These authors suggest a transition from deeper (~200 m) magmatic to surface/shallow hydrothermal magnetite based on petrographic and compositional data, particularly the decrease in Ti content (from average 0.76 to 0.02 wt.%) in drillholes through brecciated and altered andesite in the Laco Norte orebody (Fig. 1). Deeper magnetite contains ilmenite exsolutions, whereas shallower types of magnetite, Ti-poorer, can be associated with coarse diopside, crosscutting pyrite-bearing veinlets and supergene alteration products including gypsum and Fe-hydroxides.

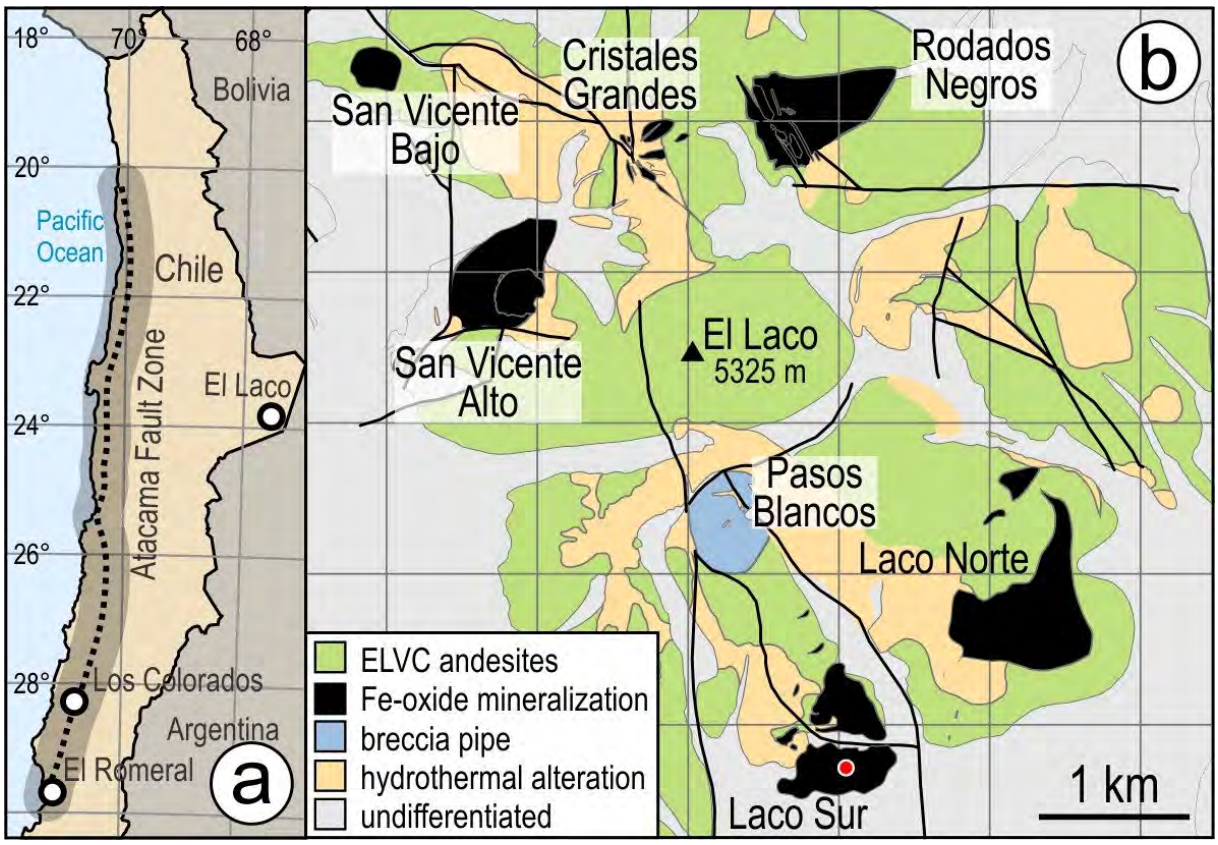

Fig. 1. (a) Location of the El Laco deposit and other selected Cenozoic magnetite-apatite deposits along the Atacama Fault Zone, Costal Cordillera. (b) Simplified geological map of the El Laco Volcanic Complex (ELVC) highlighting contacts between Fe-oxide mineralisation and host andesite and hydrothermal alteration (adapted from Tornos et al., 2017). Red circles denote sample locations.

Recognition of a comparable compositional trend (decrease of Ti+V contents) at Los Colorados prompted the introduction of the magnetite flotation model to explain the evolving geochemical signatures of igneous to presumably hydrothermal magnetite (Knipping et al., 2015). Hydrothermal magnetite from Los Colorados is typified by oscillatory zoning with respect to Al, Si, Ca, Mg and Ti, all elements that occur within an eclectic range of nanometre-scale silicate inclusions (pyroxene, amphibole, phlogopite) and Fe-Ti-oxides rather than being exclusively lattice-bound in magnetite (Deditius et al., 2018).

The flotation model is based upon the work of Edmonds et al. (2015), who proposed magnetite as an attractor for heterogeneous bubble nucleation in water-saturated melts. In this model, formation of mafic enclaves in andesites could be explained as the product of mingling resulting from instabilities at felsic/mafic melt interfaces if bubble-magnetite aggregates accumulate at such boundaries along mixing interfaces.

Accumulation of magnetite via bubble-flotation was tested experimentally via decompression of andesite-glass+H_2O±Cl mixtures homogenized under water-undersaturated conditions at 1050 °C and 250 MPa (Knipping et al., 2019). The heterogeneous distribution of fluid-vesicles and magnetite within the resulting andesite glass that accumulated at the top of the capsule was considered evidence for magnetite flotation during melt decompression. Knipping et al. (2019) considered this a feasible model to explain the formation of not only the Phanerozoic Chilean Coastal Cordillera Fe-ores, but also Precambrian deposits, such as the ~1.8 Ga Kiruna deposit (Sweden). Although considered as an example of a "intrusive magmatic" deposit (e.g., Frietsch, 1978), Kiruna and the Andean and Costal Cordilleran deposits discussed here, have more recently been re-assigned to the so-called 'Iron Oxide-Apatite' (IOA) deposit group (Williams, 2010), a subclass of the magmatic-hydrothermal Iron Oxide Copper-Gold (IOCG) clan (Groves et al., 2010).

Genesis of the El Laco deposit has been and remains hotly debated based on the stunning features observed in the Fe-oxide orebodies. These features resemble those from basaltic lava flows, e.g., ropy surfaces, vesicles and gas escape tubes exceeding 2 m in length, among others (Park, 1961; Henríquez and Martin, 1978), which cannot be readily explained by the flotation model alone. Instead, such features have been interpreted in terms of a magmatic model, in which immiscibility between a silicate and Fe-rich melts at depth results in subaerial magnetite flows and subvolcanic bodies (Tornos et al., 2016 and references therein). At shallower depths, crystallisation of an Fe-rich melt can promote exsolution of two immiscible, high and low density aqueous fluids, which produce alkali-calcic metasomatism and the acid, steam-heated alteration within andesite, respectively (Sillitoe and Burrows, 2002; Tornos et al., 2016).

Coarse pyroxene (diopside and enstatite) containing blebs of magnetite and melt inclusions are present within El Laco andesite (Velasco et al., 2016). A genetic link between magnetite, diopside (alkali-calcic alteration) and andesite is supported by comparable oxygen isotope signatures giving T estimates >900 °C (Tornos et al., 2016). Nonetheless, compositionally,

magnetite from ‘degassing pipes’ and ‘lava flows’ is considered atypical for a direct magmatic origin given the marked depletion in Ti, Al, Cr, and HFSE, and has been interpreted instead to resemble high-T hydrothermal ores (Dare et al., 2015).

In this contribution, we investigate magnetite from lava flows and acidic, steam-heated alteration, two of the most contrasting expressions of Fe-oxide mineralisation at El Laco. We show that petrographic and geochemical characterisation, complemented by a nanoscale examination of magnetite and inclusions therein, represent powerful tools to resolve the origin of such deposits in terms of magmatic or hydrothermal models.

Samples and methodology

The study was conducted on four polished blocks prepared from the two sample types representative of: (i) stratabound, vesicular magnetite (lava flow); and (ii) Fe-oxides in steam-heated altered deposits (Fig. 2a, b). In the latter, magnetite occurs as inclusions in cm-size, interpenetrated hematite crystals, resembling the so-called ‘nut-shaped’ hematite of Henríquez and Martin (1978). The 'nut'-shaped hematite was collected from below major layers of hematite-rich volcanoclastic sediments adjacent to a maar-diatreme structure in El Laco Sur (Tornos et al., 2017). Petrographic and geochemical characterisation at the micron-scale comprised scanning electron microscopy in back-scattered electron (BSE) mode, electron probe microanalysis (EPMA) using a CAMECA SX-Five electron probe microanalyzer, and laser ablation inductively coupled-plasma mass spectrometry (LA-ICP-MS) conducted on a ASI RESOlution-LR 193 nm ArF excimer laser microprobe coupled to an Agilent 7900cx quadrupole ICP-MS. Samples for nanoscale study were prepared and thinned by focused ion beam (FIB) on a FEI Helios Nanolab 600 platform. Nanoscale investigations were conducted in Bright Field (BF) and high-angle annular dark field scanning transmission electron microscopy (HAADF S/TEM) modes using a Phillips 200CM TEM and FEI Titan Themis STEM instruments. All analytical work was performed at Adelaide Microscopy, The University of Adelaide. Details of analytical procedures are given in the Supplementary Material.

Results

Mineralogy and mineral chemistry

Nut-shaped hematite from the steam-heated alteration displays a core mottled with magnetite inclusions surrounded by a ring comprising impurities and pores, and a narrow, clean margin (Fig. 2c). Stratabound magnetite grains are coarse, up to mm-sized, and display rhythmic banding with respect to silicate inclusions and their abundance (Fig. 2d). Magnetite is oscillatory zoned in both cases (Fig. 2e, f), whereas martitisation and presence of minor interstitial phosphates (±sulfates) are restricted to stratabound samples.

There is a marked difference in the grain size of magnetite in the two type of samples, whereby the smallest, 10-20 µm-sized, grains are present in the 'nut'-shaped hematite (Figs. 2f and 3a). Characteristic for this sample are sulfur-bearing phases marginally replacing magnetite inclusions within the hematite host (Fig. 2g).

EPMA mapping reveals varying degrees of magnetite replacement by the sulfur-bearing phases (up ~2.5 wt.% SO_3; Fig. 3b, c). EPMA analysis of the S-bearing domains shows that they are not enriched in Ca or Mg (i.e., present as sulfates) but rather represent intergrowths between S-bearing hematite and potentially Fe-bearing sulfates (Fig. 3d).

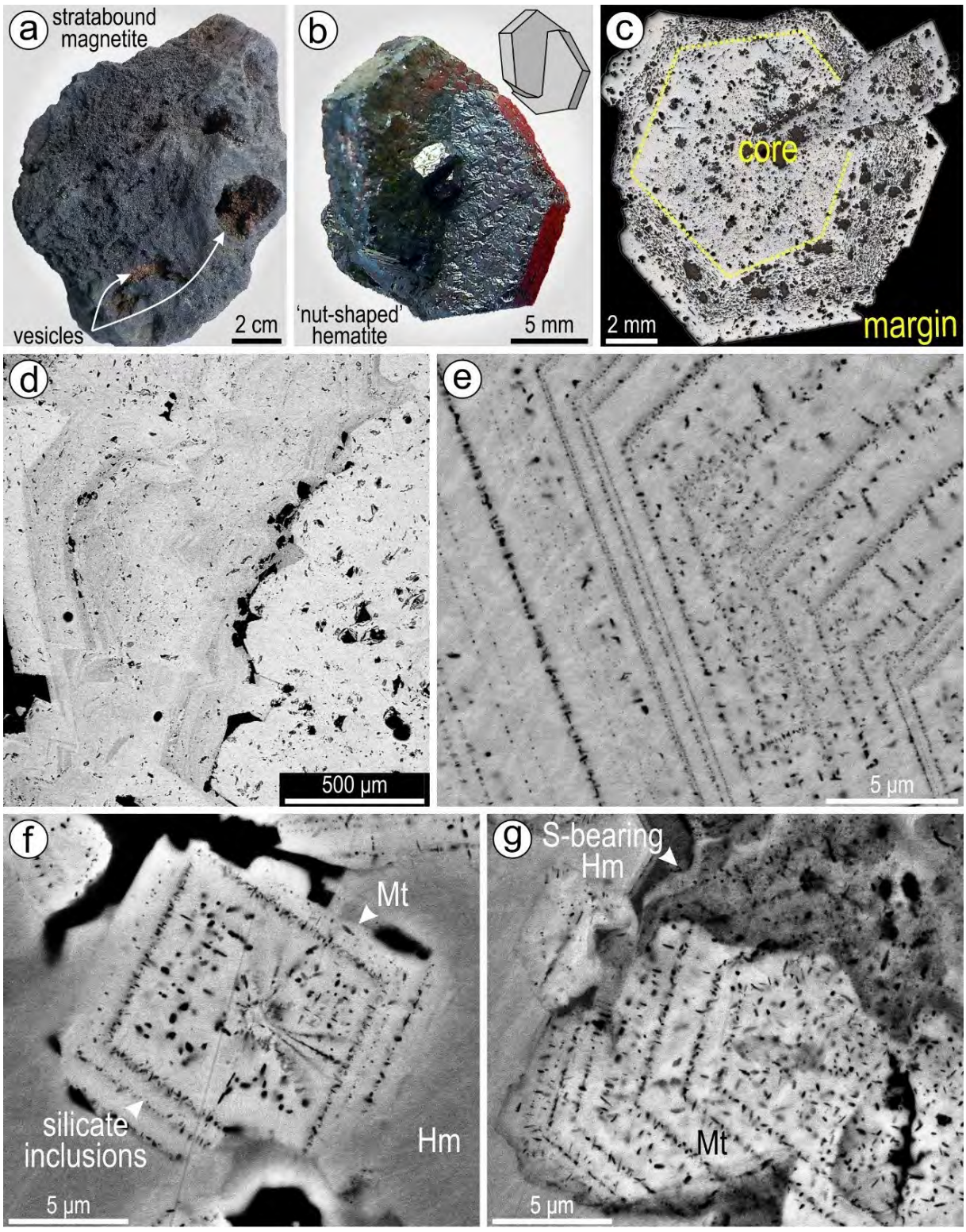

Fig. 2. Photographs of stratabound magnetite (Mt) in (a) and 'nut'-shaped hematite (Hm) in (b). Note the presence of vesicles in (a) and interpenetration of hematite crystals in (b). (c) Reflected light photomicrograph showing core (host to magnetite inclusions) to rim (ring with impurities/pores) zoning in hematite. (d-g) BSE images showing growth rhythms and inclusion-bearing zoning in stratabound (d, e) and 'nut'-shaped hosted magnetite (f, g). Note difference in size and presence of S-bearing coatings in (g).

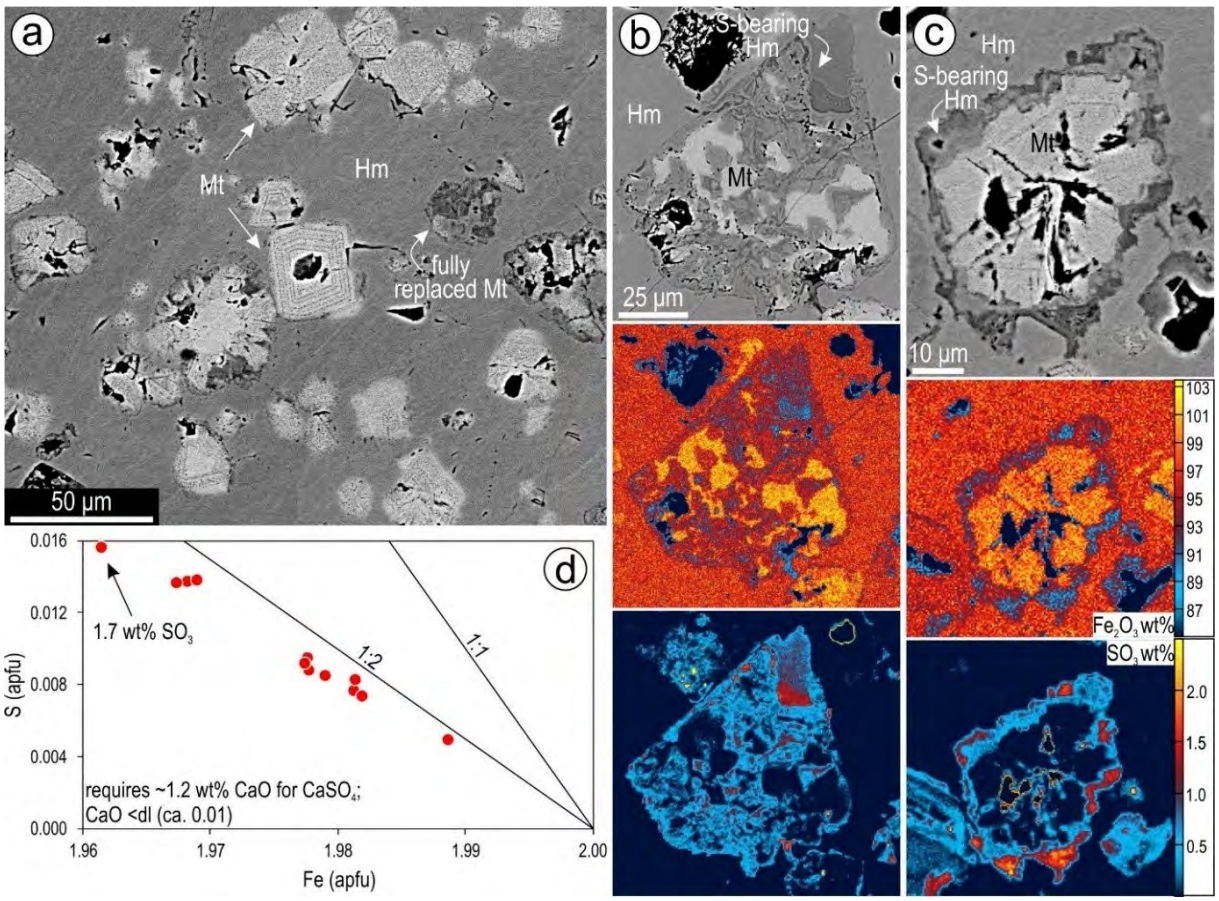

Fig. 3. (a) BSE image showing distribution of magnetite inclusions, displaying various zonation themes, within the 'nut'-shaped hematite. BSE-images (top) and EPMA maps showing the distributions of Fe and S in variably replaced magnetite inclusions within hematite (b, c). (d) Plot of S *versus* Fe showing compositional variation throughout the S-bearing hematite. Hematite calculated based on three oxygen atoms per formula unit (apfu). Increased S concentrations do not correlate with either Mg or Ca.

Trace element LA-ICP-MS data are presented in Fig. 4 and summary statistics for EPMA and LA-ICP-MS data are presented in the Supplementary Material Tables A2 and A3, respectively. Overall, there is a good agreement between the two datasets for those elements consistently above minimum detection limits (mdl). Relative to LA-ICP-MS however, EPMA results displays increased variance, in accordance with the far smaller analysed volume by EPMA. EPMA data shows also that domains seemingly devoid of silicate inclusions contain low SiO_2 (~0.05 wt.%), often below mdl, and relative Mg enrichment (~0.85 wt.% MgO), indicating that Mg is partially in solid solution, contrary to other elements which relate to silicate inclusions whenever measured at high concentrations. The concentrations of lithophile elements such as Na, K, Mg, Ca and Al increase systematically with SiO_2 contents. Concentration ranges for the two magnetite categories overlap for most trace/minor elements,

except for Mn, Zn and Mg, which are lower in hematite-hosted magnetite inclusions (Fig. 4). Trace element concentrations in hematite are typically lower than that in the other two magnetite categories.

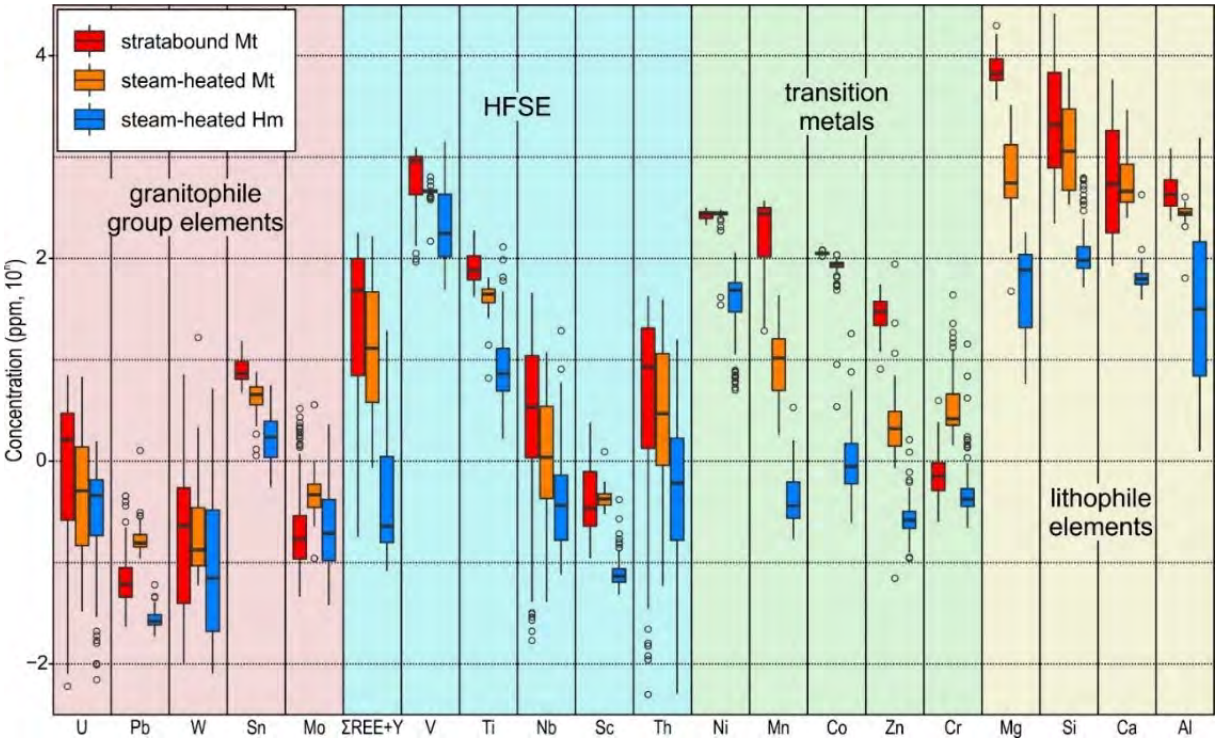

Fig. 4. Box and whisker plots displaying distribution of trace/minor element concentrations obtained by LA-ICP-MS for Fe-oxides as indicated. Element concentrations below mdl were taken as equal to the mdl value for plotting purposes. Mt─magnetite; Hm─hematite.

The micron-scale distribution of trace elements in Fe-oxides from the two samples shows zonation relative to textures as discussed above for most elements, except for some transition metals (V, Mn, Co, and Ni) and HFSE. Inclusion-rich areas from stratabound magnetite are enriched in lithophile elements (Si and Mg up to wt.% levels), HFSE, notably Th, Nb, Zr, Sc, as well as REE, and Sn and U (Fig. 5a). These relative enrichments range from a few ppm (e.g., U and Sc) to tens of ppm (e.g., Th, Nb, Ce, Y, Zr and Sn), and thousands of ppm (e.g., V). Overall, Ti contents are low, measuring up to ~190 ppm. In the 'nut'-shaped hematite, the core (magnetite-mottled) shows pervasive distribution of V, and Sn (up to ~1,400 ppm and ~6 ppm, respectively) but spotty areas of enrichment in Mg, Ni, and Co, tied to presence of magnetite inclusions. Spotty enrichment in U and P does not directly correlate with such inclusions and could be linked to secondary S-bearing phases (Fig. 5b).

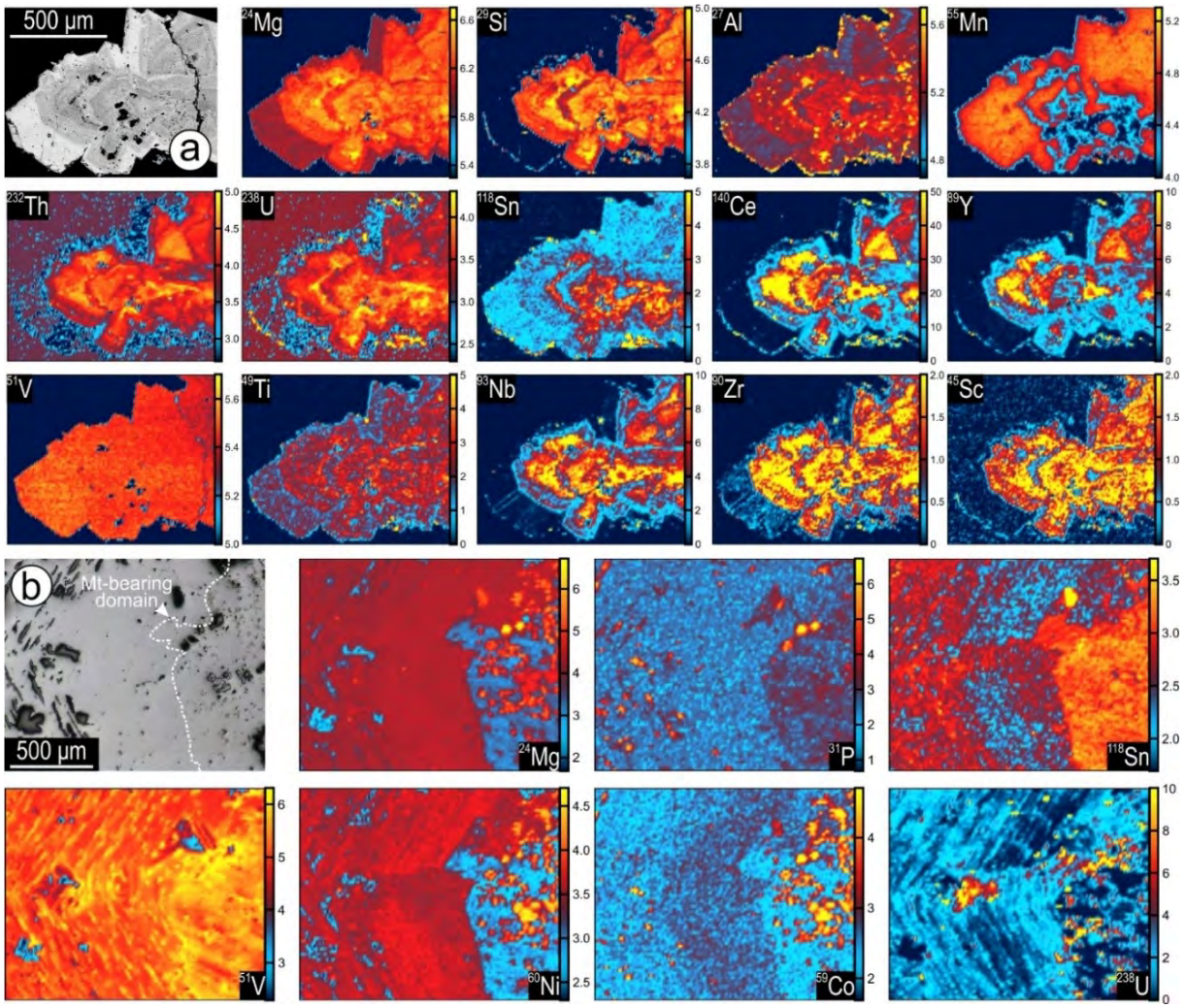

Fig. 5. LA-ICP-MS element maps of (a) stratabound magnetite displaying inclusion-rich (dark) and -poor (bright) domains (on BSE image, top left), and (b) 'nut'-shaped hematite. In (b), note compositional differences with respect to textures, i.e., from left to right: outer ring; inclusion-free, clean domain; and magnetite-bearing core (reflected light image, top left). Spotty enrichment of Mg and Ni in the core correlates with the presence of magnetite. Intensities in counts-per-second, as 10^n except in (a) where intensities for Nb, Ce and Y are displayed as $n \cdot 10^4$, whereas Ti and Zr are in $n \cdot 10^3$; U is presented as $n \cdot 10^3$ in (b).

Comparatively, the inclusion-free hematite displays homogeneous enrichment in Mg and Ni (both up to ~200 ppm). The dark ring shows some similarities with the core, e.g., comparable concentrations of Sn, P and Co, but is otherwise undistinguishable from the inclusion-free hematite, albeit with pores. Titanium is lower still than in the stratabound magnetite (average ~15 ppm).

Nanoscale characterisation

The inclusions consist dominantly of Ca-Mg-pyroxenes, with minor Si-bearing phases, in both magnetite types (Fig. 6a, b; Supplementary Material, Figs. A1 and A2). In addition, minor Fe-phosphates were identified in stratabound magnetite. The pyroxenes vary in size from a few to hundreds nm, and their abundance is lower in the steam-heated type. STEM EDX element maps reveal Mg- and Ca-rich grains, although Ca normally overlaps with Mg. Some Ca-bearing pyroxene also show Na-enrichment. Compositional data plots mostly within the augite and enstatite fields albeit across the pigeonite domain (Fig. 6c). There is a shift towards Fe-richer compositions in the pyroxenes from the steam-heated magnetite. In the steam-heated sample, hematite replacing magnetite consists of a bladed aggregate with interstitial pores and secondary S-bearing phases (Fig. 7a, b).

The aggregate is also finely mottled with respect to secondary phases. Pseudomorphic replacement of magnetite by hematite is however observed within a ~500 nm-sized domain displaying contrasting interfaces; sharp towards the magnetite and scalloped against the bladed hematite aggregate (Fig. 7c). Pyroxene inclusions inherited from pre-existing magnetite are preserved except for those along the contact with the S-bearing hematite (Fig. 7d). Sulfur enrichment correlates with the mottling within the hematite aggregate (Fig. 7a, d), whereas the inclusions are either Fe-, Mg-, Ca-bearing sulfates or Si-rich phases (Fig. 7d, e). Formation of such secondary phases starts with replacement of hematite at grain junctions as observed from S-bearing hematite preserved within a coarser inclusion of a Mg-sulfate (Fig. 7f-h).

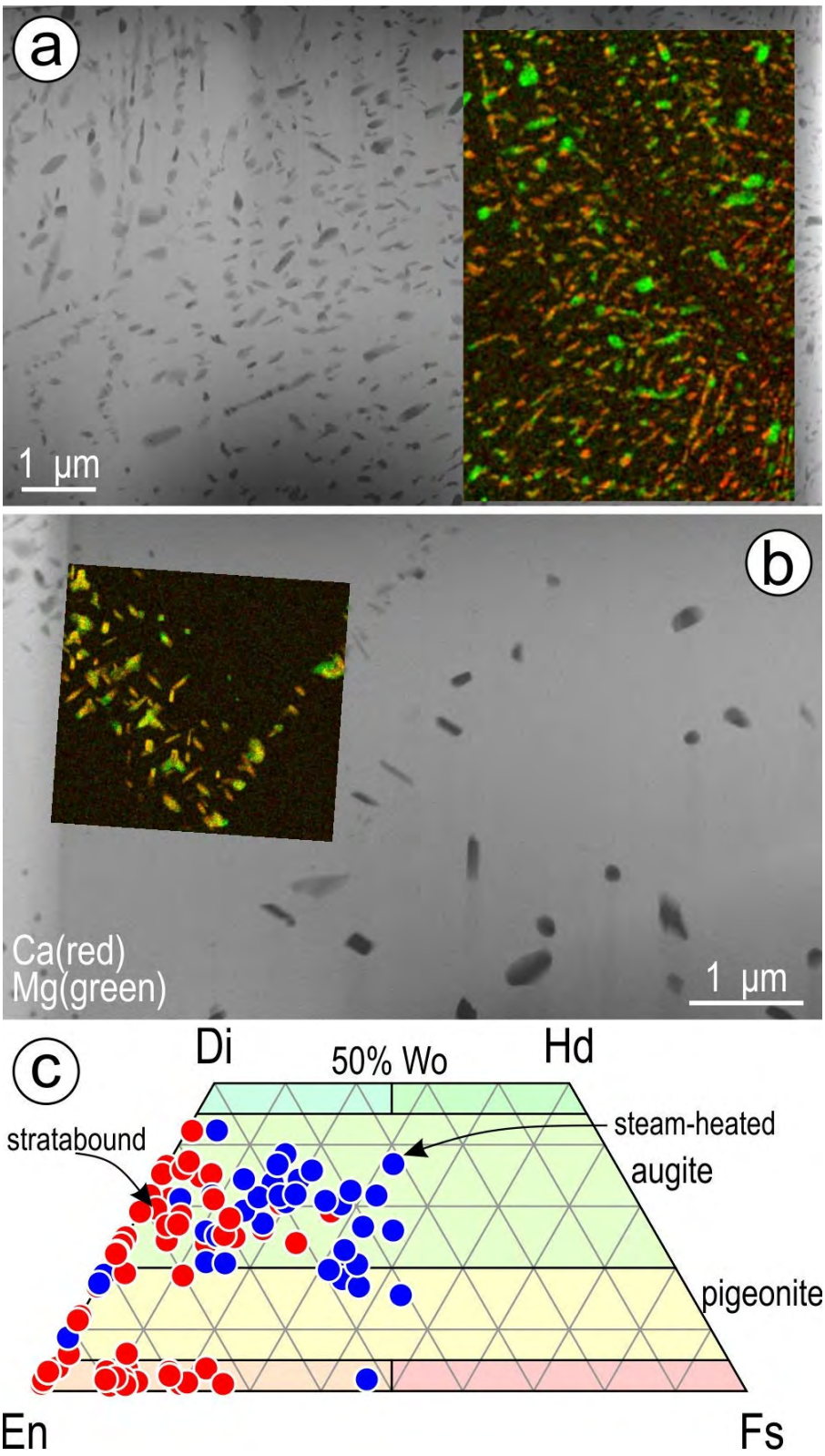

Fig. 6. HAADF STEM images and overlapped STEM-EDX maps for Ca and Mg for stratabound magnetite (a) and magnetite inclusion in 'nut'-shaped hematite (b). Colour overlap indicates paired clinopyroxenes (yellowish), whereas green-only corresponds to clinoenstatite. (c) Compositional diagram for analysed pyroxenes from magnetite categories as marked. Pyroxene formulae calculated from integrated, selected area EDX measurements. Iron calculated using pyroxene stoichiometry to eliminate interferences from host magnetite. Di−diopside; En−enstatite; Fs−ferrosilite; Hd−hedenbergite; Wo−wollastonite.

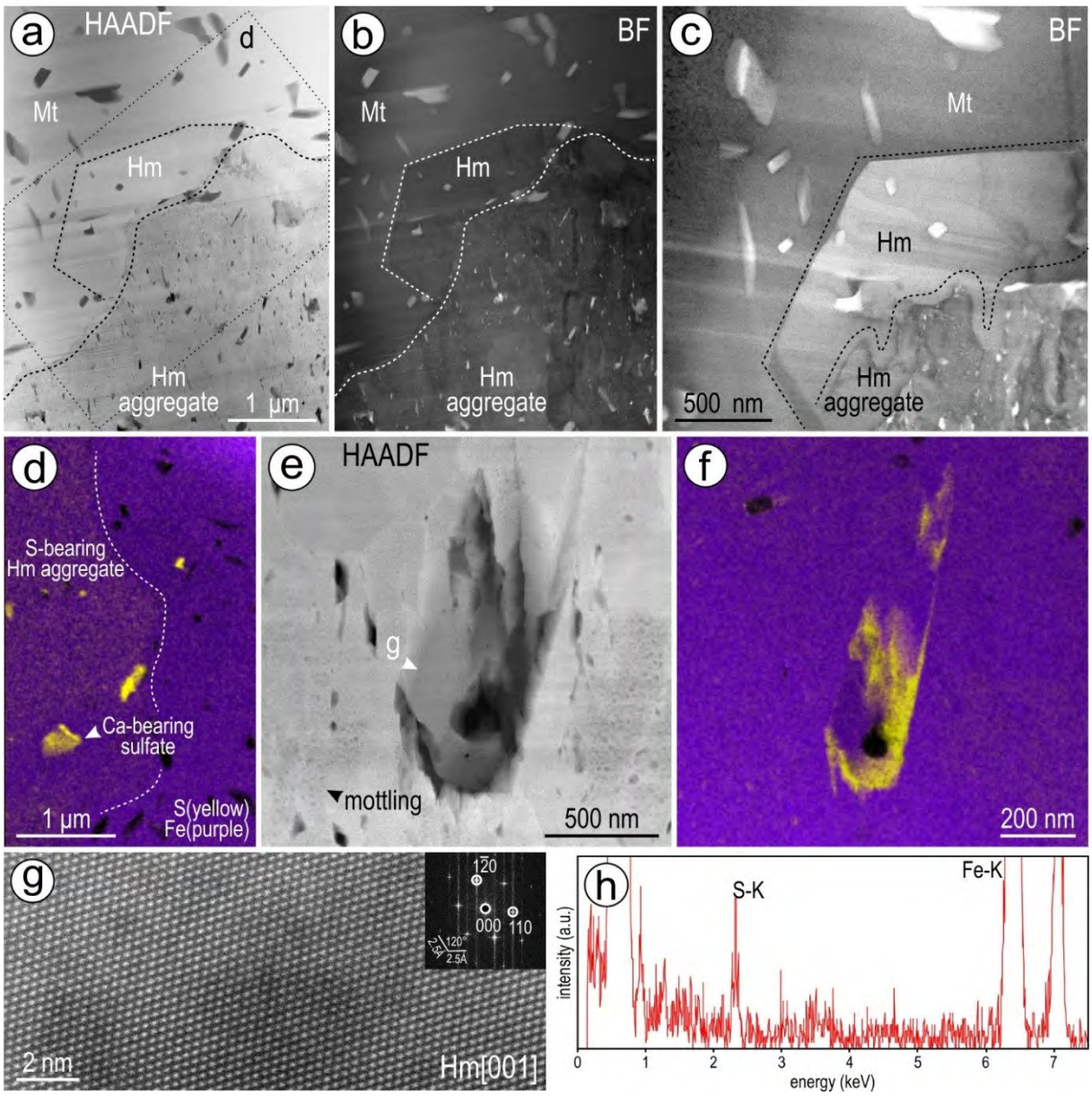

Fig. 7. HAADF and BF STEM images as marked showing replacement of magnetite (Mt) by S-bearing hematite (Hm) in the steam-heated alteration sample. Image contrast shows differences in composition and orientation in (a) and (b), respectively. Note the variable oriented domains indicating a hematite aggregate in the lower part of (b). (c) Sharp and scalloped margins of the single-hematite grain (pseudomorph after magnetite) towards magnetite (top) and the hematite-aggregate (bottom), respectively. (d) Overlapped maps of Fe and S at the contact between the two hematite grains showing S-bearing inclusions and enrichment in the aggregate. (e) Image and S+Fe maps of a Mg-bearing sulfate inclusion. Note mottling in host hematite. (g, h) High resolution image and EDX-spectrum for S-bearing hematite. Extended elemental maps are shown in the Supplementary Material Figures A3 and A4.

The inclusions show two species with coherent intergrowths along various crystallographic directions and are typified by nm-scale defects (Fig. 8a-c). Often, the two phases display sharp indentations into one another (Fig. 8b) and hair-pin defects. Fast Fourier Transform (FFT)

patterns, atomic-scale HAADF STEM imaging, STEM simulations and crystal models confirm the inclusions as clinopyroxenes (Figs. 8c-g; 9).

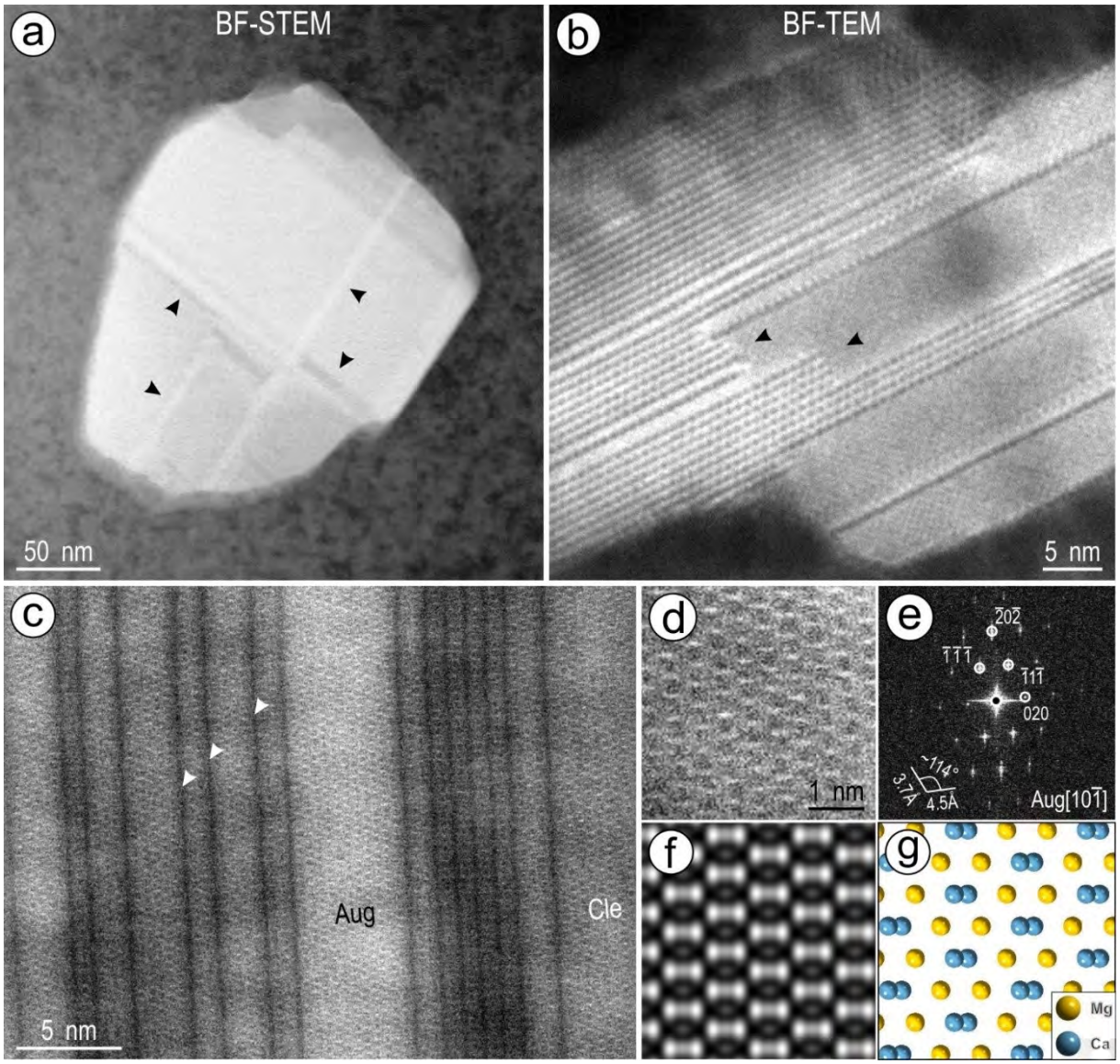

Fig. 8. (a, b) Oriented intergrowths (arrowed) within pyroxene inclusions. Note indentation between the two phases (arrowed) in (b). (c) HAADF STEM image showing epitaxial intergrowths between clinoenstatite/pigeonite on [10$\bar{1}$] zone axis. Note the presence of darker, 1-2 nm-wide bands (defects?). (d-g) Image, FFT pattern, STEM simulation and crystal model identifying the image in (c) as a clinopyroxene. Augite was used for the modelling, although there are no marked differences between the two clinopyroxenes on this orientation.

Distinctions between pyroxene and amphibole are obtained from crystal orientations exposing the full length of the cation chain, i.e., shorter in the former (Fig. 8d-g). Coherent intergrowths between magnetite and pyroxenes are common (Fig. 9a), although offsets between the crystallographic axes, by several degrees, are also observed. Identification of two distinct clinopyroxenes within the intergrowths is obtained on [010] zone axis, for example for augite

and clinoenstatite (Fig. 9b, c). Disordered lattice-scale intergrowths along the *c* axis are also common, whereby slabs of augite occur within a matrix of clinoenstatite (Fig. 9d). Notable is the fact that both pyroxenes are aligned parallel to one another, without any misfit angle between the two.

Discussion

The clinopyroxene pairs identified in the El Laco magnetite are directly comparable with augite-pigeonite inclusions, which are typical of crystallisation from mafic/ultramafic melts and are commonly reported from gabbroic/basaltic rocks.

Pyroxene intergrowths are attributed to exsolution processes with P-T conversion/inversion points between species of different symmetry and are useful for interpretation of cooling paths in metamorphic and magmatic/mantle-derived pods in layered intrusions (e.g., Arlt et al., 2000; Brizi et al., 2003; Gao et al., 2019). Coherent intergrowths between clinopyroxene pairs and Ti-rich magnetite are found in Fe-rich layered intrusions (Gao et al., 2019, and references therein), whereas the inverse relationship (i.e., crystallographically-oriented pyroxene inclusions in magnetite) is not widely reported. Nonetheless, crystallographically-oriented inclusions of clinopyroxene in chromite are known (Yamamoto et al., 2009).

Therefore, based on the identity of the observed pyroxene pairs as inclusions, a magmatic/melt origin for the studied magnetite is feasible at El Laco. The hairpin defects and indented relationships between the two phases are comparable with those reported for 'inverted pigeonites' (e.g., Ranson, 1986), whereas the lack of an offset angle between the two clinopyroxenes (Fig. 8) is concordant with crystallisation and exsolution from melts under effusive conditions or lava flows (Robinson et al., 1971, 1977).

The low Ti contents in this magnetite, noted both in our study and previously, has been used by some authors to attribute the stratabound magnetite to a hydrothermal origin as opposed to magmatic for magnetite in andesitic rocks, e.g., diagrams based on Ti *versus* Ni/Cr (Dare et al., 2015). The low Ti contents could, however, be attributed to formation of immiscible melts,

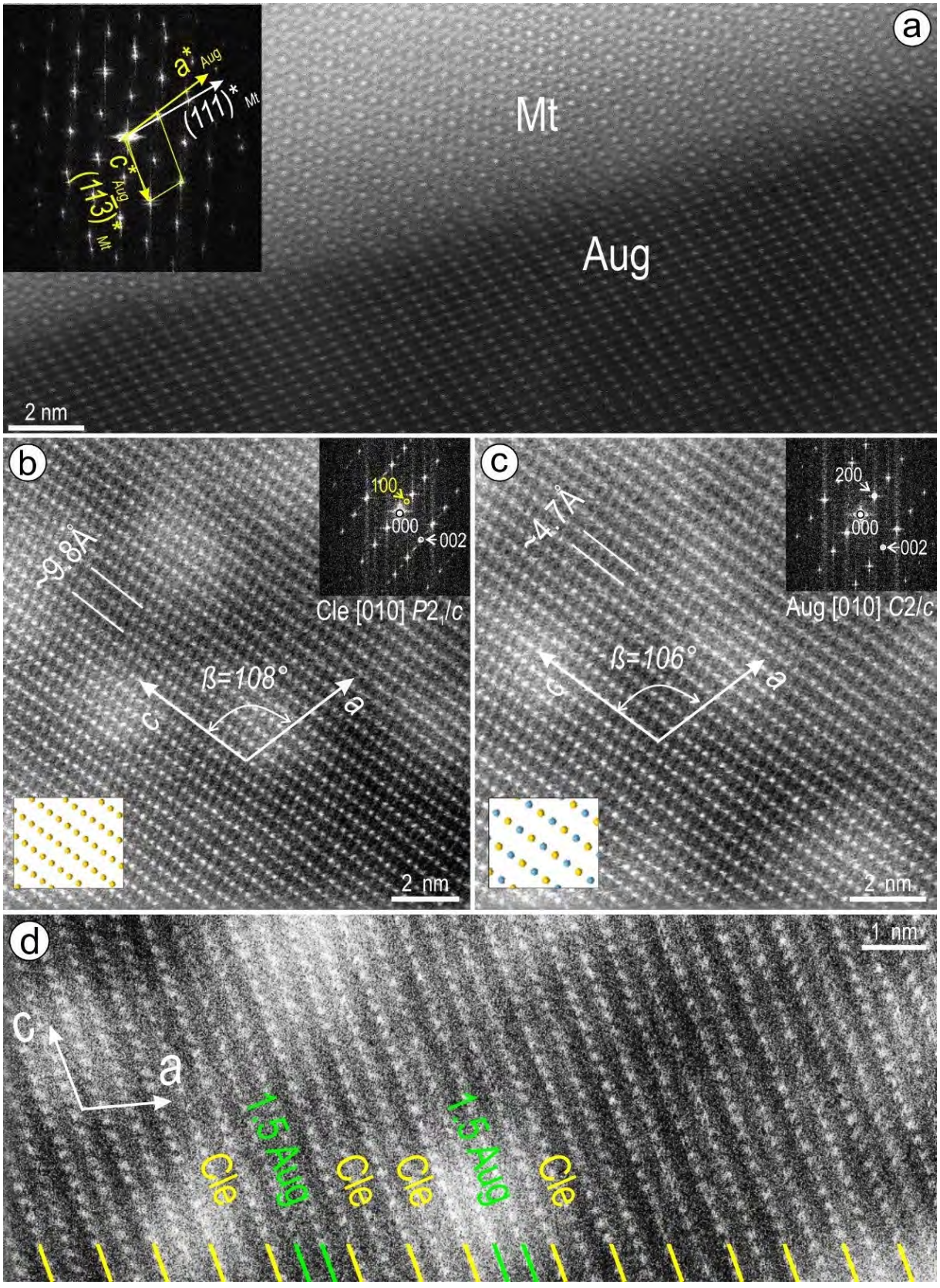

Fig. 9. (a) HAADF STEM image and FFT pattern (inset) showing orientated intergrowths between augite (Aug) and magnetite (Mt) with $c^*_{Aug}//(11\bar{3})^*_{Mt}$, the so-called 'X'-type intergrowths of Fleet et al. (1980). (b, c) High-resolution images and FFT patterns (insets) of clinoenstatite (Cle) and augite on [010] zone axis. (d) Slabs of augite within a clinoenstatite matrix.

i.e., Si- and Fe-rich conjugate melt pairs as previously suggested (Tornos et al., 2016 and references therein), if the protolith for the latter is derived from assimilation of Fe-rich but Ti-poor horizons of sedimentary or metamorphic origin into melts feeding the El Laco volcano. Such a hypothesis was proposed by Frutos and Oyarzún (1975), but later refuted (Nyström and Henríquez, 1994) based on the lack of outcropping Fe-rich units in the area. Assimilation has been reconsidered in recent models (Keller et al., 2019), since both ironstones and P-rich sediments of Silurian age are observed in outcrop from adjacent terranes in Argentina (Boso and Monaldi, 2008; Moya et al., 2012) and could be part of the thicker continental arc crust at the root of the volcanic edifice.

The hematite containing magnetite with identical inclusions as in the stratabound type can be considered in the context of sublimate crystals growing in cavities or along degassing tubes in lava flows, as previously discussed for the 'nut-shaped' hematite (Henríquez and Martin, 1978). Nonetheless, the presence of pyroxene-bearing magnetite inclusions and the debris ring in the hematite indicates a more complex, multistage formation process.

A possible scenario is presented schematically in Figure 10. Considering the Fe-Si melt immiscibility model of Keller et al. (2019), the Fe- and Si-rich melts form a stratified reservoir at a depth of ~5 km (Fig. 10a). At this stage, bubbles and magnetite grains accumulate at the contact between the two melts, as shown for water-saturated basalts underplating andesite melts (Edmonds et al., 2014; Fig 10a, inset). Injection of the Fe-rich melt (forming magnetite orebodies) along collapse faults (Keller et al., 2019) induces sudden volatile exsolution and degassing due to depressurisation (Fig. 10b). As the fluid flows upwards along conduits, the vapour bubbles coalesce and ascend with magnetite in a turbulent flow (Fig. 10b, inset). Agglomeration of magnetite with gas bubbles will entrain debris along its pathway close to the surface. The gas mixture will sublimate products within cavities and gas escape tubes at decreased temperature and pressure (Fig. 10c). Crystallisation of hematite from the gas

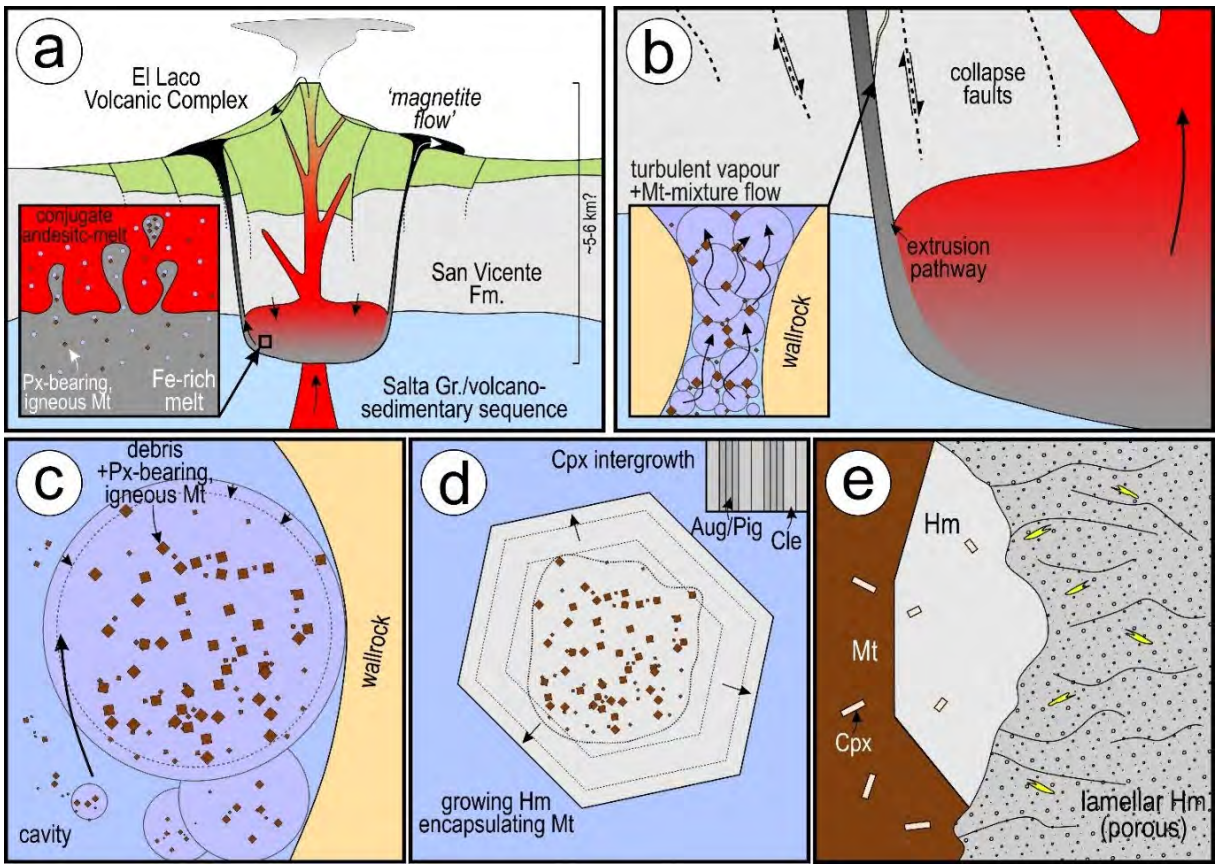

Fig. 10. Schematic illustrating igneous magnetite flotation [panels (a) and (b) adapted from Keller et al., 2019 and Edmonds et al., 2015]. (a) Due to melt immiscibility, a stratified reservoir with Fe- and Si-rich melts is formed at ~5 km depth. At the contact between the two melts, magnetite attracts heterogeneous bubble nucleation (inset). (b) Deflation causes collapse faults inducing injection of Fe-rich melts to surface and triggering depressurisation. Volatile exsolution and degassing results in a gas+fluid mixture which is channelled upwards (inset). Vapour bubbles coalesce and ascend with magnetite and debris in a turbulent flow. (c) The mixture, incorporating the magnetite, sublimates in cavities/degassing tubes due to temperature decrease at low pressure. (d, e) Crystallisation of hematite from the mixture encapsulates magnetite, whereas vapour unmixing at this stage results in acidic alteration of both Fe-oxides producing the S-bearing sublimates.

encapsulates the floated pyroxene-bearing magnetite, whereby partial martitisation occurs along mutual grain boundaries (Fig. 10d). At this stage, vapour unmixing results in acidic alteration of both magnetite and hematite, producing S-bearing sublimates and formation of hematite aggregates along their mutual boundaries (Fig. 10e). Such a scenario could explain the nanoscale textures observed in the steam-heated sample, with the mottling (Fig. 7) most likely resulting from trapping of fluids. Additionally, this scenario can explain a magmatic origin for both types of magnetite.

The Ti enrichment in accessory magnetite from the andesite relative to the overall low-Ti in the magnetite deposits (up to ~200 ppm in the present study) is discussed further. Despite

higher partitioning of Ti in Fe-rich relative to Si-rich melt (Hou et al., 2018; Keller et al., 2019), accessory magnetite in andesite will concentrate most of this Ti, making it relatively enriched compared to the bulk of the Ti content, which is evenly distributed throughout the entire magnetite orebodies. Secondly, higher fO_2 and overall low H_2S/SO_4 conditions, as inferred for melts at El Laco (presence of igneous anhydrite), could prohibit the incorporation of Ti (see discussion in Velasco et al., 2016).

Whereas the 'nut'-shaped hematite entraps valuable evidence to support the magnetite flotation model, this process is likely limited to venting or degassing conduits in the volcano. In terms of net transport, the process could have played a volumetrically important role in surficial magnetite enrichment close to vents or degassing structures. However, we consider that harvesting of magnetite by bubbles as an "efficient flotation of magmatic suspensions to form giant deposits" (Knipping et al., 2015; Ovalle et al., 2018) is unlikely, considering that there is no evidence for vapour interaction observed in the stratabound orebodies. Moreover, the homogeneous distribution of pyroxene inclusions throughout magnetite across the massive deposits shows a unique variant of a magmatic formation process, rather than predominantly hydrothermal, as put forward by other authors (Dare et al., 2015; Knipping et al., 2015; Ovalle et al., 2018).

The present data show trace elements signatures for Fe-oxides that are comparable with previous studies (e.g., Dare et al., 2015), except for the identification of U as part of the so-called 'granitophile group elements', measurable in both magnetite and hematite (Figs. 4 and 5). This signature, facilitating U-Pb dating of Fe-oxides (Courtney-Davies et al., 2019a), is recognized in IOCG systems *sensu stricto* from South Australia (Verdugo-Ihl et al., 2017, 2020; Courtney-Davies et al., 2019b). This observation could indicate a genetic link between IOCG systems and IOA deposits, such as El Laco (e.g., Ovalle et al., 2018, and references therein). The U-W-Sn-Mo signature can be transferred to felsic magmas if these are underplated by mafic

melts at the subcontinental lithospheric mantle boundary, as predicted by generic models for IOCG systems (Groves et al., 2010).

Implications and conclusions

Augite-pigeonite exsolution pairs indicate a magmatic origin for both magnetite from the stratabound and hematite within in the steam-heated deposits. Nanoscale intergrowths between the two pyroxenes support rapid growth and exsolution at low pressure and high temperature.

The S-bearing sublimate coatings are evidence for vapour transport of the magmatic magnetite, as preserved in the 'nut'-shaped hematite from El Laco. The lack of such alteration in the massive magnetite orebodies is a strong argument against considering magnetite flotation in volcanoes as a major ore-forming process. The expression of this transportation mechanism will be only surficial and likely restricted to small volumes of rock deposited around venting structures.

The present study shows that neither geochemical signatures nor textures alone can be used to infer or discriminate between a magmatic and hydrothermal origin. A complementary micron to nanoscale approach can however provide a range of criteria to underpin an integrated model for formation of the Fe-oxide orebodies.

Supplementary Materials

Appendix A: Analytical methods, additional figures, summary of EPMA results and mineral formula calculations, and summary statistics of trace element data from Fe-oxides by LA-ICP-MS.

Acknowledgments

This work is a contribution to the 'FOX' project (Trace elements in iron oxides: deportment, distribution and application in ore genesis, geochronology, exploration and mineral processing), supported by BHP Olympic Dam and the South Australian Government Mining and Petroleum Services Centre of Excellence (Grant 2015/321-0001038449). We thank Alexandra Gomez Escobar, who kindly provided sample material. We extend thanks to the staff of Adelaide

Microscopy, particularly Sarah Gilbert and Benjamin Wade, who have continuously supported this project and assisted with analytical work. N.J.C. acknowledges support from the ARC Research Hub for Australian Copper-Uranium (Grant IH130200033).

References

Arlt, T., Kunz, M., Stolz, J., Armbruster, T., Angel, R.J., 2000. P-T-X data on P21/c-clinopyroxenes and their displacive phase transitions. Contrib. to Mineral. Petrol. 138, 35–45. https://doi.org/10.1007/PL00007660

Boso, M.A., Monaldi, C.R., 2008. Cuenca Silúrico-Devónica y los depósitos ferríferos asociados en la Provincia de Juyjuy, in: XVII Congreso Geológico Argentino, Relatorio 2. pp. 155–165.

Brizi, E., Nazzareni, S., Princivalle, F., Zanazzi, P.F., 2003. Clinopyroxenes from mantle-related xenocrysts in alkaline basalts from Hannuoba (China): augite-pigeonite exsolutions and their thermal significance. Contrib. to Mineral. Petrol. 145, 578–584. https://doi.org/10.1007/s00410-003-0467-9

Courtney-Davies, L., Ciobanu, C.L., Verdugo-Ihl, M.R., Dmitrijeva, M., Cook, N.J., Ehrig, K., Wade, B.P., 2019a. Hematite geochemistry and geochronology resolve genetic and temporal links among iron-oxide copper gold systems, Olympic Dam district, South Australia. Precambrian Res. 335, 105480. https://doi.org/10.1016/j.precamres.2019.105480

Courtney-Davies, L., Tapster, S.R., Ciobanu, C.L., Cook, N.J., Verdugo-Ihl, M.R., Ehrig, K.J., Kennedy, A.K., Gilbert, S.E., Condon, D.J., Wade, B.P., 2019b. A multi-technique evaluation of hydrothermal hematite U Pb isotope systematics: Implications for ore deposit geochronology. Chem. Geol. 513, 54–72. https://doi.org/10.1016/j.chemgeo.2019.03.005

Dare, S.A.S., Barnes, S.-J., Beaudoin, G., 2015. Did the massive magnetite "lava flows" of El Laco (Chile) form by magmatic or hydrothermal processes? New constraints from magnetite composition by LA-ICP-MS. Mineralium Deposita 50, 607–617. https://doi.org/10.1007/s00126-014-0560-1

Deditius, A.P., Reich, M., Simon, A.C., Suvorova, A., Knipping, J., Roberts, M.P., Rubanov, S., Dodd, A., Saunders, M., 2018. Nanogeochemistry of hydrothermal magnetite. Contrib. to Mineral. Petrol. 173, 46. https://doi.org/10.1007/s00410-018-1474-1

Edmonds, M., Brett, A., Herd, R.A., Humphreys, M.C.S.S., Woods, A., 2015. Magnetite-bubble aggregates at mixing interfaces in andesite magma bodies. Geol. Soc. London, Spec. Publ. 410, 95–121. https://doi.org/10.1144/SP410.7

Fleet, M.E., Bilcox, G.A., Barnett, R.L., 1980. Oriented magnetite inclusions in pyroxenes from the Greenville Province. Can. Mineral. 1, 89–99.

Frietsch, R., 1978. On the magmatic origin of iron ores of the Kiruna type. Econ. Geol. 73, 478–485. https://doi.org/10.2113/gsecongeo.73.4.478

Frutos, J., Oyarzún, J., 1975. Tectonic and geochemical evidence concerning the genesis of El Laco magnetite lava flow deposits, Chile. Econ. Geol. 70, 988–990. https://doi.org/10.2113/gsecongeo.70.5.988

Gao, W., Ciobanu, C.L., Cook, N.J., Slattery, A., Huang, F., Wang, D., 2019. Nanoscale study of lamellar exsolutions in clinopyroxene from olivine gabbro: recording crystallization sequences in iron-rich layered intrusions. Am. Mineral. 104, 244–261. https://doi.org/10.2138/am-2019-6764

Groves, D.I., Bierlein, F.P., Meinert, L.D., Hitzman, M.W., 2010. Iron Oxide Copper-Gold (IOCG) Deposits through Earth History: Implications for Origin, Lithospheric Setting, and Distinction from Other Epigenetic Iron Oxide Deposits. Econ. Geol. 105, 641–654. https://doi.org/10.2113/gsecongeo.105.3.641

Henríquez, F., Martin, R.F., 1978. Crystal-growth textures in magnetite flows and feeder dykes, El Laco, Chile. Can. Mineral. 16, 581–589.

Hou, T., Charlier, B., Namur, O., Holtz, F., Veksler, I., Zhang, Z., Thomas, R., 2018. Immiscible hydrous Fe–Ca–P melt and the origin of iron oxide-apatite ore deposits. Nat. Commun. 9, 1–8. https://doi.org/10.1038/s41467-018-03761-4

Keller, T., Hanchar, J., Tornos, F., Suckale, J., 2019. Formation of the El Laco magmatic magnetite deposits by Fe-Si melt immiscibility and bubbly suspension flow along volcano tectonic faults. AGU 2018 Fall Meeting, Washington, DC. https://doi.org/10.1002/essoar.10500353.1

Knipping, J.L., Bilenker, L.D., Simon, A.C., Reich, M., Barra, F., Deditius, A.P., Lundstrom, C., Bindeman, I., Munizaga, R., 2015. Giant Kiruna-type deposits form by efficient flotation of magmatic magnetite suspensions. Geology 43, 591–594. https://doi.org/10.1130/G36650.1

Knipping, J.L., Webster, J.D., Simon, A.C., Holtz, F., 2019. Accumulation of magnetite by flotation on bubbles during decompression of silicate magma. Sci. Rep. 9, 3852. https://doi.org/10.1038/s41598-019-40376-1

Moya, M.C., Scasso, R.A., Castro, L.N., Fazio, A.M., 2012. Los fosfatos en el Ordovícico del Norte Argentino, in: Marquillas, R.A., Sánchez, M.C., Salfity, J.A. (Eds.), Aportes Sedimentológicos a La Geología Del Noroeste Argentino. XIII Reunión Argentina de Sedimentología. Salta, pp. 145–167.

Nyström, J.O., Henríquez, F., 1994. Magmatic features of iron ores of the Kiruna type in Chile and Sweden: ore textures and magnetite geochemistry. Econ. Geol. 89, 820–839. https://doi.org/10.2113/gsecongeo.89.4.820

Ovalle, J.T., La Cruz, N.L., Reich, M., Barra, F., Simon, A.C., Konecke, B.A., Rodriguez-Mustafa, M.A., Deditius, A.P., Childress, T.M., Morata, D., 2018. Formation of massive iron deposits linked to explosive volcanic eruptions. Sci. Rep. 8, 14855. https://doi.org/10.1038/s41598-018-33206-3

Park, C.F., 1961. A magnetite "flow" in northern Chile. Econ. Geol. 56, 431–436. https://doi.org/10.2113/gsecongeo.56.2.431

Ranson, W.A., 1986. Complex exsolution in inverted pigeonite: Exsolution mechanisms and temperatures of crystallization and exsolution. Am. Mineral. 71, 1322–1336.

Robinson, P., Jaffe, H.W., Ross, M., Klein, C.J., 1971. Orientation of exsolution lamellae in clinopyroxene and clinoamphiboles: Consideration of optical phase boundaries. Am. Mineral. 56, 909–939.

Robinson, P., Ross, M., Nord, G.L., Smyth, J.R., Jaffe, H.W., 1977. Exsolution lamellae in augite and pigeonite; fossil indicators of lattice parameters at high temperature and pressure. Am. Mineral. 62, 857–873.

Sillitoe, R.H., Burrows, D.R., 2002. New field evidence on the origin of the El Laco magnetite deposit, Northern Chile. Econ. Geol. 97, 1101–1109. https://doi.org/10.2113/gsecongeo.97.5.1101

Tornos, F., Velasco, F., Hanchar, J.M., 2017. The Magmatic to Magmatic-Hydrothermal Evolution of the El Laco Deposit (Chile) and Its Implications for the Genesis of Magnetite-Apatite Deposits. Econ. Geol. 112, 1595–1628. https://doi.org/10.5382/econgeo.2017.4523

Tornos, F., Velasco, F., Hanchar, J.M., 2016. Iron-rich melts, magmatic magnetite, and superheated hydrothermal systems: The El Laco deposit, Chile. Geology 44, 427–430. https://doi.org/10.1130/G37705.1

Velasco, F., Tornos, F., Hanchar, J.M., 2016. Immiscible iron- and silica-rich melts and magnetite geochemistry at the El Laco volcano (northern Chile): Evidence for a magmatic origin for the magnetite deposits. Ore Geology Reviews 79, 346–366. https://doi.org/10.1016/j.oregeorev.2016.06.007

Verdugo-Ihl, M.R., Ciobanu, C.L., Cook, N.J., Ehrig, K.J., Courtney-Davies, L., 2020. Defining early stages of IOCG systems: evidence from iron oxides in the outer shell of the Olympic Dam deposit, South Australia. Mineralium Deposita 55, 429–452. https://doi.org/10.1007/s00126-019-00896-2

Verdugo-Ihl, M.R., Ciobanu, C.L., Cook, N.J., Ehrig, K.J., Courtney-Davies, L., Gilbert, S., 2017.

Textures and U-W-Sn-Mo signatures in hematite from the Olympic Dam Cu-U-Au-Ag deposit, South Australia: Defining the archetype for IOCG deposits. Ore Geology Reviews 91, 173–195. https://doi.org/10.1016/j.oregeorev.2017.10.007

Williams, P.J., 2010. Classifying IOCG deposits, in: Corriveau, L., Mumin, H. (Eds.), Exploring for Iron Oxide Copper-Gold Deposits: Canada and Global Analogues, Short Course Notes. Geological Association of Canada, pp. 23–38.

Yamamoto, S., Komiya, T., Hirose, K., Maruyama, S., 2009. Coesite and clinopyroxene exsolution lamellae in chromites: In-situ ultrahigh-pressure evidence from podiform chromitites in the Luobusa ophiolite, southern Tibet. Lithos 109, 314–322. https://doi.org/10.1016/j.lithos.2008.05.003

CHAPTER 9

SUMMARY, RECOMMENDATIONS AND CONCLUDING REMARKS

CHAPTER 9: SUMMARY, RECOMMENDATIONS AND CONCLUDING REMARKS

9.1 Summary

In each of the chapters making up this thesis, complementary microanalytical techniques have been applied to study the two ubiquitous, and most volumetrically important Fe-oxides in IOCG systems and in the Earth's crust, hematite and magnetite. These studies have demonstrated the utility of Fe-oxides to constrain ore-forming processes at Olympic Dam, the two satellite prospects Acropolis and Wirrda Well, and in a much younger iron deposit in Chile, El Laco.

Importantly, these Fe-oxides are by no means exclusive to IOCG systems; rather, they occur in a broad range of other deposit types, either as gangue or ore minerals (e.g., in BIFs) and in geological environments that span across sedimentary, metamorphic, magmatic and hydrothermal conditions. Because of this, detailed petrographic analysis and compositional characterisation of Fe-oxides has gained significant attention in the contemporary literature. This trend is likely to continue in the years to come as researchers seek new ways to interpret ore genesis. LA-ICP-MS and EPMA, in particular, are widely available and accessible techniques that offer opportunities for precise compositional fingerprinting of Fe-oxides. Dedicated nanoscale characterisation of iron-oxides, using HAADF STEM, for example, is still gaining recognition as a powerful, additional tool. If used carefully, and on material that has been comprehensively characterised at the micron-scale, both compositionally and texturally, nanoscale study of Fe-oxides will likely play an increasingly important role in ore-deposit research, allowing the bridging of observational data at different scales, and offering novel criteria for understanding Fe-oxide mineralogy as a proxy to model mineralisation conditions.

This thesis has aimed to demonstrate and consolidate the capabilities of such a holistic approach to the study of Fe-oxides for characterising IOCG or other types of mineralising

systems following a generic concept. One of the main advantages of focusing this work on the Olympic Dam district, including the Olympic Dam deposit itself, is that substantially different products of the same type mineralisation event occur within less than ~30 km from one another. These systems display differences in terms of host lithologies, ages, proportions of magnetite relative to hematite, and contrasting Fe-oxide composition and grain morphologies, offering a basis to make a direct comparison between them. Work described in this thesis has also addressed the behaviour of minor/trace elements during superimposed overprinting of Fe-oxides during fluid-mineral interactions in terranes that have experienced a protracted geological evolution. Although poorly documented until now, overprinting is likely a common phenomenon in many deposits, and can potentially have a major impact on the composition and textures observed.

Despite major differences with other IOCG systems worldwide, in terms of mineralisation age, local geological setting, prevailing Fe-oxide speciation and their respective compositions and petrography, alteration type and overprinting, the insights gained from the characterisation of Fe-oxides in the Olympic Dam district should be applicable to broadly analogous systems elsewhere. While this work relates to specific deposits/prospects within a single district (except for the Chilean example in **Chapter 8**), it nevertheless offers conclusions of a generic nature. Because Fe-oxide mineralogy and compositions are governed by the same physical processes – ultimately linked to their physicochemical environments of formation – the body of data provides a foundation for a compare-and-contrast approach between IOCG systems *sensu lato* worldwide.

9.1.1 Geochemistry and mineralogy of hematite and magnetite from the Olympic Dam deposit

Integrated petrographical and geochemical characterisation of hematite, covering all main lithologies and across the mineralisation extent at Olympic Dam, shows a prevailing texture featuring oscillatory and sectorial compositional zonation and a geochemical signature defined by enrichment in U, W, Sn, and Mo (Verdugo-Ihl et al., 2017, **Chapter 2**). Importantly, this signature offers a direct link to granitic fluid sources, notably the Roxby Downs Granite that hosts the Olympic Dam deposit. Identifying the source(s) of hydrothermal fluids is a key question in contemporary IOCG research (Barton, 2014, and references therein). Across the Olympic Dam deposit, other textural varieties of hematite display similar granitophile signatures and represent the products of repeated cycles of replacement and recrystallisation of pre-existing Fe-oxides, including the primary zoned hematite. Fluid-mineral interactions are demonstrated to remobilise and redistribute minor/trace element components at the grain-scale within hematite, but also exchange these elements with, or release them to the infiltrating fluid, significantly modifying hematite compositions and textures. These features can, in turn, be used to track the sequence of element remobilisation in hematite. These interactions preserve, albeit in different ways, the primary granitophile signatures of zoned hematite, either as newly recrystallised grains, or as discrete mineral inclusions in overprinted domains. At the deposit-scale, in Olympic Dam, hematite is probably the most important host phase for W, Sn, and Mo by mass, a finding which carries implications for deportment models for minor elements of potential long-term economic significance. Moreover, the U-W-Sn-Mo mineral signature is an inherent feature of IOCG system across the Olympic Dam district (Courtney-Davies et al., 2019a), and reflected in multivariate statistical analyses of large whole-rock datasets at the deposit-scale (Dmitrijeva et al., 2019a, 2019b). More recently, analogous signatures are beginning to be identified in other potentially-related deposits elsewhere (e.g., Sillitoe et al., 2020).

Although hematite-dominant, the Olympic Dam orebody features a weakly-mineralised domain adjacent to the confining host granite, termed the *outer shell*, which is characterised by assemblages containing silician magnetite (Verdugo-Ihl et al., 2020a, **Chapter 3**). Iron-oxide assemblages also include hematite relatively enriched in high field strength elements (HFSE) and Ti, and various products of the interconversion between magnetite and hematite (i.e., pseudomorphic replacements). Silician magnetite was clearly one of the earliest phases to form and constrains the onset of mineralisation, as it directly overprints magmatic magnetite from the host granite, which is also tied to the breakdown of accessory magmatic Fe-Ti-oxides. The HFSE-bearing hematite, atypical for hematite elsewhere in the orebody, suggests that the *outer shell* preserves an early hydrothermal signature, supported by observation of hematite forming directly on behalf of broken-down and overprinted magmatic Fe-(Ti-)oxides. As the hydrothermal system evolves, hematite becomes systemically more enriched in U-W-Sn-Mo, and correspondingly HFSE-depleted, toward the orebody. The granular to bladed morphologies shown by silician magnetite are part of a series of Fe-oxide interconversions that follows the transition to zoned, U-W-Sn-Mo-bearing hematite from the *outer shell* to the orebody. Intimate associations between Fe-oxides and their interconversion products reflect small-scale fluctuations of fluid parameters at the stability boundaries between magnetite and hematite throughout this early stage. Geochemical modelling at 400 °C indicates that magnetite-replacement took place at pH and fO_2 conditions that coincide with stability shifts of K-feldspar to sericite, and ilmenite to rutile. As supported by nanoscale studies (Ciobanu et al., 2019), silician magnetite reflects the early alkali-calcic alteration stage, preserving fine- and nanoparticles (NPs) of calc-silicates (diopside, epidote, and (ferro)actinolite). Rock-buffered, fluid-rock interactions associated with breakdown of mafic minerals and feldspars in host granite (Kontonikas-Charos et al., 2017), could have supplied Si, Ca, Al and Mg to form the calc-silicate inclusions within the silician magnetite. Moreover, Nd isotopic signatures of

magnetite support formation by magnetite-precipitating fluids that were at equilibrium with the granite (Johnson and McCulloch, 1995).

Not all silician magnetite at Olympic Dam is, however, hydrothermal, since LA-ICP-MS dating of *outer shell* magnetite yields $^{207}Pb/^{206}Pb$ dates of 1761 ± 16 Ma, some ~160 Ma older than the host granite, implying mechanical incorporation of ~1.76-1.74 Ga Fe-rich horizons of the (meta)sedimentary Wallaroo Group (Courtney-Davies et al., 2020). Formation of the o*uter shell* could have been initiated at the depth of granite emplacement (~6-8 km), following volatile release from fluids ponding at intrusion margins. Mineralisation continued during uplift of the granite to shallower depth, with cupola collapse, incorporation of pre-existing lithologies and following extensive fluid release that facilitated brecciation and orebody formation.

9.1.2 Trace element remobilisation in hematite by fluid-mineral interaction

Micron-scale textures and compositional patterns can be linked at the nanoscale by Z-contrast imaging using HAADF STEM analysis, if the investigated TEM-foils are extracted *in-situ* from sites of petrogenetic interest that have already been well characterised at the micron-scale. Such an approach was applied to study hematite displaying atypical Cu-As-zonation and weave-twinning to determine the role of elements in solid-solution (lattice-bound) *versus* their presence in the form of discrete NPs to explain the zoning and the effect of twinning on trace element distributions (Verdugo-Ihl et al., 2019, **Chapter 4**). Nanoscale observations, including Cl-K elemental associations and rounded voids within cavities showing negative crystal shapes, fingerprint the products of fluid-mineral interactions by coupled dissolution and reprecipitation reactions (CDRR) during overprinting of hematite that generated transient porosity and formed Cu-As- and Cu-NPs associated with fluid trapping (i.e., fluid inclusions). Rapid closure of external porosity, due to ripening of the pores, can effectively trap fluids, including low-T melts, as fluid inclusions and/or mineral precipitates during CDRR (Tooth et al., 2011). These features

impact on and are reflected by the spatial distribution of minor/trace elements as imaged at the micron-scale by LA-ICP-MS mapping. The weave-twinned hematite can be considered as a precursor case to the Cu-As-zoned hematite, presenting evidence linking the formation of acicular Cu-As-NPs, associated with traceable Si-Al-K along margins, with infiltration of Si-Al-K-fluids along conjugate sets of twins. Such twins were obliterated as the reaction proceeded, with precipitation of abundant sericite lamellae that crosscut and offset twins in the weaved-twinned case, an observation consistent with the widespread hydrolytic alteration observed at Olympic Dam. The interacting fluids changed in composition from alkali-silicic to Cl- and metal-bearing, whereas fluid percolation rates could have been affected by fault activity. Importantly, the presence of Cu within hematite supports the simultaneous introduction of that element at Olympic Dam, along with Fe and U.

Hematite displaying evidence for mineral-fluid interaction, and featuring selective modifications to primary crystal zoning (i.e., antipathetic behaviour between W- and Sn-zoning preservation; Verdugo-Ihl et al., 2017), was selected for nanoscale characterisation (Verdugo-Ihl et al., 2020b, **Chapter 5**). This was undertaken to assess partial disruption of zoning patterns by remobilisation and decoupling of minor/trace elements, as shown by LA-ICP-MS maps, that affected U-Pb isotopic systematics (Courtney-Davies et al., 2019b). 'Isomineral' pseudomorphic replacement of this W-bearing hematite by W-depleted domains is traceable by compositional and crystal structural modifications. At the grain scale, such decoupling reactions can effectively strip elements from hematite, with concentrations reduced by ca. three orders of magnitude (e.g., for W) relative to elements that behave immobile, such as Sn. Differences in the transport behaviour of W at similar temperatures, in the range of 250-350 °C, and fO_2 conditions, relative to Sn, which has much lower solubility, can be invoked to explain their contrasting behaviour (Brugger et al., 2016; Wang et al., 2019). Grain-scale (re)mobilisation of trace elements (W, Pb) during CDRR is associated with crystal structural modifications in hematite associated with O-vacancies, as supported by our two-fold hematite superstructure

model with anion vacancies that reproduces such features better than other models (e.g., Chen et al., 2008; McBriarty et al., 2018). Open system behaviour, confirmed by imaging of W and Pb (re)mobilisation, responsible for U-Pb isotopic disturbances, is traceable at the nanoscale as discrete enrichment along twin-crests (W-Pb) or NPs (W) within host hematite, where evidence for the onset of CDRR is preserved. Importantly, such reactions are widespread in other geochronometers (e.g., monazite; Weinberg et al., 2020) and can result in decoupled isotopes and erroneous U-Pb dates. Twin boundaries, and associated secondary structures (splays), play an important role in element redistribution, since they provide pathways for fluid percolation and favourable metal-trapping environments for released and/or introduced element precipitation (e.g., twinned sphalerite; Šrot et al., 2003). Thus, their presence can facilitate the operation of open system mechanisms, in turn affecting the robustness of a mineral geochronometer. Recognition of such features can be a valuable indicator of open-system behaviour.

9.1.3 Magnetite nanomineralogy from IOCG and -kin systems

Dedicated nanoscale (HAADF STEM) studies of magnetite from the contrasting Acropolis and Wirrda Well prospects, within the Olympic Dam district, and from the El Laco Fe-deposit (Chile), serve as excellent case-studies to highlight the variability in terms of trace element signatures and nanoscale inclusion populations in magnetite, thus offering a glimpse at different magnetite mineralisation conditions. This variability is also seen in other recently published studies. Yin et al. (2019) studied Fe-skarn magnetite from the Baishiya deposit, China, and the role of local supersaturation upon nucleation of spinel *sensu lato* NPs at the interface of fluid-mineral interaction. Deditius et al. (2018) addressed hydrothermal magnetite from the Los Colorados iron-oxide apatite deposit, Chile, and identified diopside, clinoenstatite, amphibole, mica and Ti-bearing spinels, attributing their accumulation in minor/trace-element rich zones to supersaturation from hydrothermal fluids and entrapment. Further nanoscale studies on magnetite from IOGG systems and important kin deposits elsewhere (e.g., Kiruna), would

significantly contribute to the understanding of these deposits and will help contextualise the use of NPs as universally applicable petrogenetic indicators.

Characterisation of hydrothermal magnetite and its nanomineralogy at Acropolis (Verdugo-Ihl et al., in press, **Chapter 6**), shows differences in NP populations that relate to the minor/trace element compositions in the host Fe-oxide. Titanium-rich (titanomagnetite, ~2.0 wt.% TiO_2) and -poor varieties (~0.07 wt.% TiO_2), the later exclusively hosted in a HS granite, occur as steep veins predominantly within GRV lithologies. Primary titanomagnetite, displaying trellis exsolutions, is texturally indistinguishable from igneous magnetite from granites across the district, which also feature ilmenite and two-phase ulvöspinel-hercynite NP exsolutions (e.g., in the Roxby Downs Granite; Ciobanu et al., 2019). Titanium-poor magnetite, however, exclusively hosts monophase NPs of spinel *sensu stricto*. The mechanism for formation of oxide phases from magnetite solid-solution ($magnetite_{SS}$) can be interpreted as a process following exsolution of ilmenite and ulvöspinel-hercynite, with subsequent overprinting of magnetite *via* mineral-buffered reactions. These reactions can be interpreted in the context of vein-reopening and hydrothermal fluid recirculation. At the grain-scale, mineral-fluid interaction recycles and redistributes contained elements (e.g., Mg, Al, Ti, and Zn) that form densely-mottled and orbicular, self-organised clusters of sub-µm inclusions, comprising hercynite±gahnite+TiO_2-polymorphs (anatase/rutile) and Sc-Ti-phases. Order-disorder phenomena observed in the TiO_2 polymorphs are evidence for subtly fO_2-buffered reactions from anatase (reducing) to rutile (more oxidising) conditions. Nanothermobarometric estimates using ilmenite-magnetite pairs provide re-equilibration temperatures in the range of ~570-510±50 °C from primary to orbicular magnetite, whereas Ti-poor magnetite could have formed at even higher temperatures (670±50 °C using X_{Mg}-in-magnetite thermometry; Canil and Lacourse, 2020). The spinel-bearing magnetite can be interpreted as a case of titanomagnetite extensively overprinted by interaction with hot fluids, remobilising Ti, and subsequent recrystallisation, in which low contents of minor elements (e.g., Mg, and Al) are partially

retained, or, alternatively, as the product of a distinct fluid pulse. The lack of calc-silicate NPs, as known from silician magnetite in IOCG systems with prevailing rock-buffered alteration of host lithologies (e.g., Olympic Dam; Ciobanu et al., 2019), can be explained by open-fracture circulation of hydrothermal fluids at Acropolis, inhibiting additional supply of Si, Ca, K, etc from host lithology during magnetite precipitation. Although the HS granite at Acropolis cannot be considered the source of the mineralisation (Dmitrijeva et al., 2019a), the broader district experienced incremental magmatic activity that spanned a few Ma (Cherry et al., 2018; Courtney-Davies et al., 2020; McPhie et al., 2020), potentially with intrusion of concealed, and likely more mafic/basic, plutons sourcing Ti-rich mineralising fluids (monzonitic/dioritic?). Although this titanomagnetite does occur in other hydrothermal deposits (e.g., Hu et al., 2019, and references therein), its similarity to igneous titanomagnetite, crystallising from silicate melts and displaying nearly the same oxy-exsolution features, does complicate interpretations regarding its formation conditions in some cases.

Unlike Acropolis, silician magnetite is the predominant type of magnetite seen in the Wirrda Well prospect (Verdugo-Ihl et al., in review, a, **Chapter 7**). Drawing on new HAADF S/TEM data, this magnetite is shown to host nanoinclusions of the rare Al-amphibole, ferro-tschermakite, which are imaged down to the atomic-scale. Moreover, this amphibole contains defects that have never been previously visualised at this scale, although they are predicted and modelled from previous studies. Considering that the host ~1.85 Ga granite underwent burial metamorphism, ferro-tschermakite is interpreted to represent a metamorphic phase that formed during Kimban metamorphism at ~1.75 Ga, prior to the magmatic-hydrothermal event, at ~1.6 Ga, which deposited IOCG-style mineralisation across the district.

Nanomineralogy of the El Laco magnetite (Verdugo-Ihl et al., in review, b, **Chapter 8**) contrasts dramatically with that of Olympic Dam (Ciobanu et al., 2019), Wirrda Well and Acropolis. The new data, particularly the presence two pyroxene inclusions (clinoenstatite + augite-pigeonite) within magnetite from both stratabound (pyroclastic and vesicular)

mineralisation, or as inclusions within hydrothermal hematite links them genetically, and sets them apart from unequivocally hydrothermal magnetite within the Olympic Dam district, which feature either calc-silicate and Si-Fe-nanoprecipitates (Olympic Dam, Wirrda Well), or oxide associations (ilmenite + spinel-associations ± TiO_2-polymorphs; Acropolis). Currently, the two most popular, but contrasting models that explain formation of massive magnetite-orebodies at El Laco involve either magnetite crystallisation from immiscible, Fe-rich melts (e.g., Tornos et al., 2016, and references therein), or combined magmatic-hydrothermal processes leading "magnetite flotation" during magma degassing (Ovalle et al., 2018). Although pyroxene inclusions (diopside/enstatite) have been shown in hydrothermal magnetite at Los Colorados Fe-deposit (Chile; Deditius et al., 2018), allegedly similar to Kiruna or El Laco, and for which the magnetite flotation model was initially proposed (Knipping et al., 2015), those results differ to the ones shown here, since they are associated with more hydrous phases (amphibole, phlogopite) supporting hydrothermal conditions. As shown here, clinopyroxene intergrowths support formation by rapid growth and exsolution at low pressure and relatively high temperatures, typical for melts. The presence of fine-grained, pyroxene-bearing magnetite inclusions, like those in the massive ore, within hydrothermal hematite, is perhaps the best hard evidence to support magnetite flotation at El Laco, since: (i) it can be directly linked to magnetite precipitating from a melt, and (ii) it displays alteration features associated with hydrothermal transport (S-bearing coatings). Nevertheless, the fine-grained nature of those magnetite inclusions differs significantly from the coarse-grained ores, suggesting that overall magnetite-flotation probably played a limited role in the transport and deposition of magnetite.

9.2 Recommendations

The work outlined in this thesis: (i) Fe-oxide mineralogy and mineral chemistry at Olympic Dam (Verdugo-Ihl et al., 2017, 2020a); (ii) processes leading to hematite overprinting (Verdugo-Ihl et al., 2019, 2020b); and (iii) case studies of magnetite from IOCG and -kin deposits (Verdugo-Ihl et al., in press; in review, b, c), can benefit from further layers of

information, not only applied directly to the study of Fe-oxides themselves, but also to accessory minerals as a proxy for the formation of the rocks and ores they are contained in. Some potential avenues for future research are outlined below.

9.2.1 Hematite geochemistry and additional microanalysis

From the perspective of mineralogical study of Fe-oxides within the Olympic Dam district, several topics remain inadequately addressed, particularly those relating to the crystal-chemical variability of hematite, especially when compared to that of magnetite, which has been extensively studied by several authors. Identification of unusually high concentrations of trace elements by both EPMA and LA-ICP-MS, include the highest reported concentrations for Mo (up to 2.88 wt.% MoO_3), and Sn (up to ~25,700 ppm; Verdugo-Ihl et al., 2017) in hematite. Niobium (up to 1.72 wt.% Nb_2O_5), is also markedly enriched in some hematite varieties and shows a strong positive correlation with Ti (r^2=0.92), interpreted in the context of charged-balanced substitutions: $Nb^{5+} + Ti^{4+} + \square \leftrightarrow 3Fe^{3+}$ (Verdugo-Ihl et al., 2020a). Significant Sc concentrations have been measured in magnetite from Acropolis (albeit typically ≲50 ppm), and even imaged as a discrete phase at the nanoscale (Verdugo-Ihl et al., in press), Sc concentrations (up to 680 ppm) are higher in zoned titanohematite containing up to ~34,200 ppm Ti (Verdugo-Ihl et al., unpublished data). Although limited substitution of Sc^{3+} for Fe^{3+} does occur, Sc^{3+} has somewhat different coordination chemistry and behaviour to other transition metals; Sc may actually occur as discrete NPs. Thus, further dedicated studies would be required to clarify issues relating to the incorporation of these elements in hematite at the nanoscale to determine the role of solid solutions *versus* the presence of discrete phases. This work will assist with understanding the petrogenetic significance of these elements but knowledge of how these elements are hosted will also contribute to deportment models in future studies aimed at determining the mineralogical balance for W, Mo, Sn, Sc, Nb and other critical metals (including rare earth elements) in ores and tailings at Olympic Dam.

Despite indirect indications, there are also some outstanding uncertainties about the oxidation states of certain elements in hematite that would require testing, notably the assumption that W, Mo and U are always hexavalent in hematite. Synchrotron micro X-ray absorption near edge structure (μ-XANES) spectroscopy and X-ray absorption fine structure (μ-EXAFS) analysis should be able provide empirical support, if not fully resolve these questions. Results will provide additional evidence to support substitution mechanisms and guide work aimed at first principles modelling of the crystal structural modifications leading to minor element incorporation.

Validation would require atomistic simulations of the coordination environments of such elements (e.g., U retaining octahedral coordination in hematite; Kerisit et al., 2011) coupled with nanoscale verification of the inferred crystal structural modifications, which can show phase modifications to accommodate such compositional changes (e.g., local formation of magnetite needles in U-high hematite; Ciobanu et al., 2018).

Work primarily targeted towards understanding the deportment and sinks for radionuclides in Olympic Dam ores, has shown, using a combination of nanoscale secondary ion mass spectrometry (nanoSIMS) and electron backscatter diffraction (EBSD) mapping, the importance of mineral grain boundaries as traps in which trace elements released from their primary hosts can be effectively concentrated (e.g., Pb in chalcopyrite; Rollog et al., 2019, 2020). A nanoSIMS approach, at spatial resolutions far superior than those of LA-ICP-MS, even if data are not quantifiable, could complement the study of twin-boundaries in hematite, or other minerals. This could provide identification of pathways for fluid percolation during overprinting and help provide improved targets for TEM-foil extraction and subsequent dedicated nanoscale analysis.

Stable isotope data (Fe, O) are an important source of additional information to clarify formation conditions of magnetite, hematite and their interconversion products. The fine grain size and intimate intergrowths between the two are common to some IOCG systems and would

likely compromise attempts to generate meaningful data. Secondary ion mass spectrometry (SIMS) and femtosecond LA multi-collector ICP-MS for *in situ* measurements of O and Fe isotopes, respectively, could be potentially applied to determine intra-grain Fe-oxide isotopic variation, as shown for BIFs (Li et al., 2013), or used to infer igneous *versus* hydrothermal magnetite crystallisation (e.g., Knipping et al., 2019). The same approach should be applicable to the study of replacement reactions in hematite and magnetite (e.g., replacement of W-bearing by W-depleted hematite; igneous titanomagnetite by silician magnetite, or primary trellis-type by orbicular) to determine, in addition to the extent of compositional reworking, whether such changes are systematically caused by re-equilibration with higher/lower temperature fluids. Tracking these changes could highlight different hydrothermal stages or fluid pulses at Olympic Dam, or its satellite deposits/prospects. However, this would only be possible if allowed by the analytical precision and spatial resolution to identify such changes.

Direct comparison with Fe-oxides from analogous IOCG systems across the Olympic Cu-Au Province has been hindered by a relative lack of comparative data from many of those systems. As such, further work aimed at addressing their Fe-oxide mineralogy could be a valuable resource, since (i) the titanomagnetite occurrence at Acropolis is unlikely to be unique within this province, and (ii) it could serve to prove the importance of the water-rock ratio in controlling magnetite mineralisation, i.e., open-fracture system → Acropolis-type titanomagnetite, or rock-buffered → silician magnetite at Olympic Dam.

Some World-class IOCG deposits *sensu lato*, such as Kirunavaara, could also benefit from being revisited considering new contributions and analytical developments, particularly with respect to nanoscale mineralogy, which is currently lacking in the contemporary literature. Dedicated mineralogical studies to characterise hematite from hematite-dominant IOCGs could further help to test the hypothesis outlined in this thesis concerning the presence of granitophile-bearing hematite in other systems as a feature characteristic feature. Important case-study candidates include the newly-discovered Oak Dam West, which resembles Olympic Dam in

many ways, and other (younger) analogues world-wide in prime IOCG-provinces, such as those in Chile (see below; Verdugo-Ihl et al., in prep.).

9.2.2 Nanomineralogy of Acropolis titanohematite

Although titanomagnetite is the most important host for Ti by mass in the Acropolis prospect, a subordinate variety of fine-grained, lamellar hematite is also of interest. This *titanohematite* occurs in small pockets surrounded by, or as thin veinlets crosscutting pre-existing titanomagnetite. In some cases, it can be more enriched in Ti than the titanomagnetite, reaching up to ~15.4 wt.% TiO_2 (EPMA data; Verdugo-Ihl et al., in prep.). The *titanohematite* displays grain-scale compositional zoning characterised by Ti-rich cores, enclosed by oscillatory zones of varying abundance and thickness, as well as the presence of rutile-hematite symplectites (Fig. 9.1a). The latter can be interpreted in the broader context of fluid-mineral interaction due to the development of local porosity. STEM EDX mapping (Fig. 9.1b) shows a sharp interface between the Ti-poor ($Fe^{2+}_{0.03}Mn_{0.01}Fe^{3+}_{1.91}Al_{0.01}Ti_{0.03}Si_{0.01}O_3$; ~3.4 $mol\%_{Ilm}$) and the Ti-rich domain ($Fe^{2+}_{0.20}Mn_{0.01}Fe^{3+}_{1.57}Ti_{0.21}O_3$; ~20.7 $mol\%_{Ilm}$; integrated area analysis).

The Ti-rich domains, displaying discrete Ti-enrichment as rutile, are surrounded by Ti-poor hematite haloes, indicative of local Ti redistribution and particle coarsening (Fig. 9.1c). Considering the hematite-ilmenite solid solution solvus (Lindsley, 1973), formation temperature of this hematite, with locally greater than ~20.7 $mol\%_{Ilm}$, could have been well in excess of 500 °C. Locally however, discrete domains of ilmenite can be depicted at the nanoscale (Fig. 9.1c), raising questions concerning their origin and mechanisms of formation. Overall, a wide range of crystal structural modifications and defects are observed in this hematite. Although not illustrated here, they – and the implications they carry – are the focus of ongoing work.

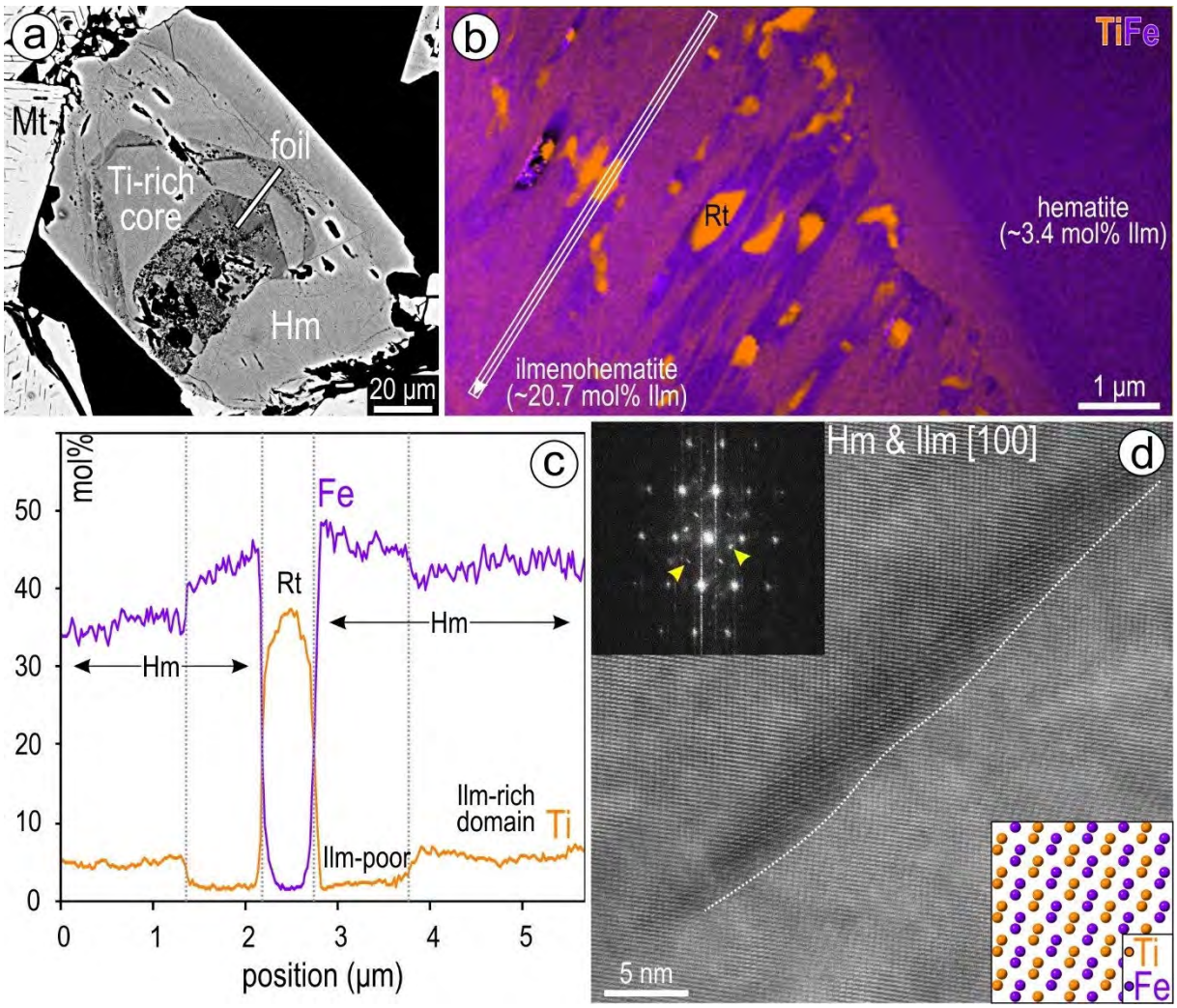

Fig. 9.1. (a) BSE image of a zoned, Ti-rich hematite. (b) STEM-EDX map across the boundary between Ti-rich and Ti-poor domains showing Ti-redistribution within the ilmenohematite core; note the presence of rutile surrounded by Ti-poor hematite. (c) Compositional profile across overprinted domain showing the distribution of Fe and Ti. (d) HAADF STEM image of ilmenite lamellae within hematite, note the presence of satellite reflections in FFT pattern (inset, top-left). Ilmenite crystal model on [100] for comparison (bottom-right). Abbreviations: Hm–hematite; Ilm–ilmenite; Mt–magnetite; Rt–rutile.

9.2.3 Granitophile element bearing hematite in IOCG systems along the Chilean Iron Belt: Geochronological implications

The Coastal Cordillera of northern Chile hosts several magnetite- to hematite-dominant, Cu(±Au)-poor to -rich systems, including the Mantoverde and Carmen de Cobre IOCG and the magnetite(±apatite) Carmen de Fierro deposits, spatially-associated with the Atacama Fault System (AFS). The genetic relationships between some of these spatially related, magnetite- to hematite-dominant systems are, however, inadequately temporally constrained in prior studies. In these systems, hematite mineralisation typically occurs paragenetically later, either replacing

earlier magnetite or as late veins (e.g., Tornos et al., 2010), yet no direct dating of hematite has been attempted until now.

Preliminary work on specular hematite from the Mantoverde and Carmen de Cobre IOCG deposits shows that they share similar trace element compositions, characterised by W and Sn enrichment (up to 813 and 185 ppm, respectively), readily depictable by LA-ICP-MS mapping (Fig. 9.1a), and with consistently measurable, albeit low, U contents (up to ~5 ppm). Despite these low concentrations, the presence of U and radiogenic Pb enabled U-Pb dating of such hematite by LA-ICP-MS, yielding lower intercept ages of 108 ± 20 and 108.6 ± 6.3 Ma for Mantoverde and Carmen de Cobre (Fig. 9.1b), respectively. Age uncertainties of Mantoverde hematite partially overlap with previously reported dates for hydrothermal alteration and mineralisation in that area (Fig. 9.1c), although the similar date obtained at Carmen de Cobre, but with higher precision, suggests that hematite-rich portions of these systems may actually be significantly younger and post-date the magnetite (±apatite) mineralisation by a few My. The younger hematite dates are supported by field relationships, which show deep intersections at Carmen de Cobre that crosscut paragenetically earlier magnetite(±apatite) mineralisation along the same fault structure that intersects magnetite(±apatite) mineralisation in the adjacent deposit at Carmen de Fierro, ~5 km north from the location of the hematite dated here.

These new ages favour paragenetically younger, hematite-mineralisation events relative to the prevalent magnetite(±apatite) mineralisation that is temporally constrained by zircon U-Pb geochronology of magmatic hosts or associated lithologies (Fig. 9.1c). In these cases, the magnetite(±apatite) mineralisation is always directly linked, both spatially and temporally, to Early Cretaceous magmatic activity and coeval magmatism along the AFS. The age difference between magnetite mineralisation and the dated hematite, relating to Cu±Au-bearing mineralisation, can strongly support super-imposed events in these districts (e.g., circulation of basinal brines with external sulfur that dissolved and reprecipitated previous Fe-oxide

mineralisation (?), or perhaps concealed, younger intrusions during the waning stages of the Early Cretaceous magmatism).

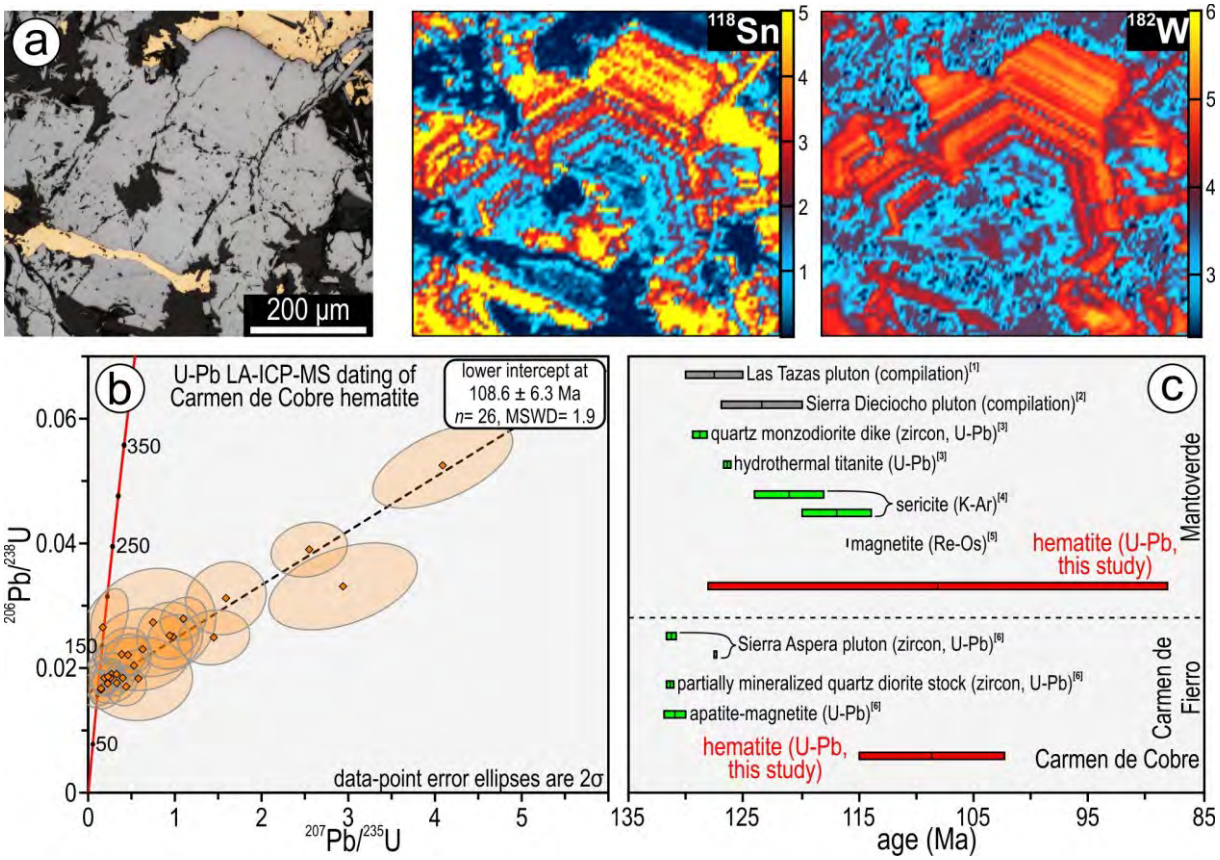

Fig. 9.2. (a) Reflected light optical image and LA-ICP-MS trace element maps (intensity in cps, 10^n) of hematite from Mantoverde. (b) Wetherill concordia diagram for Carmen de Cobre hematite. (c) New hematite age data and published age constraints on mineralisation at Mantoverde and Carmen. Data sourced from: [1] Benavides et al. (2007); [2] Rieger et al. (2010); [3] Gelcich et al. (2003); [4] Vila et al. (1998); [5], Mathur et al. (2002); and [6] Gelcich et al. (2005).

This preliminary work represents the first U-Pb dating of hematite from Chilean IOCG systems. The presence of U-bearing hematite in Chilean IOCGs enables direct dating of Fe-oxide mineralisation along and adjacent to the AFS, thus providing improved correlations between magmatism, mineralisation, fault-reactivation and/or alteration. Hematite U-Pb dating therefore offers additional, and hitherto overlooked, temporal constraints on regional-scale IOCG metallogeny that can complement mineral chemistry and isotopic data, and help revaluate the timing of mineralising events. The finding of a W-Sn-U geochemical signature in hematite from Chilean IOCGs stands as a *proof-of-concept* for the prediction of hematite with similar enrichment patterns in IOCGs elsewhere (Verdugo-Ihl et al., 2017; Courtney-Davies et

al., 2019a). Coupled with published work on IOCG systems from the Gawler Craton in South Australia, these findings suggest that such trace element signatures in hematite are indicative of IOCG systems globally, opening opportunities for direct dating of analogous systems elsewhere.

9.3 Concluding remarks

New insights into the formation and overprinting conditions of hematite and magnetite from three IOCG deposits/prospects within the Olympic Dam district, and the El Laco Fe-deposit (Chile) are provided, despite these deposits having been known for ca. 45 and 60 years, respectively. Findings presented in this thesis complement ongoing research focused on the minor/trace element analysis of Fe-oxides applied to ore-forming processes and deposit genesis. The research also provides a framework for the characterisation of Fe-oxides in the context of ore deposit research over several orders of magnitude, bridging observations from the deposit-down to the nanoscale. The approach described in this work is transferable; not only applicable to Fe-oxides and IOCG system in South Australia, but to other mineral groups and deposits elsewhere.

Above all, this research highlights the critical importance of using complementary techniques in any study of Fe-oxides in deposits where they are abundant, to allow novel re-interpretation of ore-forming mechanisms or provide additional evidence in support of existing models. Iron-oxides from IOCG systems within the Olympic Dam district and elsewhere react sensitively to their formation environments. Such conditions are captured by a wide range of textures and compositions that reflect different environments and can record subsequent overprinting. Iron-oxides are remarkably robust and the products of overprinting by mineral-fluid interaction are particularly well-preserved in hematite. This includes evidence for minor/trace element (re)mobilisation along twins and splays, trapping of fluid as fluid inclusions and nucleation of metal-bearing NPs. These processes are important because they

affect isotopic systematics and, implicitly, the accuracy of mineral geochronometers and can widely redistribute minor/trace elements.

Despite the fact that the speciation and relative proportions of Fe-oxides varies within and between systems, some features are common to the wider spectrum of deposits, including at least some stages at which granitophile elements are incorporated, thus facilitating U-Pb hematite dating of both older and younger systems. Magnetite-dominant deposits show a particularly broad range of magnetite textures and compositions. Such diversity highlights variation in fluid-rock ratios during hydrothermal deposition, i.e., the ability to source components from the fluid-rock interaction to support magnetite growth, in addition to varied fluid or melt sources, thus controlling magnetite nanomineralogy. Nanoscale studies of magnetite reveal an eclectic range of inclusion populations that serve as valuable proxies for identifying formation conditions.

9.4 References

Barton, M.D., 2014. Iron Oxide(–Cu–Au–REE–P–Ag–U–Co) Systems. In: Treatise on Geochemistry, Vol. 13, Elsevier, pp. 515–541. https://doi.org/10.1016/B978-0-08-095975-7.01123-2

Benavides, J., Kyser, T.K., Clark, A.H., Oates, C.J., Zamora, R., Tarnovschi, R., Castillo, B., 2007. The Mantoverde Iron Oxide-Copper-Gold District, III Region, Chile: The Role of Regionally Derived, Nonmagmatic Fluids in Chalcopyrite Mineralization. Economic Geology 102, 415–440. https://doi.org/10.2113/gsecongeo.102.3.415

Brugger, J., Liu, W., Etschmann, B., Mei, Y., Sherman, D.M., Testemale, D., 2016. A review of the coordination chemistry of hydrothermal systems, or do coordination changes make ore deposits? Chemical Geology 447, 219–253. https://doi.org/10.1016/j.chemgeo.2016.10.021

Canil, D., Lacourse, T., 2020. Geothermometry using minor and trace elements in igneous and hydrothermal magnetite. Chemical Geology, 119576. https://doi.org/10.1016/j.chemgeo.2020.119576

Chen, Z., Cvelbar, U., Mozetič, M., He, J., Sunkara, M.K., 2008. Long-range ordering of oxygen-vacancy planes in α-Fe_2O_3 nanowires and nanobelts. Chemistry of Materials 20, 3224–3228. https://doi.org/10.1021/cm800288y

Cherry, A.R., Ehrig, K., Kamenetsky, V.S., McPhie, J., Crowley, J.L., Kamenetsky, M.B., 2018. Precise geochronological constraints on the origin, setting and incorporation of ca. 1.59 Ga surficial facies into the Olympic Dam Breccia Complex, South Australia. Precambrian Research 315, 162–178. https://doi.org/10.1016/j.precamres.2018.07.012

Ciobanu, C.L., Slattery, A., Verdugo-Ihl, M., Courtney-Davies, L., Cook, N.J., Ehrig, K., 2018. Crystal structural modifications in U-rich, oscillatory-zoned hematite. Goldschmidt 2018 Abstract.

Ciobanu, C.L., Verdugo-Ihl, M.R., Slattery, A., Cook, N.J., Ehrig, K., Courtney-Davies, L., Wade, B.P., 2019. Silician Magnetite: Si–Fe-Nanoprecipitates and Other Mineral Inclusions in Magnetite from the Olympic Dam Deposit, South Australia. Minerals 9, 311. https://doi.org/10.3390/min9050311

Courtney-Davies, L., Ciobanu, C.L., Verdugo-Ihl, M.R., Cook, N.J., Ehrig, K.J., Wade, B.P., Zhu, Z., Kamenetsky, V.S., 2020. ~1760 Ma magnetite-bearing protoliths in the Olympic Dam deposit, South Australia: Implications for ore genesis and regional metallogeny. Ore Geology Reviews 118, 103337. https://doi.org/10.1016/j.oregeorev.2020.103337

Courtney-Davies, L., Ciobanu, C.L., Verdugo-Ihl, M.R., Dmitrijeva, M., Cook, N.J., Ehrig, K., Wade, B.P., 2019a. Hematite geochemistry and geochronology resolve genetic and temporal links among iron-oxide copper gold systems, Olympic Dam district, South Australia. Precambrian Research 335, 105480. https://doi.org/10.1016/j.precamres.2019.105480

Courtney-Davies, L., Tapster, S.R., Ciobanu, C.L., Cook, N.J., Verdugo-Ihl, M.R., Ehrig, K.J., Kennedy, A.K., Gilbert, S.E., Condon, D.J., Wade, B.P., 2019b. A multi-technique evaluation of hydrothermal hematite U–Pb isotope systematics: Implications for ore deposit geochronology. Chemical Geology 513, 54–72. https://doi.org/10.1016/j.chemgeo.2019.03.005

Deditius, A.P., Reich, M., Simon, A.C., Suvorova, A., Knipping, J., Roberts, M.P., Rubanov, S., Dodd, A., Saunders, M., 2018. Nanogeochemistry of hydrothermal magnetite. Contributions to Mineralogy and Petrology 173, 46. https://doi.org/10.1007/s00410-018-1474-1

Dmitrijeva, M., Ciobanu, C.L., Ehrig, K.J., Cook, N.J., Metcalfe, A. V., Verdugo-Ihl, M.R., McPhie, J., 2019a. Mineralization-alteration footprints in the Olympic Dam IOCG district, South Australia: The Acropolis prospect. Journal of Geochemical Exploration 205, 106333. https://doi.org/10.1016/j.gexplo.2019.106333

Dmitrijeva, M., Ehrig, K.J., Ciobanu, C.L., Cook, N.J., Verdugo-Ihl, M.R., Metcalfe, A. V., 2019b. Defining IOCG signatures through compositional data analysis: A case study of lithogeochemical zoning from the Olympic Dam deposit, South Australia. Ore Geology Reviews 105, 86–101. https://doi.org/10.1016/j.oregeorev.2018.12.013

Gelcich, S., Davis, D.W., Spooner, E.T.C., 2005. Testing the apatite-magnetite geochronometer: U-Pb and $^{40}Ar/^{39}Ar$ geochronology of plutonic rocks, massive magnetite-apatite tabular bodies, and IOCG mineralization in Northern Chile. Geochimica et Cosmochimica Acta 69, 3367–3384. https://doi.org/10.1016/j.gca.2004.12.020

Gelcich, S.H., Davis, D.W., Spooner, E.T.C., 2003. New U-Pb ages for host rocks, mineralization and alteration of iron oxide (Cu-Au) deposits in the Coastal cordillera of Northern Chile, in: IV South American Symposium on Isotope Geology, August 24th-27th. Salvador, Brazil, pp. 63–66.

Hu, H., Li, J., Harlov, D.E., Lentz, D.R., McFarlane, C.R.M., Yang, Y.-H., 2019. A genetic link between iron oxide-apatite and iron skarn mineralization in the Jinniu volcanic basin, Daye district, eastern China: Evidence from magnetite geochemistry and multi-mineral U-Pb geochronology. Geological Society of America Bulletin 132(5-6), 899–917. https://doi.org/10.1130/B35180.1

Johnson, J.P., McCulloch, M.T., 1995. Sources of mineralising fluids for the Olympic Dam deposit (South Australia): Sm-Nd isotopic constraints. Chemical Geology 121, 177–199. https://doi.org/10.1016/0009-2541(94)00125-R

Kerisit, S., Felmy, A.R., Ilton, E.S., 2011. Atomistic Simulations of Uranium Incorporation into Iron (Hydr)Oxides. Environ Science and Technology 45(7), 2770–2776. https://doi.org/10.1021/es1037639

Knipping, J.L., Bilenker, L.D., Simon, A.C., Reich, M., Barra, F., Deditius, A.P., Lundstrom, C., Bindeman, I., Munizaga, R., 2015. Giant Kiruna-type deposits form by efficient flotation of magmatic magnetite suspensions. Geology 43, 591–594. https://doi.org/10.1130/G36650.1

Knipping, J.L., Fiege, A., Simon, A.C., Oeser, M., Reich, M., Bilenker, L.D., 2019. In-situ iron isotope analyses reveal igneous and magmatic-hydrothermal growth of magnetite at the Los Colorados Kiruna-type iron oxide-apatite deposit, Chile. American Mineralogist 104, 471–484. https://doi.org/10.2138/am-2019-6623

Kontonikas-Charos, A., Ciobanu, C.L., Cook, N.J., Ehrig, K., Krneta, S., Kamenetsky, V.S., 2017. Feldspar evolution in the Roxby Downs Granite, host to Fe-oxide Cu-Au-(U) mineralisation at Olympic Dam, South Australia. Ore Geology Reviews 80, 838–859. https://doi.org/10.1016/j.oregeorev.2016.08.019

Krneta, S., Cook, N.J., Ciobanu, C.L., Ehrig, K., Kontonikas-Charos, A., 2017. The Wirrda Well and Acropolis prospects, Gawler Craton, South Australia: Insights into evolving fluid conditions through apatite chemistry. Journal of Geochemical Exploration 181, 276–291. https://doi.org/10.1016/j.gexplo.2017.08.004

Li, W., Huberty, J.M., Beard, B.L., Kita, N.T., Valley, J.W., Johnson, C.M., 2013. Contrasting behavior of oxygen and iron isotopes in banded iron formations revealed by in situ isotopic analysis. Earth and Planetary Science Letters 384, 132–143. https://doi.org/10.1016/j.epsl.2013.10.014

Lindsley, D.H., 1973. Delimitation of the Hematite-Ilmenite Miscibility Gap. Geological Society of America Bulletin 84, 657. https://doi.org/10.1130/0016-7606(1973)84<657:DOTHMG>2.0.CO;2

Mathur, R., Marschik, R., Ruiz, J., Munizaga, F., Leveille, R.A., Martin, W., 2002. Age of Mineralization of the Candelaria Fe Oxide Cu-Au Deposit and the Origin of the Chilean Iron Belt, Based on Re-Os Isotopes. Economic Geology 97, 59–71. https://doi.org/10.2113/gsecongeo.97.1.59

McBriarty, M.E., Kerisit, S., Bylaska, E.J., Shaw, S., Morris, K., Ilton, E.S., 2018. Iron vacancies accommodate uranyl incorporation into hematite. Environmental Science and Technology 52, 6282–6290. https://doi.org/10.1021/acs.est.8b00297

McPhie, J., Ehrig, K.J., Kamenetsky, M.B., Crowley, J.L., Kamenetsky, V.S., 2020. Geology of the Acropolis prospect, South Australia, constrained by high-precision CA-TIMS ages. Australian Journal of Earth Sciences 67(5), 699–716. https://doi.org/10.1080/08120099.2020.1717617

Ovalle, J.T., La Cruz, N.L., Reich, M., Barra, F., Simon, A.C., Konecke, B.A., Rodriguez-Mustafa, M.A., Deditius, A.P., Childress, T.M., Morata, D., 2018. Formation of massive iron deposits linked to explosive volcanic eruptions. Scientific Reports 8, 14855. https://doi.org/10.1038/s41598-018-33206-3

Rieger, A.A., Marschik, R., Diaz, M., Holzl, S., Chiaradia, M., Akker, B., Spangenberg, J.E., 2010. The Hypogene Iron Oxide Copper-Gold Mineralization in the Mantoverde District, Northern Chile. Economic Geology 105, 1271–1299. https://doi.org/10.2113/econgeo.105.7.1271

Rollog, M., Cook, N.J., Guagliardo, P., Ehrig, K., Ciobanu, C.L., Kilburn, M., 2019. Detection of Trace Elements/Isotopes in Olympic Dam Copper Concentrates by nanoSIMS. Minerals 9, 336. https://doi.org/10.3390/min9060336

Rollog, M., Cook, N.J., Guagliardo, P., Ehrig, K., Kilburn, M., 2020. Radionuclide distributions in Olympic Dam copper concentrates: The significance of minor hosts, incorporation mechanisms, and the role of mineral surfaces. Minerals Engineering 148, 106176. https://doi.org/10.1016/j.mineng.2019.106176

Sillitoe, R.H., Magaranov, G., Mladenov, V., Creaser, R.A., 2020. Rosen, Bulgaria: A newly recognized iron oxide-copper-gold district. Economic Geology 104, 897–904. https://doi.org/10.5382/econgeo.4731

Šrot, V., Rečnik, A., Scheu, C., Šturm, S., Mirtič, B., 2003. Stacking faults and twin boundaries in sphalerite crystals from the Trepča mines in Kosovo. American Mineralogist 88, 1809–1816. https://doi.org/10.2138/am-2003-11-1222

Tooth, B., Ciobanu, C.L., Green, L., O'Neill, B., Brugger, J., 2011. Bi-melt formation and gold scavenging from hydrothermal fluids: An experimental study. Geochimica et Cosmochimica Acta 75, 5423–5443. https://doi.org/10.1016/j.gca.2011.07.020

Tornos, F., Velasco, F., Barra, F., Morata, D., 2010. The Tropezón Cu–Mo–(Au) deposit, Northern Chile: the missing link between IOCG and porphyry copper systems? Mineralium Deposita 45, 313–321. https://doi.org/10.1007/s00126-010-0277-8

Tornos, F., Velasco, F., Hanchar, J.M., 2016. Iron-rich melts, magmatic magnetite, and superheated hydrothermal systems: The El Laco deposit, Chile. Geology 44, 427–430. https://doi.org/10.1130/G37705.1

Verdugo-Ihl, M.R., Ciobanu, C.L., Cook, N.J., Ehrig, K.J., Courtney-Davies, L., Gilbert, S., 2017. Textures and U-W-Sn-Mo signatures in hematite from the Olympic Dam Cu-U-Au-Ag deposit, South Australia: Defining the archetype for IOCG deposits. Ore Geology Reviews 91, 173–195. https://doi.org/10.1016/j.oregeorev.2017.10.007

Verdugo-Ihl, M.R., Ciobanu, C.L., Slattery, A., Cook, N.J., Ehrig, K., Courtney-Davies, L., 2019. Copper-Arsenic Nanoparticles in Hematite: Fingerprinting Fluid-Mineral Interaction. Minerals 9, 388. https://doi.org/10.3390/min9070388

Verdugo-Ihl, M.R., Ciobanu, C.L., Cook, N.J., Ehrig, K.J., Courtney-Davies, L., 2020a. Defining early stages of IOCG systems: evidence from iron oxides in the outer shell of the Olympic Dam deposit, South Australia. Mineralium Deposita 55, 429–452. https://doi.org/10.1007/s00126-019-00896-2

Verdugo-Ihl, M.R., Ciobanu, C.L., Cook, N.J., Ehrig, K., Slattery, A., Courtney-Davies, L., 2020b. Trace element remobilisation from W-Sn-U-Pb zoned hematite: Nanoscale insights into open system behaviour of a mineral geochronometer. Mineralogical Magazine 84(4), 502–516. https://doi.org/10.1180/mgm.2020.49

Verdugo-Ihl, M.R., Ciobanu, C.L., Cook, N.J., Ehrig, K., Slattery, A., Courtney-Davies, L., Dmitrijeva, M. Nanomineralogy of hydrothermal magnetite from Acropolis, South Australia: genetic implications for iron-oxide copper gold mineralisation. American Mineralogist, in press. https://doi.org/10.2138/am-2020-7557

Verdugo-Ihl, M.R., Ciobanu, C.L., Cook, N.J., Ehrig, K., Slattery, A., Courtney-Davies, L., in review, a. Ferro-tschermakite with short range disorder identified in silician magnetite. American Mineralogist.

Verdugo-Ihl, M.R., Ciobanu, C.L., Cook, N.J., Tornos, F., Ehrig, K., Slattery, A., Xu, J., Courtney-Davies, L., Hanchar, J.M., in review, b. Vapour transport of magnetite in volcanoes: evidence from igneous pyroxene pair inclusions and S-bearing sublimate coatings. Earth and Planetary Science Letters.

Vila, T., Lindsay, N., Zamora, R., 1998. Geology of the Manto Verde copper deposit, Northern Chile: A specularite-rich, hydrothermal-tectonic breccia related to the Atacama Fault Zone, in: Camus, F., Sillitoe, R.H., Petersen, R. (Eds.), Andean Copper Deposits: New Discoveries, Mineralization, Styles and Metallogeny. Special Publication 5, Society of Economic Geologists, pp. 157–169. https://doi.org/10.5382/SP.05.11

Wang, X.-S., Timofeev, A., Williams-Jones, A.E., Shang, L.-B., Bi, X.-W., 2019. An experimental study of the solubility and speciation of tungsten in NaCl-bearing aqueous solutions at 250, 300, and 350 °C. Geochimica et Cosmochimica Acta 265, 313–329. https://doi.org/10.1016/j.gca.2019.09.013

Weinberg, R.F., Wolfram, L.C., Nebel, O., Hasalová, P., Závada, P., Kylander-Clark, A.R.C., Becchio, R., 2020. Decoupled U-Pb date and chemical zonation of monazite in migmatites: The case for disturbance of isotopic systematics by coupled dissolution-reprecipitation. Geochimica et Cosmochimica Acta 269, 398–412. https://doi.org/10.1016/j.gca.2019.10.024

Yin, S., Wirth, R., Ma, C., Xu, J., 2019. The role of mineral nanoparticles at a fluid-magnetite interface: Implications for trace-element uptake in hydrothermal systems. American Mineralogist 104, 1180–1188. https://doi.org/10.2138/am-2019-6996

CHAPTER 10

SUPPLEMENTARY AND ADDITIONAL MATERIAL

SUPPLEMENTARY MATERIAL A

FOR CHAPTER 2 – TEXTURES AND U-W-SN-MO SIGNATURES IN HEMATITE FROM THE OLYMPIC DAM CU-U-AU-AG DEPOSIT, SOUTH AUSTRALIA: DEFINING THE ARCHETYPE FOR IOCG DEPOSITS

APPENDIX A: ADDITIONAL FIGURES AND FULL LA-ICP-MS MAPS

APPENDIX B: METHODOLOGY

APPENDIX C: LA-ICP-MS TRACE ELEMENT DATA

APPENDIX D: EPMA DATA

ELECTRONIC APPENDIX A FOR CHAPTER 2

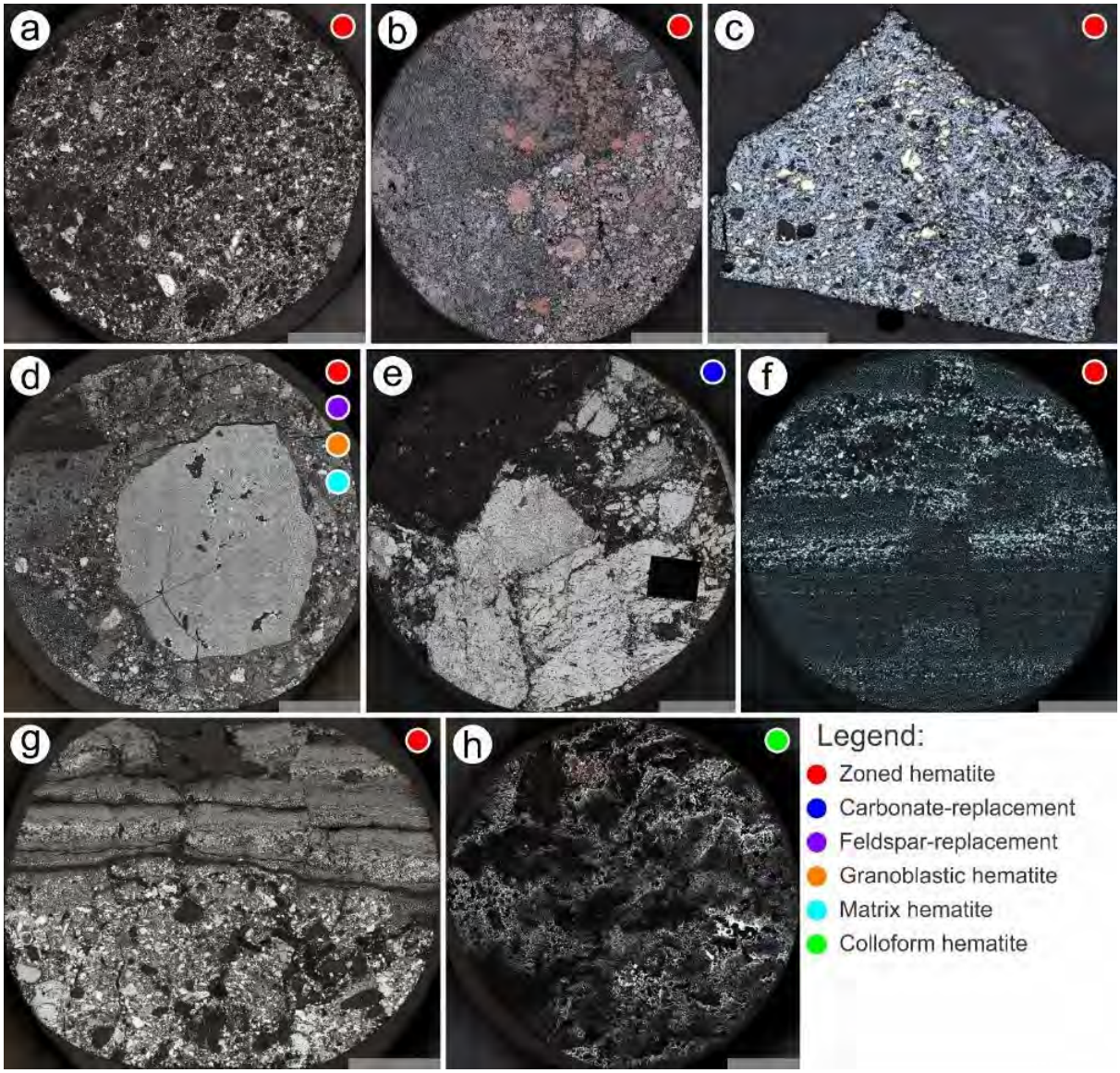

Figure A1. Optical maps in reflected light showing a selection of polished blocks representative of the main ore types. (a-c) Lithologies and granitophile-rich hematite categories (marked by circles of different colours). Grey bar on all images corresponds to 5 mm. (a) Hematite breccia from the upper, bornite-chalcocite zone (sample RX6607; drillhole RD2852A). (b) High-grade bornite ore from the NW arm (sample CLC201; drillhole RU41-9882). (c) Hematite-rich breccia from the deepest, pyrite-chalcopyrite zone (sample RX7294; drillhole RD1988). (d) Volcanoclastic, hematite-rich breccia (sample MV093; drillhole RD647). (e) Hematite replacing coarse carbonates from high-grade chalcocite ores (sample CLC053; drillhole RU34-8890). (f) Bedded, silty sandstone with hematite-rich laminae and containing disseminations of zoned hematite (sample MV027; drillhole RD2768A). (g) Contact between hematite-rich laminated facies and hematite-rich hydrothermal breccia (sample MV101; drillhole RD2765). (h) Colloform hematite in fine-grained silicate (sericite+chlorite) breccia matrix (sample MV048; drillhole RU27-7551).

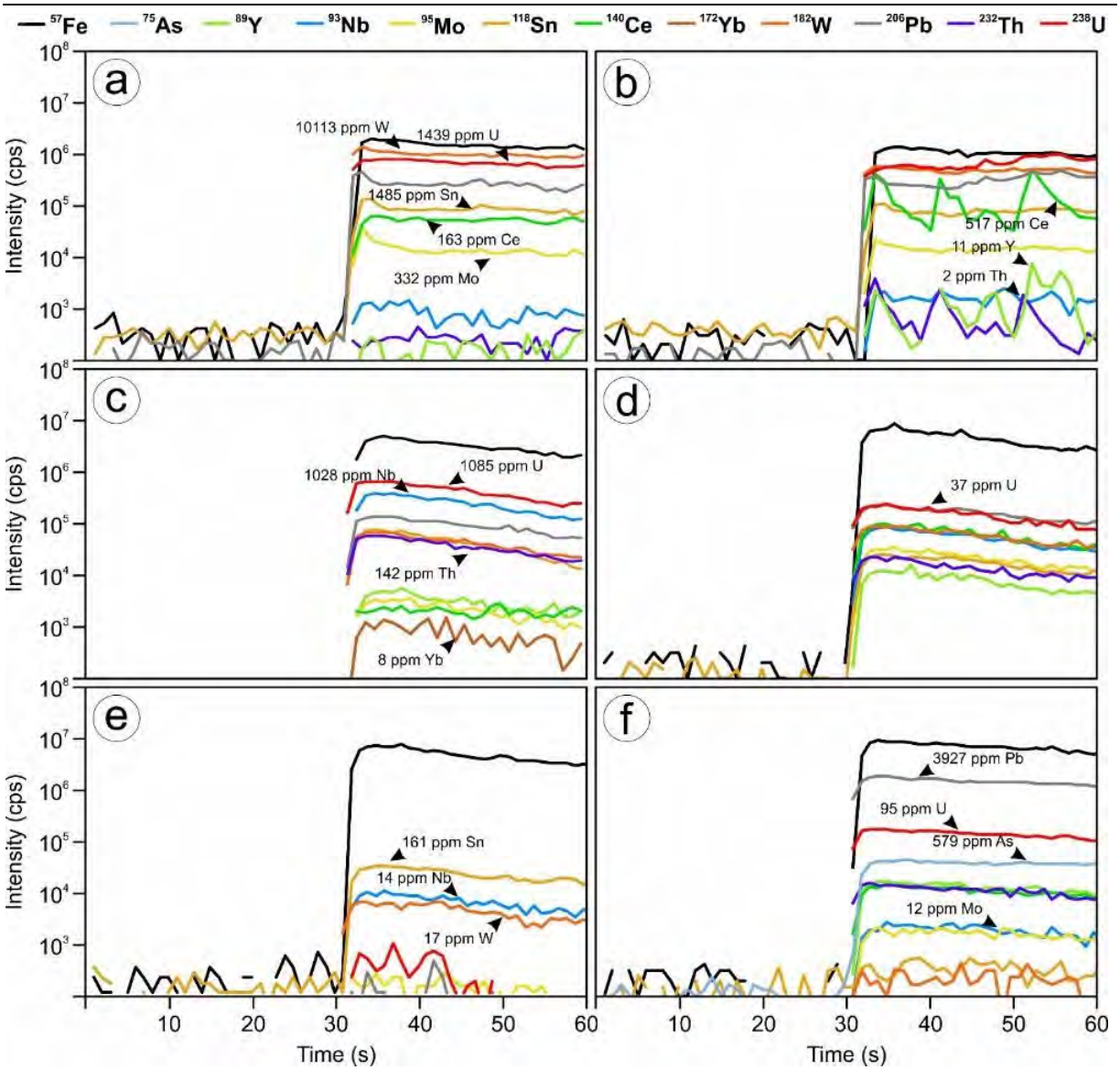

Figure A2. Representative time-resolved LA-ICP-MS down-hole profiles of different hematite textures highlighting the flat, smooth signals for elements of interest indicating homogeneous distribution of trace elements. The profiles show a background acquisition of 30 s, followed by a 30 s measurement of the hematite unknown during ablation. Measured concentrations are given for selected elements. (a) Zoned hematite. (b) REE-Th-Y-inclusions in zoned hematite. (c) Carbonate replacement hematite. (d) Matrix hematite. (e) Granoblastic hematite. (f) Colloform hematite.

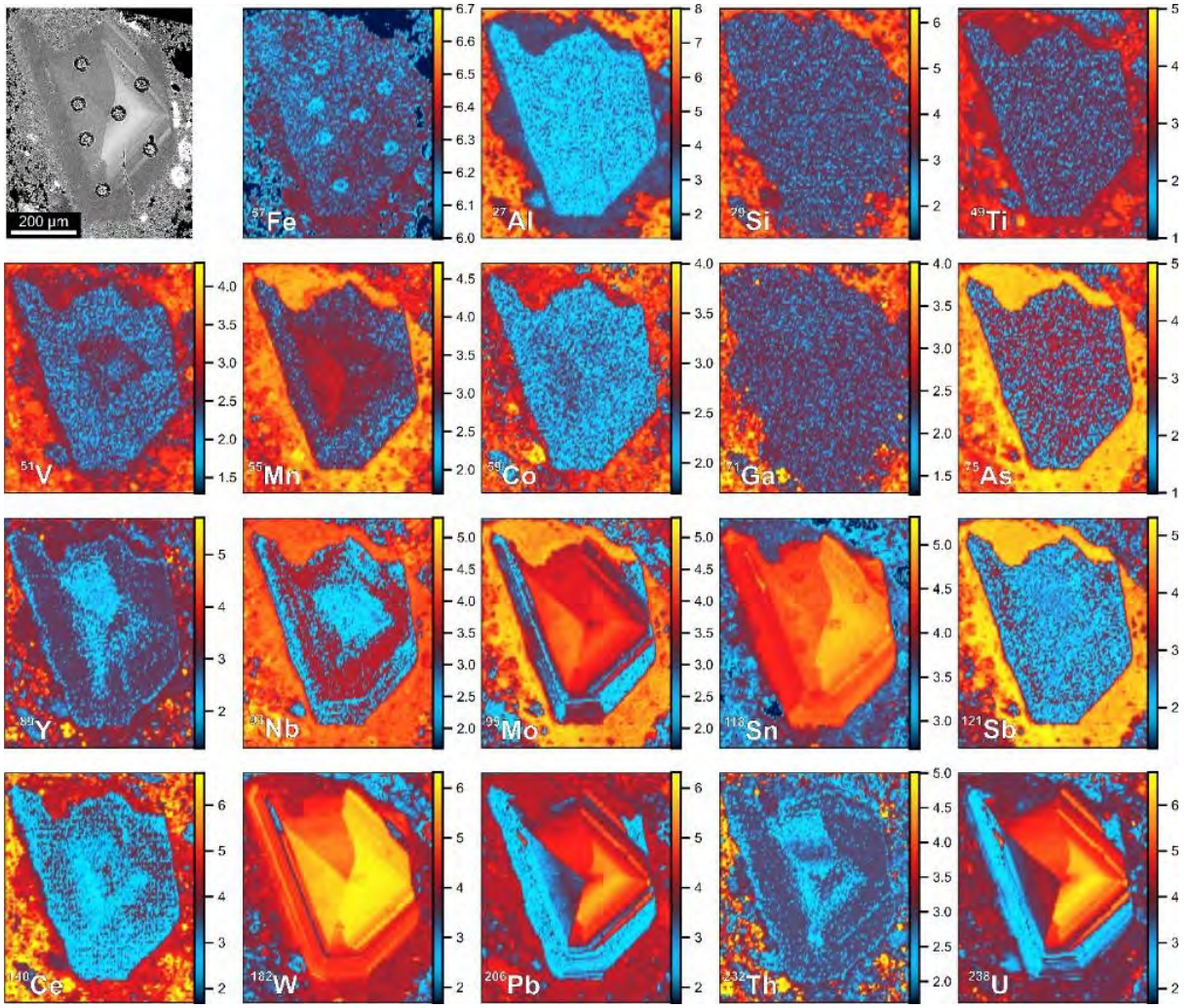

Figure A3. LA-ICP-MS element maps of zoned hematite (sample CLC046; RU49-8096) corresponding to Fig. 8 showing a reduced number of maps. The obtained intensities in counts-per-second (cps) were scaled individually using logarithmic scale (10^n) to highlight intra-grain variability and accentuate features of interest. Warmer colours represent higher intensities. Spots on the imaged grain correspond to previously acquired laser-ablation spot analysis. BSE image (upper left) shows the ablated area.

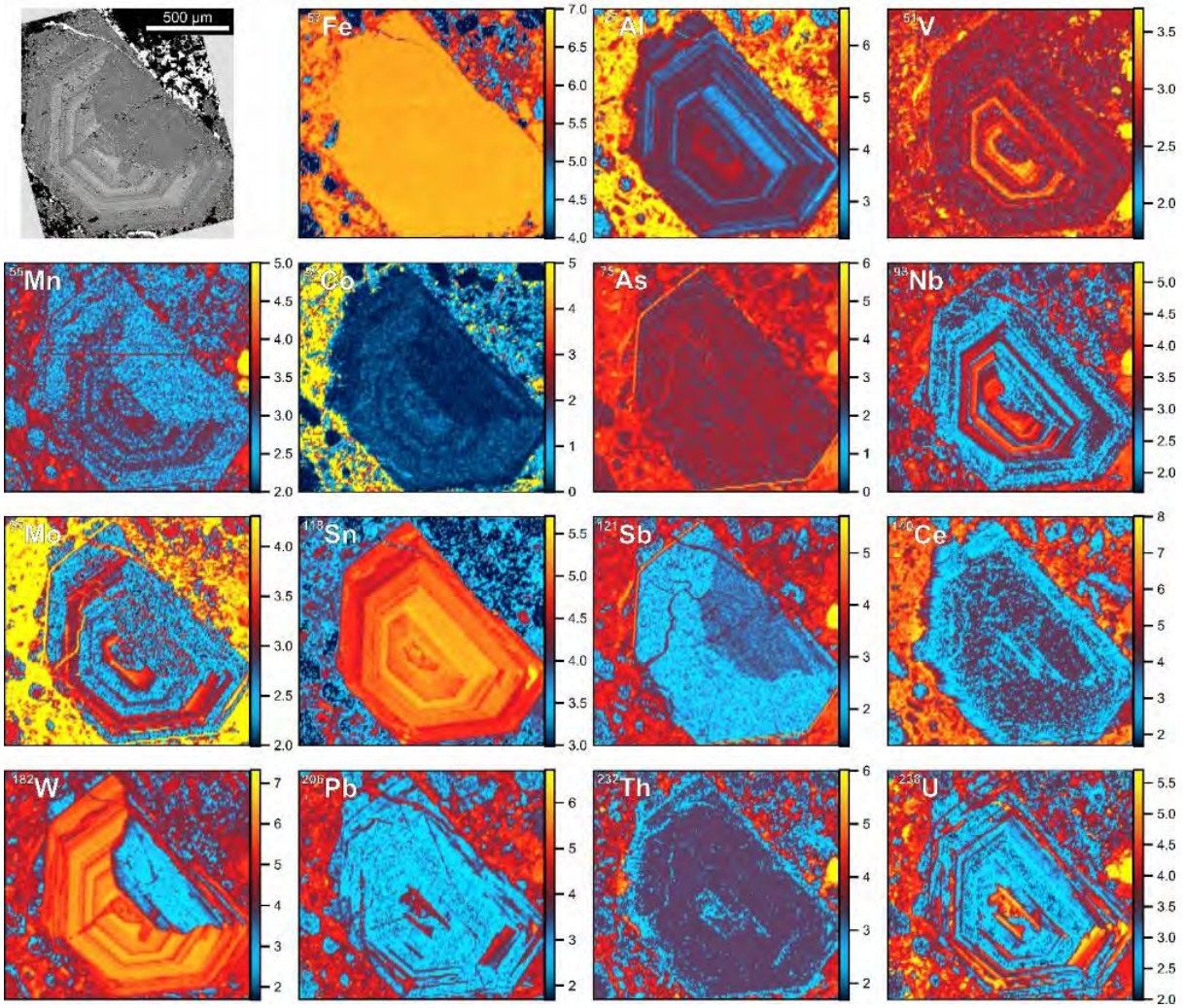

Figure A4. LA-ICP-MS element maps of zoned hematite (sample RX6607; RD2852A) corresponding to Fig. 9a showing a reduced number of maps. The obtained intensities were scaled individually using logarithmic scale (10^n).

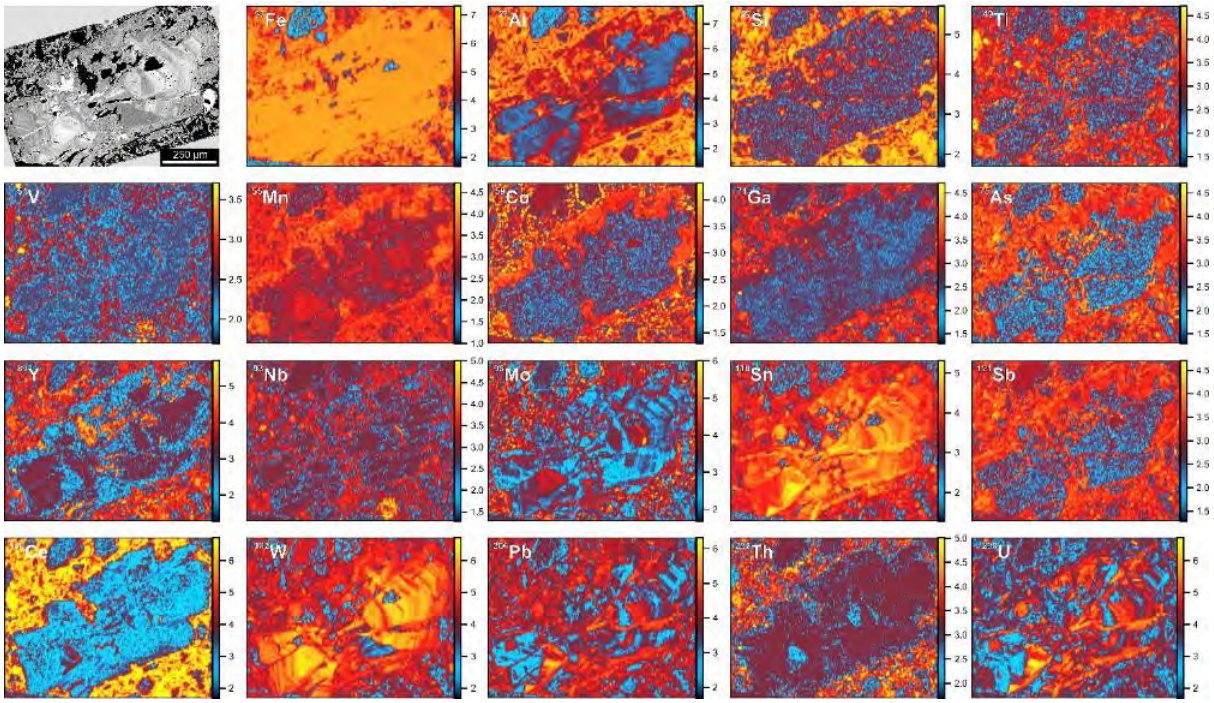

Figure A5. LA-ICP-MS element maps of zoned hematite corresponding to Fig. 9b showing a reduced number of maps (sample RX6607; drillhole RD2852A). The obtained intensities were scaled individually using logarithmic scale (10^n).

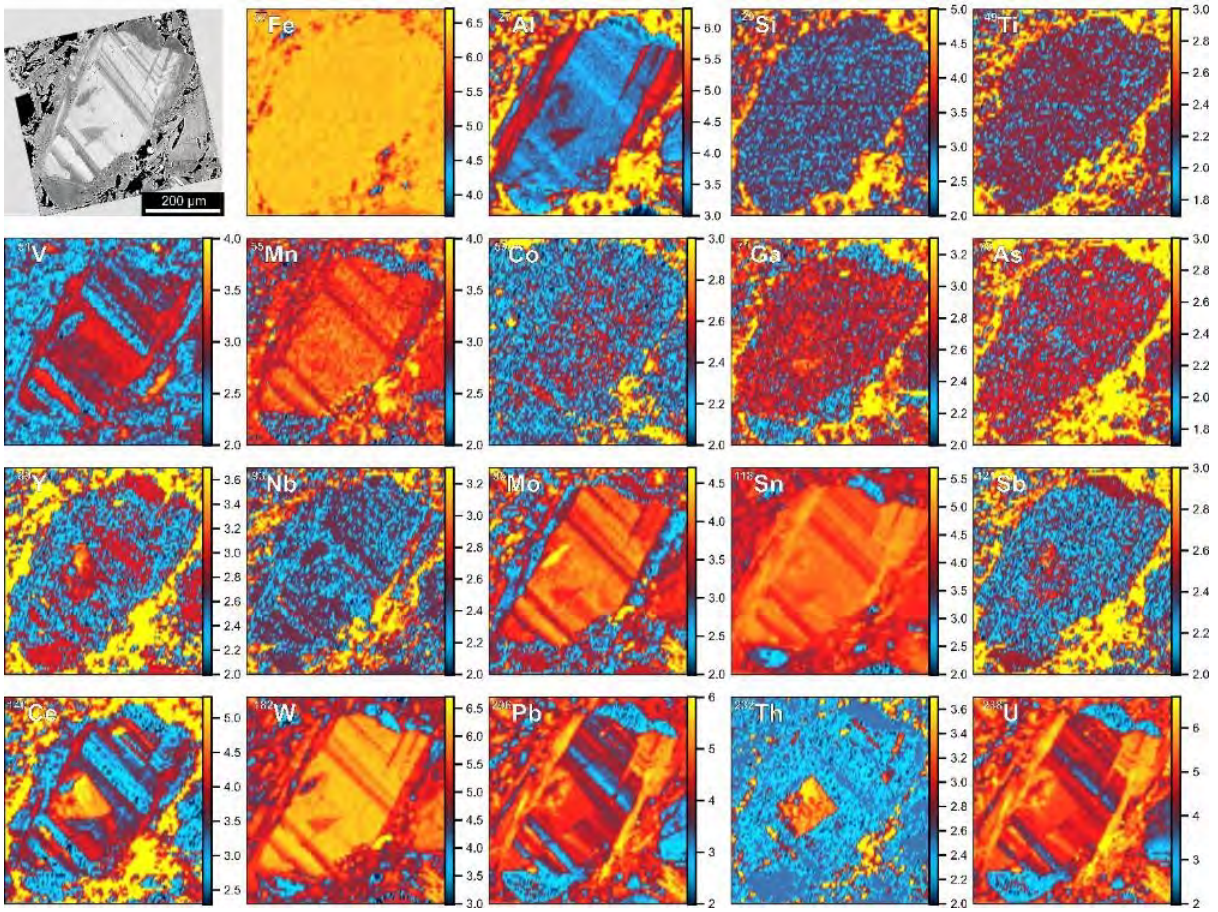

Figure A6. LA-ICP-MS element maps of zoned hematite corresponding to Fig. 10 showing a reduced number of maps (sample RX7294; drillhole RD1988). The obtained intensities were scaled individually using logarithmic scale (10^n). Upper left BSE image corresponds to the ablated area for comparison.

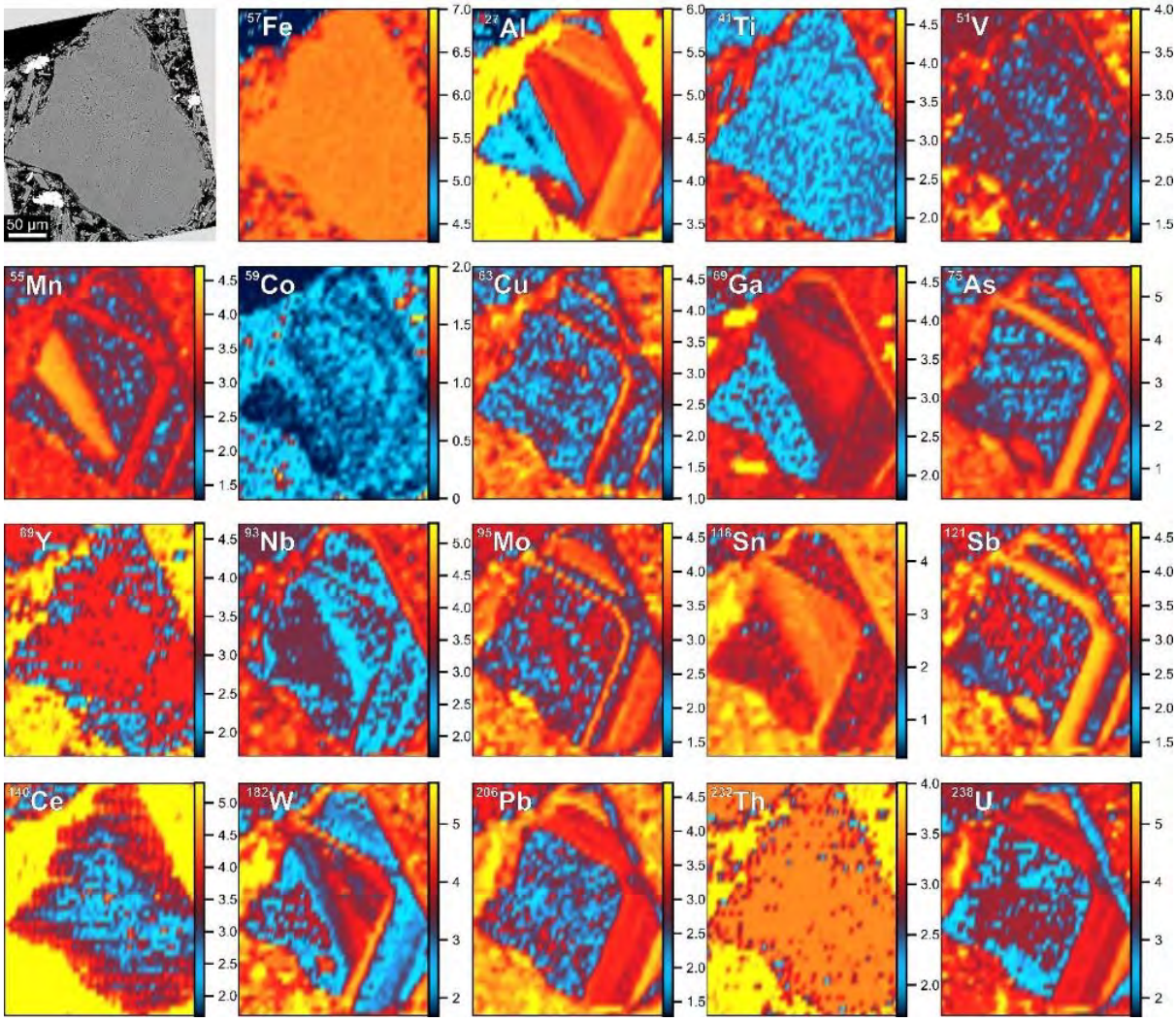

Figure A7. LA-ICP-MS element maps of zoned hematite corresponding to Fig. 11 showing a reduced number of maps (sample RX6584; drillhole RD2852A). The obtained intensities were scaled individually using logarithmic scale (10^n). Upper left BSE image corresponds to the ablated area for comparison.

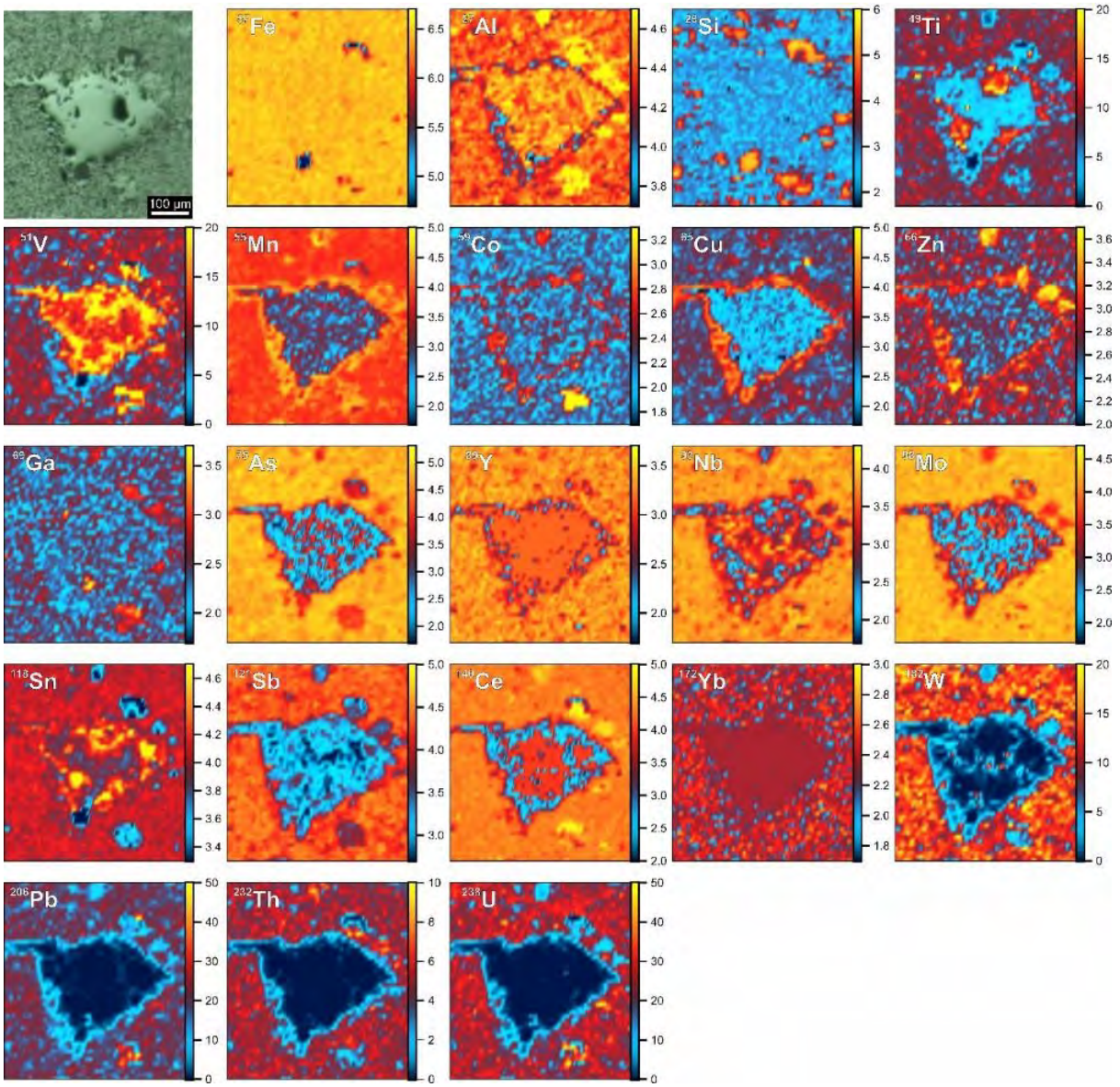

Figure A8. LA-ICP-MS element maps of granoblastic hematite corresponding to Fig. 12a showing a reduced number of maps (sample MV093; drillhole RD647). The obtained intensities were scaled individually using logarithmic scale (10^n). ^{49}Ti and ^{51}V, ^{182}W, ^{206}Pb, ^{232}Th and ^{238}U in are linearly scaled ($n \cdot 1000$). Upper left image corresponds to an optical micrograph of the ablated area.

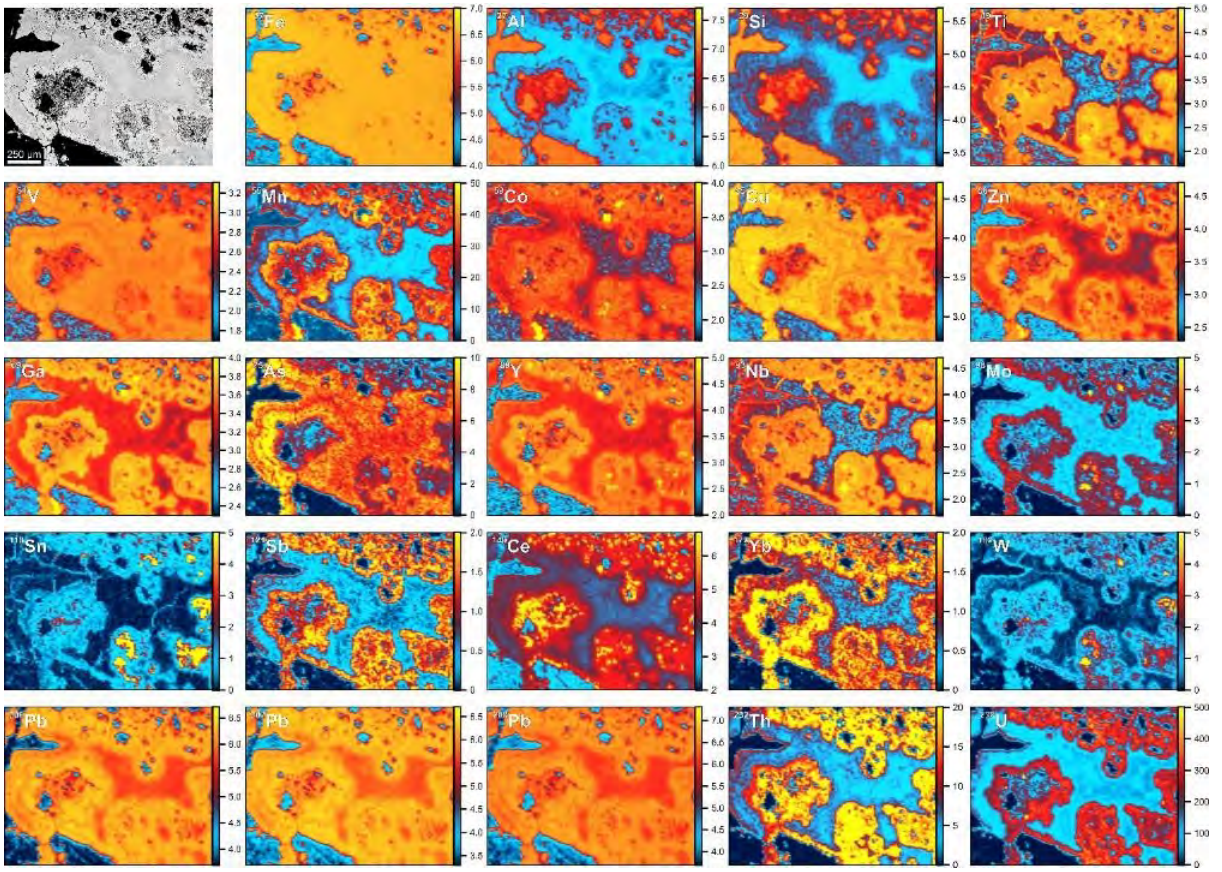

Figure A9. LA-ICP-MS element maps of colloform hematite corresponding to Fig. 12b showing a reduced number of maps (sample MV048; RU27-7551). The obtained intensities were scaled individually using logarithmic scale (10^n). ^{55}Mn, ^{75}As, ^{98}Mo, ^{118}Sn, ^{121}Sb, ^{172}Yb, ^{182}W, ^{232}Th and ^{238}U are linearly scaled (n·1000). Upper left image corresponds to a BSE micrograph of the ablated area.

ELECTRONIC APPENDIX B FOR CHAPTER 2

Analytical methods – Electron probe microanalysis (EPMA)

Quantitative major and minor oxide compositions of U-rich zoned hematite from sample RX6583 (drillhole RD2852A, SE lobe) were obtained using a CAMECA SX-Five Electron Probe Microanalyzer (EPMA), equipped with 5 wavelength-dispersive spectrometers (WDS), and hosted at Adelaide Microscopy (The University of Adelaide). The instrument was operated at a constant accelerating voltage of 15 keV and beam current of 20 nA for most of the analyzed elements, excepting for U and Pb, which were both measured at 15 keV and 100 nA. A constant beam spot-size of ~1 μm was utilized for the measurements. Individual analytical conditions for each analyzed element are listed in Tab. A1. Calibration and data reduction was conducted in the software package Probe for EPMA (Probe Software Inc.) using the mean atomic number (MAN) correction procedures (see Donovan et al., 2016, and references therein). Background times were kept constant at 40 s for the calibration of all elements in the standards. The actual backgrounds of the elements in the unknowns were not measured, as they are unnecessary using the MAN background method. Typical minimum detection limits ranged from 0.007 (U, Pb) to 0.111 wt.% (W) at 99 % confidence.

Table B1. Summary of analytical conditions/setup employed for EPMA analysis of hematite

Element	X-Ray line	Crystal	Standard	Peak count time (s)	Average mdl (wt.%)
Al	K_α	TAP	Astimex Albite	15	0.019
Ca	K_α	LPET	Astimex Plagioclase	15	0.008
Cr	K_α	LLIF	P&H block Cr_2O_3	15	0.016
Fe	K_α	LLIF	P&H block Specularite	15	0.023
Mg	K_α	TAP	Astimex Almandine Garnet	15	0.012
Mn	K_α	LLIF	P&H block Rhodonite	15	0.022
Mo	L_α	LPET	Taylor block synthetic $CaMoO_4$	15	0.028
Nb	L_α	LPET	Astimex Niobium metal	15	0.029
Ni	K_α	LLIF	Astimex Pentlandite	15	0.029
P	K_α	LPET	Astimex Apatite	15	0.010
Pb	M_α	LPET	NIST	100	0.007
Si	K_α	TAP	Astimex Albite	15	0.020
Sn	L_α	LPET	P&H block Cassiterite	15	0.024
Ti	K_α	LPET	P&H block Rutile	15	0.009
U	M_β	LPET	DAS UO_2	100	0.007
V	K_α	LLIF	Astimex Vanadium metal	15	0.018
W	L_α	LLIF	Taylor block synthetic $CaWO_4$	15	0.111
Zn	K_α	LLIF	Astimex Willemite	15	0.045
Zr	L_α	LPET	Taylor block Zircon	15	0.033

mdl: minimum detection limit.

Laser-ablation inductively-coupled mass spectrometry (LA-ICP-MS)

LA-ICP-MS spot analysis was conducted following established practices at The University of Adelaide (e.g., Ciobanu et al., 2013; Ismail et al., 2014; Xu et al., 2016) using a RESOlution-LR 193 nm excimer laser microprobe (Australian Scientific Instruments) with a large format S155 two-volume ablation cell designed by Laurin Technic Pty., coupled to an Agilent 7900x Quadrupole ICP-MS. Laser ablation was performed in an atmosphere of UHP He (0.35 1/min) and the aerosol was mixed with Ar (1.06 l/min) before exiting the sample chamber. A pulse homogenizing device (”squid”, Laurin Technic) was used in the interface tubing between the laser and ICP-MS to smooth signal fluctuations. The ICP-MS system was optimized daily to achieve maximal sensitivity and low oxide interference production. Most commonly, a laser spot size diameter of 43 µm was employed (also 30 and 60 µm depending on the requirements), using a pulse repetition rate of 5 Hz and a fluence of 3.5 J/cm^2.

Prior to each spot analysis, the selected areas were pre-ablated to avoid surface contamination. Acquisition time was a total of 60 s, comprising a 30 s measurement of the background (laser off) and 30 s acquisition of the signal while the laser ablates. Analytical standards were run before and after each individual set of ≤26 hematite unknowns using either BHVO-2G or GSD-1G as the primary standard, and NIST-610 as the secondary standard.

Data reduction was performed in Glitter (van Achterbergh et al., 2001) using the stoichiometric concentration of Fe in hematite as FeO wt.% (i.e., 89.9810) as the internal standard element. Detection limits indicated by Glitter were individually calculated for each element in each spot analysis.

The following extended suite of 45 elements, including four Pb isotopes, was measured: ^{24}Mg, ^{27}Al, ^{28}Si, ^{31}P, ^{43}Ca, ^{45}Sc, ^{49}Ti, ^{51}V, ^{52}Cr, ^{55}Mn, ^{57}Fe, ^{59}Co, ^{60}Ni, ^{63}Cu, ^{66}Zn, ^{69}Ga, ^{75}As, ^{88}Sr, ^{89}Y, ^{90}Zr, ^{93}Nb, ^{95}Mo, ^{118}Sn, ^{121}Sb, ^{137}Ba, ^{139}La, ^{140}Ce, ^{141}Pr, ^{146}Nd, ^{147}Sm, ^{153}Eu, ^{157}Gd, ^{159}Tb, ^{163}Dy, ^{165}Ho, ^{166}Er, ^{169}Tm, ^{172}Yb, ^{175}Lu, ^{178}Hf, ^{181}Ta, ^{182}W, ^{204}Pb, ^{206}Pb, ^{207}Pb, ^{208}Pb, ^{232}Th and ^{238}U.

LA-ICP-MS element maps were obtained for subsets of the previously indicated isotopes (see above). For this purpose, grids of parallel lines were ablated across the selected areas using a fluence of ~3.5 J/cm^2 and laser repetition rates of 10 Hz. A spot size of 7 and 11 µm was used with a speed of 7 and 11 µm/s respectively. Prior to the main ablation and signal acquisition phase, individual lines were pre-ablated to clean the surfaces and minimize the contribution from the deposition blanket from previous lines. An acquisition of 10 s background for each line was conducted prior to the main ablation phase. Spot analyses were conducted on the reference materials before and after each mapping run. The program Iolite (Woodhead et al., 2007; Paton et al., 2011) was used for data reduction and processing. Individual line-profiles of the measured isotopes were merged together into 2D-images by subtracting the average backgrounds from the time-resolved intensities and producing qualitative isotope intensity maps with scales in counts-per-second (cps). The obtained intensities were scaled individually using generally logarithmic-, but also linear-scales to highlight intragrain variability in hematite and to image features of interest accordingly.

References cited

Ciobanu, C.L., Wade, B.P., Cook, N.J., Schmidt Mumm, A., Giles, D., 2013. Uranium-bearing hematite from the Olympic Dam Cu–U–Au deposit, South Australia: A geochemical tracer and reconnaissance Pb–Pb geochronometer. Precambrian Research, 238, 129–147.

Donovan, J.J., Singer, J.W., Armstrong, J.T., 2016. A new EPMA method for fast trace element analysis in simple matrices. American Mineralogist 101, 1839–1853

Ismail, R., Ciobanu, C.L., Cook, N.J., Teale, G.S., Giles, D., Schmidt Mumm, A., & Wade, B., 2014. Rare earths and other trace elements in minerals from skarn assemblages, Hillside iron oxide–copper–gold deposit, Yorke Peninsula, South Australia. Lithos 184–187, 456–477.

Paton, C., Hellstrom, J., Paul, B., Woodhead, J., Hergt, J., 2011. Iolite: Freeware for the visualisation and processing of mass spectrometric data. Journal of Analytical Atomic Spectrometry 26, 2508–2518.

van Achterbergh, E., Ryan, C.G., Jackson, S.E., Griffin, W.L., 2001. Data reduction software for LA-ICP-MS. In P.J. Sylvester (Ed.), Laser-ablation-ICPMS in the Earth Sciences; Principles and Applications. Mineralogical Association of Canada, Short Course Series 29, 239–243.

Woodhead, J.D., Hellstrom, J., Hergt, J.M., Greig, A., Maas, R., 2007. Isotopic and Elemental Imaging of Geological Materials by Laser Ablation Inductively Coupled Plasma-Mass Spectrometry. Geostandards and Geoanalytical Research 31, 331-343.

Xu, J., Ciobanu, C.L., Cook, N.J., Zheng, Y., Sun, X., Wade, B.P., 2016. Skarn formation and trace elements in garnet and associated minerals from Zhibula copper deposit, Gangdese Belt, southern Tibet. Lithos 262, 213–231.

ELECTRONIC APPENDIX C FOR CHAPTER 2

Table C1. Zoned hematite in RD1988 (SE-lobe)

Drillhole	U*	Sample	Mg	Al	Si	P	Ca	Sc	Ti	V	Cr	Mn	Co	Ni	Cu	Zn	Ga	As	Sr	Zr	Nb	Mo	Sn	Sb	Ba	Hf	Ta
RD1988																											
RX7293	**L**	**Mean (n=10)**	**36.9**	**114**	**410**	**<145**	**<1088**	**<0.72**	**4.9**	**6.5**	**2.4**	**15.9**	**2.9**	**1.4**	**3.7**	**6.9**	**11.4**	**5.7**	**0.36**	**<0.02**	**0.50**	**272**	**1423**	**8.9**	**1.2**	**0.04**	**0.005**
		S.D.	19.8	36.4	124	-	-	-	0.61	6.4	0.07	5.1	0.66	0.25	0.97	0.67	1.1	1.2	0.28	-	0.48	167	379	2.7	1.3	0.05	0.007
		Min.	10.3	61.5	<209	-	-	-	3.8	0.50	<2.3	6.5	1.8	<0.79	<2.9	<6.1	9.5	<4.7	<0.07	-	0.02	33.3	860	5.2	<0.001	<0.001	<0.001
		Max.	80.5	176	652	-	-	-	4.7	21.0	2.4	23.4	4.0	1.4	6.1	8.5	13.3	8.4	0.83	-	1.5	546	1989	13.8	3.9	0.04	0.02
	M	**Mean (n=5)**	**42.1**	**488**	**863**	**<150**	**<1127**	**0.70**	**62.6**	**5.1**	**<2.5**	**16.2**	**3.4**	**1.5**	**54.6**	**7.3**	**17.6**	**17.8**	**4.1**	**<0.03**	**8.0**	**917**	**1256**	**22.4**	**117**	**0.02**	**0.05**
		S.D.	23.0	161	411	-	-	0.06	55.4	7.2	-	10.1	1.6	0.12	43.0	2.0	2.6	13.9	4.9	-	6.8	455	718	11.0	154	0.02	0.04
		Min.	22.8	210	469	-	-	0.65	8.8	<0.45	-	5.9	1.4	1.3	9.7	<6.0	14.3	<5.2	0.10	-	2.0	332	325	8.8	0.47	<0.001	0.01
		Max.	86.2	686	1598	-	-	0.65	141	19.5	-	35.2	5.9	1.3	129	11.3	21.4	37.6	13.1	-	21.2	1520	2396	38.3	385	0.04	0.11
	H	**Mean (n=3)**	**36.5**	**632**	**731**	**<151**	**<1116**	**<0.68**	**6.4**	**9.8**	**<2.5**	**16.6**	**3.1**	**<1.3**	**7.0**	**6.9**	**17.2**	**7.9**	**0.24**	**<0.04**	**2.9**	**764**	**1958**	**16.7**	**1.1**	**0.001**	**0.01**
		S.D.	5.9	179	517	-	-	-	0.93	5.7	-	1.3	0.26	-	5.6	0.42	0.56	3.5	0.13	-	1.8	246	411	0.57	0.33	0.001	0.01
		Min.	28.9	413	311	-	-	-	5.4	2.3	-	14.8	2.8	-	<3.1	<6.4	16.6	<5.2	<0.07	-	1.4	520	1462	16.0	0.67	0.001	<0.001
		Max.	43.3	852	1459	-	-	-	7.6	16.0	-	17.7	3.4	-	14.9	7.4	17.9	12.9	0.37	-	5.4	1101	2469	17.4	1.4	0.001	0.01
RX7294A	**L**	**Mean (n=19)**	**187**	**204**	**2909**	**13.8**	**316**	**0.92**	**5.9**	**6.7**	**0.79**	**13.2**	**2.0**	**0.35**	**0.54**	**4.7**	**5.7**	**15.6**	**0.71**	**0.43**	**0.62**	**180**	**413**	**Na**	**2.2**	**0.04**	**0.03**
		S.D.	133	81.9	1693	4.5	241	2.4	5.8	8.1	0.89	7.9	1.0	0.29	0.33	13.9	1.7	12.1	1.2	0.44	1.2	113	162	-	2.5	0.04	0.07
		Min.	7.3	55.2	849	<9.6	<81.8	<0.09	<2.0	0.03	<0.45	<1.1	0.32	0.06	0.24	0.41	3.5	<0.53	<0.001	<0.001	<0.001	13.8	77.9	-	0.04	<0.001	0.003
		Max.	455	340	6086	28.6	992	10.3	24.8	26.5	0.84	25.8	3.6	1.2	0.97	3.7	11.8	36.2	4.5	1.6	4.5	382	627	-	9.0	0.10	0.32
	M	**Mean (n=9)**	**81.8**	**230**	**1939**	**17.8**	**226**	**1.6**	**6.1**	**6.9**	**0.73**	**13.9**	**2.1**	**0.31**	**0.67**	**23.3**	**6.7**	**10.7**	**0.51**	**0.22**	**0.93**	**306**	**598**	**Na**	**1.7**	**0.03**	**0.007**
		S.D.	88.2	104	1057	11.7	188	2.1	5.8	5.0	0.63	6.9	1.0	0.18	0.62	62.5	2.6	9.5	0.63	0.19	1.2	164	225	-	1.8	0.02	0.005
		Min.	<7.0	25.7	844	<10.1	<76.4	<0.09	<2.1	0.39	0.38	3.5	0.49	0.10	<0.24	0.73	4.3	<0.81	<0.02	<0.03	0.03	113	352	-	<0.14	0.01	<0.004
		Max.	255	374	3939	21.3	705	5.7	19.8	14.5	0.77	23.8	3.9	0.77	2.3	200	13.4	25.4	1.6	0.63	4.1	595	915	-	4.4	0.07	0.02
RX7294B	**L**	**Mean (n=16)**	**54.0**	**128**	**437**	**<149**	**<1106**	**0.75**	**4.7**	**8.5**	**<2.5**	**20.0**	**3.4**	**1.4**	**3.6**	**6.8**	**11.6**	**6.1**	**0.15**	**0.04**	**0.45**	**396**	**1279**	**17.2**	**0.62**	**0.002**	**0.004**
		S.D.	40.4	31.2	186	-	-	0.07	0.62	5.8	-	5.6	0.99	0.43	0.51	0.50	1.4	2.1	0.11	0.06	0.59	150	460	4.7	0.94	0.009	0.009
		Min.	9.5	60.4	<203	-	-	<0.62	3.8	0.48	-	5.1	0.93	0.84	<2.9	<6.1	8.3	<5.1	0.03	<0.001	<0.04	114	195	6.9	<0.001	<0.001	<0.001
		Max.	197	185	936	-	-	0.70	3.8	21.2	-	26.1	4.9	2.4	4.6	7.9	14.5	13.7	0.43	0.09	1.9	714	1751	26.3	3.1	0.04	0.02
	M	**Mean (n=5)**	**56.7**	**389**	**741**	**162**	**<1196**	**<0.83**	**7.3**	**19.7**	**<2.6**	**19.3**	**2.8**	**1.5**	**3.4**	**<6.8**	**14.6**	**<5.6**	**0.15**	**0.001**	**2.4**	**494**	**1578**	**22.1**	**8.0**	**0.001**	**0.007**
		S.D.	35.4	295	759	22.4	-	-	4.1	20.0	-	7.7	0.78	0.17	0.26	-	4.2	-	0.16	0.001	2.9	339	641	11.5	15.0	0.001	0.009
		Min.	14.4	87.8	282	<143	-	-	<4.8	0.50	-	10.8	1.8	1.3	<3.1	-	8.7	-	0.05	0.001	0.12	114	478	6.3	0.22	0.001	<0.001
		Max.	116	945	2248	203	-	-	15.4	49.0	-	31.7	3.9	1.8	3.2	-	20.6	-	0.47	0.001	6.7	964	2475	41.7	37.9	0.001	0.02
	H		60.0	303	913	<160	2901	<0.70	<6.2	21.9	<2.7	28.0	4.7	<1.3	<3.6	11.5	16.1	46.4	3.4	0.09	1.7	1175	2648	55.2	13.5	0.04	<0.03
RX7295A	**L**	**Mean (n=8)**	**35.4**	**211**	**411**	**32.2**	**1651**	**0.38**	**16.2**	**5.8**	**0.67**	**15.6**	**1.8**	**0.26**	**7.9**	**1.6**	**5.9**	**9.4**	**1.7**	**0.12**	**1.0**	**135**	**567**	**5.0**	**55.7**	**0.04**	**0.03**
		S.D.	11.6	81.9	69.2	11.1	1012	0.19	18.0	2.1	0.39	3.2	0.47	0.11	7.0	1.0	1.6	4.7	1.5	0.11	0.87	70.0	77.9	2.0	122	0.04	0.04
		Min.	21.2	92.7	342	<23.3	<824	<0.25	3.0	2.3	<0.31	11.3	0.92	<0.11	<1.4	0.66	4.8	1.9	0.29	<0.001	0.11	28.3	459	1.5	<0.001	<0.001	<0.001
		Max.	55.4	380	543	58.6	3812	0.88	57.7	8.1	1.5	20.9	2.4	0.43	19.9	4.0	10.0	17.4	4.6	0.35	2.9	267	689	8.6	377	0.10	0.13
	M	**Mean (n=10)**	**48.8**	**372**	**555**	**43.2**	**1089**	**0.70**	**4.5**	**4.3**	**0.47**	**11.9**	**1.5**	**0.20**	**3.3**	**1.3**	**8.3**	**13.7**	**7.6**	**0.13**	**1.4**	**126**	**795**	**5.2**	**157**	**0.04**	**0.01**
		S.D.	63.4	334	285	13.4	228	0.98	2.9	4.6	0.18	3.6	0.49	0.17	2.5	0.70	3.9	10.1	13.6	0.22	2.1	134	372	2.9	312	0.04	0.01
		Min.	6.1	55.3	299	<29.5	<853	<0.29	<1.3	<0.04	<0.31	4.4	0.82	<0.001	<1.6	<0.56	4.6	2.0	<0.05	<0.001	0.05	29.3	103	1.6	<0.001	<0.001	<0.001
		Max.	235	1227	1206	76.8	1692	3.6	11.4	15.1	0.88	17.2	2.5	0.48	9.9	3.1	16.8	31.9	36.7	0.73	7.3	511	1323	11.6	932	0.10	0.03
	H		158	384	894	<30.5	<1033	<0.33	2.5	0.53	0.92	10.3	1.4	<0.19	2.3	0.74	6.6	15.6	1.2	<0.001	0.12	293	602	4.7	<0.88	0.05	<0.001
RX7295B	**M**	**Mean (n=19)**	**29.5**	**545**	**1028**	**26.8**	**829**	**0.31**	**32.7**	**1.8**	**0.51**	**14.2**	**2.1**	**0.21**	**20.4**	**2.0**	**6.2**	**24.4**	**1.2**	**0.34**	**4.8**	**438**	**579**	**11.3**	**5.4**	**0.06**	**0.05**
		S.D.	9.4	309	1083	9.2	253	0.10	33.6	1.4	0.20	4.2	1.1	0.15	23.1	1.9	1.1	14.2	1.0	0.35	5.2	200	152	7.0	11.4	0.05	0.05
		Min.	16.0	123	433	<15.7	<589	<0.19	<0.80	0.05	<0.26	7.0	0.72	<0.001	<1.2	0.31	4.9	3.8	0.14	<0.001	0.10	83.2	267	4.5	0.70	<0.001	<0.001
		Max.	58.1	1306	4179	47.9	1714	0.56	107	4.3	1.0	23.5	6.0	0.50	73.1	7.2	9.4	49.6	3.3	1.1	19.6	804	823	30.8	53.4	0.15	0.17

Table C1. (Continued) Zoned hematite in RD1988 (SE-lobe)

Drillhole	U*	Sample	Y	La	Ce	Pr	Nd	Sm	Eu	Gd	Tb	Dy	Ho	Er	Tm	Yb	Lu	∑REY	W	^{204}Pb	^{206}Pb	^{207}Pb	^{208}Pb	Th	U
RD1988																									
RX7293	**L**	**Mean (n=10)**	**0.04**	**6.6**	**8.7**	**0.39**	**0.62**	**0.04**	**0.01**	**0.06**	**0.005**	**0.02**	**0.006**	**0.02**	**0.009**	**0.04**	**0.01**	**16.6**	**12083**	**4.5**	**102**	**12.4**	**0.77**	**0.21**	**60.4**
		S.D.	0.02	9.7	12.2	0.49	0.74	0.02	0.008	0.04	0.004	0.02	0.005	0.01	0.005	0.02	0.008	23.2	5809	1.3	71.2	8.3	0.87	0.23	42.6
		Min.	<0.02	0.22	0.19	0.02	0.02	<0.001	<0.001	<0.001	<0.001	<0.001	<0.001	<0.001	<0.001	<0.001	<0.001	0.65	3101	<3.0	4.3	0.52	<0.31	0.003	2.5
		Max.	0.11	27.2	33.8	1.4	2.3	0.07	0.007	0.11	0.01	0.04	0.007	0.03	0.01	0.08	0.03	65.0	23457	7.6	203	24.5	3.3	0.76	122
	M	**Mean (n=5)**	**0.15**	**15.4**	**22.8**	**1.1**	**1.8**	**0.10**	**0.02**	**0.11**	**0.01**	**0.03**	**0.01**	**0.03**	**0.01**	**0.05**	**0.01**	**41.6**	**9388**	**5.6**	**2295**	**266**	**1.9**	**0.52**	**1301**
		S.D.	0.06	17.2	22.8	1.0	1.4	0.05	0.008	0.03	0.007	0.02	0.01	0.02	0.009	0.03	0.007	42.6	4015	2.5	810	92.4	2.0	0.58	422
		Min.	0.08	2.4	3.9	0.21	0.41	<0.07	0.006	<0.07	0.001	<0.001	<0.001	0.01	0.003	0.02	0.004	7.2	3759	<3.4	1354	159	<0.34	0.07	796
		Max.	0.24	45.0	61.9	2.8	4.1	0.18	0.03	0.16	0.001	0.04	0.03	0.05	0.03	0.09	0.02	115	14749	9.9	3214	377	5.5	1.6	1749
	H	**Mean (n=3)**	**0.25**	**10.8**	**18.4**	**0.91**	**1.8**	**0.11**	**0.01**	**0.13**	**0.01**	**0.06**	**0.009**	**0.05**	**0.02**	**0.16**	**0.02**	**32.7**	**10577**	**4.3**	**5824**	**674**	**0.44**	**0.38**	**3179**
		S.D.	0.07	1.5	2.3	0.12	0.47	0.04	0.01	0.04	0.002	0.01	0.002	0.006	0.002	0.003	0.002	4.1	2698	0.86	1645	185	0.02	0.13	839
		Min.	0.18	8.7	16.2	0.78	1.2	0.07	<0.001	<0.10	0.001	0.05	0.007	0.04	0.01	0.16	0.02	28.3	7863	<3.2	4529	523	0.41	0.21	2549
		Max.	0.35	12.3	21.5	1.1	2.3	0.17	0.01	0.19	0.001	0.07	0.01	0.06	0.02	0.17	0.03	38.2	14256	5.3	8146	934	0.47	0.49	4365
RX7294A	**L**	**Mean (n=19)**	**0.21**	**1.6**	**1.9**	**0.12**	**0.32**	**0.13**	**0.03**	**0.05**	**0.01**	**0.03**	**0.02**	**0.06**	**0.03**	**0.22**	**0.06**	**4.8**	**5675**	**NA**	**45.4**	**5.5**	**1.1**	**0.91**	**39.3**
		S.D.	0.24	2.0	2.1	0.13	0.33	0.31	0.09	0.03	0.02	0.03	0.03	0.06	0.03	0.25	0.06	5.0	2217	-	33.7	3.9	2.4	1.7	27.8
		Min.	0.01	<0.04	<0.07	0.01	0.01	<0.01	<0.001	<0.02	<0.001	0.01	<0.003	<0.007	<0.002	<0.02	<0.005	0.32	270	-	<1.3	<0.77	0.07	<0.006	3.7
		Max.	0.75	6.6	6.9	0.40	1.1	1.4	0.42	0.09	0.01	0.13	0.13	0.22	0.07	0.88	0.21	16.5	8957	-	110	14.7	11.3	5.3	97.6
	M	**Mean (n=9)**	**0.75**	**3.8**	**5.2**	**0.38**	**0.95**	**0.12**	**0.10**	**0.13**	**0.05**	**0.12**	**0.03**	**0.18**	**0.04**	**0.47**	**0.14**	**12.5**	**6337**	**NA**	**245**	**30.2**	**0.90**	**0.57**	**238**
		S.D.	0.81	3.8	5.9	0.47	1.2	0.10	0.22	0.16	0.09	0.12	0.03	0.18	0.03	0.46	0.13	12.5	1370	-	102	12.1	1.2	0.84	100
		Min.	0.02	0.08	<0.09	0.008	0.02	0.008	<0.006	<0.02	0.003	<0.008	0.003	<0.01	<0.003	0.02	0.009	0.38	4230	-	134	16.0	0.14	<0.006	124
		Max.	2.7	13.5	20.0	1.6	4.3	0.34	0.71	0.43	0.30	0.42	0.09	0.57	0.09	1.6	0.44	44.9	8514	-	411	49.3	4.0	2.9	398
RX7294B	**L**	**Mean (n=16)**	**0.04**	**2.4**	**3.5**	**0.19**	**0.29**	**0.05**	**0.009**	**0.08**	**0.006**	**0.03**	**0.007**	**0.02**	**0.004**	**0.05**	**0.008**	**6.7**	**19304**	**3.5**	**74.6**	**8.9**	**0.48**	**0.12**	**44.4**
		S.D.	0.03	1.4	2.1	0.12	0.21	0.04	0.008	0.03	0.006	0.02	0.004	0.02	0.005	0.02	0.006	3.7	5722	0.71	36.6	4.6	0.41	0.15	21.4
		Min.	0.008	0.29	0.93	0.05	0.08	<0.001	<0.001	<0.001	<0.001	<0.001	<0.001	<0.001	<0.001	<0.001	<0.001	1.8	4404	<3.0	16.4	2.0	<0.31	<0.01	7.1
		Max.	0.12	4.8	7.2	0.46	0.85	0.10	0.01	0.09	0.007	0.05	0.007	0.04	0.007	0.11	0.02	13.1	24087	5.9	149	18.4	2.0	0.60	84.1
	M	**Mean (n=5)**	**0.26**	**8.5**	**12.3**	**0.69**	**1.3**	**0.13**	**0.02**	**0.09**	**0.01**	**0.06**	**0.01**	**0.07**	**0.01**	**0.16**	**0.03**	**23.7**	**18678**	**3.5**	**525**	**61.4**	**1.6**	**1.9**	**308**
		S.D.	0.27	7.1	9.9	0.66	1.5	0.15	0.02	0.03	0.005	0.06	0.004	0.08	0.006	0.16	0.02	19.4	6918	0.58	220	25.4	1.6	2.4	127
		Min.	<0.03	0.35	0.49	0.004	<0.08	<0.001	0.006	0.05	0.004	<0.001	<0.01	0.01	0.004	0.03	0.004	1.2	8945	<3.1	263	31.1	<0.31	0.004	169
		Max.	0.70	21.6	30.5	1.9	4.3	0.41	0.06	0.14	0.02	0.17	0.02	0.23	0.02	0.45	0.06	59.7	29223	4.7	840	97.8	4.6	6.3	498
	H		7.9	58.4	109	6.7	12.2	0.91	0.19	0.47	0.07	0.49	0.08	0.44	0.10	1.1	0.22	395	22442	6.3	4181	506	11.1	1.2	2234
RX7295A	**L**	**Mean (n=8)**	**0.50**	**2.0**	**2.8**	**0.18**	**0.42**	**0.08**	**0.03**	**0.08**	**0.01**	**0.07**	**0.02**	**0.08**	**0.02**	**0.13**	**0.05**	**6.5**	**19172**	**NA**	**40.4**	**6.5**	**1.3**	**0.15**	**48.3**
		S.D.	0.25	1.3	2.0	0.13	0.25	0.03	0.02	0.03	0.008	0.02	0.01	0.03	0.009	0.05	0.02	3.6	7765	-	17.5	3.1	1.5	0.11	20.4
		Min.	0.19	0.57	0.78	0.05	<0.07	<0.04	<0.01	<0.05	<0.001	<0.04	0.006	0.05	0.008	0.06	0.01	2.8	2578	-	14.7	2.3	0.33	<0.02	17.5
		Max.	0.82	5.0	7.8	0.50	0.92	0.14	0.06	0.15	0.03	0.09	0.05	0.14	0.04	0.21	0.09	15.4	31026	-	65.0	11.7	5.2	0.34	77.3
	M	**Mean (n=10)**	**0.77**	**8.0**	**10.2**	**0.68**	**1.6**	**0.16**	**0.05**	**0.13**	**0.02**	**0.13**	**0.04**	**0.16**	**0.04**	**0.34**	**0.09**	**22.3**	**12165**	**NA**	**324**	**41.8**	**1.2**	**0.25**	**386**
		S.D.	0.78	12.0	14.2	0.94	2.2	0.25	0.04	0.12	0.02	0.12	0.04	0.17	0.04	0.34	0.06	31.2	6266	-	223	28.6	1.5	0.33	270
		Min.	<0.02	0.13	0.19	0.02	<0.07	<0.001	<0.001	<0.05	<0.001	<0.03	<0.008	0.03	<0.007	<0.001	0.01	0.64	3997	-	104	11.5	<0.03	0.02	123
		Max.	2.8	42.6	50.8	3.3	7.6	0.86	0.12	0.46	0.05	0.45	0.15	0.61	0.12	1.2	0.19	111	25639	-	733	94.8	4.4	1.2	887
	H		2.7	22.9	32.7	2.4	5.6	0.44	0.10	0.47	0.05	0.50	0.09	0.53	0.07	1.2	0.29	138	6878	NA	1320	173	0.29	<0.02	1692
RX7295B	**M**	**Mean (n=19)**	**2.0**	**19.9**	**26.9**	**1.8**	**4.7**	**0.41**	**0.08**	**0.32**	**0.05**	**0.39**	**0.09**	**0.37**	**0.08**	**0.75**	**0.18**	**58.1**	**12100**	**NA**	**772**	**94.0**	**4.2**	**0.30**	**849**
		S.D.	1.1	10.7	14.3	1.0	2.6	0.32	0.04	0.21	0.03	0.24	0.05	0.21	0.04	0.36	0.08	30.6	6385	-	368	43.0	3.3	0.16	429
		Min.	0.48	4.7	6.7	0.44	0.97	0.05	<0.02	<0.06	<0.006	<0.05	<0.01	0.07	0.04	0.16	0.05	14.4	2865	-	220	28.1	0.20	0.05	182
		Max.	3.8	37.3	50.3	3.6	9.6	1.3	0.17	0.74	0.11	0.84	0.17	0.84	0.17	1.5	0.32	107	29105	-	1784	215	11.9	0.63	1969

Table C2. Zoned hematite in RD2786A (SE-lobe)

Drillhole	U*	Sample	Mg	Al	Si	P	Ca	Sc	Ti	V	Cr	Mn	Co	Ni	Cu	Zn	Ga	As	Sr	Zr	Nb	Mo	Sn	Sb	Ba	Hf	Ta
RD2786A																											
LCD02	**L**	**Mean (n=13)**	**48.0**	**236**	**548**	**159**	**1326**	**0.91**	**10.6**	**16.3**	**<2.5**	**6.6**	**1.3**	**1.4**	**3.3**	**<5.8**	**10.7**	**6.6**	**0.68**	**0.07**	**3.0**	**258**	**4717**	**4.1**	**2.3**	**0.02**	**0.01**
		S.D.	91.9	223	271	16.2	172	0.26	7.7	20.0	-	6.1	1.1	0.46	0.75	-	4.3	4.5	1.1	0.11	3.6	402	8354	2.7	4.1	0.04	0.02
		Min.	2.6	72.8	270	<127	<921	<0.52	<3.3	<0.24	-	<1.5	<0.15	0.77	<1.7	-	3.5	<3.1	<0.001	<0.001	0.03	1.5	132	<0.96	<0.001	<0.001	<0.001
		Max.	336	937	1167	187	1537	1.6	26.8	72.8	-	18.3	3.7	2.4	4.4	-	19.1	16.4	3.9	0.39	10.7	1332	25685	8.6	15.7	0.05	0.05
	M	**Mean (n=6)**	**61.5**	**406**	**392**	**<153**	**<1273**	**<0.82**	**92.2**	**76.6**	**<2.5**	**20.8**	**3.1**	**<1.4**	**3.0**	**7.7**	**17.6**	**6.8**	**2.9**	**0.16**	**22.7**	**291**	**2253**	**17.6**	**2.8**	**0.02**	**0.04**
		S.D.	15.6	102	131	-	-	-	80.1	35.4	-	5.3	0.75	-	0.72	3.4	3.3	3.3	5.0	0.14	17.0	135	404	5.3	3.2	0.02	0.03
		Min.	41.4	297	295	-	-	-	<3.4	29.3	-	13.3	1.9	-	<1.9	<5.0	13.1	<3.5	<0.001	<0.001	1.6	165	1750	12.0	<0.001	<0.001	<0.001
		Max.	87.3	587	670	-	-	-	225	136	-	27.3	4.1	-	2.2	14.7	21.9	12.3	13.9	0.35	49.4	532	2772	26.2	8.5	0.05	0.09
	H	**Mean (n=3)**	**46.2**	**368**	**458**	**166**	**<1248**	**<0.71**	**<4.2**	**3.0**	**<2.3**	**19.8**	**3.2**	**<1.5**	**<2.8**	**<5.6**	**15.6**	**19.1**	**0.50**	**0.04**	**0.04**	**381**	**2363**	**14.0**	**1.5**	**0.001**	**0.01**
		S.D.	5.1	126	195	40.0	-	-	-	0.91	-	2.8	0.36	-	-	-	1.5	5.6	0.33	0.06	0.003	50.0	256	1.8	0.80	0.001	0.008
		Min.	39.6	200	<185	<138	-	-	-	1.9	-	16.0	2.7	-	-	-	13.6	15.0	0.15	0.001	0.04	331	2082	11.8	0.43	0.001	<0.001
		Max.	52.0	503	629	223	-	-	-	4.1	-	22.7	3.6	-	-	-	17.4	27.1	0.95	0.001	0.04	449	2701	16.2	2.3	0.001	0.02
MV023	**L**	**Mean (n=23)**	**23.7**	**129**	**125**	**6.7**	**25.4**	**0.50**	**130**	**42.2**	**0.24**	**12.9**	**1.7**	**0.35**	**0.24**	**0.62**	**5.7**	**0.99**	**0.18**	**0.44**	**64.5**	**242**	**1164**	**1.2**	**0.64**	**0.01**	**0.28**
		S.D.	23.5	76.7	30.6	3.0	17.1	0.90	259	36.3	0.26	14.0	1.6	0.37	0.63	0.45	1.9	1.0	0.49	0.72	103	333	1824	1.2	1.2	0.02	0.54
		Min.	0.08	20.3	62.9	2.1	<12.4	<0.02	2.5	5.5	<0.11	0.13	0.14	<0.04	<0.05	<0.09	3.3	<0.13	0.009	0.008	1.9	0.11	139	0.04	<0.01	<0.001	<0.001
		Max.	58.0	280	176	12.1	103	3.3	1018	141	1.4	46.6	4.1	1.7	3.1	2.2	8.3	4.3	2.4	3.1	337	826	8375	2.9	5.4	0.08	1.8
MV024	**L**	**Mean (n=12)**	**36.1**	**176**	**92.3**	**5.5**	**23.1**	**0.05**	**1.5**	**7.9**	**0.16**	**15.3**	**2.5**	**0.17**	**0.07**	**0.63**	**7.2**	**1.0**	**0.05**	**0.02**	**1.8**	**240**	**365**	**1.7**	**0.29**	**0.002**	**0.002**
		S.D.	15.4	48.4	24.2	1.9	6.2	0.05	1.5	5.0	0.05	5.4	0.86	0.07	0.009	0.19	0.53	1.4	0.09	0.03	1.8	234	141	0.61	0.60	0.002	0.002
		Min.	4.4	58.1	48.8	2.0	<15.6	0.03	<0.25	0.30	<0.10	3.7	0.60	0.05	<0.06	0.21	5.9	0.15	<0.001	<0.001	0.27	40.0	67.9	0.40	<0.001	<0.001	<0.001
		Max.	53.7	228	143	7.9	41.7	0.18	5.6	15.7	0.30	21.5	3.2	0.27	0.09	0.91	7.8	5.1	0.28	0.12	6.9	850	506	2.8	2.1	0.005	0.008
	M	**Mean (n=9)**	**15.5**	**45.8**	**118**	**5.8**	**20.7**	**0.07**	**5.5**	**0.29**	**0.15**	**4.7**	**0.98**	**0.07**	**0.08**	**0.30**	**8.9**	**2.9**	**0.17**	**0.02**	**0.60**	**554**	**42.4**	**1.5**	**0.61**	**0.003**	**0.004**
		S.D.	7.3	42.5	18.1	1.9	2.1	0.06	13.2	0.47	0.02	1.1	0.21	0.02	0.05	0.13	2.4	2.9	0.16	0.03	0.90	479	68.2	0.81	0.82	0.003	0.009
		Min.	5.0	13.6	93.4	2.5	<18.4	<0.03	<0.22	<0.008	<0.12	2.3	0.51	0.04	<0.06	<0.11	5.3	0.38	0.005	<0.001	0.001	94.9	1.1	0.70	0.03	<0.001	<0.001
		Max.	27.0	126	150	9.4	25.5	0.19	42.6	1.2	0.18	6.5	1.2	0.11	0.20	0.58	12.6	9.1	0.51	0.11	2.6	1645	187	3.1	2.8	0.01	0.03
	H	**Mean (n=5)**	**24.3**	**450**	**203**	**6.1**	**123**	**0.03**	**3.7**	**0.37**	**0.18**	**8.7**	**1.5**	**0.12**	**0.06**	**0.41**	**13.0**	**13.8**	**0.78**	**0.01**	**0.62**	**1214**	**96.2**	**3.4**	**5.8**	**0.003**	**0.002**
		S.D.	2.2	153	36.2	2.6	175	0.01	4.2	0.20	0.06	0.78	0.16	0.04	0.002	0.12	0.84	2.6	0.73	0.009	0.72	304	18.2	0.28	7.5	0.003	0.002
		Min.	21.8	275	145	<2.4	18.9	<0.02	0.77	0.17	<0.11	7.4	1.3	0.07	0.06	0.22	11.9	12.1	0.16	<0.003	0.04	884	74.5	2.8	1.4	<0.001	0.001
		Max.	27.9	706	252	8.8	472	0.06	12.0	0.76	0.28	9.7	1.7	0.16	0.07	0.55	14.3	19.0	2.2	0.03	2.0	1758	128	3.7	20.7	0.005	0.006
LCD03	**L**	**Mean (n=6)**	**15.3**	**54.2**	**465**	**<336**	**<2429**	**<1.6**	**<9.0**	**<0.88**	**<4.6**	**8.2**	**1.1**	**2.1**	**<5.8**	**10.8**	**13.9**	**9.4**	**0.26**	**0.001**	**0.15**	**94.5**	**814**	**5.1**	**1.5**	**0.09**	**0.02**
		S.D.	7.1	26.4	68.7	-	-	-	-	-	-	3.4	0.39	0.31	-	1.2	4.5	0.42	0.27	0.001	0.17	45.3	350	2.4	1.5	0.12	0.03
		Min.	<4.8	29.3	<402	-	-	-	-	-	-	<3.6	0.59	<1.7	-	<8.5	4.6	<8.8	<0.001	0.001	<0.001	29.6	534	<1.8	<0.001	0.001	<0.001
		Max.	29.1	109	563	-	-	-	-	-	-	13.0	1.6	1.8	-	12.1	18.9	9.7	0.84	0.001	0.52	179	1508	8.4	4.2	0.001	0.03
	M	**Mean (n=5)**	**13.3**	**142**	**420**	**339**	**<2352**	**2.7**	**8.8**	**10.1**	**<4.6**	**9.0**	**1.7**	**<2.4**	**5.6**	**12.6**	**25.4**	**27.0**	**5.1**	**0.11**	**4.2**	**450**	**650**	**20.8**	**9.1**	**0.06**	**0.03**
		S.D.	5.1	84.7	55.0	47.8	-	2.0	1.3	16.0	-	2.1	0.44	-	0.47	2.5	22.9	25.7	8.7	0.17	7.0	279	657	15.9	7.4	0.11	0.06
		Min.	6.9	22.3	<350	<279	-	<1.5	<7.3	<0.77	-	5.9	1.1	-	<5.0	<10.0	12.5	<8.2	<0.21	<0.001	0.08	143	217	6.0	<0.001	0.001	<0.001
		Max.	20.3	259	512	414	-	6.7	9.6	41.8	-	11.5	2.2	-	5.1	17.2	71.1	75.4	22.4	0.44	18.0	892	1948	51.2	18.3	0.001	0.15
	H		17.9	562	<504	<405	<2946	<2.0	<10.8	<1.2	<5.6	7.0	1.7	<3.9	<6.6	<14.1	22.6	<12.2	<0.25	<0.001	0.03	232	1915	9.5	<1.6	<0.001	<0.001

Table C2. (Continued) Zoned hematite in RD2786A (SE-lobe)

Drillhole	U*	Sample	Mg	Al	Si	P	Ca	Sc	Ti	V	Cr	Mn	Co	Ni	Cu	Zn	Ga	As	Sr	Zr	Nb	Mo	Sn	Sb	Ba	Hf	Ta
LCD04	**L**	**Mean (n=9)**	**18.5**	**33.3**	**354**	**<144**	**<1213**	**<0.75**	**<4.4**	**0.57**	**2.4**	**6.0**	**1.6**	**1.2**	**<2.7**	**<5.2**	**8.3**	**5.9**	**0.12**	**0.03**	**0.55**	**292**	**675**	**2.7**	**0.63**	**0.01**	**0.01**
		S.D.	10.8	18.5	110	-	-	-	-	0.37	0.57	2.6	0.70	0.31	-	-	3.1	6.2	0.11	0.04	1.3	321	402	2.2	0.73	0.03	0.02
		Min.	3.4	<7.2	<199	-	-	-	-	<0.24	<1.7	2.0	0.25	0.68	-	-	4.2	<2.9	<0.001	<0.001	<0.001	9.2	167	<0.82	<0.001	<0.001	0.001
		Max.	30.5	54.5	539	-	-	-	-	1.6	3.5	11.2	2.3	1.7	-	-	14.5	23.3	0.38	0.06	4.2	813	1240	6.5	2.4	0.03	0.001
	M	**Mean (n=8)**	**13.2**	**237**	**408**	**<150**	**<1252**	**<0.87**	**9.7**	**0.81**	**2.6**	**7.2**	**1.3**	**<1.3**	**8.5**	**5.6**	**11.9**	**18.2**	**0.45**	**0.08**	**0.79**	**631**	**922**	**10.4**	**3.7**	**0.05**	**0.05**
		S.D.	5.4	167	161	-	-	-	11.3	0.68	0.49	2.4	0.35	-	13.6	0.67	3.7	22.2	0.60	0.07	1.7	490	644	8.4	5.4	0.07	0.10
		Min.	6.5	9.3	228	-	-	-	<2.9	<0.23	<2.0	4.0	0.85	-	<1.7	<4.8	4.3	<2.9	0.02	<0.001	0.02	25.5	416	2.6	0.19	<0.001	<0.001
		Max.	20.1	525	760	-	-	-	37.3	2.5	3.7	11.9	2.0	-	44.4	6.3	16.0	74.4	1.9	0.11	5.4	1538	2084	29.2	16.9	0.05	0.30
	H	**Mean (n=3)**	**21.3**	**502**	**544**	**<152**	**<1282**	**<0.97**	**5.8**	**<0.51**	**<2.5**	**9.1**	**1.4**	**1.3**	**<3.3.**	**5.9**	**14.3**	**15.1**	**0.28**	**0.001**	**0.11**	**255**	**1380**	**12.3**	**0.88**	**0.10**	**0.001**
		S.D.	2.1	246	121	-	-	-	1.3	-	-	3.9	0.27	0.36	-	0.23	1.7	8.3	0.25	0.001	0.13	225	89.4	6.8	0.31	0.04	0.001
		Min.	18.4	173	445	-	-	-	<4.1	-	-	6.3	1.1	0.78	-	<5.7	12.1	4.7	0.03	0.001	<0.001	94.5	1254	7.2	0.55	0.05	0.001
		Max.	22.9	763	713	-	-	-	7.1	-	-	14.6	1.7	0.78	-	6.3	16.4	25.0	0.63	0.001	0.30	573	1447	21.9	1.3	0.05	0.001
MV025	**L**	**Mean (n=18)**	**19.4**	**113**	**160**	**10.2**	**73.8**	**0.18**	**23.7**	**0.52**	**0.69**	**10.8**	**1.5**	**0.22**	**0.82**	**0.63**	**7.8**	**5.9**	**0.20**	**0.02**	**0.83**	**173**	**286**	**1.4**	**1.2**	**0.004**	**0.04**
		S.D.	12.6	50.3	156	16.2	177	0.25	56.9	0.62	1.5	4.0	0.64	0.18	2.9	0.60	0.88	8.6	0.31	0.04	1.4	189	156	0.59	3.0	0.004	0.07
		Min.	7.0	74.0	68.9	<3.0	<13.3	0.03	<0.22	0.08	<0.13	5.8	0.81	0.07	<0.06	<0.14	5.5	<0.16	0.004	<0.001	0.02	25.7	125	0.81	0.02	<0.001	<0.001
		Max.	49.6	292	426	9.7	75.4	1.0	205	2.0	1.7	18.9	3.1	0.43	12.8	2.9	9.5	31.3	1.2	0.13	5.1	664	604	3.1	13.0	0.01	0.26
	M	**Mean (n=21)**	**22.4**	**193**	**511**	**50.1**	**444**	**0.66**	**12.9**	**0.85**	**3.7**	**9.1**	**1.5**	**0.85**	**1.2**	**1.9**	**8.7**	**19.4**	**0.73**	**0.12**	**1.2**	**495**	**251**	**4.0**	**5.0**	**0.01**	**0.03**
		S.D.	15.0	150	250	30.5	308	0.45	35.0	1.2	2.5	4.8	0.58	0.51	0.71	1.1	3.2	26.8	1.1	0.15	2.7	544	188	2.1	8.7	0.02	0.09
		Min.	5.8	26.7	114	3.1	<19.6	<0.03	<0.23	<0.14	<0.14	2.9	0.60	0.17	<0.07	0.22	2.8	0.83	<0.001	<0.001	<0.001	32.4	13.6	1.5	<0.001	<0.001	<0.001
		Max.	65.9	640	750	65.2	46.4	2.0	162	5.5	6.6	24.6	2.6	0.40	3.1	4.6	15.3	91.7	4.8	0.45	10.3	2646	798	9.0	27.5	0.03	0.31
	H	**Mean (n=5)**	**34.4**	**210**	**732**	**<70.0**	**807**	**0.91**	**13.8**	**0.57**	**<5.7**	**10.9**	**1.8**	**0.95**	**<1.2**	**1.8**	**10.5**	**13.4**	**0.38**	**0.22**	**0.15**	**741**	**214**	**5.6**	**0.79**	**0.005**	**0.06**
		S.D.	33.0	83.2	148	-	288	0.43	22.3	0.22	-	4.2	0.53	0.16	-	0.22	1.6	10.7	0.34	0.21	0.19	241	64.3	1.7	0.89	0.01	0.08
		Min.	11.9	130	<652	-	<547	<0.65	<2.6	0.26	-	6.1	1.0	0.77	-	<1.5	8.4	<0.69	0.02	0.03	<0.001	375	142	3.4	<0.001	<0.001	<0.001
		Max.	99.0	352	1029	-	1369	1.8	58.4	0.91	-	18.5	2.6	0.77	-	1.6	13.0	26.7	0.86	0.62	0.51	1122	314	8.3	2.4	0.03	0.22
LCD05	**L**	**Mean (n=16)**	**28.2**	**88.6**	**396**	**<159**	**<1400**	**<0.96**	**7.0**	**8.6**	**<2.7**	**9.0**	**1.9**	**1.3**	**<3.5**	**<6.1**	**11.0**	**5.2**	**0.17**	**0.05**	**1.3**	**280**	**1037**	**4.9**	**0.86**	**0.001**	**0.01**
		S.D.	53.8	77.9	330	-	-	-	3.9	17.5	-	6.3	1.1	0.40	-	-	2.6	4.1	0.17	0.06	2.6	480	837	3.6	1.1	0.001	0.01
		Min.	<3.5	18.1	182	-	-	-	<2.4	<0.23	-	2.7	0.73	<0.44	-	-	7.3	<2.7	<0.001	<0.001	0.02	3.5	230	<0.98	<0.001	0.001	<0.001
		Max.	229	287	1492	-	-	-	16.7	55.9	-	22.2	3.8	0.79	-	-	16.2	18.1	0.74	0.17	10.1	1584	3051	13.4	4.9	0.001	0.03
	M	**Mean (n=10)**	**27.0**	**363**	**370**	**<145**	**1236**	**<0.79**	**11.1**	**17.3**	**<2.4**	**9.7**	**1.7**	**1.3**	**3.5**	**<5.4**	**18.0**	**14.9**	**0.35**	**0.01**	**2.5**	**261**	**1250**	**12.4**	**1.7**	**0.03**	**0.02**
		S.D.	19.7	251	143	-	275	-	16.2	31.1	-	3.4	0.70	0.37	1.9	-	4.9	18.6	0.48	0.02	4.8	300	898	7.6	1.8	0.03	0.01
		Min.	7.6	54.6	<222	-	<783	-	<2.2	<0.21	-	4.3	0.71	<0.65	<1.5	-	11.7	<2.7	<0.001	<0.001	0.01	97.1	106	3.2	<0.001	<0.001	<0.001
		Max.	77.0	892	719	-	1293	-	58.9	79.5	-	17.0	3.1	2.0	8.5	-	24.6	65.0	1.5	0.05	14.9	1150	2744	28.2	6.2	0.05	0.03
	H	**Mean (n=3)**	**22.3**	**776**	**998**	**<143**	**<12134**	**<0.94**	**6.5**	**0.44**	**<2.4**	**12.8**	**1.4**	**<1.1**	**<3.0**	**<5.2**	**16.9**	**89.9**	**2.0**	**0.02**	**0.18**	**266**	**1181**	**29.2**	**7.6**	**0.07**	**0.009**
		S.D.	7.5	493	1133	-	-	-	3.0	0.14	-	8.6	0.37	-	-	-	3.5	115	2.6	0.03	0.20	184	808	26.6	8.8	0.09	0.006
		Min.	15.7	87.1	160	-	-	-	<3.2	0.24	-	5.0	1.1	-	-	-	14.3	7.9	0.08	<0.001	0.02	125	217	9.0	0.16	0.001	<0.001
		Max.	32.8	1217	2601	-	-	-	10.6	0.24	-	24.7	1.9	-	-	-	21.8	252	5.6	0.06	0.46	526	2193	66.8	19.9	0.001	0.01

Table C3. Zoned hematite in RD2786A (SE-lobe)

Drillhole	U*	Sample	Y	La	Ce	Pr	Nd	Sm	Eu	Gd	Tb	Dy	Ho	Er	Tm	Yb	Lu	∑REY	W	^{204}Pb	^{206}Pb	^{207}Pb	^{208}Pb	Th	U
LCD04	**L**	**Mean (n=9)**	**0.02**	**0.46**	**0.59**	**0.03**	**0.09**	**0.06**	**0.01**	**0.07**	**0.01**	**0.007**	**0.007**	**0.02**	**0.004**	**0.03**	**0.007**	**1.4**	**5521**	**2.4**	**11.2**	**1.6**	**0.19**	**0.01**	**6.0**
		S.D.	0.009	0.58	0.75	0.04	0.06	0.03	0.006	0.06	0.008	0.01	0.006	0.02	0.005	0.02	0.005	1.4	2775	0.73	11.2	1.4	0.11	0.004	5.9
		Min.	<0.001	0.10	0.10	<0.001	<0.001	0.02	<0.001	<0.001	<0.001	0.001	<0.001	<0.001	<0.001	<0.001	<0.001	0.34	946	<1.5	0.44	0.17	<0.10	0.003	0.18
		Max.	0.02	2.1	2.7	0.14	0.21	0.06	0.01	0.02	0.003	0.001	0.003	0.01	0.008	0.04	0.01	5.3	8588	3.9	37.1	5.0	0.47	0.01	19.4
	M	**Mean (n=8)**	**0.09**	**2.4**	**4.7**	**0.29**	**0.56**	**0.07**	**0.02**	**0.08**	**0.01**	**0.03**	**0.009**	**0.03**	**0.01**	**0.06**	**0.02**	**8.4**	**6066**	**2.9**	**1510**	**180**	**0.86**	**0.04**	**811**
		S.D.	0.08	2.5	5.1	0.30	0.60	0.04	0.02	0.06	0.007	0.02	0.007	0.03	0.008	0.03	0.01	8.7	3499	1.1	796	95.7	1.2	0.04	463
		Min.	0.02	0.18	0.17	0.003	<0.001	0.02	<0.001	<0.001	<0.001	<0.001	<0.001	<0.001	<0.001	<0.001	0.005	0.76	690	<1.9	641	75.9	<0.11	0.004	295
		Max.	0.22	6.6	13.7	0.75	1.7	0.06	0.05	0.03	0.02	0.05	0.02	0.10	0.01	0.11	0.05	22.9	12792	5.7	2740	330	4.0	0.13	1512
	H	**Mean (n=3)**	**0.74**	**14.9**	**27.7**	**1.8**	**3.7**	**0.29**	**0.05**	**0.20**	**0.02**	**0.14**	**0.04**	**0.15**	**0.04**	**0.27**	**0.07**	**50.1**	**3601**	**2.9**	**10290**	**1207**	**0.62**	**0.63**	**5256**
		S.D.	0.75	12.5	22.6	1.5	3.1	0.24	0.02	0.15	0.01	0.14	0.04	0.15	0.05	0.29	0.08	41.6	1988	0.30	7795	910	0.55	0.68	3637
		Min.	0.21	5.5	10.5	0.57	1.4	0.12	0.03	0.03	<0.01	0.04	0.009	0.04	0.005	0.02	<0.01	18.7	2063	<2.6	4735	562	<0.17	0.12	2599
		Max.	1.8	32.6	59.7	3.9	8.1	0.63	0.08	0.40	0.04	0.35	0.10	0.36	0.11	0.67	0.18	109	6408	3.3	21314	2494	1.4	1.6	10399
MV025	**L**	**Mean (n=18)**	**0.09**	**1.5**	**2.3**	**0.14**	**0.33**	**0.03**	**0.009**	**0.02**	**0.003**	**0.02**	**0.006**	**0.03**	**0.008**	**0.10**	**0.03**	**4.7**	**8057**	**3.5**	**28.9**	**3.7**	**0.17**	**0.02**	**25.7**
		S.D.	0.11	2.4	4.1	0.24	0.55	0.06	0.02	0.03	0.003	0.02	0.007	0.03	0.008	0.09	0.02	7.5	2389	1.1	18.6	2.3	0.23	0.04	17.2
		Min.	0.005	0.002	0.002	<0.001	0.002	<0.001	<0.001	0.002	<0.001	<0.004	<0.001	0.001	<0.001	0.01	0.003	0.06	3355	1.5	4.7	0.69	<0.006	<0.001	4.3
		Max.	0.36	8.8	14.0	0.95	2.2	0.24	0.08	0.13	0.01	0.09	0.03	0.10	0.03	0.32	0.08	26.1	12051	4.6	71.1	8.7	0.83	0.14	63.1
	M	**Mean (n=21)**	**0.52**	**4.0**	**5.9**	**0.42**	**1.0**	**0.11**	**0.03**	**0.09**	**0.02**	**0.11**	**0.03**	**0.13**	**0.03**	**0.36**	**0.09**	**12.9**	**6033**	**7.3**	**889**	**108**	**0.51**	**0.11**	**696**
		S.D.	0.78	5.1	7.9	0.61	1.5	0.13	0.03	0.08	0.02	0.14	0.05	0.21	0.05	0.49	0.12	16.2	4158	2.7	641	77.7	1.0	0.33	476
		Min.	<0.02	0.04	0.03	0.003	0.02	<0.001	<0.001	<0.001	<0.001	<0.001	<0.001	0.008	<0.001	0.04	0.007	0.44	616	3.2	130	15.7	0.01	<0.001	123
		Max.	2.8	22.4	34.6	2.7	6.5	0.49	0.13	0.33	0.06	0.47	0.17	0.89	0.21	2.3	0.55	69.9	12869	10.6	2327	282	4.7	1.6	1748
	H	**Mean (n=5)**	**2.5**	**15.2**	**23.4**	**1.8**	**4.7**	**0.57**	**0.08**	**0.44**	**0.06**	**0.43**	**0.10**	**0.47**	**0.10**	**1.0**	**0.22**	**51.0**	**6372**	**<8.0**	**3715**	**448**	**0.20**	**0.33**	**2932**
		S.D.	2.3	15.6	24.6	1.9	5.0	0.61	0.08	0.42	0.06	0.44	0.11	0.43	0.08	0.75	0.10	52.4	2472	-	871	101	0.13	0.35	605
		Min.	0.14	0.85	0.99	0.04	0.08	<0.001	<0.001	0.02	0.005	0.03	0.005	0.06	0.02	0.27	0.14	2.9	3152	-	3069	373	<0.04	0.008	2480
		Max.	5.5	36.0	57.2	4.2	11.7	1.3	0.23	1.2	0.15	1.1	0.28	1.2	0.21	2.2	0.39	123	9216	-	5416	645	0.40	0.97	4132
LCD05	**L**	**Mean (n=16)**	**0.04**	**1.0**	**1.5**	**0.09**	**0.15**	**0.06**	**0.01**	**0.10**	**0.01**	**0.03**	**0.006**	**0.03**	**0.006**	**0.04**	**0.01**	**3.0**	**7347**	**2.5**	**51.9**	**6.8**	**0.64**	**0.42**	**26.5**
		S.D.	0.03	0.90	1.3	0.07	0.09	0.04	0.008	0.04	0.008	0.04	0.006	0.02	0.007	0.03	0.007	2.4	6177	0.53	55.4	6.9	0.85	1.3	28.6
		Min.	0.007	0.11	0.14	<0.01	<0.05	<0.001	<0.001	<0.001	<0.001	<0.001	<0.001	<0.001	<0.001	<0.001	<0.001	0.58	127	<1.6	0.92	<0.31	<0.11	<0.001	0.18
		Max.	0.15	3.2	4.8	0.23	0.42	0.07	0.02	0.12	0.02	0.02	0.01	0.07	0.005	0.10	0.03	9.0	18870	4.2	220	27.7	3.0	5.1	110
	M	**Mean (n=10)**	**0.40**	**3.2**	**5.1**	**0.28**	**0.63**	**0.06**	**0.02**	**0.07**	**0.02**	**0.07**	**0.02**	**0.10**	**0.03**	**0.24**	**0.05**	**10.3**	**7152**	**2.1**	**1083**	**130**	**2.1**	**3.8**	**572**
		S.D.	0.77	3.5	5.7	0.31	0.75	0.04	0.01	0.06	0.01	0.16	0.03	0.13	0.04	0.36	0.08	10.4	4923	0.49	685	81.3	2.7	7.5	373
		Min.	<0.001	0.30	0.32	<0.03	0.06	<0.001	0.006	<0.001	0.004	<0.001	<0.001	<0.001	<0.001	<0.001	<0.007	0.93	1734	<1.2	338	40.3	<0.15	0.004	175
		Max.	2.7	9.9	15.1	0.99	2.5	0.13	0.04	0.20	0.04	0.54	0.11	0.47	0.12	1.2	0.25	27.9	17131	2.8	2381	283	7.0	19.6	1292
	H	**Mean (n=3)**	**28.5**	**128**	**253**	**17.6**	**41.7**	**4.9**	**1.4**	**2.7**	**0.63**	**4.7**	**1.1**	**4.5**	**0.91**	**6.5**	**1.1**	**498**	**3465**	**2.7**	**3707**	**442**	**0.63**	**0.06**	**2109**
		S.D.	40.0	173	345	24.1	56.8	6.7	2.0	3.7	0.88	6.6	1.5	6.2	1.3	9.0	1.5	679	2355	1.0	931	109	0.29	0.02	410
		Min.	0.20	4.3	6.8	0.44	1.0	0.13	0.02	<0.05	0.005	0.05	0.01	<0.06	0.008	<0.05	0.03	13.5	1239	<1.5	2819	336	0.22	0.04	1817
		Max.	85.0	373	741	51.7	122	14.4	4.2	8.0	1.9	14.0	3.3	13.3	2.7	19.3	3.3	1458	6723	4.1	4994	592	0.85	0.08	2688

Table C3. (Continued) Zoned hematite in RD2786A (SE-lobe)

Drillhole	U*	Sample	Mg	Al	Si	P	Ca	Sc	Ti	V	Cr	Mn	Co	Ni	Cu	Zn	Ga	As	Sr	Zr	Nb	Mo	Sn	Sb	Ba	Hf	Ta
MV026	**L**	**Mean (n=15)**	**20.5**	**40.6**	**<743**	**76.4**	**<704**	**<0.77**	**23.5**	**0.27**	**5.4**	**11.6**	**2.1**	**1.2**	**<1.3**	**1.8**	**7.9**	**9.9**	**0.37**	**0.09**	**0.30**	**273**	**180**	**4.6**	**0.95**	**0.009**	**0.03**
		S.D.	9.1	15.6	-	3.1	-	-	72.4	0.17	0.47	4.7	0.78	0.34	-	0.37	0.82	17.4	0.61	0.05	0.61	237	104	5.9	1.1	0.03	0.09
		Min.	7.7	16.7	-	<70.0	-	-	2.4	<0.12	<4.5	5.5	0.92	<0.68	-	1.0	7.1	<0.54	<0.001	<0.001	<0.001	29.7	54.9	0.97	<0.001	<0.001	<0.001
		Max.	33.4	76.9	-	78.2	-	-	294	0.81	5.6	17.4	3.4	1.2	-	1.0	10.5	69.8	2.1	0.11	1.9	649	416	25.7	3.4	0.03	0.35
	M	**Mean (n=5)**	**29.4**	**74.5**	**<726**	**<77.8**	**<714**	**<0.75**	**16.4**	**0.39**	**<5.6**	**18.4**	**2.2**	**<1.4**	**1.9**	**3.0**	**7.9**	**10.7**	**2.5**	**0.04**	**0.87**	**156**	**305**	**4.2**	**13.4**	**0.02**	**0.005**
		S.D.	20.8	30.6	-	-	-	-	27.4	0.40	-	5.2	0.32	-	0.88	1.2	0.77	5.9	2.2	0.05	1.6	89.5	49.0	1.5	14.6	0.04	0.01
		Min.	13.1	53.5	-	-	-	-	<1.7	<0.14	-	13.4	1.8	-	<1.3	<1.9	7.1	1.8	0.56	<0.001	<0.001	63.7	217	2.2	1.3	0.001	<0.001
		Max.	69.9	133	-	-	-	-	71.3	1.2	-	28.0	2.7	-	3.7	5.4	8.8	19.5	6.6	0.14	4.0	266	352	6.3	41.9	0.001	0.03
LCD06	**L**	**Mean (n=31)**	**22.0**	**97.8**	**389**	**137**	**1141**	**0.79**	**13.8**	**0.67**	**2.5**	**8.1**	**1.3**	**1.2**	**2.9**	**5.1**	**9.8**	**7.5**	**0.42**	**0.05**	**1.9**	**103**	**717**	**6.0**	**1.9**	**0.02**	**0.03**
Sediments		**S.D.**	29.8	84.8	230	61.6	526	0.34	36.1	0.69	0.85	5.6	0.82	0.61	1.5	2.4	4.4	9.8	1.1	0.07	6.0	148	458	7.2	4.1	0.04	0.08
		Min.	<4.0	<13.9	<136	<17.8	<160	<0.16	<0.56	<0.04	<0.92	2.4	<0.29	<0.19	<0.37	<0.63	1.2	<0.14	<0.001	<0.001	<0.001	10.4	51.4	0.33	<0.001	<0.001	<0.001
		Max.	129	370	1174	19.8	1614	0.65	194	3.9	4.4	33.5	3.6	1.3	5.7	10.1	17.4	48.4	6.0	0.23	32.8	576	1880	41.0	21.0	0.11	0.48
	M	**Mean (n=11)**	**14.2**	**126**	**347**	**97.5**	**<826**	**0.63**	**16.8**	**2.0**	**<2.0**	**10.3**	**1.0**	**0.78**	**2.2**	**4.4**	**12.3**	**15.7**	**1.4**	**0.04**	**1.0**	**348**	**697**	**4.9**	**4.4**	**0.01**	**0.01**
		S.D.	8.8	71.9	216	73.9	-	0.42	27.4	3.1	-	4.8	0.35	0.48	1.5	2.5	5.7	19.8	1.8	0.06	2.0	228	459	4.6	5.1	0.04	0.02
		Min.	6.5	19.1	132	<16.6	-	<0.14	<0.56	<0.04	-	4.8	0.59	<0.15	<0.34	0.54	1.3	<0.22	0.007	<0.001	0.01	92.6	188	0.48	<0.001	<0.001	<0.001
		Max.	36.9	267	942	17.0	-	1.3	83.8	10.7	-	18.9	1.8	1.1	1.5	6.6	22.9	66.5	5.6	0.06	7.0	789	1452	18.3	16.1	0.01	0.06
	H		11.6	148	541	<162	<1403	<0.93	<4.5	<0.52	<2.8	10.2	1.4	<1.2	<3.5	<6.0	11.3	42.6	0.49	<0.16	0.02	288	2425	11.3	2.9	<0.001	<0.001
MV027	**L**	**Mean (n=17)**	**8.6**	**99.6**	**<761**	**<79.7**	**675**	**<0.78**	**5.3**	**0.74**	**5.5**	**6.2**	**0.95**	**1.2**	**1.5**	**2.0**	**7.6**	**11.1**	**0.53**	**0.06**	**1.8**	**81.5**	**213**	**2.0**	**5.6**	**0.009**	**0.02**
Sediments		**S.D.**	3.8	88.7	-	-	73.0	-	6.8	1.9	0.54	1.8	0.39	0.26	0.31	0.44	1.4	18.0	0.70	0.06	4.5	113	131	1.8	11.8	0.02	0.04
		Min.	3.3	22.8	-	-	<559	-	<2.3	<0.11	<4.8	2.8	0.36	0.69	<1.2	<1.2	3.7	<0.69	<0.001	<0.001	<0.001	3.1	51.0	0.37	<0.001	<0.001	<0.001
		Max.	15.9	337	-	-	634	-	31.1	8.2	5.3	10.2	1.7	0.69	2.7	3.2	10.7	68.0	2.2	0.17	19.0	373	541	6.9	41.0	0.06	0.18
	M		27.9	282	1674	<74.5	<694	<0.74	57.2	0.77	<5.7	8.4	2.2	<0.96	<1.6	<1.8	8.0	5.9	0.22	0.11	0.59	128	209	7.1	30.6	<0.001	0.009
	H		50.7	14.6	<744	71.5	<679	<0.72	<2.3	0.24	<5.1	4.1	1.6	<0.92	<1.4	<1.7	1.5	17.5	2.9	0.03	18.2	398	576	2.8	4.6	<0.001	0.008
LCD07	**L**	**Mean (n=7)**	**26.4**	**68.7**	**551**	**<385**	**<2659**	**<1.7**	**10.4**	**2.0**	**<5.3**	**14.5**	**2.8**	**<2.7**	**6.6**	**13.1**	**13.4**	**<9.3**	**0.28**	**0.09**	**0.48**	**477**	**938**	**4.8**	**2.9**	**0.10**	**0.03**
		S.D.	12.7	24.4	152	-	-	-	1.8	2.1	-	4.9	0.89	-	0.57	2.8	2.2	-	0.20	0.13	0.64	582	461	1.4	2.4	0.15	0.04
		Min.	8.8	38.8	<444	-	-	-	8.2	<0.97	-	6.9	1.1	-	<5.9	<9.9	10.6	-	0.06	<0.001	0.03	65.4	368	2.6	<0.001	0.001	<0.001
		Max.	47.6	102	912	-	-	-	14.0	7.1	-	20.8	4.4	-	6.6	19.6	18.2	-	0.72	0.12	1.8	1858	1649	6.8	7.6	0.001	0.10
	M	**Mean (n=3)**	**21.0**	**108**	**879**	**<408**	**<2836**	**<2.3**	**21.2**	**1.0**	**<5.6**	**13.7**	**2.2**	**2.7**	**<6.7**	**<13.9**	**19.8**	**33.2**	**1.5**	**0.04**	**0.61**	**1141**	**686**	**21.2**	**3.7**	**0.11**	**0.03**
		S.D.	3.1	98.1	529	-	-	-	10.3	0.09	-	2.2	0.05	0.45	-	-	3.9	32.8	1.9	0.06	0.68	816	310	20.5	3.2	0.16	0.04
		Min.	16.8	38.0	<502	-	-	-	<12.2	<0.92	-	10.9	2.1	2.2	-	-	14.3	<9.9	<0.18	<0.001	<0.08	203	249	5.7	1.2	0.001	0.001
		Max.	24.2	247	1627	-	-	-	35.6	1.2	-	16.3	2.2	2.2	-	-	23.4	79.6	4.2	0.13	1.6	2192	927	50.2	8.2	0.001	0.001
	H		50.7	14.6	<744	71.5	<679	<0.72	<2.3	0.24	<5.1	4.1	1.6	<0.92	<1.4	<1.7	1.5	17.5	2.9	0.03	18.2	398	576	2.8	4.6	<0.001	0.008
MV031	**L**	**Mean (n=23)**	**16.6**	**161**	**148**	**6.8**	**43.0**	**0.55**	**5.3**	**2.6**	**0.16**	**10.3**	**1.5**	**0.13**	**0.15**	**0.94**	**7.2**	**8.4**	**0.78**	**0.02**	**2.2**	**81.7**	**315**	**2.1**	**2.3**	**0.004**	**0.006**
		S.D.	5.6	73.3	101	3.4	33.7	0.95	11.2	1.3	0.04	2.3	0.57	0.08	0.12	0.60	1.1	8.4	0.79	0.04	3.5	58.7	156	0.64	2.6	0.003	0.01
		Min.	6.5	92.3	45.5	<2.8	<17.4	<0.03	0.22	1.1	0.13	6.7	0.44	<0.04	<0.06	0.22	6.2	0.47	0.006	<0.001	0.07	14.8	164	1.3	0.03	<0.001	<0.001
		Max.	26.7	367	424	16.0	121	3.4	46.2	6.0	0.31	14.3	2.4	0.34	0.58	2.2	11.4	26.3	2.8	0.14	12.9	204	682	3.7	9.8	0.01	0.04
	M	**Mean (n=3)**	**43.9**	**341**	**513**	**4.5**	**31.7**	**1.7**	**15.0**	**4.3**	**0.16**	**12.3**	**0.67**	**0.19**	**0.32**	**1.3**	**8.7**	**23.2**	**2.2**	**0.24**	**9.2**	**50.7**	**679**	**3.3**	**7.2**	**0.02**	**0.01**
		S.D.	53.3	91.2	176	1.4	9.5	0.22	3.1	0.15	0.001	5.5	0.06	0.08	0.12	0.33	0.42	6.6	0.74	0.06	2.4	14.2	106	1.0	2.3	0.002	0.005
		Min.	6.0	214	290	<2.5	23.8	1.4	12.5	4.1	<0.16	6.5	0.60	0.08	0.19	0.83	8.2	14.0	1.1	0.16	6.3	39.3	564	1.8	4.0	0.02	0.007
		Max.	119	424	720	5.8	45.1	2.0	19.4	4.4	0.16	19.6	0.75	0.26	0.48	1.6	9.2	28.2	2.7	0.30	12.1	70.7	819	4.2	9.1	0.02	0.02

Table C4. Zoned hematite in RD2786A (SE-lobe)

Drillhole	U*	Sample	Y	La	Ce	Pr	Nd	Sm	Eu	Gd	Tb	Dy	Ho	Er	Tm	Yb	Lu	∑REY	W	^{204}Pb	^{206}Pb	^{207}Pb	^{208}Pb	Th	U
MV026	**L**	**Mean (n=15)**	**0.13**	**1.3**	**1.5**	**0.10**	**0.20**	**0.03**	**0.02**	**0.08**	**0.005**	**0.04**	**0.007**	**0.03**	**0.007**	**0.10**	**0.02**	**3.6**	**7679**	**8.6**	**37.5**	**5.1**	**0.44**	**0.02**	**27.1**
		S.D.	0.26	1.2	1.5	0.09	0.22	0.03	0.009	0.04	0.005	0.03	0.006	0.03	0.006	0.06	0.01	2.9	4209	1.6	40.6	5.4	0.71	0.04	27.2
		Min.	0.02	0.008	0.008	<0.001	<0.001	<0.001	0.006	<0.001	<0.001	<0.001	<0.001	<0.001	<0.001	0.01	0.008	0.24	862	<4.9	0.23	0.04	0.04	<0.001	0.20
		Max.	1.0	3.2	5.0	0.34	0.78	0.09	0.02	0.13	0.009	0.13	0.02	0.10	0.02	0.21	0.05	9.8	12107	8.1	139	19.2	2.4	0.14	88.4
	M	**Mean (n=5)**	**0.24**	**6.7**	**7.1**	**0.39**	**0.75**	**0.12**	**0.03**	**0.08**	**0.01**	**0.07**	**0.01**	**0.07**	**0.01**	**0.12**	**0.02**	**15.8**	**7832**	**<9.0**	**447**	**55.9**	**0.93**	**0.001**	**346**
		S.D.	0.19	10.0	10.0	0.51	0.85	0.15	0.004	0.001	0.002	0.06	0.007	0.05	0.003	0.08	0.009	21.8	1224	-	148	17.8	0.63	0.001	126
		Min.	0.06	0.49	0.69	0.05	<0.10	0.04	<0.02	0.08	<0.01	0.01	0.003	0.009	<0.01	0.03	0.02	1.7	6014	-	319	39.9	0.31	0.001	230
		Max.	0.48	26.7	27.0	1.4	2.4	0.41	0.03	0.08	0.01	0.15	0.02	0.17	0.02	0.26	0.04	59.2	9510	-	733	90.0	1.7	0.001	586
LCD06	**L**	**Mean (n=31)**	**0.05**	**1.0**	**1.6**	**0.11**	**0.29**	**0.05**	**0.01**	**0.08**	**0.008**	**0.02**	**0.005**	**0.03**	**0.007**	**0.04**	**0.01**	**3.4**	**5652**	**2.8**	**64.4**	**8.3**	**3.4**	**0.01**	**36.5**
Sediments		**S.D.**	0.06	0.88	1.7	0.11	0.26	0.04	0.01	0.06	0.007	0.02	0.006	0.02	0.007	0.04	0.009	3.0	3591	0.76	60.3	7.6	14.4	0.01	32.5
		Min.	<0.001	0.01	0.02	0.001	0.004	<0.001	<0.001	<0.001	<0.001	<0.001	<0.001	<0.001	<0.001	<0.001	<0.001	0.14	336	<1.2	0.85	0.19	0.01	<0.001	0.57
		Max.	0.28	3.9	8.0	0.57	1.2	0.09	0.03	0.15	0.01	0.05	0.02	0.07	0.02	0.19	0.05	14.3	16089	4.6	228	27.4	81.5	0.07	103
	M	**Mean (n=11)**	**1.7**	**2.1**	**4.1**	**0.39**	**1.3**	**0.24**	**0.13**	**0.25**	**0.06**	**0.47**	**0.10**	**0.43**	**0.08**	**0.77**	**0.10**	**12.2**	**7261**	**3.0**	**760**	**91.7**	**1.1**	**0.14**	**527**
		S.D.	4.8	2.2	6.4	0.74	2.7	0.60	0.37	0.56	0.17	1.4	0.29	1.2	0.23	2.1	0.22	23.8	2195	1.0	433	51.7	1.7	0.27	372
		Min.	0.01	0.11	0.11	0.01	0.04	<0.001	<0.001	<0.001	<0.001	<0.001	<0.001	<0.001	<0.001	0.02	0.006	0.40	3843	<2.0	208	28.6	<0.02	<0.001	203
		Max.	16.9	8.2	23.7	2.7	9.7	2.2	1.3	2.0	0.59	4.9	1.0	4.3	0.81	7.4	0.79	86.5	11657	5.8	1747	209	5.6	0.92	1369
	H		0.14	7.4	15.8	1.0	2.2	0.03	<0.02	0.10	0.01	<0.001	0.01	0.09	<0.01	<0.001	0.005	53.9	8563	<2.5	5288	623	0.25	0.03	2760
MV027	**L**	**Mean (n=17)**	**0.07**	**0.42**	**0.58**	**0.04**	**0.11**	**0.05**	**0.02**	**0.09**	**0.008**	**0.01**	**0.006**	**0.01**	**0.003**	**0.03**	**0.007**	**1.5**	**4196**	**9.6**	**15.5**	**2.4**	**0.57**	**0.07**	**11.4**
Sediments		**S.D.**	0.11	0.57	0.87	0.05	0.18	0.05	0.01	0.05	0.005	0.02	0.006	0.01	0.004	0.03	0.005	1.8	3250	1.7	19.4	2.6	1.0	0.24	15.0
		Min.	<0.001	<0.001	0.004	<0.001	<0.001	<0.001	<0.001	<0.001	<0.001	<0.001	<0.001	<0.001	<0.001	<0.001	<0.001	0.07	175	<6.6	0.25	0.02	<0.03	<0.001	0.22
		Max.	0.42	2.0	3.3	0.19	0.66	0.11	0.03	0.11	0.009	0.06	0.02	0.02	0.005	0.09	0.01	6.9	12438	8.5	74.3	9.0	4.2	1.0	57.6
	M		0.09	4.5	6.0	0.42	0.88	0.05	<0.02	<0.15	<0.001	<0.05	<0.001	<0.04	0.009	0.08	0.03	24.3	2471	<10.2	146	18.1	0.33	0.06	132
	H		0.76	17.9	30.4	2.4	5.6	0.44	0.09	0.30	0.03	0.25	0.04	0.12	0.03	0.24	0.04	117	2726	<10.9	1693	217	1.5	0.45	1297
LCD07	**L**	**Mean (n=7)**	**0.06**	**3.7**	**5.8**	**0.33**	**0.66**	**0.10**	**0.02**	**0.20**	**0.02**	**0.03**	**0.02**	**0.04**	**0.02**	**0.07**	**0.02**	**11.1**	**13196**	**4.4**	**71.3**	**8.0**	**0.56**	**0.12**	**32.1**
		S.D.	0.03	1.2	1.6	0.06	0.24	0.08	0.02	0.07	0.01	0.04	0.01	0.06	0.01	0.07	0.02	3.1	5687	0.47	41.2	4.5	0.30	0.11	19.4
		Min.	<0.001	1.9	3.0	0.25	0.35	<0.001	<0.001	0.07	0.01	<0.001	<0.001	<0.001	<0.001	<0.001	<0.001	6.2	6380	<3.7	36.2	4.0	<0.35	0.01	14.8
		Max.	0.09	5.3	8.0	0.40	1.1	0.07	0.04	0.07	0.01	0.04	0.01	0.04	0.02	0.09	0.02	15.0	24037	4.8	164	18.2	1.1	0.30	75.1
	M	**Mean (n=3)**	**0.08**	**4.6**	**10.1**	**0.34**	**0.66**	**0.11**	**0.03**	**0.14**	**0.005**	**0.001**	**0.04**	**0.07**	**0.01**	**0.18**	**0.02**	**16.3**	**10481**	**5.1**	**736**	**82.7**	**0.52**	**0.52**	**226**
		S.D.	0.01	1.2	3.9	0.12	0.37	0.04	0.009	0.14	0.005	0.001	0.006	0.03	0.01	0.03	0.01	5.6	2610	1.0	241	26.8	0.20	0.64	78.8
		Min.	0.001	3.4	6.2	0.22	0.29	0.07	0.02	0.001	<0.001	0.001	0.001	0.04	<0.001	<0.14	0.01	10.8	7583	<4.2	538	60.0	<0.36	<0.04	159
		Max.	0.001	5.7	14.0	0.45	1.0	0.15	0.04	0.001	0.01	0.001	0.001	0.04	0.02	0.21	0.01	21.9	13909	6.6	1075	120	0.80	1.4	337
	H		0.76	17.9	30.4	2.4	5.6	0.44	0.09	0.30	0.03	0.25	0.04	0.12	0.03	0.24	0.04	117	2726	<10.9	1693	217	1.5	0.45	1297
MV031	**L**	**Mean (n=23)**	**0.07**	**1.3**	**1.8**	**0.11**	**0.23**	**0.02**	**0.01**	**0.01**	**0.002**	**0.01**	**0.003**	**0.01**	**0.004**	**0.05**	**0.02**	**3.6**	**4284**	**3.6**	**35.0**	**4.9**	**0.67**	**0.09**	**30.4**
		S.D.	0.05	1.9	2.7	0.16	0.29	0.02	0.02	0.009	0.001	0.007	0.002	0.009	0.002	0.03	0.009	5.1	1641	1.0	36.8	4.6	0.53	0.11	32.6
		Min.	0.008	0.005	0.005	0.001	0.002	0.002	0.001	0.002	<0.001	0.001	0.001	0.004	<0.001	0.02	0.004	0.13	1763	2.0	2.3	0.71	0.05	0.001	1.4
		Max.	0.23	9.1	12.0	0.68	1.2	0.09	0.08	0.04	0.005	0.03	0.008	0.04	0.01	0.15	0.04	23.4	6391	7.0	138	17.6	2.2	0.39	122
	M	**Mean (n=3)**	**0.10**	**3.7**	**6.3**	**0.40**	**0.75**	**0.07**	**0.04**	**0.03**	**0.004**	**0.03**	**0.007**	**0.03**	**0.004**	**0.03**	**0.009**	**11.5**	**6067**	**2.9**	**196**	**24.8**	**0.54**	**0.003**	**190**
		S.D.	0.04	1.2	2.0	0.13	0.30	0.03	0.009	0.01	0.002	0.01	0.003	0.007	0.002	0.01	0.003	3.7	1052	0.13	42.2	5.3	0.19	0.001	43.8
		Min.	0.05	2.1	3.6	0.22	0.35	0.02	0.03	0.02	0.002	0.01	0.003	0.02	0.001	0.02	0.005	6.4	4755	2.8	138	17.6	0.27	0.002	132
		Max.	0.14	4.7	8.3	0.53	1.1	0.09	0.05	0.04	0.006	0.04	0.009	0.03	0.006	0.05	0.01	15.1	7331	3.1	237	30.2	0.70	0.005	237

Table C4. (Continued) Zoned hematite in RD2786A (SE-lobe)

Drillhole	U*	Sample	Mg	Al	Si	P	Ca	Sc	Ti	V	Cr	Mn	Co	Ni	Cu	Zn	Ga	As	Sr	Zr	Nb	Mo	Sn	Sb	Ba	Hf	Ta
MV032	**L**	**Mean (n=17)**	**20.3**	**115**	**76.6**	**5.5**	**23.0**	**0.20**	**1.1**	**1.8**	**0.16**	**11.6**	**1.7**	**0.20**	**0.09**	**0.52**	**6.7**	**0.62**	**0.05**	**0.03**	**4.1**	**142**	**477**	**1.1**	**0.54**	**0.003**	**0.01**
		S.D.	6.6	31.7	22.1	2.2	8.2	0.12	1.1	1.8	0.03	4.5	0.39	0.09	0.10	0.21	1.5	0.84	0.12	0.03	5.0	75.5	369	0.28	1.8	0.003	0.01
		Min.	6.6	48.9	41.4	<1.8	<13.2	<0.03	0.16	0.03	<0.12	3.3	0.94	<0.03	<0.05	0.11	3.0	<0.14	<0.001	<0.003	0.01	54.7	40.8	0.67	<0.001	<0.001	<0.001
		Max.	31.3	154	130	9.4	47.2	0.41	3.7	4.5	0.24	18.0	2.5	0.39	0.49	0.91	8.1	3.4	0.46	0.10	16.7	317	1038	1.5	7.8	0.01	0.04
	M	**Mean (n=6)**	**12.2**	**469**	**199**	**5.1**	**26.1**	**0.12**	**0.28**	**0.23**	**0.14**	**5.6**	**0.91**	**0.16**	**<0.06**	**0.44**	**6.6**	**5.3**	**0.16**	**0.005**	**0.04**	**208**	**306**	**1.6**	**0.62**	**0.001**	**0.001**
		S.D.	3.7	383	137	1.8	11.7	0.05	0.06	0.13	0.01	2.4	0.35	0.06	-	0.45	2.3	5.3	0.12	0.004	0.02	209	119	0.66	0.47	0.002	0.001
		Min.	6.3	66.5	53.4	2.9	<19.2	0.04	<0.21	0.06	<0.12	3.4	0.58	<0.04	-	<0.13	3.1	<0.16	0.007	<0.001	0.02	20.2	112	0.96	0.01	0.001	<0.001
		Max.	18.0	934	397	7.7	52.1	0.17	0.36	0.38	0.15	10.7	1.5	0.21	-	1.4	8.8	12.4	0.32	0.01	0.06	614	439	2.8	1.2	0.001	0.001
	H		14.0	189	170	4.7	<20.3	<0.03	<0.23	0.07	0.16	8.5	1.2	0.20	<0.07	0.24	8.6	5.5	0.14	<0.001	0.02	222	543	2.1	0.48	<0.001	0.001
MV034	**L**	**Mean (n=13)**	**27.1**	**79.4**	**114**	**9.9**	**31.4**	**3.8**	**14.1**	**8.9**	**3.9**	**16.4**	**5.6**	**4.1**	**4.2**	**4.7**	**6.7**	**8.3**	**5.3**	**4.3**	**22.2**	**83.1**	**422**	**7.3**	**8.6**	**4.7**	**4.9**
		S.D.	6.6	46.2	69.4	9.5	18.9	11.2	15.7	10.6	12.1	17.7	12.2	12.9	13.1	13.3	13.0	13.3	14.1	14.5	14.6	50.5	120	14.9	17.0	16.2	16.4
		Min.	17.9	32.0	39.7	<1.9	<12.6	0.18	1.4	2.3	0.11	4.7	1.1	0.11	<0.05	0.26	2.1	0.80	0.05	<0.001	6.2	12.5	57.7	1.8	<0.001	<0.001	0.002
		Max.	40.1	208	314	40.7	82.4	42.7	44.1	44.7	45.7	64.7	47.7	48.7	49.7	50.7	51.7	52.7	53.7	54.7	55.7	191	556	58.7	59.7	60.7	61.7
MV028	**L**	**Mean (n=21)**	**10.9**	**63.1**	**663**	**69.0**	**562**	**0.70**	**22.5**	**0.58**	**5.0**	**8.8**	**1.3**	**1.1**	**1.5**	**1.9**	**6.4**	**1.8**	**0.28**	**0.05**	**7.9**	**82.0**	**250**	**1.3**	**0.96**	**0.003**	**0.02**
		S.D.	6.6	33.6	241	25.1	225	0.28	65.0	0.42	2.0	5.2	0.45	0.50	0.53	0.63	0.71	2.4	0.84	0.07	15.4	93.8	138	0.53	2.4	0.008	0.06
		Min.	3.6	23.0	52.0	7.1	<14.5	0.03	0.19	<0.12	<0.14	3.7	0.49	0.17	<0.05	0.46	4.8	<0.63	<0.001	<0.001	0.01	8.1	36.3	0.58	<0.001	<0.001	<0.001
		Max.	27.4	128	798	9.7	75.6	0.04	287	1.4	6.7	26.5	2.1	1.4	3.0	2.9	7.4	11.6	4.0	0.24	62.7	319	567	2.8	10.6	0.03	0.25
	M	**Mean (n=10)**	**15.6**	**227**	**222**	**19.2**	**133**	**0.19**	**0.94**	**0.38**	**1.2**	**9.9**	**1.5**	**0.33**	**0.41**	**0.88**	**6.8**	**1.0**	**0.24**	**0.007**	**0.17**	**142**	**399**	**1.4**	**0.44**	**0.002**	**0.001**
		S.D.	5.3	170	258	27.6	219	0.30	0.98	0.13	2.1	3.5	0.36	0.35	0.59	0.64	0.75	1.0	0.35	0.01	0.25	73.5	104	0.30	0.55	0.002	0.001
		Min.	6.3	81.9	45.4	3.2	<18.9	<0.03	0.20	<0.13	<0.14	3.4	0.72	0.09	<0.06	0.32	6.1	<0.12	<0.001	<0.001	0.02	41.0	143	1.1	<0.001	<0.001	<0.001
		Max.	26.2	536	160	6.8	31.4	0.14	1.8	0.62	0.30	15.8	2.2	0.28	0.39	1.0	8.2	3.1	1.1	0.04	0.71	296	505	2.2	1.3	0.005	0.001
	H	**Mean (n=2)**	**14.2**	**335**	**97.8**	**5.0**	**31.1**	**<0.03**	**0.56**	**0.50**	**0.18**	**8.3**	**1.4**	**0.27**	**1.2**	**0.72**	**6.5**	**1.5**	**0.34**	**0.003**	**0.04**	**80.3**	**742**	**1.2**	**0.55**	**0.005**	**0.001**
		S.D.	1.0	30.6	11.6	1.1	5.3	-	0.35	0.06	0.008	0.27	0.06	0.07	1.1	0.03	0.16	1.2	0.34	0.003	0.04	20.5	103	0.05	0.50	0.002	0.001
		Min.	13.1	304	86.2	3.9	25.8	-	<0.22	0.44	0.18	8.1	1.4	0.19	0.14	0.69	6.4	<0.22	<0.004	0.001	0.008	59.8	639	1.1	0.06	0.002	<0.001
		Max.	15.2	365	109	6.1	36.4	-	0.91	0.56	0.19	8.6	1.5	0.34	2.3	0.74	6.7	2.7	0.68	0.001	0.08	101	845	1.2	1.0	0.002	0.002
LCD09	**L**	**Mean (n=17)**	**15.3**	**109**	**387**	**168**	**<1355**	**<0.96**	**20.3**	**4.7**	**2.7**	**9.2**	**1.6**	**1.3**	**3.6**	**6.0**	**11.7**	**14.2**	**0.25**	**0.06**	**20.4**	**157**	**872**	**12.9**	**1.2**	**0.02**	**0.05**
Sediments		**S.D.**	8.5	54.3	114	27.7	-	-	29.2	7.3	0.46	4.5	0.73	0.35	1.3	0.70	7.0	20.0	0.24	0.12	48.3	262	507	14.3	1.5	0.05	0.05
		Min.	<2.9	<13.4	<202	<130	-	-	<3.0	<0.33	<2.0	2.4	0.36	<0.55	<1.8	<4.6	1.5	<2.8	<0.06	<0.001	<0.001	0.71	66.4	1.8	<0.001	<0.001	<0.001
		Max.	38.4	206	590	261	-	-	105	25.9	3.9	19.1	3.5	1.4	7.8	6.2	37.3	79.4	0.87	0.48	200	1002	1730	59.3	5.0	0.11	0.18
	M		11.5	154	508	<159	<1446	<1.1	<7.0	1.1	<2.7	10.6	1.0	<1.8	<3.7	5.4	11.0	<4.0	0.59	<0.16	0.35	32.2	2360	4.2	0.81	<0.001	<0.001

Table C5. Zoned hematite in RD2852A (SE-lobe)

Drillhole	U*	Sample	Mg	Al	Si	P	Ca	Sc	Ti	V	Cr	Mn	Co	Ni	Cu	Zn	Ga	As	Sr	Zr	Nb	Mo	Sn	Sb	Ba	Hf	Ta
RD2852A																											
RX6581	**L**	**Mean (n=12)**	**21.0**	**65.8**	**371**	**<174**	**1551**	**0.91**	**9.9**	**0.74**	**<3.2**	**12.6**	**2.2**	**1.5**	**6.2**	**<10.2**	**13.6**	**<7.7**	**0.17**	**0.09**	**0.14**	**377**	**1057**	**6.6**	**0.47**	**0.02**	**0.01**
		S.D.	8.3	27.5	116	-	79.6	0.08	12.3	0.46	-	5.2	1.0	0.30	2.1	-	3.1	-	0.25	0.08	0.18	216	1377	3.2	0.70	0.06	0.02
		Min.	4.1	18.5	<265	-	<1423	0.70	<4.2	<0.45	-	4.2	0.67	1.1	<4.4	-	10.1	-	<0.001	<0.001	0.01	61.1	54.5	<1.6	<0.001	<0.001	<0.001
		Max.	32.7	101	588	-	1464	0.70	50.6	1.9	-	22.7	3.6	1.9	12.5	-	20.9	-	0.94	0.05	0.62	760	4272	12.0	2.6	0.05	0.03
	M	**Mean (n=5)**	**34.3**	**417**	**705**	**<177**	**<1542**	**<0.93**	**<6.4**	**0.49**	**<3.3**	**12.5**	**1.8**	**<1.5**	**8.1**	**14.1**	**18.2**	**40.7**	**21.3**	**0.02**	**0.11**	**211**	**1261**	**21.8**	**5.2**	**0.001**	**0.003**
		S.D.	32.0	144	486	-	-	-	-	0.04	-	7.1	1.1	-	2.4	4.9	5.6	35.0	41.7	0.04	0.17	156	336	9.6	5.8	0.001	0.005
		Min.	13.4	248	<267	-	-	-	-	<0.44	-	5.1	0.45	-	<4.9	<10.4	13.7	<7.8	0.06	<0.001	<0.001	83.2	969	9.6	<0.001	0.001	<0.001
		Max.	97.8	608	1407	-		-	-	0.47	-	24.8	3.6	-	11.3	23.3	29.1	86.6	105	0.10	0.44	512	1910	32.4	15.9	0.001	0.01
RX6583	**L**	**Mean (n=4)**	**45.4**	**140**	**728**	**<179**	**1595**	**1.2**	**12.5**	**2.5**	**3.4**	**16.4**	**1.8**	**<1.5**	**19.6**	**15.0**	**7.8**	**26.1**	**2.3**	**0.03**	**1.6**	**172**	**2275**	**44.7**	**7.3**	**0.01**	**0.02**
		S.D.	24.9	192	565	-	171	0.36	4.1	2.0	0.27	15.0	0.59	-	23.9	7.0	6.9	31.3	3.8	0.05	1.8	135	1805	14.0	11.4	0.02	0.02
		Min.	8.2	<11.7	<267	-	<1406	<0.80	<7.1	<0.54	<3.0	5.0	0.80	-	<4.1	<9.9	1.8	<7.6	<0.09	<0.001	<0.001	72.2	257	23.4	<0.001	<0.001	<0.001
		Max.	78.0	470	1696	-	1871	1.8	18.5	5.2	3.7	42.3	2.3	-	60.9	27.1	19.0	80.2	8.8	0.11	4.5	401	4132	61.9	27.0	0.05	0.01
	M	**Mean (n=19)**	**52.9**	**71.0**	**443**	**<174**	**<1460**	**0.93**	**18.6**	**2.2**	**3.2**	**9.6**	**2.4**	**<1.6**	**18.9**	**21.9**	**6.4**	**34.6**	**1.6**	**0.05**	**2.4**	**475**	**2054**	**288**	**8.8**	**0.03**	**0.02**
		S.D.	43.2	66.0	250	-	-	0.12	30.5	2.2	0.14	5.1	0.85	-	27.2	44.8	5.0	50.2	2.7	0.09	4.8	282	1042	754	15.5	0.05	0.02
		Min.	4.7	<11.5	<262	-	-	<0.67	<4.8	<0.42	<2.9	<2.3	0.66	-	<4.2	<8.6	0.64	<7.2	<0.001	<0.001	0.02	44.5	496	<7.4	<0.001	<0.001	<0.001
		Max.	199	260	1216	-	-	1.0	137	7.8	3.4	23.1	3.7	-	113	212	22.0	182	9.4	0.33	18.7	987	4258	2975	50.3	0.05	0.05
	H		24.7	72.2	276	<166	<1449	<0.99	<5.5	3.1	<3.2	8.9	2.3	<2.1	5.6	17.2	6.2	<7.8	<0.08	<0.15	0.35	1054	2405	18.4	<0.001	<0.14	<0.04
RX6584	**L**		140	37.5	2009	<189	<1404	<0.96	<6.3	<0.53	<3.4	7.3	2.8	<2.0	<5.0	<10.9	5.4	<8.9	<0.13	<0.001	0.02	504	862	20.7	<0.83	<0.001	<0.001
	M	**Mean (n=17)**	**41.1**	**468**	**2647**	**197**	**1656**	**1.0**	**45.8**	**2.0**	**<3.6**	**23.6**	**1.4**	**1.9**	**84.0**	**14.7**	**20.3**	**231**	**5.7**	**0.02**	**5.8**	**353**	**882**	**218**	**25.1**	**0.006**	**0.04**
		S.D.	60.9	252	1460	37.2	129	0.13	74.7	3.5	-	7.3	0.85	0.51	63.7	5.0	6.5	170	3.2	0.05	9.7	161	354	263	11.6	0.02	0.04
		Min.	5.2	28.5	300	<157	<1394	<0.76	<5.5	<0.53	-	10.3	0.53	1.2	<4.7	<10.7	5.9	9.8	<0.12	<0.001	0.02	188	280	11.5	<0.001	<0.001	<0.001
		Max.	246	847	4948	335	1966	1.1	317	12.8	-	33.6	3.5	1.7	192	31.0	28.2	794	15.3	0.10	39.4	706	1440	889	43.4	0.05	0.16
	H	**Mean (n=2)**	**74.8**	**222**	**586**	**340**	**<1583**	**1.4**	**39.1**	**9.0**	**<3.4**	**13.8**	**3.8**	**2.0**	**69.7**	**<11.5**	**6.1**	**294**	**12.1**	**0.08**	**5.9**	**758**	**1539**	**885**	**14.0**	**0.09**	**0.007**
		S.D.	29.4	206	311	171	-	0.52	31.6	8.5	-	6.6	0.33	0.66	65.1	-	2.3	285	12.0	0.08	5.9	259	239	808	13.8	0.04	0.007
		Min.	45.4	15.9	<275	<169	-	<0.86	<7.5	<0.53	-	7.2	3.4	<1.4	<4.5	-	3.8	<8.6	0.06	0.001	<0.001	499	1300	77.8	0.28	0.05	<0.001
		Max.	104	428	897	511	-	1.9	70.8	17.5	-	20.3	4.1	2.7	135	-	8.3	579	24.1	0.001	11.8	1017	1779	1693	27.8	0.05	0.01
RX6585	**L**	**Mean (n=6)**	**48.5**	**246**	**1613**	**263**	**<1799**	**<1.2**	**73.1**	**7.2**	**4.0**	**28.0**	**18.4**	**8.7**	**145**	**25.5**	**32.4**	**1169**	**10.5**	**0.05**	**2.0**	**250**	**855**	**318**	**77.4**	**0.03**	**0.03**
		S.D.	50.7	241	1866	106	-	-	97.6	9.5	0.44	32.8	24.6	9.6	161	22.2	19.2	1621	14.9	0.07	2.8	291	537	430	121	0.07	0.03
		Min.	7.5	50.4	<289	<186	-	-	<5.9	<0.55	<3.5	2.7	0.52	1.6	<4.9	<9.8	12.9	<8.1	0.03	<0.001	<0.001	6.7	137	5.2	<0.001	0.001	<0.001
		Max.	120	617	4278	463	-	-	254	22.6	4.7	85.4	53.2	22.6	387	68.2	59.3	3597	38.3	0.07	6.8	667	1604	936	324	0.001	0.07
	M	**Mean (n=7)**	**63.1**	**423**	**2550**	**213**	**1781**	**1.1**	**83.2**	**1.0**	**<3.8**	**25.5**	**2.0**	**1.7**	**94.0**	**21.8**	**18.1**	**265**	**7.9**	**0.03**	**4.4**	**593**	**1183**	**113**	**29.9**	**0.007**	**0.04**
		S.D.	41.3	420	2602	20.5	112	0.20	109	1.0	-	25.2	0.75	0.42	106	7.8	12.1	201	6.4	0.06	6.8	379	313	102	25.6	0.02	0.03
		Min.	14.8	49.4	<293	<191	1646	<0.82	<7.3	<0.56	-	2.9	0.79	<1.2	<4.9	<10.4	4.0	<8.8	0.07	<0.001	0.03	258	757	9.0	<0.001	<0.001	<0.001
		Max.	118	991	6533	258	1646	1.4	341	3.5	-	71.3	2.9	2.4	283	33.5	35.5	534	17.1	0.06	20.9	1234	1787	338	63.8	0.05	0.09
	H	**Mean (n=2)**	**87.9**	**142**	**707**	**<190**	**<1641**	**<1.0**	**63.3**	**1.6**	**<3.6**	**6.0**	**1.5**	**2.3**	**18.9**	**<10.7**	**5.0**	**205**	**4.5**	**0.001**	**20.8**	**848**	**2131**	**134**	**4.0**	**0.001**	**0.07**
		S.D.	4.7	92.2	0.96	-	-	-	4.1	0.98	-	0.78	0.60	0.54	0.55	-	0.23	55.1	3.7	0.001	19.2	591	617	9.1	1.5	0.001	0.02
		Min.	83.2	49.6	706	-	-	-	59.2	<0.57	-	5.2	0.91	<1.7	18.3	-	4.8	150	0.79	0.001	1.6	257	1515	125	2.5	0.001	<0.04
		Max.	92.6	234	708	-	-	-	67.5	2.5	-	6.8	2.1	2.8	19.4	-	5.2	260	8.3	0.001	39.9	1439	2748	143	5.5	0.001	0.09

Table C5. (continued) Zoned hematite in RD2852A (SE-lobe)

Drillhole	U*	Sample	Y	La	Ce	Pr	Nd	Sm	Eu	Gd	Tb	Dy	Ho	Er	Tm	Yb	Lu	∑REY	W	204Pb	206Pb	207Pb	208Pb	Th	U
RD2852A																									
RX6581	**L**	**Mean (n=12)**	**0.02**	**0.62**	**0.97**	**0.05**	**0.13**	**0.04**	**0.01**	**0.06**	**0.008**	**0.02**	**0.006**	**0.02**	**0.005**	**0.04**	**0.009**	**2.0**	**13407**	**4.2**	**56.7**	**7.4**	**0.57**	**0.009**	**23.7**
		S.D.	0.01	0.64	1.1	0.05	0.14	0.04	0.01	0.04	0.008	0.03	0.006	0.02	0.006	0.02	0.006	1.9	8312	1.1	56.3	6.6	0.26	0.007	20.6
		Min.	<0.001	0.01	<0.01	0.004	<0.001	<0.001	<0.001	<0.001	<0.001	<0.001	<0.001	<0.001	<0.001	<0.001	<0.001	0.27	1107	<3.3	0.71	<0.47	<0.29	<0.001	0.24
		Max.	0.03	2.0	3.6	0.17	0.51	0.03	0.02	0.06	0.009	0.02	0.009	0.01	0.005	0.04	0.01	6.4	23609	7.3	184	22.2	1.3	0.005	66.1
	M	**Mean (n=5)**	**0.14**	**9.9**	**22.0**	**1.2**	**2.0**	**0.21**	**0.03**	**0.12**	**0.01**	**0.05**	**0.006**	**0.04**	**0.008**	**0.03**	**0.02**	**35.8**	**9979**	**4.0**	**1252**	**154**	**0.72**	**0.02**	**659**
		S.D.	0.09	6.7	15.2	0.96	1.5	0.10	0.009	0.03	0.006	0.01	0.007	0.03	0.01	0.04	0.01	24.3	6436	0.53	626	74.1	0.43	0.01	338
		Min.	0.02	0.99	1.9	0.10	0.22	0.06	0.02	<0.08	<0.001	0.04	<0.001	0.01	<0.001	<0.001	<0.001	3.7	3949	<3.4	618	77.3	<0.37	0.009	322
		Max.	0.23	17.3	36.1	2.4	3.8	0.33	0.04	0.11	0.02	0.07	0.02	0.10	0.03	0.12	0.04	57.7	18224	4.4	2427	291	1.6	0.04	1303
RX6583	**L**	**Mean (n=4)**	**0.05**	**1.6**	**4.6**	**0.26**	**0.53**	**0.06**	**0.01**	**0.04**	**0.009**	**0.02**	**0.009**	**0.02**	**0.005**	**0.02**	**0.007**	**7.2**	**8889**	**3.9**	**150**	**19.8**	**2.4**	**0.02**	**77.6**
		S.D.	0.02	2.2	6.2	0.39	0.78	0.07	0.01	0.04	0.007	0.03	0.006	0.02	0.007	0.009	0.007	9.7	7644	1.1	33.5	5.3	2.4	0.02	14.5
		Min.	<0.03	0.15	0.33	<0.01	<0.07	<0.001	0.001	<0.001	<0.001	0.001	<0.001	<0.001	<0.001	<0.001	0.001	0.69	1421	<2.9	97.5	12.0	<0.36	0.005	54.9
		Max.	0.08	5.4	15.3	0.94	1.9	0.16	0.001	0.06	0.005	0.001	0.01	0.02	0.005	0.02	0.001	23.9	20845	5.6	182	25.8	6.5	0.06	95.3
	M	**Mean (n=19)**	**0.05**	**1.9**	**4.8**	**0.22**	**0.37**	**0.05**	**0.01**	**0.08**	**0.006**	**0.02**	**0.007**	**0.02**	**0.009**	**0.07**	**0.01**	**7.7**	**9659**	**4.0**	**1318**	**159**	**2.0**	**0.10**	**710**
		S.D.	0.07	3.0	7.6	0.38	0.62	0.07	0.02	0.05	0.006	0.03	0.007	0.02	0.006	0.03	0.007	11.6	6299	2.0	899	108	2.6	0.16	479
		Min.	<0.001	0.08	0.12	0.005	0.03	<0.001	<0.001	<0.001	<0.001	<0.001	<0.001	<0.001	<0.001	<0.001	<0.001	0.50	618	2.8	225	29.6	<0.30	<0.001	127
		Max.	0.32	10.2	28.2	1.6	2.7	0.28	0.07	0.18	0.02	0.08	0.01	0.07	0.02	0.14	0.02	44.0	24195	11.7	3589	437	10.0	0.66	1805
	H		0.03	0.24	0.40	0.03	0.03	0.03	<0.001	0.06	<0.001	<0.05	0.009	0.01	0.009	0.11	0.04	2.1	16505	<2.9	4396	545	<0.31	0.05	2303
RX6584	**L**		0.01	2.5	5.4	0.19	0.22	<0.09	0.02	<0.09	<0.02	0.02	<0.01	<0.04	0.005	0.09	<0.01	17.2	1831	<3.3	189	21.3	<0.35	0.04	93.0
	M	**Mean (n=17)**	**0.40**	**10.7**	**28.1**	**1.7**	**3.0**	**0.24**	**0.05**	**0.12**	**0.02**	**0.09**	**0.02**	**0.05**	**0.01**	**0.07**	**0.01**	**41.9**	**7107**	**12.6**	**1110**	**144**	**14.0**	**0.12**	**547**
		S.D.	0.41	4.3	10.9	0.71	1.3	0.13	0.03	0.06	0.02	0.07	0.01	0.03	0.01	0.04	0.007	20.1	2892	9.0	537	68.9	13.7	0.20	290
		Min.	0.04	2.2	5.6	0.30	0.50	0.07	<0.001	0.04	<0.001	<0.001	<0.001	<0.001	<0.001	<0.001	0.005	<0.001	3143	<2.9	325	40.8	0.58	0.01	173
		Max.	1.8	19.4	45.9	2.5	5.1	0.53	0.10	0.25	0.11	0.26	0.05	0.12	0.04	0.20	0.03	75.8	12314	30.3	2700	369	43.2	0.65	1344
	H	**Mean (n=2)**	**5.7**	**166**	**263**	**19.9**	**49.2**	**4.6**	**1.8**	**2.1**	**0.27**	**1.2**	**0.24**	**0.58**	**0.07**	**0.40**	**0.07**	**515**	**5779**	**7.0**	**4032**	**458**	**7.4**	**1.1**	**2166**
		S.D.	5.7	162	254	19.5	48.9	4.5	1.8	2.0	0.26	1.2	0.22	0.54	0.07	0.31	0.06	501	371	3.9	210	17.0	7.0	1.0	329
		Min.	<0.03	4.3	9.2	0.43	0.29	0.06	<0.03	<0.12	<0.01	<0.001	<0.01	<0.04	0.004	0.08	0.01	14.6	5409	<3.1	3823	441	0.37	0.10	1836
		Max.	11.3	328	517	39.5	98.1	9.1	3.6	4.1	0.53	2.3	0.46	1.1	0.14	0.71	0.13	1016	6150	10.9	4242	475	14.4	2.1	2495
RX6585	**L**	**Mean (n=6)**	**1.8**	**67.7**	**120**	**7.4**	**14.2**	**0.86**	**0.44**	**0.38**	**0.05**	**0.24**	**0.05**	**0.15**	**0.03**	**0.17**	**0.04**	**427**	**3441**	**24.4**	**154**	**52.7**	**34.6**	**0.46**	**55.2**
		S.D.	2.7	99.8	176	10.8	20.7	1.1	0.65	0.44	0.05	0.34	0.06	0.18	0.04	0.21	0.05	625	4202	29.7	44.0	46.7	48.5	0.63	39.3
		Min.	<0.001	0.03	0.08	<0.001	<0.09	<0.001	<0.001	<0.001	<0.001	<0.001	<0.001	<0.001	<0.001	<0.001	<0.001	0.66	267	<2.8	116	14.3	<0.32	0.01	7.2
		Max.	7.0	254	443	27.1	52.3	2.7	1.7	1.3	0.14	0.79	0.13	0.41	0.09	0.56	0.13	1581	9690	69.2	241	126	109	1.5	110
	M	**Mean (n=7)**	**0.47**	**7.0**	**18.4**	**1.2**	**2.5**	**0.32**	**0.05**	**0.14**	**0.03**	**0.14**	**0.02**	**0.11**	**0.01**	**0.10**	**0.02**	**30.5**	**6871**	**13.3**	**1256**	**167**	**16.7**	**0.63**	**631**
		S.D.	0.52	7.0	18.9	1.3	2.6	0.30	0.05	0.03	0.02	0.10	0.02	0.11	0.007	0.08	0.008	31.0	1990	6.7	525	69.5	10.3	1.1	290
		Min.	<0.03	0.15	0.21	0.01	<0.08	<0.001	<0.001	0.001	0.005	0.02	0.005	0.02	<0.001	<0.001	0.01	0.83	4197	4.0	595	74.2	<0.34	<0.01	332
		Max.	1.2	15.7	43.0	3.1	6.0	0.75	0.12	0.001	0.06	0.29	0.05	0.25	0.02	0.21	0.03	70.8	11148	22.9	2217	287	33.0	3.0	1160
	H	**Mean (n=2)**	**0.12**	**2.8**	**5.4**	**0.39**	**0.66**	**0.05**	**0.05**	**0.11**	**0.01**	**0.09**	**0.01**	**0.05**	**0.01**	**0.08**	**0.02**	**9.8**	**5240**	**12.7**	**8635**	**1053**	**14.8**	**0.02**	**4659**
		S.D.	0.06	1.3	1.9	0.22	0.26	0.02	0.02	0.02	0.002	0.09	0.005	0.02	0.001	0.01	0.001	3.8	3570	0.22	3023	366	3.2	0.005	1365
		Min.	<0.06	1.6	3.5	0.17	0.40	0.03	<0.04	0.10	0.01	<0.001	0.005	0.03	<0.01	0.07	0.02	6.0	1671	12.5	5612	687	11.5	0.01	3294
		Max.	0.18	4.1	7.2	0.61	0.91	0.07	0.07	0.10	0.01	0.18	0.02	0.03	0.01	0.09	0.02	13.6	8810	12.9	11658	1419	18.0	0.01	6023

Table C6. Zoned hematite in RD2852A (SE-lobe)

Drillhole	U*	Sample	Mg	Al	Si	P	Ca	Sc	Ti	V	Cr	Mn	Co	Ni	Cu	Zn	Ga	As	Sr	Zr	Nb	Mo	Sn	Sb	Ba	Hf	Ta
RX6587	**L**	**Mean (n=13)**	**10.9**	**92.4**	**463**	**<177**	**<1511**	**1.0**	**7.9**	**0.79**	**3.4**	**8.8**	**1.3**	**1.8**	**6.2**	**9.9**	**15.2**	**25.9**	**0.77**	**0.05**	**0.14**	**101**	**894**	**46.3**	**5.6**	**0.02**	**0.002**
Volcanics		**S.D.**	3.9	17.0	149	-	-	0.15	3.6	0.45	0.17	3.6	0.35	0.33	4.5	1.3	2.5	58.7	0.76	0.07	0.18	90.0	301	74.1	4.4	0.05	0.007
		Min.	6.1	60.2	283	-	-	<0.77	<4.7	<0.50	<3.1	5.3	0.54	<1.2	<4.6	<8.6	11.5	<7.1	0.06	<0.001	0.03	32.9	469	3.8	1.9	0.001	<0.001
		Max.	19.0	113	827	-	-	0.82	18.6	2.3	3.8	20.8	1.9	1.9	21.9	14.0	19.6	229	3.1	0.06	0.75	391	1333	264	16.2	0.001	0.03
	M	**Mean (n=12)**	**10.6**	**154**	**791**	**<182**	**<1528**	**1.1**	**10.9**	**1.2**	**<3.4**	**11.3**	**1.4**	**<1.8**	**8.0**	**11.1**	**16.1**	**36.9**	**1.9**	**0.06**	**0.52**	**162**	**856**	**61.6**	**16.1**	**0.01**	**0.03**
		S.D.	4.0	65.2	367	-	-	0.29	7.4	0.64	-	6.0	0.36	-	4.5	2.3	1.4	26.1	1.6	0.08	0.72	90.9	171	68.8	13.2	0.04	0.02
		Min.	<3.8	69.6	<269	-	-	<0.83	<4.7	<0.50	-	3.6	0.84	-	<4.8	<8.2	14.5	<6.9	<0.09	<0.001	0.02	71.9	622	3.8	1.2	0.001	0.01
		Max.	19.3	280	1504	-	-	2.0	29.5	2.5	-	23.3	2.1	-	17.9	16.1	18.9	88.1	4.5	0.06	2.5	365	1178	258	47.3	0.001	0.02
RX6601	**L**	**Mean (n=3)**	**25.7**	**220**	**103**	**12.2**	**47.9**	**0.17**	**4.5**	**1.4**	**<0.32**	**8.4**	**2.2**	**0.23**	**3.0**	**1.2**	**6.3**	**9.4**	**0.12**	**0.02**	**1.5**	**26.7**	**210**	**4.5**	**0.41**	**0.001**	**0.01**
		S.D.	4.4	101	31.0	6.3	18.0	0.04	4.5	0.11	-	1.8	1.2	0.10	2.0	0.60	1.5	5.9	0.04	0.02	1.9	11.1	82.3	0.86	0.12	0.001	0.01
		Min.	20.6	132	65.5	<5.1	<29.0	0.13	1.1	1.3	-	6.2	1.3	0.13	<0.18	0.36	4.3	1.1	0.08	<0.001	0.13	17.3	102	3.5	0.31	<0.001	0.001
		Max.	31.4	361	141	20.4	72.1	0.23	10.8	1.5	-	10.5	3.9	0.38	4.5	1.8	7.9	14.1	0.18	0.06	4.3	42.3	301	5.6	0.58	0.003	0.03
	M	**Mean (n=12)**	**39.8**	**345**	**117**	**6.5**	**46.5**	**0.27**	**4.1**	**1.3**	**0.28**	**10.9**	**3.7**	**0.37**	**0.25**	**0.67**	**4.6**	**1.2**	**0.25**	**0.02**	**2.5**	**181**	**139**	**5.4**	**1.3**	**0.001**	**0.008**
		S.D.	11.1	41.7	35.5	3.0	24.1	0.34	6.5	0.96	0.03	1.9	1.1	0.17	0.17	0.25	0.39	1.4	0.47	0.02	3.8	123	73.7	1.7	3.6	0.002	0.02
		Min.	18.2	249	67.5	<4.3	<26.6	<0.05	<0.32	0.28	<0.23	6.7	1.6	<0.09	<0.15	0.31	3.8	<0.23	<0.001	<0.001	0.08	75.0	52.8	3.4	<0.001	<0.001	<0.001
		Max.	56.1	400	170	13.5	109	1.3	25.3	3.8	0.35	13.7	4.5	0.69	0.79	1.2	5.3	4.5	1.6	0.09	14.0	539	267	9.4	13.1	0.008	0.06
RX6607	**L**	**Mean (n=16)**	**23.3**	**96.2**	**417**	**205**	**<1749**	**<1.1.**	**8.0**	**0.80**	**<3.7**	**12.6**	**1.8**	**2.3**	**6.0**	**11.2**	**13.2**	**14.7**	**0.90**	**0.03**	**0.10**	**476**	**931**	**12.3**	**3.7**	**0.01**	**0.02**
		S.D.	15.9	44.3	138	29.7	-	-	2.8	0.27	-	6.1	0.95	0.45	1.0	1.5	1.4	14.8	1.3	0.06	0.09	648	552	17.9	5.4	0.04	0.02
		Min.	5.8	31.8	<280	<178	-	-	<6.0	<0.62	-	2.5	0.36	<1.6	<5.3	<9.7	11.1	<7.6	0.03	<0.001	<0.001	6.0	197	3.7	<0.001	<0.001	<0.001
		Max.	60.4	196	701	314	-	-	18.6	1.7	-	21.8	3.3	2.7	9.3	14.6	16.2	67.8	3.7	0.07	0.38	1723	2040	79.9	17.5	0.06	0.05
	M	**Mean (n=3)**	**11.7**	**70.3**	**324**	**<207**	**<1812**	**<1.1.**	**8.7**	**<0.71**	**<3.9**	**7.3**	**1.4**	**1.5**	**6.6**	**12.6**	**13.3**	**15.5**	**0.28**	**0.04**	**0.37**	**126**	**1312**	**9.1**	**2.2**	**0.001**	**0.02**
		S.D.	2.6	38.2	7.2	-	-	-	1.7	-	-	2.4	0.19	0.40	0.96	1.5	1.4	10.0	0.18	0.06	0.21	69.3	457	3.9	0.67	0.001	0.02
		Min.	8.2	37.6	0.001	-	-	-	<7.0	-	-	4.1	1.1	1.0	<5.9	<10.8	11.3	<8.0	0.15	<0.001	0.09	29.2	776	3.6	1.7	0.001	<0.001
		Max.	14.3	124	0.001	-	-	-	11.1	-	-	9.5	1.5	1.4	8.0	14.6	14.5	29.7	0.54	0.13	0.61	186	1893	12.3	3.1	0.001	0.02
	H		18.4	398	546	<196	<2030	<1.2	<10.0	<0.66	<3.7	5.4	1.4	1.7	5.8	<9.7	14.3	31.8	0.47	<0.001	0.56	90.7	2162	13.2	1.4	<0.16	<0.001
RX6609	**L**	**Mean (n=11)**	**22.5**	**62.7**	**538**	**342**	**<2833**	**<2.2**	**25.0**	**2.6**	**6.1**	**7.7**	**1.9**	**3.5**	**9.8**	**<16.9**	**14.1**	**16.3**	**0.95**	**0.03**	**4.2**	**110**	**1676**	**15.0**	**2.6**	**0.02**	**0.02**
		S.D.	14.1	42.2	79.3	20.7	-	-	40.0	1.8	0.28	3.6	0.57	-	1.6	-	8.3	6.9	2.4	0.10	8.6	146	742	8.3	4.9	0.05	0.03
		Min.	<7.5	<28.0	<467	<300	-	-	<10.5	<0.93	<5.8	<4.0	1.1	-	<8.7	-	4.0	<11.2	<0.001	0.001	<0.001	9.4	620	2.4	<0.001	<0.001	<0.001
		Max.	58.4	168	779	384	-	-	151	6.4	6.6	12.6	2.7	-	14.6	-	29.6	34.8	8.6	0.001	30.3	504	2884	25.6	17.8	0.13	0.08
	M	**Mean (n=11)**	**17.2**	**103**	**569**	**<336**	**<2917**	**<2.1**	**17.4**	**1.3**	**<5.9**	**8.3**	**1.7**	**3.4**	**<8.9**	**16.5**	**16.3**	**33.9**	**0.46**	**0.19**	**0.37**	**376**	**1141**	**7.2**	**2.0**	**0.06**	**0.001**
		S.D.	13.7	117	117	-	-	-	13.8	0.63	-	4.1	0.85	0.63	-	1.3	5.9	45.2	0.67	0.15	0.80	289	511	4.5	2.6	0.11	0.001
		Min.	<7.8	<28.1	<482	-	-	-	<11.0	<0.97	-	<4.2	0.81	<2.6	-	<14.9	5.5	<11.7	0.06	<0.001	0.03	104	435	2.5	<0.001	<0.001	0.001
		Max.	57.2	409	814	-	-	-	61.0	3.3	-	16.7	4.1	2.9	-	19.4	26.6	172	2.6	0.12	2.9	976	2388	18.9	9.2	0.12	0.001

Table C6. (Continued) Zoned hematite in RD2852A (SE-lobe)

Drillhole	U*	Sample	Y	La	Ce	Pr	Nd	Sm	Eu	Gd	Tb	Dy	Ho	Er	Tm	Yb	Lu	∑REY	W	204Pb	206Pb	207Pb	208Pb	Th	U
RX6587	**L**	**Mean (n=13)**	**0.04**	**0.50**	**1.3**	**0.06**	**0.12**	**0.06**	**0.02**	**0.09**	**0.009**	**0.02**	**0.005**	**0.02**	**0.007**	**0.03**	**0.007**	**2.3**	**12620**	**5.2**	**90.5**	**13.2**	**2.6**	**0.01**	**50.8**
Volcanics		**S.D.**	0.03	0.30	0.74	0.04	0.06	0.05	0.02	0.04	0.007	0.02	0.007	0.02	0.006	0.03	0.008	1.1	6010	3.4	49.0	6.9	4.4	0.009	27.8
		Min.	0.01	0.14	0.38	0.03	<0.001	<0.001	<0.001	<0.001	<0.001	<0.001	<0.001	<0.001	<0.001	<0.001	<0.001	0.99	3426	<3.4	13.5	2.3	<0.32	<0.001	5.0
		Max.	0.12	1.2	2.6	0.13	0.23	0.03	0.06	0.03	0.02	0.02	0.01	0.03	0.01	0.06	0.03	4.0	20225	16.9	164	25.7	17.3	0.03	87.1
	M	**Mean (n=12)**	**0.05**	**2.1**	**5.3**	**0.31**	**0.55**	**0.06**	**0.009**	**0.09**	**0.009**	**0.02**	**0.01**	**0.02**	**0.008**	**0.02**	**0.007**	**8.6**	**12638**	**5.5**	**550**	**70.1**	**5.1**	**0.03**	**293**
		S.D.	0.05	1.5	4.0	0.23	0.41	0.05	0.01	0.06	0.007	0.03	0.007	0.02	0.006	0.03	0.006	6.2	4103	2.4	217	25.3	4.5	0.02	104
		Min.	0.01	0.15	0.31	0.005	0.06	<0.001	<0.001	<0.001	<0.001	<0.001	<0.001	<0.001	<0.001	<0.001	<0.001	0.74	5022	<3.5	251	30.7	<0.33	0.009	142
		Max.	0.21	5.1	12.7	0.68	1.2	0.11	0.03	0.04	0.02	0.04	0.006	0.03	0.01	0.03	0.01	20.0	18193	10.9	1033	123	13.3	0.09	542
RX6601	**L**	**Mean (n=3)**	**0.02**	**0.35**	**0.84**	**0.04**	**0.10**	**0.01**	**0.005**	**0.01**	**0.001**	**0.009**	**0.002**	**0.005**	**0.001**	**0.02**	**0.008**	**1.4**	**1246**	**3.7**	**37.6**	**5.6**	**1.1**	**0.004**	**28.9**
		S.D.	0.01	0.08	0.47	0.01	0.04	0.006	0.002	0.006	0.001	0.003	0.001	0.003	0.001	0.01	0.003	0.61	793	0.46	47.0	4.6	0.74	0.002	37.8
		Min.	0.01	0.23	0.31	0.03	0.05	0.005	<0.002	0.008	0.001	<0.005	0.001	0.001	0.001	0.01	0.005	0.69	455	3.3	3.8	2.1	<0.006	0.001	1.6
		Max.	0.04	0.41	1.5	0.06	0.14	0.02	0.008	0.02	0.002	0.01	0.004	0.007	0.002	0.03	0.01	2.2	2331	4.3	104	12.1	1.6	0.007	82.4
	M	**Mean (n=12)**	**0.06**	**0.33**	**0.52**	**0.04**	**0.09**	**0.007**	**0.003**	**0.007**	**0.001**	**0.01**	**0.004**	**0.02**	**0.008**	**0.16**	**0.05**	**1.3**	**1625**	**3.0**	**369**	**45.7**	**0.03**	**0.03**	**338**
		S.D.	0.05	0.52	0.80	0.06	0.13	0.009	0.002	0.004	0.001	0.008	0.004	0.02	0.007	0.10	0.03	1.7	1712	0.29	176	21.7	0.04	0.04	164
		Min.	0.008	0.01	0.02	<0.001	0.006	<0.001	<0.001	<0.001	0.001	<0.001	0.001	0.003	<0.001	0.04	0.01	0.20	277	2.5	151	18.6	0.006	0.002	133
		Max.	0.16	1.9	2.9	0.21	0.49	0.03	0.007	0.01	0.002	0.03	0.01	0.07	0.02	0.39	0.12	6.3	5527	3.7	773	95.2	0.15	0.13	707
RX6607	**L**	**Mean (n=16)**	**0.03**	**1.2**	**2.1**	**0.12**	**0.21**	**0.04**	**0.01**	**0.10**	**0.01**	**0.02**	**0.006**	**0.04**	**0.008**	**0.04**	**0.01**	**4.0**	**10829**	**4.9**	**46.3**	**7.0**	**1.9**	**0.02**	**23.9**
		S.D.	0.02	1.5	2.6	0.15	0.28	0.05	0.01	0.05	0.01	0.02	0.007	0.04	0.007	0.05	0.009	4.6	6980	2.1	49.4	6.1	3.5	0.03	25.8
		Min.	<0.001	<0.03	0.03	0.006	<0.001	<0.001	<0.001	<0.001	<0.001	<0.001	<0.001	<0.001	<0.001	<0.001	<0.001	0.38	1353	<3.1	<0.53	<0.59	<0.35	<0.001	0.08
		Max.	0.06	6.2	10.3	0.60	1.1	0.08	0.03	0.07	0.005	0.04	0.01	0.17	0.02	0.09	0.02	18.5	23394	11.8	176	20.9	15.2	0.12	81.7
	M	**Mean (n=3)**	**0.02**	**0.67**	**1.2**	**0.06**	**0.11**	**0.04**	**0.02**	**0.10**	**0.01**	**0.03**	**0.002**	**0.05**	**0.006**	**0.06**	**0.007**	**2.4**	**7761**	**4.8**	**527**	**63.3**	**1.8**	**0.02**	**266**
		S.D.	0.02	0.19	0.51	0.01	0.05	0.05	0.008	0.05	0.007	0.03	0.003	0.02	0.008	0.04	0.007	0.79	5427	1.3	230	26.9	1.6	0.009	132
		Min.	<0.001	0.52	0.65	0.05	0.06	0.001	0.01	0.04	0.001	<0.001	<0.001	0.02	0.001	0.001	<0.001	1.5	1093	<3.9	360	42.9	0.56	0.01	157
		Max.	0.04	0.94	1.9	0.08	0.18	0.001	0.01	0.04	0.001	0.02	0.006	0.02	0.001	0.001	0.006	3.4	14385	6.8	853	101	4.0	0.03	452
	H		0.08	5.9	13.5	0.66	1.5	0.04	<0.03	0.07	<0.001	<0.001	<0.02	0.02	<0.001	0.05	<0.02	43.7	4456	3.9	2021	244	4.4	0.01	1138
RX6609	**L**	**Mean (n=11)**	**0.05**	**0.47**	**0.85**	**0.04**	**0.10**	**0.10**	**0.02**	**0.27**	**0.03**	**0.05**	**0.02**	**0.05**	**0.01**	**0.09**	**0.01**	**2.2**	**4888**	**7.3**	**79.1**	**11.6**	**1.8**	**0.02**	**35.8**
		S.D.	0.04	0.72	1.3	0.05	0.07	0.09	0.02	0.11	0.006	0.05	0.02	0.05	0.02	0.07	0.02	2.0	5512	1.8	83.1	12.8	2.5	0.02	37.0
		Min.	<0.001	<0.03	0.03	<0.001	<0.001	<0.001	<0.001	0.07	0.01	<0.001	<0.001	<0.001	<0.001	<0.001	<0.001	0.72	15.1	<5.0	2.2	<1.1	<0.60	<0.001	0.56
		Max.	0.07	2.4	4.2	0.17	0.17	0.06	0.03	0.07	0.03	0.08	0.02	0.10	0.01	0.15	0.05	7.4	17115	11.0	271	43.2	9.1	0.05	117
	M	**Mean (n=11)**	**0.07**	**8.7**	**17.4**	**0.71**	**1.1**	**0.09**	**0.03**	**0.26**	**0.03**	**0.11**	**0.03**	**0.06**	**0.01**	**0.06**	**0.02**	**28.8**	**14566**	**6.4**	**1061**	**136**	**1.1**	**0.09**	**516**
		S.D.	0.05	11.4	20.1	0.81	1.3	0.07	0.02	0.09	0.01	0.04	0.02	0.05	0.01	0.03	0.02	33.4	5887	0.73	662	83.3	0.97	0.16	318
		Min.	<0.001	0.04	0.05	<0.001	0.05	<0.001	<0.001	0.07	<0.001	0.04	<0.001	<0.001	<0.001	<0.001	<0.001	0.80	5971	<5.6	302	38.3	<0.60	<0.001	148
		Max.	0.20	38.2	61.9	2.2	3.4	0.06	0.02	0.30	0.03	0.12	0.01	0.10	0.01	0.10	0.01	107	23535	7.9	2041	258	4.1	0.58	971

Table C7. Zoned hematite in RD2852A (SE-lobe)

Drillhole	U*	Sample	Mg	Al	Si	P	Ca	Sc	Ti	V	Cr	Mn	Co	Ni	Cu	Zn	Ga	As	Sr	Zr	Nb	Mo	Sn	Sb	Ba	Hf	Ta
RX6610	**L**	**Mean (n=11)**	**20.0**	**124**	**668**	**<417**	**<3415**	**<2.7**	**15.8**	**1.4**	**<7.2**	**9.6**	**1.8**	**4.2**	**<11.0**	**19.9**	**26.3**	**16.2**	**0.39**	**0.13**	**0.27**	**53.0**	**1301**	**18.2**	**0.62**	**0.06**	**0.03**
		S.D.	8.3	58.2	86.7	-	-	-	2.0	0.16	-	2.9	0.68	0.48	-	1.8	9.2	1.8	0.32	0.18	0.51	30.7	337	7.1	0.79	0.14	0.05
		Min.	<8.8	57.2	<577	-	-	-	<12.1	<1.2	-	5.3	0.68	<3.6	-	<17.8	13.0	<14.2	0.07	<0.001	<0.001	8.6	565	7.2	<0.001	<0.001	<0.001
		Max.	34.7	275	852	-	-	-	17.6	1.8	-	14.2	3.2	4.2	-	23.7	42.5	21.2	1.1	0.14	1.9	122	1638	30.2	1.8	0.15	0.04
	M	**Mean (n=14)**	**29.9**	**92.9**	**<606**	**<403**	**<3306**	**2.5**	**<15.2**	**2.3**	**<6.9**	**9.7**	**1.8**	**4.2**	**<10.7**	**20.3**	**25.1**	**21.4**	**0.51**	**0.06**	**1.0**	**258**	**1160**	**17.3**	**1.5**	**0.14**	**0.02**
		S.D.	24.7	87.9	-	-	-	0.31	-	3.5	-	5.1	0.92	0.87	-	3.9	14.5	12.9	0.35	0.11	2.7	332	691	12.0	1.1	0.20	0.04
		Min.	<8.8	<33.6	-	-	-	<2.1	-	<1.1	-	4.7	<0.86	2.4	-	16.1	11.1	<14.0	0.13	<0.001	0.03	26.8	347	4.6	<0.001	<0.001	<0.001
		Max.	77.8	381	-	-	-	3.4	-	15.0	-	24.0	4.5	4.9	-	28.9	56.4	62.3	1.1	0.20	10.6	1376	2864	37.8	4.1	0.15	0.04
RX6612	**L**	**Mean (n=13)**	**18.3**	**65.4**	**662**	**400**	**<3341**	**<2.5**	**<14.9**	**1.5**	**<6.9**	**10.0**	**2.0**	**<3.8**	**<10.7**	**18.2**	**12.9**	**31.4**	**0.36**	**0.09**	**0.42**	**182**	**1399**	**12.0**	**1.0**	**0.07**	**0.02**
		S.D.	10.0	29.7	107	35.4	-	-	-	0.54	-	3.9	0.73	-	-	2.2	3.8	45.0	0.24	0.15	0.49	301	1013	9.5	0.87	0.13	0.03
		Min.	<8.1	<32.2	<572	<355	-	-	-	1.2	-	<4.9	1.1	-	-	<15.8	6.1	<13.4	<0.18	<0.001	<0.001	20.3	377	3.2	<0.001	<0.001	<0.001
		Max.	37.6	126	919	507	-	-	-	3.3	-	15.6	3.7	-	-	24.9	17.7	186	0.96	0.27	1.5	1201	4494	40.9	2.5	0.29	0.07
	M	**Mean (n=17)**	**34.3**	**154**	**665**	**<388**	**<3213**	**<2.4**	**16.0**	**1.5**	**6.8**	**10.2**	**2.1**	**4.0**	**<10.4**	**17.9**	**16.1**	**24.4**	**1.1**	**0.12**	**0.31**	**353**	**1867**	**9.0**	**2.8**	**0.03**	**0.03**
		S.D.	46.6	154	132	-	-	-	2.2	0.44	0.47	4.7	0.87	0.67	-	1.7	6.8	19.5	2.6	0.17	0.38	319	1332	3.3	2.8	0.06	0.05
		Min.	<8.3	<31.6	<561	-	-	-	<12.3	<1.1	<6.2	<4.4	0.65	<2.9	-	<15.2	3.5	<13.3	0.18	<0.001	<0.001	39.4	315	4.3	<0.001	<0.001	<0.001
		Max.	210	609	1004	-	-	-	22.5	2.7	7.1	21.1	3.7	3.2	-	17.2	35.6	87.1	11.5	0.16	1.6	1089	5678	14.4	9.4	0.18	0.04
	H	**Mean (n=3)**	**14.5**	**43.4**	**658**	**<394**	**<3269**	**<2.5**	**16.3**	**<1.4**	**<6.8**	**7.6**	**2.5**	**<4.6**	**<10.5**	**19.4**	**12.3**	**22.8**	**0.36**	**0.001**	**0.07**	**1135**	**1946**	**18.3**	**0.63**	**0.05**	**0.001**
		S.D.	6.0	14.7	96.0	-	-	-	1.8	-	-	0.85	0.27	-	-	1.6	13.1	12.1	0.13	0.001	0.03	1368	984	3.3	0.89	0.08	0.001
		Min.	<9.9	<32.8	<585	-	-	-	<13.8	-	-	6.7	2.1	-	-	<17.3	2.5	<14.1	<0.26	0.001	0.03	104	626	14.5	0.001	<0.001	0.001
		Max.	23.0	64.2	793	-	-	-	17.7	-	-	8.7	2.7	-	-	19.9	30.8	40.0	0.54	0.001	0.03	3067	2987	22.7	0.001	0.16	0.001
RX6626	**L**	**Mean (n=10)**	**16.0**	**89.2**	**717**	**<437**	**<3665**	**2.9**	**<17.7**	**1.9**	**<7.6**	**8.4**	**1.7**	**4.4**	**<12.1**	**20.0**	**18.2**	**26.1**	**0.51**	**0.20**	**2.9**	**414**	**1273**	**43.0**	**2.2**	**0.13**	**0.07**
		S.D.	9.5	47.4	89.6	-	-	0.30	-	1.1	-	2.4	0.96	1.1	-	1.3	6.7	15.5	0.42	0.22	6.7	707	1020	46.4	1.4	0.23	0.05
		Min.	<8.7	<37.8	614	-	-	<2.3	-	<1.3	-	<4.7	0.55	3.0	-	<16.8	6.6	<14.4	<0.22	<0.001	0.04	17.0	255	9.0	<0.001	<0.001	<0.001
		Max.	42.3	169	951	-	-	2.6	-	5.3	-	11.8	3.7	4.4	-	20.8	32.7	61.4	1.6	0.16	22.5	2057	3591	143	5.4	0.16	0.04
	M	**Mean (n=8)**	**24.2**	**115**	**740**	**<430**	**<3523**	**<2.6**	**37.9**	**2.0**	**<7.4**	**10.8**	**2.2**	**4.2**	**13.0**	**31.4**	**14.5**	**74.0**	**0.86**	**0.04**	**1.3**	**139**	**2603**	**139**	**5.5**	**0.06**	**0.06**
		S.D.	16.6	148	157	-	-	-	34.6	1.0	-	6.6	0.58	0.98	1.9	31.3	8.8	118	1.4	0.06	1.5	98.5	2527	160	10.7	0.11	0.04
		Min.	<9.5	39.5	<638	-	-	-	<17.4	<1.3	-	<5.0	1.6	<2.7	<11.5	<16.4	3.9	<14.2	<0.20	<0.001	0.07	56.3	1018	13.9	<0.001	<0.001	<0.001
		Max.	53.7	504	1145	-	-	-	121	3.8	-	25.9	3.5	6.0	17.6	114	29.7	383	4.4	0.15	3.5	334	8736	529	33.6	0.32	0.04
	H	**Mean (n=3)**	**65.9**	**59.7**	**1444**	**<426**	**<3685**	**3.2**	**<17.5**	**<1.5**	**<7.5**	**12.7**	**1.5**	**<4.1**	**<12.2**	**19.1**	**30.1**	**115**	**1.1**	**0.30**	**0.22**	**1185**	**1309**	**169**	**3.5**	**0.16**	**0.04**
		S.D.	46.3	26.3	432	-	-	0.40	-	-	-	4.7	0.58	-	-	0.53	6.1	81.2	0.64	0.21	0.20	763	1092	106	0.80	0.23	0.05
		Min.	27.0	<38.0	940	-	-	<2.8	-	-	-	6.1	1.0	-	-	18.4	21.7	<14.9	0.22	0.001	<0.001	213	422	20.0	2.7	0.001	0.001
		Max.	131	96.7	1994	-	-	3.7	-	-	-	16.2	2.3	-	-	19.6	36.0	214	1.8	0.001	0.49	2076	2848	256	4.6	0.001	0.001

Table C7. (Continued) Zoned hematite in RD2852A (SE-lobe)

Drillhole	U*	Sample	Y	La	Ce	Pr	Nd	Sm	Eu	Gd	Tb	Dy	Ho	Er	Tm	Yb	Lu	∑REY	W	204Pb	206Pb	207Pb	208Pb	Th	U
RX6610	**L**	**Mean (n=11)**	**0.07**	**0.31**	**0.84**	**0.05**	**0.18**	**0.13**	**0.02**	**0.26**	**0.04**	**0.08**	**0.02**	**0.07**	**0.02**	**0.08**	**0.03**	**2.2**	**6105**	**8.6**	**75.3**	**9.4**	**0.91**	**0.06**	**34.2**
		S.D.	0.04	0.62	1.7	0.08	0.16	0.13	0.03	0.10	0.01	0.07	0.02	0.05	0.02	0.07	0.02	2.7	4383	0.96	40.8	4.9	0.35	0.09	19.1
		Min.	0.03	<0.04	0.03	<0.001	<0.001	<0.001	<0.001	0.08	<0.001	<0.001	<0.001	<0.001	<0.001	<0.001	<0.001	0.82	508	<6.7	3.3	<1.2	<0.70	<0.001	1.5
		Max.	0.14	2.2	6.2	0.30	0.59	0.07	0.06	0.25	0.04	0.05	0.01	0.08	0.03	0.13	0.02	10.5	11847	7.9	153	19.1	1.7	0.34	74.0
	M	**Mean (n=14)**	**0.08**	**2.3**	**6.0**	**0.29**	**0.58**	**0.11**	**0.04**	**0.23**	**0.03**	**0.06**	**0.02**	**0.09**	**0.02**	**0.12**	**0.02**	**10.0**	**7803**	**8.8**	**661**	**82.9**	**2.0**	**0.28**	**318**
		S.D.	0.06	4.5	11.4	0.61	1.0	0.11	0.03	0.10	0.02	0.06	0.02	0.06	0.02	0.10	0.02	17.8	5606	3.1	492	60.1	2.2	0.69	238
		Min.	<0.001	0.07	0.36	<0.03	0.06	<0.001	0.001	<0.001	<0.001	<0.001	<0.001	<0.001	<0.001	<0.001	<0.001	1.1	2067	<6.2	287	36.1	<0.66	<0.001	136
		Max.	0.27	18.2	46.1	2.5	4.2	0.31	0.001	0.32	0.02	0.14	0.04	0.11	0.01	0.27	0.05	72.6	20009	18.7	1829	219	8.4	2.6	834
RX6612	**L**	**Mean (n=13)**	**0.06**	**0.28**	**0.70**	**0.04**	**0.16**	**0.08**	**0.03**	**0.30**	**0.03**	**0.06**	**0.01**	**0.06**	**0.03**	**0.11**	**0.02**	**1.8**	**10775**	**7.7**	**89.8**	**12.1**	**1.1**	**0.02**	**38.4**
		S.D.	0.05	0.27	0.68	0.03	0.08	0.09	0.03	0.09	0.02	0.08	0.01	0.05	0.02	0.08	0.03	1.2	6650	0.62	64.5	8.9	0.91	0.02	31.2
		Min.	<0.001	0.01	0.05	<0.001	<0.001	<0.001	<0.001	<0.21	<0.001	<0.001	<0.001	<0.001	<0.001	<0.001	<0.001	0.38	92.7	<6.3	5.9	1.4	<0.66	<0.001	2.3
		Max.	0.03	0.74	2.0	0.12	0.32	0.08	0.02	0.22	0.05	0.10	0.04	0.04	0.01	0.05	0.02	4.0	20833	8.5	212	30.5	4.2	0.04	114
	M	**Mean (n=17)**	**0.10**	**7.2**	**16.2**	**0.68**	**1.0**	**0.13**	**0.03**	**0.28**	**0.03**	**0.06**	**0.02**	**0.09**	**0.02**	**0.13**	**0.03**	**26.0**	**13514**	**7.5**	**1257**	**148**	**1.4**	**0.14**	**572**
		S.D.	0.04	7.7	16.3	0.62	1.0	0.09	0.02	0.13	0.02	0.07	0.02	0.06	0.02	0.09	0.02	25.5	9400	1.4	763	90.1	1.5	0.20	351
		Min.	0.05	0.24	0.69	0.04	<0.001	<0.001	<0.001	<0.001	<0.001	<0.001	<0.001	<0.001	<0.001	<0.001	<0.001	1.6	822	<5.3	262	34.8	<0.64	<0.001	143
		Max.	0.17	30.3	57.1	2.2	3.5	0.15	0.02	0.30	0.04	0.09	0.06	0.16	0.02	0.28	0.03	93.3	30562	10.9	2989	357	7.1	0.78	1352
	H	**Mean (n=3)**	**0.07**	**13.3**	**33.6**	**1.2**	**1.4**	**0.14**	**0.01**	**0.33**	**0.03**	**0.08**	**0.02**	**0.08**	**0.01**	**0.11**	**0.03**	**50.4**	**8510**	**7.3**	**5255**	**584**	**0.99**	**0.13**	**2400**
		S.D.	0.02	17.6	44.4	1.5	1.8	0.10	0.02	0.11	0.008	0.06	0.02	0.07	0.02	0.09	0.02	65.7	2867	0.76	1376	149	0.37	0.15	781
		Min.	0.04	0.31	1.2	0.07	0.17	0.001	<0.001	0.001	0.02	<0.001	<0.001	<0.001	0.001	<0.001	0.001	2.2	5646	<6.5	3839	431	<0.68	<0.001	1715
		Max.	0.09	38.2	96.5	3.3	3.9	0.001	0.04	0.001	0.02	0.10	0.04	0.17	0.001	0.12	0.001	143	12428	6.9	7119	786	1.5	0.34	3493
RX6626	**L**	**Mean (n=10)**	**0.08**	**1.2**	**3.9**	**0.23**	**0.36**	**0.11**	**0.04**	**0.32**	**0.04**	**0.07**	**0.02**	**0.09**	**0.02**	**0.09**	**0.02**	**6.0**	**11692**	**8.1**	**86.2**	**12.0**	**1.7**	**0.02**	**37.0**
		S.D.	0.05	1.1	4.0	0.22	0.39	0.10	0.03	0.07	0.02	0.05	0.02	0.08	0.02	0.13	0.02	5.8	7929	1.3	76.6	9.9	0.87	0.02	34.6
		Min.	<0.001	<0.07	<0.06	0.03	<0.001	<0.001	<0.001	0.001	<0.001	<0.001	<0.001	<0.001	<0.001	<0.001	<0.001	0.77	2382	<7.0	1.9	<1.3	<0.81	<0.001	0.91
		Max.	0.12	3.5	12.1	0.71	1.3	0.23	0.02	0.001	0.03	0.06	0.02	0.04	0.02	0.07	0.02	18.4	24248	7.4	217	29.2	3.4	0.04	107
	M	**Mean (n=8)**	**0.08**	**1.0**	**3.1**	**0.15**	**0.30**	**0.08**	**0.03**	**0.35**	**0.04**	**0.10**	**0.03**	**0.14**	**0.04**	**0.13**	**0.04**	**5.7**	**10900**	**8.4**	**1175**	**141**	**3.7**	**0.04**	**497**
		S.D.	0.04	1.5	4.4	0.20	0.30	0.08	0.03	0.06	0.03	0.08	0.02	0.04	0.02	0.11	0.02	6.4	9670	1.6	814	95.5	3.1	0.03	347
		Min.	<0.001	0.06	0.05	0.01	<0.001	<0.001	<0.001	0.25	<0.001	<0.001	<0.001	0.04	<0.001	<0.001	<0.001	1.2	1172	<6.1	302	37.9	0.72	<0.001	124
		Max.	0.09	4.7	13.2	0.63	1.0	0.16	0.02	0.37	0.10	0.10	0.01	0.04	0.01	0.26	0.01	20.6	32804	11.8	2705	311	8.8	0.09	1111
	H	**Mean (n=3)**	**0.54**	**25.9**	**80.9**	**3.9**	**5.8**	**0.34**	**0.08**	**0.48**	**0.04**	**0.17**	**0.05**	**0.13**	**0.05**	**0.23**	**0.07**	**119**	**5415**	**8.3**	**8581**	**990**	**4.1**	**0.16**	**3463**
		S.D.	0.30	18.7	57.4	2.7	4.3	0.37	0.01	0.21	0.001	0.15	0.04	0.11	0.03	0.17	0.01	84.0	856	1.6	3958	440	2.4	0.09	1613
		Min.	<0.12	0.71	1.7	0.08	0.13	<0.001	0.06	0.26	0.04	<0.001	<0.001	<0.001	<0.001	<0.001	0.06	3.2	4639	<7.2	5492	641	0.80	<0.04	2270
		Max.	0.80	45.5	136	6.3	10.4	0.86	0.08	0.76	0.04	0.37	0.10	0.27	0.06	0.38	0.09	200	6607	10.5	14167	1610	6.2	0.23	5742

Table C8. Zoned hematite in RD647 (SE-lobe)

Drillhole	U*	Sample	Mg	Al	Si	P	Ca	Sc	Ti	V	Cr	Mn	Co	Ni	Cu	Zn	Ga	As	Sr	Zr	Nb	Mo	Sn	Sb	Ba	Hf	Ta
RD647																											
MV092	**L**	**Mean (n=7)**	**16.6**	**5.3**	**393**	**<43.4**	**<442**	**0.47**	**2.0**	**4.2**	**3.1**	**4.4**	**1.3**	**0.74**	**3.7**	**2.8**	**3.7**	**17.4**	**0.25**	**0.36**	**8.9**	**187**	**314**	**1.2**	**0.14**	**0.03**	**0.05**
Volcanics		**S.D.**	8.8	1.4	120	-	-	0.22	1.1	9.3	1.1	2.0	0.41	0.69	7.2	4.2	2.9	40.5	0.59	0.81	16.7	174	101	1.6	0.23	0.05	0.13
		Min.	6.9	3.2	<306	-	-	<0.32	<1.1	<0.05	0.001	1.8	0.84	0.06	<0.60	<0.89	1.7	<0.31	0.007	<0.001	<0.01	9.7	204	0.32	<0.001	<0.001	<0.001
		Max.	31.7	7.9	601	-	-	0.96	4.3	26.9	0.001	7.9	2.0	2.4	21.4	13.1	10.7	116	1.7	2.3	48.4	581	537	5.1	0.60	0.13	0.37
	M	**Mean (n=6)**	**45.8**	**12.9**	**<310**	**39.4**	**<389**	**0.40**	**4.2**	**3.2**	**<2.5**	**7.7**	**1.9**	**0.35**	**2.0**	**1.3**	**3.0**	**7.4**	**0.66**	**0.77**	**38.6**	**298**	**575**	**3.1**	**1.2**	**0.01**	**0.05**
		S.D.	33.6	11.2	-	1.6	-	0.17	6.1	4.9	-	2.7	0.76	0.11	1.2	0.55	1.3	6.6	0.52	1.5	37.0	230	234	1.3	1.1	0.01	0.05
		Min.	22.2	1.3	-	<37.6	-	<0.30	<0.97	0.48	-	3.9	0.95	0.12	<0.62	0.84	1.4	0.51	0.04	<0.001	0.06	40.2	311	1.1	0.25	<0.001	<0.001
		Max.	113	30.3	-	39.0	-	0.78	16.5	14.2	-	12.2	3.2	0.12	3.8	2.5	4.9	18.9	1.3	4.0	104	732	959	5.3	3.5	0.04	0.15
	H		88.8	1.5	297	<33.9	<365	<0.31	<1.3	1.6	<2.2	11.1	2.8	<0.23	2.0	<0.76	3.6	1.8	0.38	<0.05	1.6	814	659	3.4	0.54	<0.05	<0.001
LCD32	**L**	**Mean (n=3)**	**15.7**	**166**	**183**	**21.0**	**<197**	**0.83**	**6.0**	**2.9**	**<1.2**	**8.9**	**0.56**	**0.39**	**<0.47**	**0.71**	**11.4**	**6.2**	**0.35**	**0.02**	**6.0**	**21.3**	**228**	**1.2**	**0.86**	**0.02**	**0.01**
Volcanics		**S.D.**	11.4	20.9	22.1	0.29	-	0.73	7.4	4.0	-	2.5	0.08	0.22	-	0.11	2.1	4.9	0.23	0.02	8.4	10.2	88.9	0.90	0.53	0.02	0.02
		Min.	6.9	137	158	<20.6	-	<0.20	<0.71	0.08	-	6.3	0.45	<0.23	-	<0.56	8.4	1.7	0.04	<0.001	0.02	13.1	113	0.47	0.20	0.008	<0.001
		Max.	31.8	184	212	21.0	-	1.9	16.5	8.6	-	12.3	0.62	0.70	-	0.82	13.3	13.0	0.59	0.04	17.9	35.8	330	2.5	1.5	0.02	0.04
	M	**Mean (n=3)**	**15.6**	**533**	**272**	**21.3**	**232**	**3.7**	**9.3**	**10.6**	**<1.2**	**13.4**	**1.3**	**0.26**	**1.5**	**1.7**	**13.4**	**13.5**	**3.4**	**0.13**	**12.3**	**583**	**254**	**1.8**	**6.5**	**0.01**	**0.02**
		S.D.	2.7	119	59.9	1.9	19.3	2.7	7.4	9.7	-	4.1	0.42	0.04	1.0	0.68	0.20	7.9	2.4	0.08	9.4	410	16.5	0.48	4.6	0.01	0.02
		Min.	13.0	419	202	<18.7	<205	<0.20	<0.82	<0.05	-	7.7	0.72	0.21	<0.43	<0.76	13.3	2.4	0.05	<0.03	0.006	20.5	231	1.1	0.38	<0.001	<0.001
		Max.	19.3	698	348	23.3	250	6.9	18.9	23.5	-	16.7	1.7	0.31	2.9	2.3	13.7	20.4	5.8	0.24	22.9	985	266	2.3	11.3	0.01	0.04
	H		81.2	65.1	197	<19.4	<175	0.26	17.3	1.1	<1.1	7.7	2.2	<0.29	<0.39	1.1	3.7	1.3	0.11	0.06	1.8	572	392	2.4	0.53	0.01	0.07
MV093A	**L**	**Mean (n=4)**	**46.9**	**116**	**<268**	**<34.1**	**<317**	**<0.29**	**55.8**	**5.7**	**1.9**	**8.9**	**2.0**	**0.24**	**3.5**	**4.2**	**4.2**	**6.3**	**0.55**	**0.17**	**60.8**	**188**	**765**	**7.8**	**0.61**	**0.01**	**0.09**
Volcanics		**S.D.**	35.9	69.0	-	-	-	-	69.7	5.3	0.73	6.5	0.95	0.20	3.4	4.1	0.84	3.3	0.52	0.16	69.6	126	253	1.3	0.57	0.01	0.08
		Min.	6.2	56.3	-	-	-	-	<1.4	1.9	<1.4	1.9	0.72	<0.001	<0.51	<1.1	3.2	<0.60	<0.001	<0.001	1.9	7.5	444	6.0	<0.001	<0.001	0.007
		Max.	104	228	-	-	-	-	176	14.7	3.2	19.5	3.4	0.56	9.2	11.2	5.4	8.6	1.4	0.39	172	365	1123	9.8	1.5	0.02	0.17
	M	**Mean (n=2)**	**115**	**124**	**306**	**<32.4**	**<271**	**<0.24**	**2.5**	**0.21**	**<1.3**	**3.1**	**1.9**	**0.28**	**<0.43**	**<1.1**	**9.3**	**3.1**	**0.05**	**<0.05**	**6.4**	**492**	**893**	**3.7**	**0.09**	**<0.001**	**0.008**
		S.D.	84.5	22.2	50.2	-	-	-	1.4	0.03	-	0.25	0.03	0.10	-	-	0.41	2.5	0.02	-	6.4	80.9	49.3	1.2	0.09	-	0.008
		Min.	30.5	102	<256	-	-	-	<1.1	0.18	-	2.9	1.9	<0.18	-	-	8.9	<0.59	<0.02	-	0.02	411	844	2.4	<0.001	-	<0.001
		Max.	199	146	356	-	-	-	3.9	0.24	-	3.4	1.9	0.37	-	-	9.8	5.6	0.07	-	12.8	573	943	4.9	0.18	-	0.02
MV093B	**L**	**Mean (n=10)**	**41.5**	**246**	**492**	**115**	**<301**	**0.39**	**18.6**	**6.8**	**1.9**	**19.9**	**2.2**	**0.44**	**15.5**	**7.5**	**11.1**	**138**	**4.5**	**0.28**	**47.7**	**97.5**	**887**	**73.4**	**32.0**	**0.01**	**0.05**
Volcanics		**S.D.**	27.6	214	323	119	-	0.29	40.1	6.7	0.97	21.0	1.8	0.19	26.2	11.2	5.1	259	5.7	0.53	56.0	157	343	120	85.0	0.02	0.08
		Min.	5.0	37.8	<243	<34.4	-	<0.24	1.1	0.27	1.3	4.2	0.64	<0.20	<0.46	<1.1	3.8	<0.62	<0.001	<0.001	0.08	2.6	359	1.7	<0.001	<0.001	<0.001
		Max.	86.5	692	1083	353	-	1.3	129	20.6	4.7	77.7	6.7	0.84	86.3	35.4	17.3	869	19.7	1.5	185	545	1551	412	287	0.04	0.24
	M	**Mean (n=7)**	**170**	**161**	**762**	**80.3**	**253**	**2.4**	**20.2**	**14.3**	**1.6**	**15.6**	**2.7**	**0.26**	**5.2**	**2.7**	**5.1**	**35.7**	**6.6**	**0.09**	**156**	**134**	**1112**	**33.7**	**3.1**	**0.001**	**0.17**
		S.D.	104	173	1115	107	35.8	5.1	21.5	13.4	0.27	8.5	1.1	0.11	6.6	2.2	5.4	47.9	13.7	0.12	240	55.3	367	11.1	3.7	0.001	0.31
		Min.	12.4	<0.73	<231	<30.8	<194	<0.23	<1.1	0.12	<1.2	6.3	1.1	0.09	<0.43	<1.0	0.39	<0.60	0.006	<0.001	0.09	84.1	784	12.1	<0.001	0.001	<0.001
		Max.	292	492	3469	343	299	14.9	50.1	36.9	2.2	33.7	3.9	0.44	16.5	7.2	17.9	123	40.0	0.29	724	242	1951	49.1	9.9	0.001	0.93
	H		241	8.7	<225	<32.4	<258	3.6	195	57.6	<1.6	11.6	3.3	0.25	4.5	1.1	16.3	9.0	5.1	0.09	55.0	387	722	20.7	435	<0.001	0.13
MV094	**L**	**Mean (n=2)**	**95.0**	**280**	**41.4**	**5.0**	**62.6**	**1.4**	**12.8**	**27.6**	**0.26**	**19.5**	**3.7**	**0.29**	**2.9**	**1.2**	**5.7**	**7.0**	**0.15**	**0.06**	**528**	**110**	**513**	**5.0**	**0.33**	**0.007**	**0.23**
Volcanics		**S.D.**	33.0	162	7.9	0.27	24.8	1.4	8.7	24.9	0.03	5.9	0.005	0.11	1.8	0.16	3.8	3.8	0.15	0.04	364	78.2	214	0.64	0.28	0.001	0.18
		Min.	61.9	118	33.5	4.8	<37.7	<0.04	4.1	2.7	<0.23	13.6	3.7	0.18	1.1	0.99	1.9	3.2	0.005	0.03	164	31.7	299	4.4	0.05	0.006	0.04
		Max.	128	441	49.3	4.8	87.4	2.8	21.5	52.5	0.28	25.4	3.7	0.40	4.6	1.3	9.5	10.7	0.30	0.10	892	188	726	5.6	0.61	0.008	0.41
	M	**Mean (n=20)**	**47.3**	**128**	**107**	**12.6**	**32.4**	**0.66**	**23.7**	**12.3**	**0.48**	**8.5**	**2.0**	**0.20**	**1.2**	**0.76**	**4.8**	**9.1**	**0.34**	**0.14**	**167**	**198**	**412**	**3.6**	**0.55**	**0.006**	**0.13**
		S.D.	19.4	129	40.6	8.0	15.3	0.80	40.1	12.5	0.34	4.3	0.86	0.17	1.6	0.59	2.3	10.3	0.27	0.22	250	176	66.6	2.6	0.53	0.008	0.25
		Min.	11.1	2.3	49.6	<2.7	<13.4	<0.04	<0.21	1.1	<0.18	2.0	0.84	<0.07	<0.11	<0.15	1.8	0.29	0.004	<0.001	0.29	36.8	302	0.64	<0.001	<0.001	0.001
		Max.	75.2	430	198	36.3	85.6	2.7	165	43.6	1.5	16.8	3.9	0.85	6.6	2.6	10.1	44.4	1.1	0.79	1121	533	500	10.3	1.6	0.03	1.2
	H		19.3	2.0	136	<4.7	<25.2	0.33	0.59	0.55	0.29	3.0	1.1	<0.10	<0.16	<0.19	4.0	1.4	0.03	0.004	0.41	382	501	0.60	0.02	<0.001	0.004

Table C8. (Continued) Zoned hematite in RD647 (SE-lobe)

Drillhole	U*	Sample	Y	La	Ce	Pr	Nd	Sm	Eu	Gd	Tb	Dy	Ho	Er	Tm	Yb	Lu	∑REY	W	^{204}Pb	^{206}Pb	^{207}Pb	^{208}Pb	Th	U
RD647																									
MV092	**L**	**Mean (n=7)**	**0.09**	**0.68**	**0.78**	**0.05**	**0.13**	**0.02**	**0.006**	**0.04**	**0.007**	**0.02**	**0.01**	**0.04**	**0.007**	**0.07**	**0.01**	**2.0**	**3538**	**14.8**	**60.7**	**14.8**	**8.1**	**0.13**	**46.2**
Volcanics		**S.D.**	0.19	0.78	0.83	0.05	0.14	0.02	0.007	0.03	0.005	0.03	0.01	0.06	0.01	0.09	0.01	1.8	1893	15.2	37.6	18.7	18.2	0.30	32.8
		Min.	0.002	0.002	0.007	<0.006	<0.001	<0.001	<0.001	<0.001	0.001	<0.001	<0.001	<0.001	<0.001	0.02	0.005	0.14	448	<7.0	10.7	1.5	<0.03	<0.001	8.2
		Max.	0.54	2.2	2.1	0.14	0.38	0.009	0.02	0.11	0.02	0.10	0.04	0.17	0.04	0.28	0.04	4.4	6042	51.8	122	58.9	52.7	0.87	107
	M	**Mean (n=6)**	**0.81**	**4.8**	**7.5**	**0.53**	**1.5**	**0.16**	**0.03**	**0.13**	**0.02**	**0.19**	**0.06**	**0.25**	**0.06**	**0.66**	**0.14**	**16.9**	**2659**	**<7.4**	**451**	**56.9**	**0.83**	**0.08**	**406**
		S.D.	0.53	3.1	5.6	0.47	1.5	0.17	0.04	0.09	0.01	0.15	0.05	0.22	0.05	0.64	0.14	10.6	2215	-	220	28.1	1.2	0.06	197
		Min.	0.15	1.1	1.6	0.11	0.33	0.009	<0.001	0.008	0.002	0.01	0.008	0.04	0.007	0.12	0.03	3.6	1034	-	236	30.4	<0.03	<0.001	220
		Max.	1.5	10.8	18.7	1.5	4.5	0.52	0.11	0.27	0.04	0.43	0.13	0.66	0.13	1.8	0.36	37.4	7536	-	820	103	3.3	0.20	734
	H		1.4	14.4	22.4	1.6	4.7	0.44	0.05	0.16	0.05	0.38	0.10	0.54	0.12	1.3	0.30	47.9	4793	<8.1	2416	292	0.04	0.07	2364
LCD32	**L**	**Mean (n=3)**	**0.19**	**0.46**	**0.90**	**0.08**	**0.24**	**0.04**	**0.006**	**0.04**	**0.007**	**0.03**	**0.006**	**0.03**	**0.004**	**0.03**	**0.008**	**2.1**	**2406**	**2.5**	**23.6**	**3.1**	**0.09**	**0.01**	**22.6**
Volcanics		**S.D.**	0.10	0.47	0.93	0.08	0.22	0.03	0.003	0.007	0.003	0.01	0.003	0.02	0.002	0.01	0.003	1.9	1627	0.35	14.4	1.9	0.10	0.007	13.6
		Min.	0.06	0.11	0.19	0.02	0.05	0.02	0.001	<0.03	<0.003	<0.02	0.003	0.01	0.001	0.02	<0.004	0.71	764	2.1	5.3	0.75	0.02	0.003	4.9
		Max.	0.30	1.1	2.2	0.19	0.55	0.09	0.001	0.05	0.009	0.05	0.01	0.05	0.005	0.05	0.01	4.7	4623	2.1	40.6	5.5	0.23	0.02	37.8
	M	**Mean (n=3)**	**0.69**	**10.6**	**15.6**	**1.0**	**2.1**	**0.23**	**0.06**	**0.14**	**0.02**	**0.19**	**0.04**	**0.18**	**0.04**	**0.35**	**0.06**	**31.4**	**2650**	**2.7**	**467**	**58.8**	**0.31**	**0.06**	**452**
		S.D.	0.40	9.5	13.2	0.76	1.6	0.13	0.05	0.04	0.02	0.13	0.03	0.13	0.03	0.21	0.04	26.3	1007	0.21	179	23.2	0.25	0.02	184
		Min.	0.31	2.2	3.7	0.31	0.80	0.12	0.009	0.10	0.007	0.09	0.02	0.07	0.02	0.14	0.02	8.1	1438	<2.6	320	38.6	0.02	0.04	297
		Max.	1.2	23.9	34.1	2.1	4.4	0.42	0.12	0.19	0.04	0.37	0.09	0.36	0.09	0.64	0.11	68.1	3905	2.6	719	91.4	0.62	0.09	711
	H		0.80	11.4	17.7	1.4	3.4	0.36	0.04	0.16	0.03	0.24	0.06	0.28	0.07	0.86	0.20	36.9	3541	<2.5	3716	457	0.49	0.26	3820
MV093A	**L**	**Mean (n=4)**	**0.43**	**0.24**	**0.47**	**0.04**	**0.15**	**0.02**	**0.01**	**0.05**	**0.007**	**0.08**	**0.03**	**0.14**	**0.04**	**0.36**	**0.10**	**2.2**	**2019**	**6.0**	**93.3**	**19.2**	**8.4**	**0.13**	**63.4**
Volcanics		**S.D.**	0.35	0.26	0.45	0.04	0.15	0.02	0.009	0.03	0.003	0.07	0.02	0.09	0.03	0.24	0.06	1.7	1534	6.7	22.3	11.4	11.4	0.13	19.4
		Min.	0.02	0.03	0.08	0.003	0.01	<0.001	0.002	0.02	<0.004	0.008	0.002	<0.001	0.001	0.004	0.01	0.23	25.2	1.7	72.4	8.3	<0.03	<0.001	50.1
		Max.	0.88	0.68	1.2	0.09	0.38	0.03	0.03	0.09	0.01	0.16	0.05	0.23	0.09	0.68	0.17	4.6	4057	17.6	131	38.3	28.0	0.34	96.9
	M	**Mean (n=2)**	**0.08**	**0.51**	**0.76**	**0.05**	**0.08**	**0.007**	**0.002**	**0.02**	**0.004**	**0.01**	**0.008**	**0.02**	**0.02**	**0.21**	**0.08**	**1.9**	**3716**	**<2.2**	**507**	**59.1**	**<0.02**	**0.02**	**394**
		S.D.	0.05	0.38	0.49	0.04	0.06	0.007	0.002	0.01	0.001	0.006	0.003	0.01	0.01	0.10	0.03	1.2	1111	-	187	21.0	-	0.001	145
		Min.	0.03	0.12	0.27	0.01	0.02	<0.001	<0.001	0.007	0.004	0.008	0.004	0.01	0.006	0.11	0.06	0.68	2605	-	319	38.1	-	0.02	249
		Max.	0.12	0.89	1.2	0.08	0.15	0.01	0.003	0.007	0.004	0.02	0.01	0.03	0.03	0.31	0.11	3.0	4828	-	694	80.1	-	0.03	539
MV093B	**L**	**Mean (n=10)**	**1.4**	**2.6**	**4.1**	**0.33**	**0.99**	**0.17**	**0.07**	**0.14**	**0.03**	**0.26**	**0.08**	**0.36**	**0.09**	**0.86**	**0.23**	**11.8**	**2161**	**4.2**	**46.5**	**15.0**	**9.7**	**0.32**	**27.9**
Volcanics		**S.D.**	2.0	3.6	5.3	0.44	1.5	0.29	0.14	0.22	0.06	0.40	0.11	0.44	0.10	1.0	0.27	14.0	1659	6.1	49.2	21.4	17.9	0.34	30.5
		Min.	0.01	0.005	0.01	<0.001	0.03	<0.001	<0.001	0.007	<0.001	0.009	<0.001	<0.01	<0.001	0.005	0.002	0.16	452	<0.94	0.26	<0.04	<0.03	<0.001	0.18
		Max.	6.3	10.2	13.7	1.3	4.7	0.89	0.42	0.70	0.19	1.2	0.33	1.3	0.31	3.0	0.80	42.1	5290	19.3	128	61.4	51.7	0.92	95.3
	M	**Mean (n=7)**	**5.9**	**4.2**	**12.6**	**0.76**	**3.1**	**0.61**	**0.07**	**0.67**	**0.16**	**1.3**	**0.34**	**1.6**	**0.36**	**3.4**	**0.75**	**35.8**	**3908**	**2.4**	**1020**	**132**	**4.5**	**1.4**	**851**
		S.D.	4.8	2.9	9.7	0.53	2.1	0.49	0.06	0.53	0.13	1.1	0.30	1.3	0.32	2.8	0.58	26.8	3327	2.2	462	53.4	6.6	1.6	399
		Min.	0.11	0.03	0.03	<0.001	<0.03	<0.001	0.005	<0.001	<0.001	0.02	0.009	0.08	0.02	0.34	0.10	0.77	902	0.98	430	70.9	<0.03	<0.01	342
		Max.	13.4	7.9	28.1	1.5	5.8	1.3	0.18	1.6	0.35	3.1	0.83	3.6	0.87	8.0	1.6	78.0	9741	7.6	1791	224	18.9	4.7	1515
	H		5.1	38.4	61.2	4.1	11.8	1.2	0.13	1.0	0.18	1.3	0.35	1.7	0.39	4.1	1.0	132	3404	<1.1	6120	746	4.4	17.6	4443
MV094	**L**	**Mean (n=2)**	**1.2**	**1.3**	**2.5**	**0.25**	**0.75**	**0.09**	**0.01**	**0.14**	**0.02**	**0.22**	**0.07**	**0.33**	**0.08**	**0.89**	**0.21**	**8.1**	**2911**	**3.6**	**103**	**13.5**	**0.78**	**1.2**	**94.2**
Volcanics		**S.D.**	0.55	0.95	2.0	0.22	0.62	0.06	0.01	0.03	0.005	0.13	0.05	0.25	0.06	0.71	0.17	2.0	1460	0.03	24.3	2.1	0.37	1.1	20.8
		Min.	0.64	0.36	0.48	0.03	0.13	0.03	0.005	0.12	0.02	0.09	0.02	0.09	0.01	0.18	0.04	6.1	1451	3.6	78.5	11.4	0.42	0.02	73.5
		Max.	1.7	2.3	4.5	0.46	1.4	0.15	0.02	0.17	0.03	0.34	0.12	0.58	0.14	1.6	0.38	10.1	4371	3.7	127	15.6	1.2	2.3	115
	M	**Mean (n=20)**	**0.89**	**2.5**	**4.5**	**0.35**	**0.97**	**0.10**	**0.02**	**0.07**	**0.01**	**0.15**	**0.05**	**0.29**	**0.07**	**0.83**	**0.19**	**11.0**	**2522**	**4.5**	**466**	**58.7**	**0.84**	**0.40**	**447**
		S.D.	1.2	4.6	7.7	0.64	1.7	0.15	0.02	0.07	0.01	0.18	0.07	0.41	0.11	1.1	0.24	14.5	1643	1.7	286	35.4	1.4	0.72	286
		Min.	0.04	0.03	0.05	0.003	0.005	<0.001	<0.001	0.002	0.001	0.007	0.003	0.01	0.004	0.05	0.01	0.38	489	2.2	145	22.1	0.09	0.009	127
		Max.	3.9	20.8	34.5	2.8	7.5	0.65	0.08	0.25	0.06	0.66	0.25	1.4	0.39	4.0	0.87	67.3	5136	9.8	898	113	6.3	3.1	920
	H		0.13	2.4	3.4	0.21	0.54	0.06	0.008	0.02	0.005	0.03	0.01	0.03	0.01	0.13	0.05	7.0	2529	4.9	1652	205	0.31	0.07	1564

Table C9. Zoned hematite in RD647 (SE-lobe)

Drillhole	U*	Sample	Mg	Al	Si	P	Ca	Sc	Ti	V	Cr	Mn	Co	Ni	Cu	Zn	Ga	As	Sr	Zr	Nb	Mo	Sn	Sb	Ba	Hf	Ta
RD647																											
LCD35	**L**	**Mean (n=7)**	**42.0**	**117**	**169**	**<22.0**	**<217**	**1.5**	**121**	**27.3**	**2.4**	**10.8**	**2.3**	**0.42**	**0.78**	**1.6**	**5.9**	**5.6**	**0.42**	**0.84**	**839**	**86.7**	**654**	**3.6**	**0.92**	**0.03**	**1.7**
Volcanics		**S.D.**	16.5	106	21.8	-	-	1.7	144	22.6	2.2	3.6	0.79	0.24	0.68	1.3	1.5	7.8	0.54	1.0	824	57.6	300	2.5	1.1	0.03	2.0
		Min.	17.9	21.2	<147	-	-	<0.18	<0.79	0.11	<1.3	5.2	1.1	<0.24	<0.42	<0.52	2.7	<0.22	<0.001	0.008	1.9	15.1	404	1.8	<0.001	<0.001	<0.001
		Max.	74.2	338	220	-	-	4.7	389	64.3	7.8	15.1	3.6	0.98	2.4	4.1	7.8	21.9	1.6	2.9	1906	178	1334	8.9	2.7	0.08	5.0
	M	**Mean (n=5)**	**57.4**	**236**	**<140**	**<18.8**	**<169**	**1.7**	**67.6**	**23.2**	**2.3**	**8.3**	**1.8**	**<0.21**	**0.52**	**1.0**	**5.1**	**2.3**	**0.89**	**0.25**	**601**	**186**	**558**	**2.8**	**0.66**	**0.01**	**0.61**
		S.D.	62.7	276	-	-	-	2.5	111	27.8	1.5	4.0	0.77	-	0.21	0.17	1.8	2.0	0.93	0.42	1090	192	325	2.3	0.72	0.01	1.1
		Min.	9.5	7.3	-	-	-	<0.17	0.71	0.43	<1.1	4.2	0.83	-	<0.38	0.71	3.1	<0.21	0.004	<0.001	0.11	4.8	53.2	0.61	<0.001	<0.001	0.002
		Max.	179	686	-	-	-	6.7	287	70.4	5.1	14.9	2.9	-	0.93	1.2	7.6	5.9	2.6	1.1	2775	522	1021	7.2	1.7	0.007	2.9

Table C9. (Continued) Zoned hematite in RD647 (SE-lobe)

Drillhole	U*	Sample	Y	La	Ce	Pr	Nd	Sm	Eu	Gd	Tb	Dy	Ho	Er	Tm	Yb	Lu	∑REY	W	^{204}Pb	^{206}Pb	^{207}Pb	^{208}Pb	Th	U
RD647																									
LCD35	**L**	**Mean (n=7)**	**0.27**	**0.10**	**0.35**	**0.02**	**0.06**	**0.02**	**0.005**	**0.03**	**0.007**	**0.05**	**0.01**	**0.06**	**0.02**	**0.16**	**0.04**	**1.2**	**4173**	**5.2**	**20.2**	**5.8**	**3.6**	**0.03**	**14.5**
Volcanics		**S.D.**	0.32	0.07	0.31	0.02	0.04	0.01	0.003	0.03	0.004	0.06	0.02	0.07	0.01	0.12	0.02	1.0	1602	3.9	15.5	5.1	4.3	0.03	13.8
		Min.	0.009	0.007	0.01	0.002	0.005	<0.001	<0.001	<0.001	0.002	<0.001	<0.001	<0.01	0.004	0.05	0.02	0.13	1280	<2.4	6.5	0.77	0.02	<0.001	3.7
		Max.	0.87	0.23	0.88	0.04	0.10	0.02	0.008	0.09	0.01	0.16	0.05	0.18	0.04	0.35	0.08	2.9	6340	13.1	51.0	15.2	11.2	0.08	46.0
	M	**Mean (n=5)**	**1.9**	**2.4**	**3.5**	**0.15**	**0.39**	**0.07**	**0.01**	**0.16**	**0.04**	**0.36**	**0.11**	**0.57**	**0.13**	**1.4**	**0.30**	**11.4**	**1653**	**2.2**	**541**	**65.4**	**0.68**	**2.8**	**504**
		S.D.	3.4	4.4	6.2	0.25	0.64	0.08	0.02	0.26	0.06	0.62	0.20	1.0	0.22	2.2	0.46	13.4	1732	0.16	330	39.2	0.78	3.6	280
		Min.	0.03	0.08	0.10	0.009	<0.001	<0.001	0.001	<0.001	<0.001	<0.01	0.002	<0.008	0.001	0.03	0.01	0.32	31.5	<2.0	191	24.4	0.05	<0.001	183
		Max.	8.7	11.1	15.8	0.64	1.7	0.20	0.04	0.67	0.16	1.6	0.52	2.6	0.56	5.8	1.2	31.0	5005	2.1	1104	132	2.2	9.0	953

Table C10. Zoned hematite in RD1628-9 (SE-lobe)

Drillhole	U*	Sample	Mg	Al	Si	P	Ca	Sc	Ti	V	Cr	Mn	Co	Ni	Cu	Zn	Ga	As	Sr	Zr	Nb	Mo	Sn	Sb	Ba	Hf	Ta
RD1628-9																											
LCD36	**L**	**Mean (n=3)**	**58.2**	**16.4**	**930**	**46.0**	**<191**	**<0.20**	**22.8**	**2.3**	**<1.3**	**12.9**	**2.4**	**0.22**	**10.2**	**2.0**	**3.0**	**29.7**	**0.49**	**0.09**	**21.2**	**311**	**435**	**5.0**	**0.42**	**0.003**	**0.05**
Sediments		**S.D.**	39.6	15.1	1101	37.4	-	-	31.4	3.1	-	8.6	0.75	0.08	13.8	1.9	0.52	41.7	0.67	0.11	29.8	323	101	4.5	0.59	0.004	0.07
		Min.	29.4	5.6	<151	<19.0	-	-	<0.48	0.12	-	6.8	1.9	<0.13	<0.39	<0.64	2.3	<0.21	<0.02	<0.001	0.04	66.0	363	1.9	<0.001	<0.001	<0.001
		Max.	114	37.8	2487	98.8	-	-	67.2	6.7	-	25.1	3.5	0.32	29.7	4.7	3.5	88.6	1.4	0.24	63.4	767	578	11.4	1.3	0.008	0.15
	M	**Mean (n=6)**	**74.7**	**106**	**174**	**<19.7**	**<181**	**1.2**	**220**	**19.4**	**<1.3**	**8.1**	**1.9**	**0.21**	**<0.47**	**0.73**	**3.2**	**9.5**	**1.5**	**0.07**	**556**	**282**	**556**	**3.0**	**0.26**	**0.01**	**1.9**
		S.D.	67.1	145	43.7	-	-	1.5	313	20.5	-	7.4	1.6	0.05	-	0.12	1.5	15.5	2.2	0.10	767	363	218	1.5	0.31	0.02	3.0
		Min.	4.1	7.3	<148	-	-	<0.17	<0.74	0.13	-	<0.43	0.20	<0.14	-	<0.60	1.3	0.29	0.008	<0.001	0.14	5.8	327	0.65	<0.001	<0.001	<0.001
		Max.	182	392	271	-	-	3.6	728	58.5	-	20.1	4.5	0.16	-	0.90	5.9	43.2	6.0	0.27	1898	995	969	5.8	0.77	0.02	8.2
LCD39	**L**	**Mean (n=5)**	**41.3**	**895**	**173**	**29.7**	**<187**	**1.0**	**172**	**6.9**	**4.1**	**10.0**	**2.0**	**0.87**	**0.58**	**0.87**	**13.6**	**16.7**	**0.71**	**0.12**	**4.6**	**3259**	**233**	**26.3**	**1.9**	**0.01**	**0.09**
Sediments		**S.D.**	23.5	1031	16.8	15.2	-	1.6	272	6.9	4.7	4.7	0.49	0.75	0.19	0.29	13.9	23.9	0.81	0.14	5.2	4419	115	41.9	2.7	0.02	0.16
		Min.	13.9	46.3	<157	<20.0	-	<0.19	<0.69	0.66	<1.5	5.4	1.6	<0.20	<0.42	<0.58	3.3	0.52	0.02	<0.001	0.11	83.8	30.5	1.5	<0.001	<0.001	<0.001
		Max.	69.2	2424	204	60.0	-	4.3	706	20.2	13.4	18.7	2.9	1.9	0.95	1.2	39.4	64.2	1.9	0.37	13.6	11549	367	110	7.2	0.04	0.40
	M		96.5	202	<148	<20.0	<174	<0.15	1.7	16.8	<1.3	9.8	1.8	<0.26	<0.41	7.5	4.7	0.45	4.6	0.007	30.4	91.8	336	4.6	6.8	<0.001	<0.009
CLC109B	**L**	**Mean (n=14)**	**58.0**	**54.2**	**497**	**<197**	**<1618**	**1.7**	**196**	**26.1**	**7.6**	**26.1**	**4.2**	**2.2**	**22.8**	**16.1**	**5.8**	**162**	**5.9**	**0.09**	**9.4**	**106**	**975**	**114**	**11.3**	**0.06**	**0.14**
Sediments		**S.D.**	20.4	50.5	228	-	-	0.98	268	15.7	8.7	25.9	4.7	1.8	27.9	7.6	2.2	242	9.5	0.10	12.7	74.0	438	158	17.1	0.07	0.35
		Min.	34.0	<12.8	<292	-	-	<0.95	4.6	0.99	<3.5	7.2	1.6	<0.79	<5.0	<10.6	2.7	<8.2	<0.09	<0.001	0.10	38.6	377	13.2	<0.001	<0.001	<0.001
		Max.	100	191	965	-	-	3.7	667	57.2	37.5	81.4	21.0	8.5	82.8	37.4	10.5	656	25.9	0.36	40.9	330	1714	445	48.4	0.11	1.4
	M	**Mean (n=8)**	**72.3**	**124**	**692**	**237**	**<1555**	**1.1**	**34.1**	**9.3**	**4.4**	**17.1**	**3.5**	**1.6**	**36.6**	**12.3**	**6.6**	**431**	**4.7**	**0.06**	**1.2**	**144**	**1036**	**206**	**4.3**	**0.007**	**0.01**
		S.D.	16.5	206	503	78.2	-	0.17	44.7	5.6	2.3	12.6	2.5	0.28	59.5	2.3	5.4	814	10.8	0.08	1.6	60.9	372	357	7.9	0.02	0.01
		Min.	45.2	<11.8	<293	<176	-	<0.93	<4.8	2.1	<3.4	7.9	1.3	<1.1	<4.2	<10.6	2.4	<7.9	0.03	<0.001	0.08	46.8	630	17.6	<0.001	<0.001	<0.001
		Max.	99.6	620	1835	375	-	1.5	120	19.0	10.5	47.8	9.4	1.7	177	18.1	19.0	2414	33.1	0.18	4.9	215	1625	1082	24.4	0.05	0.03
	H		39.7	146	<291	<190	<1461	<1.1	4.3	<0.51	<3.5	7.0	2.6	1.7	<5.1	<12.3	6.5	<8.2	0.09	<0.001	0.03	297	1289	10.4	<0.001	<0.001	<0.001

Table C10. (Continued) Zoned hematite in RD1628-9 (SE-lobe)

Drillhole	U*	Sample	Y	La	Ce	Pr	Nd	Sm	Eu	Gd	Tb	Dy	Ho	Er	Tm	Yb	Lu	∑REY	W	^{204}Pb	^{206}Pb	^{207}Pb	^{208}Pb	Th	U
RD1628-9																									
LCD36	**L**	**Mean (n=3)**	**0.55**	**10.9**	**18.1**	**1.5**	**4.1**	**0.37**	**0.15**	**0.24**	**0.02**	**0.18**	**0.04**	**0.17**	**0.04**	**0.40**	**0.11**	**36.8**	**6598**	**3.4**	**78.3**	**10.8**	**1.3**	**0.07**	**73.3**
Sediments		**S.D.**	0.69	15.5	25.6	2.1	5.8	0.51	0.21	0.33	0.03	0.24	0.04	0.20	0.04	0.33	0.08	51.5	377	0.79	16.1	3.4	1.8	0.10	14.2
		Min.	0.05	0.008	0.02	<0.001	0.009	0.005	<0.001	<0.001	<0.003	<0.01	0.004	0.02	0.009	0.14	0.04	0.34	6240	<2.3	56.9	7.0	<0.01	<0.001	53.5
		Max.	1.5	32.8	54.3	4.4	12.2	1.1	0.45	0.71	0.06	0.53	0.10	0.45	0.09	0.86	0.22	110	7120	4.0	95.8	15.4	3.8	0.21	86.3
	M	**Mean (n=6)**	**1.4**	**8.4**	**18.3**	**1.4**	**4.0**	**0.36**	**0.03**	**0.21**	**0.04**	**0.31**	**0.10**	**0.42**	**0.09**	**0.99**	**0.23**	**36.3**	**3019**	**2.5**	**358**	**44.7**	**0.50**	**0.18**	**338**
		S.D.	1.1	8.2	19.3	1.7	4.7	0.31	0.02	0.15	0.03	0.27	0.08	0.36	0.07	0.79	0.16	33.5	2993	0.48	231	29.3	0.99	0.16	227
		Min.	0.11	0.08	0.33	0.03	0.11	<0.02	0.001	0.03	0.003	0.006	0.003	0.02	0.003	0.06	0.02	0.96	24.2	<1.8	152	18.4	<0.01	0.007	142
		Max.	2.8	18.6	48.8	4.4	12.7	0.81	0.06	0.39	0.09	0.71	0.23	0.97	0.20	2.2	0.48	85.4	8982	3.3	794	100	2.7	0.46	773
LCD39	**L**	**Mean (n=5)**	**0.28**	**7.7**	**7.2**	**0.35**	**0.68**	**0.05**	**0.03**	**0.06**	**0.009**	**0.06**	**0.02**	**0.09**	**0.02**	**0.27**	**0.07**	**16.9**	**2406**	**2.7**	**48.4**	**6.7**	**0.87**	**0.90**	**44.9**
Sediments		**S.D.**	0.34	14.3	13.4	0.64	1.2	0.09	0.05	0.07	0.01	0.09	0.02	0.10	0.02	0.24	0.06	30.5	1689	0.29	40.8	5.2	0.96	0.79	40.0
		Min.	0.03	0.09	0.18	0.01	0.03	<0.001	<0.001	0.02	<0.003	0.007	0.002	<0.01	0.003	0.04	0.02	0.62	337	<2.3	15.0	2.0	0.03	0.005	13.3
		Max.	0.93	36.3	33.9	1.6	3.2	0.23	0.13	0.19	0.03	0.24	0.06	0.25	0.05	0.59	0.16	77.8	4712	3.2	123	15.7	2.5	2.1	121
	M		1.3	0.04	0.08	0.003	<0.02	<0.04	<0.006	<0.03	0.009	0.23	0.08	0.57	0.14	1.6	0.42	4.5	555	<1.9	326	40.1	0.65	0.65	306
CLC109B	**L**	**Mean (n=14)**	**0.20**	**1.1**	**4.7**	**0.42**	**0.91**	**0.19**	**0.10**	**0.12**	**0.02**	**0.10**	**0.02**	**0.04**	**0.01**	**0.06**	**0.009**	**8.0**	**5201**	**29.0**	**163**	**45.1**	**30.7**	**0.34**	**61.7**
Sediments		**S.D.**	0.28	1.4	7.1	0.65	1.4	0.22	0.14	0.07	0.02	0.15	0.02	0.05	0.01	0.07	0.009	11.4	2896	41.8	83.3	50.7	49.6	0.55	23.0
		Min.	<0.001	<0.02	0.03	<0.001	<0.001	<0.001	<0.001	<0.001	<0.001	<0.001	<0.001	<0.001	<0.001	<0.001	<0.001	0.42	700	3.5	67.6	8.4	<0.33	0.005	19.8
		Max.	0.81	4.3	20.4	1.9	4.1	0.64	0.37	0.27	0.07	0.54	0.06	0.21	0.04	0.29	0.03	33.3	10165	119	317	149	132	1.6	111
	M	**Mean (n=8)**	**0.26**	**1.8**	**4.5**	**0.33**	**0.70**	**0.15**	**0.13**	**0.10**	**0.02**	**0.10**	**0.02**	**0.06**	**0.01**	**0.10**	**0.02**	**8.3**	**5970**	**19.2**	**815**	**116**	**21.3**	**0.14**	**428**
		S.D.	0.40	3.6	8.1	0.56	1.1	0.15	0.25	0.10	0.02	0.14	0.02	0.07	0.01	0.06	0.02	14.2	3397	32.0	689	92.6	44.5	0.30	380
		Min.	0.02	0.02	0.02	<0.001	0.03	<0.001	<0.001	<0.001	<0.001	<0.001	<0.001	<0.001	<0.001	0.04	<0.001	0.39	1837	<3.9	264	31.8	<0.35	<0.001	136
		Max.	1.1	10.8	22.9	1.4	2.6	0.43	0.75	0.33	0.07	0.41	0.06	0.19	0.03	0.24	0.05	40.4	11393	102	2058	243	136	0.93	1095
	H		0.16	3.2	7.9	0.32	0.76	0.03	<0.02	0.13	<0.001	0.04	0.009	0.04	<0.001	<0.06	0.02	12.5	2509	5.6	3194	372	<0.35	0.08	1806

Table C11. Zoned hematite in the deposit middle

Drillhole	U*	Sample	Mg	Al	Si	P	Ca	Sc	Ti	V	Cr	Mn	Co	Ni	Cu	Zn	Ga	As	Sr	Zr	Nb	Mo	Sn	Sb	Ba	Hf	Ta
RD2765																											
MV103	**L**	**Mean (n=2)**	**76.1**	**382**	**88.3**	**5.1**	**27.6**	**2.2**	**10.4**	**16.9**	**0.25**	**12.4**	**3.5**	**0.26**	**0.35**	**0.75**	**6.6**	**5.7**	**0.08**	**0.05**	**11.0**	**183**	**426**	**2.9**	**0.04**	**0.008**	**0.01**
		S.D.	1.5	36.4	6.8	2.2	9.1	1.1	8.5	5.6	0.09	0.60	0.10	0.08	0.04	0.28	0.38	0.53	0.002	0.04	2.5	15.8	8.7	0.04	0.005	0.008	0.008
		Min.	74.6	346	81.5	<3.0	<18.5	1.1	1.9	11.2	<0.16	11.8	3.4	0.18	0.31	0.47	6.2	5.2	0.08	0.01	8.4	168	417	2.9	0.03	<0.001	0.006
		Max.	77.7	418	95.1	7.3	36.6	3.4	18.9	22.5	0.34	13.0	3.6	0.34	0.39	1.0	6.9	6.2	0.08	0.09	13.5	199	434	3.0	0.04	0.02	0.02
	M	**Mean (n=14)**	**89.5**	**496**	**81.8**	**8.3**	**28.4**	**3.6**	**23.6**	**16.4**	**0.56**	**11.3**	**2.7**	**0.21**	**0.64**	**1.3**	**8.7**	**8.5**	**0.39**	**0.06**	**28.3**	**178**	**396**	**6.6**	**0.79**	**0.006**	**0.06**
		S.D.	24.6	148	40.1	5.7	7.3	1.4	36.8	5.4	0.53	2.9	0.59	0.09	0.53	0.98	2.1	8.4	0.50	0.05	18.7	99.1	128	2.9	0.95	0.007	0.10
		Min.	56.3	87.9	<31.4	<2.6	<15.2	<0.03	0.68	1.9	<0.13	6.2	1.9	<0.06	<0.11	0.21	2.3	2.2	0.01	<0.001	3.2	96.1	137	2.9	<0.001	<0.001	0.003
		Max.	129	672	171	25.7	38.8	5.3	114	24.3	1.7	18.0	3.8	0.35	2.1	3.8	10.6	31.8	1.7	0.16	57.5	425	686	13.6	3.3	0.02	0.42
	H	**Mean (n=2)**	**73.9**	**59.9**	**106**	**11.4**	**<25.6**	**0.09**	**3.8**	**1.7**	**0.24**	**6.5**	**2.2**	**0.21**	**0.31**	**0.44**	**2.1**	**2.4**	**0.02**	**0.008**	**0.64**	**365**	**556**	**2.1**	**0.001**	**0.001**	**0.005**
		S.D.	7.9	28.5	20.9	4.0		0.05	0.71	0.27	0.005	0.005	0.11	0.06	0.13	0.04	0.50	1.9	0.008	0.001	0.21	91.9	39.2	0.08	0.001	0.001	0.002
		Min.	66.0	31.4	84.6	7.4		<0.05	3.1	1.5	0.23	6.5	2.1	0.15	<0.18	0.40	1.6	0.49	0.009	0.008	0.44	273	516	2.0	0.001	0.001	0.003
		Max.	81.8	88.5	126	15.4		0.14	4.5	2.0	0.24	6.5	2.3	0.26	0.44	0.49	2.6	4.2	0.03	0.008	0.85	457	595	2.2	0.001	0.001	0.007
MV104	**L**	**Mean (n=17)**	**23.7**	**202**	**85.2**	**9.7**	**39.2**	**0.18**	**1.2**	**2.8**	**0.34**	**8.9**	**2.3**	**0.25**	**1.0**	**0.79**	**7.2**	**11.1**	**0.34**	**0.02**	**15.6**	**40.7**	**269**	**5.5**	**0.35**	**0.001**	**0.008**
		S.D.	15.8	96.0	38.6	6.2	18.3	0.39	1.6	1.6	0.17	7.0	3.0	0.25	2.6	0.97	3.3	22.5	0.85	0.02	18.9	34.9	36.3	2.5	0.97	0.002	0.01
		Min.	8.7	89.4	<31.2	<4.5	<14.3	<0.05	<0.25	0.47	<0.25	3.6	0.67	<0.08	<0.16	<0.19	4.3	<0.27	0.003	<0.001	0.02	2.9	183	1.8	<0.001	<0.001	<0.001
		Max.	65.7	438	201	24.3	88.5	1.7	6.7	4.9	1.0	31.5	14.1	0.94	11.3	4.1	19.5	75.7	3.6	0.06	59.0	118	332	11.5	4.2	0.006	0.03
	M	**Mean (n=4)**	**55.2**	**371**	**87.3**	**5.7**	**42.8**	**0.28**	**0.89**	**6.3**	**0.31**	**13.7**	**3.9**	**0.49**	**0.46**	**0.79**	**6.4**	**8.1**	**0.41**	**0.005**	**17.7**	**45.8**	**213**	**6.1**	**2.5**	**0.001**	**0.01**
		S.D.	4.7	123	25.7	1.3	46.5	0.16	0.67	5.0	0.11	2.8	0.52	0.22	0.49	0.40	3.9	12.6	0.70	0.007	28.9	24.6	117	1.4	3.1	0.001	0.02
		Min.	47.7	263	45.4	<4.5	<8.9	<0.04	<0.29	2.5	<0.20	9.7	3.1	0.26	<0.17	0.30	2.6	0.48	0.009	<0.001	0.34	7.4	96.5	3.8	<0.001	<0.001	<0.001
		Max.	59.6	580	114	7.8	123	0.47	1.9	14.8	0.48	16.7	4.5	0.83	1.3	1.4	11.8	30.0	1.6	0.02	67.7	73.1	374	7.4	7.7	0.003	0.06
MV101	**L**	**Mean (n=3)**	**34.9**	**200**	**<290**	**40.8**	**<276**	**<0.32**	**1.6**	**2.7**	**<1.9**	**7.3**	**2.1**	**0.26**	**2.3**	**2.4**	**5.8**	**9.4**	**0.31**	**0.005**	**0.36**	**30.3**	**602**	**4.8**	**0.41**	**0.001**	**0.001**
Sediments		**S.D.**	8.3	131	-	1.8	-	-	0.27	0.94	-	1.4	0.58	0.09	1.3	1.3	4.5	6.1	0.22	0.007	0.32	18.1	232	0.81	0.30	0.001	0.001
		Min.	23.6	18.8	-	<39.4	-	-	<1.4	1.9	-	6.2	1.6	0.17	<0.51	<1.5	1.7	2.0	0.007	<0.001	0.07	8.4	298	3.9	<0.001	0.001	0.001
		Max.	43.3	325	-	39.7	-	-	2.0	4.0	-	9.3	2.9	0.22	3.6	4.2	12.1	17.0	0.53	0.01	0.80	52.7	862	5.8	0.70	0.001	0.001
	M	**Mean (n=5)**	**167**	**343**	**657**	**119**	**<289**	**0.35**	**7.2**	**8.9**	**2.2**	**20.5**	**5.6**	**0.68**	**15.6**	**22.4**	**2.8**	**112**	**4.9**	**1.5**	**5.2**	**278**	**604**	**28.8**	**21.2**	**0.06**	**0.04**
		S.D.	88.3	564	759	151	-	0.09	7.2	7.8	1.3	13.7	5.3	0.67	24.4	37.3	2.9	183	8.6	2.7	4.3	166	314	27.4	27.2	0.10	0.05
		Min.	57.4	0.91	<261	<35.7	-	<0.27	1.4	0.39	<1.4	5.4	1.7	0.15	<0.52	<1.2	0.26	7.1	0.16	<0.001	1.6	176	230	5.9	0.35	<0.001	0.004
		Max.	267	1455	2174	421	-	0.53	19.4	19.9	4.7	42.4	16.0	2.0	64.2	96.8	8.3	478	22.0	6.9	13.4	609	1021	79.6	69.0	0.26	0.14
	H	**Mean (n=2)**	**40.3**	**0.83**	**310**	**35.4**	**<273**	**<0.29**	**1.2**	**0.22**	**<1.7**	**5.1**	**1.7**	**0.21**	**0.50**	**1.4**	**0.78**	**3.2**	**0.39**	**0.007**	**0.12**	**559**	**704**	**3.2**	**0.63**	**0.001**	**0.001**
		S.D.	3.9	0.05	50.7	1.1	-	-	0.17	0.16	-	0.89	0.21	0.005	0.03	0.26	0.11	2.5	0.39	0.007	0.09	128	25.1	0.11	0.63	0.001	0.001
		Min.	36.4	0.78	<259	<34.3	-	-	<1.1	<0.05	-	4.2	1.5	0.001	0.001	<1.1	0.67	<0.74	<0.001	<0.001	0.03	431	679	3.1	<0.001	0.001	0.001
		Max.	44.2	0.78	360	36.5	-	-	1.4	0.38	-	6.0	1.9	0.001	0.001	1.7	0.89	5.7	0.78	0.01	0.20	687	730	3.3	1.3	0.001	0.001
Underground																											
CLC057	**L**	**Mean (n=13)**	**23.3**	**139**	**151**	**8.1**	**32.9**	**0.28**	**19.2**	**43.8**	**0.32**	**6.4**	**1.5**	**0.17**	**0.19**	**0.34**	**2.3**	**0.83**	**0.05**	**0.008**	**99.6**	**76.2**	**630**	**2.1**	**0.08**	**0.002**	**0.05**
		S.D.	3.6	85.3	135	3.1	5.6	0.33	36.8	8.9	0.06	0.46	0.12	0.09	0.03	0.16	0.43	0.80	0.09	0.007	41.7	28.7	68.1	0.43	0.17	0.002	0.05
		Min.	16.4	42.2	<30.9	<5.0	<23.1	<0.05	0.32	29.4	<0.23	5.4	1.2	<0.07	<0.14	0.16	1.6	<0.28	<0.001	<0.001	39.7	13.4	564	1.6	<0.001	<0.001	0.005
		Max.	29.9	349	516	15.5	37.4	1.1	142	60.4	0.44	7.2	1.7	0.37	0.28	0.78	3.0	2.8	0.30	0.02	177	102	789	3.3	0.64	0.006	0.15

Table C11. (Continued) Zoned hematite in the deposit middle

Drillhole	U*	Sample	Y	La	Ce	Pr	Nd	Sm	Eu	Gd	Tb	Dy	Ho	Er	Tm	Yb	Lu	∑REY	W	204Pb	206Pb	207Pb	208Pb	Th	U
RD2765																									
MV103	**L**	**Mean (n=2)**	**0.21**	**0.28**	**0.55**	**0.04**	**0.11**	**0.02**	**0.006**	**0.02**	**0.004**	**0.05**	**0.01**	**0.09**	**0.02**	**0.28**	**0.06**	**1.8**	**2184**	**5.7**	**69.3**	**9.3**	**2.4**	**1.0**	**53.9**
		S.D.	0.10	0.15	0.30	0.02	0.07	0.02	0.005	0.01	0.002	0.03	0.008	0.04	0.006	0.08	0.01	0.84	8.7	0.91	20.7	3.6	1.6	0.45	16.4
		Min.	0.12	0.13	0.26	0.01	0.04	<0.001	<0.002	0.008	0.003	0.02	0.007	0.05	0.01	0.21	0.05	0.91	2175	4.8	48.6	5.7	0.82	0.57	37.5
		Max.	0.31	0.43	0.85	0.06	0.18	0.03	0.01	0.04	0.006	0.09	0.02	0.13	0.02	0.36	0.07	2.6	2193	6.6	90.0	12.9	4.0	1.5	70.3
	M	**Mean (n=14)**	**3.1**	**1.1**	**2.3**	**0.13**	**0.51**	**0.15**	**0.02**	**0.26**	**0.06**	**0.64**	**0.19**	**0.97**	**0.22**	**2.3**	**0.49**	**12.5**	**1502**	**4.9**	**370**	**48.0**	**4.7**	**8.1**	**329**
		S.D.	1.7	0.72	1.5	0.09	0.38	0.10	0.02	0.17	0.04	0.37	0.10	0.48	0.10	1.1	0.20	6.1	1131	5.5	127	15.8	5.6	3.2	114
		Min.	0.86	0.21	0.41	0.02	0.06	0.02	<0.001	0.07	0.009	0.19	0.06	0.34	0.07	0.79	0.19	3.6	609	1.0	200	25.8	0.96	2.8	187
		Max.	5.9	2.4	4.9	0.31	1.2	0.29	0.05	0.56	0.12	1.3	0.34	1.7	0.38	4.0	0.80	23.0	4301	21.4	577	77.2	22.2	13.0	507
	H	**Mean (n=2)**	**0.77**	**3.0**	**4.6**	**0.31**	**0.91**	**0.11**	**0.01**	**0.10**	**0.02**	**0.19**	**0.06**	**0.32**	**0.07**	**0.91**	**0.22**	**11.6**	**3167**	**1.9**	**5216**	**628**	**0.41**	**2.3**	**4987**
		S.D.	0.20	1.7	3.0	0.22	0.63	0.07	0.005	0.04	0.005	0.03	0.01	0.06	0.009	0.09	0.02	6.1	1259	0.63	1403	169	0.09	0.18	1572
		Min.	0.57	1.2	1.6	0.09	0.28	0.04	0.005	0.06	0.01	0.17	0.05	0.26	0.06	0.82	0.21	5.5	1909	1.3	3813	459	0.32	2.1	3415
		Max.	0.96	4.7	7.6	0.53	1.5	0.18	0.02	0.14	0.02	0.22	0.07	0.37	0.08	0.99	0.24	17.7	4426	2.6	6619	798	0.50	2.5	6559
MV104	**L**	**Mean (n=17)**	**0.24**	**0.56**	**0.93**	**0.07**	**0.19**	**0.02**	**0.006**	**0.02**	**0.004**	**0.04**	**0.01**	**0.06**	**0.02**	**0.20**	**0.05**	**2.4**	**1381**	**2.9**	**30.4**	**4.5**	**0.88**	**0.05**	**25.4**
		S.D.	0.65	1.3	2.0	0.16	0.42	0.05	0.01	0.05	0.008	0.09	0.03	0.14	0.03	0.37	0.10	5.0	1430	1.9	34.5	5.0	1.5	0.17	27.8
		Min.	0.002	<0.001	<0.002	<0.001	<0.001	<0.001	<0.001	0.002	<0.001	<0.001	<0.001	0.001	<0.001	0.007	0.002	0.05	5.0	1.4	1.6	0.19	<0.005	<0.001	1.4
		Max.	2.8	5.0	7.0	0.52	1.4	0.18	0.05	0.18	0.03	0.37	0.11	0.59	0.13	1.6	0.41	17.2	4447	8.2	130	16.2	4.7	0.73	100
	M	**Mean (n=4)**	**0.32**	**1.1**	**2.2**	**0.15**	**0.31**	**0.03**	**0.008**	**0.03**	**0.004**	**0.05**	**0.02**	**0.09**	**0.03**	**0.42**	**0.12**	**4.8**	**818**	**1.9**	**282**	**34.3**	**0.12**	**0.12**	**255**
		S.D.	0.30	0.99	2.6	0.18	0.26	0.03	0.007	0.02	0.004	0.03	0.01	0.09	0.02	0.35	0.11	3.9	494	0.60	136	16.4	0.11	0.16	117
		Min.	0.02	0.10	0.17	0.01	0.06	<0.009	0.001	<0.001	0.001	<0.004	<0.001	0.003	0.001	0.03	0.005	1.5	203	0.94	144	17.4	0.02	<0.001	123
		Max.	0.82	2.7	6.6	0.46	0.74	0.08	0.02	0.06	0.01	0.10	0.04	0.24	0.06	0.93	0.28	11.2	1510	2.5	507	61.4	0.31	0.40	444
MV101	**L**	**Mean (n=3)**	**0.15**	**0.38**	**0.73**	**0.08**	**0.19**	**0.04**	**0.003**	**0.01**	**0.004**	**0.02**	**0.006**	**0.06**	**0.02**	**0.24**	**0.07**	**2.0**	**2114**	**<1.4**	**53.3**	**7.0**	**1.1**	**0.10**	**40.1**
Sediments		**S.D.**	0.08	0.27	0.52	0.06	0.14	0.004	0.002	0.01	0.001	0.01	0.004	0.03	0.01	0.13	0.02	1.1	1446	-	28.8	3.6	0.38	0.02	21.9
		Min.	0.09	<0.001	0.003	<0.001	<0.001	0.03	<0.001	<0.001	0.003	0.005	0.001	0.03	0.002	0.07	0.05	0.50	963	-	12.9	1.9	0.59	0.08	9.3
		Max.	0.27	0.63	1.2	0.13	0.31	0.04	0.004	0.02	0.005	0.04	0.009	0.09	0.04	0.39	0.09	2.9	4153	-	77.9	10.3	1.5	0.12	57.9
	M	**Mean (n=5)**	**2.7**	**6.5**	**14.1**	**0.80**	**3.1**	**0.49**	**0.06**	**0.43**	**0.09**	**0.60**	**0.15**	**0.81**	**0.18**	**1.8**	**0.40**	**32.2**	**2786**	**17.7**	**873**	**134**	**44.5**	**1.5**	**660**
		S.D.	2.3	5.4	12.8	0.60	2.5	0.40	0.05	0.42	0.07	0.53	0.12	0.67	0.13	1.3	0.29	27.0	1688	31.4	274	63.3	82.5	1.4	252
		Min.	0.17	1.5	2.6	0.16	0.62	0.11	0.01	0.09	0.004	0.04	0.007	0.05	0.02	0.16	0.05	7.4	305	<1.2	473	51.7	<0.04	0.03	362
		Max.	5.7	15.4	35.0	1.7	7.0	1.1	0.14	1.1	0.18	1.3	0.30	1.6	0.32	3.3	0.72	74.9	4916	80.5	1178	247	209	4.1	945
	H	**Mean (n=2)**	**0.15**	**1.2**	**1.9**	**0.14**	**0.41**	**0.03**	**0.001**	**0.05**	**0.004**	**0.04**	**0.01**	**0.07**	**0.03**	**0.31**	**0.12**	**4.5**	**4380**	**1.2**	**3361**	**377**	**0.12**	**0.02**	**2745**
		S.D.	0.02	1.0	1.7	0.13	0.33	0.01	0.001	0.01	0.003	0.002	0.005	0.004	0.002	0.03	0.006	3.2	1115	0.10	684	75.5	0.10	0.002	564
		Min.	0.13	0.20	0.24	0.02	0.08	0.02	<0.001	<0.04	0.001	0.04	0.005	0.06	0.02	0.28	0.11	1.3	3265	1.1	2678	302	<0.03	0.02	2181
		Max.	0.17	2.2	3.6	0.27	0.74	0.04	0.002	0.07	0.006	0.04	0.02	0.07	0.03	0.34	0.12	7.6	5495	1.1	4045	452	0.22	0.02	3308
Underground																									
CLC057	**L**	**Mean (n=13)**	**0.15**	**0.01**	**0.02**	**0.001**	**0.006**	**0.002**	**0.001**	**0.008**	**0.001**	**0.02**	**0.01**	**0.08**	**0.02**	**0.30**	**0.06**	**0.69**	**764**	**2.9**	**26.1**	**3.3**	**0.10**	**0.09**	**22.9**
		S.D.	0.06	0.03	0.03	0.002	0.009	0.003	0.002	0.003	0.001	0.008	0.005	0.03	0.01	0.13	0.03	0.26	300	0.59	11.5	1.5	0.29	0.27	10.1
		Min.	0.01	<0.001	0.001	<0.001	<0.001	<0.001	<0.001	0.002	0.001	<0.005	0.001	0.005	0.001	0.03	0.005	0.08	464	1.6	3.6	0.42	<0.005	<0.001	3.2
		Max.	0.23	0.08	0.09	0.009	0.03	0.004	0.005	0.009	0.003	0.03	0.02	0.14	0.04	0.45	0.09	1.0	1599	4.0	43.8	5.8	1.1	1.0	39.1

Table C12. Zoned hematite in the deposit middle

Drillhole	U*	Sample	Mg	Al	Si	P	Ca	Sc	Ti	V	Cr	Mn	Co	Ni	Cu	Zn	Ga	As	Sr	Zr	Nb	Mo	Sn	Sb	Ba	Hf	Ta
RU36-9867W1																											
MV095	**L**	**Mean (n=15)**	**20.0**	**299**	**326**	**119**	**<254**	**0.68**	**62.6**	**17.1**	**2.2**	**9.5**	**4.0**	**1.2**	**2.3**	**4.8**	**5.8**	**78.6**	**3.2**	**2.3**	**96.1**	**103**	**868**	**48.9**	**0.75**	**0.09**	**0.26**
		S.D.	17.2	303	198	236	-	0.61	68.0	18.6	2.0	12.5	7.3	2.0	2.3	8.5	8.3	112	6.5	4.6	156	205	554	94.3	0.67	0.18	0.61
		Min.	3.0	5.2	<197	<30.5	-	<0.18	<0.82	0.17	<0.98	1.8	0.66	0.07	<0.29	<0.88	1.3	<0.50	<0.001	<0.001	<0.001	2.7	22.0	1.8	<0.001	<0.001	<0.001
		Max.	58.4	873	962	970	-	2.4	241	53.7	7.4	55.5	29.0	5.9	7.8	34.0	36.5	388	25.6	15.4	638	846	1814	366	1.9	0.58	2.5
	M	**Mean (n=6)**	**69.6**	**329**	**487**	**47.9**	**240**	**0.37**	**66.9**	**3.0**	**1.7**	**18.1**	**2.4**	**0.26**	**8.0**	**4.8**	**6.3**	**73.4**	**4.5**	**0.12**	**7.0**	**254**	**696**	**24.1**	**12.1**	**0.01**	**0.07**
		S.D.	25.8	181	282	24.9	34.6	0.32	103	3.7	1.1	12.0	0.40	0.10	11.6	5.3	2.2	78.5	5.3	0.15	6.3	110	195	18.3	15.0	0.02	0.12
		Min.	36.0	57.6	<182	<27.3	<183	<0.19	0.88	0.08	<0.94	6.3	1.6	0.15	<0.30	0.90	3.7	<0.44	0.004	<0.001	0.50	115	360	4.3	<0.001	<0.001	<0.001
		Max.	107	602	950	84.3	268	1.1	291	9.7	4.2	42.2	2.9	0.40	32.0	14.6	10.0	213	14.3	0.40	17.9	388	929	51.7	39.7	0.04	0.33
	H	**Mean (n=2)**	**54.2**	**274**	**338**	**306**	**<243**	**0.30**	**190**	**3.6**	**4.3**	**10.0**	**2.4**	**0.49**	**11.6**	**5.2**	**2.2**	**88.9**	**14.5**	**0.37**	**125**	**166**	**2704**	**16.5**	**1.5**	**0.02**	**0.39**
		S.D.	39.6	270	72.0	279	-	0.12	188	3.4	3.4	5.5	0.69	0.26	0.01	4.2	0.90	86.8	14.0	0.37	125	100	1044	15.7	0.76	0.02	0.39
		Min.	14.6	4.8	266	<26.8	-	<0.18	1.5	0.24	<0.99	4.6	1.7	0.24	11.5	1.1	1.3	2.1	0.52	<0.001	0.16	66.2	1660	0.75	0.79	<0.001	0.004
		Max.	93.7	544	410	584	-	0.42	378	7.0	7.7	15.5	3.1	0.75	11.6	9.4	3.1	176	28.6	0.74	250	267	3748	32.2	2.3	0.04	0.78
MV096	**L**	**Mean (n=14)**	**6.1**	**387**	**352**	**36.5**	**<376**	**2.0**	**408**	**20.4**	**3.3**	**16.1**	**2.8**	**0.61**	**15.2**	**5.5**	**6.6**	**36.2**	**0.36**	**2.4**	**564**	**57.2**	**356**	**9.3**	**0.97**	**0.16**	**1.2**
		S.D.	1.5	168	73.9	2.6	-	1.1	497	15.2	1.4	24.9	2.7	0.37	27.9	6.4	1.0	82.0	0.34	1.9	618	60.5	143	14.0	1.2	0.14	2.2
		Min.	3.6	68.9	<309	<33.2	-	<0.36	<1.5	0.32	<2.2	2.2	0.87	0.27	<0.57	0.80	5.3	<0.36	0.02	0.01	0.40	2.8	155	0.17	<0.001	<0.001	<0.001
		Max.	8.2	717	585	33.4	-	4.1	1503	48.1	6.6	83.2	9.7	1.6	92.7	19.0	8.8	324	1.0	6.0	2009	226	628	47.1	3.6	0.40	8.8
	M		27.7	316	514	<34.7	<366	39.8	11.9	74.5	2.4	16.1	2.2	0.40	7.6	6.2	16.2	16.6	6.1	<0.05	0.67	162	461	2.6	9.6	<0.05	0.01
RU49-8096-7																											
CLC046	**L**	**Mean (n=8)**	**65.2**	**10.5**	**372**	**<122**	**<975**	**0.65**	**4.0**	**0.73**	**<1.9**	**5.0**	**1.7**	**1.0**	**<2.7**	**4.3**	**0.87**	**3.5**	**0.09**	**0.04**	**0.26**	**356**	**1469**	**4.9**	**0.25**	**0.001**	**0.01**
		S.D.	69.3	3.5	149	-	-	0.10	0.73	0.49	-	4.1	0.88	0.29	-	0.42	0.20	2.3	0.07	0.05	0.41	243	371	2.3	0.25	0.001	0.007
		Min.	9.6	<8.0	187	-	-	<0.49	<2.8	<0.32	-	<1.2	0.71	0.53	-	<3.7	0.51	<2.3	0.04	0.001	0.009	10.4	873	1.8	<0.001	0.001	0.008
		Max.	229	19.3	715	-	-	0.72	5.2	1.8	-	12.4	3.2	0.77	-	4.3	1.1	9.5	0.27	0.001	1.3	724	1926	8.9	0.79	0.001	0.02
	M	**Mean (n=6)**	**34.2**	**<8.5**	**294**	**<123**	**<980**	**0.64**	**<4.0**	**0.96**	**<1.9**	**5.4**	**1.8**	**1.1**	**<2.5**	**4.1**	**0.98**	**2.5**	**0.06**	**0.01**	**1.0**	**243**	**1793**	**5.9**	**0.06**	**0.03**	**0.007**
		S.D.	13.7	-	66.8	-	-	0.10	-	0.53	-	2.0	0.30	0.24	-	0.47	0.30	0.13	0.03	0.03	1.4	103	472	3.3	0.09	0.04	0.01
		Min.	18.9	-	<176	-	-	<0.49	-	0.36	-	2.7	1.3	<0.64	-	0.001	0.67	0.001	<0.001	<0.001	0.04	124	947	2.5	<0.001	0.001	<0.001
		Max.	61.5	-	395	-	-	0.68	-	1.7	-	7.8	2.3	1.1	-	0.001	1.5	0.001	0.02	0.08	4.1	413	2343	12.7	0.19	0.001	0.02
CLC047	**L**	**Mean (n=3)**	**17.7**	**8.4**	**70.2**	**<4.6**	**53.6**	**<0.05**	**<0.25**	**7.6**	**0.33**	**3.7**	**1.3**	**0.10**	**0.22**	**0.46**	**0.85**	**0.66**	**0.23**	**0.003**	**0.35**	**143**	**282**	**0.73**	**0.25**	**0.002**	**0.001**
		S.D.	0.23	0.34	36.5	-	20.7	-	-	1.8	0.15	0.79	0.14	0.03	0.08	0.25	0.08	0.57	0.32	0.002	0.31	18.8	37.8	0.09	0.32	0.003	0.001
		Min.	17.6	7.9	<30.3	-	24.8	-	-	5.0	<0.21	2.9	1.1	0.08	<0.17	<0.28	0.77	<0.25	0.007	<0.001	0.08	123	230	0.67	<0.001	0.001	<0.001
		Max.	18.1	8.8	119	-	72.7	-	-	8.9	0.55	4.8	1.4	0.15	0.33	0.82	0.96	1.5	0.68	0.004	0.78	168	318	0.86	0.69	0.001	0.001
	M	**Mean (n=10)**	**153**	**28.1**	**93.1**	**5.7**	**33.2**	**0.05**	**0.30**	**14.5**	**0.26**	**13.9**	**3.2**	**0.15**	**0.35**	**0.72**	**1.6**	**0.77**	**0.40**	**0.005**	**2.9**	**315**	**382**	**3.7**	**0.31**	**0.002**	**0.001**
		S.D.	105	18.8	34.0	2.1	14.6	0.02	0.05	8.2	0.06	7.7	1.5	0.05	0.44	0.34	0.63	0.71	0.53	0.004	2.1	152	133	2.2	0.51	0.002	0.002
		Min.	15.0	4.8	35.1	<3.5	<21.0	<0.04	<0.25	4.4	<0.21	3.1	1.1	0.10	<0.15	<0.23	0.73	<0.25	<0.001	<0.001	0.04	114	251	0.55	<0.001	<0.001	<0.001
		Max.	302	51.9	149	9.6	63.0	0.11	0.42	28.5	0.42	22.8	5.0	0.23	1.6	1.3	2.4	2.4	1.7	0.004	7.1	506	693	6.2	1.7	0.003	0.005
CLC050	**M**	**Mean (n=5)**	**238**	**<16.6**	**<311**	**213**	**<1793**	**<1.3**	**<8.2**	**4.9**	**<3.5**	**29.9**	**4.4**	**2.1**	**18.0**	**21.0**	**1.3**	**20.5**	**1.5**	**0.001**	**412**	**116**	**2006**	**77.1**	**2.2**	**0.07**	**0.04**
		S.D.	38.1	-	-	35.3	-	-	-	0.68	-	17.1	2.0	0.52	13.6	25.2	0.41	19.2	1.9	0.001	190	10.1	121	13.9	2.3	0.08	0.007
		Min.	186	-	-	<151	-	-	-	4.2	-	16.2	2.7	0.001	<2.8	<5.0	0.68	4.9	<0.07	0.001	155	96.2	1777	57.0	<0.001	<0.001	<0.03
		Max.	300	-	-	261	-	-	-	6.2	-	61.8	8.3	0.001	38.7	70.8	1.9	50.9	5.1	0.001	727	124	2114	97.0	6.4	0.08	0.04

Table C12. (Continued) Zoned hematite in the deposit middle

Drillhole	U*	Sample	Y	La	Ce	Pr	Nd	Sm	Eu	Gd	Tb	Dy	Ho	Er	Tm	Yb	Lu	∑REY	W	^{204}Pb	^{206}Pb	^{207}Pb	^{208}Pb	Th	U
RU36-9867W1																									
MV095	**L**	**Mean (n=15)**	**0.13**	**1.2**	**1.5**	**0.11**	**0.30**	**0.04**	**0.01**	**0.04**	**0.005**	**0.03**	**0.008**	**0.04**	**0.01**	**0.13**	**0.03**	**3.6**	**1636**	**4.2**	**34.9**	**14.0**	**10.7**	**1.9**	**19.0**
		S.D.	0.15	2.7	3.1	0.20	0.52	0.06	0.009	0.04	0.005	0.04	0.01	0.04	0.01	0.19	0.04	6.9	2045	5.5	33.4	18.4	17.2	3.2	20.0
		Min.	<0.006	<0.004	<0.004	<0.001	<0.001	<0.001	<0.001	0.006	<0.001	0.003	<0.001	0.003	0.001	0.003	0.001	0.07	3.0	0.73	0.99	0.19	0.02	<0.001	0.76
		Max.	0.56	10.1	11.7	0.74	1.9	0.21	0.02	0.14	0.02	0.14	0.03	0.12	0.05	0.66	0.14	26.1	5565	21.8	126	70.0	66.2	9.4	82.7
	M	**Mean (n=6)**	**1.3**	**2.8**	**4.8**	**0.34**	**0.95**	**0.14**	**0.05**	**0.15**	**0.04**	**0.31**	**0.09**	**0.44**	**0.10**	**1.0**	**0.23**	**12.8**	**1819**	**4.2**	**317**	**48.9**	**10.8**	**0.66**	**237**
		S.D.	0.70	3.2	5.0	0.40	0.99	0.13	0.06	0.15	0.03	0.19	0.04	0.20	0.04	0.39	0.08	10.5	883	4.3	89.7	13.7	12.7	0.78	76.5
		Min.	0.28	0.16	0.24	0.02	0.04	0.005	0.003	<0.001	0.005	0.07	0.03	0.12	0.04	0.39	0.08	1.5	884	<0.69	192	28.0	0.04	0.04	139
		Max.	2.1	9.7	15.2	1.2	3.0	0.37	0.18	0.38	0.07	0.60	0.16	0.76	0.15	1.5	0.33	33.7	3534	12.6	470	70.9	34.9	2.1	379
	H	**Mean (n=2)**	**3.6**	**149**	**206**	**15.7**	**30.2**	**2.6**	**0.60**	**1.2**	**0.15**	**0.96**	**0.20**	**0.57**	**0.10**	**0.80**	**0.16**	**412**	**1149**	**4.7**	**8786**	**1037**	**14.0**	**2.6**	**7981**
		S.D.	3.3	147	204	15.5	29.8	2.6	0.59	1.1	0.14	0.87	0.18	0.45	0.07	0.33	0.02	406	351	4.0	5642	635	13.9	2.6	4888
		Min.	0.33	1.6	2.3	0.18	0.37	0.03	0.005	0.05	0.01	0.08	0.02	0.12	0.03	0.47	0.14	5.7	798	<0.75	3144	402	0.11	0.03	3092
		Max.	6.9	296	410	31.2	60.0	5.1	1.2	2.3	0.29	1.8	0.38	1.0	0.16	1.1	0.18	818	1500	8.7	14428	1672	27.9	5.2	12869
MV096	**L**	**Mean (n=14)**	**0.17**	**0.03**	**0.09**	**0.01**	**0.05**	**0.07**	**0.01**	**0.06**	**0.009**	**0.06**	**0.01**	**0.04**	**0.007**	**0.05**	**0.009**	**0.68**	**937**	**25.7**	**28.2**	**21.5**	**19.9**	**2.0**	**8.6**
		S.D.	0.26	0.02	0.08	0.01	0.06	0.11	0.02	0.06	0.009	0.10	0.01	0.05	0.008	0.07	0.006	0.65	1155	30.2	36.7	32.1	29.8	3.1	10.9
		Min.	0.002	0.003	<0.007	<0.001	<0.001	<0.001	<0.001	0.009	<0.001	<0.001	<0.001	<0.001	<0.001	<0.001	0.001	0.12	37.4	<5.3	0.14	<0.07	<0.03	<0.001	0.11
		Max.	0.73	0.08	0.26	0.04	0.17	0.45	0.05	0.23	0.03	0.30	0.05	0.16	0.03	0.25	0.02	2.2	3545	100	116	94.9	87.8	11.0	32.9
	M		0.36	3.6	6.0	0.47	1.2	0.08	0.02	0.06	<0.009	0.08	0.03	0.09	0.01	0.22	0.07	24.4	3305	<7.0	244	34.9	6.0	0.29	217
RU49-8096-7																									
CLC046	**L**	**Mean (n=8)**	**0.03**	**0.22**	**0.33**	**0.03**	**0.09**	**0.03**	**0.007**	**0.04**	**0.006**	**0.03**	**0.006**	**0.02**	**0.005**	**0.05**	**0.01**	**0.90**	**4732**	**1.8**	**63.2**	**8.2**	**0.31**	**0.03**	**37.5**
		S.D.	0.04	0.22	0.36	0.03	0.05	0.03	0.006	0.03	0.004	0.02	0.005	0.02	0.004	0.03	0.007	0.71	2549	0.23	42.8	5.3	0.22	0.03	25.3
		Min.	<0.001	<0.01	0.04	0.006	0.02	<0.001	<0.001	<0.001	<0.001	<0.001	<0.001	<0.001	<0.001	<0.001	<0.001	0.20	7.6	1.5	7.4	0.99	<0.13	0.003	4.4
		Max.	0.11	0.60	0.93	0.08	0.17	0.06	0.006	0.06	0.003	0.02	0.01	0.06	0.01	0.12	0.02	2.0	6705	2.2	138	17.1	0.62	0.11	79.2
	M	**Mean (n=6)**	**0.05**	**0.05**	**0.07**	**0.009**	**0.03**	**0.03**	**0.01**	**0.07**	**0.007**	**0.02**	**0.007**	**0.04**	**0.008**	**0.08**	**0.02**	**0.51**	**6835**	**2.1**	**747**	**92.0**	**0.47**	**0.08**	**434**
		S.D.	0.06	0.009	0.02	0.001	0.02	0.02	0.008	0.02	0.003	0.03	0.007	0.03	0.01	0.06	0.009	0.18	3188	0.54	436	52.6	0.23	0.14	242
		Min.	<0.02	0.04	0.03	<0.008	<0.001	<0.001	<0.001	0.001	0.003	<0.001	<0.001	<0.001	<0.001	0.01	0.006	0.35	1639	<1.6	298	38.2	<0.14	0.003	149
		Max.	0.19	0.07	0.11	0.01	0.05	0.02	0.02	0.001	0.009	0.08	0.02	0.08	0.03	0.20	0.03	0.89	10792	3.2	1579	192	0.72	0.40	857
CLC047	**L**	**Mean (n=3)**	**0.007**	**0.02**	**0.04**	**0.003**	**0.006**	**0.001**	**0.001**	**0.004**	**0.001**	**0.003**	**0.001**	**0.004**	**0.002**	**0.04**	**0.01**	**0.14**	**3310**	**2.7**	**28.1**	**3.5**	**0.01**	**0.006**	**25.5**
		S.D.	0.001	0.02	0.04	0.002	0.005	0.001	0.001	0.004	0.001	0.002	0.001	0.001	0.001	0.003	0.002	0.07	630	0.57	11.8	1.3	0.01	0.003	10.7
		Min.	0.006	0.005	0.01	0.001	<0.001	0.001	<0.001	<0.001	0.001	0.001	0.001	<0.004	0.001	0.03	0.009	0.09	2496	2.1	15.0	2.1	<0.004	0.002	13.6
		Max.	0.007	0.06	0.10	0.006	0.01	0.001	0.001	0.002	0.001	0.001	0.001	0.004	0.003	0.04	0.01	0.24	4030	3.5	43.6	5.3	0.03	0.01	39.6
	M	**Mean (n=10)**	**4.6**	**4.5**	**16.7**	**1.3**	**5.3**	**0.86**	**0.11**	**0.71**	**0.14**	**1.1**	**0.32**	**1.5**	**0.31**	**3.1**	**0.63**	**41.2**	**2627**	**3.1**	**1419**	**176**	**0.86**	**4.8**	**1348**
		S.D.	4.0	4.8	17.3	1.4	5.7	0.86	0.11	0.67	0.13	1.0	0.28	1.3	0.26	2.6	0.51	40.6	833	0.53	328	39.7	0.82	5.3	319
		Min.	0.008	0.003	0.008	<0.001	<0.001	<0.001	0.001	<0.008	<0.001	<0.001	0.001	0.006	0.002	0.02	0.01	0.09	843	2.1	1067	132	<0.006	0.005	986
		Max.	10.7	14.7	50.2	4.2	16.5	2.4	0.32	1.9	0.34	2.8	0.76	3.5	0.70	6.8	1.3	117	3389	4.0	2077	257	2.2	14.6	2020
CLC050	**M**	**Mean (n=5)**	**1.9**	**0.70**	**3.6**	**0.20**	**0.78**	**0.24**	**0.04**	**0.22**	**0.05**	**0.45**	**0.12**	**0.43**	**0.10**	**1.2**	**0.17**	**10.2**	**1269**	**4.7**	**2372**	**298**	**4.5**	**3.1**	**1231**
		S.D.	0.62	0.34	1.1	0.07	0.26	0.09	0.02	0.07	0.02	0.08	0.05	0.17	0.03	0.17	0.07	2.1	87.5	2.2	98.8	11.6	3.1	0.74	71.5
		Min.	1.3	0.21	2.0	0.08	0.42	<0.12	0.02	<0.13	<0.03	0.38	0.07	0.27	0.08	1.0	0.11	7.3	1159	<2.3	2249	286	2.5	2.0	1140
		Max.	3.1	1.1	5.5	0.31	1.1	0.38	0.07	0.30	0.08	0.59	0.22	0.77	0.15	1.5	0.30	12.7	1357	8.7	2515	319	10.8	4.3	1331

Table C13. Zoned hematite in RU41-9882 (NW-arm)

Drillhole	U*	Sample	Mg	Al	Si	P	Ca	Sc	Ti	V	Cr	Mn	Co	Ni	Cu	Zn	Ga	As	Sr	Zr	Nb	Mo	Sn	Sb	Ba	Hf	Ta
RU41-9882																											
CLC201A	**L**	**Mean (n=8)**	**23.9**	**156**	**136**	**9.1**	**<30.6**	**0.73**	**117**	**17.5**	**0.29**	**4.1**	**1.0**	**0.46**	**2.2**	**0.88**	**4.9**	**0.98**	**0.87**	**0.08**	**140**	**63.8**	**254**	**1.3**	**2.9**	**0.006**	**0.22**
		S.D.	54.2	203	146	5.8	-	1.2	234	27.6	0.04	5.0	1.3	0.31	4.9	1.0	1.8	1.2	1.6	0.13	302	91.8	267	0.84	6.7	0.008	0.43
		Min.	0.32	9.3	<36.0	<3.5	-	<0.05	0.26	0.81	<0.22	0.20	0.15	<0.06	<0.14	0.19	1.5	<0.26	0.002	<0.001	0.14	10.4	81.4	0.59	<0.001	<0.001	<0.001
		Max.	167	616	514	23.0	-	3.7	704	82.0	0.32	14.1	4.0	1.2	15.0	3.4	6.4	3.8	5.1	0.37	921	293	903	3.5	20.4	0.03	1.3
	M	**Mean (n=10)**	**96.7**	**215**	**109**	**8.7**	**30.4**	**1.5**	**83.7**	**28.8**	**0.33**	**7.3**	**2.0**	**0.31**	**0.30**	**0.53**	**5.1**	**1.4**	**1.6**	**0.13**	**202**	**171**	**199**	**2.9**	**1.0**	**0.005**	**0.43**
		S.D.	82.1	155	23.4	4.5	8.9	2.8	206	46.2	0.13	5.2	1.5	0.13	0.29	0.41	0.42	2.1	4.4	0.35	524	160	110	1.8	2.8	0.01	1.1
		Min.	0.34	16.5	58.6	3.6	<18.7	<0.05	<0.38	2.4	<0.20	0.28	0.16	0.14	<0.13	<0.20	4.6	<0.24	<0.004	<0.001	1.5	19.6	105	0.70	<0.001	<0.001	<0.001
		Max.	222	559	139	16.3	47.9	9.8	699	164	0.64	15.1	4.3	0.54	1.2	1.7	5.8	7.5	14.8	1.2	1767	475	413	5.1	9.5	0.03	3.9
CLC201B	**L**	**Mean (n=17)**	**23.2**	**284**	**200**	**25.3**	**152**	**1.0**	**83.2**	**27.8**	**0.70**	**3.6**	**2.1**	**0.86**	**1.6**	**0.84**	**5.3**	**7.7**	**1.4**	**0.09**	**143**	**40.4**	**562**	**3.0**	**1.4**	**0.006**	**0.58**
		S.D.	39.8	247	70.4	20.7	125	2.0	132	26.2	0.50	3.7	3.9	1.4	2.8	0.65	4.7	14.3	2.8	0.14	108	39.4	596	4.9	2.6	0.02	0.98
		Min.	<0.19	20.7	<34.4	<4.2	<14.5	<0.05	<0.97	5.9	<0.17	<0.40	0.02	<0.07	<0.13	<0.15	0.57	<0.19	<0.001	<0.001	12.2	0.40	13.9	0.05	<0.001	<0.001	<0.001
		Max.	147	746	323	94.1	58.9	8.6	523	108	0.42	13.7	16.3	5.9	11.4	2.8	18.5	58.0	10.6	0.58	396	131	2285	16.5	9.2	0.07	3.9
	M	**Mean (n=7)**	**18.5**	**517**	**426**	**54.0**	**<222**	**0.51**	**62.4**	**28.8**	**<1.1**	**7.5**	**5.8**	**3.4**	**2.7**	**1.5**	**4.7**	**15.3**	**4.3**	**0.03**	**107**	**16.5**	**1053**	**3.8**	**2.3**	**0.001**	**0.64**
		S.D.	20.9	410	424	66.2	-	0.41	110	24.8	-	15.2	12.3	7.1	5.1	1.5	3.1	26.9	7.4	0.05	81.3	16.5	1727	4.5	4.5	0.001	1.2
		Min.	0.27	38.4	93.7	8.5	-	<0.20	<1.2	7.6	-	<0.44	<0.001	<0.15	<0.34	0.16	0.79	1.6	0.005	<0.001	22.1	0.98	17.3	0.99	0.05	0.001	0.008
		Max.	58.1	1049	1434	215	-	1.4	330	84.9	-	44.9	35.8	20.7	15.1	5.1	9.2	81.1	22.0	0.15	275	45.8	5008	14.6	13.4	0.001	3.5
	H		13.1	270	599	<28.7	<218	0.55	4.9	2.4	<1.0	6.0	1.2	0.34	0.90	0.93	3.4	94.1	2.8	0.07	18.6	159	5840	13.5	4.9	0.007	0.14
CLC201C	**L**	**Mean (n=12)**	**11.6**	**257**	**385**	**40.6**	**277**	**0.41**	**64.9**	**7.4**	**1.9**	**5.8**	**3.9**	**1.2**	**19.4**	**3.3**	**4.4**	**8.5**	**1.2**	**0.05**	**80.0**	**87.5**	**609**	**1.3**	**1.5**	**0.001**	**0.52**
		S.D.	13.7	198	201	2.6	34.5	0.18	125	9.8	0.25	9.2	6.5	2.1	47.4	6.5	2.4	11.8	1.4	0.06	115	106	647	1.0	2.0	0.003	0.90
		Min.	0.74	9.6	<250	<37.1	<233	<0.27	<1.3	<0.07	1.4	<0.59	0.23	0.06	<0.44	<1.1	1.4	<0.72	<0.001	<0.001	0.05	1.7	24.2	0.41	<0.001	<0.001	<0.001
		Max.	54.5	568	1013	45.5	236	0.91	431	28.6	2.0	35.6	19.2	6.0	167	24.7	10.2	36.8	3.9	0.19	405	359	2178	3.9	5.7	0.01	2.7
	M	**Mean (n=5)**	**14.9**	**388**	**515**	**88.1**	**<206**	**1.5**	**57.5**	**11.8**	**<1.6**	**10.7**	**4.5**	**1.4**	**76.1**	**10.7**	**3.3**	**10.7**	**8.8**	**0.32**	**302**	**398**	**1923**	**2.8**	**1.2**	**0.005**	**1.4**
		S.D.	8.8	298	260	91.1	-	2.2	80.4	8.6	-	12.2	7.3	2.3	97.7	17.6	2.2	10.6	13.4	0.51	554	661	2312	1.4	0.88	0.01	2.7
		Min.	3.3	14.4	<281	<34.3	-	<0.30	<1.5	0.10	-	0.91	0.08	0.05	<0.52	<0.99	1.0	<0.72	0.05	0.01	0.01	3.3	103	1.2	<0.001	<0.001	<0.001
		Max.	28.0	724	994	269	-	5.8	215	22.7	-	31.1	19.1	6.0	239	45.7	7.2	27.6	35.2	1.3	1411	1717	6372	4.7	2.7	0.03	6.8

Table C13. (Continued) Zoned hematite in RU41-9882 (NW-arm)

Drillhole	U*	Sample	Y	La	Ce	Pr	Nd	Sm	Eu	Gd	Tb	Dy	Ho	Er	Tm	Yb	Lu	∑REY	W	^{204}Pb	^{206}Pb	^{207}Pb	^{208}Pb	Th	U
RU41-9882																									
CLC201A	**L**	**Mean (n=8)**	**0.31**	**0.16**	**0.36**	**0.03**	**0.09**	**0.03**	**0.009**	**0.04**	**0.009**	**0.07**	**0.02**	**0.11**	**0.02**	**0.25**	**0.06**	**1.6**	**242**	**2.6**	**86.5**	**10.9**	**0.46**	**1.7**	**73.9**
		S.D.	0.75	0.24	0.55	0.04	0.14	0.04	0.01	0.06	0.02	0.17	0.05	0.26	0.06	0.62	0.14	2.9	423	0.93	39.3	4.5	0.79	4.2	35.6
		Min.	<0.003	<0.002	0.006	<0.001	<0.001	<0.001	<0.001	<0.001	<0.001	<0.001	<0.001	<0.001	<0.001	0.001	<0.001	0.03	6.6	1.2	32.1	4.1	<0.006	<0.001	25.6
		Max.	2.3	0.66	1.4	0.12	0.38	0.11	0.04	0.20	0.05	0.52	0.16	0.80	0.18	1.9	0.42	8.9	1308	3.6	140	16.9	2.2	12.8	119
	M	**Mean (n=10)**	**1.1**	**0.40**	**1.3**	**0.07**	**0.32**	**0.10**	**0.02**	**0.13**	**0.03**	**0.27**	**0.08**	**0.41**	**0.09**	**1.0**	**0.22**	**5.6**	**753**	**2.2**	**394**	**47.6**	**1.8**	**10.5**	**360**
		S.D.	1.4	0.45	1.6	0.09	0.44	0.15	0.03	0.19	0.04	0.33	0.10	0.45	0.10	1.0	0.21	6.3	737	0.86	156	19.0	3.0	17.2	150
		Min.	0.001	0.01	0.02	0.002	0.004	<0.001	<0.001	0.002	<0.001	<0.001	<0.001	<0.001	<0.001	<0.001	0.001	0.06	34.8	1.4	144	17.1	<0.007	<0.001	128
		Max.	4.4	1.2	4.2	0.27	1.3	0.43	0.08	0.50	0.11	0.94	0.29	1.3	0.27	2.8	0.58	16.5	2412	4.2	592	71.2	10.4	59.2	536
CLC201B	**L**	**Mean (n=17)**	**0.14**	**0.46**	**0.69**	**0.06**	**0.16**	**0.03**	**0.02**	**0.04**	**0.005**	**0.05**	**0.01**	**0.04**	**0.007**	**0.07**	**0.01**	**1.8**	**2034**	**1.8**	**41.3**	**5.6**	**0.55**	**0.06**	**37.6**
		S.D.	0.34	0.74	0.91	0.08	0.24	0.04	0.02	0.06	0.007	0.08	0.02	0.07	0.01	0.12	0.02	2.3	2465	1.2	34.6	4.8	1.1	0.07	35.8
		Min.	<0.001	0.004	0.009	0.002	<0.001	<0.001	<0.001	<0.001	<0.001	<0.001	<0.001	<0.001	<0.001	<0.001	<0.001	0.07	42.6	0.42	0.08	<0.04	<0.02	<0.001	0.04
		Max.	1.5	3.2	3.3	0.33	0.98	0.15	0.08	0.18	0.03	0.29	0.06	0.31	0.05	0.42	0.07	8.4	7072	4.9	108	15.4	3.0	0.26	109
	M	**Mean (n=7)**	**0.73**	**1.2**	**2.8**	**0.19**	**0.70**	**0.16**	**0.10**	**0.27**	**0.04**	**0.28**	**0.06**	**0.20**	**0.03**	**0.22**	**0.03**	**7.0**	**813**	**1.4**	**229**	**28.8**	**2.0**	**0.17**	**195**
		S.D.	1.4	1.2	3.6	0.25	0.93	0.22	0.17	0.36	0.07	0.55	0.13	0.40	0.06	0.45	0.07	8.2	1148	0.47	81.1	10.3	2.4	0.30	71.1
		Min.	<0.007	0.01	0.03	0.004	0.005	<0.001	<0.001	0.01	<0.001	<0.001	<0.001	<0.001	<0.001	<0.001	<0.001	0.12	43.3	0.80	128	15.4	<0.02	<0.001	123
		Max.	3.9	3.1	10.2	0.66	2.4	0.56	0.46	0.86	0.21	1.5	0.34	1.1	0.18	1.2	0.18	18.5	3324	2.4	395	50.2	6.7	0.90	348
	H		3.0	10.7	19.3	1.9	4.8	0.98	0.39	0.76	0.24	1.7	0.35	1.1	0.22	1.8	0.26	93.1	1404	<0.78	3782	457	1.0	0.39	3602
CLC201C	**L**	**Mean (n=12)**	**2.7**	**3.4**	**5.9**	**0.51**	**1.5**	**0.33**	**0.18**	**0.56**	**0.18**	**1.4**	**0.35**	**1.1**	**0.18**	**1.1**	**0.15**	**19.4**	**1489**	**2.9**	**44.5**	**7.2**	**1.7**	**0.16**	**34.9**
		S.D.	7.4	4.0	6.8	0.59	1.7	0.57	0.37	1.3	0.50	3.9	1.0	3.2	0.52	3.1	0.42	30.8	1586	1.5	46.4	8.0	4.1	0.27	35.1
		Min.	0.005	0.002	0.003	<0.001	<0.001	<0.001	<0.001	0.009	<0.001	<0.001	<0.001	0.004	<0.001	0.005	0.001	0.13	15.2	<1.4	1.7	0.24	<0.03	<0.001	0.59
		Max.	26.9	12.2	18.6	1.6	5.2	2.0	1.3	4.6	1.8	14.2	3.7	11.8	1.9	11.2	1.5	113	4608	7.3	151	22.6	14.8	1.0	96.0
	M	**Mean (n=5)**	**0.42**	**8.0**	**10.8**	**0.68**	**1.6**	**0.13**	**0.05**	**0.17**	**0.02**	**0.14**	**0.03**	**0.08**	**0.01**	**0.13**	**0.02**	**22.3**	**1583**	**9.4**	**249**	**44.4**	**14.4**	**0.69**	**230**
		S.D.	0.54	10.2	12.0	0.65	1.4	0.13	0.06	0.17	0.02	0.19	0.04	0.11	0.02	0.16	0.02	24.0	2198	12.1	84.7	33.4	25.3	1.3	59.6
		Min.	<0.01	0.01	0.03	<0.001	<0.001	<0.001	0.002	0.009	0.001	<0.02	<0.005	<0.01	<0.001	0.005	<0.005	0.12	5.8	<2.5	153	18.4	<0.03	<0.001	133
		Max.	1.3	25.4	31.1	1.7	3.8	0.33	0.15	0.44	0.05	0.47	0.11	0.26	0.05	0.40	0.05	62.8	5847	33.5	356	109	64.7	3.2	288

Table C14. Hematite replacing carbonates (middle)

Drillhole	U*	Sample	Mg	Al	Si	P	Ca	Sc	Ti	V	Cr	Mn	Co	Ni	Cu	Zn	Ga	As	Sr	Zr	Nb	Mo	Sn	Sb	Ba	Hf	Ta
RU34-8889-91																											
CLC052	**M**	**Mean (n=29)**	**141**	**1004**	**2168**	**292**	**1957**	**<1.3**	**65.4**	**259**	**<3.6**	**56.8**	**21.5**	**5.1**	**373**	**16.7**	**26.8**	**283**	**6.8**	**0.15**	**570**	**73.1**	**1426**	**77.8**	**10.1**	**0.02**	**0.46**
		S.D.	70.1	524	957	119	367	-	47.0	68.4	-	63.3	12.2	4.2	361	7.3	7.3	148	7.1	0.19	844	54.8	481	21.3	10.5	0.05	0.50
		Min.	2.3	270	885	<148	<1215	-	9.1	10.1	-	<1.7	1.8	<1.4	53.3	<7.8	17.7	57.4	1.6	<0.001	9.4	34.1	147	50.4	0.50	<0.001	<0.001
		Max.	309	2516	4640	658	3008	-	186	364	-	374	59.1	22.1	1919	39.6	61.7	893	36.1	0.99	4690	289	2522	153	51.3	0.15	2.3
	H		238	672	2147	<261	<2152	<1.3	<10.2	207		60.2	51.6	4.2	397	14.6	29.3	515	5.3	<0.26	88.6	55.9	1447	81.7	6.9	<0.001	0.06
CLC053A	**M**	**Mean (n=29)**	**44.7**	**864**	**2228**	**247**	**2114**	**<1.4**	**170**	**424**	**4.1**	**29.9**	**21.2**	**11.3**	**440**	**13.6**	**31.0**	**324**	**4.5**	**0.13**	**893**	**53.2**	**1584**	**49.5**	**27.5**	**0.02**	**0.52**
		S.D.	24.0	194	453	43.9	438	-	53.0	35.7	0.92	13.8	5.1	6.6	310	5.3	2.5	79.0	2.1	0.30	491	9.6	415	12.2	27.6	0.04	0.36
		Min.	11.5	594	1445	<160	<1313	-	96.5	305	<2.4	11.7	10.5	2.7	113	<6.2	23.0	107	2.1	<0.001	276	36.0	694	30.3	5.7	<0.001	0.10
		Max.	114	1258	3322	308	2932	-	294	477	6.5	66.2	37.1	26.6	1449	29.3	34.8	482	10.5	1.7	2527	75.1	2579	77.0	130	0.09	1.7
	H	**Mean (n=3)**	**65.0**	**788**	**2317**	**298**	**<2361**	**<1.4**	**201**	**458**	**<4.4**	**92.7**	**26.6**	**11.8**	**350**	**18.2**	**30.9**	**262**	**9.2**	**0.09**	**1671**	**45.0**	**1541**	**47.8**	**28.8**	**0.13**	**0.99**
		S.D.	14.0	192	480	56.1	-	-	50.1	27.9	-	49.2	9.9	6.2	117	3.6	1.5	85.9	5.3	0.07	226	9.0	171	2.9	16.6	0.06	0.11
		Min.	47.3	624	1947	<245	-	-	157	429	-	55.7	18.2	3.8	185	14.0	29.0	193	3.7	<0.001	1353	37.0	1306	43.8	6.7	0.09	0.85
		Max.	81.6	1058	2995	376	-	-	271	496	-	162	40.5	19.1	450	22.8	32.7	384	16.5	0.18	1848	57.6	1710	50.7	46.7	0.09	1.1
CLC053B	**L**		228	733	878	46.2	220	0.21	94.3	210	0.52	70.4	14.0	4.2	88.5	5.4	10.3	88.7	1.9	0.08	1373	10.4	558	6.6	1.5	0.02	3.5
	M	**Mean (n=46)**	**174**	**942**	**952**	**56.1**	**393**	**0.21**	**103**	**317**	**0.80**	**48.3**	**16.8**	**5.7**	**116**	**7.1**	**12.3**	**84.4**	**3.6**	**0.13**	**1107**	**34.1**	**608**	**16.4**	**8.8**	**0.02**	**0.93**
		S.D.	118	170	274	22.0	274	0.18	44.9	49.6	0.55	22.9	6.2	3.1	52.1	3.5	1.9	18.2	1.4	0.13	782	12.8	231	5.1	10.1	0.03	0.64
		Min.	36.7	654	329	<21.0	112	0.04	44.4	214	0.20	18.8	5.1	1.5	47.9	2.3	8.7	37.1	1.2	<0.001	235	17.2	135	9.5	<0.001	<0.001	0.18
		Max.	473	1381	1832	126	1250	0.86	210	424	1.8	102	43.6	15.8	289	17.8	16.1	124	7.7	0.81	2898	96.0	1111	30.5	56.6	0.08	2.4
CLC054A	**M**	**Mean (n=24)**	**257**	**1060**	**871**	**46.2**	**260**	**0.20**	**388**	**390**	**0.74**	**76.8**	**29.1**	**2.7**	**108**	**7.1**	**11.8**	**82.6**	**2.3**	**0.10**	**2337**	**39.3**	**715**	**11.3**	**60.2**	**0.02**	**4.4**
		S.D.	78.1	150	277	8.9	42.4	0.15	125	41.0	0.20	22.3	8.4	1.9	84.4	2.5	4.5	33.9	1.9	0.08	654	17.1	177	2.0	270	0.04	1.1
		Min.	148	863	586	27.8	<165	<0.08	113	336	<0.57	43.5	15.1	0.16	31.4	2.3	9.9	25.1	0.88	<0.001	789	20.2	410	8.6	0.55	<0.001	1.6
		Max.	460	1500	1717	61.5	408	0.80	647	506	1.6	139	43.9	7.2	358	12.0	33.0	188	10.6	0.26	3734	110	1049	17.4	1356	0.09	6.3
CLC054B	**L**		285	1497	2043	197	<166	0.86	864	238	0.66	63.0	21.4	2.5	101	11.1	10.0	99.7	10.1	1.1	290	26.8	582	33.6	28.5	0.18	1.8
	M	**Mean (n=23)**	**105**	**1166**	**1355**	**76.9**	**294**	**0.31**	**215**	**370**	**0.67**	**37.4**	**14.9**	**4.0**	**156**	**6.0**	**12.9**	**99.3**	**3.6**	**0.27**	**885**	**38.6**	**662**	**20.1**	**16.5**	**0.03**	**0.94**
		S.D.	68.2	278	582	46.6	126	0.33	103	54.7	0.08	15.7	5.4	3.0	107	2.9	1.4	29.6	1.7	0.25	392	19.3	186	9.9	34.8	0.05	0.63
		Min.	26.9	812	741	39.5	<224	<0.08	83.0	220	<0.57	12.3	7.6	0.69	50.6	1.1	9.1	36.3	0.91	0.04	497	22.4	123	10.5	0.85	<0.001	0.34
		Max.	384	1882	2818	235	770	1.3	434	443	0.88	72.5	29.9	16.2	411	11.0	14.7	152	9.0	1.0	2132	116	1002	51.0	177	0.09	2.7
CLC055	**M**	**Mean (n=11)**	**139**	**1180**	**1206**	**62.6**	**148**	**0.48**	**189**	**291**	**0.73**	**37.9**	**20.4**	**4.0**	**51.3**	**6.9**	**11.0**	**83.1**	**6.1**	**0.39**	**516**	**36.0**	**675**	**14.2**	**2.9**	**0.06**	**1.1**
		S.D.	104	240	558	43.1	22.8	0.33	143	34.4	0.18	22.7	8.3	2.6	40.1	3.6	1.2	65.8	11.0	0.32	363	13.3	114	4.3	2.4	0.08	0.96
		Min.	27.0	929	529	23.7	<111	<0.05	29.7	235	<0.53	8.9	8.9	0.36	<5.9	1.5	8.3	4.5	0.13	<0.001	151	22.7	478	8.1	<0.001	<0.001	0.17
		Max.	385	1623	2171	184	190	1.0	461	343	1.1	76.9	37.7	8.5	136	14.4	13.1	217	38.5	0.95	1385	76.2	844	21.0	7.4	0.29	3.0
	H	**Mean (n=3)**	**132**	**1328**	**1650**	**50.5**	**309**	**1.1**	**298**	**270**	**0.70**	**36.2**	**21.7**	**3.5**	**27.8**	**9.6**	**11.0**	**87.7**	**3.7**	**2.4**	**617**	**31.8**	**731**	**22.5**	**3.8**	**0.06**	**0.99**
		S.D.	86.7	121	516	16.6	240	0.43	147	46.1	0.22	11.9	7.8	2.2	6.1	5.2	0.29	24.5	2.8	0.59	456	11.1	138	5.5	2.0	0.04	0.28
		Min.	27.0	1229	1202	36.2	<138	0.50	96.2	218	<0.51	19.6	12.1	1.3	19.9	2.4	10.6	54.0	1.5	1.9	165	18.2	547	15.4	1.8	<0.001	0.63
		Max.	239	1497	2372	73.9	649	1.5	443	330	1.0	46.8	31.2	6.6	34.7	14.6	11.3	111	7.7	3.2	1241	45.3	880	28.7	6.5	0.10	1.3
CLC056	**M**	**Mean (n=23)**	**141**	**1290**	**1241**	**88.6**	**177**	**0.20**	**228**	**285**	**0.85**	**47.6**	**28.5**	**1.6**	**51.7**	**8.2**	**11.9**	**6.3**	**6.0**	**0.50**	**617**	**32.6**	**801**	**13.4**	**5.8**	**0.04**	**2.1**
		S.D.	32.2	222	556	38.2	72.6	0.15	80.8	18.1	0.81	17.5	13.4	1.5	29.6	4.4	0.91	8.3	7.9	0.63	181	8.1	120	2.8	4.3	0.12	0.79
		Min.	101	1084	338	8.3	<113	<0.05	125	244	0.44	20.3	2.3	0.18	8.7	0.48	10.2	<0.05	<0.04	<0.001	382	16.2	556	8.9	<0.001	<0.001	1.1
		Max.	207	1989	2466	154	364	0.55	417	317	4.5	78.9	45.8	6.6	150	14.7	13.3	42.9	41.1	3.2	976	61.4	988	19.4	16.0	0.17	3.9

Table C14. (Continued) Hematite replacing carbonates (middle)

Drillhole	U*	Sample	Y	La	Ce	Pr	Nd	Sm	Eu	Gd	Tb	Dy	Ho	Er	Tm	Yb	Lu	∑REY	W	^{204}Pb	^{206}Pb	^{207}Pb	^{208}Pb	Th	U
RU34-8889-91																									
CLC052	**M**	**Mean (n=29)**	**4.1**	**4.4**	**11.9**	**1.1**	**3.3**	**0.59**	**0.16**	**0.51**	**0.09**	**0.72**	**0.2**	**0.83**	**0.18**	**1.7**	**0.32**	**30.1**	**835**	**14.7**	**1577**	**193**	**49.4**	**52.8**	**854**
		S.D.	4.5	6.3	10.8	1.2	4.5	0.95	0.27	0.71	0.1	0.62	0.14	0.43	0.09	0.65	0.17	25	191	10.8	387	43.8	17.1	20.1	215
		Min.	0.97	0.49	1.9	0.15	0.19	0.08	<0.03	<0.12	0.02	0.13	0.04	0.11	0.03	0.6	0.07	7.4	516	2.6	696	125	1.7	4.6	249
		Max.	25.7	33	53.4	4.9	23.6	5.1	1.4	3.9	0.5	3.1	0.68	1.9	0.38	3.3	0.89	109	1405	49.2	2428	285	93	104	1199
	H		13.6	6.7	29.8	2.8	8.1	1.6	0.39	1.2	0.29	2.2	0.52	2.6	0.46	3.3	0.72	74.2	777	6.2	2981	315	43.5	76.2	1800
CLC053A	**M**	**Mean (n=29)**	**6.7**	**3.2**	**13.8**	**1.2**	**4.1**	**0.76**	**0.31**	**0.98**	**0.21**	**1.4**	**0.39**	**1.5**	**0.28**	**2.6**	**0.48**	**38.1**	**685**	**11.7**	**2384**	**281**	**58.8**	**77.7**	**1233**
		S.D.	7.8	2.7	14	1.9	6.7	1	0.59	1.6	0.33	2	0.46	1.8	0.25	2.3	0.38	40.4	130	5.1	448	50.7	13.4	40.5	289
		Min.	1.6	0.77	3.4	0.29	0.65	<0.13	0.01	0.16	0.04	0.25	0.1	0.4	0.09	0.88	0.2	10.9	300	4.8	1164	157	31.8	33.8	485
		Max.	36.9	14.7	81.9	10.8	37.9	4.7	2.7	6.8	1.4	9.8	2.2	9.8	1.4	12.8	2.2	225	989	26	3249	384	79.9	237	1915
	H	**Mean (n=3)**	**12.8**	**8**	**35.4**	**2.9**	**8.4**	**1.7**	**0.83**	**2**	**0.37**	**3.6**	**0.88**	**3.4**	**0.7**	**5.3**	**1.1**	**87.2**	**708**	**18.6**	**4050**	**470**	**98.4**	**179**	**2649**
		S.D.	1.3	4.8	19.4	1.7	5.1	0.99	0.79	1.3	0.19	1.1	0.15	0.2	0.08	1.3	0.41	34.4	231	1.5	330	29.1	13.3	51	137
		Min.	11	1.4	11.8	1.3	4.7	0.65	0.14	0.91	0.23	2.8	0.7	3.2	0.6	3.9	0.57	46.0	427	17.3	3630	430	79.6	111	2525
		Max.	14	12.6	59.4	5.3	15.6	3	1.9	3.8	0.64	5.1	1.1	3.6	0.79	7	1.6	130	993	20.7	4435	497	108	234	2840
CLC053B	**L**		0.54	3.1	3.9	0.33	0.67	0.12	0.08	0.17	0.03	0.21	0.04	0.15	0.04	0.28	0.07	9.8	211	NA	115	17.3	4	2.3	95
	M	**Mean (n=46)**	**8.7**	**2.4**	**5.9**	**0.54**	**1.9**	**0.48**	**0.15**	**0.65**	**0.17**	**1.6**	**0.49**	**2.3**	**0.49**	**4.8**	**1**	**31.5**	**357**	**NA**	**613**	**81.5**	**18.9**	**90.8**	**589**
		S.D.	3.1	1.3	3.4	0.34	1.2	0.3	0.12	0.29	0.07	0.55	0.15	0.67	0.15	1.4	0.29	10.8	171		197	21.6	7.1	36	187
		Min.	0.42	0.68	1.9	0.18	0.63	0.14	0.04	0.12	0.02	0.17	0.04	0.13	0.03	0.33	0.09	5.1	125		170	24.9	5.5	3.9	146
		Max.	17.7	6.5	17.5	1.7	7.1	1.8	0.73	1.6	0.42	3.5	0.99	4.2	0.9	8.3	1.6	73.3	1275		952	117	37	178	951
CLC054A	**M**	**Mean (n=24)**	**10.1**	**2.2**	**6.4**	**0.47**	**1.9**	**0.43**	**0.1**	**0.72**	**0.21**	**2**	**0.59**	**2.8**	**0.56**	**5.7**	**1.4**	**35.5**	**504**	**NA**	**603**	**86.1**	**30.3**	**158**	**636**
		S.D.	1.7	2	4.9	0.29	1	0.19	0.04	0.2	0.05	0.41	0.12	0.52	0.11	0.97	0.23	8.4	106		93.9	11.9	6.5	33.6	99.8
		Min.	7.4	0.4	1.5	0.09	0.36	<0.08	0.03	0.31	0.12	1.2	0.39	2	0.35	3.8	0.94	19.5	317		409	65	20.3	103	419
		Max.	14.5	9.7	22.6	1.3	4.6	0.83	0.22	1.1	0.3	2.7	0.84	3.9	0.73	7.7	1.8	57.6	790		807	119	42.5	228	842
CLC054B	**L**		2.5	29.3	47.9	4.3	13	0.95	0.28	0.92	0.09	0.71	0.16	0.72	0.06	1.2	0.17	102	160	NA	127	43.1	31.4	17.2	86
	M	**Mean (n=23)**	**11.4**	**3.5**	**9.7**	**0.83**	**3**	**0.69**	**0.16**	**1**	**0.25**	**2.1**	**0.67**	**3**	**0.6**	**5.8**	**1.3**	**44.1**	**443**	**NA**	**740**	**99.6**	**24.2**	**97**	**745**
		S.D.	3.5	2	4.7	0.37	1.4	0.32	0.06	0.34	0.08	0.61	0.2	1	0.19	2	0.43	10.6	123		254	30.1	6.3	37.7	263
		Min.	4.7	1.2	4.1	0.3	1.3	0.11	0.07	0.37	0.1	0.69	0.26	1.1	0.21	1.9	0.37	19.1	306		173	38.6	12.3	20.1	141
		Max.	16.1	8.9	23.2	1.8	6.5	1.5	0.28	1.5	0.41	3.2	1	4.5	0.9	8.5	2	73.8	862		1101	148	37.3	151	1093
CLC055	**M**	**Mean (n=11)**	**8.2**	**3.3**	**8.9**	**0.79**	**3.1**	**0.63**	**0.14**	**0.71**	**0.18**	**1.5**	**0.47**	**2.3**	**0.49**	**4.7**	**1**	**36.3**	**378**	**NA**	**663**	**80.8**	**21.6**	**90.7**	**618**
		S.D.	2.1	3.1	7.2	0.7	2.9	0.43	0.08	0.3	0.07	0.46	0.14	0.62	0.1	1.3	0.27	13.2	157		205	23	6.1	24	191
		Min.	4.8	0.49	1.7	0.1	0.46	0.07	0.05	0.15	0.08	0.63	0.28	1.3	0.35	3	0.61	24.8	161		291	53.1	10.5	66.4	234
		Max.	10.5	11.8	22.8	2.3	10.5	1.8	0.35	1.4	0.27	2.2	0.71	3	0.64	7.2	1.5	66.9	797		940	116	28.9	149	850
	H	**Mean (n=3)**	**21**	**5**	**16.2**	**1.7**	**6.3**	**3.2**	**1.1**	**3.8**	**0.93**	**6.2**	**1.5**	**5.9**	**1.1**	**9**	**1.7**	**84.6**	**287**	**NA**	**1702**	**198**	**33.9**	**121**	**1733**
		S.D.	3.8	3.5	9.5	0.43	0.97	1.3	0.42	1.5	0.32	1.7	0.23	0.76	0.06	0.37	0.17	12.6	55		133	6.5	8.9	28.4	275
		Min.	17.9	0.69	5.8	1.3	5	1.9	0.52	1.8	0.55	4.1	1.3	5	1	8.5	1.6	69.6	210		1514	193	24.3	84.1	1348
		Max.	26.3	9.2	28.8	2.3	7.4	5	1.4	5.4	1.3	8.3	1.9	6.9	1.2	9.4	2	100	336		1798	207	45.7	153	1976
CLC056	**M**	**Mean (n=23)**	**13.9**	**3.5**	**9.1**	**0.61**	**2.4**	**0.58**	**0.18**	**1.1**	**0.33**	**2.8**	**0.86**	**3.9**	**0.82**	**7.4**	**1.5**	**48.9**	**331**	**NA**	**1094**	**123**	**22.9**	**92.6**	**1061**
		S.D.	2.6	3.5	7.4	0.64	1.8	0.28	0.13	0.35	0.1	0.59	0.18	0.82	0.17	1.6	0.36	12.8	129		231	22.7	5.7	17.1	226
		Min.	5.7	0.33	1.5	0.06	0.35	0.24	0.02	0.54	0.16	1.3	0.27	1	0.24	2.6	0.46	34.7	110		383	56.6	13.9	37.1	355
		Max.	18.2	16.8	36	3.1	8.1	1.3	0.5	1.8	0.65	4.6	1.2	4.9	1.2	10.6	2.2	97	840		1334	143	33.3	126	1284

Table C15. Overprinted zoned hematite (various locations)

Drillhole	U*	Sample	Mg	Al	Si	P	Ca	Sc	Ti	V	Cr	Mn	Co	Ni	Cu	Zn	Ga	As	Sr	Zr	Nb	Mo	Sn	Sb	Ba	Hf	Ta
RU36-9867W1																											
MV097	**M**	**Mean (n=6)**	**24.6**	**1240**	**2340**	**176**	**52.3**	**0.89**	**1257**	**219**	**8.3**	**41.8**	**9.3**	**6.4**	**15.4**	**32.5**	**10.1**	**389**	**5.3**	**6.3**	**282**	**203**	**78.4**	**61.2**	**6.6**	**0.44**	**1.2**
		S.D.	8.5	154	276	14.9	25.8	0.13	233	45.5	1.3	2.4	0.67	1.2	1.8	5.1	0.30	23.0	0.66	0.54	48.6	33.1	44.6	4.7	1.3	0.07	0.19
		Min.	17.6	997	1913	149	<26.6	0.71	917	165	6.4	37.9	8.4	4.5	13.5	26.6	9.6	365	4.4	5.7	198	166	29.6	54.7	4.8	0.36	0.82
		Max.	42.2	1481	2793	198	95.5	1.0	1643	302	10.2	44.8	10.4	8.1	18.6	39.4	10.5	422	6.2	7.0	345	259	134	68.0	8.2	0.54	1.4
MV099	**L**	**Mean (n=4)**	**377**	**415**	**705**	**79.7**	**171**	**0.19**	**58.6**	**76.1**	**0.23**	**90.0**	**16.3**	**2.9**	**18.5**	**7.5**	**8.7**	**74.9**	**13.3**	**0.15**	**3035**	**31.3**	**106**	**5.0**	**2.8**	**0.007**	**9.0**
		S.D.	78.4	38.1	174	28.2	39.7	0.08	10.7	2.3	0.06	9.1	1.9	0.57	4.4	0.76	0.40	7.4	8.1	0.05	405	7.5	30.2	0.94	1.5	0.005	1.0
		Min.	301	349	485	54.7	110	0.10	51.9	73.4	<0.14	77.3	13.8	2.4	12.4	6.5	8.1	66.1	4.0	0.08	2519	22.1	61.3	4.0	0.80	<0.001	7.6
		Max.	502	438	876	128	206	0.27	77.2	79.2	0.30	102	19.0	3.9	24.3	8.4	9.1	86.2	24.6	0.21	3488	42.7	145	6.5	5.1	0.01	10.4
	M	**Mean (n=36)**	**386**	**544**	**657**	**60.4**	**166**	**0.37**	**124**	**105**	**0.26**	**88.3**	**17.0**	**3.2**	**40.4**	**9.9**	**8.2**	**91.4**	**8.0**	**0.57**	**1991**	**33.8**	**185**	**10.3**	**11.3**	**0.007**	**5.1**
		S.D.	127	125	339	26.0	113	0.15	60.8	16.1	0.09	25.7	5.8	0.99	28.8	2.0	0.78	17.5	9.2	0.36	818	21.8	85.9	3.0	25.7	0.006	2.4
		Min.	89.4	383	188	23.0	27.4	0.13	41.2	57.0	<0.13	37.7	6.3	1.4	8.5	6.2	7.0	50.1	2.2	0.14	708	10.5	39.5	4.5	1.5	<0.001	1.9
		Max.	617	966	1720	137	500	0.68	256	132	0.58	141	27.9	5.4	132	15.0	10.0	122	53.6	1.3	3497	84.9	340	18.5	120	0.03	11.3
	H	**Mean (n=2)**	**270**	**654**	**382**	**63.3**	**158**	**0.61**	**130**	**83.4**	**<0.20**	**79.2**	**9.8**	**4.2**	**29.7**	**12.9**	**7.8**	**110**	**5.3**	**3.2**	**1718**	**36.9**	**125**	**13.3**	**10.0**	**0.06**	**6.0**
		S.D.	127	277	0.001	9.9	0.001	0.11	15.8	17.2	-	27.7	5.0	0.06	15.6	1.6	0.46	26.4	2.5	2.2	837	4.5	75.6	7.6	8.0	0.05	1.7
		Min.	143	377	382	53.4	158	0.50	114	66.3	-	51.6	4.8	4.1	14.2	11.3	7.4	83.8	2.8	1.0	881	32.5	49.5	5.7	1.9	0.009	4.3
		Max.	397	931	382	73.2	158	0.72	146	101	-	107	14.8	4.2	45.3	14.5	8.3	137	7.8	5.4	2556	41.4	201	20.8	18.0	0.11	7.7
MV100	**M**	**Mean (n=18)**	**272**	**643**	**761**	**144**	**154**	**2.7**	**368**	**158**	**0.29**	**84.0**	**21.3**	**3.1**	**16.9**	**10.5**	**16.5**	**99.6**	**7.2**	**2.6**	**3620**	**15.0**	**244**	**7.9**	**5.6**	**0.01**	**19.0**
		S.D.	72.5	109	216	48.6	97.2	1.7	72.1	18.0	0.09	27.9	6.3	1.0	11.8	3.6	1.5	18.1	6.2	1.0	1613	2.5	86.7	2.4	7.7	0.008	9.5
		Min.	153	516	447	54.7	25.6	1.3	287	113	<0.14	51.5	11.1	1.1	3.8	5.4	14.0	62.3	1.3	1.6	2279	10.9	74.1	5.1	0.67	0.003	12.0
		Max.	402	882	1138	241	341	8.2	546	181	0.51	170	30.6	4.5	55.7	22.2	18.9	121	30.0	4.7	8436	19.2	376	15.4	34.6	0.03	50.6
RU49-8096																											
CLC047	**M**	**Mean (n=7)**	**32.9**	**418**	**3522**	**322**	**1142**	**<0.72**	**8.0**	**92.9**	**<2.1**	**38.9**	**14.8**	**3.2**	**276**	**29.9**	**7.1**	**376**	**12.1**	**0.05**	**1328**	**32.8**	**314**	**41.9**	**6.0**	**0.03**	**0.40**
		S.D.	10.5	225	947	99.9	67.0	-	2.9	6.4	-	4.7	1.8	0.69	78.6	3.5	0.66	80.1	3.9	0.06	334	5.5	137	1.5	1.3	0.03	0.10
		Min.	21.5	261	2239	188	<1058	-	<4.3	81.0	-	30.6	12.5	2.2	167	23.0	6.0	283	7.5	<0.001	731	26.1	170	39.5	3.9	<0.001	0.19
		Max.	49.7	945	5221	512	1286	-	12.6	100	-	45.5	17.1	4.6	386	34.6	8.2	480	17.9	0.17	1681	44.2	566	44.1	8.0	0.03	0.50
RD2765																											
MV105	**M**	**Mean (n=7)**	**10.7**	**546**	**497**	**43.8**	**72.3**	**0.08**	**152**	**341**	**0.29**	**29.5**	**8.5**	**6.5**	**147**	**16.0**	**9.8**	**77.0**	**4.6**	**0.25**	**832**	**50.2**	**223**	**11.4**	**10.0**	**0.01**	**0.91**
		S.D.	4.3	173	259	36.1	73.8	0.03	15.5	72.0	0.08	12.1	4.3	1.4	73.2	7.6	1.7	57.4	2.2	0.25	183	27.5	129	4.6	2.0	0.01	0.11
		Min.	3.8	380	184	5.2	<21.6	<0.03	125	215	0.21	10.0	4.4	4.7	59.8	4.3	6.7	16.6	1.4	0.02	456	15.4	71.7	5.8	7.0	<0.001	0.75
		Max.	17.3	902	1028	101	244	0.12	173	417	0.39	46.8	18.8	9.1	307	26.2	11.4	194	7.3	0.64	1128	90.0	461	19.3	13.0	0.04	1.1
RU41-9882																											
MV043	**M**	**Mean (n=16)**	**94.6**	**1733**	**1904**	**20.4**	**82.7**	**0.22**	**61.1**	**205**	**0.28**	**30.1**	**17.5**	**1.5**	**582**	**11.1**	**9.9**	**561**	**5.4**	**1.1**	**241**	**48.7**	**353**	**7.6**	**29.8**	**0.05**	**0.18**
		S.D.	39.3	396	507	27.2	48.0	0.36	35.2	62.9	0.26	14.9	4.4	0.81	430	3.7	1.1	218	3.4	1.1	93.9	16.7	64.8	1.3	37.8	0.08	0.23
		Min.	40.8	1191	1261	<2.7	20.2	<0.04	25.6	34.4	<0.12	14.4	11.2	0.33	124	5.6	7.4	144	2.8	0.08	64.3	26.9	205	5.9	2.5	<0.001	0.05
		Max.	199	2374	2829	117	170	1.5	146	246	1.2	77.3	28.7	2.9	1656	19.1	11.4	1004	15.9	3.7	412	92.4	458	10.4	137	0.28	1.0

Table C15. (Continued) Overprinted zoned hematite (various locations)

Drillhole	U*	Sample	Y	La	Ce	Pr	Nd	Sm	Eu	Gd	Tb	Dy	Ho	Er	Tm	Yb	Lu	∑REY	W	^{204}Pb	^{206}Pb	^{207}Pb	^{208}Pb	Th	U
RU36-9867W1																									
MV097	**M**	**Mean (n=6)**	**3.9**	**5.4**	**13.9**	**1.1**	**3.9**	**0.88**	**0.31**	**0.81**	**0.16**	**1.2**	**0.27**	**1.1**	**0.22**	**2.2**	**0.39**	**35.8**	**950**	**30.4**	**797**	**125**	**31.7**	**14.4**	**730**
		S.D.	0.49	2.2	4.1	0.32	0.94	0.11	0.03	0.06	0.02	0.15	0.03	0.16	0.03	0.27	0.04	7.4	286	2.7	145	16.9	3.5	2.5	142
		Min.	3.4	2.9	8.5	0.76	2.8	0.71	0.26	0.71	0.13	1.1	0.24	0.94	0.18	1.8	0.33	25.6	682	28.0	543	95.3	29.1	10.1	486
		Max.	4.8	8.4	19.3	1.6	5.3	0.99	0.34	0.88	0.20	1.5	0.35	1.4	0.27	2.6	0.47	45.0	1542	36.2	1025	150	39.4	17.6	958
MV099	**L**	**Mean (n=4)**	**1.2**	**6.2**	**10.7**	**1.1**	**3.6**	**0.40**	**0.09**	**0.23**	**0.03**	**0.20**	**0.04**	**0.17**	**0.03**	**0.38**	**0.07**	**24.3**	**28.4**	**9.2**	**32.9**	**12.2**	**8.9**	**1.8**	**23.1**
		S.D.	0.21	3.5	5.7	0.57	1.9	0.15	0.04	0.08	0.008	0.03	0.01	0.05	0.008	0.09	0.01	12.1	5.1	0.78	1.6	1.1	1.1	0.39	1.8
		Min.	0.88	2.0	3.5	0.32	1.1	0.21	0.03	0.10	0.02	0.17	0.03	0.11	0.03	0.25	0.05	8.8	24.7	8.1	30.6	11.0	7.6	1.2	20.5
		Max.	1.5	10.5	16.5	1.7	5.6	0.63	0.13	0.31	0.04	0.23	0.06	0.24	0.05	0.48	0.08	37.3	37.1	10.0	35.2	13.9	10.6	2.2	25.2
	M	**Mean (n=36)**	**13.3**	**5.2**	**12.6**	**1.1**	**4.4**	**1.3**	**0.38**	**1.7**	**0.36**	**2.9**	**0.76**	**3.3**	**0.65**	**6.3**	**1.2**	**55.2**	**195**	**13.0**	**996**	**132**	**33.7**	**142**	**982**
		S.D.	4.1	5.7	11.3	1.0	3.5	0.97	0.43	1.2	0.22	1.3	0.27	1.0	0.19	1.9	0.36	21.6	109	2.8	319	39.4	9.1	54.4	311
		Min.	6.3	0.71	3.0	0.25	1.2	0.38	0.09	0.65	0.16	1.4	0.35	1.8	0.34	3.1	0.51	24.8	88.2	6.1	442	64.8	19.7	37.7	405
		Max.	24.1	28.0	52.6	5.1	17.6	4.6	1.9	5.6	1.1	7.6	1.6	5.8	1.0	9.1	1.7	131	527	20.3	1848	237	53.3	253	1808
	H	**Mean (n=2)**	**14.4**	**5.4**	**16.9**	**2.1**	**9.9**	**5.3**	**1.8**	**4.8**	**0.90**	**5.6**	**1.1**	**3.5**	**0.58**	**4.9**	**0.77**	**77.8**	**498**	**17.0**	**1856**	**240**	**28.3**	**91.3**	**2544**
		S.D.	9.6	1.9	6.6	1.1	6.3	4.6	1.7	4.1	0.77	4.6	0.80	2.3	0.34	2.4	0.23	47.3	316	2.2	837	101	2.9	13.9	248
		Min.	4.8	3.5	10.3	1.0	3.6	0.71	0.13	0.70	0.13	0.97	0.26	1.1	0.24	2.5	0.53	30.5	182	14.8	1020	139	25.4	77.4	2296
		Max.	24.0	7.3	23.5	3.1	16.2	9.9	3.5	8.9	1.7	10.2	1.9	5.8	0.92	7.2	1.0	125	813	19.3	2693	341	31.2	105	2792
MV100	**M**	**Mean (n=18)**	**7.9**	**8.2**	**17.0**	**1.4**	**5.0**	**0.90**	**0.22**	**1.0**	**0.22**	**1.8**	**0.50**	**2.3**	**0.48**	**4.9**	**1.0**	**52.7**	**102**	**12.7**	**641**	**88.4**	**35.4**	**147**	**590**
		S.D.	2.0	11.5	21.0	2.0	6.1	0.76	0.17	0.87	0.19	1.1	0.23	0.73	0.14	1.0	0.19	44.1	22.5	2.7	171	18.8	10.1	79.0	176
		Min.	6.2	0.58	1.4	0.14	0.63	0.29	0.08	0.45	0.12	1.1	0.35	1.6	0.35	3.6	0.75	20.4	78.9	6.7	430	67.0	24.8	77.0	403
		Max.	15.5	47.8	83.5	8.6	26.0	3.1	0.80	4.4	0.96	6.2	1.4	5.0	0.99	8.5	1.6	187	148	18.3	977	128	55.9	319	960
RU49-8096																									
CLC047	**M**	**Mean (n=7)**	**13.0**	**7.2**	**24.1**	**2.8**	**9.7**	**1.8**	**0.58**	**1.6**	**0.31**	**2.9**	**0.67**	**2.6**	**0.57**	**4.8**	**0.92**	**73.5**	**384**	**25.3**	**1493**	**202**	**70.2**	**101**	**836**
		S.D.	7.5	3.9	11.3	1.5	6.5	1.3	0.39	1.1	0.19	1.7	0.38	1.3	0.29	1.7	0.36	35.2	42.0	3.7	184	21.0	5.4	8.7	103
		Min.	5.2	3.5	11.8	1.2	3.2	0.54	0.25	0.47	0.13	1.1	0.30	1.5	0.39	3.5	0.60	33.6	332	19.2	1186	173	62.6	87.7	646
		Max.	29.9	15.7	45.1	5.1	20.4	4.4	1.3	4.0	0.72	6.6	1.5	5.6	1.3	8.8	1.8	134	448	28.9	1810	243	80.8	114	1011
RD2765																									
MV105	**M**	**Mean (n=7)**	**3.8**	**4.9**	**9.0**	**0.75**	**2.0**	**0.23**	**0.15**	**0.23**	**0.07**	**0.67**	**0.22**	**1.2**	**0.26**	**2.7**	**0.58**	**26.7**	**233**	**15.5**	**373**	**58.8**	**26.9**	**76.0**	**334**
		S.D.	0.88	0.99	2.2	0.21	0.58	0.06	0.05	0.07	0.02	0.13	0.05	0.26	0.07	0.68	0.15	5.2	41.5	9.9	115	10.0	7.8	22.3	117
		Min.	1.9	2.9	5.1	0.38	1.0	0.15	0.08	0.15	0.04	0.41	0.12	0.62	0.13	1.3	0.27	19.6	173	1.7	205	44.1	15.5	38.7	158
		Max.	4.6	5.9	12.1	1.1	2.9	0.31	0.25	0.36	0.09	0.82	0.27	1.4	0.35	3.4	0.73	33.7	296	29.3	517	74.5	40.0	111	478
RU41-9882																									
MV043	**M**	**Mean (n=16)**	**9.8**	**4.2**	**9.1**	**0.85**	**3.1**	**0.60**	**0.20**	**0.80**	**0.19**	**1.8**	**0.48**	**2.0**	**0.36**	**3.3**	**0.63**	**37.3**	**678**	**26.5**	**628**	**99.2**	**41.4**	**98.5**	**615**
		S.D.	6.6	2.9	5.6	0.56	1.9	0.29	0.10	0.33	0.08	0.91	0.22	0.64	0.09	0.69	0.13	13.0	410	8.3	181	21.4	10.2	38.2	167
		Min.	4.4	1.1	3.2	0.26	1.1	0.29	0.09	0.44	0.11	0.84	0.24	1.1	0.22	2.1	0.39	20.7	328	14.8	211	46.0	15.6	5.9	229
		Max.	28.4	13.6	26.3	2.5	8.8	1.3	0.42	1.5	0.40	4.0	1.1	3.5	0.52	4.6	0.98	69.7	1972	41.1	883	122	61.9	150	874

Table C16. Other hematite textures in MV093 (RD647)

Texture	U*	Sample	Mg	Al	Si	P	Ca	Sc	Ti	V	Cr	Mn	Co	Ni	Cu	Zn	Ga	As	Sr	Zr	Nb	Mo	Sn	Sb	Ba	Hf	Ta
Granoblastic	**L**	**Mean (n=16)**	**12.6**	**378**	**212**	**35.7**	**170**	**3.6**	**741**	**105**	**48.7**	**4.4**	**0.88**	**0.39**	**10.1**	**1.3**	**1.9**	**74.0**	**0.22**	**10.5**	**8.1**	**6.0**	**188**	**34.6**	**0.49**	**0.39**	**0.05**
		S.D.	6.5	29.5	97.6	30.3	115	1.2	384	19.0	18.9	1.9	0.40	0.20	25.6	0.95	0.27	139	0.25	6.6	7.0	8.6	87.0	17.5	0.64	0.23	0.05
		Min.	1.2	309	55.9	<2.9	<14.4	0.99	213	79.3	12.6	0.96	0.15	<0.09	0.24	0.17	1.4	<0.64	<0.001	1.5	0.42	0.15	92.8	9.9	<0.001	0.09	0.007
		Max.	20.4	429	437	116	164	5.4	1417	141	90.7	8.0	1.5	0.82	108	4.6	2.5	563	0.87	22.1	27.2	35.7	404	71.7	2.2	0.91	0.22
Matrix	**L**	**Mean (n=6)**	**30.9**	**275**	**1467**	**838**	**320**	**1.7**	**950**	**63.5**	**86.9**	**48.2**	**0.89**	**0.19**	**39.4**	**23.4**	**2.0**	**2631**	**20.2**	**8.6**	**17.7**	**174**	**86.0**	**187**	**24.3**	**0.27**	**0.05**
		S.D.	9.6	13.4	1107	57.6	122	0.11	47.5	1.3	2.4	7.7	0.16	0.07	7.4	8.0	0.14	162	0.49	0.86	1.5	9.7	1.8	16.0	1.7	0.05	0.009
		Min.	24.9	258	487	749	171	1.6	875	61.7	82.7	42.1	0.66	<0.07	32.7	17.2	1.8	2350	19.6	7.1	14.8	158	82.9	157	22.3	0.16	0.03
		Max.	51.7	292	3474	934	494	1.9	1025	64.9	90.3	64.8	1.1	0.31	54.2	40.8	2.2	2865	21.1	9.6	19.4	186	88.5	210	27.5	0.32	0.05
Feldspar-	**L**	**Mean (n=9)**	**65.1**	**237**	**2811**	**293**	**277**	**1.3**	**1404**	**80.4**	**71.0**	**77.2**	**4.9**	**0.67**	**328**	**192**	**5.9**	**581**	**66.3**	**5.5**	**81.9**	**137**	**212**	**214**	**56.3**	**0.16**	**0.32**
replacement		**S.D.**	49.7	172	1332	153	25.5	0.85	840	103	91.7	25.2	3.8	0.33	165	228	3.0	171	40.7	4.0	47.7	73.6	225	85.0	40.9	0.12	0.20
		Min.	22.2	41.4	681	<34.9	241	<0.28	42.9	1.9	<1.5	44.5	1.7	0.22	164	21.1	3.0	221	11.1	0.05	18.3	16.7	38.0	44.1	9.5	<0.001	0.01
		Max.	182	532	4524	449	312	2.7	2388	279	249	129	14.0	1.1	656	624	11.4	759	133	10.9	157	219	707	294	136	0.36	0.60
	M	**Mean (n=3)**	**29.3**	**580**	**4864**	**497**	**<312**	**2.4**	**2497**	**251**	**241**	**72.7**	**3.3**	**0.94**	**305**	**79.4**	**10.4**	**792**	**83.9**	**10.4**	**131**	**234**	**130**	**291**	**85.9**	**0.35**	**0.61**
		S.D.	3.2	15.5	514	37.8	-	0.30	52.7	6.2	9.7	1.9	0.17	0.28	7.4	1.6	0.41	14.3	1.1	0.43	1.5	4.9	1.7	18.8	34.9	0.02	0.06
		Min.	24.7	559	4254	461	-	2.0	2450	242	228	70.0	3.1	0.65	297	77.1	9.9	772	82.7	9.8	130	228	129	266	58.6	0.34	0.53
		Max.	31.7	596	5511	549	-	2.8	2570	255	251	74.2	3.5	1.3	315	80.7	10.9	805	85.5	10.8	133	240	133	311	135	0.38	0.67

Table C16. (Continued) Other hematite textures in MV093 (RD647)

Texture	U*	Sample	Y	La	Ce	Pr	Nd	Sm	Eu	Gd	Tb	Dy	Ho	Er	Tm	Yb	Lu	∑REY	W	^{204}Pb	^{206}Pb	^{207}Pb	^{208}Pb	Th	U
Granoblastic	**L**	**Mean (n=16)**	**0.04**	**0.23**	**0.44**	**0.04**	**0.12**	**0.02**	**0.006**	**0.02**	**0.002**	**0.01**	**0.003**	**0.01**	**0.002**	**0.02**	**0.002**	**0.98**	**8.7**	**2.7**	**2.3**	**1.4**	**1.2**	**0.08**	**0.34**
		S.D.	0.06	0.28	0.57	0.05	0.17	0.03	0.008	0.02	0.002	0.02	0.003	0.01	0.002	0.02	0.003	1.2	10.1	1.4	2.2	1.3	1.2	0.09	0.33
		Min.	0.002	<0.001	<0.001	<0.001	<0.001	<0.001	<0.001	<0.001	<0.001	<0.001	<0.001	<0.001	<0.001	<0.001	<0.001	0.02	0.56	<1.4	0.04	<0.005	0.003	<0.001	0.004
		Max.	0.19	1.0	2.1	0.18	0.61	0.10	0.03	0.09	0.006	0.06	0.01	0.05	0.009	0.06	0.01	4.4	35.7	5.2	7.3	4.2	3.4	0.28	1.0
Matrix	**L**	**Mean (n=6)**	**5.9**	**15.5**	**38.5**	**3.7**	**12.3**	**2.0**	**0.86**	**1.4**	**0.29**	**2.1**	**0.42**	**1.3**	**0.22**	**1.5**	**0.18**	**86.1**	**86.5**	**35.9**	**116**	**50.4**	**40.3**	**6.1**	**30.4**
		S.D.	0.25	1.3	2.2	0.15	0.41	0.14	0.05	0.09	0.03	0.13	0.02	0.07	0.01	0.05	0.01	3.6	8.5	1.7	5.9	1.5	1.2	0.17	2.2
		Min.	5.6	14.3	36.3	3.6	11.6	1.8	0.81	1.2	0.24	1.9	0.40	1.2	0.20	1.4	0.17	82.2	70.1	32.9	108	48.6	38.7	5.8	26.3
		Max.	6.3	17.6	42.2	3.9	12.9	2.2	0.97	1.5	0.33	2.3	0.46	1.4	0.23	1.6	0.20	91.9	95.4	38.3	125	53.1	42.0	6.3	32.8
Feldspar-	**L**	**Mean (n=9)**	**13.1**	**15.8**	**45.5**	**5.5**	**18.2**	**3.4**	**1.2**	**2.6**	**0.61**	**4.4**	**0.91**	**3.0**	**0.52**	**3.6**	**0.45**	**119**	**192**	**74.8**	**407**	**254**	**213**	**7.1**	**57.3**
replacement		**S.D.**	8.1	9.4	29.4	3.4	11.2	2.0	0.86	1.6	0.39	2.9	0.60	1.9	0.34	2.4	0.29	72.0	140	31.2	177	100	85.5	6.4	36.3
		Min.	0.81	3.6	7.2	0.78	2.3	0.42	0.14	0.22	0.05	0.37	0.08	0.22	0.04	0.26	0.04	16.7	73.7	21.6	142	84.9	66.2	0.19	25.6
		Max.	22.0	30.8	92.8	10.2	32.0	5.7	2.2	4.4	1.1	8.0	1.7	5.5	0.95	6.9	0.81	215	492	115	651	411	345	18.1	121
	M	**Mean (n=3)**	**18.3**	**28.8**	**90.7**	**9.8**	**31.8**	**5.3**	**2.1**	**3.8**	**0.91**	**6.8**	**1.3**	**4.2**	**0.79**	**5.5**	**0.66**	**211**	**319**	**109**	**610**	**336**	**289**	**17.2**	**138**
		S.D.	0.009	1.2	1.1	0.15	0.32	0.15	0.02	0.07	0.03	0.04	0.02	0.22	0.01	0.18	0.02	2.7	3.3	4.3	13.4	9.1	6.1	0.22	1.0
		Min.	18.3	27.1	89.5	9.6	31.3	5.0	2.1	3.8	0.88	6.8	1.3	4.0	0.78	5.3	0.64	207	315	103	592	324	280	17.0	138
		Max.	18.4	29.8	92.1	10.0	32.0	5.4	2.2	3.9	0.94	6.9	1.4	4.5	0.81	5.7	0.69	213	323	114	624	346	293	17.5	140

Table C17. Colloform hematite (various locations)

Drillhole	U*	Sample	Mg	Al	Si	P	Ca	Sc	Ti	V	Cr	Mn	Co	Ni	Cu	Zn	Ga	As	Sr	Zr	Nb	Mo	Sn	Sb	Ba	Hf	Ta
RD2786A																											
MV025	**L**	**Mean (n=2)**	**6.6**	**191**	**640**	**17.6**	**<121**	**0.46**	**934**	**5.8**	**1.6**	**56.1**	**<0.19**	**<0.04**	**258**	**3.1**	**6.7**	**1014**	**28.3**	**1.3**	**78.1**	**78.8**	**52.1**	**105**	**145**	**<0.03**	**1.3**
		S.D.	0.28	0.03	29.9	0.15	-	0.04	73.1	0.33	0.24	1.8	-	-	13.3	0.39	0.001	20.0	0.05	0.005	3.2	0.02	4.7	2.4	2.6	-	0.09
		Min.	6.3	191	610	17.5	-	0.41	861	5.5	1.4	54.3	-	-	244	2.7	6.7	994	28.2	1.3	74.9	78.8	47.5	103	142	-	1.2
		Max.	6.9	191	669	17.8	-	0.50	1007	6.1	1.9	57.8	-	-	271	3.5	6.7	1034	28.3	1.3	81.3	78.8	56.8	108	148	-	1.4
RD647																											
MV093B	**L**	**Mean (n=5)**	**22.8**	**771**	**4399**	**694**	**377**	**1.7**	**1128**	**99.7**	**31.7**	**60.8**	**1.8**	**0.48**	**714**	**32.2**	**3.1**	**674**	**108**	**3.7**	**34.3**	**124**	**29.8**	**92.0**	**64.3**	**0.10**	**0.20**
		S.D.	7.9	138	1199	342	118	0.50	200	40.6	3.0	13.5	0.27	0.13	429	3.8	0.99	301	22.3	2.2	3.6	89.9	9.1	15.0	6.5	0.06	0.04
		Min.	12.8	594	2647	191	<260	0.97	886	74.9	27.3	41.2	1.5	0.34	324	27.3	1.8	334	68.2	1.5	29.5	10.8	18.0	77.3	58.3	0.03	0.17
		Max.	30.4	962	5738	1008	537	2.2	1392	180	35.7	79.2	2.4	0.64	1375	38.4	4.4	1146	127	7.4	39.3	250	40.1	116	76.5	0.19	0.28
RU27-7551																											
MV048	**L**	**Mean (n=19)**	**5.3**	**2366**	**5303**	**236**	**125**	**2.4**	**165**	**1.1**	**20.3**	**55.5**	**3.8**	**0.53**	**523**	**205**	**4.8**	**433**	**20.7**	**1.0**	**3.0**	**9.8**	**0.87**	**3.1**	**45.8**	**0.05**	**0.14**
		S.D.	2.2	483	964	84.5	81.6	0.38	159	0.43	14.3	12.6	1.2	0.14	50.2	67.3	0.94	57.3	7.6	0.86	3.0	3.2	1.1	2.3	19.0	0.05	0.22
		Min.	2.0	1804	4094	101	<20.2	1.5	24.5	0.51	8.6	37.1	2.2	0.20	442	117	3.3	360	9.3	0.25	0.42	4.6	<0.25	1.4	22.2	<0.001	0.002
		Max.	9.7	3562	7427	416	156	3.1	538	2.6	77.8	76.9	6.4	0.74	605	344	7.6	579	34.4	4.0	12.6	19.8	4.6	11.4	86.1	0.18	0.90
	M	**Mean (n=24)**	**23.8**	**4019**	**8307**	**249**	**244**	**5.5**	**1231**	**4.6**	**36.6**	**161**	**8.7**	**0.70**	**899**	**477**	**12.4**	**509**	**56.4**	**5.0**	**23.8**	**31.3**	**4.3**	**32.6**	**134**	**0.22**	**0.75**
		S.D.	36.2	735	1559	82.4	53.2	0.82	469	1.7	25.7	32.9	2.0	0.21	585	132	4.0	59.2	10.7	2.2	8.6	11.8	2.3	7.0	37.2	0.10	0.33
		Min.	6.1	2671	5574	106	<184	4.0	407	1.5	9.7	83.0	5.0	0.27	539	246	5.9	368	39.3	1.3	6.6	11.5	1.4	12.3	66.0	0.03	0.15
		Max.	141	5838	13773	500	409	7.2	1838	6.9	105	228	13.0	1.1	3547	848	19.4	590	82.3	9.9	35.7	49.3	13.2	40.2	239	0.37	1.2

Table C17. (Continued) Colloform hematite (various locations)

Drillhole	U*	Sample	Y	La	Ce	Pr	Nd	Sm	Eu	Gd	Tb	Dy	Ho	Er	Tm	Yb	Lu	∑REY	W	^{204}Pb	^{206}Pb	^{207}Pb	^{208}Pb	Th	U
RD2786A																									
MV025	**L**	**Mean (n=2)**	**9.6**	**17.1**	**29.7**	**2.3**	**5.9**	**0.97**	**0.82**	**0.86**	**0.25**	**2.2**	**0.54**	**2.1**	**0.35**	**2.6**	**0.38**	**151**	**1076**	**47.6**	**338**	**87.1**	**55.5**	**3.7**	**58.1**
		S.D.	0.55	0.01	0.14	0.02	0.02	0.04	0.04	0.01	0.007	0.09	0.02	0.07	0.004	0.11	0.02	0.19	32.7	1.7	0.31	0.67	0.94	0.23	0.14
		Min.	9.1	17.1	29.5	2.3	5.9	0.93	0.78	0.85	0.24	2.1	0.52	2	0.34	2.5	0.36	151	1043	45.9	337	86.4	54.5	3.4	58
		Max.	10.2	17.1	29.8	2.3	5.9	1	0.86	0.87	0.25	2.3	0.57	2.2	0.35	2.7	0.4	151	1108	49.3	338	87.7	56.4	3.9	58.3
RD647																									
MV093B	**L**	**Mean (n=5)**	**8.1**	**4.9**	**20**	**2.6**	**9.1**	**1.8**	**0.87**	**1.4**	**0.35**	**2.9**	**0.54**	**1.7**	**0.33**	**2.3**	**0.27**	**116**	**50.9**	**81.1**	**354**	**239**	**207**	**3.5**	**39.8**
		S.D.	1.5	0.99	3.8	0.49	1.5	0.31	0.17	0.24	0.05	0.48	0.1	0.22	0.06	0.39	0.06	20.7	7.9	24.1	77.9	68.6	60.1	0.32	4
		Min.	5.2	3.4	14.2	1.9	6.6	1.3	0.56	1	0.26	1.9	0.35	1.2	0.22	1.6	0.16	79.7	40.6	61.6	299	182	155	2.9	34.9
		Max.	9.4	5.8	24.4	3.1	10.8	2.2	1	1.7	0.4	3.3	0.62	1.8	0.38	2.7	0.31	137	62.3	127	502	369	320	3.9	46.9
RU27-7551																									
MV048	**L**	**Mean (n=19)**	**17.5**	**3.8**	**11.8**	**1.5**	**5.8**	**1.5**	**0.65**	**1.8**	**0.43**	**3.4**	**0.85**	**3.1**	**0.51**	**3.7**	**0.62**	**57**	**0.97**	**2783**	**3646**	**4196**	**3882**	**6**	**70.9**
		S.D.	3.5	1.2	3.4	0.33	1.2	0.31	0.13	0.36	0.08	0.63	0.14	0.55	0.1	0.68	0.12	11.5	0.55	1539	838	975	906	0.87	17.1
		Min.	12.6	2.2	6.7	0.93	3.9	0.89	0.44	1.2	0.3	2.5	0.58	2.2	0.38	2.6	0.42	38.5	0.17	828	2622	3020	2767	5	38.7
		Max.	26.2	7.1	18.5	2.1	8	2	0.94	2.6	0.64	5	1.2	4.5	0.82	5.2	0.95	80.1	2.8	5486	5622	6520	6027	9.2	115
	M	**Mean (n=24)**	**52.2**	**10.9**	**39.5**	**5.3**	**21.2**	**5.7**	**2.5**	**6.6**	**1.7**	**12.2**	**2.8**	**9.3**	**1.6**	**9.2**	**1.6**	**182**	**5.7**	**1915**	**5488**	**5927**	**5498**	**16.3**	**236**
		S.D.	9	5.5	15.6	1.7	6.3	1.5	0.6	1.6	0.33	2.3	0.47	1.5	0.24	1.4	0.22	43	1.6	1216	1080	1276	1127	5.2	50.1
		Min.	34.5	4.9	16.9	2.3	9.6	3	1.2	3.5	0.91	6.8	1.7	5.9	1	6.4	1.2	100	2	1056	3336	3538	3364	8.2	126
		Max.	70.8	33.8	89.1	10.6	38.4	9	3.8	9.4	2.1	16.4	3.4	12	2	12.1	2.1	293	8.7	7590	8012	9131	8580	25.2	317

Notes: dash line (-) denotes values that could be not calculated based on the available data; bdl: below detection limit; NA: not analysed; different Pb isotopes indicate total concentration of Pb based on the measurement of that particular isotope.

ELECTRONIC APPENDIX D FOR CHAPTER 2

Table D1. EPMA data for hematite in sample RX6583

Analysis #	**1**	**2**	**3**	**4**	**5**	**6**	**7**	**8**	**9**	**10**	**11**	**12**	**13**
MgO	bdl	0.03	0.03	0.04	0.03	0.05	0.07	0.04	0.05	0.04	0.07	0.07	0.04
TiO_2	bdl	bdl	bdl	bdl	bdl	bdl	bdl	bdl	bdl	bdl	0.02	bdl	bdl
Fe_2O_3	96.31	95.37	94.15	95.41	95.98	95.88	97.45	97.28	97.60	96.59	99.45	99.22	97.07
WO_3	1.61	1.53	1.56	1.46	1.49	1.47	1.25	1.30	1.07	1.02	0.34	0.23	1.48
ZnO	bdl	bdl	bdl	bdl	bdl	bdl	bdl	bdl	bdl	bdl	bdl	0.06	bdl
ZrO_2	bdl	bdl	bdl	bdl	bdl	bdl	bdl	bdl	bdl	0.05	bdl	bdl	bdl
MoO_3	0.17	0.14	0.14	0.15	0.14	0.18	0.16	0.17	0.16	0.14	bdl	bdl	0.13
SnO_2	0.11	0.10	0.14	0.11	0.09	0.06	0.09	0.09	0.12	0.09	0.09	0.06	0.13
UO_3	2.33	2.33	2.23	2.08	1.93	1.57	1.53	1.57	1.46	1.46	0.05	0.03	0.74
PbO	0.55	0.57	0.53	0.51	0.47	0.38	0.37	0.38	0.35	0.35	0.03	0.03	0.20
Total	101.06	100.07	98.79	99.76	100.14	99.58	100.92	100.82	100.81	99.73	100.05	99.70	99.81
Calculated hematite formula based on 3 O (apfu)													
Mg	-	0.001	0.001	0.001	0.001	0.002	0.003	0.001	0.002	0.002	0.003	0.003	0.002
Ti	-	-	-	-	-	-	-	-	-	-	0.000	-	-
Fe	1.944	1.945	1.944	1.948	1.950	1.954	1.958	1.957	1.961	1.962	1.991	1.993	1.964
W	0.011	0.011	0.011	0.010	0.010	0.010	0.009	0.009	0.007	0.007	0.002	0.002	0.010
Zn	-	-	-	-	-	-	-	-	-	-	-	0.001	-
Zr	-	-	-	-	-	-	-	-	-	0.001	-	-	-
Mo	0.002	0.002	0.002	0.002	0.002	0.002	0.002	0.002	0.002	0.002	-	-	0.001
Sn	0.001	0.001	0.002	0.001	0.001	0.001	0.001	0.001	0.001	0.001	0.001	0.001	0.001
U	0.013	0.013	0.013	0.012	0.011	0.009	0.008	0.009	0.008	0.008	0.000	0.000	0.004
Pb	0.004	0.004	0.004	0.004	0.003	0.003	0.003	0.003	0.003	0.003	0.000	0.000	0.001
Total	1.975	1.976	1.976	1.978	1.979	1.980	1.983	1.982	1.984	1.984	1.998	1.999	1.985

bdl: below detection limit; apfu: atoms per formula unit. Al_2O_3, CaO, Cr_2O_3, MnO, Nb_2O_5, NiO, P_2O_5, SiO_2 and V_2O_3 were consistently below the minimum detection limit.

SUPPLEMENTARY MATERIAL B

FOR CHAPTER 3 –DEFINING EARLY STAGES OF IOCG SYSTEMS: EVIDENCE FROM IRON-OXIDES IN THE OUTER SHELL OF THE OLYMPIC DAM DEPOSIT, SOUTH AUSTRALIA

APPENDIX A: METHODOLOGY

APPENDIX B: ADDITIONAL TABLES AND EPMA AND LA-ICP-MS RESULTS

APPENDIX C: ADDITIONAL FIGURES AND FULL LA-ICP-MS MAPS

ELECTRONIC APPENDIX A FOR CHAPTER 3

Analytical methods – Electron probe microanalysis (EPMA)

Quantitative major and minor oxide compositions of different sub-types of Fe-oxides were obtained using a CAMECA SX-Five Electron Probe Microanalyzer (EPMA), equipped with 5 wavelength-dispersive spectrometers (WDS), and hosted at Adelaide Microscopy, The University of Adelaide. The instrument was operated at a constant accelerating voltage of 15 keV and variable beam current. A constant beam spot-size of ~1 μm was utilized for the measurements. Individual analytical conditions for each analyzed element are listed in Table A1. Calibration and data reduction was conducted in the software package Probe for EPMA (see Donovan et al. 2016, and references therein). Background times were kept constant at 40 s for the calibration of all elements in the standards. Typical minimum detection limits ranged from 0.004 (Mg) to 0.051 wt% (W) at 99 % confidence. The error/precision was calculated separately for each individual spot based on analytical conditions and concentration of the elements in the unknown. On average, the absolute precision values were smaller for those elements present at higher concentrations, varying from 0.27 % (Fe) to -101 % (Zr). Elemental concentrations measured on standards over a 4-year period indicate that the internal accuracy is good.

Table A1. Summary of analytical conditions/setup employed for EPMA analysis of Fe-oxides

Element	Line	Current (nA)	Crystal	Standard	Peak count time (s)		Average mdl (wt%)	Error* (%)
					on-	off- (H/L)		
Al	K_α	20	TAP	Astimex Plagioclase An65	20	10	0.012	37
Ca	K_α	20	LPET	Titanite	20	10	0.011	6.8
Co	K_α	100	LLIF	Cobaltite	50	25	0.012	-46
Cr	K_α	20	LLIF	P&H Cr_2O_3	20	10	0.022	25
Cu	K_α	20	LLIF	Chalcopyrite	20	10	0.046	-8.4
Fe	K_α	20	LLIF	P&H Specularite	20	10	0.03	0.27
Mg	K_α	100	TAP	Astimex Almandine Garnet	50	25	0.004	1.2
Mn	K_α	20	LLIF	P&H Rhodonite	20	10	0.028	-31
Mo	L_α	100	LPET	Astimex Molybdenum metal	20	10	0.017	-46
Nb	L_α	100	LPET	Astimex Niobium metal	20	10	0.017	-3.3
Ni	K_α	100	LLIF	Astimex Pentlandite	35	15	0.013	68
P	K_α	20	LPET	Astimex Apatite	20	10	0.017	90
Pb	M_α	100	LPET	K227 Pb glass	20	30/40	0.011	66
Si	K_α	20	TAP	Astimex Plagioclase An65	20	10	0.013	2.4
Sn	L_α	100	LPET	P&H Cassiterite	20	10	0.016	-32
Ti	K_α	20	LPET	Titanite	50	25	0.008	33
U	M_β	100	LPET	DAS UO_2	20	30/40	0.017	-82
V	K_α	100	LLIF	Astimex Vanadium metal	35	20	0.007	-64
W	L_α	100	LLIF	Astimex Tungsten metal	40	15	0.051	-33
Zn	K_α	100	LLIF	Astimex Willemite	50	25	0.019	40
Zr	L_α	100	LPET	GJ1 Zircon	20	10	0.017	-101

* average error based on individual analysis conditions considering on-peak and off-peak counting statistic for zoned, Si-magnetite from sample OD11. Absolute values become increasingly smaller when measured on-peak intensities are substantially above local background. mdl: minimum detection limit.

Analytical methods – Laser-ablation inductively-coupled mass spectrometry (LA-ICP-MS)

LA-ICP-MS spot analysis was conducted following established practices at Adelaide Microscopy (e.g., Verdugo-Ihl et al. 2017) using a RESOlution-LR 193 nm excimer laser microprobe (Australian Scientific Instruments) with a large-format S155 two-volume ablation

cell designed by Laurin Technic Pty., coupled to an Agilent 7900x Quadrupole ICP-MS. Laser ablation was performed in an atmosphere of UHP He (0.35 1/min) and the aerosol was mixed with Ar (1.06 l/min) before exiting the sample chamber. A pulse homogenizing device ('squid', Laurin Technic) was used in the interface tubing between the laser and ICP-MS to smooth signal fluctuations. The ICP-MS system was optimized daily to achieve maximal sensitivity and low oxide interference production. Most commonly, a laser spot size diameter of 43 µm was employed (also 29 and 51 µm depending on the requirements), using a pulse repetition rate of 5 Hz and a fluence of 3.5 J/cm^2.

Prior to each spot analysis, the selected areas were pre-ablated to avoid surface contamination. Acquisition time comprised a 30 s measurement of the background (laser off) and either 30 or 40 s acquisition of the signal while the laser ablates. Analytical standards were run before and after each individual set of ≤26 Fe-oxide unknowns using either BHVO-2G or GSD-1G as the primary standard, and NIST-610 as the secondary standard.

Data reduction was performed in Glitter (van Achterbergh et al. 2001) using stoichiometric concentrations of Fe in hematite or magnetite expressed as FeO (89.9810 and 93.0899 wt%, respectively) as the internal standard element. Detection limits indicated by Glitter were individually calculated for each element in each spot analysis.

The following suite of 45 elements, including four Pb isotopes, was measured: ^{24}Mg, ^{27}Al, ^{28}Si, ^{31}P, ^{43}Ca, ^{45}Sc, ^{49}Ti, ^{51}V, ^{52}Cr, ^{55}Mn, ^{57}Fe, ^{59}Co, ^{60}Ni, ^{63}Cu, ^{66}Zn, ^{69}Ga, ^{75}As, ^{88}Sr, ^{89}Y, ^{90}Zr, ^{93}Nb, ^{95}Mo, ^{118}Sn, ^{121}Sb, ^{137}Ba, ^{139}La, ^{140}Ce, ^{141}Pr, ^{146}Nd, ^{147}Sm, ^{153}Eu, ^{157}Gd, ^{159}Tb, ^{163}Dy, ^{165}Ho, ^{166}Er, ^{169}Tm, ^{172}Yb, ^{175}Lu, ^{178}Hf, ^{181}Ta, ^{182}W, ^{204}Pb, ^{206}Pb, ^{207}Pb, ^{208}Pb, ^{232}Th and ^{238}U.

LA-ICP-MS element maps were obtained for subsets of the previously indicated isotopes (see above). For this purpose, grids of parallel lines were ablated across the selected areas using a fluence of ~3.5 J/cm^2 and laser repetition rates of 10 Hz. A spot size of 7 and 11 µm was used with a speed of 7 and 11 µm/s respectively. Prior to the main ablation and signal acquisition phase, individual lines were pre-ablated to clean the surfaces and minimize the contribution from the deposition blanket from previous lines. An acquisition of 15 or 20 s background for each line was conducted prior to the main ablation phase. Spot analyses were conducted on the reference materials before and after each mapping run. The program Iolite (Paton et al. 2011) was used for data reduction and processing. Individual line-profiles of the measured isotopes were merged together into 2D-images by subtracting the average backgrounds from the time-resolved intensities and producing qualitative isotope intensity maps with scales in counts-per-second (cps). The obtained intensities were scaled individually using generally logarithmic-, but also linear-scales to highlight intragrain variability in hematite and to image features of interest accordingly.

References

Donovan JJ, Singer JW, Armstrong JT (2016) A new EPMA method for fast trace element analysis in simple matrices. Am Mineral 101:1839–1853. doi: 10.2138/am-2016-5628

Paton C, Hellstrom J, Paul B, et al (2011) Iolite: Freeware for the visualisation and processing of mass spectrometric data. J Anal At Spectrom 26:2508–2518. doi: 10.1039/c1ja10172b

van Achterbergh E, Ryan CG, Jackson SE, Griffin WL (2001) Data reduction software for LA-ICP-MS. In: Sylvester PJ (ed) Laser-ablation-ICPMS in the Earth Sciences; Principles and Applications.

Mineralogical Association of Canada, Short Course Series 29. pp 239–243
Verdugo-Ihl MR, Ciobanu CL, Cook NJ, et al (2017) Textures and U-W-Sn-Mo signatures in hematite from the Olympic Dam Cu-U-Au-Ag deposit, South Australia: Defining the archetype for IOCG deposits. Ore Geol Rev 91:173–195. doi: 10.1016/j.oregeorev.2017.10.007

ELECTRONIC APPENDIX B FOR CHAPTER 3

Table S1. Sample list and key characteristic from the Magnetite drillhole (RU65-7976)

Depth -RL (downhole) m	Sample	Magnetite			Hematite				Type	Characteristics
		magmatic	silician	(pseudo) mushketovite	zoned	specular/ bladed	replacing carbonates	martite		
678.9 (65)	CLC02					X				Hm-rich breccia intercalated within variably altered, pink- to greenish-coloured granite; lithologies partially resemble orebody-breccias.
692 (90.4)	CLC05					X				
692.2 (90.7)	CLC06					X				
692.2 (90.8)	CLC07					X				
711.8 (128.7)	CLC08A/B						X		B	Rhythmically banded Hm and breccia interval Hm replacing carbonates(?)
731.3 (166.3)	CLC10				X			(X)		
849.5 (397.3)	CLC18					X				
851.5 (410.3)	CLC20		(X)	X		X				Mt(±Hm)-rich metasomatised granite (±pinkish- to greenish-coloured, altered granite clasts), Msk-predominant
856.6 (411.3)	CLC21		(X)	X		X				
863 (424)	CLC22		(X)	X		X				
866.6 (431)	OD11A		X	(X)		(X)				Carbonate-hosted, massive Mt-interval
	OD11B		(X)	(X)		(X)				
	OD11C		X	(X)		X				
866.8 (431.4)	CLC23			(X)		X				Mt(±Hm)-rich breccia with pinkish- to greenish-coloured, altered granite clasts and Sd; intermittent presence of Sd-veins.
878.4 (454.3)	CLC25		X			(X)				Carbonate-replacement of Mt.
884.8 (467)	CLC26		X			X				
885.6 (468.5)	CLC27		X	X		(X)				
892 (481.2)	CLC28					(X)	X			Carbonate-vein with specular Hm.
894 (485.2)	CLC29		X	X		(X)				
900 (496.6)	CLC30		X							
901 (498.7)	CLC31	(X)	X	X		X				
901.7 (500)	CLC32		(X)	(X)		X				Hm-rich, metasomatised granite

B: band; brackets denote Fe-oxide sub-types present within the sample but not analysed by LA-ICP-MS.

Abbreviations: Hm–hematite; Msk–mushketovite; Mt–magnetite; Sd–siderite.

Table S2. Sample list and key characteristic from the *Nodular Fe-oxide granite* (RD2366)

Depth -RL (downhole) m	Sample	Magnetite			Hematite			Type	Characteristics
		magmatic	silician	(pseudo) mushketovite	Zoned	specular/ bladed	Martite		
265.2 (366.3)	MV20						(X)		Ser-altered granite (preservation of Kfsp), carbonate-replacements.
282.3 (383.4)	MV19				X			N	
357.4 (458.6)	MV18B				(X)	(X)		B	
	MV18A	(X)			(X)	X	(X)	B	
381.8 (483)	MV17				(X)		(X)		
414 (515.2)	MV16					X		N	Brecciated granite with intervals Hm-rich breccias; presence of orbicular aggregates; predominantly Ser(±Chl)-altered but local preservation of magmatic Kfsp.
472 (573.2)	MV15				(X)	X	(X)	N	
504.3 (605.5)	MV14					X		N	
509.2 (610.4)	MV13				(X)		(X)		
600 (701.3)	MV12				(X)	X	(X)	N	
618.5 (719.8)	MV11				(X)	(X)			
637.3 (738.6)	MV10		(X)			(X)	(X)		
664 (765.3)	MV09		(X)	(X)		(X)			
756 (857.4)	MV08		(X)			X		B	
864.2 (965.6)	MV07B	X	(X)	(X)	(X)	(X)			
	MV07A		X	X		(X)		B	Up to several tens of m thick, Mt-Hm-rich breccias, with variable degree of granitic clasts, intercalated within brecciated granite; predominantly Ser(±Chl)-altered but local preservation of Kfsp; variably preserved magmatic Fe-Ti-oxides
880.8 (982.2)	MV06		(X)	X	X	(X)			
915.6 (1017)	MV05B		X	X	X				
	MV05A	X	(X)	X	X	X^N	(X)	N	
942.4 (1043.8)	MV04	X	X	X		X		N	
988 (1089.5)	MV03		(X)	X		X			
1033 (1134.5)	MV02	X	(X)	X	X	(X)	(X)		
1146.5 (1248)	MV01						(X)		Ser-altered granite (preservation of magmatic Kfsp), carbonate-replacements.

N: nodule; B: band; brackets denote Fe-oxide sub-types present within the sample but not analysed by LA-ICP-MS.

Abbreviations: Chl–chlorite; Hm–hematite; Msk–mushketovite; Mt–magnetite; Sd–siderite; Ser–sericite; Kfsp–K-feldspar.

Table S3. Sample list and key characteristic from the *Deep Mineralisation* (DM; RD2773)

Depth -RL (downhole) m	Sample	Magnetite		Hematite			Characteristics
		silician	mushketovite	zoned	specular/ bladed	martite	
1889.6 (1998)	RD2773-5	X	(X)		X	X	Granite-breccia with clast derived from a felsic volcanic; Ser(±Chl)-altered; replacements after Kfsp(?).
2073.3 (2181.8)	CLC111B		X		X		Hm-veins cross-cutting the *Felsic unit*; Ser-altered.
2150.4 (2259)	RX7568		X		X		
2197.6 (2306.2)	CLC113		X	(X)	X		Brecciated-granite with coarse Hm; Ser(±Chl)-altered.

Brackets denote Fe-oxide sub-types present within the sample but not analysed by LA-ICP-MS.

Abbreviations: Chl–chlorite; Hm–hematite; Ser–sericite; Kfsp–K-feldspar.

Table S4. Sample list and key characteristic from the *Distal satellite mineralisation* (DSM; RD2316)

Depth -RL (downhole) m	Sample	Magnetite	Hematite			Characteristics
		silician	zoned	specular /bladed	martite	
155.3 (253.4)	LCD18		X			
253.3 (351.4)	MV51		X		(X)	
281.2 (379.3)	MV52		X		(X)	Intermittent presence of Hm-veins crosscutting coarse-grained granite, featuring minor brecciation and locally rock-flour, ±Ser-altered.
341 (439.2)	LCD19		X		(X)	
	MV53		X		X	
445 (543.3)	MV54				(X)	
457 (555.2)	MV55		X		(X)	Granite-breccia with abundance of Hm; preservation of magmatic Kfsp (±Ser-altered); onset of sulfide-mineralization.
469.6 (567.8)	LCD21		X			
481.8 (580)	MV56	(X)			X	
522 (620.2)	MV57	X		X	X	Mt-predominant, granite-breccia with abundance of Fe-oxides; minor presence of carbonates, Ap and Fl; Ser(±Chl)-altered.
539.8 (638)	LCD22A	(X)	X		X	
542 (640.2)	MV58	X	X		X	
561 (659.2)	MV59	X		(X)	X	
581 (679.2)	MV60	X	X		X	
613 (711.3)	MV61	X			X	
630.2 (728.5)	MV62	(X)		X	(X)	From ca. 730 m downwards albitized.
649 (747.3)	MV63	X			X	
686.2 (784.5)	MV64	(X)		(X)	(X)	
699.8 (798.1)	MV65				(X)	

Brackets denote Fe-oxide sub-types present within the sample but not analysed by LA-ICP-MS.

Abbreviations: Ap–apatite; Chl–chlorite; Fl–fluorite; Hm–hematite; Ser–sericite; Kfsp–K-feldspar.

Table S5. Quantitative major and minor oxide compositions of the studied Fe-oxide sub-types as determined by EPMA

	CLC22 (*n*=9) Si-magnetite			MV06 (*n*=7) Si-magnetite			MV59 (*n*=13) Si-magnetite			OD11 (*n*=64) Si-magnetite			MV07 (*n*=7) magmatic magnetite			MV19 (*n*=12) HFSE-rich zoned hematite		
Sample	min.	max.	ave.	min.	max.	ave.	min.	max.	ave.	min.	max.	ave.	min.	max.	ave.	min.	max.	ave.
CaO	0.06	0.52	0.28	0.1	0.67	0.46	0.02	1.05	0.46	0.02	1.23	0.24	0.01	0.01	0.01	0.07	0.29	0.18
MgO	0.01	0.03	0.02	0.01	0.23	0.08	0.12	0.91	0.56	0.01	0.25	0.06				0.12	0.12	0.12
TiO_2				0.04	0.32	0.17	0.03	0.41	0.22	0.01	0.06	0.03	0.21	0.33	0.27	0.15	0.93	0.42
SiO_2	0.41	1.83	1	0.23	3.38	2.32	0.07	4.46	2.73	0.13	3.09	1.12	0.03	0.17	0.07	0.06	0.88	0.43
Al_2O_3	0.03	0.03	0.03	0.26	0.54	0.39	0.07	0.4	0.24	0.02	0.07	0.03	0.07	0.23	0.11	0.11	0.19	0.14
FeO	88.28	92.47	90.73	86.94	92.38	88.83	85.91	93.27	88.92	85.56	93.06	90.87	92.98	93.87	93.24	96.28*	99.35*	97.96*
MnO	0.02	0.04	0.03	0.04	0.04	0.04	0.03	0.1	0.05	0.02	0.05	0.03	0.04	0.04	0.04	0.04	0.04	0.04
Cr_2O_3										0.02	0.03	0.03						
P_2O_5	0.02	0.02	0.02				0.02	0.02	0.02	0.02	0.04	0.02				0.02	0.02	0.02
Nb_2O_5							0.03	0.03	0.03	0.02	0.03	0.02	0.02	0.02	0.02	0.37	1.72	0.84
V_2O_3	0.01	0.01	0.01	0.01	0.04	0.03	0.05	0.08	0.07	0.01	0.01	0.01	0.03	0.06	0.05	0.06	0.09	0.08
WO_3										0.04	0.06	0.05				0.08	0.08	0.08
ZnO							0.03	0.03	0.03				0.03	0.05	0.04	0.04	0.04	0.04
ZrO_2													0.02	0.02	0.02			
MoO_3										0.02	0.03	0.03						
SnO_2				0.02	0.02	0.02				0.01	0.01	0.01				0.07	0.1	0.09
NiO				0.01	0.01	0.01	0.02	0.02	0.02	0.01	0.01	0.01						
CoO	0.01	0.01	0.01	0.03	0.05	0.04	0.01	0.03	0.02	0.01	0.03	0.02	0.02	0.03	0.02	0.02	0.03	0.02
Cu_2O							0.03	0.03	0.03	0.03	0.05	0.04				0.05	0.05	0.05
UO_3	0.03	0.03	0.03	0.03	0.05	0.04	0.03	0.09	0.05	0.03	0.04	0.03				0	0.09	0.03
PbO																0	0.04	0.02
Sum	90.63	92.94	92.07	91.99	92.84	92.29	92.42	93.57	93.14	90.31	93.4	92.36	93.36	94.35	93.74	99.17	100.54	100.01
No. of ions based on X apfu O																		
Cu							0.008	0.008	0.008	0.009	0.014	0.011				0.001	0.001	0.001
$\sum M^{+}$							0.008	0.008	0.008	0.009	0.014	0.011						
Mg	0.006	0.012	0.009	0.005	0.105	0.035	0.052	0.4	0.247	0.003	0.114	0.028				0.005	0.005	0.005
Ca	0.019	0.173	0.093	0.031	0.217	0.15	0.007	0.338	0.146	0.006	0.407	0.081	0.005	0.005	0.005	0.002	0.008	0.005
Mn	0.007	0.01	0.008	0.01	0.011	0.011	0.007	0.027	0.013	0.006	0.014	0.009	0.01	0.01	0.01	0.001	0.001	0.001
Fe^{2+}	7.664	7.932	7.816	7.317	7.946	7.532	7.083	7.974	7.443	7.372	7.972	7.794	7.905	7.964	7.941			
Co							0.004	0.004	0.004	0.004	0.007	0.005				0	0.001	0
Ni				0.003	0.003	0.003	0.005	0.005	0.005	0.004	0.004	0.004						
Zn							0.006	0.006	0.006				0.006	0.011	0.009	0.001	0.001	0.001
Pb																		
$\sum M^{2+}$	7.847	7.962	7.92	7.567	7.987	7.716	7.656	8.001	7.808	7.797	7.998	7.9	7.91	7.983	7.947	0.001	0.013	0.005
Al	0.01	0.012	0.011	0.093	0.191	0.137	0.026	0.14	0.084	0.006	0.024	0.011	0.024	0.083	0.04	0.004	0.006	0.004
V	0.002	0.002	0.002	0.003	0.009	0.006	0.012	0.019	0.016	0.002	0.004	0.003	0.007	0.015	0.011	0.001	0.002	0.002

Cr										0.005	0.007	0.006						
Fe^{3+}	15.329	15.864	15.633	14.635	15.891	15.065	14.166	15.948	14.886	14.745	15.944	15.589	15.81	15.929	15.883	1.914	1.981	1.952
$\sum M^{3+}$	15.34	15.864	15.636	14.835	15.899	15.189	14.323	15.96	14.971	14.768	15.948	15.594	15.9	15.941	15.929	1.919	1.987	1.958
Si	0.126	0.568	0.311	0.07	1.022	0.704	0.021	1.32	0.814	0.04	0.954	0.345	0.01	0.053	0.023	0.002	0.023	0.011
Ti				0.008	0.072	0.039	0.008	0.09	0.049	0.002	0.015	0.007	0.049	0.075	0.063	0.003	0.018	0.008
Zr													0.002	0.002	0.002			
Sn				0.002	0.002	0.002				0.002	0.002	0.002				0.001	0.001	0.001
$\sum M^{4+}$	0.126	0.568	0.311	0.079	1.082	0.743	0.029	1.41	0.863	0.04	0.969	0.351	0.049	0.113	0.077	0.004	0.032	0.017
P	0.004	0.004	0.004				0.005	0.005	0.005	0.004	0.009	0.006				0.001	0.001	0.001
Nb							0.004	0.004	0.004	0.002	0.004	0.003	0.002	0.003	0.003	0.004	0.02	0.01
$\sum M^{5+}$	0.004	0.004	0.004				0.004	0.005	0.005	0.002	0.009	0.006	0.002	0.003	0.003	0.004	0.02	0.01
Mo										0.002	0.004	0.003						
W										0.003	0.005	0.004				0.001	0.001	0.001
U	0.002	0.002	0.002	0.002	0.003	0.002	0.002	0.006	0.003	0.002	0.003	0.002						
$\sum M^{6+}$	0.002	0.002	0.002	0.002	0.003	0.002	0.002	0.006	0.003	0.002	0.005	0.003				0.001	0.001	0.001
Sum	23.758	23.942	23.869	23.486	23.964	23.649	23.434	23.99	23.646	23.641	23.986	23.849	23.927	23.973	23.954	1.996	2	1.999

Minimum, maximum and average data for values above detection; otherwise blanks (i.e., all values bellow detection limit).

*reported as Fe_2O_3.

Table S6. Summary statistics of LA-ICP-MS data for individual samples and Fe-oxide sub-types from the Magnetite drillhole - RU65-7976.

Sample	Type		Mg	Al	Si	P	Ca	Sc	Ti	V	Cr	Mn	Co	Ni	Cu	Zn	Ga	As	Sr	Y	Zr	Nb	Mo	Sn	Sb	Ba
CLC002	Hm	min	125	407	<109	<20.4	122	0.118	261	142	<0.66	30.3	4.51	<0.22	<0.45	1.37	5.78	<0.001	0.94	3.55	0.7	1070	7.42	212	4.61	<0.001
	(n=22)	max	431	1350	955	98.6	603	0.68	665	235	2.2	94	28.8	6.22	24.2	13.3	9.65	0.001	10.1	13.7	2.91	5000	29.6	903	13.3	13.5
		ave	274	819	522	55.1	263	0.31	402	191	1.32	66.3	16.9	2.99	11.4	6.3	8.07	0.001	3.57	8.75	1.54	2270	21.2	539	7.86	2.73
		GM	260	774	455	49.2	241	0.27	389	190	1.25	63.7	15.2	2.34	8.28	5.69	8.01	0.001	3.02	8.27	1.4	2060	20.3	496	7.45	1.35
		Std	88.9	292	243	24.7	123	0.183	107	24.2	0.434	17.6	7.05	1.65	7.5	2.75	0.916	0.001	2.13	2.88	0.69	1040	5.62	207	2.67	2.89
CLC005	Hm	min	4.82	972	579	<16.2	<129	0.32	130	11.7	<0.001	15.9	2.34	2.15	<0.001	<0.74	2.35	26.6	2.03	5.03	<0.001	449	13.7	292	6.25	<0.001
	(n=23)	max	201	1620	1800	113	614	16.3	364	204	1.52	57.6	30	9.5	60.1	8.3	10.7	213	10.6	26	2.32	3070	116	4880	22.9	8.43
		ave	106	1230	1210	30.1	267	1.53	236	175	0.821	27.9	15.8	5.92	21.5	4.35	8.66	79.7	3.75	13.1	0.766	1130	31.2	818	10.9	3.19
		GM	90.6	1220	1170	26.2	235	0.861	229	162	0.613	26.5	13.9	5.65	12.3	3.72	8.41	73	3.39	12.2	0.411	1050	27.2	652	10.4	1.49
		Std	45.8	182	324	21.3	158	3.25	56.9	38.4	0.314	9.59	7.36	1.77	13.6	2.11	1.61	37.4	1.99	4.83	0.523	520	22.5	914	3.8	2.21
CLC006	Hm	min	38.6	288	561	<164	<1160	<0.6	8.79	62.5	<2.58	9.77	2.63	2.66	7.99	<7.55	13.4	99.3	0.81	0.73	<0.001	75.3	30.5	416	19.7	<0.001
	(n=37)	max	294	888	2630	449	3980	2.21	67.4	175	6.23	49.6	35.5	16.1	256	57.4	30.7	356	7.06	5.5	0.4	1420	354	3010	51.1	12.3
		ave	102	482	1410	326	2300	1.52	25.7	131	4.61	28.8	13.9	8.58	59.6	26.1	21.3	193	3.27	2.28	0.118	575	61.5	1400	33.3	3.72
		GM	91.7	468	1330	307	2150	1.41	21.4	127	4.4	26.8	12.2	7.59	43.6	24.1	21.1	184	2.86	2.07	0.021	435	53.5	1230	32.1	0.784
		Std	49.8	121	469	101	774	0.525	17.2	31	1.3	10.1	7.12	4.01	55.6	10.5	3.08	62.9	1.59	1.02	0.124	373	52.8	671	8.79	3.32
CLC007	Hm	min	15	275	<411	<115	<763	<0.5	<4.53	95.7	<1.88	9.55	4.84	1.76	2.75	<7.65	13.7	60.1	0.41	1.29	<0.001	6.92	18.5	160	13.8	<0.001
	(n=39)	max	280	653	1500	356	2790	1.71	27.9	176	4.99	43.9	38.4	11.7	76.7	57.8	24.9	355	9.17	7.53	0.36	1420	70.9	2220	39.9	15.2
		ave	124	451	989	246	1800	1.18	12.3	142	3.6	23.6	12.7	5.81	21.6	21.8	18.4	147	3.15	2.93	0.058	438	46.1	1220	25.6	3.15
		GM	106	441	933	233	1680	1.09	11.2	141	3.45	22.2	11	5.21	17.2	19.9	18.2	133	2.54	2.67	0.007	272	44.4	1050	24.6	0.586
		Std	64.3	93.7	316	72.7	608	0.411	5.36	15.9	0.974	8.38	7.62	2.54	15.5	9.97	2.54	72.2	1.99	1.37	0.089	336	11.8	567	6.93	3.23
CLC008A	Hm	min	62.2	200	161	<18.5	27.2	0.172	130	124	<0.62	16.1	6.02	0.32	1.82	1.5	7.07	8.91	0.38	0.44	0.1	1050	10.3	251	7.35	<0.001
	rep. carbonates	max	456	3930	3480	788	2560	2.28	686	214	5.96	134	51.3	10.3	91.3	31.6	20.6	339	143	9.41	11.8	4400	68.6	2820	39.7	18.6
	(n=51)	ave	275	775	766	223	1320	0.935	316	178	2.84	82.4	28.3	3.76	22.3	11.4	12.7	88.4	8.38	4.12	1.15	2240	28.8	1170	19.2	3.59
		GM	253	592	624	155	810	0.678	295	177	2.31	76.2	24.7	3.07	15.3	8.78	11.9	71.4	3.79	2.84	0.743	2110	26	978	17.2	1.47
		Std	98.9	713	583	168	944	0.635	123	19.2	1.64	28	12.7	2.42	20.1	8.01	4.59	59	22.6	3.01	1.68	750	13.6	673	8.77	3.71
CLC008B	Hm	min	95	281	460	13	<62.4	0.057	141	123	0.13	35.5	6.54	0.97	1.65	2.14	6.21	15.8	0.53	0.969	0.19	849	14.3	441	7.2	<0.001
	rep. carbonates	max	436	3110	2030	340	1500	1.5	721	208	2.68	137	44.6	7.4	53.5	30.9	24.1	238	55.6	13.1	2.91	5030	85.4	2120	32.7	9.08
	(n=39)	ave	239	808	944	116	451	0.482	334	175	0.973	76.8	22.3	3.26	16.5	9.84	11.3	92.1	5.3	5.07	1.26	2550	29.5	992	16	2.47
		GM	223	679	867	90.6	273	0.388	300	174	0.616	73.1	20.4	2.89	12.9	7.86	10.6	72.9	3.1	4.03	1.01	2270	27.3	889	14.5	1.55
		Std	90.3	601	408	78.8	434	0.302	164	17.6	0.914	24	9.02	1.54	11.4	7.41	4.4	61.7	9.21	3.07	0.754	1260	13.2	506	7.48	1.9
CLC010	Hm	min	14.8	10.2	<260	<162	<1160	<0.75	<2.51	<0.45	<3.07	3.65	1.55	0.78	<4.32	<10.1	3.05	<6.72	<0.001	<0.001	<0.001	0.48	94.8	1070	8.94	<0.001
	zoned	max	190	553	1020	195	1550	14	130	127	3.48	17.3	4.85	2.19	9.5	17.3	21.2	24.6	1.46	0.492	0.199	1200	1480	5010	68	3.68
	(n=18)	ave	52.3	140	479	174	1300	2.17	11.9	28.3	3.24	8.3	3.09	1.53	5.53	12.1	9.07	8.9	0.158	0.12	0.032	172	687	2890	25.5	0.312
		GM	38.5	57.7	452	174	1300	1.42	5.43	13.7	3.23	7.67	2.97	1.48	5.39	11.9	7.48	8.36	0.068	0.051	0.004	34.8	552	2590	21.3	0.004
		Std	48.2	154	185	9.2	93.5	3.15	29.5	33.6	0.123	3.55	0.884	0.389	1.43	2.28	5.58	4.26	0.329	0.158	0.061	299	399	1330	16.5	0.891
CLC018	Hm	min	41.8	202	670	66.5	<494	<0.27	4.94	24.2	<0.94	15.2	4.47	1.16	2.54	<3.42	6.95	25.8	1.22	1.58	<0.001	102	10.8	80	11.6	0.92
	(n=25)	max	522	983	1800	336	782	1.88	97.4	240	1.72	89.8	52.2	7.19	26.6	18.2	16.8	238	19.8	9.95	0.47	6230	50.6	1430	44.5	18.4
		ave	244	570	1070	164	638	0.493	55.1	155	1.24	47.8	29.4	4.03	13.3	10.5	11.8	80	6.95	4.97	0.067	872	31.8	673	25.7	6.42
		GM	222	544	1020	147	632	0.448	44.5	137	1.22	44.7	25.1	3.57	11.9	9.46	11.5	65.8	5.46	4.49	0.021	487	30	565	24.6	5.12
		Std	99.9	164	348	80.4	86.3	0.312	27.9	59.3	0.17	17	14.2	1.82	5.9	4.34	2.51	58.8	5.08	2.22	0.098	1370	9.83	354	7.65	4.17
CLC020	Hm	min	4.61	86.6	360	<85	<585	<0.35	<1.37	27	<1.24	15.9	5.02	2.43	<1.84	<4.51	2.73	10.4	0.555	2.6	<0.001	2.35	6.45	14.4	20.7	0.4
	(n=13)	max	307	585	2300	105	1110	0.59	45.6	105	1.45	37.1	13.2	5.92	9.57	22.8	12.9	51.5	29.8	10.5	0.95	261	88.8	916	31.9	4.09
		ave	77.9	276	959	95.9	730	0.456	10.6	71.9	1.36	24.3	8.03	4.53	3.92	10.8	5.87	25.2	3.84	5.91	0.267	53.4	40.1	239	26	1.88
		GM	36.8	230	810	95.7	722	0.452	7.47	68.4	1.36	23.5	7.78	4.38	3.41	9.82	5.19	23.1	1.84	5.21	0.11	27.4	32.8	145	25.8	1.57
		Std	95.2	168	618	5.85	126	0.066	11.4	20.5	0.077	6.42	2.15	1.13	2.33	5.03	3.28	11.1	7.84	3.09	0.296	67.6	23.1	241	3.25	1.06
CLC020	pMsk	min	189	1180	35000	<111	<964	<0.56	<2.73	15.3	<1.74	133	2.54	6.99	61.2	68.8	29.7	34.6	15.7	5.15	0.04	6.78	0.16	15.1	12	11.5
	(n=13)	max	631	1480	42700	174	3280	1.38	9.46	19.3	2.44	378	11.6	10.6	645	150	43.1	40.2	34.2	6.86	0.45	17.2	0.41	23.6	20	24.1
		ave	408	1290	38900	147	1950	0.747	5.47	17.4	2.09	234	4.38	8.44	191	102	36.2	37.1	22.6	5.77	0.189	13.3	0.253	19.6	17.1	18.7
		GM	384	1290	38900	146	1800	0.724	5.04	17.3	2.08	225	3.79	8.39	138	99.4	36	37.1	22.1	5.75	0.141	12.8	0.243	19.4	17	18.3
		Std	142	85.7	1950	17.7	802	0.221	2.35	1.17	0.215	68.4	3.1	1.03	185	25.3	3.98	1.94	5.31	0.521	0.138	3.34	0.078	2.77	2.1	3.74
CLC021	Hm	min	5.9	70.6	434	<6.31	<21.6	<0.06	5.5	64.3	<0.001	16.5	5.9	0.44	<0.001	0.49	1.48	3.4	0.393	4.28	<0.001	10.4	15.7	85.2	11.2	0.42
	(n=19)	max	204	1640	2460	72.8	332	0.385	125	115	2.81	48	12.1	3.88	10.7	33.5	7.38	11.6	3.28	15	0.764	166	102	527	19.7	11.2
		ave	66.2	420	1010	14.7	106	0.12	46.5	86.4	0.694	28.4	9.14	1.99	2.05	11.3	2.89	8.33	1.34	9.32	0.306	39.4	31.2	257	15	2.36
		GM	39.7	318	894	11	75	0.107	36.5	85	0.428	27.2	9	1.7	0.586	7.85	2.69	7.96	1.14	8.87	0.181	28.6	28.4	226	14.7	1.73
		Std	62.7	357	543	16	91.3	0.075	30.4	15.8	0.612	9.08	1.64	0.965	2.63	8.64	1.32	2.32	0.777	2.9	0.229	38.9	18.4	130	2.64	2.38
CLC021	pMsk	min	91.4	401	4930	<8.5	838	0.28	21.1	15.1	<0.307	32.2	4.13	3.32	3.12	32	8.35	1.11	2.46	4.3	<0.034	1.09	0.15	8.01	<0.13	3.35
	(n=12)	max	767	3630	30300	306	8470	1.24	378	25.9	3.49	170	22.1	7.91	206	126	24.4	43.3	161	25.6	4.6	34.7	1.92	16.7	14.5	31.7
		ave	421	1960	24400	75.2	3920	0.683	240	21.5	1.09	110	15	5.62	65.3	96.6	21.3	23.2	49.8	18.8	1.87	7.46	0.641	10.8	11.3	21.5
		GM	371	1770	22700	43.6	3520	0.634	206	21.3	0.797	104	13.4	5.43	42.6	91.7	20.7	18.8	33.4	17.6	1.34	5.38	0.531	10.7	8.27	19.4
		Std	202	773	6540	89.5	1760	0.264	88.9	2.76	1.01	31.2	6.42	1.46	59.2	26.7	4.27	9.71	46.4	5.23	1.1	8.74	0.461	2.15	4.08	6.95
CLC022	Hm	min	4.08	62.7	<124	<19.3	<115	<0.11	<3.67	50.3	0.27	12.5	5.23	0.28	0.41	1.29	1.62	1.6	0.5	0.929	<0.001	2.87	14.8	76.8	5.16	<0.001
	(n=22)	max	326	926	2200	143	537	0.65	444	158	1.09	196	24.1	4.63	24.5	40.4	15.6	48.5	56.1	23.6	3.91	764	117	630	21.4	14.6
		ave	68.3	435	659	47.4	224	0.221	98.5	97.3	0.721	51.9	13.3	2.04	4.08	11.6	5.41	18.3	10.6	13.6	0.811	177	40.8	309	10.1	3.69
		GM	43.1	371	477	36.2	193	0.189	24.9	92	0.688	37.8	11.7	1.72	1.92	8.31	4.45	12.9	3.93	11.2	0.158	52.6	35.6	270	9.62	0.991
		Std	71.2	216	553	39.6	140	0.15	145	33.2	0.205	50.4	6.57	1.09	5.76	9.75	3.81	14.2	16.3	6.64	1.17	236	24.8	147	3.53	3.6
CLC022	pMsk	min	96.5	406	43300	<301	<2180	<1.57	<8.9	14.9	4.72	86.3	3.99	6.42	<5.98	43.6	23.9	51.1	9.39	1.81	<0.001	21.6	<0.23	35.7	18.8	7.55
	(n=12)	max	307	604	53000	390	3820	2.28	15.5	18.3	5.92	101	7.31	12.4	15.1	93.5	41	67.3	76	4.03	0.37	31.7	0.65	43	25.3	19.3
		ave	199	488	48200	350	2800	1.85	11.5	16.7	5.42	95.4	4.92	9.23	8	66.4	31.2	60.9	25.9	2.86	0.113	26.2	0.455	39.7	20.7	13.5
		GM	190	483	48100	349	2770	1.84	11.3	16.7	5.4	95.3	4.83	8.99	7.69	65.2	30.7	60.7	19.6	2.81	0.01	26.1	0.438	39.6	20.6	13.1

Sample	Type		Mg	Al	Si	P	Ca	Sc	Ti	V	Cr	Mn	Co	Ni	Cu	Zn	Ga	As	Sr	Y	Zr	Nb	Mo	Sn	Sb	Ba
		Std	63.4	68.1	3200	28.3	432	0.201	2.2	1.14	0.405	4.7	1.05	2.18	2.65	13.1	5.54	5.27	23.1	0.556	0.16	2.97	0.123	2.17	2.12	3.26
OD11A	Si-Mt	min	803	309	14200	37.5	5030	0.039	7.15	16.1	<0.079	52.3	1.44	2.34	0.198	19.3	6.49	11.5	11	49.6	0.02	109	0.193	7.6	0.912	3.54
	(n=16)	max	2650	1180	20700	122	13900	0.103	107	23.6	0.404	106	2.69	3.03	90.2	31.1	10.2	16.3	21.2	91.5	0.126	239	0.63	10.6	1.29	8.37
		ave	1680	579	19300	74.6	7420	0.063	47.9	19	0.124	79	1.91	2.72	6.6	25	8.62	14.2	16.2	79	0.048	201	0.324	9.39	1.15	6.19
		GM	1620	555	19300	70.7	7250	0.06	40.8	18.9	0.111	78	1.87	2.71	1.17	24.8	8.56	14.1	16.1	78.3	0.042	198	0.306	9.36	1.15	6.08
		Std	459	190	1690	25.5	1880	0.022	25.3	2.23	0.08	12.6	0.385	0.239	22.3	3.25	1.03	1.33	2.17	10.2	0.029	32.9	0.122	0.775	0.102	1.12
OD11A	Si-Mt	min	57.1	134	4750	22.8	187	0.015	8.23	0.059	<0.102	36	0.61	0.72	0.2	11.2	2.6	78.7	0.542	46.9	0.045	0.642	0.86	4.16	4.15	0.57
	(n=28)	max	1900	2280	16800	690	5570	0.42	313	37.8	1.38	199	19.6	7.14	4.01	41.9	6.11	1320	36.7	869	3.77	91.2	35	47.8	62.9	18
		ave	665	600	9000	82	2010	0.16	99.7	14	0.741	66.5	2.65	3.93	1.19	22.4	4.04	266	11.2	312	0.835	21.2	13.5	20.5	15.4	6.73
		GM	510	483	8560	57.1	1490	0.107	70.2	4.55	0.594	61.9	2.04	3.59	0.871	21.1	3.93	210	7.98	249	0.484	10.7	10.7	15.8	4.67	2.67
		Std	478	455	2970	124	1400	0.118	70.8	14.9	0.371	31.3	3.41	1.5	0.939	8.25	0.97	241	8.24	222	0.848	22.7	7.69	13.5	15.3	5.35
OD11A	Si-Mt	min	49.5	377	<750	8.65	318	0.03	51.7	29.9	<0.21	30.9	0.451	2.61	<0.16	15.1	2.39	1.03	1.38	0.496	0.23	2.23	0.044	2.76	0.078	0.42
	(n=25)	max	1660	13400	25000	507	17300	0.656	817	75.8	2.05	1900	2.75	7.26	7.33	61	14.1	10.6	22.1	13.7	1.62	174	76.8	17.6	2.87	10.7
		ave	495	3130	10500	73.8	2390	0.238	306	46.4	0.804	192	1.4	4.54	1.56	36.1	7.07	4.23	8.35	6.01	0.79	36.9	6.75	6.52	1.01	6.43
		GM	327	1920	7310	32	1720	0.199	247	44.8	0.712	105	1.27	4.39	1.08	34	6.41	3.53	7.5	5.15	0.714	25.4	0.431	6	0.81	2.3
		Std	429	3370	7790	121	3190	0.131	211	13.1	0.381	370	0.605	1.19	1.53	12.2	2.92	2.46	3.96	3.06	0.352	38.6	20.2	3.04	0.823	3.08
OD11C	Si-Mt	min	194	464	6420	<6.04	724	<0.106	93.4	28.7	<0.53	47.4	0.71	2.82	0.57	24.5	2.59	3.21	3.99	3.59	0.34	16.9	<0.001	3.16	NA	NA
	(n=8)	max	431	3550	15200	114	2570	0.235	374	42.3	3.65	1320	3.36	5.07	122	43	9.19	7.51	13.4	10.4	1.38	315	31.2	8.38	NA	NA
		ave	301	1700	11200	28.5	1590	0.14	215	36.2	1.14	252	1.39	4.04	18.1	32.3	6.34	4.25	7.07	5.3	0.93	103	5.57	6.76	NA	NA
		GM	292	1430	10700	17.6	1470	0.135	192	35.9	0.92	116	1.24	3.96	4.12	31.8	5.77	4.09	6.6	4.97	0.86	59.8	0.527	6.54	NA	NA
		Std	78.3	986	3430	36.2	662	0.045	102	4.37	1.04	436	0.841	0.814	41.8	6.29	2.65	1.43	3.01	2.28	0.339	113	10.8	1.57	NA	NA
OD11C	pMsk	min	21.2	158	562	<5.66	<199	<0.087	72.6	17.6	<0.45	42.8	1.23	2.39	0.68	18.7	1.81	<1.59	3.27	1.93	0.76	72.4	26.9	8.26	NA	NA
	(n=9)	max	337	1740	3960	7.31	3590	0.124	157	38.7	2.03	145	3.59	12.4	8.37	105	3.91	5.47	13.1	17.6	5.73	1530	67	106	NA	NA
		ave	73.8	501	1620	6.53	760	0.108	109	27.1	0.896	72.7	1.87	4.34	2.85	51.2	2.47	3.3	7.14	8.29	1.71	329	46.7	36.9	NA	NA
		GM	49.4	385	1370	6.51	456	0.108	106	26.1	0.807	67.4	1.76	3.79	2.18	42.8	2.37	3.13	6.28	6.77	1.39	199	45	27.2	NA	NA
		Std	99.7	486	1060	0.576	1090	0.014	29	8.15	0.482	32.7	0.739	3.09	2.37	32.2	0.746	1.1	3.96	5.39	1.54	461	13.2	31	NA	NA
CLC023	Hm	min	7.39	146	110	<9.85	<83.3	<0.064	4.41	3.05	<0.001	27.4	6.63	<0.133	0.21	5.69	2.28	2.87	1.55	2.43	<0.001	17.8	2.78	15.4	4.36	1.87
	(n=27)	max	566	1800	9090	1720	6270	0.393	769	250	2.96	209	41.7	8.04	49.6	65.6	15.6	110	67.5	36.8	2.29	2190	112	711	57.6	24.4
		ave	105	649	2420	108	1120	0.134	351	159	0.667	71.3	16.4	3.61	12.8	24.7	6.37	16	11.5	19.3	0.795	836	35.6	416	24.1	6.52
		GM	62.9	565	1230	22.2	452	0.119	245	127	0.477	57	13.9	2.36	6.24	19.5	5.22	9.64	5.8	17	0.499	529	29.5	326	21.1	5.35
		Std	117	375	2710	350	1480	0.078	207	68.6	0.516	54	10.5	2.47	14.5	17.5	4.35	24.9	16.3	7.85	0.539	615	22.2	194	11.9	4.99
CLC025	Hm	min	2.26	39.1	480	<85.9	<605	<0.35	8.44	5.8	<1.25	1.3	0.43	<0.55	<1.57	<4.51	2.54	2.94	0.337	0.028	0.03	3.45	0.149	5.7	0.63	0.31
	(n=21)	max	185	1860	6590	239	1360	0.63	707	30.8	1.82	156	82.2	8.35	41	30.6	19.9	362	117	6.41	2.07	100	457	491	27.5	10.9
		ave	35.9	771	2950	132	878	0.527	142	16.5	1.56	31.2	8.64	2.18	6.67	12.4	9.39	88.4	37.9	1.29	0.438	29	58.1	81	10.5	3.55
		GM	17.7	584	2310	127	862	0.52	74.4	15.1	1.55	19.2	2.69	1.67	4.55	10.2	8.47	49.4	14.3	0.465	0.265	17.4	6.12	27	6.73	2.53
		Std	47.3	475	1900	40.6	177	0.082	162	7.06	0.144	35.8	18	1.96	8.51	8.12	4.11	104	37.9	1.78	0.464	28.7	117	150	7.71	2.66
CLC025	Si-Mt	min	1600	181	28400	<94.7	3840	<0.45	<1.71	6.9	<1.27	60.9	2.1	1.78	<1.66	11.9	14.9	49.5	11.9	17.9	<0.001	79.8	0.156	12.5	6.58	5.2
	(n=27)	max	3450	809	39600	264	7240	0.87	73.7	10.7	1.81	116	32.8	4.79	51.8	35.5	34.8	75.9	20.1	39.4	0.239	278	1.02	41.6	11	16.9
		ave	2570	338	34900	127	5410	0.551	13.7	8.43	1.46	88.2	5.23	2.95	5.86	23.1	21.7	61.6	16.2	28.3	0.046	174	0.508	28.5	8.55	11.3
		GM	2520	307	34800	124	5330	0.544	6.6	8.36	1.45	86.8	3.78	2.83	3.38	22.5	21.2	61.2	16.1	27.6	0.013	167	0.478	27.7	8.47	11
		Std	504	174	2940	36.3	953	0.098	19.4	1.11	0.121	15.8	6.61	0.872	10	5.47	4.86	7.14	2.07	6.59	0.059	50.7	0.172	6.36	1.23	2.42
CLC026	Hm	min	<0.001	42.5	134	<8.83	<66.8	<0.057	<0.85	<0.039	<0.37	0.89	<0.059	<0.001	<0.163	0.21	0.285	<0.39	0.019	<0.001	<0.001	<0.001	<0.105	<0.053	<0.13	<0.001
	(n=17)	max	498	2360	1320	42.2	439	2.01	10.1	59.6	2.2	282	0.73	1.91	1.44	1.83	4.36	32.1	2.04	1.03	5.86	58.9	12.6	39	45.2	4.06
		ave	66.7	696	510	15	139	0.647	2.2	8.26	0.631	43.8	0.242	0.417	0.46	0.693	3.2	8.16	0.361	0.301	0.434	7.08	3.01	5.12	9.27	0.738
		GM	6.59	332	400	12.8	120	0.368	1.71	0.678	0.561	11.7	0.172	0.129	0.39	0.536	2.84	3.35	0.159	0.116	0.024	0.174	2.03	0.567	3.1	0.088
		Std	130	741	369	10.9	95.4	0.629	2.29	18.7	0.428	75.1	0.207	0.48	0.322	0.538	1.08	10	0.511	0.329	1.4	17.7	2.87	11.3	12.2	1.13
CLC026	Si-Mt	min	337	180	5170	11.5	519	<0.054	2.44	7.27	<0.001	51.9	2.5	1	2.14	7.21	6.83	3.77	2.32	7.17	<0.001	24.2	<0.05	5.21	<0.36	1.57
	(n=13)	max	3240	611	22700	78.6	7350	0.434	21.9	14.2	0.87	327	217	39.3	102	165	12.9	56.6	24.9	95.1	0.31	486	0.7	46.9	41.1	87.3
		ave	1330	471	13600	26.9	3300	0.182	10.3	10.9	0.578	137	49.7	10.2	36.7	52.3	10.4	26.1	14.5	39.8	0.094	199	0.22	17.9	11.8	20.4
		GM	960	447	12400	22.6	2510	0.148	8.7	10.7	0.365	111	14	5.08	16.9	30.1	10.2	19.3	12	30.5	0.018	127	0.158	13.5	5.33	11.5
		Std	1010	136	5830	18.5	2270	0.124	5.88	1.84	0.25	102	79.9	13.6	40	62.6	1.9	15.9	7.04	26	0.114	175	0.199	15.6	14.7	23.8
CLC027	pMsk	min	213	217	18000	<131	<1040	<0.63	<3.12	7.7	<1.9	76.5	2.41	2.2	<2.76	30.9	13.1	<0.001	10.9	1.97	<0.001	110	<0.134	22.6	11.9	7.28
	(n=20)	max	2170	732	35300	273	3700	1.21	14.6	13.1	5.23	158	7.37	8.81	46.6	309	17.4	45.8	40.1	16.6	0.145	342	0.44	120	36.5	30.9
		ave	379	453	21400	179	1500	0.88	6.68	12.1	2.73	128	3.75	4	29.9	214	15.3	28.3	23	3.24	0.058	204	0.259	71	25	21.4
		GM	309	443	21000	177	1410	0.871	6.09	12.1	2.66	127	3.58	3.74	25.8	199	15.2	11.1	22.5	2.72	0.014	198	0.247	68.2	24	20.5
		Std	426	98	4640	35.6	630	0.133	3.26	1.15	0.702	16.5	1.27	1.69	11.6	61.6	1.33	10.8	5.14	3.21	0.058	50.8	0.082	18.6	6.95	5.76
CLC028	Hm	min	3.94	218	295	<84.5	<613	<0.39	1.81	3	<1.27	3.84	0.218	<0.54	1.68	<3.57	3.01	<1.95	0.299	0.014	<0.001	0.634	2.17	22.9	0.82	0.58
	rep. carbonates	max	295	1600	939	105	817	0.54	171	170	1.94	97.4	25.1	6.36	20.5	69.4	10.3	34.8	5.96	2.98	0.56	2120	102	1020	25.7	10.4
	(n=25)	ave	47.7	776	522	95.6	722	0.448	42.1	97.3	1.4	28.2	4.57	3.15	7.53	22.4	4.82	12.3	2.5	1.36	0.098	611	23.5	413	13.2	3.44
		GM	24.3	634	501	95.4	721	0.447	20.1	52.5	1.39	19.7	2.3	2.26	5.51	16.8	4.7	9.08	1.98	0.466	0.04	109	12.8	224	9.45	2.74
		Std	61.3	483	157	5.01	44.5	0.04	40.6	68.5	0.139	23.9	5.4	2.06	5.91	16.6	1.29	8.66	1.48	1.12	0.118	644	23	347	8.13	2.37
CLC029	Hm	min	57.7	77.1	256	<109	<807	<0.46	115	63.2	<1.68	49.7	2.39	1.43	<2.51	5.66	2.29	11.7	1.05	0.053	<0.001	3640	1.73	228	16.9	0.2
	(n=4)	max	133	542	794	115	928	0.71	263	74.3	1.78	91.4	4	3.96	3.25	11.4	5.86	13.8	1.63	0.14	0.21	6440	3.21	337	20.6	0.93
		ave	90.1	253	421	112	868	0.595	178	68.5	1.72	68.1	3.21	2.67	2.75	7.89	3.7	12.6	1.25	0.092	0.109	5560	2.3	295	18.1	0.618
		GM	84.3	194	378	112	866	0.586	168	68.4	1.72	66.5	3.15	2.51	2.73	7.63	3.49	12.6	1.23	0.087	0.04	5430	2.23	292	18	0.532
		Std	37.6	208	251	3.16	61.6	0.116	70.7	4.64	0.045	17.3	0.675	1.05	0.349	2.47	1.52	1.06	0.26	0.036	0.086	1300	0.686	49.2	1.74	0.325
CLC029	Si-Mt	min	329	415	10600	<104	<896	<0.62	9.39	12.7	1.71	65.2	<0.147	2.33	<2.24	38.3	8.29	<2.23	3.02	0.98	<0.001	21.1	<0.105	11.8	<0.72	1.7
	(n=9)	max	2310	1110	25600	127	2810	0.78	40.6	25.2	2.05	1700	3.71	8.47	15.8	59.9	19.5	10.2	6.66	4.78	0.117	86.4	0.23	23.5	4.42	8.03
		ave	948	717	18500	117	1860	0.678	17.1	20.4	1.86	375	0.977	4.53	4.81	49.1	14.3	5.28	4.74	2.75	0.039	39.9	0.172	17.2	1.75	3.8
		GM	791	679	17900	117	1750	0.676	15.1	20	1.86	208	0.64	4.25	3.91	48.6	13.9	4.62	4.63	2.57	0.007	36.1	0.166	16.8	1.48	3.43
		Std	622	247	4630	7.15	657	0.054	10.3	3.87	0.15	533	1.09	1.81	4.25	7.48	3.19	2.85	1.06	0.983	0.048	20.5	0.044	3.7	1.21	1.93

Sample	Type		Mg	Al	Si	P	Ca	Sc	Ti	V	Cr	Mn	Co	Ni	Cu	Zn	Ga	As	Sr	Y	Zr	Nb	Mo	Sn	Sb	Ba
CLC029	pMsk	min	122	646	17600	<142	<807	0.51	23	15.2	<1.69	83.1	<0.26	<1.5	<2.48	55.2	11	7.28	3.94	1.44	<0.001	44.9	<0.093	18.3	1.79	1.56
	(n=23)	max	2080	9080	36800	263	4150	1.4	74.4	30.4	5.05	728	15.8	5.96	314	180	20.3	41.2	35.4	3.99	0.5	2040	0.7	54.3	36	73
		ave	521	2610	28400	185	1890	0.965	47	25.9	2.86	181	1.65	2.41	93.2	99.8	14.8	30.3	29.7	2.59	0.258	1440	0.278	43.1	26.9	48.6
		GM	365	2040	28000	183	1780	0.944	45	25.7	2.79	162	0.957	2.3	65.5	96.3	14.6	29.2	28.1	2.51	0.131	1230	0.248	42	24.4	41.9
		Std	530	2280	4600	30.1	746	0.197	14	3.1	0.689	126	3.14	0.904	74.6	28.9	2.54	6.26	6.51	0.652	0.147	533	0.143	8.9	7.58	16.8
CLC030	Hm	min	28.1	246	890	<11.3	<83	<0.06	1.39	18.7	<0.49	15.1	3.14	<0.18	1.11	2.19	1.46	16.7	3.43	2.85	<0.001	38.4	30.5	130	14.9	2.43
	(n=17)	max	155	1350	3310	122	387	0.67	64.6	62.7	0.94	379	14.1	2.17	6.16	17.1	6.48	60.1	29.8	11.1	6.6	893	111	450	37.5	20.3
		ave	77.4	700	1600	60	216	0.255	16.7	35.2	0.668	74.8	8.03	0.998	2.69	6.94	4.47	41.1	9.64	6.13	1.12	326	62.3	229	26.1	8.21
		GM	67.8	640	1440	51	198	0.195	12.6	33.2	0.656	45.2	7.57	0.822	2.3	6.25	4.28	39.4	8.02	5.73	0.115	248	58.5	211	25.4	6.99
		Std	40.8	287	798	30.2	91.1	0.191	14.4	12.4	0.134	95.7	2.77	0.578	1.62	3.4	1.14	10.9	6.93	2.33	2.11	225	23	106	6.39	5.09
CLC031	Hm	min	7.34	106	<60.8	<8.01	<0.001	<0.047	13.9	74.6	<0.001	43.6	3.38	0.76	0.37	5.16	1.79	2.2	0.35	<0.001	<0.001	199	0.99	53.6	7.96	<0.001
	(n=28)	max	149	720	1600	395	3090	2.17	1020	190	6.31	438	17.2	7.66	34.4	73.2	6.86	33.9	6.74	7.96	2.33	8820	113	1070	55.4	12.7
		ave	61	322	425	164	1290	0.913	271	105	2.75	152	8.56	3.75	7.8	24.8	3.55	13.4	2.67	2.46	0.53	3430	29.4	378	27.3	3.2
		GM	49.6	293	339	59.7	310	0.405	161	101	0.68	130	7.44	3.23	5.45	20.6	3.27	11.6	2.2	0.627	0.309	2380	11.9	290	24.7	0.564
		Std	35.8	145	309	165	1290	0.873	251	29.4	2.47	90.3	4.61	1.96	6.6	16.4	1.47	6.47	1.67	2.91	0.542	2190	32.1	264	12	3.32
CLC031	Si-Mt	min	566	295	9060	<16.1	2050	<0.108	1.75	6.41	<0.001	62.8	0.57	<0.36	0.2	13	10.2	4.75	3.94	17.4	<0.001	52.4	<0.059	5.55	1.12	1.59
	(n=23)	max	2900	1090	21000	56	6910	0.69	259	22	1.18	164	16.8	3.94	15.2	37.2	23.8	33.3	47.1	95.3	0.33	338	1.79	22.5	10.4	14.3
		ave	1720	614	18200	30.4	5340	0.357	41.8	13.3	0.201	86.2	2.85	2.51	5.58	22.6	16.7	21.2	16.6	65.6	0.034	220	0.371	12.2	6.16	8.23
		GM	1630	588	18000	28.7	5200	0.315	23.5	12.9	0.007	84.4	1.93	2.29	3.29	22	16.3	20	15.3	62.6	0.003	206	0.241	11.7	5.68	7.6
		Std	514	184	2540	10.9	1090	0.18	59.2	3.39	0.339	20.6	3.76	0.879	5.06	5.49	3.69	6.18	7.68	17.5	0.075	71.4	0.442	3.3	2.12	2.85
CLC031	pMsk	min	240	432	39300	<362	<2730	<1.81	19.1	17.6	<5.74	91.8	2.03	<3.33	114	131	20.2	59.1	13.3	0.66	<0.001	244	<0.42	60.3	22.1	17.4
	(n=14)	max	590	819	48900	497	3990	3.29	59.1	22.2	7.8	117	7.94	8.82	800	225	27	71.8	39.3	1.31	0.38	535	1.68	107	39.3	37.7
		ave	391	507	44200	435	3440	2.46	45	20.1	6.71	98.9	4.65	5.81	323	185	24.3	64.4	21.3	0.949	0.138	423	0.742	84	31.2	26.5
		GM	380	500	44100	433	3420	2.43	42.9	20	6.68	98.6	4.39	5.62	239	183	24.2	64.3	20	0.92	0.022	414	0.681	83	30.9	25.8
		Std	94.2	98.2	2960	41.3	368	0.412	12.8	1.19	0.651	7.7	1.59	1.55	264	25	2.17	3.47	8.4	0.245	0.141	84.8	0.353	13.4	4.68	6.26
CLC032	Si-Mt	min	213	209	8050	<11.2	1720	0.067	<0.78	7.86	<0.33	45.8	0.73	1.21	<0.32	19.6	8.06	3.01	4.2	13.7	<0.001	31	0.062	6.7	0.27	<0.001
	(n=26)	max	4080	3650	26700	58	9560	0.74	11.3	16.3	2.46	154	4.98	19.2	56.6	42	22.2	36.4	23.3	119	0.17	410	0.57	21.4	5.55	15.6
		ave	2140	927	20100	34.4	6450	0.278	3.22	12.5	0.909	86.7	2.3	4.21	12.5	31	16.1	24.3	18	87.3	0.053	296	0.264	16.9	2.39	8.03
		GM	1870	781	19500	31.8	6150	0.223	2.54	12.3	0.796	83.9	2.12	3.44	5.79	30.5	15.7	21.8	16.9	79.2	0.02	262	0.224	16.3	2.01	5.26
		Std	812	675	3950	12.9	1550	0.181	2.43	1.91	0.54	22.7	1.01	3.6	14.3	5.41	3.24	7.58	4.62	27.5	0.052	104	0.141	3.63	1.22	3.76

Table S6. (continued) Summary statistics of LA-ICP-MS data for individual samples and Fe-oxide sub-types from the Magnetite drillhole - RU65-7976.

Sample		La	Ce	Pr	Nd	Sm	Eu	Gd	Tb	Dy	Ho	Er	Tm	Yb	Lu	Hf	Ta	W	Pb204	Pb206	Pb207	Pb208	Th	U	Pb	ΣREY
CLC002	min	0.058	0.208	0.052	0.278	0.099	<0.013	0.27	0.056	0.86	0.296	1.19	0.218	1.8	0.39	<0.001	3.86	60.3	NA	44.6	5.61	4.72	45	207	55.6	16.2
	max	5.75	16.1	1.58	4.39	1.66	0.74	2.52	0.76	5.3	1.17	4.93	1.06	7.6	1.87	0.096	18.4	243	NA	168	20.6	15.1	192	803	203	58.7
	mean	2.06	5.49	0.532	1.89	0.783	0.225	1.08	0.264	2.17	0.641	2.82	0.609	5.34	1.25	0.034	8.72	189	NA	121	13.6	9.41	120	596	144	33.9
	GM	1.4	4.02	0.4	1.55	0.635	0.169	0.87	0.226	1.93	0.6	2.67	0.566	5.08	1.19	0.011	8.02	183	NA	117	13.1	9.02	113	574	139	32
	Std	1.56	3.89	0.39	1.12	0.449	0.163	0.701	0.157	1.12	0.24	0.946	0.225	1.54	0.351	0.033	3.81	42	NA	29.5	3.41	2.73	39.7	144	34.8	11.8
CLC005	min	0.332	0.68	0.14	1.85	0.43	0.071	0.49	0.091	1.23	0.313	1.45	0.254	2.1	0.219	<0.001	1.44	30.6	NA	13.6	4.84	5.03	40.2	45.1	28.3	19
	max	7.53	14.7	1.62	11.1	2.93	0.76	2.69	0.708	4.61	1.13	4.84	1.01	9.6	2.14	0.89	10.6	653	NA	244	30.7	16.7	216	1360	290	77.1
	mean	2.56	9.74	0.962	4.53	1.22	0.259	1.48	0.343	2.84	0.746	3.27	0.674	6.37	1.28	0.108	3.52	414	NA	157	20.1	11.4	118	726	189	49.4
	GM	2.24	8.57	0.86	4.11	1.1	0.221	1.4	0.318	2.69	0.707	3.1	0.634	5.93	1.16	0.013	3.08	375	NA	141	18.8	10.9	110	637	173	46.6
	Std	1.38	3.68	0.398	2.16	0.573	0.168	0.492	0.126	0.887	0.229	1.03	0.223	2.18	0.467	0.224	2.21	127	NA	54.8	6.32	3.06	40	275	62.8	15.7
CLC006	min	0.582	2.17	0.112	0.4	<0.001	<0.001	<0.129	0.019	<0.16	<0.001	0.126	0.028	0.355	0.079	<0.001	0.111	405	<0.059	131	18.7	6.9	6.98	312	165	7.9
	max	8.67	34.6	3.85	13.6	1.65	0.37	0.57	0.117	1.06	0.418	1.13	0.274	2.05	0.655	0.33	2.27	1930	0.277	826	91.3	39.8	59	1780	944	65.7
	mean	2.66	10.7	0.826	2.24	0.369	0.084	0.303	0.054	0.429	0.122	0.493	0.12	1.1	0.219	0.078	0.522	732	0.143	487	55.1	22.7	34.9	1020	565	22
	GM	2.2	8.83	0.635	1.69	0.264	0.054	0.281	0.049	0.38	0.097	0.44	0.102	1.01	0.195	0.006	0.384	686	0.131	464	52.9	21.1	30.9	973	540	19.3
	Std	1.84	7.02	0.69	2.28	0.284	0.071	0.123	0.025	0.221	0.072	0.222	0.068	0.453	0.114	0.127	0.453	311	0.059	140	15	7.76	14.4	283	159	12.3
CLC007	min	0.44	2.3	0.098	0.35	<0.069	0.011	0.058	<0.001	0.128	0.022	0.163	0.039	0.4	0.088	<0.001	<0.001	220	<0.028	165	18.4	8.21	19.9	384	191	7.47
	max	8.85	39.4	4.16	9.14	0.95	0.377	1.18	0.177	1.47	0.422	1.24	0.288	2.52	0.59	0.259	0.77	900	0.281	796	87.8	34.9	78.3	1690	905	76
	mean	2.3	9.36	0.724	1.91	0.29	0.061	0.286	0.059	0.506	0.148	0.627	0.145	1.41	0.266	0.04	0.248	530	0.109	488	54.2	20.8	45	1110	563	21
	GM	1.82	7.41	0.511	1.38	0.242	0.048	0.232	0.047	0.456	0.129	0.569	0.129	1.32	0.244	0.003	0.188	514	0.1	469	52.1	20.1	43.4	1070	542	18.4
	Std	1.68	7.21	0.739	1.79	0.192	0.059	0.227	0.036	0.254	0.079	0.257	0.067	0.471	0.112	0.086	0.143	131	0.047	131	14.5	5.1	12.3	284	148	12.6
CLC008A	min	<0.045	0.338	0.031	0.084	<0.001	<0.001	<0.001	0.016	0.062	0.016	0.072	0.015	0.33	0.055	<0.001	1.74	137	<0.049	39.2	5.18	4.93	15.1	183	50.7	2.14
	max	33.1	59.2	4.05	10.3	1.23	0.494	2.38	0.54	3.76	0.846	2.97	0.66	6.45	1.29	0.37	19.3	2020	0.253	642	72.9	35.1	136	1430	742	128
	mean	2.76	7.37	0.641	1.91	0.452	0.144	0.568	0.136	1.09	0.288	1.25	0.293	2.77	0.574	0.038	6.11	400	0.13	175	21.1	15.3	62.9	506	211	24.4
	GM	1.32	4.13	0.363	1.14	0.254	0.097	0.363	0.089	0.718	0.192	0.857	0.207	1.91	0.39	0.005	5.34	336	0.339	146	17.7	13.2	55.8	473	177	18.2
	Std	5.09	10.9	0.819	2.03	0.338	0.116	0.548	0.128	0.938	0.224	0.943	0.211	2.04	0.429	0.079	3.36	315	0.05	113	13.3	8.3	30.3	206	133	20.7
CLC008B	min	0.174	0.562	0.061	0.156	0.063	0.011	<0.061	0.012	0.139	0.053	0.238	0.052	0.474	0.068	<0.001	2.08	169	<0.033	31.6	5.32	5.6	24.4	116	43.3	5.56
	max	20.9	34.9	3.22	9.01	1.5	0.512	3	0.811	5.48	1.14	4.49	0.784	6.39	1.47	0.139	17.6	1190	0.183	463	50.5	42.3	184	1080	541	84.2
	mean	2.79	6.95	0.633	2.04	0.495	0.157	0.756	0.179	1.37	0.362	1.58	0.338	3.35	0.71	0.018	7.2	354	0.098	156	18.7	14.5	75.7	469	189	26.8
	GM	1.63	4.46	0.401	1.38	0.371	0.102	0.486	0.116	0.955	0.259	1.18	0.27	2.7	0.556	0.004	6.2	312	0.435	128	15.8	12.2	68.3	420	157	22.1
	Std	4.04	7.96	0.743	2.14	0.378	0.132	0.746	0.18	1.19	0.276	1.06	0.196	1.84	0.412	0.03	3.98	217	0.057	106	11.8	9.4	36	227	126	17.8
CLC010	min	0.053	0.071	0.009	<0.001	<0.001	<0.001	<0.001	<0.001	<0.001	<0.001	<0.001	<0.001	0.018	<0.001	<0.001	<0.001	1290	<0.031	19.5	1.97	<0.153	0.012	37.7	21.6	0.552
	max	36.6	65.2	3.55	6.42	0.57	0.071	0.129	0.032	0.208	0.042	0.132	0.025	0.329	0.069	0.126	0.66	18300	0.048	2580	266	2.36	5.02	5270	2850	113

Sample		La	Ce	Pr	Nd	Sm	Eu	Gd	Tb	Dy	Ho	Er	Tm	Yb	Lu	Hf	Ta	W	Pb204	Pb206	Pb207	Pb208	Th	U	Pb	∑REY
	mean	2.95	5.53	0.283	0.619	0.096	0.016	0.066	0.009	0.04	0.012	0.04	0.012	0.106	0.024	0.019	0.062	10500	0.038	546	56.3	0.425	0.622	1160	603	9.93
	GM	0.594	1.18	0.064	0.164	0.018	0.007	0.041	0.005	0.013	0.009	0.021	0.009	0.075	0.014	0.003	0.011	8460	0.038	299	30.8	0.295	0.095	624	331	2.71
	Std	8.48	15.1	0.822	1.5	0.143	0.021	0.039	0.008	0.051	0.011	0.035	0.008	0.092	0.02	0.04	0.153	5610	0.004	630	65.1	0.534	1.32	1300	695	26.2
CLC018	min	0.223	1.05	0.168	0.721	0.177	0.037	0.23	0.027	0.32	0.103	0.398	0.071	0.89	0.098	<0.001	0.202	92.2	0.04	62	7.44	5.18	7.58	124	74.7	9.39
	max	29.5	69.4	5.79	15.6	2.19	0.48	1.63	0.245	2.14	0.693	2.5	0.476	4.45	0.87	0.06	3.72	512	0.103	517	56.2	26.2	162	1400	593	142
	mean	5.02	12.4	1.09	3.52	0.619	0.149	0.586	0.127	0.98	0.297	1.18	0.254	2.35	0.436	0.019	0.95	310	0.065	305	32.9	15.6	89.6	852	354	34
	GM	3.23	8.52	0.767	2.54	0.498	0.125	0.508	0.113	0.892	0.27	1.08	0.232	2.17	0.392	0.004	0.728	289	0.063	279	30.2	14.3	76	774	324	27.7
	Std	5.85	13.8	1.18	3.48	0.482	0.099	0.352	0.061	0.427	0.135	0.497	0.1	0.926	0.196	0.025	0.841	105	0.017	116	12.5	5.93	42.5	313	133	27.4
CLC020	min	0.235	1.12	0.067	0.398	0.226	0.024	0.127	0.059	0.548	0.17	0.652	0.153	1	0.204	<0.001	0.01	125	0.039	122	12.8	4.52	14.7	442	139	9.48
	max	6.25	16.1	1.92	7.45	2.52	0.593	2.51	0.515	3.73	0.782	2.29	0.46	4.14	0.68	0.061	0.595	898	0.082	472	48.8	7.18	37.8	1600	527	53.2
	mean	2.36	7.84	0.847	3.21	1.07	0.239	0.939	0.244	1.75	0.367	1.31	0.274	2.3	0.369	0.022	0.159	440	0.057	256	25.7	5.99	23	988	288	29
	GM	1.71	6.5	0.65	2.45	0.786	0.159	0.66	0.192	1.41	0.31	1.18	0.255	2.11	0.346	0.007	0.095	384	0.055	239	23.9	5.91	22.2	919	269	25.8
	Std	1.73	4.43	0.544	2.19	0.804	0.195	0.745	0.167	1.16	0.231	0.641	0.112	0.983	0.143	0.024	0.153	231	0.014	98.5	10.1	0.967	6.45	383	109	14.2
CLC020	min	58.9	129	15.5	43.8	3.74	0.184	1.43	0.113	0.708	0.152	0.493	0.082	0.66	0.095	<0.001	0.044	0.363	0.039	11.3	1.6	2.71	1.02	4.69	15.9	266
	max	82.6	170	19.7	55.5	5.55	0.405	2.28	0.269	1.2	0.247	0.86	0.15	1.08	0.18	0.039	0.278	0.8	0.096	17.4	2.97	5.91	2.29	6.65	26.3	346
	mean	72.4	146	17.3	49	4.54	0.299	1.8	0.166	0.912	0.194	0.665	0.115	0.846	0.136	0.012	0.126	0.571	0.071	13.8	2.07	3.73	1.59	6.01	19.7	300
	GM	72	145	17.3	48.9	4.51	0.293	1.77	0.162	0.902	0.192	0.655	0.114	0.838	0.134	0.003	0.109	0.557	0.069	13.8	2.04	3.66	1.53	5.98	19.6	299
	Std	7.27	12.6	1.28	3.6	0.577	0.058	0.309	0.041	0.146	0.03	0.121	0.019	0.119	0.025	0.017	0.071	0.131	0.018	1.43	0.323	0.834	0.46	0.526	2.5	24.5
CLC021	min	0.371	1.17	0.099	0.414	0.063	0.016	0.185	0.063	0.81	0.251	1.19	0.244	2.42	0.475	<0.001	0.014	184	NA	56.4	6.25	1.71	15.6	359	67.5	18
	max	85.5	168	15.7	47.3	4.89	0.615	2.66	0.341	3.68	0.774	3.93	0.92	7.42	1.59	0.08	0.907	1020	NA	196	20.3	4.81	68	1260	221	347
	mean	6.58	15.2	1.24	3.97	0.634	0.106	0.812	0.196	1.77	0.512	2.38	0.544	4.89	0.989	0.02	0.159	348	NA	122	12.3	2.78	27.5	813	137	49.2
	GM	1.7	5.41	0.364	1.35	0.356	0.073	0.672	0.182	1.63	0.489	2.29	0.52	4.73	0.957	0.005	0.101	321	NA	117	11.8	2.65	25.8	784	132	33.6
	Std	19.3	37.9	3.54	10.6	1.07	0.132	0.569	0.073	0.771	0.151	0.676	0.17	1.24	0.256	0.027	0.204	179	NA	33.1	3.41	0.944	11.7	214	36.8	74
CLC021	min	6.4	17.1	2.12	8.26	1.66	0.039	0.76	0.129	0.94	0.16	0.46	0.13	0.9	0.057	<0.001	0.024	0.36	NA	0.81	0.093	0.243	0.239	1.63	1.15	43.4
	max	383	771	75.7	233	29.3	3.42	17.1	1.35	4.39	0.973	3.63	0.63	4.3	0.91	0.059	0.561	3.48	NA	13.6	1.79	4.35	7.18	23.5	19.7	1550
	mean	145	289	31	99	11.8	1.12	7.09	0.678	3.02	0.702	2.39	0.43	3.21	0.567	0.024	0.229	1.09	NA	9.18	1.2	2.5	4.38	10.9	12.9	614
	GM	107	216	24.1	79	9.72	0.756	5.83	0.602	2.85	0.652	2.2	0.403	3.02	0.497	0.009	0.188	0.823	NA	7.98	1.03	2.17	3.66	9.32	11.2	475
	Std	105	211	20.4	62.3	7.72	0.987	4.27	0.305	0.912	0.212	0.739	0.135	0.934	0.193	0.023	0.133	0.966	NA	3.05	0.422	0.928	1.55	5.61	4.36	416
CLC022	min	0.548	3.95	0.25	0.76	0.327	0.075	0.58	0.068	0.295	0.051	0.147	0.02	0.288	0.093	<0.001	<0.001	137	NA	12.7	1.78	1.41	0.536	58.1	15.9	19.3
	max	16.2	39.6	3.35	11.2	2.47	0.544	2.83	0.9	7.33	1.58	5.93	1.31	10.1	1.98	0.084	3.16	962	NA	235	23.9	12.9	111	1520	262	91.4
	mean	4.31	13.8	1.15	4.43	1.16	0.226	1.49	0.372	3.05	0.781	3.13	0.701	5.96	1.23	0.021	0.67	348	NA	151	15.3	4.19	42.6	983	171	55.4
	GM	2.78	11.1	0.869	3.5	0.975	0.188	1.34	0.304	2.51	0.639	2.45	0.558	4.91	1.02	0.005	0.077	295	NA	130	13.5	3.46	24.9	816	148	51.4
	Std	4.32	9.77	0.948	3.15	0.678	0.142	0.684	0.221	1.71	0.398	1.63	0.339	2.72	0.553	0.027	0.99	231	NA	59.3	5.83	2.95	34.4	423	65.7	19.7
CLC022	min	35.5	90.5	9.48	21.4	1.09	<0.048	0.33	<0.041	0.25	0.066	0.185	<0.026	0.25	0.011	<0.001	<0.001	0.63	0.072	49.2	6.82	13.5	1.46	36.9	69.5	163
	max	43.6	143	13.5	30.8	3.33	0.32	1.13	0.128	0.82	0.17	0.56	0.125	0.58	0.162	0.35	0.095	1.21	0.248	102	13.4	27	1.96	59.8	143	239
	mean	39.1	120	11.6	27	2.42	0.176	0.629	0.079	0.507	0.107	0.305	0.059	0.445	0.057	0.079	0.035	0.941	0.181	72.7	9.71	19.4	1.69	43.7	102	205
	GM	39	119	11.5	26.8	2.3	0.16	0.576	0.074	0.47	0.102	0.293	0.053	0.427	0.048	0.006	0.008	0.919	0.171	71.3	9.52	19	1.68	43.2	100	204
	Std	2.93	17.3	1.3	3.34	0.712	0.073	0.282	0.029	0.199	0.034	0.097	0.033	0.124	0.037	0.133	0.037	0.209	0.055	14.6	2.02	3.87	0.169	6.86	20.5	25.6
OD11A	min	99.9	249	30.2	112	14.9	1.05	11.2	1.54	9.13	1.86	6.3	0.87	6.71	1.01	<0.001	0.028	0.414	<0.004	4.47	0.587	0.765	7.53	15.7	5.82	595
	max	188	418	49.6	185	25.1	1.84	18	2.57	16.4	3.64	12.2	1.89	14.3	2.17	0.01	0.304	0.753	0.037	10.4	1.11	2.06	22.7	37	12.7	999
	mean	155	352	43.6	161	22.6	1.58	16.5	2.24	13.9	3.03	9.84	1.47	11.1	1.72	0.003	0.074	0.555	0.018	7.37	0.848	1.69	18.9	28.4	9.92	874
	GM	153	350	43.3	160	22.5	1.57	16.4	2.23	13.8	3	9.74	1.45	11	1.7	0.002	0.059	0.551	0.016	7.23	0.837	1.65	18.4	27.8	9.77	868
	Std	21.6	41.4	4.95	17.9	2.63	0.212	1.78	0.253	1.77	0.425	1.4	0.24	1.83	0.267	0.003	0.067	0.071	0.008	1.47	0.138	0.32	3.89	5.61	1.72	103
OD11A	min	17.8	42.2	3.82	13.4	3.03	0.2	3.12	0.613	4.91	1.58	6.02	1.25	11.4	2.9	<0.001	<0.001	15.8	<0.006	1.21	0.121	<0.021	0.195	5.27	1.35	160
	max	742	1470	141	475	82.7	7.5	102	17.3	117	28.7	104	20.5	222	62.9	0.008	1.68	104	0.041	30.1	3.17	2.71	13.5	128	33.8	4420
	mean	211	436	41.7	143	26.1	2.29	30.7	5.33	39.2	9.94	37.2	7.22	76.6	21.3	0.004	0.324	42.4	0.025	10.2	1.19	0.524	3.11	43.5	11.9	1400
	GM	156	333	31.6	110	20.7	1.67	24.2	4.19	31	7.89	29.1	5.53	56.5	15.4	0.24	0.051	36.9	0.381	8.12	0.946	0.371	2.14	35.1	9.55	1110
	Std	165	320	31.1	105	18.4	1.78	22.5	3.94	28.2	7.23	27.5	5.51	60.3	16.9	0.003	0.481	23.6	0.013	7.19	0.809	0.526	3	29.2	8.23	995
OD11A	min	6.34	16.6	2	6.52	0.62	0.066	0.406	0.025	0.088	0.031	0.09	0.015	0.188	0.032	<0.01	0.15	<0.001	<0.007	0.165	0.055	0.153	0.432	0.336	0.421	40.1
	max	197	446	37.9	128	12.5	1.99	7.36	0.691	2.75	0.519	1.85	0.395	2.52	0.545	0.102	3.3	802	0.05	165	16.9	2.6	20	844	185	846
	mean	35.3	83.6	7.8	25.1	3.09	0.397	1.9	0.225	1.18	0.234	0.743	0.122	1.28	0.342	0.036	1.18	58.7	0.026	15.6	1.73	0.808	3.43	72.9	18.1	167
	GM	21.5	55.3	5.77	18.9	2.45	0.284	1.55	0.189	1	0.202	0.642	0.103	1.15	0.309	0.475	0.994	0.405	0.461	2.32	0.389	0.63	1.97	4.41	3.64	120
	Std	42.2	93.5	7.69	25.1	2.51	0.409	1.46	0.139	0.631	0.122	0.39	0.077	0.528	0.121	0.038	0.674	193	0.017	40.4	4.15	0.583	4.58	204	45	172
OD11C	min	7.24	17.6	2.03	6.89	0.85	0.114	0.58	0.114	0.65	0.156	0.54	0.052	0.68	0.186	Inf	0.94	0.119	NA	1.2	0.117	0.442	1.15	1.64	1.79	45.1
	max	45.5	123	11.6	32.7	4.75	0.63	2.57	0.37	2.02	0.435	1.26	0.269	1.86	0.57	0.001	2.98	93.2	NA	32	3.19	2.84	10.2	134	38.1	238
	mean	19.1	49.4	4.88	15.8	2.11	0.248	1.46	0.177	1.11	0.227	0.735	0.139	1.39	0.399	NA	1.85	27.1	NA	9.61	0.956	0.874	3.35	35.6	11.4	102
	GM	15.5	40.8	4.18	14.1	1.8	0.212	1.32	0.162	1.04	0.216	0.707	0.127	1.33	0.375	1	1.7	3.39	NA	5.07	0.53	0.714	2.61	12.9	6.56	88.1
	Std	14.1	35	3.18	8.45	1.28	0.172	0.634	0.09	0.449	0.087	0.241	0.062	0.4	0.137	NA	0.788	40.2	NA	11.4	1.13	0.799	3.01	51.2	13.2	65.1
OD11C	min	13.1	27.9	2.47	6.47	0.97	0.107	0.16	0.053	0.49	0.12	0.45	0.071	1.6	0.34	Inf	0.354	178	NA	97.6	9.62	0.826	5.73	490	109	63.3
	max	98	191	15.4	46.1	6.7	1.38	5.08	0.77	6.75	1.22	4.25	0.88	8	1.19	0.001	5.93	453	NA	291	29.9	8.23	66.2	1590	329	380
	mean	41.7	95.6	7.74	21.9	2.7	0.512	1.68	0.304	2.38	0.529	1.9	0.365	3.42	0.637	NA	1.71	303	NA	180	18.2	3.83	30.3	961	202	190
	GM	35.3	79.6	6.33	17.5	2.07	0.343	1.06	0.218	1.66	0.381	1.5	0.291	3.01	0.587	1	1.18	292	NA	168	17.1	3.15	25	877	188	159
	Std	25.5	55.5	4.81	14.8	2.14	0.434	1.61	0.258	2.18	0.43	1.38	0.252	2.03	0.287	NA	1.73	87.3	NA	70.6	6.9	2.49	18.8	431	79.1	110
CLC023	min	1.94	10.3	0.766	3.52	0.374	0.059	0.361	0.104	0.4	0.122	0.441	0.046	0.444	0.163	<0.001	<0.001	27.3	NA	2.22	0.355	0.231	0.027	7.43	2.81	24.1
	max	40.4	121	12.7	44.2	6.69	0.92	5.89	0.893	5.99	1.52	6.41	1.46	13.9	2.69	0.69	4.97	596	NA	341	39.3	48	220	1750	394	256
	mean	8.82	32.5	2.74	11.4	2.29	0.26	2.35	0.489	3.59	0.949	3.76	0.824	7.16	1.42	0.054	1.53	222	NA	172	19.9	11.6	106	915	204	97.8
	GM	6.27	26.3	1.94	8.63	1.9	0.206	2.08	0.43	3.13	0.816	3.19	0.645	5.64	1.14	0.011	0.856	184	NA	125	15	8.27	45.3	551	151	85.8
	Std	9.29	25.2	2.94	10.6	1.51	0.208	1.1	0.213	1.48	0.415	1.77	0.441	3.81	0.745	0.136	1.13	128	NA	90.5	10.2	10.5	71.9	570	104	52.4
CLC025	min	0.168	0.353	0.053	0.098	0.016	0.009	0.031	0.002	0.028	<0.001	<0.001	0.003	0.011	<0.001	<0.001	<0.001	0.01	0.036	1.08	0.338	0.542	0.088	1.6	2.39	0.872
	max	21.9	62.2	5.94	19.4	2.76	0.556	1.33	0.309	1.92	0.383	1.33	0.234	1.83	0.289	0.47	0.398	4670	0.356	632	69.9	23.5	10.5	2040	710	126
	mean	6.77	17.5	1.49	4.27	0.472	0.112	0.314	0.056	0.397	0.074	0.26	0.048	0.379	0.06	0.043	0.089	620	0.078	102	12.4	3.56	2.18	292	118	33.5
	GM	4.66	11.9	1.06	2.85	0.242	0.058	0.165	0.024	0.151	0.028	0.079	0.018	0.119	0.018	0.008	0.046	25.1	0.066	17.6	3.35	2.28	0.938	32.3	25.9	22.8

Sample		La	Ce	Pr	Nd	Sm	Eu	Gd	Tb	Dy	Ho	Er	Tm	Yb	Lu	Hf	Ta	W	Pb204	Pb206	Pb207	Pb208	Th	U	Pb	∑REY
	Std	5.21	14.1	1.28	4.14	0.62	0.145	0.411	0.082	0.61	0.103	0.387	0.071	0.567	0.09	0.101	0.101	1230	0.067	186	20.6	4.95	3.1	573	208	28.2
CLC025	min	79.3	233	25.8	78.1	9.69	0.674	4.7	0.61	3.78	0.655	1.84	0.292	2.21	0.189	<0.001	<0.001	0.64	<0.018	10	1.17	1.68	4.45	21.4	12.9	459
	max	168	465	50	160	20.2	1.58	9.65	1.34	8.04	1.66	4.64	0.8	5.41	0.668	0.072	0.031	1.56	0.406	28.6	3.19	4.25	15.3	61.1	34.2	930
	mean	116	331	35.7	112	14.1	1.04	6.71	0.944	5.5	1.08	3.15	0.523	3.68	0.426	0.017	0.008	1.15	0.04	18.7	2.24	3.02	8.78	41.5	24	660
	GM	113	324	35.1	110	13.8	1.01	6.55	0.918	5.36	1.04	3.06	0.506	3.57	0.407	0.004	0.004	1.13	0.027	18.2	2.18	2.93	8.35	40.2	23.4	646
	Std	25.1	67	7.21	23.3	3.04	0.254	1.48	0.226	1.27	0.28	0.754	0.135	0.929	0.127	0.027	0.009	0.205	0.074	4.31	0.501	0.73	2.87	10.5	5.14	137
CLC026	min	<0.007	<0.012	<0.01	<0.033	<0.001	0.005	<0.03	<0.005	0.01	<0.001	0.009	<0.004	<0.019	0.005	<0.001	<0.001	0.008	NA	<0.011	<0.008	0.027	<0.001	0.025	0.064	0.408
	max	0.277	1.43	0.236	1.01	0.42	0.045	0.323	0.055	0.326	0.101	0.331	0.147	1.62	0.323	0.152	0.114	4.49	NA	3.52	1.94	3.68	0.313	9.32	9.15	5.21
	mean	0.111	0.343	0.066	0.231	0.088	0.018	0.119	0.019	0.098	0.033	0.112	0.033	0.323	0.052	0.026	0.016	0.733	NA	0.733	0.322	0.628	0.052	1.84	1.68	1.95
	GM	0.07	0.175	0.038	0.128	0.047	0.015	0.083	0.014	0.063	0.02	0.062	0.016	0.142	0.028	0.008	0.006	0.175	NA	0.196	0.089	0.193	0.018	0.64	0.51	1.33
	Std	0.092	0.416	0.074	0.298	0.115	0.011	0.106	0.016	0.086	0.03	0.115	0.043	0.464	0.077	0.036	0.027	1.42	NA	1.14	0.545	1.02	0.084	2.65	2.69	1.64
CLC026	min	4.54	15	2.04	8.57	1.29	0.134	0.72	0.175	1.01	0.254	0.95	0.184	1.45	0.291	<0.001	<0.001	0.028	NA	2.24	0.395	0.742	0.699	7.72	3.37	44.2
	max	170	394	46.2	162	23.2	2.14	16.8	2.46	18.2	3.77	12.9	2.24	15.8	2.2	0.84	0.113	1	NA	104	19.9	37.6	36.8	2800	162	968
	mean	55.3	125	15.4	53.7	8.47	0.746	6.06	1.08	7.42	1.65	5.68	1.02	7.41	1.13	0.079	0.069	0.357	NA	28.1	5.27	10	12.9	519	43.4	330
	GM	34	75.9	9.75	34.1	5.53	0.538	4.08	0.809	5.48	1.2	4.45	0.81	6.11	0.967	0.006	0.045	0.257	NA	12.5	2.29	4.53	8.23	82.9	19.4	221
	Std	51	118	14.1	49.1	7.12	0.613	4.88	0.736	5.06	1.15	3.46	0.615	4.08	0.56	0.229	0.04	0.258	NA	39.1	7.37	13.9	10.5	949	60.3	283
CLC027	min	19.3	25.9	3.46	8.28	0.49	0.057	0.135	0.036	0.237	0.061	0.137	0.01	0.123	0.017	<0.001	0.021	0.28	0.033	12.1	1.28	2.47	1.86	10.9	15.9	61.5
	max	69.1	214	23.1	70.6	8.35	0.616	4.39	0.576	3.27	0.652	1.84	0.256	2.07	0.2	0.108	0.134	0.95	0.23	79.1	12	13.3	8.23	30.3	104	416
	mean	25.4	41.7	5.38	14.5	1.34	0.125	0.67	0.1	0.581	0.126	0.354	0.06	0.423	0.045	0.027	0.059	0.549	0.146	35.4	5.1	9.07	3.05	16.8	49.7	94.1
	GM	24.1	34.9	4.71	12.2	1.03	0.103	0.495	0.079	0.47	0.103	0.288	0.05	0.352	0.038	0.004	0.052	0.528	0.137	33.7	4.76	8.66	2.68	16.2	47.5	82.2
	Std	11	41.5	4.34	13.7	1.68	0.12	0.891	0.114	0.644	0.128	0.36	0.05	0.4	0.039	0.041	0.032	0.163	0.044	12	1.97	2.36	1.99	5.2	15.7	77.9
CLC028	min	0.115	0.193	0.032	0.075	<0.001	<0.001	<0.001	0.002	<0.001	<0.001	<0.001	<0.001	<0.001	<0.001	<0.001	<0.001	6.44	<0.015	0.764	0.086	0.195	0.026	0.486	1.13	0.533
	max	11.4	23.1	2.18	5.97	0.67	0.158	0.389	0.117	0.734	0.202	0.757	0.192	1.9	0.362	0.064	2.62	1490	0.11	192	23	14.1	102	586	229	49.2
	mean	1.45	3.3	0.303	0.889	0.166	0.043	0.148	0.036	0.282	0.082	0.346	0.089	0.877	0.148	0.013	0.693	242	0.044	82.3	9.48	6.72	41.6	285	98.5	9.51
	GM	0.635	1.81	0.166	0.458	0.086	0.015	0.087	0.02	0.136	0.032	0.114	0.033	0.21	0.045	0.003	0.134	104	0.038	29.1	3.53	3.61	4.72	49.9	37.1	5.34
	Std	2.48	4.97	0.468	1.36	0.178	0.05	0.135	0.034	0.251	0.07	0.288	0.071	0.716	0.126	0.02	0.721	296	0.023	66	7.63	4.94	34.3	232	78.4	11
CLC029	min	0.326	0.975	0.077	0.154	0.022	0.007	<0.048	0.006	<0.001	0.003	<0.001	<0.001	<0.034	<0.007	<0.001	11.8	1.69	0.025	4.67	1.42	2.63	0.127	8.13	9.72	1.85
	max	1.74	2.62	0.396	0.6	0.058	0.018	0.089	0.015	0.044	0.024	0.023	0.007	0.065	0.018	0.001	29.1	6.7	0.144	8.66	3.43	6.87	1.68	15.1	19.1	5.64
	mean	0.855	1.56	0.174	0.313	0.045	0.013	0.064	0.009	0.023	0.009	0.016	0.003	0.049	0.012	0.001	20.1	3.14	0.069	6.29	2.04	3.93	0.718	10.8	12.3	3.24
	GM	0.713	1.46	0.138	0.275	0.042	0.012	0.061	0.008	0.011	0.006	0.01	0.002	0.048	0.012	0.001	19.1	2.64	0.056	6.11	1.91	3.63	0.467	10.5	11.8	2.97
	Std	0.614	0.725	0.15	0.196	0.016	0.005	0.02	0.004	0.021	0.01	0.01	0.003	0.014	0.006	0.001	7.34	2.39	0.052	1.79	0.933	1.98	0.699	3.03	4.54	1.66
CLC029	min	3.83	13.5	1.8	6.06	0.36	0.069	0.4	0.037	0.303	0.05	0.115	0.03	0.157	0.011	<0.001	<0.001	<0.001	<0.02	0.723	0.124	0.189	0.331	1.64	1.09	27.7
	max	15.2	52.6	6.01	17.7	2.26	0.218	1.2	0.144	0.97	0.179	0.428	0.09	0.72	0.09	0.001	0.209	0.31	0.038	2.75	0.408	0.915	1.21	4.73	3.96	103
	mean	8.78	31.1	3.7	11.9	1.6	0.146	0.812	0.087	0.586	0.099	0.276	0.05	0.445	0.055	0.001	0.052	0.147	0.026	1.57	0.239	0.529	0.603	2.43	2.36	62.3
	GM	8.18	29.1	3.5	11.3	1.45	0.14	0.772	0.08	0.539	0.092	0.261	0.047	0.407	0.046	0.001	0.027	0.076	0.025	1.44	0.217	0.452	0.559	2.29	2.15	58.7
	Std	3.49	11.9	1.29	3.68	0.56	0.042	0.26	0.036	0.251	0.039	0.091	0.021	0.181	0.027	0.001	0.062	0.117	0.006	0.682	0.11	0.285	0.272	1	1.04	22.3
CLC029	min	8.8	30.5	3.9	13.6	1.39	0.109	0.46	0.028	0.142	0.028	0.101	0.009	0.249	0.028	<0.001	0.015	0.18	0.021	0.939	0.161	0.316	0.525	1.9	1.44	63.7
	max	42.8	89.6	10.6	31.1	3.73	0.257	1.78	0.167	0.88	0.172	0.51	0.087	0.6	0.106	0.155	3.62	1.69	0.18	33.7	4.39	9.57	8.12	25.1	47.8	181
	mean	35.5	74.9	8.77	25	2.45	0.177	0.977	0.085	0.45	0.088	0.284	0.047	0.37	0.057	0.01	1.98	1.11	0.109	25.9	3.18	6.81	6.13	16.2	36	152
	GM	34.4	73.4	8.63	24.6	2.38	0.172	0.92	0.076	0.417	0.082	0.259	0.042	0.359	0.054	0.001	1.59	1.01	0.1	23.2	2.88	6.13	5.62	14.8	32.4	149
	Std	6.64	12.7	1.42	4.12	0.556	0.045	0.347	0.041	0.17	0.034	0.117	0.02	0.099	0.02	0.034	0.803	0.404	0.04	6.36	0.81	1.79	1.71	5.47	8.75	24.9
CLC030	min	2.19	5.85	0.56	2.1	0.43	0.132	0.247	0.134	0.97	0.187	0.631	0.124	1.01	0.122	<0.001	0.014	266	NA	29	4.77	1.61	1.09	150	38.6	18.5
	max	7.35	20.1	2.04	7.09	2.6	0.6	2.72	0.853	4.89	0.8	2.4	0.395	3.51	0.524	0.46	0.68	1710	NA	108	12.8	5.7	7.55	622	123	51.7
	mean	4.05	12.2	1.1	3.85	0.969	0.272	0.873	0.258	1.85	0.376	1.26	0.255	2.11	0.295	0.063	0.183	773	NA	63.9	8.3	3.95	2.82	361	76.2	35.9
	GM	3.8	11.6	1.05	3.62	0.837	0.246	0.754	0.226	1.64	0.341	1.17	0.245	2.02	0.276	0.01	0.116	686	NA	60.3	8.01	3.77	2.43	335	72.6	34.6
	Std	1.49	3.66	0.362	1.42	0.62	0.131	0.565	0.174	1.08	0.178	0.515	0.072	0.648	0.104	0.118	0.172	403	NA	22.3	2.25	1.11	1.73	134	24.2	9.44
CLC031	min	0.256	0.786	0.05	0.096	<0.001	<0.001	0.066	<0.001	<0.001	<0.001	<0.001	<0.001	<0.001	<0.001	<0.001	0.128	0.99	<0.058	2.65	0.519	0.384	0.074	10.9	4.12	2.06
	max	18.8	32	1.59	4.87	0.69	0.131	0.61	0.157	1.57	0.476	2.32	0.61	6.33	1.17	0.54	48	377	0.13	276	31	27.3	220	785	333	69.1
	mean	2.36	5.68	0.369	1.04	0.199	0.05	0.285	0.059	0.477	0.141	0.673	0.158	1.49	0.294	0.038	9.58	126	0.085	70.3	8.52	7.32	46.9	311	86.2	15.7
	GM	1.49	3.98	0.256	0.631	0.091	0.031	0.24	0.041	0.112	0.057	0.238	0.05	0.284	0.083	0.004	3.24	28	0.313	31.9	4.66	4.65	6.86	121	42.3	10.8
	Std	3.46	6.15	0.345	1.16	0.154	0.037	0.164	0.044	0.544	0.156	0.807	0.192	1.89	0.373	0.104	10.8	127	0.025	76.6	8.47	7.19	57.5	299	91.8	14
CLC031	min	17.7	47.9	6.47	24	4.32	0.236	3.27	0.45	2.72	0.64	2.13	0.335	2.75	0.363	<0.001	0.006	0.054	NA	0.561	0.106	0.215	2.76	2.83	0.881	131
	max	141	343	40.6	152	21.4	1.56	16.9	2.38	15.6	3.44	12.2	1.91	13.7	1.98	0.094	1.28	6.73	NA	7.98	0.879	2.19	27.1	35.5	10.3	863
	mean	93.5	235	28.3	105	15.4	1.08	11.9	1.71	11.3	2.44	8.24	1.31	9.48	1.38	0.024	0.14	0.714	NA	4.52	0.537	1.36	17.7	19.6	6.41	592
	GM	87.6	222	26.9	99.8	14.7	1.03	11.4	1.63	10.8	2.32	7.82	1.25	9	1.3	0.005	0.052	0.426	NA	4.1	0.496	1.26	16.3	17.6	5.88	561
	Std	28.2	66.5	7.73	28.2	3.97	0.292	3.15	0.466	3.02	0.662	2.35	0.375	2.78	0.41	0.034	0.309	1.33	NA	1.62	0.183	0.449	6.04	7.73	2.16	164
CLC031	min	17.9	51	4.59	9.97	0.58	0.021	0.25	0.021	0.096	0.011	0.042	<0.001	<0.001	<0.001	<0.001	0.057	1.1	<0.086	23.3	4.59	10.8	2.17	11.3	39.8	85.8
	max	25.9	79.5	7.08	18.1	1.74	0.155	0.82	0.099	0.41	0.074	0.33	0.082	0.33	0.098	0.45	0.24	2.23	0.234	43.1	7.06	14.6	3.33	22	63.5	133
	mean	22.3	66.3	6.05	13.2	1.11	0.091	0.43	0.045	0.225	0.041	0.157	0.035	0.198	0.032	0.054	0.135	1.69	0.162	31.8	5.58	12.3	2.77	16.6	49.9	111
	GM	22.2	65.7	5.99	13	1.07	0.082	0.399	0.042	0.202	0.036	0.135	0.022	0.132	0.019	0.003	0.124	1.66	0.157	31.4	5.54	12.3	2.75	16.3	49.5	110
	Std	2.06	8.86	0.862	2.27	0.283	0.036	0.183	0.021	0.104	0.02	0.09	0.023	0.096	0.026	0.126	0.054	0.337	0.04	5.49	0.633	1.23	0.318	2.96	6.65	13.9
CLC032	min	14	35.7	5.06	18	3.53	0.225	2.02	0.323	2.28	0.389	1.42	0.27	1.38	0.32	<0.001	0.01	0.042	NA	1.03	0.21	0.423	2.29	2.19	1.69	98.9
	max	177	419	51.1	191	27.9	1.91	22.1	3.29	20.7	4.93	16.3	2.54	18.5	2.83	0.241	0.244	0.74	NA	11.3	1.48	3.05	34.4	40.8	15.8	1070
	mean	128	312	39.1	141	21.2	1.35	16.3	2.44	15.2	3.42	11.5	1.92	13.2	2.08	0.025	0.062	0.523	NA	6.87	0.945	1.97	23	27.2	9.78	796
	GM	112	277	34.9	126	19.4	1.24	14.8	2.21	13.7	3.06	10.3	1.73	11.8	1.87	0.006	0.045	0.452	NA	6.15	0.857	1.8	19.6	23	8.85	710
	Std	44.8	103	12.6	44.8	6.46	0.408	5.05	0.763	4.81	1.11	3.8	0.63	4.53	0.702	0.047	0.052	0.193	NA	2.45	0.342	0.693	9.15	10.4	3.4	260

mean corresponds to the arithmetic mean, whereas *GM* corresponds to the geometric mean; Std represents 1σ

Mt: magnetite; Hm: hematite; pMsk: pseudomushketovite; Si-: silician

Table S7. Summary statistics of LA-ICP-MS data for individual samples and Fe-oxide sub-types from the *Nodular Fe-oxide granite* - RD2366.

Sample	Type		Mg	Al	Si	P	Ca	Sc	Ti	V	Cr	Mn	Co	Ni	Cu	Zn	Ga	As	Sr	Y	Zr	Nb	Mo	Sn	Sb	Ba
MV019	Hm	min	93	688	146	<73.3	<591	<0.37	623	431	<1.18	15.1	2.46	0.34	<1.72	<3.08	14.1	<1.53	0.014	0.068	<0.001	2100	27.7	1310	16.4	<0.001
	zoned	max	387	1440	1780	904	4280	2.9	3090	533	8.07	45.4	7.17	4.41	11.6	22.6	18.9	57.9	31.3	7.31	1.5	6920	80.3	1830	67.1	10.5
	nodule	mean	140	1030	691	161	1120	0.752	1200	490	2.05	23.6	4.06	1.38	3.1	8.14	16.3	9.41	2.75	3.34	0.286	3530	39.9	1590	30.3	0.936
	(n=42)	GM	132	1020	556	124	935	0.646	1140	490	1.74	22.8	3.93	1.14	2.64	6.79	16.2	4.96	0.712	2.62	0.132	3410	38.9	1580	28.2	0.034
		Std	60.2	146	462	163	884	0.547	452	22.3	1.58	6.71	1.12	0.944	2.34	5.34	1.14	12.4	5.19	1.77	0.275	1010	10.1	115	13.5	1.87
MV018A	Hm	min	15.2	318	487	<92.4	<522	<0.38	<1.42	230	<1.32	8.11	9.29	<0.76	<2.99	<3.93	23.5	171	0.81	4.37	<0.001	1.22	34.8	573	57.5	0.28
	band	max	117	876	1780	332	685	1.87	337	269	1.88	31	20.4	7.03	14.4	15.6	46.5	937	19.4	8.05	0.63	33.4	64.4	1340	109	19.5
	(n=20)	mean	62.1	599	850	160	609	0.905	56.1	255	1.5	17.5	14.2	3.11	5.73	8.08	36.7	344	4.59	5.98	0.107	7.51	43.7	998	77.4	3.97
		GM	56.6	580	789	151	608	0.808	12.2	254	1.49	16.8	13.9	2.46	4.98	7.3	36.2	304	3.08	5.9	0.036	3.87	43.2	973	76.1	2.72
		Std	24.3	149	358	60.7	42.3	0.437	88.9	9.17	0.129	5.19	2.88	2.06	3.4	3.86	6.07	206	4.66	1.02	0.141	9.79	6.94	216	14.5	4.08
MV016	Hm	min	7.51	302	<172	<82.9	<700	<0.44	2.75	68.7	<1.78	4.62	8.16	<0.84	<1.96	4.6	13.4	8.64	1.67	0.205	<0.001	33.7	14.8	586	18	<0.001
	nodule	max	368	506	905	236	2720	1.29	18.8	118	5.88	58.3	38	18	123	170	28.7	148	24.5	1.65	0.78	178	184	1740	60.3	91.1
	(n=32)	mean	121	387	455	134	1180	0.711	8.23	93.3	2.73	16.2	17.6	5.33	12.8	39.4	20	54.6	6.42	0.892	0.105	87.8	58.4	1240	34	17.6
		GM	88.3	384	408	129	1110	0.697	7.5	92.7	2.65	13.5	16.5	4.11	7.58	25.8	19.7	43.3	5.08	0.824	0.019	79.5	52.1	1190	32.7	8.46
		Std	88.3	46.7	211	39.8	450	0.156	3.69	10.2	0.757	11.9	7.25	3.77	21.8	46.3	3.73	38.3	5	0.324	0.15	39.6	34.2	326	9.8	19.8
MV015	Hm	min	2.18	578	278	<92	611	<0.48	8.89	6.71	<1.26	<1.04	<0.001	0.98	<2.11	<3.46	56.6	24.8	0.41	0.015	<0.001	0.48	12.7	53.5	50.2	<0.001
	nodule	max	288	3020	9340	973	3300	21.2	512	338	2.43	439	63.1	37.9	59.2	135	105	620	45.6	54.2	1.43	101	2030	1450	141	55.9
	(n=29)	mean	117	1140	4200	271	1070	2.96	143	245	1.67	70.8	19.9	18.4	18.4	38.4	71.8	286	12.1	14	0.349	26.7	190	957	76.2	12.9
		GM	89.6	1040	3490	236	966	1.25	98.5	204	1.64	50.7	12	13.7	13.8	31.2	70.9	257	8.64	7.44	0.208	16.5	83	823	72.6	5.19
		Std	64	532	2130	167	580	5.81	121	83.2	0.324	75.8	11.3	12.1	14.2	26	12.6	111	9.2	13.8	0.312	25.6	422	337	26	13.1
MV014	Hm	min	31.1	241	373	<84.6	<696	<0.44	<3.4	26	<1.92	4.39	1.57	2.95	<3.74	<4.93	8.44	23.7	1.44	0.183	<0.001	0.24	28.8	94.3	19.6	<0.001
	nodule	max	589	6280	9120	456	1510	1.76	52.2	175	4.49	1460	10.4	17.8	61.6	108	17.8	264	10.2	81.1	2.04	3.82	109	1680	53.5	35.8
	(n=24)	mean	119	1080	1910	186	1030	0.761	13.2	124	2.77	80.7	6.29	9.23	16.9	26.6	13.5	138	5.65	7.08	0.197	1.48	57.5	680	33.3	11.6
		GM	84	655	1270	165	1010	0.732	10	115	2.7	17	5.82	8.11	12.7	17.3	13.2	124	5.11	1.85	0.01	1.18	53.7	563	32	7.16
		Std	142	1460	2240	103	186	0.251	12.6	37.3	0.642	296	2.23	4.46	14.3	28.8	2.51	56.1	2.38	16.8	0.44	0.958	22.4	389	9.6	7.22
MV012	Hm	min	6.3	269	189	89.6	<687	0.48	<2.04	3.17	<1.38	2.5	0.37	<1.15	<2.03	<3.08	14.5	35.2	0.66	0.07	<0.001	0.109	1.37	21.2	5.12	<0.001
	nodule	max	127	2180	6180	330	1680	1.68	263	81.7	3.52	102	17	30	17.6	59	46.4	427	31.6	4.39	4.76	126	138	1160	116	35.2
	(n=14)	mean	41.4	998	1920	154	919	0.896	55.6	32.9	1.91	21.8	5.62	9.59	6	15	31.6	133	8.23	0.904	0.513	16.9	40.3	291	45.6	10.3
		GM	26.4	838	1380	140	887	0.837	20.2	22.4	1.83	12.4	3.06	6.18	4.4	10.5	30.1	105	4.15	0.42	0.079	5.1	16.7	91.2	35.3	2.36
		Std	38.3	590	1590	75.3	284	0.356	75.2	24.7	0.655	29.9	5.27	9.6	5.19	15.1	9.82	105	9.93	1.23	1.24	32.4	47.8	421	31	9.78
MV008	Hm	min	14.7	268	239	<94.1	<761	0.39	14.8	165	<1.99	3.5	8.9	1.7	5.05	<3.7	13.6	15.4	1.39	0.043	<0.001	218	18.2	115	12.6	2.83
	band	max	187	1150	2590	1280	2550	1.74	210	373	5.91	36.4	32.5	24.2	120	59.1	28.6	321	16.4	6.83	0.94	2430	311	2450	186	87.2
	(n=28)	mean	72.9	458	1350	426	1200	0.699	132	313	2.72	16.1	17.1	15.8	37.4	17.7	20.7	188	7.1	1.19	0.286	1070	67.9	758	42.7	14.5
		GM	63.7	433	1240	364	1140	0.669	110	306	2.66	13.6	16.5	14.6	26.6	14.5	20.3	160	6.25	0.866	0.037	861	50.2	553	35.6	11.2
		Std	37.6	188	486	239	436	0.245	59	59.2	0.708	8.84	4.94	4.86	33.3	11.5	4.12	79	3.55	1.21	0.317	642	66.9	632	33.3	15.4
MV007A	Si-Mt	min	217	326	1670	<2.61	356	0.125	375	124	<0.086	9.59	5	12.4	0.05	27.6	4.73	0.61	0.353	0.604	0.36	3.83	0.106	5.21	0.208	0.458
	band	max	2150	3110	12900	44.6	2260	0.777	1300	476	22.3	34	9.85	18.5	26.6	184	10.2	7.14	10.2	8.9	4.45	36.1	85.9	22.2	1.34	45.2
	(n=13)	mean	1150	1880	8060	14.4	1300	0.411	696	197	3.25	23.3	6.26	15.2	3.2	65.5	7.04	4.36	5.02	4.21	1.66	20	15.4	12.6	0.574	17.4
		GM	923	1580	6810	9.54	1130	0.364	661	175	0.382	22.3	6.13	15.1	0.71	55.3	6.86	3.78	4.08	3.5	1.33	17.1	1.86	11.7	0.511	10.3
		Std	687	932	3970	14	627	0.192	248	124	7.48	6.67	1.47	1.63	7.25	46.8	1.69	1.8	2.56	2.19	1.12	9.91	26.8	5.09	0.296	14.5
MV007A	pMsk	min	14.9	379	479	<2.26	166	<0.04	67.3	33.4	<0.147	18.7	5.17	8.4	<0.065	33.5	4.11	2.24	1.5	1.28	0.184	11.9	0.079	4.82	<0.104	2.25
	band	max	4230	7470	25300	26.1	5960	3.49	1990	177	0.54	1370	21.7	15.8	20.4	464	13.1	9.23	24.5	10.2	3.37	102	541	26.2	8.83	158
	(n=17)	mean	1080	2070	7430	7.88	1660	0.782	669	96.6	0.243	111	8.82	12.6	3.36	150	6.78	4.71	9.69	4.2	1.15	30.2	72.2	12.7	1.82	31.5
		GM	331	1230	3370	6.36	993	0.245	267	82.1	0.221	37.9	7.95	12.3	1.08	100	6.37	4.38	7	3.56	0.703	24.8	5.3	11.4	1.08	14.8
		Std	1370	2330	7870	5.72	1640	1.12	799	52.9	0.126	324	4.9	2.48	5.1	140	2.71	1.88	7.38	2.71	1.1	22.9	132	6.08	2.11	46.1
MV007B	Mt	min	0.889	692	238	14.1	<15.3	13.1	1190	307	1.5	8.08	4.9	10.2	<0.059	53.7	4.1	<0.25	<0.001	<0.002	<0.001	<0.002	<0.03	0.97	<0.03	<0.001
	magmatic	max	50.9	1120	998	40.9	43.6	45.7	2610	432	36.4	29.5	6.62	19.4	0.2	329	11.2	13.7	9.31	19.8	31.9	25.9	0.39	3.56	0.89	12.3
	(n=23)	mean	9.42	873	454	29.7	22.2	28.8	1850	360	15.2	12.6	6.02	15.4	0.102	218	6.35	2.22	1.05	2.05	2.52	3.41	0.094	1.52	0.176	2.37
		GM	4.68	861	425	28.8	21.4	26.9	1820	358	11.8	11.8	6.01	15.2	0.094	203	6.11	1.27	0.126	0.225	0.095	0.296	0.071	1.41	0.082	0.308
		Std	13.3	148	188	7.01	7	9.97	376	34.7	9.89	5.61	0.463	2.43	0.044	74.5	1.91	3.23	2.3	4.87	7.22	6.73	0.084	0.693	0.263	3.87
MV006	Hm	min	0.085	83.3	241	4	<11.9	<0.021	<0.112	0.444	<0.066	0.168	0.361	2.22	<0.026	0.187	9.2	<0.28	<0.001	<0.001	<0.001	0.012	14	5.89	0.051	<0.001
	zoned	max	25.9	1030	2670	125	750	0.61	115	63.8	1.76	34.7	3.1	19.4	8.03	19.4	31.6	94.9	53.4	4.06	0.339	94.8	248	343	21.5	6.02
	(n=21)	mean	5.83	318	770	51.5	302	0.232	12	20.9	0.726	3.72	1.22	9.3	2.19	3.43	18.5	28.5	10.7	0.815	0.039	11	112	65.2	6.11	2.08
		GM	2.46	227	604	28.9	111	0.132	3.13	11.4	0.396	1.18	1.07	7.39	0.856	1.7	17.3	8.7	0.654	0.075	0.008	1.37	82.2	32.4	2.01	0.217
		Std	8.36	294	626	43.6	302	0.203	24.8	18.9	0.649	8.39	0.675	5.66	2.2	4.47	7.13	30.5	17.2	1.27	0.074	21.1	75.8	92.4	7.07	1.98
MV006	pMsk	min	33.5	239	1170	<81.8	557	<0.33	20.1	35	<1.24	22.9	0.52	12.8	<3.62	33.7	7.91	26.7	14.2	7.83	0.098	27.4	0.118	11.1	9.12	29.8
	(n=8)	max	402	3510	14600	116	1410	0.6	122	74.1	2.45	88.1	6.76	20.6	14.2	536	16.6	61.6	45.4	11.1	1.82	392	227	1090	19.8	295
		mean	140	1320	9170	105	850	0.491	87.7	64.3	1.65	40.5	1.63	15.3	5.53	129	13.1	49.3	21	9.97	1.22	274	37.8	162	16.5	68
		GM	109	989	7070	104	811	0.485	73	62.4	1.62	37.6	1.11	15.2	4.89	73.1	12.7	47.1	19.2	9.92	0.927	202	1.12	43.5	15.9	46
		Std	116	1040	4790	11	300	0.076	41.9	14.6	0.35	19.9	2.09	2.37	3.65	177	3.02	14.1	10.9	1.05	0.631	148	80.5	375	4.27	91.9
MV005B	Hm	min	0.97	10.5	130	3.93	<4.69	<0.007	<0.98	<0.171	<0.05	<0.79	0.223	0.081	<0.026	0.335	2.06	<0.13	<0.001	<0.01	<0.001	<0.001	0.45	40.2	0.87	<0.001
	zoned	max	70.2	581	1160	108	762	0.57	58.5	46.5	5.71	19.3	11.4	9.65	5.54	16.2	25.4	153	9.2	2.84	0.084	38.4	1960	1080	48.5	10.2
	(n=26)	mean	33.1	210	325	47.1	287	0.196	10.5	18.3	0.879	9.39	2.69	0.922	1.93	3.42	9.91	14.9	0.806	0.382	0.02	11.2	213	532	7.83	1.24
		GM	21.4	131	256	30.2	70.2	0.074	4.36	5.52	0.411	6.94	1.92	0.485	0.86	1.8	8.87	2.56	0.06	0.145	0.007	1.59	51.8	444	5.19	0.131
		Std	18.6	162	288	36.6	287	0.187	14.9	15.5	1.13	5.13	2.69	1.83	1.65	4.23	5	33.1	2.03	0.632	0.024	11.7	421	270	9.4	2.46
MV005B	Si-Mt	min	11.6	250	1180	<2.69	61.1	<0.043	64.3	8.31	<0.141	6.9	0.404	9.12	<0.055	27.9	3.38	0.33	0.161	0.19	0.061	3.15	0.057	5.37	<0.05	0.248
	(n=22)	max	1960	4460	19500	25.2	15900	1.3	348	128	0.38	35.7	8.36	17.1	8.92	136	13	32.6	53.8	15	4.76	72.9	0.71	23.7	1.1	26.6
		mean	866	1110	9180	11.2	4400	0.353	181	61.3	0.205	17.5	1.66	11	1.16	52.8	5.41	6.72	12	8.08	1.78	21.5	0.314	14	0.441	6.58
		GM	472	796	6840	8.81	2210	0.206	155	44.6	0.199	15.3	1.13	10.9	0.273	49.1	5.18	4.52	5.9	5.93	0.947	16.4	0.267	12.1	0.344	3.85

Sample	Type		Mg	Al	Si	P	Ca	Sc	Ti	V	Cr	Mn	Co	Ni	Cu	Zn	Ga	As	Sr	Y	Zr	Nb	Mo	Sn	Sb	Ba
		Std	692	1050	6110	7.02	4110	0.358	99.2	40.9	0.059	8.83	2	1.77	2.26	23.7	1.98	7.2	12.8	4.69	1.54	15.6	0.176	7.04	0.273	6.59
MV005B	pMsk	min	28.7	180	807	<2.34	148	<0.039	89.9	46.4	<0.131	9.9	0.225	9.01	<0.06	27.1	2.7	<0.14	0.851	0.545	0.22	9.06	0.162	4.49	0.119	1.31
	(n=10)	max	232	1670	5150	22.5	3080	0.298	272	77.1	0.18	41.6	4.1	10.8	10.9	246	6.44	9.63	30.7	5.46	0.754	441	293	63.3	14.7	26.1
		mean	91.4	657	2310	7.01	795	0.133	163	66	0.157	20.7	1.77	9.91	3.39	135	3.78	5.68	9.41	2.61	0.438	104	115	22.3	6.66	11.3
		GM	70.3	520	1880	5.07	517	0.108	154	64.8	0.157	18.5	1.25	9.9	1.2	98.3	3.66	3.97	6.17	2.03	0.405	47.2	44	15.6	3.7	8.35
		Std	74.2	509	1570	6.58	878	0.085	57.3	12.5	0.016	10.7	1.31	0.603	3.29	90.5	1.13	3.18	8.82	1.73	0.182	145	109	20.1	5.51	7.51
MV005A	Hm	min	<1.97	135	95.3	3.93	<4.69	<0.007	1.12	0.48	<0.05	<1.08	0.27	0.031	<0.019	0.08	5.99	<0.13	<0.001	0.018	<0.001	0.032	4.09	29.1	2.14	<0.001
	zoned	max	114	994	3680	684	852	0.79	144	110	5.71	1240	38.5	12.7	15.8	48.7	25.4	508	32.6	2.84	0.157	63.3	1100	2170	30	9.75
	(n=37)	mean	41.7	259	501	64.9	180	0.151	19.3	32.7	0.773	65.9	5.05	1.77	1.88	4.73	8.82	47.7	2.08	0.412	0.023	17.7	141	573	6.7	1.4
		GM	35.3	231	245	20.2	24.9	0.035	8.3	24.2	0.28	13.7	2.64	0.446	0.401	1.12	8.04	2.28	0.157	0.18	0.007	11	68.3	486	4.58	0.226
		Std	22.2	162	853	143	326	0.254	29.7	24.8	1.17	220	8.45	3.52	3.57	10.2	4.92	133	6.25	0.656	0.036	13.4	196	370	7.27	2.37
MV005A	Hm	min	12.1	381	1180	<124	<638	<0.51	<2.79	99.8	<1.38	8.3	22.2	2.57	8.41	5.38	18.4	207	3.07	0.232	<0.001	3.11	24.8	436	12.5	1.33
	nodule	max	123	1640	8980	532	1050	1.27	39.8	196	2.08	23.7	58.3	14.1	62.8	33.5	34.7	463	12.7	2.49	0.12	38.5	92.6	3300	36.3	11.2
	(n=15)	mean	60.2	820	2990	388	837	0.64	10.6	146	1.69	14.6	33.7	7.8	30	18.9	23.1	364	5.83	1.35	0.041	15.5	53.9	1570	23.6	4.98
		GM	50.2	784	2560	367	827	0.623	6.78	143	1.68	13.9	32.6	6.94	25.4	17.1	22.8	356	5.42	1.04	0.008	13.2	51.1	1430	22.5	4.15
		Std	33.6	270	2050	114	129	0.184	11.9	29.9	0.224	4.9	9.52	3.55	17.7	7.84	3.98	77.6	2.48	0.782	0.047	9.22	17.2	671	7.28	2.91
MV005A	Mt	min	1.05	483	427	7.34	<11.3	2.43	1050	558	309	6.55	0.233	17.4	0.043	74.9	3.76	<0.12	<0.001	0.001	<0.001	0.017	0.55	1.27	<0.019	<0.014
	magmatic	max	89.8	987	1290	80.2	159	10	2340	901	416	10.1	0.713	26.6	0.318	235	7.94	3.21	1.49	0.913	0.523	1.51	0.998	1.8	0.407	7.74
	(n=7)	mean	21.1	693	611	20.9	49.9	6.28	1590	774	370	7.97	0.476	22.4	0.102	134	5.58	1.17	0.727	0.204	0.13	0.515	0.743	1.59	0.107	2.53
		GM	8.39	678	563	14.2	32.6	5.64	1520	764	369	7.89	0.449	22.2	0.081	126	5.28	0.782	0.231	0.04	0.03	0.246	0.728	1.58	0.064	0.878
		Std	31.6	162	312	26.4	53.7	2.81	521	128	35.7	1.27	0.168	3.39	0.097	54.7	1.98	1.04	0.632	0.324	0.191	0.602	0.163	0.184	0.136	2.9
MV005A	pMsk	min	91	701	1420	21.4	<100	0.081	69.4	76.1	0.064	13.1	0.874	8.81	2.61	45.1	2.49	3.64	3.43	0.7	<0.001	8.76	10	11.1	0.19	6.21
	(n=28)	max	633	8160	10200	848	12300	0.64	324	225	4.21	606	52.8	36.4	58.3	231	8.65	20.6	57.6	14.6	9.65	2720	699	352	48.6	94
		mean	193	1980	3230	330	2970	0.235	150	142	0.646	49.8	7.21	13.1	12.2	115	4.25	10.7	17.5	7.41	0.933	724	202	59.1	13.8	31.5
		GM	178	1730	2960	229	2080	0.213	139	137	0.318	29.9	4.88	12.5	8.45	106	4.1	9.83	14.7	6.07	0.514	551	149	36.5	10.3	26.7
		Std	99.8	1370	1680	258	2780	0.114	63.5	39.9	0.926	110	9.7	5.34	14.6	50.3	1.28	4.32	10.9	3.75	1.73	510	163	75.5	9.91	18.7
MV004	Hm	min	0.629	23	306	5.25	16.7	<0.016	<1.55	0.99	<0.072	<0.74	0.6	0.49	0.318	1.58	1.29	5.21	0.148	0.004	<0.001	0.168	47.6	73.7	3.09	0.47
	(n=14)	max	79.3	1710	1700	131	697	0.565	2360	121	1.45	11.4	7.33	9.5	4.48	24.7	24.8	102	23	2.01	0.301	915	651	1350	17.1	19.7
		mean	26.7	427	724	52.3	351	0.295	180	25.5	0.765	4.2	3.04	4.44	2.18	6.96	10.6	50.8	6.31	0.663	0.06	75.8	186	449	11.1	6.64
		GM	10.9	250	625	33.6	207	0.162	9.23	12.9	0.494	2.99	2.32	3.23	1.57	5.03	8.27	39.5	4.14	0.223	0.026	7.72	145	272	9.77	4.4
		Std	26.8	444	435	42.6	276	0.207	628	31.7	0.585	3.33	2.06	2.97	1.55	6.3	6.73	29.9	5.46	0.758	0.077	242	155	441	5.01	5.86
MV004	Mt	min	1.13	676	226	3.68	<7.21	5.33	1450	311	<0.086	6.03	2.78	9.97	<0.037	29.9	4.92	<0.105	<0.001	<0.001	<0.001	0.007	<0.001	0.565	<0.017	<0.001
	magmatic	max	188	2330	2020	93.4	915	16.7	3400	592	64	11.9	10.6	16.7	22.9	213	26	3.13	3.19	0.744	0.131	14.9	0.187	11.5	0.66	11.2
	(n=42)	mean	33.1	904	459	40.7	139	11.3	2250	407	5.92	8.15	4.12	12.9	1.78	85.1	11.5	0.865	0.531	0.054	0.019	0.59	0.064	3.18	0.134	1.24
		GM	17.6	872	406	30.4	36.9	10.9	2180	404	1.36	8.05	3.97	12.7	0.496	76.5	10.8	0.693	0.129	0.018	0.008	0.137	0.046	2.61	0.057	0.286
		Std	44.2	327	312	29.2	242	3.03	536	55.9	14.8	1.38	1.37	1.8	3.69	42.2	4.22	0.556	0.745	0.125	0.026	2.29	0.045	2.4	0.192	2.3
MV004	Mt	min	17.2	724	938	23.7	83	5.56	1250	162	<0.095	7.32	2.94	9.82	0.073	38.4	5.82	<0.8	0.543	0.08	0.043	0.183	<0.02	1.92	<0.019	0.762
	magmatic	max	875	4930	7690	96.5	1780	36.4	2610	405	2.45	73.3	15.2	21	37.9	261	22.8	3.5	13.8	6.07	1.02	25.2	0.142	11.3	1.06	19
	Si-overprint	mean	384	1690	3610	55.1	768	18.7	1960	238	0.935	15.2	5.51	13.4	6.67	97.1	10.6	1.57	4.31	1.25	0.264	3.69	0.062	4.76	0.296	7.14
	(n=19)	GM	278	1510	3090	48.3	638	16.7	1930	227	0.681	12.9	4.96	13.2	1.58	79.9	9.64	1.44	2.81	0.732	0.171	1.88	0.056	4.08	0.169	5.51
		Std	273	973	1930	27.2	446	8.72	325	81.3	0.674	14.3	3.1	2.68	10.7	67.4	5.03	0.703	4.21	1.46	0.264	6.25	0.031	2.97	0.296	4.84
MV004	Si-Mt	min	1010	673	5780	4.99	1440	0.136	48.4	58.2	<0.17	18.2	2.74	7.18	<0.048	34.6	6.03	1.03	2.5	3.56	0.241	8.02	0.05	9.74	0.066	1.66
	(n=5)	max	4090	4660	23900	21.7	7150	1	160	80.2	0.2	45.3	3.89	11.6	0.58	74.6	15.3	7.96	24	20.9	1.54	48.9	0.49	24.1	0.847	64.2
		mean	1810	1900	11400	11.2	3020	0.449	83.9	67.9	0.188	25.8	3.43	9.18	0.187	48.7	9	2.46	7.08	7.84	0.573	18.4	0.226	15.7	0.246	20.3
		GM	1560	1370	9830	9.6	2540	0.357	76.1	67.3	0.187	24.3	3.4	9.06	0.11	46.5	8.49	1.62	4.33	6.12	0.444	14.3	0.158	14.9	0.145	6.42
		Std	1280	1760	7520	6.77	2330	0.344	45.2	9.98	0.013	11.1	0.457	1.65	0.229	17.3	3.71	3.07	9.49	7.35	0.544	17.2	0.198	5.51	0.337	27.9
MV004	pMsk	min	13.9	249	631	7.18	1040	0.89	20.2	41	0.09	11.9	1.86	12	0.219	48.1	3.39	4.18	11.1	2.13	0.058	8.02	57.3	5.72	1.5	18.7
	(n=3)	max	128	1900	4290	17.6	3950	1.27	43.6	59.2	0.41	18.7	4.09	13.4	2.16	298	5.67	8.73	23.9	7.37	0.228	22.8	124	7.26	4.79	45.9
		mean	80	1290	2470	12.4	2360	1.12	28.3	48.7	0.197	15.1	2.7	12.7	1.01	146	4.57	6.22	17.2	5.5	0.134	15.9	83.7	6.41	2.79	32.7
		GM	55.9	931	1890	11.6	2050	1.11	26.5	48.1	0.15	14.8	2.54	12.7	0.671	110	4.47	5.95	16.4	4.79	0.115	14.6	79.2	6.38	2.46	30.6
		Std	59	903	1830	5.2	1470	0.201	13.2	9.41	0.184	3.41	1.21	0.713	1.02	133	1.14	2.31	6.45	2.92	0.086	7.44	35.3	0.783	1.76	13.6
MV003	Hm	min	6.94	40.5	336	<86.6	<655	0.46	<1.64	2.48	<1.4	0.99	<0.112	<0.75	<2.14	<3.24	5.28	7.07	0.1	<0.014	<0.001	5.23	1.08	34.9	<0.68	<0.001
	(n=17)	max	256	1020	2630	169	1720	0.89	746	202	2.17	72.8	23.6	25.1	43.9	41.5	45.8	168	157	6.95	3.72	3580	503	1640	46.6	22.6
		mean	48.4	378	1060	121	918	0.619	124	69.5	1.71	13.8	8.12	6.15	8.43	11.1	15.1	50.8	22.1	1.63	0.505	281	107	427	20.4	6.41
		GM	29.2	282	876	118	894	0.609	25.7	43.4	1.7	6.68	4.12	3.85	5.94	8.1	13	38.7	8.96	0.752	0.077	42.8	53.2	209	14.4	3.25
		Std	59.8	292	709	24.3	242	0.117	218	62.9	0.204	20.2	7.64	6.64	9.81	10.7	10	40	36.2	1.78	0.985	856	117	501	12.1	5.16
MV003	pMsk	min	10.8	20.5	251	<98.2	<883	<0.47	9.49	28.2	<1.53	6.67	0.22	5.87	<2.97	80.6	7.97	<2.76	0.088	0.044	<0.001	0.437	<0.148	19.3	0.82	0.2
	(n=30)	max	303	973	5220	6950	11200	2.3	388	329	3.09	365	39.3	38	145	666	13.8	54.5	77	43.5	8.1	1810	1310	2490	410	181
		mean	72.8	391	1310	3040	4790	0.767	77.9	198	1.97	51.7	12.9	24.2	44	282	10.7	25	28.8	10.6	1.71	616	336	833	86	51.8
		GM	46.8	280	945	1580	3530	0.724	53.4	171	1.94	35.4	7.41	22.7	30.3	240	10.6	21	21	4.72	0.447	289	163	443	48	32.5
		Std	70.3	300	1150	2290	3270	0.342	79.7	90.4	0.349	68.1	11.8	7.75	36.2	158	1.75	12.4	17.2	10.2	1.92	544	362	751	92.7	41.6
MV002	Hm	min	23.3	11.1	86.2	6.09	<5.61	<0.009	<0.001	3.57	<0.061	5.02	1.06	0.08	<0.022	0.175	3.18	0.429	0.005	0.023	<0.001	0.163	15.4	222	4.48	0.112
	zoned	max	105	153	207	15.5	52.4	0.047	9.48	15.4	0.18	23.9	3.35	0.32	0.08	3.32	4.18	20.9	1.13	0.234	0.046	2.6	441	282	6.77	3.16
	(n=6)	mean	57.4	75	153	11.2	17	0.022	2.04	9.79	0.09	11.9	2.04	0.156	0.037	1.27	3.68	6.69	0.381	0.114	0.012	1.16	185	247	5.3	1.27
		GM	48.9	50.1	148	10.7	12	0.018	0.107	8.5	0.083	10.2	1.87	0.141	0.033	0.727	3.66	2.59	0.127	0.088	0.005	0.734	98.2	246	5.22	0.629
		Std	33.4	56.3	40.3	3.38	18.1	0.016	3.71	4.98	0.046	7.24	0.91	0.085	0.022	1.25	0.421	8.65	0.475	0.076	0.017	0.945	168	23	1.06	1.36
MV002	Mt	min	1.63	442	373	18.3	<14.6	0.514	843	619	14.9	5.48	0.455	19	<0.056	44	5.4	<0.22	<0.001	0.002	<0.006	0.017	0.623	4.41	<0.034	<0.001
	magmatic	max	107	2250	2700	156	221	11.7	21300	1030	74.7	12.7	1.18	27.6	0.285	221	11.6	7.84	10.1	3.31	0.289	19.6	2.83	17.9	0.96	35.3
	(n=26)	mean	11.7	1180	638	42.4	40.2	7.05	14300	918	34.2	8.76	0.923	23.4	0.12	97.9	7.21	1.64	1.44	0.424	0.077	1.85	1.3	12.1	0.131	3.4
		GM	7.59	1120	583	36.7	28.6	5.83	11500	911	32	8.65	0.903	23.3	0.108	88.1	7.03	1.08	0.302	0.071	0.052	0.307	1.26	11.5	0.079	0.256
		Std	20	353	430	32.9	48	2.94	5910	113	13.8	1.42	0.181	2.02	0.064	49.3	1.78	1.79	2.51	0.825	0.077	4.58	0.387	3.35	0.198	7.21

Table S7. (Continued) Summary statistics of LA-ICP-MS data for individual samples and Fe-oxide sub-types from the *Nodular Fe-oxide granite* - RD2366.

Sample		La	Ce	Pr	Nd	Sm	Eu	Gd	Tb	Dy	Ho	Er	Tm	Yb	Lu	Hf	Ta	W	Pb204	Pb206	Pb207	Pb208	Th	U	Pb	∑REY
MV019	min	0.2	0.44	0.047	0.151	<0.001	<0.001	<0.033	0.005	0.019	0.002	0.014	0.007	0.073	0.011	<0.001	0.51	299	<0.015	55.8	6.18	0.4	1.97	143	62.4	1.14
	max	34.1	52.4	3.9	13.3	1.44	0.163	0.88	0.212	1.56	0.5	1.97	0.4	3.76	0.6	0.35	3.96	1120	0.343	358	39.3	47	291	951	427	113
	mean	4.17	9.22	0.795	2.44	0.356	0.042	0.293	0.071	0.614	0.168	0.752	0.16	1.65	0.26	0.026	1.5	474	0.05	216	24	22.7	143	593	263	24.3
	GM	1.78	4.87	0.381	1.25	0.179	0.018	0.214	0.051	0.472	0.124	0.584	0.128	1.3	0.215	0.004	1.38	436	0.032	204	22.6	18.9	117	554	247	15.9
	Std	6.55	11.7	1.05	3.12	0.361	0.046	0.222	0.053	0.381	0.103	0.409	0.081	0.82	0.124	0.06	0.669	230	0.068	64.2	7.21	9.1	57.2	193	78.8	24.5
MV018A	min	0.625	2.8	0.173	0.577	0.249	0.05	0.263	0.077	0.84	0.217	0.96	0.231	1.91	0.417	<0.001	<0.001	419	0.033	467	52.2	24.8	161	1240	544	15.1
	max	18.9	34.1	3.23	12.8	1.96	0.547	1.2	0.249	1.94	0.381	1.57	0.367	3.47	0.667	0.056	0.195	649	0.424	598	69.8	51	240	1560	713	87.4
	mean	2.67	7.66	0.693	2.54	0.556	0.142	0.596	0.14	1.2	0.301	1.33	0.293	2.68	0.513	0.013	0.042	521	0.151	537	62.4	38.4	198	1410	638	27.3
	GM	1.78	6.16	0.533	1.88	0.468	0.116	0.542	0.132	1.18	0.297	1.32	0.29	2.64	0.51	0.003	0.012	516	0.121	536	62.3	37.7	197	1410	637	24.8
	Std	3.95	6.99	0.69	2.74	0.416	0.113	0.281	0.048	0.269	0.05	0.183	0.043	0.443	0.058	0.02	0.059	72.1	0.1	32.3	4.35	7.15	22.4	84.9	39.6	15.9
MV016	min	0.06	0.91	0.07	0.123	<0.001	<0.001	<0.001	0.007	<0.001	<0.001	0.036	<0.013	<0.053	0.015	<0.001	0.055	184	0.024	78.4	11.7	6.1	6.73	201	99.8	3.54
	max	33.1	70.2	7.02	21.9	2.5	0.52	0.73	0.098	0.59	0.116	0.44	0.204	1.5	0.274	0.2	1.28	2430	0.325	382	43.6	24.9	49.5	1030	441	137
	mean	3.34	7.16	0.616	1.79	0.35	0.132	0.206	0.031	0.238	0.051	0.232	0.06	0.516	0.098	0.01	0.374	765	0.147	240	28.7	14.5	27.6	622	283	15.7
	GM	1.55	3.86	0.31	0.854	0.16	0.062	0.128	0.026	0.177	0.04	0.206	0.051	0.442	0.083	0.001	0.289	700	0.13	224	27.2	13.6	25.2	582	266	10.3
	Std	5.97	12.4	1.23	3.81	0.487	0.131	0.168	0.02	0.144	0.03	0.1	0.035	0.276	0.053	0.038	0.267	373	0.069	79.9	8.69	4.88	10.5	207	91.3	23.8
MV015	min	0.038	0.052	0.007	<0.037	<0.043	<0.001	<0.04	<0.001	<0.035	0.005	<0.019	0.005	<0.039	0.01	<0.001	<0.001	20.1	<0.028	12.4	1.21	0.221	0.242	32.5	13.9	0.372
	max	224	403	32.2	119	18.2	4.07	11.7	1.97	12	2.06	5.43	0.676	5.29	0.88	0.075	0.5	1400	21.1	1440	584	1240	254	1610	3280	761
	mean	30.3	70.8	7.05	24.1	4.15	1.18	3.07	0.486	3.01	0.585	1.78	0.274	2.47	0.437	0.012	0.108	552	1.29	453	75.6	97.8	152	1030	628	164
	GM	12.6	32	3.22	11.2	2.26	0.573	1.66	0.262	1.76	0.358	1.18	0.202	1.85	0.333	0.002	0.036	444	0.519	340	49.4	47.6	101	792	447	87.6
	Std	44.3	88.7	8.11	27.4	4.28	1.18	3.11	0.48	3.02	0.5	1.3	0.156	1.23	0.21	0.025	0.129	291	3.82	263	101	221	61.3	478	557	178
MV014	min	0.45	1.9	0.119	0.19	<0.001	0.024	0.09	<0.014	<0.001	<0.001	<0.001	<0.001	0.117	0.015	<0.001	<0.001	316	0.029	30.4	6.94	8.05	1.9	69.7	47.6	4.86
	max	7.26	16.2	1.62	9.26	6.31	2.65	10.9	2.04	11.6	2.79	5.83	1.11	8.11	1.23	0.127	0.027	2300	0.418	812	92.8	26.8	54	2580	932	137
	mean	1.76	5.17	0.531	2.14	0.868	0.38	1.14	0.236	1.27	0.276	0.631	0.117	1.02	0.143	0.027	0.003	999	0.195	153	20.5	14.8	19.2	404	189	22.8
	GM	1.42	4.36	0.419	1.57	0.261	0.146	0.346	0.067	0.305	0.06	0.201	0.05	0.508	0.075	0.004	0.001	872	0.174	116	17.3	14	12.8	278	151	15.3
	Std	1.46	3.66	0.409	1.98	1.46	0.685	2.39	0.457	2.52	0.595	1.24	0.222	1.7	0.252	0.041	0.006	575	0.09	156	17	4.93	15.1	497	176	27.8
MV012	min	0.261	0.577	0.053	0.096	<0.001	<0.001	<0.001	<0.006	<0.001	0.002	0.015	<0.001	<0.026	<0.001	<0.001	<0.001	2.98	<0.018	1.91	0.536	0.311	0.177	3.12	3.49	1.52
	max	16.7	44.9	5.12	18.1	4.31	1.06	1.98	0.273	1.96	0.338	0.84	0.186	1.77	0.211	0.073	0.48	4540	0.401	264	30.5	21.3	33.8	737	310	102
	mean	2.06	5.5	0.654	2.39	0.524	0.134	0.294	0.043	0.275	0.048	0.138	0.026	0.226	0.03	0.011	0.068	973	0.133	43.4	6.93	6.85	3.27	113	57.3	13.3
	GM	0.929	2.3	0.279	0.89	0.133	0.03	0.08	0.02	0.065	0.017	0.064	0.009	0.096	0.012	0.002	0.019	140	0.085	16.1	3.54	3.79	0.933	32.4	25.3	5.93
	Std	4.25	11.5	1.3	4.61	1.12	0.274	0.513	0.074	0.521	0.09	0.217	0.049	0.452	0.055	0.025	0.126	1500	0.123	70.4	8.44	6.84	8.8	198	82.9	25.9
MV008	min	1.25	5.3	0.213	0.46	<0.001	<0.001	0.075	<0.001	<0.001	<0.001	<0.001	<0.001	<0.001	<0.015	<0.001	0.291	208	0.04	34.6	4.17	1.14	0.671	86.7	40	9.75
	max	9.63	26.2	3.15	7.98	1.68	0.25	0.94	0.135	1.46	0.281	1.13	0.284	3.25	0.62	0.31	3.68	1450	5.07	497	175	352	84.9	974	973	58.4
	mean	4.37	12	0.977	2.69	0.361	0.108	0.286	0.045	0.248	0.059	0.234	0.067	0.661	0.127	0.039	1.44	515	0.648	217	39	53.9	40.8	437	311	23.5
	GM	3.98	10.8	0.782	2.01	0.146	0.08	0.217	0.033	0.159	0.03	0.15	0.035	0.41	0.089	0.005	1.17	477	0.316	183	28.8	29.9	32.1	380	248	20.9
	Std	1.86	5.97	0.688	2.07	0.426	0.069	0.245	0.032	0.271	0.057	0.213	0.066	0.605	0.118	0.069	0.872	236	1.13	119	36.7	77.8	18.3	211	218	12.1
MV007A	min	1.63	3.13	0.329	0.799	0.188	0.04	0.149	0.027	0.158	0.032	0.175	0.014	0.131	0.024	<0.008	0.088	<0.006	0.022	0.493	0.082	0.099	0.17	1.92	0.734	7.54
	max	88.7	136	10.8	31.3	3.17	0.486	1.78	0.348	2.29	0.54	1.55	0.196	2.24	0.392	0.082	2.68	752	1.6	51.1	25.8	53.9	6.18	123	130	283
	mean	12.2	24	2.28	7.98	1.06	0.167	0.808	0.126	0.883	0.177	0.608	0.091	0.849	0.149	0.034	1.31	148	0.251	10	3.82	7.38	1.52	31.6	21.5	55.6
	GM	6.1	15.3	1.61	5.86	0.844	0.137	0.653	0.104	0.705	0.139	0.526	0.075	0.693	0.12	0.028	0.934	9.09	0.084	3.1	0.639	0.844	0.792	12.5	5	38
	Std	23.2	34.4	2.65	7.45	0.758	0.117	0.49	0.081	0.615	0.131	0.349	0.055	0.522	0.095	0.021	0.799	244	0.481	17.9	8.24	16.8	1.91	43	43	69.9
MV007A	min	2.11	5.82	0.692	2.93	0.354	0.061	0.227	0.035	0.182	0.055	0.189	0.036	0.384	0.053	<0.004	0.127	0.034	<0.01	0.556	0.083	0.113	0.176	1.89	0.762	14.5
	max	53	79.5	7.13	19	2.07	0.339	1.61	0.27	1.56	0.357	1.41	0.221	2.08	0.455	0.177	1.2	1700	12	299	206	434	17.3	772	951	166
	mean	12.4	24.5	2.37	7.76	1.04	0.178	0.705	0.113	0.723	0.175	0.628	0.119	1.05	0.234	0.047	0.586	386	1.09	60	22.1	39.5	3.93	173	123	56.2
	GM	7.47	17.8	1.88	6.53	0.923	0.151	0.601	0.095	0.63	0.151	0.539	0.108	0.962	0.212	0.021	0.472	22.1	0.138	10.7	2.05	2.49	1.54	42.2	16.2	44
	Std	14.3	22.4	1.85	5.04	0.528	0.099	0.428	0.07	0.397	0.098	0.358	0.051	0.437	0.101	0.056	0.33	483	2.97	87.3	51.2	108	4.97	219	239	44.1
MV007B	min	<0.001	<0.002	<0.001	<0.001	<0.001	<0.001	<0.001	0.001	<0.001	<0.001	<0.001	<0.001	<0.001	<0.001	<0.001	<0.001	<0.007	<0.005	0.004	<0.004	0.016	<0.002	<0.001	0.038	0.057
	max	4.23	7.25	2.15	13.1	6.79	2.34	6.51	1.31	7.39	1.3	4.21	0.643	4.63	0.607	0.206	0.224	19.4	0.234	21.2	2.65	4.53	17.4	419	23.9	78
	mean	0.287	1.13	0.245	1.36	0.703	0.257	0.671	0.143	0.895	0.156	0.483	0.083	0.551	0.072	0.032	0.031	2.4	0.022	3.66	0.575	0.542	1.99	54.3	4.8	9.1
	GM	0.021	0.111	0.021	0.135	0.051	0.023	0.071	0.019	0.077	0.019	0.051	0.013	0.062	0.011	0.012	0.007	0.192	0.012	0.566	0.139	0.151	0.122	2.77	1.06	1.19
	Std	0.877	2.12	0.535	3.23	1.64	0.605	1.58	0.321	1.91	0.326	1.04	0.17	1.16	0.153	0.057	0.058	5.1	0.047	5.83	0.871	1.12	4.4	114	7.29	19.5
MV006	min	<0.002	<0.002	<0.001	<0.001	<0.001	<0.001	<0.001	<0.001	<0.001	0.001	<0.001	<0.001	<0.001	<0.001	<0.001	0.001	232	0.013	0.026	0.007	<0.006	0.009	0.027	0.073	0.049
	max	25.1	63.2	5	14	1.31	0.224	0.67	0.142	1.08	0.217	0.7	0.145	1.47	0.318	0.073	1.14	2780	0.082	295	32.7	4.14	16	878	332	117
	mean	2.07	5.5	0.488	1.51	0.21	0.046	0.146	0.023	0.169	0.04	0.159	0.029	0.284	0.059	0.013	0.093	1330	0.035	49.1	5.68	0.943	1.85	167	55.7	11.6
	GM	0.165	0.387	0.056	0.187	0.037	0.014	0.048	0.008	0.035	0.011	0.028	0.01	0.06	0.014	0.004	0.013	981	0.029	4.52	0.664	0.221	0.244	13.1	6.07	1.6
	Std	5.48	13.7	1.09	3.08	0.335	0.065	0.204	0.037	0.279	0.059	0.222	0.039	0.401	0.084	0.02	0.244	893	0.021	76.7	8.58	1.21	3.67	260	86.1	25.4
MV006	min	14.4	28.1	3.27	10.5	3.41	1.15	2.14	0.426	2.34	0.441	1.26	0.183	1.18	0.291	<0.001	0.073	8.86	0.189	73.2	11.3	12.3	6.4	960	97	81.3
	max	161	368	32.3	91.8	8.46	1.58	3.06	0.774	5.41	0.99	2.84	0.438	3.59	0.348	0.067	8.53	9180	0.738	353	46.8	55.7	11.7	1550	429	681
	mean	35.6	78.5	8.53	26	4.84	1.32	2.63	0.673	4.52	0.777	2.27	0.37	2.82	0.312	0.036	5.67	1260	0.479	156	27.3	36.1	9.8	1320	219	179
	GM	23.3	49.2	6.38	20.3	4.68	1.32	2.62	0.662	4.39	0.757	2.22	0.359	2.7	0.312	0.017	2.89	40.3	0.452	141	25.5	33.5	9.62	1300	203	135
	Std	50.5	117	9.64	26.7	1.51	0.147	0.301	0.119	1	0.172	0.491	0.079	0.747	0.021	0.025	3.45	3210	0.151	83.9	10.3	12.5	1.87	194	95.7	203
MV005B	min	<0.006	0.011	<0.005	0.01	<0.001	<0.001	<0.001	0.001	0.005	<0.001	<0.001	0.002	<0.001	<0.001	<0.001	<0.001	0.088	0.008	6.31	0.731	<0.031	0.002	12.7	7.1	0.142
	max	3.42	5.63	0.569	2.27	0.28	0.081	0.108	0.027	0.425	0.172	0.911	0.233	2.66	0.672	0.068	0.052	9370	0.149	192	21.6	9.79	28.1	807	214	11.6
	mean	0.786	1.25	0.109	0.321	0.043	0.013	0.033	0.007	0.064	0.022	0.115	0.029	0.361	0.094	0.009	0.017	2960	0.033	42.9	5.11	0.932	2.56	160	48.9	3.63
	GM	0.308	0.468	0.042	0.1	0.023	0.006	0.016	0.005	0.035	0.009	0.041	0.012	0.122	0.03	0.003	0.007	443	0.025	28.8	3.58	0.214	0.289	94.3	33.7	1.87
	Std	0.962	1.7	0.161	0.599	0.058	0.019	0.032	0.007	0.092	0.037	0.212	0.055	0.611	0.154	0.017	0.017	2670	0.033	41.9	4.64	2.13	6.48	179	46.3	3.77
MV005B	min	0.737	2.11	0.244	1.01	0.152	0.01	0.104	0.017	0.034	0.006	0.033	0.008	0.037	0.004	<0.004	0.088	0.019	<0.007	0.038	0.012	0.016	0.089	0.089	0.088	4.7
	max	31.8	79.1	9.15	32.1	4.35	0.351	3.19	0.436	2.97	0.561	1.62	0.265	2.27	0.536	0.047	6.8	1.38	0.061	5.27	1.4	3.17	5.59	12.1	9.55	181
	mean	8.59	23.3	2.94	11.3	1.69	0.183	1.27	0.177	1.22	0.268	0.867	0.137	1.16	0.24	0.014	2.39	0.268	0.027	1.92	0.367	0.731	1.65	3.52	3.05	61.5
	GM	6.59	18.7	2.39	9.31	1.4	0.149	1.02	0.143	0.932	0.199	0.652	0.1	0.794	0.148	0.011	1.21	0.142	0.021	1.36	0.234	0.389	1.2	2.71	2.09	50
	Std	7.13	17	1.97	6.96	0.974	0.096	0.761	0.104	0.724	0.155	0.494	0.085	0.752	0.173	0.012	2.1	0.335	0.018	1.32	0.34	0.835	1.34	2.37	2.44	39.1

Sample		La	Ce	Pr	Nd	Sm	Eu	Gd	Tb	Dy	Ho	Er	Tm	Yb	Lu	Hf	Ta	W	Pb204	Pb206	Pb207	Pb208	Th	U	Pb	∑REY
MV005B	min	0.81	2.09	0.168	0.91	0.162	0.043	0.05	0.005	0.115	0.017	0.062	0.021	0.261	0.053	<0.001	0.262	6.93	0.013	0.498	0.017	0.082	0.071	0.619	0.614	6.22
	max	64.2	105	7.42	18.7	1.63	0.381	0.775	0.126	1.03	0.215	0.96	0.174	1.7	0.355	0.013	2.74	1670	2.35	291	60.6	99.6	42.6	731	433	207
	mean	17.7	32.2	2.63	7.31	0.739	0.152	0.423	0.062	0.474	0.109	0.458	0.097	0.907	0.182	0.006	1.09	670	0.909	104	24.2	37.9	9.48	223	167	66
	GM	7.83	16	1.46	4.63	0.571	0.112	0.305	0.047	0.372	0.086	0.324	0.077	0.728	0.154	0.006	0.78	371	0.329	48.5	8.77	13.3	2.05	72.8	74.7	36.7
	Std	22.7	38.6	2.82	7.14	0.524	0.129	0.277	0.037	0.312	0.063	0.325	0.06	0.553	0.1	0.003	0.869	531	0.885	103	23.5	37.1	13.4	251	162	73.8
MV005A	min	0.046	0.085	0.002	0.007	<0.001	0.001	<0.001	0.001	<0.001	0.001	<0.001	0.001	<0.001	<0.006	<0.001	<0.001	31.6	<0.003	8.79	1.09	0.036	0.034	11.3	10.1	0.294
	max	10.4	17.4	1.22	3.22	0.38	0.221	0.23	0.064	0.58	0.172	0.911	0.233	2.66	0.672	0.095	0.184	17700	0.719	192	21.6	38	28.1	807	214	33.1
	mean	1.07	1.95	0.163	0.439	0.05	0.013	0.038	0.009	0.077	0.021	0.1	0.027	0.316	0.085	0.007	0.036	4040	0.071	51.3	6.82	3.15	2.77	191	61.3	4.77
	GM	0.486	0.805	0.053	0.147	0.02	0.004	0.016	0.004	0.03	0.009	0.04	0.012	0.154	0.045	0.002	0.02	2030	0.03	36.5	4.72	0.504	0.699	126	43.8	2.43
	Std	1.89	3.53	0.294	0.807	0.083	0.037	0.054	0.014	0.12	0.034	0.187	0.048	0.518	0.131	0.019	0.036	3560	0.144	42.8	5.82	8.18	6.06	177	49.7	6.9
MV005A	min	0.716	1.66	0.106	0.56	<0.001	<0.001	0.044	<0.001	0.029	0.009	<0.02	<0.007	0.035	0.007	<0.001	<0.001	1440	0.283	30.5	10.4	16.7	2.01	49.6	65	4.12
	max	10.4	30.5	3.81	7.65	0.7	0.25	0.42	0.071	0.63	0.122	0.659	0.116	1.76	0.338	0.069	0.114	3520	0.859	252	36	47.2	126	666	331	57.2
	mean	2.52	6.83	0.704	1.97	0.249	0.081	0.187	0.028	0.304	0.076	0.291	0.059	0.687	0.173	0.016	0.05	2170	0.52	137	25.1	34.3	47.8	320	197	15.5
	GM	1.87	4.96	0.46	1.48	0.153	0.048	0.153	0.019	0.213	0.057	0.206	0.044	0.403	0.101	0.004	0.034	2080	0.494	111	23	32.5	26.5	244	170	12
	Std	2.48	7.18	0.906	1.84	0.186	0.073	0.12	0.022	0.197	0.042	0.185	0.035	0.52	0.118	0.024	0.035	653	0.167	74.4	9.7	11	39.2	189	93.5	13.4
MV005A	min	0.013	0.038	0.001	0.005	<0.001	<0.002	<0.001	<0.001	<0.001	<0.001	<0.003	<0.001	<0.003	<0.001	<0.001	<0.001	<0.006	0.01	0.05	0.009	0.102	0.002	0.022	0.221	0.082
	max	0.63	0.965	0.246	0.819	0.215	0.082	0.181	0.065	0.445	0.072	0.229	0.027	0.302	0.057	0.035	0.064	1.41	0.078	9.24	2.12	3.47	1.45	49.2	14.9	4.75
	mean	0.15	0.369	0.044	0.191	0.05	0.017	0.045	0.015	0.08	0.014	0.046	0.007	0.069	0.011	0.01	0.018	0.298	0.025	2.26	0.485	0.732	0.256	8.07	3.5	1.31
	GM	0.074	0.21	0.011	0.06	0.015	0.008	0.013	0.005	0.01	0.004	0.016	0.003	0.022	0.003	0.005	0.007	0.084	0.019	0.61	0.128	0.301	0.034	0.593	1.18	0.582
	Std	0.216	0.395	0.089	0.293	0.075	0.029	0.064	0.024	0.164	0.026	0.082	0.01	0.109	0.021	0.012	0.025	0.51	0.024	3.38	0.769	1.23	0.531	18.2	5.38	1.72
MV005A	min	0.672	1.23	0.084	0.219	<0.02	0.008	0.086	0.008	0.096	0.041	<0.001	0.023	0.128	0.032	<0.001	0.309	<0.001	0.153	14.7	4.38	9.06	0.259	0.848	28.4	5.32
	max	40.9	82	8.25	28.4	3.53	0.67	2.93	0.584	2.56	0.468	1.65	0.267	2.44	0.575	0.083	27.8	452	11.3	604	213	432	81.7	309	1220	181
	mean	19.3	39.1	3.83	12.9	1.66	0.289	1.35	0.191	1.15	0.254	0.875	0.16	1.53	0.355	0.012	2.98	226	3.05	185	64.6	128	39.1	130	380	90.4
	GM	14.5	29.1	2.77	9.5	1.22	0.204	1.03	0.144	0.924	0.224	0.65	0.146	1.37	0.321	0.006	1.94	140	2.13	146	48.4	94.8	30.6	98.5	293	70.7
	Std	11.8	24.7	2.5	8.21	1.02	0.198	0.837	0.123	0.648	0.114	0.384	0.061	0.564	0.128	0.017	4.99	100	2.62	132	50.6	102	19.3	72.2	285	52.7
MV004	min	0.018	0.061	0.004	0.022	0.014	<0.001	0.026	<0.001	<0.001	<0.001	<0.001	0.002	<0.025	<0.001	<0.001	<0.001	379	0.012	2.01	0.534	0.293	<0.001	6.5	3.27	0.444
	max	33	45.6	3.56	11	0.96	0.295	0.658	0.061	0.484	0.126	0.405	0.101	1.25	0.242	0.028	5.7	5840	0.071	404	45.8	4.68	9.87	1800	452	97.4
	mean	7.16	12.4	1.12	3.14	0.287	0.067	0.188	0.021	0.145	0.037	0.14	0.032	0.323	0.068	0.005	0.497	2290	0.041	62.4	7.49	1.63	1.89	246	71.6	25.8
	GM	1.45	2.86	0.272	0.695	0.123	0.025	0.103	0.01	0.056	0.014	0.059	0.016	0.146	0.027	0.002	0.038	1750	0.036	19.1	3.11	1.27	0.177	58	25.5	7.19
	Std	10.4	16.7	1.44	4.21	0.342	0.088	0.207	0.023	0.159	0.044	0.151	0.035	0.416	0.087	0.009	1.5	1570	0.02	108	12	1.19	3.42	482	120	34.5
MV004	min	0.002	0.002	0.001	<0.001	<0.001	0.001	<0.001	0.001	<0.001	0.001	<0.001	0.001	<0.001	0.001	<0.001	0.001	<0.001	<0.003	<0.003	<0.001	<0.002	<0.001	<0.002	0.021	0.044
	max	0.216	0.74	0.461	0.257	0.133	0.06	0.106	0.014	0.118	0.024	0.106	0.017	0.086	0.032	0.084	0.343	2.73	0.082	3.15	0.664	0.92	0.284	31.6	4.68	2.39
	mean	0.047	0.098	0.021	0.039	0.014	0.005	0.015	0.003	0.015	0.004	0.012	0.002	0.014	0.003	0.009	0.012	0.178	0.013	0.208	0.053	0.085	0.027	1.07	0.359	0.345
	GM	0.026	0.046	0.006	0.024	0.007	0.003	0.008	0.002	0.007	0.002	0.006	0.002	0.006	0.002	0.003	0.003	0.019	0.01	0.05	0.018	0.035	0.01	0.062	0.129	0.221
	Std	0.05	0.137	0.072	0.048	0.022	0.009	0.019	0.003	0.023	0.005	0.019	0.003	0.018	0.005	0.017	0.053	0.584	0.013	0.588	0.133	0.192	0.057	4.91	0.909	0.431
MV004	min	0.063	0.069	0.008	0.046	<0.001	<0.001	0.058	<0.001	<0.001	0.005	<0.001	0.003	0.028	<0.001	<0.001	<0.001	<0.007	<0.004	0.079	0.019	0.019	<0.006	0.046	0.124	0.398
	max	1.72	7.53	1.48	7.8	2.37	0.734	2.46	0.524	3.23	0.473	1.54	0.2	1.37	0.192	0.064	0.12	3.38	0.039	11.3	1.28	1.74	1.88	256	13.4	37.1
	mean	0.505	1.82	0.295	1.32	0.34	0.09	0.318	0.059	0.364	0.065	0.21	0.027	0.209	0.035	0.017	0.021	0.478	0.019	1.12	0.23	0.343	0.224	21.4	1.72	6.92
	GM	0.351	1.05	0.149	0.724	0.138	0.038	0.178	0.023	0.126	0.033	0.09	0.014	0.116	0.022	0.01	0.01	0.117	0.016	0.355	0.108	0.169	0.046	0.817	0.73	4.46
	Std	0.428	2.13	0.413	1.9	0.59	0.174	0.541	0.119	0.735	0.107	0.348	0.045	0.32	0.042	0.015	0.032	0.877	0.011	2.61	0.32	0.436	0.55	62.6	3.06	8.61
MV004	min	3.23	12.2	1.78	7.38	1.5	0.111	0.84	0.101	0.686	0.128	0.481	0.108	0.908	0.178	<0.004	0.48	<0.008	<0.005	0.455	0.045	0.089	0.586	1.01	0.602	35.7
	max	23.1	65.6	8.6	34.2	5.27	0.57	4.38	0.576	3.48	0.837	2.7	0.411	3.64	0.71	0.013	5.7	0.176	0.044	4.94	1.27	2.44	6.1	3.77	8.69	175
	mean	8.27	25.3	3.4	13.8	2.3	0.219	1.7	0.213	1.38	0.315	1.09	0.187	1.59	0.335	0.007	1.63	0.099	0.021	1.66	0.357	0.703	1.8	2.04	2.74	67.9
	GM	6.23	20.2	2.77	11.3	1.99	0.175	1.36	0.165	1.11	0.243	0.868	0.163	1.37	0.295	0.006	0.953	0.066	0.016	1.01	0.167	0.277	1.09	1.85	1.51	54.7
	Std	8.31	22.6	2.92	11.5	1.66	0.197	1.51	0.204	1.19	0.296	0.925	0.127	1.16	0.215	0.004	2.28	0.066	0.016	1.94	0.518	1.02	2.41	1.07	3.47	60
MV004	min	7.11	16.3	1.31	4.15	0.591	0.158	0.363	0.039	0.486	0.072	0.371	0.079	0.86	0.146	<0.001	0.058	569	0.412	46.3	10.3	13.7	0.615	132	70.6	39.4
	max	30	37.6	3.28	8.91	1.07	0.274	0.785	0.161	0.757	0.188	0.697	0.098	1.01	0.189	0.004	0.155	1190	1.06	120	27.7	47	2.47	294	187	84.8
	mean	17.9	27.6	2.45	7.05	0.803	0.201	0.554	0.098	0.637	0.124	0.51	0.087	0.918	0.161	0.002	0.12	854	0.76	84	21.3	33.1	1.38	187	139	64.6
	GM	15.2	26.1	2.28	6.69	0.779	0.195	0.527	0.084	0.626	0.115	0.493	0.087	0.916	0.159	0.002	0.11	817	0.707	78.1	19.5	29.2	1.17	174	128	61.5
	Std	11.5	10.7	1.02	2.54	0.246	0.064	0.214	0.061	0.138	0.059	0.168	0.01	0.083	0.025	0.002	0.054	311	0.325	37	9.59	17.3	0.968	92.3	61	23.1
MV003	min	0.209	0.283	0.016	0.099	<0.001	<0.001	<0.001	<0.001	0.011	<0.001	<0.001	<0.001	<0.001	<0.006	<0.001	<0.001	22.8	0.017	3.41	1.11	2.31	<0.001	0.62	6.89	0.828
	max	16.3	35.6	2.93	7.86	1.32	0.222	0.58	0.096	0.64	0.135	0.74	0.23	2.18	0.444	0.132	41.7	4820	0.162	493	54.2	17.9	67.4	1280	556	66.5
	mean	3.68	9.53	0.868	2.58	0.323	0.089	0.194	0.035	0.227	0.054	0.26	0.062	0.617	0.126	0.023	3.01	1270	0.083	148	17.5	6.17	12.5	380	172	20.3
	GM	2.16	5.38	0.466	1.28	0.137	0.051	0.108	0.013	0.132	0.025	0.123	0.028	0.25	0.066	0.003	0.163	780	0.072	75.8	11.1	5.48	2.39	141	98.1	11.9
	Std	4.27	10.1	0.906	2.79	0.366	0.073	0.181	0.033	0.198	0.047	0.229	0.059	0.602	0.128	0.039	10	1120	0.041	135	14.5	3.55	16.8	360	151	20
MV003	min	0.088	0.384	0.037	0.342	0.022	<0.001	<0.001	<0.001	0.016	<0.001	0.029	<0.001	<0.001	0.003	<0.001	<0.001	<0.001	<0.027	0.479	0.245	0.347	<0.008	0.123	1.1	1.09
	max	127	300	32	98	12.9	2.03	9.33	1.6	8.1	1.66	4.73	0.56	4.62	0.48	0.134	4.51	4670	13.6	2510	526	859	70.1	1120	3910	618
	mean	56.6	136	13.5	41.3	4.76	0.63	2.69	0.354	1.81	0.368	1.01	0.14	1.09	0.167	0.018	1.06	1180	3.53	587	129	214	20	226	933	271
	GM	34	80.4	7.54	22.9	2.58	0.33	1.08	0.153	0.865	0.17	0.566	0.075	0.557	0.101	0.002	0.502	611	1.61	278	62.3	97.1	7.26	119	446	160
	Std	36.1	89.2	9.13	28.7	3.47	0.506	2.47	0.358	1.77	0.374	1.01	0.124	1.01	0.129	0.037	1.17	963	3.59	619	131	220	18.3	225	968	181
MV002	min	0.055	0.147	0.008	0.026	<0.009	<0.001	<0.006	0.001	<0.004	<0.001	0.004	0.001	<0.002	0.004	<0.001	<0.001	104	0.012	2.96	0.311	0.011	0.002	10.7	3.3	0.641
	max	1.11	2.85	0.2	0.572	0.072	0.024	0.07	0.006	0.062	0.013	0.08	0.018	0.233	0.071	0.007	0.013	4580	0.057	49.1	5.46	1.57	0.401	195	54.6	5.54
	mean	0.479	0.954	0.08	0.218	0.031	0.009	0.023	0.003	0.026	0.007	0.032	0.008	0.098	0.027	0.002	0.005	2020	0.032	14.3	1.8	0.595	0.11	55.8	16.7	2.11
	GM	0.236	0.499	0.046	0.145	0.025	0.005	0.014	0.002	0.019	0.005	0.02	0.005	0.041	0.018	0.002	0.003	1030	0.027	8.96	1.26	0.192	0.028	33.6	11.1	1.5
	Std	0.493	1.08	0.077	0.201	0.022	0.009	0.026	0.002	0.02	0.005	0.028	0.008	0.092	0.024	0.002	0.005	1800	0.018	17.4	1.84	0.712	0.159	69.7	19	1.95
MV002	min	<0.001	0.008	<0.001	<0.001	<0.001	<0.001	<0.001	0.001	<0.001	<0.001	<0.001	<0.001	<0.001	<0.001	<0.001	<0.001	<0.007	0.006	0.002	<0.004	0.011	0.003	0.002	0.025	0.066
	max	2.57	9.86	0.535	2	0.383	0.105	0.444	0.088	0.713	0.223	0.487	0.084	0.578	0.118	0.07	12	10	0.153	11.5	3.3	6.58	1.39	3.49	21.5	20.3
	mean	0.328	0.921	0.067	0.218	0.042	0.01	0.054	0.012	0.088	0.024	0.079	0.013	0.111	0.021	0.013	0.747	1.1	0.018	0.666	0.235	0.48	0.1	0.255	1.4	2.41
	GM	0.036	0.113	0.01	0.038	0.017	0.004	0.015	0.004	0.017	0.006	0.024	0.005	0.028	0.007	0.009	0.059	0.122	0.013	0.123	0.059	0.145	0.02	0.061	0.374	0.506
	Std	0.708	2.21	0.149	0.457	0.08	0.022	0.102	0.023	0.173	0.049	0.134	0.022	0.183	0.035	0.014	2.37	2.68	0.028	2.23	0.64	1.28	0.278	0.68	4.16	4.81

Mean corresponds to the arithmetic mean, whereas *GM* corresponds to the geometric mean; Std represents 1σ
Mt: magnetite; Hm: hematite; pMsk: pseudomushketovite; Si-: silician

Table S8. Summary statistics of LA-ICP-MS data for individual samples and Fe-oxide sub-types from the *Deep Mineralisation* - RD2773.

Sample	Type		Mg	Al	Si	P	Ca	Sc	Ti	V	Cr	Mn	Co	Ni	Cu	Zn	Ga	As	Sr	Y	Zr	Nb	Mo	Sn	Sb	Ba
RD2773-5	Hm	min	0.418	24.4	135	18.7	<9.76	0.023	<0.001	<0.009	<0.073	6.85	0.005	0.032	<0.03	<0.041	1.19	0.85	<0.001	0.001	<0.001	0.001	0.011	0.358	<0.02	<0.001
	(n=23)	max	10.2	1540	262	36.4	65.8	1.97	9.63	6.32	0.264	24.1	0.13	0.62	0.224	1.66	9.4	3.64	0.13	0.088	0.061	0.244	13.6	19.4	0.633	0.152
		mean	1.99	540	180	27.5	18.1	0.223	1.35	0.391	0.133	13.8	0.042	0.272	0.057	0.337	4.54	1.54	0.016	0.008	0.005	0.03	1.13	3.31	0.106	0.027
		GM	1.5	273	178	27.2	15.3	0.121	0.259	0.078	0.125	13.2	0.026	0.224	0.047	0.217	3.51	1.46	0.004	0.002	0.002	0.005	0.057	1.4	0.058	0.01
		Std	2.02	523	32.8	4.44	14	0.403	2.54	1.3	0.052	4.17	0.036	0.142	0.046	0.374	3.03	0.612	0.031	0.021	0.013	0.066	3.43	5.05	0.16	0.037
RD2773-5	Mrt	min	0.474	278	193	20.6	<9.58	2.97	41.7	161	<0.075	2.75	0.072	3.21	<0.037	0.288	22.9	4.66	0.11	0.046	<0.001	0.025	<0.009	0.217	0.049	0.116
	(n=23)	max	143	874	1710	83.6	1770	20.6	1400	241	0.65	354	45.7	21.7	72.5	50.1	54.4	105	42.7	0.607	0.166	5.38	0.916	1.53	16.3	50.4
		mean	27.8	524	540	29.5	145	7.86	805	210	0.296	77.8	4.44	8.46	5.36	19.7	39.9	30.9	3.96	0.227	0.048	1.59	0.175	0.684	3.2	4.75
		GM	13.8	504	473	27.9	54.7	7.02	636	209	0.233	42.1	1.83	7.54	1.01	11	39	21.9	1.44	0.162	0.026	0.769	0.109	0.623	1.01	1.77
		Std	33.4	150	325	13.1	361	4.02	382	24.9	0.194	83.8	9.2	4.46	14.9	15.4	7.95	26.5	8.69	0.17	0.047	1.46	0.199	0.29	5.17	10.2
RD2773-5	Si-Mt	min	3.52	202	494	15.5	<9.93	0.451	583	183	<0.083	108	5.96	5.54	<0.036	43.8	2.53	0.61	<0.001	0.022	<0.001	0.001	<0.011	0.207	<0.022	<0.001
	(n=32)	max	199	1650	3020	38	564	19.2	4090	237	1.06	164	9.72	11.9	24.3	711	3.45	2.74	0.574	1.11	0.278	1.34	0.21	2.66	0.145	2.03
		mean	49.1	680	1130	24.2	118	3.84	1290	216	0.276	132	6.84	8.11	2.39	224	2.94	1.66	0.15	0.302	0.058	0.094	0.062	0.554	0.049	0.468
		GM	30.9	623	991	23.7	61.6	2.11	1150	215	0.221	132	6.78	8.01	0.28	174	2.93	1.6	0.062	0.173	0.025	0.029	0.046	0.442	0.044	0.163
		Std	49.5	304	661	5.09	137	4.89	803	12.1	0.208	14.2	0.904	1.33	5.73	160	0.231	0.429	0.186	0.337	0.076	0.234	0.051	0.547	0.026	0.527
CLC111B	Hm	min	0.36	32.5	382	<17.3	<544	<0.18	<0.8	0.031	<0.21	3.19	<0.001	<0.001	<0.65	<0.46	2.7	<0.64	<0.02	<0.001	<0.001	<0.001	0.034	0.26	<0.13	<0.001
	veinlet	max	177	2060	1310	54.9	1060	9.11	229	7.15	0.95	62.1	0.184	0.51	1.62	16.2	7.95	9.43	0.62	0.663	0.214	228	9.76	6.36	4.38	9.93
	(n=20)	mean	13.2	1050	561	25.8	658	2.66	61.7	2.04	0.349	11.9	0.042	0.184	0.969	3.21	4.18	3.06	0.212	0.14	0.066	63.5	3.08	3.39	1.29	1.38
		GM	3.38	668	531	24.6	648	1.26	19.3	0.816	0.319	9.59	0.03	0.108	0.943	2.02	3.94	2.41	0.141	0.057	0.021	9.52	1.36	2.25	0.894	0.173
		Std	39	673	225	9.25	130	2.91	70.6	2.09	0.184	12.2	0.039	0.122	0.247	3.57	1.63	2.11	0.164	0.17	0.066	67.7	2.71	2.23	1.14	2.46
CLC111B	Msk	min	<0.21	27.6	367	<30.5	<1280	<0.31	<0.82	<0.087	<0.56	10.2	<0.001	<0.001	<0.63	<0.57	2.4	<1.01	<0.001	<0.02	<0.001	0.023	<0.094	<0.26	<0.74	<0.001
	(n=20)	max	15.7	2090	1110	124	6820	4.42	117	4.88	1.55	471	0.38	1.44	5.32	92	14.3	27.7	15.3	0.359	0.168	138	8.12	5.42	28.3	275
		mean	4.05	597	611	44.9	2460	0.996	12.4	0.553	0.774	68.9	0.111	0.442	1.06	8.84	5.9	10.1	1.43	0.084	0.047	13.6	1.25	1.52	7.53	33.7
		GM	2.09	284	593	41.4	2130	0.643	3.33	0.221	0.735	39.1	0.08	0.239	0.897	3.23	5.4	6.39	0.292	0.058	0.009	0.986	0.525	0.891	4.6	2.16
		Std	4.86	674	163	22.7	1560	1.23	28.1	1.13	0.287	102	0.077	0.31	1.02	20	2.67	8.51	3.37	0.089	0.053	34.7	2.01	1.58	6.94	79
RX7568	Hm	min	0.64	85	216	<7.51	76.7	1.63	<1.5	0.465	<0.218	3.29	<0.023	<0.001	<0.127	<0.39	0.88	0.41	<0.001	<0.009	<0.001	<0.001	0.41	0.45	0.46	<0.001
	veinlet	max	337	3390	1660	19.9	628	175	166	54.3	1.08	88.2	0.308	1.05	3.64	280	4.09	18.9	1.34	0.699	1.4	6.79	2.52	4.06	38	82.3
	(n=20)	mean	35.8	1800	635	10.1	169	79.3	35.9	12.5	0.542	15.4	0.07	0.196	0.894	33.2	2.45	5.49	0.448	0.189	0.363	1.07	1.34	1.62	7.33	8.44
		GM	5.65	1500	514	9.71	135	57.2	13	8.95	0.519	10.3	0.054	0.028	0.62	9.86	2.32	3.49	0.257	0.089	0.14	0.164	1.13	1.38	3.97	1.99
		Std	94.1	838	469	3.15	143	52.1	53.1	11.1	0.166	20.1	0.066	0.27	0.863	65.1	0.784	4.96	0.391	0.204	0.386	1.78	0.738	1.02	9.54	18.8
RX7568	Msk	min	0.73	452	314	<8.29	117	29.9	1.64	3.3	<0.35	9.35	<0.043	<0.001	0.165	6.78	0.92	0.61	0.053	0.047	<0.029	<0.03	0.15	0.59	1.55	<0.13
	(n=4)	max	3.36	1040	2050	12.8	314	79	22.7	63.1	0.93	15.4	12.5	2.29	1.16	339	5.35	7.08	0.931	0.087	0.82	0.8	0.86	6.19	46.9	106
		mean	2.37	754	1090	9.57	238	47.4	11	21.9	0.6	11.9	3.18	0.858	0.444	132	3.03	4.3	0.468	0.071	0.415	0.234	0.405	2.59	20	42.7
		GM	2.05	722	835	9.41	222	44.2	7.73	11.7	0.564	11.7	0.251	0.163	0.311	52.1	2.55	3.15	0.229	0.069	0.225	0.087	0.331	1.84	10.3	5.96
		Std	1.16	241	821	2.15	89.5	21.7	8.74	27.9	0.245	2.52	6.21	0.997	0.48	155	1.81	2.7	0.473	0.019	0.377	0.378	0.312	2.48	20.7	51.5
CLC113	Hm	min	<2.64	17.9	<283	<167	<1200	<0.89	<3.29	<0.53	<3.16	2.24	0.07	<0.96	<4.28	<10.4	1.8	<7.26	<0.001	0.01	<0.001	<0.001	<0.31	<1.45	<2.69	<0.001
	veinlet	max	35.8	596	1160	205	2290	5.86	40.4	46.8	3.79	37	0.3	1.94	10.2	25.4	6.75	31.7	1.23	0.106	0.263	35.1	3.86	14.2	48.1	59.8
	(n=20)	mean	8.02	277	588	188	1480	2.18	11.7	7.74	3.47	11.5	0.214	1.6	5.17	13.8	4.57	13.2	0.351	0.036	0.05	5.31	1.26	3.51	13.3	5.19
		GM	6.01	202	535	187	1470	1.83	8.71	4.76	3.46	9.52	0.203	1.57	5.06	13.3	4.38	11.7	0.137	0.029	0.006	0.65	1	2.87	8.92	0.16
		Std	7.9	184	259	9.67	212	1.38	10.3	10.1	0.191	7.71	0.064	0.274	1.31	3.98	1.32	7.24	0.348	0.025	0.075	8.46	0.875	2.95	12.9	13.3
CLC113	Msk	min	<2.93	32.7	<315	<186	<1430	<0.9	<4.78	<0.63	<3.68	7.79	<0.176	<1.44	<5.15	<12.2	5.6	<9.19	<0.093	<0.001	<0.001	<0.001	0.47	<1.66	<5.76	<0.001
	(n=10)	max	22.8	283	1300	239	1870	2.3	10.6	5.51	5.67	158	0.4	2.73	6.62	31.6	9.88	20.7	8.86	0.09	0.23	2.85	2.97	5.76	32.9	586
		mean	7.19	120	593	212	1650	1.21	6.33	2.85	4.16	49.4	0.278	2.1	5.6	16.3	7.13	13	1.8	0.04	0.041	0.487	1.53	4.01	18	88
		GM	5.73	87.4	533	212	1640	1.17	6.17	2.45	4.13	30.4	0.269	2.06	5.59	15.4	6.99	12.5	0.572	0.021	0.003	0.109	1.22	3.59	15.6	8.5
		Std	6.08	98.1	311	14.2	143	0.398	1.65	1.48	0.554	50.1	0.073	0.4	0.439	6.39	1.56	4.04	2.84	0.029	0.085	0.877	0.952	1.7	9.19	183

Table S8. (continued) Summary statistics of LA-ICP-MS data for individual samples and Fe-oxide sub-types from the *Deep Mineralisation* - RD2773.

Sample		La	Ce	Pr	Nd	Sm	Eu	Gd	Tb	Dy	Ho	Er	Tm	Yb	Lu	Hf	Ta	W	Pb204	Pb206	Pb207	Pb208	Th	U	Pb	∑REY
RD2773-5	min	0.001	0.001	0.001	<0.001	<0.001	0.001	<0.001	0.001	<0.001	0.001	<0.001	0.001	<0.001	0.001	<0.001	<0.001	<0.003	0.004	<0.001	0.001	<0.004	0.001	<0.001	0.014	0.023
	max	0.07	0.155	0.022	0.084	0.014	0.024	0.042	0.004	0.014	0.006	0.01	0.002	0.011	0.003	0.004	0.01	452	0.029	15.6	1.32	0.528	0.012	0.719	17.5	0.525
	mean	0.01	0.019	0.003	0.012	0.005	0.003	0.008	0.001	0.004	0.001	0.003	0.001	0.004	0.001	0.003	0.002	40.6	0.013	1.14	0.135	0.09	0.002	0.087	1.38	0.085
	GM	0.002	0.005	0.001	0.005	0.004	0.002	0.006	0.001	0.003	0.001	0.003	0.001	0.004	0.001	0.002	0.001	0.217	0.011	0.031	0.014	0.022	0.002	0.012	0.106	0.055
	Std	0.021	0.038	0.005	0.022	0.003	0.005	0.008	0.001	0.003	0.001	0.002	0.001	0.002	0.001	0.001	0.002	128	0.008	3.41	0.319	0.162	0.003	0.191	3.85	0.117
RD2773-5	min	0.015	0.054	0.005	<0.004	0.005	<0.001	<0.001	0.001	<0.003	<0.001	<0.003	0.001	0.004	0.001	<0.001	0.001	0.496	<0.004	0.035	0.025	0.029	0.01	0.058	0.127	0.181
	max	0.438	0.97	0.107	0.512	0.195	0.069	0.252	0.021	0.171	0.027	0.091	0.012	0.102	0.023	0.023	0.026	28.3	0.139	19.6	3.01	5.37	0.317	3.54	28.1	3.3
	mean	0.218	0.493	0.053	0.217	0.058	0.02	0.072	0.009	0.066	0.01	0.033	0.005	0.034	0.006	0.006	0.009	7.77	0.048	2.43	0.847	1.67	0.113	1.15	4.99	1.52
	GM	0.163	0.377	0.036	0.138	0.035	0.012	0.037	0.006	0.042	0.007	0.021	0.003	0.021	0.003	0.004	0.005	4.65	0.037	1.11	0.525	0.981	0.08	0.803	2.87	1.12
	Std	0.138	0.307	0.038	0.162	0.053	0.018	0.069	0.007	0.051	0.008	0.026	0.003	0.031	0.006	0.006	0.008	7.06	0.035	4.24	0.775	1.5	0.082	0.892	5.99	1.02
RD2773-5	min	0.017	0.173	0.012	0.03	<0.005	0.002	<0.001	0.001	<0.001	0.001	0.003	0.001	<0.001	0.001	<0.001	0.001	<0.001	<0.003	0.008	<0.001	<0.002	0.002	0.028	0.033	0.436
	max	8.04	24.7	1.85	5.83	0.882	0.111	0.661	0.047	0.181	0.04	0.1	0.013	0.13	0.016	0.052	0.034	0.445	0.063	0.841	0.799	1.78	0.159	2.21	3.49	43.7
	mean	0.623	2.47	0.184	0.603	0.097	0.014	0.075	0.01	0.051	0.01	0.03	0.004	0.027	0.004	0.012	0.005	0.082	0.016	0.108	0.044	0.093	0.022	0.378	0.261	4.51
	GM	0.167	0.683	0.056	0.235	0.047	0.007	0.024	0.005	0.026	0.005	0.019	0.003	0.015	0.003	0.008	0.003	0.029	0.013	0.053	0.015	0.029	0.015	0.181	0.123	1.65
	Std	1.5	5.48	0.4	1.11	0.158	0.021	0.128	0.011	0.057	0.011	0.03	0.003	0.031	0.004	0.013	0.007	0.129	0.011	0.173	0.139	0.311	0.027	0.529	0.609	8.92
CLC111B	min	<0.011	0.003	<0.001	<0.001	<0.001	<0.001	<0.001	0.004	<0.001	0.004	<0.001	<0.001	<0.001	<0.001	<0.001	<0.001	<0.024	NA	0.027	0.023	<0.017	0.003	0.003	0.124	0.136
	max	1.16	2.68	0.257	0.86	0.214	0.026	0.207	0.027	0.225	0.018	0.08	0.022	0.129	0.034	0.078	5.76	31.6	NA	5.09	1.84	3.9	0.165	20.5	9.71	6.56
	mean	0.212	0.471	0.044	0.168	0.06	0.011	0.048	0.009	0.046	0.009	0.022	0.007	0.036	0.007	0.035	1.46	9.18	NA	1.27	0.418	0.831	0.047	3.11	2.52	1.29
	GM	0.097	0.161	0.017	0.081	0.041	0.009	0.023	0.008	0.029	0.008	0.017	0.006	0.024	0.005	0.017	0.418	2.52	NA	0.685	0.257	0.41	0.027	0.981	1.57	0.767
	Std	0.266	0.624	0.059	0.21	0.054	0.006	0.047	0.005	0.047	0.004	0.016	0.005	0.029	0.007	0.025	1.64	9.2	NA	1.33	0.413	0.927	0.044	4.82	2.35	1.48
CLC111B	min	0.013	0.015	<0.014	<0.085	<0.001	0.022	<0.001	0.014	<0.001	<0.001	<0.061	<0.015	0.053	<0.024	<0.001	<0.001	0.13	NA	<0.039	<0.042	<0.054	<0.02	<0.025	0.154	0.974
	max	0.227	0.39	0.122	0.35	0.77	0.092	0.36	0.077	0.154	0.051	0.18	0.087	0.26	0.17	0.54	2.22	36.5	NA	8.63	4.87	10.3	0.074	24.8	23.8	2.13
	mean	0.086	0.147	0.038	0.18	0.206	0.057	0.161	0.031	0.091	0.03	0.09	0.037	0.146	0.05	0.132	0.293	6.5	NA	1.4	0.687	1.5	0.043	4.28	3.58	1.44
	GM	0.06	0.108	0.034	0.17	0.141	0.054	0.124	0.029	0.072	0.025	0.087	0.032	0.137	0.045	0.054	0.057	1.66	NA	0.517	0.249	0.501	0.041	1.21	1.37	1.4
	Std	0.076	0.106	0.024	0.065	0.162	0.019	0.073	0.014	0.038	0.013	0.029	0.021	0.051	0.032	0.118	0.535	11	NA	2.15	1.22	2.61	0.014	7.02	5.96	0.348
RX7568	min	<0.013	0.012	<0.007	<0.001	<0.034	<0.001	<0.029	<0.001	<0.001	<0.001	0.011	<0.001	<0.001	<0.001	<0.001	<0.001	1.12	NA	0.034	0.008	0.01	<0.008	0.124	0.053	0.235
	max	1.09	3.17	0.341	1.44	0.4	0.036	0.237	0.038	0.216	0.029	0.144	0.049	0.199	0.04	0.122	0.235	63.5	NA	3.13	1.25	2.2	0.897	15.4	6.08	7.66
	mean	0.294	0.812	0.087	0.363	0.095	0.013	0.073	0.013	0.054	0.012	0.04	0.012	0.052	0.012	0.032	0.038	14.3	NA	0.995	0.457	0.833	0.394	3.48	2.28	2.12
	GM	0.176	0.459	0.056	0.201	0.076	0.009	0.06	0.01	0.026	0.008	0.03	0.009	0.028	0.008	0.01	0.007	7.86	NA	0.57	0.21	0.379	0.226	1.89	1.24	1.5
	Std	0.278	0.785	0.084	0.351	0.084	0.009	0.057	0.009	0.056	0.008	0.038	0.012	0.055	0.011	0.035	0.068	16	NA	0.977	0.41	0.801	0.287	4.09	2.01	1.81
RX7568	min	<0.001	0.025	0.008	<0.027	0.026	<0.007	<0.001	0.006	0.014	<0.006	<0.019	<0.004	<0.018	<0.004	<0.001	<0.001	2.46	NA	0.151	0.135	0.332	0.019	0.201	0.617	0.402
	max	0.038	0.162	0.04	0.085	0.066	0.035	0.065	0.03	0.034	0.019	0.036	0.014	0.068	0.012	0.028	0.013	26.6	NA	0.659	0.567	1.17	0.165	1.31	2.4	0.639
	mean	0.022	0.081	0.019	0.064	0.054	0.02	0.039	0.013	0.022	0.014	0.027	0.008	0.038	0.007	0.012	0.006	9.77	NA	0.343	0.266	0.648	0.066	0.718	1.26	0.499
	GM	0.013	0.064	0.015	0.058	0.051	0.017	0.019	0.01	0.02	0.013	0.026	0.007	0.033	0.007	0.005	0.003	6.24	NA	0.297	0.22	0.58	0.047	0.59	1.1	0.491
	Std	0.016	0.06	0.015	0.026	0.019	0.012	0.027	0.011	0.009	0.006	0.009	0.004	0.022	0.003	0.014	0.006	11.3	NA	0.22	0.205	0.368	0.067	0.456	0.79	0.106
CLC113	min	0.006	<0.016	<0.001	<0.001	<0.001	<0.001	<0.001	<0.001	<0.001	<0.001	<0.001	<0.001	<0.001	<0.001	<0.001	<0.001	0.105	<0.036	<0.115	<0.121	<0.174	<0.001	<0.011	0.455	0.251
	max	0.525	1.92	0.161	0.47	0.136	0.035	0.158	0.018	0.086	0.023	0.052	0.02	0.078	0.019	0.14	0.133	215	0.182	28.3	5.84	9.47	0.037	60.3	35.1	3.31
	mean	0.122	0.411	0.04	0.094	0.038	0.013	0.069	0.007	0.03	0.009	0.026	0.008	0.026	0.005	0.02	0.03	22.9	0.061	7.86	1.59	1.92	0.016	14.8	11.4	0.935
	GM	0.051	0.159	0.015	0.031	0.01	0.006	0.039	0.004	0.013	0.006	0.015	0.005	0.008	0.003	0.002	0.015	3.72	0.055	3.41	0.966	0.964	0.011	3.47	6.27	0.675
	Std	0.152	0.512	0.049	0.112	0.042	0.012	0.043	0.006	0.026	0.007	0.017	0.007	0.027	0.006	0.043	0.03	49.3	0.036	7.99	1.5	2.32	0.01	16.6	10.8	0.82
CLC113	min	0.006	0.013	0.006	<0.001	<0.001	<0.001	<0.001	<0.001	<0.001	<0.001	<0.001	<0.001	<0.001	<0.001	<0.001	<0.001	0.103	0.042	0.302	<0.13	<0.205	<0.001	0.082	0.701	0.214
	max	0.199	0.92	0.118	0.2	0.096	0.033	0.13	0.02	0.1	0.015	0.04	0.014	0.064	0.015	0.158	0.227	20.6	0.118	13.2	1.62	3.38	0.056	76.9	15.4	1.89
	mean	0.063	0.203	0.023	0.077	0.052	0.012	0.036	0.006	0.051	0.006	0.01	0.007	0.028	0.005	0.023	0.037	5.58	0.057	5.25	0.801	0.785	0.016	26.1	6.89	0.619
	GM	0.04	0.104	0.014	0.025	0.014	0.005	0.008	0.003	0.034	0.003	0.003	0.004	0.007	0.003	0.003	0.007	2.45	0.054	3.05	0.597	0.506	0.009	6.45	4.72	0.51
	Std	0.063	0.271	0.034	0.067	0.045	0.013	0.045	0.006	0.03	0.006	0.013	0.006	0.031	0.005	0.051	0.069	6.8	0.023	4.2	0.506	0.96	0.016	25.4	4.66	0.481

Mean corresponds to the arithmetic mean, whereas *GM* corresponds to the geometric mean; Std represents 1σ

Mt: magnetite; Hm: hematite; Msk: mushketovite; Mrt: martite; Si-: silician-.

Table S9. Summary statistics of LA-ICP-MS data for individual samples and Fe-oxide sub-types from the Distal satellite mineralisation - RD2316.

Sample	Type		Mg	Al	Si	P	Ca	Sc	Ti	V	Cr	Mn	Co	Ni	Cu	Zn	Ga	As	Sr	Y	Zr	Nb	Mo	Sn	Sb	Ba
LCD18	Hm	min	<0.22	51.4	<68.5	<8.11	<36.5	0.984	<0.74	0.233	<0.45	1	<0.016	0.069	<0.081	<0.37	11.7	<0.33	<0.001	0.005	<0.021	0.151	0.043	1.53	<0.074	<0.001
	veinlet	max	58.1	2180	1990	28.7	240	55	6820	44.8	1.54	70.8	0.823	0.87	4	24.1	56.3	30.8	1.93	2.2	9.37	227	15.4	403	7.87	14.2
	(n=48)	mean	11.4	1230	522	10.9	75.5	21.5	1470	15	0.628	11.2	0.283	0.287	0.368	4.07	22.3	5.25	0.393	0.288	1.99	56.8	2.67	165	1.65	2.23
		GM	5.12	986	277	10.5	71.1	16.6	475	9.24	0.599	7.18	0.219	0.238	0.253	2.28	20.9	2.65	0.14	0.094	0.972	27	1.21	104	0.686	0.294
		Std	15	581	552	3.45	33.7	12.5	1470	11.4	0.244	12.6	0.167	0.193	0.57	4.52	9.47	6.09	0.462	0.417	1.99	49.3	3.02	114	2.09	2.96
MV051	Hm	min	1.31	335	108	<1.8	<11.6	2.75	516	4.4	<0.092	3.13	0.022	0.03	<0.046	0.401	5.31	1.74	0.202	0.008	0.171	34.3	0.354	2.3	0.307	0.028
	veinlet	max	46.4	2100	1700	11.3	85.4	23.6	2900	38.7	0.47	30	0.522	0.625	0.56	10	22.1	12.4	0.832	1.77	7.75	126	5.35	410	4.52	7.92
	(n=21)	mean	16.3	1360	689	5.03	27.9	13.7	1600	18.7	0.19	16.6	0.31	0.229	0.216	4.45	13.4	7.1	0.497	0.641	3.42	72.1	2.39	263	1.91	4.11
		GM	11.4	1280	562	4.39	22.2	12.7	1510	16.4	0.17	14.8	0.245	0.184	0.176	3.59	13	6.46	0.467	0.439	2.65	66	1.95	188	1.68	3.13
		Std	12.8	422	420	2.63	21.8	4.91	538	10.1	0.102	6.88	0.138	0.131	0.144	2.51	3.1	2.93	0.169	0.41	1.9	31.8	1.43	135	1.01	1.88
MV052	Hm	min	<0.171	142	<55.5	<7.28	<42.8	0.275	<0.41	<0.027	<0.35	0.66	0.018	<0.094	<0.07	<0.22	4.22	<0.29	<0.007	<0.005	<0.001	<0.007	<0.026	0.346	<0.053	<0.001
	veinlet	max	33.2	2780	2100	27.1	138	100	14800	75.1	3.18	36.9	1.97	0.9	1.33	17.6	20	160	1.76	1.82	9.84	217	12.7	244	87.9	17.1

Sample	Type		Mg	Al	Si	P	Ca	Sc	Ti	V	Cr	Mn	Co	Ni	Cu	Zn	Ga	As	Sr	Y	Zr	Nb	Mo	Sn	Sb	Ba
	(n=24)	mean	12.6	1450	644	10.8	64.4	35.2	3440	30.3	0.91	15.2	0.597	0.278	0.367	4.47	11.7	14.6	0.71	0.607	2.55	47.9	3.26	79.7	6.57	4.08
		GM	5.13	1070	323	9.73	60.4	15.9	1280	15.7	0.743	8.27	0.256	0.23	0.239	1.8	10.9	5.29	0.265	0.185	0.556	23.2	1.08	35.6	1.58	1.21
		Std	11.1	894	623	6.1	26.9	31	3620	24	0.692	12.5	0.611	0.191	0.354	4.72	4.01	31.7	0.616	0.641	2.65	43.8	3.41	72.1	17.5	4.18
LCD19	Hm	min	<0.22	305	<71	<9.3	<51	0.271	<0.9	<0.032	<0.48	0.44	<0.016	<0.15	<0.097	<0.36	4.25	<0.129	<0.009	0.004	<0.001	<0.006	<0.001	0.18	<0.062	<0.001
	veinlet	max	55.2	2230	1580	38.9	181	160	8620	165	3.53	47.1	0.93	0.66	1.4	13.1	49.2	47	2	2.75	4.76	308	33.5	223	14.8	9.8
	(n=39)	mean	7.63	1190	336	14.9	102	56.3	2290	36.3	1.04	9.85	0.197	0.258	0.359	2.31	21.1	7.95	0.268	0.475	1.41	71	4.45	49.1	2.45	1.33
		GM	3.85	1090	198	14	92	32.7	1170	16.8	0.915	4.08	0.116	0.237	0.266	1.23	18.6	2.47	0.06	0.07	0.537	39.9	1.3	17.8	0.781	0.086
		Std	10.6	483	374	5.7	46.8	36.1	1950	40.9	0.634	14.7	0.211	0.121	0.318	3.06	9.39	10.5	0.46	0.81	1.31	61.1	6.08	58.6	3.4	2.27
MV053	Mrt	min	16.6	1100	662	66.3	<50.2	5	3810	377	14.7	89.8	4.3	2.68	0.55	4.62	27.4	173	0.971	1.32	0.674	4.85	85.8	13.1	19.1	1.14
	(n=5)	max	82.3	1650	1510	120	170	14.2	34800	602	39.8	671	17.2	8.39	1.54	47.2	58.9	270	1.64	7.79	6.44	138	211	69.8	46	5.99
		mean	45.9	1320	1110	98.1	93.1	9.93	20300	535	29.2	352	10.6	5.76	0.95	23.2	43.9	217	1.31	3.74	2.73	70.8	139	42.5	33.8	3.07
		GM	39.8	1310	1060	95.3	83.8	9.19	13900	528	27.3	259	9.56	5.23	0.894	16	42.6	214	1.3	2.98	2.06	32	131	36	32.5	2.64
		Std	25.5	231	377	25	49.8	4.09	14900	93.7	11.2	255	5.03	2.55	0.378	18.6	11.3	41.8	0.239	2.68	2.26	64.1	52.8	23.9	9.73	1.86
MV053	Hm	min	<0.18	234	<54.8	<6.82	<42.1	4.16	6.64	4.94	<0.37	1.4	<0.011	<0.095	<0.077	<0.23	7.13	<0.28	<0.001	<0.005	0.034	1.32	<0.047	2.61	<0.053	<0.001
	veinlet	max	7.89	1490	406	19.2	84	231	8300	154	2.13	7.66	0.325	0.77	0.313	0.65	41.5	17.1	0.364	0.675	5.76	333	94	451	6.36	2.04
	(n=17)	mean	4.05	984	222	8.64	51.6	81	3620	26.7	0.911	3.22	0.085	0.242	0.165	0.357	17.9	7.2	0.072	0.232	2.13	143	12.9	77.8	2.88	0.545
		GM	3.31	868	183	8.3	50.4	49.5	1920	14.4	0.759	2.81	0.053	0.197	0.148	0.341	16.1	4.06	0.038	0.121	1.13	93.1	1.48	38.4	1.13	0.095
		Std	1.95	406	116	3.04	12.5	72.7	2240	42.3	0.59	1.88	0.089	0.18	0.081	0.123	9.07	5.49	0.09	0.188	1.93	92.1	25.6	105	2.41	0.557
MV055	Hm	min	0.048	1.55	29.4	<1.78	<13.1	<0.02	0.27	0.264	<0.081	0.563	0.07	0.163	<0.041	0.101	2.02	<0.24	0.003	0.001	<0.001	<0.001	0.247	1.4	<0.081	<0.001
	zoned	max	14.3	1510	1500	17.5	77.1	24.3	2630	637	0.49	117	3.72	7.58	424	2.58	51.4	56.4	1.28	1.52	6.85	16.4	44.7	70.8	25.1	19.2
	(n=46)	mean	2.02	386	165	8.16	30.2	3.32	405	148	0.218	11.4	0.508	2.3	36.4	0.695	34.4	9.26	0.324	0.156	0.507	1.99	7.58	11.8	4.08	1.69
		GM	0.928	146	105	7.07	26.6	0.71	53.3	32.1	0.192	5.79	0.34	1.74	0.885	0.506	32.1	4.61	0.123	0.023	0.061	0.251	3.48	6.3	2.36	0.325
		Std	2.95	374	250	4.11	16.6	5.25	653	180	0.107	19.6	0.601	1.73	114	0.564	8.99	11.9	0.37	0.342	1.36	3.49	11	16.8	4.41	3.4
LCD21	Hm	min	0.585	60.7	<34	<4.38	<19.4	0.378	<0.25	0.407	<0.23	1.55	<0.011	<0.064	<0.049	<0.15	4.92	<0.187	<0.004	<0.001	<0.001	0.008	0.14	1.89	<0.084	<0.001
	(n=27)	max	16.3	2050	382	20.2	136	60.2	4400	781	1.04	11.2	0.186	0.53	8.37	72.2	23.4	16.8	0.749	0.4	0.6	7.91	141	691	4.75	6.05
		mean	5.52	989	148	6.95	40.8	6.74	592	97.2	0.352	5.64	0.087	0.171	0.787	3.21	10.3	5.47	0.177	0.124	0.085	1.48	14.3	217	1.44	0.88
		GM	4.2	635	111	6.33	36.2	3.36	28.6	12.5	0.327	5.06	0.067	0.14	0.141	0.489	8.74	2.54	0.07	0.04	0.035	0.225	3.04	81.3	0.815	0.118
		Std	4.05	666	105	3.61	25.7	11.6	1180	202	0.172	2.61	0.051	0.124	1.92	13.8	6.36	4.99	0.191	0.137	0.149	2.47	30.7	201	1.39	1.31
MV056	Mrt	min	4.71	190	107	<3.5	36.8	2.18	53	3.93	<0.18	22	0.963	0.224	<0.05	1.99	6.39	5.8	0.53	0.106	0.086	0.647	0.897	93.1	1.11	0.94
	(n=26)	max	40.6	490	514	17.4	401	4.71	2050	273	0.77	137	6.08	7.24	19.1	7.08	11.6	21.3	2.6	2.13	0.988	30.2	8.01	589	5.45	8.91
		mean	13.9	306	239	6.95	166	3.29	984	124	0.288	76.2	2.56	1.99	1.39	4.22	8.23	13.1	1.54	0.98	0.471	11.5	3.4	266	2.63	5.06
		GM	11.9	297	223	6.12	138	3.23	804	98.4	0.27	71.9	2.27	1.44	0.515	4.02	8.12	12.4	1.48	0.874	0.415	9.38	2.95	245	2.5	4.6
		Std	8.55	77.1	93.1	3.83	99.9	0.627	529	65.9	0.128	24	1.32	1.81	3.69	1.26	1.45	3.99	0.394	0.423	0.229	6.56	1.81	114	0.884	1.86
MV057	Mrt	min	2.25	336	95.4	<3.63	<19.3	3.72	656	378	<0.18	86.6	3.1	11.1	<0.044	6.81	7.94	<0.14	0.082	0.006	<0.008	<0.005	0.052	1.66	<0.031	<0.001
	(n=8)	max	154	527	1370	12.8	109	6.05	798	469	1	278	20	18	0.138	43.8	26.8	4.18	0.563	0.95	0.121	0.355	8.53	5.19	0.83	0.94
		mean	74.3	408	805	7.08	54	4.96	740	415	0.332	189	15.3	15.3	0.081	29.6	15.2	1.09	0.294	0.212	0.065	0.23	2.53	2.26	0.243	0.331
		GM	50.2	404	575	6.28	45.2	4.92	738	413	0.275	178	13.7	15.2	0.074	25.1	14.4	0.587	0.244	0.09	0.049	0.125	1.04	2.09	0.163	0.147
		Std	45.2	65	494	3.67	33.3	0.69	48	42.3	0.279	64	5.54	2.12	0.037	14.5	5.46	1.38	0.169	0.306	0.038	0.137	2.77	1.19	0.253	0.29
MV057	Hm	min	<0.13	46	<27.7	<3.49	<19.3	0.942	<0.25	<0.015	<0.175	0.74	0.018	0.39	<0.03	<0.137	2.74	0.28	0.005	<0.002	<0.001	<0.001	<0.021	0.234	<0.036	<0.001
	(n=20)	max	11.8	1130	774	21.1	169	18.6	839	82.2	1.02	29.3	0.782	28.1	0.49	5.11	26.9	43.5	3.5	58.8	0.115	2.59	35.5	47.3	7.43	9.99
		mean	2.38	464	156	9.77	50.7	7	91.2	15.9	0.335	5.4	0.347	10.4	0.108	0.755	15	8.57	0.447	7.55	0.02	0.312	2.77	8.25	1.4	1.37
		GM	1.63	297	108	8.53	38.8	4.76	9.88	3.85	0.3	3.27	0.223	4.91	0.08	0.431	13.1	4.15	0.167	0.257	0.008	0.055	0.411	4.46	0.547	0.211
		Std	2.43	346	178	5.01	45	5.9	189	21.1	0.2	7.12	0.24	10.3	0.109	1.13	6.76	10.8	0.809	15.6	0.027	0.612	8.14	10.7	2.03	2.27
MV057	Si-Mt	min	8.61	279	209	<8.66	<52.9	3.21	357	332	<0.43	92.4	10.9	12.3	<0.043	23	7.17	<0.31	<0.014	0.012	0.014	0.016	<0.031	1.16	<0.064	<0.001
	(n=24)	max	1410	1070	6320	53.8	1090	35.5	1660	490	1.58	144	18.9	21.1	0.481	85.9	16.3	2.68	3.06	3.76	1.03	2.14	0.32	3.3	0.401	3.35
		mean	132	424	1430	15.7	163	7.47	704	417	0.681	110	14.9	15.3	0.133	44.4	10	0.638	0.339	0.41	0.126	0.386	0.065	1.72	0.122	0.472
		GM	41.1	395	1050	13.7	95	6.3	670	415	0.642	109	14.7	15.2	0.121	41.7	9.79	0.517	0.106	0.121	0.064	0.23	0.057	1.68	0.109	0.051
		Std	314	204	1440	10.2	254	6.51	256	37.4	0.28	15.6	1.99	2.03	0.078	17.1	2.21	0.597	0.659	0.894	0.21	0.472	0.056	0.457	0.073	0.776
LCD22A	Hm	min	0.627	217	107	<4.34	28.6	2.3	4.7	5.75	<0.24	3.12	<0.011	0.58	0.049	<0.18	3.19	10.5	0.207	0.014	<0.001	<0.004	0.341	6.22	2.41	0.079
	(n=19)	max	84.1	1930	973	14.1	862	12.6	160	148	0.53	100	1.46	32.4	51.3	4.31	47.6	90.2	3.03	0.299	2.09	23.6	11.8	348	56.6	3.72
		mean	15.1	1240	443	8.11	145	5.17	59.9	52.5	0.335	15.6	0.318	8.91	3.03	1.56	23.6	48.7	1.25	0.1	0.189	1.55	2.89	89.4	23.4	1.64
		GM	8.12	1070	379	7.36	82.9	4.57	40.2	41.5	0.326	9.33	0.174	6.1	0.198	1.08	20.7	42.3	0.964	0.066	0.05	0.216	2.23	51.7	18	1.23
		Std	20.2	520	226	3.68	203	2.89	50	36.3	0.084	22	0.377	8.11	11.7	1.24	11.1	24.3	0.918	0.093	0.467	5.34	2.45	103	15.3	1.07
LCD22A	Mrt	min	3.4	415	59.5	<4.76	<27.1	3.75	1270	464	<0.23	11.4	0.335	8.61	<0.061	0.52	22.9	48.4	0.477	0.036	0.015	0.213	1.33	1.5	5.16	0.056
	(n=8)	max	18.3	1140	485	14.7	104	8.94	2050	604	0.9	22.1	1.12	21.9	0.86	5.23	42.3	179	5.16	0.383	0.208	2.06	12.9	4.91	24.8	6.35
		mean	9.58	676	310	7.11	56	5.19	1570	517	0.365	17.4	0.62	16.1	0.249	1.94	27.9	97.6	1.89	0.132	0.066	1	6.72	3.35	13.9	2.7
		GM	8.22	644	258	6.57	51.2	5.01	1550	515	0.33	17	0.568	15.4	0.174	1.55	27.3	88.8	1.36	0.099	0.048	0.712	5.08	3.15	12.3	1.6
		Std	5.32	231	154	3.44	25.5	1.64	247	51.5	0.22	4.22	0.292	4.92	0.263	1.51	6.36	48	1.59	0.114	0.064	0.715	4.68	1.19	7.07	1.97
MV058	Hm	min	0.54	237	176	<23.7	139	4.43	<0.92	0.298	<0.88	1.17	0.013	0.85	<0.25	0.75	5.22	4.4	0.019	0.01	<0.001	<0.001	0.493	0.61	1.66	<0.001
	zoned	max	7.07	1350	652	36.1	231	24.6	1120	173	1.59	63.1	0.086	63.9	0.57	0.96	18.4	117	1.57	1.9	1.04	29.6	37.2	557	185	9.12
	(n=10)	mean	2.78	688	392	27.5	192	11.9	134	36.1	1.14	12.7	0.044	8.86	0.338	0.862	10.5	28.3	0.382	0.403	0.144	3.95	5.9	327	31.6	1.44
		GM	1.95	595	352	27.2	191	10.4	7.85	13.3	1.13	5.4	0.038	3.39	0.328	0.859	9.89	17.2	0.153	0.146	0.015	0.084	2.36	179	12.8	0.196
		Std	2.37	387	178	3.96	26.5	6.59	348	52.4	0.198	19.3	0.023	19.4	0.094	0.07	3.69	33.8	0.524	0.601	0.32	9.21	11.2	172	55.8	2.77
MV058	Mrt	min	5.91	88	97.6	<3.68	<19.9	1.34	37.2	5.72	<0.17	20.7	1.11	3.33	<0.051	<0.77	12.6	1.3	0.171	0.099	0.015	0.346	0.183	10.7	0.396	<0.001
	(n=38)	max	211	744	783	34.9	1120	6.41	1490	377	1.66	296	51.3	78.7	51.1	18.5	31.2	147	5.78	3.16	0.474	4.15	37.7	892	15.3	351
		mean	68	332	303	13.8	179	3.95	541	69	0.561	72.9	6.86	23.3	1.83	4.53	21.6	18.6	1.25	0.878	0.129	1.61	5.41	112	3.77	13.7
		GM	46	294	263	10.6	124	3.63	368	39	0.407	58.1	4.79	16.5	0.413	3.44	20.7	13.2	1.04	0.678	0.095	1.42	2.94	52	2.7	3.3
		Std	52.4	153	173	9.56	186	1.47	410	81.7	0.475	60.1	8.8	20.1	8.22	3.85	6.05	23.2	0.923	0.646	0.106	0.842	6.93	191	3.14	56.6
MV058	Si-Mt	min	14.5	284	580	<4.15	119	2.1	423	110	<0.21	82.8	1.28	10.7	<0.059	13.7	12.7	<0.16	<0.001	0.065	<0.001	0.106	<0.001	1.82	<0.034	<0.001
	(n=41)	max	3710	3350	21700	45.1	7330	79.6	2550	561	1.71	231	22	19.8	48.8	69.4	46.4	11.9	55.3	138	3.82	14.1	0.33	112	1.9	94.6
		mean	1200	827	5630	16.9	1250	21.6	1260	345	0.709	120	4.18	14.4	3.39	28.8	20.6	1.6	6.36	15	0.853	2.35	0.07	23.7	0.345	12.4
		GM	606	717	4000	12.2	771	15.5	1170	326	0.534	117	3.04	14.2	0.601	27	19.8	0.731	1.32	3.45	0.446	1.33	0.053	12.4	0.176	1.95

Sample	Type		Mg	Al	Si	P	Ca	Sc	Ti	V	Cr	Mn	Co	Ni	Cu	Zn	Ga	As	Sr	Y	Zr	Nb	Mo	Sn	Sb	Ba
		Std	1100	530	4820	12.6	1480	17	443	108	0.532	30.5	4.5	2.21	9.03	10.9	6.52	2.41	11.5	27.6	0.802	2.81	0.058	27.9	0.398	22.4
MV059	Mrt	min	1.39	67.4	<27.8	<3.73	<19	0.244	<0.4	0.082	<0.2	2.9	<0.006	<0.061	<0.027	<0.15	1.57	<0.19	0.006	0.004	<0.001	0.014	0.147	2.33	0.138	<0.001
	(n=17)	max	70.6	2200	737	21.8	355	28.5	1140	722	0.66	64.3	6.88	23.4	5.09	3.66	49.2	91.1	1.34	1.58	1.62	25.4	38.5	1130	61.9	3.79
		mean	12.7	515	189	9.69	52.1	4.85	296	188	0.315	11.6	1.75	6.94	0.737	0.945	16.6	21.3	0.523	0.157	0.327	4.95	4.31	269	9.76	0.936
		GM	6.24	322	137	8.04	34.8	2.48	82.8	22.8	0.293	7.62	0.188	1.44	0.159	0.614	9.46	6.34	0.197	0.039	0.088	0.771	1.16	72.3	2.02	0.118
		Std	19.1	552	170	6.09	79.6	6.68	382	231	0.133	15.5	2.5	7.51	1.55	0.945	14.9	28.1	0.489	0.375	0.439	8.72	9.18	335	16.6	1.16
MV059	Si-Mt	min	5.76	166	344	<4.07	<24.6	3.34	156	209	<0.23	75	0.768	10.3	<0.044	13.6	9.87	<0.16	0.026	0.037	0.021	0.053	<0.001	0.94	<0.036	<0.001
	(n=35)	max	2690	1560	9990	15.9	1840	47.2	2890	616	0.46	259	68.2	22.6	38.2	49.8	23.6	1.76	4.21	16.4	1.34	4.91	0.192	18.1	0.35	7.45
		mean	307	419	2110	7.72	317	9.9	822	365	0.301	126	6.49	15.1	4.35	26.1	14.6	0.375	0.809	2.14	0.231	0.72	0.048	2.51	0.095	1.21
		GM	82	362	1530	6.96	138	7.34	574	352	0.297	117	3.48	14.7	0.353	24.8	14.2	0.306	0.279	0.531	0.105	0.401	0.036	1.77	0.078	0.159
		Std	595	282	2130	3.61	467	10.1	739	97	0.056	50.6	11.5	3.54	10.4	8.82	3.56	0.316	1.29	3.89	0.347	0.993	0.038	3.59	0.073	1.99
MV060	Hm	min	0.362	285	344	<2.43	<19.9	1.8	1.02	37.5	<0.14	0.914	0.047	0.295	<0.044	<0.2	4.04	0.52	<0.007	0.006	0.007	0.019	0.113	7.08	0.159	0.122
	zoned	max	4.91	1560	1450	21.3	192	139	1700	470	0.2	24.1	0.527	12.5	0.14	1.67	12.5	100	1.07	0.653	0.487	15.1	174	610	24.9	2.21
	(n=13)	mean	2.25	921	838	7.21	47.8	43.9	322	194	0.156	8.75	0.234	2.72	0.073	0.474	6.97	33	0.444	0.269	0.165	2.88	43.5	280	6.85	0.975
		GM	1.8	773	758	5.83	35.5	15.3	82.8	155	0.155	5.37	0.182	1.68	0.068	0.386	6.59	16.3	0.268	0.129	0.091	0.875	6.15	173	3.08	0.696
		Std	1.32	509	373	5.28	49.3	51.8	484	126	0.017	7.27	0.161	3.25	0.031	0.392	2.46	30.8	0.342	0.244	0.151	4.41	53.6	196	7.26	0.689
MV060	Mrt	min	19.1	255	122	1.81	<14.7	4.53	728	416	<0.083	36.1	4.89	8.66	<0.046	2.9	12.2	0.262	0.143	0.007	<0.001	0.007	0.026	1.29	<0.019	<0.001
	(n=20)	max	1310	1000	1190	15	2420	16.3	1480	569	0.26	430	68.3	34.1	283	63.6	23.9	7.49	2.21	0.862	0.967	2.71	29.8	30.7	1.16	3.89
		mean	187	463	518	6.32	166	8.03	1030	491	0.148	137	13.5	12.4	18.4	22.1	18	2.58	0.7	0.304	0.219	0.677	7.55	5.61	0.445	1.11
		GM	116	429	394	5.59	44.4	7.64	1010	489	0.136	117	10	11.8	0.307	14.7	17.6	2.01	0.509	0.156	0.044	0.232	1.8	3.59	0.269	0.486
		Std	277	203	358	3.15	531	2.76	242	40.5	0.064	87.4	15	5.27	64.6	18.4	3.63	1.83	0.608	0.279	0.309	0.773	9.46	7.25	0.371	1.15
MV060	Si-Mt	min	15.7	137	491	<1.96	<15	6.98	163	137	<0.09	76.2	1.23	9.97	<0.055	15.6	10.1	<0.112	0.045	0.054	0.015	0.035	<0.001	0.826	<0.022	<0.001
	(n=39)	max	2230	960	8860	14.7	2300	55.5	1660	628	0.43	287	78.2	24.4	151	103	32.5	2.33	12.2	25.1	1.27	3.99	0.98	4.75	0.476	15.2
		mean	476	510	2740	5.4	497	17.4	862	376	0.157	131	10.1	15.3	9.63	43.1	18.7	0.476	2.1	4.37	0.208	0.874	0.103	2.21	0.069	3
		GM	240	462	2160	4.47	235	15.3	630	354	0.147	125	5.91	14.9	0.389	40.3	18	0.293	0.801	1.7	0.129	0.543	0.042	2.06	0.047	0.915
		Std	555	209	2080	3.41	571	10.6	572	118	0.068	46.6	13.7	3.39	28.5	16.6	4.98	0.583	3.09	6.64	0.275	0.93	0.178	0.867	0.09	4.15
MV061	Mrt	min	21.8	240	<31.5	<3.7	<20.3	5.21	533	562	<0.2	52.2	0.684	15.9	<0.036	1.68	13.6	0.33	0.213	<0.003	<0.001	<0.003	0.021	1.2	<0.032	<0.001
	(n=29)	max	343	752	1250	153	456	22.1	4190	767	2.57	230	26	67.1	13	13.8	33.8	25.7	1.35	1.55	0.162	6.31	12.4	4.28	1.93	16.5
		mean	120	411	203	12.3	51.5	12.7	1300	667	0.516	98.8	8.98	29.1	0.617	6.41	22.8	3.42	0.647	0.156	0.015	0.547	0.984	2.04	0.281	1.48
		GM	98.4	390	151	7.23	36.6	11.9	1170	665	0.395	93.6	6.43	27.4	0.103	5.81	22.3	2.2	0.585	0.062	0.005	0.11	0.271	1.9	0.164	0.61
		Std	76.1	140	223	27.3	80	4.53	699	60.5	0.512	35.3	7.43	11.5	2.4	2.82	5.12	4.58	0.301	0.304	0.03	1.26	2.39	0.852	0.369	3.04
MV061	Si-Mt	min	69	468	842	<4.4	<28.3	9.32	1590	542	<0.19	96.9	4.33	18	<0.048	25.1	6.45	<0.18	0.023	0.107	0.03	0.025	<0.001	1.6	<0.037	0.128
	(n=22)	max	1620	1030	7050	15.7	1880	146	6020	738	0.71	161	25.7	31.7	33.9	78	12.6	0.41	3.93	5.2	0.989	2.13	0.112	4.02	0.181	7.55
		mean	398	667	2300	7.81	353	35.5	2560	643	0.386	114	6.55	23.9	2.58	51.3	8.27	0.251	0.774	1.13	0.288	0.439	0.057	2.42	0.064	1.2
		GM	281	650	2000	7.01	190	26.6	2430	641	0.362	113	5.95	23.6	0.225	48.8	8.14	0.244	0.524	0.7	0.216	0.277	0.045	2.35	0.059	0.675
		Std	398	161	1450	3.93	440	33.8	971	57.6	0.147	16.8	4.42	3.48	7.72	16.1	1.64	0.063	0.811	1.23	0.228	0.466	0.029	0.614	0.032	1.72
MV062	Hm	min	0.473	92.2	101	<3.75	<22.1	5.36	<0.29	<0.019	<0.2	1.57	<0.015	0.345	0.033	<0.122	0.723	4.5	0.026	0.008	<0.001	<0.001	0.309	<0.051	1.16	0.107
	(n=26)	max	77	3520	5150	16.4	179	360	572	370	0.88	70.1	1.75	55.2	26.5	6.02	5.08	320	2.86	1.87	3.7	3.94	7.46	93.3	56.8	15.5
		mean	14.9	1250	1690	7.79	61.6	104	137	41.1	0.291	25.2	0.504	8.47	3.15	1.7	2.13	103	1.09	0.483	0.749	0.812	2.24	9.19	21.8	4.9
		GM	7.34	764	1050	6.79	48.6	56.4	34.5	6.95	0.273	18.7	0.239	3.91	0.194	1.09	1.91	61.7	0.728	0.284	0.146	0.143	1.65	1.74	13.9	3.42
		Std	18.6	1070	1460	4.23	46.1	100	169	80.1	0.141	18.7	0.579	13	7.86	1.53	1.05	90.2	0.873	0.499	1.08	1.1	1.77	19.4	16.4	3.82
MV063	Mrt	min	66.5	224	69.7	<1.68	<11.2	10	445	657	<0.117	92.2	1.91	19.6	<0.046	3.37	11.2	0.54	0.192	<0.003	<0.001	<0.001	<0.016	1.05	0.03	0.134
	(n=25)	max	645	1240	1010	21.7	1090	46.6	3090	859	37.3	251	21.5	35.2	3.22	23.6	22.6	15.7	1.8	0.734	3.21	0.897	1.36	5.78	0.932	4.48
		mean	207	462	313	8.28	95.3	20.4	1470	758	8.62	137	6.48	25.8	0.321	9.04	16.5	3.81	0.76	0.147	0.202	0.18	0.404	2.21	0.263	1.33
		GM	168	413	233	6.95	35.3	19.1	1350	756	2.02	133	5.33	25.6	0.135	7.95	16.3	2.81	0.675	0.077	0.032	0.062	0.231	2.04	0.174	1.02
		Std	152	254	267	4.91	231	8.19	620	58.8	13.1	35.3	4.82	3.26	0.67	4.95	2.49	3.36	0.364	0.164	0.637	0.255	0.414	0.988	0.244	0.978
MV063	Si-Mt	min	292	500	1420	<4.84	67.3	10.1	1980	515	<0.24	117	10.9	26.3	<0.061	22.9	5.37	<0.23	0.864	1.79	0.121	0.158	<0.019	2.06	<0.053	1.03
	(n=10)	max	1400	867	6190	9.03	1820	65.7	3800	727	0.51	155	28.9	30.8	3.84	65.8	10	0.73	18.6	23.4	1.13	2.54	0.053	3.23	0.129	22.4
		mean	659	625	3220	5.84	592	28.9	2890	590	0.326	135	21.4	27.8	0.463	49.4	8.21	0.327	5.42	7.31	0.43	0.757	0.035	2.68	0.077	5.84
		GM	590	616	2950	5.7	404	24.6	2850	586	0.319	134	20.3	27.8	0.125	46.6	8.04	0.306	3.36	5.16	0.36	0.537	0.034	2.65	0.074	3.6
		Std	352	118	1480	1.42	553	18.1	507	74.7	0.075	12.4	6.26	1.43	1.19	15.7	1.67	0.15	5.96	7.23	0.291	0.761	0.01	0.405	0.026	7.08
MV065	Mrt	min	29.8	239	<32.6	<4.22	22.5	3.87	596	656	0.53	46	0.795	20.2	<0.041	1.63	16.9	<0.34	0.108	<0.002	<0.001	0.003	0.028	0.839	<0.047	<0.001
	(n=17)	max	346	962	847	18.9	69.2	7.63	1870	839	4.32	114	3.13	43.5	0.182	14.8	31.7	5.81	1.01	1.22	6.83	4.95	3.71	2.22	0.421	1.81
		mean	79.6	366	171	8.85	37.3	5.47	1100	783	1.76	70.2	1.99	25.3	0.068	5.12	27.6	1.43	0.397	0.159	0.755	0.533	0.441	1.43	0.119	0.311
		GM	64.6	345	122	7.8	34.5	5.37	1050	782	1.47	67.6	1.89	24.9	0.064	4.24	27.3	1.09	0.324	0.044	0.018	0.057	0.18	1.37	0.092	0.094
		Std	72.6	163	190	4.58	16.7	1.08	346	42.1	1.1	20.7	0.631	5.45	0.032	3.64	3.89	1.3	0.266	0.299	2.06	1.21	0.883	0.42	0.104	0.429
MV065	Mrt	min	28.6	949	265	<4.34	<27.2	1.41	914	660	51.3	76.2	2.74	19	<0.055	19.6	8.78	0.65	0.426	0.058	0.501	0.416	0.566	1.4	0.045	0.226
	a. magmatic Mt	max	399	2050	2300	9.19	116	3.83	1680	744	72.5	123	4.07	25.9	0.761	53.1	10.3	2.45	1.68	14.8	36.9	11.2	1.71	1.94	0.325	5.14
	(n=5)	mean	175	1240	1020	5.65	72.1	2.36	1130	703	58.6	105	3.22	22	0.236	43.1	9.58	1.27	0.95	4.22	12.2	5.06	1.18	1.66	0.149	1.51
		GM	119	1190	745	5.43	63.3	2.24	1100	703	58.2	103	3.18	21.9	0.142	40.7	9.56	1.14	0.829	0.953	5.23	3.08	1.08	1.65	0.117	0.82
		Std	153	460	850	2	36.6	0.896	320	31	8.44	19.6	0.54	2.58	0.297	13.9	0.635	0.698	0.523	6.12	15	4.33	0.516	0.192	0.115	2.05
MV065	Mt	min	14.9	426	271	<5.18	<26.1	6.29	1120	756	63.7	119	5.18	24.5	<0.071	50	8.17	<0.2	<0.001	0.006	<0.008	0.002	0.125	1.4	<0.037	<0.001
	magmatic	max	94.5	500	458	11.9	79.7	7.86	2700	772	75.9	135	6.04	26.2	0.08	68	9.43	0.58	0.224	0.047	0.03	0.028	0.222	2.99	0.049	0.57
	(n=4)	mean	38.6	461	363	7.7	40.5	7.12	1790	762	71.5	125	5.55	25.6	0.075	59.4	8.71	0.32	0.062	0.019	0.018	0.01	0.189	2	0.041	0.152
		GM	29	460	356	7.27	35.8	7.1	1690	762	71.4	124	5.54	25.6	0.075	59	8.69	0.291	0.008	0.013	0.016	0.006	0.185	1.91	0.041	0.012
		Std	37.5	31.6	84.9	3.11	26.2	0.645	707	7	5.37	7.08	0.431	0.794	0.004	8.15	0.612	0.176	0.108	0.019	0.01	0.012	0.044	0.735	0.005	0.279

Table S9. (Continued) Summary statistics of LA-ICP-MS data for individual samples and Fe-oxide sub-types from the Distal satellite mineralisation - RD2316.

Sample		La	Ce	Pr	Nd	Sm	Eu	Gd	Tb	Dy	Ho	Er	Tm	Yb	Lu	Hf	Ta	W	Pb204	Pb206	Pb207	Pb208	Th	U	Pb	∑REY
LCD18	min	<0.001	0.004	<0.001	<0.001	<0.001	<0.002	<0.001	<0.001	<0.001	0.001	<0.001	0.001	<0.001	0.001	<0.001	<0.003	8	<0.011	0.005	<0.001	<0.008	0.003	<0.002	0.041	0.123
	max	3.23	8.19	0.761	2.57	0.708	0.124	0.735	0.148	0.899	0.14	0.339	0.056	0.488	0.055	0.567	29.1	3560	0.128	4.13	2.53	6.08	3.74	5.71	12.9	16.8
	mean	0.733	1.67	0.162	0.541	0.122	0.017	0.106	0.02	0.098	0.017	0.046	0.008	0.055	0.009	0.179	2.85	431	0.032	0.476	0.218	0.538	0.675	0.992	1.26	3.89
	GM	0.222	0.504	0.062	0.215	0.068	0.011	0.053	0.01	0.044	0.009	0.024	0.005	0.03	0.005	0.091	0.714	227	0.027	0.203	0.09	0.218	0.214	0.331	0.633	1.71
	Std	0.831	1.85	0.174	0.589	0.132	0.02	0.127	0.025	0.143	0.022	0.059	0.009	0.078	0.01	0.152	5.09	555	0.023	0.633	0.371	0.895	0.792	1.12	1.9	4.19
MV051	min	0.062	0.128	0.013	0.028	0.014	<0.001	0.006	0.001	0.008	0.001	<0.001	0.001	<0.004	<0.001	0.034	0.922	110	0.02	0.178	0.057	0.234	0.236	0.093	0.489	0.278
	max	2.13	3.81	0.352	1.04	0.341	0.065	0.348	0.064	0.379	0.072	0.193	0.042	0.244	0.034	0.475	5.3	920	0.109	2.22	1.4	3.26	1.81	3.15	6.96	8.96
	mean	0.967	1.96	0.194	0.65	0.175	0.025	0.174	0.033	0.2	0.034	0.095	0.016	0.113	0.015	0.251	2.65	298	0.055	1.19	0.716	1.7	1.01	1.91	3.66	5.29
	GM	0.803	1.64	0.165	0.535	0.145	0.019	0.13	0.025	0.156	0.026	0.066	0.011	0.082	0.011	0.215	2.45	249	0.05	1.04	0.598	1.47	0.913	1.61	3.17	4.38
	Std	0.47	0.886	0.084	0.269	0.082	0.015	0.087	0.017	0.1	0.019	0.053	0.011	0.067	0.01	0.119	1.07	209	0.023	0.525	0.353	0.795	0.416	0.764	1.69	2.3
MV052	min	0.002	0.002	<0.001	<0.001	<0.022	<0.001	<0.001	<0.001	<0.001	0.002	<0.007	<0.002	0.008	<0.002	<0.001	0.004	1.96	<0.012	<0.004	<0.007	<0.008	0.002	0.003	0.032	0.09
	max	7.59	13.3	1.09	3.6	0.73	0.102	0.555	0.097	0.661	0.13	0.322	0.044	0.379	0.058	1.07	24.4	1990	0.056	1.89	0.87	2.26	4.53	7.43	5.06	28.6
	mean	1.4	2.98	0.299	1.03	0.253	0.032	0.209	0.038	0.217	0.036	0.105	0.017	0.129	0.018	0.27	3.22	183	0.024	0.861	0.288	0.758	1.37	2.29	1.93	7.38
	GM	0.408	0.825	0.095	0.327	0.12	0.015	0.084	0.017	0.081	0.016	0.051	0.01	0.068	0.01	0.083	1.22	62	0.021	0.374	0.135	0.301	0.407	0.784	0.934	2.8
	Std	1.72	3.33	0.322	1.1	0.255	0.032	0.204	0.036	0.214	0.039	0.104	0.015	0.121	0.018	0.3	4.92	409	0.012	0.683	0.263	0.701	1.32	1.99	1.6	7.82
LCD19	min	<0.001	0.002	<0.001	<0.001	<0.001	<0.001	<0.001	<0.001	<0.001	<0.001	<0.001	<0.001	<0.001	<0.001	<0.001	<0.005	3.24	0.02	<0.005	<0.001	<0.004	<0.001	<0.003	0.04	0.047
	max	6.71	18.9	1.77	5.35	1.05	0.147	0.89	0.159	0.934	0.181	0.563	0.086	0.6	0.076	0.539	9.84	1330	0.103	2.77	1.32	3.3	6.87	4.83	7.45	35.8
	mean	1.27	3.16	0.31	0.97	0.244	0.026	0.189	0.029	0.177	0.029	0.09	0.014	0.106	0.015	0.154	3.35	182	0.035	0.576	0.234	0.561	1.08	1.38	1.41	7.1
	GM	0.178	0.326	0.051	0.152	0.063	0.009	0.059	0.009	0.037	0.008	0.023	0.006	0.035	0.007	0.071	1.74	77.1	0.031	0.124	0.047	0.091	0.132	0.27	0.402	1.51
	Std	1.73	4.52	0.431	1.37	0.31	0.038	0.262	0.042	0.268	0.048	0.15	0.021	0.164	0.021	0.142	2.88	288	0.019	0.786	0.379	0.928	1.66	1.69	2.07	9.49
MV053	min	1.13	2.05	0.231	0.671	0.339	0.042	0.238	0.06	0.336	0.058	0.273	0.039	0.257	0.028	0.054	0.126	9.91	0.023	1.63	0.43	0.878	1.43	5.5	2.96	7.1
	max	15.3	20.9	2.32	7.16	1.38	0.291	1.48	0.32	2.8	0.49	1.81	0.262	1.54	0.24	0.73	18.4	103	0.078	34.7	4.21	3.79	17.2	89.6	42.8	57
	mean	7.1	11.1	1.17	3.51	0.823	0.149	0.819	0.175	1.17	0.23	0.741	0.113	0.744	0.117	0.346	8.16	57.4	0.05	9.73	1.51	1.93	7.34	27.1	13.2	31.7
	GM	4.75	7.83	0.822	2.55	0.713	0.118	0.642	0.143	0.889	0.173	0.574	0.09	0.584	0.088	0.26	2.08	44.5	0.045	5.15	1.1	1.7	5.42	16.3	8.22	23.6
	Std	5.82	8.3	0.903	2.64	0.459	0.103	0.546	0.111	0.994	0.174	0.631	0.089	0.544	0.087	0.246	7.97	36.2	0.024	14	1.53	1.14	6.07	35.2	16.7	21.9
MV053	min	0.007	0.005	<0.002	<0.001	<0.001	0.004	<0.001	<0.001	<0.001	<0.001	<0.007	<0.001	0.009	0.002	<0.001	0.006	3.16	<0.014	0.008	<0.006	<0.007	0.006	0.007	0.035	0.092
	max	3.54	10.1	1.14	3.24	1	0.036	0.516	0.088	0.423	0.036	0.169	0.015	0.188	0.026	0.836	12.3	667	0.045	0.776	0.136	0.297	2.41	3.27	1.16	20.6
	mean	1.57	4.32	0.413	1.19	0.262	0.012	0.16	0.022	0.104	0.014	0.04	0.007	0.055	0.009	0.307	5.47	209	0.02	0.386	0.071	0.138	0.94	1.51	0.615	8.4
	GM	0.535	1.21	0.133	0.351	0.111	0.009	0.068	0.013	0.053	0.01	0.025	0.005	0.036	0.007	0.125	2.58	94.1	0.019	0.22	0.054	0.091	0.403	0.685	0.423	3.29
	Std	1.25	3.52	0.349	1.07	0.288	0.009	0.148	0.023	0.107	0.009	0.044	0.004	0.051	0.007	0.309	3.51	222	0.009	0.279	0.039	0.09	0.85	1.15	0.387	6.88
MV055	min	<0.002	0.003	0.001	<0.001	<0.001	0.001	<0.001	0.001	<0.001	0.001	<0.001	0.001	<0.001	0.001	<0.001	<0.001	1.18	<0.005	0.091	0.011	<0.003	<0.001	0.139	0.134	0.038
	max	1.81	2.62	0.193	0.626	0.095	0.029	0.223	0.035	0.267	0.076	0.241	0.034	0.301	0.049	0.233	0.247	1140	0.122	8.86	2.82	5.07	0.422	27.4	16.1	8.11
	mean	0.167	0.254	0.019	0.059	0.015	0.004	0.021	0.004	0.03	0.007	0.025	0.004	0.03	0.006	0.022	0.03	218	0.024	1.13	0.306	0.46	0.067	3.65	1.92	0.801
	GM	0.059	0.092	0.008	0.023	0.008	0.003	0.01	0.002	0.01	0.003	0.008	0.002	0.011	0.003	0.009	0.009	57.1	0.018	0.594	0.136	0.149	0.024	1.86	0.994	0.328
	Std	0.295	0.437	0.033	0.106	0.02	0.006	0.038	0.007	0.056	0.015	0.053	0.007	0.062	0.011	0.04	0.048	302	0.023	1.6	0.567	0.98	0.093	4.87	3.08	1.43
LCD21	min	0.001	0.002	0.002	<0.009	<0.009	<0.001	<0.001	0.001	<0.001	<0.001	0.003	0.001	<0.006	<0.001	<0.001	<0.001	2.23	0.009	<0.003	<0.003	<0.005	0.001	<0.001	0.046	0.07
	max	7.68	12.3	1.1	2.8	0.415	0.085	0.276	0.023	0.138	0.04	0.074	0.012	0.197	0.022	0.051	0.29	4980	0.074	73.2	8.26	0.499	3.18	287	81.9	23.9
	mean	1.77	3.1	0.268	0.72	0.098	0.02	0.052	0.007	0.035	0.008	0.022	0.003	0.037	0.006	0.011	0.049	1040	0.032	8.97	1.05	0.199	0.593	34.9	10.2	6.27
	GM	0.265	0.45	0.069	0.198	0.045	0.01	0.022	0.004	0.019	0.004	0.013	0.003	0.022	0.004	0.007	0.011	201	0.026	0.398	0.122	0.121	0.035	0.898	1.05	1.66
	Std	2.25	3.98	0.33	0.891	0.115	0.025	0.069	0.007	0.04	0.01	0.023	0.003	0.046	0.006	0.011	0.074	1470	0.019	19.6	2.19	0.157	0.985	77.3	21.9	7.81
MV056	min	0.289	0.615	0.049	0.15	<0.01	0.006	0.037	0.003	0.096	0.003	<0.005	<0.001	0.052	0.004	0.008	0.016	389	0.008	0.417	0.377	0.773	0.009	0.385	1.59	1.81
	max	3.27	4.92	0.355	0.89	0.209	0.09	0.206	0.058	0.449	0.11	0.38	0.067	0.538	0.092	0.154	0.872	3660	0.153	4.33	2.77	5.91	0.476	4.16	13.1	12
	mean	0.928	1.68	0.135	0.411	0.091	0.037	0.099	0.027	0.224	0.047	0.161	0.028	0.237	0.043	0.055	0.343	1590	0.087	2.45	1.49	3.24	0.18	2.68	7.27	5.13
	GM	0.806	1.5	0.121	0.366	0.075	0.032	0.088	0.022	0.208	0.04	0.135	0.023	0.205	0.038	0.043	0.281	1340	0.075	2.28	1.41	3.06	0.151	2.42	6.85	4.65
	Std	0.608	0.923	0.069	0.207	0.049	0.021	0.051	0.015	0.085	0.023	0.078	0.014	0.125	0.02	0.038	0.199	926	0.037	0.799	0.466	1.02	0.098	1	2.26	2.46
MV057	min	0.023	0.064	<0.002	<0.014	0.005	<0.001	<0.001	0.001	<0.004	<0.002	<0.001	<0.001	<0.001	0.002	<0.001	<0.001	0.038	0.01	0.051	0.014	0.02	0.001	0.013	0.127	0.175
	max	0.287	0.723	0.04	0.161	0.058	0.012	0.051	0.009	0.101	0.035	0.11	0.016	0.158	0.017	0.03	0.044	3.97	0.071	1	0.23	0.621	0.015	2.71	1.93	2.72
	mean	0.123	0.302	0.025	0.1	0.017	0.005	0.017	0.003	0.027	0.009	0.033	0.006	0.05	0.008	0.011	0.022	0.738	0.035	0.358	0.083	0.169	0.004	0.65	0.645	0.939
	GM	0.101	0.242	0.019	0.079	0.013	0.004	0.012	0.002	0.018	0.006	0.02	0.004	0.028	0.007	0.008	0.013	0.265	0.031	0.221	0.062	0.112	0.003	0.226	0.466	0.712
	Std	0.078	0.207	0.014	0.058	0.017	0.003	0.015	0.003	0.031	0.011	0.033	0.005	0.048	0.005	0.009	0.017	1.32	0.018	0.348	0.068	0.189	0.005	0.905	0.593	0.785
MV057	min	0.006	0.024	<0.001	<0.006	0.005	0.001	<0.001	<0.001	0.006	<0.001	<0.001	0.001	0.005	<0.001	<0.001	<0.001	0.394	<0.009	0.018	0.005	<0.005	<0.001	0.033	0.053	0.093
	max	83.4	145	14.6	59	9.83	3.67	9.46	1.29	7.8	1.7	6.21	0.901	5.53	0.982	0.075	0.191	108	0.16	5.91	2.55	4.81	0.026	2.39	13.4	377
	mean	11.3	19.9	2.02	8.12	1.48	0.609	1.51	0.194	1.09	0.246	0.814	0.101	0.702	0.113	0.01	0.02	11.3	0.05	0.509	0.217	0.396	0.006	0.667	1.17	55.8
	GM	0.613	1.25	0.102	0.361	0.081	0.024	0.078	0.013	0.083	0.02	0.061	0.011	0.081	0.015	0.005	0.006	2.91	0.037	0.173	0.062	0.102	0.003	0.393	0.433	3.44
	Std	21.3	37.6	3.83	15.8	2.85	1.14	2.9	0.386	2.17	0.481	1.67	0.222	1.41	0.237	0.017	0.042	24.6	0.04	1.28	0.554	1.05	0.007	0.583	2.91	105
MV057	min	0.01	0.035	0.004	<0.017	<0.001	<0.001	<0.001	0.002	<0.001	<0.001	0.005	<0.001	<0.012	0.002	<0.001	<0.001	<0.001	<0.018	0.006	<0.005	<0.007	0.001	0.006	0.042	0.201
	max	5.37	15.5	1.75	6.23	0.92	0.162	0.862	0.115	0.562	0.152	0.379	0.049	0.623	0.139	0.066	0.122	0.041	0.092	1.03	0.276	0.621	0.026	0.991	2.01	36.5
	mean	0.483	1.41	0.17	0.628	0.099	0.02	0.105	0.013	0.071	0.016	0.052	0.008	0.07	0.015	0.021	0.035	0.019	0.04	0.102	0.03	0.05	0.004	0.172	0.221	3.58
	GM	0.135	0.381	0.046	0.167	0.04	0.009	0.043	0.006	0.021	0.006	0.023	0.006	0.035	0.008	0.011	0.024	0.014	0.034	0.033	0.014	0.015	0.004	0.089	0.113	1.14
	Std	1.14	3.35	0.383	1.42	0.2	0.035	0.2	0.025	0.141	0.034	0.094	0.01	0.129	0.028	0.017	0.031	0.01	0.022	0.233	0.06	0.134	0.005	0.246	0.436	8.04
LCD22A	min	0.09	0.168	0.01	0.045	<0.001	<0.001	0.01	<0.001	0.006	<0.001	<0.001	0.001	<0.006	0.001	<0.001	<0.001	98.4	<0.01	0.153	0.03	0.035	0.007	0.422	0.308	0.426
	max	2.56	6.03	0.447	0.984	0.105	0.023	0.049	0.014	0.053	0.018	0.114	0.007	0.091	0.015	0.253	0.121	1510	0.096	3.88	0.603	0.847	0.176	4.83	5.21	10.3
	mean	0.882	2.31	0.168	0.377	0.042	0.008	0.021	0.004	0.021	0.005	0.023	0.003	0.028	0.006	0.027	0.009	521	0.043	0.94	0.226	0.336	0.074	2.31	1.55	4
	GM	0.659	1.69	0.114	0.28	0.029	0.006	0.019	0.003	0.017	0.003	0.014	0.002	0.02	0.004	0.008	0.003	373	0.036	0.708	0.168	0.245	0.052	1.88	1.21	3.03
	Std	0.609	1.55	0.117	0.256	0.031	0.007	0.011	0.003	0.015	0.005	0.026	0.002	0.026	0.004	0.058	0.027	425	0.025	0.825	0.166	0.245	0.055	1.34	1.16	2.61
LCD22A	min	0.443	0.693	0.047	0.115	<0.011	<0.001	<0.001	<0.001	<0.009	0.002	<0.004	0.001	<0.006	0.002	<0.007	0.013	26.8	0.014	0.589	0.113	0.061	0.027	1.61	1.02	1.57
	max	1.08	1.88	0.133	0.348	0.072	0.012	0.051	0.009	0.062	0.02	0.079	0.021	0.082	0.017	0.042	0.075	2150	0.136	2.43	0.804	1.21	0.176	7.07	4.54	3.73

Sample		La	Ce	Pr	Nd	Sm	Eu	Gd	Tb	Dy	Ho	Er	Tm	Yb	Lu	Hf	Ta	W	Pb204	Pb206	Pb207	Pb208	Th	U	Pb	∑REY
	mean	0.761	1.21	0.081	0.207	0.035	0.005	0.022	0.004	0.03	0.008	0.031	0.005	0.04	0.007	0.015	0.044	1080	0.058	1.04	0.326	0.506	0.087	2.96	1.93	2.58
	GM	0.731	1.16	0.075	0.191	0.028	0.004	0.015	0.003	0.026	0.006	0.024	0.003	0.028	0.005	0.012	0.036	528	0.046	0.936	0.274	0.369	0.076	2.65	1.7	2.47
	Std	0.225	0.39	0.033	0.09	0.022	0.004	0.016	0.003	0.016	0.006	0.023	0.007	0.03	0.006	0.012	0.026	811	0.039	0.597	0.221	0.374	0.045	1.77	1.17	0.815
MV058	min	0.074	0.14	0.018	<0.001	<0.001	<0.001	<0.027	<0.001	<0.001	<0.001	0.006	<0.001	<0.001	<0.001	<0.001	<0.001	84.1	<0.01	0.232	0.039	<0.01	<0.001	0.678	0.32	0.374
	max	2.06	6.67	0.643	1.85	0.431	0.031	0.196	0.02	0.256	0.083	0.406	0.078	0.629	0.142	0.033	0.024	2570	0.064	6.06	2.73	5.39	0.198	13.9	14.2	12
	mean	0.748	1.82	0.171	0.468	0.093	0.009	0.067	0.007	0.068	0.019	0.076	0.017	0.103	0.024	0.01	0.008	1210	0.019	1.36	0.525	0.995	0.051	3.26	2.9	4.1
	GM	0.465	1.11	0.1	0.193	0.031	0.005	0.056	0.005	0.029	0.008	0.027	0.006	0.02	0.007	0.004	0.005	893	0.015	0.834	0.195	0.204	0.019	2.24	1.42	2.64
	Std	0.734	1.92	0.189	0.534	0.128	0.01	0.049	0.007	0.082	0.026	0.125	0.024	0.195	0.043	0.012	0.008	825	0.016	1.76	0.853	1.71	0.067	3.88	4.31	3.79
MV058	min	0.391	0.571	0.046	0.099	<0.001	0.005	0.008	<0.001	0.025	<0.001	0.018	0.005	0.06	0.009	<0.001	<0.001	22.3	<0.009	0.563	0.249	0.271	<0.001	0.656	1.53	1.77
	max	3.91	7.62	0.816	2.43	0.56	0.25	0.88	0.168	1.28	0.208	0.565	0.1	0.85	0.132	0.066	0.073	4400	0.112	25.1	3.05	2.73	0.444	204	29	22.9
	mean	1.3	2.2	0.179	0.513	0.082	0.035	0.088	0.02	0.157	0.039	0.149	0.027	0.239	0.044	0.012	0.022	1030	0.044	5.03	1.08	1.41	0.055	20.5	7.57	5.96
	GM	1.12	1.85	0.148	0.421	0.045	0.025	0.055	0.013	0.104	0.025	0.113	0.021	0.198	0.036	0.005	0.016	625	0.038	2.92	0.916	1.27	0.022	5.71	5.61	5.05
	Std	0.763	1.4	0.134	0.391	0.094	0.04	0.14	0.027	0.208	0.038	0.119	0.021	0.16	0.028	0.015	0.017	893	0.022	6.1	0.657	0.613	0.091	40.1	6.66	3.92
MV058	min	0.019	0.041	0.012	0.05	<0.001	<0.001	<0.001	<0.001	<0.016	<0.001	<0.001	<0.001	0.016	<0.004	<0.001	<0.001	<0.001	<0.009	0.011	0.004	<0.004	0.001	0.049	0.052	0.322
	max	96.1	210	25.6	96.8	19.3	4.27	18.7	3.16	19.3	4.95	18	2.85	21.3	4.26	0.209	0.275	4.44	0.031	5.47	0.472	0.124	0.083	297	6.02	683
	mean	11.1	27.3	3.3	12.4	2.3	0.508	2.25	0.339	2.21	0.542	1.89	0.287	2.29	0.486	0.05	0.089	0.559	0.019	0.451	0.053	0.038	0.021	16.3	0.561	82.2
	GM	3.57	9.32	1.12	4.06	0.604	0.105	0.541	0.076	0.571	0.129	0.41	0.066	0.681	0.157	0.027	0.064	0.093	0.017	0.174	0.03	0.025	0.01	1.05	0.288	25.9
	Std	18.5	42.2	5.15	19.6	3.86	0.896	3.86	0.613	3.89	0.987	3.53	0.537	4.08	0.838	0.05	0.061	1	0.007	0.957	0.082	0.034	0.023	57.4	1.05	136
MV059	min	0.015	0.022	0.002	<0.001	<0.001	<0.001	<0.001	<0.001	<0.001	<0.001	<0.004	<0.001	<0.001	0.001	<0.001	<0.001	3.4	<0.008	0.08	0.013	<0.005	<0.001	0.086	0.123	0.121
	max	1.63	4.46	0.366	0.871	0.146	0.063	0.087	0.037	0.386	0.067	0.194	0.043	0.252	0.04	0.107	0.104	2280	0.077	21.3	3.36	3	0.407	103	27.8	7.9
	mean	0.397	0.865	0.073	0.181	0.035	0.009	0.02	0.005	0.041	0.007	0.023	0.005	0.034	0.006	0.025	0.026	418	0.019	2.78	0.459	0.438	0.055	11.5	3.7	1.86
	GM	0.206	0.385	0.029	0.071	0.019	0.005	0.014	0.003	0.011	0.003	0.01	0.002	0.013	0.003	0.008	0.016	146	0.015	0.784	0.172	0.153	0.016	1.81	1.28	0.954
	Std	0.41	1.13	0.101	0.231	0.043	0.015	0.02	0.009	0.092	0.016	0.046	0.01	0.06	0.009	0.033	0.028	615	0.018	5.47	0.847	0.735	0.103	25.7	7.02	2.22
MV059	min	0.024	0.108	0.012	0.055	<0.009	0.002	<0.001	<0.001	<0.006	0.001	<0.006	<0.001	0.009	0.002	<0.001	0.003	<0.001	<0.008	0.012	0.003	0.005	<0.001	0.027	0.052	0.426
	max	14.5	39.1	4.5	15.6	3.19	0.501	2.68	0.389	2.88	0.627	1.71	0.214	1.56	0.302	0.107	0.205	0.082	0.038	1.47	0.223	0.462	0.09	13.6	1.76	103
	mean	1.86	5.08	0.614	2.31	0.411	0.074	0.394	0.054	0.362	0.078	0.253	0.032	0.235	0.046	0.021	0.046	0.02	0.013	0.141	0.05	0.065	0.008	0.614	0.268	13.9
	GM	0.439	1.37	0.168	0.689	0.12	0.02	0.106	0.014	0.087	0.019	0.06	0.008	0.067	0.016	0.011	0.03	0.012	0.012	0.077	0.029	0.038	0.003	0.152	0.197	3.85
	Std	3.46	9.22	1.08	3.9	0.731	0.134	0.705	0.099	0.667	0.145	0.451	0.055	0.39	0.075	0.024	0.05	0.019	0.007	0.245	0.054	0.084	0.018	2.28	0.296	24.7
MV060	min	0.105	0.33	0.022	0.071	0.009	0.002	<0.008	<0.002	0.005	<0.001	0.004	<0.001	<0.005	<0.001	<0.006	<0.001	388	0.007	0.087	0.012	<0.007	0.002	0.278	0.148	0.635
	max	8.87	18.8	2.14	6.84	0.85	0.315	0.49	0.028	0.16	0.042	0.168	0.026	0.278	0.059	0.044	0.083	6180	0.041	1.71	0.627	1.26	0.102	5.93	3.48	39
	mean	1.7	3.19	0.307	0.982	0.109	0.031	0.068	0.01	0.06	0.015	0.052	0.009	0.092	0.016	0.019	0.013	2160	0.018	0.744	0.221	0.366	0.027	2.47	1.35	6.91
	GM	0.931	1.87	0.164	0.453	0.045	0.008	0.031	0.006	0.035	0.008	0.025	0.006	0.038	0.008	0.016	0.005	1590	0.015	0.456	0.11	0.125	0.015	1.56	0.767	4.05
	Std	2.34	4.81	0.554	1.8	0.225	0.086	0.129	0.009	0.053	0.014	0.056	0.009	0.1	0.017	0.012	0.023	1770	0.011	0.626	0.21	0.39	0.029	2.03	1.21	9.96
MV060	min	0.007	0.017	<0.001	<0.004	<0.001	<0.001	<0.001	0.001	<0.003	0.001	<0.001	0.001	<0.001	0.001	<0.001	0.001	0.051	0.004	0.077	0.062	0.111	0.001	0.005	0.317	0.067
	max	0.639	1.43	0.144	0.62	0.136	0.029	0.103	0.025	0.191	0.054	0.168	0.032	0.264	0.043	0.06	0.043	35.6	0.061	11.4	1.66	1.8	2.07	21.7	14.9	4.3
	mean	0.255	0.52	0.056	0.221	0.044	0.011	0.046	0.009	0.071	0.018	0.057	0.009	0.071	0.014	0.011	0.013	7.61	0.027	3.94	0.652	0.745	0.397	6.74	5.37	1.71
	GM	0.14	0.299	0.029	0.126	0.021	0.007	0.025	0.005	0.035	0.009	0.022	0.005	0.021	0.007	0.004	0.005	2.59	0.023	1.63	0.422	0.558	0.037	1.35	2.93	0.965
	Std	0.211	0.441	0.048	0.184	0.042	0.009	0.037	0.009	0.069	0.017	0.057	0.009	0.079	0.013	0.016	0.015	10.1	0.014	3.68	0.496	0.503	0.665	7.96	4.62	1.43
MV060	min	0.026	0.117	0.014	0.019	<0.01	0.004	0.011	0.002	0.008	0.001	0.006	0.001	0.016	0.001	<0.001	0.003	<0.001	<0.004	0.008	0.002	0.002	0.001	0.017	0.025	0.306
	max	10.9	27.4	3.5	14.9	3.27	0.955	4.07	0.618	4.37	1.11	3.74	0.6	5	0.897	0.088	0.219	0.887	0.034	3.01	1.24	1.96	0.095	4.09	6.23	101
	mean	1.99	5.48	0.717	3.05	0.656	0.161	0.746	0.105	0.699	0.172	0.579	0.086	0.651	0.129	0.019	0.055	0.107	0.015	0.254	0.062	0.081	0.018	0.507	0.411	19.6
	GM	0.998	2.83	0.364	1.47	0.3	0.065	0.314	0.045	0.276	0.059	0.189	0.028	0.225	0.047	0.011	0.035	0.032	0.013	0.087	0.014	0.013	0.007	0.246	0.146	9.18
	Std	2.44	6.46	0.855	3.76	0.862	0.239	1.07	0.155	1.1	0.281	0.965	0.148	1.15	0.215	0.018	0.053	0.197	0.008	0.541	0.201	0.315	0.025	0.727	1.04	26
MV061	min	0.014	0.045	0.002	<0.001	<0.001	<0.001	<0.001	0.001	<0.001	<0.001	0.002	0.001	0.004	<0.001	<0.001	0.001	<0.007	<0.009	0.041	0.034	0.074	<0.001	0.01	0.164	0.13
	max	3.64	6.84	0.654	2.02	0.365	0.04	0.286	0.035	0.207	0.079	0.234	0.042	0.422	0.062	0.022	0.248	12	0.125	4.13	2.41	4.7	0.371	2.82	11.4	16.4
	mean	0.344	0.613	0.049	0.154	0.031	0.005	0.029	0.004	0.03	0.008	0.03	0.006	0.049	0.008	0.005	0.023	1.9	0.028	0.65	0.397	0.795	0.055	0.321	1.87	1.52
	GM	0.133	0.258	0.018	0.058	0.015	0.003	0.013	0.003	0.013	0.004	0.015	0.003	0.021	0.005	0.003	0.006	0.544	0.022	0.354	0.274	0.568	0.013	0.124	1.25	0.685
	Std	0.717	1.3	0.122	0.37	0.066	0.008	0.054	0.007	0.043	0.015	0.052	0.01	0.101	0.013	0.005	0.051	2.74	0.026	0.893	0.45	0.857	0.1	0.584	2.2	3.13
MV061	min	0.107	0.492	0.064	0.236	0.016	0.012	0.034	<0.001	<0.01	0.004	<0.011	0.001	0.012	0.002	<0.001	0.005	<0.001	<0.009	0.046	<0.003	<0.004	<0.001	0.168	0.066	1.12
	max	11.5	30.4	3.44	12.5	2.32	0.35	2	0.237	1.07	0.153	0.335	0.041	0.343	0.113	0.185	0.075	0.049	0.02	0.661	0.129	0.222	0.032	1.05	0.893	70
	mean	1.77	4.84	0.564	2.13	0.382	0.065	0.367	0.048	0.202	0.034	0.076	0.011	0.101	0.029	0.032	0.034	0.012	0.012	0.15	0.02	0.024	0.006	0.406	0.206	11.8
	GM	1.01	2.88	0.338	1.37	0.239	0.047	0.244	0.025	0.11	0.021	0.051	0.007	0.072	0.02	0.017	0.028	0.008	0.012	0.105	0.012	0.01	0.004	0.362	0.147	7.33
	Std	2.48	6.63	0.749	2.69	0.481	0.073	0.42	0.056	0.245	0.037	0.078	0.011	0.092	0.026	0.041	0.02	0.01	0.003	0.165	0.028	0.052	0.007	0.216	0.223	15.2
MV062	min	0.102	0.228	0.013	0.046	0.006	0.002	<0.008	0.001	<0.007	0.002	<0.005	0.006	0.027	0.009	<0.001	0.001	<0.007	<0.008	0.093	0.057	0.096	0.002	0.252	0.255	0.506
	max	6.67	14.1	1.06	1.94	0.171	0.033	0.228	0.032	0.368	0.108	0.501	0.09	1.09	0.357	0.481	0.051	77.7	0.267	7.15	3.13	6.12	1.29	18.1	16.7	27.9
	mean	2.06	4.58	0.317	0.608	0.059	0.012	0.049	0.008	0.088	0.028	0.123	0.028	0.3	0.08	0.071	0.008	10.1	0.066	2.06	0.971	2.03	0.309	3.94	5.12	8.82
	GM	1.36	2.79	0.182	0.357	0.04	0.008	0.033	0.005	0.06	0.016	0.072	0.02	0.188	0.048	0.015	0.004	2.76	0.046	1.46	0.748	1.56	0.105	2.56	3.86	5.67
	Std	1.76	4.11	0.301	0.562	0.048	0.009	0.051	0.009	0.088	0.031	0.131	0.024	0.308	0.087	0.117	0.013	18.9	0.056	1.84	0.678	1.36	0.363	4.38	3.8	7.7
MV063	min	0.013	0.035	0.003	<0.009	0.006	<0.001	<0.004	0.001	<0.001	0.001	<0.001	0.001	<0.003	0.001	<0.001	<0.001	<0.001	<0.01	0.103	0.134	0.244	0.001	0.004	0.512	0.117
	max	0.981	1.39	0.119	0.291	0.079	0.02	0.092	0.012	0.112	0.027	0.088	0.012	0.134	0.029	0.036	0.094	3.06	0.085	1.32	1.05	2.38	0.57	1.45	4.64	3.37
	mean	0.297	0.511	0.042	0.106	0.025	0.005	0.024	0.004	0.03	0.007	0.023	0.004	0.028	0.005	0.008	0.013	0.595	0.039	0.588	0.456	0.999	0.082	0.316	2.08	1.26
	GM	0.179	0.335	0.027	0.073	0.019	0.004	0.018	0.003	0.017	0.005	0.014	0.003	0.018	0.003	0.003	0.006	0.206	0.034	0.478	0.394	0.861	0.021	0.169	1.78	0.842
	Std	0.272	0.422	0.035	0.086	0.021	0.005	0.021	0.003	0.031	0.007	0.021	0.003	0.029	0.007	0.011	0.021	0.81	0.021	0.371	0.249	0.548	0.143	0.368	1.16	1.03
MV063	min	0.473	1.28	0.167	0.85	0.259	0.053	0.285	0.037	0.308	0.071	0.249	0.017	0.107	0.035	<0.008	0.004	<0.008	<0.01	0.054	0.004	0.005	<0.003	0.185	0.076	6
	max	8.54	21.4	3	13.7	3.52	1.01	4.45	0.672	4.4	0.877	2.18	0.236	1.1	0.29	0.11	0.114	0.086	0.013	0.316	0.039	0.015	0.101	1.28	0.381	88.8
	mean	2.59	6.81	0.98	4.39	1.15	0.298	1.33	0.197	1.3	0.279	0.755	0.078	0.43	0.093	0.037	0.035	0.029	0.012	0.123	0.016	0.007	0.023	0.517	0.157	28
	GM	1.89	5.06	0.727	3.26	0.856	0.197	0.927	0.134	0.891	0.19	0.572	0.058	0.329	0.072	0.026	0.023	0.022	0.012	0.102	0.013	0.006	0.014	0.446	0.136	20.6
	Std	2.45	6.15	0.867	4	1.06	0.324	1.38	0.206	1.34	0.283	0.667	0.069	0.361	0.083	0.034	0.036	0.025	0.001	0.092	0.01	0.003	0.029	0.334	0.103	26.2
MV065	min	0.009	0.02	<0.002	<0.008	0.006	<0.001	<0.001	<0.001	<0.005	0.001	<0.004	0.001	0.004	<0.001	<0.001	0.001	<0.007	<0.007	0.035	0.021	0.052	<0.001	0.005	0.117	0.118
	max	0.25	0.488	0.052	1.15	0.078	0.015	0.066	0.018	0.138	0.053	0.181	0.029	0.178	0.033	0.116	0.033	1.34	0.041	2.17	0.481	1.21	1.48	4.83	3.59	2.77
	mean	0.071	0.143	0.014	0.111	0.024	0.004	0.021	0.005	0.028	0.008	0.033	0.006	0.036	0.006	0.016	0.008	0.173	0.019	0.386	0.195	0.476	0.177	0.456	1.08	0.669
	GM	0.038	0.082	0.008	0.034	0.019	0.004	0.014	0.003	0.017	0.004	0.015	0.003	0.016	0.003	0.004	0.003	0.062	0.017	0.204	0.143	0.335	0.014	0.082	0.725	0.381

Sample		La	Ce	Pr	Nd	Sm	Eu	Gd	Tb	Dy	Ho	Er	Tm	Yb	Lu	Hf	Ta	W	Pb204	Pb206	Pb207	Pb208	Th	U	Pb	∑REY
	Std	0.084	0.158	0.016	0.272	0.019	0.003	0.017	0.006	0.035	0.013	0.05	0.008	0.056	0.008	0.034	0.011	0.317	0.01	0.55	0.148	0.35	0.444	1.17	0.989	0.761
MV065	**min**	0.048	0.118	0.012	0.106	0.028	0.002	0.012	<0.002	0.016	0.002	0.006	<0.001	<0.006	<0.002	0.024	0.007	0.057	<0.009	0.489	0.256	0.657	0.346	0.226	1.41	0.423
	max	0.82	2.5	0.175	0.83	0.226	0.115	0.89	0.277	2.34	0.706	2.11	0.308	2.78	0.348	1.39	0.276	0.574	0.112	4	1.32	3.9	7.59	8.83	9.02	28.2
	mean	0.399	1.05	0.087	0.386	0.137	0.032	0.278	0.085	0.699	0.194	0.57	0.087	0.714	0.093	0.397	0.127	0.226	0.038	2.69	0.891	2.51	3.79	3.36	6.13	9.03
	GM	0.237	0.57	0.055	0.276	0.094	0.013	0.095	0.024	0.207	0.033	0.142	0.023	0.138	0.025	0.164	0.052	0.158	0.022	2.19	0.775	2.14	2.29	1.96	5.16	3.45
	Std	0.351	1.04	0.072	0.33	0.1	0.047	0.362	0.113	0.955	0.294	0.88	0.128	1.17	0.146	0.57	0.118	0.21	0.045	1.39	0.422	1.27	3.35	3.31	3.09	11.3
MV065	**min**	0.002	0.042	0.002	0.015	<0.001	0.002	0.006	0.002	0.004	0.001	<0.005	<0.001	<0.007	<0.002	<0.001	0.002	<0.009	<0.011	0.009	<0.002	<0.003	<0.003	0.051	0.028	0.126
	max	0.085	0.172	0.014	0.056	0.017	0.005	0.016	0.002	0.006	0.004	0.007	0.003	0.017	0.003	0.022	0.003	0.11	0.015	0.034	0.026	0.045	0.036	0.078	0.12	0.401
	mean	0.044	0.107	0.008	0.027	0.011	0.004	0.012	0.002	0.005	0.002	0.006	0.002	0.01	0.002	0.01	0.003	0.036	0.013	0.018	0.01	0.014	0.014	0.07	0.055	0.261
	GM	0.02	0.088	0.006	0.024	0.007	0.004	0.012	0.002	0.005	0.002	0.005	0.002	0.009	0.002	0.006	0.003	0.02	0.013	0.016	0.006	0.008	0.009	0.069	0.045	0.232
	Std	0.04	0.07	0.006	0.019	0.007	0.001	0.005	0.001	0.001	0.001	0.001	0.001	0.005	0.001	0.009	0.001	0.049	0.002	0.011	0.011	0.02	0.015	0.013	0.044	0.138

Mean corresponds to the arithmetic mean, whereas *GM* corresponds to the geometric mean; Std represents 1σ
Mt: magnetite; Hm: hematite; Mrt: martite; Si-: silician

ELECTRONIC APPENDIX C FOR CHAPTER 3

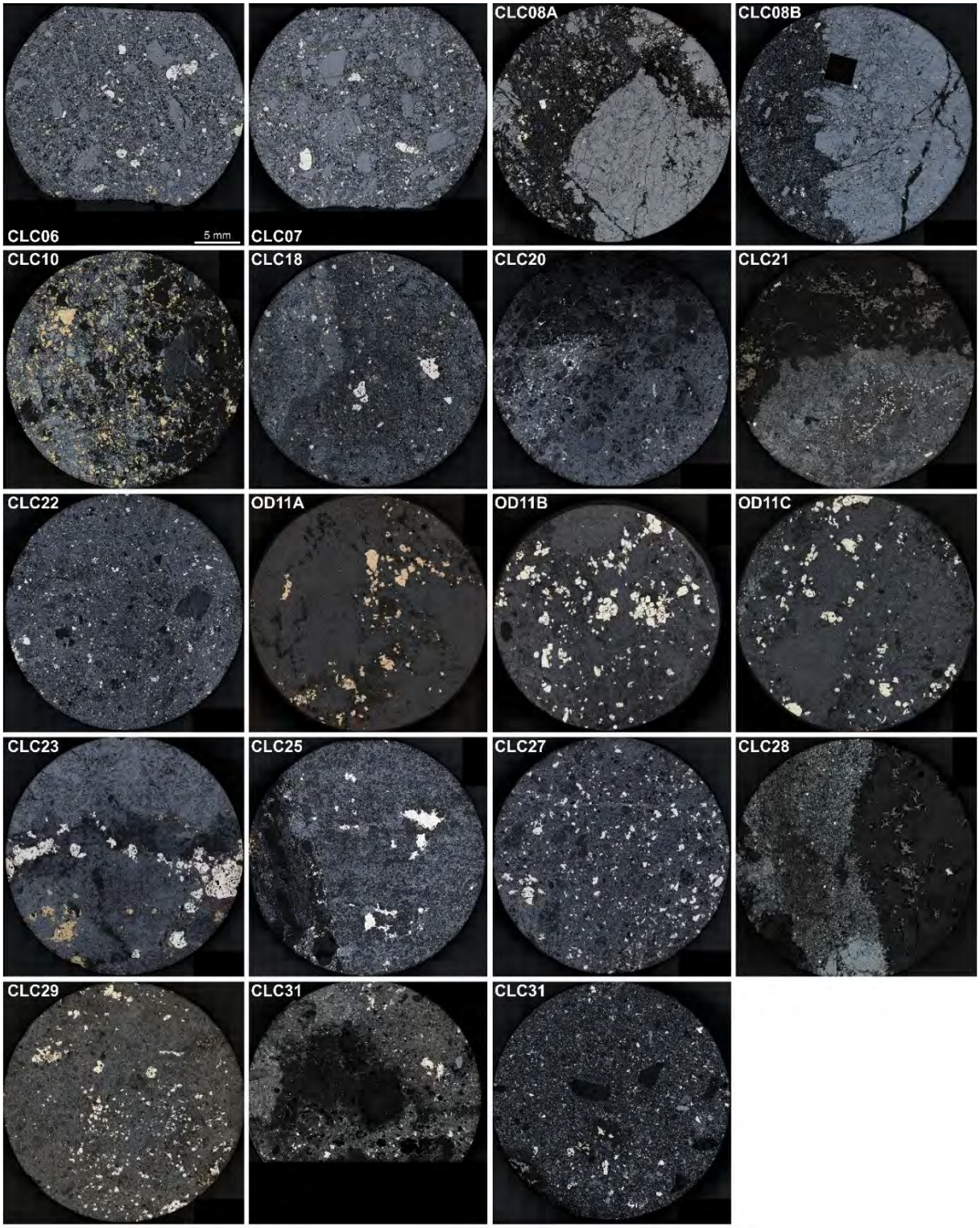

Fig. 1. Reflected light scans of one-inch polished blocks from the *Magnetite drillhole* (RU65-7976). Note the transition downwards on the page from hematite-rich samples (CLC06-CLC10) towards more magnetite-dominant samples. OD11 (A to C) correspond to the massive, siderite-hosted magnetite interval.

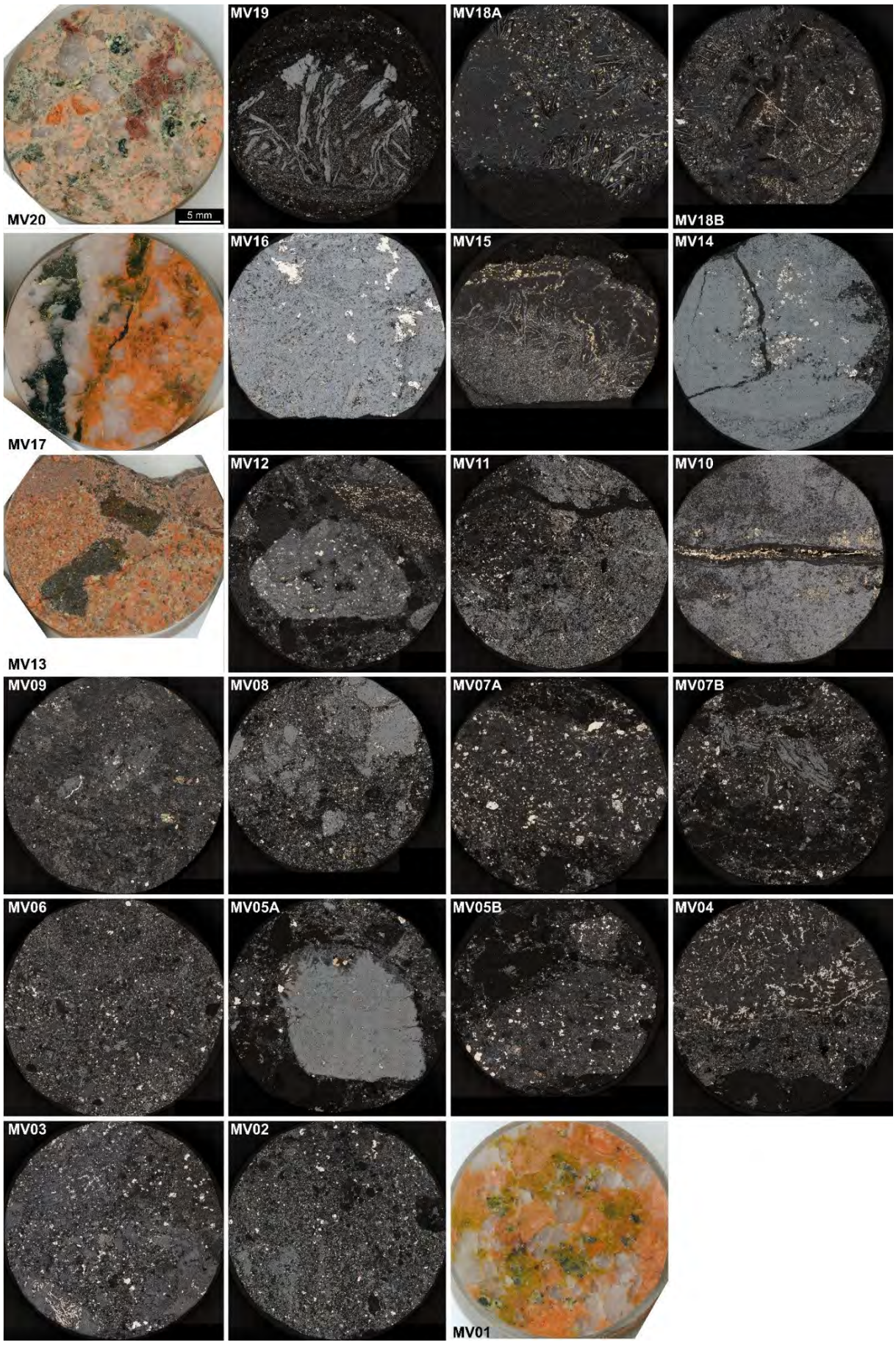
MV20
5 mm
MV19
MV18A
MV18B
MV17
MV16
MV15
MV14
MV13
MV12
MV11
MV10
MV09
MV08
MV07A
MV07B
MV06
MV05A
MV05B
MV04
MV03
MV02
MV01

Fig. 2. Optical and reflected light scans of one-inch polished blocks from the *Nodular Fe-oxide drillhole* (RD2366). Optical scans of altered granite samples were preferred, - given the lack, or low abundance of reflective, opaque minerals and due to the alteration becoming more apparent.

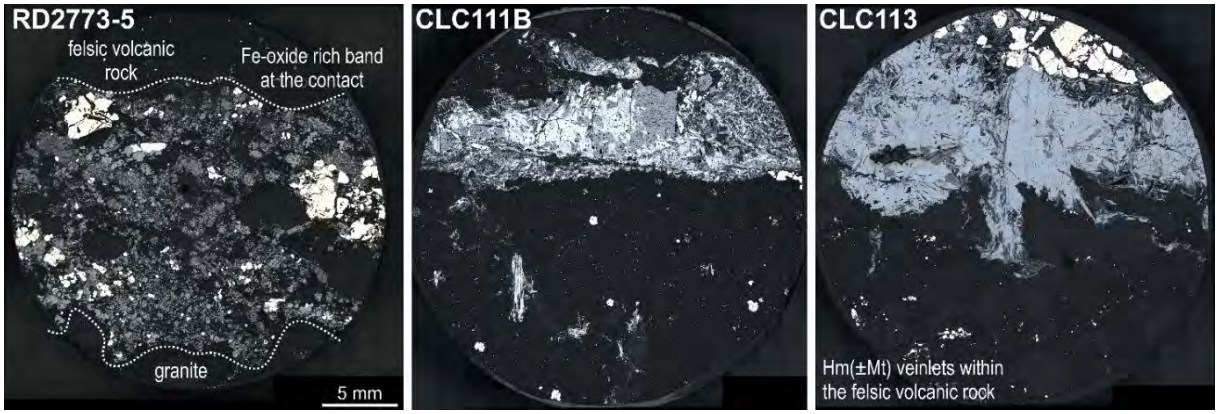

Fig. 3. Optical and reflected light scans of one-inch polished blocks from the *Deep mineralization* (DM; RD2773). Sample RD2773-5 displays an Fe-oxide rich, magnetite-bearing band at the contact of felsic volcanic clast, and brecciated granite, whereas samples CLC111B and -113 show typical aspects of hematite-rich veinlets within the altered, *Felsic unit*, and local mushketovitization.

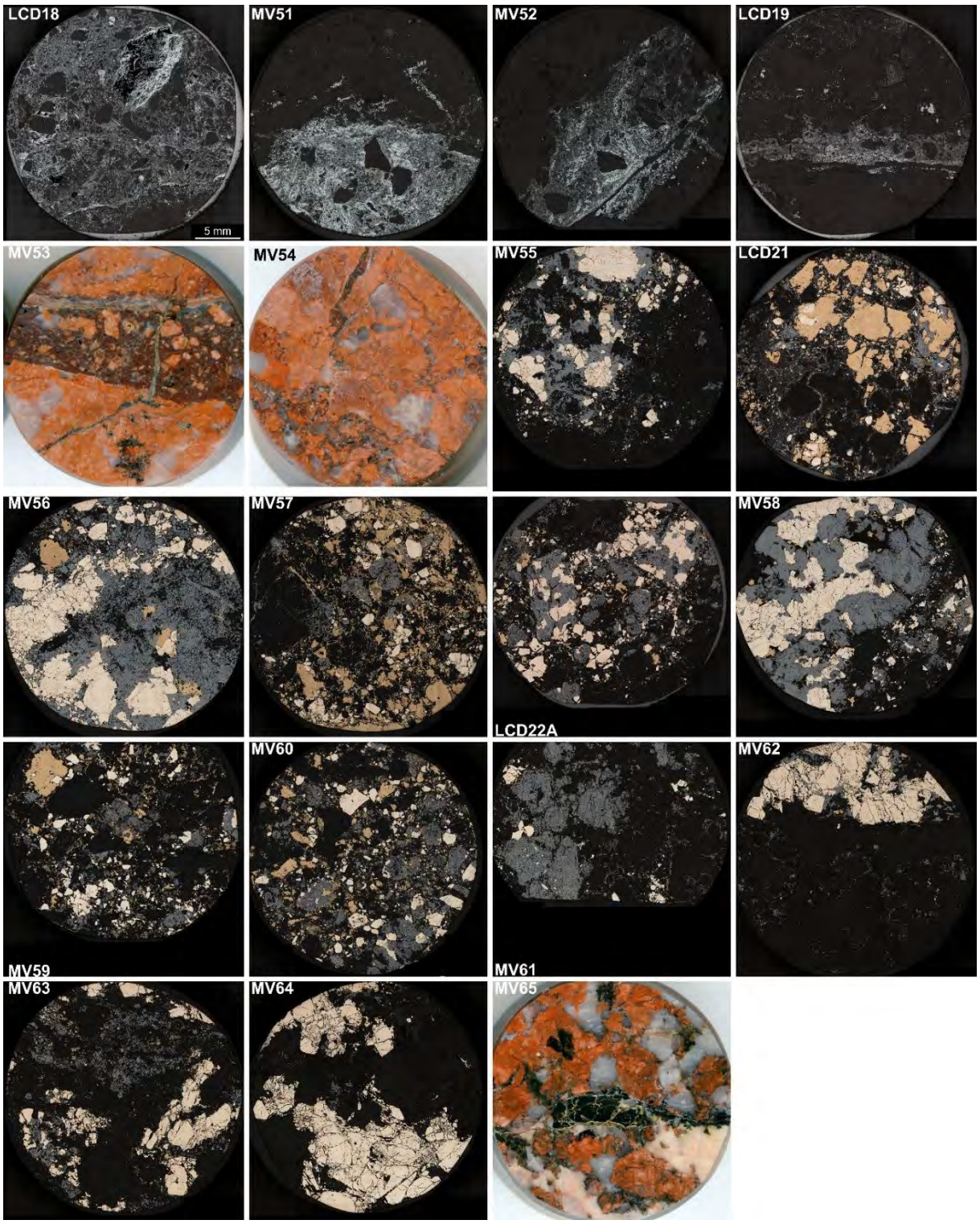

Fig. 4. Optical and reflected light scans of one-inch polished blocks from the *Distal satellite mineralization* (DSM; RD2316). Samples LCD18 to MV54 represent the upper section of the drillcore, where hematite-rich veins predominate, typically displaying elevated Ti-concentrations. Samples MV55 to -65 correspond to the lower, magnetite-bearing interval, where martitization can be locally observed. Fe-oxide rich mineralization mostly occurs as spread pockets within the granite, variably-enriched in Cu(-Fe)-sulfides.

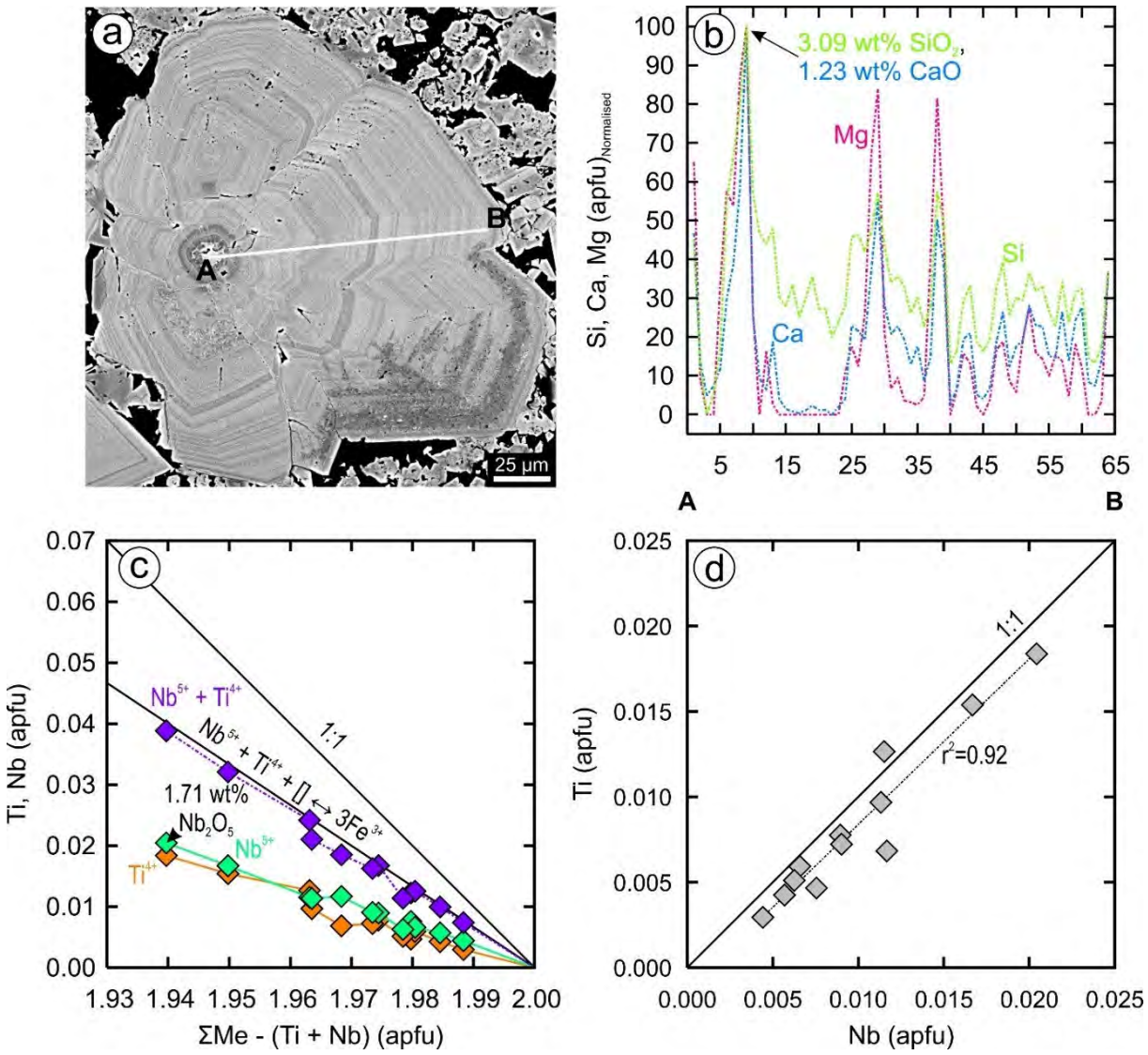

Fig. 5. (a) BSE-image of zoned magnetite from the massive, siderite-hosted, magnetite interval (sample OD11A; *Magnetite drillhole* - RU65-7976) showing transect location and (b) normalized elemental variation across the transect; maximum, individual Si, Ca and Mg apfu normalized to 100. Note the good correlation between Ca and Mg, which can be partially mimicked by Si at higher Mg+Ca concentrations. (c, d) Compositional variation in apfu of HFSE-rich hematite from the *Nodular Fe-oxide drillhole* (RD2366; sample MV19) in terms of: Ti and Nb, relative to ∑Me-(Si+Nb) (c), and linear correlation between Nb and Ti suggesting coupled substitution in hematite in (d).

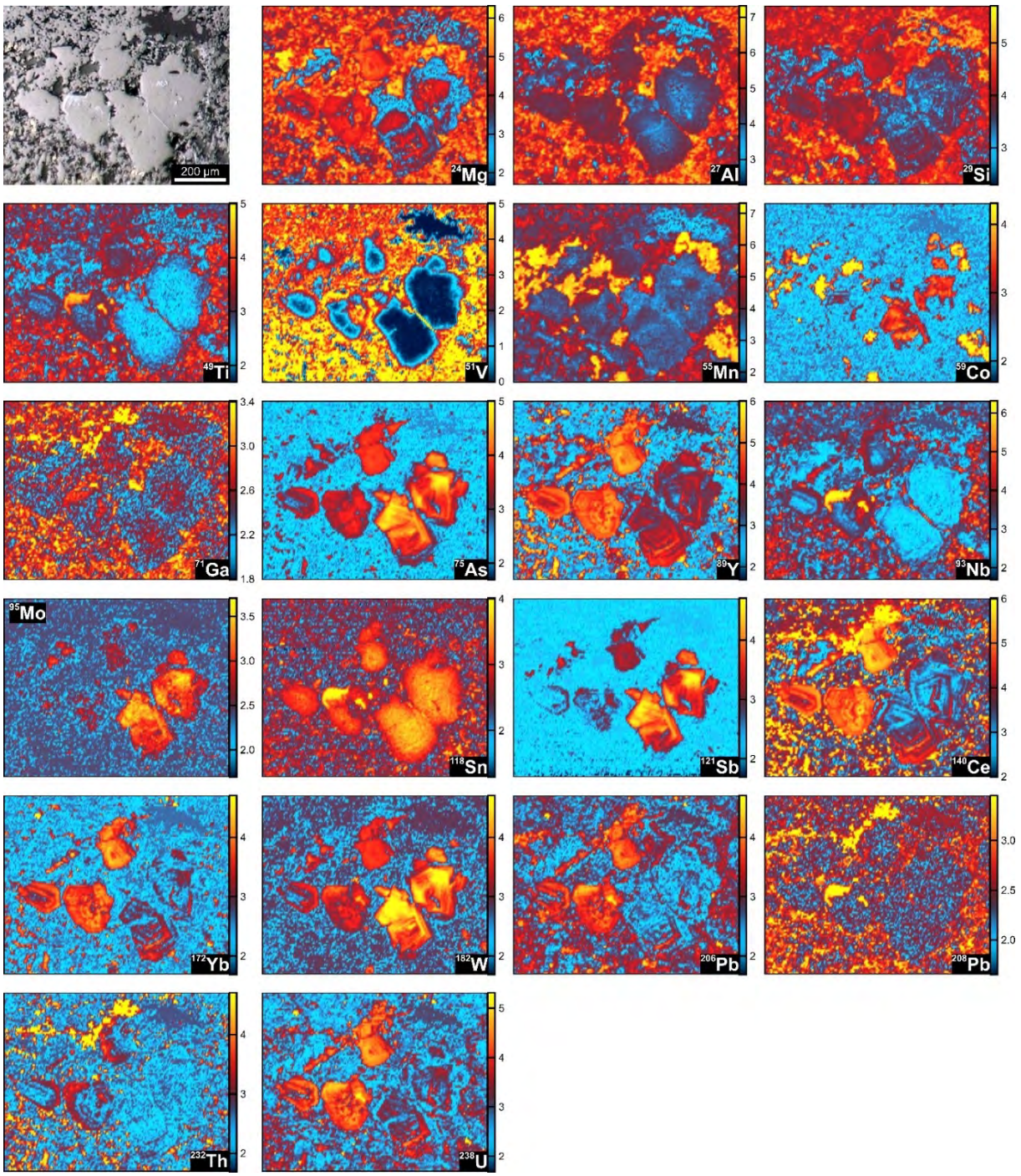

Fig. 6. Reflected-light micrograph and corresponding LA-ICP-MS elemental maps of Si-magnetite in the massive, carbonate-hosted magnetite interval (sample OD11A; *Magnetite drillhole* - RU65-7976). Note the marked compositional differences between adjacent, coarser grains in the fine-grained matrix. Intensities in counts-per-second (cps), logarithmically-scaled (10^n), except for ^{51}V (linear scale, $n \cdot 10^3$).

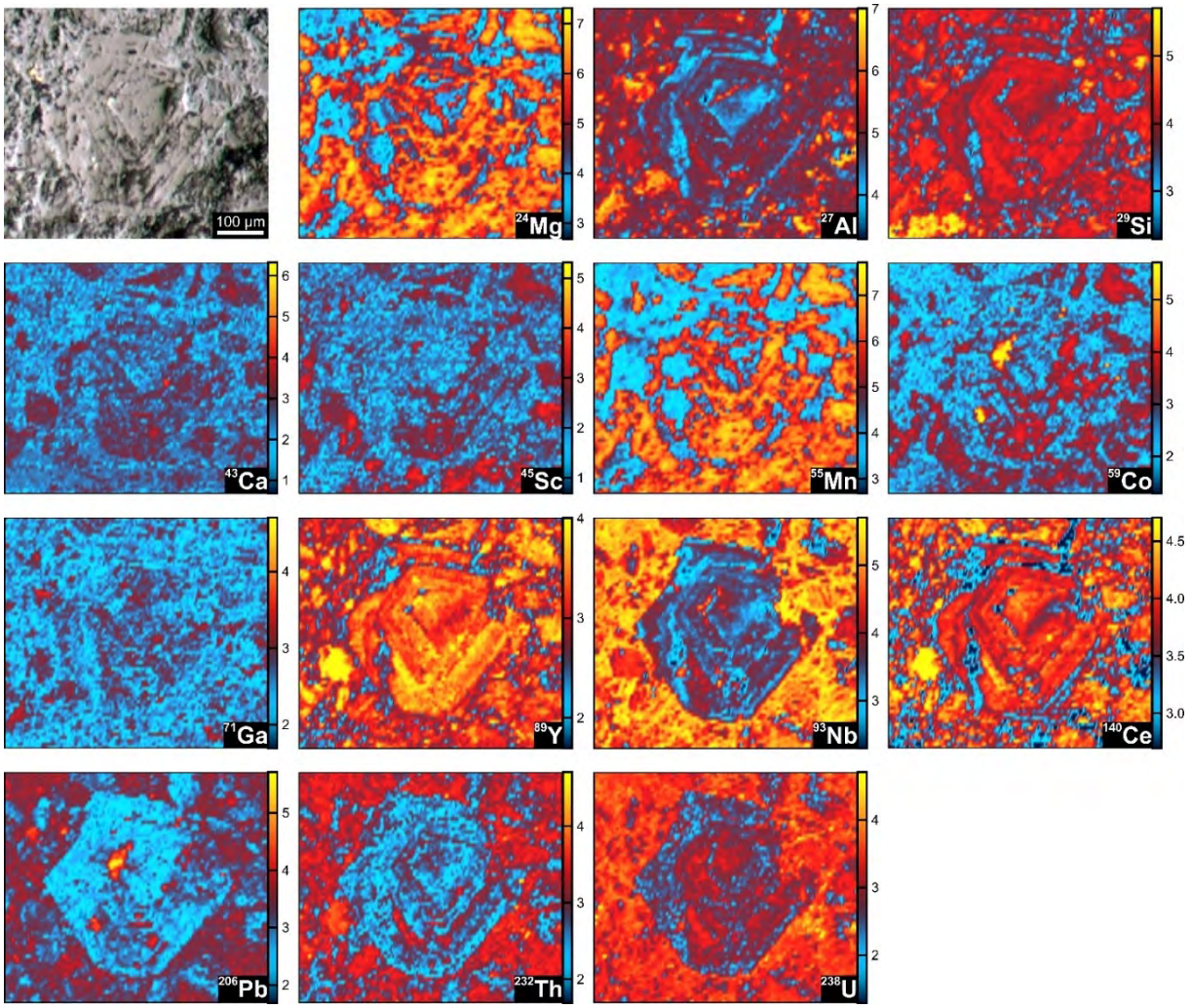

Fig. 7. Reflected-light micrograph and corresponding LA-ICP-MS elemental maps of overprinted Si-magnetite outside the massive, carbonate-hosted magnetite interval (sample CLC29; *Magnetite drillhole* - RU65-7976). Strongest enrichment in Y and Ce coincide with Si-rich domains. Logarithmically-scaled intensities (cps, 10^n).

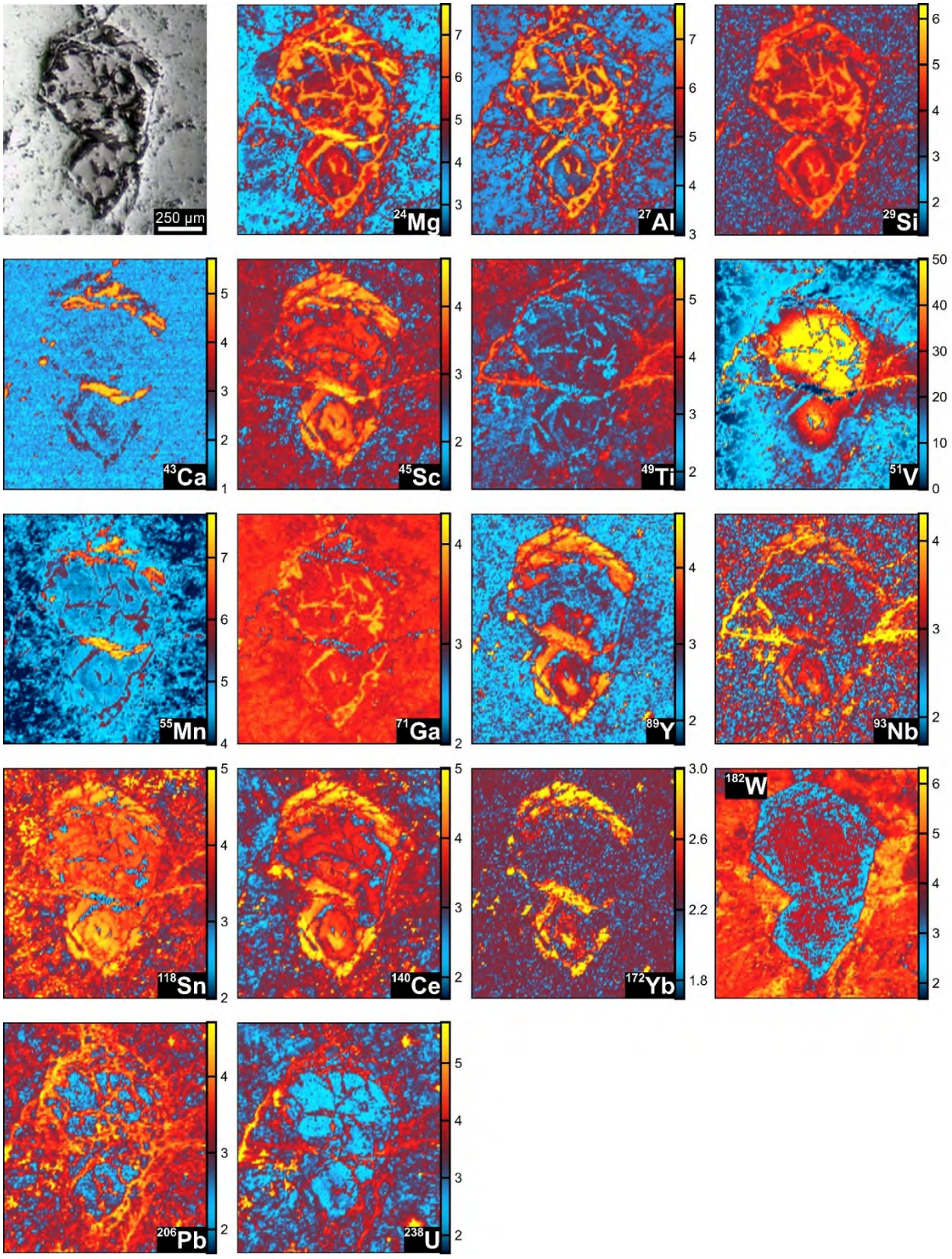

Fig. 8. Reflected-light micrograph and corresponding LA-ICP-MS elemental maps of Si-magnetite in hematite matrix (sample MV58; *Distal satellite mineralization* - RD2316). Note the marked compositional differences between hematite-matrix and the Si-magnetite, typically richer in HFSE. Logarithmically-scaled intensities (cps, 10^n), except for ^{51}V (linear scale, $n \cdot 10^3$).

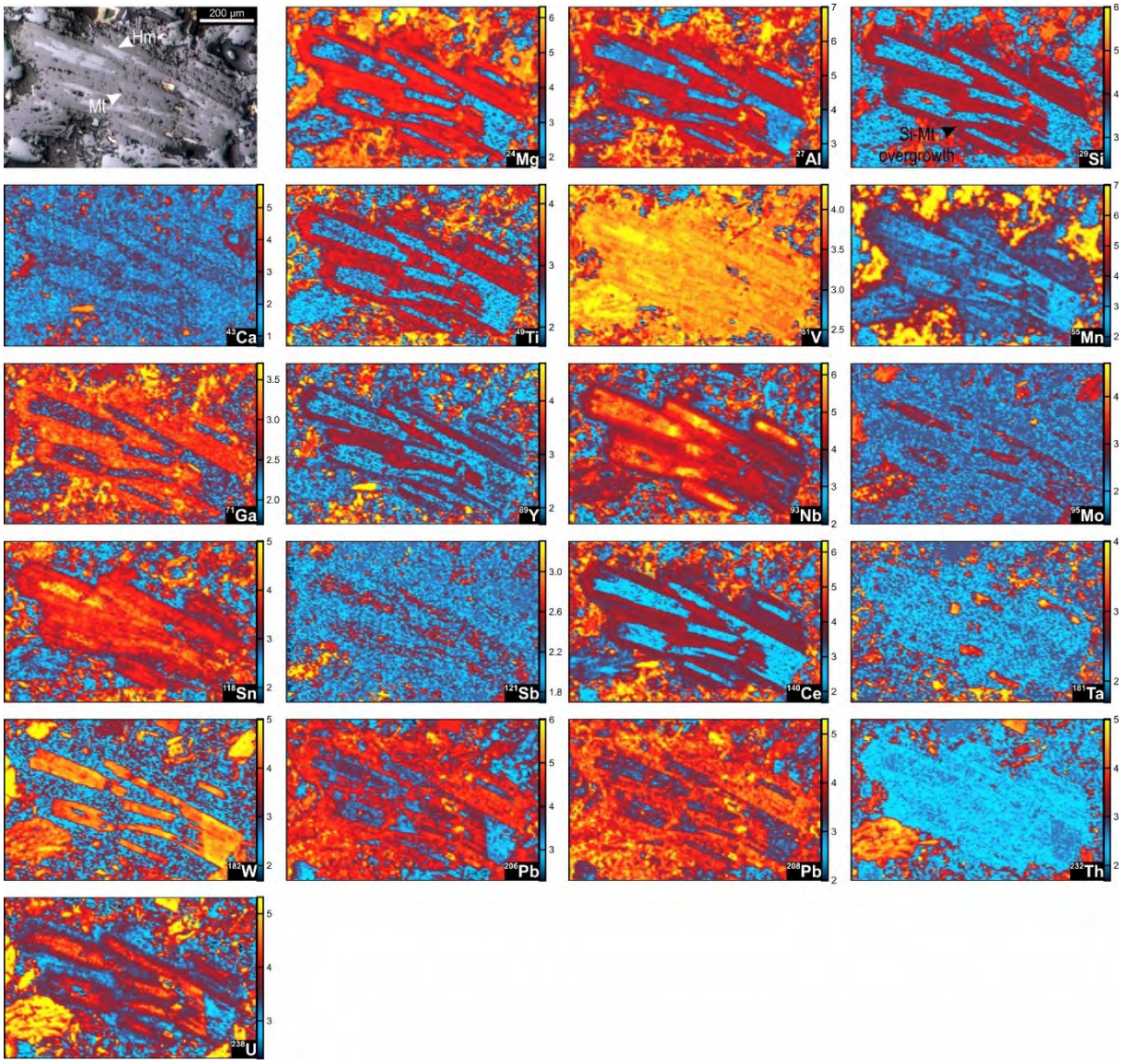

Fig. 9. Reflected-light micrograph and corresponding LA-ICP-MS elemental maps of a lamellar aggregate of Fe-oxide interconversion products displaying inner hematite domains, partially mushketovitized and Si-magnetite overgrowths (sample MV03; *Nodular Fe-oxide drillhole* - RD2366). Note the marked compositional differences predominantly between hematite/mushketovite and the Si-magnetite overgrowth, which is distinctly enriched in Mg, Al, Si, Ti, Y and Ce. Logarithmically-scaled intensities (cps, 10^n).

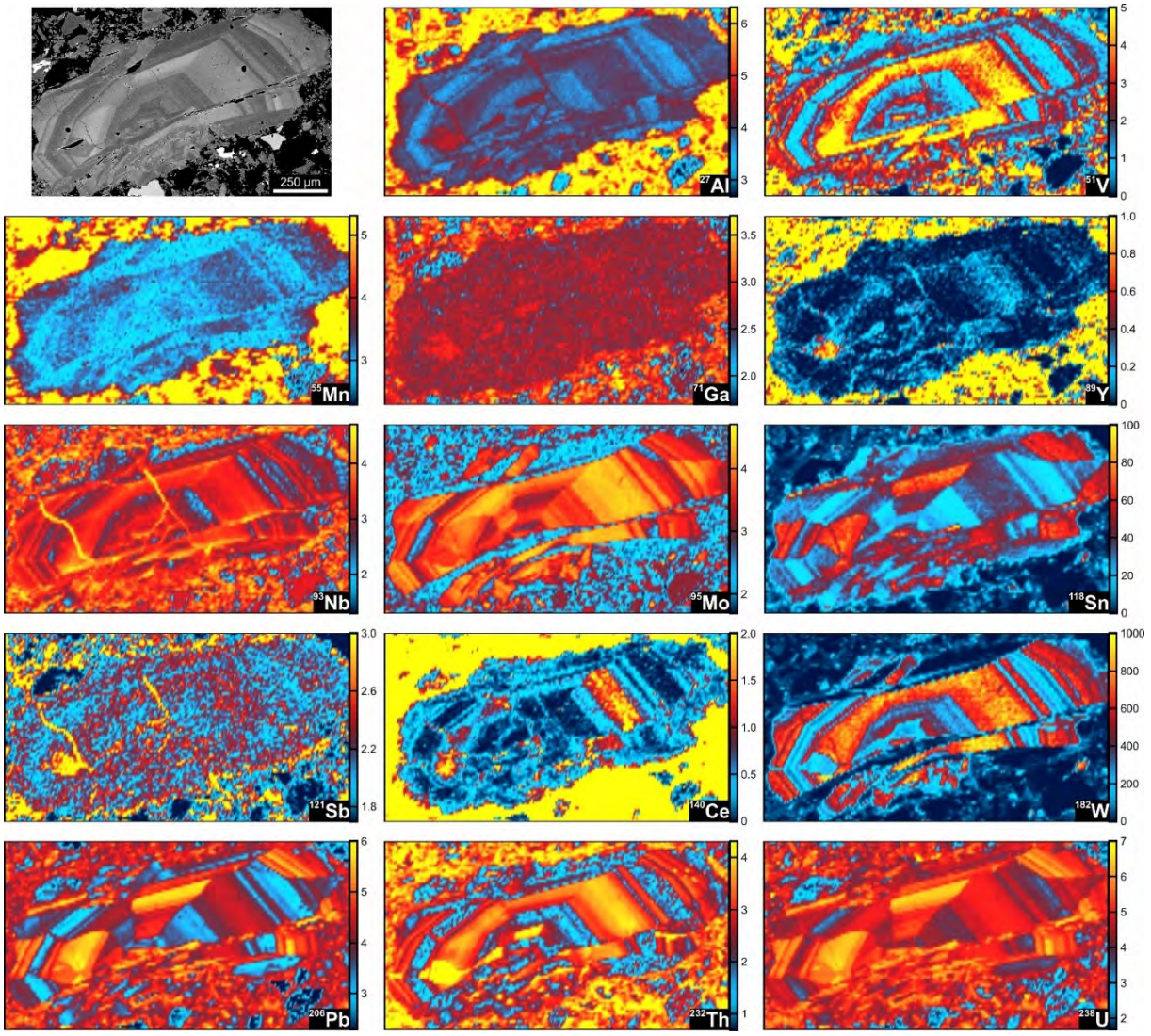

Fig. 10. BSE-image and corresponding LA-ICP-MS elemental maps of a fractured, granitophile-zoned hematite grain displaying both sectorial and oscillatory zonation, with clear HFSE-enrichment, and particularly Th (sample MV05A; *Nodular Fe-oxide drillhole* - RD2366). Logarithmically-scaled intensities (cps, 10^n), except for ^{51}V, ^{81}Y, ^{118}Sn, ^{140}Ce and ^{182}W (linear scale, $n \cdot 10^3$).

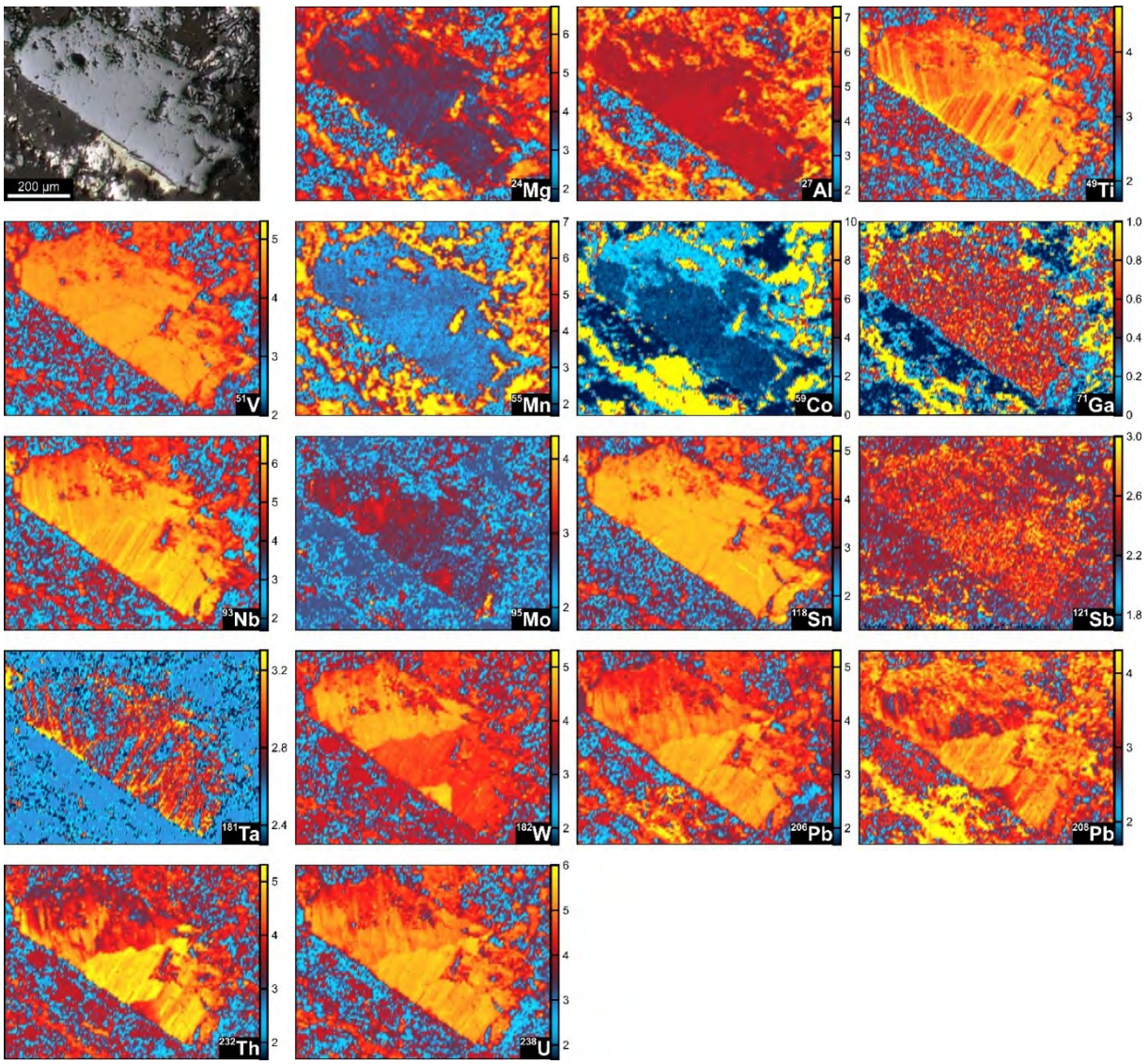

Fig. 11. Reflected-light micrograph and corresponding LA-ICP-MS elemental maps of HFSE-rich, hematite displaying fine-scale oscillatory zonation (sample MV19; *Nodular Fe-oxide drillhole* - RD2366). Note the contrasting styles of HFSE distribution within the mapped grain; whereas Ti, Nb, Ta and Th display fine-scale oscillatory zonation, the distribution of V is relatively even throughout the grain. Logarithmically-scaled intensities (cps, 10^n), except for ^{59}Co and ^{71}Ga (linear scale, $n \cdot 10^3$).

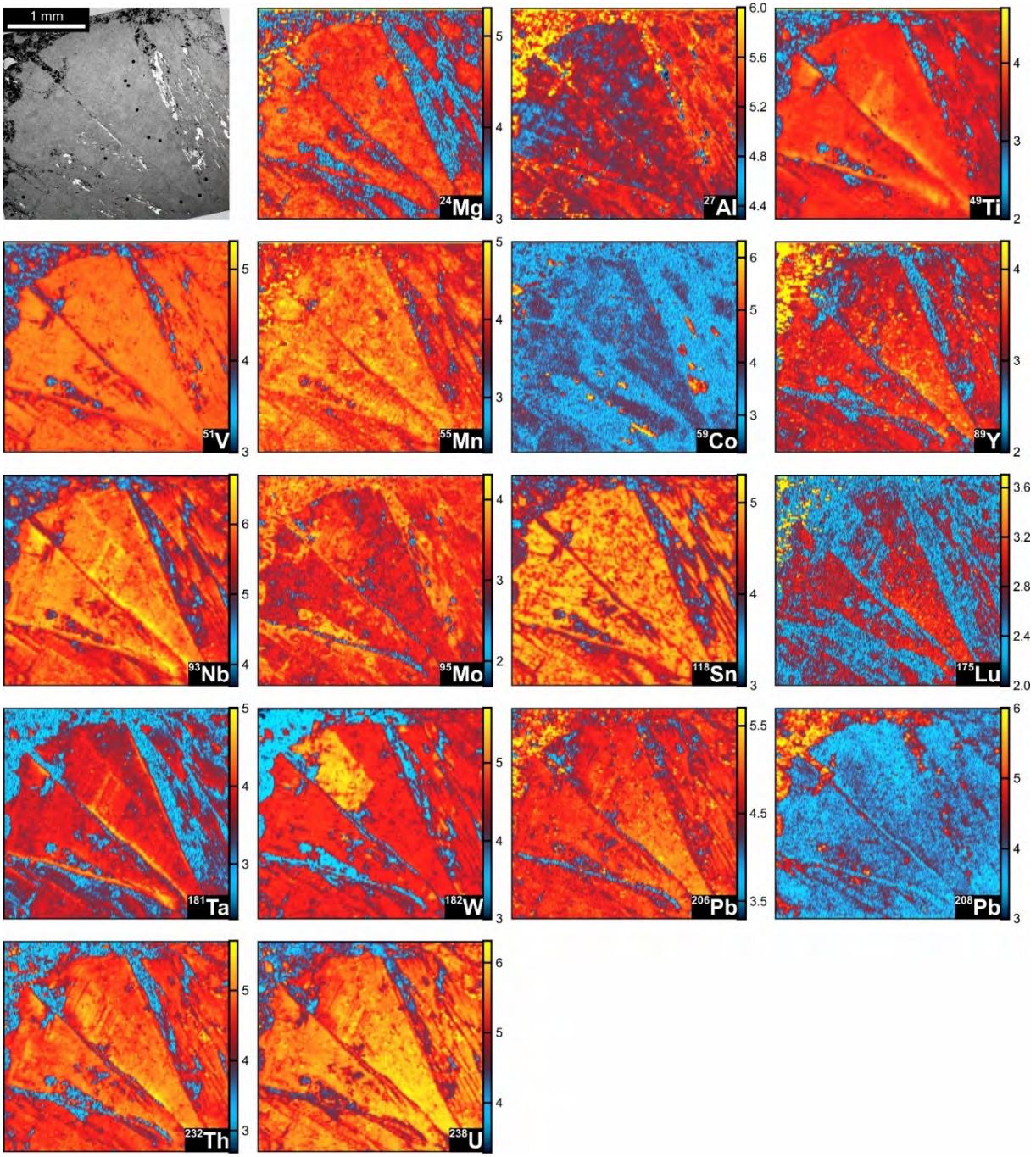

Fig. 12. BSE-image and corresponding LA-ICP-MS elemental maps hematite replacing carbonates(?) (banded interval, sample CLC08B; *Magnetite drillhole* - RU65-7976). The hematite grains display oscillatory zoning with respect to both granitophile elements and HFSE (Nb, Mo, Ta, Pb, Th, U) despite being polycrystalline. Distinct sectorial zoning can be also recognized (e.g., W) although other elements appear to be more homogeneously distributed. Logarithmically-scaled intensities (cps, 10^n).

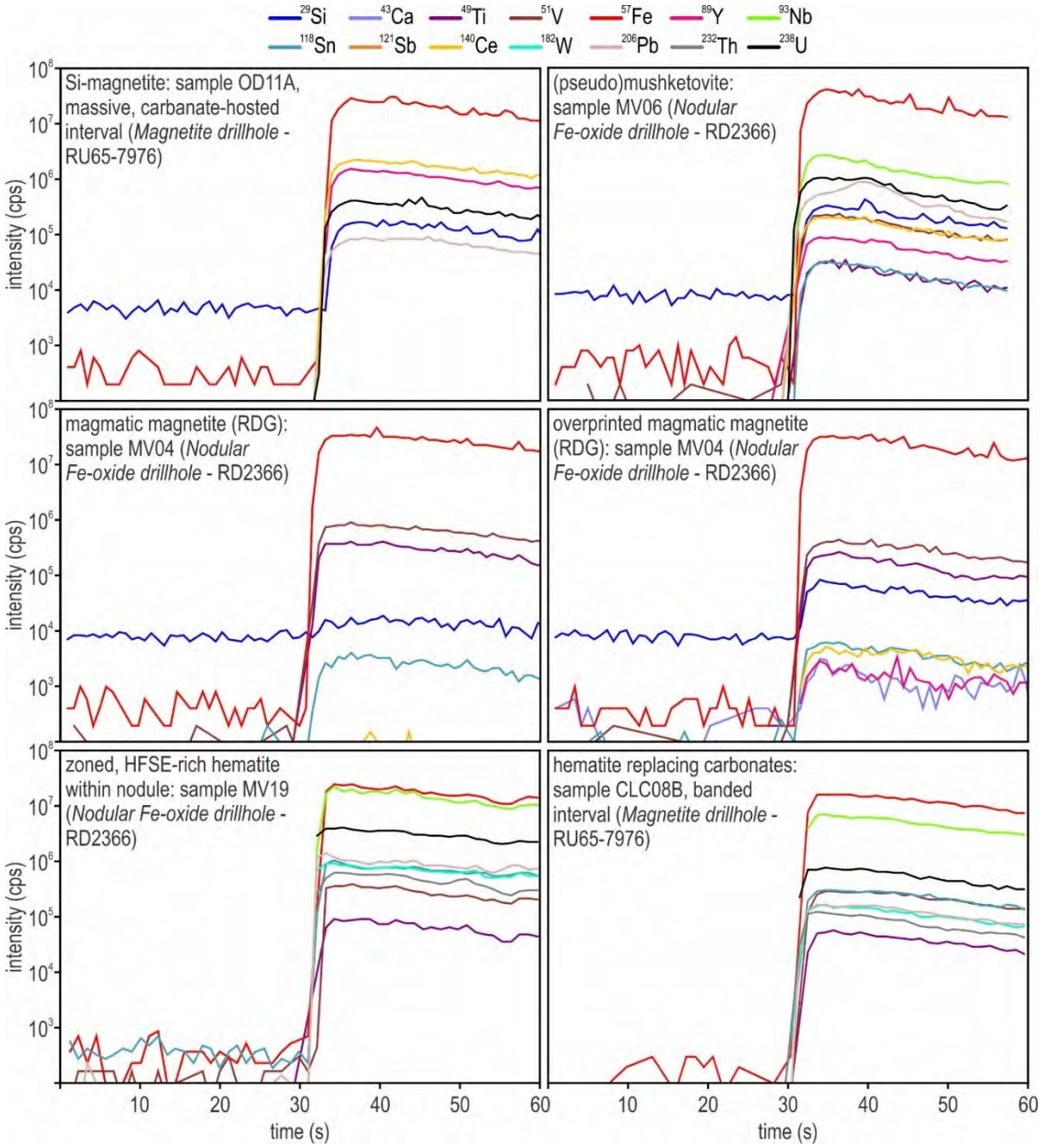

Fig. 13. Selected LA-ICP-MS time-resolved profiles of studied Fe-oxides. For displaying purposes, only selected elements shown.

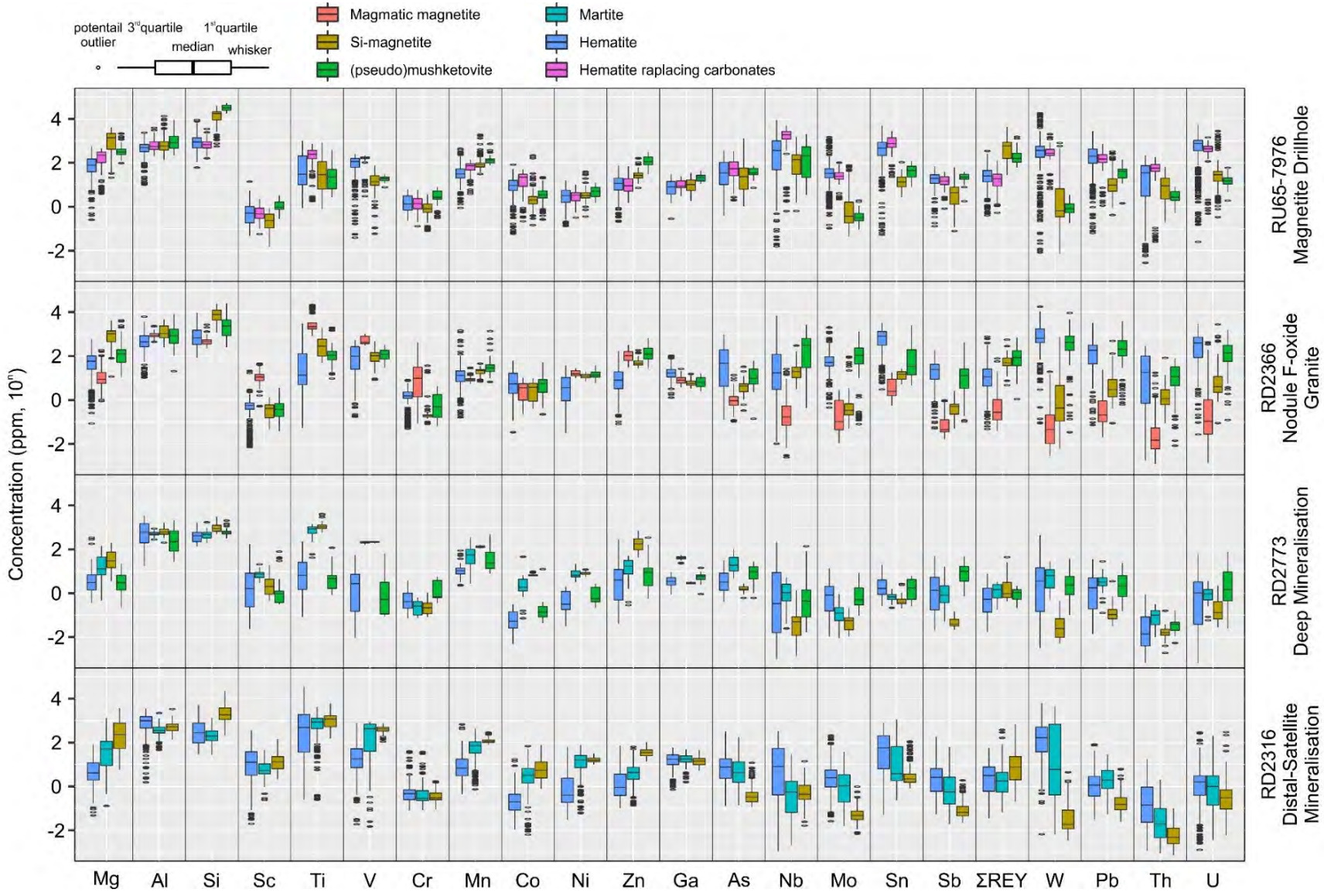

Fig. 14. Box plots of selected elements analysed by LA-ICP-MS from the different types of Fe-oxides as defined in the text and grouped by location.

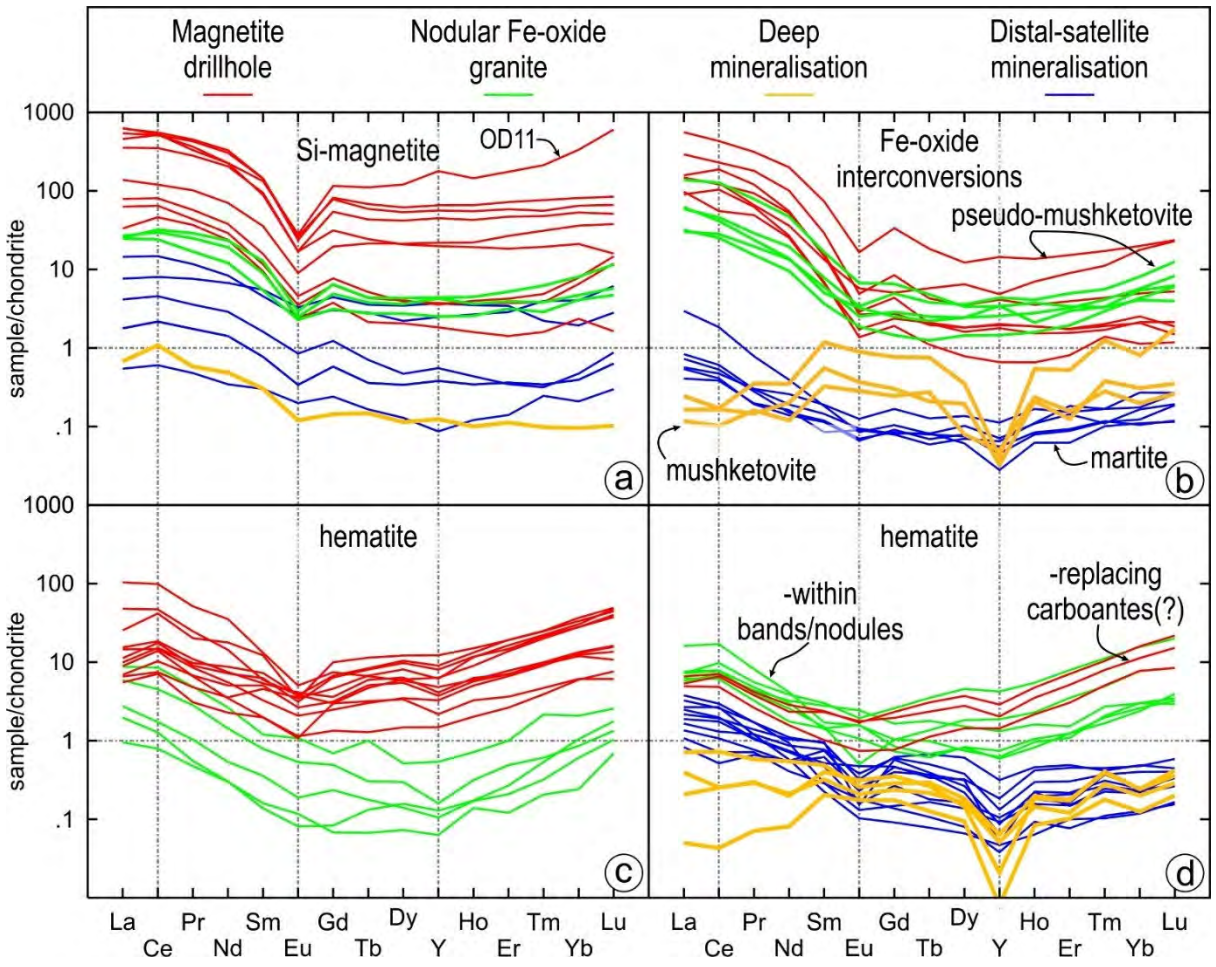

Fig. 15. Representative chondrite-normalised REY-fractionation trends of sample/texture-averages of the different Fe-oxides types (geometric means).

SUPPLEMENTARY MATERIAL C

FOR CHAPTER 4 – COPPER-ARSENIC NANOPARTICLES IN HEMATITE: FINGERPRINTING FLUID-MINERAL INTERACTION

APPENDIX S: ADDITIONAL FIGURES

ELECTRONIC APPENDIX S FOR CHAPTER 4

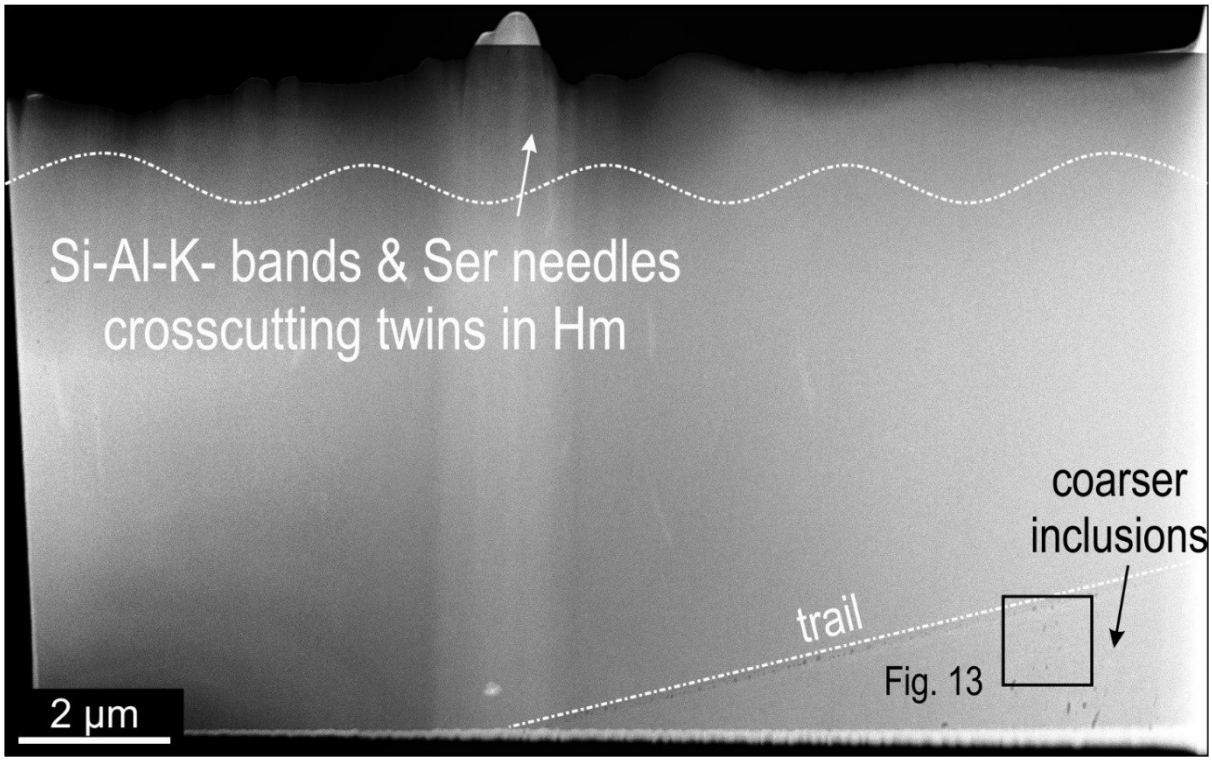

Figure S1. Low-magnification HAADF STEM image of the foil (foil #4) from the weave-twinned hematite showing areas of interest. Ser-sericite; Hm-hematite.

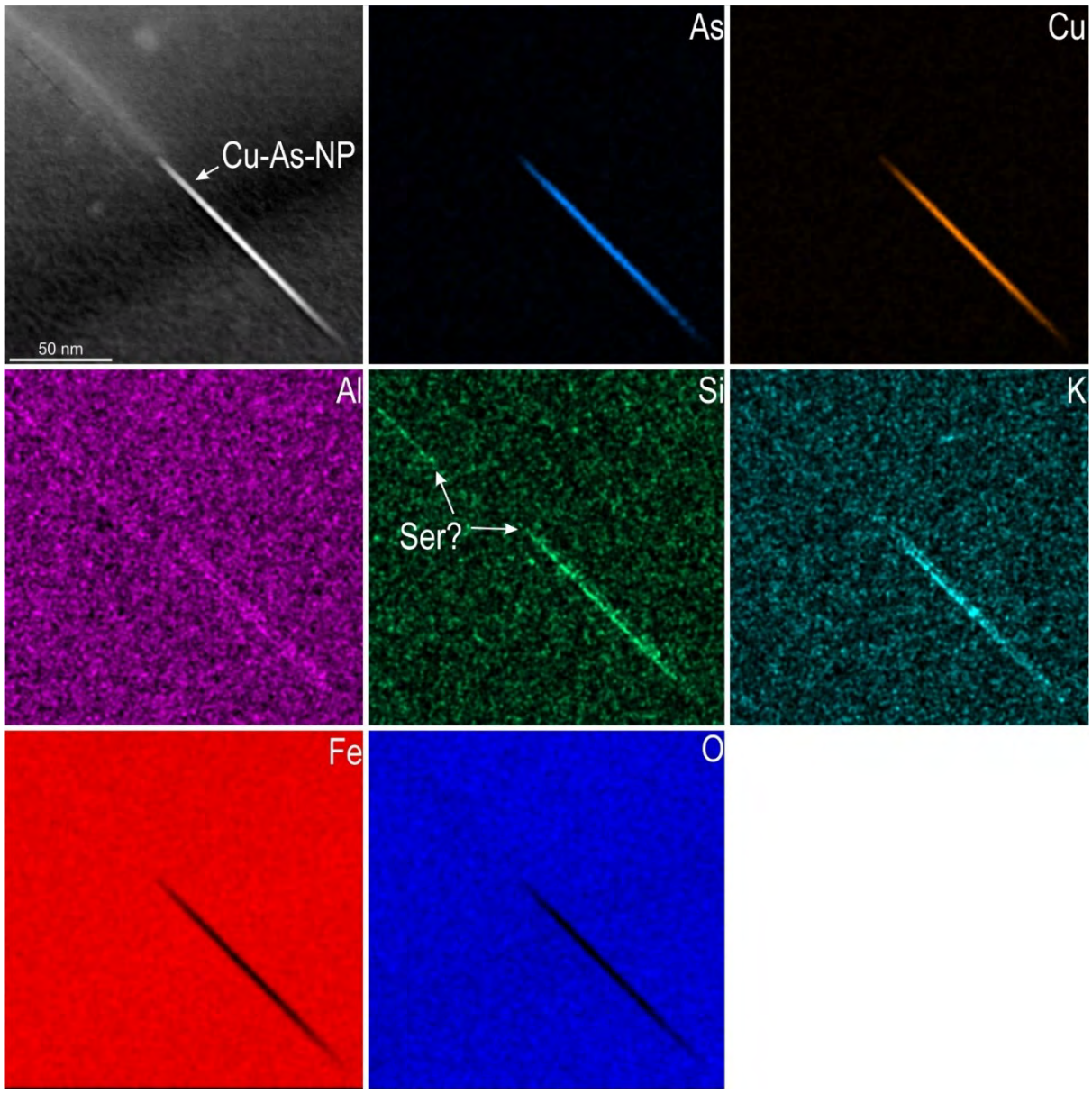

Figure S2. HAADF STEM and STEM EDX maps of Cu-As NP with acicular morphology hosted within bright band (foil #1). Note the presence of Si, K and Al surrounding the margins of the needle and/or proximal to it. Ser-sericite.

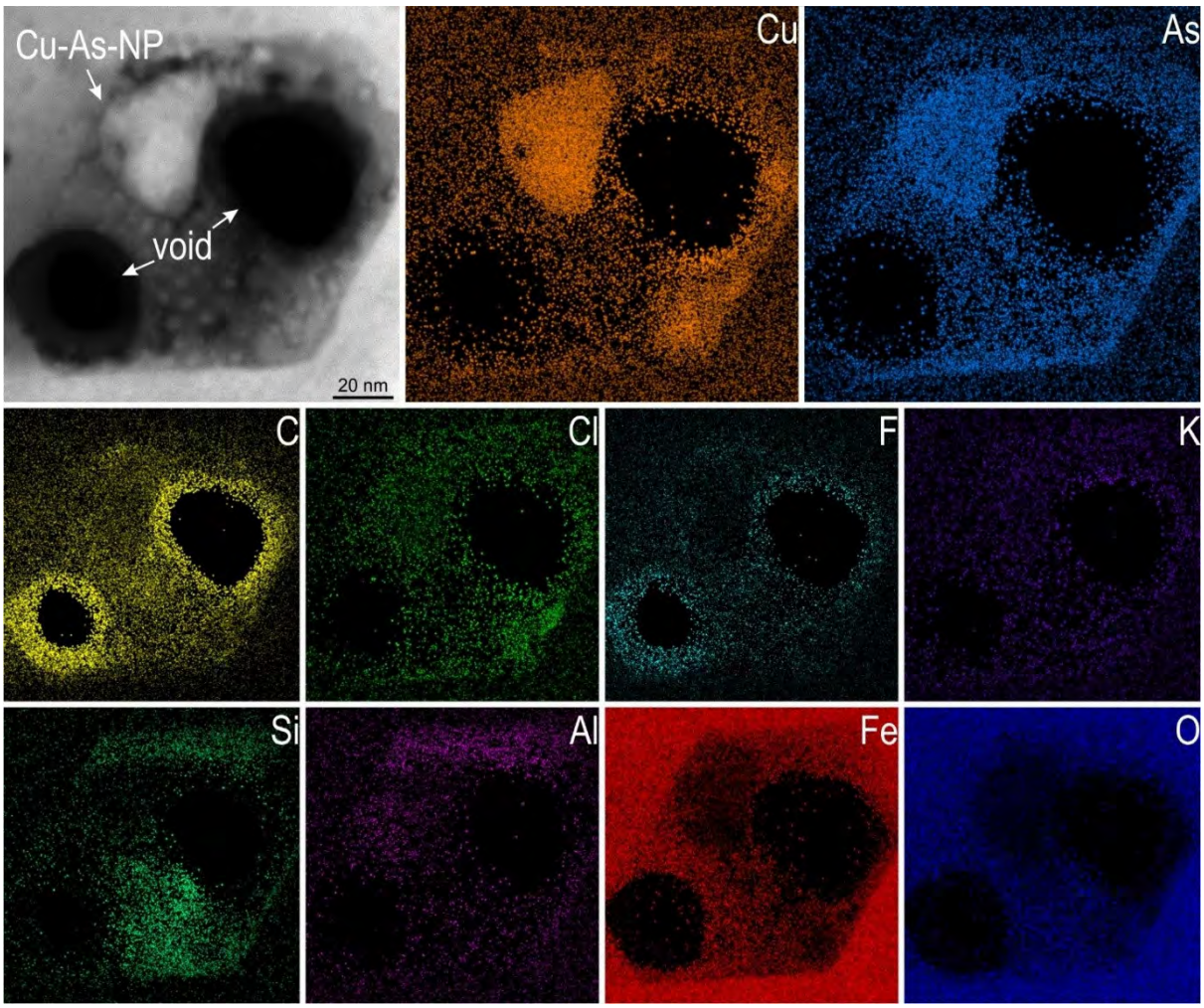

Figure S3. HAADF STEM and STEM-EDX maps of hexagonal cavity in Foil #3 (domain B) featuring the presence of voids and a Cu-As NP. Though F-Kα partially overlaps with Fe-Lα in the lower energy spectrum, note that enrichment of F is observed within the cavity, rather than outside, in the host hematite.

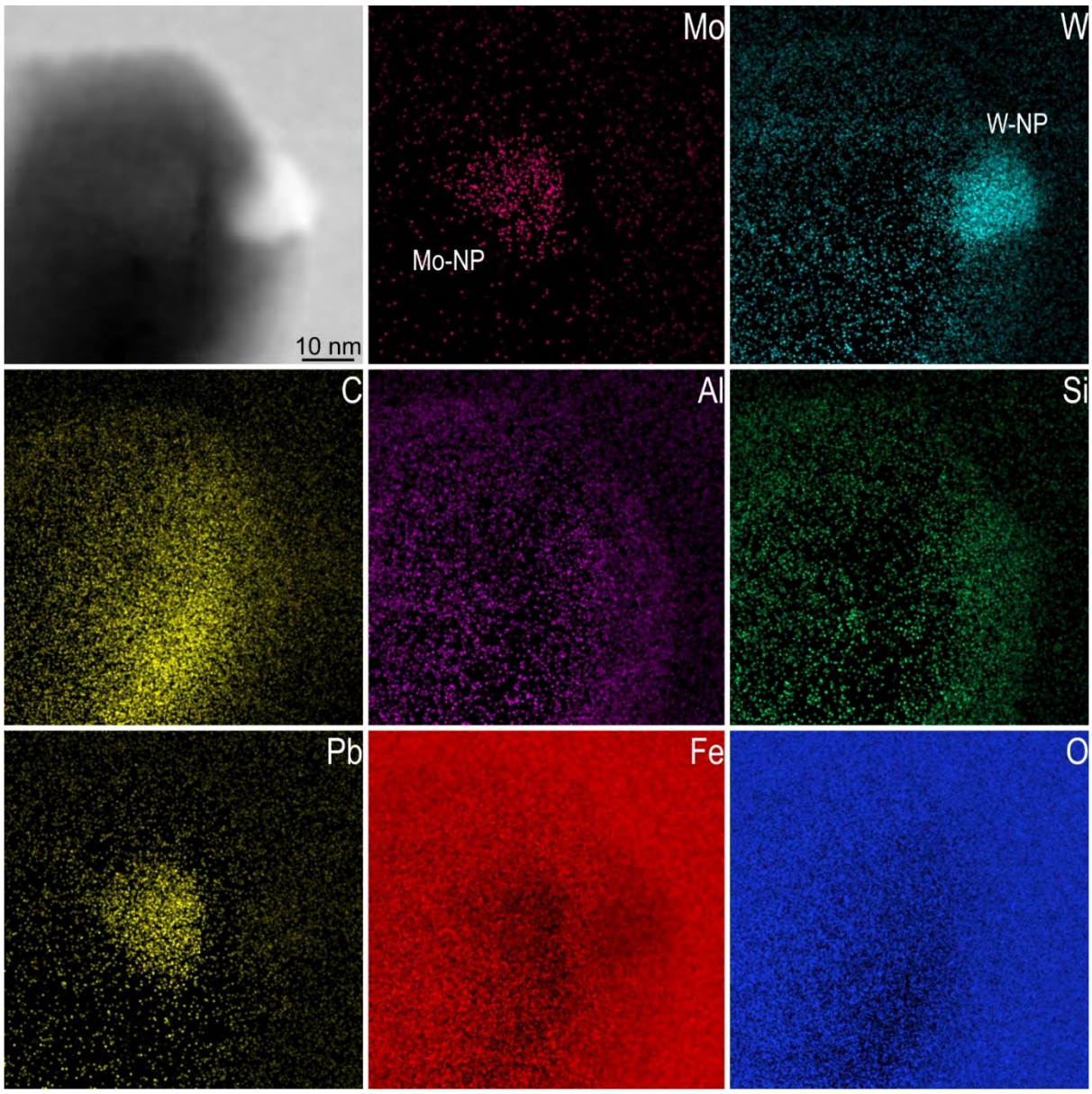

Figure S4. HAADF STEM and STEM-EDX maps of cavity hosting W- and Mo-bearing NPs (foil #3, domain B). Although the EDX peak position of Mo-Lα partially overlaps with that of Pb Mα, the presence of characteristic Mo-Kα peaks is observed in the higher energy interval of the spectrum.

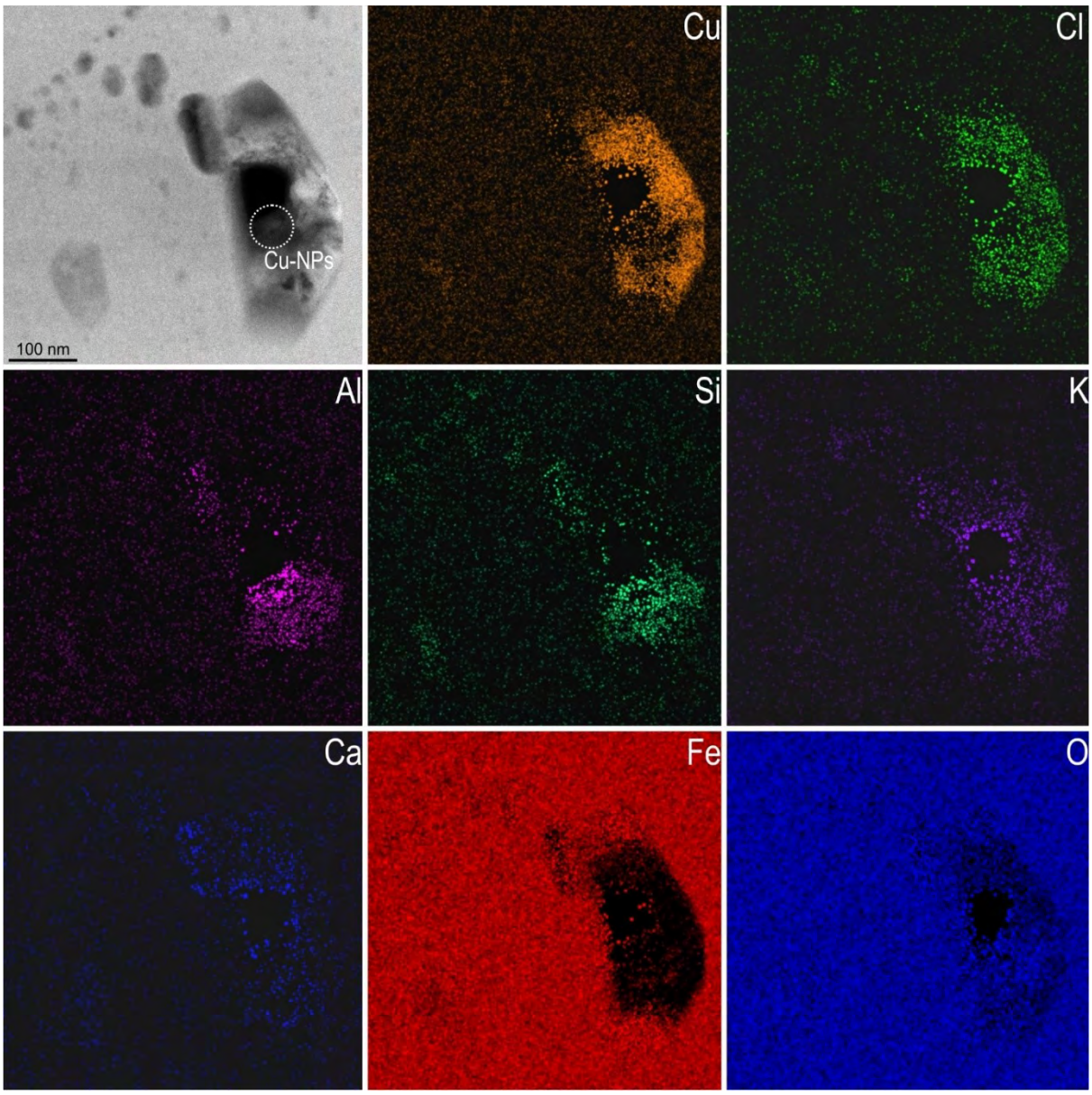

Figure S5. HAADF STEM and STEM-EDX maps of large cavity in foil #1 displaying the presence of a void and strong enrichment in Cu correlating with Cl. Native copper NPs are observed proximal to the void.

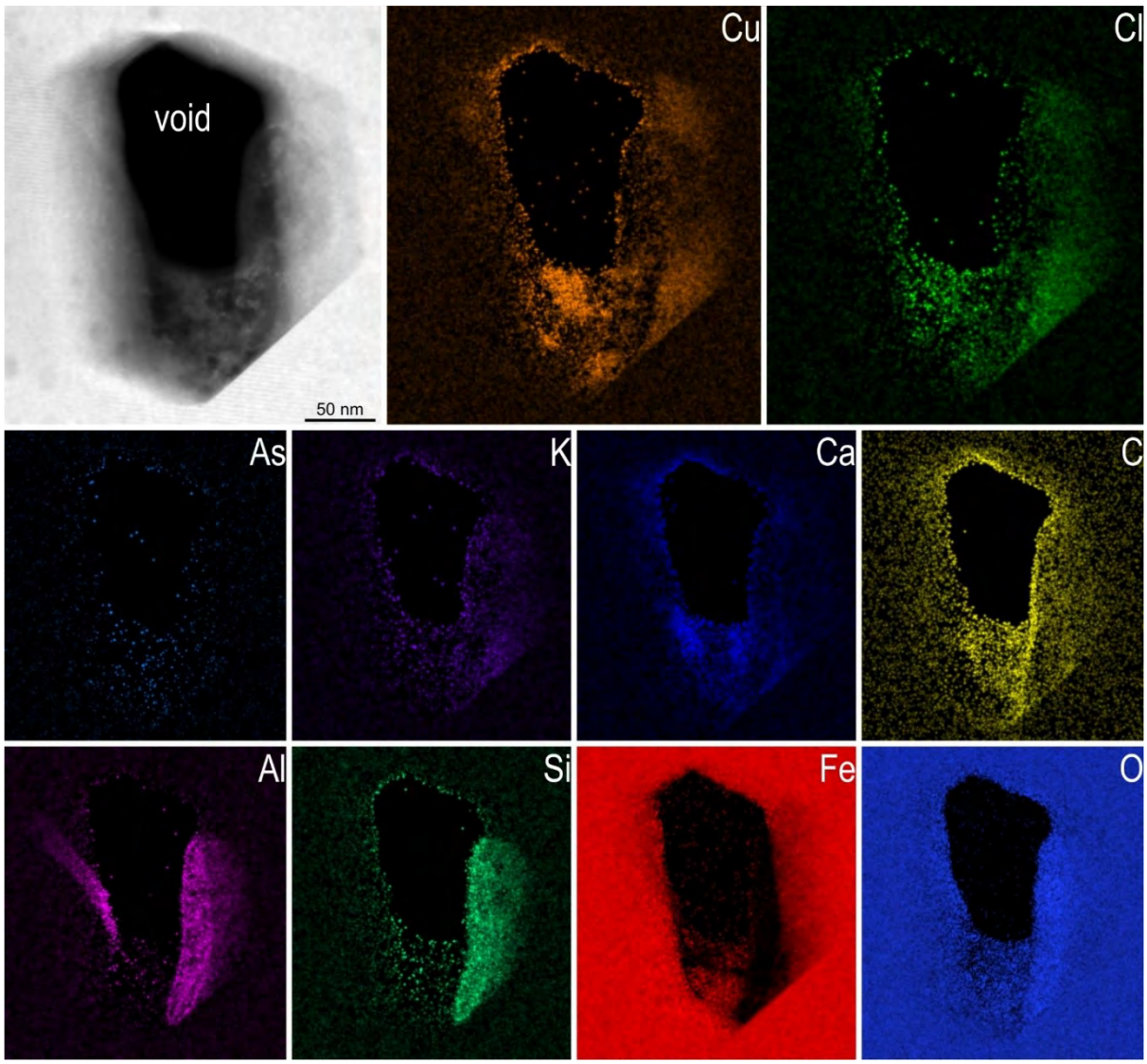

Figure S6. HAADF STEM and STEM-EDX maps of cavity in foil #2 (domain A) displaying the presence of a void and compositional heterogeneity within the inclusion (compare distributions of Ca *versus* Si and Al).

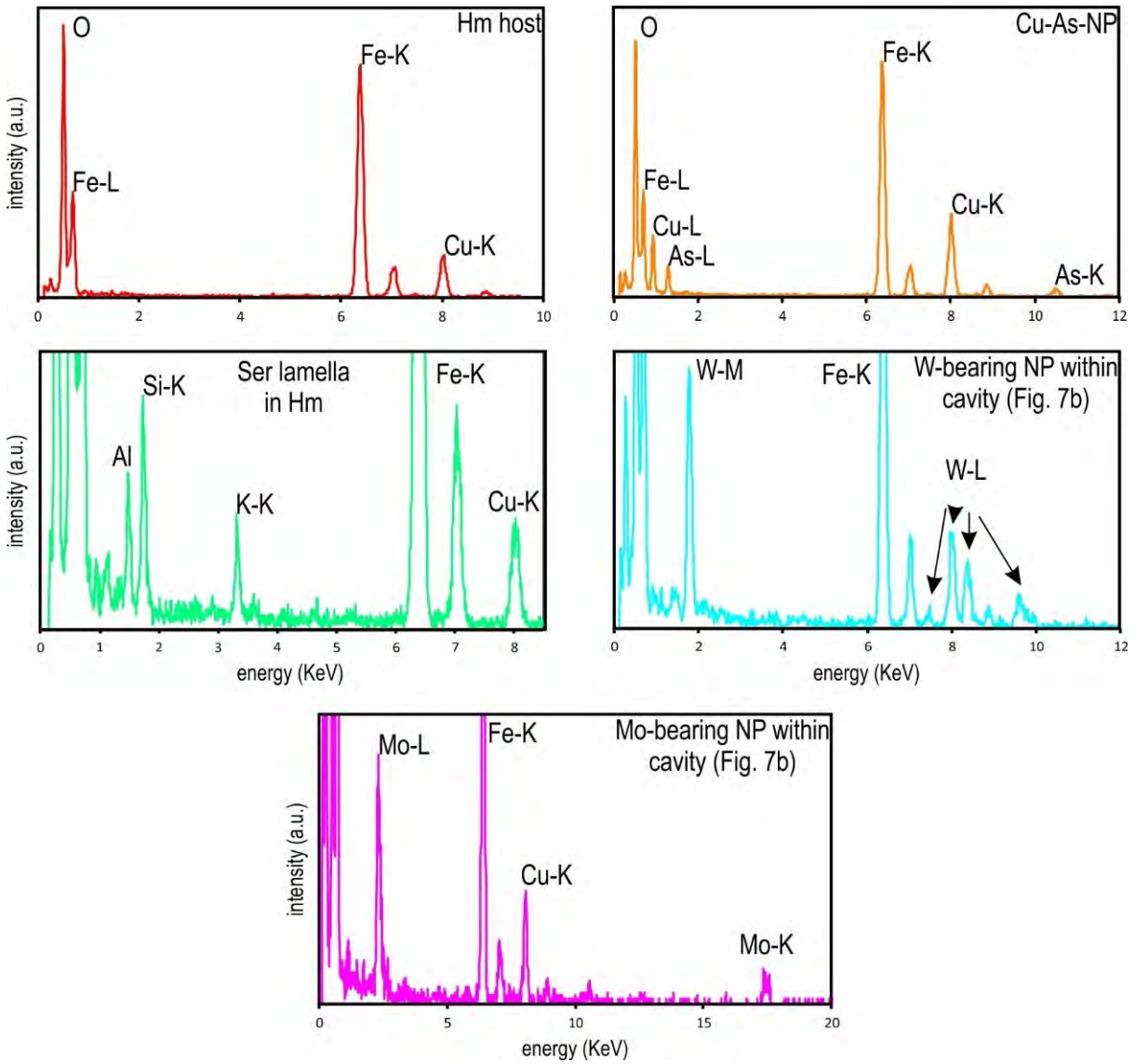

Figure S7. Representative STEM EDX spectra for observed NPs within cavities or directly hosted by hematite. The spectra are scaled individually to emphasise features of interest; typical hematite spectrum is shown (top left) for comparison. Note the relative differences between the Fe-K and Cu-K intensities in hematite host relative to the Cu-As-bearing NP.

SUPPLEMENTARY MATERIAL D

FOR CHAPTER 5 – TRACE ELEMENT REMOBILISATION FROM W-SN-U-PB ZONED HEMATITE: NANOSCALE INSIGHTS INTO OPEN SYSTEM BEHAVIOUR OF A MINERAL GEOCHRONOMETER

APPENDIX A: LA-ICP-MS TRACE ELEMENT DATA IN PPM FOR HEMATITE

APPENDIX B: ADDITIONAL FIGURES

APPENDIX C: .CIF-FILE OF HEMATITE SUPERSTRUCTURE WITH INDICATED VACANCY SITES

ELECTRONIC APPENDIX A FOR CHAPTER 5

Table S1. LA-ICP-MS trace element data in ppm for hematite

Domain		Analysis	Mg	Al	Si	P	Ca	Sc	Ti	V	Mn	Co	Ni	Cu	Zn	Ga	As	Sr	Y	Zr	Nb	Mo	Sn
Tungsten depleted	Rim	11[a]	6.86	127	423	4.11	41	<0.04	0.23	0.41	4.25	0.53	0.2	0.18	0.37	7.36	5.44	0.53	0.12	0.007	0.05	2.82	522
		10[a]	7.45	99.4	401	12.8	<20.5	0.06	<0.16	0.43	3.2	0.65	0.28	<0.05	<0.21	5.31	2.41	0.2	0.02	0.01	0.04	6.56	423
		9	7.43	131	446	7.88	<21.2	<0.04	<0.12	0.75	3.67	0.52	0.35	<0.06	<0.22	7.53	0.16	0.009	0.01	0.005	0.008	2.35	693
		8	7.81	95.2	381	<2.3	32.5	0.07	<0.19	1.6	3.57	0.55	0.34	0.13	<0.21	9.23	<0.13	<0.005	0.004	0.008	0.06	1.86	622
		7	5.6	55.1	308	8.57	<20.2	0.04	<0.21	2.15	2.83	0.5	0.29	<0.06	<0.21	5.66	0.38	<0.001	0.004	0.005	1.47	2.84	596
	Transect #1	6	7.14	77	405	2.38	<20.9	0.14	<0.08	4.4	3.52	0.37	0.33	<0.05	<0.19	5.67	0.19	0.009	<0.003	0.008	1.42	0.93	1000
		5	4.83	34.7	385	7.49	<23	0.17	0.65	2.31	2.29	0.31	0.21	0.09	<0.17	4.17	0.18	0.007	<0.001	0.02	8.77	1.06	985
		4	6.69	41.5	379	9.47	<25.3	0.07	<0.001	2.29	3.6	0.44	0.4	<0.06	0.68	4.36	<0.18	<0.004	0.003	<0.007	0.75	1.69	1050
		3	14.5	120	473	<2.3	<21.1	0.39	<0.08	3.43	3.93	0.48	0.17	0.09	<0.18	6.03	1.92	0.02	0.09	<0.007	0.13	2.25	1080
		2	6.85	89.1	448	2.94	<23.2	0.04	0.76	2.49	2.59	0.36	0.22	0.3	0.38	5.25	<0.23	<0.001	0.003	<0.005	0.5	1.16	828
		1	6.66	103	330	5.25	24.1	<0.04	<0.001	2.57	3.29	0.41	0.41	0.11	0.22	6.18	<0.31	<0.001	0.003	<0.005	0.1	1.47	705
	Core	12	8.23	67.3	376	5.33	23.7	0.08	0.48	0.41	3.72	0.46	0.37	0.09	0.45	5.34	<0.17	<0.007	0.06	<0.007	0.29	1.43	801
	Foil #3	15	6.98	90.7	320	4.74	<19	0.15	0.31	4.69	3.27	0.47	0.43	1.15	<0.22	160	3.13	0.03	0.007	<0.007	0.81	1.82	849
		16	6.56	101	342	3.28	<20.9	0.05	0.42	2.51	3.64	0.49	0.27	0.95	1.83	11.9	4.47	0.07	0.02	0.01	0.75	3.03	583
Patchy core	Foil #2	13	27.6	140	587	<2.15	<18.2	0.06	1.21	1.08	9.32	1.38	0.16	0.3	0.62	6.99	27.2	4.41	0.38	0.03	9.17	43.7	566
		14	21.6	124	585	17.3	23.8	0.13	1.1	1.16	8.57	1.07	0.17	0.52	1.39	6.05	33.5	1.3	0.08	0.02	7.06	20	455
		17	23.7	119	388	10.4	<19.4	0.07	<0.11	0.46	7.73	1.04	0.42	0.12	0.43	7.48	1.5	0.02	0.16	<0.001	0.32	15	810
Tungsten rich	Core	18	18.4	222	373	9.17	24.4	0.29	3.53	7.75	8.38	1.05	0.26	<0.05	0.62	5.79	4.57	0.19	0.04	0.01	57.1	27.7	713
	Transect #2	19	14.8	158	377	2.78	<21.8	0.04	0.33	3.18	6.37	0.77	0.4	<0.05	0.2	5.71	4.31	0.53	0.02	0.02	7.71	10.8	637
		20[b]	17.4	139	312	6.31	<18.6	0.11	3.58	4.78	6.73	0.95	<0.06	<0.06	0.3	4.95	1.15	0.03	0.03	0.03	67.4	10.2	746
		21	17.9	135	393	7.2	<21.9	0.32	1.62	5.24	7.42	0.78	0.46	0.36	<0.21	5.46	<0.14	0.01	0.02	0.02	17.3	12.6	855
		22	14.3	132	406	9.98	32.3	0.09	0.65	4.51	6.1	0.77	0.25	<0.05	0.37	5.58	0.15	0.01	0.01	<0.007	21.5	6.52	760
		23	17.4	150	424	<2.23	25.5	<0.04	0.38	1.73	7.47	0.76	<0.05	<0.06	<0.22	6.49	0.16	<0.005	0.01	0.006	2.1	25.2	616
		24	14.7	135	449	7.34	133	0.09	2.51	0.68	7.93	1	<0.05	1.32	0.86	4.74	14.7	0.86	0.03	0.009	0.28	32.3	338
		25	6.78	82.4	438	<2.21	43.6	<0.04	0.55	0.77	2.82	0.6	0.24	<0.06	<0.21	5.68	0.12	<0.001	<0.002	0.01	2.75	7.37	248
		26	7.68	57.7	405	7.17	<19.5	<0.03	0.53	0.22	2.95	0.59	0.17	0.06	<0.19	4.54	2.85	<0.003	0.006	<0.004	0.25	6.35	292
	Rim	27	12.6	279	463	6.74	19.4	<0.04	0.18	1.4	13.5	0.56	0.26	0.63	1.6	8.22	3.86	2.43	0.18	<0.006	0.1	5.89	558
	Core	28	15.8	128	393	10.6	<21.3	<0.04	2.54	3.05	5.9	1	0.16	0.09	0.39	5.03	0.7	0.06	0.005	0.02	19	19.1	610
	Transect #3	29	18.6	154	458	13.9	<20.2	0.06	0.91	1.94	7.6	0.98	0.12	0.13	<0.19	6.72	0.33	0.02	0.02	0.03	3.15	25.6	623
		30	18.4	150	531	18.6	129	0.11	12.7	0.67	9.63	1.16	0.12	1.09	8.98	6.33	63.6	7.36	0.13	0.03	0.95	73.1	618
	Rim	31	9.23	144	385	<2.17	<19	0.2	16.7	1.07	3.76	0.88	0.11	<0.05	<0.18	4.7	1.7	0.04	0.02	0.007	0.91	25	245

Table S1. (Continued) LA-ICP-MS trace element data in ppm for hematite

Domain		Analysis	Sb	Ba	Pr	Nd	Tb	Dy	Ho	Er	Tm	Yb	Lu	Ta	W	Th	U	^{204}Pb	^{206}Pb	^{207}Pb	^{208}Pb	∑Pb
Tungsten depleted	Rim	11[a]	1.19	1.9	0.03	0.08	<0.001	0.01	<0.003	0.009	<0.001	0.02	0.008	<0.002	1070	0.02	6.17	<0.006	1.81	0.4	0.48	2.7
		10[a]	4.96	0.24	0.04	0.11	<0.002	<0.004	0.003	<0.008	<0.001	0.008	0.006	<0.002	182	0.003	15.7	<0.008	3.69	0.45	0.05	4.2
		9	5.13	<0.03	<0.003	0.03	<0.002	<0.008	<0.002	<0.004	<0.002	0.01	0.003	<0.001	13.8	<0.003	2.41	<0.008	0.58	0.08	0.04	0.7
		8	5.13	<0.001	<0.002	<0.007	<0.002	<0.007	<0.002	<0.005	<0.002	0.04	0.007	<0.003	7.34	<0.003	1.05	<0.007	0.3	0.04	0.01	0.36
		7	4.82	<0.001	<0.001	<0.009	0.002	0.005	<0.002	<0.005	<0.001	0.008	<0.002	<0.002	9.25	<0.003	0.5	<0.006	0.12	0.03	0.008	0.16
	Transect	6	5.97	<0.001	<0.001	<0.007	0.001	<0.005	<0.001	<0.006	<0.002	<0.007	0.01	0.003	11.3	0.002	0.41	<0.006	0.1	0.006	0.009	0.12
	#1	5	4.81	<0.02	<0.001	0.02	<0.002	<0.006	<0.002	<0.007	<0.002	0.01	<0.002	0.01	11.7	<0.002	0.17	0.01	0.08	0.009	<0.006	0.11
		4	6.76	<0.001	0.003	<0.007	<0.002	0.02	<0.002	<0.008	<0.002	<0.01	0.004	0.004	13.4	0.01	0.59	<0.007	0.14	0.02	0.01	0.17
		3	6.28	0.29	0.04	0.09	0.006	0.02	<0.002	0.007	<0.002	0.05	0.004	<0.001	118	0.05	11.9	<0.007	2.97	0.27	0.04	3.28
		2	5.22	<0.001	0.002	0.03	<0.003	<0.007	0.002	<0.009	<0.001	0.02	0.005	<0.002	5.34	<0.002	1.18	0.02	0.13	0.03	0.006	0.18
		1	4.83	<0.001	0.002	<0.01	<0.002	<0.01	<0.002	<0.008	<0.002	0.009	0.006	<0.002	21.2	<0.003	0.6	0.02	0.15	0.02	<0.005	0.2
	Core	12	6.92	<0.02	<0.002	0.01	0.003	0.01	0.002	0.01	0.009	0.03	0.01	<0.002	16.8	<0.002	1.04	<0.006	0.32	0.04	0.02	0.39
	Foil	15	5.61	0.22	0.004	<0.009	<0.001	0.009	<0.001	<0.006	<0.002	0.02	<0.002	0.003	63.1	0.008	0.77	0.01	0.58	0.37	0.72	1.68
	#3	16	5.79	0.38	0.01	0.02	<0.002	<0.007	0.003	0.01	<0.001	0.04	<0.003	0.003	43.8	0.003	1.84	0.07	1.16	0.6	1.35	3.17
Patchy core	Foil #2	13	4.94	3.01	0.006	0.12	0.005	0.06	0.02	0.12	0.05	0.47	0.15	0.03	6470	0.11	91.5	0.01	22.4	3.07	0.88	26.4
		14	5.48	1.83	0.02	0.01	<0.002	0.008	0.003	0.02	0.01	0.11	0.04	0.01	932	0.02	1.3	0.05	1.92	1.3	2.75	6.02
		17	4.95	0.1	<0.001	0.06	0.007	0.01	<0.002	0.07	0.01	0.19	0.04	<0.001	1910	0.04	103	<0.006	24.2	2.75	0.1	27.1
Tungsten rich	Core	18	3	0.64	<0.001	<0.01	0.003	0.005	0.005	0.005	0.003	0.06	0.03	0.08	7900	<0.002	3.97	0.01	1.29	0.41	0.62	2.33
		19	1.78	0.46	<0.001	<0.009	<0.002	<0.008	<0.002	<0.01	0.002	0.03	0.01	0.02	6280	0.003	1.26	0.02	0.46	0.26	0.4	1.13
		20[b]	1.63	<0.02	<0.002	<0.01	<0.002	0.009	<0.002	0.01	0.002	0.07	0.02	0.06	6170	<0.001	0.69	<0.006	0.25	0.05	0.04	0.33
		21	1.9	<0.001	<0.002	<0.01	<0.002	<0.005	<0.001	<0.005	0.005	0.06	0.02	0.01	7800	<0.001	0.61	0.01	0.22	0.03	0.02	0.28
	Transect	22	1.69	<0.001	<0.001	0.05	<0.002	0.01	0.004	<0.004	0.005	0.03	0.01	0.02	5040	0.008	0.23	<0.005	0.17	0.03	<0.006	0.21
	#2	23	1.59	<0.001	<0.002	<0.001	<0.002	<0.008	<0.002	<0.006	<0.002	0.08	0.04	0.006	8080	<0.003	1.79	<0.007	0.54	0.05	0.007	0.61
		24	2.77	1.61	0.04	0.12	<0.002	<0.01	<0.003	<0.005	0.006	0.02	0.004	0.005	4060	<0.002	7.29	0.02	2.3	0.5	0.61	3.43
		25	0.93	<0.02	0.006	0.04	<0.002	0.01	<0.002	<0.003	0.002	<0.005	0.002	<0.002	904	<0.002	0.64	0.01	0.22	0.01	0.006	0.25
		26	0.9	<0.03	<0.002	0.04	<0.001	<0.007	<0.002	<0.006	0.002	<0.007	0.004	0.002	1260	0.01	3.77	0.01	1.04	0.12	0.02	1.19
	Rim	27	1.17	6.42	0.07	0.1	0.003	0.06	0.005	0.04	0.005	0.04	0.01	<0.002	3400	0.13	25.5	<0.007	5.9	0.84	0.21	6.97
	Core	28	1.77	<0.02	<0.001	<0.009	0.001	<0.001	0.002	0.02	0.002	0.05	0.02	0.05	5050	<0.003	5.16	<0.006	1.46	0.19	0.01	1.68
	Transect	29	2.05	0.11	<0.002	<0.007	0.003	<0.007	0.003	0.008	0.006	0.05	0.02	0.02	8420	<0.003	2.65	<0.006	0.7	0.1	0.02	0.84
	#3	30	6.14	3.98	0.01	0.04	0.006	0.007	0.007	0.07	0.02	0.17	0.06	0.02	8640	0.08	69.7	0.07	17	2.92	2.44	22.4
	Rim	31	1.9	0.29	0.006	<0.009	<0.002	<0.008	0.005	0.004	<0.002	<0.01	0.007	0.02	2590	<0.003	1.14	0.02	0.89	0.19	0.25	1.35

Concentrations for Cr, Sm, Eu, Gd and Hf are not indicated due to being consistently bellow minimum detection limits in >66.7 % of the analyses.

[a] intersects partially preserved W.

[b] on band intersected by foil #1.

ELECTRONIC APPENDIX B FOR CHAPTER 5

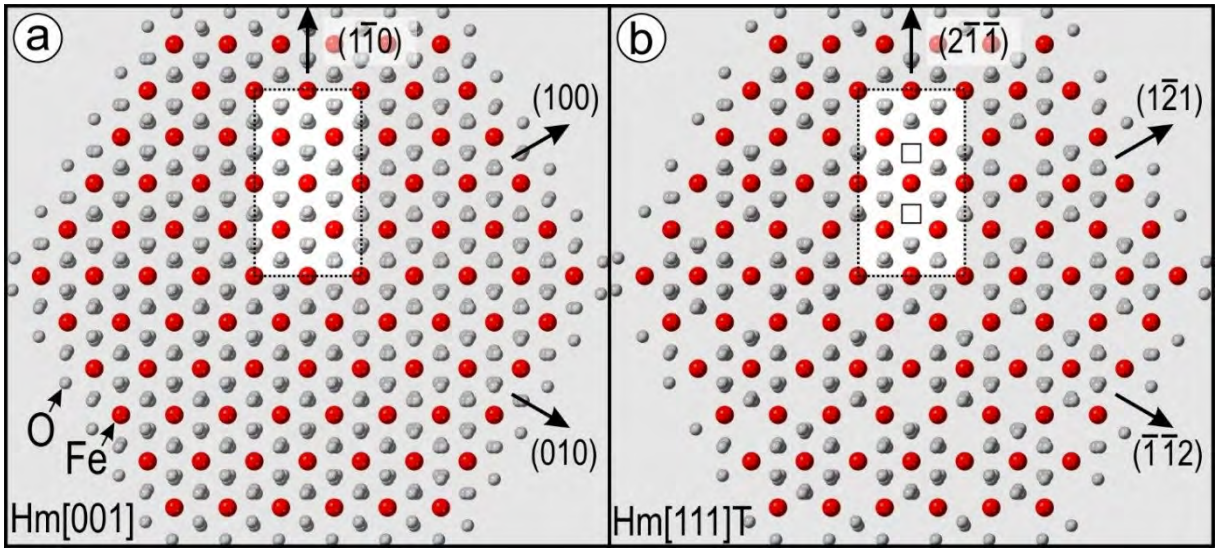

Fig. S1. Schematic showing (a) ideal distribution of Fe and O in hematite on the [001] zone axis (hexagonal setting) and (b) two-fold superstructure model on the $[111]T_{P1}$ zone axis (rhombohedral axes) showing location of proposed vacancies as empty squares along directions as marked.

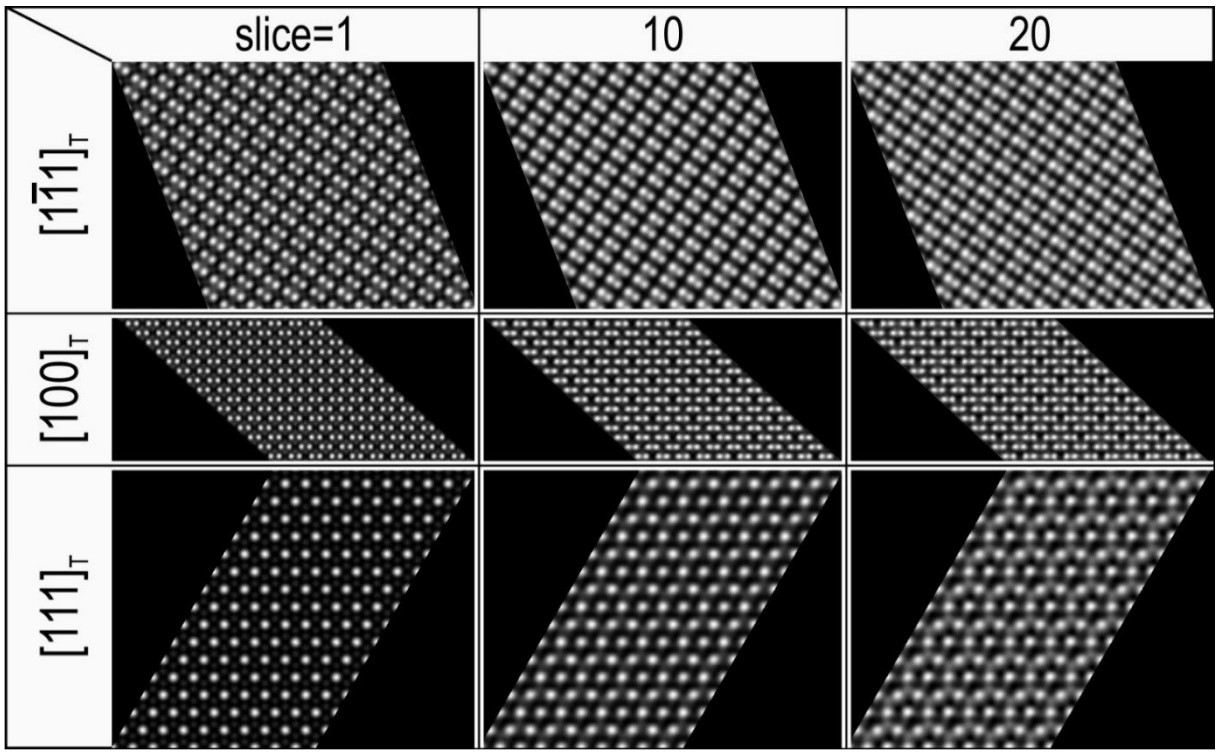

Fig. S2. STEM simulations for the two-fold superstructure with oxygen vacancies in hematite for three difference slices using probe = 1. Note enhanced 'phantom effects' in the higher-order slices for $[100]T$.

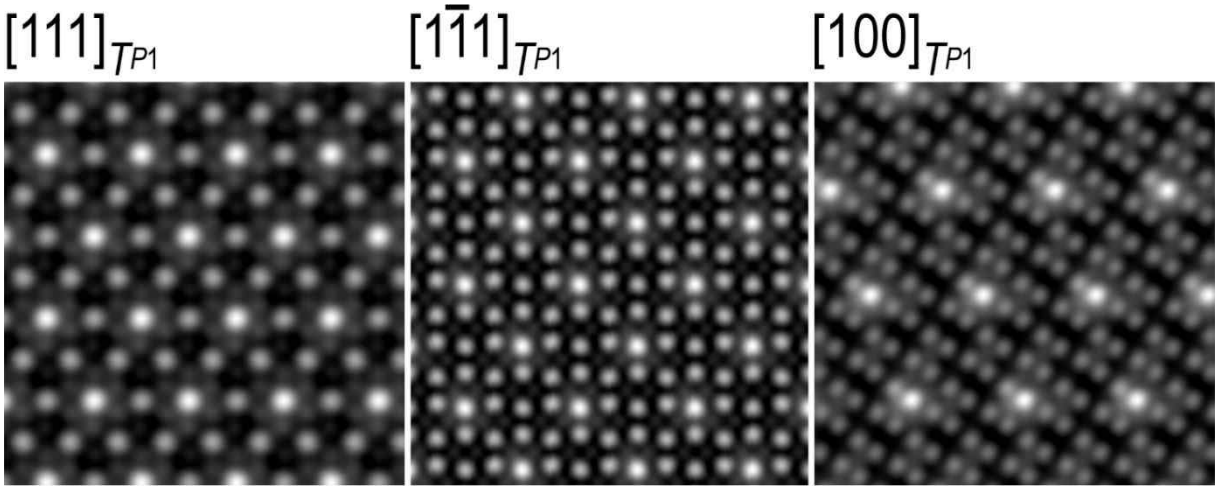

Fig. S3. STEM simulations for the 2-fold superstructure of U-bearing hematite using the model of McBriarty *et al*. (2018). The superstructure is well marked by strong increase in the intensity for the U. Note good match with models in Fig. 10, except for $[100]T$. In the latter case the rhombic motif is enhanced but the motif periodicity is four-fold rather than two-fold.

References

McBriarty M.E., Kerisit S., Bylaska E.J., Shaw S., Morris K. and Ilton E.S. (2018) Iron vacancies accommodate uranyl incorporation into hematite. *Environmental Science & Technology*, **52**, 6282–6290. doi: 10.1021/acs.est.8b00297

ELECTRONIC APPENDIX C FOR CHAPTER 5

```
data_global
_cell_length_a                10.853602
_cell_length_b                10.853602
_cell_length_c                10.853602
_cell_angle_alpha              55.284235
_cell_angle_beta               55.284235
_cell_angle_gamma              55.284235

_symmetry_space_group_name_H-M     'P 1'

loop_
_symmetry_equiv_pos_as_xyz
'+x,+y,+z'

loop_
_atom_site_label
_atom_site_type_symbol
_atom_site_occupancy
_atom_site_fract_x
_atom_site_fract_y
_atom_site_fract_z
   Fe01   Fe   1   0.32239   0.32239   0.32239
   Fe02   Fe   1   0.32239   0.32239   0.82239
   Fe03   Fe   1   0.32239   0.82239   0.32239
   Fe04   Fe   1   0.32239   0.82239   0.82239
   Fe05   Fe   1   0.82239   0.32239   0.32239
   Fe06   Fe   1   0.82239   0.32239   0.82239
   Fe07   Fe   1   0.82239   0.82239   0.32239
   Fe08   Fe   1   0.82239   0.82239   0.82239
   Fe09   Fe   1   0.42761   0.42761   0.42761
   Fe10   Fe   1   0.42761   0.42761   0.92761
   Fe11   Fe   1   0.42761   0.92761   0.42761
   Fe12   Fe   1   0.42761   0.92761   0.92761
   Fe13   Fe   1   0.92761   0.42761   0.42761
   Fe14   Fe   1   0.92761   0.42761   0.92761
   Fe15   Fe   1   0.92761   0.92761   0.42761
   Fe16   Fe   1   0.92761   0.92761   0.92761
   Fe17   Fe   1   0.17761   0.17761   0.17761
   Fe18   Fe   1   0.17761   0.17761   0.67761
   Fe19   Fe   1   0.17761   0.67761   0.17761
   Fe20   Fe   1   0.17761   0.67761   0.67761
   Fe21   Fe   1   0.67761   0.17761   0.17761
   Fe22   Fe   1   0.67761   0.17761   0.67761
   Fe23   Fe   1   0.67761   0.67761   0.17761
   Fe24   Fe   1   0.67761   0.67761   0.67761
   Fe25   Fe   1   0.07239   0.07239   0.07239
   Fe26   Fe   1   0.07239   0.07239   0.57239
   Fe27   Fe   1   0.07239   0.57239   0.07239
   Fe28   Fe   1   0.07239   0.57239   0.57239
   Fe29   Fe   1   0.57239   0.07239   0.07239
   Fe30   Fe   1   0.57239   0.07239   0.57239
   Fe31   Fe   1   0.57239   0.57239   0.07239
   Fe32   Fe   1   0.57239   0.57239   0.57239
   O01   O   1   0.375   0.221975   0.028025
```

```
O02  O  1  0.375  0.221975  0.528025
O03  O  1  0.375  0.721975  0.528025
O04  O  1  0.875  0.221975  0.028025
O05  O  1  0.875  0.721975  0.028025
O06  O  1  0.875  0.721975  0.528025
O07  O  1  0.278025  0.471975  0.125
O08  O  1  0.278025  0.471975  0.625
O09  O  1  0.278025  0.971975  0.125
O10  O  1  0.778025  0.471975  0.625
O11  O  1  0.778025  0.971975  0.125
O12  O  1  0.778025  0.971975  0.625
O13  O  1  0.471975  0.125  0.278025
O14  O  1  0.471975  0.625  0.278025
O15  O  1  0.471975  0.625  0.778025
O16  O  1  0.971975  0.125  0.278025
O17  O  1  0.971975  0.125  0.778025
O18  O  1  0.971975  0.625  0.778025
O19  O  1  0.125  0.278025  0.471975
O20  O  1  0.125  0.278025  0.971975
O21  O  1  0.125  0.778025  0.971975
O22  O  1  0.625  0.278025  0.471975
O23  O  1  0.625  0.778025  0.471975
O24  O  1  0.625  0.778025  0.971975
O25  O  1  0.221975  0.028025  0.375
O26  O  1  0.221975  0.028025  0.875
O27  O  1  0.221975  0.528025  0.375
O28  O  1  0.721975  0.028025  0.875
O29  O  1  0.721975  0.528025  0.375
O30  O  1  0.721975  0.528025  0.875
O31  O  1  0.028025  0.375  0.221975
O32  O  1  0.028025  0.875  0.221975
O33  O  1  0.028025  0.875  0.721975
O34  O  1  0.528025  0.375  0.221975
O35  O  1  0.528025  0.375  0.721975
O36  O  1  0.528025  0.875  0.721975
V01  O  0  0.221975  0.528025  0.875  # vacancy site
V02  O  0  0.721975  0.028025  0.375  # vacancy site
V03  O  0  0.028025  0.375  0.721975  # vacancy site
V04  O  0  0.528025  0.875  0.221975  # vacancy site
V05  O  0  0.375  0.721975  0.028025  # vacancy site
V06  O  0  0.875  0.221975  0.528025  # vacancy site
V07  O  0  0.278025  0.971975  0.625  # vacancy site
V08  O  0  0.778025  0.471975  0.125  # vacancy site
V09  O  0  0.471975  0.125  0.778025  # vacancy site
V10  O  0  0.971975  0.625  0.278025  # vacancy site
V11  O  0  0.125  0.778025  0.471975  # vacancy site
V12  O  0  0.625  0.278025  0.971975  # vacancy site
```

SUPPLEMENTARY MATERIAL E

FOR CHAPTER 6 – NANOMINERALOGY OF HYDROTHERMAL MAGNETITE FROM ACROPOLIS, SOUTH AUSTRALIA: GENETIC IMPLICATIONS FOR IRON–OXIDE COPPER GOLD MINERALIZATION

APPENDIX A: ADDITIONAL MATERIAL, FIGURES AND TABLES

ELECTRONIC APPENDIX A FOR CHAPTER 6

Supplementary Material – Methodology

Electron probe microanalysis (EPMA)

Quantitative EPMA were obtained using a CAMECA SX-Five Electron Probe Microanalyzer (EPMA), equipped with 5 wavelength-dispersive spectrometers (Adelaide Microscopy, The University of Adelaide). The instrument was operated at a constant accelerating voltage of 15 keV and variable beam current (see below). A constant beam spot-size of ~1 µm was utilized for the measurements. Individual analytical conditions for each analyzed element are listed below. Calibration and data reduction were conducted using 'Probe for EPMA' software (Donovan et al. 2016).

<mdl: less than minimum limit of detection.

Element	Line	Current (nA)	Crystal	Standard	Peak count (s)	Bkgd count (s)	Mean mdl (wt%)
Al	Kα	20	TAP	Astimex Plagioclase An65	20	10	0.012
Ca	Kα	20	LPET	Titanite	20	10	0.011
Fe	Kα	20	LLIF	P&H Specularite	20	10	0.03
Mg	Kα	100	TAP	Astimex Almandine	50	25	0.004
Mn	Kα	20	LLIF	P&H Rhodonite	20	10	0.028
Si	Kα	20	TAP	Astimex Plagioclase An65	20	10	0.013
Ti	Kα	20	LPET	Titanite	50	25	0.008
V	Kα	100	LLIF	Astimex Vanadium metal	35	20	0.007
Zn	Kα	100	LLIF	Astimex Willemite	50	25	0.019

Laser ablation inductively coupled plasma mass spectrometry (LA-ICP-MS)

^{57}Fe was used as the internal standard element, assuming a stoichiometric Fe content in magnetite. External reference materials GSD-1G and NIST-610 were used for trace element quantification and instrument drift correction. A laser spot diameter of 43 or 51 µm, pulse repetition rate of 5 Hz and fluence of 3.5 J/cm^2 were used. Data reduction was performed in Glitter (van Achterbergh et al. 2001). Analysis comprised 44 elements by measurement of the following isotopes: ^{24}Mg, ^{27}Al, ^{28}Si, ^{31}P, ^{43}Ca, ^{45}Sc, ^{49}Ti, ^{51}V, ^{52}Cr, ^{55}Mn, ^{59}Co, ^{60}Ni, ^{63}Cu, ^{66}Zn, ^{69}Ga, ^{75}As, ^{88}Sr, ^{89}Y, ^{90}Zr, ^{93}Nb, ^{95}Mo, ^{118}Sn, ^{121}Sb, ^{137}Ba, ^{139}La, ^{140}Ce, ^{141}Pr, ^{146}Nd, ^{147}Sm, ^{153}Eu, ^{157}Gd, ^{159}Tb, ^{163}Dy, ^{165}Ho, ^{166}Er, ^{169}Tm, ^{172}Yb, ^{175}Lu, ^{178}Hf, ^{181}Ta, ^{182}W, ^{232}Th, ^{238}U, and four isotopes of lead (^{204}Pb, ^{206}Pb, ^{207}Pb and ^{208}Pb).

Supplementary Material – Additional figures

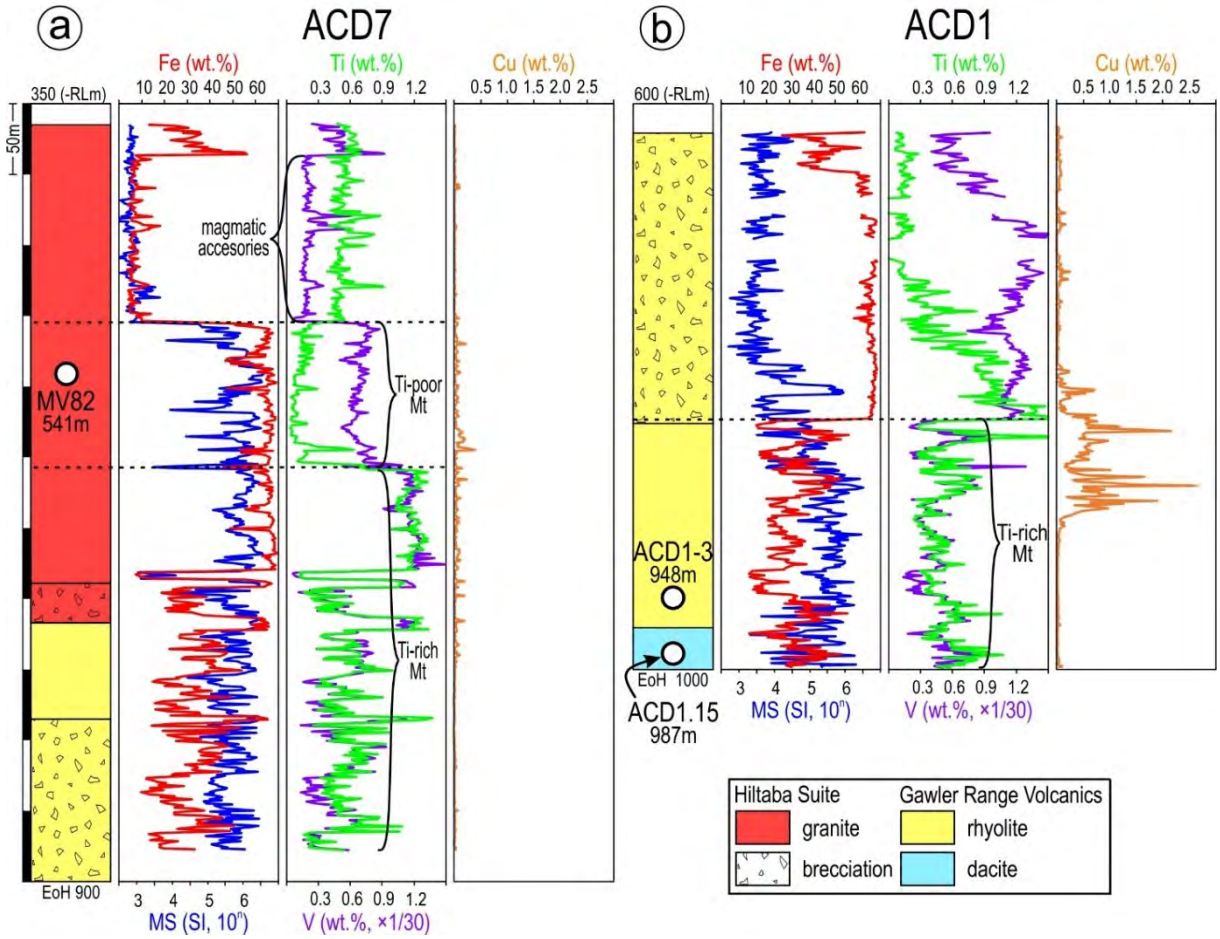

Fig. A1. (a, b) Schematic drillhole logs for holes ACD7 and ACD1, respectively, showing sample locations, simplified lithologies and downhole distributions of Ti, V, and Cu, relative to Fe and magnetic susceptibility (MS; standard international-SI). Whole-rock assays are at 1-meter intervals. Note the good spatial correlation between V and Ti relative to increases in Fe and MS associated with magnetite-rich intervals. Divergences between measured Fe contents and MS relate to the presence of hematite. High Ti-contents in the upper part of drillhole ACD7 relate to the presence of Ti-bearing magmatic accessories. Abbreviation: Mt−magnetite. Iron-oxides are present within cm-wide veins that are locally interconnected (stockwork, patches and disseminations).

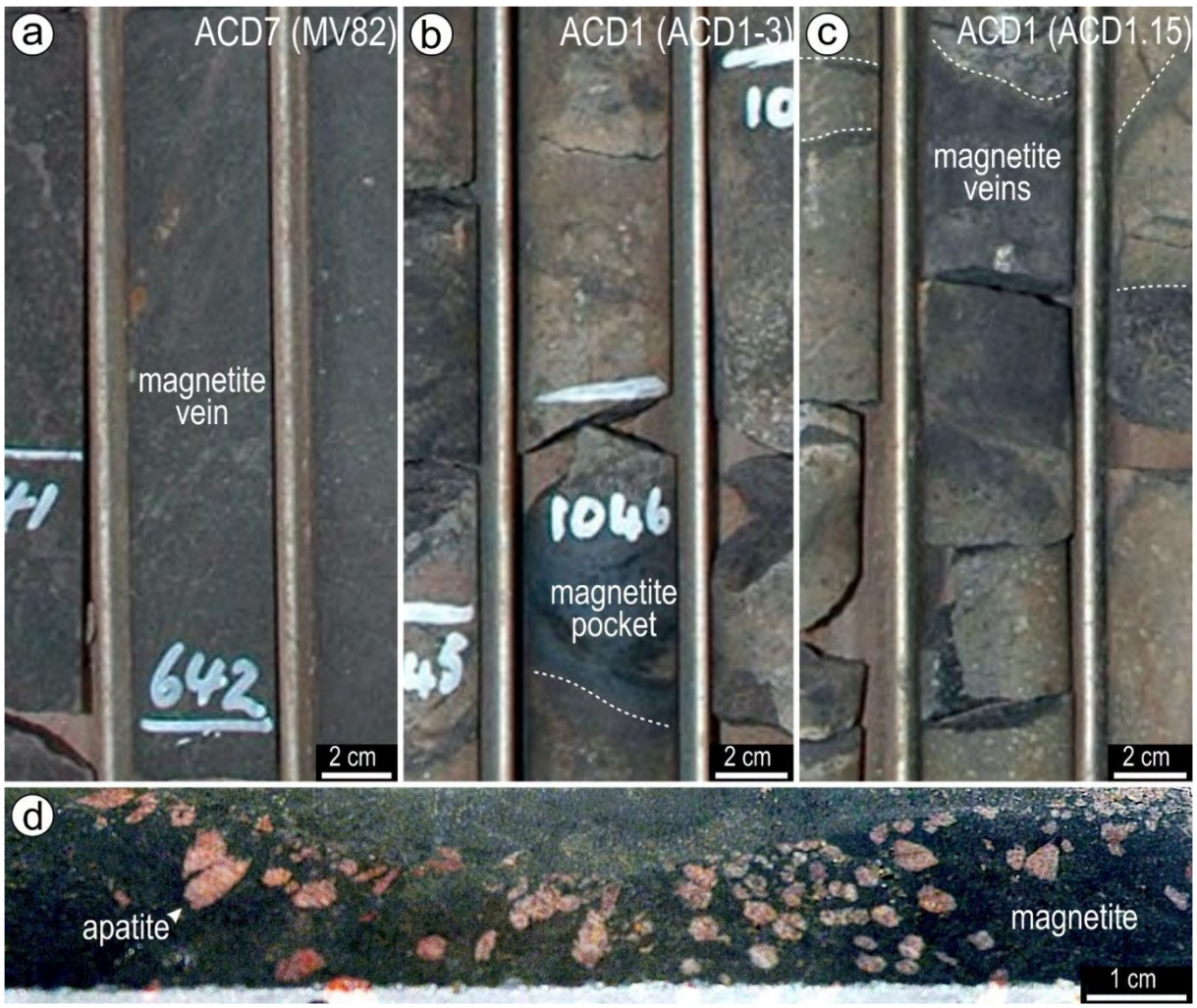

Fig. A2. Photographs of Acropolis drillcore showing sampled sections. (a) Vein of massive magnetite sectioned along dip within Hiltaba Suite (HS) granite (drillhole ACD7; sample MV82). (b, c) Magnetite-rich intervals hosted within altered Gawler Range Volcanics (GRV) lithologies from drillhole ACD1; in (b) rhyolite (sample ACD1-3) and (c) dacite (sample ACD1.15). (d) Interstitial apatite grains within magnetite vein in HS granite (drillhole ACD7).

Supplementary Material – Petrographic background for nanoscale study

In two samples (samples MV82 and ACD1.15), magnetite is coarse-grained (~300 μm-diameter), relatively equigranular, and represents >90 % of the polished block. In the third sample (ACD1-3 SK), magnetite occurs as veinlets within a groundmass of altered rhyolite.

The uppermost ~100 m-thick segment of granite partially preserves magmatic Fe-Ti-oxides, albeit with strong martitization of magnetite and replacement of titanite(+ilmenite?) by symplectites consisting of rutile, secondary silicates and carbonates (Fig. A3a). Symplectitic intergrowths among Fe-Ti-oxides, filling discrete grains in titanomagnetite from the same drillhole, ACD7, are attributable to breakdown of ilmenite$_{ss}$ within Ti-bearing hematite (Fig. A3b). Two S/TEM foils were prepared from the Ti-poor magnetite hosted in granite (Fig. A3c,

d). This magnetite displays thin, ~10 µm-wide hematite veinlets (Fig. A3e). Up to ~15 % hematite is estimated within this sample (MV82).

Trellis magnetite hosted in GRV was sampled from the deeper part of drillhole ACD1 (sample ACD1.15; Fig. A4). In this case, veinlets filled with Fe-Ti-oxides, Ti-bearing hematite and secondary Fe-hydroxides (+carbonates and quartz) are also observed and display boxwork textures typical of supergene/fault gouge alteration (Fig. A4a, b). The S/TEM foil was obtained from the margin of a grain adjacent to hematite zoned with respect to Ti and also contains nanoscale inclusions of ilmenite and rutile (Fig. A4c, d).

A second type of trellis Ti-rich magnetite, displaying various overprinting textures, was studied from the upper interval of the same drillhole (sample ACD1-3 SK; Fig. A5). Coarser, mm-sized magnetite occurs along a vein of baryte (Fig. A5a-c). The magnetite is otherwise fine-grained and brecciated to partially milled. One of the two textural varieties consist of magnetite densely mottled with inclusions, whereby the trellis networks are partially obliterated towards the grain margin (Fig. A5d). The second type displays orbicular textures developed within and across some of the lamellae forming the trellis frameworks (Fig. A5e). Three S/TEM foils were obtained from the margin of a densely mottled grain and two from the orbicular patterned grain (Fig. A5f, g).

Diverse textures relate to the martitization of Ti-rich magnetite (hosted by either HS granite or GRV rocks) towards the upper part of each drillhole (Fig. A6). Marginal martitization evolves into wider embayed domains where hematite replaces Ti-rich magnetite (Fig. A6a, b). In such cases the trellis network is still partially visible within the hematite aggregate at the direct contact with magnetite, but is partly obliterated in the patchy, outwards-growing aggregates of hematite (Fig. A6b). The occurrence of fine-grained symplectitic intergrowths of Fe-Ti-oxides surrounded by Ti-rich hematite (Fig. A6c) is typical of Ti-rich magnetite undergoing martitization. Such intergrowths are ubiquitous throughout the Ti-rich magnetite in the prospect but decrease in abundance towards the upper part of each drillhole. Recrystallization of such Ti-rich oxide aggregates results in coarser grained rutile and Ti-zoned hematite forming aggregates within pockets or along veinlets throughout the Ti-rich magnetite (Fig. A6d-f). Development of lamellar to acicular Ti-bearing hematite along some of the veinlets affected by supergene/fault gouge alteration results in typical boxwork textures host to secondary Fe-hydroxides, siderite and quartz (Fig. A6g).

Although hematite inherits a Ti-signature from magnetite during martitization, this changes to U-W-Sn-Mo in martite in the uppermost part of some drillholes, e.g., ACD2 (Courtney-Davies et al. 2019a; Fig. A6h). Some of the Ti-(Fe)-oxides forming parts of Ti-zoned hematite may be attributed to the breakdown of ilmenite$_{ss}$ within Ti-bearing hematite. Formation of later hematite can be accompanied by replacement of magnetite by bornite (Fig. A6i). In this case, hematite appears as stubby lamellae associated with covellite. The presence of covellite and hematite (and lack of Fe-hydroxides) may indicate highly acidic and oxidized fluids for sulfide precipitation prior to martite formation.

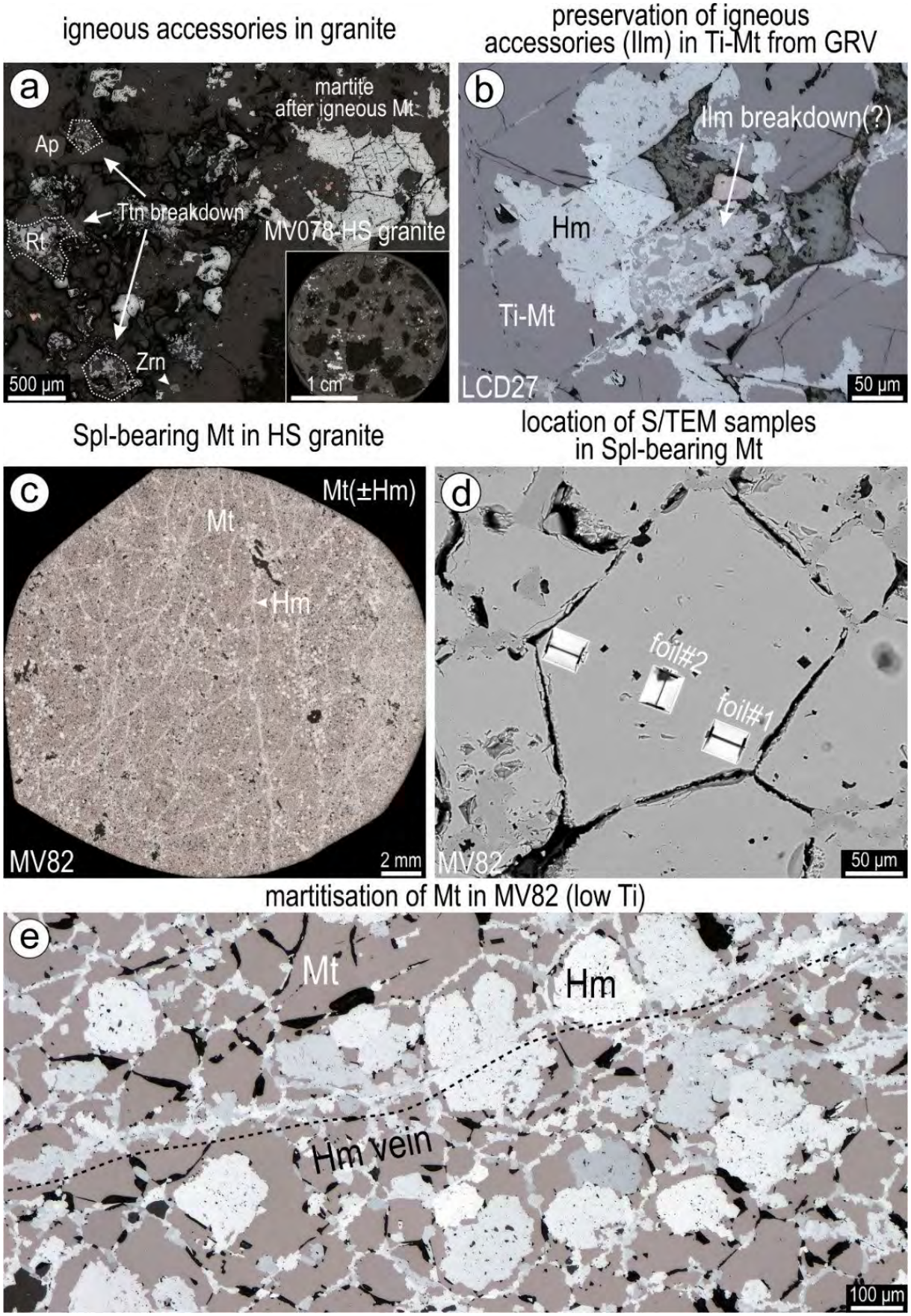

Fig. A3. Reflected light photographs (a-c, e) and BSE image (d) showing petrographic aspects of Fe-oxides in samples from drillhole ACD7. (a) Magmatic accessories in HS granite. (b) Fine-grained symplectites of rutile+hematite interpreted as breakdown ilmenite in volcanic rock

(GRV). (c, d) Map of polished block in (c) and location of S/TEM samples in (d) from the magnetite with nanoinclusions of spinel. (e) Martitization of magnetite shown in (c). Abbreviations: Ap−apatite; Hm−hematite; Ilm−ilmenite; Mt−magnetite; Rt−rutile; Spl−spinel; Ttn−titanite; Ti-Mt−titanomagnetite; Zrc−zircon. Additional samples in drillhole ACD7 and RL depth: MV078, 366 m; LCD27, 878 m.

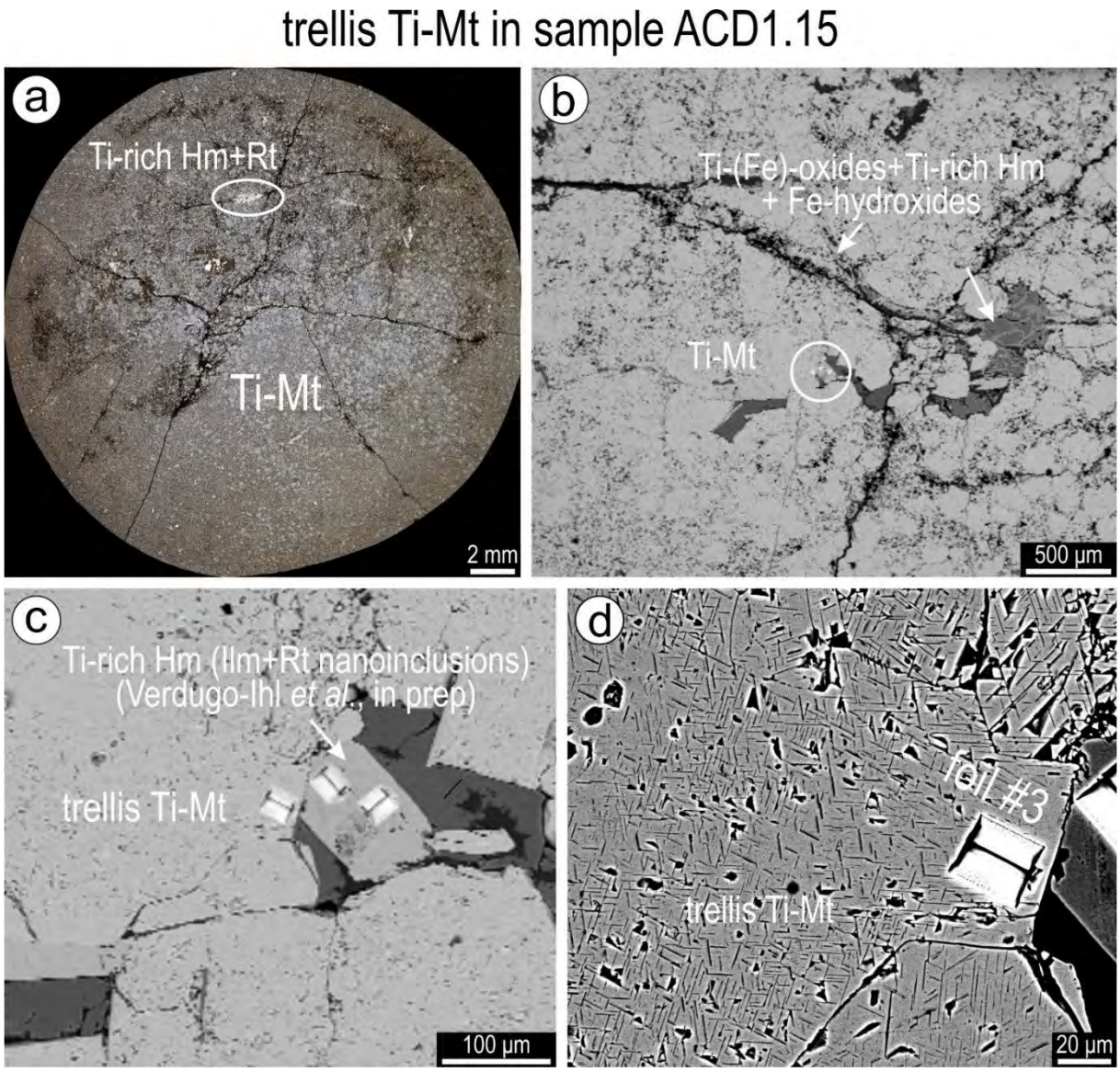

Fig. A4. Reflected light photograph (a) and BSE images (b-d) of trellis titanomagnetite. (a) Map of polished block of titanomagnetite. (b) Area of sample in (a) with fractures and pockets of Fe-Ti-oxides and Fe-hydroxides (arrowed). (c) Close up of the area circled in (b) showing typical trellis titanomagnetite adjacent to a coarse grain of Ti-rich hematite. (d) Location of S/TEM sample across trellis lamellae (Ti-rich). Abbreviations: Hm−hematite; Ilm−ilmenite; Ti-Mt−titanomagnetite; Rt−rutile.

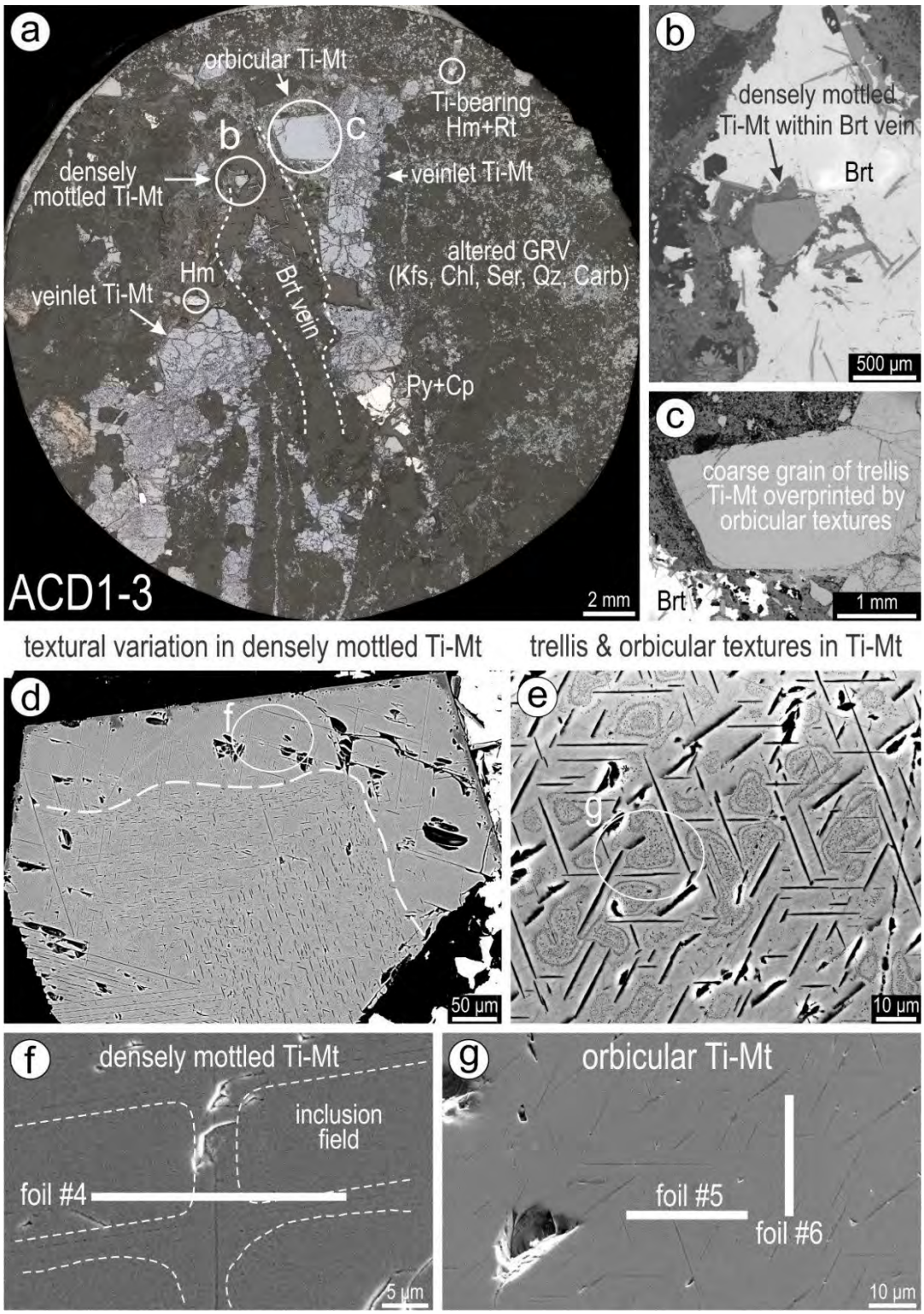

Fig. A5. Reflected light photograph (a) and BSE images (b-g) showing petrographic aspects of trellis titanomagnetite with overprint. (a) Map of polished block of veinlets of titanomagnetite in altered volcanic rock. (b, c) Details of the two magnetite grains that were sampled for nanoscale study. (d) Grain of titanomagnetite with margin depleted in trellis lamellae (dashed line) and enriched in densely mottled nanoinclusions. (e) Detail of trellis titanomagnetite with orbicular texture. (f, g) Location of S/TEM samples obtained from the two magnetite grains obtained from the circled areas marked in (d, e). Abbreviations: Brt−barite; Carb−carbonates; Chl−chlorite; Cp−chalcopyrite; Hm−hematite; Kfs−potassium feldspar; Py−pyrite; Qz−quartz; Ti-Mt−titanomagnetite; Rt−rutile; Ser−sericite.

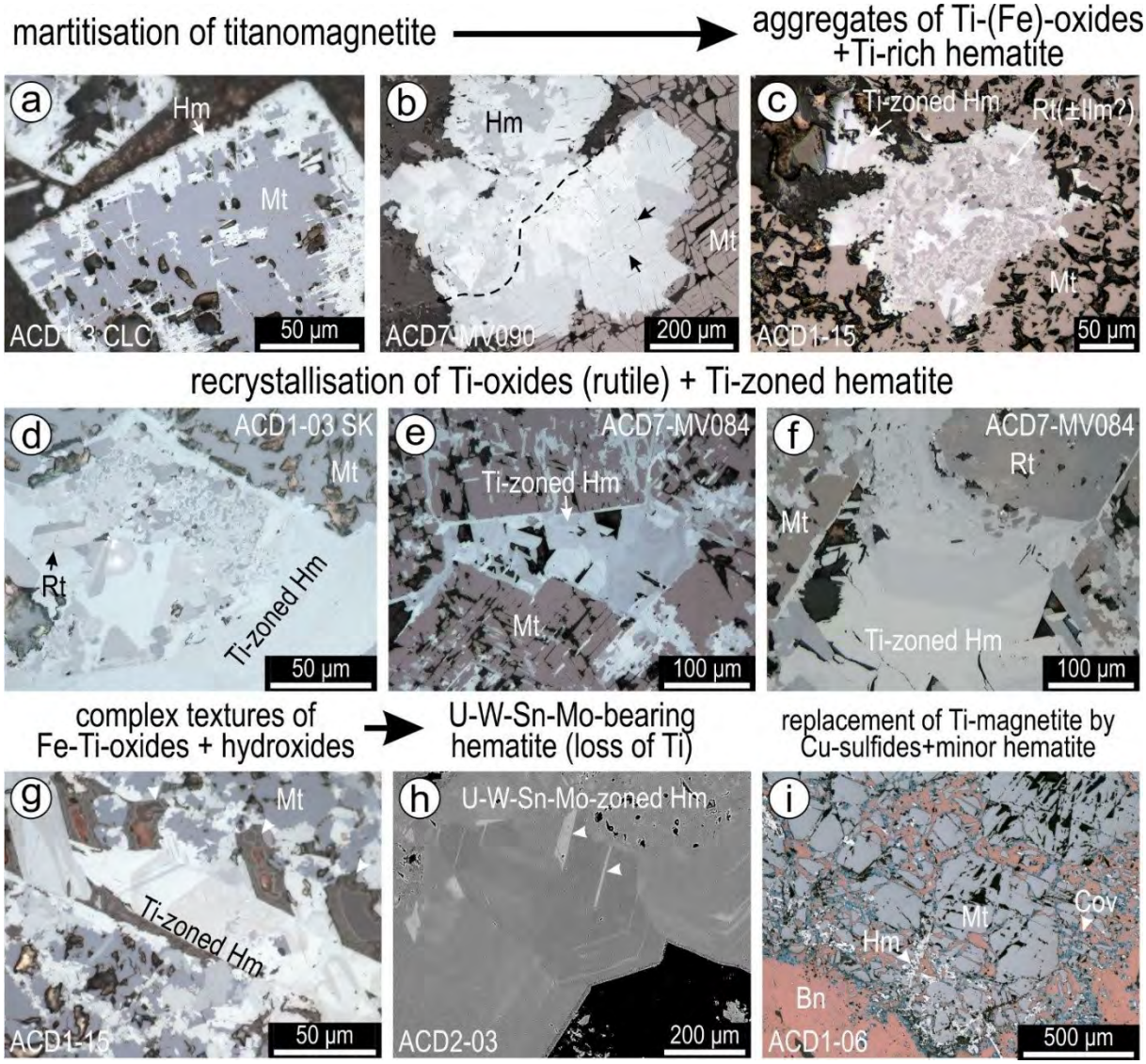

Fig. A6. Reflected light photographs showing titanomagnetite martitization (a-h) and replacement by Cu-sulfides in (i). (a) Martitization along grain boundary. (b) Coarse aggregate of hematite partially preserving trellis lamellae (dashed line). Fine-grained aggregates of Ti-(Fe)-oxides and hematite within titanomagnetite. (d-f) Titanium-bearing/rich zoned hematite associated with rutile resulting from recrystallisation as shown in (c). (g) Iron-hydroxides with rhythmic-orbicular textures typical of gauge-fault alteration surrounding Ti-zoned hematite. (h) U-W-Sn-Mo-zoned hematite that was dated at ~1.6 Ga (U-Pb LA-ICP-MS; Courtney-Davies et al. 2019). Arrows show some of the highest U-bearing bands. (i) Bornite replacing magnetite. Note the presence of covellite and hematite throughout the replaced magnetite. Abbreviations: Bn−bornite; Cov−covellite; Hm−hematite; Ilm−ilmenite; Mt−magnetite; Rt−rutile. Additional samples location and RL depth: Drillhole ACD1: ACD1-3CLC: 806.8 m; ACD1-06: 866.6 m; Drillhole ACD7: MV084: 619 m; MV090: 810 m.

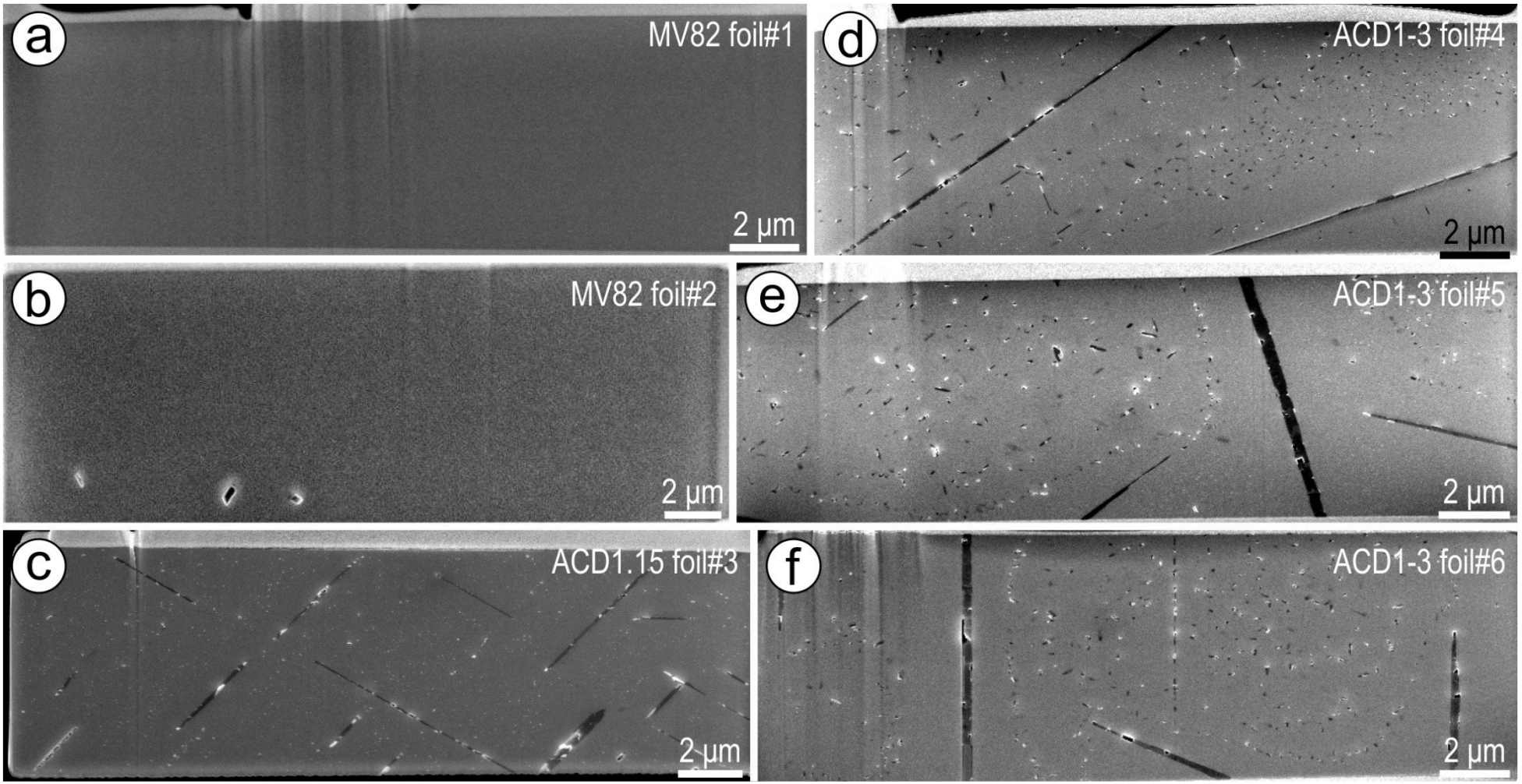

Fig. A5. SE images of the six FIB- extracted slices (#1-#6) prior to thinning and cleaning. (a, b) Titanium-poor magnetite; (d-f) Ti-rich magnetite: (c) trellis-textured magnetite, (d) densely mottled magnetite, and (e, f) orbicular magnetite.

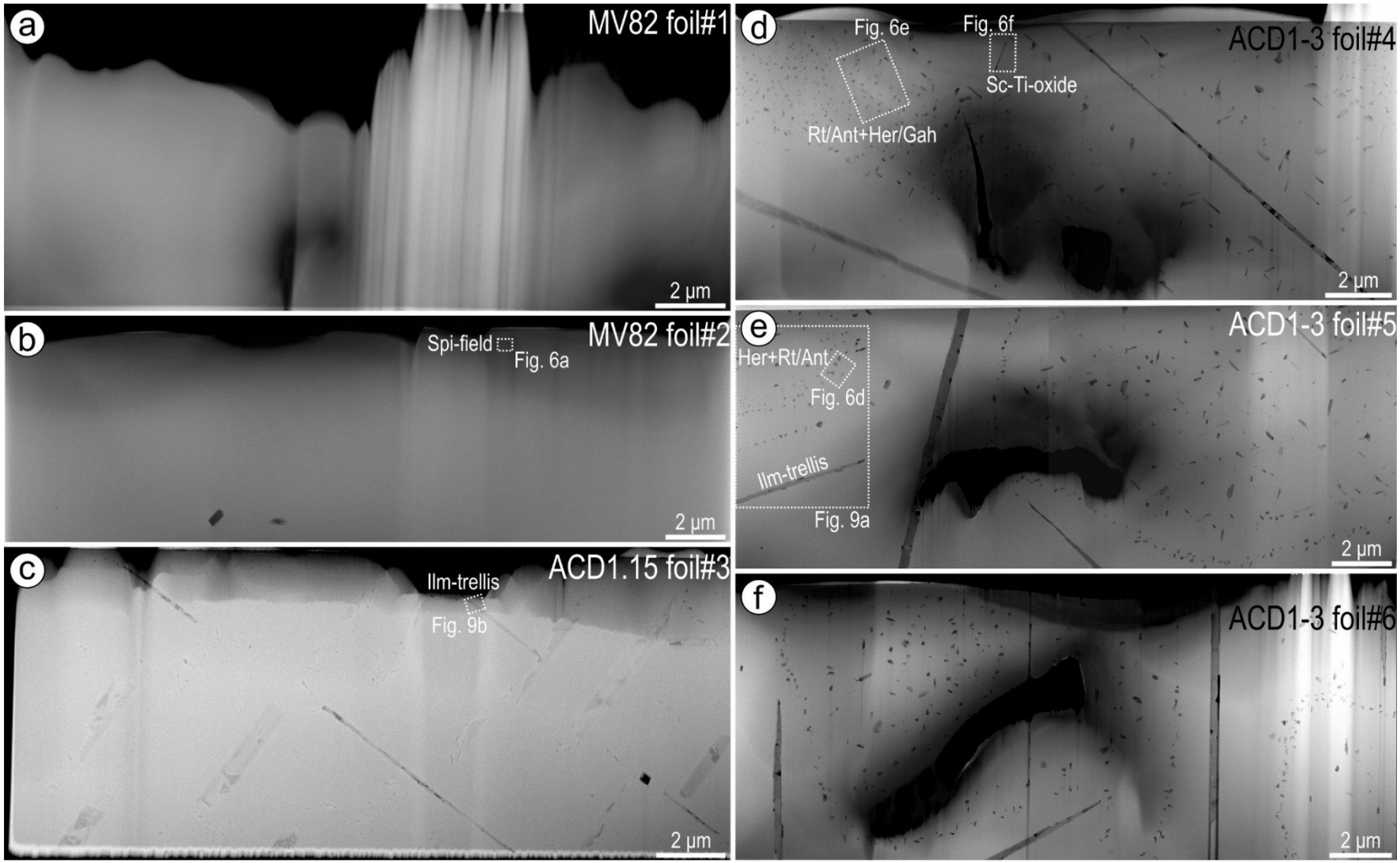

Fig. A6. (a-f) High angle annular dark field (HAADF) scanning transmission electron microscopy (STEM) images showing location of STEM-EDX maps of lamellae and/or associated inclusion fields. Abbreviations: Ant−anatase; Gah−gahnite; Her−hercynite; Ilm−ilmenite; Rt−rutile; Spi−spinel.

Supplementary Materials – Additional tables

Table A1. Summary of magnetite compositions as determined by EPMA and mineral formulae

Sample	Ti-rich magnetite									Ti-poor magnetite		
	trellis (ACD1.15, *n*=5)			orbicular (ACD1-3, *n*=10)			orbicular, ilm (ACD1-3, *n*=6)			(MV82, *n*=15)		
Concentration, wt%	Min.	Max.	Mean	Min.	Max.	Mean	Min.	Max.	Mean	Min.	Max.	Mean
CaO	0.02	0.03	0.03		<0.02			<0.02		<0.02	0.03	0.00
MgO		<0.01		<0.04	0.25	0.14	0.54	1.62	0.80	0.26	0.54	0.45
TiO_2	0.62	3.09	1.75	0.27	1.70	0.75	4.27	12.72	6.52	0.03	0.07	0.05
SiO_2	<0.02	0.06	0.04	0.03	0.06	0.05	0.03	0.06	0.05	0.03	0.11	0.05
Al_2O_3	0.32	0.39	0.36	0.32	0.54	0.44	0.38	0.76	0.54	0.23	0.33	0.29
$Fe_2O_{3(Total)}$	99.36	102.71	100.93	101.14	105.35	103.82	88.34	99.65	97.03	101.61	104.36	102.83
FeO	31.61	33.79	32.57	31.56	32.94	32.16	34.17	38.68	35.80	30.07	31.23	30.54
Fe_2O_3	61.98	67.44	64.73	65.43	69.63	68.08	45.35	61.67	57.24	68.20	69.65	68.89
MnO		<0.02		<0.05	0.08	0.02	<0.05	2.20	0.76	<0.05	0.13	0.07
ZnO	0.03	0.04	0.04	<0.06	0.10	0.01		<0.06			<0.06	
V_2O_3	0.05	0.07	0.06	<0.05	0.09	0.06	<0.06	0.09	0.02		<0.05	
Sum	99.04	100.28	99.57	99.24	103.11	101.70	100.17	102.73	101.73	99.27	101.57	100.34
Calculated formulae (atoms per formula unit; apfu) based on 32 O atoms												
Mg	0.000	0.000	0.000	0.000	0.111	0.062	0.240	0.716	0.354	0.117	0.249	0.204
Ca	0.006	0.010	0.008	0.000	0.000	0.000	0.000	0.000	0.000	0.000	0.011	0.001
Mn	0.000	0.000	0.000	0.000	0.019	0.004	0.000	0.551	0.190	0.000	0.034	0.017
Fe^{2+}	8.137	8.715	8.401	7.996	8.404	8.118	8.560	9.577	8.931	7.760	7.904	7.806
Zn	0.007	0.009	0.008	0.000	0.021	0.002	0.000	0.000	0.000	0.000	0.000	0.000
$\sum M^{2+}$			8.417			8.185			9.475			8.028
Al	0.115	0.142	0.130	0.114	0.197	0.156	0.136	0.267	0.189	0.083	0.117	0.103
V	0.014	0.017	0.015	0.000	0.022	0.015	0.000	0.022	0.005	0.000	0.000	0.000
Fe^{3+}	14.385	15.561	15.020	15.022	15.717	15.458	10.103	13.902	12.856	15.807	15.864	15.841
$\sum M^{3+}$			15.165			15.629			13.050			15.944
Si	0.000	0.018	0.011	0.010	0.018	0.014	0.010	0.017	0.013	0.009	0.035	0.017
Ti	0.142	0.718	0.406	0.062	0.391	0.172	0.963	2.832	1.462	0.008	0.016	0.011
$\sum M^{4+}$			0.417			0.185	0.974	2.844	1.475	0.019	0.046	0.028
Sum			24			24			24			24
X_{Mg}	-	-	-	0.0019	0.0047	0.0029	-	-	-	0.0049	0.010	0.0086
Temperature, °C	-	-	-	531	608	565	-	-	-	613	690	667

Sample means calculated considering values below minimum detection limits as zero. Blanks denote that all measurements within a sample were below minimum detection limits. Temperature estimates calculated using the empirical thermometer of Canil and Lacourse (2020). Abbreviations: Min.−minimum; Max.−maximum.

Table A2. Summary statistics of magnetite trace element data by LA-ICP-MS, concentrations in ppm.

Type	Ti-rich magnetite										Ti-poor magnetite				
variety/	trellis (ACD1.15, *n*=37)					orbicular (ACD1-3, *n*=30)					(MV82, *n*=21)				
sample	Min.	Max.	Mean	G.M.	S.D.	Min.	Max.	Mean	G.M.	S.D.	Min.	Max.	Mean	G.M.	S.D.
Mg	48.5	1,450	404	242	424	18.9	1,480	341	216	343	1,150	3,250	2,130	2,050	612
Al	1,610	3,910	2,610	2,570	450	1,910	2,560	2,230	2,230	176	1,440	1,560	1,490	1,490	27.8
Si	518	4,750	1,520	1,270	1,020	63.9	492	164	154	71.2	224	687	318	306	103
P	<28.9	186	58.3	50.8	35.6	<2.46	12.2	5.84	5.12	3.04	<2.7	25.3	13.9	12.3	6.45
Ca	NA	NA	NA	NA	NA	<16.5	49.3	22.8	21.8	8.09	<23.6	79.7	36.6	34.0	16.2
Sc	11.4	36.6	24.6	23.6	7.12	27.1	44.7	37.2	36.9	4.22	4.46	5.05	4.77	4.77	0.12
Ti	6,700	16,400	12,800	12,600	2,180	9,600	14,700	11,200	11,200	1,230	371	419	399	399	13.3
V	356	473	414	413	29.1	419	479	442	442	16.6	230	249	235	235	4.35
Cr	<0.77	7.06	2.83	2.63	1.12	<0.17	67.1	5.91	1.54	12.5	<0.19	1.10	0.29	0.25	0.21
Mn	32.9	118	58.3	56.5	15.8	48.3	534	126	99.2	111	155	681	343	312	150
Co	14.9	26.5	20.1	20.0	2.42	26.6	42.0	31.2	31	3.77	116	128	121	121	3.16
Ni	24.6	50.6	34.7	34.1	6.49	29.9	43.2	34.8	34.7	2.84	59.7	65.0	61.8	61.8	1.33
Cu	<0.92	39.4	7.46	4.27	8.52	<0.076	1.77	0.22	0.15	0.32	0.88	3.1	1.61	1.52	0.58
Zn	64.1	267	188	179	53.3	72.7	400	134	120	73.3	63.8	77.1	69.9	69.8	3.76
Ga	31.4	52.9	40.7	40.4	5.09	42.3	57.1	48.9	48.8	4.06	14.5	16.2	15.2	15.2	0.40
As	<0.81	3.99	2.16	1.93	1.01	<0.13	0.64	0.22	0.20	0.11	<0.16	0.35	0.20	0.20	0.047
Sr	0.054	10.8	3.01	2.09	2.29	<0.001	3.88	0.34	0.032	0.84	0.003	0.072	0.024	0.016	0.022
Y	<0.03	3.26	1.00	0.72	0.67	<0.002	1.16	0.13	0.016	0.26	0.019	0.41	0.10	0.064	0.10
Zr	0.32	3.31	1.28	1.10	0.70	0.088	0.73	0.31	0.25	0.22	0.089	0.28	0.17	0.17	0.046
Nb	0.321	4.50	1.56	1.36	0.89	0.17	3.46	1.57	1.11	1.15	1.83	4.33	3.25	3.17	0.71
Mo	<0.001	5.67	0.45	0.19	0.96	0.042	0.19	0.13	0.12	0.036	<0.011	0.26	0.16	0.15	0.053
Sn	5.26	21.6	12.3	11.4	4.63	5.94	10.3	7.71	7.66	0.92	13.7	15.7	14.7	14.7	0.44
Sb	0.16	1.47	0.47	0.39	0.31	<0.032	0.22	0.062	0.056	0.035	<0.035	0.086	0.046	0.045	0.013
Ba	<0.001	35.5	7.47	1.16	9.31	<0.001	2.07	0.27	0.028	0.51	<0.001	0.39	0.089	0.029	0.11
La	0.06	45.7	7.60	2.93	10.8	<0.001	1.00	0.079	0.014	0.19	0.002	0.58	0.15	0.056	0.18
Ce	0.11	40.7	7.41	3.73	9.15	0.001	1.75	0.15	0.025	0.35	0.012	1.33	0.32	0.16	0.34
Pr	<0.02	4.53	0.75	0.36	1.00	0.001	0.24	0.023	0.006	0.05	0.002	0.18	0.041	0.018	0.047
Nd	<0.13	8.15	1.77	0.96	1.94	0.003	1.19	0.12	0.029	0.25	<0.009	0.66	0.14	0.074	0.17
Sm	<0.001	1.22	0.25	0.18	0.22	0.006	0.29	0.035	0.018	0.06	<0.01	0.13	0.034	0.025	0.033
Eu	<0.001	0.75	0.11	0.066	0.13	0.002	0.21	0.018	0.006	0.041	<0.002	0.007	0.004	0.004	0.001
Gd	<0.001	1.03	0.25	0.17	0.18	<0.008	0.31	0.041	0.023	0.065	<0.01	0.10	0.025	0.021	0.021
Tb	<0.01	0.44	0.05	0.037	0.071	0.001	0.065	0.006	0.003	0.012	0.001	0.017	0.004	0.003	0.004
Dy	<0.06	0.81	0.32	0.26	0.20	<0.004	0.40	0.04	0.016	0.081	<0.006	0.094	0.022	0.015	0.023
Ho	<0.001	1.15	0.10	0.052	0.19	0.001	0.056	0.006	0.003	0.011	0.001	0.015	0.004	0.003	0.004
Er	<0.04	0.78	0.24	0.19	0.16	0.002	0.17	0.025	0.01	0.042	0.006	0.03	0.011	0.01	0.006
Tm	<0.001	0.50	0.06	0.042	0.081	0.001	0.023	0.004	0.003	0.005	0.001	0.008	0.003	0.002	0.002
Yb	<0.07	0.60	0.20	0.18	0.11	0.005	0.091	0.016	0.011	0.02	<0.005	0.051	0.013	0.011	0.011
Lu	<0.001	0.22	0.05	0.036	0.046	0.001	0.015	0.004	0.003	0.004	0.001	0.007	0.002	0.002	0.001
Hf	<0.001	0.97	0.14	0.054	0.17	<0.001	0.10	0.031	0.022	0.021	<0.001	0.045	0.017	0.013	0.011
Ta	<0.001	0.51	0.11	0.061	0.11	0.02	0.097	0.06	0.056	0.021	0.46	0.68	0.56	0.56	0.057
W	<0.001	2.80	0.59	0.34	0.60	<0.001	0.99	0.09	0.021	0.20	0.006	0.026	0.011	0.01	0.004
^{204}Pb	0.004	0.71	0.13	0.063	0.15	<0.006	0.18	0.02	0.014	0.032	<0.006	0.023	0.01	0.009	0.004
^{206}Pb	0.04	13.5	2.53	1.21	2.98	<0.003	3.14	0.18	0.02	0.58	<0.003	0.038	0.008	0.007	0.008
^{207}Pb	0.06	10.6	1.82	0.90	2.16	0.002	3.21	0.16	0.019	0.58	<0.003	0.028	0.007	0.006	0.005
^{208}Pb	0.06	26.6	4.62	2.17	5.75	<0.004	7.17	0.36	0.038	1.31	<0.004	0.049	0.013	0.011	0.011
∑Pb	0.22	51.4	9.11	4.46	11.0	0.016	13.7	0.72	0.11	2.5	0.02	0.12	0.038	0.035	0.022
Th	<0.05	31.9	4.44	2.44	5.69	0.001	1.99	0.15	0.013	0.39	0.002	0.28	0.042	0.018	0.065
U	0.08	92.2	6.00	1.25	16.9	<0.001	0.71	0.073	0.009	0.17	0.003	0.044	0.01	0.008	0.009

Summary statistics treat concentrations lying below their respective detection limit as that mdl value. Calcium values are omitted for ACD1.15 due to high background. Abbreviations: Min.−minimum; Max.−maximum; G.M.−geometric mean; S.D.−standard deviation; NA−not available.

Table A3. Nano-thermooxybarometric estimations based on magnetite and ilmenite pairs from STEM-EDX data.

Sample	trellis, ACD1.15									
oxide, wt%	Mt1	Ilm1	Mt2	Ilm1	Mt1	Ilm2	Mt2	Ilm2	Mt-mean	Ilm-mean
TiO_2	0.51	49.47	0.59	49.47	0.51	49.35	0.59	49.35	0.55	49.41
Al_2O_3	0.08	0.24	0.06	0.24	0.08	0.29	0.06	0.29	0.07	0.26
$FeO_{(Total)}$	98.17	46.73	98.10	46.73	98.17	46.82	98.10	46.82	98.13	46.77
MnO	0.87	3.31	0.87	3.31	0.87	3.25	0.87	3.25	0.87	3.28
MgO	0.23	<mdl	0.23	<mdl	0.23	0.01	0.23	0.01	0.23	0.01
ZnO	0.08	0.20	0.08	0.20	0.08	0.16	0.08	0.16	0.08	0.18
V_2O_3	0.06	0.05	0.07	0.05	0.06	0.12	0.07	0.12	0.07	0.08
Sum	100.00	100.00	100.00	100.00	100.00	100.00	100.00	100.00	100.00	100.00
APFU										
Ti	0.014	0.935	0.016	0.935	0.014	0.933	0.016	0.933	0.015	0.934
Al	0.003	0.007	0.002	0.007	0.003	0.008	0.002	0.008	0.003	0.008
Fe^{3+}	1.968	0.121	1.964	0.121	1.968	0.124	1.964	0.124	1.966	0.122
Fe^{2+}	0.973	0.861	0.975	0.861	0.973	0.860	0.975	0.860	0.974	0.861
Mn	0.027	0.070	0.026	0.070	0.027	0.069	0.026	0.069	0.026	0.070
Mg	0.012	0.000	0.012	0.000	0.012	0.000	0.012	0.000	0.012	0.000
Zn	0.002	0.004	0.002	0.004	0.002	0.003	0.002	0.003	0.002	0.003
V	0.002	0.001	0.002	0.001	0.002	0.002	0.002	0.002	0.002	0.002
Sum	3.000	2.000	3.000	2.000	3.000	2.000	3.000	2.000	3.000	2.000
Calc. Methods (Mol frac.)	Ulv	Ilm	Ulv	Ilm	Ulv	Ilm	Ulv	Ilm	Ulv	Ilm
Lindsley & Spencer (1982)	0.014	0.937	0.016	0.937	0.014	0.935	0.016	0.935	0.015	0.936
Stormer (1983)	0.013	0.937	0.015	0.937	0.013	0.936	0.015	0.936	0.014	0.936
Geothermobarometer by										
X'Ulv & X'Ilm from:	T, °C	$\log_{10}fO_2$	T, °C	$\log_{10}fO_2$	T, °C	$\log_{10}fO_2$	T, °C	$\log_{10}fO_2$	T, °C	$\log_{10}fO_2$
Lindsley & Spencer (1982)	562	-19.20	569	-19.07	564	-19.04	572	-18.91	567	-19.05
Stormer (1983)	560	-19.24	567	-19.11	562	-19.11	569	-18.99	564	-19.11
Mean	561	-19.22	568	-19.09	563	-19.08	570	-18.95	566	-19.08

Table A3. (Continued) Nano-thermooxybarometric estimations based on magnetite and ilmenite pairs from STEM-EDX data.

Sample	orbicular, ACD1-3									
oxide, wt%	Mt	Ilm1	Mt	Ilm2	Mt	Ilm3	Mt	Ilm5	Mt	Ilm-mean
TiO_2	0.06	51.12	0.06	50.30	0.06	50.37	0.06	50.57	0.06	50.57
Al_2O_3	0.51	0.21	0.51	0.20	0.51	0.12	0.51	0.17	0.51	0.17
$FeO_{(Total)}$	98.61	33.43	98.61	34.20	98.61	34.79	98.61	33.51	98.61	33.51
MnO	0.54	10.94	0.54	11.37	0.54	11.36	0.54	11.13	0.54	11.13
MgO	0.19	4.30	0.19	3.93	0.19	3.37	0.19	4.61	0.19	4.61
ZnO	NA	NA	NA	NA	NA	NA	NA	NA	NA	NA
V_2O_3	0.08	<mdl	0.08	<mdl	0.08	<mdl	0.08	<mdl	0.08	<mdl
Sum	100.00	100.00	100.00	100.00	100.00	100.00	100.00	100.00	100.00	100.00
APFU										
Ti	0.002	0.934	0.002	0.921	0.002	0.927	0.002	0.921	0.002	0.921
Al	0.022	0.006	0.022	0.006	0.022	0.003	0.022	0.005	0.022	0.005
Fe^{3+}	1.973	0.126	1.973	0.152	1.973	0.143	1.973	0.152	1.973	0.152
Fe^{2+}	0.975	0.553	0.975	0.544	0.975	0.569	0.975	0.527	0.975	0.527
Mn	0.016	0.225	0.016	0.234	0.016	0.235	0.016	0.228	0.016	0.228
Mg	0.010	0.156	0.010	0.143	0.010	0.123	0.010	0.167	0.010	0.167
Zn	NA	NA	NA	NA	NA	NA	NA	NA	NA	NA
V	0.002	0.000	0.002	0.000	0.002	0.000	0.002	0.000	0.002	0.000
Sum	3.000	2.000	3.000	2.000	3.000	2.000	3.000	2.000	3.000	2.000
Calc. methods (Mol frac.)	Ulv	Ilm	Ulv	Ilm	Ulv	Ilm	Ulv	Ilm	Ulv	Ilm
Lindsley & Spencer (1982)	0.002	0.919	0.002	0.901	0.002	0.907	0.002	0.901	0.002	0.901
Stormer (1983)	0.002	0.920	0.002	0.903	0.002	0.910	0.002	0.902	0.002	0.902
Geothermobarometer by										
X'Ulv & X'Ilm from	T, C	$\log_{10}fO_2$	T, C	$\log_{10}fO_2$	T, C	$\log_{10}fO_2$	T, C	$\log_{10}fO_2$	T, C	$\log_{10}fO_2$
Lindsley & Spencer (1982)	493	-19.41	507	-18.32	503	-18.64	507	-18.35	503	-18.65
Stormer (1983)	492	-19.47	505	-18.45	499	-18.88	506	-18.37	501	-18.77
Mean	492	-19.44	506	-18.38	501	-18.76	506	-18.36	502	-18.71

APFU calculations are based on totals of four and three oxygen atoms in magnetite and ilmenite, respectively, using the ILMAT spreadsheet of Lepage (2003, and references therein). Average temperature and log(fO_2) from thermooxybarometers of Lindsley and Spencer (1982), Stormer (1983), and calibrations of Andersen and Lindsley (1985). Stability of buffering assemblages calculated from data provided in Frost (1991). Note that Zn was not observed in the orbicular magnetite and therefore it was not among the elements measured. Abbreviations: M−magnetite; Ilm−ilmenite; Ulv−ulvöspinel; NA−not analysed.

Additional references

Andersen, D.J., and Lindsley, D.H. (1985) New (and final!) model for the Ti-magnetite/ilmenite geothermometer and oxygen barometer. Abstract, AGU 1985 Spring Meet. Eos Transactions, 66, 416.

Canil, D., and Lacourse, T. (2020) Geothermometry using minor and trace elements in igneous and hydrothermal magnetite. Chemical Geology, 541, 119576. https://doi.org/10.1016/j.chemgeo.2020.119576

Courtney-Davies, L., Ciobanu, C.L., Verdugo-Ihl, M.R., Dmitrijeva, M., Cook, N.J., Ehrig, K., and Wade, B.P. (2019a) Hematite geochemistry and geochronology resolve genetic and temporal links among iron-oxide copper gold systems, Olympic Dam district, South Australia. Precambrian Research, 335, 105480. https://doi.org/10.1016/j.precamres.2019.105480

Donovan JJ, Singer JW, Armstrong JT (2016) A new EPMA method for fast trace element analysis in simple matrices. Am Mineral 101, 1839–1853. https://doi.org/10.2138/am-2016-5628

Lepage, L.D. (2003) ILMAT: an Excel worksheet for ilmenite–magnetite geothermometry and geobarometry. Computers and Geosciences 29, 673–678. https://doi.org/10.1016/S0098-3004(03)00042-6

Lindsley, D.H., and Spencer, K.J. (1982) Fe−Ti oxide geothermometry: Reducing analyses of coexisting Ti-magnetite (Mt) and ilmenite (Ilm). Transactions, American Geophysical Union 63, 471.

Stormer, J.C. (1983) The effects of recalculation on estimates of temperature and oxygen fugacity from analyses of multicomponent iron-titanium oxides. American Mineralogist, 68, 586–594.

van Achterbergh, E., Ryan, C.G., Jackson, S.E., and Griffin, W.L. (2001) Data reduction software for LA-ICP-MS, in: Sylvester, P.J. (Ed.), Laser-Ablation-ICPMS in the Earth Sciences; Principles and Applications. Mineralogical Association of Canada, Short Course Series, 29. pp. 239–243.

SUPPLEMENTARY MATERIAL F

FOR CHAPTER 7 –FERRO-TSCHERMAKITE WITH SHORT RANGE DISORDER IDENTIFIED IN SILICIAN MAGNETITE

APPENDIX A: ADDITIONAL FIGURES AND TABLES.

ELECTRONIC APPENDIX A FOR CHAPTER 7

Supplementary Material – Additional figures and tables

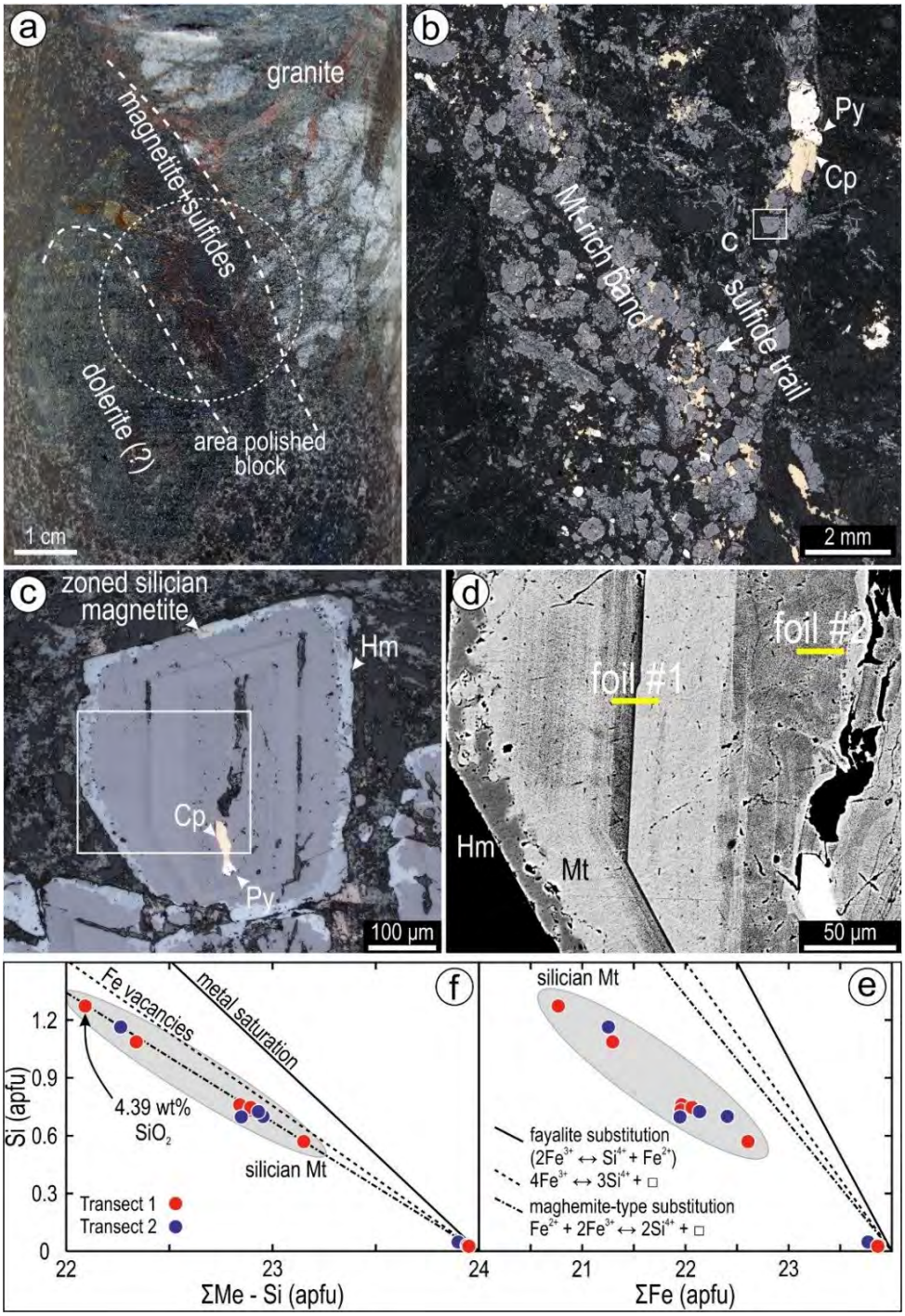

Figure A1. (a) Photograph of drill core sample from where the studied sample was cut. Magnetite (Mt) forms a band at the contact between altered granite and dolerite (?). (b, c) Reflected light images showing details of magnetite grains. Note trails of sulfides crosscutting the magnetite band in (b). Crystal zoning with respect to fine, dusty inclusions in magnetite can be seen in (c). Back scatter electron (BSE) image showing location of the two FIB cuts from where S/TEM foils were prepared. (e) Plot of Si (a.p.f.u.) *vs.* Me-Si (a.p.f.u.), and (f) Si (a.p.f.u.) *vs.* Fe (a.p.f.u.), for silician magnetite. Mineral formula calculated using the approach of Huberty et al. (2012). Abbreviations: Cp–chalcopyrite; Hm Abbreviations: Cp–chalcopyrite; Py–pyrite. hematite; Py–pyrite.

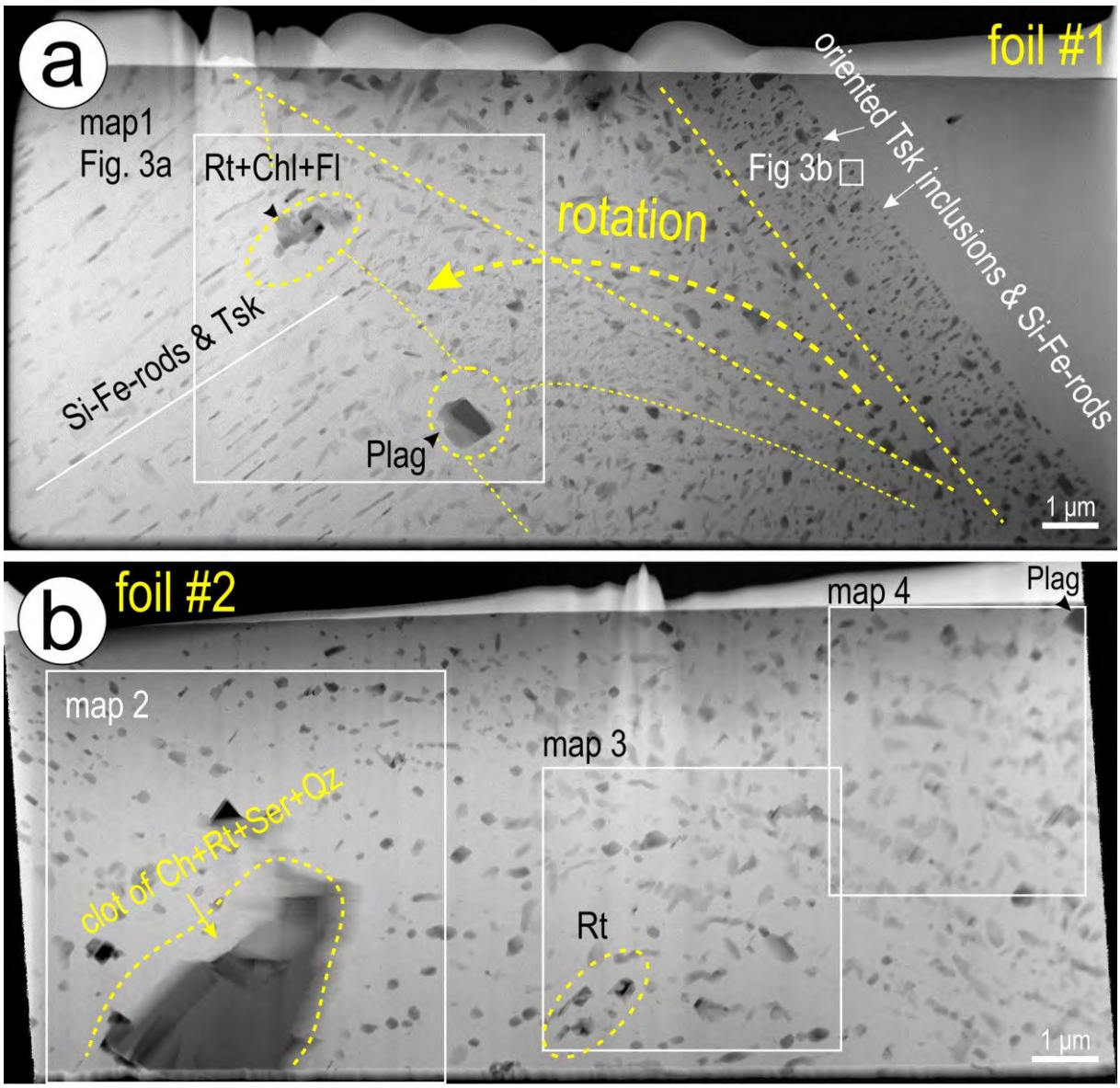

Figure A2. Overview of the studied TEM foils, also indicating mapped areas and locations of inclusions and Si-Fe-nanorods discussed in the text. Abbreviations: Chl–chlorite; Plag–plagioclase; Qz–quartz; Rt–rutile; Ser–sericite; Tsk–tschermakite.

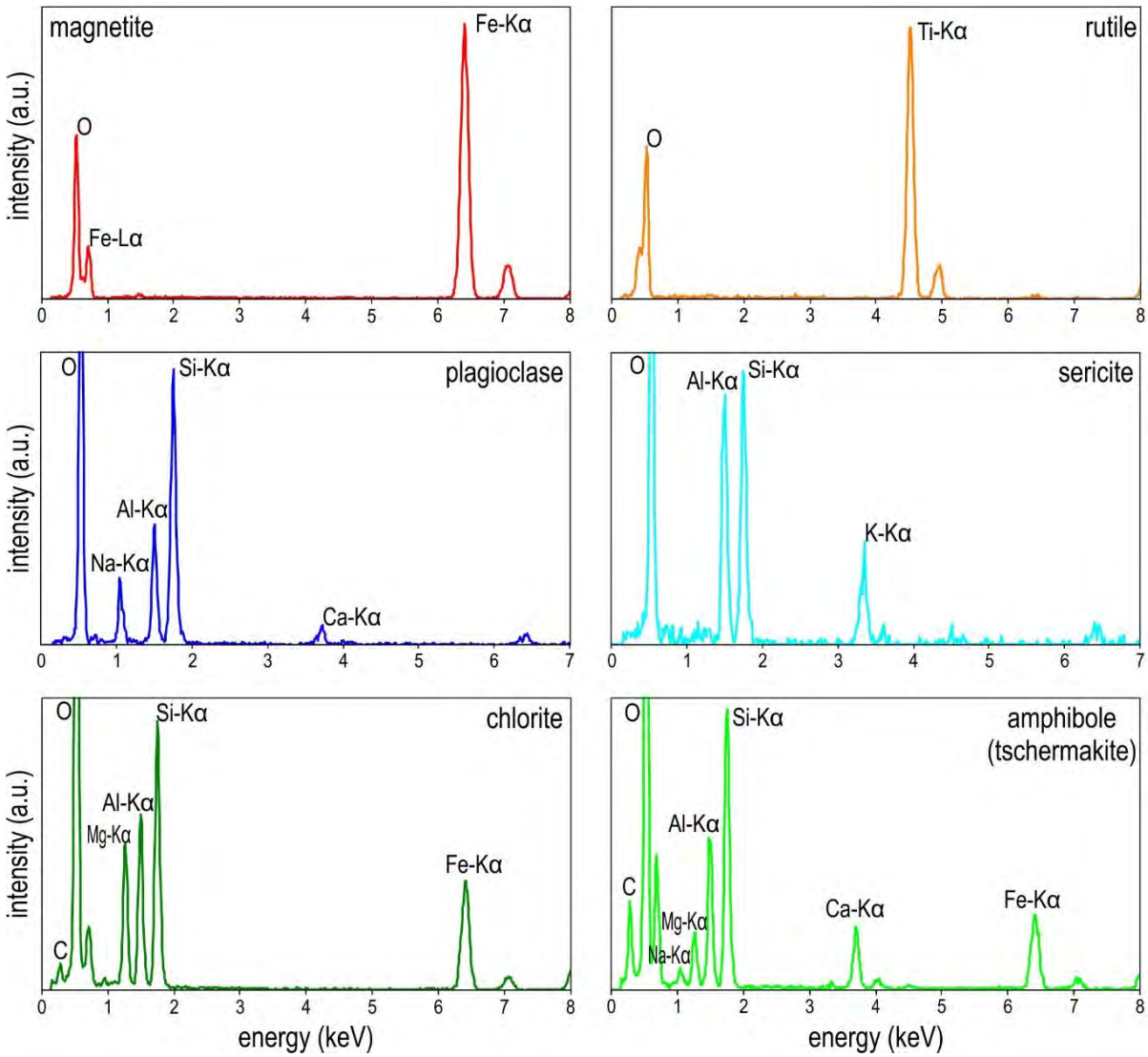

Figure A3. Representative EDX spectra for magnetite, rutile, plagioclase, sericite, chlorite and tschermakite.

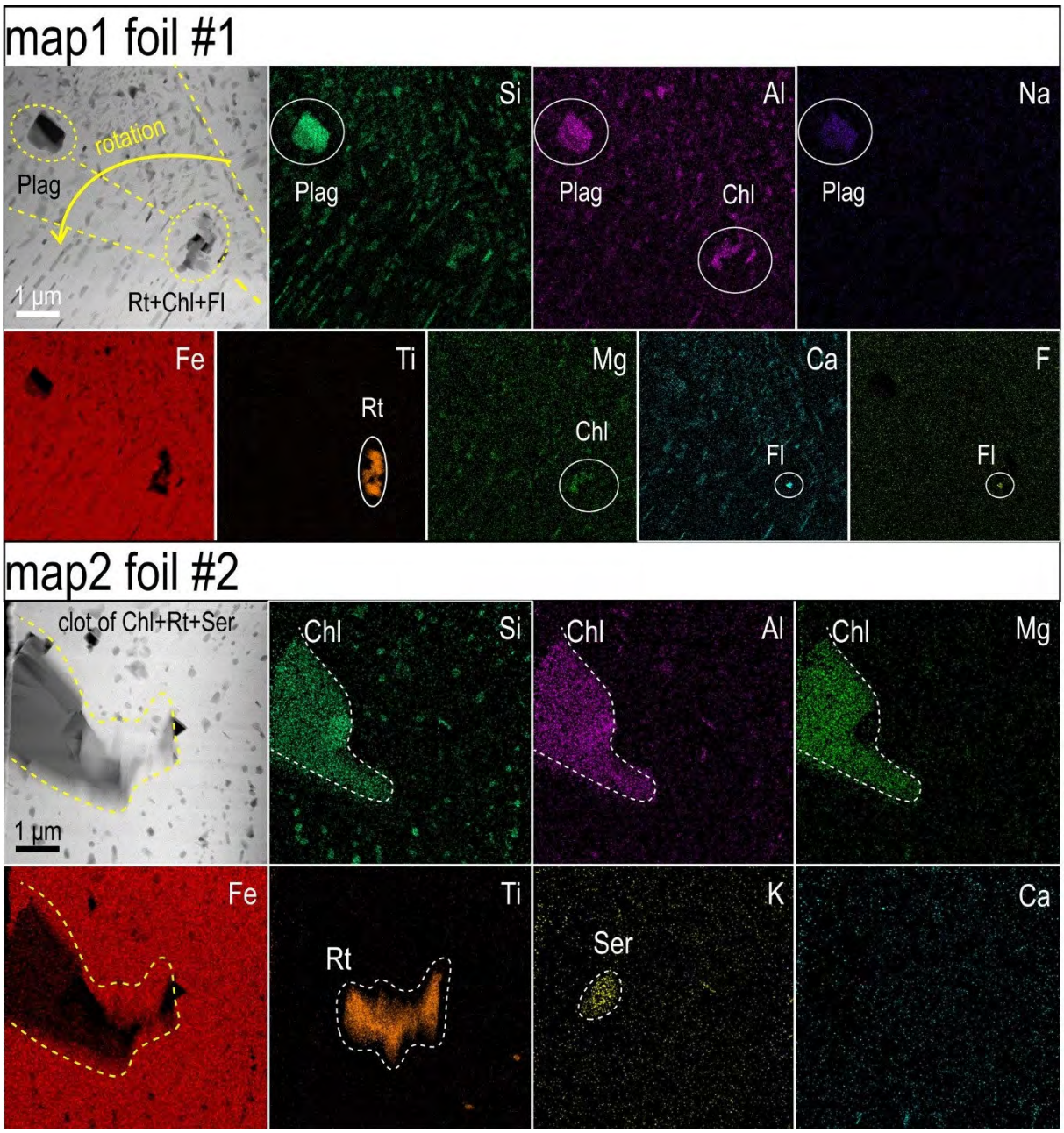

Figure A4. STEM EDX element maps of areas in magnetite showing the presence of coarser inclusions and clots. Mineral clots at junctions between zones of changing direction of inclusion orientation with rotational fabric indicated in map 1 (top). Abbreviations: Chl–chlorite; Fl–fluorite; Rt–rutile; Ser–sericite; Plag-plagiocalse.

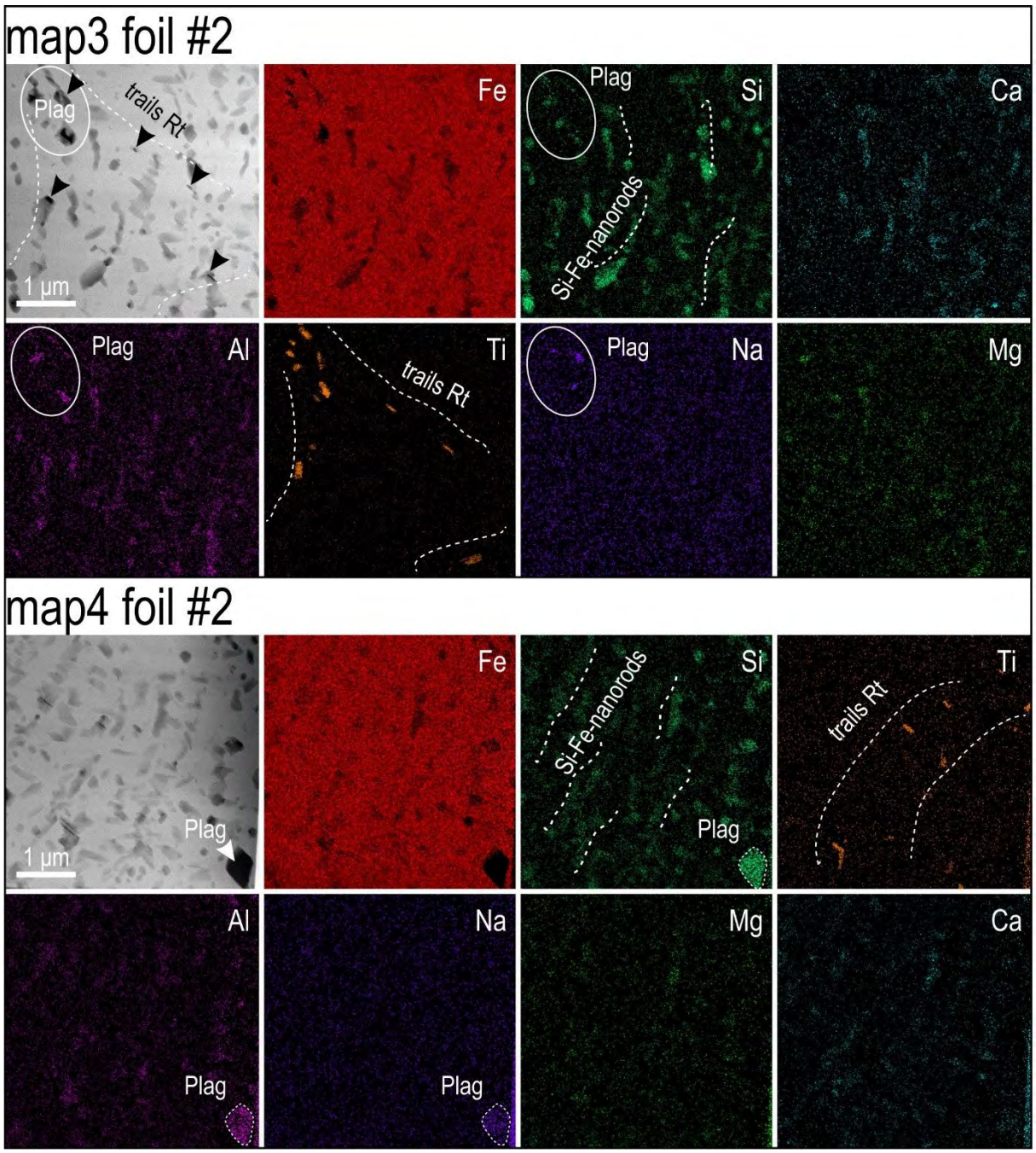

Figure A5. STEM EDX element maps of domains in magnetite containing Si-Fe-nanorods and trails of rutile. Abbreviations: Plag–plagioclase, Rt–rutile.

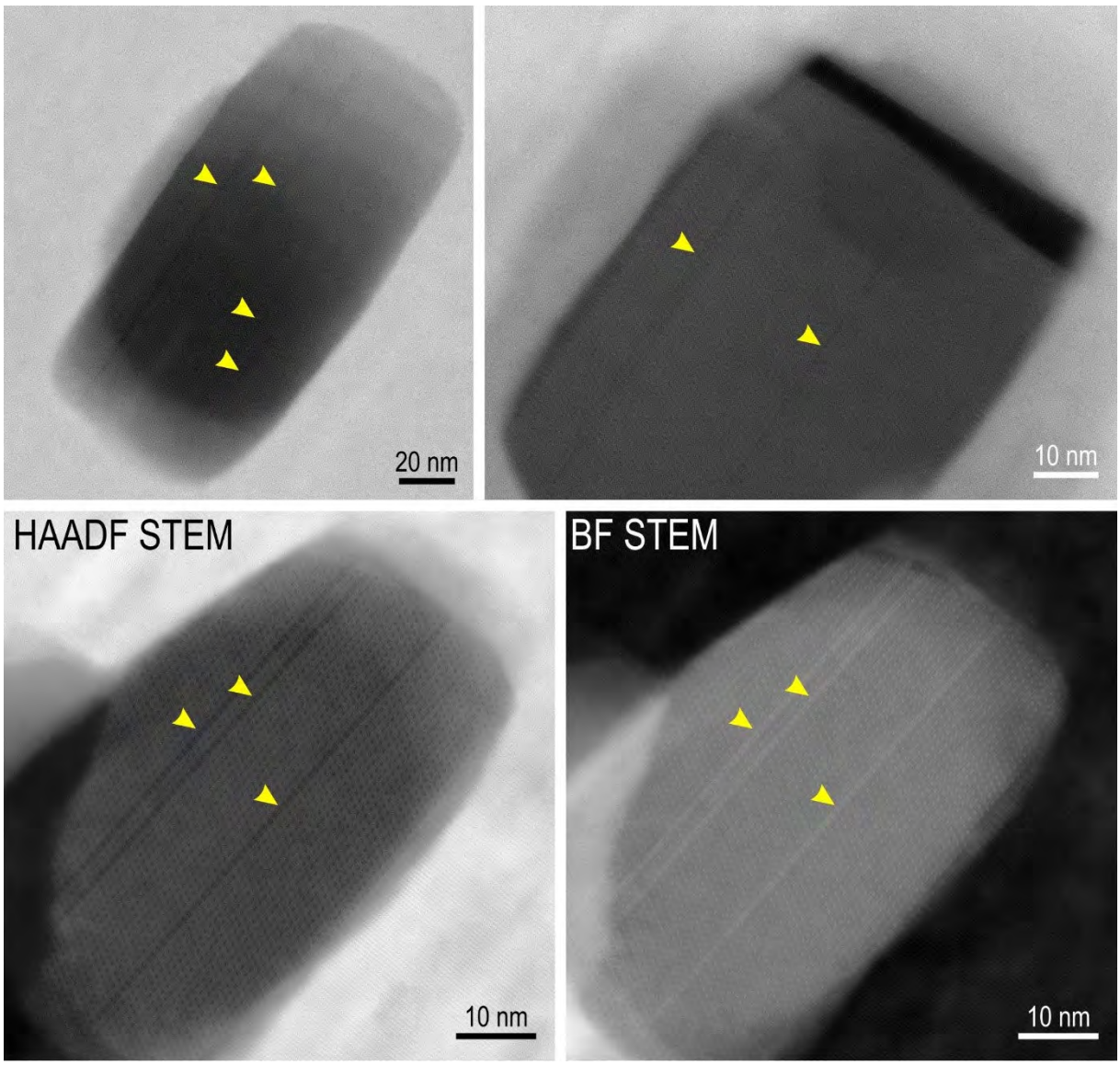

Figure A6. HAADF STEM images of selected tschermakite inclusions on [001]. Stacking disorder is indicated by yellow arrows.

Supplementary Material Table 1. EPMA data for silician magnetite

Conc.,	Transect#1								Transect#2					
wt%	Mt1-1	Mt1-2	Mt1-3	Mt1-4	Mt1-5	Mt1-6	Mt1-7	Mt1-8	Mt2-1	Mt2-2	Mt2-3	Mt2-4	Mt2-5	Mt2-6
MgO	0.34	0.23	0.57	0.47	0.55	0.28	<mdl	0.01	<mdl	<mdl	0.25	0.44	0.36	0.54
CaO	0.33	0.30	0.33	0.38	0.70	0.56	<mdl	<mdl	0.02	0.02	0.26	0.41	0.38	0.42
MnO	<mdl	0.04	<mdl	<mdl	0.05	<mdl	0.04	<mdl	<mdl	<mdl	<mdl	0.05	<mdl	0.05
CoO	0.05	0.04	0.05	0.05	0.03	0.04	0.04	0.05	0.03	<mdl	0.03	0.04	0.04	0.06
NiO	<mdl	<mdl	<mdl	0.02	0.02	<mdl	0.02	<mdl	<mdl	0.02	0.03	<mdl	0.02	0.02
ZnO	<mdl	<mdl	<mdl	<mdl	<mdl	<mdl	<mdl	<mdl	0.03	<mdl	<mdl	0.02	<mdl	<mdl
PbO	<mdl	<mdl	0.02	<mdl	<mdl	<mdl	<mdl	<mdl	<mdl	<mdl	<mdl	<mdl	0.03	<mdl
Al_2O_3	1.65	0.81	1.33	1.27	2.33	1.95	0.06	0.11	0.11	0.09	0.88	1.11	0.91	1.66
V_2O_3	0.05	0.06	0.05	0.05	0.05	0.05	0.05	0.05	0.05	0.05	0.05	0.05	0.04	0.05
FeO_{total}	88.84	90.33	88.92	88.91	85.61	86.10	93.61	92.84	92.87	93.44	90.26	89.04	88.40	87.21
Fe_2O_3	61.04	63.61	61.33	61.58	55.67	56.92	69.33	68.52	68.20	68.93	62.74	61.86	60.07	57.66
FeO	33.91	33.09	33.73	33.50	35.52	34.88	31.23	31.19	31.51	31.42	33.81	33.37	34.34	35.32
SiO_2	2.57	1.90	2.48	2.52	4.39	3.67	<mdl	0.08	0.16	0.10	2.36	2.44	2.35	3.99
TiO_2	0.11	0.11	0.40	0.14	0.16	0.19	0.04	0.07	0.24	0.07	0.08	0.18	1.24	0.13
UO_2	<mdl	0.02	<mdl	<mdl	<mdl	<mdl	<mdl	<mdl	<mdl	<mdl	<mdl	<mdl	<mdl	0.04
Sum	100.05	100.21	100.29	99.96	99.47	98.54	100.82	100.09	100.35	100.69	100.49	99.98	99.78	99.95
Atoms per formula unit (APFU) based on 32 O														
Mg	0.153	0.105	0.253	0.209	0.246	0.125	0.000	0.005	0.000	0.000	0.114	0.197	0.163	0.241
Ca	0.106	0.098	0.107	0.123	0.223	0.183	0.000	0.000	0.006	0.006	0.084	0.132	0.123	0.135
Mn	0.000	0.011	0.000	0.000	0.013	0.000	0.012	0.000	0.000	0.000	0.000	0.014	0.000	0.012
Fe^{2+}	8.527	8.379	8.462	8.440	8.850	8.839	7.983	8.025	8.082	8.035	8.516	8.419	8.691	8.819
Co	0.011	0.010	0.011	0.013	0.008	0.009	0.010	0.012	0.008	0.000	0.008	0.009	0.009	0.013
Ni	0.000	0.000	0.000	0.004	0.004	0.000	0.006	0.000	0.000	0.005	0.006	0.000	0.004	0.004
Zn	0.000	0.000	0.000	0.000	0.000	0.000	0.000	0.000	0.007	0.000	0.000	0.006	0.000	0.000
Pb	0.000	0.000	0.002	0.000	0.000	0.000	0.000	0.000	0.000	0.000	0.000	0.000	0.003	0.000
$\sum M^{2+}$	8.797	8.602	8.835	8.789	9.344	9.156	8.010	8.042	8.104	8.046	8.729	8.776	8.993	9.225
Al	0.585	0.288	0.472	0.452	0.818	0.698	0.023	0.040	0.040	0.031	0.311	0.394	0.324	0.585
V	0.012	0.013	0.012	0.011	0.011	0.013	0.013	0.012	0.012	0.012	0.013	0.012	0.010	0.012
Fe^{3+}	13.809	14.494	13.846	13.960	12.483	12.978	15.944	15.863	15.739	15.865	14.219	14.042	13.680	12.953
$\sum M^{3+}$	14.406	14.796	14.330	14.423	13.312	13.688	15.980	15.915	15.792	15.908	14.543	14.448	14.014	13.550
Si	0.773	0.576	0.744	0.758	1.307	1.113	0.000	0.026	0.048	0.031	0.710	0.735	0.711	1.192
Ti	0.024	0.024	0.091	0.031	0.037	0.042	0.010	0.017	0.056	0.015	0.019	0.041	0.282	0.030
U	0.000	0.001	0.000	0.000	0.000	0.000	0.000	0.000	0.000	0.000	0.000	0.000	0.000	0.002
$\sum M^{4+}$	0.797	0.601	0.835	0.789	1.344	1.156	0.010	0.042	0.104	0.046	0.729	0.776	0.993	1.224
Sum	24	24	24	24	24	24	24	24	24	24	24	24	24	24

Quantitative EPMA were obtained using a CAMECA SX-Five Electron Probe Microanalyzer (EPMA), equipped with 5 wavelength-dispersive spectrometers (WDS) (Adelaide Microscopy, The University of Adelaide). The instrument was operated at a constant accelerating voltage of 15 keV and variable beam current (see below). A constant beam spot-size of ~1 μm was utilized for the measurements. Individual analytical conditions for each analyzed element are listed below. Calibration and data reduction were conducted using the software package 'Probe for EPMA' (Donovan et al. 2016).

<mdl: less than minimum limit of detection.

Element	Line	Current (nA)	Crystal	Standard	Peak count (s)	Bkgd count (s)	Mean mdl (wt%)
Al	Kα	20	TAP	Astimex Plagioclase An65	20	10	0.012
Ca	Kα	20	LPET	Titanite	20	10	0.011
Fe	Kα	20	LLIF	P&H Specularite	20	10	0.03
Mg	Kα	100	TAP	Astimex Almandine	50	25	0.004
Mn	Kα	20	LLIF	P&H Rhodonite	20	10	0.028
Si	Kα	20	TAP	Astimex Plagioclase An65	20	10	0.013
Ti	Kα	20	LPET	Titanite	50	25	0.008
V	Kα	100	LLIF	Astimex Vanadium metal	35	20	0.007
Zn	Kα	100	LLIF	Astimex Willemite	50	25	0.019

Supplementary Material Table A2. Compositional data for ferro-tschermakite

Concentration (wt.%)	Integrated Area (Schreiber-Wims)	Integrated Area (Brown-Powell)	Mean
SiO_2	45.4	46.8	46.1
TiO_2	0.6	0.6	0.6
Al_2O_3	18.8	19.4	19.1
MnO	0.4	0.3	0.3
Fe_2O_3	20.0	17.9	19.0
MgO	5.4	5.6	5.5
CaO	7.8	7.8	7.8
Na_2O	1.3	1.3	1.3
K_2O	0.3	0.3	0.3
Sum	100.0	100.0	100.0
Recalculated wt%			
FeO	18.0	16.1	17.1
H_2O^+	2.1	2.1	2.1
Total	100.1	100.3	100.2
APFU			
Si	6.60	6.70	6.65
Al	1.40	1.30	1.35
∑T	8.00	8.00	8.00
Ti	0.07	0.06	0.06
Al	1.82	1.97	1.89
Fe^{2+}	1.95	1.77	1.86
Mg	1.17	1.20	1.18
∑C	5.00	5.00	5.00
Mn^{2+}	0.05	0.04	0.04
Fe^{2+}	0.25	0.16	0.20
Ca	1.22	1.19	1.21
Na	0.36	0.37	0.37
∑B	1.88	1.76	1.82
K	0.06	0.06	0.06
∑A	0.06	0.06	0.06
∑T,C,B,A	14.94	14.82	14.88
O	22	22	22
OH	2	2	2

Calculations used software by Locock (2014). Schreiber-Wims, and Brown-Powel denote ionization cross-section models used in Velox for EDX quantification. Abbreviation: apfu – atoms per formula unit.

Calculated formulae:

$K_{0.06}(Ca_{1.22}Na_{0.36}Fe_{0.25}Mn_{0.05})_{\Sigma 1.88}(Fe^{2+}_{1.95}Al_{1.82}Mg_{1.17}Ti_{0.07})_{\Sigma 5}(Si_{6.6}Al_{1.4})_{\Sigma 8}O_{22}(OH)_2$ (Schreiber-Wims)

$K_{0.06}(Ca_{1.19}Na_{0.37}Fe_{0.16}Mn_{0.04})_{\Sigma 1.76}(Al_{1.97}Fe^{2+}_{1.77}Mg_{1.2}Ti_{0.06})_{\Sigma 5}(Si_{6.7}Al_{1.3})_{\Sigma 8}O_{22}(OH)_2$ (Brown-Powell)

$K_{0.06}(Ca_{1.21}Na_{0.37}Fe_{0.2}Mn_{0.04})_{\Sigma 1.82}(Al_{1.89}Fe^{2+}_{1.86}Mg_{1.18}Ti_{0.06})_{\Sigma 5}(Si_{6.65}Al_{1.35})_{\Sigma 8}O_{22}(OH)_2$ (Mean)

Additional references

Huberty JM, Konishi H, Heck PR, Fournelle JH, Valley JW, Xu H (2012) Silician magnetite from the Dales Gorge Member of the Brockman Iron Formation, Hamersley Group, Western Australia. Am Mineral 97, 26–37. https://doi.org/10.2138/am.2012.3864

Locock, A.J. (2014) An Excel spreadsheet to classify chemical analyses of amphiboles following the IMA2012 recommendations. Computers & Geosciences 62, 1–11. https://doi.org/10.1016/j.cageo.2013.09.011

Donovan JJ, Singer JW, Armstrong JT (2016) A new EPMA method for fast trace element analysis in simple matrices. Am Mineral 101, 1839–1853. https://doi.org/10.2138/am-2016-5628

SUPPLEMENTARY MATERIAL G

FOR CHAPTER 8 – VAPOUR TRANSPORT OF MAGNETITE IN VOLCANOES: EVIDENCE FROM IGNEOUS PYROXENE PAIR INCLUSIONS AND S-BEARING SUBLIMATE COATINGS

APPENDIX A: DETAILS ON ANALYTICAL CONDITIONS, ADDITIONAL FIGURES AND TABLES.

ELECTRONIC APPENDIX A FOR CHAPTER 8

Supplementary material

1 Analytical methods

1.1 Electron probe microanalysis (EPMA)

Quantitative major and minor oxide compositions were obtained using a CAMECA SX-Five electron probe microanalyzer (EPMA), equipped with five wavelength-dispersive spectrometers, and housed at Adelaide Microscopy, The University of Adelaide. The instrument was operated at a constant accelerating voltage of 15 keV and variable beam current. A beam size of 2 or 3 µm was utilized for spot analyses. Individual analytical conditions for each analysed element are listed in Table A1. Calibration and data reduction was conducted in the software package Probe for EPMA (Donovan et al. 2016, and references therein). Background measurement consisted of standard 2-point linear fits, with total count times varying from 10 to 40 s dependant on element analysed. Typical minimum detection limits ranged from 0.008 (S) to 0.054 wt.% (Fe) at 99 % confidence.

Table A1. Summary of analytical conditions/setup employed for EPMA analysis of Fe-oxides

Element	Line	Current (nA)	Crystal	Standard	Peak count time (s)		Average mdl
					on-	off- (H/L)	(wt.%)
Al	K_α	20	TAP	NMNH-122142 Augite	15	5	0.022
Ca	K_α	20	LPET	P&H Wollastonite	15	5	0.015
Cl	K_α	20	LPET	Astimex Tugtupite	15	5	0.019
Cr	K_α	20	LLIF	P&H Cr_2O_3	30	15	0.017
Fe	K_α	20	LLIF	P&H Specularite	15	5	0.054
K	K_α	20	LPET	Astimex Sanidine	15	5	0.015
Mg	K_α	100	TAP	NMNH-113312-44 Olivine	15	5	0.027
Mn	K_α	20	LLIF	P&H Rhodonite	15	5	0.041
Na	K_α	20	TAP	P&H Amelia Albite	15	5	0.044
Nb	L_α	100	LPET	Astimex Niobium metal	40	20	0.049
Ni	K_α	100	LLIF	Nickel Olivine	30	15	0.030
P	K_α	20	LPET	Astimex Apatite	15	5	0.020
S	K_α	20	LPET	Astimex Celestine	40	20	0.008
Si	K_α	20	TAP	P&H Amelia Albite	40	20	0.010
Sn	L_α	100	LPET	P&H Cassiterite	45	20	0.023
Ti	K_α	20	LPET	P&H Rutile	30	15	0.010
V	K_α	100	LLIF	Astimex Vanadium metal	15	5	0.033
Zn	K_α	100	LLIF	Astimex Willemite	30	15	0.048
Zr	L_α	100	LPET	GJ1 Zircon	45	20	0.026

Sulfur-bearing hematite-magnetite intergrowths were quantitatively mapped for S and Fe concentrations using the same instrument. Beam conditions were set at an accelerating voltage of 15 kV and 50 nA, utilizing a focused beam and pixel resolution/step size of 1 µm. Pixel dwell time in the two maps were set to 150 and 200 ms. Calibration and quantitative data reduction of obtained maps was conducted in Calcimage (Probe for EPMA) and processed in XMapTools 3.2.2 (Lanari et al., 2014, 2019). Calibration was performed on certified synthetic standards from P&H and Associates (barite for S, hematite for Fe). In order to attain better detection limits, quantitative mapping of S was achieved by measurement of S-Kα on 4 separate spectrometers (3 LPET and 1 PET crystal) and aggregated using the function in Probe for EPMA, whereas Fe-Kα was measured on a single LLIF crystal. Background subtraction on the maps was performed via the Mean Atomic Number (MAN) background correction (Donovan et al. 2016, and references therein), omitting the need for a second pass "off-peak" map

acquisition. Following this, each pixel goes through full φ(ρz) corrected quantification identical to traditional spot analysis.

1.2 Laser-ablation inductively-coupled-plasma mass-spectrometry (LA-ICP-MS)

LA-ICP-MS spot analysis was conducted following established practices at Adelaide Microscopy (e.g., Verdugo-Ihl et al. 2019) using a RESOlution-LR 193 nm excimer laser microprobe (Australian Scientific Instruments) with a large-format S155 two-volume ablation cell designed by Laurin Technic Pty., coupled to an Agilent 7900x Quadrupole ICP-MS. Laser ablation was performed in an atmosphere of UHP He (0.35 1/min) and the aerosol was mixed with Ar (1.06 l/min) before exiting the sample chamber. A pulse homogenizing device ('squid', Laurin Technic) was used in the interface tubing between the laser and ICP-MS to smooth signal fluctuations. The ICP-MS system was optimized daily to achieve maximal sensitivity and low oxide interference production. Most commonly, a laser spot size diameter of 43 µm was employed (also 29 and 51 µm depending on the requirements), using a pulse repetition rate of 5 Hz and a fluence of 3.5 J/cm^2.

Prior to each spot analysis, the selected areas were pre-ablated to avoid surface contamination. Acquisition time comprised a 30 s measurement of the background (laser off) and 30 s acquisition of the signal while the laser ablates. Analytical standards were run before and after sets of Fe-oxide unknowns comprising less than 1 hr intervals of analysis run duration, using GSD-1G and NIST-610 as the primary and secondary standards, respectively.

Data reduction was performed in Iolite (Paton et al. 2011) using stoichiometric concentrations of Fe in magnetite and hematite (72.3596 and 69.9431 wt%, respectively) as the internal standard element. Detection limits were individually calculated by the program for each element in each spot analysis based on analytical conditions.

The following suite of 45 elements, including four Pb isotopes, was measured: ^{24}Mg, ^{27}Al, ^{28}Si, ^{31}P, ^{43}Ca, ^{45}Sc, ^{49}Ti, ^{51}V, ^{52}Cr, ^{55}Mn, ^{57}Fe, ^{59}Co, ^{60}Ni, ^{63}Cu, ^{66}Zn, ^{69}Ga, ^{75}As, ^{88}Sr, ^{89}Y, ^{90}Zr, ^{93}Nb, ^{95}Mo, ^{118}Sn, ^{121}Sb, ^{137}Ba, ^{139}La, ^{140}Ce, ^{141}Pr, ^{146}Nd, ^{147}Sm, ^{153}Eu, ^{157}Gd, ^{159}Tb, ^{163}Dy, ^{165}Ho, ^{166}Er, ^{169}Tm, ^{172}Yb, ^{175}Lu, ^{178}Hf, ^{181}Ta, ^{182}W, ^{204}Pb, ^{206}Pb, ^{207}Pb, ^{208}Pb, ^{232}Th and ^{238}U. Reported Pb contents correspond to total Pb concentrations calculated from the individual abundances of ^{204}Pb, ^{206}Pb, ^{207}Pb and ^{208}Pb to correct for overestimation due to radioactive decay of Th and U.

LA-ICP-MS element maps were obtained for subsets of the previously indicated isotopes (see above). For this purpose, grids of parallel lines were ablated across the selected areas using a fluence of 3.5 J/cm^2 and laser repetition rates of 10 Hz. A spot size of 11 and 16 µm was used with a speed of 11 and 16 µm/s respectively. Prior to the main ablation and signal acquisition phase, individual lines were pre-ablated to clean the surfaces and minimize the contributions from ablation blankets of the previous lines. An acquisition of 20 s background for each line was conducted prior to the main ablation phase. Spot analyses were conducted on the reference materials before and after each mapping run. Data reduction was conducting in Iolite. Individual line-profiles of the measured isotopes were merged into 2D-images by subtracting the average backgrounds from the time-resolved intensities and producing qualitative isotope intensity maps with scales in counts-per-second (cps). The obtained intensities were scaled individually to highlight intragrain variability.

1.3 Nanoscale investigations

Transmission electron microscopy (TEM) foils were extracted using established dual-beam focussed ion beam (FIB)-SEM methods (Ciobanu et al., 2011) using a FEI Helios Nanolab 600

instrument (FEI, Hillsboro, OR, USA). The obtained foils were cut across features of interest, close or perpendicular to zoning and boundaries.

Electron diffractions and bright field TEM imaging using a Philips CM200 TEM (Philips, Eindhoven, The Netherlands) operated at 200 kV. The instrument was equipped with a LaB_6 source, double-tilt holder and Gatan Orius digital camera (Gatan Inc., Pleasanton, CA, USA).

High angle annular dark field (HAADF) scanning TEM (S/TEM) imaging and energy-dispersive X-ray (EDX) spectrometry in spot analysis and mapping modes were conducted with an ultra-high resolution, probe corrected, FEI Titan Themis STEM (FEI, Hillsboro, OR, USA) operated at 200 kV. This instrument is equipped with a X-FEG Schottky source and Super-X EDX geometry. The Super-X EDX detector provides geometrically symmetric EDX detection with an effective solid angle of 0.8 Sr. Probe correction delivered sub-Ångstrom spatial resolution and an inner collection angle greater than 50 mrad was used for HAADF imaging with a Fischione detector.

Indexing of diffraction patterns obtained from Fast-Fourier-Transformed (FFT) images was conducted with WinWulff© (version 1.5.2) and publicly available data from the American Mineralogist Crystal Structure Database (http://rruff.geo.arizona.edu/AMS/amcsd.php). Crystal structure models were generated in CrystalMaker® (version 10.2) and STEM for xHREMTM Version 4.1 software. All instruments are housed at Adelaide Microscopy, The University of Adelaide.

References

Ciobanu, C.L., Cook, N.J., Utsunomiya, S., Pring, A., Green, L., 2011. Focussed ion beam–transmission electron microscopy applications in ore mineralogy: Bridging micro- and nanoscale observations. Ore Geol. Rev. 42, 6–31. https://doi.org/10.1016/j.oregeorev.2011.06.012

Donovan, J.J., Singer, J.W., Armstrong, J.T., 2016. A new EPMA method for fast trace element analysis in simple matrices. Am. Mineral. 101, 1839–1853. https://doi.org/10.2138/am-2016-5628

Lanari, P., Vho, A., Bovay, T., Airaghi, L., Centrella, S., 2019. Quantitative compositional mapping of mineral phases by electron probe micro-analyser. Geol. Soc. London, Spec. Publ. 478, 39–63. https://doi.org/10.1144/SP478.4

Lanari, P., Vidal, O., De Andrade, V., Dubacq, B., Lewin, E., Grosch, E.G., Schwartz, S., 2014. XMapTools: A MATLAB©-based program for electron microprobe X-ray image processing and geothermobarometry. Comput. Geosci. 62, 227–240. https://doi.org/10.1016/j.cageo.2013.08.010

Paton, C., Hellstrom, J., Paul, B., Woodhead, J., Hergt, J., 2011. Iolite: Freeware for the visualisation and processing of mass spectrometric data. J. Anal. At. Spectrom. 26, 2508–2518. https://doi.org/10.1039/c1ja10172b

Verdugo-Ihl, M.R., Ciobanu, C.L., Cook, N.J., Ehrig, K.J., Courtney-Davies, L., 2019. Defining early stages of IOCG systems: evidence from iron oxides in the outer shell of the Olympic Dam deposit, South Australia. Miner. Depos. https://doi.org/10.1007/s00126-019-00896-2

2 Additional figures

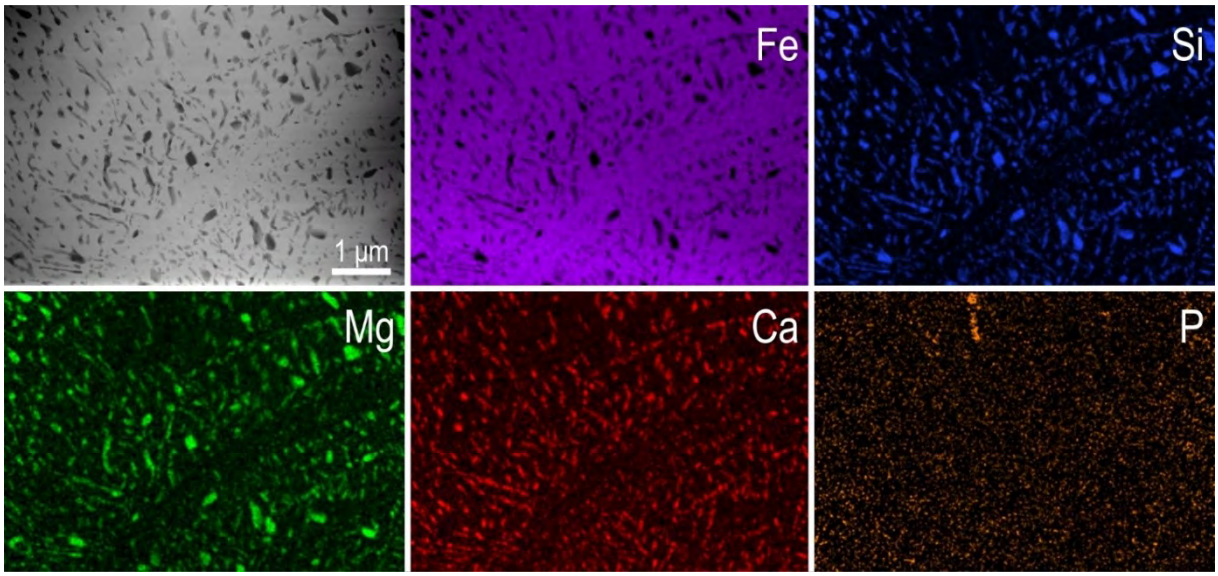

Fig. A1. HAADF-STEM and selected STEM-EDX maps showing aspects of concentric/orbicular zoning from vesicular, massive stratabound magnetite (foil Laco2, map#1051). Note the presence of a Fe-bearing phosphate, which is otherwise rarely observed.

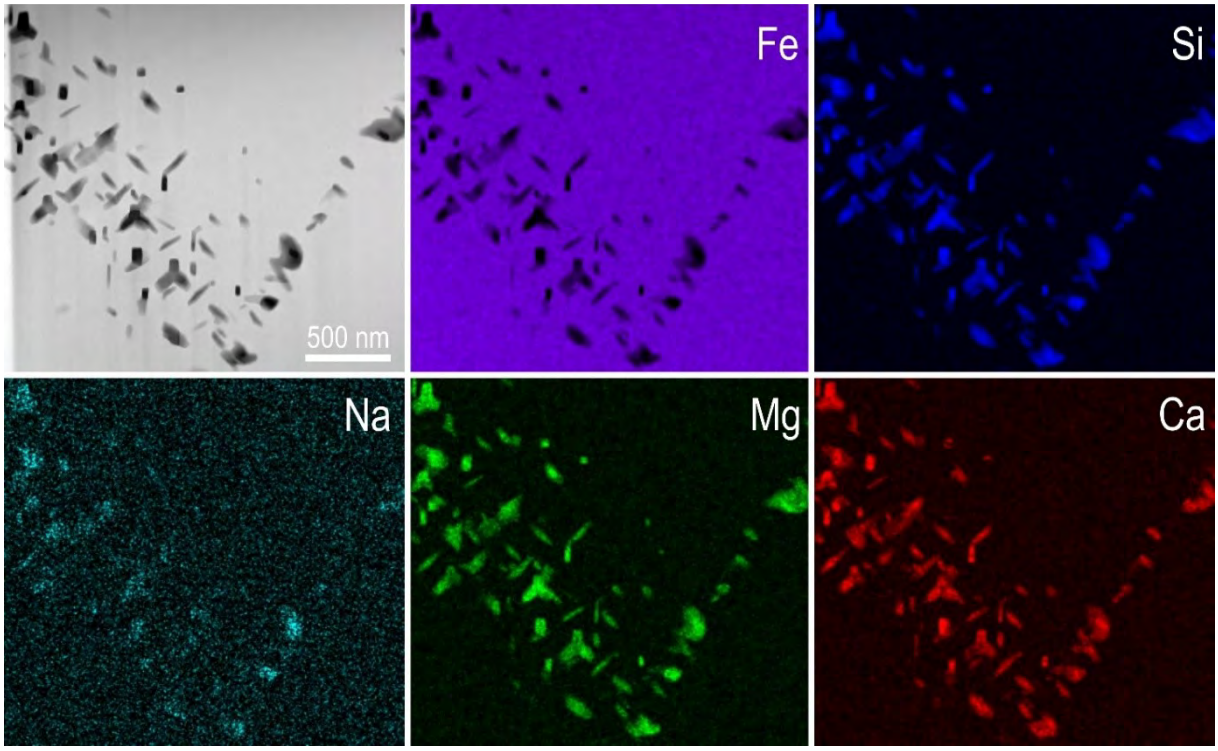

Fig. A2. HAADF-STEM and selected STEM-EDX maps showing orientation of pyroxene inclusions within band, displaying crystallographically oriented relationships to host magnetite (magnetite within 'nut-shaped'-hematite, steam-heated alteration; Laco4, map#1830).

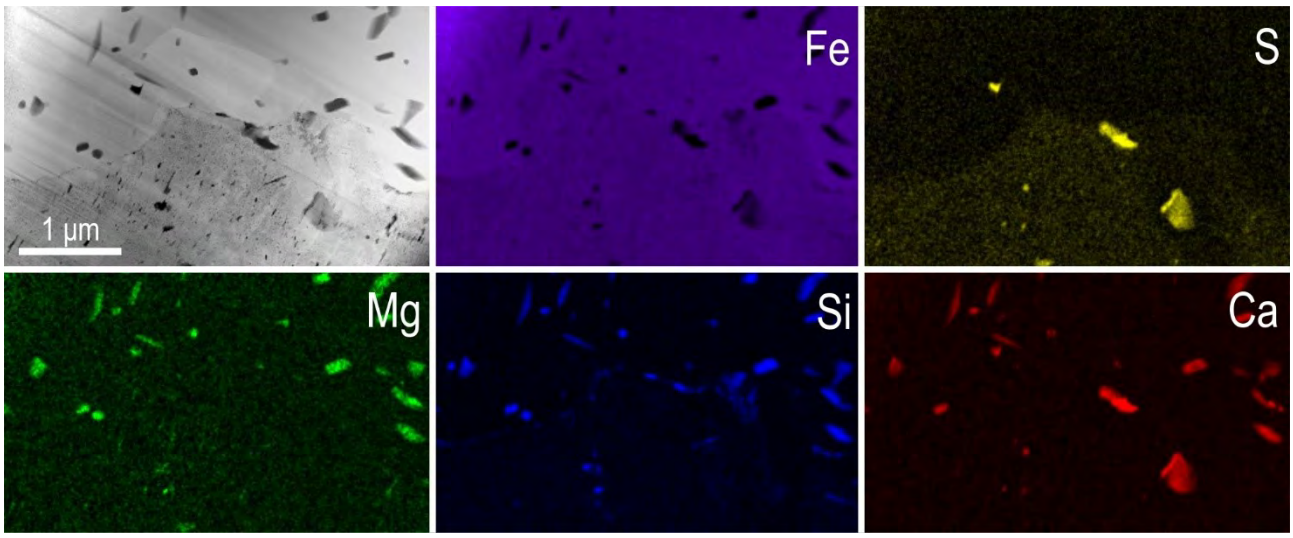

Fig. A3. HAADF-STEM and selected STEM-EDX maps of boundary between magnetite, martitised domain and mottled hematite displaying S-enrichment (hematite replacing magnetite within 'nut-shaped'-hematite, steam-heated alteration; foil Laco5, map#1319).

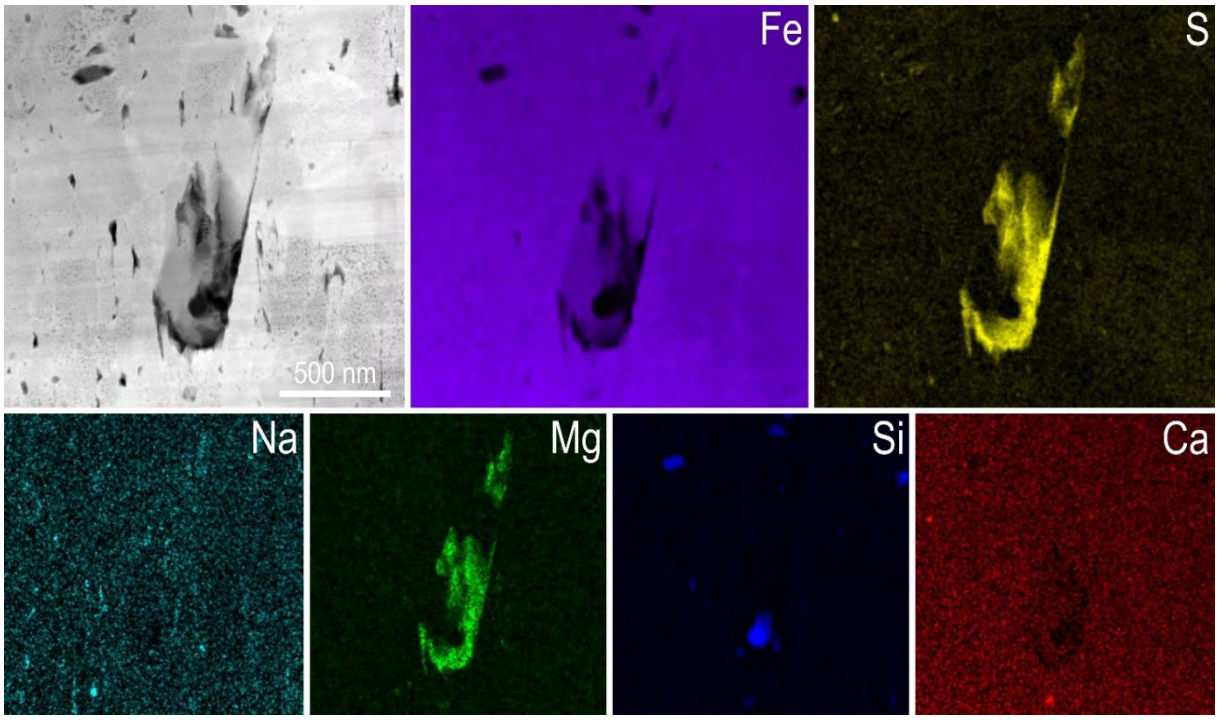

Fig. A4. HAADF-STEM and selected STEM-EDX maps of Mg(-Fe?)-bearing sulfate within mottled domain in hematite. Note that while S is distinctly enriched within the sulfate-phase, S is also present within the finely mottled hematite, displaying no characteristic enrichment in other elements (hematite replacing magnetite within 'nut-shaped'-hematite, steam-heated alteration; foil Laco5, map#1808).

Table A2. Summary of analytical conditions/setup employed for EPMA analysis of Fe-oxides

Sample	magnetite, LCO-285						magnetite, EL-A (*n*= 25)			LCO-72								
	inclusion-rich (*n*= 61)			inclusion-poor (*n*= 9)						magnetite (*n*= 6)			S-bearing martite (*n*= 14)			hematite host (*n*= 9)		
	Min.	Max.	Mean	Min.	Max.	Mean	Min.	Max.	Mean	Min.	Max.	Mean	Min.	Max.	Mean	Min.	Max.	Mean
CaO	0.20	1.08	0.49	<0.02	0.03	0.01	0.07	0.49	0.24	0.08	0.26	0.16	<0.02	0.16	0.01		<0.02	
MgO	1.34	7.01	2.18	0.77	0.91	0.85	0.47	1.90	1.25	0.19	0.56	0.37	0.05	0.26	0.02	<0.04	0.05	0.01
TiO_2	<0.02	0.04	0.01	<0.02	0.02	0.00	<0.02	0.03	0.01		<0.02		<0.02	0.02	0.01		<0.02	
SiO_2	1.06	9.95	2.86	<0.02	0.13	0.04	0.59	2.52	1.36	0.53	1.21	0.89	0.04	0.99	0.23	<0.02	0.08	0.01
Al_2O_3	<0.04	1.45	0.14	0.07	0.15	0.11	0.09	1.06	0.20	0.07	0.12	0.10	0.04	0.17	0.08	<0.04	0.09	0.02
Fe_2O_3	83.99	102.42	94.88	102.43	105.40	103.62	97.91	102.56	100.69	99.82	101.33	100.69	93.58	98.71	95.81	96.19	100.33	98.72
MnO	<0.05	0.09	0.02	<0.05	0.08	0.01	<0.05	0.05	0.00	<0.05	0.06	0.01		<0.05			<0.05	
Cr_2O_3	<0.02	0.04	0.00		<0.02		<0.02	0.03	0.00		<0.02			<0.02			<0.02	
K_2O	<0.02	0.11	0.05	<0.02	0.02	0.00	<0.02	0.04	0.01	<0.02	0.02	0.01	<0.02	0.03	0.00		<0.02	
P_2O_5	<0.04	0.23	0.01		<0.04		<0.04	0.07	0.00		<0.04		<0.05	0.07	0.00	<0.05	0.05	0.01
Na_2O	<0.06	0.29	0.15	<0.06	0.07	0.01	<0.06	0.17	0.02		<0.06			<0.06		<0.06	0.08	0.01
ZnO	<0.06	0.29	0.01	<0.06	0.08	0.01	<0.06	0.06	0.01		<0.06			<0.06			<0.06	
V_2O_3	0.06	0.18	0.12	<0.05	0.10	0.07	0.11	0.20	0.16	<0.05	0.11	0.06	<0.05	0.11	0.06	<0.05	0.05	0.01
SnO_2	<0.03	0.04	0.00	<0.03	0.03	0.00		<0.03			<0.03		<0.03	0.03	0.00		<0.03	
NiO	NA	NA	NA	NA	NA	NA	NA	NA	NA	<0.04	0.06	0.01	<0.04	0.05	0.01		<0.04	
SO_3	NA	NA	NA	NA	NA	NA	NA	NA	NA	NA	NA	NA	0.31	1.67	0.98	<0.02	0.14	0.02
Sum			100.93			104.74			103.96			102.29			97.22			98.80
Calculated formulae in atoms per formula unit (apfu)																		
Na	0.000	0.023	0.012	0.000	0.006	0.001	0.000	0.013	0.001	0.000	0.000	0.000	0.000	0.000	0.000	0.000	0.002	0.000
K	0.000	0.006	0.002	0.000	0.001	0.000	0.000	0.002	0.001	0.000	0.001	0.000	0.000	0.000	0.000	0.000	0.000	0.000
$\sum M^{+}$			0.015			0.001			0.002			0.000			0.000			0.000
Mg	0.077	0.472	0.135	0.045	0.052	0.049	0.028	0.112	0.073	0.011	0.033	0.022	0.000	0.005	0.000	0.000	0.001	0.000
Ca	0.008	0.052	0.022	0.000	0.001	0.000	0.003	0.021	0.010	0.003	0.011	0.007	0.000	0.002	0.000	0.000	0.000	0.000
Mn	0.000	0.003	0.001	0.000	0.002	0.000	0.000	0.002	0.000	0.000	0.002	0.000	0.000	0.000	0.000	0.000	0.000	0.000
Fe^{2+}	7.605	7.954	7.895	7.982	7.986	7.984	7.910	7.972	7.946	7.964	7.983	7.973	-	-	-	-	-	-
Ni	-	-	-	-	-	-	-	-	-	0.000	0.002	0.000	0.000	0.001	0.000	0.000	0.000	0.000
Zn	0.000	0.009	0.000	0.000	0.002	0.000	0.000	0.002	0.000	0.000	0.000	0.000	0.000	0.000	0.000	0.000	0.000	0.000
$\sum M^{2+}$			8.053			8.034			8.030			8.002			0.001			0.000
Al	0.000	0.077	0.007	0.003	0.007	0.005	0.004	0.051	0.010	0.003	0.006	0.005	0.001	0.002	0.001	0.000	0.001	0.000
V	0.002	0.006	0.004	0.000	0.003	0.002	0.003	0.006	0.005	0.000	0.003	0.002	0.000	0.001	0.001	0.000	0.001	0.000
Cr	0.000	0.001	0.000	0.000	0.000	0.000	0.000	0.001	0.000	0.000	0.000	0.000	0.000	0.000	0.000	0.000	0.000	0.000
Fe^{3+}	15.210	15.909	15.789	15.965	15.972	15.968	15.820	15.945	15.893	15.927	15.966	15.946	1.961	1.989	1.976	1.994	2.000	1.999
$\sum M^{3+}$			15.800			15.975			15.907			15.952			1.977			1.999
Si	0.041	0.449	0.119	0.000	0.005	0.001	0.023	0.100	0.053	0.021	0.048	0.035	0.000	0.012	0.003	0.000	0.001	0.000
Ti	0.000	0.001	0.000	0.000	0.000	0.000	0.000	0.001	0.000	0.000	0.000	0.000	0.000	0.000	0.000	0.000	0.000	0.000
Sn	0.000	0.001	0.000	0.000	0.001	0.000	0.000	0.000	0.000	0.000	0.000	0.000	0.000	0.000	0.000	0.000	0.000	0.000
$\sum M^{4+}$			0.119			0.002			0.054			0.035			0.003			0.000
P	0.000	0.009	0.000	0.000	0.000	0.000	0.000	0.002	0.000	0.000	0.000	0.000	0.000	0.001	0.000	0.000	0.000	0.000
S	-	-	-	-	-	-	-	-	-	-	-	-	0.003	0.016	0.009	0.000	0.001	0.000
Sum			23.987			24.011			23.993			23.989			1.990			2.000

- All values below minimum detection limits

Table A3. Summary statistics of magnetite and hematite trace element data by LA-ICP-MS, concentrations in ppm.

Sample	Stratabound magnetite															Steam-heated alteration									
	EL-A (*n*= 31)					LCO-285 (*n*=103)					LCO-287 (*n*= 33)					LCO-72 (magnetite, *n*= 77)					LCO-72 (hematite, *n*= 102)				
	Min.	Max.	Mean.	G.M.	S.D.	Min.	Max.	Mean.	G.M.	S.D.	Min.	Max.	Mean.	G.M.	S.D.	Min.	Max.	Mean.	G.M.	S.D.	Min.	Max.	Mean.	G.M.	S.D.
Mg	5360	8210	6280	6230	887	5550	19800	9330	8870	3130	3660	6650	4360	4330	529	47.5	3270	940	690	774	5.75	182	69.9	49.5	46.2
Al	489	611	554	553	32.5	239	1220	491	443	233	233	560	397	389	73.8	64.0	404	286	281	43.0	1.25	1560	113	32.0	200
Si	222	7500	1550	758	2130	285	26200	6960	4030	6080	398	6540	1510	1270	1130	340	7520	1970	1230	1950	52.0	623	143	116	125
P	<25.6	223	57.3	48.2	41.8	<13.3	251	83.7	68.2	49.8	<21.1	223	85.3	77.0	40.3	<60.4	212	99.7	95.0	33.9	<10.7	74.0	23.0	20.8	11.6
Ca	<127	1940	461	273	584	<84.4	5850	1670	932	1440	89.0	2240	448	347	402	<252	2950	745	585	626	<39.1	426	68.2	64.4	38.4
Sc	0.17	0.71	0.30	0.275	0.16	<0.11	2.41	0.80	0.61	0.58	0.12	0.80	0.24	0.23	0.12	<0.30	1.24	0.44	0.43	0.12	<0.048	0.417	0.085	0.079	0.046
Ti	74.2	107	89.1	88.6	9.84	42.3	190	91.4	85.3	34.9	51.2	72.5	60	59.8	4.86	6.60	64.8	43.5	42.0	9.78	1.66	130	14.4	8.89	18.9
V	911	1240	1090	1090	88.1	92.9	1090	794	706	282	405	440	418	418	7.93	148	636	459	456	49.2	49.1	1440	282	205	247
Cr	<0.59	1.34	0.96	0.94	0.19	<0.25	1.50	0.71	0.66	0.28	0.34	3.96	0.87	0.70	0.75	<1.44	43.7	4.79	3.43	6.07	<0.22	14.3	0.75	0.50	1.57
Mn	69.3	359	210	193	81.0	39.4	372	292	279	63.0	19.4	67.1	45.4	43.7	11.8	<1.8	43.8	11.0	8.85	7.29	0.17	3.39	0.511	0.42	0.42
Co	109	120	114	114	3.18	105	121	112	112	3.43	108	121	114	114	3.40	3.45	109	83.8	79.2	17.1	0.25	18.1	1.31	0.97	1.92
Ni	271	319	296	296	10.2	215	302	272	271	18.8	232	255	243	243	4.93	<34.7	304	269	261	43.8	5.02	115	44.1	34.6	23.7
Cu	<0.24	3.33	0.52	0.41	0.59	<0.13	32.9	2.78	0.71	5.88	<0.15	29.0	2.83	0.70	6.89	<0.69	158	4.38	1.30	19.8	<0.109	3.10	0.26	0.21	0.34
Zn	13.1	46.0	28.2	26.6	9.59	18.6	55.1	35.2	34.1	8.56	8.10	55.5	18.2	16.9	8.82	0.070	88.0	4.04	2.32	10.1	0.11	1.63	0.30	0.27	0.19
Ga	1.21	1.77	1.57	1.56	0.14	0.97	39.6	2.18	1.67	4.31	0.43	0.87	0.56	0.56	0.081	0.055	80.0	1.25	0.20	9.09	0.075	0.37	0.20	0.19	0.053
As	<0.51	4.96	1.40	1.01	1.40	<0.23	17.0	5.10	2.93	4.21	<0.27	1.95	0.78	0.70	0.36	<1.2	68.5	4.07	2.63	8.06	0.20	13.8	3.37	2.09	3.19
Sr	<0.001	2.58	0.48	0.064	0.81	<0.001	8.19	2.32	0.95	2.02	0.23	32.7	3.22	1.38	6.82	<0.001	5.18	1.21	0.52	1.44	<0.001	4.28	0.093	0.019	0.44
Zr	<0.029	3.14	0.77	0.31	1.06	0.053	15.8	2.51	1.20	3.00	0.20	3.40	0.98	0.86	0.56	<0.001	3.59	0.67	0.31	0.72	<0.001	3.44	0.22	0.057	0.49
Nb	<0.001	5.92	1.14	0.21	1.85	0.029	46.1	10.8	5.24	10.3	0.36	7.37	2.92	2.59	1.31	<0.041	11.8	2.24	0.99	2.51	0.076	19.4	1.02	0.44	2.22
Mo	<0.001	0.41	0.17	0.14	0.066	<0.001	2.72	0.45	0.24	0.60	<0.046	3.30	0.21	0.11	0.56	<0.001	3.60	0.52	0.43	0.41	<0.001	2.31	0.35	0.20	0.42
Sn	4.74	7.91	6.04	6.00	0.74	5.10	15.4	9.22	8.94	2.34	5.70	12.4	6.73	6.66	1.14	1.14	7.64	4.46	4.20	1.38	0.56	5.63	2.01	1.73	1.16
Sb	<0.13	0.36	0.24	0.23	0.058	<0.084	1.79	0.59	0.44	0.43	<0.076	0.39	0.15	0.14	0.069	<0.38	3.81	0.70	0.64	0.43	<0.069	1.49	0.37	0.27	0.30
Ba	<0.001	2.39	0.54	0.078	0.74	<0.001	8.90	2.16	0.95	1.96	0.30	18.0	2.55	1.59	3.36	<0.001	5.10	1.23	0.34	1.36	<0.001	2.06	0.17	0.05	0.27
Hf	<0.001	0.043	0.024	0.02	0.01	0.007	0.14	0.025	0.02	0.02	0.010	0.085	0.025	0.022	0.014	0.029	0.15	0.061	0.057	0.021	<0.001	0.052	0.011	0.009	0.007
Ta	<0.007	0.38	0.075	0.038	0.096	0.012	1.43	0.29	0.15	0.31	0.012	0.23	0.097	0.087	0.042	<0.01	0.50	0.12	0.079	0.11	0.001	0.96	0.049	0.01	0.13
W	<0.001	0.58	0.11	0.046	0.16	<0.001	1.15	0.40	0.20	0.33	<0.027	7.20	0.61	0.20	1.38	<0.001	16.6	0.47	0.17	1.89	<0.008	5.21	0.28	0.086	0.59
Pb	0.044	0.22	0.073	0.068	0.036	0.023	0.45	0.089	0.072	0.079	0.028	0.22	0.063	0.054	0.046	0.11	1.28	0.19	0.17	0.13	0.019	0.06	0.028	0.028	0.006
Th	<0.005	23.2	4.33	0.34	7.49	<0.011	43.0	15.8	7.21	12.4	<0.63	23.9	7.16	5.91	4.07	0.059	39.5	8.07	2.82	10.1	<0.004	15.9	1.56	0.50	2.62
U	<0.006	1.83	0.37	0.11	0.53	<0.01	7.02	2.24	1.17	1.81	<0.22	4.61	2.30	1.89	1.19	0.033	6.79	0.96	0.48	1.24	<0.007	1.57	0.51	0.32	0.40
∑REY	0.18	109	21.6	2.49	36.3	0.34	179	76.3	38.0	56.4	6.11	123	38.3	31.4	24.1	0.86	166	34.8	13.8	43.7	0.085	19.5	1.49	0.43	3.44

Summary statistics treat concentrations lying below their respective detection limit as that mdl value. Abbreviations: Min.−minimum; Max.−maximum; G.M.−geometric mean; S.D.−standard deviation; NA−not available.

ADDITIONAL MATERIAL H

CO-AUTHORED ARTICLE ABSTRACT:

SILICIAN MAGNETITE: SI–FE-NANOPRECIPITATES AND OTHER MINERAL INCLUSIONS IN MAGNETITE FROM THE OLYMPIC DAM DEPOSIT, SOUTH AUSTRALIA

Cristiana L. Ciobanu [1], **Max R. Verdugo-Ihl** [1], Ashley Slattery [2], Nigel J. Cook [1], Kathy Ehrig [3], Liam Courtney-Davies [1], Benjamin P. Wade [2]

[1] *School of Chemical Engineering and Advanced Materials, The University of Adelaide, Adelaide, SA 5005, Australia*

[2] *Adelaide Microscopy, The University of Adelaide, Adelaide, SA 5005, Australia*

[3] *BHP Olympic Dam, Adelaide, SA 5000, Australia*

Article published in *Minerals* (2019) 9(5), 311.

minerals

MDPI

Article

Silician Magnetite: Si–Fe-Nanoprecipitates and Other Mineral Inclusions in Magnetite from the Olympic Dam Deposit, South Australia

Cristiana L. Ciobanu [1,*], Max R. Verdugo-Ihl [1], Ashley Slattery [2], Nigel J. Cook [1], Kathy Ehrig [3], Liam Courtney-Davies [1] and Benjamin P. Wade [2]

1 School of Chemical Engineering, The University of Adelaide, Adelaide, SA 5005, Australia; max.verdugoihl@adelaide.edu.au (M.R.V.-I.); nigel.cook@adelaide.edu.au (N.J.C.); liam.courtney-davies@adelaide.edu.au (L.C.-D.)

2 Adelaide Microscopy, The University of Adelaide, Adelaide, SA 5005, Australia; ashley.slattery@adelaide.edu.au (A.S.); benjamin.wade@adelaide.edu.au (B.P.W.)

3 BHP Olympic Dam, Adelaide, SA 5000, Australia; kathy.ehrig@bhp.com

* Correspondence: cristiana.ciobanu@adelaide.edu.au; Tel.: +61-432-955-000

Received: 19 April 2019; Accepted: 16 May 2019; Published: 20 May 2019

check for updates

Abstract: A comprehensive nanoscale study on magnetite from samples from the outer, weakly mineralized shell at Olympic Dam, South Australia, has been undertaken using atom-scale resolution High Angle Annular Dark Field Scanning Transmission Electron Microscopy (HAADF STEM) imaging and STEM energy-dispersive X-ray spectrometry mapping and spot analysis, supported by STEM simulations. Silician magnetite within these samples is characterized and the significance of nanoscale inclusions in hydrothermal and magmatic magnetite addressed. Silician magnetite, here containing Si–Fe-nanoprecipitates and a diverse range of nanomineral inclusions [(ferro)actinolite, diopside and epidote but also U-, W-(Mo), Y-As- and As-S-nanoparticles] appears typical for these samples. We observe both silician magnetite nanoprecipitates with spinel-type structures and a γ-$Fe_{1.5}SiO_4$ phase with maghemite structure. These are distinct from one another and occur as bleb-like and nm-wide strips along d_{111} in magnetite, respectively. Overprinting of silician magnetite during transition from K-feldspar to sericite is also expressed as abundant lattice-scale defects (twinning, faults) associated with the transformation of nanoprecipitates with spinel structure into maghemite via Fe-vacancy ordering. Such mineral associations are characteristic of early, alkali-calcic alteration in the iron-oxide copper gold (IOCG) system at Olympic Dam. Magmatic magnetite from granite hosting the deposit is quite distinct from silician magnetite and features nanomineral associations of hercynite-ulvöspinel-ilmenite. Silician magnetite has petrogenetic value in defining stages of ore deposit evolution at Olympic Dam and for IOCG systems elsewhere. The new data also add new perspectives into the definition of silician magnetite and its occurrence in ore deposits.

Keywords: silician magnetite; high angle annular dark field scanning transmission electron microscopy; Olympic Dam

1. Introduction

Magnetite ($Fe^{2+}Fe^{3+}{}_2O_4$), an abundant mineral in ore deposits of various genetic types, is one of the '2-3 oxide spinels', $A^{2+}B^{3+}{}_2O_4$; Table 1 ([1] and references therein). The oxide spinel structure has a cubic close packing of anions (O), with the cations hosted either in tetrahedral (T) or octahedral (M) sites (e.g., [2]). Displacement of metal ions along the [111] direction leads to a lowering of $Fd\bar{3}m$ symmetry, for example $F\bar{4}3m$ symmetry was reported in natural magnetite ([3]; Table 1). Cation disorder

ADDITIONAL MATERIAL I

CO-AUTHORED ARTICLE ABSTRACT:

ADVANCES AND OPPORTUNITIES IN ORE MINERALOGY

Nigel J. Cook [1], Cristiana L. Ciobanu [1], Kathy Ehrig [2], Ashley Slattery [3],

Max R. Verdugo-Ihl [1], Liam Courtney-Davies [1], Wenyuan Gao [4]

[1] *School of Chemical Engineering and Advanced Materials, The University of Adelaide, Adelaide, SA 5005, Australia*

[2] *Adelaide Microscopy, The University of Adelaide, Adelaide, SA 5005, Australia*

[3] *BHP Olympic Dam, Adelaide, SA 5000, Australia*

[4] *Key Laboratory of Ministry of Education on Safe Mining of Deep Metal Mines, School of Resources and Civil Engineering, Northeastern University, Shenyang 110819, China*

Article published in *Minerals* (2017) 7, 233.

minerals

MDPI

Review

Advances and Opportunities in Ore Mineralogy

Nigel J. Cook [1,*], Cristiana L. Ciobanu [1], Kathy Ehrig [2], Ashley Slattery [3], Max R. Verdugo-Ihl [1], Liam Courtney-Davies [1] and Wenyuan Gao [1,4]

1 School of Chemical Engineering, The University of Adelaide, Adelaide, SA 5000, Australia; cristiana.ciobanu@adelaide.edu.au (C.L.C.); max.verdugoihl@adelaide.edu.au (M.R.V.-I.); liam.courtney-davies@adelaide.edu.au (L.C.-D.); wenyuan.gao@adelaide.edu.au (W.G.)
2 BHP Olympic Dam, Adelaide, SA 5000, Australia; Kathy.ehrig@adelaide.edu.au
3 Adelaide Microscopy, The University of Adelaide, Adelaide, SA 5000, Australia; ashley.slattery@adelaide.edu.au
4 Key Laboratory of Ministry of Education on Safe Mining of Deep Metal Mines, School of Resources and Civil Engineering, Northeastern University, Shenyang 110819, China
* Correspondence: nigel.cook@adelaide.edu.au; Tel.: +61-8-8313-1096

Received: 28 October 2017; Accepted: 22 November 2017; Published: 24 November 2017

Abstract: The study of ore minerals is rapidly transforming due to an explosion of new micro- and nano-analytical technologies. These advanced microbeam techniques can expose the physical and chemical character of ore minerals at ever-better spatial resolution and analytical precision. The insights that can be obtained from ten of today's most important, or emerging, techniques and methodologies are reviewed: laser-ablation inductively-coupled plasma mass spectrometry; focussed ion beam-scanning electron microscopy; high-angle annular dark field scanning transmission electron microscopy; electron back-scatter diffraction; synchrotron X-ray fluorescence mapping; automated mineral analysis (Quantitative Evaluation of Mineralogy via Scanning Electron Microscopy and Mineral Liberation Analysis); nanoscale secondary ion mass spectrometry; atom probe tomography; radioisotope geochronology using ore minerals; and, non-traditional stable isotopes. Many of these technical advances cut across conceptual boundaries between mineralogy and geochemistry and require an in-depth knowledge of the material that is being analysed. These technological advances are accompanied by changing approaches to ore mineralogy: the increased focus on trace element distributions; the challenges offered by nanoscale characterisation; and the recognition of the critical petrogenetic information in gangue minerals, and, thus the need to for a holistic approach to the characterization of mineral assemblages. Using original examples, with an emphasis on iron oxide-copper-gold deposits, we show how increased analytical capabilities, particularly imaging and chemical mapping at the nanoscale, offer the potential to resolve outstanding questions in ore mineralogy. Broad regional or deposit-scale genetic models can be validated or refuted by careful analysis at the smallest scales of observation. As the volume of information at different scales of observation expands, the level of complexity that is revealed will increase, in turn generating additional research questions. Topics that are likely to be a focus of breakthrough research over the coming decades include, understanding atomic-scale distributions of metals and the role of nanoparticles, as well how minerals adapt, at the lattice-scale, to changing physicochemical conditions. Most importantly, the complementary use of advanced microbeam techniques allows for information of different types and levels of quantification on the same materials to be correlated.

Keywords: ore mineralogy; microanalysis; instrumental techniques

ADDITIONAL MATERIAL J

CO-AUTHORED ARTICLE ABSTRACT:

~1760 MA MAGNETITE-BEARING PROTOLITHS IN THE OLYMPIC DAM DEPOSIT, SOUTH AUSTRALIA: IMPLICATIONS FOR ORE GENESIS AND REGIONAL METALLOGENY

Liam Courtney-Davies [1], Cristiana L. Ciobanu [1], **Max R. Verdugo-Ihl** [1], Nigel J. Cook [1], Kathy J. Ehrig [2], Benjamin P. Wade [3], Zhi-Yong Zhu [4], and Vadim S. Kamenetsky [5]

[1]School of Chemical Engineering and Advanced Materials, The University of Adelaide, Adelaide, SA 5005, Australia

[2]BHP Olympic Dam, Adelaide, SA 5000, Australia

[3]Adelaide Microscopy, The University of Adelaide, Adelaide, SA 5005, Australia

[4] MNR Key Laboratory of Isotope Geology and Deep-Earth Dynamics, Institute of Geology, Chinese Academy of Geological Sciences, Beijing, China

[5] ARC Centre of Excellence in Ore Deposits (CODES), School of Natural Sciences, University of Tasmania, Hobart, Tasmania 7001, Australia

Article published in *Ore Geology Reviews* (2020) 118, 103337.

Ore Geology Reviews 118 (2020) 103337

Contents lists available at ScienceDirect

Ore Geology Reviews

journal homepage: www.elsevier.com/locate/oregeorev

~1760 Ma magnetite-bearing protoliths in the Olympic Dam deposit, South Australia: Implications for ore genesis and regional metallogeny

Liam Courtney-Davies[a,*], Cristiana L. Ciobanu[a], Max R. Verdugo-Ihl[a], Nigel J. Cook[a], Kathy J. Ehrig[b], Benjamin P. Wade[c], Zhi-Yong Zhu[d], Vadim S. Kamenetsky[e]

[a] School of Chemical Engineering and Advanced Materials, The University of Adelaide, SA 5005, Australia
[b] BHP Olympic Dam, Adelaide, SA 5000, Australia
[c] Adelaide Microscopy, The University of Adelaide, SA 5005, Australia
[d] MNR Key Laboratory of Isotope Geology and Deep-Earth Dynamics, Institute of Geology, Chinese Academy of Geological Sciences, Beijing, China
[e] ARC Centre of Excellence in Ore Deposits (CODES), School of Natural Sciences, University of Tasmania, Hobart, Tasmania 7001, Australia

ARTICLE INFO

Keywords:
Olympic Dam
Magnetite U-Pb dating
IOCG
Gawler Craton

ABSTRACT

Spatial associations between banded iron formation and iron-oxide Cu-Au (IOCG) style mineralization are well documented in the Gawler Craton (South Australia), but the possible genetic relationships between these two distinct types of mineralization are hitherto unclear. A texturally conspicuous generation of coarse-grained silician magnetite, intergrown with carbonates and quartz, is observed in drillholes intersecting the 'outer shell' of the Olympic Dam IOCG-type deposit. This magnetite is characterised by high U-content (~50 ppm), siliceous chemistry, and unusual zonal textures with respect to Si-Fe-nanoprecipitates. Direct dating of this magnetite by laser ablation inductively coupled plasma mass spectrometry yields reproducible $^{207}Pb/^{206}Pb$ dates (1761 ± 16 Ma) that are significantly older than the granite hosting the deposit (1593 Ma), or the mineralized breccias constituting the Cu-U-Au-Ag resource (~1592–1589 Ma). The older, Fe-rich crustal material can be correlated with the ~1.76–1.74 Ga (meta)sedimentary Wallaroo Group, host to Fe-rich horizons across the Gawler Craton, including locations ~15 km NW of Olympic Dam. A generation of granitic rocks, which intruded bedrock at ~1.75 Ga are present ~30 km NE of Olympic Dam, and likely exsolved hydrothermal fluids that enriched pre-existing magnetite-bearing protoliths in both U and REE. Such material was physically, and likely chemically, incorporated into the 'outer shell' at Olympic Dam some ~150 Ma later, during granite uplift along faults. The coincidence between Fe-rich horizons/BIF and ~1750 Ma granitoids may have provided IOCG systems with an additional source of both Fe and U that predates the ~1.59 Ga craton-scale metallogenic event. The uranium concentrations in some South Australian IOCG systems represent major global anomalies in the element. A combination of the fortuitous geological circumstances outlined here, may help explain the highly anomalous accumulation of uranium found at Olympic Dam.

1. Introduction

Olympic Dam is by far the largest iron-oxide copper gold (IOCG) system within a N-S-striking, 500 km-long belt defined as the Olympic Cu-Au Province (e.g., Skirrow et al., 2007; Reid, 2019), located on the eastern margin of the Gawler Craton, South Australia. The IOCG mineralization is associated with bimodal intrusive rocks of the Hiltaba Suite (Fanning et al., 1988) and subaerial Gawler Range Volcanics (GRV; Blissett et al., 1993), which together comprise the ~1.6 Ga Gawler Silicic Large Igneous Province (SLIP; Fig. 1A; Allen et al., 2008). The Olympic Dam district contains numerous IOCG-style deposits and prospects which are concealed by post-mineralization sedimentary cover (Reid, 2019), making the area highly prospective and the current focus of exploration (Wise, 2019).

Basement rocks of the district comprise the 2.5 Ga Mulgathing Metamorphic Complex, ~1.85 Ga Donington Suite granitoid rocks, and the 1.76–1.74 Ga Wallaroo Group (meta)sedimentary rocks, which are intruded, and unconformably overlain by, the Hiltaba Suite granitoids and GRV, respectively (Fig. 1B). The Wallaroo Group is a diverse suite of siltstone-dominated metasedimentary, felsic and mafic metavolcanic rock packages, including the Wandearah and Weetulta Formations (Cowley et al., 2003; Conor et al., 2010), which comprise metasedimentary units, including a range of feldspathic, carbonaceous and calc-silicate-bearing members. Iron-rich horizons attributed to Banded Iron

* Corresponding author.
E-mail address: liam.courtney-davies@adelaide.edu.au (L. Courtney-Davies).

https://doi.org/10.1016/j.oregeorev.2020.103337
Received 25 October 2019; Received in revised form 10 January 2020; Accepted 13 January 2020
Available online 17 January 2020
0169-1368/ © 2020 Elsevier B.V. All rights reserved.

ADDITIONAL MATERIAL K

CO-AUTHORED ARTICLE ABSTRACT:

A MULTI-TECHNIQUE EVALUATION OF HYDROTHERMAL HEMATITE U-PB ISOTOPE SYSTEMATICS: IMPLICATIONS FOR ORE DEPOSIT GEOCHRONOLOGY

Liam Courtney-Davies [1], Simon R. Tapster [2], Cristiana L. Ciobanu [1], Nigel J. Cook [1],

Max R. Verdugo-Ihl [1], Kathy J. Ehrig [3], Allen K. Kennedy [4],

Sarah E. Gilbert [5], Daniel J. Condon [2], Benjamin P. Wade [5]

[1] *School of Chemical Engineering and Advanced Materials, The University of Adelaide, Adelaide, SA 5005, Australia*

[2] *NIGL, British Geological Survey, Keyworth, Nottingham, NG12 5GG, UK*

[3] *BHP Olympic Dam, Adelaide, SA 5000, Australia*

[4] *Adelaide Microscopy, The University of Adelaide, Adelaide, SA 5005, Australia*

[5] *John de Laeter Centre, Curtin University of Technology, Bentley, WA 6102, Australia*

Article published in *Chemical Geology* (2019) 513, 54–72.

Chemical Geology 513 (2019) 54–72

Contents lists available at ScienceDirect

Chemical Geology

journal homepage: www.elsevier.com/locate/chemgeo

A multi-technique evaluation of hydrothermal hematite U–Pb isotope systematics: Implications for ore deposit geochronology

Liam Courtney-Davies[a,*], Simon R. Tapster[b], Cristiana L. Ciobanu[a], Nigel J. Cook[a], Max R. Verdugo-Ihl[a], Kathy J. Ehrig[c], Allen K. Kennedy[d], Sarah E. Gilbert[e], Daniel J. Condon[b], Benjamin P. Wade[e]

[a] School of Chemical Engineering, The University of Adelaide, Adelaide, SA 5005, Australia
[b] NIGL, British Geological Survey, Keyworth, Nottingham, NG12 5GG, UK
[c] BHP Olympic Dam, Adelaide, SA 5000, Australia
[d] John de Laeter Centre, Curtin University of Technology, Bentley, WA 6102, Australia
[e] Adelaide Microscopy, The University of Adelaide, Adelaide, SA 5005, Australia

ARTICLE INFO

Editor: Balz Kamber

Keywords:
Hematite
U-Pb
Micro-sampled ID-TIMS
LA-ICP-MS mapping
Geochronology
Olympic Dam
IOCG

ABSTRACT

Hematite (α-Fe_2O_3) is a common iron-oxide mineral known to incorporate U into its crystal lattice at up to wt% concentrations and has been previously used to date ore formation within iron-oxide copper gold and banded iron formation deposits. However, there has been no detailed evaluation of the potential challenges this novel mineral geochronometer may present for accurate temporal interpretation. We report a multi-technique U–Pb geochronological study comprising laser ablation-inductively coupled plasma-mass spectrometry (LA-ICP-MS), sensitive high-resolution ion microprobe (SHRIMP) and the first isotope dilution-thermal ionization mass spectrometry (ID-TIMS) procedure and analyses using an in-situ grain micro-sampling technique. We assess intra- and inter-sample data reproducibility, and examine the compatibility of spatial and analytical resolutions to texturally and compositionally diverse samples.

Five samples of hydrothermal, primary, oscillatory-zoned hematite were analysed from distinct lithologies throughout the ~1.59 Ga Olympic Dam Cu-U-Au-Ag deposit, with typical U concentrations ranging between ~20 and 1000 ppm. LA-ICP-MS mapping of isotope distributions across mm-sized grains allows pinpointing of U-rich and relatively U/Pb isotopically 'homogeneous' domains. Micro-domains were extracted via laser-cut square shaped trenches (100 × 100 μm). U–Pb datum range in complexity, with concordant age domains measured by ID-TIMS indicating that hematite can retain a near-closed U–Pb system over ~1.6 Ga, while also demonstrating that younger Pb-loss events may be recorded. Significant reverse discordance is common in the data, likely to be a real feature due to both internal decoupling and mobility of Pb within a single grain and U–Pb fractionation during microbeam analysis. These effects will obscure the interpretation of real ages for Proterozoic samples where non-zero age Pb-loss events occur, and restricts the evaluation of common Pb mixing components. As a result, microbeam analyses may be biased younger or older in terms of $^{207}Pb/^{206}Pb$ dates in samples with complex histories. Microbeam datum compare favourably with high precision ID-TIMS ages. Although reproducible ID-TIMS U–Pb dates were generally not obtained, in the best-case example, a $^{207}Pb/^{206}Pb$ weighted mean age of 1589.91 ± 0.91 Ma (MSWD = 1.3, n = 5), within 0.2% of the Olympic Dam granite host rock age (1593.87 ± 0.21 Ma) was generated. All five hematite samples dated by LA-ICP-MS and SHRIMP yield weighted mean $^{207}Pb/^{206}Pb$ dates within 2% of the host granite age after small degrees of data rejection. The results demonstrate that with careful sample petrography, screening and data interpretation, hematite can be considered a very useful U–Pb mineral geochronometer, with potential application to all U-bearing Fe-oxide rich mineral systems.

Editor: Balz Kamber

* Corresponding author.
E-mail address: liam.courtney-davies@adelaide.edu.au (L. Courtney-Davies).

https://doi.org/10.1016/j.chemgeo.2019.03.005
Received 8 October 2018; Received in revised form 28 February 2019; Accepted 4 March 2019
Available online 07 March 2019
0009-2541/ © 2019 Elsevier B.V. All rights reserved.

ADDITIONAL MATERIAL L

CO-AUTHORED ARTICLE ABSTRACT:

HEMATITE GEOCHRONOLOGY AND GEOCHEMISTRY RESOLVE GENETIC AND TEMPORAL LINKS AMONG IRON-OXIDE COPPER GOLD SYSTEMS, OLYMPIC DAM DEPOSIT, SOUTH AUSTRALIA

Liam Courtney-Davies [1], Cristiana.L. Ciobanu [1], **Max R. Verdugo-Ihl** [1],

Marija Dmitrijeva [1], Nigel J. Cook [1], Kathy Ehrig [2], Benjamin P. Wade [3]

[1] School of Chemical Engineering and Advanced Materials, The University of Adelaide, Adelaide, SA 5005, Australia

[2] BHP Olympic Dam, Adelaide, SA 5000, Australia

[3] Adelaide Microscopy, The University of Adelaide, SA 5005, Australia

Article published in *Precambrian Research* (2019) 335.

Precambrian Research 335 (2019) 105480

Contents lists available at ScienceDirect

Precambrian Research

journal homepage: www.elsevier.com/locate/precamres

Hematite geochemistry and geochronology resolve genetic and temporal links among iron-oxide copper gold systems, Olympic Dam district, South Australia

Liam Courtney-Davies[a,*], Cristiana.L. Ciobanu[a], Max R. Verdugo-Ihl[a], Marija Dmitrijeva[a], Nigel J. Cook[a], Kathy Ehrig[b], Benjamin P. Wade[c]

[a] School of Chemical Engineering and Advanced Materials, The University of Adelaide, Adelaide, SA 5005, Australia
[b] BHP Olympic Dam, Adelaide, SA 5000, Australia
[c] Adelaide Microscopy, The University of Adelaide, SA 5005, Australia

ARTICLE INFO

Keywords:
Hematite U-Pb dating
IOCG
Wirrda Well
Acropolis
Olympic Cu-Au province

ABSTRACT

The Wirrda Well and Acropolis prospects, ~25 km south from the Olympic Dam deposit, are among several dozen examples of iron-oxide copper gold (IOCG) mineralisation forming a 600 km-long province in the eastern Gawler Craton, South Australia. IOCG systems across the province differ in terms of host lithology, iron-oxide mineral associations, intensity of brecciation, and grade of Cu-(U)-Au mineralisation. Previous efforts to provide a geochronological framework for mineralisation, and correlate this with igneous activity, were inhibited by a lack of clear crosscutting features (particularly in breccia-hosted systems) and a scarcity of reliable hydrothermal mineral geochronometers. The earliest generation of hematite, characterised by enrichment in U-W-Sn-Mo and previously reported from Olympic Dam, provides confident U-Pb dates and insights into hydrothermal fluid signatures. Similar hematite is recognised from Wirrda Well and Acropolis, allowing direct comparison between the three IOCG systems. Relationships between early, silician (Wirrda Well) and titaniferous (Acropolis) magnetite and U-bearing hematite at the two prospects differ. Inferred martitisation of magnetite at Acropolis has generated zoned hematite with U-W-Mo-enrichment at constant Sn concentration, but with a marked loss of REE + Y (REY) and Ti, whereas at Wirrda Well, single-crystal zoned hematite, resembling that from Olympic Dam, retains high REY and Sn concentrations. Although morphologies, textures and compositions of U-bearing hematite at Olympic Dam, Wirrda Well and Acropolis vary significantly, a common U-Pb (laser ablation-inductively coupled plasma-mass spectrometry) age of ~1590 Ma is obtained from the most reliable data ($^{207}Pb/^{206}Pb$: 1598.9 ± 6.3 Ma at Wirrda Well and 1590.6 ± 6.5 Ma at Acropolis). The geochemical signatures of iron-oxides from the two prospects share common trends for U, W, Sn, Mo, high field strength and siderophile elements, comparable with signatures of Fe-oxides from the 'outer shell' of the Olympic Dam deposit. Given that datable iron-oxides would seem to be ubiquitous phases throughout the eastern Gawler Craton, the commonality in geochemistry and age of U-bearing hematite from the Olympic Dam district is significant, as it provides a single, traceable mineral to compare IOCG systems across the province.

1. Introduction

Mesoproterozoic magmatic-hydrothermal ore deposits and prospects occur within a Cu-Au ± U-rich metallogenic province, extending for 600 km along the eastern margin of the Gawler Craton, South Australia (Fig. 1A). Climaxing at ~1.6 Ga, a craton-scale tectonothermal event resulted in emplacement of voluminous, bi-modal intrusive and volcanic rocks of the co-magmatic Gawler Range Volcanics (GRV) and Hiltaba Suite (Drexel et al., 1993, and references therein). Together, these rocks form an intracontinental Large Igneous Province (LIP), which unlike most mantle plume derived LIP's (Ernst, 2014), is dominated by felsic rather than mafic rocks (Allen et al., 2008). The magmatism, and associated metallogenesis in the region, has been temporally correlated with the episodic breakup of the Columbia/Nuna supercontinent (Goldfarb et al., 2010; Groves et al., 2010).

Based on geophysical and geochemical data, lithospheric models for the region acknowledge the important role of mantle-derived components and, moreover, recognise delamination of metasomatised

* Corresponding author.
E-mail address: liam.courtney-davies@adelaide.edu.au (L. Courtney-Davies).

https://doi.org/10.1016/j.precamres.2019.105480
Received 12 June 2019; Received in revised form 4 October 2019; Accepted 4 October 2019
Available online 05 October 2019
0301-9268/ © 2019 Elsevier B.V. All rights reserved.

ADDITIONAL MATERIAL M

CO-AUTHORED ARTICLE ABSTRACT:

ZIRCON AT THE NANOSCALE RECORDS METASOMATIC PROCESSES LEADING TO LARGE MAGMATIC-HYDROTHERMAL ORE SYSTEMS

Liam Courtney-Davies [1], Cristiana L. Ciobanu [1], **Max R. Verdugo-Ihl** [1], Ashley Slattery [2], Nigel J. Cook [1], Marija Dmitrijeva [1], William Keyser [1], Benjamin P. Wade [2], Urs I. Domnick [1], Kathy Ehrig [3], Jing Xu [1,4], Alkiviadis Kontonikas-Charos [1]

[1] *School of Chemical Engineering and Advanced Materials, The University of Adelaide, Adelaide, SA 5005, Australia*

[2] *Adelaide Microscopy, The University of Adelaide, Adelaide, SA 5005, Australia*

[3] *BHP Olympic Dam, Adelaide, SA 5000, Australia*

[4] *Key Laboratory of Mineral Resources, Institute of Geology and Geophysics, Chinese Academy of Sciences, Beijing 100029, China*

Article published in *Minerals* (2019) 9, 364.

minerals

MDPI

Article

Zircon at the Nanoscale Records Metasomatic Processes Leading to Large Magmatic–Hydrothermal Ore Systems

Liam Courtney-Davies [1,*], Cristiana L. Ciobanu [1], Max R. Verdugo-Ihl [1], Ashley Slattery [2], Nigel J. Cook [1], Marija Dmitrijeva [1], William Keyser [1], Benjamin P. Wade [2], Urs I. Domnick [1], Kathy Ehrig [3], Jing Xu [1,4] and Alkiviadis Kontonikas-Charos [1]

1 School of Chemical Engineering and Advanced Materials, The University of Adelaide, Adelaide, SA 5005, Australia; cristiana.ciobanu@adelaide.edu.au (C.L.C.); max.verdugoihl@adelaide.edu.au (M.R.V.-I.); nigel.cook@adelaide.edu.au (N.J.C.); marija.dmitrijeva@adelaide.edu.au (M.D.); william.keyser@adelaide.edu.au (W.K.); urs.domnick@adelaide.edu.au (U.I.D.); j.xu@adelaide.edu.au (J.X.); alkiviadis.kontonikas-charos@adelaide.edu.au (A.K.-C.)

2 Adelaide Microscopy, The University of Adelaide, Adelaide, SA 5005, Australia; ashley.slattery@adelaide.edu.au (A.S.); benjamin.wade@adelaide.edu.au (B.P.W.)

3 BHP Olympic Dam, Adelaide, SA 5000, Australia; kathy.ehrig@bhp.com

4 Key Laboratory of Mineral Resources, Institute of Geology and Geophysics, Chinese Academy of Sciences, Beijing 100029, China; xujing3800@126.com

* Correspondence: liam.courtney-davies@adelaide.edu.au

Received: 30 April 2019; Accepted: 13 June 2019; Published: 16 June 2019

check for updates

Abstract: The petrography and geochemistry of zircon offers an exciting opportunity to better understand the genesis of, as well as identify pathfinders for, large magmatic–hydrothermal ore systems. Electron probe microanalysis, laser ablation inductively coupled plasma mass spectrometry, high-angle annular dark-field scanning transmission electron microscopy (HAADF-STEM) imaging, and energy-dispersive X-ray spectrometry STEM mapping/spot analysis were combined to characterize Proterozoic granitic zircon in the eastern Gawler Craton, South Australia. Granites from the ~1.85 Ga Donington Suite and ~1.6 Ga Hiltaba Suite were selected from locations that are either mineralized or not, with the same style of iron-oxide copper gold (IOCG) mineralization. Although Donington Suite granites are host to mineralization in several prospects, only Hiltaba Suite granites are considered "fertile" in that their emplacement at ~1.6 Ga is associated with generation of one of the best metal-endowed IOCG provinces on Earth. Crystal oscillatory zoning with respect to non-formula elements, notably Fe and Cl, are textural and chemical features preserved in zircon, with no evidence for U or Pb accumulation relating to amorphization effects. Bands with Fe and Ca show mottling with respect to chloro–hydroxy–zircon nanoprecipitates. Lattice defects occur along fractures crosscutting such nanoprecipitates indicating fluid infiltration post-mottling. Lattice stretching and screw dislocations leading to expansion of the zircon structure are the only nanoscale structures attributable to self-induced irradiation damage. These features increase in abundance in zircons from granites hosting IOCG mineralization, including from the world-class Olympic Dam Cu–U–Au–Ag deposit. The nano- to micron-scale features documented reflect interaction between magmatic zircon and corrosive Fe–Cl-bearing fluids in an initial metasomatic event that follows magmatic crystallization and immediately precedes deposition of IOCG mineralization. Quantification of α-decay damage that could relate zircon alteration to the first percolation point in zircon gives ~100 Ma, a time interval that cannot be reconciled with the 2–4 Ma period between magmatic crystallization and onset of hydrothermal fluid flow. Crystal oscillatory zoning and nanoprecipitate mottling in zircon intensify with proximity to mineralization and represent a potential pathfinder to locate fertile granites associated with Cu–Au mineralization.

ADDITIONAL MATERIAL N

CO-AUTHORED ARTICLE ABSTRACT:

SYNTHESIS OF U-PB DOPED HEMATITE USING A HYDRATED FERRIC OXIDE APPROACH

Liam Courtney-Davies [1], Cristiana L. Ciobanu [1], Marcus W. Richardson [2], Ned Prosser [1], **Max Verdugo-Ihl [1]**, Benjamin P. Wade [3], Sarah E. Gilbert 3, Kathy J. Ehrig [4], Nigel J.Cook [1]

[1] *School of Chemical Engineering, The University of Adelaide, Adelaide, S.A. 5005, Australia*

[2] *6 Ophir Street, Goodwood, S.A. 5034, Australia*

[3] *Adelaide Microscopy, The University of Adelaide, Adelaide, S.A. 5005, Australia*

[4] *BHP Olympic Dam, Adelaide, S.A. 5000, Australia*

Article published in *Journal of Crystal Growth* (2019) 513, 48–57.

Journal of Crystal Growth 513 (2019) 48–57

Contents lists available at ScienceDirect

Journal of Crystal Growth

journal homepage: www.elsevier.com/locate/jcrysgro

Synthesis of U-Pb doped hematite using a hydrated ferric oxide approach

Liam Courtney-Davies[a,*], Cristiana L. Ciobanu[a], Marcus W. Richardson[b], Ned Prosser[a], Max Verdugo-Ihl[a], Benjamin P. Wade[c], Sarah E. Gilbert[c], Kathy J. Ehrig[d], Nigel J. Cook[a]

[a] School of Chemical Engineering, The University of Adelaide, Adelaide, S.A. 5005, Australia
[b] 6 Ophir Street, Goodwood, S.A. 5034, Australia
[c] Adelaide Microscopy, The University of Adelaide, Adelaide, S.A. 5005, Australia
[d] BHP Olympic Dam, Adelaide, S.A. 5000, Australia

ARTICLE INFO

Communicated by T. Nishinaga

Keywords:
U-Pb geochronology
Hematite
Reference material
Hydrated ferric oxide
Doping experiments

ABSTRACT

Hematite (α-Fe_2O_3) has been successfully co-doped with uranium and lead using hydrated ferric oxide (HFO) as an intermediary, precipitated by ammonia from a ferric nitrate solution. A novel synthesis approach has been developed, involving a wet stage of doping colloidal HFO by absorption from nitrate solution containing U and Pb nitrates, followed by drying and heating to 700 °C to convert HFO to Fe_2O_3. The crystal phase present in the sample was confirmed as hematite by X-ray powder diffraction. Scanning electron microscopy was used to determine sample morphology and U/Pb isotope homogeneity was assessed using laser-ablation inductively-coupled-plasma mass spectrometry (LA-ICP-MS). Although reasonably homogeneous at the scale of a LA-ICP-MS ablation analysis spot, conspicuous domains are recognized that appear 'bright' or 'dark' on backscatter electron images. These domains display distinctly different element concentrations and U/Pb ratios on LA-ICP-MS isotope maps. Nevertheless, this synthetic U-Pb-doped hematite represents a potential reference material for use in microbeam U-Pb geochronology and the results show that the preparation methods and doping conditions are effective. The observed chemical and isotopic heterogeneity between bright and dark domains may, however, inhibit widespread use of the synthesized hematite as a reference material. U/Pb heterogeneity may be controlled by the heating and cooling regimes of the method. Assuming the 'bright and dark domains' can be analytically or mechanically separated through refinement of the preparation method, then a suitable reference material may be produced. Subject to validation via high-precision chemical analysis, this reference material can be used to date uranium-bearing hematite from various types of deposits. The high speed and precision of LA-ICP-MS analyses will allow measurement of geological ages in a very common mineral, providing new insights for mineral exploration worldwide.

1. Introduction

Iron-oxide minerals such as magnetite (Fe_3O_4) and hematite (α-Fe_2O_3) are ubiquitous in many types of ore deposits. The recognition that Fe-oxides can contain measurable concentrations of uranium and radiogenic lead [1] has raised the potential of developing new U-Pb mineral geochronometers that can be widely applied to establish the age of mineral systems that may not otherwise be accurately dated. This is because conventionally dated (hydrothermal) minerals can be either absent, U-poor, or represent isotopically open systems. Zircon ($ZrSiO_4$) is the most commonly used mineral for U-Pb geochronology but has limited applicability in many hydrothermal ore bodies, due to open system behavior originating from mineral/fluid interaction and metamictization due to high U contents producing large alpha decay doses [2].

Geochronology represents a powerful tool for mineral exploration research, whereby constraints on the relative timing of magmatic and hydrothermal events can underpin models for regional-scale metallogeny and the genesis of individual ore deposits. Radiometric dating of minerals is achieved by observing a known decay of a parent isotope which was substituted into the crystal lattice of the mineral during crystallization (e.g. [3]). The uranium-to-lead decay series provides dates that can be calculated from two uranium decay chains (^{238}U and ^{235}U).

Critical for routine application of U-Pb geochronology is a suitable reference material (RM) that contains known concentrations of U and Pb isotopes, and ratios that can be accurately measured [4,5]. If this material is to be used for analysis by microbeam techniques, such as

* Corresponding author.
E-mail address: liam.courtney-davies@adelaide.edu.au (L. Courtney-Davies).

https://doi.org/10.1016/j.jcrysgro.2019.02.053
Received 8 January 2019; Received in revised form 14 February 2019; Accepted 21 February 2019
Available online 22 February 2019
0022-0248/ © 2019 Elsevier B.V. All rights reserved.

ADDITIONAL MATERIAL O

CO-AUTHORED ARTICLE ABSTRACT:

DEFINING IOCG SIGNATURES THROUGH COMPOSITIONAL DATA ANALYSIS: A CASE STUDY OF LITHOGEOCHEMICAL ZONING FROM THE OLYMPIC DAM DEPOSIT, SOUTH AUSTRALIA

Marija Dmitrijevaa [1], Kathy J. Ehrig [2], Cristiana L. Ciobanu [1],

Nigel J. Cook [1], **Max R. Verdugo-Ihl** [1], Andrew V. Metcalfe [3]

[1] *School of Chemical Engineering, The University of Adelaide, Adelaide, SA 5005, Australia*

[2] *BHP Olympic Dam, Adelaide, SA 5000, Australia*

[3] *School of Mathematical Sciences, The University of Adelaide, Adelaide, SA 5005, Australia*

Article published in *Ore Geology Reviews* (2019) 105, 86–101.

Ore Geology Reviews 105 (2019) 86–101

Contents lists available at ScienceDirect

Ore Geology Reviews

journal homepage: www.elsevier.com/locate/oregeorev

Defining IOCG signatures through compositional data analysis: A case study of lithogeochemical zoning from the Olympic Dam deposit, South Australia

Marija Dmitrijeva[a,*], Kathy J. Ehrig[b], Cristiana L. Ciobanu[a], Nigel J. Cook[a], Max R. Verdugo-Ihl[a], Andrew V. Metcalfe[c]

[a] School of Chemical Engineering, The University of Adelaide, Adelaide, SA 5005, Australia
[b] BHP Olympic Dam, Adelaide, SA 5001, Australia
[c] School of Mathematical Sciences, The University of Adelaide, Adelaide, SA 5005, Australia

ARTICLE INFO

Keywords:
Principal component analysis
Hierarchical clustering
Whole-rock dataset
IOCG deposits
Lithogeochemical zoning
Olympic Dam

ABSTRACT

The Olympic Dam Cu-U-Au-Ag deposit is dominantly composed of mineralised hematite-breccias and occurs entirely within the Roxby Downs Granite. Multivariate statistical analysis of a large whole-rock, 15 m-interval geochemical dataset (10,565 samples) was undertaken to identify geochemical signatures characteristic of iron-oxide copper gold (IOCG)-style mineralization and constrain the conspicuous lithogeochemical zonation observed at Olympic Dam. Statistical analyses include principal component analysis on centred logratio (clr)-transformed data coupled with hierarchical clustering. Certain groups of elements that can be interpreted in terms of an evolving hydrothermal system relative to host lithologies are derived from data analysis: granitophile (U-W-Sn-Mo); siderophile (Ni-Co); chalcophile (Ag-Bi) and related elements (As-Sb and Au-Te). The distributions of elements within each group are investigated through three vertical cross-sections and are compared with known lithological and Cu-(Fe)-sulphide zonation. Throughout the Olympic Dam Breccia Complex, the IOCG signature is defined by multi-element combinations of the commodity metals Cu, U, Au, and Ag, coupled with a range of trace elements. Overall, the IOCG signature overlaps well with Fe-metasomatism despite mismatch which is likely due to discrete styles of mineralisation found only on the margins of the deposit and also to the presence of mineralised domains within Fe-poor zones. The IOCG signature is composed of two geochemical associations, which exhibit distinct spatial distributions. The first group, Cu-U_3O_8-Se-S, shows concentric zonation whereas the second group, Au-W-Mo-Sb-As, forms a vertical ~1800 m deep corridor in the southeastern lobe of the deposit. The specific Au-W-Mo-As-Sb signature could potentially be generic within IOCG systems across the Olympic Cu-Au province and if so, would provide a proxy model for near-mine exploration.

1. Introduction

A distinctive feature of many magmatic-hydrothermal ore deposits is the presence of systematic spatial distribution patterns, commonly expressed by zoned alteration assemblages and/or paragenetic sequences (e.g., Guilbert and Park, 1986). The spatial distribution of minerals, and hence the suite of elements that each contains, occurs due to fluid flow in and around intrusive bodies and conduits for hydrothermal fluids as a response to pH, Eh, temperature gradients and other factors. Investigation of the spatial distribution of mineral assemblages and mineral compositions in deposits formed by dynamic fluid/rock reactions as, for example, in skarn deposits (e.g., Meinert, 1997) is crucial for the development and validation of hypotheses concerning ore genesis that can underpin conceptual exploration models.

Magmatic-hydrothermal iron-oxide copper gold (IOCG) deposits (e.g. in Olympic Cu-Au Province, South Australia; the Cloncurry District, Queensland, or the Carajás Mineral Province, Brazil) represent an economically significant source of Cu, Au, Ag, and in some cases, also U. These deposits are also enriched in, and thus represent potential resources for rare earth elements (REE), and several minor elements, including Co, Nb, and Te (Barton, 2014). The IOCG clan encompasses a diverse group of deposits found in a range of geological settings, and formed from the Archean to Tertiary (e.g., Groves et al., 2010). Despite such a broad spectrum of IOCG systems in terms of age, regional setting, genetic characteristics, host rocks, and ore grade, they are all inherently associated with zoned alteration envelopes and contain significant, often dominant concentrations of Fe-oxides (Barton, 2014, and references therein). In conceptual models for IOCG systems, the expression of regional-scale hydrothermal alteration varies from distal alkali-rich to proximal hydrolytic sericite-chlorite assemblages (Hitzman et al.,

* Corresponding author.

https://doi.org/10.1016/j.oregeorev.2018.12.013
Received 8 October 2018; Received in revised form 8 December 2018; Accepted 17 December 2018
Available online 18 December 2018
0169-1368/ © 2018 Elsevier B.V. All rights reserved.

ADDITIONAL MATERIAL P

CO-AUTHORED ARTICLE ABSTRACT:

MINERALIZATION-ALTERATION FOOTPRINTS IN THE OLYMPIC DAM IOCG DISTRICT, SOUTH AUSTRALIA: THE ACROPOLIS PROSPECT

Marija Dmitrijeva [1], Cristiana L. Ciobanu [1], Kathy J. Ehrig [2], Nigel J. Cook [1], Andrew V. Metcalfe [3], **Max R. Verdugo-Ihl** [1], Jocelyn McPhie [4]

[1] *School of Chemical Engineering and Advanced Materials, The University of Adelaide, Adelaide, SA 5005, Australia*

[2] *BHP Olympic Dam, Adelaide, SA 5001, Australia*

[3] *School of Mathematical Sciences, The University of Adelaide, Adelaide, SA 5005, Australia*

[4] *ARC Centre of Excellence in Ore Deposits, School of Natural Sciences, University of Tasmania, Hobart, TAS 7005, Australia*

Article published in *Journal of Geochemical Exploration* (2019) 205.

Journal of Geochemical Exploration 205 (2019) 106333

Contents lists available at ScienceDirect

Journal of Geochemical Exploration

journal homepage: www.elsevier.com/locate/gexplo

Mineralization-alteration footprints in the Olympic Dam IOCG district, South Australia: The Acropolis prospect

Marija Dmitrijeva[a,*], Cristiana L. Ciobanu[a], Kathy J. Ehrig[b], Nigel J. Cook[a], Andrew V. Metcalfe[c], Max R. Verdugo-Ihl[a], Jocelyn McPhie[d]

[a] School of Chemical Engineering and Advanced Materials, The University of Adelaide, Adelaide, SA 5005, Australia
[b] BHP Olympic Dam, Adelaide, SA 5001, Australia
[c] School of Mathematical Sciences, The University of Adelaide, Adelaide, SA 5005, Australia
[d] ARC Centre of Excellence in Ore Deposits, School of Natural Sciences, University of Tasmania, Hobart, TAS 7005, Australia

ARTICLE INFO

Keywords:
Acropolis prospect
Magnetite-dominant IOCG
K-means clustering
PCA
Implicit 3D modelling

ABSTRACT

The Acropolis prospect, 20 km southwest from the Olympic Dam Cu-U-Au-Ag deposit, South Australia, is a vein-style magnetite (± apatite ± hematite) system. A whole-rock dataset comprising 4864 core samples from 14 drillholes was analysed using multivariate statistical analyses to understand and identify geochemical signatures of mineralization, as well as the expressions and extents of hydrothermal alteration. Statistical analysis included unsupervised (principal component analysis, hierarchical and *k*-means clustering) and supervised (random forests) machine learning algorithms. The geology of the Acropolis prospect is presented as a 3D geological model complemented by cross-sections. The results of statistical analyses are overlaid and interpreted relative to the geological model, and encompass a projection of sodic and propylitic alteration as PC3, and mineralization signature as PC1.

Although the mineralization footprint of the Acropolis prospect partially overlaps with a Hiltaba Suite granite, it is not centred on the granite body. A distinct 'magnetite' signature of Fe-V-Ni-Co is developed in the southwestern part of Acropolis and represents samples containing > 60 wt% Fe. In contrast, the 'hematite' signature displays an association of REE, W, Sn, Sb, U, Th, Ca and P, and is present throughout the Acropolis prospect with the exception of drillhole ACD5, which is non-mineralized. Interpolated values of Cu (> 200 ppm) indicate an offset from Fe-rich veins, thus supporting a genetic model in which Cu-bearing mineralization overprints Cu-Au-deficient magnetite-dominant veins. The results obtained provide insights into the evolution from magnetite to hematite-dominant IOCG systems and may provide a proxy for exploration of shallow and economically significant IOCG deposits in the eastern Gawler Craton.

1. Introduction

Iron-oxide copper gold (IOCG) deposits encompass a diverse group of mineralization styles found in a range of geological settings, and formed from the Archean to Tertiary (Groves et al., 2010). In the last three decades, IOCG systems spanning a continuum from magnetite- to hematite-rich end-members have been subject to many studies aimed at defining common mineralogical and geochemical characteristics and ore genesis (Hitzman et al., 1992; Hitzman, 2000; Williams et al., 2005; Corriveau, 2005; Barton, 2014 and references therein). These deposits are well known for their broad alteration haloes – particularly alkali-(calcic) alteration, and also for their marked deposit-scale zoning, as seen for the IOCG systems at Olympic Dam deposit, South Australia (Ehrig et al., 2012 and references therein; Mauger et al., 2016; Dmitrijeva et al., 2019), or Ernest Henry, Queensland (Mark et al., 2006).

Conceptualization of IOCG-style mineralization and ore genesis has become increasingly problematic, however, particularly since diverse end-members have been added to this group. These include Cu-Au-poor ore systems, such as the Kiruna and El Laco types, which were initially considered as magnetite-apatite deposits of magmatic origin (Geijer, 1931; Frietsch, 1978; Park, 1961), albeit of very different ages (1888 ± 6 Ma, Romer et al., 1994, vs. 2.1 ± 0.1 Ma, Maksaev et al., 1988). As more Kiruna-type magnetite-apatite deposits were identified, notably in the Chilean Iron Belt (El Algarrobo, Ruiz et al., 1968; El Romeral, Bookstrom, 1977), and as detailed geochemical studies

* Corresponding author.
E-mail address: marija.dmitrijeva@adelaide.edu.au (M. Dmitrijeva).

https://doi.org/10.1016/j.gexplo.2019.106333
Received 16 April 2019; Received in revised form 13 June 2019; Accepted 8 July 2019
Available online 17 July 2019
0375-6742/ © 2019 Elsevier B.V. All rights reserved.

ADDITIONAL MATERIAL Q

CO-AUTHORED ARTICLE ABSTRACT:

NUMERICAL MODELLING OF RARE EARTH ELEMENT FRACTIONATION TRENDS IN GARNET: A TOOL TO MONITOR SKARN EVOLUTION

Jing Xu [1,2,3], Cristiana L. Ciobanu [3], Nigel J. Cook [3], Youye Zheng [1], Xiaofeng Li [2,4],

Benjamin P. Wade [5], **Max R. Verdugo-Ihl [3]**, Wenyuan Gao [6], Qiaoqiao Zhu [3,7]

[1] *State Key Laboratory of Geological Processes and Mineral Resources, China University of Geosciences, Beijing 100083, China*

[2] *Key Laboratory of Mineral Resources, Institute of Geology and Geophysics, Chinese Academy of Sciences, Beijing 100029, China*

[3] *School of Chemical Engineering and Advanced Materials, The University of Adelaide, Adelaide, SA 5005, Australia*

[4] *College of Earth and Planetary Sciences, University of Chinese Academy of Sciences, Beijing 100049, China*

[5] *Adelaide Microscopy, The University of Adelaide, Adelaide, SA 5005, Australia*

[6] *Key Laboratory of Ministry of Education on Safe Mining of Deep Metal Mines, Northeastern University, Shenyang 110819, China*

[7] *Key Laboratory of Metallogeny and Mineral Assessment, Institute of Mineral Resources, Chinese Academy of Geological Sciences, Beijing 100037, China*

Article published in *Contributions to Mineralogy and Petrology* (2020) 175:30.

Contributions to Mineralogy and Petrology (2020) 175:30
https://doi.org/10.1007/s00410-020-1670-7

ORIGINAL PAPER

Numerical modelling of rare earth element fractionation trends in garnet: a tool to monitor skarn evolution

Jing Xu[1,2,3] · Cristiana L. Ciobanu[3] · Nigel J. Cook[3] · Youye Zheng[1] · Xiaofeng Li[2,4] · Benjamin P. Wade[5] · Max R. Verdugo-Ihl[3] · Wenyuan Gao[6] · Qiaoqiao Zhu[3,7]

Received: 12 November 2019 / Accepted: 1 March 2020
© Springer-Verlag GmbH Germany, part of Springer Nature 2020

Abstract
Proximal and distal garnets from skarns at Jiaduobule, Tibet, are used to demonstrate how variation in the fluid composition and parameters such as salinity, pH, fO_2, and X_{CO_2} will impact on rare earth element (REE) distribution in garnets, and also to constrain skarn evolution across the orefield from proximal (Fe mineralization) to distal (Cu mineralization). These garnets display a diversity from proximal to distal skarn which is expressed in mineral assemblages, textures, major to trace element contents, and particularly, chondrite-normalized REE fractionation trends. The empirical variation among REE fractionation trends, determined from laser ablation inductively coupled-plasma mass spectrometry data, can be numerically modelled in terms of variable fluid compositions and physicochemical parameters, among which the key determining factors are salinity, pH, X_{CO_2} and Ca content buffered from the rock-fluid reaction with carbonate rocks. Modelling REE trends in skarn garnet is shown to be valuable for constraining conditions during garnet formation and a useful tool for monitoring the evolution of complex skarn deposits.

Keywords Garnet · Numerical modelling · Rare earth elements · Skarn evolution · Jiaduobule · Tibet

Introduction

Garnet, a common rock-forming mineral in skarn deposits, can incorporate a broad range of trace elements, making it a pivotal mineral for the study of skarn evolution (e.g., Smith et al. 2004; Gaspar et al. 2008; Xu et al. 2016). One particularly informative group of elements are the rare earth elements (REE), which together with yttrium (Y) can be significantly enriched in skarn garnet. REE + Y (hereafter REY) incorporation in garnet is achieved via a number of different substitution mechanisms, including 'alkali-type', 'menzerite-type', and 'yttrogarnet-type (YAG substitution), e.g., Carlson et al. (2014).

Gaspar et al. (2008) concluded that grossular-rich garnet from the Crown Jewel Au skarn, Washington, USA, typically displays a chondrite-normalized REY fractionation trend enriched in heavy rare earth elements (HREE) and depleted in light rare earth elements (LREE). In contrast, andradite-dominant garnet shows relative LREE-enrichment

Communicated by Hans Keppler.

Electronic supplementary material The online version of this article (https://doi.org/10.1007/s00410-020-1670-7) contains supplementary material, which is available to authorized users.

✉ Jing Xu
xujing3800@126.com

[1] State Key Laboratory of Geological Processes and Mineral Resources, China University of Geosciences, Beijing 100083, China

[2] Key Laboratory of Mineral Resources, Institute of Geology and Geophysics, Chinese Academy of Sciences, Beijing 100029, China

[3] School of Chemical Engineering and Advanced Materials, The University of Adelaide, Adelaide, SA 5005, Australia

[4] College of Earth and Planetary Sciences, University of Chinese Academy of Sciences, Beijing 100049, China

[5] Adelaide Microscopy, The University of Adelaide, Adelaide, SA 5005, Australia

[6] Key Laboratory of Ministry of Education on Safe Mining of Deep Metal Mines, Northeastern University, Shenyang 110819, China

[7] Key Laboratory of Metallogeny and Mineral Assessment, Institute of Mineral Resources, Chinese Academy of Geological Sciences, Beijing 100037, China

Published online: 16 March 2020

ADDITIONAL MATERIAL R

CONFERENCE ABSTRACT AND POSTER:

TRACE ELEMENT SIGNATURES IN U-W-SN-MO ZONED HEMATITE FROM THE IOCG DEPOSIT AT OLYMPIC DAM, SOUTH AUSTRALIA

Max R. Verdugo-Ihl [1], Cristiana L. Ciobanu [1], Nigel J. Cook [1],

Liam Courtney-Davies [1], Kathy J. Ehrig [2], Sarah Gilbert [1]

[1] *University of Adelaide, Australia*

[2] *BHP Billiton Olympic Dam, Australia*

Extended conference abstract and poster presentation at Mineral Resources to Discover. Proceedings of the 14th SGA Biennial Meeting, Québec, Canada, August 20th-23rd, 2017. ISBN: 978-2-9816898-0-1, Volume 3, 967–970.

Trace element signatures in U-W-Sn-Mo zoned hematite from the IOCG deposit at Olympic Dam, South Australia

Max R. Verdugo-Ihl, Cristiana L. Ciobanu, Nigel J. Cook, Liam Courtney-Davies
University of Adelaide, Australia

Kathy J. Ehrig
BHP Billiton Olympic Dam, Australia

Sarah Gilbert
University of Adelaide, Australia

Abstract. Hematite is the dominant gangue component of the Olympic Dam Cu-U-Au-Ag orebody, South Australia. A distinct oscillatory-zoned hematite, conspicuously rich in 'granitophile' elements (U, W, Sn, Mo) is recognized throughout the ~2 km vertical extent of deposit zonation, from deep pyrite-chalcopyrite to shallow bornite-chalcocite orezones, as well as throughout the entire NW-SE strike of the orebody. Concentrations of granitophile elements are retained, albeit at lower concentrations, in later replacement hematites. Comparison of trace element datasets for U-W-Sn-Mo-zoned hematite relative to replacement hematite provides evidence for localized fluid-mineral reaction and for the importance of reactions coupling dissolution with reprecipitation rates in driving element exchange. The oscillatory-zoned hematite is analogous to that previously dated by LA-ICP-MS, confirming that this generation of hematite was formed at ~1.6 Ga during the onset of the IOCG mineralising system. Such 'granitophile'-rich hematite may be common in other IOCG deposits, and typifies precipitation from fluids rich in these elements during the main hydrothermal stages. Lack of evidence for this type elsewhere is most likely attributable to advanced overprinting in which such signatures are largely obliterated.

1 Introduction

Inherent to all iron-oxide copper gold (IOCG) deposits is the abundance of Fe-oxides as hematite (α-Fe_2O_3) and/or magnetite (Fe_3O_4). The increasing volume of published trace/minor element data for minerals from hydrothermal ores (Cook et al. 2016 and references therein) include studies of Fe-oxides for fingerprinting mineral deposits of different types (e.g. Dupuis and Beaudoin 2011). Trace element signatures of magnetite from end-member IOCG deposits *sensu lato* such as Kiruna (Sweden) and El Laco (Chile) have been obtained to support debates around their magmatic versus hydrothermal origins (Dare et al. 2015; Knipping et al. 2015). In contrast, trace elements in Fe-oxides from *sensu stricto* IOCG-systems, and specifically hematite, have not been studied in detail despite being the main products of alteration closely associated with mineralising processes. Among the exceptions is hematite from the IOCG deposit at Olympic Dam (OD), South Australia (S.A.), which was found to incorporate a wide range of trace elements, including HFSE, REE+Y (REY) and is particularly rich in U, W, Sn, and Mo (hereafter 'granitophile' elements) (Ciobanu et al. 2013; 2015; Cook et al. 2016). Incorporation of U and its decay products within grains showing oscillatory zonation patterns facilitates its use as a mineral geochronometer for directly dating hydrothermal ore-forming processes in IOCG deposits from S.A. and elsewhere (Ciobanu et al. 2013; Courtney-Davies et al. 2016). Hematite from OD shows incredible textural diversity including pseudomorphic replacement of pre-existing minerals and/or rock fragments, overgrowths of hematite with distinct trace/minor element signatures, as well as cycles of (inter)conversion with magnetite, all of which is mirrored by a complexity of preserved trace element signatures (Ciobanu et al. 2013; 2015; Cook et al. 2016). Hence, studies of hematite signatures and their variation can offer insights into the processes responsible for the genesis and overprinting of IOCG-deposits, as well as providing a temporal context for regional metallogenic events.

2 Geological background

Olympic Dam is a giant, Cu-U-Au-Ag deposit (10,400 Mt @ 0.77 % Cu, 250 ppm U_3O_8, 1 ppm Ag and 0.32 ppm Au; BHP Billiton 2016) located on the eastern margin of the Gawler Craton. It belongs to the Olympic Cu-Au Province (e.g. Skirrow et al. 2007) in which IOCG mineralisation is associated with ~1.6 Ga magmatism (Hiltaba Intrusive Suite; HIS and Gawler Range Volcanics, GRV), although ongoing work at OD shows the importance of subsequent overprinting events to account for the spectacular metal endowment of the deposit. The deposit is hosted within the Olympic Dam Breccia Complex (ODBC), which is confined to the Roxby Downs Granite (RDG; Fig. 1), a HIS granitoid. Latest, high-precision U-Pb dating of magmatic and hydrothermal zircon in RDG and ODBC shows that brecciation and hydrothermal alteration (at least the early stage) is coeval with RDG crystallisation at ~1595 Ma (e.g. Jagodzinski 2005 and unpublished data). U-Pb geochronology of oscillatory-zoned hematite from two locations in the deposit shows overlaps with the zircon ages (Ciobanu et al. 2013; Courtney-Davies et al. 2016).

The RDG displays a gradational continuum from altered, through fractured to brecciated lithologies, associated with an increase in Fe-metasomatism and

multiple episodes of brecciation and displacement. OD is mineralogically zoned at the deposit scale, characterized by an inwards-, roughly concentric and quasi-continuous Cu(-Fe)-sulphide zonation that spans vertically and horizontally from pyrite-chalcopyrite (Py-Cp) through chalcopyrite-bornite (Cp-Bn) to bornite-chalcocite (Bn-Cc) dominated assemblages (Ehrig et al. 2012), a pattern considered to represent a primary feature of hypogene ore precipitation (Ciobanu et al. 2017). Hematite is the main Fe-oxide within the orebody, even though at depth and along the deposit margins magnetite is also present and shows various, complex replacement textures with hematite (Ehrig et al. 2012; Ciobanu et al. 2015).

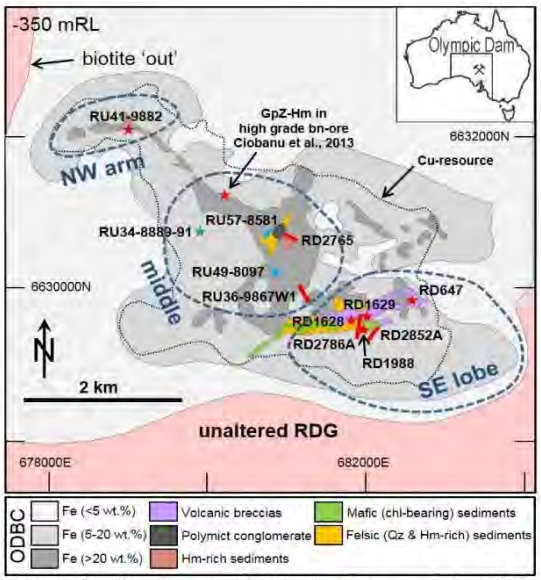

Figure 1. Sketch map of OD showing sampled drillholes. Different categories of hematite (Hm) as follows: red: oscillatory-zoned (GpZ-Hm); green: carbonate replacement (RC-Hm); blue: replacement, undifferentiated. After Ehrig et al. (2012).

3 Sampling approach and methodology

The present study is undertaken on ~50 samples collected from drillholes intersecting different parts of the OD orebody along its ~6 km strike and throughout the entire ~2 km vertical zonation in the SE lobe. These were selected to represent the lithological complexity, e.g. (i) presence of blocks of sediments and brecciated felsic volcanics in the SE lobe; (ii) sediments in the 'barren core' from the middle part of the deposit (>20 wt.% Fe); (iii) high-grade chalcocite and bornite ores from the middle (RU34-8889-8891) and NW arm (RU41-9882) of the deposit, respectively. Polished blocks were analysed using reflected light microscopy, scanning electron microscopy in back-scatter electron mode (BSE), electron probe microanalysis (EPMA) and laser ablation inductively-coupled plasma mass spectrometry (LA-ICP-MS) for trace elements using BHVO-2G and NIST610 as reference standards. All instrumentation is housed at Adelaide Microscopy, The University of Adelaide.

4 Results

Oscillatory zonation in hematite with respect to concentrations of U+W+Sn+Mo is recognised throughout most samples from across the deposit area, including from the shallow Bn-Cc orezone in the SE lobe, in hematite-richest breccias from the 'barren core', and in high-grade bornite ores from the NW arm of the deposit (Fig. 1). This type of hematite (GpZ-Hm; Fig. 2) occurs as single grains of variable size (tens to hundreds of µm), and more rarely as lamellar aggregates. Remarkable concentrations of granitophile elements, routinely measured by LA-ICP-MS (see below), are confirmed by EPMA analysis (e.g. up to wt.% levels of UO_3 and WO_3; Fig. 2a). Overprinting of such hematite is recognised, including marginal corrosion and replacement, brecciation, porosity, fields of discrete inclusions (U-, W-, or REE-minerals), as well as cross-cutting veinlets. In most cases, GpZ-Hm grains display varying degrees of pseudomorphic replacement, leading to overgrowths of hematite poor in granitophile elements (Fig. 2a). There are, however, also grains with a clast-like morphology, little apparent replacement, and excellent preservation of compositional zoning (Fig. 2b). These are specific to samples from the 'barren core', or from entrapped sediments from the SE lobe.

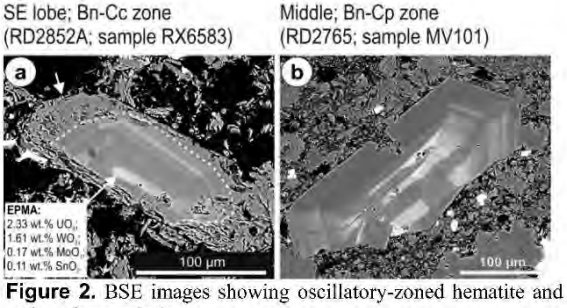

Figure 2. BSE images showing oscillatory-zoned hematite and styles of overprinting.

Although the abundance of GpZ-Hm is higher in samples analysed here from the SE lobe, this type of hematite is relatively minor on the deposit-scale (~10 vol.% within a given sample) relative to other hematite types. These include porous aggregates, and fine-grained hematite filling single grains of other minerals (feldspars in RDG or volcanic rocks), other rock fragments, or the dominant fine-grained hematite that makes up the matrix for breccias, notably in samples from the 'barren core' of the deposit. One type of replacement hematite is defined by fine aggregates of hematite filling coarser lamellae (mm-size) arranged within an overall rhombic outline (RC-Hm). The pre-existing mineral may have been a carbonate. Importantly, such aggregates host abundant chalcocite and define high-grade chalcocite-only ores in the middle part of the deposit.

Trace element data for zoned hematite show variation with respect to REY, HFSE (particularly Nb and V), as well as in the relative proportions of the granitophile elements, e.g. U vs. W+Sn+Mo (Fig. 3). Concentrations of U and W can both reach up to several wt.%; in some cases, hematite grains rich in U and W co-exist in the same sample (e.g. in the Cp-Py zone at depth in the SE lobe). Sn and Mo concentrations are generally subordinate: up to hundreds of ppm (exceptionally thousands of ppm Sn in samples from the SE lobe). Such variation is, however, neither systematic with respect to location within the deposit nor throughout its vertical extent. Replacement hematite, particularly in samples from the middle part of the deposit (included here for comparison) can also be relatively rich in granitophile elements, albeit 1-2 orders of magnitude lower than in GpZ-Hm (Fig. 3). There is an apparent decrease in the U content of hematite from SE to NW. GpZ-Hm in samples from the SE lobe and 'barren core' appear the poorest in HFSE relative to other types.

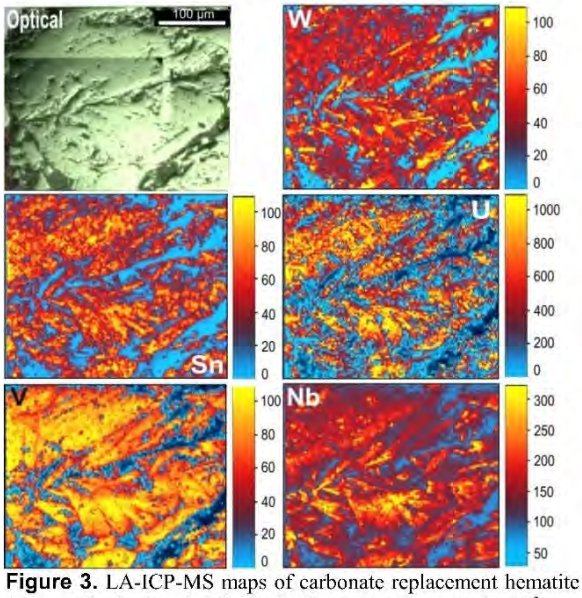

Figure 3. LA-ICP-MS maps of carbonate replacement hematite (see text for further detail). Scales in counts-per-second x 10^3.

The relatively homogenous distribution of granitophile elements and HFSE in the RC-Hm type (Fig. 4) seems to map out the coarse lamellae rather than fine-grained nature of the hematite filling. RC-Hm also stands out by having the highest, consistent Nb+V concentrations (Fig. 4c). In contrast, ΣREY concentrations display a relatively constant spread, with a wide range across several orders of magnitude, irrespective of hematite type (Fig. 4a).

Chondrite-normalised REY fractionation trends (Fig. 5) show that GpZ-Hm is, for the most part, poor in REY, but nevertheless displays a consistent pattern defined by relative LREE enrichment. Other REY trends, including flat to slightly concave profiles, are obtained from grains with higher-ΣREY throughout all categories of hematite. RC-Hm is an exception, however, and shows conspicuous, concave, HREE-enriched trends throughout all analyses.

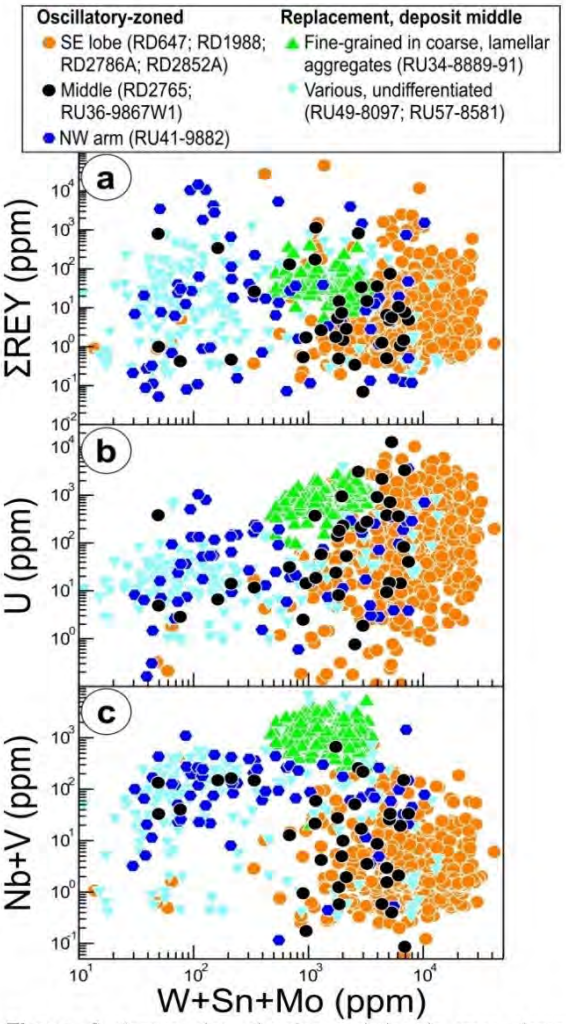

Figure 4. Scatter plots showing variation in trace element signatures of different types of hematite.

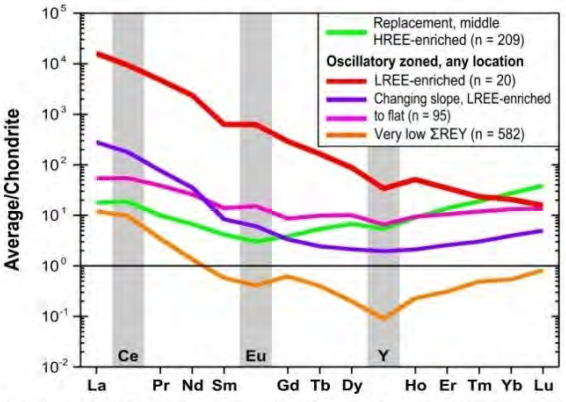

Figure 5. Chondrite normalized REY fractionation trends of different types of hematite.

5 Discussion and implications

'Granitophile'-rich, oscillatory-zoned hematite previously reported from a couple of locations in the OD deposit (Ciobanu et al. 2013; 2015) is now recognised as present throughout the ~2 km vertical extent of deposit zonation (from deep Py-Cp to shallow Bn-Cc orezones), as well as throughout the entire NW-SE strike of the orebody. Such hematite has been also dated by LA-ICP-MS, using GJ-1 zircon as primary standard, and shows the same ~1.6 Ga age (Courtney-Davies et al. unpublished data), firmly indicating that this generation of hematite was formed during the onset of the IOCG mineralising system.

GpZ-Hm is a poor host for REY; higher ΣREY are mostly attributable to discrete inclusions of REE-minerals. The change in REY fractionation trend from LREE, dominant throughout most hematite types, to HREE-enriched, as documented here for RC-Hm, can be related to pH variation, as this parameter can strongly impact on REE solubility (Midgisov et al. 2016 and references therein). This is concordant with the interpretation of replacement of a pre-existing carbonate, strongly reactive to the acidic fluids leading to hydrolytic (sericite-hematite) alteration, and could also account for the formation of high-grade chalcocite ore. One of the interesting findings is the potential that HFSE may have for understanding primary deposit zonation, or the importance of different protoliths relative to granitophile-rich hydrothermal fluids.

The fact that concentrations of U and other granitophile elements are retained throughout all replacement hematites, some of which are clearly formed on behalf of the oscillatory-zoned type, suggests the importance of reactions coupling dissolution with reprecipitation rates (CDRR) throughout the ODBC, retaining such elements close to the sites of fluid-mineral interaction. The data for U-W-Sn-Mo-zoned hematite can be considered as evidence for localised fluid-mineral reaction throughout the ODBC and the importance of CDRR in driving element exchange as was shown for OD uraninite (Macmillan et al. 2016a, b) and for feldspar alteration in the RDG outside the orebody (Kontonikas-Charos et al. 2017).

Comparable compositional zonation with respect to W+U was shown for hematite from other deposits in the Olympic Cu-Au Province and from Carajas, Brazil (Courtney-Davies et al. 2016), irrelevant of host lithologies (granitoid hosted or not). It is likely that 'granitophile'-rich hematite is one of the main types in IOCG deposits, and typifies precipitation from fluids rich in these elements during the main hydrothermal stages, assuming no other minerals that are normally good 'granitophile' carriers are formed at the same time (e.g. skarn calc-silicates). A lack of evidence for this type elsewhere is most likely attributable to advanced overprinting (obliteration of such signature), and/or poor mineralogical/petrological studies.

Acknowledgments

This is a contribution to the 'FOX' project, supported by BHP Billiton Olympic Dam and South Australian Mining and Petroleum Services Centre of Excellence.

References

BHP Billiton (2016) http://www.bhpbilliton.com/~/media/bhp/documents/investors/annual-reports/2016/bhpbillitonannualreport2016.pdf.

Ciobanu CL, Cook NJ, Ehrig K (2017) Ore minerals down to the nano-scale: Cu-(Fe)-sulphides from the Iron Oxide Copper Gold deposit at Olympic Dam, South Australia. Ore Geol Rev 81:1218-1235

Ciobanu CL, Cook NJ, Ehrig K, Wade BP, Kamenetsky VS (2015) Trace element signatures in iron oxides from the Olympic IOCG deposit, South Australia. Mineral Resources in a Sustainable World, 13th SGA Biennial Meeting 2015, Nancy:1071-1074

Ciobanu CL, Wade B, Cook NJ, Schmidt Mumm A, Giles D (2013) Uranium-bearing hematite from the Olympic Dam Cu-U-Au deposit, South Australia; a geochemical tracer and reconnaissance Pb-Pb geochronometer. Precambr Res 238:129-147

Cook NJ, Ciobanu CL, George L, Zhu Z-Y, Wade BP, Ehrig K (2016) Trace element analysis of minerals in magmatic-hydrothermal ores by laser ablation inductively-coupled plasma mass spectrometry: approaches and opportunities. Minerals 6(4), 111; doi:10.3390/min6040111

Courtney-Davies L, Zhu Z, Ciobanu CL, Wade BP, Cook NJ, Ehrig K, Cabral AR, Kennedy A (2016) Matrix-matched iron-oxide laser ablation ICP-MS U-Pb geochronology using mixed solution standards. Minerals 6(3), 85; doi:10.3390/min6030085

Dare SAS, Barnes S-J, Beaudoin G (2015) Did the massive magnetite "lava flows" of El Laco (Chile) form by magmatic or hydrothermal processes? New constraints from magnetite composition by LA-ICP-MS. Mineral Deposita 50:607-617

Dupuis C, Beaudoin G (2011) Discriminant diagrams for iron oxide trace element fingerprinting of mineral deposit types. Mineral Deposita 46:319–335

Ehrig K, McPhie J, Kamenetsky V (2012) Geology and mineralogical zonation of the Olympic Dam Iron Oxide Cu-U-Au-Ag deposit, South Australia. SEG Spec Publ 16:237-267

Jagodzinski EA (2005) Compilation of SHRIMP U–Pb Geochronological Data. Olympic Domain, Gawler Craton, South Australia, 2001–2003. Geoscience Australia, Record 2005/20

Knipping JL, Bilenker LD, Simon AC, Reich M, Barra F, Deditius AP, Lundstrom C, Bindeman I, Munizaga R (2015) Giant Kiruna-type deposits form by efficient flotation of magmatic magnetite suspensions. Geology 43:591-594

Kontonikas-Charos A, Ciobanu CL, Cook NJ, Ehrig K, Krneta S, Kamenetsky VS (2017) Feldspar evolution in the Roxby Downs Granite, host to Fe-oxide Cu-Au-(U) mineralisation at Olympic Dam, South Australia. Ore Geol Rev 80:838-859

Macmillan E, Ciobanu CL, Ehrig K, Cook NJ, Pring A (2016a) Chemical zoning and lattice distortion: Uraninite from Olympic Dam, South Australia. Amer Mineral 101:2351-2354

Macmillan E, Cook NJ, Ehrig E, Ciobanu CL, Pring A (2016b) Uraninite from the Olympic Dam IOCG-U-Ag deposit: linking textural and compositional variation to temporal evolution. Amer Mineral 101:1295-1320

Migdisov A, Williams-Jones A, Brugger J, Caporuscio F (2016) Hydrothermal transport, deposition, and fractionation of the REE: Experimental data and thermodynamic calculations. Chem Geol 439:13-42

Skirrow RG, Bastrakov E, Evgeniy N, Barovich K, Fraser GL, Creaser RA, Fanning CM, Raymond OL, Davidson GJ (2007) Timing of iron oxide Cu-Au-(U) hydrothermal activity and Nd isotope constraints on metal sources in the Gawler craton, South Australia. Econ Geol 102:1441-1470

Trace element signatures in U-W-Sn-Mo zoned hematite from the IOCG deposit at Olympic Dam, South Australia

Max R. Verdugo-Ihl[1]*, Cristiana L. Ciobanu[1], Nigel J. Cook[1], Liam Courtney-Davies[1], Kathy J. Ehrig[2], Sarah Gilbert[3]

[1]*School of Chemical Engineering, The University of Adelaide;* [2]*BHP Olympic Dam;* [3]*Adelaide Microscopy, The University of Adelaide*

*max.verdugoihl@adelaide.edu.au

Introduction

Hematite is the dominant gangue component of the Olympic Dam (OD) iron oxide copper gold (IOCG) deposit in South Australia (SA). Oscillatory-zoned hematite enriched in 'granitophile' elements (U-W-Sn-Mo), is recognized throughout the ~2 km vertical extent of deposit zonation, from deep pyrite-chalcopyrite (Py-Cp) to shallow bornite-chalcocite (Bn-Cc) orezones, as well as throughout the entire NW-SE strike of the orebody. Comparison of trace element datasets for U-W-Sn-Mo-zoned hematite relative to replacement and overprinted hematites provides evidence for localized fluid-mineral reaction and for the importance of reactions coupling dissolution with reprecipitation, driving element exchange. This type of zoned hematite has been previously dated by LA-ICP-MS[1-2], confirming its formation at ~1.6 Ga during the onset of a regional-scale metallogenic event.

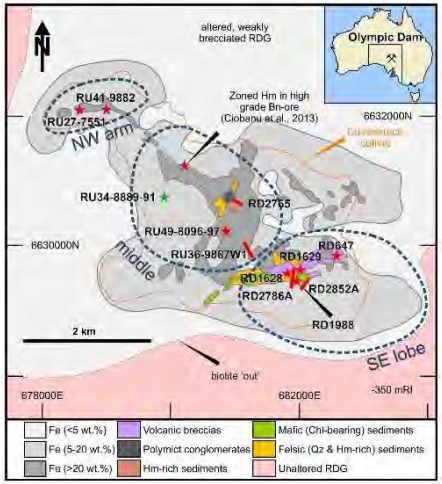

Figure 1. Sketch map of OD indicating sampled drillholes across deposit area. Green star denotes the exclusive location of carbonate- replacement hematite. After Ehrig et al.[19].

Geological background and approach

Olympic Dam (**Fig. 1**) is located on the eastern margin of the Gawler Craton in the Olympic Cu-Au Province[4], where IOCG mineralisation is associated with ~1.6 Ga magmatism of the Hiltaba Intrusive Suite (HIS) and Gawler Range Volcanics (GRV). The deposit is confined to the Roxby Downs Granite (RDG)[5], a HIS-granitoid, and hosted within the Olympic Dam Breccia Complex (ODBC). The complex features an inwards-, roughly concentric and quasi-continuous Cu(-Fe)-sulphide zonation that spans vertically and horizontally, and that possibly represents a primary 'feature of hypogene ore precipitation'[6]. Hematite is the main Fe-oxide within the orebody, even though at depth, and along the deposit margins, magnetite can be locally abundant and displays various complex replacement textures with hematite[7-9].

The analysed samples were collected from drillholes that intersect various parts of the OD orebody along its ~6 km strike and throughout the entire ~2 km vertical zonation in the SE lobe (**Fig. 1**).These locations represent the lithological complexity of the deposit, eg., (i) presence of blocks of sediments and brecciated felsic volcanics in the SE lobe; (ii) sediments in the 'barren core' from the middle part of the deposit (>20 wt.% Fe); (iii) high-grade chalcocite and bornite ores from the middle (RU34-8889-8891) and NW arm (RU41-9882) of the deposit, respectively. Hematite in the polished blocks was analysed by reflected light microscopy, scanning electron microscopy in back-scatter electron mode (BSE), electron probe microanalysis (EPMA) and laser ablation inductively-coupled plasma mass spectrometry (LA-ICP-MS).

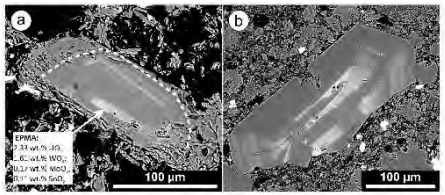

Figure 2. BSE images showing oscillatory-zoned hematite and styles of overprinting. (a) SE lobe in Bn-Cc zone (RD2852A- RX6583). (b) Middle in barren zone (RD2765 - MV101).

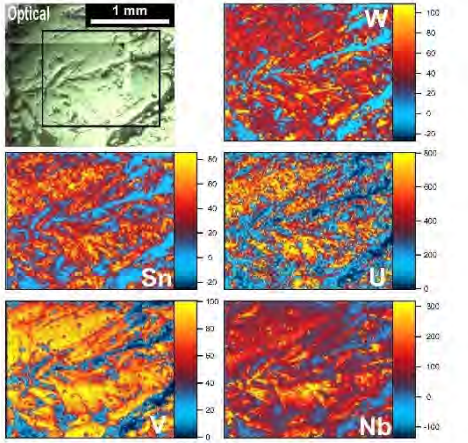

Figure 3. LA-ICP-MS maps of carbonate replacement hematite (RC-Hm); intensity in counts-per-second x10[1].

Results

Oscillatory zoned hematite is recognised throughout the deposit area (**Fig. 1**). This type of hematite (GpZ-Hm; **Fig. 2**) occurs as single grains of variable size (10s to 100s of µm) and as lamellar aggregates. Remarkable concentrations of granitophile elements, routinely measured by LA-ICP-MS, are confirmed by EPMA analysis, eg., up to wt.% levels of UO_2 and WO_3 **(Fig. 2a)**. Overprinting of such hematite is recognised, including marginal corrosion (**Fig. 2b**), replacement, brecciation, porosity development and fields of discrete inclusions (U-, W-, or REE-phases). Other hematite types include porous aggregates, fine-grained hematite filling single grains of other minerals (feldspars in RDG or volcanic rocks), repacking other rock fragments, or as the dominant fine-grained matrix for breccias. One particular type of replacement hematite (**Fig. 3**) is defined by fine aggregates of hematite filling coarser lamellae (mm-size) arranged within an overall rhombic outline (RC-Hm), possibly representing a replacement after pre-existing carbonates. These aggregates host abundant chalcocite and define high-grade chalcocite-only ores in the middle part of the deposit.

Trace element data for zoned hematite show variation with respect to concentrations of REY, HFSE, particularly Nb and V, and granitophile elements (e.g. U vs. W+Sn+Mo; **Fig. 3**). Concentrations of U and W can reach up to several wt.%, in some cases, whereas Sn and Mo concentrations are generally subordinate (up to 100s of ppm). Such variation is, however, neither systematic with respect to location within the deposit nor throughout its vertical extent.Replacement hematite, particularly in samples from the middle part of the deposit (included here for comparison) can also be relatively rich in granitophile elements, albeit 1-2 orders of magnitude lower than in GpZ-Hm (**Fig. 3**). There is an apparent decrease in the U content of hematite from SE to NW. GpZ-Hm in samples from the SE lobe and 'barren core' appear the poorest in HFSE relative to other types.

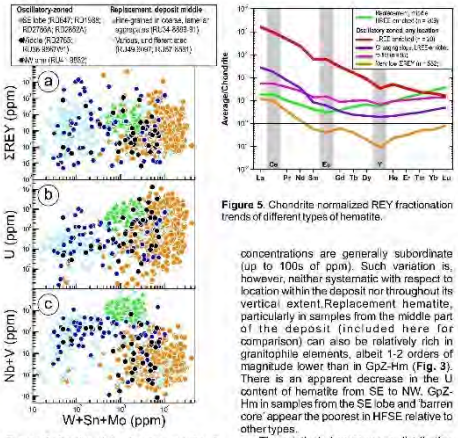

Figure 4. Scatter plots showing variation in trace element signatures of different types of hematite.

Figure 5. Chondrite normalized REY fractionation trends of different types of hematite.

The relatively homogenous distribution of granitophile elements and HFSE in the RC-Hm type (**Fig. 3**) seems to map out the coarse lamellae rather than fine-grained nature of the hematite filling. RC-Hm also stands out by having the highest, consistent Nb+V concentrations (**Fig. 4c**). In contrast, ΣREY concentrations display a relatively consistent spread, with a wide range across several orders of magnitude, irrespective of hematite type (**Fig. 4a**). Chondrite-normalised REY-fractionation trends (**Fig. 5**) show that GpZ-Hm is poor in REY but nevertheless displays a consistent pattern defined by relative LREE enrichment. Other REY trends, including flat to slightly concave profiles, are obtained from grains with higher-ΣREY throughout all categories of hematite. RC-Hm is an exception, however, and shows conspicuous, concave, HREE-enriched trends throughout all analyses.

Discussion and implications

'Granitophile'-rich, oscillatory-zoned hematite is now recognised as present throughout the ~2 km vertical extent of the deposit zonation and throughout the entire NW-SE strike of the orebody. GpZ-Hm is a poor host for REY, and higher ΣREY are normally attributed to discrete inclusions of REE-minerals. The change in REY-fractionation trends from LREE, dominant throughout most hematite types, to HREE-enriched, as documented here for RC-Hm, can be related to pH variation, as this parameter can strongly impact on REE solubility[3]. One of the interesting findings is the potential that HFSE may have for understanding primary deposit zonation, or the importance of different protoliths relative to granitophile-rich hydrothermal fluids. The fact that granitophile elements are retained throughout all replacement hematites, suggests the importance of reactions coupling dissolution with reprecipitation (CDRR)[10] throughout the ODBC, retaining such elements close to the sites of fluid-mineral interaction. The data for GpZ-Hm can be considered as evidence for localised fluid-mineral reaction throughout the ODBC and the importance of CDRR in driving element exchange, as shown for OD uraninite[11] and feldspars in the RDG outside the orebody[12]. Comparable compositional zonation with respect to W-U was shown for hematite from other deposits in the Olympic Cu-Au Province and from Carajas (Brazil)[13], irrelevant of host lithologies. It is likely that 'granitophile'-rich hematite is one of the main types in IOCG deposits, and typifies precipitation from fluids rich in these elements during the main hydrothermal stages, assuming no other minerals that are normally good 'granitophile' carriers are formed at the same time (e.g. skarn calc-silicates). A lack of evidence for this type elsewhere could be attributed to advanced overprinting, in which such textures and characteristics signatures are largely obliterated.

[1] Ciobanu CL, Wade B, Cook N J, Schmidt Mumm A, Ehrig K (2013) Uraninite-bearing hematite breccias in the Olympic Dam South Australia IOCG deposit: Evidence for multistage, fluid-mediated uranium remobilization. Precamb. Res. 238: 75-97. [2] Courtney-Davies L, Ciobanu CL, Wade BP, Cook NJ, Ehrig K, Gilbert SE, Kontonikas-Charos A (2016) Mineralogical and trace element characterization of IOCG-type hematite using mixed isotope datasets. Ore Geol Rev 78: 460-475. [3] Ehrig K, Morris J, Kamenetsky V (2012) Geology and mineralogical zonation of the Olympic Dam Iron Oxide Cu-Au-U-Ag deposit, South Australia. SEG Spec Pub 16:237-267. [4] Skirrow RG, Bastrakov EN, Barovich K, Fraser GL, Creaser RA, Fanning CM, Raymond OL, Davidson GJ (2007) Timing of iron oxide Cu-Au-(U) hydrothermal activity and Nd isotope constraints on metal sources in the Gawler Craton, South Australia. Economic 102: 1441-1470. [5] Johnson JP, Cross KC (1995) U-Pb geochronology of the Roxby Downs Granite, and its bearing on the timing and duration of Olympic Dam-type mineralization. Econ Geol 90: 1046-1063. [6] Ciobanu CL, Cook NJ, Ehrig K (2017) Ore-forming fluids and the olympic dam story. Ore Geol Rev 80:1130-1156. [7] Macmillan E, Williams-Jones AE, Boggs C, Goodall P (2013) Hydrothermal alteration, and mineralization of the Prominent Hill IOCG deposit, South Australia. Econ Geol 108: 1301-1330. [8] Verdugo-Ihl MR, Ciobanu CL, Cook NJ, Ehrig K, Courtney-Davies L, Gilbert S (2017) Multi-stage origin of hematite in IOCG deposits: Evidence from the Olympic Dam district. Ore Geol Rev 80: 1078-1106. [9] Verdugo-Ihl MR, Ciobanu CL, Cook NJ, Ehrig K, Courtney-Davies L, Gilbert S (2017) Hematite at Olympic Dam: Breccia evolution and fluid-mineral interactions. Chem Geol 466:478-494. [10] Putnis A (2002) Mineral replacement reactions: from macroscopic observations to microscopic mechanisms. Mineral Mag 66: 689-708. [11] Courtney-Davies L, Ehrig K, Cook NJ, Ciobanu CL (2016) Deciphering the diagenetic history of sandstone-hosted uranium deposits: Olympic Dam, South Australia. Amer Mineral 101:2257-2270. doi: 10.2138/am-2016-5783

Acknowledgements

This work is a contribution to the 'FOX' project (Trace elements in iron oxides: deportment, distribution and application in ore genesis, geochronology, exploration and mineral processing), supported by BHP Olympic Dam and the South Australian Government Mining and Petroleum Services Centre of Excellence.

ADDITIONAL MATERIAL S

CONFERENCE ABSTRACT AND POSTER:

COPPER NANOPARTICLES ALONG FLUID INCLUSION TRAILS IN HEMATITE

Max R. Verdugo-Ihl [1], Cristiana L. Ciobanu [1], Nigel J. Cook [1],

Ashley Slattery [2], Kathy Ehrig [4]

[1] *University of Adelaide, Adelaide, SA 5005, Australia*

[2] *BHP Olympic Dam, Adelaide, SA 5000, Australia*

Conference abstract and poster presentation (presented by Cristiana L. Ciobanu) at Goldschmidt Conference 2018, Boston, U.S.A., August 12th-17th.

Goldschmidt2018 Abstract

Copper nanoparticles along fluid inclusion trails in hematite

M.R. VERDUGO-IHL[1]*, C.L. CIOBANU[1], N.J. COOK[1], A. SLATTERY[1], K.J. EHRIG[2]

[1]University of Adelaide, Adelaide, SA 5005, Australia (correspondence*: max.verdugoihl@adelaide.edu.au; cristiana.ciobanu@adelaide.edu.au; nigel.cook@adelaide.edu.au; ashley.slattery@adelaide.edu.au

[2]BHP Olympic Dam, Adelaide, SA 5000, Australia (Kathy.J.Ehrig@bhpbilliton.com)

Interaction between minerals and hydrothermal fluids can lead to pseudomorphic replacement if the dissolution and precipitation rates are coupled to one another (CDRR). Such reactions are mediated by a reaction interface along which transient porosity occurs and within which mineral inclusions can precipitate as products of fluid-mineral interaction [1]. Hydrothermal hematite (Hm) from granite-hosted, iron-oxide copper gold (IOCG) deposits such as Olympic Dam (OD), South Australia, display a prominent geochemical signature comprising U-Pb-W-Sn-Mo (granitophile elements; GS) [2]. Such a signature can change within grains that show partial pseudomorphic replacement of Hm resulting in newly-formed Hm that features either pores, and/or inclusion-attached pores. The geochemical signature of the new-formed Hm is always distinct from that of the precursor Hm [2].

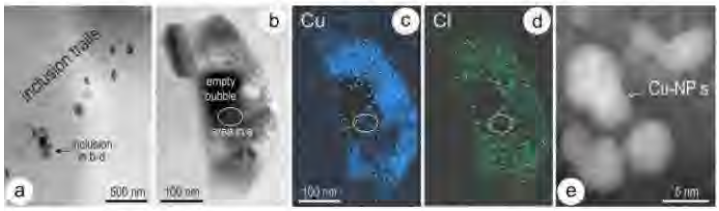

Fig. 1. HAADF-STEM images (a, b, e) and EDX maps (c, d) showing inclusion trails, their morphology and selected composition. Cu-NPs are shown in (e). Images and maps obtained at 200 kV.

FIB-prepared TEM foils cut across unusual Cu-As-rich zones in one such GS-bearing Hm from OD were analysed by HAADF-STEM imaging and EDX-STEM mapping. Results show the presence of nm- to µm-scale composite inclusions along trails parallel to crystal zoning (Fig. 1a). Coarser inclusions contain empty 'bubbles', and display elements typical of fluid inclusions (e.g., Cl, Na, K, C; Fig. 1b-d). Metal-bearing (Cu, As, Mo, W, Sn) nanoparticles (NPs) are identified within such inclusions. The presence of Cu-NPs (Fig. 1e) is concordant with the sulphide-poor environment for the analysed Hm. We suggest these metal-bearing NPs formed during CDRR-driven replacement of GS-bearing Hm.

[1] Tooth, B. et al. (2011) Geochim Cosmochim. Acta 75, 5423-5443;
[2] Verdugo-Ihl, M.R. et al. (2017), Ore Geo. Rev., 91, 173-195.

Copper nanoparticles along fluid inclusion trails in hematite

Max R. Verdugo-Ihl[1]*, Cristiana L. Ciobanu[1], Nigel J. Cook[1], Ashley Slattery[1], Kathy J. Ehrig[2]

[1]University of Adelaide, Adelaide, SA 5005, Australia

[2]BHP Olympic Dam, Adelaide, SA 5000, Australia

*Corresponding author: max.verdugoihl@adelaide.edu.au

ABSTRACT

Variations to the zonation patterns can be observed in hematite formed by pseudomorphic replacement of a precursor hematite. Commonly, this process can be associated with porosity development and/or presence of inclusions attached to pores. FIB-prepared TEM foils, cut across unusual Cu-As-bands within zoned, granitophile element (U, Pb, W, Sn, Mo) bearing hematite from the iron-oxide-Cu-Au (IOCG) deposit at Olympic Dam (OD), were analysed by HAADF-STEM imaging and EDX-STEM mapping. The investigations revealed nm- to µm-scale, composite inclusions arranged parallel to crystal zoning. Within these trails, coarser inclusions contain voids and display the presence of elements typically associated with fluid inclusions (e.g., Cl, Na, K, C). Various metal-bearing (Cu, As, Mo, W, Sn) nanoparticles (NPs) can be identified within such inclusions. HAADF-STEM imaging of hematite from inclusion wall-zone areas shows nano-domains of variable orientation, sets of twining and defects, contrasting with the host hematite almost devoid of such defects. These domains suggest that such hematite is a fine-grained precipitate formed during interaction between the precursor hematite and pervading fluids. This process can locally drive the formation of metal-bearing NPs in hematite and produce unusual trace element signatures as depicted by other analyses.

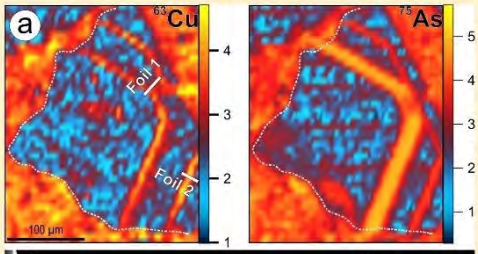

Fig. 1. (a) LA-ICP-MS maps of selected elements (As and Cu), intensity in counts-per-second (10^n); adapted from [2]. White bars indicate location of the extracted TEM-foils. HAADF-STEM aspects of the obtained foils: (b) foil 1 and (c) foil 2, displaying brighter bands (inset).

BACKGROUND

Replacement processes develop across mineral-fluid interfaces, in which transient porosity can host mineral inclusions attached to pores [1]. Laser-ablation inductively-coupled-plasma mass-spectrometry (LA-ICP-MS) mapping of hematite from OD [2] indicates that hematite has been affected by coupled dissolution and re-precipitation reactions (CDRR). In particular, trace element distributions patterns of hematite from a sulphide-poor interval within the SE-lobe of the deposit revealed unusual As- and Cu-zoning (Fig. 1). Nano-scale investigations of such zones were conducted to assess the character of the unusual zoning observed at the micron-scale.

Acknowledgements:
This work is a contribution to the **'FOX'** project (Trace elements in iron oxides: deportment, distribution and application in ore genesis, geochronology, exploration and mineral processing), supported by BHP Olympic Dam and the South Australian Government Mining and Petroleum Services Centre of Excellence.

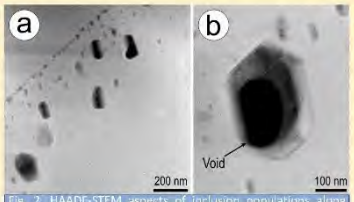

Fig. 2. HAADF-STEM aspects of inclusion populations along trails. (a) Fine to medium size inclusions. (b) Coarser (up to hundreds of nm) inclusion displaying hexagonal outline, accompanied by finer inclusions. Coarser inclusions are mostly composite, hosting metal-bearing NP and displaying the presence of void(s).

METHODOLOGY

Transmission electron microscopy (TEM) foils of an As-Cu-zoned hematite (Fig. 1) were obtained by focused ion beam (FIB) milling using a FEI-Helios nanoLab (Fig. 1b-c). The sample surface was re-polished prior to selecting the foil locations, which were aligned across the unusual zoning. The obtained foils were analysed by High Angle Annular Dark Field (HAADF) scanning-TEM (STEM) and energy dispersive X-ray spectrometry (EDX)-STEM mapping using a Titan Themis operated at 200 kV. All employed instrumentation is hosted at Adelaide Microscopy, The University of Adelaide.

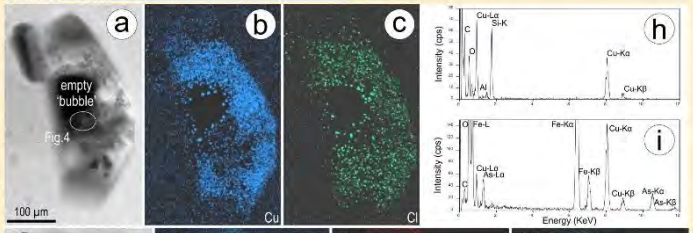

Fig. 3. HAADF-STEM images of composite, NP-bearing inclusions (a, d). Selected STEM-EDX element maps (b-c, e-g). EDX spectra of: (h) a Cu-NP in (a) and Fig. 4, and (i) Cu-As-bearing NP within brighter bands (Fig. 1c, inset).

RESULTS

Hematite displays trails of inclusions, comprising swarms of fine (tens of nm) and sporadic, up to ~300 nm inclusions (Fig. 2). Brighter bands that host Cu-As-bearing NP, of different orientation to the trails, are also observed (Fig. 1c, inset). Coarsest inclusions are generally multicomponent, and comprise metal-bearing NPs (e.g., Cu, As, Mo, W, Sn). STEM-EDX mapping of coarser inclusions typically show element associations including Cl, Cu, As, and C, among others (Fig. 3). Voids are generally observed within coarser inclusions (Fig. 2 and 3), which can be ascribed to the presence of volatile phases freed during FIB-milling. These features suggest that medium to coarser inclusions correspond to fluid inclusions. Occasionally, clustered Cu-NPs (Fig. 3) are present within coarser inclusions. HAADF-STEM imaging of hematite proximal to inclusion wall areas reveals nanodomains of variable orientation, defects and sets of twinning (Fig. 5). Contrasting with the host hematite almost devoid of defects, such domains along the inclusion trails indicate that such hematite is a fine-grained precipitate formed during interaction between precursor hematite and pervading fluids.

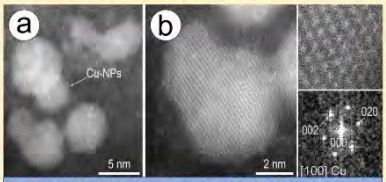

Fig. 4. HAADF-STEM images of clustered Cu-NPs (a) and detail of a Cu-NP (b) with corresponding zone axis, indexed from Fast Fourier Transform (FFT; inset).

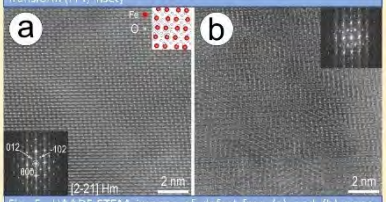

Fig. 5. HAADF-STEM images of defect-free (a) and (b) nano-domains of variable orientations (note satellite reflections in FFT, inset), close to inclusion (no change of tilt).

DISCUSSION and CONCLUSIONS

Nano-domains, defects and twining in hematite proximal to inclusions, suggest that such hematite formed as a precipitate during mineral-fluid interaction.

Metal-bearing NPs within fluid inclusions and isolated within brighter bands can be sourced from the release of primary incorporated elements in the zonation patterns (e.g., W, Mo) and the interacting fluids. Transient porosity development during CDRR and local precipitation of NPs can promote trapping of metals resealed during this process. Such processes result in 'open system' behaviour for several elements, including U, bearing on the U-Pb systematics of those domains and notably affecting their trace element composition at the micron-scale. In this case, S-depleted fluids can be invoked to explain precipitation of native elements as NPs, correlating with the presence of Cu-Au alloys and the sulphide-poor interval that the sample represents.

References:
[1] Tooth, B. et al., 2011. Geochim. Cosmochim. Acta 75, 5423-5443. doi: 10.1016/j.gca.2011.07.020
[2] Verdugo-Ihl, M.R. et al., 2017. Ore Geol. Rev. 91, 173-195. doi: 10.1016/j.oregeorev.2017.10.007

ADDITIONAL MATERIAL T

CONFERENCE ABSTRACT:

METAL-BEARING NANOPARTICLES IN HEMATITE

Max R. Verdugo-Ihl [1], Cristiana L. Ciobanu [1], Nigel J. Cook [1],

Ashley Slattery [2], Kathy Ehrig [3], Liam Courtney-Davies [1]

[1] *School of Chemical Engineering and Advanced Materials, The University of Adelaide, Adelaide, SA 5005, Australia*

[2] *Adelaide Microscopy, The University of Adelaide, Adelaide, SA 5005, Australia*

[3] *BHP Olympic Dam, Adelaide, SA 5000, Australia*

Conference abstract and oral presentation at 15th Quadrennial IAGOD Symposium, Salta, Argentina, August 28th-31st. Symposium Volume, SEGEMAR, 189–190.

15th Quadrennial IAGOD International Association on the Genesis of Ore Deposits Symposium, Salta, Argentina.

METAL-BEARING NANOPARTICLES IN HEMATITE

Max R. Verdugo-Ihl, Cristiana L. Ciobanu[1], Nigel J. Cook, Ashley Slattery, Kathy J. Ehrig, Liam Courtney-Davies

[1]*School of Chemical Engineering, The University of Adelaide - max.verdugoihl@adelaide.edu.au*

BACKGROUND

Interaction between minerals and hydrothermal fluids can result in pseudomorphic replacements if dissolution- and (re-)precipitation rates are coupled with one another (CDRR). Such processes are mediated by reaction interfaces along which transient porosity is generated, in which mineral inclusions as products of fluid-mineral interactions can precipitate (Tooth *et al.*, 2011). Hydrothermal hematite from the granite-hosted, iron-oxide-copper-gold deposit at Olympic Dam, South Australia, displays a distinct enrichment in granitophile elements (U-Pb-W-Sn-Mo) (Verdugo-Ihl *et al.*, 2017). These geochemical signatures can be modified within grains featuring partial to complete pseudomorphic replacement of hematite that results in a newly-formed hematite featuring new sets of zonation, porosity, and/or micron-scale inclusion-attached pores. Commonly, the composition of the new hematite differs markedly from that of its precursor.

Among the products of hematite replacement via CDRR discussed in (Verdugo-Ihl *et al.*, 2017), samples from bornite-chalcocite and sulphide-poor intervals represent two unusual cases. These samples, studied here at the nanoscale, originate from the upper mineralised level in the SE-part of the orebody, ~170 m apart from one another. In the first case, a mm-sized hematite grain is partially replaced by hematite depleted in W but preserves some of the other primary elements (e.g., Sn). In the second case, newly-formed oscillatory zonation patterns in hematite are defined by As and Cu-rich bands. Such patterns form overgrowths on the more common U-Pb-W-Sn-Mo oscillatory zoning.

Here, we present evidence for metal-bearing nanoparticles (NPs) occurring along trails of inclusions in such hematites and for the re-precipitation of the host hematite. These observations assist in understanding the behaviour of trace elements during CDRR and, thus, constrain mechanisms of metal remobilisation during superimposed fluid percolation.

METHODS

Foils were prepared for transmission electron microscopy (TEM) by focused ion beam (FIB)- SEM, cut across: (I) a relict U-Pb-W-Sn-Mo zonation pattern showing microfractures/pores, and (II) the unusual Cu-As-rich overgrowths. The foils were analysed using High Angle Annular Dark Field (HAADF) scanning-TEM (STEM) imaging and energy dispersive X-ray spectrometry (EDX)-STEM mapping (Titan Themis instrument operated at 200 kV).

RESULTS

Case-I hematite displays nm-sized inclusions along densely populated, longer trails (Fig. 1a) and shorter sets of splays (Fig. 1b) branching from the main trails. Up to ~200-300 nm sized inclusions occur sporadically along swarms of smaller NPs (1-5 nm). All inclusions along the main trails have comparable contents of Si, Cl, K, Na, and occasionally As (EDX-STEM spot- analysis/mapping). Metal-bearing NPs, mostly W-bearing phases (ferberite and/or WO_3; Fig. 1c) occur attached to silica-bearing inclusions (Fig. 1b).

Case-II hematite displays inclusion trails comparable to *case-I* but also shows As-rich bands of different orientation to the trails, which host As(±Pb)-bearing NPs. As in *case-I*, the trails feature inclusion populations of variable size (from ~5 up to hundreds of nm). However, the coarsest inclusions are multicomponent and often comprise metal-bearing NPs (Cu, As, Mo, W, and Sn; Fig. 1d). As in *case-I*, elements such as K, Na, and Cl are measurable throughout the composite inclusions. The presence of such elements, as well as rounded voids (Fig. 1a, d), suggest that coarser inclusions correspond to fluid inclusions containing a volatile phase that were opened during FIB-milling. The occurrence of clustered Cu-NPs (5-10 nm) is also noted on the walls of voids. High-resolution HAADF-STEM imaging of hematite along the trails displays nanodomains of variable orientation, defects and sets of twinning (Fig. 1e), which differs from the host hematite that consists of a single grain almost devoid of defects. This is evidence that the hematite along the inclusion trails is a fine-grained precipitate formed during interaction between precursor hematite and pervading fluids.

DISCUSSION AND CONCLUSIONS

Metal-bearing NPs along splays branching with fluid inclusion trails are sourced by the release of W and other elements from primarily-zoned domains in host hematite. Evolution of this process led to precipitation of W-depleted

domains adjacent to areas studied here. The antipathetic behaviour of W relative to other granitophile elements (e.g., Sn) may be attributed to their different complexation behaviour during interaction with the pervading fluid at the reaction front. Given the close association between W- and silica-bearing NPs along the splays, we speculate about the reaction of silica-bearing fluids interactive with W but not with other elements.

Results indicate 'open system behaviour' of granitophile elements, including U, in domains that may otherwise be considered reliable for high-precision U-Pb dating (see Courtney-Davies *et al.*, 2018). The presence of metal-bearing fluid inclusions also shows the role played by CDRR in trapping metals released during interaction with fluids. In this case, S-depleted fluids can be invoked to explain precipitation of native elements as NPs, correlating with the presence of Cu-Au alloys, and indeed coarser particles of native copper (Verdugo-Ihl *et al.*, 2017).

REFERENCES

Courtney-Davies, L., Ciobanu, C.L., Tapster, S.R., Cook, N.J., Ehrig, K.J., Kennedy, A.K., Condon, D.J., Verdugo-Ihl, M.R., Wade, B.S., Gilbert, S.E., 2018. The U-Pb systematics of hydrothermal hematite; Insights from the IOCG system at Olympic Dam, South Australia, 15th Quadrennial Symposium of the International Association on the Genesis of Ore Deposits (IAGOD) this volume.

Tooth, B., Ciobanu, C.L., Green, L., O'Neil, B., Brugger, J., 2011. Bi-melt formation and gold scavenging from hydrothermal fluids: An experimental study, Geochimica et Cosmochimica Acta, 75, 5423-5443. doi: 10.1016/j.gca.2011.07.020.

Verdugo-Ihl, M.R., Ciobanu, C.L., Cook, N.J., Ehrig, K.J., Courtney-Davies, L., Gilbert, S., 2017. Textures and U-W-Sn-Mo signatures in hematite from the Olympic Dam Cu-U-Au-Ag deposit, South Australia: Defining the archetype for IOCG deposits, Ore Geology Reviews, 91, 173-195. doi: 10.1016/j.oregeorev.2017.10.007.

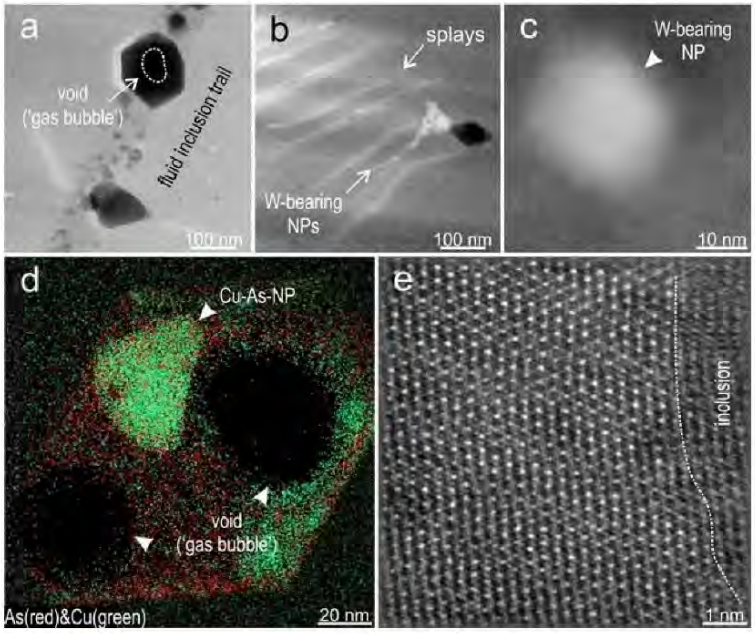

Fig. 1. HAADF-STEM images (a-c, e) and EDX-STEM map (d) showing aspects of inclusions and metal-bearing NPs in recrystallised hematite. See text for further explanations.

ADDITIONAL MATERIAL U

CONFERENCE ABSTRACT AND POSTER:

TUNGSTEN-BEARING NANOPARTICLES IN HEMATITE: INSIGHTS INTO OPEN SYSTEM BEHAVIOUR OF MINERAL GEOCHRONOMETERS

Max R. Verdugo-Ihl [1], Cristiana L. Ciobanu [1], Nigel J. Cook [1],

Liam Courtney-Davies [1], Kathy Ehrig [2], Ashley Slattery [3]

[1] *School of Chemical Engineering and Advanced Materials, The University of Adelaide, Adelaide, SA 5005, Australia*

[2] *BHP Olympic Dam, Adelaide, SA 5000, Australia*

[3] *Adelaide Microscopy, The University of Adelaide, Adelaide, SA 5005, Australia*

Conference abstract and poster presentation at TIGeR 2019, Perth, Australia, September 11th-13th.

Tungsten-bearing nanoparticles in hematite: insights into open system behaviour of mineral geochronometers

Max R. Verdugo-Ihl[1,], Cristiana L. Ciobanu[1], Nigel J. Cook[1], Liam Courtney-Davies[1], Kathy Ehrig[2], Ashley Slattery[3]*

[1] School of Chemical Engineering and Advanced Materials, The University of Adelaide, Adelaide, SA, 5005, Australia;*max.verdugoihl@adelaide.edu.au; cristiana.ciobanu@adelaide.edu.au; nigel.cook@adelaide.edu.au; liam.courtney-davies@adelaide.edu.au

[2] BHP Olympic Dam, Adelaide, SA 5000, Australia; kathy.ehrig@bhp.com

[3] Adelaide Microscopy, The University of Adelaide, Adelaide, SA, 5005, Australia; ashley.slattery@adelaide.edu.au

Formation of metal-bearing nanoparticles (NPs) in minerals can fingerprint replacement processes at the atomic scale, at which element exchange occurs. Advanced transmission electron microscopy, particularly Z-contrast imaging using high-angle annular dark field scanning transmission electron microscopy (HAADF STEM), on a sample extracted *in-situ* from locations of petrogenetic interest is a powerful approach for understanding trace element incorporation in and their release from a host mineral (Ciobanu et al. 2016). Copper-As NPs were documented from oscillatory-zoned U-W-Sn-Mo-bearing hematite that also shows atypical Cu-As-zoning and weave-twinning patterns (Verdugo-Ihl et al. 2017, 2019). These NPs occur either along (i) trails of inclusions interpreted as inclusions opened during sample preparation, or (ii) within Si-Al-K-bearing planes that also host sericite. Formation of the two types of NPs was interpreted as due to interaction between hematite and hydrolytic fluids whereby fluid supersaturation and phase separation during depressurisation account for different regimes of fluid-rate infiltration along pre-existing twin planes. Uranium-Pb systematics in the same type of hematite have been addressed by various microbeam techniques and high-precision U-Pb ID TIMS on material microsampled from U-rich domains (Courtney-Davies et al. 2019), which showed both closed and open system behaviour for U-Pb isotopes.

Here we address the issue of nanoscale manifestation of open system behaviour in hematite from samples that display compositional zoning affected by preferential removal of some elements, in this case W. Selective removal of different elements from the zonation patterns was previously interpreted as replacement reactions coupling dissolution with reprecipitation rates (CDRR; Verdugo-Ihl et al. 2017). The sample was collected from ~170 m below the hematite hosting Cu-As-NPs from a downwards-plunged block in the SE part of the Olympic Dam deposit, South Australia. The TEM foil was obtained by focused ion beam SEM by cutting across microfractures occurring along the boundary between preserved U-W-Sn-Mo zonation (microsampled for ID TIMS U-Pb geochronology) and a W-depleted domain (Verdugo-Ihl et al. 2017). Bright field (BF) and HAADF STEM imaging, as well as STEM energy-dispersive X-ray spectrometry (EDX) mapping and spot analysis, were performed using a high-resolution, probe-corrected FEI Titan Themis S/TEM at 200 kV (all instruments are housed at Adelaide Microscopy). Imaging of the foil shows domains with fractures and splays adjacent to twin planes in hematite which all display W and Pb enrichment on STEM EDX maps (Fig. 1a, b). In addition, W-bearing NPs occur along trails proximal to such structures (Fig. 1c). High-resolution HAADF STEM imaging shows the twin planes have nm-wide crests with defects showing swelling and displacement (Fig. 1d). The hematite on each of the twin planes shows sets of misorientation directions, in addition to superstructuring. In detail, arrangements of the Fe atoms in the dumbbell motif typical of $[12\bar{1}]_{\text{hematite}}$ show alternating brighter and darker units indicative of a 2-fold superstructure (Fig. 1e), and also indicated by Fast Fourier Transforms displaying satellite reflections.

The results allow for the following interpretation. Micron-scale fracturing of the oscillatory zoned hematite results in mechanical twinning and these provide nm-wide channels for fluid infiltration resulting in removal of W and Pb from primary zoning. The twin directions are marked by measurable W and Pb inferring these structures are effective traps for them. In contrast, the W-bearing NPs do not concentrate Pb, implying that this element is lost from the

system during fluid channeling. Defects and structural modifications of hematite are evidence for strain-induced effects in the crystal lattice during fluid percolation. As in the case of the Cu-As-NPs, we show that nanoscale studies can fingerprint fluid-mineral interaction. Additionally, the data demonstrates open system behaviour of U-Pb systematics in hematite. This is concordant with ID TIMS data recording high common Pb in the aliquots prepared from this grain (Courtney-Davies et al. 2019).

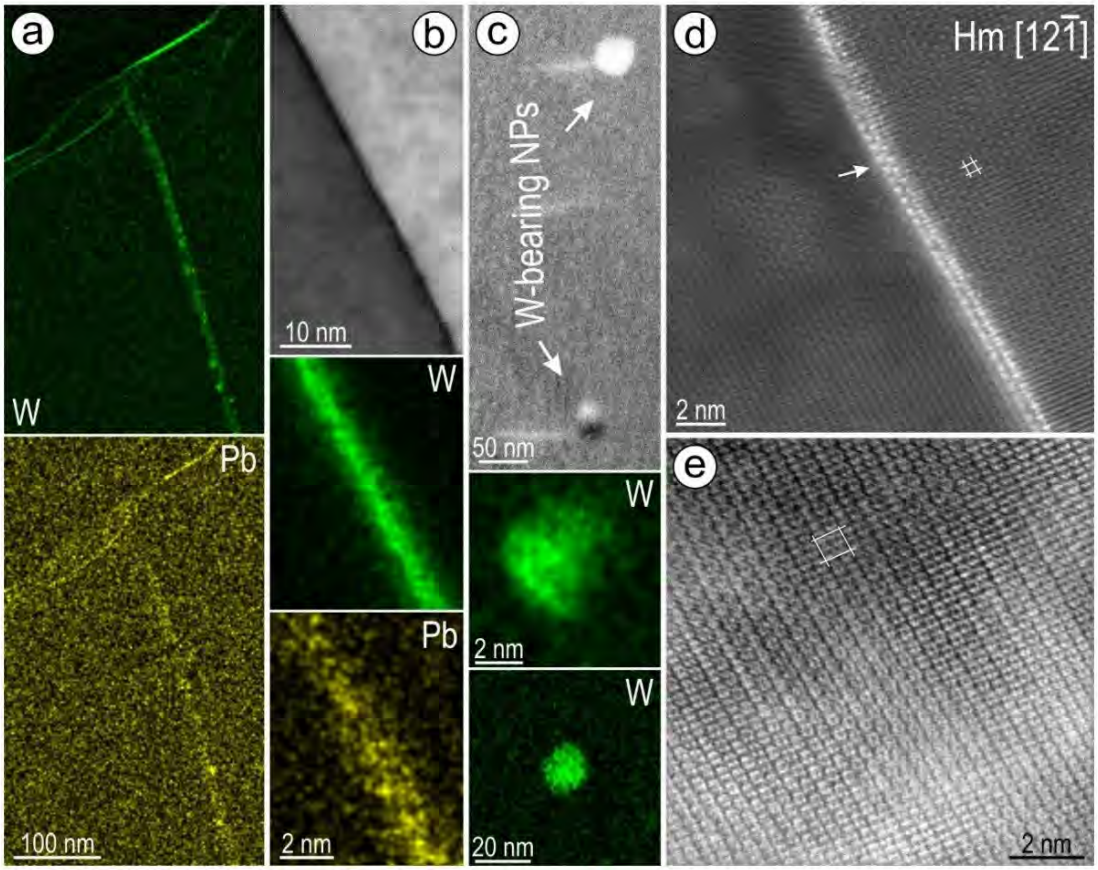

Figure 1. (a) STEM EDX maps of hematite (Hm) domain with fractures and splays adjacent to a twin plane featuring W- and Pb-enrichment. (b) BF STEM and STEM EDX maps of W- and Pb-enrichment along twin boundary. (c) HAADF STEM image and TEM EDX maps of W-bearing NPs along a trail; note that no Pb is detected within such NPs. (d) HAADF STEM image of Hm with a twin crest (arrowed) enriched in W-Pb, and featuring defects (swelling and displacement). (e) HAADF STEM image of Hm adjacent to the twin plane displaying 2-fold superstructuring (white lines) of the basic dumbbell motif on the [12$\bar{1}$] zone axis.

Overall, these results attest to the importance of CDRR in the formation of NPs and domains that are relatively enriched in certain trace elements, and how these impact on trace element signatures measured by microbeam techniques (LA-ICP-MS and/or EPMA). If characterized at appropriate scales of observation, such features can provide evidence for open system behaviour in hematite and other minerals. This, in turn, carries implications for the separation of daughter radionuclides from parent isotopes (Rollog et al. 2019) and the modification of isotopic systematics, both impacting on the accuracy and precision of geochronometers (e.g. U-Pb system in hematite; Courtney-Davies et al. 2019).

References

Ciobanu CL, Cook NJ, Maunders C, Wade BP, Ehrig, K (2016). Minerals 6, 112; doi:10.3390/min6040112.

Courtney-Davies L, Tapster S, Ciobanu CL, Cook NJ, Verdugo-Ihl MR, Ehrig KJ, Kennedy AK, Gilbert SE, Condon DJ, Wade BP (2019). Chem. Geol. 513, 54–72. doi:10.1016/j.chemgeo.2019.03.005.

Rollog M, Cook NJ, Guagliardo P, Ehrig KJ, Kilburn M (2019) Geochem.: Explor. Environm. Analysis. doi:10.1144/geochem2018-038.

Verdugo-Ihl MR, Ciobanu CL, Slattery A, Cook NJ, Ehrig K, Courtney-Davies L (2019) Minerals 9, doi:10.3390/min9070388.

Verdugo-Ihl MR, Ciobanu CL, Cook NJ, Ehrig KJ, Courtney-Davies L, Gilbert S (2017) Ore Geol. Rev. 91, 173–195. doi:10.1016/j.oregeorev.2017.10.007.

Tungsten-(Pb) remobilisation from W-Sn-U-Pb zoned hematite: Insights into open system behaviour of mineral geochronometers

Max R. Verdugo-Ihl[1], Cristiana L. Ciobanu[1], Nigel J. Cook[1], Liam Courtney-Davies[1], Kathy Ehrig[2], Ashley Slattery[3]

[1]School of Chemical Engineering and Advanced Materials, The University of Adelaide
[2]BHP Olympic Dam, Adelaide
[3]Adelaide Microscopy, The University of Adelaide

Introduction/Background: Z-contrast imaging using high-angle annular dark field (HAADF) scanning transmission electron microscopy (S/TEM) is a powerful approach to asses the incorporation of trace elements into, and their release from a host mineral at the nanoscale. Such processes can be related to replacement reactions at the atomic scale, where element exchange occurs, and induce locally the formation of metal-bearing nanoparticles (NPs), trace element enriched/depleted domains and modification to the crystal structure of the host. We address the nanoscale manifestation of such an open system behaviour in W-Sn-U-Pb-bearing hematite that displays compositional zoning, but that has been affected by preferential remobilisation of some elements, particularly W. Such remobilisation has been interpreted (Verdugo-Ihl et al. 2017) in the context of coupled dissolution and reprecipitation reactions (CDRR). The U-Pb systematics of this type of hematite addressed by microbeam techniques and high-precision U-Pb ID TIMS on microsampled material from U-rich domains (Courtney-Davies et al. 2019), shows both closed and open system behaviour for U-Pb isotopes. These phenomena can be linked to the replacement process as inferred from modification to primary crystal zoning. We thus undertook detailed nanoscale investigations to understand how the involved processes operated, what were their products and how the decoupling of parent-daughter isotope pairs occurred.

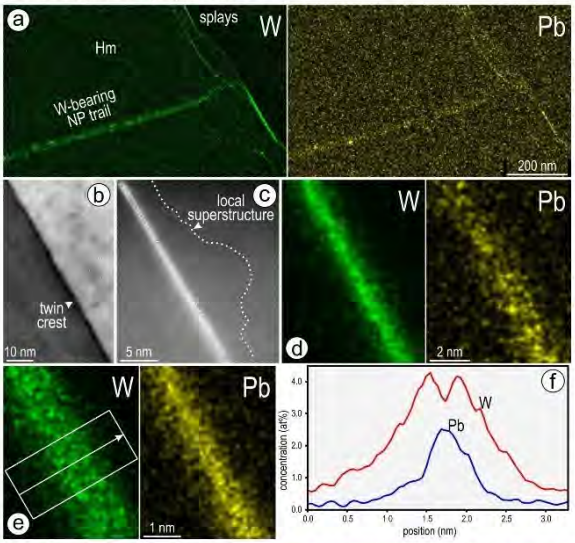

Figure 2. (a) STEM-EDX maps of hematite (Hm) displaying local enrichment of W and Pb along trails and splays. (b) BF-STEM image of twin boundary. (C) HAADF-STEM aspect of local super-structure development adjacent to twin-plane. (d, e) STEM-EDX maps showing enrichment of W and Pb along twin-boundary. (f) Integrated STEM-EDX profile across twin boundary as shown in (e).

Results: Within the preserved zonation (foil#1), domains with fractures and splays adjacent to twin planes in hematite display W and Pb enrichment (Fig. 2). In addition, W-bearing NPs (ferberite?) occur along trails proximal to such structures (Fig. 2a, 3), which are also observed in other domains (e.g., foil#2). High-resolution HAADF-STEM imaging shows that the twin planes have nm-wide crests with defects featuring swelling and displacement (Fig. 2b, c). On each side of the twin plane, hematite shows sets of misorientation directions and superstructuring. In detail, Fe atoms arranged in a dumbbell motif on $[12\bar{1}]_{hematite}$ show alternating brighter and darker units indicative of a 2-fold superstructure, supported by Fast Fourier Transforms (FFT) displaying additional, satellite reflections (Fig. 4b, arrowed).

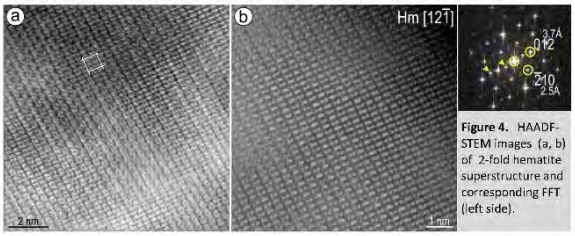

Figure 4. HAADF-STEM images (a, b) of 2-fold hematite superstructure and corresponding FFT (left side).

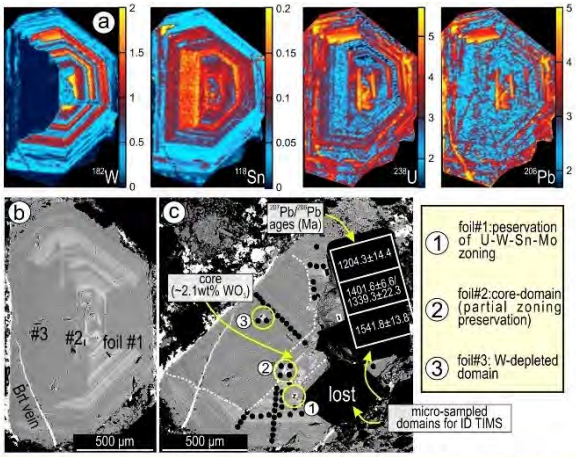

Figure 1. (a) LA-ICP-MS maps of hematite displaying contrasting zonation patterns for W relative to Sn (linear scale, n*10^6), and U-Pb (log scale, 10^n); intensities in cps. (b, c) BSE images of the same grain re-polished after mapping showing location of FIB-prepared S/TEM foils on different domains. The micro-sampled domains for U-Pb ID-TIMS and ages are shown in (c). The grain is crosscut by a barite (Brt) vein.

Methodology: S/TEM foils were obtained using dual-beam focused ion beam (FIB)-SEM by cutting the grain at locations as marked on Figure 1. Bright field (BF) and HAADF-STEM imaging, as well as STEM energy-dispersive X-ray spectrometry (EDX) mapping and spot analysis, were performed using a high-resolution, probe-corrected FEI Titan Themis S/TEM at 200 kV at Adelaide Microscopy.

Figure 3. (a) HAADF-STEM image showing W-bearing NPs along a trail and corresponding W-maps for the two NPs. (b) Representative EDX profile of a W-bearing NP as shown in (a). Note the presence of characteristic higher energy peaks for W. Note small concentration of Mn could suggest that the NP corresponds to Mn-bearing ferberite.

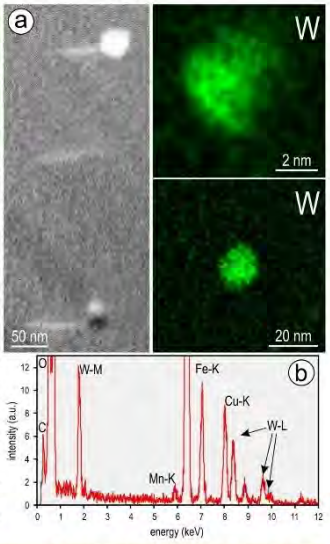

Discussion/Conclusions: Twins and micron-scale fracturing in hematite provides nm-wide fluid pathways for infiltration, resulting in the removal of W and Pb from primary zoning. Twin boundaries trapped W and Pb removed from hematite zoning since these elements are mapped along such structures (Fig. 2). Tungsten-bearing NPs do not, however, concentrate measurable Pb, implying that Pb is lost from the system during fluid channelling. Lattice-scale defects in hematite are evidence for strain-induced effects in the crystal structure during fluid percolation, comparable with findings in other studies of hematite (Verdugo-Ihl et al. 2019).

Remobilisation of Pb is concordant with U-Pb open system behaviour in hematite as reflected in the ID TIMS data recording high common Pb in aliquots prepared from this grain (Fig. 1c), i.e., markedly younger than the ~1.6 Ga age obtained for well-preserved U-bearing hematite (Courtney-Davies et al. 2019). Our results attest to the importance of CDRR in the formation of NPs and trace element remobilisation. In turn, such fluid-mineral interaction impacts on measured trace element concentrations by microbeam techniques (e.g., LA-ICP-MS/EPMA). If characterised at appropriate scales of observation, such features provide evidence for open system behaviour in mineral geochronometers, which carries implications for the decoupling of daughter radionuclides from parent isotopes (Rollog et al. 2019). Grain scale Pb remobilisation leads to modifications of U-Pb isotopic systematics and thus affects the accuracy/precision of mineral geochronometers at different scales.

Acknowledgements: This is a contribution to the FOX project, supported by BHP Olympic Dam and the Government of South Australia Mining and Petroleum Services Centre of Excellence.
References: Courtney-Davies et al. 2019 (Chem Geol 513, 54-72); Rollog et al. 2019 (Geochem Explor Environm Anal 19, 245–254); Verdugo-Ihl et al. 2017 (Ore Geol Rev 91, 173–195); Verdugo-Ihl et al. 2019 (Minerals 9, 388).

ADDITIONAL MATERIAL V

CO-AUTHORED CONFERENCE ABSTRACT:

CRYSTAL STRUCTURAL MODIFICATIONS IN U-RICH, OSCILLATORY ZONED HEMATITE

Cristiana L. Ciobanu [1], Ashley Slattery [1], **Max R. Verdugo-Ihl** [1],

Liam Courtney-Davies [1], Nigel J. Cook [1], Kathy Ehrig [2]

[1] *The University of Adelaide, Adelaide, SA 5005, Australia*

[2] *BHP Olympic Dam, Adelaide, SA 5000, Australia*

Conference abstract and oral presentation (presented by Cristiana L. Ciobanu) at Goldschmidt Conference 2018, Boston, U.S.A., August 12th-17th.

Goldschmidt2018 Abstract

Crystal structural modifications in U-rich, oscillatory-zoned hematite

C.L. CIOBANU[1,*], A.SLATTERY[1], M.VERDUGO-IHL[1], L. COURTNEY-DAVIES[1], N.J. COOK[1], K.EHRIG[2]

[1] The University of Adelaide, SA 5005, Australia (*correspondence: cristiana.ciobanu@adelaide.edu.au; ashley.slattery@adelaide.edu.au; max.verdugoihl@adelaide.edu.au; liam.courtney-davies@adelaide.edu.au; nigel.cook@adelaide.edu.au)

[2] BHP Olympic Dam, Adelaide SA 5000, Australia (Kathy.J.Ehrig@bhpbilliton.com)

Hematite, (α-Fe_2O_3; rhombohedral) is the most common phase among the five Fe_2O_3 polymorphs [1]. Hematite from U-rich deposits is shown to incorporate this element up to several wt.% UO_3 [2,3]. This is commonly associated with a more complex signature comprising radiogenic Pb, W, Sn, and Mo and expressed in crystals with pronounced oscillatory zoning. TEM study of FIB-prepared foils extracted from high-U grains has shown crystal structural modifications interpreted as vacancy-induced supertructures [2].

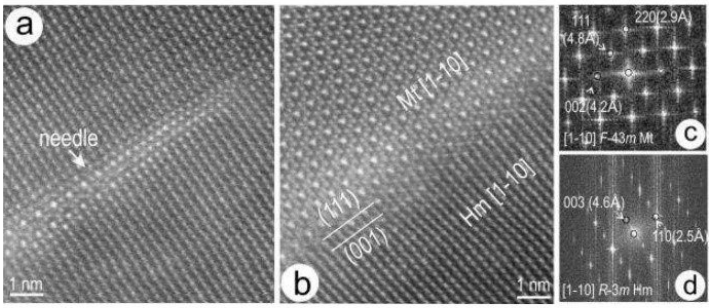

Fig. 1. HAADF-STEM images of atom-wide (a) and tens of nm-wide (b) magnetite (Mt) needles in U-rich hematite. (c, d) FFTs obtained from hematite (Hm) and Mt in (a) and (b), respectively. Images obtained at 200 kV (Titan Themis; Adelaide Microscopy).

HAADF-STEM imaging shows modification of the crystal lattice from [1-10] rhombohedral to [1-10] cubic across domains nm- to tens of nm wide (Fig. 1). TEM-STEM mapping shows these domains are Fe-richer and O-poorer relative to matrix hematite, suggesting these represent nm-scale needles of magnetite (Fe_3O_4) instead of cubic (β-, γ-) Fe_2O_3 polymorphs. Such needles are not found in high-W (up to several wt% WO_3) or low-U (up to thousands of ppm U) hematite. Results suggest that such magnetite needles occur at the upper U solubility limit in the U-bearing hematite lattice. This is most significant for understanding reliability of such grains for high-precision U-Pb dating.

[1] Lee, S., Xu, H. (2016) J Phys Chem 120, 13316−13322.
[2] Ciobanu, C.L. et al. (2013) Precambr Res 238, 129-147.
[3] Verdugo-Ihl, M. et al. (2017) Ore Geol Rev 91, 173–195.

ADDITIONAL MATERIAL W

CO-AUTHORED CONFERENCE ABSTRACT:

NANOSCALE STUDY OF SILICIAN MAGNETITE FROM IOCG SYSTEMS EXAMPLES FROM THE OLYMPIC DAM DISTRICT, SOUTH AUSTRALIA

Cristiana L. Ciobanu [1], **Max R. Verdugo-Ihl** [1], Ashley Slattery [2],

Nigel J. Cook [1], Kathy Ehrig [3], Liam Courtney-Davies [1]

[1] School of Chemical Engineering and Advanced Materials, The University of Adelaide, Adelaide, SA 5005, Australia

[2] Adelaide Microscopy, The University of Adelaide, Adelaide, SA 5005, Australia

[3] BHP Olympic Dam, Adelaide, SA 5000, Australia

Conference abstract and oral presentation (presented by Cristiana L. Ciobanu) at 15th Quadrennial IAGOD Symposium, Salta, Argentina, August 28th-31st. Symposium Volume, SEGEMAR, 185–186.

15th Quadrennial IAGOD International Association on the Genesis of Ore Deposits Symposium, Salta, Argentina.

NANOSCALE STUDY OF SILICIAN MAGNETITE FROM IOCG SYSTEMS: EXAMPLES FROM THE OLYMPIC DAM DISTRICT. SOUTH AUSTRALIA

Cristiana L. Ciobanu[1], Max R. Verdugo-Ihl, Ashley Slattery, Nigel J. Cook, Kathy J. Ehrig, Liam Courtney- Davies

[1]*School of Chemical Engineering, University of Adelaide, Adelaide, Australia - cristiana.ciobanu@adelaide.edu.au*

BACKGROUND

'Silician magnetite' (Si-magnetite) refers to magnetite with variable Si (up to ~10 wt.% SiO_2) and occurs in deposits spanning the magmatic-hydrothermal spectrum, low-T metamorphosed BIF ores as well as in mafic and ultramafic rocks (Huberty *et al.*, 2012 and references therein). Definition of Si-magnetite nanoprecipitates as $Si^{IV}[(vacancy)_{0.5}Fe^{2+}_{0.5}]^{VI}[Fe^{3+}]^{VI}O_4$ with maghemite-type vacancy-ordering was only recently possible by using Z-contrast techniques for high-resolution Scanning Transmission Electron Microscopy (STEM) imaging (Xu *et al.*, 2014). Formation of Si-magnetite in hydrothermal systems can be considered as co- precipitation of aqueous silica and Fe-silicate complexes during crystal growth (Xu *et al.*, 2014). It is thus important in modelling deposits where regional/orefield zonation patterns result from fluid evolution. In Iron-Oxide Copper Gold (IOCG) systems, magnetite is associated with early, higher-T, alkali/calcic metasomatism, in turn associated with chalcopyrite-pyrite mineralization in the Olympic Dam District (ODD), South Australia, but not necessarily elsewhere. The Olympic Dam (OD) deposit is hosted within hematite-bearing breccias placed in the central, upper part of the Roxby Downs Granite (RDG) associated with ~1.6 Ga IOCG mineralization and magmatism.

Here we discuss Si-magnetite from 5 locations: 4 from the outer, weakly-mineralised shell of brecciated RDG at OD, and one from the older (~1.85 Ga) Donington granite hosting the Wirrda Well (WW) IOCG prospect, ~17 km SW from OD. These samples are representative of Si-magnetite found in concentrations varying from massive intervals with carbonate gangue at OD to cm-dm-sized nodules or irregular pockets in variably altered granite (OD, WW) and at depths from ~700 m to 2 km. We aim to: (i) characterise; and (ii) explore the petrogenetic significance of Si-magnetite in IOCG systems from terranes with protracted geological histories.

METHODS

Si-magnetite foils prepared for TEM using focused ion beam (FIB)-SEM methods were cut across zonation patterns. Seven foils were analysed using High Angle Annular Dark Field (HAADF) STEM imaging and energy dispersive X-ray spectrometry (EDX)-STEM mapping.

RESULTS

In all samples, magnetite features µm-scale zonation patterns (Fig. 1a) which consists of Si- magnetite nanoprecipitates (Fig. 1b). An eclectic range of other nanomineral inclusions comprising silicates, carbonates, rutile, and U-, and Y±As-bearing nanoparticles (NPs; Fig.1b) were identified using EDX-STEM spot analysis/mapping, and HR-HAADF STEM imaging. Calc-silicates (±rutile) are present in Si-magnetite on the eastern side of OD and at WW, whereas NPs were only identified from the carbonate-hosted Si-magnetite.

Si-magnetite nanoprecipitates occur as darker inclusions on HAADF STEM images (Fig. 1c), varying in size from few to tens of nm, shape and density. Narrower bands (1-2 unit cells wide) of still darker Si-magnetite are stacked along d111 magnetite within the coarser precipitates, or directly in magnetite (Fig. 1c, d). Minor Al and K are measured in Si-magnetite bands from the irregular patches at the location with Fe-oxide nodules in RDG. Although both magnetite and Si-magnetite have very similar crystal structures, intensity line profiles show variation attributable to Si substitution and vacancies comparable with the maghemite model (Xu *et al.*, 2014) (Fig. 1e). Satellite reflections on Fast Fourier Transform (FFT; inset Fig. 1c) are concordant with interpretation of maghemite superstructures.

The strongest overprint is recognised as: (i) abundant lattice-scale defects (twinning, faults), K- and Al-banding, SiO_2-rich inclusion subpopulation and replacement by fluorite in the magnetite from RDG with Fe-oxide nodules; and (ii) conspicuous U, Y and As-enrichment along trails cross-cutting zonation (Fig. 1b and inset), in the carbonate-hosted, massive magnetite occurrence. Calc-silicates are present within Si-magnetite from RDG on the eastern side at OD whereas Ca-Al-bearing amphibole (tschermakite - used as a proxy for the crystal structure model (Abdu and Hawthorne, 2009)) is identified by imaging (Fig. 1f) and mapping of inclusions in magnetite from WW.

DISCUSSION AND CONCLUSIONS

Formation of mineral inclusions in all samples analysed here is attributable to coarsening of Si-magnetite nanoprecipitates during interaction with fluids enriched in elements typical of that evolution stage, e.g., K-Al-

banding and calc-silicates are compatible with early alkali- calcic alteration in IOCGs. Some of these elements can be enriched during early-mineral replacement of granite (Ca, Al, Mg, Ti from plagioclase+mica in RDG). Higher-T for the Ca- Al-amphibole stability may be a response to post-Donington metamorphism. Carbonate- hosted magnetite could be inherited from pre-existing BIF horizons in sediments intruded by RDG but with an IOCG overprint as recognised from the U-Y-As signature. Si-magnetite in samples studied here is distinct from magmatic magnetite in RDG (Cook *et al.*, 2017), or vein-magnetite in volcanics from ODD, both typified by exsolutions of ilmenite±rutile+hercynite. It also differs from occurrences elsewhere studied at the nanoscale, e.g., kin IOCG deposits containing both Ti-spinel and calc-silicates (Deditius *et al.*, 2018), or low-T metamorphosed BIFs (Huberty *et al.*, 2012; Xu *et al.*, 2014). Si-magnetite represents a petrogenetic tool if used in a given context and with the complexity of crystal- chemical phenomena adequately characterised down to the nanoscale.

REFERENCES

Abdu Y.A., Hawthorne F.C., 2009. Crystal structure and Mössbauer spectroscopy of tschermakite from the ruby locality at Fisknaesset, Greenland. Canadian Mineralogist 47, 917-926.

Cook, N.J., Ciobanu, C.L., Ehrig, K., Slattery, A., Verdugo-Ihl, M.R., Courtney-Davies, L. and Gao, W., 2017. Advances and opportunities in ore mineralogy. Minerals 7(12), 233; doi:10.3390/min7120233.

Deditius A.P., Reich, M., Simon, A.C., Suvorova, A., Knipping, J., Roberts, M.R., Rubanov, S., Dodd, A., Saunders, M., 2018. Nanogeochemistry of hydrothermal magnetite. Contributions to Mineralogy and Petrology, 173, 46; https://doi.org/10.1007/s00410-018-1474-1.

Huberty, J.M., Konishi, H., Heck, P.R., Fournette, J.H., Valley, J.W., Xu, H.F., 2012. Silician magnetite from the Dales Gorge Member of the Broc kman Iron Formation, Hamersley Group, Western Australia. American Mineralogist 97, 26–37.

Xu, H., Shen, Z., Konishi, H., 2014. Si-magnetite nano-precipitates in silician magnetite from banded iron formation: Z-contrast imaging and ab initio study. American Mineralogist 99, 2196–2202.

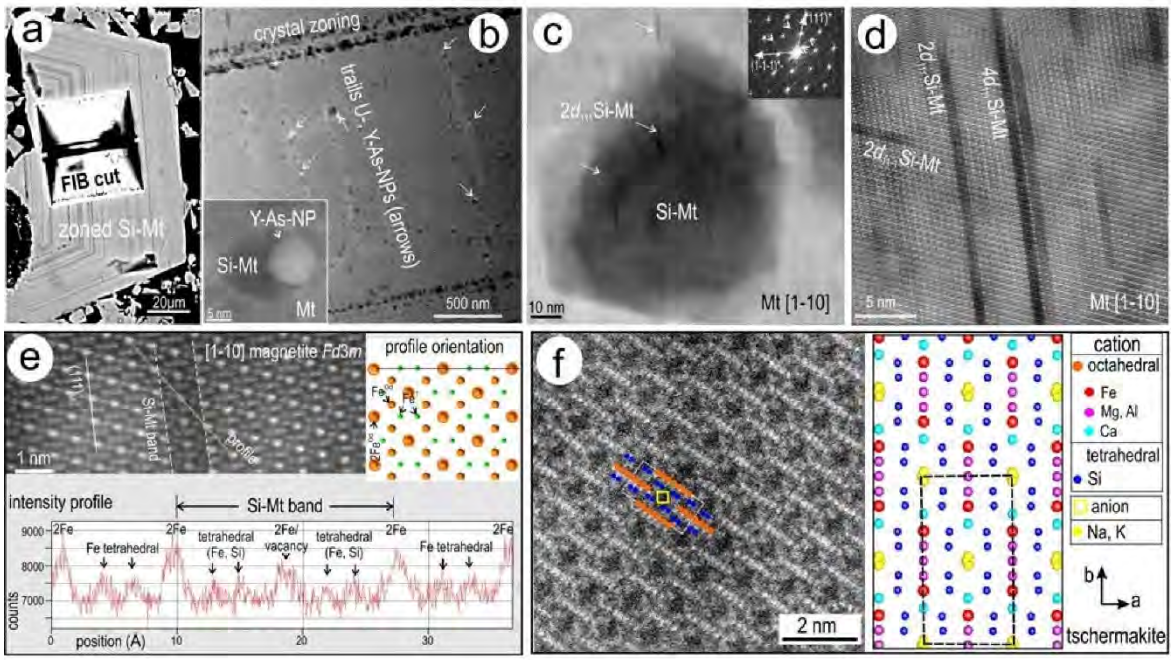

Fig. 1 (a) Back-scatter electron image showing location of FIB-cut across zoning in Si- magnetite. HAADF STEM images of Si-magnetite (b-e) and amphibole (f). Satellite reflections arrowed on FFT (inset) obtained from image in (c). Intensity profile (e) and crystal-structure models (e,f). Tschermakite (Abdu and Hawthorne, 2009) is used as a proxy for the Ca-Al-amphibole. The (Na,K) position has the best fit for the image compared to other potential Ca- amphiboles (e.g., actinolite). Imaging and EDX-STEM at 200 kV (Titan Themis; Adelaide Microscopy).

ADDITIONAL MATERIAL X

CO-AUTHORED CONFERENCE ABSTRACT:

WHY DETAILED MINERALOGY IS IMPORTANT UNDERSTANDING EVOLUTION OF THE OLYMPIC DAM IRON-OXIDE COPPER-GOLD SYSTEM, SOUTH AUSTRALIA

Nigel Cook [1], Kathy Ehrig [2], Cristiana Ciobanu [1], Liam Courtney-Davies [1],

Max Verdugo-Ihl [1], Mark Rollog [1], Danielle Schmandt [1], Nicholas Owen [1],

Edeltraud Macmillan [2], Alkiviadis Kontonikas-Charos [1], Sasha Krneta [1], Marija Dmitrijeva [1]

[1] *School of Chemical Engineering and Advanced Materials, The University of Adelaide, Adelaide, SA 5005, Australia*

[2] *BHP Olympic Dam, Adelaide, SA 5000, Australia*

Conference abstract and oral presentation (presented by Nigel J. Cook) at 15th Quadrennial IAGOD Symposium, Salta, Argentina, August 28th-31st. Symposium Volume, SEGEMAR, 371–372.

15th Quadrennial IAGOD International Association on the Genesis of Ore Deposits Symposium, Salta, Argentina.

WHY DETAILED MINERALOGY IS IMPORTANT: UNDERSTANDING EVOLUTION OF THE OLYMPIC DAM IRON-OXIDE COPPER-GOLD SYSTEM, SOUTH AUSTRALIA

Nigel Cook[1], Kathy Ehrig, Cristiana Ciobanu, Liam Courtney-Davies, Max Verdugo-Ihl, Mark Rollog, Danielle Schmandt, Nicholas Owen, Edeltraud Macmillan, Alkiviadis Kontonikas-Charos, Sasha Krneta, Marija Dmitrijeva

[1]*School of Chemical Engineering, University of Adelaide, Australia - nigel.cook@adelaide.edu.au*

Olympic Dam is one of the largest deposits on Earth and a significant producer of copper, uranium, gold and silver (Ehrig, *et al.*, 2013). Uranium-Pb geochronology using undisturbed magmatic and hydrothermal minerals allows interpretation of the initial and major hydrothermal ore- forming event at ~1593 Ma, associated with emplacement of the Gawler Silicic Large Igneous Province. The >10 billion-tonne resource is heterogeneous and contained within a breccia complex, itself confined to the ~1593 Ma Roxby Downs Granite. Ore textures suggest multiple episodes of replacement, remobilization and recrystallization and are supported by (radio) isotope data yielding a range of younger ages. Conceptual models for ore formation, necessary for exploration in the region, and optimised processing of complex fine-grained ores characterised by enrichment in an extraordinarily wide variety of elements are dependent on an exceptionally thorough understanding of mineralogy and geochemistry underpinned by high-quality, high-resolution assay data, extensive MLA datasets, and deportment models for multiple elements.

Micron - to nanoscale studies of feldspars and accessory phases within the alteration envelope, and of Fe-oxides, Cu-(Fe)-sulphides, sulphates, U- and REE-bearing minerals within the deposit all point to common mechanisms involved in formation of the mineral assemblages as observed today, the prevailing Mm-scale mineral textures, and measured variations in mineral compositions. Detailed mineralogical investigation has proven pivotal in establishing a framework for ore evolution.

Each of the 100 minerals in the Olympic Dam deposit has a story to tell. The complex fine- grained, intergrown, heterogeneous assemblages necessitate ultra-careful investigation on multiple representative samples and with compositional data requiring verification by examination at the nanoscale. We therefore use a combination of whole rock assay, optical and scanning electron microscopy, electron probe microanalysis (EPMA), laser-ablation inductively-coupled plasma mass spectrometry, complemented by imaging and nanoscale compositional analysis by transmission electron microscopy (TEM) on foils extracted *in-situ* by focussed ion beam SEM methods.

Investigation of feldspars from within and outside the deposit allows an understanding of the magmatic to hydrothermal transition and early Fe-metasomatism (Kontonikas-Charos, *et al.*, 2017). Nanoscale characterization of feldspars undergoing transformation from early post-magmatic (deuteric) to hydrothermal stages in granites hosting the deposit reveals complex perthitic textures, anomalously Ba, Fe, or REE-rich compositions, and REE-fluorocarbonate+molybdenite assemblages that pseudomorph feldspars (Kontonikas-Charos, *et al.*, 2018). Epitaxial orientations between (igneous) cryptoperthite, (deuteric) patch and albite replacive within vein perthite support interface-mediated reactions between pre-existing alkali-feldspars and pervading fluid, irrespective of micron-scale crystal morphology. Such observations are consistent with coupled dissolution-replacement reactions (CDRR), indicating that albitization enhances rock permeability via the generation of transient pores which facilitate grain-scale element remobilization and trap elements as nanoscale inclusions. These inclusions represent the earliest stage of REE remobilization at the grain-scale, and reflect the significant role feldspar replacement reactions play in concentrating REE during hydrothermal alteration.

Hematite is by far the most abundant hydrothermal mineral and preserves oscillatory and sectorial zoning and incorporation of U, W, Mo, Sn and other trace elements, including REE (Verdugo-Ihl, *et al.*, 2017). The presence of U and Pb allows application of hematite U-Pb geochronology [e.g., Courtney-Davies, *et al.*, 2018]. These primary textures give way to repeated processes of brecciation, fluid-assisted reworking, element redistribution, recrystallization and overprinting. CDRR permits release of trace elements from the lattice to be trapped as nm- to Mm-scale inclusions (e.g., uraninite), or to form discrete minerals (e.g., scheelite molybdenite) in the near vicinity.

EPMA-scale compositional data combined with TEM investigation of chalcocite-group minerals, bornite and chalcopyrite has shown that Cu-Fe-sulphides from different ore zones feature nanoscale intergrowths, lattice defects, superstructure domains and antiphase boundary domains (Ciobanu, *et al.*, 2017). Such features can be interpreted as having originated via a combination of exsolution, coarsening, and phase transformation during cooling from high-T solid solutions (e"400°C) in the system Cu-Fe-S and sub-systems. A scenario of 'exsolution from primary solid-solution, corroborated by the consistency in phase relations within each zone across different scales of observation from deposit- to nanoscale, supports a model of primary hypogene ore precipitation rather than replacement, and

accounts for the observed zoning patterns at OD. Nonetheless, evidence for CDRR, replacement, phase transformation and local (Mm- to tens m-wide) remobilization is evident.

Uraninite, coffinite, brannerite and hematite are the dominant U hosts [Courtney-Davies, *et al.*, 2018, Macmillan, *et al.*, 2016, Macmillan, *et al.,* 2017). Although some uraninite and hematite retain U and daughter isotopes, breakdown and replacement can lead to release, remobilization and redistribution of radionuclides (RN) at scales from nm upwards. New minerals may be formed (late uraninite, coffinite) and U and Pb can also be incorporated into existing minerals (barite, svanbergite-woodhouseite). RN are, however, also concentrated as sub-microscopic particles within pores, microfractures and at grain boundaries in the near vicinity of altered or replaced U-bearing mineral grains (Rollog, *et al.*, 2018) attesting to fluid-mediated processes. Such redistribution carries implications for ore processing and, potentially also for the interpretation of geochronological data.

Three groups of REE-minerals are observed: REE-fluorocarbonates (bastnosite and subordinate synchysite (Schmandt, *et al.*, 2017), which appear paragenetically early; REE-phosphates (dominantly florencite of variable age and association but also minor xenotime, the main carrier of HREE); and Ca-, Sr-, REE-bearing phosphate-sulphates (svanbergite- woodhouseite], which are generally late and replace earlier-formed minerals (Owen, *et al.,* 2018). Minor REE are also contained in apatite, which displays evolving chondrite-normalized REE fractionation trends that can be explained in terms of changes in fluid parameters and speciation of REY in ore-forming fluids (Krneta, *et al.,* 2017). Under hydrothermal conditions typical of iron- oxide copper gold mineralization, a decrease in salinity, pH and temperature is associated with hematite-sericite alteration sufficient to produce a characteristic MREE-enriched apatite. However, anomalous high-pH (~7) fluids at 300 °C may account for high-grade Cu ores as modelled from apatite with strong positive Eu anomalies (Krneta, *et al.*, 2017).

Although primary assemblages are identified, a persistent narrative is offered by multiple episodes of fluid-assisted replacement, phase transition, remobilization, migration, and re- precipitation of all ore components. These processes played a major role in the modification of textural and geochemical patterns in many minerals. However, more refractory minerals, notably hematite, apatite, pyrite, some REE-minerals, and some sub-types of U-minerals, can preserve primary geochemical signatures and can also record and retain evidence of evolving and overprinting fluid signatures. Fluid regimes were likel heterogeneous given observations of texturally and geochemically distinct generations of the same mineral within single samples.

REFERENCES

Ehrig, K., McPhie, J., Kamenetsky, V., 2013. Geology and mineralogical zonation of the Olympic Dam iron oxide Cu-U-Au-Ag deposit, South Australia. In: Hedenquist, J.W., Harris, M., Camus, F. (Eds), Geology and Genesis of Major Copper Deposits and Districts of the World, a Tribute to Richard Sillitoe. SEG Special Publication 16, pp. 237-268.

Kontonikas-Charos, A., Ciobanu, C.L., Cook, N.J., Ehrig, K., Krneta, S., Kamenetsky, V.S., 2017. Feldspar evolution in the Roxby Downs Granite, host to Fe-oxide Cu-Au-(U) mineralization at Olympic Dam, South Australia. Ore Geology Reviews, 80, 838-859.

Kontonikas-Charos, A., Ciobanu, C.L., Cook, N.J., Ehrig, K., Ismail, R., Krneta, S., Basak, A., 2018. Feldspar mineralogy and rare earth element (re)mobilization in iron-oxide copper gold systems from South Australia: a nanoscale study. Mineralogical Magazine 82 (S1), S173–S197.

Verdugo-Ihl, M.R., Ciobanu, C.L., Cook, N.J., Ehrig, K., Courtney-Davies, L., Gilbert, S., 2017. Textures and U-W-Sn-Mo signatures in hematite from the Cu-U-Au-Ag orebody at Olympic Dam, South Australia: defining the archetype for IOCG deposits. Ore Geology Reviews 91, 173–195.

Courtney-Davies, L., Ciobanu, C.L., Tapster, S.R., Cook, N.J., Ehrig, K.J., Kennedy, A.K., Condon, D.J., Verdugo-Ihl, M.R., Wade, B.S., Gilbert, S.E., 2018. The U-Pb systematics of hydrothermal hematite; insights from the IOCG system at Olympic Dam, South Australia. IAGOD Symposium, Salta (this volume).

Ciobanu, C.L., Cook, N.J., Ehrig, K., 2017. Ore minerals down to the nanoscale: Cu-(Fe)- sulphides from the iron oxide copper gold deposit at Olympic Dam, South Australia. Ore Geology Reviews 81, 1218-1235.

Macmillan, E., Cook, N.J., Ciobanu, C.L., Ehrig, E., Pring, A., 2016. Uraninite from the Olympic Dam IOCG-U-Ag deposit: linking textural and compositional variation to temporal evolution. American Mineralogist 101, 1295–1320.

Macmillan, E., Cook, N.J., Ehrig, K., Pring, A., 2017. Chemical and textural interpretation of late-stage coffinite and brannerite from the Olympic Dam IOCG-Ag-U deposit. Mineralogical Magazine 81, 1323-1366.

Rollog, M., Cook, N.J., Gugliardo, P., Ehrig. K., Kilburn, M., 2018. In situ spatial distribution mapping of radionuclides in minerals by nanoSIMS. Geochemistry – Exploration, Environment, Analysis (in press).

Schmandt, D.S., Cook, N.J., Ciobanu, C.L., Ehrig, K., Wade, B.P., Gilbert, S., Kamenetsky, V.S., 2017. Rare earth element fluorocarbonate minerals from the Olympic Dam Cu-U-Au-Ag deposit, South Australia. Minerals 7(10), 202; doi: 10.3390/min7100202.

Owen, N.D., Ciobanu, C.L., Cook, N.J., Slattery, A., Basak, A., 2018. Nanoscale study of clausthalite-bearing symplectites in Cu-Au-(U) ores: Implications for ore genesis. Minerals, 8(2), 67; doi:10.3390/min8020067.

Krneta, S., Ciobanu, C.L., Cook, N.J., Ehrig, K., Kontonikas-Charos, A., 2017. Rare earth element behaviour in apatite from the Olympic Dam Cu-U-Au-Ag deposit, South Australia. Minerals 7(8), 135; doi:10.3390/min7080135.

ADDITIONAL MATERIAL Y

CO-AUTHORED CONFERENCE ABSTRACT:

OSCILLATORY-ZONED HEMATITE: A RELIABLE U-PB MINERAL GEOCHRONOMETER

Liam Courtney-Davies [1], Cristiana L. Ciobanu [1], Nigel J. Cook [1], **Max Verdugo-Ihl** [1],

Simon R. Tapster [2], Daniel J. Condon [2], Allen K. Kennedy [3],

Kathy Ehrig [4], Benjamin P. Wade [5], Sarah E. Gilbert [5]

[1] School of Chemical Engineering and Advanced Materials, The University of Adelaide, Adelaide, SA 5005, Australia

[2] NIGL, British Geological Survey, Keyworth, Nottingham, NG12 5GG, UK

[3] John de Laeter Centre, Curtin University of Technology, Bentley, WA 6102, Australia

[4] BHP Olympic Dam, Adelaide, SA 5000, Australia

[5] Adelaide Microscopy, The University of Adelaide, Adelaide, SA 5005, Australia

Conference abstract and oral presentation (presented by Liam Courtney-Davies) at Goldschmidt 2017, Paris, France, August 13th-18th.

Goldschmidt2017 Abstract

Oscillatory-zoned hematite: a reliable U-Pb mineral geochronometer

L. COURTNEY-DAVIES[1*], C.L. CIOBANU[1], N.J. COOK[1], M. VERDUGO-IHL[1], S.R. TAPSTER[2], D.J. CONDON[2], A.K. KENNEDY[3], K. EHRIG[4], B.P. WADE[5], S.E. GILBERT[5]

[1]School of Chemical Engineering, Univ. of Adelaide, Adelaide, SA 5005, Australia (correspondence: Liam.Courtney-Davies@adelaide.edu.au; Cristiana.Ciobanu@adelaide.edu.au; Nigel.Cook @adelaide.edu.au; Max.Verdugolhl@adelaide.edu.au)

[2]NERC, British Geological Survey, Keyworth, U.K. (simont@bgs.ac.uk; dcondon@bgs.ac.uk)

[3]John de Laeter Centre, Curtin University, Bentley, WA, Australia (A.Kennedy@exchange.curtin.edu.au)

[4]BHP Billiton Olympic Dam, Adelaide, SA 5000, Australia (Kathy.J.Ehrig@bhpbilliton.com)

[5]Adelaide Microscopy, Adelaide, SA 5005, (Benjamin.Wade @adelaide.edu.au; Sarah.Gilbert@adelaide.edu.au)

Uranium-bearing oscillatory-zoned hematite has previously been proposed as a U-Pb geochronometer [1,2]. The presence of lattice bound U-W-Sn-Mo-Pb bearing hematite featuring oscillatory zonation was shown across the 6 km strike and 2 km vertical extent of the Iron Oxide Copper Gold (IOCG) deposit at Olympic Dam, South Australia [3]. LA-ICP-MS dating of these U-W-Sn-Mo oscillatory-zoned hematites displays a common $^{207}Pb/^{206}Pb$ upper intercept age of ~1.6 Ga. However the reliability of LA-ICP-MS U-Pb data is difficult to assess without a matrix-matched standard and poorly constrained matrix-effects.

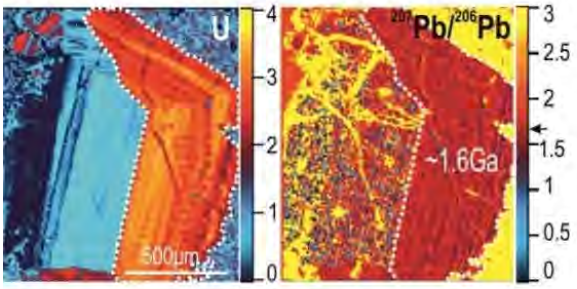

Fig. 1: LA-ICP-MS chemical maps of oscillatory-zoned hematite from Olympic Dam (U map in counts-per-second 10^n; Pb/Pb map in Ga).

LA-ICP-MS mapping of zoned grains show consistent ~1.6 Ga $^{207}Pb/^{206}Pb$ ages within the higher U domains (Fig. 1). Further asessment of the U-Pb sytematics has been conducted using SHRIMP and ID-TIMS micro-sampled domain analysis. The data confirm the presence of low common Pb, near-closed system crystals domains and zero-age open-system behaviour. Results show: (i) oscillatory zoning traps radiogenic daughter isotopes in hematite; and (ii) such hematite, confirmed in IOCGs worldwide [2], marks the onset of mineralisation.

[1] Ciobanu, C.L. et al. (2013), Precambr. Res. 238,129-147 [2] Courtney-Davies, L. et al. (2016), Minerals 6(3), 85 ; doi:10.3390/min6030085 [3] Verdugo-Ihl, M. et al. (2017) Extended abstract, SGA-2017, Quebec.

ADDITIONAL MATERIAL Z

CO-AUTHORED CONFERENCE ABSTRACT:

U-PB DOPED SYNTHETIC REFERENCE MATERIAL FOR IN-SITU HEMATITE GEOCHRONOLOGY

Liam Courtney-Davies [1], Marcus W. Richardson [2], Sarah E. Gilbert [3], Cristiana L. Ciobanu [1],

Max Verdugo-Ihl [1], Nigel J. Cook [1], Kathy Ehrig [4], Benjamin P. Wade [3]

[1] *School of Chemical Engineering and Advanced Materials, The University of Adelaide, Adelaide, SA 5005, Australia*

[2] *6 Ophir Street, Goodwood, SA 5060, Australia*

[3] *Adelaide Microscopy, The University of Adelaide, Adelaide, SA 5005, Australia*

[4] *BHP Billiton Olympic Dam, Adelaide, SA 5000, Australia*

Conference abstract and poster presentation (presented by Liam Courtney-Davies) at Geoanalysis 2018, Sydney, Australia, July 10th-14th.

U-Pb doped synthetic reference material for *in-situ* hematite geochronology

LIAM COURTNEY-DAVIES[1], MARCUS RICHARDSON[2], SARAH E. GILBERT[3], CRISTIANA L. CIOBANU[1], MAX R. VERDUGO-IHL[1], NIGEL J. COOK[1], KATHY EHRIG[4], BENJAMIN P. WADE[3]

[1]School of Chemical Engineering, University of Adelaide, 5005 SA, Australia, Liam.Courtney-Davies@adelaide.edu.au, Cristiana.Ciobanu@adelaide.edu.au, Max.Verdugolhl @adelaide.edu.au, Nigel.Cook@adelaide.edu.au
[2]6 Ophir Street, Goodwood, 5034 SA, Australia, wcamar@internode.on.net
[3]Adelaide Microscopy, University of Adelaide, Australia, Sarah.Gilbert@adelaide.edu.au, Benjamin.Wade@adelaide.edu.au
[4]BHP Olympic Dam, Adelaide, 5000 SA, Australia, Kathy.J.Ehrig@bhpbilliton.com

Uranium-bearing hematite is widespread within iron-oxide-Cu-Au deposits and ores associated with banded iron formations of South Australia [1-4]. Valuable age data has been obtained via LA-ICP-MS applying GJ-1 Zircon and mixed U-Pb solutions as the primary reference materials [1,2,5], as well as high precision ID-TIMS U-Pb data, which is independent of the need for solid reference materials [6]. However, routine high-accuracy microbeam dating of hematite requires near-matrix-matched reference materials, of which suitable natural specimens have currently not been identified. We report a method to produce U-Pb doped hydrated ferric oxide, through slow introduction of ~150 ppm U/Pb solutions, calcinated at 700 °C to dehydrate and convert to hematite. Polycrystalline hematite fragments, up to 1 cm-long, are commonly produced through this method. The material was mounted in epoxy, polished, and imaged by SEM in backscatter electron mode (BSE) to check for potential heterogeneity or inclusions of U-Pb-bearing phases. Further characterisation by LA-ICP-MS showed that the precision of the $^{207}Pb/^{235}U$ and $^{206}Pb/^{238}U$ (50 spot analyses) was 0.2% (95% confidence interval) and with a MSWD of 0.61, compared to the zircons GJ-1 (0.5% *n*=36), Plesovice (0.6% *n*=18), and 91500 (0.6% *n*=9) analysed in the same analytical session. U concentrations are ~70 ppm, and Pb ~35 ppm. The material displays both dark and bright areas under BSE, with slightly varying U/Pb most likely formed during heating steps. Downhole U-Pb profiles for the synthetic material displayed a similar fractionation trend to natural hematite analysed within the same analytical session. To further evaluate homogeneity, the samples will be measured by ID-TIMS to define absolute U-Pb ratios, and subsequently by SHRIMP to examine U-Pb isotope homogeneity at the micron-scale. Our aspiration is that this material can be used routinely as a reference material for microbeam techniques.

[1] Ciobanu et al. (2013) *Precambr. Res.* ***238****, 129-147.* [2] Courtney-Davies et al. (2016) *Minerals.* ***6****, 3, 85.* [3] Verdugo-Ihl et al. (2017) *Ore Geol. Rev.* ***91****, 173-195.* [4] Keyser et al. (2018) *Ore Geol. Rev.* ***93****, 337-360.* [5] Apukhtina et al. (2017) *Econ. Geol.* ***112****, 1531-1542.* [6] Courtney-Davies et al. (2018) *Chem. Geol. (in review).*

ADDITIONAL MATERIAL AA

CO-AUTHORED CONFERENCE ABSTRACT:

THE U-PB SYSTEMATICS OF HYDROTHERMAL HEMATITE: INSIGHTS FROM THE IOCG SYSTEM AT OLYMPIC DAM, SOUTH AUSTRALIA

Liam Courtney-Davies [1], Cristiana L. Ciobanu [1], Simon R. Tapster [2], Nigel J. Cook [1],

Kathy Ehrig [4], Allen K. Kennedy [3], Daniel J. Condon [2],

Max Verdugo-Ihl [1], Benjamin P. Wade [5], Sarah E. Gilbert [5]

[1] *School of Chemical Engineering and Advanced Materials, The University of Adelaide, Adelaide, SA 5005, Australia*

[2] *NIGL, British Geological Survey, Keyworth, Nottingham, NG12 5GG, UK*

[3] *BHP Olympic Dam, Adelaide, SA 5000, Australia*

[4] *John de Laeter Centre, Curtin University of Technology, Bentley, WA 6102, Australia*

[5] *Adelaide Microscopy, The University of Adelaide, Adelaide, SA 5005, Australia*

Conference abstract and oral presentation (presented by Liam Courtney-Davies) at 15th Quadrennial IAGOD Symposium, Salta, Argentina, August 28th-31st. Symposium Volume, SEGEMAR, 171–172.

15th Quadrennial IAGOD International Association on the Genesis of Ore Deposits Symposium, Salta, Argentina.

THE U-Pb SYSTEMATICS OF HYDROTHERMAL HEMATITE: INSIGHTS FROM THE IOCG SYSTEM AT OLYMPIC DAM, SOUTH AUSTRALIA

Liam Courtney Davies[1], Cristiana L. Ciobanu, Simon R. Tapster, Nigel J. Cook, Kathy J. Ehrig, Allen K. Kennedy, Daniel J. Condon, Max R. Verdugo-Ihl, Benjamin S. Wade, Sarah E. Gilbert

[1]*The University of Adelaide - liam.courtney-davies@adelaide.edu.au*

BACKGROUND

Uranium-bearing minerals that have been isotopically closed since crystallization can be used to accurately constrain geologic events via the coupled U-Pb decay chain. However, the primary isotopic signature of a mineral can be easily modified, through multiple episodes of fluid exsolution, overprinting processes, regional metamorphism and protracted thermal events. Defining a chronology within complex environments such as Proterozoic ore deposits can therefore prove challenging.

The iron-oxide-Cu-Au (IOCG) deposit at Olympic Dam (OD), South Australia, is the largest publicly declared U resource. Located within the ~1.6 Ga Gawler Silicic Large Igneous Province, the deposit is entirely contained within the Olympic Dam Breccia Complex (ODBC); [1, 2], hosted and dominantly derived from the enclosing Roxby Downs Granite (RDG). The magmatic system at OD has been well constrained to ~1593 Ma, however, dating of hydrothermal mineralization has so far yielded low-resolution dates broadly coeval with the magmatism (e.g. uraninite and apatite from altered RDG and pene- contemporaneous volcanic units [3]). We aim to understand if the magmatic-hydrothermal transition can be accurately recorded in minerals that can have only a hydrothermal origin [4, 5], and are closely associated with the ores.

As has been shown at OD [6], hematite is a ubiquitous component of IOCG systems and can contain wt% levels of U, as well as elevated concentrations of W, Mo, Sn, and Pb. The occurrence of primary, often well-preserved oscillatory-zoned, U-W-Sn-Mo-bearing hematite throughout OD provides a mechanism for accurately constraining the timing of hydrothermal mineralization. This type of hematite is present throughout all ore zones and major lithologies at OD (e.g. breccias, sedimentary and volcanic rocks), occurring along the orebody's entire 6 km NW-SE strike [7] and depths of up to ~2 km. There is an intimate association between hematite-rich breccias and primary economic Cu-U-Au-Ag mineralization, which is manifested as concentric zonation with respect to sulphides [2]. Remobilisation of uranium is noted within the ODBC at scales from sub-micron upwards. Deposited as flooding, veinlets and pockets, remobilised uraninite accounts for local U enrichment and is clearly late relative to the widespread disseminations, inferring (probably multiple) processes of dissolution and re-precipitation. Therefore, understanding the principal sources and timing of metal introduction relative to the ~1.6 Ga primary magmatic-hydrothermal event is pivotal in understanding the genesis of OD, as remobilisation or isotopic resetting of minerals may be misinterpreted as new metal influxes and late mineralization events.

The potential of zoned hematite at OD for U-Pb geochronology was first recognised in a reconnaissance geochronological study [6]. Calibration with a non-matrix-matched reference material restricted full assessment of dating accuracy, however, 207Pb/206Pb weighted mean laser-ablation inductively-coupled-plasma mass-spectrometry (LA-ICP-MS) dates broadly tied hematite mineralization as coeval to the RDG. Further LA-ICP-MS studies [8], complemented previous work, but did not critically improve temporal constraints. The biggest obstacle for routine U-Pb hematite dating is the lack of homogeneous reference materials. We have therefore implemented isotope-dilution thermal-ionization-mass- spectrometry (ID-TIMS) to constrain robust ages at OD. Through combined U-Pb isotope- mapping (LA-ICP-MS) and ID-TIMS, targeted grain domains in Proterozoic samples can provide accurate ages down to ~0.05% precision. Data features such as common Pb, discordancy, and reverse discordance are assessed, their mechanisms proposed, and the analytical precision achievable at different resolutions at OD defined.

METHODS

Elevated concentrations of U in hematite can be directly imaged under backscattered electron imaging by scanning electron microscopy, which enables selective targeting of U- rich and inclusion-free domains within grains, ranging from tens of Mm to cm in size. The combination of LA-ICP-MS spot-analysis/mapping, sensitive high-resolution ion microprobe (SHRIMP) and ID-TIMS, allows investigation into the U-Pb systematics of hematite at different analytical and spatial resolutions. Isotopic measurements were collected at Adelaide Microscopy (LA-ICP-MS), Curtin University (SHRIMP) and the British Geological Survey (ID-TIMS). The developing, experimental approach to hematite isotope-dilution required micro-sampling of grains in-situ, by ablating trenches to form ~100 x 100 Mm squares within polished blocks which could be manually extracted under a microscope.

RESULTS AND DISCUSSION

Hematite 207Pb/206Pb weighted mean ID-TIMS ages can be used to interpret ore forming events to a precision of ~0.05%, compared to >1% for microbeam techniques (LA-ICP-MS and SHRIMP). However, as with any mineral, some are subject to chemical overprinting effects yielding lower resolution data. Isotope mapping demonstrates the susceptibility of zoned hematite to overprinting, with low-U, high-common Pb domains affected by fluid- mineral interactions. Potential Pb-diffusion from high- to low-U zones can also be imaged using LA-ICP-MS, where excess, unsupported radiogenic Pb produces reverse discordance.

Nevertheless, in the best-case scenarios, ID-TIMS yields a 207Pb/206Pb hematite weighted mean age of 1592.1 ± 0.88 Ma (MSWD=0.52, n=5), signifying pene-contemporaneous mineralization after RDG crystallization (1593.9 ± 0.4 Ma; [9]), while near-concordant ID- TIMS aliquots point towards negligible disturbance of the U-Pb system. Furthermore, the lifespan of the major mineralizing event is demonstrated to be short when using hematite as a proxy, as there is no robust divergence in age from ~1590 Ma. This does not however rule out mineralization post-dating the oscillatory-zoned hematite but is representative of the bulk of Cu-U mineralization. The ubiquitous presence of hematite within the orebody, and the fact that many subsequent hematite types at OD can be tied to replacement of the zoned type, clearly indicate that the U resource is associated with the magmatic-hydrothermal IOCG system at OD rather than other exotic sources. Dating of zoned hematite in sandstones from a depth of ~1.6 km yields ~1590 Ma dates. Such sediments may be older than the ODBC, and entrapped within the RDG during uplift and brecciation, supporting a deep, rather than shallow granite emplacement.

CONCLUSIONS

The key to robust temporal interpretations, particularly for deposits like OD, is a well- constrained magmatic U-Pb framework combined with a sufficiently large n sample set of hydrothermal grains. This enables interpretation of different, deposit-wide processes, which is rapidly achievable with hematite. Iron-oxide minerals, including magnetite, can become important tools for directly dating mineralization in ore deposits, particularly where other datable minerals are either absent, metamict or not representative of the ore-forming event. The ubiquitous presence of hematite in IOCG deposits, as well as banded iron formation deposits, suggests it has far reaching value in both old, and new, ore deposit research.

REFERENCES

Apukhtina O. B., Kamenetsky V. S., Ehrig, K., Kamenetsky, M. B., Maas, R., Thompson, J., McPhie, J., Ciobanu, C. L., Cook N. J., 2017. Early, deep magnetite-fluorapatite mineralization at the olympic dam cu-u-au-ag deposit, south australia. Economic Geology 112, 1531-1542.

Ciobanua C. L., Wadec B. P., Cook N. J., Schmidt M. A., Giles, D., 2013. Uranium-bearing hematite from the Olympic Dam Cu–U–Au deposit, South Australia: A geochemical tracer and reconnaissance Pb–Pb geochronometer. Precambrian Research, 238, 129-147.

Courtney-Davies, L., Zhu, Z., Ciobanu, C. L., Wade, B.P., Cook, N.J., Ehrig, K., 2016. Matrix-matched iron-oxide laser ablation ICP-MS U–Pb geochronology using mixed solution standards. Minerals, 6 (3), 85.

Ehrig, K., McPhie, J., Kamenetsky, V., 2012. Geology and mineralogical zonation of the Olympic Dam iron oxide Cu-U-Au-Ag deposit, South Australia, In: Hedenquist, J.W., Harris, M., F. Camus (Eds.), Geology and Genesis of Major Copper Deposits and Districts of the World. SEG Special Publication 16, 237-268.

Jagodzinski, E.A., 2016. http://minerals.statedevelopment.sa.gov.au/latest_ updates /mineral_ systems_ drilling_ program _ open_day_presentations.

Krneta, S., Ciobanu, C., Cook, N., Ehrig, K., Kontonikas Charos, A., 2017. Rare Earth Element Behaviour in Apatite from the Olympic Dam Cu–U–Au–Ag Deposit, South Australia. Minerals, 7, 135.

Macmillan, E., Ciobanu, C.L., Ehrig, K., Cook, N.J., and Pring, A., 2016. Chemical zoning and lattice distortion in uraninite from Olympic Dam, South Australia. American Mineralogist, 101, 2351–2354.

Reeve JS, Cross KC, Smith RN & Oreskes N. 1990. Olympic Dam copper-uranium-gold deposit. In: Hughes FE (ed), Geology of the Mineral Deposits of Australia and Papua New Guinea. The Australasian Institute of Mining and Metallurgy, 1009-1035.

Verdugo Ihl, M., Ciobanu, C., Cook, N., Ehrig, K., Courtney-Davies, L., Gilbert, S., 2017. Textures and U-W-Sn-Mo signatures in hematite from the Olympic Dam Cu-U-Au-Ag deposit, South Australia: Defining the archetype for IOCG deposits. Ore Geology Reviews, 10, 1016.

ADDITIONAL MATERIAL BB

CO-AUTHORED CONFERENCE ABSTRACT:

CHLORO-HYDROXY-ZIRCON NANOPRECIPITATES FINGERPRINT FERTILITY AND MINERALIZATION POTENTIAL OF GRANITIC MAGMAS

Liam Courtney-Davies [1], Cristiana L. Ciobanu [1], **Max Verdugo-Ihl** [1],

Ashley Slattery [2], Nigel J. Cook [1], Kathy Ehrig [3]

[1] *School of Chemical Engineering and Advanced Materials, The University of Adelaide, Adelaide, SA 5005, Australia*

[2] *Adelaide Microscopy, The University of Adelaide, Adelaide, SA 5005, Australia*

[3] *BHP Olympic Dam, Adelaide, SA 5000, Australia*

Conference abstract and poster presentation (presented by Liam Courtney-Davies) at TIGeR 2019, Perth, Australia, September 11th-13th.

Chloro-hydroxy-zircon nanoprecipitates fingerprint fertility and mineralization potential of granitic magmas

Liam Courtney-Davies[1], Cristiana L. Ciobanu[1], Max Verdugo-Ihl[1], Ashley Slattery[2], Nigel J. Cook[1], Kathy Ehrig[3]

[1]The School of Chemical Engineering and Advanced Materials; liam.courtney-davies@adelaide.edu.au; cristiana.ciobanu@adelaide.edu.au; max.verdugo-ihl@adelaide.edu.au; nigel.cook@adelaide.edu.au
[2]Adelaide Microscopy; Ashley.slattery@adelaide.edu.au
[3]BHP Olympic Dam; kathy.ehrig@bhp.com

Zircon micron- to nanoscale structures and trace element signatures offer an exciting opportunity to delve into the genesis of large magmatic-hydrothermal ore systems (Courtney-Davies et al., 2019a). Based on zircon within different Proterozoic granites in the Olympic Cu-Au province (Gawler Craton, South Australia), either hosting, proximal to, or distal from iron-oxide-Cu-(U)-Au (IOCG) style mineralization, we characterize and interpret features that have application as potential discriminants in exploration for IOCG deposits. This subject is of interest to igneous petrologists and mineral deposit specialists alike, since the evidence contradicts long-held consensus regarding the processes and timescales of zircon alteration in magmatic-hydrothermal environments (Geisler et al., 2007 and references therein).

Magmatic zircon was studied from two distinct granite suites: ~1.85 Ga Donington Suite and ~1.6 Ga Hiltaba Suite. Although both suites host mineralisation, only the Hiltaba Suite granites are genetically associated with IOCG mineralization. The Hiltaba Suite-affiliated Roxby Downs Granite (1593.87+0.21; Cherry et al., 2018), host to the Olympic Dam deposit, is an outstanding case of a fertile granite, whereas the Donington Suite provides examples of pristine (Cape Donington, Eyre Peninsula) to hydrothermally-altered zircon (Wirrda Well prospect), the latter impacted by the same ~1.6 Ga hydrothermal event.

Zircon grains were studied by complementary micron- and nanoscale techniques: High Angle Annular Dark Field Scanning Transmission Electron Microscopy (HAADF STEM) imaging and STEM energy-dispersive (EDS) X-ray spectrometry mapping and spot analysis, supported by STEM simulations and complemented by electron microprobe analysis (EPMA). The aims were to characterise and interpret; (1) crystal zoning with respect to 'non-formulae' elements such as Fe, Ca and Cl; (2) the nature of a characteristic inclusion mottling in zoned bands; (3) lattice defects; and (4) the relationship between metamictization and alteration. Zircon grains were selected after imaging in BSE mode. Foils for TEM study were extracted in-situ, thinned to <100 nm by ion beam (Ga+) milling, and attached to Cu grids on a FIB-SEM platform. Of seven foils, five were cut across oscillatory zoning observed on grain surfaces in zircon to target their development at depth, also allowing correlation between micron- and nanoscale characteristics. HAADF STEM imaging and EDS spot analysis and mapping, was performed using an ultra-high resolution, probe-corrected, FEI Titan Themis S/TEM operated at 200 kV.

Crystal oscillatory zoning is expressed in all zircons, but with respect to different elements. In unaltered zircon, variation is, as expected, expressed with respect to common magmatic trace elements (REE and actinides), whereas altered zircon features crystal oscillatory zoning with non-formula elements, particularly Fe, Ca and Cl. Such patterns are depicted on both EPMA and STEM-EDS maps. In zircon proximal to mineralisation dense inclusion mottling becomes typical within bands enriched in non-formula elements. At higher resolution, the mottled areas (dark nanodomains in HAADF STEM images), concentrate Cl in particles ranging in size from nanoparticles (<100 nm) to fine particles (up to hundreds of nm). The largest particles, with well-defined geometrical shapes are crosscut by veinlets with lattice-scale defects proving they are inclusions rather than pores; the latter can nonetheless be present within the inclusions. Based on EPMA data and nanoscale characterisation we define these as chloro–hydroxy–zircon nano-precipitates formed by substitution mechanisms involving replacement of O by Cl and/or OH^-. Remobilised U and Pb was not found to be concentrated within such precipitates.

High-resolution imaging on four main zone axes in zircon shows lattice-scale disorder expressed as screw dislocations and lattice stretching but no amorphous domains, despite a

'metamict' appearance at the micron-scale. The most complex defects were imaged in Fe-rich bands from Roxby Downs Granite zircon on [1$\bar{1}$1] zone axis. In this case, changes in the atomic arrangement along (011) can be interpreted as displacements with anti-phase modulation along fault planes. In contrast, defects within the particles described above are interpreted as the result of local fluid–mineral interaction leading to an increase in OH/halogen content.

Overall, chloro-hydroxy-zircon nanoprecipitates in the Fe-Ca-rich zones become volumetrically more significant in close proximity to the Olympic Dam deposit. An association between Fe and Cl would be expected in early IOCG fluids exsolved after granite crystallization. We thus conclude that Cl is inherent to hydrothermal fluids derived from the Hiltaba Suite granites, which also affected and altered the older Donington Suite granites at Wirrda Well. The absence of non-formula elements in fresh Donington Suite zircon from the Eyre Peninsula rules out a magmatic origin for such elements.

Zircon metasomatism can be attributed to an initial low-fluid, mineral-buffered diffusion-reaction process, followed by formation of chloro–hydroxy–zircon nanoprecipitates when fluids become highly focused. Preservation of pre-existing crystal orientation in zircon nanoprecipitates and host zircon is characteristic of reactions via a sharp interface, typical of replacement via coupling of dissolution with reprecipitation rates (CDRR). Transient porosity developed during the progression of CDRR provides sites for deposition of such nanoprecipitates (Putnis 2002).

From high-precision dating of hematite, iron metasomatism is known to have occurred at Olympic Dam shortly after granite crystallization (~2 to 4 Ma later; Courtney-Davies et al., 2019b). The α-dose required to relate zircon alteration to metamictization is calculated at ~100 Ma after crystallization, a period that cannot be reconciled with the timing of Fe-metasomatism in the region (Courtney-Davies et al., 2019a).

These results show that early metasomatic alteration can be recorded in magmatic zircon and that these patterns can be preserved over geological time, even when superimposed by the effects of metamictization. Marked differences in the geochemistry and nanoscale features of zircon across the sample suite imply that nanoscale studies of magmatic zircon, if coupled with careful characterization of textures and compositions at the micron-scale, represent a pathfinder tool that could be used to locate mineralisation. In turn, the presence of chloro-hydroxy-zircon nanoprecipitates would represent a diagnostic tool to assess the 'fertility' of granitic magmas.

References

Cherry AR, Ehrig K, Kamenetsky VS, et al (2018) Precise geochronological constraints on the origin, setting and incorporation of ca. 1.59 Ga surficial facies into the Olympic Dam Breccia Complex, South Australia. Precambrian Research, *315*, 162–178.

Courtney-Davies, L., Ciobanu, C.L., Verdugo-Ihl, M.R., Slattery, A., Cook, N.J., Dmitrijeva, M., Keyser, W., Wade, B.P., Dominick, U.I., Ehrig, K., Xu, J., Kontonikas-Charos, A., 2019a. Zircon at the nanoscale records metasomatic processes leading to large magmatic-hydrothermal ore deposits. Minerals, *9*(6), 364.

Courtney-Davies, L. Tapster, S. Ciobanu, C. Cook, N.J. Verdugo-Ihl, M.R. Ehrig, K.J. Kennedy, A.K. Gilbert, S.E. Condon, D.J. Wade, B.P., 2019b. A multi-technique evaluation of hydrothermal hematite U-Pb isotope systematics: Implications for ore deposit geochronology. Chemical Geology, *513*, 54–72.

Geisler, T., Schaltegger, U., Tomaschek, F., 2007. Re-equilibration of zircon in aqueous fluids and melts. Elements, *3*, 43–50.

Putnis, A., 2002. Mineral replacement reactions: from macroscopic observations to microscopic mechanisms. Mineralogical Magazine, 66(5), 689-708.

ADDITIONAL MATERIAL CC

CO-AUTHORED CONFERENCE ABSTRACT:

MULTIVARIATE STATISTICAL ANALYSIS OF LA-ICP-MS TRACE ELEMENT DATA FOR IRON-OXIDES: EXAMPLES FROM GENETICALLY DISTINCT ORE DEPOSITS FROM SOUTH AUSTRALIA

Marija Dmitrijeva [1], Cristiana L. Ciobanu [1], Andrew V. Metcalfe [2], Nigel J. Cook [1],

Max R. Verdugo-Ihl [1], William M. Keyser [1], Kathy Ehrig [3]

[1] School of Chemical Engineering and Advanced Materials, The University of Adelaide, Adelaide, SA 5005, Australia

[2] 2School of Mathematical Sciences, The University of Adelaide, Adelaide, SA 5005, Australia

[3] BHP Olympic Dam, Adelaide, SA 5000, Australia

Conference abstract and oral presentation (presented by Marija Dmitrijeva) at IAMG 2017, Perth, Australia, September 3rd-9th.

69: MULTIVARIATE STATISTICAL ANALYSES OF LA-ICP-MS TRACE ELEMENT DATA FOR IRON-OXIDES: EXAMPLES FROM GENETICALLY DISTINCT ORE DEPOSITS FROM SOUTH AUSTRALIA

Dmitrijeva, M.[1], Ciobanu, C. L.[1], Metcalfe, A. V.[2], Cook, N. J.[1], Verdugo-Ihl, M. R. [1], Keyser, W.M. [1], Ehrig, K.[3]

[1]School of Chemical Engineering, The University of Adelaide, Adelaide, SA 5005, Australia
[2]School of Mathematical Sciences, The University of Adelaide, Adelaide, SA 5005, Australia
[3]BHP Billiton Olympic Dam, Adelaide, SA 5001, Australia

Abstract: Magnetite and hematite are ubiquitous components of banded iron formations (BIF) and iron-oxide copper-gold-type (IOCG) deposits. These minerals can incorporate anomalous concentrations of large number of trace elements, which in turn, are expected to deliver unique geochemical signatures mirroring conditions of mineral formation and superimposed tectonothermal events. In contrast to whole-rock data approach, prone to averaging-out effects, trace element signatures in minerals (TESIM) are governed by crystal structure and the ability to record changes in physical- chemical parameters, and are thus more suitable for fingerprinting distinct stages of mineralization. With improvements in laser-ablation inductively-coupled plasma-mass spectrometry (LA-ICP- MS), present-day TESIM datasets may be very large, yet are often presented without reference to mineral texture or detailed analysis of mineral assemblage, and apart from bi/trivariate visualizations, often lack a numerical approach. The complexity of TESIM data demands statistical formalism, as the full potential of these data cannot be realized without being able to mathematically model dependencies and understand the relationships among elements.

Trace element distributions expose inter/intra-grain variability, along with relative variation conjugated with position of the mineral assemblage within a given ore system. This has potential for development of exploration vectors, particularly for discrimination of distal/proximal positions of mineralization.

We evaluate suitability and limitations of multivariate statistical analyses to describe, and model dependencies within TESIM data, and formalize a general TESIM concept for building geochemical vectors accounting for interdependence of elements for spatial and temporal factors. We present trace element signatures of Fe-oxides from South Australian deposits (the IOCG-type Olympic Dam Cu-U-Au-Ag deposit and BIF-type iron deposits of the Middleback Ranges) and provide recommendations for LA-ICP-MS data treatment, which acknowledge and address issues of inter/intra-grain zoning, censoring, missing data and dependence modelling. The potential of TESIM to become a viable too for deciphering evolution of complex IOCG and BIF-type ore systems is demonstrated.

ADDITIONAL MATERIAL DD

CO-AUTHORED CONFERENCE ABSTRACT:

COPULA FUNCTIONS AS A TOOL FOR STATISTICAL MODELLING OF TRACE ELEMENT SIGNATURES IN IRON-OXIDES: EXAMPLES FROM SOUTH AUSTRALIAN ORE DEPOSITS

Marija Dmitrijeva [1], Andrew V. Metcalfe [2], Cristiana L. Ciobanu [1], Nigel J. Cook [1],

Max R. Verdugo-Ihl [1], William M. Keyser [1], Kathy Ehrig [3]

[1] School of Chemical Engineering and Advanced Materials, The University of Adelaide, Adelaide, SA 5005, Australia

[2] 2School of Mathematical Sciences, The University of Adelaide, Adelaide, SA 5005, Australia

[3] BHP Olympic Dam, Adelaide, SA 5000, Australia

Conference abstract and poster presentation (presented by Marija Dmitrijeva) at IAMG 2017, Perth, Australia, September 3rd-9th.

18TH ANNUAL CONFERENCE
IAMG2017
2-9 SEPTEMBER • PERTH, AUSTRALIA

70: COPULA FUNCTIONS AS A TOOL FOR STATISTICAL MODELLING OF TRACE ELEMENT SIGNATURES IN IRON-OXIDES: EXAMPLES FROM SOUTH AUSTRALIAN ORE DEPOSITS.

~~Dmitrijeva, M.[1],~~ Metcalfe, A. V.[2], Ciobanu, C. L.[1], Cook, N. J.[1], Verdugo-Ihl, M. R.[1], Keyser, W. M.[1], Ehrig, K.[3]

[1] School of Chemical Engineering, The University of Adelaide, Adelaide, SA 5005, Australia
[2] School of Mathematical Sciences, The University of Adelaide, Adelaide, SA 5005, Australia
[3] BHP Billiton Olympic Dam, Adelaide, SA 5001, Australia

Trace elements are impurities 'dissolved' in a mineral lattice, and account for a small percentage of the total bulk composition of a given grain. Their concentrations are, implicitly, extremely low by comparison with the major components. Concentrations need, therefore, to be treated as either non-compositional data, or as compositional relative to the sum of the concentrations of all trace elements[1]. These alternatives provide different descriptions of the dataset. The concentrations of trace elements vary over several orders of magnitude, and standard multivariate analysis techniques (typically developed for dealing with samples from multivariate Gaussian distributions) tend to be dominated by outlying values unless the original data are transformed. Various options of transformations are compared. Moreover, large trace element signatures in mineral (TESIM) datasets may comprise multiple sub-populations (related to e.g., different samples or textural types), and analysis should be performed separately for each.
Trace element data is commonly analyzed by computing either Pearson's product-moment or Spearman's rank-order correlation coefficients between pairs of elements. However, correlation coefficients and empirical marginal distributions do not define dependence structure unless a multivariate Gaussian distribution is assumed. Copulas are multivariate distribution functions with one-dimensional uniform margins, and provide a greater flexibility since they can combine various marginal distributions with a variety of copula distributions. Copulas can therefore provide a better fit to data from sub-populations, and offer a powerful method for distinguishing sub-populations in a quantitative manner.
We present, for the first time, successive steps for building copula models for parts-per-million- level trace element concentrations in hematite and magnetite (the main iron-oxides considered here) from different types of deposits in South Australia. We fit various elliptical and Archimedean bivariate copulas to pre-defined textural types and evaluate goodness of fit. Further studies using copulas on larger datasets with extension to pair-copula constructions and spatial modelling are proposed.

ADDITIONAL MATERIAL EE

CO-AUTHORED CONFERENCE ABSTRACT:

DEFINING IOCG SIGNATURES THROUGH COMPOSITIONAL DATA ANALYSIS: A CASE STUDY OF LITHOGEOCHEMICAL ZONING AT OLYMPIC DAM, SOUTH AUSTRALIA

Marija Dmitrijeva [1], Kathy Ehrig [2], Cristiana L. Ciobanu [1],

Nigel J. Cook [1], **Max R. Verdugo-Ihl** [1], Andrew V. Metcalfe [3]

[1] School of Chemical Engineering and Advanced Materials, The University of Adelaide, Adelaide, SA 5005, Australia

[2] BHP Olympic Dam, Adelaide, SA 5000, Australia

[3] School of Mathematical Sciences, The University of Adelaide, Adelaide, SA 5005, Australia

Conference abstract and oral presentation (presented by Marija Dmitrijeva) at 15th Quadrennial IAGOD Symposium, Salta, Argentina, August 28th-31st. Symposium Volume, SEGEMAR, 246–247.

15th Quadrennial IAGOD International Association on the Genesis of Ore Deposits Symposium, Salta, Argentina.

A | 118

DEFINING IOCG SIGNATURES THROUGH COMPOSITIONAL DATA ANALYSIS: A CASE STUDY OF LITHOGEOCHEMICAL ZONING AT OLYMPIC DAM, SOUTH AUSTRALIA

Marija Dmitrijeva[1], Kathy J. Ehrig, Cristiana L. Ciobanu, Nigel J. Cook, Max R. Verdugo-Ihl, Andrew V. Metcalfe

[1]*University of Adelaide - marija.dmitrijeva@adelaide.edu.au*

BACKGROUND

Iron-oxide–Cu-Au (IOCG) comprises a diverse clan of ore deposits that are found in a wide spectrum of geological settings spanning the Archean to Tertiary (Groves *et al.*, 2010). These deposits are inherently associated with zoned alteration assemblages represented by distal alkali-rich, and proximal hydrolytic alteration, with respect to the main Fe-oxide (±Cu-Au) mineralization (Barton, 2014). This zonation is observed at different scales, from regional down to individual orebodies, and results from the circulation and evolution of hydrothermal fluids. Understanding the spatio-temporal distribution of metals and minerals relative to fluid sources is thus crucial to constrain genetic models and develop exploration strategies.

The Olympic Dam (OD) deposit, South Australia, shows a regional and deposit-scale zoning with respect to alteration assemblages. The sulphide-zonation is roughly concentric, displaying a deeper-to-shallower transition from pyrite-chalcopyrite (Py-Cp) through chalcopyrite-bornite (Cp-Bn) to bornite-chalcocite (Bn-Cc) (Ehrig *et al.*, 2012). The deposit is hosted within the Olympic Dam Breccia Complex (ODBC), itself within the ~1.59 Ga Roxby Downs Granite and is predominantly derived from progressive brecciation and increasing Fe-metasomatism of the host granite. This relatively simple geological setting and mineralogical zonation make OD a prime target to investigate geochemical patterns potentially associated with zoning and concentration gradients relative to metal source(s). As a first step towards constraining zoning within the ODBC, principal component analysis (PCA) was performed to derive lithogeochemical zonation and identify key elements defining IOCG signatures.

METHODS

The whole-rock dataset consists of 10,546 samples from 533 drillholes and forms a dense grid in the south-eastern part of ODBC. Each sample represents a 15 m-long drillhole interval, which was assayed for 39 elements (as on Fig. 1). The PCA was performed on the centred logratio transformed data containing all elements, and the PC1 interpolated in Leapfrog3D software (Fig. 1a).

We present only the first principal component (PC1), which governs the greatest variability (~32%) within the dataset and represents an interpretable geological process. As an example, the NW-SE partial cross-section (Fig. 1b) represents the majority of lithologies/alteration types documented in the ODBC. The combination of multivariate statistics, i.e. PCA/hierarchical clustering, with a large whole-rock dataset, allows a comparison of empirical lithological/alteration and sulphide and gangue mineralogical zonation (obtained from Cu:S ratios and supported by modal mineralogy data), with an IOCG geochemical signature represented as the PC1, and provides data-driven decisions for element groupings.

RESULTS AND DISCUSSION

Relationships among elements within whole-rock geochemical datasets are governed by the mixture of minerals and their stoichiometries. The PCA transforms data into a set of linear combinations of elements or PCs, whereby the dominant PC1 reflects mineralogy and describes geological processes, which are mirrored by a relative increase or decrease of elements. The resulting PC1 and dendrogram shows two main element groups (Fig. 1c), defined as Class 1, and an antithetic association represented by Classes 2, 3 and 4. These two distinct groups represent the inverse relationship between (i) trace elements in host rocks (unmineralized granite, mafic and carbonate units), and (ii) elements typifying an IOCG geochemical signature within the ODBC. Notably, the highest loadings on PC1 are given by Class 3 elements Au-W-As-Mo-Sb (Fig. 1d).

If compared with the lithological/alteration cross-section (Fig. 1b), the distribution of positive PC1 values only partially overlaps with the distribution of >20 wt% Fe hematite breccias and vice versa. This may suggest that: (i) in some areas mineralization may not be associated with the Fe-metasomatism; and (ii) the presence of some Fe-rich lithologies may pre- or postdate IOCG mineralization.

The Cu(-Fe)-sulphide zone interfaces represent a complex but mappable feature. However, when compared to the significant correlation between PC1 and lithological/alteration zones, no pattern can be observed. This mismatch may be attributed to the low-resolution sampling and/or pervasive distribution of abundant Cu(-Fe)-

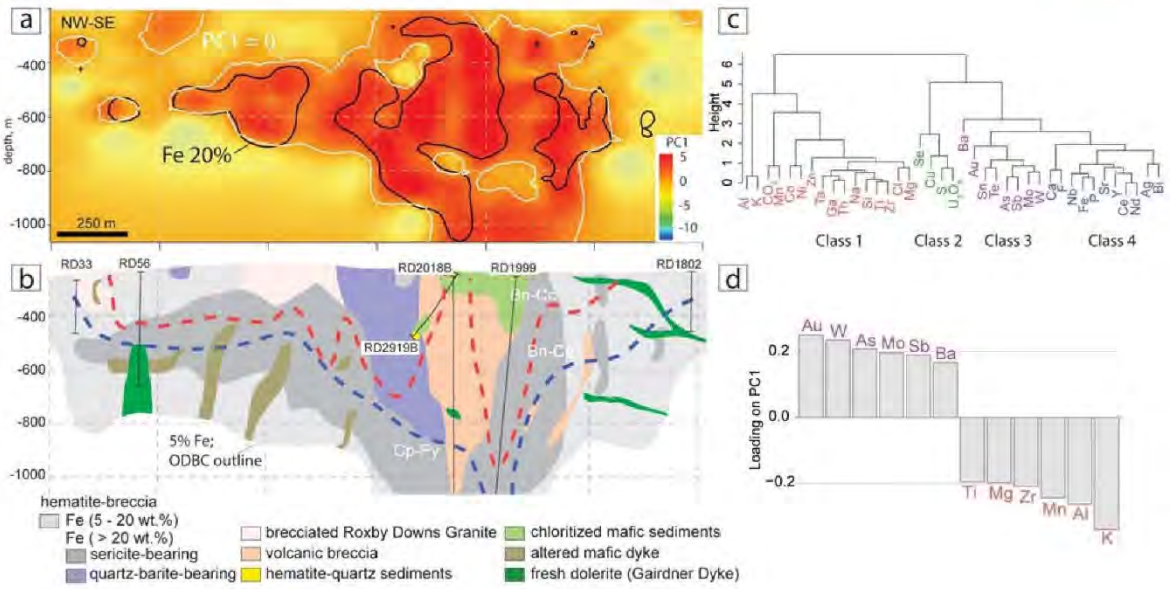

Figure 1. (a) NW-SE cross-section showing interpolated values of PC1 scores; (b) corresponding geological sketch; (c) dendrogram of analysed elements; (d) highest absolute element loadings on PC1.

sulphides and Fe-oxides that host trace elements. The latter stresses the necessity for investigation of individual metal gradients with emphasis on statistically defined classes, such as the Au-W-As-Mo-Sb signature.

CONCLUSIONS

The PCA has implications for delineation of the ODBC from the enclosing granite by deriving groups of elements representing IOCG mineralization. Although PC1 overlaps with Fe- metasomatism, it neither gives solid gradients nor defines zonation. This may signify that data-driven grouping of elements is the next step for further metal zonation investigation with a potential to detect primary/replacement patterns. However, given the complexity of ore assemblages in response to multiple episodes of mineral dissolution and (re)precipitation, trace element signatures in individual minerals (e.g. Cu(-Fe)-sulphides, Fe- oxides) may prove better at constraining the spatiotemporal evolution of the ODBC.

REFERENCES

Groves, D.I., Bierlein, F.P., Meinert, L.D., and Hitzman, M.W., 2010. Iron oxide copper- gold (IOCG) deposits through Earth history: Implications for origin, lithospheric setting, and distinction from other epigenetic iron oxide deposits: Economic Geology, 105, 641–654.

Barton, M.D., 2014. Iron Oxide (–Cu–Au–REE–P–Ag–U–Co) Systems, in: Treatise on Geochemistry. Elsevier, 13, pp. 515–541.

Ehrig, K., McPhie, J., Kamenetsky, V., 2012. Geology and Mineralogical Zonation of the Olympic Dam Iron Oxide Cu-U-Au-Ag Deposit, South Australia, in: Hedenquist, J.W., Harris, M., Camus, F. (Eds.), Geology and Genesis of Major Copper Deposits and Districts of the World: A Tribute to Richard H. Sillitoe. Society of Economic Geologists, Special Publication 16, pp. 237–267.

ADDITIONAL MATERIAL FF

CO-AUTHORED CONFERENCE ABSTRACT:

MINERALIZATION SIGNATURES OF THE MAGNETITE-DOMINANT ACROPOLIS PROSPECT, OLYMPIC DAM IOCG DISTRICT, SOUTH AUSTRALIA

Marija Dmitrijeva [1], Cristiana L. Ciobanu [1], Kathy Ehrig [2], Nigel J. Cook [1],

Andrew V. Metcalfe [3], **Max R. Verdugo-Ihl** [1], Jocelyn McPhie [4]

[1] School of Chemical Engineering and Advanced Materials, The University of Adelaide, Adelaide, SA 5005, Australia

[2] BHP Olympic Dam, Adelaide, SA 5000, Australia

[3] School of Mathematical Sciences, The University of Adelaide, Adelaide, SA 5005, Australia

[4] School of Natural Sciences and Centre of Excellence in Ore Deposits (CODES), University of Tasmania, Hobart, Tasmania 7001, Australia

Published conference abstract and oral presentation (presented by Marija Dmitrijeva) at AEGC 2019, Perth, Australia, September 2nd-5th.

AEGC2019 Data to Discovery

Mineralization signatures of the magnetite-dominant Acropolis prospect, Olympic Dam IOCG district, South Australia

Marija Dmitrijeva[*,1] marija.dmitrijeva@adelaide.edu.au
Cristiana L. Ciobanu[1] cristiana.ciobanu@adelaide.edu.au
Kathy J. Ehrig[2] kathy.j.ehrig@bhp.com
Andrew V. Metcalfe[3] andrew.metcalfe@adelaide.edu.au
Max R. Verdugo-Ihl[1] max.verdugoihl@adelaide.edu.au
Jocelyn McPhie[4] j.mcphie@utas.edu.au
Nigel J. Cook[1] nigel.cook@adelaide.edu.au

[1]*School of Chemical Engineering, The University of Adelaide*
[2]*BHP Olympic Dam, Adelaide*
[3]*School of Mathematical Sciences, The University of Adelaide*
[4]*CODES, The University of Tasmania*

SUMMARY

The Acropolis prospect is a vein-style magnetite (±apatite ±hematite) system located ~20 km southwest from the giant Olympic Dam iron-oxide copper gold (IOCG) deposit, South Australia. A whole rock dataset comprising 4,864 core samples from fourteen drillholes was analysed using multivariate statistics to understand and identify geochemical signatures of mineralization at Acropolis. Statistical analyses included principal component analysis, hierarchical and k-means clustering. The results of statistical analyses are overlaid and interpreted relative to a 3D implicit geological model of the prospect, and encompass a projection of mineralization signature as PC1.

The mineralization footprint of Acropolis is multi-element and typified by a distinct 'magnetite' signature of Fe-V-Ni-Co. Such a signature is developed in the western part of the prospect and represents samples containing >60 wt% Fe. In contrast, the 'hematite' signature displays an association of REE, W, Sn, Sb, U, Th, Ca, and P and is present throughout the prospect. Furthermore, kriged values of Cu (> 200 ppm) demonstrate an offset from Fe-rich veins, thus supporting a genetic model in which (earlier) Cu-Au-deficient veins in which magnetite is the dominant Fe-oxide are subsequently overprinted by Cu-bearing hematite-dominant mineralization.

Results obtained provide insights into the evolution from magnetite- to hematite-dominant IOCG systems and may offer a proxy for exploration and discovery of economically significant IOCG deposits at shallower levels in the eastern Gawler Craton.

Key words: Acropolis, magnetite-dominant IOCG, statistical analysis, implicit modelling

INTRODUCTION

Acropolis is a magnetite-dominant hematite-bearing prospect located ~20 km southwest from the giant Olympic Dam (OD) deposit. Displaying a range of mineralogical-petrological similarities to OD, Acropolis is considered to be broadly cotemporaneous with mineralisation at OD (Mortimer et al., 1988). Nevertheless, unlike the OD deposit, which displays disseminated Cu(-Fe)-sulphides within hematite breccias hosted in Roxby Downs Granite of Hiltaba Suite (HS) affiliation, the Acropolis prospect represents a vein-style mineralization with weakly-developed brecciation (Cross, 1993) within felsic Gawler Range Volcanics (GRV) (Mortimer et al., 1988). Both magmatic suites, HS and GRV, form the Large Igneous Province emplaced at ~ 1.6 Ga in the Gawler Craton, South Australia (Allen et al., 2008).

At Acropolis, the GRV units are comprised of rhyolitic, dacitic and andesitic lavas, as well as minor ignimbrites (McPhie, 2016). Within the area, the basement is composed of Donington Suite granitoids (~1850 Ma; Jagodzinski, 2005) which, also host mineralization. Weakly-brecciated Hiltaba Suite-affiliated granite (drillhole ACD7), is also as a relatively minor host rock for mineralization (McPhie, 2016).

Because of the proximity of Acropolis and evident similarities with the styles of alteration at Olympic Dam (Ehrig et al., 2017), this case study aims at obtaining geochemical signatures of this magnetite-rich end-member of the IOCG clan, using statistical analyses of whole rock data. Multivariate statistical analyses are effectively applied to find structures and patterns within geochemical data which lack pre-defined categorical variables (Caciagli 2016). Such an approach allows identification of mineralized domains with distinct geochemical characteristics, combining the chemistry of protolith lithologies and superimposed geochemical signatures of the mineralization. Coupled with an implicit 3D geological model of Acropolis, these techniques allow visualization of the associations of key elements and mineralization within 3D space. The results obtained here provide insight into the development of IOCG systems from a magnetite- to hematite-dominant end-member.

METHODS

In this case study, principal component analysis (PCA), hierarchical and k-means clustering are applied to a large multi-element data set (4,864 samples, total of 36 elements), collected from fourteen drillholes at the Acropolis prospect (Figure 1). Hierarchical clustering was applied to a variation matrix containing the variances of log-ratios of every possible element pairs:

$$\tau_{ij} = var(\ln (x_i/x_j) \quad (1)$$

The compositional properties of the geochemical data were respected by obtaining isometric log-ratio (ilr) and centred log-ratio (clr) coordinates, which were further utilized for k-means clustering and PCA respectively. In the k-means procedure, the bootstrapping algorithm was used to test the stability of each cluster by calculating a Jaccard similarity value. The optimal number of k clusters was determined as seven based on the sufficient minimal value of the within-cluster sum of squares.

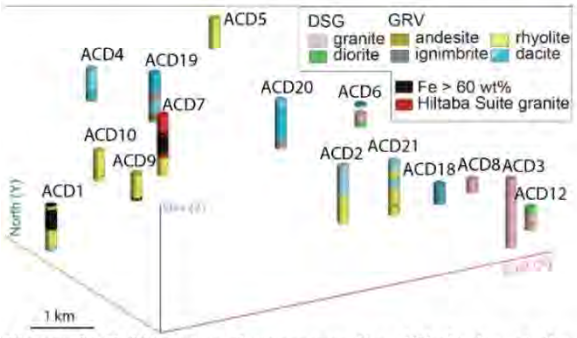

Figure 1. Drillholes and corresponding lithologies at the Acropolis prospect.

This study incorporates 3D modelling of the major faults, intrusions and lithological groups at the Acropolis prospect using the fault interpretations of McPhie (2016; Figure 2), and careful correlation of felsic GRV units using the Ti/Zr and Ti/Al ratios. Using the 3D model, we are able to overlay the lithologies of Acropolis with the interpolated results of statistical analyses as PC1 scores, the most geochemically meaningful clusters obtained from k-means algorithm and the outlines of 25 wt% Fe and 200 ppm Cu. Such a holistic approach allows us to understand the extents of mineralization signatures and relate these to the lithologies present within the Acropolis prospect.

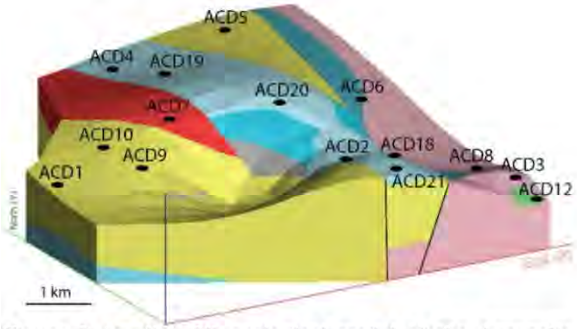

Figure 2. Implicit 3D geological model of the Acropolis prospect based on the fourteen drillholes created in Leapfrog Geo software. The legend is as in Figure 1.

RESULTS

The hierarchical dendrogram (Figure 3) provides a summary of the associations among the elements and suggests four main geochemical groups.

Group 1, comprising Ba, Zr, Al, Si, Na, K and Rb represents a geochemical signature of granites and GRV felsic units and is also indicative of silicate minerals which are the products of hydrothermal alteration within the host rocks. In contrast, the mineralization signature is typified by Groups 2, 3 and 4, whereby Group 4 is associated with Fe-dominant mineralization, thus reflecting the strong co-dependence among Fe, V, Ni and Co, i.e. 'magnetite' signature, along with sulphide signature of Cu, Mo and Bi. Group 3, which encompasses W, Sb, Zn, Ti, Sc, Mg, Li, Ca and P, is evidently associated with Group 4, and represents a range of indicator and pathfinder elements typically present within a deposit of IOCG sensu stricto type (Groves et al., 2010). Combined, Groups 3 and 4 form an indicative IOCG-signature within magnetite-dominant mineralization at Acropolis.

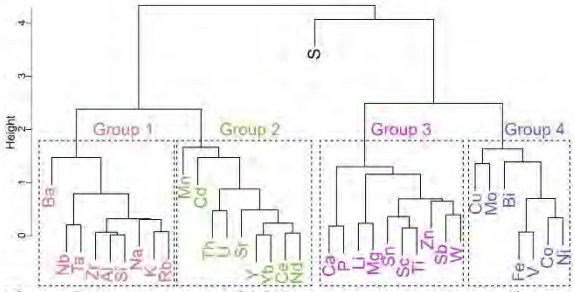

Figure 3. Dendrogram of 36 elements grouped according to their geochemical affinities. The dissimilarity measure was obtained from variation matrix based on Equation. 1.

The seven clusters identified by the k-means algorithm are used to define geochemical domains which have direct implication for characterization of data, as they reflect the original lithology along with the superimposed alteration and mineralization (Table 1).

The most geologically significant clusters are Cluster 2, 3 and 6. Cluster 2 represents early sodic alteration within the Donington Suite granite and diorite in the western part of the prospect (Figure 4). Cluster 6 represents Fe-rich veins, predominantly composed of magnetite. Finally, Cluster 3 is comprised of rhyolites and dacites with relatively higher Fe content of 30 wt% and is distributed throughout the prospect independently from the Fe-rich veins. The interpolation of Fe 25 wt% and Cu 200 ppm provides additional comparison with the lithologies and clusters at Acropolis and indicates a Cu mineralization offset from Fe-rich veins (Figure 4). A plot of magnetic susceptibility values over clusters also suggest that Cluster 3 is predominantly hematite-bearing (Figure 5).

The projection of 4,864 samples on PC1 and PC2 demonstrate geochemical affinities of Clusters and significantly complements the result of hierarchical and k-means analyses. The PC1-2 projection distinguishes Cluster 6 and its strong association with IOCG-signature elements: Fe-V-Ni-Co and with less pronounced loadings of Ti, Mn and Zn on PC1. (Figure 6). Similarly, Cluster 3 shows a strong correlation with Group 2 and Group 3 elements, thus likely representing altered and/or partially mineralized/vein samples, i.e. 'hematite' signature rather than the magnetite-dominant mineralization itself.

Finally, the spatial projection of PC1 scores in 3D indicates mineralisation signatures within the western zone of the prospect, namely in drillholes ACD1, ACD9 and ACD7. Additionally, a mineralization signature is present within the Donington Suite granite in the western zone (Figure 7).

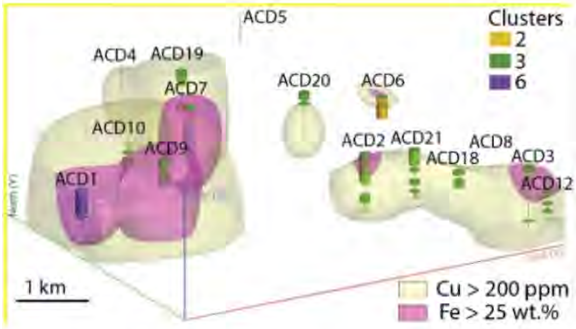

Figure 4. Spatial projection of Clusters 2, 3 and 6 in oblique view, overlaid by the outlines of Cu > 200 ppm and Fe > 25 wt%.

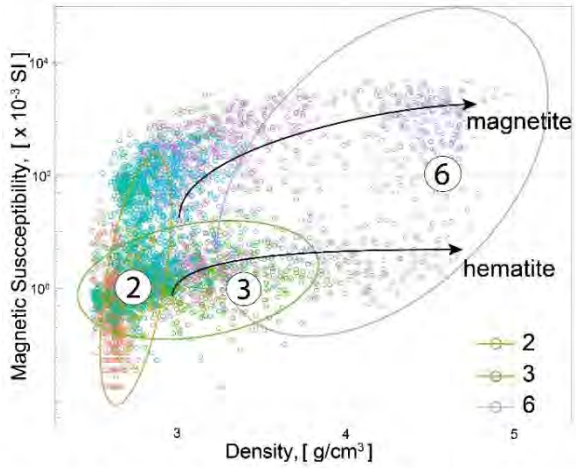

Figure 5. Magnetic susceptibility versus density, colour-coded according to a cluster membership and outlined by 0.95 confidence ellipses for Cluster 2, 3 and 6.

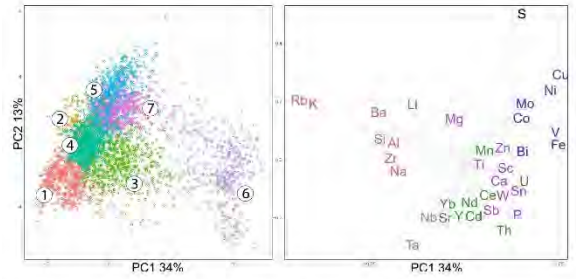

Figure 6. Projection of clr-transformed data demonstrating seven clusters obtained from k-mean algorithm and corresponding element loadings. Each circle represents a single data point. Elements are colour-coded according to the Groups (as in Figure 3).

DISCUSSION

Many magnetite-dominant IOCG systems are known to be deficient with respect to Cu and Au (Barton, 2014). Similarities among alteration types, ore and gangue mineralogy as well as the presence of early magnetite-apatite assemblages within many IOCG deposits has prompted a genetic relation between IOCG and Kiruna-type magnetite-apatite deposits (Hitzman et al., 1992), in spite of the lack of an evident transition between the two. Within the eastern Gawler Craton, and specifically in the immediate proximity of Olympic Dam, magnetite-apatite (± siderite ± chlorite) assemblages correspond to low-grade Cu-U-Au and are regarded as the envelopes of larger IOCG systems (Ehrig et al., 2012).

Analogous to the clan of IOCG systems, which are known to display elevated concentrations of many elements (Groves et al. 2010), the manifestation of the Acropolis IOCG signature is multi-element (Figure 5). The U-W-Sn-Mo signature in hematite at Olympic Dam (Verdugo-Ihl et al., 2017) is recognised in geochemical studies as a distinct W-Mo-Sn subset besides the dominant Fe, Cu, Au association in the IOCG signature obtained from PCA analysis (Dmitrijeva et al., 2019). Although Acropolis is deficient in terms of Au (> 70% of values are below the minimum detection limit) and contains geochemically anomalous, but low concentrations of Cu, it demonstrates a mineralisation signature analogous to that at Olympic Dam, with high loadings of W, Sn, Sb, U, Th and REE (Cluster 3), albeit at trace concentrations.

At Acropolis, sulphide minerals, particularly chalcopyrite, are predominantly associated with hematite-sericite-chlorite assemblages, which replace early magnetite-apatite (Krneta et al., 2017). An analogue mineral assemblage of early sulphide-poor magnetite-apatite overprinted by later sulphur-enriched Fe-oxide-Cu-Au mineralization is recorded at other IOCG systems outside the Gawler Craton (Ernest Henry, Queensland; Mark et al., 2006). The results of statistical analyses demonstrate that although Fe-oxide and Cu(-Fe)-sulphide mineralization are associated, they offset each other in some measure, reaffirming that assemblages observed in petrographic records correspond to patterns within the whole rock data. Cluster 3, which is characterised by Ca-P-Li-Mg-Sc-Ti-Zn-W-Sn-Sb, along with REE, Sr, U and Th is evidently associated with hematite-dominant alteration (Figure 5), and likely represents its geochemical footprint, overprinting early Cu-deficient magnetite-apatite assemblages. The projection of Cluster 3 in Leapfrog (Figure 4), indicates that such a signature does not form haloes around Fe-rich veins (Cluster 6), but is actually ubiquitous throughout the Acropolis prospect, confirming that a transition from magnetite- to a hematite dominant system involves significant metal endowment.

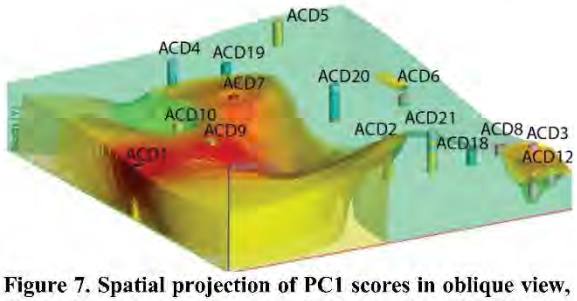

Figure 7. Spatial projection of PC1 scores in oblique view, displaying zones of most intense mineralization at Acropolis.

Overall, these results suggest that recognition of magnetite-dominant members of the IOCG clan are of critical importance in establishing the spatio-temporal model of entire IOCG systems and can facilitate discovery of metal endowed hematite-dominant IOCG deposits. This is particularly relevant in productive mineral districts, such as the Olympic Cu-Au province, where basement and the mineralization contained within is buried beneath a thick, barren sedimentary cover. Therefore, an improved understanding of the genesis and full

extent of zonation in IOCG systems is fundamental for effective exploration, both at the local and regional scales.

CONCLUSIONS

Application of statistical analyses combined with implicit 3D geological modelling is an effective way to identify patterns and structures within the data in the absence of detailed petrographic and mineralogical data.

Despite being magnetite-dominant, the Acropolis prospect displays a multi-element mineralisation signature, which is partially similar to that of Olympic Dam, with W, Sn, Mo, and REE distributed throughout the prospect. Within Acropolis, Fe and Cu mineralization are slightly offset, thus being consistent with observation of Cu-deficient magnetite-apatite veins in the western part of Acropolis and overprinting Cu-endowed hematite-dominant assemblages that extend throughout the prospect area, represented as Cluster 3. This conclusion is supported by the low magnetic susceptibility of Cluster 3 and a range of indicator elements which are typically hosted within a hematite-dominant assemblage: U, Th, REE, W, Sn and Sb. In contrast, magnetite mineralization (Cluster 6) is typified by a Fe-V-Ni-Co signature with less pronounced loadings of Ti, Mn and Zn. The magnetite veins may represent the upper part, or alternatively, the roots of an eroded or undiscovered Cu-Au mineralization, which, although partially coincident, is not centred on the HS granite. The Fe-V-Ni-Co signature is an indicator of relatively early IOCG mineralization and is a significant proxy for exploration of fertile hematite-dominant IOCG deposits at shallower crustal levels.

ACKNOWLEDGEMENTS

This work is a contribution to the FOX project 'Trace elements in iron-oxides: deportment, distribution and application in ore genesis, geochronology, exploration and mineral processing', supported by BHP Olympic Dam and the South Australian Mining and Petroleum Services Centre of Excellence. N.J.C. acknowledges additional support from the ARC Research Hub for Australian Copper-Uranium (Grant IH130200033).

REFERENCES

Allen, S.R., McPhie, J., Ferris, G., and Simpson, C., 2008, Evolution and architecture of a large felsic Igneous Province in western Laurentia: the 1.6 Ga Gawler Range Volcanics, South Australia. Journal of Volcanology and Geothermal Research 172, 132–147.

Barton, M.D., 2014, Iron oxide (–Cu–Au–REE–P–Ag–U–Co) systems: In: Holland, H.D., and Turekian, K.K. (Eds.), Treatise on Geochemistry, 2nd ed., Elsevier, Oxford, 515–541.

Caciagli, N., 2016, Multielement geochemical modelling for mine planning: case study from an epithermal gold deposit: In: Martín-Fernández, J.A., and Thió-Henestrosa, S. (Eds.), Compositional Data Analysis. Springer Proceedings in Mathematics and Statistics, 187, 45–61.

Cross, K.C., 1993, Acropolis and Wirrda Well: In: Drexel, J.F., Preiss, W.V., and Parker, A.J. (eds.), The Geology of South Australia. vol. 1, The Precambrian. Geological Survey of South Australia, South Australia, 138 pp.

Dmitrijeva, M., Ehrig, K., Ciobanu, C., Cook, N. Verdugo-Ihl, M., and Metcalfe, A., 2019, Defining IOCG signatures through compositional data analysis: A case study of lithogeochemical zoning from the Olympic Dam deposit, South Australia: Ore Geology Reviews, 105, 86-101.

Ehrig, K., McPhie, J., and Kamenetsky, V., 2012, Geology and mineralogical zonation of the Olympic Dam iron oxide Cu-U-Au-Ag deposit, South Australia: Economic Geology, Special Publication 16, 237-267.

Ehrig, K. Kamenetsky, V.S., McPhie, J. Apukhtina, O., Ciobanu, C., Cook, N., Kontonikas-Charos, A., and Krneta, S. 2017, The IOCG-IOA Olympic Dam Cu-U-Au-Ag deposit and nearby prospects, South Australia: Proceedings, 14th Biennial SGA Meeting 'Mineral Resources to Discover' Québec City, Canada, vol. 3, p. 823-826.

Groves, D.I., Bierlein, F.P., Meinert, L.D., and Hitzman, M.W., 2010, Iron Oxide Copper-Gold (IOCG) deposits through earth history: implications for origin, lithospheric setting, and distinction from other epigenetic iron oxide deposits: Economic Geology, 105, 641–654.

Hitzman, M.W., Oreskes, N., and Einaudi, M.T., 1992, Geological characteristics and tectonic setting of Proterozoic iron oxide (Cu-U-Au-REE) deposits: Precambrian Research, 58, 241–287.

Jagodzinski, E.A., 2005, Compilation of SHRIMP U–Pb geochronological data – Olympic Domain, Gawler Craton, South Australia, 2001–2003: Geoscience Australia Record 2005/20, 197 pp.

Krneta, S., Cook, N.J., Ciobanu, C.L., Ehrig, K.J., and Kontonikas-Charos, A., 2017, The Wirrda Well and Acropolis prospects, Gawler Craton, South Australia: Insights into evolving fluid conditions through apatite chemistry: Journal of Geochemical Exploration, 181, 276-291.

Mark, G., Oliver, N.H.S., and Williams, P.J. 2006, Mineralogical and chemical evolution of the Ernest Henry Fe oxide–Cu–Au ore system, Cloncurry district, northwest Queensland, Australia: Mineralium Deposita 40, 769-801.

McPhie, J., 2016, Acropolis Report (unpublished): BHP Billiton Olympic Dam.

Mortimer, G.E., Cooper, J.A., Paterson, H.L., Cross, K., Hudson, G.R.T., and Uppill, R.K., 1988, Zircon U–Pb Dating in the Vicinity of the Olympic Dam Cu–U–Au Deposit, Roxby Downs, South-Australia: Economic Geology, 83, 694–709.

Verdugo-Ihl, M.R., Ciobanu, C.L., Cook, N.J., Ehrig, K., Courtney-Davies, L., and Gilbert, S., 2017, Textures and U-W-Sn-Mo signatures in hematite from the Cu-U-Au-Ag orebody at Olympic Dam, South Australia: defining the archetype for IOCG deposits: Ore Geology Reviews, 91, 173–195.

Table 1. Characteristics of seven clusters obtained from k-means cluster analysis.

Cluster	n, samples	Jaccard similarity value, j_i	Predominant cluster lithology and median values of Fe, K and Cu	Median density, kg/m^3	Median magnetic susceptibility, $\times 10^{-3}$ SI
1	779	0.57	Altered, least-veined rhyolites and minor dacites with 5% Fe, 5-6% K and 35 ppm Cu.	2.6	0.86
2	171	0.74	Altered Donington granite and diorite with pronounced sodic alteration; 8% Fe, 3.5 % K and 85 ppm Cu	2.7	0.94
3	619	0.84	Altered and intensively veined rhyolites and dacites with 30% Fe, 2.7% K and 137 ppm Cu	3.1	1.52
4	1384	0.69	Altered and moderately veined rhyolites, dacites, HS and Donington granite with 10% Fe, 5% K and 180 ppm Cu	2.7	1.91
5	712	0.74	Altered Donington granite and diorite with minor dacites; 20% Fe, 4% K and high Cu content (530 ppm)	2.9	28
6	441	0.93	Fe-rich veins; Fe >60%, K <0.1% and high Cu content (430 ppm)	4.2	306
7	759	0.75	Altered and veined rhyolites, dacites and ignimbrites with Fe 25% and K 2% and 280 ppm Cu	3.1	28

ADDITIONAL MATERIAL GG

CO-AUTHORED CONFERENCE ABSTRACT:

'INVISIBLE' AU IN PYRITE FROM OLYMPIC DAM DEPOSIT, SOUTH AUSTRALIA: BRIDGING TEXTURES WITH STATISTICAL ANALYSES

Marija Dmitrijeva [1], **Max R. Verdugo-Ihl** [1], Kathy Ehrig [2],

Cristiana L. Ciobanu [1], Nigel J. Cook [1]

[1] School of Chemical Engineering and Advanced Materials, The University of Adelaide, Adelaide, SA 5005, Australia

[2] BHP Olympic Dam, Adelaide, SA 5000, Australia

Conference abstract and poster presentation (presented by Marija Dmitrijeva) at TIGeR 2019, Perth, Australia, September 11th-13th.

'Invisible' Au in pyrite from Olympic Dam deposit, South Australia: bridging textures with statistical analyses

Marija Dmitrijeva[1*], Max R. Verdugho-Ihl[1], Kathy J. Ehrig[2], Cristiana L. Ciobanu[1], Nigel J. Cook[1]

[1]School of Chemical Engineering and Advanced Materials, The University of Adelaide, SA 5005, Australia; *marija.dmitrijeva@adelaide.edu.au; max.verdugoihl@adelaide.edu.au; cristiana.ciobanu@adelaide.edu.au; nigel.cook@adelaide.edu.au

[2]BHP Olympic Dam, Adelaide, SA 5000, Australia; kathy.ehrig@bhp.com

'Invisible' Au in pyrite refers to gold present within the sulphide lattice or as discrete nanoparticle inclusions, making it undetectable by conventional optical and scanning electron microscopy (SEM) (Cook and Chryssoulis 1990). Incorporation of Au into pyrite is often mediated by incorporation of As (Reich et al. 2005). Nevertheless, pore-attached Au-Ag-telluride nanoparticles have been documented within As-free pyrite (Ciobanu et al. 2012) thus representing an alternative mechanism for incorporation of Au into pyrite.

Olympic Dam, is an an archetypal iron-oxide copper gold (IOCG) deposit that contains >100 minerals and displays complex, finely intergrown sulphide assemblages (Ehrig et al. 2012). Of these, pyrite makes up ~0.5 wt% of the orebody. There currently exists a significant knowledge gap with respect to the potential presence of 'invisible' Au within pyrite from such IOCG ores, at Olympic Dam and elsewhere. Identification of the physical and chemical state of Au allows new constraints to be placed on ore genesis and also carries implications for mineral processing.

In a first attempt to address this issue, we combine multivariate statistical analyses of LA-ICP-MS trace element datasets for pyrite from Olympic Dam (OD) with micron-scale characterization. Trace element datasets are often presented with a relatively low-level statistical treatment such as two-three component projections accompanied by summary statistics. However, given the ever-increasing size and complexity of LA-ICP-MS datasets, a data-driven, reproducible and quantitative approach is required for processing (Winderbaum et al. 2012). Sixty-seven pyrite grains with measurable Au content were studied from a single polished block representative of a pyrite-chalcopyrite orezone at OD. Pyrite features oscillatory zoning with respect to As(-Co,-Ni) in individual grains (Fig. 1a) and sub-micron-scale inclusions of Bi- and Au-tellurides, among others (Fig. 1b). Gold-tellurides are also found in As-poor pyrite with no visible compositional zoning (Fig. 1c-d). The LA-ICP-MS dataset shows measurable concentrations of Ag, As, Au, Bi, Cd, Co, Cu, Mn, Mo, Ni, Pb, Se, Sn, Sb, Te, Ti, Tl, Th, ^{238}U, W, and Zn (192 spot analyses). Such elements are likely to be present as lattice-bound as well as inclusion within pyrite. Arsenic concentrations attain up to 3 wt%; mean and median values are 0.64 and 0.72 wt%, respectively.

Principal component analysis (PCA) coupled with construction of hierarchical dendrogram were used to depict geochemical associations among trace elements. Two distinct sub-groups are found: (i) Au-bearing (>10 ppm Au); and (ii) Au-poor pyrite (Fig. 1e-g). These sub-groups are clearly distinguished by different geochemical associations (Fig. 1f-g). In group (i), Au correlates strongly with As and Ag, and to a lesser extent, also with Bi, Sb, Cu, Sn and Pb. This confirms that compositionally zoned pyrite is a host for 'invisible' Au. Group (ii) features the element associations Ni-Co, Te-Se, elements that are easily incorporated in the pyrite structure, and other elements likely to occur as discrete mineral inclusions (Ti, Mn, W, Zn, U and Th). Although Bi-telluride inclusions are observed within As-bearing pyrite (Fig. 1b), PCA results show that Te and As are placed within different clusters. Microscopic observations suggest the presence of Te as telluride inclusions and As-poor pyrite. A possible scenario is that Au is essentially lattice-bond in As-bearing pyrite but present as inclusions of Au-bearing tellurides in As-poor pyrite. This hints at different mechanisms and/or conditions of Au incorporation, consistent with the complex evolution of the ores at Olympic Dam including reworking of primary zoning patterns. Further work includes nanoscale characterization of pyrite which will allow improved discrimination of NPs populations and their formation from lattice-bound elements or by other mechanisms. Statistical analysis could

be an important, novel tool to recognise populations of NPs in pyrite relative to well-defined generations and formation mechanisms e.g., exsolutions from solid solution in grains with crystal zoning, or fluid-assisted brecciation leading to pore-attached NPs.

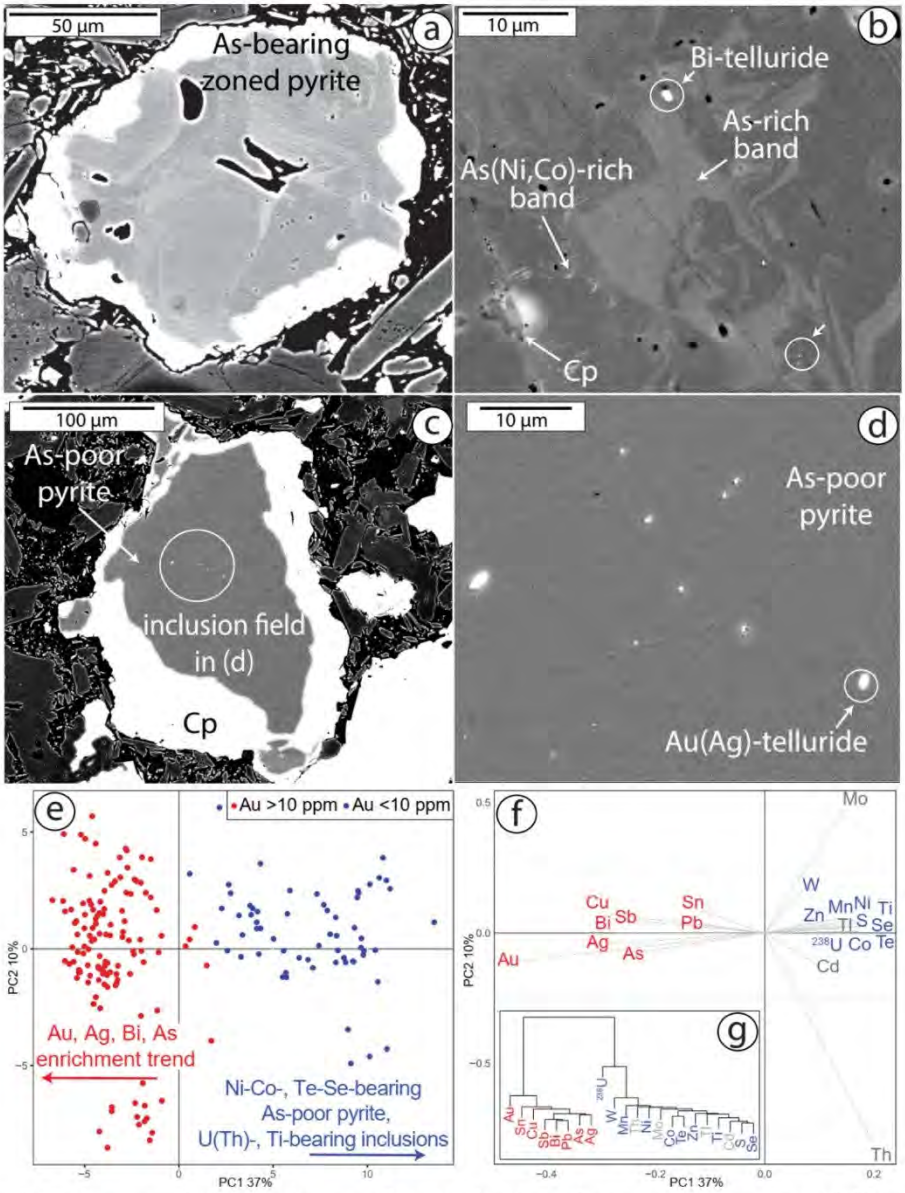

Figure 1. (a-d) Back-scattered electron images of pyrite showing relevant textures as marked. Note presence of sub-micron-sized tellurides. (e) PC scores showing geochemical distinctions among Au-bearing (>10 ppm Au) and Au-poor (<10 ppm Au) pyrite; (f) PC loadings showing geochemical groups associated with distinct pyrite types. Grey colours represent elements with >20% values falling below minimum limits of detection. (g) Hierarchical cluster dendrogram of analysed elements.

References

Ciobanu CL, Cook NJ, Utsunomiya S, Kogagwa M, Green L, Gilbert S, Wade B (2012) Gold-telluride nanoparticles revealed in arsenic-free pyrite, Am. Mineral. 97:1515-1518

Cook NJ, Chryssoulis SL (1990) Concentrations of invisible old in the common sulfides. Can. Mineral. 28: 1-16.

Ehrig K, McPhie J, Kamenetsky V (2012) Geology and mineralogical zonation of the Olympic Dam iron oxide Cu-U-Au-Ag deposit, South Australia. SEG Spec. Publ. 16:237–267

Reich M, Kesler SE, Utsunomiya S, Palenik CS, Chryssoulis SL, Ewing RC (2005) Solubility of gold in arsenian pyrite. Geochim. Cosmochim. Acta 69: 2781-2796

Winderbaum L, Ciobanu CL, Cook NJ, Paul M, Metcalfe A, Gilbert S (2012) Multivariate Analysis of an LA-ICP-MS Trace Element Dataset for Pyrite. Mathem. Geosci. 44: 823-842.

ADDITIONAL MATERIAL HH

CO-AUTHORED CONFERENCE ABSTRACT:

OSCILLATORY GROWTH PATTERNS IN HEMATITE DEFINED BY SI-FE-NANOPRECIPITATES: ORE ENRICHMENT PROCESSES IN BIFS

William Keyser [1], Cristiana L. Ciobanu [1], **Max Verdugo-Ihl** [1],

Nigel J. Cook [1], Ashley Slattery [2], Kathy Ehrig [3]

[1] *School of Chemical Engineering and Advanced Materials, The University of Adelaide, Adelaide SA 5000,*

[2] *Adelaide Microscopy, The University of Adelaide, Adelaide SA 5000, Australia*

[3] *BHP Olympic Dam, Adelaide SA 5000, Australia*

Conference abstract and poster presentation (presented by William Keyser) at TIGeR 2019, Perth, Australia, September 11th-13th.

Oscillatory growth patterns in hematite defined by Si-Fe-nanoprecipitates: ore enrichment processes in BIFs

William Keyser[1], Cristiana L. Ciobanu[1], Max Verdugo-Ihl[1], Nigel J. Cook[1], Ashley Slattery[2], Kathy Ehrig[3]

[1]School of Chemical Engineering and Advanced Materials, The University of Adelaide, Adelaide SA 5000, Australia; william.keyser@adelaide.edu.au; cristiana.ciobanu@adelaide.edu.au; max.verdugo-ihl@adelaide.edu.au; nigel.cook@adelaide.edu.au

[2]Adelaide Microscopy, The University of Adelaide, Adelaide SA 5000, Australia; ashley.slattery@adelaide.edu.au

[3]BHP Olympic Dam, Adelaide SA 5000, Australia; kathy.ehrig@bhp.com

'Silician magnetite' refers to magnetite containing up to several wt.% SiO_2 and is well-known from oscillatory-zoned crystals in a variety of ore types. Nanoscale studies using Z-contrast techniques imaging such as High Angle Annular Dark Field Scanning Transmission Electron Microscopy (HAADF STEM) have shown that the Si-bearing zonation patterns are due to the presence of Si-Fe-nanoprecipitates (NPs) in two different ore types (Xu et al. 2014; Ciobanu et al. 2019). The NPs form crystallographically-oriented strips of n x d_{111} (n=even number) in host magnetite and are considered as γ-$Fe_{1.5}SiO_4$, one of the maghemite-type structures with vacancy ordering, resulting in $P4_332$ symmetry, a subgroup of $Fd3m$ group known for the spinels (Xu et al. 2014). Rounded to sub-euhedral NPs with no detectable structural changes were also found and interpreted as a variant of the same phase but with disordered vacancies (Ciobanu et al. 2019). Hematite, α-Fe_2O_3, is a polymorph of maghemite but with rhombohedral structure. Oscillatory zoned silician hematite (1.8 wt.% SiO_2) was reported from Neoarchean BIF ores at Iron Knight, Middleback Ranges, South Australia (Keyser et al. 2018). The samples display textures indicative of hematite forming from iron-hydroxides, thus implying re-burial of the deposit after supergene enrichment.

Considering that 'silician hematite' is a new discovery, we undertook a nanoscale study to understand: (i) the nature of the Si-bearing zoning in the zoned hematite; and (ii) how this can be used to constrain the model put forward for ore enrichment. The samples were prepared using focused ion beam SEM by cutting across zoning in hematite (Fig. 1A). HAADF STEM imaging and STEM energy-dispersive (EDS) X-ray mapping and spot analysis were performed using a high-resolution, probe-corrected, FEI Titan Themis S/TEM at 200 kV (all instruments are housed at Adelaide Microscopy).

STEM-EDS maps show that the Si-enriched, Fe-depleted, fine-scale bands in hematite display a mottled texture with respect to Si-Fe nanoparticles with rounded to hexagonal morphology (Fig. 1B, C). Chaotic agglomeration of the NPs is observed in areas were the bands are interrupted by microfractures along which discrete SiO_2 inclusions are present and Al is also established as present by mapping, in addition to Si. High-resolution imaging of exposed NPs with hexagonal morphology shows these have atom arrangements different to host hematite viewed on [12-1] zone axis (Fig. 1D). The structure corresponds to [1-10] cubic maghemite (Fig. 1E) as shown for Si-Fe-NPs in magnetite (Ciobanu et al. 2019). Fast Fourier Transform (FFT) patterns obtained show that the NPs are epitaxially related to host hematite. They display satellite reflections indicative of vacancy ordering towards a γ-$Fe_{1.5}SiO_4$ maghemite phase (Fig. 1F, G).

A model for formation of silician hematite from iron-hydroxides can be outlined. The oscillatory zoned texture is inherited from the iron-hydroxides ($Fe^{3+}O(OH)$), which are fine-grained and typically disply concentric banding. Impurities, such as Si and Al, are often part of such aggregates in iron-hydroxides. Upon burial, dewatering and recrystallization of these compounds into hematite leads to formation of Si-Fe-NPs along the bands rich in impurities. During NP coarsening, vacancy ordering in a γ-$Fe_{1.5}SiO_4$ maghemite type structure occurs within the rhombohedral lattice of hematite. The presence of fractures with other impurities, such as Al, or discrete SiO_2 inclusions, is further evidence for the heterogeneity of the initial material compatible with the assumption of a iron-hydroxide protore. Phase transition between goethite and hematite via dehydration was shown in TEM experiments (Watari et al. 1983).

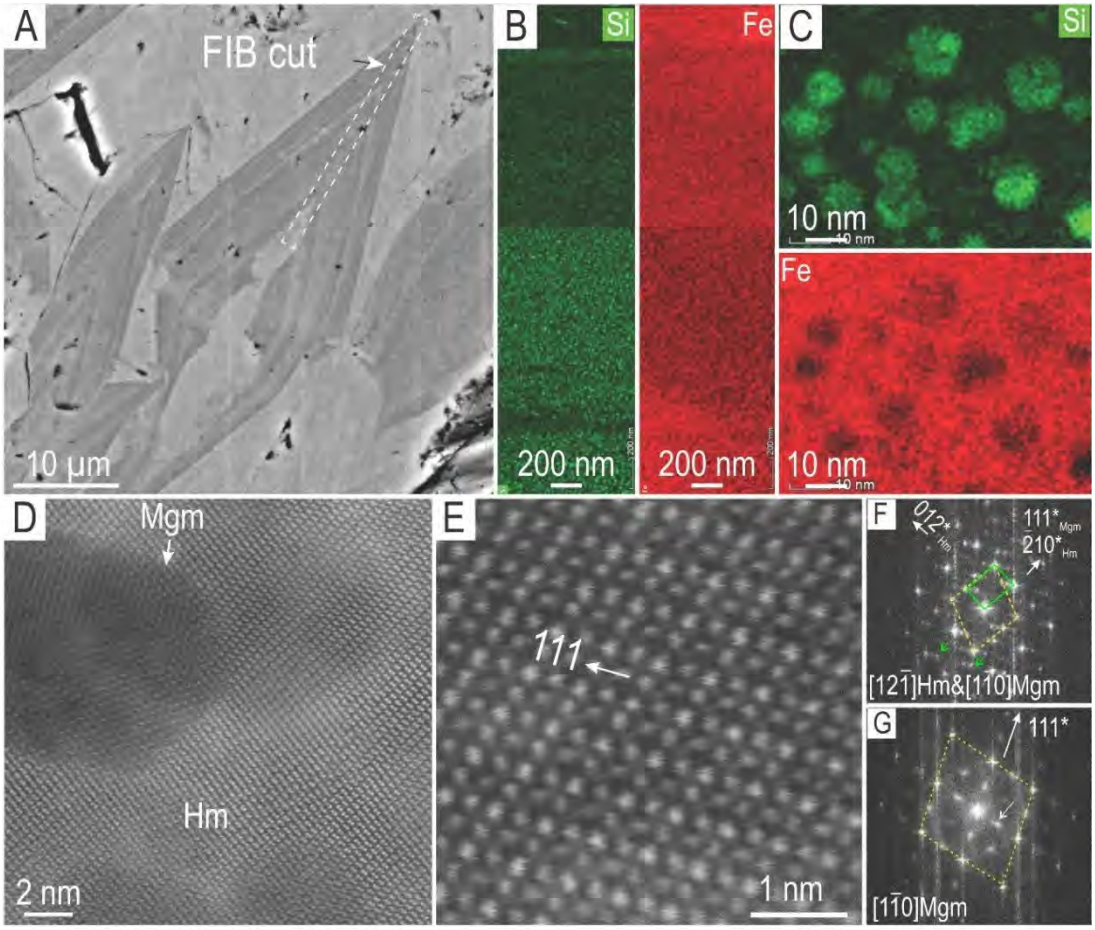

Figure 1. (A) BSE image showing oscillatory-zoned silician hematite. (B, C) STEM-EDS maps of Si and Fe showing banding and the mottled texture formed by Si-Fe NPs. High-resolution images showing a Si-Fe-NP with maghemite (Mgm) structure in hematite (Hm) (D) and detail of Mgm (E). (F, G) FFT from D and E, respectively showing orientation of Hm and Mgm as marked. Satellite reflections arrowed.

Although further work is needed in order to confirm the above interpretations, preliminary findings support a burial/dehydration model for formation of silician hematite, recognized as a 'microplaty type' in BIF ores at Iron Knight (Keyser et al. 2018). This follows a regional extensional event and contemporaneous emplacement of Gairdner dyke swarms at ~800 Ma. The supergene enriched ores underwent a second burial cycle to form an upgraded hematite ore at ~680 Ma (LA-ICP-MS U-Pb dating of hematite; Keyser et al. in review). 'Silician hematite' may thus represent a potential signature for reburial processes leading to enrichment of BIF ores. These findings carry potentially important implications for ore formation due to the common presence of microplaty hematite ores in BIF-hosted iron ore deposits elsewhere.

References

Ciobanu CL, Verdugo-Ihl MR, Slattery S, Cook NJ, Ehrig K, Courtney-Davies L, Wade BP, 2019. Silician magnetite: Si-Fe-nanoprecipitates and other mineral inclusions in magnetite from the Olympic Dam deposit, South Australia. Minerals, *9*, 311.

Keyser W, Ciobanu CL, Cook NJ, Johnson G, Feltus H, Johnson S, Dmitrijeva M, Ehrig K, Nguyen PT, 2018. Petrography and trace element signatures of iron-oxides in deposits from the Middleback Ranges, South Australia: from banded iron formation to ore. Ore Geology Reviews, *93*, 337-360.

Keyser W, Ciobanu CL, Cook NJ, Wade BP, Kennedy A, Kontonikas-Charos A, Ehrig K, Feltus H, Johnson G, in review. Episodic mafic magmatism in the Eyre Peninsula: defining syn- and post-depositional BIF environments for iron deposits in the Middleback Ranges, South Australia. Precambrian Research.

Watari F, Delavignette P, van Landuyt J, Amelinckx S, 1983. Electron Microscopic Study of Dehydration Transformations. Part III: High Resolution Observations of the Reaction Process FeOOH→Fe_2O_3. Journal of Solid State Chemistry, *48*, 49-64.

Xu H, Shen Z, Konishi H, 2014. Si magnetite nano-precipitates in silician magnetite from banded iron formation: Z-contrast imaging and ab initio study. American Mineralogist, *99*, 2196-2202.

ADDITIONAL MATERIAL II

CO-AUTHORED CONFERENCE ABSTRACT:

A MULTIPLATFORM APPROACH TO UNRAVELLING GEOLOGICAL PROBLEMS: A CASE STUDY FROM OLYMPIC DAM, SOUTH AUSTRALIA

Angus K.O. Netting [1], Benjamin P. Wade [1], **Max R. Verdugo-Ihl** [2], Liam Courtney-Davies [2],

Cristiana L. Ciobanu [2], Nigel. J Cook [2], Kathy Ehrig [3],

Ashley Slattery [1], Sarah E. Gilbert [1], Ken Neubauer [1]

[1] Adelaide Microscopy, The University of Adelaide, Adelaide, SA 5005, Australia

[2] School of Chemical Engineering and Advanced Materials, The University of Adelaide, Adelaide, SA 5005, Australia

[3] BHP Olympic Dam, Adelaide, SA 5001, Australia

Published conference abstract and oral presentation (presented by Angus K.O. Netting), Microscopy and Microanalysis 2019, Portland, U.S.A., 4th-8th August, 2019. 25(S2):2432–2433.

2432
doi:10.1017/S1431927619012893
Microsc. Microanal. 25 (Suppl 2), 2019
© Microscopy Society of America 2019

A Multi-platform Microanalysis Approach to Unravelling Geological Problems: a Case Study from Olympic Dam South Australia

Netting A.K.O.*[1], Wade, B.P.[1], Verdugo-Ihl, M.R.[2], Courtney-Davies, L.[2], Ciobanu, C.L.[2], Cook, N.[2], Ehrig, K.[3], Slattery, A.[1], Gilbert, S.[1], Neubauer, K.[1]

1. Adelaide Microscopy, University of Adelaide, Adelaide, Australia.
2. School of Chemical Engineering, University of Adelaide, Adelaide, Australia.
3. BHP Olympic Dam, Adelaide, Australia
* Corresponding author: angus.netting@adelaide.edu.au

The ca. 1.6 Ga iron-oxide-Cu-Au (IOCG) Olympic Dam (OD) deposit in South Australia is considered the archetypal example of IOCG formation. It is the largest known IOCG system on Earth, with a Cu-U-Au-Ag resource in excess of 10 Bt [1]). Like other IOCG systems worldwide, the OD ores record an extended complex formation history that is expressed in a diverse package of preserved mineral assemblages [2]. Pulling apart both the chemical and temporal complexity at the micro/nano scale is key to understanding the evolution of the deposit.

Iron-oxides (dominant hematite α-Fe_2O_3 and subordinate magnetite Fe_3O_4) are the most dominant minerals within the deposit, and the most visible expression of hydrothermal alteration of the host granite. These iron-oxides can be directly related to the mineralizing process thus information contained within them such as chemical composition, crystal structure, and age of formation, provides direct information on the processes responsible for the genesis of the OD IOCG deposit [3,4,5].

Imaging and microanalysis of hematite using complimentary techniques that bridge scales of observation from the millimetre to Angstrom scales, such as FIB-SEM, EPMA, LA-ICP-MS, and HR-TEM, have been used to better understand into the OD deposit. Distinct chemical signatures are found to be preserved at the micro and nanoscale, indicating that whereas some primary iron-oxides are well preserved, others have passed through replacement, reworking, and recrystallization events during multiple cycles of interaction with fluids [3-6].

An example of this complex relationship of preservation vs overprinting is displayed in Figure 1. Primary oscillatory zoned hematite displays embayments of hematite replacement as evidenced by the dark area on the grain in BSE. This overprinting is characterised by decoupling between the granitophile elements W and Sn evident in the LA-ICPMS maps. Selective removal of trace elements can be invoked by evolving redox conditions, resulting in disequilibrium of the fluid involved affecting elements with differences in the stability of cationic oxidation states (Sn^{4+} vs W^{6+}; [5]).

This is further evidenced in HR-TEM images of FIB-SEM foils of overprinted hematite (Figure 2). Overprinted areas display extensive inclusion trails comprising voids, silica bearing nanoparticles, and a range of metallic nanoparticles (W, Cu, As). In addition to this wispy splays of WO_3 (Ferberite) were present. Atomic resolution HAADF-STEM imaging of hematite immediately adjacent inclusion trails show nanodomains of dense twin sets, indicating localised reprecipitation of hematite. Combined with the diverse complex inclusion population, and gross scale elemental zonation in LA-ICPMS maps, a mechanism of *in-situ* combined dissolution reprecipitation reaction (CDRR [7]) is concluded as the primary replacement mechanism for hematite at Olympic Dam.

References
[1] BHP Billiton, 2016. Annual Report 2016.
[2] Hitzman *et al.*, Precambrian Research 58 (1992), p. 241-287.
[3] Ciobanu et al., Precambrian Research 238 (2013), p. 129-147.
[4] Ciobanu et al., 13th SGA Biennial Meeting 2015. Miner. Resour. Sustainable World 3, 1071-1074.
[5] Verdugo-Ihl et al., Ore Geology Reviews 91 (2017), p. 173-195.
[6] Verdugo-Ihl et al., 15th Quadrennial IAGOD, 189-190.
[7] Putnis, Mineralogical Magazine 80 (2002), p. 689-708.

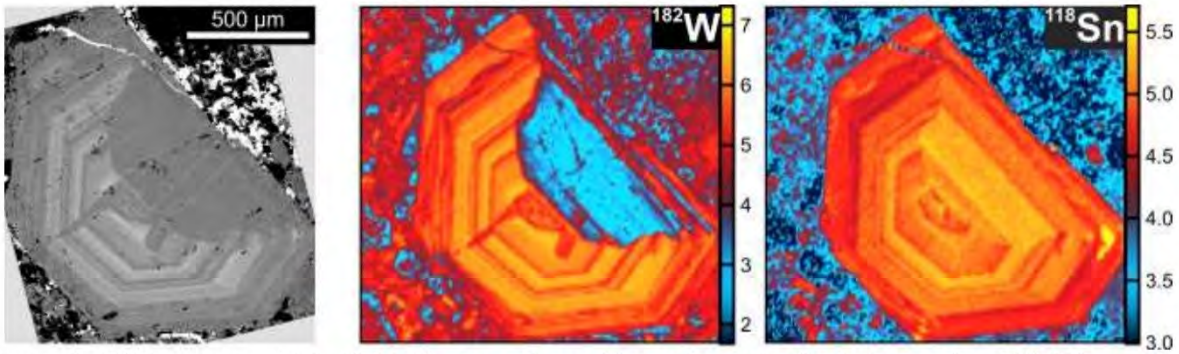

Figure 1. BSE image and LA-ICP-MS maps of zoned hematite grain. Scale in cps (log 10^n) [5]

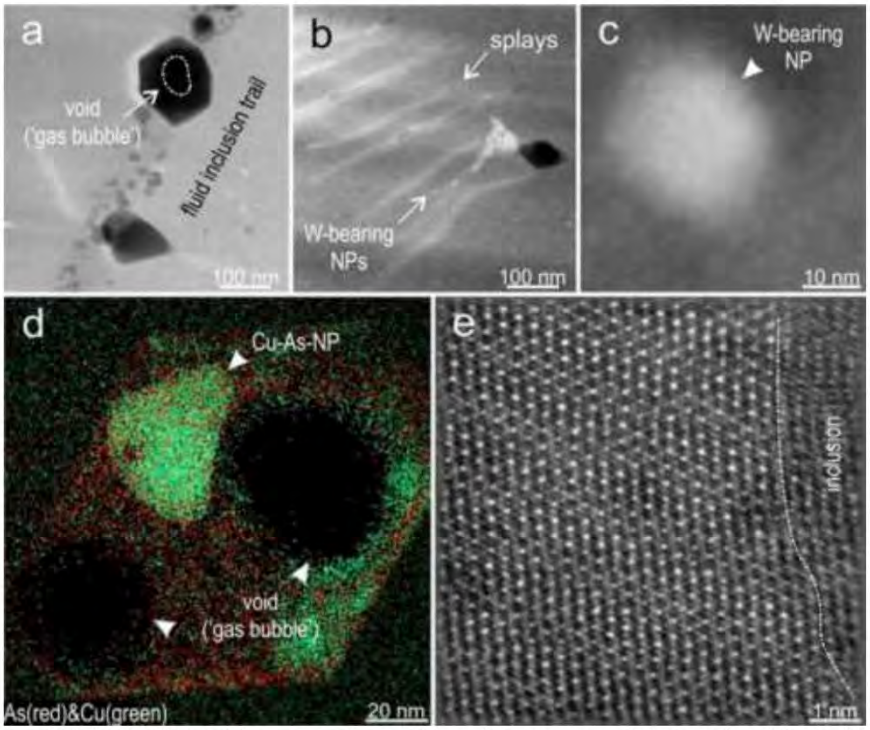

Figure 2. (a-c,e) HAADF-STEM images of metal bearing nanoparticles and voids inside hematite; (d) EDS-STEM map of metal bearing nanoparticle [6]

CHAPTER 11

REFERENCES

CHAPTER 11: REFERENCES

Abakumov, A.M., Batuk, D., Hadermann, J., Rozova, M.G., Sheptyakov, D.V., Tsirlin, A.A., Niermann, D., Waschkowski, F., Hemberger, J., Van Tendeloo, G., Antipov, E.V., 2011. Antiferroelectric $(Pb,Bi)_{1-x}Fe_{1+x}O_{3-y}$ perovskites modulated by crystallographic shear planes. Chemistry of Materials 23(2), 255–265. https://doi.org/10.1021/cm102907h

Abakumov, A.M., Hadermann, J., Bals, S., Nikolaev, I.V., Antipov, E.V., Van Tendeloo, G., 2006. Crystallographic shear structures as a route to anion-deficient perovskites. Angewandte Chemie International Edition 45, 6697–6700. https://doi.org/10.1002/anie.200602480

Abdu, Y.A., Hawthorne, F.C., 2009. Crystal structure and Mössbauer spectroscopy of tschermakite from the Ruby locality at Fiskenaesset, Greenland. Canadian Mineralogist 47, 917–926. https://doi.org/10.3749/canmin.47.4.917

Allen, S.R., McPhie, J., Ferris, G., Simpson, C., 2008. Evolution and architecture of a large felsic Igneous Province in western Laurentia: The 1.6 Ga Gawler Range Volcanics, South Australia. Journal of Volcanology and Geothermal Research 172, 132–147. https://doi.org/10.1016/j.jvolgeores.2005.09.027

Andersen, D.J., Lindsley, D.H., 1985. New (and final!) model for the Ti-magnetite/ilmenite geothermometer and oxygen barometer. Abstract, AGU 1985 Spring Meet. Eos Transactions 66, p. 416.

Apukhtina, O.B., Kamenetsky, V.S., Ehrig, K., Kamenetsky, M.B., Maas, R., Thompson, J., McPhie, J., Ciobanu, C.L., Cook, N.J., 2017. Early, deep magnetite-fluorapatite mineralization at the Olympic Dam Cu-U-Au-Ag deposit, South Australia. Economic Geology 112, 1531–1542. https://doi.org/10.5382/econgeo.2017.4520

Apukhtina, O.B., Kamenetsky, V.S., Ehrig, K., Kamenetsky, M.B., McPhie, J., Maas, R., Meffre, S., Goermann, K., Rodermann, T., Cook, N.J., Ciobanu, C.L., 2016. Postmagmatic magnetite–apatite assemblage in mafic intrusions: A case study of dolerite at Olympic Dam, South Australia. Contributions to Mineralogy and Petrology 171, 2. https://doi:10.1007/s00410-015-1215-7

Arguin, J.-P., Pagé, P., Barnes, S.-J., Girard, R., Duran, C., 2018. An integrated model for ilmenite, Al-spinel, and corundum exsolutions in titanomagnetite from oxide-rich layers of the Lac Doré Complex (Québec, Canada). Minerals 8, 476. https://doi.org/10.3390/min8110476

Arlt, T., Kunz, M., Stolz, J., Armbruster, T., Angel, R.J., 2000. P-T-X data on $P2_1/c$-clinopyroxenes and their displacive phase transitions. Contributions to Mineralogy and Petrology 138, 35–45. https://doi.org/10.1007/PL00007660

Barkov, A.Y., Martin, R.F., Shi, L., LeBarge, W., Fedortchouk, Y., 2008. Oscillatory zoning in stanniferous hematite and associated W- and Bi-rich minerals from Canadian Creek, Yukon, Canada. Canadian Mineralogist 46, 59–72. https://doi.org/10.3749/canmin.46.1.59

Barton, M.D., 2014. Iron Oxide(–Cu–Au–REE–P–Ag–U–Co) Systems, in: Treatise on Geochemistry, Vol. 13. Elsevier, pp. 515–541. https://doi.org/10.1016/B978-0-08-095975-7.01123-2

Bastrakov E.N., Skirrow R.G., Davidson G.J., 2007 Fluid Evolution and Origins of Iron Oxide Cu-Au Prospects in the Olympic Dam District, Gawler Craton, South Australia. Economic Geology 102, 1415–1440. https://doi.org/10.2113/gsecongeo.102.8.1415

Batuk, D., Batuk, M., Abakumov, A.M., Tsirlin, A.A., McCammon, C., Dubrovinsky, L., Hadermann, J., 2013, Effect of lone-electron-pair cations on the orientation of crystallographic shear planes in anion-deficient perovskites. Inorganic Chemistry 52, 10009–10020. https://doi.org/10.1021/ic4012845

Baurier-Aymat, S., Jiménez-Franco, A., Roqué-Rosell, J., González-Jiménez, J.M., Gervilla, F., Proenza, J.A., Mendoza, J., Nieto, F., 2019. Nanoscale Structure of Zoned Laurites from the Ojén Ultramafic Massif, Southern Spain. Minerals 9, 288. https://doi.org/10.3390/min9050288

Benavides, J., Kyser, T.K., Clark, A.H., Oates, C.J., Zamora, R., Tarnovschi, R., Castillo, B., 2007. The Mantoverde Iron Oxide-Copper-Gold District, III Region, Chile: The Role of Regionally Derived, Nonmagmatic Fluids in Chalcopyrite Mineralization. Economic Geology 102, 415–440. https://doi.org/10.2113/gsecongeo.102.3.415

BHP Billiton, 2016. Annual Report 2016. http://www.bhpbilliton.com/~/media/bhp/documents/investors/annual-reports/2016/bhpbillitonannualreport2016.pdf?la=en

Biagioni, C., Pasero, M., 2014. The systematics of the spinel-type minerals: An overview. American Mineralogist 99, 1254–1264. https://doi.org/10.2138/am.2014.4816

Blanchin, M.G., Bursill, L.A., Hutchison, J.L., Gai, P.L., 1981. Direct observation of disorder within crystallographic shear defects in deformed and non-stoichiometric rutiles. Journal de Physique Colloques 42 (Suppl. C3), 95-112. https://doi.org/10.1051/jphyscol:1981310

Blissett, A.H., Creaser, R.A., Daly, S.J., Flint, R.B., Parker, A.J., 1993. Gawler Range Volcanics, in: Drexel, J.F., Preiss, W. V., Parker, A.J. (Eds.), The Geology of South Australia., Vol. 1, The Precambrian, Bulletin 54. Geological Survey of South Australia, pp. 107–124.

Bodnar, R.J., 2003. Reequilibration of fluid inclusions. In Fluid inclusions: Analysis and interpretation, Short Course 32, Samson, I., Anderson, A., Marshal, D., Eds., Mineralogical Association of Canada, Ottawa, pp. 213–230.

Bosi, F., Biagioni, C., Pasero, M., 2019. Nomenclature and classification of the spinel supergroup. European Journal of Mineralogy 31, 183–192. https://doi.org/10.1127/ejm/2019/0031-2788

Boso, M.A., Monaldi, C.R., 2008. Cuenca Silúrico-Devónica y los depósitos ferríferos asociados en la Provincia de Juyjuy, in: XVII Congreso Geológico Argentino, Relatorio 2, pp. 155–165.

Bowles, J.F.W., Howie, R.A., Vaughan, D.J., Zussman, J., 2011. Rock-forming Minerals: Non-Silicates: Oxides, Hydroxides and Sulphides. The Geological Society of London, 920 pp.

Brizi, E., Nazzareni, S., Princivalle, F., Zanazzi, P.F., 2003. Clinopyroxenes from mantle-related xenocrysts in alkaline basalts from Hannuoba (China): augite-pigeonite exsolutions and their thermal significance. Contributions to Mineralogy and Petrology 145, 578–584. https://doi.org/10.1007/s00410-003-0467-9

Broughm, S.G., Hanchar, J.M., Tornos, F., Westhues, A., Attersley, S., 2017. Mineral chemistry of magnetite from magnetite-apatite mineralization and their host rocks: examples from Kiruna, Sweden, and El Laco, Chile. Mineralium Deposita 52, 1223–1244. https://doi.org/10.1007/s00126-017-0718-8

Brugger, J., Liu, W., Etschmann, B., Mei, Y., Sherman, D.M., Testemale, D., 2016. A review of the coordination chemistry of hydrothermal systems, or do coordination changes make ore deposits? Chemical Geology 447, 219–253. https://doi.org/10.1016/j.chemgeo.2016.10.021

Buddington, A.F., Lindsley, D.H., 1964. Iron-titanium oxide minerals and synthetic equivalents. Journal of Petrology 5, 310–357. https://doi.org/10.1093/petrology/5.2.310

Bykova, E., Dubrovinsky, L., Dubrovinskaia, N., Bykov, M., McCammon, C., Ovsyannikov, S.V., Liermann, H.-P., Kupenko, I., Chumakov, A.I., Rüffer, R., Hanfland, M., Prakapenka, V., 2016 Structural complexity of simple Fe_2O_3 at high pressures and temperatures. Nature Communications 7, 10661. https://doi.org/10.1038/ncomms10661

Canil, D., Lacourse, T., 2020. Geothermometry using minor and trace elements in igneous and hydrothermal magnetite. Chemical Geology 541, 119576. https://doi.org/10.1016/j.chemgeo.2020.119576

Champness, P.E., 2002. Applications of Transmission Electron Microscopy. Advances in Imaging and Electron Physics 121, 53–90, https://doi.org/10.1016/S1076-5670(02)80025-8

Chen, T., Jin, Z., Zhang, J., Wang, L., 2019. Calcium amphibole exsolution lamellae in chromite from the Semail ophiolite: Evidence for a high-pressure origin. Lithos 334–335, 273–280. https://doi.org/10.1016/j.lithos.2019.03.020

Chen, Z., Cvelbar, U., Mozetič, M., He, J., Sunkara, M.K., 2008. Long-Range Ordering of Oxygen-Vacancy Planes in α-Fe_2O_3 Nanowires and Nanobelts. Chemistry of Materials 20(9), 3224–3228. https://doi.org/10.1021/cm800288y

Cherry, A.R., Ehrig, K., Kamenetsky, V.S., McPhie, J., Crowley, J.L., Kamenetsky, M.B., 2018. Precise geochronological constraints on the origin, setting and incorporation of ca. 1.59 Ga surficial facies into the Olympic Dam Breccia Complex, South Australia. Precambrian Research 315, 162–178. https://doi.org/10.1016/j.precamres.2018.07.012

Ciancio, R., Vittadini, A., Selloni, A., Aruta, C., Scitti di Uccia, U., Rossi, G., Carlino, E., 2012. Atomic structure and crystallographic shear planes in epitaxial TiO_2 anatase thin films. Microscopie, September 2012, 50–56. https://doi.org/10.4081/microscopie.2012.4985

Ciobanu, C.L., 2015. Trace element signatures in sulfides at Olympic Dam and satellite prospects: a reconnaissance study for ore vectoring using Cu-(Fe)-sulfides in Iron Oxide Copper Gold Deposits. Unpublished Report. The University of Adelaide.

Ciobanu, C.L., Cook, N.J., Utsunomiya, S., Pring, A., Green, L., 2011. Focussed ion beam–transmission electron microscopy applications in ore mineralogy: Bridging micro- and nanoscale observations. Ore Geology Reviews 42, 6–31. https://doi.org/10.1016/j.oregeorev.2011.06.012

Ciobanu, C.L., Cook, N.J., Utsunomiya, S., Kogagwa, M., Green, L., Gilbert, S., Wade, B. 2012. Gold-telluride nanoparticles revealed in arsenic-free pyrite. American Mineralogist 97, 1515–1518. https://doi.org/10.2138/am.2012.4207

Ciobanu, C.L., Wade, B.P., Cook, N.J., Schmidt Mumm, A., Giles, D., 2013. Uranium-bearing hematite from the Olympic Dam Cu–U–Au deposit, South Australia: A geochemical tracer and reconnaissance Pb–Pb geochronometer. Precambrian Research 238, 129–147. https://doi.org/10.1016/j.precamres.2013. 10.007

Ciobanu, C.L., Cook, N.J., Wade, B.P., Ehrig, K., 2014. Ore minerals down to nanoscale: Petrogenetic implications. Acta Geologica Sinica, English Edition 88, 1441–1443. https://doi.org/10.1111/1755-6724.12382_2

Ciobanu, C.L., Cook, N.J., Ehrig, K., Wade, B.P., Kamenetsky, V.S., 2015. Trace Element Signatures in Iron Oxides from the Olympic Dam IOCG Deposit, South Australia. In: 13th SGA Biennial Meeting 2015, Mineral Resources for a Sustainable World, Vol. 3, pp. 1071–1074.

Ciobanu, C.L., Cook, N.J., Ehrig, K., Courtney-Davies, L., Keyser, W., Wade, B.P., Maunders, C., Kamenetsky, V.S., 2016. Towards a suitable natural standard for routine U-Pb dating of iron oxides. Abstract, Australian Earth Sciences Convention, Adelaide.

Ciobanu, C., Cook, N., Maunders, C., Wade, B., Ehrig, K., 2016. Focused Ion Beam and Advanced Electron Microscopy for Minerals: Insights and Outlook from Bismuth Sulphosalts. Minerals 6, 112. https://doi.org/10.3390/min6040112

Ciobanu, C.L., Cook, N.J., Ehrig, K., 2017. Ore minerals down to the nanoscale: Cu-(Fe)-sulphides from the iron oxide copper gold deposit at Olympic Dam, South Australia. Ore Geology Reviews 81, 1218–1235. https://doi.org/10.1016/j.oregeorev.2016.08.015

Ciobanu, C.L., Slattery, A., Verdugo-Ihl, M.R., Courtney-Davies, L., Cook, N.J., Ehrig, K., 2018. Crystal structural modifications in U-rich, oscillatory-zoned hematite. Goldschmidt Conference 2018, Boston, U.S.A., August 12th-17th.

Ciobanu, C.L., Verdugo-Ihl, M.R., Slattery, A., Cook, N.J., Ehrig, K.J., Courtney-Davies L., 2018. Nanoscale study of silician magnetite from IOCG systems: Examples from the Olympic Dam District, South Australia. Proceedings of the 15th Quadrennial IAGOD Symposium, August 28th-31st, Salta, Argentina, pp. 185–186.

Ciobanu, C.L., Verdugo-Ihl, M.R., Slattery, A., Cook, N.J., Ehrig, K., Courtney-Davies, L., Wade, B.P., 2019. Silician Magnetite: Si–Fe-Nanoprecipitates and Other Mineral Inclusions in Magnetite from

the Olympic Dam Deposit, South Australia. Minerals 9(5), 311. https://doi.org/10.3390/min9050311

Conor, C., Raymond, O., Baker, T., Teale, G., Say, P., Lowe, G., 2010. Alteration and mineralisation in the Moonta-Wallaroo Cu–Au mining field region, Olympic Domain, South Australia. In: Porter, T.M. (Ed.), Hydrothermal Iron Oxide Copper–Gold and Related Deposits, Vol. 3, pp. 1–24.

Cook, N.J., Ciobanu, C.L., George, L., Zhu, Z.-Y., Wade, B., Ehrig, K., 2016. Trace Element Analysis of Minerals in Magmatic-Hydrothermal Ores by Laser Ablation Inductively-Coupled Plasma Mass Spectrometry: Approaches and Opportunities. Minerals 6(4), 111. https://doi.org/10.3390/min6040111

Cook, N.J., Ciobanu, C.L., Ehrig, K.J., Slattery, A., Verdugo-Ihl, M.R., Courtney-Davies, L., Gao, W., 2017. Advances and opportunities in ore mineralogy. Minerals 7(12), 233. https://doi.org/10.3390/min7120233

Cook, N.J., Ehrig, K., Ciobanu, C.L., Courtney-Davies, L., Verdugo-Ihl, M.R., Rollog, M., Schmandt, D.S., Owen, N.D., Macmillan, E., Kontonikas-Charos, A., Krneta, S., Dmitrijeva, M., 2018. Why detailed mineralogy is important: understanding evolution of the Olympic Dam iron-oxide-copper-gold system, South Australia. Proceedings of the 15th Quadrennial IAGOD Symposium, August 28th-31st, Salta, Argentina, pp. 371–372.

Courtney-Davies, L., Zhu, Z., Ciobanu, C.L., Wade, B.P., Cook, N.J., Ehrig, K., Cabral, A.R., Kennedy, A., 2016. Matrix-matched iron-oxide laser ablation ICP-MS U-Pb geochronology using mixed solution standards. Minerals 6, 85. https://doi.org/10.3390/min6030085

Courtney-Davies, L., Ciobanu, C.L., Cook, N.J., Verdugo-Ihl, M., Tapster, S.R., Condon, D.J., Kennedy, A.K., Ehrig, K., Wade, W.P., Gilbert, S.E., 2017. Oscillatory-zoned hematite: a reliable U-Pb mineral geochronometer. Goldschmidt Conference 2017, Paris, France, August 13th-18th.

Courtney-Davies, L., Ciobanu, C.L., Tapster, S.R., Cook, N.J., Ehrig, K.J., Kennedy, A.K., Condon, D.J., Verdugo-Ihl, M.R., Wade, B.S., Gilbert, S.E. 2018. The U-Pb systematics of hydrothermal hematite: Insights from the IOCG system at Olympic Dam, South Australia. Proceedings of the 15th Quadrennial IAGOD Symposium, August 28th-31st, Salta, Argentina, pp. 171–172.

Courtney-Davies, L., Richardson, M.W., Gilbert, S.E., Ciobanu, C.L., Verdugo-Ihl, M., Cook, N.J., Ehrig, K., Wade, B.P., 2018. U-Pb doped synthetic reference material for in-situ hematite geochronology. Geoanalysis 2018 Conference, Sydney, Australia, July 10th-14th.

Courtney-Davies, L., Ciobanu, C.L., Richardson, M.W., Prosser, N., Verdugo-Ihl, M.R., Wade, B.P., Gilbert, S.E., Ehrig, K., Cook, N.J., 2019. Synthesis of U-Pb doped hematite using a hydrated ferric oxide approach. Journal of Crystal Growth 513, 48–57. https://doi.org/10.1016/j.jcrysgro.2019.02.053

Courtney-Davies, L., Ciobanu, C.L., Verdugo-Ihl, M., Slattery, A., Cook, N.J., Ehrig, K., 2019. Chloro-hydroxy-zircon nanoprecipitates fingerprint fertility and mineralization potential of granitic magmas. TIGeR Conference 2019, Curtin University, Perth, W.A., Australia, September 11th-13th, pp. 51–52.

Courtney-Davies, L., Ciobanu, C.L., Verdugo-Ihl, M.R., Dmitrijeva, M., Cook, N.J., Ehrig, K., Wade, B.P., 2019. Hematite geochemistry and geochronology resolve genetic and temporal links among iron-oxide copper gold systems, Olympic Dam district, South Australia. Precambrian Research 335, 105480. https://doi.org/10.1016/j.precamres.2019.105480

Courtney-Davies, L., Ciobanu, C.L., Verdugo-Ihl, M.R., Slattery, A., Cook, N.J., Dmitrijeva, M., Keyser, W., Wade, B.P., Dominick, U.I., Ehrig, K., Xu, J., Kontonikas-Charos, A., 2019. Zircon at the nanoscale records metasomatic processes leading to large magmatic-hydrothermal ore deposits. Minerals 9(6), 364. https://doi.org/10.3390/min9060364

Courtney-Davies, L., Tapster, S.R., Ciobanu, C.L., Cook, N.J., Verdugo-Ihl, M.R., Ehrig, K.J., Kennedy, A.K., Gilbert, S.E., Condon, D.J., Wade, B.P., 2019. A multi-technique evaluation of hydrothermal hematite U Pb isotope systematics: Implications for ore deposit geochronology. Chemical Geology 513, 54–72. https://doi.org/10.1016/j.chemgeo.2019.03.005

Courtney-Davies, L., Ciobanu, C.L., Verdugo-Ihl, M.R., Cook, N.J., Ehrig, K., Wade, B.P., Zhu, Z-Y., Kamenetsky, V.S., 2020. ~1760 Ma magnetite-bearing protoliths in the Olympic Dam deposit: Implications for ore genesis and regional metallogeny. Ore Geology Reviews 118, 103337 https://doi.org/10.1016/j.oregeorev.2020.103337

Courtney-Davies, L., Ciobanu, C.L., Tapster, S.R., Cook, N.J., Ehrig, K., Crowley, J.L., Verdugo-Ihl, M.R., Wade, B.P., Condon, D.J., 2020. Opening the Magmatic-Hydrothermal Window: High-Precision U-Pb Geochronology of the Mesoproterozoic Olympic Dam Cu-U-Au-Ag Deposit, South Australia. Economic Geology, in press. https://doi.org/10.5382/econgeo.4772

Cowley, W., Conor, C., Zang, W., 2003. New and revised Proterozoic stratigraphic units on northern Yorke Peninsula. MESA Journal 29, 46–58.

Creaser, R.A., 1989. The geology and petrology of Middle Proterozoic felsic magmatism of the Stuart Shelf, South Australia. Unpublished PhD thesis, La Trobe University.

Creaser, R.A., 1996. Petrogenesis of a Mesoproterozoic quartz latite-granitoid suite from the Roxby Downs area, South Australia. Precambrian Research 79, 371–394. https://doi.org/10.1016/S0301-9268(96)00002-2

Dare, S.A.S., Barnes, S.-J., Beaudoin, G., 2015. Did the massive magnetite "lava flows" of El Laco (Chile) form by magmatic or hydrothermal processes? New constraints from magnetite composition by LA-ICP-MS. Mineralium Deposita 50, 607–617. https://doi.org/10.1007/s00126-014-0560-1

Deditius, A.P., Reich, M., Simon, A.C., Suvorova, A., Knipping, J., Roberts, M.P., Rubanov, S., Dodd, A., Saunders, M. (2018) Nanogeochemistry of hydrothermal magnetite. Contributions to Mineralogy and Petrology 173, 46. https://doi.org/10.1007/s00410-018-1474-1

Dmitrijeva, M., Ciobanu, C.L., Metcalfe, A.V., Cook, N.J., Verdugo-Ihl, M.R., Keyser, W., Ehrig, K., 2017. Multivariate statistical analyses of LA-ICP-MS trace element data for iron-oxides: examples from genetically distinct ore deposits from South Australia. 18th International Association for Mathematical Geosciences Conference 2017, Perth, Australia, September 2nd-9th, p. 110.

Dmitrijeva, M., Metcalfe, A.V., Ciobanu, C.L., Cook, N.J., Verdugo-Ihl, M.R., Keyser, W.M., Ehrig, K., 2017. Copula Functions as A Tool for Statistical Modelling of Trace Element Signatures in Iron-Oxides: Examples from South Australian Ore Deposits. International Association of Mathematical Geosciences, Perth, Australia, September 2nd-9th., p. 207.

Dmitrijeva, M., Ehrig, K.J., Ciobanu, C.L., Cook, N.J., Verdugo-Ihl, M.R., Metcalfe, A.V., 2018. Defining IOCG signatures through compositional data analysis: a case study of lithogeochemical zoning at Olympic Dam, South Australia. Proceedings of the 15th Quadrennial IAGOD Symposium, August 28th-31st, Salta, Argentina, pp. 246–247.

Dmitrijeva, M., Metcalfe, A.V., Ciobanu, C.L., Cook, N.J., Frenzel, M., Keyser, W.M., Johnson, G., Ehrig, K., 2018. Discrimination and variance structure of trace element signatures in Fe-oxides: A case study of BIF-mineralisation from the Middleback Ranges, South Australia. Mathematical Geosciences 50, 381–415. https://doi.org/10.1007/s11004-018-9734-1

Dmitrijeva, M., Ciobanu, C.L., Ehrig, K.J., Cook, N.J., Metcalfe, A. V., Verdugo-Ihl, M.R., McPhie, J., 2019. Mineralization-alteration footprints in the Olympic Dam IOCG district, South Australia: The Acropolis prospect. Journal Geochemical Exploration 205, 106333. https://doi.org/10.1016/j.gexplo.2019.106333

Dmitrijeva, M., Ciobanu, C.L., Ehrig, K.J., Metcalfe, A. V., Verdugo-Ihl, M.R., McPhie, J., Cook, N.J., 2019. Mineralization signatures of the magnetite-dominant Acropolis prospect, Olympic Dam IOCG district, South Australia. ASEG Extended Abstracts 2019, 1–5. https://doi.org/10.1080/22020586.2019.12073050

Dmitrijeva, M., Ehrig, K.J., Ciobanu, C.L., Cook, N.J., Verdugo-Ihl, M.R., Metcalfe, A.V., 2019. Defining IOCG signatures through compositional data analysis: A case study of lithogeochemical zoning from the Olympic Dam deposit, South Australia. Ore Geology Reviews 105, 86–101. https://doi.org/10.1016/j.oregeorev.2018.12.013

Dmitrijeva, M., Verdugo-Ihl, M.R., Ehrig, K.J., Ciobanu, C.L., Cook, N.J., 2019. 'Invisible' Au in pyrite from Olympic Dam deposit, South Australia: bridging textures with statistical analyses TIGeR Conference 2019, Curtin University, Perth, W.A., Australia, September 11th-13th, pp. 52–53.

Donovan, J.J., Singer, J.W., Armstrong, J.T., 2016. A new EPMA method for fast trace element analysis in simple matrices. American Mineralogist 101, 1839–1853. https://doi.org/10.2138/am-2016-5628

Duff, M.C., Coughlin, J.U., Hunter, D.B., 2002. Uranium co-precipitation with iron oxide minerals. Geochimica et Cosmochimica Acta 66, 3533–3547. https://doi.org/10.1016/S0016-7037(02)00953-5

Dupuis, C., Beaudoin, G., 2011. Discriminant diagrams for iron oxide trace element fingerprinting of mineral deposit types. Mineralium Deposita 46, 319–335. https://doi.org/10.1007/s00126-011-0334-y

Edmonds, M., Brett, A., Herd, R.A., Humphreys, M.C.S., Woods, A., 2015. Magnetite-bubble aggregates at mixing interfaces in andesite magma bodies. Geological Society of London, Special Publication 410, 95–121. https://doi.org/10.1144/SP410.7

Ehrig, K., McPhie, J., Kamenetsky, V., 2012. Geology and Mineralogical Zonation of the Olympic Dam Iron Oxide Cu-U-Au-Ag Deposit, South Australia, in: Hedenquist, J.W., Harris, M., Camus, F. (Eds.), Geology and Genesis of Major Copper Deposits and Districts of the World: A Tribute to Richard H. Sillitoe, Society of Economic Geologists, Special Publication 16, pp. 237–267. https://doi.org/10.5382/SP.16.11

Ehrig, K., Kamenetsky, V.S., McPhie, J., Apukhtina, O., Ciobanu, C.L., Cook, N.J., Kontonikas-Charos, A., Krneta, S., 2017. The IOCG-IOA Olympic Dam Cu-U-Au-Ag deposit and nearby prospects, South Australia. Proceedings, 14th SGA Biennial Meeting 2017, Mineral Resources to Discover, pp. 823–826.

Ehrig, K., Kamenetsky, V.S., McPhie, J., Cook, N.J., Ciobanu, C.L., 2017. Olympic Dam iron oxide Cu-U-Au-Ag deposit, in: Phillips, G.N. (Ed.), Australian Ore Deposits, The Australasian Institute of Mining and Metallurgy, Melbourne, pp. 601–610.

Fanning, C.M., Flint, R.B., Parker, A.J., Ludwig, K.R., Blissett, A.H., 1988. Refined Proterozoic evolution of the Gawler Craton, South Australia, through U-Pb zircon geochronology. Precambrian Research 40–41, 363–386. https://doi.org/10.1016/0301-9268(88)90076-9

Ferracutti, G.R., Gargiulo, M.F., Ganuza, M.L., Bjerg, E.A., Castro, S.M., 2015. Determination of the spinel group end-members based on electron microprobe analyses. Mineralogy and Petrology 109, 153–160. https://doi.org/10.1007/s00710-014-0363-1

Fleet, M.E., Bilcox, G.A., Barnett, R.L., 1980. Oriented magnetite inclusions in pyroxenes from the Grenville Province. Canadian Mineralogist 18, 89–99.

Frietsch, R., 1978. On the magmatic origin of iron ores of the Kiruna type. Economic Geology 73, 478–485. https://doi.org/10.2113/gsecongeo.73.4.478

Frost, B.R., 1991. Introduction to oxygen fugacity and its petrologic importance, in: Lindsley, D.H. (Ed.), Oxide Minerals. De Gruyter, Berlin, Boston, pp. 1–10. https://doi.org/10.1515/9781501508684-004

Frutos, J., Oyarzún, J., 1975. Tectonic and geochemical evidence concerning the genesis of El Laco magnetite lava flow deposits, Chile. Economic Geology 70, 988–990. https://doi.org/10.2113/gsecongeo.70.5.988

Fougerouse, D., Kirkland, C., Saxey, D., Seydoux-Guillaume, A.-M., Rowles, M.R., Rickard, W.D., Reddy, S.M., 2020. Nanoscale Isotopic Dating of Monazite. Geostandards and Geoanalytical Research. https://doi.org/10.1111/ggr.12340

Gao, W., Ciobanu, C.L., Cook, N.J., Huang, F., Meng, L., Gao, S., 2017. Petrography and trace element signatures in silicates and Fe–Ti oxides from the Lanjiahuoshan deposit, Panzhihua layered intrusion, Southwest China. Lithos 294–295, 164–183. https://doi.org/10.1016/j.lithos.2017.10.003

Gao, W., Ciobanu, C.L., Cook, N.J., Slattery, A., Huang, F., Song, D., 2019. Nanoscale study of titanomagnetite from the Panzhihua Layered Intrusion, Southwest China: Multistage exsolutions record ore formation. Minerals 9, 513. https://doi.org/10.3390/min9090513

Gao, W., Ciobanu, C.L., Cook, N.J., Slattery, A., Huang, F., Wang, D., 2019. Nanoscale study of lamellar exsolutions in clinopyroxene from olivine gabbro: Recording crystallization sequences in iron-rich layered intrusions. American Mineralogist 104, 244–261. https://doi.org/10.2138/am-2019-6764

Gelcich, S., Davis, D.W., Spooner, E.T.C., 2005. Testing the apatite-magnetite geochronometer: U-Pb and 40Ar/39Ar geochronology of plutonic rocks, massive magnetite-apatite tabular bodies, and IOCG mineralization in Northern Chile. Geochimica et Cosmochimica Acta 69, 3367–3384. https://doi.org/10.1016/j.gca.2004.12.020

Gelcich, S.H., Davis, D.W., Spooner, E.T.C., 2003. New U-Pb ages for host rocks, mineralization and alteration of iron oxide (Cu-Au) deposits in the Coastal cordillera of Northern Chile, in: IV South American Symposium on Isotope Geology, August 24th-27th. Salvador, Brazil, pp. 63–66.

Gotić, M., Dražić, G., Musić, S.,2011. Hydrothermal synthesis of α-Fe_2O_3 nanorings with the help of divalent metal cations, Mn^{2+}, Cu^{2+}, Zn^{2+} and Ni^{2+}. Journal of Molecular Structure 993, 167–176. https://doi.org/10.1016/j.molstruc.2010.12.063

Groves, D.I., Bierlein, F.P., Meinert, L.D., Hitzman, M.W., 2010. Iron Oxide Copper-Gold (IOCG) Deposits through Earth History: Implications for Origin, Lithospheric Setting, and Distinction from Other Epigenetic Iron Oxide Deposits. Economic Geology 105, 641–654. https://doi.org/10.2113/gsecongeo.105.3.641

Halkoaho, T., Ahven, M., Rämö, O.T., Hokka, J., Huhma, H., 2020. Petrography, geochemistry, and geochronology of the Sc-enriched Kiviniemi ferrodiorite intrusion, eastern Finland. Mineralium Deposita, in press. https://doi.org/10.1007/s00126-020-00952-2

Hannington, M., Garbe-Schönberg, D., 2019. Detection of Gold Nanoparticles in Hydrothermal Fluids. Economic Geology 114, 397–400. http://dx.doi.org/10.5382/econgeo.2019.4636

Hawthorne, F.C., Della Ventura, G., Oberti, R., Robert, J.-L., Iezzi, G., 2005. Short-range order in minerals: Amphiboles. Canadian Mineralogist 43, 1895–1920. https://doi.org/10.2113/gscanmin.43.6.1895

Hawthorne, F.C., Oberti, R., Harlow, G.E., Maresch, W.V., Martin, R.F., Schumacher, J.C., Welch, M.D., 2012. Nomenclature of the amphibole supergroup. American Mineralogist 97, 2031–2048. https://doi.org/10.2138/am.2012.4276

Haynes, D.W., Cross, K.C., Bills, R.T., Reed, M.H., 1995. Olympic Dam ore genesis: a fluid-mixing model. Economic Geology 90, 281–307. https://doi.org/10.2113/gsecongeo.90.2.281

Henríquez, F., Martin, R.F., 1978. Crystal-growth textures in magnetite flows and feeder dykes, El Laco, Chile. Canadian Mineralogist 16, 581–589.

Hitzman, M.W., 2000. Iron-oxide-Cu-Au deposits: What, where, when, and why. In: Porter TM (ed) Hydrothermal Iron Oxide Copper-Gold & Related Deposits: A Global Perspective. PGC Publishing, Adelaide, pp. 9–25.

Hitzman, M.W., Oreskes, N., Einaudi, M.T., 1992. Geological characteristics and tectonic setting of Proterozoic iron oxide (Cu-U-Au-REE) deposits. Precambrian Research 58, 241–287. https://doi.org/10.1016/0301-9268(92)90121-4

Hou, T., Charlier, B., Namur, O., Holtz, F., Veksler, I., Zhang, Z., Thomas, R., 2018. Immiscible hydrous Fe–Ca–P melt and the origin of iron oxide-apatite ore deposits. Nature Communications 9, 1–8. https://doi.org/10.1038/s41467-018-03761-4

Hu, H., Li, J., Harlov, D.E., Lentz, D.R., McFarlane, C.R.M., Yang, Y.-H., 2019. A genetic link between iron oxide-apatite and iron skarn mineralization in the Jinniu volcanic basin, Daye district, eastern China: Evidence from magnetite geochemistry and multi-mineral U-Pb geochronology. Geological Society of America Bulletin, 1–19. https://doi.org/10.1130/B35180.1

Huang, Q., Kamenetsky, V.S., McPhie, J., Ehrig, K., Meffre, S., Maas, R., Thompson, J., Kamenetsky, M., Chambefort, I., Apukhtina, O., Hu, Y., 2015. Neoproterozoic (ca. 820–830Ma) mafic dykes at Olympic Dam, South Australia: Links with the Gairdner Large Igneous Province. Precambrian Research 271, 160–172. https://doi.org/10.1016/j.precamres.2015.10.001

Huang, Q., Kamenetsky, V.S., Ehrig, K., McPhie, J., Kamenetsky, M., Cross, K., Meffre, S., Agangi, A., Chambefort, I., Direen, N.G., Maas, R., Apukhtina, O., 2016. Olivine-phyric basalt in the Mesoproterozoic Gawler silicic large igneous province, South Australia: Examples at the Olympic Dam Iron Oxide Cu–U–Au–Ag deposit and other localities. Precambrian Research 281, 185–199. https://doi.org/10.1016/j.precamres.2016.05.019

Huberty, J.M., Konishi, H., Heck, P.R., Fournelle, J.H., Valley, J.W., Xu, H., 2012. Silician magnetite from the Dales Gorge Member of the Brockman Iron Formation, Hamersley Group, Western Australia. American Mineralogist 97, 26–37. https://doi.org/10.2138/am.2012.3864

Ismail, R., Ciobanu, C.L., Cook, N.J., Teale, G.S., Giles, D., Schmidt Mumm, A.S., Wade, B., 2014. Rare earths and other trace elements in minerals from skarn assemblages, Hillside iron oxide–copper–gold deposit, Yorke Peninsula, South Australia. Lithos 184–187, 456–477. https://doi.org/10.1016/j.lithos. 2013.07.023

Jagodzinski, E.A., 2005. Compilation of SHRIMP U-Pb geochronological data Olympic Domain, Gawler Craton, South Australia, 2001–2003. Geoscience Australia Record 2005/20, 211 pp.

Jagodzinski, E.A., 2014 The Age of Magmatic and Hydrothermal Zircon at Olympic Dam. In Proceedings of 2014 Australian Earth Sciences Convention (AESC), Sustainable Australia, Newcastle, NSW, Australia, 7–10 July 2014, Vol. 110, p. 260.

Johnson, J.P., McCulloch, M.T., 1995. Sources of mineralising fluids for the Olympic Dam deposit (South Australia): Sm-Nd isotopic constraints. Chemical Geology 121, 177–199. https://doi.org/10.1016/0009-2541(94)00125-R

Junge, M., Wirth, R., Oberthür, T., Melcher, F., Schreiber, A. 2015. Mineralogical siting of platinum-group elements in pentlandite from the Bushveld Complex, South Africa. Mineralium Deposita 50, 41–54. https://doi.org/10.1007/s00126-014-0561-0

Karkhanavala, M.D., 1958. On radioactive uraniferous iron oxides. Geochimica et Cosmochimica Acta 15, 229–236. https://doi.org/10.1016/0016-7037(58)90060-7

Keller, T., Hanchar, J., Tornos, F., Suckale, J., 2019. Formation of the El Laco magmatic magnetite deposits by Fe-Si melt immiscibility and bubbly suspension flow along volcano tectonic faults. AGU 2018 Fall Meeting, Washington, DC. https://doi.org/10.1002/essoar.10500353.1

Kerisit, S., Felmy, A.R., Ilton, E.S., 2011. Atomistic Simulations of Uranium Incorporation into Iron (Hydr)Oxides. Environmental Science & Technology 45, 2770–2776. https://doi.org/10.1021/es1037639

Keyser, W.M., Ciobanu C.L., Cook, N.J., Courtney-Davies L., Ehrig K., Gilbert S., McPhie, J., 2017. Links between sedimentary protoliths and IOCG-skarn alteration, Island Dam, South Australia. Extended abstract, 14th Biennial SGA Conference, Québec, Canada, Vol. 3, pp. 935–938.

Keyser, W., Ciobanu, C.L., Cook, N.J., Johnson, G., Feltus, H., Johnson, S., Dmitrijeva, M., Ehrig, K., Nguyen, P.T., 2018. Petrography and trace element signatures of iron-oxides in deposits from the Middleback Ranges, South Australia: From banded iron formation to ore. Ore Geology Reviews 93, 337–360. https://doi.org/10.1016/j.oregeorev.2018.01.006

Keyser, W., Ciobanu, C.L., Cook, N.J., Dmitrijeva, M., Courtney-Davies, L., Feltus, H., Gilbert, S., Johnson, G., Ehrig, K., 2019. Iron-oxides constrain BIF evolution in terranes with protracted geological histories: The Iron Count prospect, Middleback Ranges, South Australia. Lithos 324–325, 20–38. https://doi.org/10.1016/j.lithos.2018.10.035

Keyser, W., Ciobanu, C.L., Cook, N.J., Feltus, H., Johnson, G., Slattery, A., Wade, B.P., Ehrig, K., 2019. Mineralogy of Zirconium in Iron-Oxides: A Micron- to Nanoscale Study of Hematite Ore from Peculiar Knob, South Australia. Minerals 9, 244. https://doi.org/10.3390/min9040244

Keyser, W., Ciobanu, C.L., Verdugo-Ihl, M., Cook, N.J., Slattery, A., Ehrig, K., 2019. Oscillatory growth patterns in hematite defined by Si-Fe- nanoprecipitates: ore enrichment processes in BIFs. TIGeR Conference 2019, Curtin University, Perth, W.A., Australia, September 11th-13th, pp. 54–55.

Knauss, K.G., Dibley, M.J., Bourcier, W.L., Shaw, H.F., 2001. Ti(IV) hydrolysis constants derived from rutile solubility measurements made from 100 to 300°C. Applied Geochemistry 16, 1115–1128. https://doi.org/10.1016/S0883-2927(00)00081-0

Knipping, J.L., Bilenker, L.D., Simon, A.C., Reich, M., Barra, F., Deditius, A.P., Lundstrom, C., Bindeman, I., Munizaga, R., 2015. Giant Kiruna-type deposits form by efficient flotation of magmatic magnetite suspensions. Geology 43, 591–594. https://doi.org/10.1130/G36650.1

Knipping, J.L., Bilenker, L.D., Simon, A.C., Reich, M., Barra, F., Deditius, A.P., Wälle, M., Heinrich, C.A., Holtz, F., Munizaga, R., 2015. Trace elements in magnetite from massive iron oxide-apatite deposits indicate a combined formation by igneous and magmatic-hydrothermal processes. Geochimica et Cosmochimica Acta 171, 15–38. https://doi.org/10.1016/j.gca. 2015.08.010

Knipping, J.L., Fiege, A., Simon, A.C., Oeser, M., Reich, M., Bilenker, L.D., 2019. In-situ iron isotope analyses reveal igneous and magmatic-hydrothermal growth of magnetite at the Los Colorados Kiruna-type iron oxide-apatite deposit, Chile. American Mineralogist 104, 471–484. https://doi.org/10.2138/am-2019-6623

Knipping, J.L., Webster, J.D., Simon, A.C., Holtz, F., 2019. Accumulation of magnetite by flotation on bubbles during decompression of silicate magma. Scientific Reports 9, 3852. https://doi.org/10.1038/s41598-019-40376-1

Kontonikas-Charos, A., Ciobanu, C.L., Cook, N.J., 2014. Albitization and redistribution of REE and Y in IOCG systems: Insights from Moonta-Wallaroo, Yorke Peninsula, South Australia. Lithos 208–209, 178–201. https://doi.org/10.1016/j.lithos.2014.09.001

Kontonikas-Charos, A., Ciobanu, C.L., Cook, N.J., Ehrig, K., Ismail, R., Krneta, S., Basak, A., 2017. Feldspar mineralogy and rare earth element (re)mobilization in iron-oxide copper gold systems from South Australia: a nanoscale study. Mineralogical Magazine 82(S1), S173–S197. https://doi.org/10.1180/minmag.2017. 081.040

Kontonikas-Charos, A., Ciobanu, C.L., Cook, N.J., Ehrig, K., Krneta, S., Kamenetsky, V.S., 2017. Feldspar evolution in the Roxby Downs Granite, host to Fe-oxide Cu-Au-(U) mineralisation at Olympic Dam, South Australia. Ore Geology Reviews 80, 838–859. https://doi.org/10.1016/j.oregeorev.2016.08.019

Kreissl, S., Bolanz, R., Göttlicher, J., Steininger, R., Tarassov, M., Markl, G., 2016. Structural incorporation of W^{6+} into hematite and goethite: A combined study of natural and synthetic iron oxides developed from precursor ferrihydrite and the preservation of ancient fluid compositions in hematite. American Mineralogist 101, 2701–2715. https://doi.org/10.2138/am-2016-5690

Krneta, S., Ciobanu, C.L., Cook, N.J., Ehrig, K., Kontonikas-Charos, A., 2016. Apatite at Olympic Dam, South Australia: A petrogenetic tool. Lithos 262, 470–485. https://doi.org/10.1016/j.lithos.2016.07.033

Krneta, S., Ciobanu, C.L., Cook, N.J., Ehrig, K., Kontonikas-Charos, A., 2017. Rare Earth Element Behaviour in Apatite from the Olympic Dam Cu–U–Au–Ag Deposit, South Australia. Minerals 7(8), 135. https://doi:10.3390/min7080135

Krneta, S., Cook, N.J., Ciobanu, C.L., Ehrig, K., Kontonikas-Charos, A., 2017. The Wirrda Well and Acropolis prospects, Gawler Craton, South Australia: Insights into evolving fluid conditions through apatite chemistry. Journal of Geochemical Exploration 181, 276–291. https://doi.org/10.1016/j.gexplo.2017.08.004

Krneta, S., Ciobanu, C., Cook, N., Ehrig, K., 2018. Numerical modeling of REE fractionation patterns in fluorapatite from the Olympic Dam deposit (South Australia). Minerals 8, 342. https://doi.org/10.3390/min8080342

Kusiak, M.A., Whitehouse, M.J., Wilde, S.A., Wilde, S.A., Nemchin, A.A., Clark, C., 2013. Mobilization of radiogenic Pb in zircon revealed by ion imaging: Implications for early Earth geochronology. Geology 41, 291–294. https://doi.org/10.1130/G33920.1

Kusiak M.A., Dunkley D.J., Wirth R., Whitehouse M.J., Wilde S., Marquardt K., 2015. Metallic lead nanospheres discovered in ancient zircons. Proceedings of the National Academy of Science 112, 4958–4963. https://doi.org/10.1073/pnas.1415264112

Kusiak, M.A., Kovaleva, E., Wirth, R., Klötzli, U., Dunkley, D.J., Yi, K., Lee, S., 2019. Lead oxide nanospheres in seismically deformed zircon grains. Geochimica et Cosmochimica Acta 262, 20–30. https://doi.org/.1016/j.gca.2019.07.026

Lanari, P., Vidal, O., De Andrade, V., Dubacq, B., Lewin, E., Grosch, E.G., Schwartz, S., 2014. XMapTools: A MATLAB©-based program for electron microprobe X-ray image processing and geothermobarometry. Computers & Geosciences 62, 227–240. https://doi.org/10.1016/j.cageo.2013.08.010

Lanari, P., Vho, A., Bovay, T., Airaghi, L., Centrella, S., 2019. Quantitative compositional mapping of mineral phases by electron probe micro-analyser. Geological Society of London, Special Publication 478, 39–63. https://doi.org/10.1144/SP478.4

Lattard, D., 1995. Experimental evidence for the exsolution of ilmenite from titaniferous spinel. American Mineralogist 80, 968–981. https://doi.org/10.2138/am-1995-9-1013

Lee, S., Xu, H., 2016. Size-dependent phase map and phase transformation kinetics for nanometric iron(III) oxides ($\gamma \rightarrow \varepsilon \rightarrow \alpha$ pathway). The Journal of Physical Chemistry C 120, 13316–13322. https://doi.org/10.1021/acs.jpcc.6b05287

Léger, A., Ferry, J.M., 1991. Highly aluminous hornblende from low-pressure metacarbonates and a preliminary thermodynamic model for the Al content of calcic amphibole. American Mineralogist 76, 1002–1017.

Lepage, L.D., 2003. ILMAT: an Excel worksheet for ilmenite–magnetite geothermometry and geobarometry. Computers & Geosciences 29, 673–678. https://doi.org/10.1016/S0098-3004(03)00042-6

L'Heureux, I., Katsev, S., 2006. Oscillatory zoning in a $(Ba,Sr)SO_4$ solid solution: macroscopic and cellular automata models. Chemical Geology 225(3) 230-243. https://doi.org/10.1016/j.chemgeo.2005.08.017

Li, W., Huberty, J.M., Beard, B.L., Kita, N.T., Valley, J.W., Johnson, C.M., 2013. Contrasting behavior of oxygen and iron isotopes in banded iron formations revealed by in situ isotopic analysis. Earth and Planetary Science Letters 384, 132–143. https://doi.org/10.1016/j.epsl.2013.10.014

Lindsley, D.H., 1973. Delimitation of the Hematite-Ilmenite Miscibility Gap. Geological Society of America Bulletin 84, 657. https://doi.org/10.1130/0016-7606(1973)84<657:DOTHMG>2.0.CO;2

Lindsley, D.H., Spencer, K.J., 1982. Fe–Ti oxide geothermometry: Reducing analyses of coexisting Ti-magnetite (Mt) and ilmenite (Ilm). Transactions, American Geophysical Union 63, 471.

Liu, Y., Ciobanu, C.L., 2016. Crystal-structural and nanoscale characterization of iron oxides from the Olympic Dam Cu-U-Au-Ag deposit, South Australia. Unpublished Research Report, The University of Adelaide.

Locock, A.J., 2014. An Excel spreadsheet to classify chemical analyses of amphiboles following the IMA2012 recommendations. Computers & Geosciences 62, 1–11. https://doi.org/10.1016/j.cageo.2013.09.011

Lüders, V., Romer, R.L., Cabral, A.R., Schmidt, C., Banks, D.A., Schneider, J., 2005. Genesis of itabirite-hosted Au–Pd–Pt-bearing hematite-(quartz) veins, Quadrilátero Ferrífero, Minas Gerais, Brazil: constraints from fluid inclusion infrared microthermometry, bulk crush-leach analysis and U–Pb systematics. Mineralium Deposita 40, 289–306. https://doi.org/10.1007/s00126-005-0024-8

Lund, C.R.F., Dumesic, J.A., 1981. Strong oxide-oxide interactions in silica-supported magnetite catalysts. 1. X-ray diffraction and Mössbauer spectroscopy evidence for interaction. The Journal of Physical Chemistry A 85, 3175–3180. https://doi.org/10.1021/j150621a034

Lyon, I.C., Kusiak, M.A., Wirth, R., Whitehouse, M.J., Dunkley, D.J., Wilde, S.A., Schaumlöffel, D., Malherbe, J., Moore, K.L., 2019. Pb nanospheres in ancient zircon yield model ages for zircon formation and Pb mobilization. Scientific Reports, 9, 13702. https://doi.org/10.1038/s41598-019-49882-8

Macmillan, E., Ciobanu, C.L., Ehrig, K., Cook, N.J., Pring, A., 2016. Chemical zoning and lattice distortion in uraninite from Olympic Dam, South Australia. American Mineralogist 101, 2351–2354. https://doi.org/10.2138/am-2016-5753

Macmillan, E., Ciobanu, C.L., Ehrig, K., Cook, N.J., Pring, A., 2016. Replacement of uraninite by bornite via coupled dissolution-reprecipitation: Evidence from texture and microstructure. Canadian Mineralogist 54, 1369–1383. https://doi.org/10.3749/canmin.1600031

Macmillan, E., Cook, N.J., Ehrig, K., Ciobanu, C.L., Pring, A., 2016. Uraninite from the Olympic Dam IOCG-U-Ag deposit: Linking textural and compositional variation to temporal evolution. American Mineralogist 101, 1295–1320. https://doi.org/10.2138/am-2016-5411

Maslen E.N., Streltsov V.A., Streltsova N.R., Ishizawa N., 1994. Synchrotron X-ray study of the electron density in alpha-Fe_2O_3. Acta Crystallographica B 50, 435–441. https://doi.org/10.1107/S0108768194002284

Mathur, R., Marschik, R., Ruiz, J., Munizaga, F., Leveille, R.A., Martin, W., 2002. Age of Mineralization of the Candelaria Fe Oxide Cu-Au Deposit and the Origin of the Chilean Iron Belt, Based on Re-Os Isotopes. Economic Geology 97, 59–71. https://doi.org/10.2113/gsecongeo.97.1.59

Mauger, A.J., Ehrig, K., Kontonikas-Charos, A., Ciobanu, C.L., Cook, N.J., Kamenetsky, V.S., 2016. Alteration at the Olympic Dam IOCG–U deposit: insights into distal to proximal feldspar and phyllosilicate chemistry from infrared reflectance spectroscopy. Australian Journal of Earth Sciences 63, 959–972. https://doi.org/10.1080/08120099.2016.1264474

McBriarty, M.E., Kerisit, S., Bylaska, E.J., Shaw, S., Morris, K., Ilton, E.S., 2018. Iron vacancies accommodate uranyl incorporation into hematite. Environmental Science & Technology 52, 6282–6290. https://doi.org/10.1021/acs.est.8b00297

McPhie, J., Kamenetsky, V.S., Chambefort, I., Ehrig, K., Green, N., 2011. Origin of the supergiant Olympic Dam Cu-U-Au-Ag deposit, South Australia: Was a sedimentary basin involved? Geology 39, 795–798. https://doi.org/10.1130/G31952.1

McPhie, J., Orth, K., Kamenetsky, V., Kamenetsky, M., Ehrig, K., 2016. Characteristics, origin and significance of Mesoproterozoic bedded clastic facies at the Olympic Dam Cu–U–Au–Ag deposit, South Australia. Precambrian Research 276, 85–100. https://doi.org/10.1016/j.precamres.2016.01.029

McPhie, J., Ehrig, K.J., Kamenetsky, M.B., Crowley, J.L., Kamenetsky, V.S., 2020. Geology of the Acropolis prospect, South Australia, constrained by high-precision CA-TIMS ages. Australian Journal of Earth Sciences,67(5), 699–716. https://doi.org/10.1080/08120099.2020.1717617

Meinert, L.D., Dipple, G.M., Nicolescu, S., 2005. World Skarn Deposits. Economic Geology 100, 299–336. https://doi.org/10.1130/0091-7613(1993)021

Michard, A., Michard, G., Stüben, D., Stoffers, P., Cheminée, J., Binard, N., 1993. Submarine thermal springs associated with young volcanos: The Teahitia vents, Society Islands, Pacific Ocean. Geochimica et Cosmochimica Acta 57, 4977-4986. https://doi.org/10.1016/S0016-7037(05)80003-1

Migdisov, A., Williams-Jones, A.E., Brugger, J., Caporuscio, F.A., 2016. Hydrothermal transport, deposition, and fractionation of the REE: Experimental data and thermodynamic calculations. Chemical Geology 439, 13–42. https://doi.org/10.1016/j.chemgeo.2016.06.005

Moore, P.B., 1968. Substitutions of the type $(Sb_{0.5}^{5+}Fe_{0.5}^{3+} \rightleftarrows Ti^{4+})$: the crystal structure of melanostibite. American Mineralogist 53, 1104–1109.

Morales Ruano, S., Both, R.A., Golding, S.D., 2002. A fluid inclusion and stable isotope study of the Moonta copper–gold deposits, South Australia: evidence for fluid immiscibility in a magmatic

hydrothermal system. Chemical Geology 192, 211–226. https://doi.org/10.1016/S0009-2541(02)00197-3

Moya, M.C., Scasso, R.A., Castro, L.N., Fazio, A.M., 2012. Los fosfatos en el Ordovícico del Norte Argentino, in: Marquillas, R.A., Sánchez, M.C., Salfity, J.A. (Eds.), Aportes Sedimentológicos a La Geología Del Noroeste Argentino. XIII Reunión Argentina de Sedimentología. Salta, 145–167.

Muan, A., Hauck, J., Löfall, T., 1972. Equilibrium studies with a bearing on lunar rocks. Third Lunar Science Conference, Vol. 3, pp. 185–196.

Najorka, J., Gottschalk, M., 2003. Crystal chemistry of tremolite–tschermakite solid solutions. Physics and Chemistry of Minerals 30, 108–124. https://doi.org/10.1007/s00269-002-0291-1

Netting, A.K.O, Wade, B.P., Verdugo-Ihl, M.R., Courtney-Davies, L., Ciobanu, C.L., Cook, N.J., Ehrig, K., Slattery, A., Gilbert, S., Neubauer, K., 2019. A Multiplatform approach to unravelling geological problems: a case study from Olympic Dam, South Australia, 2019. 16th European Workshop on Modern Developments and Applications in Microbeam Analysis (EMAS 2019), Norwegian University of Technology and Science, Trondheim, Norway, 19th-23rd May. Microscopy and Microanalysis 25 (Suppl. 2), 2432–2433, https://doi.org/10.1017/S1431927619012893

Nickel, E.H., 1973. The new mineral cuprospinel ($CuFe_2O_4$) and other spinels from an oxidized ore dump at Baie Verte, Newfoundland. Canadian Mineralogist 11, 1003–1007.

Nyström, J.O., Henríquez, F., 1994. Magmatic features of iron ores of the Kiruna type in Chile and Sweden: ore textures and magnetite geochemistry. Economic Geology 89, 820–839. https://doi.org/10.2113/gsecongeo.89.4.820

Oberti, R., Boiocchi, M., Hawthorne, F.C., Ciriotti, M.E., 2018. Ferro-tschermakite from the Ploumanac'h granitic complex, Brittany, France: mineral description. European Journal of Mineralogy 30, 171–176. https://doi.org/10.1127/ejm/2018/0030-2700

Ohkawa, M., Miyahara, M., Ohta, E., Hoshino, K., 2007. Silicon-substituted magnetite and accompanying iron oxides and hydroxides from the Kumano mine, Yamaguchi Prefecture, Japan: Reexamination of the so-called maghemite (γ-Fe_2O_3). Journal of Mineralogical and Petrological Sciences 102, 182–193. https://doi.org/10.2465/jmps.050706

Oreskes, N., 1990. Uranium content of Olympic Dam hematite: Implications for fluid chemistry and ore depositional mechanisms. Program with Abstracts, 8th Quadrennial IAGOD Conference, Ottawa, Canada, p. A137.

Oreskes, N., Einaudi, M.T., 1990. Origin of rare earth element-enriched hematite breccias at the Olympic Dam Cu-U-Au-Ag deposit, Roxby Downs, South Australia. Economic Geology 85, 1–28. https://doi.org/10.2113/gsecongeo.85.1.1

Oreskes, N., Einaudi, M.T., 1992. Origin of hydrothermal fluids at Olympic Dam: preliminary results from fluid inclusions and stable isotopes. Economic Geology 87, 64–90. https://doi.org/10.2113/gsecongeo.87.1.64

Otake, T., Wesolowski, D.J., Anovitz, L.M., Allard, L.F., Ohmoto, H., 2007. Experimental evidence for non-redox transformations between magnetite and hematite under H_2-rich hydrothermal conditions. Earth and Planetary Science Letters 257, 60–70. https://doi.org/10.1016/j.epsl.2007.02.022

Otake, T., Wesolowski, D.J., Anovitz, L.M., Allard, L.F., Ohmoto, H., 2010. Mechanisms of iron oxide transformations in hydrothermal systems. Geochimica et Cosmochimica Acta 74, 6141–6156. https://doi.org/10.1016/j.gca.2010.07.024

Ovalle, J.T., La Cruz, N.L., Reich, M., Barra, F., Simon, A.C., Konecke, B.A., Rodriguez-Mustafa, M.A., Deditius, A.P., Childress, T.M., Morata, D., 2018. Formation of massive iron deposits linked to explosive volcanic eruptions. Scientific Reports 8, 14855. https://doi.org/10.1038/s41598-018-33206-3

Owen, N.D., Ciobanu, C.L., Cook, N.J., Slattery, A., Basak, A., 2018. Nanoscale Study of Clausthalite-Bearing Symplectites in Cu-Au-(U) Ores: Implications for Ore Genesis. Minerals 8, 28. https://doi.org/10.3390/min8020067

Padayachee, D., Mahomed, A.S., Singh, S., Friedrich, H.B., 2020. The effect of the TiO_2 anatase:rutile ratio and interface for the oxidative activation of n-octane. ACS Catalysis 10, 2211-2220. https://doi.org/10.1021/acscatal.9b04004

Palenik, C.S., Utsunomiya, S., Reich, M., Kesler, S.E., Wang, L., Ewing, R.C., 2004. "Invisible" gold revealed: Direct imaging of gold nanoparticles in a Carlin-type deposit. American Mineralogist 89, 1359–1366. https://doi.org/10.2138/am-2004-1002

Park, C.F., 1961. A magnetite "flow" in northern Chile. Economic Geology 56, 431–436. https://doi.org/10.2113/gsecongeo.56.2.431

Paton, C., Hellstrom, J., Paul, B., Woodhead, J., Hergt, J., 2011. Iolite: Freeware for the visualisation and processing of mass spectrometric data. Journal of Analytical Atomic Spectrometry 26, 2508–2518. https://doi.org/10.1039/c1ja10172b

Pollard, P.J., 2001. Sodic(-calcic) alteration in Fe-oxide-Cu-Au districts: an origin via unmixing of magmatic H_2O-CO_2-NaCl ± $CaCl_2$-KCl fluids. Mineralium Deposita 36, 93–100. https://doi.org/10.1007/s001260050289

Putnis, A., 1992. Introduction to Mineral Sciences. Cambridge University Press, Cambridge, U.K., 457 pp.

Putnis, A., 2002. Mineral replacement reactions: from macroscopic observations to microscopic mechanisms. Mineralogical Magazine 66, 689–708. https://doi.org/10.1180/0026461026650056

Putnis, A., 2009. Mineral Replacement Reactions. Reviews in Mineralogy and Geochemistry 70, 87–124. https://doi.org/10.2138/rmg.2009.70.3

Putnis, A., 2015. Transient Porosity Resulting from Fluid–Mineral Interaction and its Consequences. Reviews in Mineralogy and Geochemistry 80, 1–23. https://doi.org/10.2138/rmg.2015.80.01

Putnis, A., Fernandez-Diaz, L., Prieto, M., 1992. Experimentally produced oscillatory zoning in the $(Ba,Sr)SO_4$ solid solution. Nature 358, 743–745. https://doi.org/doi:10.1038/358743a0

Putnis, C.V., Tsukamoto, K., Nishimura, Y., 2005. Direct observations of pseudomorphism: compositional and textural evolution at a fluid-solid interface. American Mineralogist 90, 1909–1912. https://doi.org/10.2138/am.2005.1990

Ranson, W.A., 1986. Complex exsolution in inverted pigeonite: Exsolution mechanisms and temperatures of crystallization and exsolution. American Mineralogist 71, 1322–1336.

Reeve, J.S., Cross, K.C., Smith, R.N., Oreskes, N., 1990. Olympic Dam Copper-Uranium-gold-silver Deposit. In F.E. Hughes (Ed.), Geology of the Mineral Deposits of Australia and Papua New Guinea, Australasian Institute of Mining and Metallurgy, pp. 1009–1035.

Reich, M., Kesler, S.E., Utsunomiya, S., Palenik, C.S., Chryssoulis, S.L., Ewing, R.C., 2005. Solubility of gold in arsenian pyrite. Geochimica et Cosmochimica Acta 69, 2781–2796. https://doi.org/10.1016/j.gca.2005.01.011

Reich, M., Hough, R.M., Deditius, A., Utsunomiya, S., Ciobanu, C.L., Cook, N.J. 2011. Nanogeoscience in ore systems research: Principles, methods, and applications. Ore Geology Reviews 42, 1–5. https://doi.org/10.1016/j.oregeorev.2011.06.007

Reid, A., 2019. The Olympic Cu-Au Province, Gawler Craton: A Review of the Lithospheric Architecture, Geodynamic Setting, Alteration Systems, Cover Successions and Prospectivity. Minerals 9, 371. https://doi.org/10.3390/min9060371

Richards, J.P., Mumin, A.H., 2013. Magmatic-hydrothermal processes within an evolving Earth: Iron oxide-copper-gold and porphyry Cu±Mo±Au deposits. Geology 41, 767–770. https://doi.org/10.1130/G34275.1

Rieger, A.A., Marschik, R., Diaz, M., Holzl, S., Chiaradia, M., Akker, B., Spangenberg, J.E., 2010. The Hypogene Iron Oxide Copper-Gold Mineralization in the Mantoverde District, Northern Chile. Economic Geology 105, 1271–1299. https://doi.org/10.2113/econgeo.105.7.1271

Righter, K., Keller, L.P., Rahman, Z., Christoffersen, R., 2014. Redox-driven exsolution of iron-titanium oxides in magnetite in Miller Range (MIL) 03346 nakhlite: Evidence for post

crystallization oxidation in the nakhlite cumulate pile? American Mineralogist 99, 2313–2319. https://doi.org/10.2138/am-2014-4926

Roberts, D.E., Hudson, G.R.T., 1983. The Olympic Dam copper-uranium-gold deposit, Roxby Downs, South Australia. Economic Geology 78, 799–822. https://doi.org/10.2113/gsecongeo.78.5.799

Robinson, P., Jaffe, H.W., Ross, M., Klein, C.J., 1971. Orientation of exsolution lamellae in clinopyroxene and clinoamphiboles: Consideration of optical phase boundaries. American Mineralogist 56, 909–939.

Robinson, P., Ross, M., Nord, G.L., Smyth, J.R., Jaffe, H.W., 1977. Exsolution lamellae in augite and pigeonite; fossil indicators of lattice parameters at high temperature and pressure. American Mineralogist 62, 857–873.

Roedder, E., 1984. Fluid inclusions. Reviews in Mineralogy, 12, 646 pp.

Rollog M., Cook N.J., Guagliardo P., Ehrig K., Kilburn M., 2019. In situ spatial distribution mapping of radionuclides in minerals by nanoSIMS. Geochemistry: Exploration, Environment, Analysis 19(3), 245–254. https://doi.org/10.1144/geochem2018-038

Rollog, M., Cook, N.J., Guagliardo, P., Ehrig, K., Ciobanu, C.L., Kilburn, M., 2019. Detection of Trace Elements/Isotopes in Olympic Dam Copper Concentrates by nanoSIMS. Minerals 9, 336. https://doi.org/10.3390/min9060336

Rollog, M., Cook, N.J., Guagliardo, P., Ehrig. K.J., Kilburn, M., 2019. Radionuclide-bearing minerals in Olympic Dam copper concentrates. Hydrometallurgy 189, 105153. https://doi.org/10.1016/j.hydromet.2019.105153

Rollog, M., Cook, N.J., Guagliardo, P., Ehrig, K., Kilburn, M., 2020. Radionuclide distributions in Olympic Dam copper concentrates: The significance of minor hosts, incorporation mechanisms, and the role of mineral surfaces. Minerals Engineering 148, 106176. https://doi.org/10.1016/j.mineng.2019.106176

Rosiere, C.A., Rios, F.J., 2004. The origin of hematite in high-grade iron ores based on infrared microscopy and fluid inclusion studies: The example of the Conceição Mine, Quadrilátero Ferrífero, Brazil. Economic Geology 99, 611–624. https://doi.org/10.2113/gsecongeo.99.3.611

Sejkora, J., Števko, M., Ozdín, D., Pršek, J., Jeleň, S., 2015. Unusual morphological forms of hodrušite from the Rozália vein, Hodruša-Hámre near Banská Štiavnica (Slovak Republic). Journal of Geosciences 60, 11–22. https://doi.org/10.3190/jgeosci.188

Seydoux-Guillaume A.-M., Goncalves P., Wirth R., Deutsch A., 2003. Transmission electron microscope study of polyphase and discordant monazites: Site-specific specimen preparation using the focused ion beam technique. Geology 31, 973–976. https://doi.org/10.1130/G19582.1

Seydoux-Guillaume, A.-M., Fougerouse, D., Laurent, A.T., Gardés, E., Reddy, S.M., Saxey, D.W., 2019. Nanoscale resetting of the Th/Pb system in an isotopically-closed monazite grain: A combined atom probe and transmission electron microscopy study. Geosciences Frontiers, 10, 65–76 https://doi.org/10.1016/j.gsf.2018.09.004

Sibson, R.H., Robert, F., Poulsen, K.H., 1988. High-angle reverse faults, fluid-pressure cycling, and mesothermal gold-quartz deposits. Geology 16, 551–555. https://doi.org/10.1130/0091-7613(1988)016<0551:HARFFP>2.3.CO;2

Sillitoe, R.H., Burrows, D.R., 2002. New field evidence on the origin of the El Laco magnetite deposit, Northern Chile. Economic Geology 97, 1101–1109. https://doi.org/10.2113/gsecongeo.97.5.1101

Sillitoe, R.H., Magaranov, G., Mladenov, V., Creaser, R.A., 2020. Rosen, Bulgaria: A newly recognized iron oxide-copper-gold district. Economic Geology 104, 897–904. https://doi.org/10.5382/econgeo.4731

Skirrow, R.G., Bastrakov, E.N., Barovich, K., Fraser, G.L., Creaser, R.A., Fanning, C.M., Raymond, O.L., Davidson, G.J., 2007. Timing of Iron Oxide Cu-Au-(U) Hydrothermal Activity and Nd Isotope Constraints on Metal Sources in the Gawler Craton, South Australia. Economic Geology 102, 1441–1470. https://doi.org/10.2113/gsecongeo.102.8.1441

Šrot, V., Rečnik, A., Scheu, C., Šturm, S., Mirtič, B., 2003. Stacking faults and twin boundaries in sphalerite crystals from the Trepča mines in Kosovo. American Mineralogist 88, 1809–1816. https://doi.org/10.2138/am-2003-11-1222

Stormer, J.C., 1983. The effects of recalculation on estimates of temperature and oxygen fugacity from analyses of multicomponent iron-titanium oxides. American Mineralogist 68, 586–594.

Subramanian, P.R., Laughlin, D.E., 1988. The As−Cu (arsenic-copper) system. Bulletin of Alloy Phase Diagrams 9, 605–618. https://doi.org/10.1007/BF02881964

Tarassov, M., Mihailova, B., Tarasova, E., Konstantinov, L., 2002. Chemical composition and vibrational spectra of tungsten-bearing goethite and hematite from Western Rhodopes, Bulgaria. European Journal of Mineralogy 14, 977-986. https://doi.org/10.1127/0935-1221/2002/0014-097

Timofeev, A., Migdisov, A.A., Williams-Jones, A.E., 2015. An experimental study of the solubility and speciation of niobium in fluoride-bearing aqueous solutions at elevated temperature. Geochimica et Cosmochimica Acta 158, 103–111. https://doi.org/10.1016/j.gca.2015.02.015

Tkachev, A.V., 2011. Evolution of metallogeny of granitic pegmatites associated with orogens throughout geological time. Geological Society of London, Special Publication 350, 7–23. https://doi.org/10.1144/SP350.2

Tooth, B., Ciobanu, C.L., Green, L., O'Neill, B., Brugger, J., 2011. Bi-melt formation and gold scavenging from hydrothermal fluids: An experimental study. Geochimica et Cosmochimica Acta 75, 5423–5443. https://doi.org/10.1016/j.gca.2011.07.020

Tornos, F., Velasco, F., Barra, F., Morata, D., 2010. The Tropezón Cu–Mo–(Au) deposit, Northern Chile: the missing link between IOCG and porphyry copper systems? Mineralium Deposita 45, 313–321. https://doi.org/10.1007/s00126-010-0277-8

Tornos, F., Velasco, F., Hanchar, J.M. 2016. Iron-rich melts, magmatic magnetite, and superheated hydrothermal systems: The El Laco deposit, Chile. Geology 44, 427–430. https://doi.org/10.1130/G37705.1

Tornos, F., Velasco, F., Hanchar, J.M., 2017. The Magmatic to Magmatic-Hydrothermal Evolution of the El Laco Deposit (Chile) and Its Implications for the Genesis of Magnetite-Apatite Deposits. Economic Geology 112, 1595–1628. https://doi.org/10.5382/econgeo.2017.4523

Valley, J.W., Cavosie, A.J., Ushikubo, T., Reinhard, D.A., Lawrence, D.F., Larson, D.J., Clifton, P.H., Kelly, T.F., Wilde, S.A., Moser, D.E., Spicuzza, M.J., 2014. Hadean age for a post-magma-ocean zircon confirmed by atom-probe tomography. Nature Geosciences 7, 219–223. https://doi.org/10.1038/ngeo2075

van Achterbergh, E., Ryan, C.G., Jackson, S.E., Griffin, W.L., 2001. Data reduction software for LA-ICP-MS. In P.J. Sylvester (Ed.), Laser-ablation-ICPMS in the Earth Sciences; Principles and Applications. Mineralogical Association of Canada, Short Course Series 29, pp. 239–243.

Van Landuyt, J., Amelinckx, S., 1970. Shear structures in titanium oxide. Materials Research Bulletin 5(4), 267–274. https://doi.org/10.1016/0025-5408(70)90123-6

Van Tendeloo, G., Bals, S., Van Aert, S., Verbeeck, J., Van Dyck, D., 2012. Advanced Electron Microscopy for Advanced Materials. Advanced Materials 24, 5655–5675. https://doi.org/10.1002/adma.201202107

Veblen, D.R., Burnham, C.W., 1978. New biopyriboles from Chester, Vermont: II. The crystal chemistry of jimthompsonite, clinojimthompsonite, and chesterite, and the amphibole-mica reaction. American Mineralogist 63, 1053–1073.

Veblen, D.R., Buseck, E.R., 1979. Chain-width order and disorder in biopyriboles. American Mineralogist 64, 687–700.

Velasco, F., Tornos, F., Hanchar, J.M., 2016. Immiscible iron- and silica-rich melts and magnetite geochemistry at the El Laco volcano (northern Chile): Evidence for a magmatic origin for the magnetite deposits. Ore Geology Reviews 79, 346–366. https://doi.org/10.1016/j.oregeorev.2016.06.007

Verdugo-Ihl, M.R., Ciobanu, C.L., Cook, N.J., Ehrig, K.J., Courtney-Davies, L., Gilbert, S., 2017. Textures and U-W-Sn-Mo signatures in hematite from the Olympic Dam Cu-U-Au-Ag deposit, South Australia: Defining the archetype for IOCG deposits. Ore Geology Reviews 91, 173–195. https://doi.org/10.1016/j.oregeorev.2017.10.007

Verdugo-Ihl, M.R., Ciobanu, C.L., Cook., N.J., Courtney-Davies, L., Ehrig, K.J., Gilbert, S., 2017. Trace element signatures in U-W-Sn-Mo zoned hematite from the IOCG deposit at Olympic Dam, South Australia, Extended abstract, 14th SGA Biennial Meeting 2017, Mineral Resources to Discover, Québec, Canada, Vol. 3, pp. 967–970.

Verdugo-Ihl, M.R., Ciobanu, C.L., Cook, N.J., Slattery, A., Ehrig, K. 2018. Copper Nanoparticles along fluid inclusion trails in hematite. Goldschmidt Conference 2018, Boston, U.S.A., August 12th-17th.

Verdugo-Ihl, M.R., Ciobanu, C.L., Cook, N.J., Slattery, A., Ehrig, K., Courtney-Davies, L., 2018. Metal-bearing nanoparticles in hematite. Proceedings of the 15th Quadrennial IAGOD Symposium, August 28th-31st, Salta, Argentina, pp. 189–190.

Verdugo-Ihl, M.R., Ciobanu, C.L., Slattery, A., Cook, N.J., Ehrig, K., Courtney-Davies, L., 2019. Copper-Arsenic Nanoparticles in Hematite: Fingerprinting Fluid-Mineral Interaction. Minerals 9, 388. https://doi.org/10.3390/min9070388

Verdugo-Ihl, M.R., Ciobanu, C.L. Cook, N.J., Courtney-Davies, L., Ehrig, K., Slattery, A., 2019. Tungsten-bearing nanoparticles in hematite: insights into open system behaviour of mineral geochronometers. TIGeR Conference 2019, Curtin University, Perth, W.A., Australia, September 11th-13th, pp. 66–67.

Verdugo-Ihl, M.R., Ciobanu, C.L., Cook, N.J., Ehrig, K.J., Courtney-Davies, L., 2020. Defining early stages of IOCG systems: evidence from iron oxides in the outer shell of the Olympic Dam deposit, South Australia. Mineralium Deposita 55, 429–452. https://doi.org/10.1007/s00126-019-00896-2

Verdugo-Ihl, M.R., Ciobanu, C.L., Cook, N.J., Ehrig, K., Slattery, A., Courtney-Davies, L., 2020b. Trace element remobilisation from W-Sn-U-Pb zoned hematite: Nanoscale insights into open system behaviour of a mineral geochronometer. Mineralogical Magazine 84(4), 502–516. https://doi.org/10.1180/mgm.2020.49

Verdugo-Ihl, M.R., Ciobanu, C.L., Cook, N.J., Ehrig, K., Slattery, A., Courtney-Davies, L., Dmitrijeva, M. Nanomineralogy of hydrothermal magnetite from Acropolis, South Australia: Genetic implications for iron-oxide copper gold mineralization. American Mineralogist, in press. https://doi.org/10.2138/am-2020-7557

Verdugo-Ihl, M.R., Ciobanu, C.L., Cook, N.J., Ehrig, K., Slattery, A., Courtney-Davies, L., in review. Ferro-tschermakite with short range disorder identified in silician magnetite. American Mineralogist.

Verdugo-Ihl, M.R., Ciobanu, C.L., Cook, N.J., Tornos, F., Ehrig. K., Slattery, A., Xu, J., Courtney-Davies, L., Hanchar, J.M., in revision. Vapour transport of magnetite in volcanoes: evidence from igneous pyroxene pair inclusions and S-bearing sublimate coatings. Earth and Planetary Science Letters.

Verdugo-Ihl, M.R., Courtney-Davies, L., Ciobanu, C.L., Cook, N.J., Ehrig, K., Tornos, F., Hanchar, J.M., in review. Hematite U-Pb age constraints on the timing of IOCG mineralization along the Atacama Fault Zone, Chile. Abstract, SEG 2020 Vision, Celebrating a Century of Discovery, September 15-18. Whistler, B.C., Canada.

Vila, T., Lindsay, N., Zamora, R., 1998. Geology of the Manto Verde copper deposit, Northern Chile: A specularite-rich, hydrothermal-tectonic breccia related to the Atacama Fault Zone, in: Camus, F., Sillitoe, R.H., Petersen, R. (Eds.), Andean Copper Deposits: New Discoveries, Mineralization, Styles and Metallogeny. Society of Economic Geologists, Special Publication 5, pp. 157–169. https://doi.org/10.5382/SP.05.11

Viti, C., Frezzotti, M.-L., 2001. Transmission electron microscopy applied to fluid inclusion investigations. Lithos 55, 125–138. https://doi.org/10.1016/S0024-4937(00)00042-6

Wang, X., Wei, W., Lv, X., Fan, X., Wang, S., 2017. Stanniferous magnetite composition from the Haobugao skarn Fe-Zn deposit, southern Great Xing'an Range: Implication for mineral depositional mechanism. Geological Journal 53(5), 1–17. https://doi.org/10.1002/gj.3009

Wang, X.-S., Timofeev, A., Williams-Jones, A.E., Shang, L.-B., Bi, X.-W., 2019. An experimental study of the solubility and speciation of tungsten in NaCl-bearing aqueous solutions at 250, 300, and 350 °C. Geochimica et Cosmochimica Acta 265, 313–329. https://doi.org/10.1016/j.gca.2019.09.013

Weinberg, R.F., Wolfram, L.C., Nebel, O., Hasalová, P., Závada, P., Kylander-Clark, A.R.C., Becchio, R., 2020. Decoupled U-Pb date and chemical zonation of monazite in migmatites: The case for disturbance of isotopic systematics by coupled dissolution-reprecipitation. Geochimica et Cosmochimica Acta 269, 398–412. https://doi.org/10.1016/j.gca.2019.10.024

Wernicke, R.S., Lippolt, H.J., 1993. Botryoidal hematite from the Schwarzwald (Germany): heterogeneous uranium distributions and their bearing on the helium dating method. Earth and Planetary Science Letters 114, 287-300. https://doi.org/10.1016/0012-821X(93)90031-4

Whitehouse, M.J., Kusiak, M.A., Wirth, R., Ravindra Kumar, G.R., 2017. Metallic Pb nanospheres in ultra-high temperature metamorphosed zircon from southern India. Mineralogy and Petrology, 111, 467–474. https://doi.org/10.1007/s00710-017-0523-1

Williams, P.J., 2010. Classifying IOCG deposits, in: Corriveau, L., Mumin, H. (Eds.), Exploring for Iron Oxide Copper-Gold Deposits: Canada and Global Analogues, Geological Association of Canada, Short Course Notes, pp. 23–38.

Wirth, R., Reid, D., Schreiber, A., 2013. Nanometer-sized platinum-group minerals (PGM) in base metal sulfides: New evidence for an orthomagmatic origin of the Merensky Reef PGE ore deposit, Bushveld Complex, South Africa. Canadian Mineralogist 51, 143–155. https://doi.org/10.3749/canmin.51.1.143

Woodhead, J.D., Hellstrom, J., Hergt, J.M., Greig, A., Maas, R., 2007. Isotopic and Elemental Imaging of Geological Materials by Laser Ablation Inductively Coupled Plasma-Mass Spectrometry. Geostandards and Geoanalytical Research 31, 331–343. https://doi.org/10.1111/j.1751-908X.2007.00104.x

Xia, F., Brugger, J., Chen, G., Ngothai, Y., O'Neill, B., Putnis, A., Pring, A., 2009. Mechanism and kinetics of pseudomorphic mineral replacement reactions: A case study of the replacement of pentlandite by violarite. Geochimica et Cosmochimica Acta 73, 1945–1969. https://doi.org/10.1016/j.gca.2009.01.007

Xu, H., Shen, Z., Konishi, H., 2014. Si-magnetite nano-precipitates in silician magnetite from banded iron formation: Z-contrast imaging and ab initio study. American Mineralogist 99, 2196–2202. https://doi.org/10.2138/am-2014-4964

Xu, J., Ciobanu, C.L., Cook, N.J., Zheng, Y., Sun, X., Wade, B.P., 2016. Skarn formation and trace elements in garnet and associated minerals from Zhibula copper deposit, Gangdese Belt, southern Tibet. Lithos 262, 213–231. https://doi.org/10.1016/j.lithos.2016.07.010

Xu, J., Ciobanu, C.L., Cook, N.J., Slattery, A., 2019. Crystals from the scheelite-powellite solid-solution series at the nanoscale: the Zhibula Cu skarn, Gangdese Belt, Tibet. Minerals 9(6), 340. https://doi.org/10.3390/min9060340

Xu, J., Ciobanu, C.L., Cook, N.J., Zheng, Y., Li, X., Wade, B.P., Verdugo-Ihl, M.R., Gao, W., Zhu, Q., 2020. Numerical modelling of rare earth element fractionation trends in garnet: a tool to monitor skarn evolution. Contributions to Mineral and Petrology 175, 30. https://doi.org/10.1007/s00410-020-1670-7

Yamamoto, S., Komiya, T., Hirose, K., Maruyama, S., 2009. Coesite and clinopyroxene exsolution lamellae in chromites: In-situ ultrahigh-pressure evidence from podiform chromitites in the Luobusa ophiolite, southern Tibet. Lithos 109, 314–322. https://doi.org/10.1016/j.lithos.2008.05.003

Yin, S., Wirth, R., Ma, C.Q., Xu, J.N., 2019. The role of mineral nanoparticles at a fluid-magnetite interface: Implications for trace-element uptake in hydrothermal systems. American Mineralogist 104, 1180–1188. https://doi.org/10.2138/am-2019-6996

Zhou, M.-F., Robinson, P.T., Lesher, C.M., Keays, R.R., Zhang, C.-J., Malpas, J., 2005. Geochemistry, petrogenesis and metallogenesis of the Panzhihua gabbroic layered intrusion and associated Fe–Ti–V oxide deposits, Sichuan Province, SW China. Journal of Petrology 46, 2253–2280. https://doi.org/10.1093/petrology/egi054

Zimmer, K., Zhang, Y., Lu, P., Chen, Y., Zhang, G., Dalkillic, M., Zhu, C., 2016. SUPCRTBL: A revised and extended thermodynamic dataset and software package of SUPCRT92. Computers & Geosciences 90, 97–111. https://doi.org/10.1016/j.cageo.2016.02.013